*ADVANCES IN*

# ATOMIC, MOLECULAR, AND OPTICAL PHYSICS

*Edited by*

Benjamin Bederson
DEPARTMENT OF PHYSICS
NEW YORK UNIVERSITY
NEW YORK, NEW YORK

Herbert Walther
UNIVERSITY OF MUNICH AND
MAX-PLANCK-INSTITUT FÜR QUANTENOPTIK
MUNICH, GERMANY

Volume 49

2003

**ELSEVIER**
ACADEMIC
PRESS

Amsterdam · Boston · Heidelberg · London · New York · Oxford
Paris · San Diego · San Francisco · Singapore · Sydney · Tokyo

*Advances in*

*ATOMIC, MOLECULAR, AND OPTICAL PHYSICS*

*VOLUME 49*

## Editors

## Supplements

1. *Atoms in Intense Laser Fields*, Mihai Gavrila, Ed.
2. *Cavity Quantum Electrodynamics*, Paul R. Berman, Ed.
3. *Cross Section Data*, Mitio Inokuti, Ed.

# *Contents*

**Applications of Optical Cavities in Modern Atomic, Molecular, and Optical Physics**

*Jun Ye and Theresa W. Lynn*

**Resonance and Threshold Phenomena in Low-Energy Electron Collisions with Molecules and Clusters**

*H. Hotop, M.-W. Ruf, M. Allan and I. I. Fabrikant*

**Coherence Analysis and Tensor Polarization Parameters of $(\gamma, e\gamma)$ Photoionization Processes in Atomic Coincidence Measurements**

*B. Lohmann, B. Zimmermann, H. Kleinpoppen and U. Becker*

**Quantum Measurements and New Concepts for Experiments with Trapped Ions**

*Ch. Wunderlich and Ch. Balzer*

**Scattering and Reaction Processes in Powerful Laser Fields**

*Dejan B. Milošević and Fritz Ehlotzky*

**Hot Atoms in the Terrestrial Atmosphere**

*Vijay Kumar and E. Krishnakumar*

This page
intentionally
left blank

# Contributors

Numbers in parentheses indicate the pages on which the author's contributions begin.

JUN YE (1), JILA, National Institute of Standards and Technology and University of Colorado, Boulder, Colorado 80309-0440

THERESA W. LYNN (1), Norman Bridge Laboratory of Physics, Room 12-33, California Institute of Technology, Pasadena, California 91125

H. HOTOP (85), Fachbereich Physik, Universität Kaiserslautern, 67653 Kaiserslautern, Germany

M.-W. RUF (85), Fachbereich Physik, Universität Kaiserslautern, 67653 Kaiserslautern, Germany

M. ALLAN (85), Département de Chimie, Université de Fribourg, 1700 Fribourg, Switzerland

I. I. FABRIKANT (85), Department of Physics and Astronomy, University of Nebraska, Lincoln, NE, USA

B. LOHMANN (217), Fritz-Haber-Institut der Max-Planck Gesellschaft, Faradayweg 4 – 6, D-14195 Berlin/Dahlem, Germany

B. ZIMMERMANN (217), Fritz-Haber-Institut der Max-Planck Gesellschaft, Faradayweg 4 – 6, D-14195 Berlin/Dahlem, Germany

H. KLEINPOPPEN (217), Fritz-Haber-Institut der Max-Planck Gesellschaft, Faradayweg 4 – 6, D-14195 Berlin/Dahlem, Germany

U. BECKER (217), Fritz-Haber-Institut der Max-Planck Gesellschaft, Faradayweg 4 – 6, D-14195 Berlin/Dahlem, Germany

Ch. WUNDERLICH (293), Institut für Laser-Physik, Universität Hamburg, Jungiusstr. 9, 20355 Hamburg, Germany

Ch. BALZER (293), Institut für Laser-Physik, Universität Hamburg, Jungiusstr. 9, 20355 Hamburg, Germany

DEJAN B. MILOŠEVIĆ (373), Faculty of Science, University of Sarajevo, Zmaja od Bosne 35, 71000 Sarajevo, Bosnia and Herzegovina

Fritz Ehlotzky (373), Institute for Theoretical Physics, University of Innsbruck, Technikerstrasse 25, A-6020 Innsbruck, Austria

Vijay Kumar (533), Tata Institute of Fundamental Research, Homi Bhabha Road, Colaba, Mumbai-400 005, India

E. Krishnakumar (533), Tata Institute of Fundamental Research, Homi Bhabha Road, Colaba, Mumbai-400 005, India

# *APPLICATIONS OF OPTICAL CAVITIES IN MODERN ATOMIC, MOLECULAR, AND OPTICAL PHYSICS*

*JUN YE*[1,*] *and THERESA W. LYNN*[2]

[1]*JILA, National Institute of Standards and Technology and University of Colorado, Boulder, Colorado 80309-0440*
[2]*Norman Bridge Laboratory of Physics, Room 12-33, California Institute of Technology, Pasadena, California 91125*

*E-mail: ye@jila.colorado.edu

1

# I. Introduction

For many contemporary physics experiments, the use of an optical cavity has become a powerful tool for enhancement in detection sensitivities, nonlinear interactions, and quantum dynamics. Indeed, an optical cavity allows one to extend the interaction length between matter and field, to build up the optical power, to impose a well-defined mode structure on the electromagnetic field, to enable extreme nonlinear optics, and to study manifestly quantum mechanical behavior associated with the modified

vacuum structure and/or the large field associated with a single photon confined to a small volume. Experimental activities that have benefited from the use of optical cavities appear in such diverse areas as ultra-sensitive detection for classical laser spectroscopy, nonlinear optical devices, optical frequency metrology and precision measurement, and cavity quantum electrodynamics (cavity QED). Of course the most important application of optical cavities is in laser physics itself. However, in this article we will concentrate on the various applications of external optical cavities (independent from lasers) that take advantage of the common physical properties associated with resonator physics.

One of the important themes in laser spectroscopy is to utilize an extended interaction length between matter and field inside a high finesse cavity for an increased detection sensitivity. Two key ingredients are needed to achieve the highest sensitivity possible in detection of atomic and molecular absorptions: enhancement of the absorption signal and elimination of technical noise. While the absorption signal is enhanced by an optical cavity, it is important also to take measures to avoid technical noise; the sharp resonances of the cavity can introduce additional noise through frequency-to-amplitude noise conversion. Cavity vibration and drifts can also contribute noise beyond the fundamental, quantum-noise limit. In this article (Sections IV and V), we will discuss the application of various modulation techniques combined with suitable experimental configurations that let one benefit from the signal enhancement aspect of a cavity, at the same time suppressing the technical noise in the detection process. Such achievement has enabled studies of molecular vibration dynamics of weak transitions.

Another important theme is the application of optical frequency metrology for precision measurements. Section VI addresses the role of optical cavities in this context. Certainly the use of an optical cavity for laser frequency stabilization is critical for the development of super-stable optical local oscillators. The extreme quality factor ($10^{15}$) associated with some "forbidden" optical transitions in cold and trapped samples of atoms and ions demands a similar or even higher quality factor on the optical probe source to take full advantage of the system coherence. Although the advent of femtosecond-laser-based optical frequency combs has to a certain degree reduced the utility of cavity-based frequency reference systems, stable optical cavities continue to provide important services in laser laboratories; either the cavity modes themselves provide optical frequency markers or a cavity helps enhance optical to microwave frequency coupling via an intracavity modulator. And one of the most important applications of optical cavities is still for laser frequency stabilization, with the scope now extended to cover ultrafast lasers as well. In fact, cavity-based ultra-sensitive detection of atomic/molecular absorptions represents an important approach to produce

accurate and precise frequency references throughout the visible and near-infrared wavelength regions. We also note that some of the most demanding work in precision measurement is now associated with cavity-enhanced Michelson interferemetry to search for gravitational waves or violation of relativity laws.

A third theme that will be covered in this article (Section VII) is the exploration of quantum dynamics associated with the enhanced interaction between atoms and cavity field; where the structure of the cavity enables a large field amplitude associated with single intracavity photons, the system dynamics can become manifestly quantum and nonlinear. A high cavity finesse suppresses the dissipation rate associated with photon decay while a well-defined spatial mode of the cavity output field (associated with cavity decay) permits recovery of information about the intracavity dynamics with high quantum efficiency. Although cavities in the optical domain have not significantly influenced the atomic radiative properties in a direct manner, the enhanced coherent interactions between them present an ideal platform to study open quantum systems.

Before addressing these topics in detail, we begin with some broad comments and historical context in the remainder of this introduction. Section II is devoted to description and characterization of the optical cavities themselves, while Section III gives some simple physical arguments for the cavity enhancement effect that is crucial for applications ranging from classical spectroscopy to cavity QED.

## A. Signal Enhancement and Optical Field Buildup Inside a Cavity

Improving sensitivity for spectroscopy on an atomic or molecular sample by placing it inside an optical resonator is a well-known technique and is most commonly explained in terms of the multipass effect. In fact, it was realized in the early days of laser development that a laser cavity was useful for absorption enhancement [1], owing to the multipass effect and the delicate balance between the laser gain and intracavity absorption [2,3]. However, in most recent implementations, it is often preferable to separate the absorber from the laser, in order to extend the experimental flexibility and to characterize better working parameters. Kastler first suggested that a Fabry-Perot cavity be employed for the sensitivity of its transmission to small variations in absorption within the cavity [4]. The external cavity approach has since been applied to record both linear and high-resolution nonlinear molecular spectra [5–7]. In particular, enhancement cavities in the form of cavity ring down spectroscopy [8,9] have been extensively applied in the field of physical chemistry to study molecular dynamics and reaction kinetics.

While we defer a detailed discussion of cavity enhancement effects to Section III, here we make a quick note of the advantages associated with an optical resonator. The well-known multipass effect leads to an enhancement of the effective absorption length by a factor of $2F/\pi$, where $F$ is the cavity finesse. Additionally, the intracavity optical power is built up relative to the input power via constructive interference, which allows for the study of nonlinear interactions even with low-power laser sources. An often taken-for-granted benefit in practice is that although the intracavity interaction is powered by a high field amplitude, the cavity reduces the output power to a reasonable level acceptable for subsequent photo-detectors. Alternatively, high intracavity power can be extracted using high-speed optical switching devices; this forms the basis of a cavity-based optical amplifier to be discussed in Section VI.D. Additionally, the geometrical self-cleaning and mode matching of the optical waves inside a cavity is important both for eliminating pointing-direction related noise and for obtaining narrow, unshifted resonance lines [10]. Finally, a stable cavity can be used to stabilize a laser's frequency by locking the laser to a cavity resonance, thereby reducing the detection noise in measurements involving the laser.

## B. Issues Related to Technical and Fundamental Noise

Direct absorption measurements often suffer from intensity noise on the laser. Noise amplitudes typically rise toward the low-frequency region of the intensity spectrum where many important signals reside; this problem has motivated development of modulation schemes, such as frequency-modulation spectroscopy, to encode and recover signals in frequency intervals with minimal technical noise. The use of an optical cavity, while effective in enhancing a signal, can also introduce some extra technical noise. For example, when the relative frequency fluctuation between the laser and the cavity resonance is of the same order as the cavity linewidth, frequency noise will be converted to amplitude noise in the detected signal if a naïve, direct absorption approach is adopted. Because this noise conversion is inversely proportional to the cavity linewidth, the same enhancement factor that has improved the signal size can play an equal—but deleterious—role. Thus, while it is important to reduce noise amplitudes in the first place, it is usually equally imperative to employ some clever signal recovery techniques that minimize the influence of noise on the detection result. For any absorption spectroscopy, the fundamental detection limit is reached when the minimum signal amplitude equals the noise level associated with the discrete nature of a photon flux, which has a Poisson distribution for an ordinary laser output without technical noise. Such performance can be

achieved when the technical noise is minimized by a differential measurement. For a true differential measurement, quick comparisons of on-resonance and off-resonance information are required; that is, some sort of modulation technique should be employed. When combined with an effective modulation technique, the resonant cavity scheme approaches its full potential for signal enhancement without added noise.

When cavity finesse is sufficiently high, then in order to limit the intracavity power to some useful level below system saturation, the power level associated with the cavity input and transmission will usually be maintained low. Detection of these small transmission signals with high signal-to-noise ($S/N$) is therefore a technical challenge. Although photon counting has been an effective approach to detect low light levels and construct useful photon statistics, it is not suitable for coherent detections if the field phase is the desired quantity to measure. As discussed in Ref. [11], a balanced heterodyne detection would allow a full construction of the quantum susceptibility of intracavity absorbers. Optical heterodyne detection with the aid of a large optical local oscillator field is also an effective and necessary approach to overcome serious electronic noise limitations.

## C. Change of Boundary Conditions—Quantum Effect

Optical elements present boundary conditions that alter the free-space quantization structure of the electromagnetic field. This modified electromagnetic mode structure in turn affects the interactions of an atomic dipole with light, including decay into the now-altered vacuum. Diverse observations have demonstrated changes in atomic radiative processes caused by the presence of a boundary; for example, boundary-induced atomic level shifts form the basis of the Casimir effect and numerous other phenomena. For a review of these effects and their development into the field of cavity QED, see for example Ref. [12].

The boundary conditions imposed by an optical cavity create a set of electromagnetic field modes confined between the cavity mirrors. These resonant cavity modes are well-defined in frequency and in spatial structure. The modes of an optical cavity typically subtend a small fraction of $4\pi$ in solid angle, and thus do not significantly suppress free-space atomic spontaneous emission. However, the presence of the cavity introduces a new rate, the rate of coherent exchange of excitation between atom and cavity field. Through this coherent coupling the atom and cavity decay linewidths do in fact alter one another, at first perturbatively and then strongly as the coherent coupling becomes large relative to both decays. Finally, when the physical size of a cavity is reduced until the cavity mode volume is near

the atomic ''radiative'' volume, a whole new set of quantum dynamics associated with the full quantum susceptibility can be explored within the setting of cavity quantum electrodynamics [11,13].

### D. Applications of Sensitive Detection, Field Enhancement, and Cavity QED

Sensitive, cavity-enhanced detection schemes have found many different applications, including the characterization of dielectric stacks [14]; measurement of ultraslow reflector velocities [15]; atmospheric sensing [16,17]; detection of trace gaseous species [18]; absolute determination of absorption band strengths and species concentration [19]; analysis of combustion and plasma dynamics [20,21]; study of chemical kinetics and molecular dynamics [22,23]; tests of fundamental physical postulates such as quantum spin statistics [24–26], gravitational wave detections [27,28], thermal noise detection and control [29], and magnetically induced vacuum birefringence [30,31]; improvements in laser stabilization and optical frequency metrology [32–34]; novel schemes for laser cooling [35]; and research into quantum dynamics and quantum information [36–38], nonlinear optics [39], and quantum measurement limits [40–42]. The extension of these methods to study surfaces and condensed matter [43] and their potential applications as medical instruments only make the field more exciting [44,45].

## II.  Mode Structure and Relevant Characteristics of Fabry–Perot Cavities

In this section we briefly lay out the properties of an optical cavity that will be relevant to all the scientific applications discussed in this article. Since Fabry-Perot cavities are by far the most widely used optical cavities to date and in the immediate future, we concentrate on them in our treatment. More exotic cavity geometries and fabrication methods are touched upon only very briefly, in Section VII.G. While this section lays the groundwork for further discussions, some later sections revisit the issues of precise measurement of cavity mode spacings, mirror coating properties, and subtleties of cavity mode structure.

### A. Mode Structure and Basic Definitions

Figure 1 shows a Fabry-Perot optical resonator created by aligning two highly reflective mirrors at separation $d$ measured along the cavity axis.

$$(\alpha d)_{enhanced} = \left( \frac{g_0^2}{\gamma} \cdot \tau_{cavity} \right) \approx (\alpha d) \cdot \frac{2F}{\pi} \quad \text{F: cavity finesse}$$
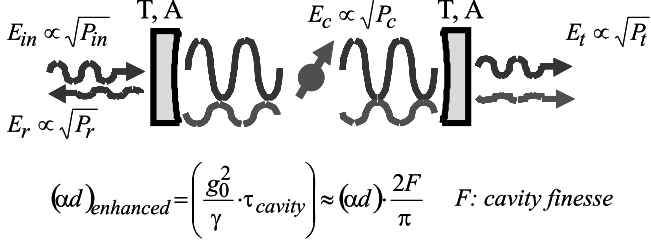
FIG. 1. Notation for the fields in and out of an optical cavity. The standing-wave field built-up inside the cavity is shown, along with the radiation field from the prepared atomic dipole.

Modes of the cavity possess a standing-wave structure along the axis, so the cavity supports a set of longitudinal modes separated in frequency by a *free spectral range* (FSR) of $c/2d$ where $c$ is the speed of light. (Mirror coatings cause the FSR to deviate very slightly from this simple formula, as will be discussed in Section VI.) At each longitudinal mode the cavity supports a complete set of transverse modes of different spatial profiles, perpendicular to the cavity axis. The TEM$_{00}$ mode has a cylindrically symmetric Gaussian profile, characterized by a beam waist $w_0$.

If the two mirrors are assumed to be identical, the cavity is characterized by the per-mirror power transmission $T$ and loss $A$. The total empty cavity loss is $L_{cav} = 2(T + A)$. The cavity finesse ($F$) is given by

$$F = \frac{2\pi}{L_{cav}} = \frac{\pi}{T + A}. \tag{1}$$

The finesse can also be expressed as the ratio of free spectral range to cavity linewidth. It is closely related to another commonly used quantity, the resonator quality factor $Q$, which is the ratio of the resonant optical frequency to the cavity decay linewidth. The use of finesse is attractive as it depends only on the mirror properties and not directly on the cavity dimension. When the cavity length changes, both the *FSR* and linewidth of the cavity vary as the inverse of the cavity length, and hence the finesse remains nearly constant. $Q$ and $F$ are related by the ratio of the optical frequency to the *FSR*; the latter lies normally in the RF/microwave frequency domain.

B.  Realization of High-Finesse Cavities

High-finesse cavities are typically constructed from superpolished substrates coated with a "stack" (40–50 or so alternating layers) of dielectric materials

so that coating layers have alternating high and low index of refraction. The layer thickness sets the center wavelength of the coating. These coating techniques are capable of producing mirror transmission $T$ at or below $10^{-6}$ (1 ppm). However, current technology has yet to push mirror loss $A$ below one to a few ppm. Thus cavity finesses in the range of $10^5$ to $10^6$ constitute the current state of the art for high-reflectivity, low-loss mirrors and coatings. Mirror absorption/scatter losses set a limit on $F$ and are furthermore a hindrance to signal extraction when nonlinear interactions are present. For example, they are a critical limiting factor in the loss rate for present cavity QED systems—for the very short cavities used in these experiments, loss rates associated with $A$ are usually similar in size to the atomic spontaneous emission rates. To build robust quantum computing/communications devices from cavity QED components, it is necessary to improve the ratio of mirror transmission (useful information) to mirror losses (loss of coherence).

Different cavity lengths are desirable for each application of optical cavity technology. The smallest cavity mode volumes are demanded by cavity QED applications, which currently use cavities with transverse mode waists as small as $w_0 \sim 10$ μm and cavity lengths $d \sim 10$ μm or slightly shorter. At these lengths it is important to consider that the standing-wave light field inside a cavity penetrates into the mirror coatings, giving a larger mode-volume than would be otherwise expected from the physical distance between the mirror surfaces. When the micro-cavities are pushed to shorter lengths in the quest for greater interaction strengths, the leakage field into the mirror coatings will have a non-negligible effect on the cavity mode structure.

## III. Cavity Enhancement: A Simple Physics Picture

In this section we will discuss the basic physics associated with the cavity enhancement effect. We will derive some useful equations from different perspectives and show that, as with many other subjects, the cavity-enhancement principle manifests itself in different and yet eventually equivalent forms. It is useful to explore these different aspects as each highlights distinct practical consequences and can lead to effective experimental techniques.

### A. Enhanced Optical Radiation and Interaction Length

We start our discussion of cavity-enhancement by directly looking into the cavity properties. The basic understanding can be developed by placing

the absorbing atoms or molecules in an optical cavity and then comparing the absorption level to the intrinsic loss of the cavity. Thus low-loss mirrors (and consequently high-finesse cavities) help to enhance the signal contrast. Beginning with the empty-cavity case, we denote the optical input power as $P_{\text{in}}$, the cavity-reflected power as $P_{\text{r}}$, and the cavity-transmitted power as $P_{\text{t}}$ (see Fig. 1). The resonant cavity reflection efficiency, transmission efficiency, and intracavity build-up power, $P_{\text{c}}$, can be expressed, respectively, as

$$\frac{P_{\text{r}}}{P_{\text{in}}} = \left(\frac{A}{T+A}\right)^2,$$
$$\frac{P_{\text{t}}}{P_{\text{in}}} = \left(\frac{T}{T+A}\right)^2, \quad \text{and} \tag{2}$$
$$\frac{P_{\text{c}}}{P_{\text{in}}} = T\left(\frac{1}{T+A}\right)^2.$$

These equations can be easily derived following any modern optics textbook [46].

Consider a cavity of roundtrip length $2d$, filled with a weakly absorbing gas sample with an absorption coefficient of $\alpha$ per unit length. (By weakly absorbing we mean the cavity round trip fractional power loss can be written as $1 - \exp(-2\alpha d) \approx 2\alpha d$. We will also use the assumption that $\alpha d \ll T, A$). In a direct absorption measurement with a sample cell of length $d$, the output power is; $P_{\text{out}} = P_{\text{in}} \cdot e^{-\alpha d} \sim P_{\text{in}} (1 - \alpha d)$. Therefore, the absorption signal is $(P_{\text{in}} \cdot \alpha d)$, with contrast $\delta P_{\text{out}}/P_{\text{out}} = -\alpha d$. When the sample is placed inside a cavity, the transmitted power is modified according to Eq. (2),

$$\frac{P_{\text{t}}}{P_{\text{in}}} = \left(\frac{T}{T+A+\alpha d}\right)^2 \approx \left(\frac{T}{T+A}\right)^2 \left(1 - 2\frac{\alpha d}{T+A}\right). \tag{3}$$

The detected signal contrast in the cavity transmission is therefore enhanced to

$$\frac{\delta P_{\text{t}}}{P_{\text{t}}} = -2\frac{\alpha d}{T+A} = -\frac{2F}{\pi} \cdot (\alpha d). \tag{4}$$

In practice, the anticipated sample absorption may actually be of the same order or larger than the mirror transmission coefficients. In this case input and output mirror parameters should be individually selected to maximize the resonant cavity transmission under the "impedance-matching"

boundary conditions in the presence of intracavity gas absorption. It is also worth noting that, although the cavity finesse is determined by the sum of the mirror transmission $T$ and loss $A$ and neither quantity appears explicitly in Eq. (4), it is optimal for $T$ to be dominant over $A$, because this increases the absolute size of the absorption signal [cf. Eq. (3)]. The ratio of $T$ to $A$ is even more important for studying nonlinear dynamics; for cavity QED experiments, for example, $T$ represents an accessible communication channel for information flow from the cavity to the outside world while $A$ represents irreversible loss of coherence.

## B. Enhanced Radiation (Absorption) of Atomic/Molecular Dipole Moments Inside the Cavity

Perhaps cavity enhancement can be most simply understood from the cartoon picture shown in Fig. 2. Suppose a single atom is present within the mode volume of a resonant light field propagating through a length $d$. The total absorption coefficient ($\alpha d$) can be interpreted as arising from an atomic transition rate $R$ multiplied by the interaction time, $d/c$. From this intuitive picture, we can immediately understand that if a cavity is placed around the atom with the intracavity photon lifetime resonantly increased to $\tau_{\text{cavity}} = (2F/\pi) \cdot d/c$, the absorption coefficient becomes $(\alpha d)_{\text{enhanced}} = R \cdot \tau_{\text{cavity}} = (2F/\pi)(\alpha d)$.

To explore other factors determining the strength of interaction, we take another look at the microscopic origins of the absorption coefficient ($\alpha d$) itself. Denoting the atomic dipole moment $\mu$ and the transition wavelength $\lambda$ angular frequency $\omega = 2\pi c\lambda$, with $c$ being the speed of light), we have the atomic decay rate $\gamma \propto \mu^2/\lambda^3$ via the Fermi golden rule. For a cavity mode of cross-sectional area $a$, the coupling between the atom and the electric field of a single photon is $g_0 \propto \mu \cdot \sqrt{\omega/(a \cdot d)}$. Here the factor within the square root arises from the energy density for a single photon within the designated



What is $\alpha$?
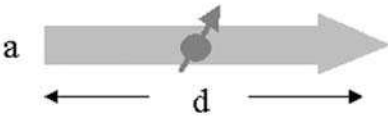
$$\alpha d = \frac{g_0^2}{\gamma} \cdot \frac{d}{c} \qquad g_0 \propto \mu \cdot \sqrt{\frac{\omega}{d \cdot a}} \ , \quad \gamma \propto \frac{\mu^2}{\lambda^3}$$

$$\alpha d \propto \frac{\lambda^2}{a} \approx \frac{\sigma_0}{a}$$

FIG. 2. An intuitive picture of atomic absorption: $\mu$ is the atomic dipole moment, $\lambda$ the transition wavelength, $\gamma$ the spontaneous decay rate, $g_0$ the coherent coupling between the atomic dipole and the light field quantized within the volume of ($a \cdot d$), and $\sigma_0$ represents the resonant atomic absorption cross-section.

mode volume. The transition rate $R$ above is then given by $g_0^2(1/\gamma)$. Therefore $\alpha d \propto (g_0^2/\gamma) \cdot d/c \approx \lambda^2/a \approx \sigma_0/a$, with $\sigma$ being the resonant absorption cross-section of the atom. Cavity enhancement of the interaction lifetime adds a factor of $2F/\pi$ as above, so the absorption scales as the cavity finesse over the cross-sectional area of the mode.

## C. Constructive Interference of Atomic/Molecular Radiation

It is clear from Eq. (2) that the intracavity circulating power can be much larger than the input power. This power buildup is essential to have an appreciable level of saturation for nonlinear spectroscopy involving very weak transitions. The strong light field phase-coherently drives the atomic or molecular dipole moments. The radiation from these prepared dipole moments is the signal to be detected. However, the strong background of the unabsorbed incoming light sets the detection noise level, the shot-noise level in the ideal case (cf. Section IV). With the build-up cavity approach, this potentially large noise contribution from the intracavity field is reduced after the sample has been prepared and before the final detection. When the cavity is tuned onto a molecular line, the major part of the molecular signal will leak out of the cavity to reach a detector, while a similar, or smaller, portion of the input power will be transmitted by the cavity and reach the same detector to set the shot-noise limit. The large intracavity buildup power, however, will remain trapped inside, where it prepares the phase-coherent molecular dipole moment of an enhanced magnitude. This result, although explained here from yet another perspective, is the same cavity enhancement effect discussed in the previous paragraphs.

To mathematically clarify the preceding discussion, we note that the intracavity field $E_c$ is related to the input field $E_{in}$ by $E_c = E_{in} \cdot \sqrt{T}/(T + A)$ (cf. Fig. 1). The radiation field of the prepared dipole moment can be written as $E_{atom} = -E_c \cdot (\alpha d/2)$, where the minus sign accounts for the negative interference between the sample radiation and the original field that leads to absorption. The integrated intracavity (single-pass) absorption signal is $(\alpha d)$ and the factor of $1/2$ reflects the fact that we are now dealing with the field amplitude. When the cavity is tuned to the atomic resonance, this atomic signal will be resonantly enhanced by constructive interference, by a factor of $2/(T + A)$. Here the factor of 2 accounts for the bi-directional effect in the cavity. Finally the field leaking out of the cavity is attenuated by $\sqrt{T}$ before reaching the photodetector. The final field can thus be expressed as

$$E_{atom,output} = -\sqrt{T} \cdot E_c \left(\frac{\alpha d}{2}\right) \cdot \left(\frac{2}{T + A}\right) = -\frac{T}{T + A} E_{in} \cdot \left(\frac{\alpha d}{2}\right) \cdot \left(\frac{2F}{\pi}\right) \quad (5)$$

$$(E_{in} + E_{atom})^2 \approx E_{in}^2 + 2E_{in} \cdot E_{atom}$$

$$\frac{S}{N} \propto \frac{2E_{in} \cdot (E_{in} \cdot \alpha d)}{\sqrt{E_{in}^2}} \sim E_{in} \cdot \alpha d$$
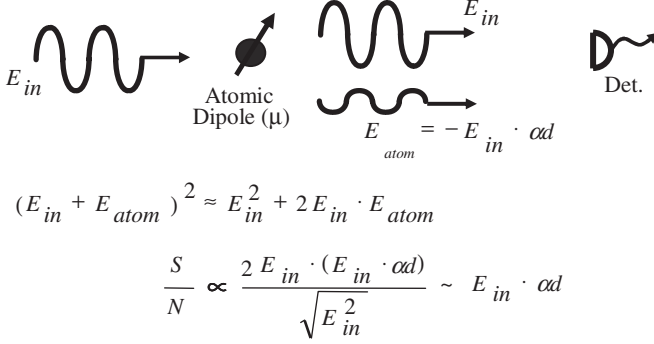
FIG. 3. Principle of optical (homodyne) heterodyne detection of an absorption signal, showing the destructive interference between the incident and the radiating fields. Derivation of a simple shot noise limited $S/N$ ratio is shown.

When this quantity is small compared to the transmitted local oscillator field, $E_{in} \cdot T/(T + A)$, the change in output power due to the atom is proportional to their cross-term, and thus the signal enhancement factor is again $(2F/\pi)$. This will be explained in a more detailed manner in Section IV.B, in the context of discussions about heterodyne detection (Fig. 3). In Section IV.E we will also show how the same cavity enhancement factor manifests itself in the detected phase shift of an output field from the cavity.

From a practical point of view, using a cavity is also attractive when the laser source has a relatively large amplitude noise. Indeed, when a buildup cavity is used, the subsequent photodetector does not have to receive a large intensity, even when there is a large interactivity field to enhance the signal of interest. This allows for high $S/N$ detection outside the cavity with transmitted power low enough for shot noise to dominate over technical noise. This effect is similar to the result of polarization spectroscopy [47] or interference filtering.

### D. Field Quantization—Influence of the Cavity Physical Size and Strong Coupling Regime in Cavity QED

Although our discussion so far has focused mainly on the semiclassical aspect of the light-matter interaction, it is nonetheless interesting to make a quick note on the connection between this classical picture of cavity-enhanced spectroscopy and optical cavity-based quantum electrodynamics (QED). When the cavity volume ($\sim \pi w_0^2 d/4$) is comparable to the critical radiation volume of a single atom, namely $V_{critical} = \lambda^2 \cdot c/\gamma$, the atom-cavity interaction needs to be treated in a fully quantum picture.

Crucial to the realization of manifestly quantum effects in cavity QED is *strong coupling*, a condition in which the coherent coupling between atom and cavity field dominates dissipative rates in the system. For a two-level atom optimally coupled to a cavity mode, the dipole-field coupling is given by the Jaynes-Cummings interaction Hamiltonian [48]

$$\hat{H}_{\text{int}} = \hbar g_0(\hat{\sigma}^+\hat{a} + \hat{\sigma}\hat{a}^+), \tag{6}$$

where $(\hat{\sigma}^+, \hat{\sigma})$ are atomic dipole raising and lowering operators, $(\hat{a}, \hat{a}^+)$ are field annihilation and creation operators for the cavity mode, and $g_0$ is one half of the single-photon Rabi frequency. This rate describes the exchange of excitation between the atomic dipole $\vec{\mu}$ and the electric field $\vec{E}$ built up by a single photon of frequency $\omega$ residing in the mode volume $V_m$ of the optical cavity:

$$g_0 = \vec{\mu} \cdot \vec{E} = \mu\sqrt{\frac{\hbar\omega}{2\varepsilon_0 V_m}}. \tag{7}$$

Thus $g_0$ is a rate of coherent evolution that must be compared with the dissipative rates for the system. These, in turn, are the atomic spontaneous emission rate $\gamma_\perp$ and the cavity field decay rate $\kappa$. While the regime of $(\kappa, \gamma_\perp) \gg g_0$ is described by the classical treatments developed above, we will see in Section VII that a quantum theory is necessary to account for physics at $g_0 \gg (\kappa, \gamma_\perp)$, in the strong coupling regime [49–51].

Though atom-cavity behavior in the strong coupling limit must be calculated in an inherently quantum treatment, the onset of this regime can be estimated from quantities well known from classical spectroscopy. In the optical bistability and cavity QED literature [52,53], there is an atomic co-operativity parameter defined as $Ng_0^2/2\kappa\gamma$, where $N$ is the number of atoms. This quantity signifies the level of modification of the empty cavity properties by the presence of atoms. Calculation reveals that the co-operativity parameter is nothing but the now familiar $(2F/\pi)\alpha d$, the enhanced intracavity absorption signal. This understanding leads to a natural definition of the critical atom number: $N_0 = 2\kappa\gamma/g_0^2$, which signifies the level of influence by a single atom on the cavity dynamics. Similarly, the critical photon number can be defined as $m_0 = \gamma^2/2g_0^2$, which is basically the number of intracavity photons required to saturate an atom, and is directly related to the aforementioned ratio of cavity mode volume to atomic radiative volume. More extensive discussions in Section VII will further

clarify the physical meanings of these quantities and their significance related to the latest generation of optical cavity QED experiments.

## IV.  Weak Absorption Measured by Field-Phase (Frequency-Domain)

In parallel with signal enhancement, the issues of detection noise and how to reach the fundamental noise limit are equally critical to the implementation of sensitive spectroscopy. In this section, we will concentrate our discussions in the frequency domain on the relevant issues related to signal extraction and noise suppression.

The ultimate detection sensitivity is achieved when we are able to observe each absorption event individually, and when the noise is limited by the uncertainty of an event occurrence. This is referred to as the shot-noise limit. The shot noise is associated with the discrete nature of the interaction between matter and the photon stream. The shot noise is fundamental in that it reflects the quantum nature of light from ordinary thermal sources and lasers far above threshold, sources that carry Poissonian statistics. Radiation fields can also be "squeezed" to have sub-Poissonian levels of fluctuation, providing an anomalously low fluctuation level for the photocurrent (i.e., sub-shot noise).

The signal exiting the cavity can also be measured using phase sensitive detection methods, i.e., in frequency-domain applications. The phase of the light, along with the cavity resonance structure, is perturbed by the molecular radiation, which leads to additional phase shifts. The objective of this section is to discuss phase-sensitive optical-heterodyne spectroscopy, using an enhancement-cavity, as a tool for signal acquisition. The advantage of this approach lies in the characteristic property of frequency modulation (FM) spectroscopy: the simultaneous and continuous observation and subtraction of the signal and background optical phases.

A.  Fundamental Detection Limits in Classical Spectroscopy

As noted in Section III, the physical origin of the absorption process can be understood as destructive interference between the incident radiation and the electric field generated by the coherently driven dipole moments of the sample. Therefore, direct absorption can be viewed as a homodyne detection between two interfering fields that have the same frequency. Maximum sensitivity occurs when the probe field has no amplitude noise beyond its intrinsic quantum fluctuations. Given a detection bandwidth of $B$ and the

average photocurrent $i_{dc}$, the associated shot-noise current is given by $i_n = \sqrt{2ei_{dc}B}$, where $e$ is the electron charge. Taking the photodetector responsivity as $\eta$ (dimensions of electrical current per unit power incident on the detector) and $P_0$ as the incident radiation power, then $i_{dc} = \eta P_0$ and the absorption signal $i_{sig} = (\alpha d)\eta P_0$. The shot noise will set the fundamental sensitivity limit for straight absorption spectroscopy. When the $S/N$ ratio is one, i.e., when the molecular absorption is equivalent to the shot noise in the measurement bandwidth, we obtain a minimum detectable absorption of

$$(\alpha d)_{min} = \sqrt{\frac{2eB}{\eta P_0}}. \tag{8}$$

This direct absorption sensitivity is capable of detecting an absorption of $2 \times 10^{-8}$ over a 1 s averaging time over $P_0 = 1\,\text{mW}$ and a reasonable $\eta$ ($\approx 0.8\,\text{A/W}$).

Needless to say, this number seems optimistic when compared to experience. In practice, noise of various technical origins usually dominates in the low frequency ranges, and actual laser systems display vastly more noise than the shot noise limit. This extra technical noise may originate in inadequately smoothed power-supply potentials, laboratory vibrations that randomly dither the laser's alignment and mode structure, electromagnetic pickup from high-frequency or high-current devices, or unwanted optical feedback. In order to avoid excessive low-frequency noise of technical origins, one can use modulation techniques, either on the laser amplitude or frequency, to encode and then detect the absorption at a higher frequency and within a narrower bandwidth. Of course amplitude modulation of the laser will result in an enhanced $S/N$ only if the signal response is nonlinear. Otherwise one just has a high $S/N$ way to see that the laser's power is unsteady. Reduced-background detection techniques (such as polarization and interference spectroscopy) are also often employed to suppress excessive noise.

## B.  Introduction to Optical Heterodyne Detection

Before we delve into the details of modulation techniques, it is useful to first discuss the principle of optical heterodyne detection. The reason is that modulation detection can often be understood as a heterodyne interaction between one optical field (the carrier) and another (a modulation sideband). The optical power will generally have a time-dependent term if the applied laser field is the sum from two sources, i.e., $[E_1(t) + E_2(t)]^2$. For simplicity

we have neglected important interference details by assuming the two contributing fields to be mutually mode-matched. With $E_1(t) = E_1 \cos(\omega_1 t)$ and similarly for $E_2$ and $\omega_2$, when the difference of the two applied frequencies is within the detector's response bandwidth, we expect a detected photocurrent of the form $i(t) = \left(i_1 + 2\sqrt{i_1 i_2} \sin(\omega_1 - \omega_2)t + i_2\right)$. We refer to the cross-term at the difference frequency as the heterodyne response. If we had chosen to think of the field $E_2$ as somehow different, such as a weak field produced by an atomic/molecular sample, one can see one of the advantages of the heterodyne approach; the scale of the beat current can be increased by increasing the amplitude of $E_1$, which is referred to as the "local oscillator" (LO) field. It is important that the $S/N$ is not degraded by use of a larger LO power, as discussed below.

Any real photodetector will have some output noise, even in total darkness. If we attempt direct detection of a weak signal, the incident power will need to be sufficiently high to overcome the detector's intrinsic noise. Consider the heterodyne case: now the signal-bearing light power is represented by the cross-term between the local oscillator field and the weak signal field, i.e., $i_{\text{sig}} \propto E_1 E_2$. On the other hand, because $E_1 \gg E_2$, the shot noise of the total photocurrent will be dominated by the LO power, i.e., $i_n \propto \sqrt{E_1^2} = E_1$. It is only this noise term that needs to be adequately large to mask the detector noise. So by merely using a stronger LO field, we can overcome the appreciable noise produced by the amplifier circuit that converts the photocurrent into an output voltage. Ideally then, the $S/N$ of the heterodyne detection depends only on the amplitude of the signal beam ($E_2$) and the LO amplitude is cancelled out in the final $S/N$ ratio (see Fig. 3).

Of course, this LO power can carry laser intensity noise to the detector as well. Any non-fundamental noise imposed on this intensity will be directly converted into unwelcome detection noise. But typically this noise, called "technical noise" to identify its origin, is concentrated at lower frequencies and arises from noise processes with "1/f" frequency dependence. So an important step toward achieving low-noise performance is to place the information-carrying heterodyne signal at a frequency sufficiently high that a negligible level of technical noise is carried by the LO field. This is the usual motivation for using some form of modulation-based signal recovery approach.

Optical heterodyne detection also plays a critically important role in retrieving the full quantum information related to vanishingly small optical power exiting from a cavity QED system operating in the strong coupling regime where the critical photon number is below one. A broad detection bandwidth is desired for a full recovery of quantum dynamics associated with atom–cavity interactions. In this case a balanced heterodyne detection is usually adopted to cancel out the noise associated with the LO.

C. Motivation and Concept of Modulation:
   Signal Encoding and Extraction

From a time-domain point-of-view, signal detection schemes employing modulation (AC) methods permit comparison of two cases in quick succession. With suitable modulation schemes, these states can represent on-resonance and off-resonance cases, sampled in rapid succession. By simultaneously obtaining and subtracting these two pieces of information, one provides a signal channel with no output unless there is a resonance. The modulation approach therefore allows efficient extraction of weak signals from a noisy background. Lorentzian signal recovery with modulation methods has been well documented [54,55]. In this type of modulation spectroscopy, the modulation frequency is often chosen to be relatively low to avoid distortions of the spectral profile by the auxiliary resonances associated with modulation-induced spectral sidebands. However, this choice of low-frequency operation usually limits the achievable $S/N$, because of the excess noise of the laser source at low frequencies. To recover the optimum signal size, large (comparable to the absorption resonance width) modulation amplitudes can be employed. In this case, however, the intrinsic line shape is masked by the signal acquisition process.

On the other hand, using modulation frequencies much greater than the width of the spectral feature under study, frequency-modulation (FM) spectroscopy has become one of the most powerful techniques available for sensitive and high-speed detection of weak absorption signals [56–58]. In principle, FM spectroscopy offers detection sensitivity close to that of Eq. (6) by operating at high frequencies where the amplitude noise of the laser source approaches shot noise. A reasonable modulation index is still needed to recover an adequate signal. However, the linewidth broadenings and line shape distortions associated with low-frequency modulation processes are not present in high-frequency FM spectroscopy. Instead, one obtains added spectral features. When scanning through an absorption resonance, each component of the FM spectrum, which consists of a central carrier and weaker sidebands, interacts with a spectral feature, thereby preserving the resolution of the laser. The high bandwidth, or equivalently speaking, a high Nyquist sampling frequency, associated with the high-frequency modulation enables rapid signal recovery.

When received by a square-law photodiode, a pure frequency-modulated spectrum will display no photocurrent at the modulation frequency. This is because the two heterodyne beat signals between the carrier and either sideband are equal in magnitude but opposite in phase. Hence the net result is a perfect cancellation. However, the presence of an absorption feature is revealed as an attenuation and phase shift of one or several of the FM

components. The perfect FM balance is therefore upset, and the resultant optical signal has an amplitude-modulated component. The photocurrent signal can then be phase-sensitively detected using standard radio frequency techniques, yielding an absorption or dispersion line shape, depending upon the detection phase. The redistribution by deliberate FM modulation of some of the carrier power into FM sidebands causes only a slight penalty in the recovered signal size. When the modulation index $\beta$ is on the order of unity or less, the FM spectrum can be approximated by a carrier [$\approx J_0(\beta)$] and two first order sidebands [$\approx J_1(\beta)$]. (Here $J_i$ is the $i$th order Bessel function.) If only the carrier is tuned to interact with a narrow sub-Doppler resonance, then the detection process is intrinsically dispersion-sensitive. Assuming the total probe power is still $P_0$, the detected shot noise current is given by $\sqrt{2eB\eta P_0(J_0^2 + 2J_1^2)} \approx \sqrt{2eB\eta P_0}$. The signal current arising from the heterodyne beat between the carrier and the sidebands becomes $\sqrt{2}\eta P_0 J_0 J_1 \cdot \phi$, where $\phi$ is the associated resonance phase shift. The relative magnitudes of dispersion and absorption ($\phi = \Delta n \cdot \omega d/c$ and $\Delta n = \alpha \cdot \lambda/4\pi$, where $\Delta n$ is the resonance-inflicted change of refractive index) set the scale of the equivalent minimum detectable absorption at the shot-noise limit:

$$(\alpha d)_{\min} = \sqrt{\frac{2eB}{\eta P_0}} \frac{\sqrt{2}}{J_0(\beta)J_1(\beta)}. \tag{9}$$

The modulation-dependent function $J_0(\beta) J_1(\beta)$ has its maximum value of 0.34 at $\beta \approx 1.1$. Compared to Eq. (8) for the ideal case of homodyne detection, FM heterodyne detection suffers a factor of $\sim 4$ loss in sensitivity for fixed total optical power. This is a small price to pay for completely avoiding the laser's technical noise. The $S/N$ loss arises in part because of the power reduction resulting from conversion of some of the main carrier to sidebands and in part from the down-conversion of shot-noise from two additional spectral windows by the two sidebands. Carefully executed FM detection can often nearly reach the sensitivity limit set in Eq. (9).

## D. Combining Cavity Enhancement with Modulation: Introduction to Cavity-Enhanced FM Spectroscopy

In this and the next sections, we will describe two techniques that combine the cavity enhancement approach with modulation techniques to reach the shot-noise limit. These techniques improve the detection sensitivity by a factor of $2F/\pi$, without the additional noise factors potentially associated with the use of an enhancement cavity. The two approaches are seemingly

quite different, with the first one related to the frequency modulation spectroscopy discussed above, while the second one is related to a time-domain picture in the context of cavity field ring-down. In cavity-enhanced FM spectroscopy [59], the on-resonance and off-resonance information is compared at a radio frequency rate. This technique can be applied to both linear and nonlinear (sub-Doppler resolution) spectroscopy. In AC ring-down spectroscopy [60], two slightly different ring-down time constants are compared, one associated with an empty cavity and the other with additional intracavity loss. Typically the comparison rate is in the audio frequency range. The technique is suitable for linear absorption measurements. The differential measurement approach of both techniques allows them to achieve near shot-noise limited absorption sensitivity. As will be evident in the following discussions, the two approaches are intimately related, through the common features of cavity signal enhancement and technical noise rejection toward the shot-noise limit.

As one considers how to probe an external cavity signal with FM techniques, the first approach that comes to mind is to lock the laser frequency to a cavity resonance and then modulate that cavity mode around the desired molecular resonance while monitoring the cavity transmission. This approach represents a simple lock-in derivative line shape recovery process. In order for this method to be successful, it is important to have a tight frequency lock loop between the laser and the cavity because any laser frequency noise relative to the cavity will be converted to amplitude noise. To implement this scheme, a piezoelectric transducer (PZT) is mounted on one of the cavity mirrors. This assembly is used to modulate the cavity length, and the laser tracks the modulation. The modulation frequency is usually limited to the audio range due to mechanical resonances and roll-off in the frequency response of the PZT and mirror assembly. Depending upon the laser's amplitude noise spectral distribution, the attainable modulation frequency may be too low to reach shot-noise limited detection. Using a solid-state Nd:YAG laser locked to a high-finesse ($F = 100,000$) cavity (corresponding to a $\approx 1\,\mathrm{mHz}$ relative linewidth), a cavity dither at $500\,\mathrm{Hz}$, and lock-in detection, an absorption detection sensitivity of $3 \times 10^{-11}$ ($6.4 \times 10^{-13}$/cm) has been measured at $1\,\mathrm{s}$ averaging [61].

To benefit from the full noise-reduction advantages of FM spectroscopy, one needs to introduce a high-frequency phase-modulation of the probe field, usually much larger than the resonance linewidth under study. In addition to the laser-cavity locking issue, another obstacle remains; namely, the cavity bandwidth limit. Specifically, FM sidebands at a high frequency are needed to eliminate low-frequency laser amplitude noise, but at the same time the cavity must respond to the sidebands in exactly the same manner as

it responds to the carrier. This will reduce the frequency-to-amplitude noise conversion process. This goal can be realized by frequency modulating the input laser beam at exactly the free-spectral range of the cavity. We then detect and demodulate the cavity-transmitted light at the modulation frequency. Any small residual frequency variations of the laser will still lead to some amplitude fluctuations and phase shifts of the transmitted carrier, but these will also lead to exactly the same amplitude fluctuations and phase shifts of the sidebands, which are transmitted on nearby cavity axial orders. So the transmitted light still accurately represents an FM spectral triplet, with minimal AM conversion caused by the relative laser/cavity frequency jitter. Thus the noise level can approach the intrinsic AM noise level of the laser at the *FSR* frequency.

### E. Operation Sensitivity of NICE-OHMS

Figure 4 shows the case where the central component is used to detect the intracavity molecular resonance, illustrating how the sub-Doppler molecular dispersion causes an unbalance of the laser FM spectrum by a phase shift on the carrier component. Initially, all the FM components coincide with their respective cavity modes. When the central cavity mode is tuned over an atomic/molecular resonance, the mode frequency will be pulled by
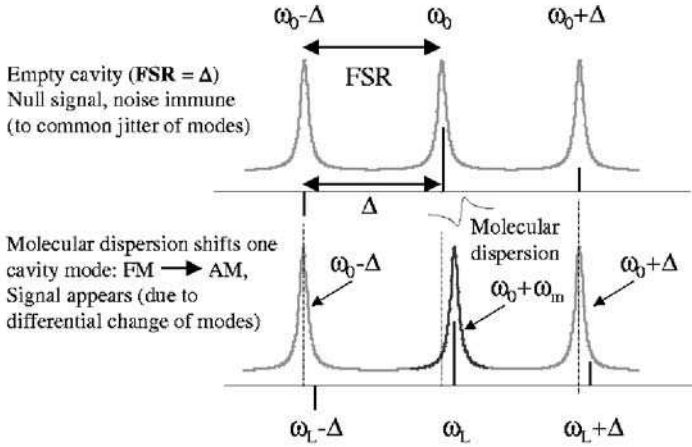


FIG. 4. The optical spectrum and the detection principle for NICE-OHMS: $\omega_L$ denotes the laser frequency and $\Delta$ is the phase-modulation frequency that matches the cavity FSR. The empty cavity resonance modes are denoted by $\omega_0$ and $\omega_0 \pm \Delta$. The original FM symmetry is upset when the molecular dispersion shifts the cavity resonance ($\omega_0$) by $\omega_m$.

the additional phase shift attributable to the intracavity dispersion. After the phase sensitive demodulation, the detector viewing the transmitted light will generate a dispersion signal in the RF beat. We refer to this technique as (laser frequency-) noise-immune, cavity-enhanced, optical-heterodyne molecular spectroscopy (NICE-OHMS) [34,59,61,62]. This modulation and detection scheme makes it possible to use a high-finesse cavity without introducing additional noise.

To estimate the sensitivity associated with NICE-OHMS, we notice that the cavity-enhancement effect applies only to the signal; no additional noise source has been introduced. Therefore the noise-equivalent absorption signal is that of Eq. (9) for ordinary FM spectroscopy, divided by the cavity enhancement factor $(2F/\pi)$. The power in the denominator should be that of the cavity transmitted light, $P_t$.

This argument can be supplemented with a more rigorous proof. Suppose the molecular dispersion changes the intracavity refractive index by $\Delta n$, with the shift of cavity resonance given by $(\Delta n \cdot \omega_0)$. Light going through the cavity will thus acquire an extra phase shift of $\phi = \arctan(\Delta n \cdot \omega_0/\gamma)$, where $\gamma$ is the cavity HWHM (measured in radians). Following the previous treatment and under the assumption of a small $\phi$, we derive

$$\phi \approx \Delta n \cdot \omega_0/\gamma = \frac{\lambda}{4\pi} \alpha \frac{\omega_0}{\gamma} = \frac{c}{2\gamma} \frac{\alpha d}{d} = \frac{FSR}{\gamma} \cdot (\alpha d) = \frac{2F}{\pi} \left( \frac{\alpha d}{2} \right). \quad (10)$$

The signal amplitude is $\sqrt{2}\eta P_t J_0 J_1 \cdot \phi$ and the shot noise limit is $\sqrt{2eB\eta P_t}$. The minimum detectable absorption at $S/N = 1$ is thus,

$$(\alpha d)_{\min} = \frac{\pi}{2F} \sqrt{\frac{2eB}{\eta P_t}} \frac{\sqrt{2}}{J_0(\beta)J_1(\beta)}. \quad (11)$$

A numerical example follows. Suppose the modulation index, $\beta$, is 0.5, and the photodiode responsivity, $\eta$, is 0.85 A/W. Also, take the optical power, $P_t$, to be 5 mW and the detection bandwidth, $B$, to be $1/2\pi$ Hz, which corresponds to a 1 s time constant. Then, for a single-pass cell, the noise-equivalent integrated absorption, $(\alpha d)_{\min}$, is $2.2 \times 10^{-8}$. Under the same conditions, a cavity with a finesse of 100,000 improves the sensitivity to $3.5 \times 10^{-13}$. As discussed below, a noise-equivalent sensitivity of $5.2 \times 10^{-13}$ of an integrated absorption at 1 s averaging has been achieved. This corresponds to an absorption of $1 \times 10^{-14}$/cm for a cavity length of 50 cm [61].

F. Implementing a NICE-OHMS Experiment:
   Signal Line Shape, Size, and Sensitivity

An experimental schematic is shown in Fig. 5. Two electro-optic phase modulators are used to impose two sets of FM sidebands on the laser beam. Modulation at a low frequency, $\delta$, is detected in the cavity-reflected signal and is used to produce a servo error signal for locking the laser to the cavity. Sidebands at a higher modulation frequency, $\Delta$ are set to match the cavity's free-spectral range ($FSR$) and are used to probe the intracavity molecular resonance. This signal is detected in transmission, with adequate optical isolation between the cavity and the photodiode. To study the resonance signal line shape and width, precise scanning capability is important. A frequency-offset locking loop is implemented to permit laser frequency sweeps at an RF resolution. During the scan, the cavity $FSR$ changes slightly. To maintain the noise-immune property, the sideband frequency should track this changing $FSR$.

  As shown in Fig. 4, the laser spectrum has three major components: the carrier at $\omega_L$ and two phase-modulation sidebands at $\omega_L \pm \Delta$. Each of these three components has its own two sidebands located at $\pm \delta$ away from itself, namely at $\omega_L \pm \delta$ $\omega_L + \Delta \pm \delta$ and $\omega_L - \Delta \pm \delta$ which are not shown in Fig. 4. The three corresponding cavity resonant peaks are denoted as $\omega_0$ and $\omega_0 \pm FSR$, with $FSR = \Delta$. The beam reflected from the cavity carries all these frequency components and is detected by a photodetector. Demodulation at frequency $\delta$ produces the servo error signal used to lock the laser frequency to the narrow-linewidth cavity. Because of the additional modulation, this locking error signal now has three contributions. These are
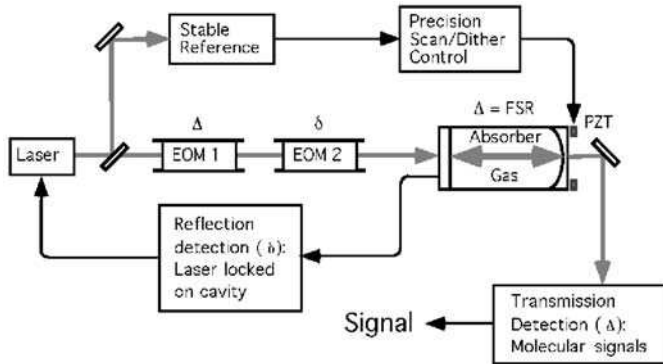


F<small>IG</small>. 5. General schematic of the NICE-OHMS spectrometer, showing the major components of the laser/cavity locking, detection of the transmitted FM triplets, and the precision tuning control.

the two sideband resonances of strength $J_1(\beta)^2$ near $\omega_0 \pm \Delta$, and the carrier contribution $J_0(\beta)^2$ near $\omega_0$. Together, these additively define the lock point. When none of the laser frequency components is affected by a resonance of the intracavity molecules, the servo error signal keeps the carrier, $\omega_L$, and its two sidebands, $\omega_L \pm \Delta$, on the cavity resonance, $\omega_0$ and $\omega_0 \pm \Delta$. Thus, the transmitted beam has the original, perfectly balanced FM spectrum because the carrier ($\omega_L$) and the sidebands ($\omega_L \pm \Delta$) experience the same phase shifts and amplitude attenuations. However, when a molecular resonance affects any of these three components, the interaction converts part of the FM into AM, which is then detected by the photodetector viewing the transmitted light.

For example, as shown in Fig. 4, when a molecular resonance is near the cavity resonance $\omega_0$ the carrier will experience a modified intracavity refractive index, which has been changed by $\Delta n$ because of the molecular absorption. As a result, $\omega_0$ is shifted by $\omega_m = -\omega_0 \Delta n$. If we neglect for the moment the servo contributions from the two sidebands, then the carrier $\omega_L$ could be kept at the new cavity resonance center ($\omega_0 + \omega_m$). On the other hand, the sidebands, after being shifted to the new positions $\omega_L \pm \Delta + \omega_m$, will no longer line up with cavity resonances. The resulting phase shifts then lead to an AM signal recovered by the detector viewing the transmitted light. In practice, the two sidebands also make limited contributions to the overall laser-cavity locking error signal and they will partially offset the contribution provided by the carrier. The net result is that the laser frequency will be shifted back by its servo in the amount of $x = 2\omega_m J_1(\beta)^2$, where $x$ is derived from the requirement that $x J_0(\beta)^2 - 2(\omega_m - x)J_1(\beta)^2 = 0$. Here we have used the approximation that $J_0(\beta)^2 + 2 J_1(\beta)^2 = 1$, valid for the interesting range $\beta \leq 1$. However, this shift of locking point causes little effect on the signal detection because it is very small ($<100\,\text{Hz}$) compared with the cavity linewidth, which is typically a few tens of kHz.

Taking into account the nonlinear molecular phase shift $\phi$ and the additional phase shift $\phi_x$ due to the small change in the locking offset, we can express the field of the cavity-transmitted light in the following form,

$$E_t(t) = E_t(0)[J_0 \exp[-i(\omega t - \phi_x)] + J_1 \exp[-i((\omega + \Delta)t + \phi - \phi_x)]$$
$$- J_1 \exp[-i((\omega - \Delta)t + \phi - \phi_x)]] \qquad (12)$$

We can see that the locking offset phase shift ($\exp[-i\phi_x]$) is a common factor for all three contributions and can be factored out. The signal current at the modulation frequency $\Delta$ can be readily derived as

$$i_s \propto J_0(\beta)J_1(\beta) \sin(\phi) \sin(\Delta t) \approx J_0(\beta)J_1(\beta)\phi \sin(\Delta t). \qquad (13)$$

The signal has a pure dispersion line shape and is independent of the laser/ cavity locking point. An important aspect of this line shape is that it contains only the odd-symmetric response $\sim \phi \sin(\Delta t)$, and so the line shape and the apparent line center position are independent of any less than optimal setting of the RF detection phase at $\Delta$.

To reject further noise and minimize baseline drift, a small dither can be applied on the cavity resonance (with the modulation amplitude matching the width of molecular resonance) at a low audio frequency. This allows a lock-in detector to process the demodulated RF signal from the output of the double-balanced mixer that is driven at frequency $\Delta$. Hence, the line shape from the RF channel, resulting from modulation detection of an isolated dispersion resonance, approximates the derivative of a dispersion profile [55]. Indeed, a theoretical line shape fits the experimental data rather well, as shown in the bottom curve of Fig. 6.

As explained earlier, another way to detect the intracavity signal is by simply dithering the cavity resonance onto which the laser frequency is locked. Lock-in detection is applied to the transmitted light. We refer to this low-frequency operation as DC detection, to differentiate it from the high-frequency RF approach of NICE-OHMS. The line shape
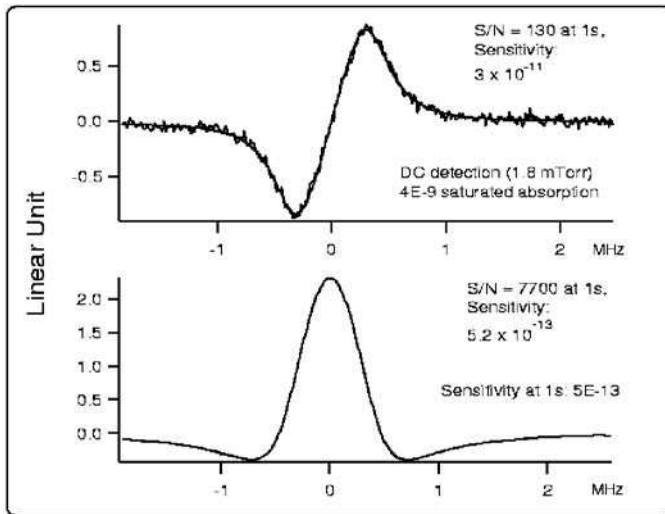


Fig. 6. Sensitivity measurement of the NICE-OHMS technique. The upper graph shows the size of the saturated absorption signal while the lower graph shows the corresponding $S/N$ obtained via NICE-OHMS detection. The noise equivalent detection sensitivities (normalized to 1s time constant) are $3 \times 10^{-11}$ for cavity dither detection and $5.2 \times 10^{-13}$ for NICE-OHMS.

measured by DC detection follows the original Wahlquist formula for a modulation-broadened, derivative line shape [54,55]. Figure 6 shows the experimental sensitivity achieved using 1.8 mTorr of gaseous $C_2HD$. The transition under study is the $(\nu_2 + 3\nu_3)$ P(5) overtone line of $C_2HD$. The cavity finesse here is 100,000 and the intracavity power $\approx 300\,\mathrm{W}$, giving a saturation parameter of $\approx 1.75$ and a saturation peak contrast of 13.2%. The single-pass (46.9-cm-long cavity) linear absorption is about $3 \times 10^{-8}$. Therefore the absolute level of saturated absorption by the intracavity molecules is $4 \times 10^{-9}$. This is verified by the DC detection of the cavity transmission, shown in the top graph of the figure. With the laser locked to the cavity with a relative linewidth of $\approx 1\,\mathrm{mHz}$, the simple cavity-dither and lock-in detection of the transmission yields a $S/N$ (amplitude/rms noise) of 130 at 1 s averaging. This corresponds to a detection sensitivity of $3 \times 10^{-11}$ at 1 s. The corresponding $S/N$ from NICE-OHMS detection is 7700 with a 1 s time constant, as shown in the bottom graph of the figure. This translates into a noise-equivalent detection sensitivity of $5.2 \times 10^{-13}$ at 1 s averaging, $\approx 1.5$ times worse than the calculated shot-noise limit. The NICE-OHMS result is about sixty times better than the straightforward dither detection, because of its higher modulation frequency and its insensitivity to the laser frequency noise relative to the cavity. We emphasize that the gain in sensitivity by NICE-OHMS over simple dither detection is even more impressive when the laser is not well stabilized to the cavity. This high detection sensitivity of the NICE-OHMS method has opened up many possible spectroscopic applications, especially for studies of weak, high-order vibration overtone transitions of various molecules of interest. For example, weak transitions of $C_2HD$ [59], $C_2H_2$ [62,63], $CO_2$ [61], $O_2$ [26], $CH_4$ [64], $CH_3I$ [65], and $H_2O$ in the near infrared regions have already been investigated using the NICE-OHMS approach.

Comparing NICE-OHMS and DC signals gives us an appreciation for the noise-immune nature of the NICE-OHMS detection, as shown in Fig. 7. This figure shows signals collected using the two techniques under two different laser/cavity lock conditions. In one set of experiments, the laser and cavity were tightly locked, and in the second, the laser/cavity lock was deliberately set to be loose and even oscillating. We can now compare the recovered $S/N$ ratios before and after the lock was sabotaged. The DC detection of the intracavity molecular absorption (upper row) is shown to be critically dependent upon the performance of the laser/cavity lock. (A fast laser/cavity frequency-lock servo was used for the graphs obtained in the left column while a slow and noisy servo was used for those in the right column.) However, increased laser frequency noise relative to the cavity has little effect on FM detection (bottom row).
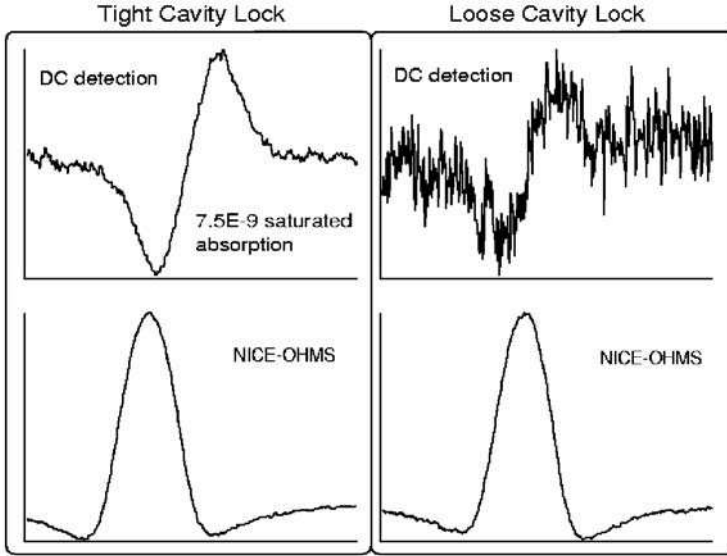
Fig. 7. Demonstration of the noise-immune property of the NICE-OHMS technique. The $C_2HD$ ($\nu_2 + 3\nu_3$) P(5) resonance signal is recovered by both cavity-dither lock-in (DC) detection and the NICE-OHMS technique, under the conditions of a tight laser/cavity lock (left column) and a poor lock (right column).

There is an optimum value of the intracavity sample pressure for the maximum signal size. An increase of pressure raises the linear absorption, but at the same time reduces the level of saturation because of the pressure-broadening of the homogeneous transition width. For fixed cavity parameters, change of pressure also influences the input power coupling. A useful model of this behavior is based on an axially averaged field picture [66,67] in which the moving molecules interact with the average standing intracavity field. At line center, the counter-propagating waves interact with the same molecules, thus causing the absorption coefficient to be reduced from the off-resonance value of $\alpha_0/\sqrt{1+S}$ to $\alpha_0/\sqrt{1+2S}$. Here $\alpha_0$ is the linear absorption coefficient at the center of the Doppler profile and $S$ is the saturation parameter. The observed nonlinear signal is thus proportional to

$$\Delta\alpha = \frac{\alpha_0}{\sqrt{1+S}} - \frac{\alpha_0}{\sqrt{1+2S}}.\tag{14}$$

To perform detailed calculations on signal size, we use Eqs. (2) and (3) to determine the cavity transmission, along with the following useful

relations: $\Delta n = (\Delta \alpha \lambda)/(4\pi)$, $\alpha_0 = \alpha_p \cdot P$, $S = I/I_{\text{sat}}$, and $I_{\text{sat}} = I_0 \cdot (\Gamma_T + \Gamma_0 \cdot P)^2$. Here $\Delta n$ is the refractive index change caused by the saturated molecular resonance; $\alpha_p$ is the molecular absorption coefficient per unit length and unit pressure; $P$ is the gas pressure; $I_{\text{sat}}$ is the required saturation intensity; $\Gamma_T$ is the residual linewidth, at zero pressure and zero power attributable to transit time broadening; $\Gamma_0$ is the pressure broadening coefficient; and $I_0$ is a power-scaling constant that can be determined experimentally. The natural linewidth ($\approx$ kHz) of a vibrational overtone transition is negligible in a saturation calculation because transit time broadening at room temperature is typically a few hundred kilohertz for a normal cavity mode waist size. Under the current settings of cavity finesse and $C_2HD$ overtone transition strength, the optimal pressure is $\sim 10$ mTorr.

## G. NICE-OHMS Application: Highly Stable Optical Frequency Standards and Molecular Dynamics of High-Vibration States

The NICE-OHMS technique can provide information about the line centers for weak molecular lines in the visible wavelength region at metrological precision. The narrow linewidths associated with saturated line shapes are especially useful, as the line centers are narrowly defined, which improves the long-term stability of a light source locked to such a transition. Moreover, the high $S/N$ ratio improves short-term stability, permitting more effective comparisons between various frequency standards. For example, although the transition strength of the $C_2HD$ overtone line is $\sim 1$ million times weaker than the $I_2$ electronic transition commonly used for laser frequency stabilization at 532 nm, the obtained $S/N$ for $C_2HD$ via NICE-OHMS is only slightly smaller than that of $I_2$. With a narrower linewidth, the resultant frequency stability of a $C_2HD$-based system becomes comparable to that of the $I_2$-stabilized system [68,69].

The NICE-OHMS spectrometer provides laser frequency discrimination information relative to both the cavity resonance and the molecular transition. It is thus an ideal system with which to achieve simultaneously good short- and long-term frequency stabilizations. We should note that although the required laser/cavity locking is much more relaxed for NICE-OHMS than for direct cavity transmission detection, the laser linewidth still needs to be narrowed so that a stable optical power is effectively coupled into the cavity. For metrology purposes, this laser/cavity locking loop serves as the short-term frequency stabilizer. Modern laser cavity stabilization loops can routinely track the laser frequency to the cavity resonance to within a few millihertz. The vibrational noise and long-term drift in the cavity can be suppressed by stabilizing the cavity to an

intracavity molecular resonance. The NICE-OHMS signal is intrinsically dispersive when the molecular resonance is probed by the carrier of the FM triplet. Used for locking, this could basically eliminate the influence of the local oscillator frequency drift on the recovered line center. In practice it is necessary also to dither the cavity length and make a second-harmonic signal recovery of the RF mixer output. This is partly to suppress the baseline-offset problem associated with the imperfect FM modulation at the *FSR* frequency. Another important issue concerns the final line shape under the conditions of FM with a residual AM part (RAM) [70,71]. The effect of RAM is to add an even-symmetric absorption-phase component to the originally pure dispersion line shape. Unfortunately, this line shape alteration caused by RAM cannot be corrected by the cavity-dither process. To achieve the best stabilization results, it is crucial that the FM has a zero (or at least a small constant) residual AM.

   To demonstrate that NICE-OHMS is useful for laser frequency-stabilization, a Nd:YAG laser at 1.064 μm stabilized on an overtone transition of $C_2HD$ is compared against a frequency-doubled Nd:YAG/$I_2$ reference system [68]. (The 532 nm-stabilized laser has a stability $\approx 5 \times 10^{-14}$ at 1 s, as determined from beating experiments with two $I_2$-stabilized systems.) Figure 8 shows the counted beat frequency versus time. The drift is $\sim 5$ Hz/h and has a 60 Hz frequency noise at 1-s counter gate time, in agreement with the $S/N$ available from the $C_2HD$ resonance at 1.064 μm. One representation of frequency stability is the Allan variance [72], which is determined by comparing adjacent frequency measurements and then averaging over the whole data set. For a set of $N$ frequency measurements, $f_n$, each with a sampling time $\tau$, the corresponding Allan variance is defined as $\sigma_y^2(\tau) = 1/(2(N-1)) \sum_{n=1}^{N-1} (f_{n+1} - f_n)^2$. The Allan variance permits one to separate and isolate different noise processes based on their
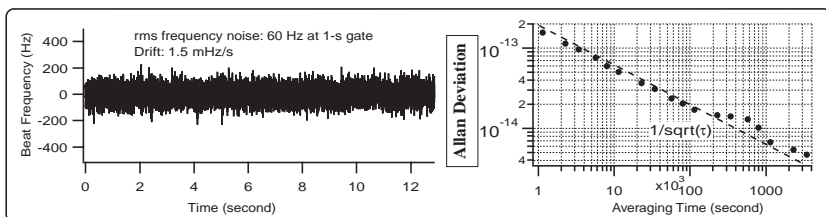


FIG. 8. Stability of beat between $I_2$-stabilized and $C_2HD$-stabilized Nd:YAG lasers. Allan deviation is determined from the beat record. The frequency noise of the beat is still limited by the $C_2HD$ system, which is about three times worse than the $I_2$ system. However, the strength of the $C_2HD$ transition is about one million times weaker than the $I_2$ transition.

characteristic time scales. Rather than the variance, it is customary to plot its square-root, called the Allan deviation. In the short-time domain, the Allan deviation typically displays a slope of $1/\sqrt{\tau}$, where $\tau$ is the averaging time. This is because the main contribution to the fast noise originates from white frequency noise, for example, shot noise. One sees from this argument that the level of this short-term deviation is controlled by the ratio between the frequency discrimination linewidth and its $S/N$. Figure 8 also shows the Allan deviation determined from the beat record of the two stabilized lasers. The frequency deviation is normalized to the optical carrier frequency, i.e., $282\,\mathrm{THz}$ ($1.064\,\mu m$). The Allan deviation of $\sigma_y = 2 \times 10^{-13}/\sqrt{\tau}$ improves to $6 \times 10^{-15}$ at a longer integration time ($>1000$ s). This frequency stability, achieved by locking to an extremely weak reference transition, is a direct result of the spectrometer's high detection sensitivity. Notice that the $C_2HD$-stabilized system shows only three times more frequency noise than the $I_2$ system, which is notable because the $I_2$ transition strength is approximately a million times stronger.

One approach to reducing some of the systematic shifts of the reference frequency is to slow down the motion of the target quantum absorber, thereby reducing the second order Doppler effect. Slower speeds also imply longer interaction times. Slower molecules give a narrower linewidth because the natural lifetime of vibrational transitions usually far exceeds (more than 300 times, for the acetylenes) the transit-controlled interaction time, limited by the laser field dimensions. While effective schemes for molecular cooling and trapping are emerging, optical selection of slow molecules based on interaction time has been actively pursued since the late 1980s [73–75]. The idea is this: the homogeneous linewidth originating from collisional broadening can be reduced by lowering the gas pressure until the mean-free-path of molecules becomes much larger than the transverse dimension of the optical field. This is referred to as the transit-time regime. To optically select slow molecules, a low optical power is necessary so that the low Rabi frequency leads to appreciable saturation only for the slowest molecules. The observed signal is thus dominated by interaction with the slowest molecules and consequently the effective interaction time is increased, limited finally by saturation and residual pressure broadening. Unfortunately, this avenue toward linewidth reduction is expensive in $S/N$, scaling approximately according to the fifth power of the instrumental resolution increase.

In the free-flight regime, molecules with the mean thermal velocity cross the laser beam without suffering any collision. In other words, if we define the collision-broadened homogeneous linewidth (the half-width at half maximum) as $\Gamma_p$ and the transit-time linewidth as $\Gamma_T$, then $\Gamma_p \ll \Gamma_T$, with

$\Gamma_T = (\pi/4) \langle V_\perp \rangle/w_0$, where $w_0$ is the laser beam-waist radius and $\langle V_\perp \rangle$ is the mean transverse velocity. The situation changes for the slowly moving molecules. In fact, the slowest molecules are those with transit times longer than the inverse of the collisional linewidth $\Gamma_p$. Therefore these molecules are in a collisional regime and they have a constant and velocity-independent saturation parameter $S$, controlled primarily by the collisional broadening,

$$S = \frac{\mu^2 E^2}{\hbar^2 \Gamma_p^2},\tag{15}$$

where $\mu$ is the transition dipole moment and $E$ is the optical field amplitude. Faster molecules with transit time shorter than $1/\Gamma_p$ are in a free-flight regime, and their saturation parameter depends on their transverse velocity. Defining $\tau$ as the interaction time ($\approx 4w_0/V_\perp$), then $S$ equals unity when $(\mu E/\hbar)\tau = \pi$. The optical power required to saturate molecules with transverse velocity $V_\perp$ is thus

$$\text{Power}_{(S=1)} = \left(\frac{c\varepsilon_0}{2} E^2\right)\pi w_0^2/2 = \frac{c\varepsilon_0}{2}\left(\frac{\pi\hbar}{\mu}\frac{V_\perp}{4w_0}\right)^2\frac{\pi w_0^2}{2} = \frac{\pi^3}{64}\frac{\hbar^2 c\varepsilon_0}{\mu^2}V_\perp^2.\tag{16}$$

Interestingly, the saturation power is independent of the optical field mode size in the free-flight regime. However, the necessary saturation power does increase as the square of the transverse velocity, and it can be vastly different for slow and average thermal molecules because it has been assumed that $\Gamma_p \ll \Gamma_T$. In short, a sufficiently low gas pressure can be used to create a free-flight regime, and a low power laser beam then optically selects for the slow molecules. The selection is based on the saturation effect in the recovered resonance signal. The resulting signal linewidth becomes strongly inhomogeneous, with molecules from different transverse velocity groups contributing different intensities and widths. Slow molecules will dominate the contribution to the signal amplitude, and the width is essentially the homogeneous linewidth $\Gamma_p$. Faster moving molecules will see a reduced saturation and will mostly contribute to the wings of the resonance. The width is caused by transit effects and increases with velocity.

   This concept has been demonstrated using NICE-OHMS. In the experiment, a $< 2\,\text{mTorr}$ sample gas was used, and the mean-free-path of molecules is $\sim 30$ times longer than the transverse optical field dimension. The cavity input power was reduced by almost two orders of magnitude from normal operation. Although the intrinsic transition width associated

with the $(\nu_2 + 3\nu_3)$ P(5) line of $C_2HD$ is on the order of kHz, the observed linewidth (FWHM) is 705 kHz under normal experimental conditions similar to those of Fig. 6. This linewidth includes contributions from the power-saturation and pressure-broadenings of the 270 kHz transit time linewidth. Working with slow molecules Fig. 9 shows a resonance linewidth of $\sim 20$ kHz. This is thirteen times narrower than that set by the room temperature transit-time-limit and is mainly limited by the relatively high pressure (1.8 mTorr). The selected molecules have a temperature of $\approx 1.8$ K. The $S/N$ ratio is vastly reduced, as the optical power is much smaller than usual and the majority of molecules do not contribute to the observed saturation signal. In fact, compared with the number of molecules participating in normal saturation spectroscopy, the slow molecule selection process has selected only a fraction of 0.75%. At present the limited $S/N$ associated with the low power has prevented us from taking full advantage of this narrow linewidth. With an improved system this approach will enable us to access the information of free molecules with minimized second order Doppler shift, thereby creating an optical frequency standard of potentially high accuracy.
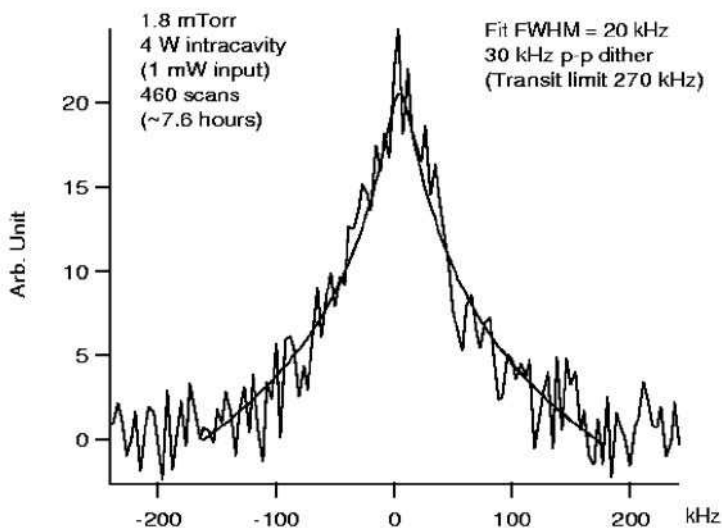


FIG. 9. With low power and low gas pressure, optical selection of slow molecules produces a linewidth thirteen times below the room-temperature transit-time-limit.

# V. Weak Absorption Measured by Field Decay (Time-Domain)

This section discusses cavity-enhanced methods for measuring very weak absorptions in the time domain. In these measurements, two cavity modes, one probing the empty cavity and the other probing intracavity absorption, are present simultaneously but their intensities are switched temporally out of phase, with one mode decaying and the other rising, when viewed in cavity transmission. Heterodyne detection between the two modes reveals the dynamic time constants associated with the empty cavity and the intracavity gas absorption. Quick, differential measurement eliminates low frequency technical noise. This is essentially an improved version of the cavity ring-down technique and it yields a $1 \times 10^{-10}$ absorption sensitivity using microwatt-level laser powers.

## A. Introduction to Cavity Ring-Down Spectroscopy and Overview of the Field

Inside a high-finesse cavity, light completes many round-trips, and this effectively increases the path length by $(2F/\pi)$. Cavity ring-down spectroscopy (CRDS) exploits this cavity-enhancement property by measuring the decay of the intracavity field during these many round-trips. Because the decay rate increases when an absorber is placed inside the cavity, this method can be used as a spectroscopic tool. For example, an unknown absorption coefficient is determined by comparing the known mirror losses to the cavity losses in the presence of the absorber. Ideally, the mirror losses should be of the same order of magnitude as the absorption level to be measured, because this makes the "background" comparable to the "signal" and increases the measurement sensitivity. Because CRDS measures the decay dynamics after the field has built up inside the cavity, it largely eliminates the technical noise of the incident radiation field.

However, as commonly implemented, CRDS has two shortcomings. The first is that CRDS, in its ordinary form, is a long time-interval measurement. Two decay-time measurements are made, one on the empty cavity decay and the other on cavity plus sample. The difference between the two measured decay rates contains the desired intracavity absorption information. However, the time between the two measurements allows slow drifts and other technical noise to contaminate the data. The second problem is that technical noise is the dominant noise source in the signal beyond the point where the field's shot noise equals the instrument's technical noise. To overcome this limitation, a heterodyne technique was developed [76] that

superimposes a large local oscillator field onto the decay field so that the resultant beat signal can always be shot-noise limited. However some form of modulation strategy is still needed to achieve a rapid differential measurement.

With a modulation technique to compare signal against background at short time intervals, one can accurately subtract background noise from the useful signal. In the context of CRDS, two decay constants are to be compared in quick succession, one associated with the empty cavity loss (off-resonance from the intracavity gas sample) and the other associated with the total intracavity loss. This concept can be realized if two different optical fields are coupled into two cavity modes, one mode centered on the molecular transition and the other far away from it. With the aid of a quick switching between the two frequency components and a subsequent heterodyne detection for their product, it is possible to reach the quantum-noise limited detection sensitivity to within a factor of 4 [60].

## B. Concept of AC Ring-Down—Separating the Ring-Down Fields Associated with Cavity and Molecules

Figure 10 illustrates the basic scheme of the alternating-constant (AC) ring-down method. A continuous-wave (cw) laser beam is split by two acousto-optic modulators (AOMs) into two beams with a frequency offset such that both beams resonate with respective cavity modes simultaneously. The frequency offset is large enough so that only one beam can be tuned onto the intracavity Doppler-limited molecular resonance at a time. The two beams are spatially combined and mode-coupled into the cavity. However, the two optical beams are switched by their respective AOMs, such that only one beam at a time is present at the cavity input. Despite the switching, a detector viewing in cavity reflection is able to maintain the laser/cavity lock using the FM technique [77]. Inside the cavity there is one decaying mode and one rising mode. That is, on the scale of one ring-down time constant, the cavity mode that is being coupled in will rise exponentially while the other mode, with its input switched off, will decay exponentially. The heterodyne beat waveform between the two modes is detected in transmission. Demodulation against the known carrier frequency then yields the heterodyne beat amplitude, which contains information on the dynamic variation of both modes. In the case of an empty cavity, the beat amplitude waveform remains unchanged at neighboring switching cycles. However, when a mode is tuned to a molecular resonance, the system exhibits two slightly different time constants. The beat waveform becomes asymmetric between the adjacent cycles, and the difference is related to the intracavity absorption. The period of a switching cycle can be chosen to
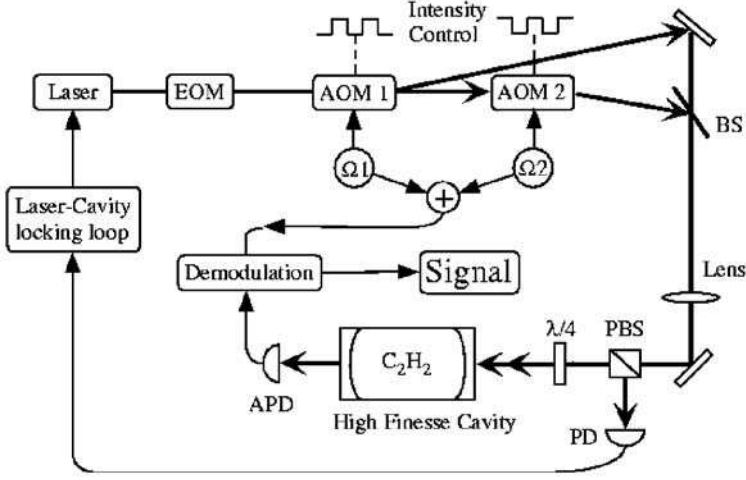
F<span>IG</span>. 10. Experimental set-up for switched heterodyne ring-down spectroscopy. The two AOMs provide the necessary frequency offset between the two cavity modes and are switched out-of-phase. Both beams are stabilized to their respective cavity resonance modes. The heterodyne beat between the two modes at the cavity transmission is demodulated against the known carrier frequency to produce the decay signal. PD: photodiode; APD: avalanche photodiode; PBS: polarized beam splitter.

roughly match the field decay time ($1/e$) of the empty cavity. This technique thus offers a quick comparison of on-resonance and off-resonance information and substantially suppresses technical noise. Because each ring-down waveform is measured during a switching period that is on the order of the $1/e$ field decay time, shot noise dominates throughout the signal acquisition.

To expand the foregoing discussion, consider the following theoretical model for this technique. Suppose the round-trip loss of the empty cavity is $L_{cav}$, the round-trip absorption of the intracavity medium is $2\alpha d$, and the round-trip time of flight within the cavity is $t_{round\text{-}trip}$. For a cavity mode that is far detuned from the sample resonance, the characteristic time constant associated with the mode dynamics is given by

$$\tau_{cav} = \frac{2t_{round\text{-}trip}}{L_{cav}}. \tag{17}$$

We note that this is the $1/e$ decay time of the *field*, a relevant quantity because the heterodyne signal is proportional to the product of the two

fields. For the mode that is tuned to the absorption, the decay time constant becomes

$$\tau_{\text{abs}} = \frac{2t_{\text{round-trip}}}{L_{\text{cav}} + 2\alpha d}. \tag{18}$$

Following the intensity-switching scheme of Fig. 10, let us assume that during the interval $[0, \Delta t/2]$, mode 1 ($E_1$) of the empty cavity is switched on, while mode 2 ($E_2$), which sees the additional intracavity absorption, is switched off. The two field amplitudes evolve as

$$E_1 = c_1[1 + \exp(-\Delta t/2\tau_{\text{cav}}) - \exp(-t/\tau_{\text{cav}})],$$
$$E_2 = c_2 \exp(-t/\tau_{\text{abs}}) \tag{19}$$

Here $c_1$ and $c_2$ are amplitude coefficients for $E_1$ and $E_2$, respectively. In the next half cycle, $[\Delta t/2, \Delta t]$, we reverse the two fields such that mode 1 is switched off and mode 2 on. The product of the two field amplitudes is what we detect in the demodulated signal of the cavity transmitted heterodyne beat. If we compare the signal of the two neighboring half-cycles, we obtain the absorption-dependent signal in the following form:

$$(E_1 E_2)_{[0,\Delta t/2]} - (E_1 E_2)_{[\Delta t/2,\Delta t]} = c_1 c_2 \Big[\big(1 + e^{-(\Delta t/2\tau_{\text{cav}})}\big)e^{-(t/\tau_{\text{abs}})} \\ - \big(1 + e^{-(\Delta t/2\tau_{\text{abs}})}\big)e^{-(t/\tau_{\text{cav}})}\Big]. \tag{20}$$

To determine the fundamental limit of sensitivity obtainable by this method, suppose the two modes have the same amplitude coefficients, $c_1 = c_2 = \sqrt{P_0}$, in transmission, and the light is converted to a photocurrent according to $i = \eta \times P$, where $\eta$ is as before the detector responsivity. The demodulated beat current is $\eta \times 2E_1 E_2/\sqrt{2}$. For simplicity of presentation, we take the small absorption limit, $\tau_{\text{cav}} \approx \tau_{\text{abs}}$, and assume $\Delta t/\tau_{\text{cav}} \geq 10$. The difference signal of Eq. (20) becomes

$$i_{\text{signal}} \approx \eta \frac{2}{\sqrt{2}} P_0 \big[e^{-(t/\tau_{\text{abs}})} - e^{-(t/\tau_{\text{cav}})}\big] = -\eta\sqrt{2}P_0 e^{-(t/\tau_{\text{cav}})}\big[1 - e^{-t((1/\tau_{\text{abs}})-(1/\tau_{\text{cav}}))}\big]$$

$$= -\eta\sqrt{2}P_0\left(\frac{1}{\tau_{\text{abs}}} - \frac{1}{\tau_{\text{cav}}}\right) \times t \times e^{-(t/\tau_{\text{cav}})}. \tag{21}$$

Because the beat amplitude reaches a maximum when $E_1 = E_2$, we have $\exp(-t/\tau_{\text{cav}}) \approx 1/2$, and $t = \tau_{\text{cav}} \ln 2$. Using Eqs. (17) and (18), we obtain

$$i_{\text{signal}} = -\eta\sqrt{2}P_0\tau_{\text{cav}}\frac{\ln 2}{2}\frac{2\alpha d}{2t_{\text{round-trip}}} = -\eta P_0 \frac{\ln 2}{\sqrt{2}}\frac{2\alpha d}{L_{\text{cav}}}. \tag{22}$$

The shot noise produced by the photocurrent, $i_{DC} = \eta \cdot 2\big((\sqrt{P_0})/2\big)^2 = \eta P_0/2$, is $i_{noise} = \sqrt{2eB \times \eta P_0/2}$. The resultant $S/N$ is thus,

$$\left|\frac{i_{signal}}{i_{noise}}\right|_{\substack{shot\\noise}} = \sqrt{\frac{\eta P_0}{eB}} \frac{\ln 2}{\sqrt{2}} \frac{2\alpha d}{L_{cav}}. \tag{23}$$

To find the noise-equivalent sensitivity of single pass integrated absorption, we set $S/N = 1$, and obtain

$$(\alpha d)_{min} = \frac{1}{\ln 2} \sqrt{\frac{2eB}{\eta P_0}} \frac{L_{cav}}{2} = \frac{2}{\ln 2} \sqrt{\frac{2eB}{\eta P_0}} \frac{\pi}{2F}. \tag{24}$$

Compared to Eq. (8), we see that except for a numerical factor of $\sim 3$, shot noise limited AC ring-down spectroscopy provides a detection sensitivity enhanced by the familiar factor of $(2F/\pi)$ over the fundamental limit of direct absorption measurement.

To relate the model to experimental observations, Fig. 11 visualizes switching results obtained from Eqs. (19) and (20). The switching period, $\Delta t$, is chosen to be $4\tau_{cav}$, and the time axes have been normalized to $\tau_{cav}$. In the case of an empty cavity, shown in the right column, the switched waveforms of mode 1 and mode 2 are totally symmetric, resulting in an equivalent signal of the beat amplitude during adjacent half-cycles; thus the difference gives a zero baseline. When mode 1 and mode 2 see different intracavity loss, as shown in the left column of the figure, there is a clear asymmetry in the heterodyne beat amplitudes between the adjacent half-cycles. The differences, as plotted in the bottom curve, show the level of additional absorption. In this case, the sample absorption is 10% of the empty cavity loss.

## C. Experimental Results of AC Ring-Down Spectroscopy

The concept discussed in the preceding section has been demonstrated in the measurement of rovibrational transitions of acetylene. The experiment used a Yb:YAG laser. The transition involved was the $3\nu_3$ R(29) overtone resonance of $C_2H_2$, located at 1031.6528 nm, with an absorption coefficient of $4 \times 10^{-6}$ $(Torr \cdot cm)^{-1}$. In the 46.9 cm long cavity with a finesse of 90,000, a few milliTorr (1 Torr = 133 Pa) of gas was typically used, giving an adsorption level of $1 \times 10^{-6}$. The beam switching frequency was 1.4 kHz, corresponding to $\Delta t = 714$ µs. The cavity transmission was received by an avalanche photodiode (APD), and the beat signal was sent to an RF
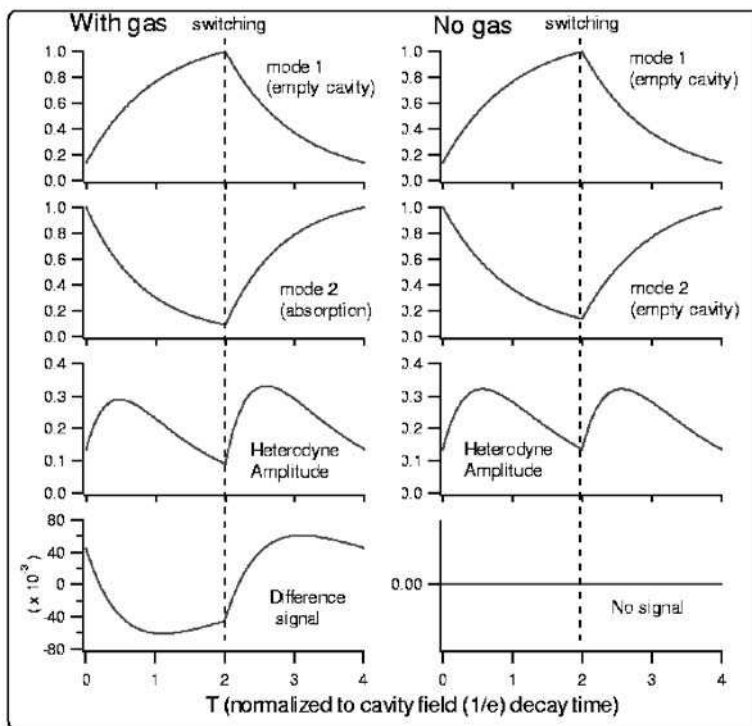
FIG. 11. Comparison of the demodulated ring-down curve between the empty cavity (right column) and the cavity with additional absorption (left column). The switching period $\Delta t = 4\tau_{cav}$, and the time axes are normalized to $\tau_{cav}$. Shown from top to bottom are the switching dynamics of mode 1, mode 2, their product (beat), and the difference signal between the neighboring half cycles.

spectrum analyzer for demodulation. The frequency reference of the RF spectrum analyzer was connected to the RF signals used to drive the AOMs. In the linear amplitude display mode, the video output of the spectrum analyzer in zero-span-mode provides a phase-insensitive demodulation for the heterodyne beat. To measure the empty cavity finesse, both mode 1 and mode 2 were tuned out of the molecular resonance. The experimental results were in excellent agreement with the model presented above.

Mode 2 is then tuned to the center of the acetylene resonance, and the ring-down waveform becomes clearly asymmetric in the neighboring half cycles. Figure 12 shows a set of experimental data where intracavity gas pressure was varied to generate four different intracavity absorption levels (expressed in terms of single-pass in the graph). The respective ring-down

Fig. 12. Demodulated heterodyne beat amplitudes between the two switched cavity modes (left column) in the presence of intracavity absorption (labeled in the graph). Shown in the right column is the absorption signal obtained by differencing the beat amplitudes in the adjacent half cycles.

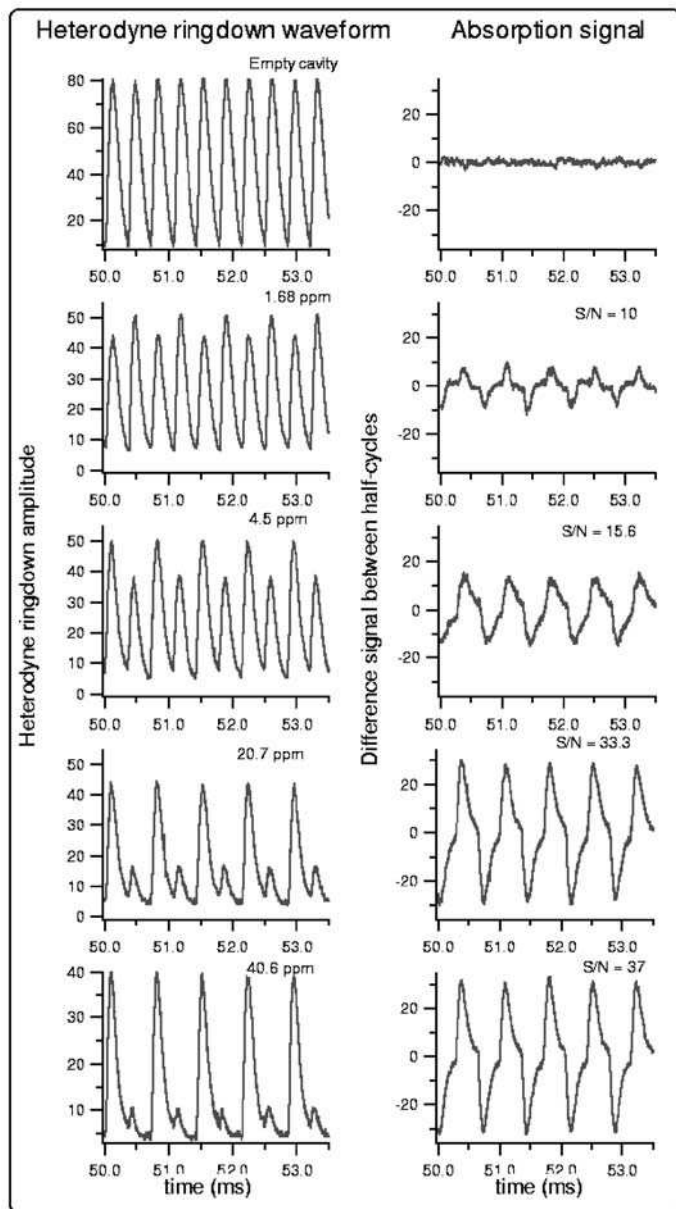beat waveforms are shown in the left column of the figure. The absorption data (shown in the right column) were produced in the following way. First, a copy of the original data was shifted by a half switching cycle along the time axis. The differences between the original data and the shifted data gave the absorption signals. With a single pass absorption of $1.7 \times 10^{-6}$, the absorption sensitivity normalized to 1 s averaging time was $1.6 \times 10^{-10}$. In steady state (no switching), each mode has $3\,\mu\text{W}$ ($P_0$) in the cavity transmission. Given an $\eta$ for the APD of $0.3\,\text{A/W}$, the shot-noise limited sensitivity is $\sim 1.2 \times 10^{-11}$ at 1 s averaging. However, because the APD has an excess noise factor of $\sim 3$ the expected minimum absorption sensitivity was $\approx 4 \times 10^{-11}$, which is within a factor of 4 of the experimental results.

Further improvement of the system includes the use of faster switching cycles and the replacement of the APD with a sensitive P-I-N diode in a resonant matching circuit. At present the switching frequency is limited by the locking loop between the laser and the cavity. After all, the sideband locking system also uses the heterodyne principle, in this case the beat is between the field of the direct reflection off the cavity input mirror and the field leaked out from the cavity storage. If the mode is switched too fast, the cavity field does not have sufficient time to establish itself as the frequency/phase reference for the incident instantaneous laser field to compare against. An alternative is to stabilize the laser on the cavity with a third mode, completely away from the molecular resonance and independent of the other two modes. The third mode can be left on continuously to maintain lock while the switching can go on as before between the first two modes. The heterodyne detection RF system can conveniently filter out the contribution from the third mode. The only penalty in this arrangement is a somewhat increased level of shot noise, resulting from the added contribution of the third mode to the photocurrent. A hybrid of the on-resonance/off-resonance switch with transmission heterodyne detection against the third mode is another clear avenue for high-sensitivity detection.

# VI. From Optical Frequency Metrology
# to Ultrafast Technology

Optical cavities have played a central role in laser stabilization and related precision optical frequency metrology over the past three decades [78]. To stabilize a laser, one needs to employ some kind of resonance information to derive a frequency/phase-dependent discrimination signal. The resonance can be of material origin, such as modes of an optical cavity, or of natural origin, such as atomic or molecular transitions. The saturation of an atomic

transition limits the attainable $S/N$ for the servo error signal, which in turn limits the useful bandwidth of the stabilization loop. In contrast, an optical cavity can provide a high contrast and basically unlimited $S/N$ for resonance information. Suitably narrow resonance linewidths can be easily accommodated with modern technologies of low loss mirror coatings. Careful design and control of the material properties can bring the stability of an optical cavity to a satisfactory level. For the most demanding applications in ultrahigh-resolution laser spectroscopy [79] and high-precision optical frequency metrology, an optical cavity has become an indispensable tool to narrow the linewidth of a laser so that it can be effectively used to interrogate optical transitions of extraordinary $Q$. When the desired property of a stabilized laser is its long-term stability or reproducibility, the use of a natural resonance then becomes necessary, often in combination with the use of a pre-stabilization cavity. Discussions presented in Section IV.G provide an example of this strategy. With the recent emergence of a remarkable synergy between cw laser-based precision optical frequency metrology and mode-locked ultrafast lasers [80], precision control of the frequency spectrum of a mode-locked laser, and consequently of the time-domain evolution of its carrier-envelope phase, has been actively pursued with great success [81]. A passive optical cavity has now been used to directly stabilize a mode-locked femtosecond laser [82].

To accommodate this diverse set of applications, it is important to develop an improved understanding of the cavity and associated mirror properties. This knowledge is essential for achieving enhanced detection sensitivity, for obtaining optimum system design, and for reducing systematic errors. For example, in cavity QED, one needs to know the mode structure of the intracavity field in order to quantitatively predict the atom-cavity coupling; for frequency metrology, accurate determination of phase shifts of the resonant fields can provide precision frequency markers; for ultrafast laser applications, *a priori* information on spectral phase shift of cavity mirrors determines the intracavity dispersion compensation schemes; and in quantitative spectroscopy, knowledge of the mirror loss sets the accuracy scale of absorption measurement. On the technology development side, the knowledge gained from careful mirror characterization could provide guidelines for the optic coating community to develop in situ measurement and control capabilities of the coating process.

The progress in preparation and understanding of mirrors of exceedingly low reflection losses has indeed been spectacular, with feasible cavity finesse now exceeding 1 million. The art of "superpolishing" substrates to Angstrom-level surface roughness has been developed, augmented by the technique of depositing 40–50 alternating layers of high and low index dielectric materials, leading to mirrors with losses guaranteed to be below

5 parts in a million. Losses of about 1 ppm have been documented over selected submillimeter-squared areas [83]. The resulting sharpness of the associated cavity fringes is breathtaking to contemplate; one fringe full width is represented by a distance below $10^{-2}\,\text{Å} = 10^{-12}\,\text{m}$. When we now feed this interferometer with a milliWatt of technically quiet coherent light, in a 1-s averaging time – if all goes well and we have only shot noise as the limitation – these fringes can be effectively subdivided into about 10 million parts. The resulting distance resolution is $10^{-19}\,\text{m}$! Sensitivity to these incredibly small distances changes has attracted wide attention in many potential applications, including the possibility of building interferometric antennas for gravitational-wave radiation [27,28].

In the following two sub-sections (VI.A and VI.B) we will discuss the application of the cavity-based optical frequency metrology techniques to various precision measurement tasks, such as characterizing cavity birefringence to a level of $\Delta n/n \sim 10^{-17}$ at 1-s averaging time for potential search of vacuum birefringence [84], or establishing a cavity-based optical frequency reference grid with sub-Hertz precision [85]. In VI.C and VI.D we will establish a connection between the recently developed femtosecond-laser-based optical frequency comb technology and high-finesse optical cavities [82] and explore an interesting application of passive amplification of ultrashort pulses based on cavity-assisted control of pulse repetition frequency and its carrier-envelope phase [86].

## A. Mirror Birefringence – A Case Study of Precision Measurement of Cavity Fringes

We will present an example of measurement of optical phase anisotropy across the mirror surface as a useful illustration of the powerful potential of cavity-based precision measurement. Basically by incorporating mirrors of interest as part of an optical cavity, one can expect an immediate precision-enhancement factor similar to the cavity finesse. Shot noise limited determination of the cavity resonance frequency with orthogonal polarizations can potentially resolve birefringence effects another factor of 1 million smaller, limited by one's ability to split the cavity linewidth. Such measurement capability will open up interesting measurements regarding intrinsic mirror properties and their modification by light beams: the Cotton–Mouton effect in various gases [87], the influence of parity-nonconserving effects in chiral molecules, and an interesting test of QED based on magnetically induced birefringence of the vacuum, the so-called "light-by-light" scattering Feynman diagram [30,31,88,89]. With the intracavity light beam of a high-finesse cavity threaded through a string

of strong dipole magnets, the shot-noise limited measurement sensitivity of the cavity resonance would allow detection (and measurement!) of the predicted $\Delta n$ (birefringence) due to QED vacuum polarization ($1.4 \times 10^{-22}$). Furthermore, such an experiment would allow a search for light scalar and pseudoscalar particles (such as the axion), which can couple by a two-photon vertex. The limit for the axion – two photon coupling constant measured by this technique should be comparable to the bound set from astrophysical arguments.

All high grade mirrors are observed to have a different reflection phase-shift (or effective plane of reflection) depending upon the state of polarisation of the incident light. The level of birefringent behavior can be as small as 0.1 µrad differential phase-shift per bounce. Indeed, it is extremely difficult to robustly mount fused silica mirrors without inducing stress-related birefringence. A cavity formed with birefringent mirrors will accumulate the differential phase shift incurred per mirror bounce and magnify it by a factor of $2F/\pi$ at the cavity transmission. This mirror-related cavity birefringence presents an adversity to many high precision measurements using a high finesse cavity. For example, in the measurement of parity nonconservation in Cs atoms, a small systematic error is introduced when the two counter-propagating waves inside the cavity have slightly different polarizations, which results from the existence of cavity birefringence [90]. In optical cavity QED experiments, cavity birefringence prevents the full realization of strong coupling between a closed (cycling) atomic transition and the cavity mode [11]. However, one could also take advantage of this intrinsic birefringence to boost the useful signal level. With an appropriate polarimetric setup, this DC bias can be gainfully employed to convert a quadratic signal of interest to a linear one, with a scaling factor equal to the magnitude of cavity birefringence [91]. Accurately measuring the mirror birefringence could also lead to useful information on surface science. As to scale, a reasonable contemporary "gyro-quality" mirror may show $\sim 10^{-6}$ waves of phase difference at normal incidence for light polarized in two perpendicular linear polarizations. Exceptional mirrors may be three- or even ten-fold less. Note that the high $S/N$ enabled by a cavity configuration (splitting of linewidth) offers us access to another factor of $\sim 10^7$ in terms of sensitivity enhancement.

How can we measure these subtle optical phase shifts precisely? Ideally we will be able to measure them accurately enough so that two measurements taken with some time separation can be found to agree at the level of precision demanded by our applications. But first, operationally, how can we measure the effect accurately? What are the possible tools? It is instantly clear from the numbers quoted above that it is only with frequency-based metrology that we can hope to have the accuracy necessary to deal with an

effect that can range from ~1 wave (one cavity fringe) to $\sim 10^{-13}$ waves ($10^{-6} \times 10^{-7}$) as the dynamic range. The ability of the two polarizations to coexist between the cavity mirrors and then be separated externally with a polarizing prism is very useful since it enables measurement of the birefringent effects differentially between the two polarization modes. If we have a minor amount of residual mirror axial motion (very small relative to the laser wavelength), there will be a tremendous reduction of its consequences because of the "common-mode" nature of this excursion as viewed by the spatially coincident but orthogonally polarized beams. This is exactly the difference between this approach and the gravitational wave experiments such as LIGO that must use the Michelson geometry: In that case the two distant mirrors exist at different spatial locations and the common-mode concept is not present. Only complex and expensive vibration isolation will work to produce the necessary inertial-frame mirrors. By contrast, for a high-finesse birefringence interferometer, the two beams will be spatially overlaid and sample the same mirror surfaces. We need isolation only as good as the fringe-width.

In many cases in precision measurement physics it turns out that an equivalent signal/noise performance can be realized in several different ways. For example, in the proposed QED birefringence experiment, two polarization states of light are resonantly interacting with mirrors with small polarization phase shifts. Theoretically one finds that good performance and sensitivity can be obtained by measuring the differences in the apparent transmission when tuned near the high-slope regions around the half-height of the resonance line shape. A simpler method would be to illuminate the cavity with light polarized at $+45°$ to the birefringence axes, and analyze the transmitted light with a crossed polarizer [92,93]. Another technique is to add some external ellipticity modulation to the beam in order to linearize the signal again via cross-product [94]. Because of the cavity resonance effect, a very small birefringence will detune the two cavity polarization modes by a significant part of a linewidth. A compensating phase-plate in the exit beam can delay the faster component so that the dark fringe condition can be re-established in the polarizer-transmitted light. The birefringence is then the measured phase divided by the cavity finesse $F$. One sees an inconvenience for this method: What happens if our birefringent phase shift is larger than $\pi/F$. Now we cannot excite both modes of the cavity simultaneously, so a lower finesse – broader cavity resonance – must be used.

However, it is clear we prefer to use a very high finesse – this directly increases the sensitivity. We want to use a frequency-based scheme to provide the large dynamic range. For laser-cavity locking, one also prefers to use some appropriate modulation method so that the desired

anti-symmetric resonance curve is produced by synchronous detection at the central tuning condition. A particularly attractive modulation/ detection scheme dubbed the Pound-Drever-Hall technique [77] produces this ''discriminator'' line shape using laser light reflected from the cavity. It is desirable to use a modulation frequency well above the cavity resonance width so that the modulation sidebands are non-resonant, and are therefore essentially reflected from the cavity input mirror. Upon being steered to the detector, these two optical frequencies form the ''local oscillator'' for heterodyne detection of the resonant electric field at the carrier frequency. For the birefringence measurement, there actually are two optical carriers, of crossed polarizations, which are presented to the cavity. They are near or at resonance, leading to strong resonant power buildup inside and to a resulting phase shift of the reflected light that is related to the detuning. Some of these two internal fields leak out, returning to the detector along with the sidebands that were directly reflected as noted before. In this way one can generate the two desired polarization-separated discriminator signals. These detector voltages could be digitized and analyzed for the subtle detuning difference between the two polarization modes, as brought about by the mirror birefringence. For small signals, this would work well. But we need a seven-decade dynamic range to cover the range between the shot noise level and the full signal of one fringe width, and another six or so decades to deal with larger fractional signals where the equivalent birefringence is approaching one wavelength. To deal with such an extreme dynamic range, clearly a possible better choice is to lock two tunable coherent optical sources onto these cavity resonances, one in each polarization, and heterodyne their outputs to recover our signal as a frequency to be counted by a contemporary frequency counter, capable of offering, for example, 12 digits resolution and accuracy in 1 second. Another feasible approach would be to use digitally synthesized frequency sources that can offer a sine-wave output up to tens of megahertz and can be programmed in steps as small as $1 \mu Hz$. Thus this frequency synthesis approach also offers the $> 10^{12}$ dynamic range.

Consider the following reasonable laboratory case of a 1 m-long cavity with $F = 10^5$, working at a wavelength near $0.5 \mu m$. The fringe order numbers are $\sim 2 \times 10^6$, and a change by unity results in the corresponding frequency change of one $FSR$, which is 150 MHz. This $FSR$ is the optical frequency difference we would have if the birefringence were 1/2 wavelength (one fringe). The fringe width is $FSR/F = 1.5$ kHz. For $\sim 1$ mW detected power, the shot noise-determined $S/N$ is $\sim 6 \times 10^4$ in a typical 100 kHz control bandwidth, leading to frequency excursions of $\Delta = 25$ mHz rms. The equivalent noise spectral density is $\sqrt{S_\nu} = \Delta/\sqrt{B} = 80 \mu Hz/\sqrt{Hz}$.

Since the modulations at the fast Fourier frequencies accumulate little optical phase, one can expect that the Lorentzian linewidth of the stabilized laser under these ideal conditions would be $\delta\nu_L = \pi \cdot \left(\sqrt{S_\nu}\right)^2 = \pi \cdot S_\nu = 0.02\,\mu\text{Hz}$ [95]. In principle we can lock the laser this accurately to the cavity fringes. The shot noise-limited equivalent birefringence for a 1 s measurement would be $\sqrt{2}\sqrt{S_\nu}/\sqrt{2\pi\tau} = 45\,\mu\text{Hz}$. (The $\sqrt{2}$ comes from subtracting two somewhat noisy values to obtain the birefringence.) This $45\,\mu\text{Hz}$ sensitivity is to be compared to the 150 MHz that corresponds to the *FSR* (i.e., a phase change of $\pi$), giving an ideal sensitivity of $3 \times 10^{-13}$ of a fringe in 1 s, or equivalently $1 \times 10^{-13}$ radians. The cavity resonance linewidth can be split by a fraction of $45\,\mu\text{Hz}/1.5\,\text{kHz} = 3 \times 10^{-8}$. Of course, the ultimate resolution limit of the minimum-detectable birefringence changes can be as small as $\sqrt{2} \times 20\,\text{nHz} \approx 28\,\text{nHz}$, provided that the experimental integration time can be extended until the discussion of the coherent laser linewidth becomes meaningful and can be gainfully employed for the measurement process. Of course, given the linewidth of 20 nHz, this integration process may not seem practical. In terms of a differential index of refraction sensitivity, if the entire cavity were filled with some gas with magnetically induced birefringence (the Cotton–Mouton effect) for example, this rather straightforward approach would bring us in a 1 s averaging time a birefringent index of refraction sensitivity of $5 \times 10^{-23}$. Here we have used the relation $\Delta n/n = \Delta f/f$. This shows the powerful potential of a cavity-based frequency measurement approach.

## B. Mirror Dispersions, Cavity Mode Spacing, and Cavity-Based Frequency References

In addition to discussions presented in the previous section, precise measurement of reflective mirror phase shifts is instrumental for accurate determination of wavelengths [96,97]. This has not only played an important role in length metrology, but has also served as an attractive route for the determination of optical frequencies in the visible region since the speed of light is now a defined quantity. Of course the second scenario has changed dramatically since the recent introduction of the femtosecond comb laser for direct absolute optical frequency measurement. There has also been extensive research on using the cavity resonant modes to serve as a bridge between RF/microwave frequencies (represented by *FSR*) and the optical frequencies in the visible [85,98,99]. For this approach to work effectively, it is important that the cavity mode spacing (*FSR*) is examined and characterized at a high precision. Considering the inevitable dispersion

associated with mirror coatings (especially for the low loss dielectric coatings), the cavity *FSR* is expected to vary with wavelength.

DeVoe *et al.* reported the first detailed and precise measurement of the wavelength-dependent variation of cavity *FSR* near the center wavelength of a mirror coating [85]. That work indicates that the cavity *FSR* will generally vary quadratically around the coating center wavelength and the variation can be determined with sub-hertz precision. High cavity finesse and precision splitting of cavity fringes facilitated by FM-sideband-based laser-cavity locking helped to achieve this level of measurement precision. Empirical calibration of the cavity modes allows the cavity to be used effectively for difference frequency measurement in the optical domain without systematic errors associated with theoretical modeling based on Maxwell's equations. However, this difference frequency measurement is incoherent as all information about the relative optical phase is lost. Furthermore, the attempt to perform absolute optical frequency measurement is still hampered by the need to determine the geometry-related diffraction phase shift and the inevitable drift of cavity properties.

The DeVoe work first introduced the two-tone EOM approach for cavity-related frequency measurement, and was thus the inspiration for the NICE-OHMS technique presented earlier. Indeed, NICE-OHMS also provides an attractive approach for measurement of cavity *FSR*. The basic principle has been illustrated in Section IV; here we will concentrate on some operational details. For NICE-OHMS to take full advantage of noise cancellation, it is important that we maintain a perfect match between the cavity *FSR* and the FM sideband frequency. However, since the laser itself is locked on the cavity, the information about the match between the sideband frequency and *FSR* cannot be obtained by simply detecting and demodulating at the sideband frequency in the cavity reflected light, which always yields a null signal. We choose to use an additional FM dither modulation on the sideband frequency itself, along with synchronous detection of this component in the cavity-reflected or transmitted light. To maintain a clean separation between the modulation and control processes, the RF sideband frequency is synthesized from two signal sources, a stable frequency synthesizer and a tunable frequency voltage-controlled crystal oscillator (VCXO). The sum frequency is band-pass filtered and amplified before it is fed to the corresponding electro-optic modulator. This configuration allows us to separate the modulation process, where an FM dither signal is applied to the frequency synthesizer, from the servo process where the frequency of the VCXO is controlled from the cavity error signal. In doing so we are able to obtain a better modulation quality and also avoid any change of modulation parameters

when the VCXO is tuned. This additional dither frequency is low, typically in the range of 10–300 kHz. Phase-sensitive detection is at the dither frequency and allows locking for the maximum transmission of the sideband. This leads to tracking between the sideband frequency and cavity *FSR*. Figure 13 shows the counted (gate time 1 s) frequency record of the VCXO under the locked condition, with the same cavity used for NICEOHMS detection of the $C_2HD$ resonance at 1.064 μm ($FSR \sim 320$ MHz and a finesse of 96,000). After removal of the cavity-associated frequency drift of 5 mHz/s, we have rms noise in the frequency readout about of 40 mHz at 1-s averaging time. We have not achieved shot-noise limited performance in this case due to the technical noise arising from the residual amplitude modulation (RAM) associated with the FM sideband generation. The RAM also degrades the long-term stability of this VCXO-*FSR* tracking system.

If the desired precision in *FSR* measurement is only moderate, then a short-length cavity offers an efficient alternative for characterizing *FSR* vs. wavelength [14]. As will be discussed in Section VII, the strong coupling condition for optical cavity QED experiments is achieved by using a small cavity length, of the order of 10 μm for the shortest length reported to date. A 10 μm cavity length translates to a *FSR* of $\sim 15$ THz, or a wavelength difference of a few tens of nanometers for neighboring cavity modes. Therefore a straightforward 6-digit measurement of the wavelengths of the cavity modes (by a commercial wavelength meter) acquires a precision of the order of $5 \times 10^{-5}$ for accurate determination of the equivalent optical length of the cavity, from which details of the index of refraction
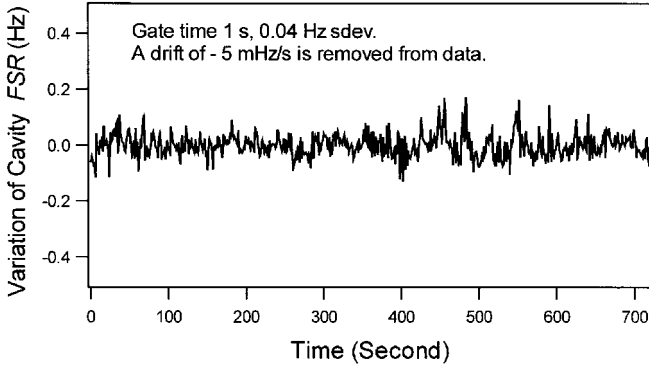


FIG. 13. Measurement of the cavity FSR via the NICE-OHMS technique: matching the FM sideband frequency to the cavity FSR. Counter gate time 1 s. The average value of the counted frequency (FSR) is 319.694953 MHz.

and layer thickness of materials in the mirror stack can be adequately inferred.

   The cavity finesse and overall cavity transmission can be measured directly to determine the mirror losses, $A$, and transmission, $T$. This information can be combined with the *FSR* measurement in two useful ways: Firstly, the *FSR* measurement is sensitive to the difference in refractive index $(n_H - n_L)$ of the two alternating materials making up the multilayer mirror stack [85], whereas the transmission $T$ depends on the ratio $n_H/n_L$. As a result, a precise measurement of both the *FSR* and $T$ can be used to determine the values of $n_H$ and $n_L$ independently. Moreover, by mapping out the wavelength dependence of the *FSR*, the thickness of layers in the mirror stack can be determined. Figure 14 shows the variation of the cavity *FSR* with respect to wavelength. The measurement is carried out with high ($\sim$ half a million) finesse mirrors forming a 10 μm scale cavity used for cavity QED experiments presented later in Section VII. Secondly, if one of the refractive indices is pre-determined, then the *FSR* measurement determines the other one, and an independent value for the mirror transmission $T$ can then be calculated from $n_H$ and $n_L$ and compared to the experimentally measured result.
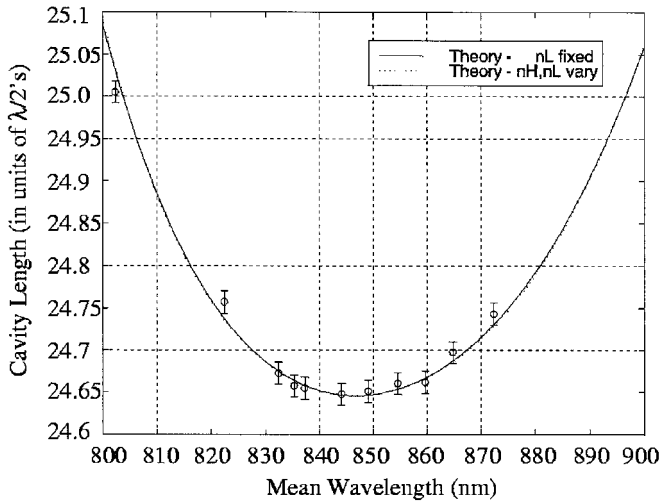


Fig. 14. The effective cavity length measured from the cavity mode splitting frequency (FSR) has a quadratic variation around the designed wavelength center of the coating. Fitting a model to these data points gives a measure of mirror transmission (from fitting of the difference $n_H - n_L$) and center wavelength (from fitting layer thickness). The measurement was made on a 10 μm long cavity with a finesse of $\sim$ 500,000.

Indeed, it is often useful to make complementary and mutually confirming measurements of the cavity properties by the two approaches, i.e., measurements of the direct cavity loss and the dispersion of the cavity modes. It is worth noting that the mirror phase shift (*FSR* measurement) is related only to the transmission (index contrast) and center wavelength (layer thickness). Therefore, if absorption/scatter losses are added to the model (by introducing an imaginary component to the refractive index) the cavity resonance wavelengths do not change.

Clearly, the wavelength-dependent phase shift due to the mirror coating, i.e., the mirror dispersion, makes it impossible to use the *FSR* of an empty cavity as a constant frequency marker. However, one can introduce an active (or passive) modulation element inside the cavity that actively "mode-locks" different cavity modes together to produce a regularly spaced optical frequency comb. One of the most effective approaches to optical difference frequency measurement across a few-terahertz gap is EOM-based optical frequency comb generation, in which an RF electro-optic modulator (EOM) is placed inside a low-loss optical cavity [100,101]. The cavity *FSR* matches with the RF sideband frequency. The optical cavity enhances modulation efficiency by resonating with the seeding optical carrier and all subsequently generated sidebands, leading to a spectral comb of frequency-calibrated lines spanning a few THz. The schematic of such an optical frequency comb generation process is shown in Fig. 15. The single frequency cw laser is locked on one of the resonance modes of the EOM cavity, with the *FSR* of the loaded cavity being an integer multiple of the EOM modulation frequency. The cavity output produces a comb spectrum with an intensity profile of $\exp\{-|k|\pi/\beta F\}$, where $k$ is the order of generated sideband from the original carrier, $\beta$ is the EOM frequency modulation index, and $F$ is the loaded cavity finesse [100]. The uniformity of the comb frequency spacing has been carefully verified [102]. These optical frequency comb generators (OFCG) have produced spectra extending a few tens of THz [103], nearly 10% of the optical carrier frequency. Some unique OFCG configurations have been developed at JILA. For example, by using an auxiliary cavity as a resonant output-coupling element, one can select a single comb line in the cavity output [104]. Another scheme uses a single crystal ($LiNbO_3$) to function both as an EO modulator and as an Optical Parametric Oscillator, leading to an effective intracavity gain within desired frequency ranges to enhance the sideband generation efficiency [105].

OFCGs had an immediate impact on the field of optical frequency measurement. Kourogi and co-workers produced an optical frequency map (accurate to $10^{-9}$) in the telecommunication band near 1.5 μm, using an OFCG that produced a 2-THz wide comb in that wavelength region,
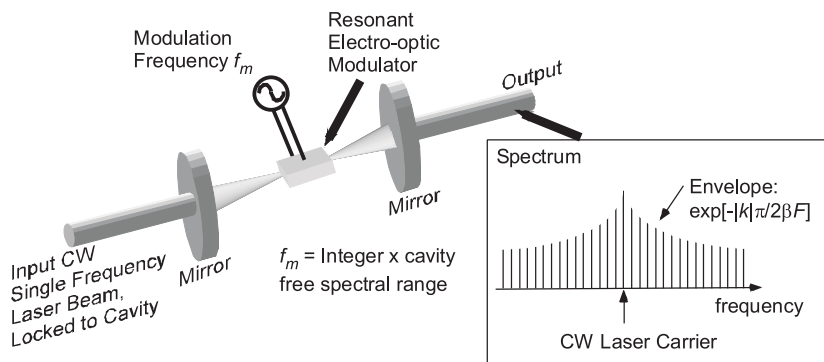
FIG. 15. Schematic of optical frequency comb generator (OFCG) based on an intracavity electro-optic modulator. OFCG converts a single optical frequency (cw) at the cavity input to a comb spectrum (pulse) at the cavity output. A high finesse (typically a few hundreds) of the loaded cavity and a high FM modulation index ($\beta$) are instrumental to a broad bandwidth of the generated comb (typically a few THz).

connecting various molecular overtone transition bands of $C_2H_2$ and HCN [33]. The absolute frequency of the Cs $D_2$ transition at 852 nm was measured against the fourth harmonic of the HeNe/$CH_4$ standard, with an OFCG bridging the remaining frequency gap of 1.78 THz [106]. At JILA, we used an OFCG to measure the absolute optical frequency of the iodine stabilized Nd:YAG frequency near 532 nm [69]. The results obtained using OFCGs have made the advantages of larger bandwidth very clear. However the bandwidth achievable by a simple EOM-based OFCG is limited by cavity dispersion and modulation efficiency. To achieve even larger bandwidth, mode-locked lasers became a natural choice, thus triggering a true revolution in optical frequency measurement [80,107]. We note in passing that the OFCGs described above actually generate a train of short pulses from a cw laser input. This is simply due to interference among modes with a fixed phase relationship. Indeed the first OFCG was built to generate short optical pulses [108] rather than for optical frequency synthesis or metrology. Later work provided even shorter pulses from an OFCG [109].

C. Femtosecond Laser Optical Frequency Comb
   and its Interaction with a Cavity

A laser that can sustain simultaneous oscillation on multiple longitudinal modes can emit short pulses; it just requires a mechanism to lock the phases

of all the modes, which occurs automatically in an OFCG due to the action of the EOM. Lasers that include such a mechanism are referred to as "mode-locked" (ML). While the term "mode-locking" comes from this frequency domain description, the actual processes that cause mode-locking are typically described in the time domain. The inclusion of gain [105,110] and dispersion compensation [111] in OFCGs brings them even closer to ML lasers. Indeed the use of ML lasers as optical comb generators has been developed in parallel with OFCG, starting with the realization that a regularly spaced train of pulses could excite narrow resonances because of the correspondence with a comb in the frequency domain [112–115]. Attention was quickly focused on ML lasers as the source of a train of short pulses [116–119]. In addition, the mode-locked lasers tend to be "self adjusting" in the sense that they do not require the active matching between cavity length and modulator frequency that an OFCG does. The recent explosion of measurements based on ML lasers [107,120–122] has been largely due to development of the Kerr-lens-mode-locked (KLM) Ti:sapphire laser [123–125] and its ability to generate pulses so short that the spectral width approaches an optical octave. Many recent results have obtained a spectral width exceeding an octave by spectral broadening external to the laser cavity [126].

To understand the connection between the ultra-stable world of optical frequency metrology and the ultra-fast world of ML lasers, we begin by comparing the unique characters of each field. The ultra-stable field is typified by high-resolution spectroscopy and high-precision measurements based on cw lasers that can be best described by their near delta-function frequency spectra. In sharp contrast, the field of ultra-fast phenomena encompasses the study of sub-picosecond events utilizing laser pulses that approach the limit of time domain delta-functions. In fact, at this point in time state-of-the-art laser sources from these two fields share nearly the same delta-function "figure of merit" with frequency and temporal widths on the order of a few parts in $10^{15}$ Hz and seconds, respectively. The connection between the ultra-stable and the ultra-fast arises from the fact that femtosecond (fs) laser oscillators produce pulses in a periodic train via mode-locking, with a corresponding rigorous periodicity in the spectral domain. In fact, the frequency domain spectrum consists of a comb of discrete modes separated by the repetition frequency $f_{\mathrm{rep}} = 1/\tau_{\mathrm{r.t.}}$, where $\tau_{\mathrm{r.t.}}$ is the cavity round trip time. The extent of the time domain pulse train provides the frequency resolution of individual comb components, while the total extent of the frequency domain mode comb is approximately limited to the inverse of the pulse duration. The generation of ultrashort pulses requires that the group velocity ($v_{\mathrm{g}}$) dispersion inside the laser cavity be minimized across the pulse's frequency spectrum [127]. This criterion is not

directly related to the frequency comb spacing, since the individual mode frequencies correspond to eigenmodes of the phase-velocity ($v_p$) of the light. In general, we have $v_g \neq v_p$ due to laser cavity dispersion. This fact results in a pulse envelope function that is not fixed with respect to the underlying optical oscillation frequencies – there is a phase slip between the "carrier" phase and the envelope peak for each of the successive pulses emitted by the laser [120,128].

The concept of carrier-envelope phase is based on the decomposition of the pulses into an envelope function, $\hat{E}(t)$, that is superimposed on a continuous carrier wave with frequency $\omega_c$, so that the electric field of the pulse is written $E(t) = \hat{E}(t)e^{i\omega_c t}$. The carrier-envelope phase, $\phi_{ce}$, is the phase shift between the peak of the envelope and the closest peak of the carrier wave, as illustrated in Fig. 16(a). In any dispersive material, the difference between group and phase velocities will cause $\phi_{ce}$ to evolve. And the pulse-to-pulse carrier-envelope phase slip is denoted as $\Delta\phi$ as shown in Fig. 16(a). In the frequency domain, $\Delta\phi$ yields an offset of the mode comb from exact harmonics of the $f_{rep}$ by the amount $f_{ceo} = \Delta\phi\, f_{rep}/2\pi$ Hence each optical comb frequency is effectively given by $f_n = nf_{rep} + f_{ceo}$, as shown in Fig. 16(b). Here $n$ represents an integer ($\sim$1 million depending up the ratio of the optical frequency and $f_{rep}$) harmonic number of the optical comb line. One sees that the frequency-domain control of both $f_{rep}$ and $f_{ceo}$ makes it possible to establish a ML-laser based optical comb at a high precision for absolute optical frequency measurement and distribution. Precision control of the time-domain carrier-envelope phase, which has been a highly desirable and yet elusive goal in ultrafast science since the advent of few-cycle pulses, also becomes a reality [129,130]. Control of $\Delta\phi$ requires maintaining a stable ratio between $f_{ceo}$ and $f_{rep}$. It is straightforward to measure $f_{ceo}$ when the bandwidth of the frequency comb spans an optical octave, which can be facilitated by spectral broadening outside a ML-laser cavity. Basically we measure the heterodyne beat between comb lines on the high frequency extreme of the spectrum and the second harmonic of the corresponding comb lines at the low frequency end of the spectrum. The resulting beat frequency is $|f_{2n} - 2f_n| = |(f_{ceo} + 2nf_{rep}) - 2(f_{ceo} + nf_{rep})| = f_{ceo}$.

An optical cavity can also be used to control the two degrees of freedom associated with a ML-laser comb [82,131]. Appropriate servo error signals can be obtained if one compares the $f_{rep}$ of the comb against the cavity $FSR$, while the average frequency of a selected collection of comb lines is compared against the center frequencies of the corresponding cavity modes. Just as for the CW laser case, an optical cavity can provide large $S/N$ ratios for the respective servo error signals that would permit
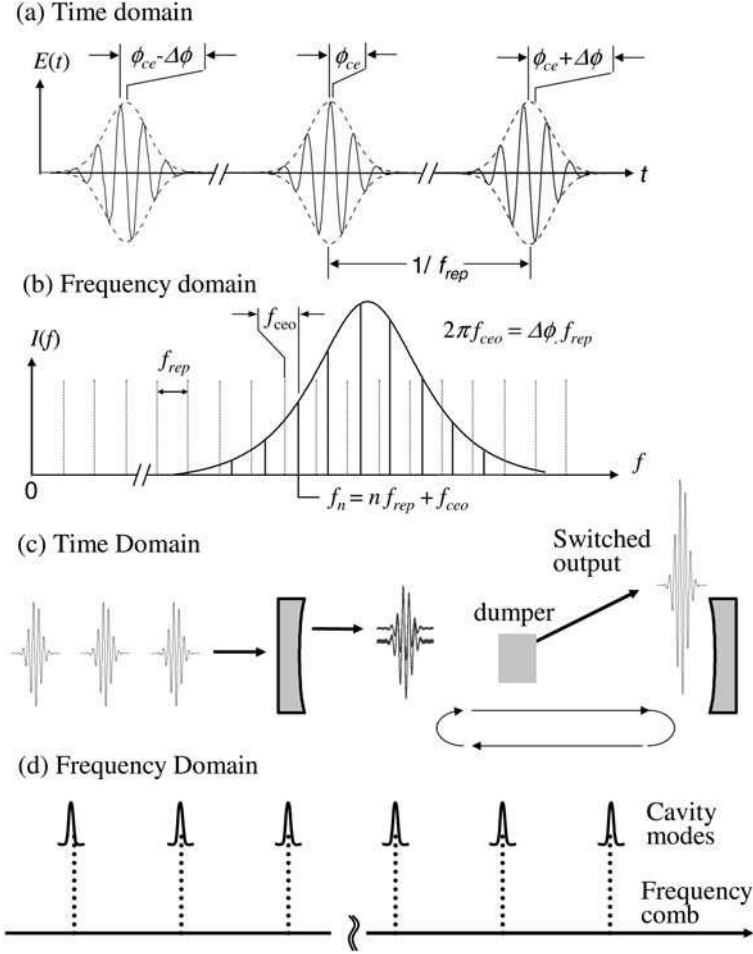
FIG. 16. Time-frequency correspondence between $\Delta\phi$ and $f_{ceo}$. (a) In the time domain, the relative phase between the carrier (solid) and the envelope (dotted) evolves from pulse to pulse by the amount $\Delta\phi$. $\phi_{ce}$ is an unknown but controllable, overall constant phase. (b) In the frequency domain, the elements of the frequency comb of a mode-locked pulse train are spaced by $f_{rep}$. The entire comb (solid) is offset from integer multiples (dotted) of $f_{rep}$ by an offset frequency $f_{ceo} = \Delta\phi f_{rep}/2\pi$. Without active stabilization, $f_{ceo}$ is a dynamic quantity, which is sensitive to perturbation of the laser. Hence $\Delta\phi$ changes in a nondeterministic manner from pulse to pulse in an unstabilized laser. (c) Principle of coherent pulse amplification scheme with the aid of an optical cavity with the time domain picture showing matching of the pulse repetition period with the cavity round trip time. The intracavity pulse is switched out when sufficient energy is built up in the cavity. Intracavity dispersion compensation is not shown. (d) Frequency domain illustration showing the matching of the pulse comb structure with corresponding cavity modes. This ensures the efficient coupling of pulse energy into the cavity.

superb short-term stability of the passive reference cavity to be transferred to the ML laser. Another interesting application is to use a passive optical cavity as a means to temporarily store and coherently enhance the pulsed electric field [86]. By simultaneously controlling the repetition and carrier frequencies, the phase coherent superposition of a collection of successive pulses from a mode-locked laser can be realized inside an optical cavity. Coherent delay and constructive interference of sequential pulses will continue until a cavity dump is enabled to switch out the "amplified" pulse. This approach will lead to an effective amplification process through decimation of the original pulse rate while preserving the overall coherence from the oscillator. This will be the subject of the next section.

### D.  Gainless Amplifier for Ultrafast Pulses Based on Control of Carrier-Envelope Phase

With the recent realization of phase control of femtosecond lasers, its potentially powerful applications in extreme nonlinear optics and novel coherent processes are being actively explored [132]. Ordinarily, the peak power offered by pulses emitted from a simple oscillator is not sufficient to drive the high-order nonlinear processes of interest. Naturally, researchers are interested in the development of phase-controlled pulse amplification [133,134]. However, the use of conventional amplifiers can introduce a great deal of phase noise owing to effects such as beam pointing variation, pump power fluctuation, and amplifier medium instability. A unique approach for pulse amplification without the use of an active gain medium is the coherent addition of neighboring pulses inside an optical cavity. The technique relies on coherent superposition of successive components from a pulse train to increase the amplitude of a single pulse while reducing the repetition frequency. This requires not only a suitable delay mechanism to line up successive pulses, but also the ability to control the phase evolution of the electric field underlying the pulse. These requirements are similar to those already realised in coherent pulse synthesis from separate femtosecond lasers. In that work, precise control of both timing synchronization and carrier phase locking was achieved to successfully synthesize a single pulse from two independent pulses. An amplification scheme based on coherent addition would maintain the carrier-envelope phase coherence of the original oscillator.

   The operation principle of the proposed "amplifier" design is illustrated in Fig. 16, with time domain action depicted in part (c) and the frequency domain correspondence in part (d). To ensure efficient coupling into the

cavity and subsequent power buildup, the repetition rate and carrier-envelope phase of the input pulses must match those of the pulse circulating inside the passive cavity. The equivalent frequency domain requirement is that all frequency components making up the pulse train are tuned into resonance with corresponding cavity modes as depicted in Fig. 16(d). The cavity decay time is directly proportional to the overall cavity finesse and is predetermined to match with the desired pulse amplification factor. For example, suppose a laser pulse train has a 100 MHz repetition rate and we wish to convert it to an output pulse train with a 1 MHz repetition rate with 100 times amplification in the peak power. We would then design the cavity finesse to be ~314 such that the linewidth is 0.32 MHz and the field decay time is roughly 1 μs. This allows the electric fields of roughly 100 pulses to add coherently inside the cavity before being switched out.

Resonant enhancement cavities are commonly used with cw lasers to improve efficiencies in nonlinear optical interactions or to increase sensitivity in spectroscopic applications [135]. Based on these cw techniques, similar intracavity experiments using ML lasers have been demonstrated [136–139]. These approaches, however, address only one parameter (repetition rate or laser average frequency), while both are required for coherent pulse manipulation. Hence coherent superposition of successive short pulses for significant amplification would not be feasible. In order to efficiently couple sub-100 femtosecond (fs) pulses into an optical cavity with a finesse sufficiently high to build up pulse energy by 100 to greater than 1000 times, two key criteria must be met: (i) the carrier *and* repetition frequency of the fs laser must be simultaneously stabilized to those of the cavity, and (ii) the cavity itself must be designed such that dispersion does not severely distort the intracavity pulse.

As discussed in previous sections, inevitable dispersion inside an optical cavity arising from intracavity elements and mirror-reflection phase shifts leads to a nonuniform cavity mode spacing throughout relevant spectral regions. This fact will place a practical limit on the spectral bandwidth (and therefore pulse duration) one can employ in this scheme since the modes of the fs pulse train are rigorously equally spaced. In addition, relevant laser comb components coupled into the cavity cannot be simultaneously locked to the center of corresponding cavity modes, in contrast to the ideal case shown in Fig. 16(d), leading to a frequency dependent phase shift imposed on the intracavity spectrum and therefore distorting the pulse temporal profile. If higher cavity finesse is desired for greater pulse enhancement, the cavity linewidth will become narrower and the increased mismatch between the cavity modes and the fs comb will lead to a further reduction in the useful bandwidth of the cavity. These facts can also be easily understood from time domain considerations where

pulses bouncing back and forth in the cavity are broadened and distorted due to dispersive phase shifts. As a result, the overlap of the incoming pulse envelopes with the stored pulse is reduced and their constructive interference is compromised.

Let us assume a four-mirror linear cavity with a pair of fused silica prisms for dispersion compensation and an intracavity fused silica Brewster-angled Bragg deflector for switching out the pulse. Two of the mirrors are used to create an intracavity focus to decrease the switching time of the Bragg deflector. It should be noted that in order to reduce intracavity peak powers to avoid substantial nonlinear effects, the input pulse may be chirped and later recompressed as is commonly practiced in traditional optical amplifiers. This operation would have no effect on the results shown here. The input mirror should have a transmission coefficient matched to the remaining part of the total cavity loss (impedance matching). The maximum finesse, and hence maximum pulse magnification, will then be limited by scattering losses in the fused silica, residual losses at the Brewster angled surfaces, and reflection loss at the remaining cavity mirrors. We expect a cavity finesse of greater than 1000 will be experimentally feasible.

The round trip phase shift inside the cavity can be expressed in a power series expansion: $\Phi_{RT}(\omega) = \Phi_0 + \Phi_1(\omega - \omega_0) + \Phi_2(\omega - \omega_0)^2/2! + \Phi_3(\omega - \omega_0)^3/3! + \cdots$, where $\omega_0$ is the center angular frequency of the mirror coating. The frequency independent phase shift $\Phi_0$ describes the carrier-envelope phase shift per round trip of the intracavity pulse while the group delay $\Phi_1$ determines the cavity free-spectral range (*FSR*) at $\omega_0$. These terms are not important to the evaluations as the pulse train incident on the cavity will be matched to these values when properly stabilized. The group-delay dispersion will be set to zero at $\omega_0$ with prism compensation. The phase shifts due to reflection from the dielectric mirrors depend strongly on the coating design. For initial calculations we have chosen to use standard quarter-wave stack mirrors for which dispersion characteristics are well known, although better performance may be achieved using mirrors custom designed for dispersion compensation. A total path length of 0.9 cm through the fused silica components was assumed with a 30 cm separation between the prisms. The dispersion coefficients used for the given cavity parameters are $\Phi_2 = 0$, $\Phi_3 = 400\,\text{fs}^3$, and $\Phi_4 = -1060\,\text{fs}^4$.

A time dependent calculation visualizes the evolving intracavity pulse one round-trip at a time. The calculation is performed in a straightforward manner by repeatedly solving for the transmitted and reflected fields at the input mirror after propagating the pulse once through the cavity. Figure 17 illustrates the evolution of a 50 fs pulse inside a cavity with a finesse of
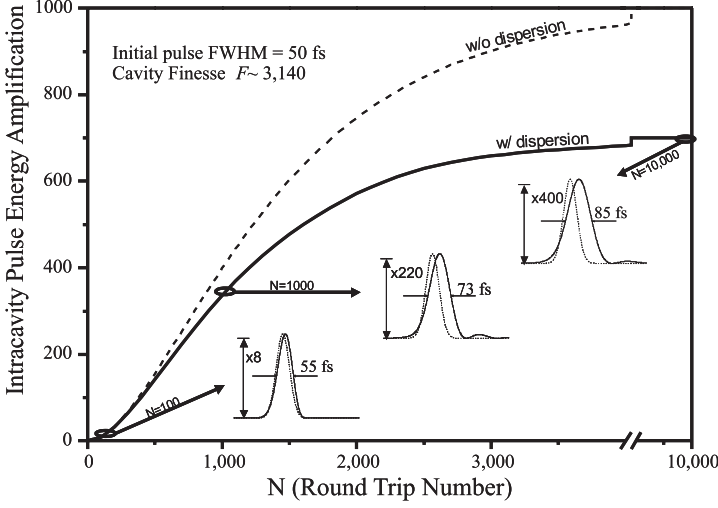
FIG. 17. Time dependent calculation of the intracavity pulse propagation shows the coherent evolution of a 50 fs pulse inside a cavity of finesse 3140. Dashed line indicates the ideal case of a dispersion free cavity perfectly matched with the incident pulse train, while the solid line shows the effect of cavity dispersion in limiting the amount of energy coupled into the cavity. Three representative pulses at different stages of "amplification" are also shown.

3140 under the conditions of zero cavity dispersion (dashed curve) and finite dispersion (solid curve). Three representative pulses at different stages of "amplification" are also shown. Although the 50 fs pulse is stretched by the dispersive cavity, it is not severely distorted due to its coupling with the incident pulse train. If the incident pulses become too short, the cavity finesse becomes too high, or the laser repetition frequency deviates significantly from the cavity *FSR* at $\omega_0$, the intra-cavity pulse may quickly "pull apart" into several pulses, and the meaning of a single pulse width will be lost.

The results shown here demonstrate the feasibility of a pulse amplification scheme based on coherent storage and constructive interference of pulsed electric fields inside a passive optical cavity. Such a technique will preserve the carrier-envelope phase coherence characteristics of the original pulses from the oscillator while enabling pulse energies to be increased by 2 or 3 orders of magnitude. This indicates that sub-100 fs pulses with microjoule energies can be obtained given the nanojoule level of pulse energy available from current ultrafast lasers. Future cavity designs based on custom dispersion compensating mirrors may extend the usefulness of this technique to the sub-20 fs regime. Initial experimental exploration with a picosecond

laser has already produced an amplification factor of greater than 50 without any noticeable pulse distortion, using a loaded cavity finesse of ∼200.

# VII.  Quantum Dynamics

The last two decades have witnessed the emergence of a qualitatively new set of phenomena in the physics of optical cavities: light-matter interactions that derive their character explicitly from the quantized nature of individual atoms and light fields. Such interactions are manifest in the current generation of cavity QED experiments thanks to a steady progression of developments in both atomic and optical physics. Technical improvements have allowed optical cavities with ever higher finesse and smaller mode volumes; as we shall see, these are the requirements for coherent dynamics to dominate the interaction of single quanta in the cavity setting. On the other hand, techniques in atomic physics and laser cooling have provided the means to deliver into these small cavity mode volumes single atoms with appropriately chosen internal states and nonlinear response functions. Today, these capabilities combine to allow experimental exploration of quantum state estimation and control, including progress toward quantum logic and quantum communication using optical cavities. The signal enhancement effects that make optical cavities so suitable for classical spectroscopy find their analogs in the quantum regime, making cavity QED a powerful tool for probing the physics of open quantum systems.

## A.  Connection and Difference Between Classical and Quantum Regimes

In a classical description of spectroscopy in an optical cavity, an atomic sample acts as a dispersive medium for the coherent light field circulating in the cavity mode volume. Classical behavior gives way to quantum when single quanta, whether of the atomic sample or of the light field itself, begin to induce nonlinear response in the system. Some critical parameters delineating this transition have already been briefly introduced. We expand that intuitive discussion here and complement it with a more quantitative development in the following sections.

Consider an atomic sample placed inside the cavity mode. The sample scatters the optical field, producing a wavelength-dependent refractive index in the cavity mode volume. The atomic sample affects the resonance properties of the optical cavity if the atom-field interaction strength and the

number of atoms are sufficient to noticeably alter the free-space dispersion relation for the light. Thus, if a single atom placed within the mode volume is to act as a nonlinear medium, it must have a large effective cross-section for scattering intracavity light. First, the atom should have a near-resonant dipole interaction with the optical field mode supported by the cavity. Second, scattering should be enhanced by ensuring that optical wavefronts have every opportunity to interact with the atom in the process of being transmitted through the cavity. This second requirement is accomplished by constructing cavities with high finesse and tightly confined modes, so that light traverses the distance between the mirrors many times before exiting the cavity and furthermore has a high chance of interacting with the atomic cross-section on each pass. Tight mode confinement has the additional benefit that the light is thoroughly diffractively mixed and thus the interaction is truly with a single cavity mode that is well-defined throughout the interaction process. Quantitatively, the importance of a single atom for the response of the intracavity field is described by the single-atom cooperativity parameter $C_1 = g_0^2/2\gamma_\perp \kappa$, or by its inverse, the critical atom number, $N_0 = 2\gamma_\perp \kappa/g_0^2$ [51]. Here $g_0$, $\gamma_\perp$, and $\kappa$ are as introduced in Section III.D. By re-expressing the single-atom cooperativity in terms of familiar properties of the cavity and the atomic transition, one finds it scales simply as $C_1 \sim 2F\lambda^2 \ \pi w_0^2$; the ratio $\lambda^2/w_0^2$ can be interpreted as the ratio of atomic absorption cross-section to cross-sectional area of the cavity mode, and $2F/\pi$ is the cavity enhancement factor we have already seen in the classical context. Note that $C_1$ does not scale explicitly with the length of a Fabry-Perot cavity.

On the other side of the coin, consider the circumstances necessary to make the quantized nature of the light field relevant to observations of the cavity system. In the classical regime the cavity mode volume is occupied by a large-amplitude coherent field. To fully probe the atomic response function, the electric field associated with the light must be strong enough to saturate the atomic dipole. How, then, is a single photon to accomplish this saturation? Simply put, the photon must be confined to a small volume so its electric field strength within that volume becomes large. A field of Rabi frequency $\Omega$ saturates an atomic transition when $\Omega \sim \gamma$. Since the Rabi frequency is proportional to the electric field and thus to the square root of photon number, the $m$-photon Rabi frequency is just $\sqrt{m}g_0$. Therefore we can define a saturation photon number $m_0 = \gamma_\perp^2/2g_0^2$ [51] representing the number of intracavity photons required to saturate the atom. As promised, this quantity is inversely proportional to the cavity mode volume through the factor $1/g_0^2$; it is, however, completely independent of the cavity finesse.

We now turn to a more formal treatment of the atom-cavity system. As is often the case, the conceptually and computationally simplest starting point

is the purely quantum limit, where the atom and cavity evolve via their coherent coupling in the absence of dissipation. This system simply obeys the Schrodinger equation with the Jaynes-Cummings Hamiltonian [48],

$$H_{JC} = \hbar\omega\hat{a}^+\hat{a} + \hbar\omega\hat{\sigma}^+\hat{\sigma} + \hbar g_0(\hat{a}\hat{\sigma}^+ + \hat{a}^+\hat{\sigma}). \tag{25}$$

Here we consider a two-level atom and $\omega$ is the common resonance frequency of both atom and cavity. Diagonalizing this Hamiltonian gives rise to the well-known Jaynes-Cummings ladder of eigenstates for the coupled atom-cavity system, as illustrated in Fig. 18. The coupled eigenstates are characterized by the equal sharing of excitation between the atomic dipole and cavity field, so that the $n$-excitation bare states $|g,n\rangle$ and $|e, n-1\rangle$ of energy $n\hbar\omega$ are replaced by

$$|\pm_n\rangle = \frac{1}{\sqrt{2}}\big(|g,n\rangle \pm |e, n-1\rangle\big), \tag{26}$$
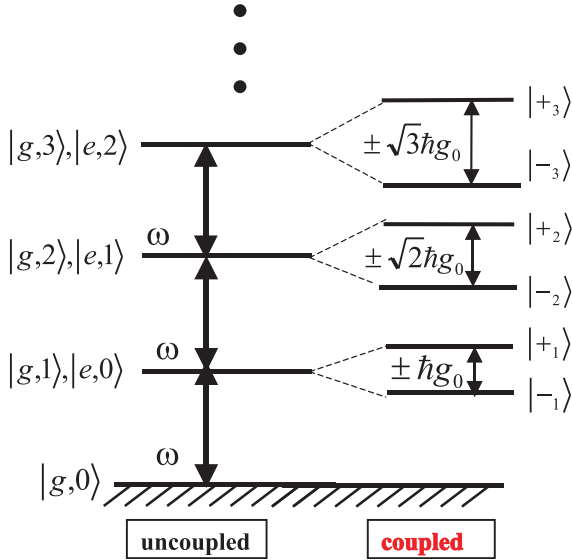


FIG. 18. Jaynes-Cummings ladder of eigenstates for the coupled atom-cavity system. Bare eigenstates of the atom and cavity field are shown on the left, labeled by atomic internal state and number of photons in the cavity mode, under the condition $\omega_c = \omega_a = \omega$. When the atomic dipole is coupled to the cavity field with single-photon Rabi frequency $2g_0$, the energy eigenstates form the ladder shown on the right. The Jaynes-Cummings ladder has pairs of strong- and weak-field-seeking states with each pair split by an energy that rises as the square root of the number of excitations.

with corresponding energy eigenvalues

$$E_{\pm_n} = n\hbar\omega \pm \sqrt{n}\,\hbar g_0. \tag{27}$$

To quantitatively predict actual atom-cavity dynamics, a treatment that moves beyond this idealized picture to include dissipation and driving terms will be necessary. Two qualitative features, however, are worth noting immediately from the Jaynes–Cummings ladder itself.

First, in the most fully quantum regime, the atom and cavity field are best described in a symmetric treatment where they combine to create a single entity sharing excitation equally. Most notably, for $n \geq 1$ excitation, there exist strong-field-seeking states $|-_n\rangle$ that can be thought of as atom-cavity states bound together by the sharing of a quantum of excitation. If we permit a detuning $\Delta_{ac}$ between the atom and cavity resonance frequencies, the sharing of excitation in these "bound states" becomes asymmetric but the qualitative properties of the ladder remain unchanged.

Second, while a ladder of strong-field- and weak-field-seeking states recalls the dressed states of atomic interaction with a coherent light field (e.g., in free space) [140], the Jaynes-Cummings ladder reflects atomic coupling to a small number of quantized excitations in the cavity mode rather than to a strong classical field in free space. The anharmonic nature of the level splittings with increasing $n$ is a feature arising explicitly from the quantized nature of the cavity field. Thus, to observe effects of field quantization on the spectrum of atom-cavity response, we can expect that experiments must probe the saturation behavior of the system and not simply rely on spectroscopy in the weak-driving limit of $n < 1$ system excitations. One caveat to this observation, however, is that nonclassical aspects of the system *dynamics* can in fact be observed for weak driving; for example, photon statistics of the cavity output field in time are of interest even for experiments in the weak-excitation limit.

In the presence of dissipation and driving, and allowing for detuning between the probe field and the atom and cavity resonant frequencies, the Jaynes-Cummings Hamiltonian becomes part of a master equation for the joint atom-cavity density operator $\rho$. We consider a driving (and probing) field $\varepsilon$ of frequency $\omega_p$, a cavity resonant at $\omega_c = \omega_p + \Delta_{cp}$, and an atomic resonance frequency $\omega_a = \omega_p + \Delta_{ap}$ approximations, and in the interaction picture with respect to the probe frequency, the evolution is described by

$$\dot{\rho} = -\frac{i}{\hbar}\left[\hat{H}_0, \rho\right] + \gamma_\perp(2\hat{\sigma}\rho\hat{\sigma}^+ - \hat{\sigma}^+\hat{\sigma}\rho - \rho\hat{\sigma}^+\hat{\sigma}) + \kappa(2\hat{a}\rho\hat{a}^+ - \hat{a}^+\hat{a}\rho - \rho\hat{a}^+\hat{a}),$$

$$\hat{H}_0 = \hbar\Delta_{cp}\hat{a}^+\hat{a} + \hbar\Delta_{ap}\hat{\sigma}^+\hat{\sigma} + \hbar g(\vec{r})\left[\hat{a}\hat{\sigma}^+ + \hat{a}^+\hat{\sigma}\right] + \varepsilon(\hat{a} + \hat{a}^+). \tag{28}$$

Here $g(\vec{r})$ is the coupling strength which takes into account the atomic position $\vec{r}$ within the cavity mode. For a Fabry-Perot cavity supporting a standing wave mode with Gaussian transverse profile, $g(\vec{r}) = g_0 \psi(\vec{r}) = g_0 \cos(2\pi x) \exp[-(y^2 + z^2)/w_0^2]$. In the fully quantum treatment, the atomic position $\vec{r}$ is itself an operator; in experiments to date a quasiclassical treatment suffices, so the atom may be considered a wavepacket with $\vec{r}$ a classical center-of-mass position variable.

This master equation provides a valid description of the atom-cavity system in any range of parameters $(g_0, \kappa, \gamma_\perp)$. It can in general be solved only numerically, but certain limits, either of inherent rates or of driving strengths, permit analytical treatments of limited application. In the sections below, we discuss behavior exhibited by theory and experiment in several parameter regimes from semiclassical to very strongly coupled.

## B. Cavity Bistability and Intracavity Nonlinear Optics

Certain parameter regimes are well described by an approximation in which the joint operator moments in Eq. (28) can be factored. This corresponds to a semiclassical treatment in which the field is described by its coherent amplitude $\langle \hat{a} \rangle = \alpha$. Such a replacement is valid in the limit of large critical parameters $(N_0, m_0) \gg 1$, in which case a collection of atoms acts as a classical nonlinear intracavity medium. Within this approximation, Eq. (28) yields an analytic expression for the driving field $\varepsilon = \kappa \sqrt{m_0}\, Y$ as a function of the intracavity field $\langle \hat{a} \rangle \leftrightarrow \sqrt{m_0} X$. This relation is the well-known optical bistability state equation [52]:

$$Y = X \left[ 1 + \frac{2C}{1 + \delta^2 + X^2} + i \left( \phi - \frac{2C\delta}{1 + \delta^2 + X^2} \right) \right]. \tag{29}$$

Here we have employed the standard notation for the bistability equation, related to our previous discussions by detunings $\delta = \Delta_{ap}/\gamma_\perp$ and $\phi = \Delta_{cp}/\kappa$, and $N$-atom cooperativity parameter $C = NC_1$. The system saturation behavior described by this relation is shown in the dotted curve of Fig. 19. The correspondence between the semiclassical amplitude $X$ and the actual operator expectation value $\langle \hat{a} \rangle$ is only approximate; in general the intracavity state is not an exact coherent state, but the bistability equation gives an input–output relation between the driving power $\sim Y^2$ and a transmitted photocurrent $\sim X^2$ which is valid in the limit discussed above.

Optical bistability effects in general have a long history in measurements within the context of laser physics. Specific cavity QED experiments measuring optical bistability in two-level systems date from the early 1980s

$(\mathbf{P_{out}})_{full}/(\mathbf{P_{out}})_{empty}$
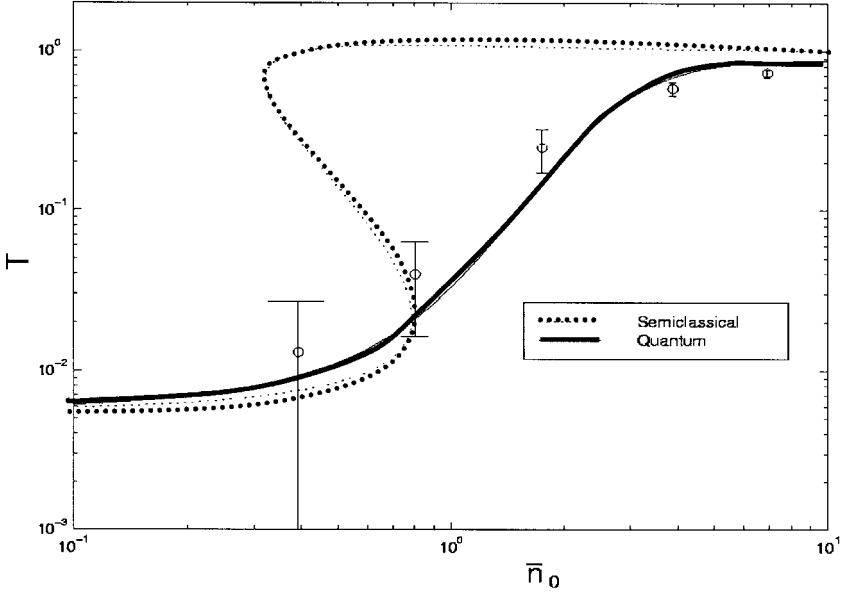


**Drive strength (photon number in empty cavity)**

Fig. 19. Saturation curves for the atom-cavity system of [158], based on semiclassical and quantum theory. Here $\omega_c = \omega_a = \omega_p$. The probe strength is varied over a range corresponding to 0.1 to 10 photons in the empty cavity. The system saturation is investigated by recording at each drive strength the ratio of cavity output power for the coupled system as compared with the empty cavity. The dotted curve shows the prediction of the optical bistability state equation (semiclassical theory), while the solid curve shows the solution of the master equation (fully quantum in the field). The semiclassical prediction clearly deviates from the quantum solution and from the data in this strongly coupled system [158].

([141,142]) and are realizable in relatively low-finesse cavities interacting with a sample of atoms crossing the cavity mode in a thermal atomic beam. However, the bistability state equation is also valid when $(N_0, m_0) < 1$ in the special case of very weak driving, $n \ll 1$ excitations in the system. In this case, only the first $(n = 1)$ excited states of the system must be considered, and the resulting relationship of joint operator moments makes factoring formally valid. This fact comes as no surprise in the light of our earlier discussion of the Jaynes-Cummings ladder; the structure of the spectrum reflects the quantized field only for higher drive strengths that sample the anharmonicity of the system eigenvalues. Optical bistability also describes

the steady-state behavior of an atom-cavity system where inherent strong coupling is washed out by the simultaneous interaction of many atoms with the cavity mode.

Even in the regime of the optical bistability equation, nonclassical dynamics of the atom-cavity system are accessible. Experiments measuring the photon statistics of the cavity output field have demonstrated non-classical correlation functions of the output light with similar work pushing from this limit to the inherently strong-coupling regime [143–146].

Another instance of intracavity nonlinear optics is the use of optical cavities to study atomic samples exhibiting electromagnetically induced transparency (EIT). In an EIT system, three or more atomic levels are used to create a configuration in which a powerful "coupling" beam on one transition prepares the atomic sample and thus strongly influences the index of refraction for a weak probe beam on a second transition [147,148]. In EIT one can obtain various interesting effects, such as: large Kerr nonlinearity, very sharp features in the index as a function of probe frequency, slow or stopped light, and nonlinear behavior at low light intensities. Placing the EIT medium inside an optical cavity, where the "probe" beam is a resonant mode of the cavity, enhances these EIT effects so that they can be more easily measured by means of resonant cavity transmission [149]. For example, if EIT is present while scanning the cavity length across the probe resonance, the Kerr nonlinearity induces asymmetry in the cavity line shape; this asymmetry can be used as a sensitive measurement of the intensity-dependent index of refraction [150]. Other observations in this setting include cavity linewidth narrowing related to the slow-light effect [151] as well as several realizations of all-optical switching where the probe transmission is gated by the coupling beam amplitude or detuning [39]. While these observations take place in a weakly coupled regime, other cavity QED effects have also been pointed out for EIT in combination with strong coupling [152].

## C. Interacting Single Quanta: The 1-D Atom

By increasing cavity finesse and decreasing mode volume, we move from a semiclassical regime to a regime of small critical parameters $(N_0, m_0) < 1$. Here single atoms and photons induce nonlinear effects in the system response. However, this condition is still consistent with overall dissipative dynamics if the cavity decay rate is fast relative to the coherent coupling $g_0$. This regime, known as the "bad cavity" limit, is realized for $\kappa > g_0^2/\kappa > \gamma_\perp$. In this limit single quanta within the cavity mode interact strongly with one another, but coherence and information leak rapidly from the system into

the output channel defined by cavity decay. Thus the atom-cavity coupling is essentially perturbative, and the atom and cavity each retain their distinct identities but with decay rates modified by the interaction. For instance, an atomic excitation, rather than decaying via spontaneous emission at rate $\gamma_\perp$, is much more likely to be exchanged into the cavity field and subsequently decay via the cavity; this preferential decay via the cavity mode at rate $g_0^2/\kappa$ gives an effectively "1-D atom."

Experiments in this parameter regime include the quantum phase gate [153] and the use of squeezed light in cavity QED [154]. Both of these effects involve the production of nonclassical effects on the light field due to nonlinearities mediated by a "1-D atom" effect [53]. Thus single photons can interact with one another by means of their common coupling to an intracavity atom. These effects are seen with single strongly coupled atoms; since these experiments delivered atoms to the cavity via thermal beams of atoms transiting a cavity mode, a background of weakly coupled or "spectator" atoms acted to dilute the inherent single-atom effect.

### D. Cavity QED: Single Atom Detection, Trapping, and Quantum Aspects of Detection

By further increasing cavity finesse, we decrease $\kappa$ relative to $g_0$ and arrive at the regime of strong coupling for the atom-cavity system. In this regime, where $g_0 \gg (\kappa, \gamma_\perp)$, single quanta are significant and, furthermore, their coherent interaction dominates other rates in the system. It is in this limit that observations most closely reflect the ideal structure of the Jaynes-Cummings ladder. Exchange of excitation at rate $g_0$ is no longer perturbative, and the system crosses over to a set of joint atom-cavity eigenstates with widths set by decay rates $\kappa$ and $\gamma_\perp$. The coupled atom-cavity transmission spectrum reflects this eigenvalue structure via the vacuum Rabi splitting [155], in which the empty-cavity Lorentzian line profile is transformed into a double-peaked transmission function as shown in Fig. 20 and first directly observed in [156]. The positions and widths of the vacuum Rabi sidebands depend on the strength of the driving field $E$ as well as the parameters $(g(\vec{r}), \kappa, \gamma_\perp)$, and are found via steady-state numerical solution of the master equation.

To fully realize the quantum mechanical phenomena inherent in Eq. (28) for strong coupling, yet another rate must be made small relative to the coherent coupling. This is the rate for decoherence as information exits the system via movement of the individual atoms contributing to the effective atom number $N$. If excitation is distributed among an ensemble of atoms, each poorly coupled or coupled for a short time as it flies across the cavity
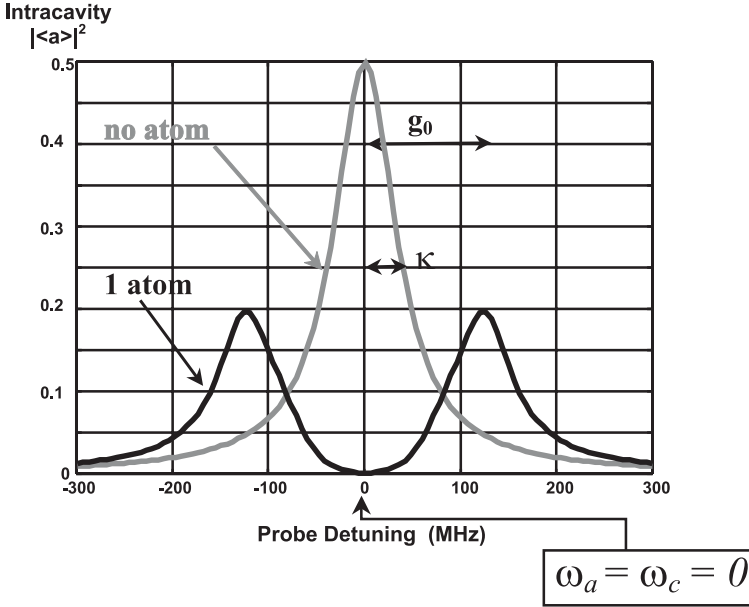
**Intracavity**
**|<a>|²**



FIG. 20. Vacuum Rabi splitting for the atom-cavity system of [158]. Intracavity $|\langle a \rangle|^2$, proportional to transmission as measured by balanced heterodyne detection, is shown as a function of probe detuning for a fixed probe intensity incident on the cavity. The gray trace shows the Lorentzian line profile of the empty cavity, while the black trace shows the system's spectrum when an atom is strongly coupled to the field, creating a Jaynes-Cummings structure as in Fig. 18.

mode, the true structure of the single-atom Jaynes-Cummings ladder cannot be observed. Thus experiments designed to probe the strong coupling regime must be carried out with cold atoms, in a situation where atom number $N \sim 1$ is realized through an actual single atom strongly coupled for a time $T$ satisfying $1/T \ll g_0$. Experiments of this type to date have involved a cloud of atoms trapped in a magneto-optical trap (MOT), cooled via standard sub-Doppler techniques, and then dropped or launched so that single atoms arrive in the cavity mode volume with small velocities and interact one-at-a-time with the cavity field. Such an experiment is shown schematically in Fig. 21; single atoms fall through the cavity mode and are detected via real-time changes in the transmission of a continuously monitored cavity probe beam [11,157–160]. More recently, single atoms have also been caught within the cavity by means of the quantized field [36,37] or trapped there using a separate far-off-resonance trap (FORT) [38,161]. Other efforts in progress include the use of cavities with magnetic traps for atoms [13],
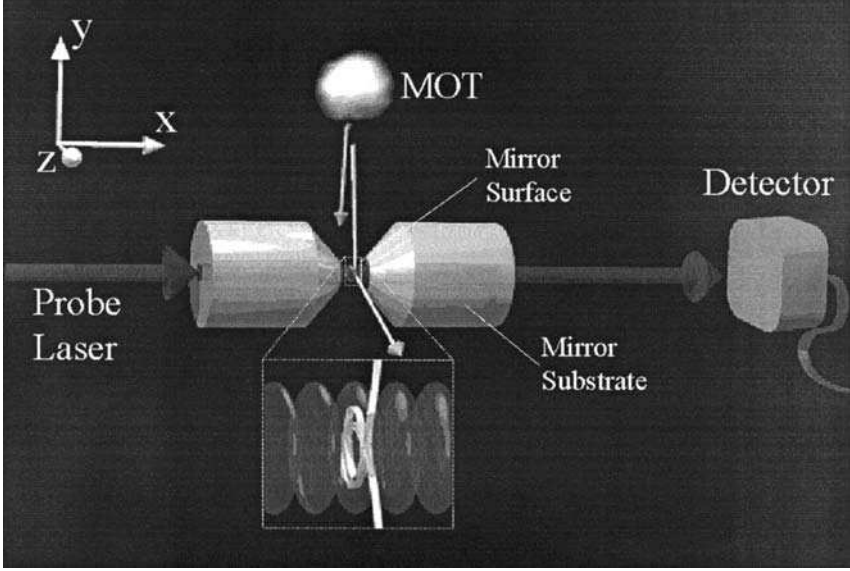
Fig. 21. Experimental schematic for use of cold atoms in cavity QED [36]. A cloud of atoms is collected in a magneto-optical trap (MOT) directly above the cavity mirrors, cooled to a few microkelvin, and released to fall over the cavity. Geometry cuts off the flux of atoms to the actual cavity mode volume so that single atoms arrive one-at-a-time to traverse the cavity field. As an atom moves through the mode volume, a probe beam is continuously applied and its transmission through the cavity monitored in real time.

trapped and cooled ions [162,163], and FORTs chaining atoms through the cavity in the transverse direction [164,165].

Cavity QED with cold atoms in the strong coupling regime has enabled observation of the vacuum Rabi splitting for single atoms in an optical cavity, and of the quantum saturation of the atom-cavity response. In the work of Ref. [158], for example, measurements of cavity transmission vs. input driving field strength clearly deviate from the prediction of the optical bistability equation and are instead consistent with numerical solutions of the quantum master equation itself (Fig. 19, solid line and experimental data points). This work was carried out with laser-cooled Cesium atoms dropped through an optical cavity of length $d = 10.1\,\mu$m and finesse $F = 180{,}000$, leading to $(g_0, \kappa, \gamma_\perp) = 2\pi(120, 40, 2.6)$ MHz and critical parameters $(N_0, m_0) = (0.014, 2 \times 10^{-4})$. This and subsequent experiments [36–38,166] thus operate in a regime of critical atom number and saturation photon number orders of magnitude below unity. In this case driving fields which populate the cavity mode with coherent amplitudes at or even below

one photon are sufficient to induce nonlinear response in the system. Likewise, effective atom numbers well below one interact strongly with the cavity field and alter the cavity transmission spectrum. Therefore the presence of a single atom, even when poorly coupled or just entering the cavity mode volume, can be detected with high $S/N$ via the transmission of a probe beam through the cavity.

A striking demonstration of strong coupling in optical cavity QED comes in recent experiments which actually bind an atom in the cavity by creating the ''bound state'' $|-\rangle$ of the Jaynes-Cummings ladder [36,37]. Figure 22(a)
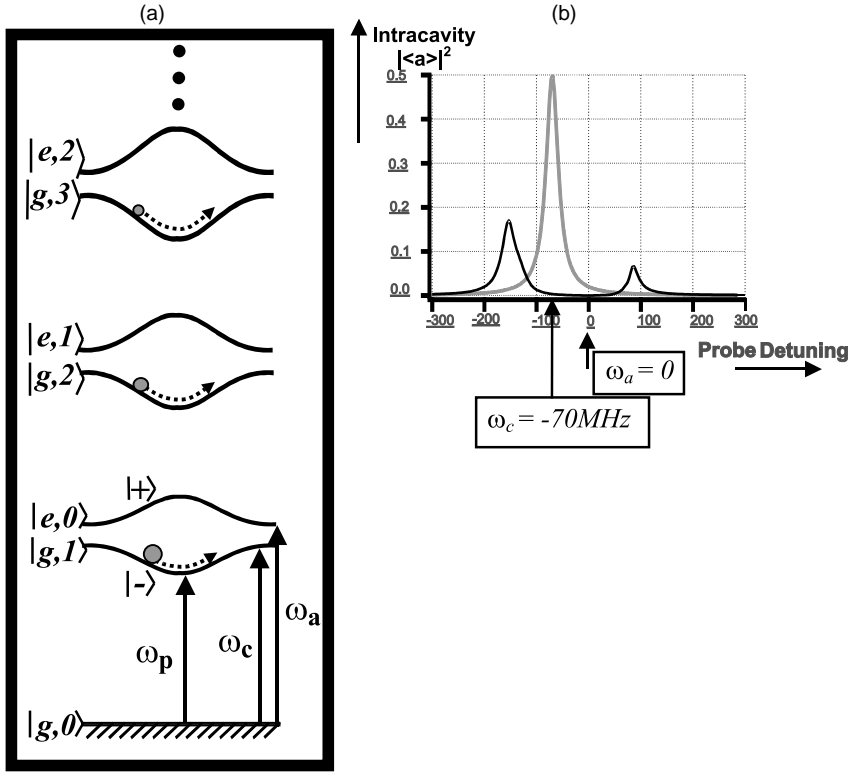


FIG. 22. Jaynes-Cummings ladder and vacuum Rabi splitting to enable trapping of single atoms with the quantized field. (a) This ladder reflects the continuous evolution of energy eigenvalues as an atom moves from outside the cavity (no coupling) to the center and back out again. A driving field at $\omega_p < \omega_c < \omega_a$ populates strong-field-seeking states, leading to an attractive effective potential for the atom in the cavity. (b) Vacuum Rabi spectrum corresponding to (a) for the atom-cavity system of [36]. Note the asymmetry in the spectrum arising from the atom-cavity detuning in this case. A probe beam tuned to the lower Rabi sideband will see a rise in transmission when an atom is coupled to the cavity mode.

shows the ladder of atom-cavity energy eigenvalues with emphasis on the continuous evolution from bare to joint eigenstates as an atom moves from regions of low coupling to regions where the cavity field is strong. Concentrating on the ground and first excited states of the manifold, we will see that this eigenvalue structure enables both sensing and trapping of an atom by means of the cavity field.

If the cavity is probed at its bare resonance frequency $\omega_p \approx \omega_c$, this probe will be moved out of resonance as the atom-cavity coupling increases, causing a drop in transmitted light as an atom moves into the cavity. If, on the other hand, the probe is tuned below the cavity resonance $\omega_p < \omega_c$ and instead near the lower dressed state, it will move into resonance as an atom becomes more strongly coupled. In this case the cavity transmission is originally low and increases as an atom moves toward regions of strong coupling. To see these effects quantitatively, we find steady-state solutions of the master equation to obtain the vacuum Rabi spectrum in Fig. 22(b). As seen already in the data of [158], resonant probe transmission can be reduced by factors of $10^2$–$10^3$, providing enormous $S/N$ for detection of an intracavity atom. For a probe on the lower vacuum Rabi sideband, the transmission increase is less drastic, but probing at this frequency is nevertheless often preferable because of its effect on the atomic motion.

Thus far we have discussed strong coupling between the cavity field and atomic dipole, or internal state. We can define a further condition of strong coupling for the *external* atomic degrees of freedom, which occurs when the coherent coupling dominates the atomic kinetic energy as well. Under these circumstances the position-dependent energy eigenvalues cause an impor-tant mechanical effect on an atom interacting with the cavity mode. For instance, an attractive effective potential is felt by an atom when a probe field tuned to the lower vacuum Rabi sideband is used to populate the strong-field-seeking state $|-\rangle$. When this potential is large relative to the atomic kinetic energy, experimental observations range from atom-cavity scattering effects to largely conservative binding of an atom by a single-photon cavity field [36,37,158,167].

In the work of Refs. [36,167], the sensing and trapping aspects of strong coupling are exploited to realize atom–photon binding within an optical cavity. A deep ($\sim 2.5\,\text{mK}$) potential associated with the single-quantum interaction arises from the use of a short cavity with very small mode volume ($d = 10.9\,\mu\text{m}$, $w_0 = 14.1\,\mu\text{m}$). This cavity, with mirror finesse $F = 480,000$ and $(g_0, \kappa, \gamma_\perp)/2\pi = (110, 14.2, 2.6)$ MHz, gives critical photon and atom numbers $m_0 = 2.7 \times 10^{-4}$, $N_0 = 6 \times 10^{-3}$. The coherent interaction energy exceeds other relevant energies in the problem, in particular the atomic kinetic energy $E_k \sim k_B(0.5\,\text{mK})$ acquired in the 3-mm fall from the MOT to the cavity mode. Thus an atom can be caught within the cavity if

the system can be driven from its ground state to the trapping state when the atom is at a maximum of the cavity field [168–171].

To implement this triggering strategy, atoms are dropped through the cavity mode while cavity transmission is monitored with a weak probe beam of frequency $\omega_p < \omega_c < \omega_a$ and 0.05 intracavity photons. Such a weak probe tuned near the lower vacuum Rabi sideband allows high $S/N$ for observation of an atom entering the cavity mode, but does not significantly populate the excited states of the atom-cavity system. Once the probe transmission rises above a predetermined threshold, indicating that an atom is in a region of strong coupling to the cavity mode, the probe power is increased to a level of about 0.3 intracavity photons to create a confining potential around the atom.

The resulting cavity transmission for an atom trapped in this way is shown in Fig. 23. It exhibits oscillations between the increased probe level of 0.3 intracavity photons and values as high as $|\langle \hat{a} \rangle|^2 \sim 1$ due to the atom's motion within the cavity field. Regular oscillations in transmission arise from atomic motion toward and away from the cavity axis, with the level falling back to 0.3 photons when the atom eventually heats out of the trap and escapes from the cavity. Using this protocol, mean atom dwell times in
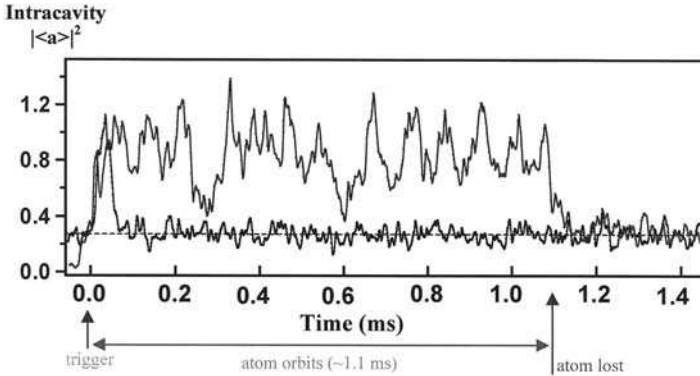


FIG. 23. Single atoms trapped in orbit with single photons using cavity QED [36]. The main trace shows probe light transmission through the cavity as a single atom is trapped there. The probe field, tuned to the lower vacuum Rabi sideband, is initially set to a weak "sensing" level that does not significantly populate excited states of the system. A rise in probe transmission signals an atom falling through the center of the cavity mode, triggering a switch to a stronger "driving" light level. The light now drives the system to strong-field-seeking states and the atom orbits within the cavity, leading to regular oscillations in cavity transmission as shown. The overlaid trace shows an atom transit signal for constant driving field (no triggered trapping) for comparison. For this data, $\omega_p = \omega_a - 2\pi$ (125 MHz) and $\omega_c = \omega_a - 4\pi$ (47 MHz). The transmission signal, detected via balanced heterodyne, is proportional to intracavity $|\langle a \rangle|^2$ and is shown in those units.

the cavity of 340 µs are observed, with some rare events lasting up to several milliseconds. For comparison, the overlaid trace shows a typical transmission signal for an atom falling through the cavity mode with constant input field; this no-triggering case shows a ∼75 µs free-fall time for an atom to traverse the cavity mode. Triggered-trapping lifetimes are limited by heating associated with the many decays and re-excitations the atom-cavity system experiences during a single atomic dwell time. It is important to note that, while atoms are trapped via their dipole interaction with a red-detuned light field in a manner reminiscent of the more familiar free-space situation, the dynamics associated with the atom-cavity system are quantitatively and qualitatively different from that case [167]. In particular, a free-space potential of equal intensity would exhibit much greater diffusive heating and thus would largely fail to trap the atoms seen in this experiment; furthermore, the single-atom sensing which enables the trapping strategy is only available through the use of the cavity QED system.

The most interesting feature of the measurement record for a trapped atom is undoubtedly the oscillation in transmission. The period and amplitude of these oscillations agrees quantitatively with atomic orbital motion in the Gaussian mode transverse to the cavity axis. For the parameters of [36] trapped atoms are tightly confined close to a single antinode of the field and detectable signatures from axial motion are not observed [36,167], leading to bounds on the size of any small-amplitude axial excursion. Thus transmission provides a direct, real-time record of an atom's radial distance from the cavity axis; this record can also be used along with the known effective potential to reconstruct two-dimensional trajectories. Such reconstructions, as tested by applying the method to simulated atomic trajectories, represent an atomic position measurement which is about a factor of 5 above the standard quantum limit (SQL) [36,172].

Current experimental efforts focus on use of this real-time position information to feed back to actively control atomic positions within the cavity mode [173]. Progress in this direction aims to use cavity QED to investigate fundamental questions of quantum measurement and optimal state estimation and control. The ability to trap an atom with a single photon field is a dramatic illustration of single-quantum physics in optical cavities; however, it is the sensing power and $S/N$ for real-time observation of the system that make the optical cavity unique.

E. Broader Application of Real-Time Sensing Capabilities:
   Quantum State Preparation and Detection

Optical cavity QED in the strong coupling regime provides, as we have seen, a nearly-closed environment for interactions between single quanta.

Furthermore, it retains the chief merit of optical cavity spectroscopy in the classical regime: enhanced $S/N$ for observation of intracavity dynamics through the well-defined output channel of cavity decay. While in the language of open quantum systems the cavity decay at rate $\kappa$ introduces decoherence into the system, the decay is a single output mode that can be directed toward some use that actually keeps information within the system of interest. In the context of optimal state estimation and control, this may mean measuring the transmitted field and using that information to control the system via active feedback. Alternatively, for quantum logic and communication, it may mean measuring the output field to obtain the result of a computation or sending it efficiently to a distant cavity where it will coherently interact with a second atom.

One measure of the capability for observation is the so-called "optical information" rate for monitoring intracavity dynamics through measurement of transmitted light. For a simple estimate of optical information, we consider the case of a resonant probe, $\omega_p = \omega_c = \omega_a$, whose transmission drops as an atom enters the cavity mode. The presence of an atom is thus signaled by a rate $dI/dt$ of "missing" photons at the cavity output. This rate is given by $dI/dt = \kappa(|\langle \hat{a} \rangle|^2_{\text{empty}} - |\langle \hat{a} \rangle|^2_{\text{full}}) \approx \kappa |\langle \hat{a} \rangle|^2_{\text{empty}}$ provided that $|\langle \hat{a} \rangle|^2_{\text{full}}$ is very small. This is the case for strong coupling conditions but driving strength still small enough to prevent complete saturation of the atomic response. Thus $dI/dt$ is maximized for $|\langle \hat{a} \rangle|^2_{\text{full}} \approx m_0$ and $|\langle \hat{a} \rangle|^2_{\text{empty}} \approx C_1^2 |\langle \hat{a} \rangle|^2_{\text{full}} \approx g_0^2/\kappa^2$. This rough argument yields an optical information rate $dI/dt = g_0^2/\kappa$; the same quantity appears in a formal treatment of the resonant-probing case as well as in calculations of probing on the lower vacuum Rabi sideband and in analytic expressions for various schemes to monitor both atomic position and atom-cavity internal states in a strong-driving limit [174].

The quantity $dI/dt = g_0^2/\kappa$ corresponds to information about some aspect of the atom-cavity state accessible at a rate of over $10^9$ per second for the current generation of strong-coupling Fabry-Perot cavities with alkali atoms. This must be compared with a rate for monitoring the same atom via light scattering in free space, where fluorescence rates do not exceed $\sim 10^7$ per second and it is nearly impossible to imagine effective collection of the light emitted over $4\pi$ solid angle. The orders-of-magnitude increase in detection capability represents one of the main strengths of cavity QED in quantum state control.

The cavity-enabled sensing ability can be brought to bear in diverse ways. In a current experiment [38,161], an atom entering the cavity mode is detected via a cavity QED probe field and then trapped by a separate light field in a different longitudinal mode of the cavity. This far-off-resonant trap (FORT) takes advantage of the cavity buildup power to obtain

intensities large enough to trap the atom even in the face of mechanical effects caused by the probe field. Furthermore, the sensing power provided by that probe field allows trapping of one and only one atom in the FORT, offering opportunities for schemes in quantum information science that rely on deterministic interaction of a single atom with the field.

Many such schemes fall under the general heading of quantum state synthesis, using the single-atom medium to prepare single photons and other nonclassical states of the light field. Existing methods of single-photon generation encounter difficulty in providing true determinism of the output field, either in timing or in spatial output channel. The output channel difficulty is naturally solved in cavity QED, and efficient single-atom trapping is bringing true on-demand state generation within the realm of possibility. Proposals encompass not only single photon generation but also numerous other state preparations, such as the photon turnstile and the single atom laser [175], as well as schemes for entanglement generation made possible by the high detection efficiency.

Another direction which relies on real-time sensing in cavity QED is quantum state estimation and quantum feedback. Real-time active feedback methods infer the system state and steer it toward some target value; as cavity-assisted state measurement approaches its fundamental quantum limit, a servo will be limited by measurement back-action effects. Performance of such a control loop will depend on minimal-disturbance measurements for the variable of interest, and the dynamics will exhibit the evolution-and-collapse patterns characteristic of quantum trajectory theory [176,177]. Experiments on real-time feedback to atomic position explore this issue from one direction, but the concept applies equally to other aspects of the overall atom-cavity state. For instance, ongoing experiments [178] also apply real-time sensing and feedback toward the goal of designing novel states of the cavity output field itself.

## F. Quantum Logic and Communication Protocols

Cavity QED in the strong coupling regime offers the possibility for efficient measurement and control of single quanta, as we have seen, and for rapid and controlled coherent interactions between these single quanta. In the language of quantum information theory, cavity QED is one of several viable platforms for quantum logic and quantum communication. Ongoing technical progress brings the field closer to achieving atomic position control that is fine enough and stable enough to perform a series of atom-field logic gates at high fidelity; position control is required for this purpose because it means a precise knowledge of the coherent coupling rate $g(\vec{r})$. This

ability in turn will allow for on-demand atom-cavity interactions to prepare and coherently couple novel quantum states of the atom and field.

For purposes of quantum information science, optical cavity QED has the advantage of offering clock rates that are fast in absolute terms, with current experiments in the range $g_0/2\pi \approx 100$–$200\,\text{MHz}$. Its chief strength, however, may lie in the marriage of atomic internal states, easily accessible for preparation and robust enough for storage, with states of the light field which can be easily and rapidly transported across large distances. In other words, optical cavity QED provides an attractive setting for the implementation of diverse protocols in quantum communication, quantum teleportation and entanglement distribution, and thus eventually extended quantum networking.

Quantum communication schemes in optical cavity QED generally involve information (e.g., coherence or entanglement) written onto the internal state of an atomic sample. The cavity QED interaction transfers that coherence onto the state of the cavity field, which then exits the cavity via the decay $\kappa$ in a well-defined mode and can be sent to the receiving station. Here the light may be injected into a second cavity and thus its state can be written onto a "target" atom. Numerous detailed proposals have been developed, with attention to realistic conditions for reversibility and to technical challenges such as atomic localization for high gate fidelity [179]. A closely related variant is the use of similar protocols for teleportation of atomic (motional) states via light fields [180].

For these schemes as well as for quantum state synthesis protocols, our previous schematic is typically altered in two important ways. First, to store information and particularly coherence in the atom, some internal structure beyond the two-level atom is helpful. A useful internal state configuration is the lambda system, which consists of two ground states interacting with a single electronic excited state. The transitions may be distinguished by frequency (e.g., due to hyperfine splitting between the ground states) or by polarization, so that the cavity mode interacts selectively with one ground state and not the second. In such a scheme classical light pulses on the second leg of the lambda system can also be used to "gate" a cavity QED interaction and control the dynamics in detail.

The second technical modification is the use of "one-sided" cavities to replace the symmetric ones we have discussed so far. This change is driven by the desire for a truly unique, coherent output mode for the cavity. We envision a cavity with single-mirror transmissions $(T_1, T_2)$ and losses $(A_1, A_2)$. The current generation of cavities have $(T_1 = T_2) > (A_1 = A_2)$, allowing cavity decay to send light out both cavity mirrors equally. A better situation for quantum communication and nonclassical light generation would instead be $T_1 \gg (T_2, A_1, A_2)$. To achieve this situation while remaining

in the strong coupling regime, mirrors with very low transmission and losses
are necessary, since one typically desires even $T_1$ about 10 ppm or smaller.

G.  Future Outlook for Cavity QED

The rich interplay between optical cavity technology and fundamental
questions of cavity QED promises to continue for some time. One area of
emerging research is cavity-assisted cooling of atoms or molecules, with a
number of theoretical schemes just beginning to be realized in experiment
[181–184]. Some cooling mechanisms rely explicitly on active feedback or on
strong coupling, but others can be thought of as free-space cooling
mechanisms adapted to operate in an optical cavity. Since cooling rates and
temperatures depend on decay rates in the system, the introduction of new
rates through cavity QED and the modification of bare atomic decay rates
can offer substantial gains under some circumstances. As colder atoms
interact in cavity QED, we also approach a situation where the quantization
of atomic external degrees of freedom is important, leading to the regime of
the ''well-dressed'' atom and novel effects associated with quantized center-
of-mass motion [170,185–189]. As the sensing and cooling effects in cavity
QED are better understood, another prospect is the identification of ways in
which they can be exploited in dispersive settings rather than in the special
case of a single near-resonant transition. Such developments would open up
these techniques of trapping, cooling, and real-time microscopy for
application to more general atomic and molecular systems.

   Cavities for these future developments may come in some unfamiliar
guises. Fabry-Perot technology is inherently limited in the mode volume and
thus coupling strengths it can offer; in particular, conventional high-
reflection coating stacks become ''soft'' boundaries for very short cavities as
a larger and larger fraction of the cavity mode actually resides in the coating
layers themselves [14]. Numerous other cavity designs are being developed
as options. Fairly extensive work, both theoretical and experimental, has
been devoted to whispering gallery modes of microspheres [190]; one of the
main challenges here is coupling light in and out of the mode without
excessive degradation in $Q$. Another emerging field is the design of optical
cavities using photonic bandgap structures in solids, where cavity properties
can be selected by tuning the lattice and defect structures [191–193].

# VIII.  Concluding Remarks on Cavity Enhancement

Dramatic progress has been achieved in optical detection sensitivity by
joining laser spectroscopy with resonator physics. The methods discussed in

this article emphasize the importance of separating the atomic signal from the cavity's stored field, and the advantage of detecting signals where only fundamental physical processes introduce noise. We note the importance of determining the cavity's response simultaneously for the on-resonance and off-resonance cases, so that these quantities can be compared from the measured signal to reveal the atomic/molecular absorption of interest. We have discussed how the FM method of NICE-OHMS can be used to implement this signal isolation and subtraction in real time. A repetitive transient heterodyne detection scheme, with lowered technical requirements on the laser system, that meets these design principles has also been discussed. One exciting application of the spectroscopic method discussed in the article is high-resolution, vibration overtone spectroscopy. Coupling this method with large, intracavity beam modes and slow moving molecules [194–196], we expect hyperfine structures and recoil splittings will be measured in overtone transitions in the near future. The precision with which these transitions can be measured will be facilitated by the recently developed femtosecond-comb-referenced laser sources [197,198]. Detailed and precise studies of systematic variations in the overtone spectra can now be carried out in a vast range of spectral coverage. Extension of these cavity-based sensitive laser spectroscopic approaches is destined to have a strong impact on certain active research areas in condensed matter physics where detailed information of system dynamics and structures are being vigorously pursued.

Besides this significant application of optical cavities for ultrasensitive spectroscopy, the technologies of high finesse and large bandwidth mirror coating will continue to play major and fascinating roles in optical frequency metrology and precision tests. The art of producing ultra-narrow and stable cavity interference fringes and the ability to accurately split these fringes to a fraction of parts per million will be critical to a vast array of laser-based modern precision experiments, some of which are mentioned in Section I.D. The emerging synergy between ultrafast lasers and optical cavities will not only present a wonderful opportunity for the extension of sensitive laser spectroscopy to wide spectral coverage, but also offer the prospect of enhanced nonlinear interactions when ultrafast pulses are optimally introduced to interact with an intracavity medium. The continued pursuit of coherent-evolution-dominated open quantum systems will also push the technological envelope of optical cavities and the related science. We hope that our brief account of optical cavities and the related subsequent discussions have helped to thread together a seemingly disparate set of actively pursued research topics ranging from ultra-sensitive to ultrafast, and from ultraprecision to ultraquantum.

## IX.  Acknowledgements

## X.  References

 1. Hansch, T.W., Schawlow, A.L., and Toschek, P. (1972). *IEEE J. Quantum Electron.* **QE-8**, 802.
 2. Kimble, H.J. (1980). *IEEE J. Quantum Electron.* **16**, 455.
 3. Harris, T.D. (1983). In: D.S. Kliger (Ed.), "Ultrasensitive Laser Spectroscopy." p. 343, Academic Press, New York.
 4. Kastler, A. (1962). *Appl. Optics* **1**, 17.
 5. Cerez, P., Brillet, A., Manpichot, C.N., and Felder, R. (1980). *IEEE Trans. Instrum. Meas.* **29**, 352.
 6. Ma, L.S., and Hall, J.L. (1990). *IEEE J. Quantum Electron.* **26**, 2006.
 7. Delabachelerie, M., Nakagawa, K., and Ohtsu, M. (1994). *Opt. Lett.* **19**, 840.
 8. Anderson, D.Z., Frisch, J.C., and Masser, C.S. (1984). *Appl. Optics* **23**, 1238.
 9. Okeefe, A., and Deacon, D.A.G. (1988). *Rev. Sci. Instrum.* **59**, 2544.
10. Hall, J.L., and Borde, C.J. (1976). *Appl. Phys. Lett.* **29**, 788.
11. Mabuchi, H., Ye, J., and Kimble, H.J. (1999). *Appl. Phys. B-Lasers Opt.* **68**, 1095.
12. Hinds, E.A. (1990). *Adv. At. Mol. Opt. Phys.* **28**, 237.
13. Mabuchi, H., and Doherty, A.C. (2002). *Science* **298**, 1372.
14. Hood, C.J., Kimble, H.J., and Ye, J. (2001). *Phys. Rev. A* **64**, 033804.
15. An, K.W., Yang, C.H., Dasari, E.E., and Feld, M.S. (1995). *Opt. Lett.* **20**, 1068.
16. Sappey, A.D., Hill, E.S., Settersten, T., and Linne, M.A. (1998). *Opt. Lett.* **23**, 954.
17. Steinfeld, J.I. (1999). *Chin. J. Chem.* **17**, 204.
18. Paul, B., Scherer, J.J., Okeefe, A., and Saykally, R.J. (1997). *Laser Focus World* **33**, 71.
19. Romanini, D., and Lehmann, K.K. (1993). *Journal of Chemical Physics* **99**, 6287.
20. Scherer, J.J., Voelkel, D., and Rakestraw, D.J. (1997). *Appl. Phys. B-Lasers Opt.* **64**, 699.
21. Spaanjaars, J.J.L., terMeulen, J.J., and Meijer, G. (1997). *Journal of Chemical Physics* **107**, 2242.
22. Park, J., Chakraborty, D., Bhusari, D.M., and Lin, M.C. (1999). *J. Phys. Chem. A* **103**, 4002.
23. Pushkarsky, M.B., Zalyubovsky, S.J., and Miller, T.A. (2000). *Journal of Chemical Physics* **112**, 10695.

24.  Modugno, G., Inguscio, M., and Tino, G.M. (1998). *Phys. Rev. Lett.* **81**, 4790.
25.  Mazzotti, D., Cancio, P., Giusfredi, G., Inguscio, M., and De Natale, P. (2001). *Phys. Rev. Lett.* **86**, 1919.
26.  Gianfrani, L., Fox, R.W., and Hollberg, L. (1999). *J. Opt. Soc. Am. B-Opt. Phys.* **16**, 2247.
27.  Abramovici, A., Althouse, W.E., Drever, R.W.P., Gursel, Y., Kawamura, S., Raab, F.J., Shoemaker, D., Sievers, L., Spero, R.E., Thorne, K.S., Vogt, R.E., Weiss, R., Whitcomb, S.E., and Zucker, M.E. (1992). *Science* **256**, 325.
28.  Fritschel, P., Gonzalez, G., Lantz, B., Saha, P., and Zucker, M. (1998). *Phys. Rev. Lett.* **80**, 3181.
29.  Cohadon, P.F., Heidmann, A., and Pinard, M. (1999). *Phys. Rev. Lett.* **83**, 3174.
30.  Semertzidis, Y., Cameron, R., Cantatore, G., Melissinos, A.C., Rogers, J., Halama, H., Prodell, A., Nezrick, F., Rizzo, C., and Zavattini, E. (1990). *Phys. Rev. Lett.* **64**, 2988.
31.  Cameron, R., Cantatore, G., Melissinos, A.C., Ruoso, G., Semertzidis, Y., Halama, H.J., Lazarus, D.M., Prodell, A.G., Nezrick, F., Rizzo, C., and Zavattini, E. (1993). *Phys. Rev. D* **47**, 3707.
32.  Delabachelerie, M., Nakagawa, K., Awaji, Y., and Ohtsu, M. (1995). *Opt. Lett.* **20**, 572.
33.  Nakagawa, K., deLabachelerie, M., Awaji, Y., and Kourogi, M. (1996). *J. Opt. Soc. Am. B-Opt. Phys.* **13**, 2708.
34.  Ye, J., Ma, L.S., and Hall, J.L. (1997). *IEEE Trans. Instrum. Meas.* **46**, 178.
35.  Vuletic, V., and Chu, S. (2000). *Phys. Rev. Lett.* **84**, 3787.
36.  Hood, C.J., Lynn, T.W., Doherty, A.C., Parkins, A.S., and Kimble, H.J. (2000). *Science* **287**, 1447.
37.  Pinkse, P.W.H., Fischer, T., Maunz, P., and Rempe, G. (2000). *Nature* **404**, 365.
38.  Ye, J., Vernooy, D.W., and Kimble, H.J. (1999). *Phys. Rev. Lett.* **83**, 4987.
39.  Wang, H., Goorskey, D., and Xiao, M. (2002). *Phys. Rev. A* **65**, 051802.
40.  Bose, S., Jacobs, K., and Knight, P.L. (1999). *Phys. Rev. A* **59**, 3204.
41.  Braginsky, V.B., Khalili, F.Y., and Volikov, P.S. (2001). *Phys. Lett. A* **287**, 31.
42.  Braginsky, V.B., and Vyatchanin, S.P. (2002). *Phys. Lett. A* **293**, 228.
43.  Pipino, A.C.R. (1999). *Phys. Rev. Lett.* **83**, 3093.
44.  Dohlman, A.W., Black, H.R., and Royall, J.A. (1993). *Am. Rev. Respir. Dis.* **148**, 955.
45.  Olopade, C.O., Zakkar, M., Swedler, W.I., and Rubinstein, I. (1997). *Chest* **111**, 862.
46.  Siegman, A.E. (1986). "Lasers." University Science Books, Mill Valley, CA.
47.  Wieman, C.E., and Hansch, T.W. (1976). *Phys. Rev. Lett.* **36**, 1170.
48.  Jaynes, E.T., and Cummings, F.W. (1963). *Proc. IEEE* **51**, 89.
49.  Haroche, S. (1992). In: J. Dalibard, J.-M. Raimond, and J. Zinn-Justin (Eds.), "Fundamental Systems in Quantum Optics, Les Houches Session LIII." North-Holland, Amsterdam.
50.  Kimble, H.J. (1994). In: P. Berman (Ed.), "Cavity Quantum Electrodynamics." Academic Press, San Diego.
51.  Kimble, H.J. (1998). *Phys. Scr.* **T76**, 127.
52.  Lugiato, L.A. (1984). *Progress in Optics* **21**, 69.
53.  Turchette, Q.A., Thompson, R.J., and Kimble, H.J. (1995). *Appl. Phys. B-Lasers Opt.* **60**, S1.
54.  Wahlquist, H. (1961). *J. Chem. Phys.* **35**, 1708.
55.  Smith, R.L. (1971). *J. Opt. Soc. Am.* **61**, 1015.
56.  Bjorklund, G.C. (1980). *Opt. Lett.* **5**, 15.
57.  Hall, J.L., Hollberg, L., Baer, T., and Robinson, H.G. (1981). *Appl. Phys. Lett.* **39**, 680.
58.  Bjorklund, G.C., Levenson, M.D., Lenth, W., and Ortiz, C. (1983). *Applied Physics B-Photophysics and Laser Chemistry* **32**, 145.
59.  Ye, J., Ma, L.S., and Hall, J.L. (1996). *Opt. Lett.* **21**, 1000.
60.  Ye, J., and Hall, J.L. (2000). *Phys. Rev. A* **61**, 061802.

61. Ye, J., Ma, L.S., and Hall, J.L. (1998). *J. Opt. Soc. Am. B-Opt. Phys.* **15**, 6.

62. Ma, L.S., Ye, J., Dube, P., and Hall, J.L. (1999). *J. Opt. Soc. Am. B-Opt. Phys.* **16**, 2255.

63. Ye, J., Ma, L.S., and Hall, J.L. (2000). *J. Opt. Soc. Am. B-Opt. Phys.* **17**, 927.

64. Ishibashi, C., and Sasada, H. (1999). *Jpn. J. Appl. Phys. Part 1 - Regul. Pap. Short Notes Rev. Pap.* **38**, 920.

65. Ishibashi, C., and Sasada, H. (2000). *J. Mol. Spectrosc.* **200**, 147.

66. Letokhev, V.S., and Chebotayev, V.P. (1977). "Nonlinear Laser Spectroscopy." Springer-Verlag, Berlin.

67. Stenholm, S. (1983). "Foundation of Laser Spectroscopy." Wiley, New York.

68. Ye, J., Robertsson, L., Picard, S., Ma, L.S., and Hall, J.L. (1999). *IEEE Trans. Instrum. Meas.* **48**, 544.

69. Hall, J.L., Ma, L.S., Taubman, M., Tiemann, B., Hong, F.L., Pfister, O., and Ye, J. (1999). *IEEE Trans. Instrum. Meas.* **48**, 583.

70. Werle, P. (1995). *Appl. Phys. B-Lasers Opt.* **60**, 499.

71. Wong, N.C., and Hall, J.L. (1985). *J. Opt. Soc. Am. B-Opt. Phys.* **2**, 1527.

72. Allan, D.W. (1987). *IEEE Trans. Ultrason. Ferroelectr. Freq. Control* **34**, 647.

73. Borde, C.J., Hall, J.L., Kunasz, C.V., and Hummer, D.G. (1976). *Phys. Rev. A* **14**, 236.

74. Bagayev, S.N., Chebotayev, V.P., Dmitriyev, A.K., Om, A.E., Nekrasov, Y.V., and Skvortsov, B.N. (1991). *Applied Physics B-Photophysics and Laser Chemistry* **52**, 63.

75. Chardonnet, C., Guernet, F., Charton, G., and Borde, C.J. (1994). *Appl. Phys. B-Lasers Opt.* **59**, 333.

76. Levenson, M.D., Paldus, B.A., Spence, T.G., Harb, C.C., Harris, J.S., and Zare, R.N. (1998). *Chem. Phys. Lett.* **290**, 335.

77. Drever, R.W.P., Hall, J.L., Kowalski, F.V., Hough, J., Ford, G.M., Munley, A.J., and Ward, H. (1983). *Applied Physics B-Photophysics and Laser Chemistry* **31**, 97.

78. Salomon, C., Hils, D., and Hall, J.L. (1988). *J. Opt. Soc. Am. B-Opt. Phys.* **5**, 1576.

79. Rafac, R.J., Young, B.C., Beall, J.A., Itano, W.M., Wineland, D.J., and Bergquist, J.C. (2000). *Phys. Rev. Lett.* **85**, 2462.

80. Udem, T., Reichert, J., Holzwarth, R., and Hänsch, T.W. (1999). *Phys. Rev. Lett.* **82**, 3568.

81. Cundiff, S.T., and Ye, J. (2003). Femtosecond optical frequency combs. *Rev. Modern Phys.*, **75**, 325.

82. Jones, R.J., and Diels, J.C. (2001). *Phys. Rev. Lett.* **86**, 3288.

83. Rempe, G., Thompson, R.J., Kimble, H.J., and Lalezari, R. (1992). *Opt. Lett.* **17**, 363.

84. Hall, J.L., Ye, J., and Ma, L.S. (2000). *Phys. Rev. A* **62**, 013815.

85. Devoe, R.G., Fabre, C., Jungmann, K., Hoffnagle, J., and Brewer, R.G. (1988). *Phys. Rev. A* **37**, 1802.

86. Jones, R.J., and Ye, J. (2002). *Opt. Lett.* **27**, 1848.

87. Cotton, A., Mouton, H., and Hebd, C.R. (1905). *Seances Acad. Sci.* **141**, 317.

88. Adler, S.L. (1971). *Ann. Phys.* **67**, 599.

89. Raffelt, G., and Stodolsky, L. (1988). *Phys. Rev. D* **37**, 1237.

90. Wood, C.S., Bennett, S.C., Cho, D., Masterson, B.P., Roberts, J.L., Tanner, C.E., and Wieman, C.E. (1997). *Science* **275**, 1759.

91. Chauvat, D., Le Floch, A., Vallet, M., and Bretenaker, F. (1998). *Appl. Phys. Lett.* **73**, 1032.

92. Moriwaki, S., Sakaida, H., Yuzawa, T., and Mio, N. (1997). *Appl. Phys. B-Lasers Opt.* **65**, 347.

93. Brandi, F., DellaValle, F., DeRiva, A.M., Micossi, P., Perrone, F., Rizzo, C., Ruoso, G., and Zavattini, G. (1997). *Appl. Phys. B-Lasers Opt.* **65**, 351.

94. Bakalov, D., Brandi, F., Cantatore, G., Carugno, G., Carusotto, S., Della, F., Valle De, A.M., Riva, Gastaldi, U., Iacopini, E., Micossi, P., Milotti, E., Onofrio, R., Pengo, R.,

Perrone, F., Petrucci, G., Polacco, E., Rizzo, C., Ruoso, G., Zavattini, E., and Zavattini, G. (1998). *Quantum Semiclass. Opt.* **10**, 239.

95. Zhu, M., and Hall, J.L. (1993). *J. Opt. Soc. Am. B-Opt. Phys.* **10**, 802.
96. Lichten, W. (1985). *J. Opt. Soc. Am. A-Opt. Image Sci. Vis.* **2**, 1869.
97. Lichten, W. (1986). *J. Opt. Soc. Am. A-Opt. Image Sci. Vis.* **3**, 909.
98. Devoe, R.G., and Brewer, R.G. (1984). *Phys. Rev. A* **30**, 2827.
99. Devoe, R.G., and Brewer, R.G. (1984). *J. Opt. Soc. Am. A-Opt. Image Sci. Vis.* **1**, 1307.
100. Kourogi, M., Nakagawa, K., and Ohtsu, M. (1993). *IEEE J. Quantum Electron.* **29**, 2693.
101. Brothers, L.R., Lee, D., and Wong, N.C. (1994). *Opt. Lett.* **19**, 245.
102. Imai, K., Zhao, Y., Kourogi, M., Widiyatmoko, B., and Ohtsu, M. (1999). *Opt. Lett.* **24**, 214.
103. Imai, K., Kourogi, M., and Ohtsu, M. (1998). *IEEE J. Quantum Electron.* **34**, 54.
104. Ye, J., Ma, L.S., Day, T., and Hall, J.L. (1997). *Opt. Lett.* **22**, 301.
105. Diddams, S.A., Ma, L.S., Ye, J., and Hall, J.L. (1999). *Opt. Lett.* **24**, 1747.
106. Udem, T., Reichert, J., Hänsch, T.W. and Kourogi, M. (2000). *Phys. Rev. A* **62**, 1801.
107. Udem, T., Reichert, J., Holzwarth, R., and Hänsch, T.W. (1999). *Opt. Lett.* **24**, 881.
108. Kobayashi, T., Sueta, T., Cho, Y., and Matsuo, Y. (1972). *Appl. Phys. Lett.* **21**, 341.
109. Macfarlane, G.M., Bell, A.S., Riis, E., and Ferguson, A.I. (1996). *Opt. Lett.* **21**, 534.
110. Ho, K.P., and Kahn, J.M. (1993). *IEEE Photonics Technol. Lett.* **5**, 721.
111. Brothers, L.R., and Wong, N.C. (1997). *Opt. Lett.* **22**, 1015.
112. Hänsch, T.W. (1976). In A. Mooradain, T. Jaeger, and P. Stokseth, (Eds.), "Tunable Lasers and Applications." Springer-Verlag, Berlin.
113. Baklanov, Y.V., and Chebotayev, V.P. (1977). *Applied Physics* **12**, 97.
114. Teets, R., Eckstein, J., and Hänsch, T.W. (1977). *Phys. Rev. Lett.* **38**, 760.
115. Salour, M.M. (1978). *Rev. Mod. Phys.* **50**, 667.
116. Eckstein, J.N., Ferguson, A.I., and Hänsch, T.W. (1978). *Phys. Rev. Lett.* **40**, 847.
117. Ferguson, A.I., and Taylor, R.A. (1983). *Proceedings of the Society of Photo-Optical Instrumentation Engineers* **369**, 366.
118. Bramwell, S.R., Ferguson, A.I., and Kane, D.M. (1987). *Opt. Lett.* **12**, 666.
119. Wineland, D.J., Bergquist, J.C., Itano, W.M., Diedrich, F., and Weimer, C.S. (1989). In: G.F. Bassani, M. Inguscio, and T.W. Hänsch (Eds.), "The Hydrogen Atom." p. 123, Springer-Verlag, Berlin.
120. Reichert, J., Holzwarth, R., Udem, T., and Hänsch, T.W. (1999). *Opt. Commun.* **172**, 59.
121. Diddams, S.A., Jones, D.J., Ye, J., Cundiff, T., Hall, J.L., Ranka, J.K., Windeler, R.S., Holzwarth, R., Udem, T., and Hansch, T.W. (2000). *Phys. Rev. Lett.* **84**, 5102.
122. Ye, J., Yoon, T.H., Hall, J.L., Madej, A.A., Bernard, J.E., Siemsen, K.J., Marmet, L., Chartier, J.-M., and Chariter, A. (2000). *Phys. Rev. Lett.* **85**, 3797.
123. Negus, D.K., Spinelli, L., Goldblatt, N., and Feugnet, G. (1991). In: "Advanced Solid-State Lasers." Vol. 10, OSA.
124. Spence, D.E., Kean, P.N., and Sibbett, W. (1991). *Opt. Lett.* **16**, 42.
125. Asaki, M.T., Huang, C.P., Garvey, D., Zhou, J.P., Kapteyn, H.C., and Murnane, M.M. (1993). *Opt. Lett.* **18**, 977.
126. Ranka, J.K., Windeler, R.S., and Stentz, A.J. (2000). *Opt. Lett.* **25**, 25.
127. Diels, J.-C., and Rudolph, W. (1996). "Ultrashort Laser Pulse Phenomena: Fundamentals, Techniques, and Applications on a Femtosecond Timescale." Academic Press, San Diego.
128. Telle, H.R., Steinmeyer, G., Dunlop, A.E., Stenger, J., Sutter, D.H., and Keller, U. (1999). *Appl. Phys. B* **69**, 327.
129. Jones, D.J., Diddams, S.A., Ranka, J.K., Stentz, A., Windeler, R.S., Hall, J.L., and Cundiff, S.T. (2000). *Science* **288**, 635.

130. Apolonski, A., Poppe, A., Tempea, G., Spielmann, C., Udem, T., Holzwarth, R., T.W. Hänsch, and Krausz, F. (2000). *Phys. Rev. Lett.* **85**, 740.
131. Jones, R.J., Diels, J.C., Jasapara, J., and Rudolph, W. (2000). *Opt. Commun.* **175**, 409.
132. Brabec, T., and Krausz, F. (2000). *Rev. Mod. Phys.* **72**, 545.
133. Baltuska, A., Fuji, T., and Kobayashi, T. (2002). *Phys. Rev. Lett.* **88**, 133901.
134. Baltuska, A., Udem, T., Uiberacker, M., Hentschel, M., Goulielmakis, E., Gohle, C., Holzwarth, R., Yakoviev, V.S., Scrinzi, A., Hansch, T.W., and Krausz, F. (2003). *Nature* **421**, 611.
135. Heupel, T., Weitz, M., and Hansch, T.W. (1997). *Opt. Lett.* **22**, 1719.
136. Malcolm, G.P.A., Ebrahimzadeh, M., and Ferguson, A.I. (1992). *IEEE J. Quantum Electron.* **28**, 1172.
137. Crosson, E.R., Haar, P., Marcus, G.A., Schwettman, H.A., Paldus, B.A., Spence, T.G., and Zare, R.N. (1999). *Rev. Sci. Instrum.* **70**, 4.
138. Yanovsky, V.P., and Wise, F.W. (1994). *Opt. Lett.* **19**, 1952.
139. McConnell, G., Ferguson, A.I., and Langford, N. (2001). *J. Phys. D-Appl. Phys.* **34**, 2408.
140. Cohen-Tannoudji, C., Dupont-Roc, J., and Grynberg, G. (1992). "Atom-Photon Interactions." Wiley, New York.
141. Grant, D.E., and Kimble, H.J. (1982). *Opt. Lett.* **7**, 353.
142. Weyer, K.G., Wiedenmann, H., Rateike, M., Gillivray, W.R.M., Meystre, P., and Walther, H. (1981). *Opt. Commun.* **37**, 426.
143. Rempe, G., Thompson, R.J., Brecha, R.J., Lee, W.D., and Kimble, H.J. (1991). *Phys. Rev. Lett.* **67**, 1727.
144. Mielke, S.L., Foster, G.T., and Orozco, L.A. (1998). *Phys. Rev. Lett.* **80**, 3948.
145. Foster, G.T., Orozco, L.A., Castro-Beltran, H.M. and Carmichael, H.J. (2000). *Phys. Rev. Lett.* **85**, 3149.
146. Foster, G.T., Mielke, S.L., and Orozco, L.A. (2000). *Phys. Rev. A* **61**, 053821.
147. Arimondo, E. (1996). *Progress in Optics*, **35**, 257.
148. Harris, S.E. (1997). *Phys. Today* **50**, 36.
149. Lukin, M.D., Fleischhauer, M., Scully, M.O., and Velichansky, V.L. (1998). *Opt. Lett.* **23**, 295.
150. Wang, H., Goorskey, D., and Xiao, M. (2001). *Phys. Rev. Lett.* **87**, 073601.
151. Wang, H., Goorskey, D.J., Burkett, W.H., and Xiao, M. (2000). *Opt. Lett.* **25**, 1732.
152. Rebic, S., Parkins, A.S., and Tan, S.M. (2002). *Phys. Rev. A* **65**, 063804.
153. Turchette, Q.A., Hood, C.J., Lange, W., Mabuchi, H., and Kimble, H.J. (1995). *Phys. Rev. Lett.* **75**, 4710.
154. Turchette, Q.A., Georgiades, N.P., Hood, C.J., Kimble, H.J., and Parkins, A.S. (1998). *Phys. Rev. A* **58**, 4056.
155. Sanchez-Mondragon, J.J., Narozhny, N.B., and Eberly, J.H. (1984). *J. Opt. Soc. Am. B-Opt. Phys.* **1**, 518.
156. Thompson, R.J., Rempe, G., and Kimble, H.J. (1992). *Phys. Rev. Lett.* **68**, 1132.
157. Mabuchi, H., Turchette, Q.A., Chapman, M.S., and Kimble, H.J. (1996). *Opt. Lett.* **21**, 1393.
158. Hood, C.J., Chapman, M.S., Lynn, T.W., and Kimble, H.J. (1998). *Phys. Rev. Lett.* **80**, 4157.
159. Munstermann, P., Fischer, T., Maunz, P., Pinkse, P.W.H., and Rempe, G. (1999). *Phys. Rev. Lett.* **82**, 3791.
160. Shimizu, Y., Shiokawa, N., Yamamoto, N., Kozuma, M., Kuga, T., Deng, L., and Hagley, E.W. (2002). *Phys. Rev. Lett.* **89**, 233001.
161. McKeever, J., Buck, J.R., Boozer, A.D., Kuzmich, A., Naegerl, H.-C., Stamper-Kurn, D.M., and Kimble, H.J. (2003). *Phys. Rev. Lett.*, **90**, 133–602.

162. Mundt, A.B., Kreuter, A., Becher, C., Leibfried, D., Eschner, J., Schmidt-Kaler, F., and Blatt, R. (2002). *Phys. Rev. Lett.* **89**, 103001.
163. Walther, H. (2002). private communications.
164. Kuhr, S., Alt, W., Schrader, D., Muller, M., Gomer, V., and Meschede, D. (2001). *Science* **293**, 278.
165. Chapman, M. (2002). private communications.
166. Hood, C.J., Lynn, T.W., Doherty, A.C., Vernooy, D.W., Ye, J., and Kimble, H.J. (2001). *Laser Phys.* **11**, 1190.
167. Doherty, A.C., Lynn, T.W., Hood, C.J., and Kimble, H.J. (2001). *Phys. Rev. A* **63**, 013401.
168. Haroche, S., Brune, M., and Raimond, J.M. (1991). *Europhys. Lett.* **14**, 19.
169. Englert, B.G., Schwinger, J., Barut, A.O., and Scully, M.O. (1991). *Europhys. Lett.* **14**, 25.
170. Scully, M.O., Meyer, G.M., and Walther, H. (1996). *Phys. Rev. Lett.* **76**, 4144.
171. Doherty, A.C., Parkins, A.S., Tan, S.M., and Walls, D.F. (1997). *Phys. Rev. A* **56**, 833.
172. Mabuchi, H. (1998). *Phys. Rev. A* **58**, 123.
173. Fischer, T., Maunz, P., Pinkse, P.W.H., Puppe, T., and Rempe, G. (2002). *Phys. Rev. Lett.* **88**, 163002.
174. Soklakov, A., and Schack, R. (2002). quant-ph/0210024.
175. Feld, M.S., and An, K.W. (1998). *Sci. Am.* **279**, 56.
176. Mabuchi, H., and Wiseman, H.M. (1998). *Phys. Rev. Lett.* **81**, 4620.
177. Warszawski, P., Wiseman, H.M., and Mabuchi, H. (2002). *Phys. Rev. A* **65**, 023802.
178. Smith, W.P., Reiner, J.E., Orozco, L.A., Kuhr, S., and Wiseman, H.M. (2002). *Phys. Rev. Lett.* **89**, 133601.
179. Briegel, H.J., Cirac, J.I., Dur, W., van, S.J., Enk, Kimble, H.J., Mabuchi, H., and Zoller, P. (1999). *Quantum Computing and Quantum Communications* **1509**, 373.
180. Parkins, A.S., and Kimble, H.J. (1999). *J. Opt. B-Quantum Semicl. Opt.* **1**, 496.
181. Domokos, P., Horak, P., and Ritsch, H. (2001). *J. Phys. B-At. Mol. Opt. Phys.* **34**, 187.
182. Gangl, M., and Ritsch, H. (2001). *Phys. Rev. A* **64**, 063414.
183. van Enk, S.J., McKeever, J., Kimble, H.J., and Ye, J. (2001). *Phys. Rev. A* **64**, 013407.
184. Chan, H.W., Black, A.T., and Vuletic, V. (2003). quant-ph/0208100.
185. Meystre, P., Schumacher, E., and Stenholm, S. (1989). *Opt. Commun.* **73**, 443.
186. Ren, W., and Carmichael, H.J. (1995). *Phys. Rev. A* **51**, 752.
187. Herkommer, A.M., Carmichael, H.J., and Schleich, W.P. (1996). *Quantum Semiclass. Opt.* **8**, 189.
188. Doherty, A.C., Parkins, A.S., Tan, S.M., and Walls, D.F. (1998). *Phys. Rev. A* **57**, 4804.
189. Vernooy, D.W., and Kimble, H.J. (1997). *Phys. Rev. A* **56**, 4287.
190. Vernooy, D.W., Furusawa, A., Georgiades, N.P., Ilchenko, V.S., and Kimble, H.J. (1998). *Phys. Rev. A* **57**, R2293.
191. Yamamoto, Y., and Slusher, R.E. (1993). *Phys. Today* **46**, 66.
192. Chang, R.K., and Campillo, A.J. (1996). (World Scientific, Singapore.
193. Khitrova, G., Gibbs, H.M., Jahnke, F., Kira, M., and Koch, S.W. (1999). *Rev. Mod. Phys.* **71**, 1591.
194. Bethlem, H.L., Berden, G., Crompvoets, F.M.H., Jongma, R.T., van Roij, A.J.A., and Meijer, G. (2000). *Nature* **406**, 491.
195. Gupta, M., and Herschbach, D. (1999). *J. Phys. Chem. A* **103**, 10670.
196. Doyle, J.M., and Friedrich, B. (1999). *Nature* **401**, 749.
197. Jost, J.D., Hall, J.L., and Ye, J. (2002). *Optics Express* **10**, 515.
198. Foreman, S., Jones, D.J., and Ye, J. (2003). *Opt. Lett.* **28**, 370.

This page
intentionally
left blank

# RESONANCE AND THRESHOLD PHENOMENA IN LOW-ENERGY ELECTRON COLLISIONS WITH MOLECULES AND CLUSTERS

## H. HOTOP[1], M.-W. RUF[1], M. ALLAN[2] and I. I. FABRIKANT[3]

[1]*Fachbereich Physik, Universität Kaiserslautern, 67653 Kaiserslautern, Germany*
[2]*Département de Chimie, Université de Fribourg, 1700 Fribourg, Switzerland*
[3]*Department of Physics and Astronomy, University of Nebraska, Lincoln, NE, USA*

# I. Introduction

## A. SETTING THE SCENE

Low-energy collisions of electrons with atoms and molecules are among the most important elementary processes in gaseous environments such as

*E-mail: hotop@physik.uni-kl.de

discharges, arcs, gas lasers, gaseous dielectrics and the earth's atmosphere. Correspondingly these processes have been studied for a long time, most notably over the last forty years following the improvement of instrumental technology and the detection of prominent resonance structure in electron scattering cross-sections due to the formation of temporary negative ions (TNI) (Schulz, 1973a, b). A wealth of information has been gained on the dynamics of these collisions, as documented by many reviews and books (e.g. Schulz, 1973a, b; Lane, 1980; Trajmar *et al.*, 1983; Christophorou, 1984; Shimamura and Takayanagi, 1984; Allan, 1989; Domcke, 1991; Buckman and Clark, 1994; Crompton, 1994; Filippelli *et al.*, 1994; Trajmar *et al.*, 1994; Huo and Gianturco, 1995; Andersen and Bartschat, 1996; Chutjian *et al.*, 1996; Zecca *et al.*, 1996; Becker *et al.*, 2000; Illenberger, 2000; Winstead and McKoy, 2000; Christophorou and Olthoff, 2001a, b; Karwacz *et al.*, 2001a, b; Brunger and Buckman, 2002). In spite of this progress, however, the exploration of threshold phenomena in electron–molecule collisions at low energies – both in the limit of zero electron energy and in the neighborhood of onsets for vibrational excitation – has remained a major challenge for experiment and theory. Experimentally, it is difficult to achieve the desired resolution (energy width in the meV range) and to handle electron beams at energies below about 0.1 eV. Theoretically, it is demanding to incorporate the nuclear dynamics, using descriptions which go beyond local complex potential models (Burke, 1979; Lane, 1980; Kazansky and Fabrikant, 1984; Morrison, 1988; Domcke, 1991; Huo and Gianturco, 1995; Winstead and McKoy, 2000). In this article, we shall survey some of the insight gained over the past ten years through experimental investigations and theoretical descriptions of resonance and threshold phenomena occurring in low-energy electron collisions with molecules and molecular clusters. We concentrate on work carried out with very high resolution (energy width 1–10 meV) and electron energies typically below 1 eV. Much of that work has been devoted to anion formation through electron attachment, but we shall also present examples for total, elastic and vibrationally inelastic electron scattering. Electron impact induced neutral dissociation, electronic excitation, and ionization processes are not considered in this article. We mention, however, recent intriguing observations on vibrational resonances in *positron*-annihilation collisions with molecules. In the remaining part of Section I, we present a brief qualitative introduction into the field of low-energy electron–molecule collisions. Recent complementary surveys on electron collisions with molecules and clusters include several articles in journals (Hashemi *et al.*, 1990; Domcke, 1991; Märk, 1991; Illenberger, 1992; Smith and Španel, 1994; Dunning, 1995; Chutjian *et al.*, 1996; Ingolfsson *et al.*, 1996; Zecca *et al.*, 1996; Burrow *et al.*, 1997; Field *et al.*, 2001a; Karwacz *et al.*,

2001a, b; Brunger and Buckman, 2002) and book chapters (Trajmar *et al.*, 1994; Huo and Gianturco, 1995; Becker *et al.*, 2000; Illenberger, 2000; Winstead and McKoy, 2000; Christophorou and Olthoff, 2001a,b; Hotop, 2001; Tanaka and Sueoka, 2001).

## B. Dynamics of Low-Energy Electron–Molecule Collisions

The dynamical behaviour of slow electrons traversing gases is to a large extent determined by two effects: the energy dependent evolution of the scattering phases for the relevant partial waves and the influence of temporary negative ion states (resonances). For quite a few atoms and molecules, special behaviour of the s-wave ($l = 0$) phase shift leads to a deep Ramsauer-Townsend minimum in the scattering cross-section between 0 and 1 eV which strongly affects the electron mobility in these gases. Even more importantly, resonances (compound states of the electron–molecule system with lifetimes ranging typically from $10^{-15}$ to $10^{-11}$ s) are often found to dominate the dynamics of electron–molecule collisions over the energy range 0–10 eV. The extended time interval (compared with the direct transit time which is below 1 fs), spent by the incoming electron close to the target while in the resonance state (lifetime $\tau = \eta/\Gamma$, $\Gamma$ = resonance width), has profound effects especially on collision channels which involve a reaction of the nuclear framework, i.e. on vibrational excitation VE and on dissociative attachment DA (forming negative ions). Apart from well-known shape resonances such as $H_2^-(^2\Sigma_u)$, $N_2^-(^2\Pi_g)$, $CO^-(^2\Pi)$, $O_2^-(^2\Pi_g, v \geq 4)$ (Schulz 1973b; Shimamura and Takayanagi, 1984; Allan, 1989; Domcke, 1991; Brunger and Buckman, 2002) which are located below the lowest limit for DA and owe their lifetime to the centrifugal barrier of the electron, repulsive anion states above the DA limit are important for VE as well as DA. The importance of resonances for vibrational excitation (VE) as well as negative ion formation via dissociative attachment (DA) is illustrated in Fig. 1.

A resonance is formed when the incoming electron, possessing an energy $E$ close to the resonance energy, is captured into a low-lying unoccupied molecular orbital (LUMO) which typically has anti-bonding character. During the lifetime of the resonance the nuclei start to move to larger distances under the influence of the destabilizing force brought into the system by the captured electron. When the electron leaves the negative ion complex by autodetachment after a time comparable to $\tau$, the nuclei find themselves at a distance substantially larger than the equilibrium distance of the neutral molecule, i.e. in a vibrationally excited state. If the lifetime is sufficiently long to allow propagation of the nuclei
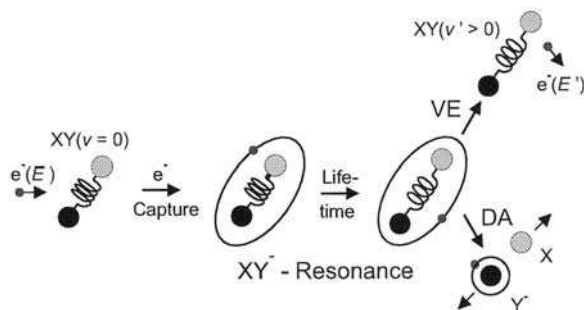
Fig. 1. Dynamics of vibrational excitation (VE) and dissociative attachment (DA) in electron–molecule scattering through resonances (from Hotop, 2001).

to large distances, dissociative attachment (DA, i.e. formation of $X + Y^-$ or $X^- + Y$) occurs. The occurrence of VE and DA is thus mediated by electron scattering through resonances $XY^{-*}$, as summarized in the reaction scheme (1):

$$e^-(E) + XY(n, v, J) \to XY^{-*} \text{ (Resonance)}$$
$$\to XY(n', v', J') + e^-(E') \qquad \text{(Scattering)} \qquad \text{(1a)}$$
$$\to X + Y^- \qquad \text{(Dissociative Attachment)} \qquad \text{(1b)}$$
$$\to XY^- \qquad \text{(Non-dissociative Attachment)} \qquad \text{(1c)}$$
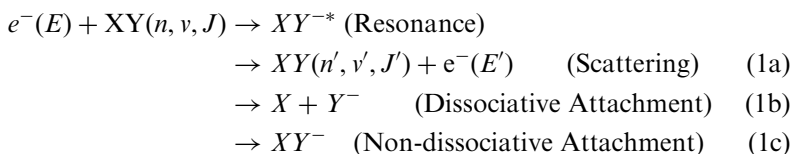
Process (1a) describes elastic scattering ($E = E'$) when the electronic ($n$), vibrational ($v$) and rotational ($J$) quantum numbers all remain the same. A reaction with $v' > v$ and $n = n'$ corresponds to VE within the initial electronic state. Process (1c) describes nondissociative attachment (NDA), i.e. formation of negative ions $XY^-$ with lifetimes sufficiently long to allow mass spectrometric detection. Figure 2 illustrates the dynamics of vibrational excitation (VE), dissociative attachment (DA) and non-dissociative attachment (NDA) in a potential curve diagram responsible for the nuclear motion along the normal coordinate $R$.

For the situation described by the potential curves in Fig. 2, VE and DA proceed through electron capture from the neutral ground state potential $V_0(R)$ into the repulsive TNI state $XY^{-*}$ (potential $V_-^*(R)$) which possesses a resonance width $\Gamma(R)$ accounting for autodetachment of the TNI at internuclear separations smaller than the crossing radius $R_C$; the width normally rises with decreasing $R$, but may saturate towards smaller $R$. The shaded area represents the Franck-Condon region for the primary electron capture process involving a molecule $XY$ in its vibrational ground

Fig. 2. Potential curve diagram for low-energy electron–molecule collisions.

state $v = 0$. The energy dependences of the cross-section $\sigma_{vv'}(E)$ for VE and $\sigma_{DA}(E)$ for DA (which are similar, but not identical in shape (O'Malley, 1966, 1967; Chu and Burrow, 1994) reflect the Franck-Condon overlap of the initial $v = 0$ level with the nuclear wave function in the $XY^{-*}$ resonance state in combination with the effects of autodetachment. For vibrationally excited states in $V_0(R)$, the effective threshold energy for DA moves to lower energies, and a substantial effect of initial vibrational excitation is thus expected on the shape of the attachment spectrum (O'Malley, 1967; Massey, 1976).

At energies close to $0\,\text{eV}$, electron capture occurs into the low-lying anion state $XY^-$ (potential $V_-(R)$) with favorable Franck-Condon factors. In the depicted case, dissociation out of this anion state is not accessible at low electron energies. For small molecules (e.g. $O_2^-\,(^2\Pi_g, v \geq 4)$), autodetachment occurs within the characteristic lifetime of the resonance, unless the TNI is stabilized by vibrational deexcitation in collisions with other particles (as possible in high density media or in clusters). For molecules with sufficient complexity (such as $SF_6$, $C_6F_6$ or $C_{60}$), however, the total energy of the $XY^-$ system may be distributed efficiently over the rich vibrational manifold by intramolecular vibrational redistribution (IVR) in such a way that it can take a long time before the system finds itself again in a situation favourable for autodetachment, i.e. nondissociative attachment with formation of a metastable anion occurs. The effective lifetime of the $XY^-$ anion in general depends on the initial vibrational energy. The energy dependence of the cross-section for NDA typically peaks at zero energy and decreases rapidly with rising energy (Christophorou, 1978; Illenberger, 2000).

There are quite a number of important cases (e.g. $F_2$, $Cl_2$, $O_3$, $CCl_4$, $CFCl_3$) for which the repulsive branch of the lowest potential surface for the $XY^-$ anion cuts the neutral ground state potential near the minimum of the latter (as in Fig. 2), but has its lowest asymptotic limit $X + Y^-$ lying energetically below the vibrational ground state of $XY$. In this case, DA is exothermic at zero electron energy, and one expects to observe a zero energy peak in the DA cross-section due to s-wave attachment unless the $l = 0$ partial wave is forbidden by symmetry considerations. Like neutron capture by nuclei at low energies, the cross-section for s-wave electron attachment to molecules follows the $1/v$ law (Bethe, 1935; Wigner, 1948) when the electron velocity $v$ goes to zero. While beautiful confirmations of this law have been made in neutron absorption experiments some time ago (e.g. Blatt and Weisskopf, 1952), clear demonstrations for electron capture collisions had to wait until sub-meV resolution was achieved in laser photoelectron attachment experiments (Klar *et al.*, 1992a, b; Schramm *et al.*, 1998).

Interesting resonance and threshold phenomena may occur close to onsets for vibrational excitation: the channels of the electron–molecule scattering system (1a,b,c) are coupled and thus 'feel' each other. This channel coupling leads to special structure (Wigner cusps of different shapes, vibrational Feshbach resonances) in open channels when the collision energy $E$ passes through the onset for a new inelastic channel. High energy resolution is needed to reveal these features. For a variety of molecules, threshold peaks, i.e. large enhancements in VE cross-sections within a narrow region above the VE onset, are observed, as first discovered for HF and HCl by Rohr and Linder (1975, 1976). Towards higher energies, VE cross-sections may exhibit oscillatory 'boomerang' structures (Birtwistle and Herzenberg, 1971; Herzenberg, 1984), found more recently even in molecules like HCl where they would initially not be expected because of a large resonance width (Cvejanovic, 1993; Allan *et al.*, 2000; Čížek *et al.*, 2001). Very narrow 'outer well resonances', superimposed on the broader boomerang structures, have been identified, initially theoretically, in molecules where the potential curve of the anion has a secondary minimum at large internuclear separation (Allan *et al.*, 2000; Čizek *et al.*, 2001). Remarkable progress towards a deeper understanding of these phenomena has been recently achieved in a systematic joint experimental and theoretical investigation of the hydrogen halides (see Section IV.).

For molecules with sufficiently strong long-range electron–molecule interactions (e.g. due to the molecular polarizability or dipole moment) the existence of a quasi-discrete low-energy anion state in the continuum ($V_d(R)$, electron attached to the LUMO) leads to two potential curves $V_{res,1}(R)$ and $V_{res,2}(R)$ (Domcke and Cederbaum, 1981; Gauyacq and Herzenberg, 1982), as sketched in Fig. 3b. Note that without the long-range
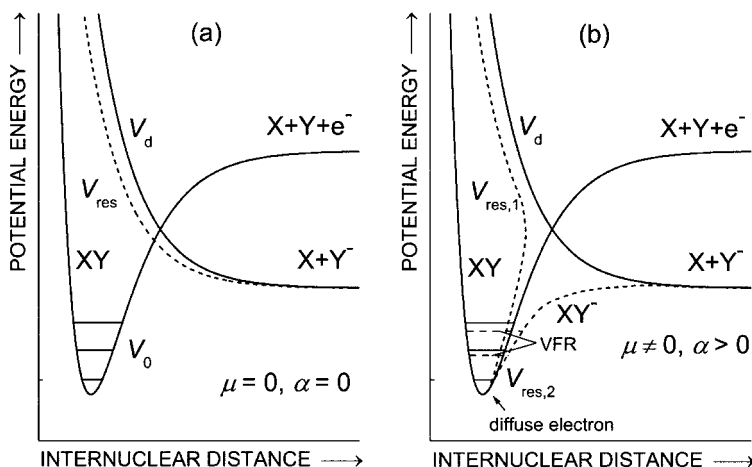
FIG. 3. On the origin of vibrational Feshbach resonances: sketch of potentials without (a) and with (b) long-range electron–molecule interaction.

attraction, only one resonance $V_{res}(R)$ exists (somewhat shifted below $V_d(R)$ by the interaction of $V_d$ with the continuum), as shown in Fig. 3a.

For internuclear distances around the equilibrium separation $R_e$ of the neutral curve $V_0(R)$, the potential curve $V_{res,2}(R)$ lies close to, but below $V_0(R)$; in this range, the anion state $V_{res,2}(R)$ may be viewed as a composite of the neutral molecule with a diffuse electron bound by long-range forces (with no need to invoke a centrifugal barrier for the electron). As evident from Fig. 3b, the low-lying vibrational levels $v_2$ in $V_{res,2}(R)$ are located just below the corresponding vibrational levels $v_0 = v_2$ in the neutral molecule. The level $v_2 = 0$ may be – when sufficiently bound with respect to the influence of rotational effects – a stable, detectable anion state (such as a dipole-bound state, Desfrançois et al., 1996) which is not accessible in collisions of the molecule with free continuum electrons. The quasi-bound vibrational levels in $V_{res,2}(R)$ with $v_2 \geq 1$ lie in the electron–molecule continuum and correspond to vibrational Feshbach resonances (VFR, Schramm et al., 1999); they were previously addressed as nuclear-excited Feshbach resonances (Bardsley and Mandl, 1968; Gauyacq and Herzenberg, 1982; Knoth et al., 1989a; Thümmel et al., 1993). In the depicted case, the VFRs can only decay by autodetachment through indirect coupling to the continuum (via kinetic coupling of the two resonance states). The VFRs are thus expected to live quite long and to appear as narrow features below vibrational thresholds in elastic or vibrationally inelastic electron scattering cross-sections (Knoth et al., 1989a; Thümmel et al., 1993; Schramm et al.,

1999; Sergenton *et al.*, 2000); their observation requires high energy resolution. If the asympotic energy of the discrete anion state $V_d(R)$ lies below a given VFR, then this and higher-lying VFRs may also decay by dissociation and thus be observed in DA as well (Schramm *et al.*, 1999, 2002). Interestingly, vibrational resonances have been recently also observed in the energy dependent cross-sections for positron annihilation involving polyatomic molecules in the gas phase (Gilbert *et al.*, 2002), see Section IV.D.

   The following article is organized as follows. In Section II, we survey the relevant aspects of the underlying theory. In Section III, we describe experimental aspects with emphasis on recent developments. In Section IV, selected case studies highlight some of the recent progress in the field. In Section V, we conclude with a brief summary and address some unsolved problems.

## II. Theory

Theoretical developments in the field of electron–molecule collisions during the past twenty-five years were covered in several reviews (Burke, 1979; Lane, 1980; Herzenberg, 1984; Kazansky and Fabrikant, 1984; Morrison, 1988; Domcke, 1991; Huo and Gianturco, 1995). Some aspects of resonance and threshold phenomena were discussed in these reviews, as well as by Sadeghpour *et al.* (2000). The theoretical description of electron–molecule collisions generally requires an adequate description of electronic, vibrational and rotational degrees of freedom. However, if the typical collision time is short compared to the rotational period, the molecule can be treated as having a fixed orientation during the collision process, and the result for the cross-section can be averaged over orientations. Treatment of vibrational dynamics is usually more important and more challenging to the theory. In the electron energy region important for applications, many inelastic processes such as vibrational excitation and dissociative electron attachment are driven by negative-ion resonances, as already addressed in the introduction. The lifetime of these resonance states is quite often comparable to the vibrational period (e.g., for $N_2$, CO and $CO_2$ molecules) and sometimes even exceeds it substantially (e.g., for the $O_2$ molecule). The theoretical description of vibrational dynamics in these cases is usually based on the nonlocal complex potential describing the nuclear motion in the intermediate negative-ion state (O'Malley, 1966; Bardsley, 1968; Domcke, 1991). An alternative method is based on the *R*-matrix approach (Schneider *et al.*, 1979; Fabrikant, 1990). For studies of resonance and threshold phenomena the latter one is especially attractive, particularly in the case

of a strong long-range interaction between the incident electron and the molecular target. The $R$ matrix allows a convenient parametrization, and all strong energy dependences of transition amplitudes and cross-sections can be accounted for by inclusion of the long-range interaction in electronic channels. In what follows we will briefly describe this approach formulated by Wigner (1948) and its application to electron–molecule collisions.

## A. Multichannel $R$-Matrix Theory

The fundamental paper of Wigner (1948) gives a unified method for the description of inelastic processes in the near-threshold region. The method is based on the $R$-matrix theory (Wigner and Eisenbud, 1947) which was initially developed for nuclear reactions, but later on applied to electron–atom and electron–molecule collisions. The $R$-matrix theory is a very powerful tool for analytical studies of near-threshold and resonance phenomena, as well as for *ab initio* numerical calculations.

   The basic concept of Wigner's theory is the reaction sphere outside which only long-range interactions between reactants are important. Initially it was assumed that this interaction is diagonal, that is interchannel transitions are impossible outside the sphere. This assumption is not always valid in the theory of electron–molecule collisions. In particular, the dipolar interaction can cause transitions between different rotational states. The $R$-matrix theory can be generalized for a nondiagonal dipolar interaction outside the sphere (Gailitis and Damburg, 1963). However, most of the analytical results (with the exception of dipolar interaction between degenerate channels) were obtained assuming a diagonal long-range interaction, and we will use this approximation at the first stage.

### A.1. Analytical Theory of Threshold Behavior, Resonances, and Cusps: Short-Range Interaction

We consider an $N$-channel system and introduce the multichannel wave function in the form of an $N \times N$ matrix $\boldsymbol{\psi}$ which has the following form outside the reaction sphere, $r > r_0$,

$$\boldsymbol{\psi} = \boldsymbol{h}^{-1} - \boldsymbol{h}^{(+)}\boldsymbol{S} \tag{2}$$

where $\boldsymbol{S}$ is the scattering matrix and $\boldsymbol{h}^{(\pm)}$ are channel wavefunctions with the following asymptotic behavior

$$h_{ij}^{\pm} \sim \delta_{ij}k_i^{-1/2} \exp[i(k_i r - l_i\pi/2)], \tag{3}$$

where $k_i$ and $l_i$ are linear and angular momenta in channel $i$. The asymptotic form (3) assumes that all $N$ channels are open. However, the whole treatment can be easily generalized if there are $N_c$ additional closed channels. The corresponding diagonal matrix elements of $h^{(+)}$ behave like $\exp -i|k_i|r : \exp(-i|k_i|r)$, and the matrice $h^{(-)}$ and $S$ become rectangular with $N + N_c$ rows and $N$ columns. For simplicity we will not dwell on further details related to closed channels.

The partial (for a given set of angular momenta) cross-section for transitions from an initial state $i$ to a final state $f$ is proportional to $|T_{fi}|^2$ where $T$ is the transition matrix related to the scattering matrix by

$$T = 1 \ (= \text{unity matrix}) - S \tag{4}$$

The function (2) is matched with the internal wavefunction in the form

$$\psi = R \frac{d\psi}{dr} \tag{5}$$

where $R$ is the Wigner $R$ matrix which is a meromorphic function of energy having poles only on the real axis (Lane and Thomas, 1958). For the purpose of derivation of the threshold laws we assume that the $R$ matrix can be considered as an analytical function of energy and expanded in powers of energy $E$. This is the essence of the effective range theory (ERT). A special treatment is necessary if there is a bound, a virtual, or a resonance state near the threshold.

Using analytical properties of $h^{(+)}$, one can obtain the equation of Ross and Shaw (1961)

$$T = -2ik^{l+1/2}(M - ik^{2l+l})^{-1}k^{l+1/2}, \tag{6}$$

where $M$ is a meromorphic function of energy. This equation allows us to obtain threshold laws for elastic and inelastic processes. In particular the threshold law for an inelastic process is given by

$$T_{fi} \sim k_f^{l_f+1/2}. \tag{7}$$

This is the Wigner threshold law. Usually we are interested in the total (that is, summed over all orbital angular momenta) cross-section. Then $l_f$ is the lowest angular momentum allowed by the symmetry of the problem. For example, photodetachment of a bound s electron gives a $k_f^3$ or $E_f^{3/2}$ behavior of the cross-section (p-wave emission), whereas photodetachment

of a bound p electron leads to the $k_f$ behavior (s-wave emission) near threshold because of the dipole selection rules (the d-wave is suppressed strongly by the $k_f^5$ dependence).

In nonresonant collision processes, when there is no selection rule in $l$, the lowest allowed angular momentum is $l_f = 0$, therefore we obtain $\sigma_{fi} \propto k_f$ for the cross-section of an endothermic process. This law can be usually applied to the process of electron impact excitation of atoms and molecules, if there is no dipolar interaction in the final channel. If heavy particles are formed in the final state (for example in DA and electron impact dissociation processes) the range of validity of the Wigner law is very narrow (Fabrikant *et al.*, 1991), therefore, if there is no activation barrier for the process, the cross-section as a function of energy in the near-threshold region exhibits a vertical onset (O'Malley, 1966).

Another example is the Wigner-Baz' cusp (Baz', 1958). Just for illustration we will consider now a two-channel case and investigate the behavior of $|T_{11}|^2$ near the threshold for excitation of the channel 2. Note that $k_2$ is real above the threshold, and purely imaginary below the threshold. This allows us to write $|T_{11}|^2$ in the following form

$$|T_{11}|^2 = \frac{a}{b + ck_2^{2l_2+1}}, \quad k_2^2 > 0 \tag{8}$$

$$|T_{11}|^2 = \frac{a + d|k_2|^{2l_2+1}}{b + f|k_2|^{2l_2+1}}, \quad k_2^2 < 0 \tag{9}$$

where the constants $a$, $b$, $c$, $d$, and $f$ are expressed through the elements of the $M$-matrix. Equation (9) explicitly demonstrates the discontinuity of $d|T_{11}|^2/dE$ at threshold (the threshold cusp) for $l_2 = 0$. If $l_2 > 0$, we still have formally a nonanalytical behavior appearing as a discontinuity of higher derivatives. However, this behavior is very hard to detect experimentally. The paper of Baz' (1958) shows that this discontinuity results directly from the conservation of probability or the unitarity of the $S$ matrix.

Note that the explicit expressions for the coefficients allow us to prove (Fabrikant, unpubl.) that $a$, $b$, and $c$ are positive meaning that the *elastic* cross-section is always *decreasing* above the threshold. At the same time there is no certain relation between $d$ and $f$, therefore the sign of the energy derivative *below* the threshold might be both positive and negative. This result can be generalized to some multichannel cases. For example, if there are two open channels and we look at the transition $1 \rightarrow 2$, it can be shown that in the vicinity of the threshold for channel 3 the cross-section $\sigma_{12}$ exhibits the same type of behavior: the sign of $d\sigma_{12}/dE$ might be both
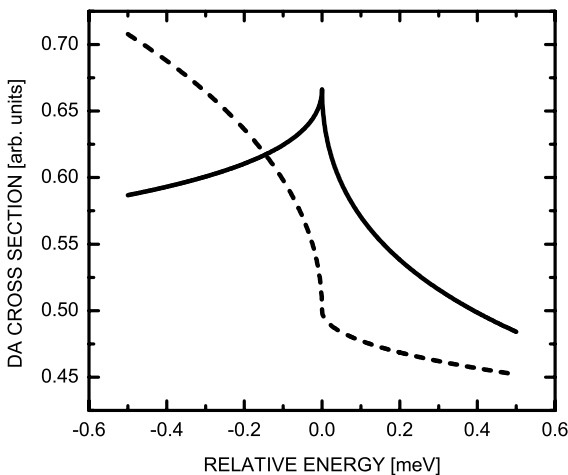
Fig. 4. Illustration of cusp structure in partial cross-sections due to interchannel coupling (see text).

positive and negative below threshold, but is always negative above threshold. This behaviour is illustrated in Fig. 4 and can be found, e.g., in cross-sections for dissociative attachment around a vibrational excitation threshold. Indeed, in all observed and calculated cases which involve long-range interactions decaying faster than $r^{-2}$ the DA cusp goes downward above the VE threshold.

Although these results seem to be natural (a cross-section in the 'old' channel is decreasing because of the growing cross-section for a transition into a 'new' channel), they are not generally true. In particular, they do not apply when there is a long-range (dipolar) interaction outside the $R$-matrix sphere. The case of the Coulomb interaction gives a completely different behavior, but we do not discuss it here since this review is concerned with electron scattering by neutral targets.

Equation (6) contains also information about near-threshold resonances and virtual states. Let us again consider for simplicity a two-channel case with $l_2 = 0$. Assume first that interchannel coupling is negligible, that is $M_{12} = 0$. Then the $T$-matrix has a pole in the complex $k_2$ plane whose position is $k_2 = -iM_{22}$. This corresponds to a bound state when $M_{22} < 0$ and a virtual state when $M_{22} > 0$. If $M_{12} \neq 0$, $k_2$ acquires a nonzero real part. When $M_{22} < 0$ it corresponds to a Feshbach resonance whereas the case $M_{22} > 0$ corresponds to a virtual state coupled to channel 1. In the first case there is a time delay in scattering, and the cross-section exhibits a Lorentzian or a Fano profile, whereas in the second case the cross-section

exhibits an enhancement at the threshold. This phenomenon is closely connected to the threshold cusps discussed above. In the case of a virtual state whose corresponding pole is close to $k_2 = 0$ the cross-section exhibits a very sharp cusp with a positive derivative at $k_2^2 < 0$ and a negative derivative at $k_2^2 > 0$. If the interaction in the channel 2 becomes more attractive, the cusp turns into a Feshbach resonance below the threshold. Examples illustrating this behavior will be given in Section II.A.4.

### A.2. Dipolar Interaction: Stationary Dipole

A similar approach can be applied in the case of a long-range interaction outside the reaction sphere. In case of electron interaction with a nonrotating dipolar molecule the problem is reduced to diagonalization of the operator (Mittleman and von Holdt, 1965)

$$L = l(l+1) - 2D, \tag{10}$$

where $D$ is the dipole moment matrix obtained by calculating the matrix element of the dipolar interaction between the angular momentum eigenstates.

Diagonalization of the matrix $L$ allows us to express the solution of the Schrödinger equation outside the reaction sphere as a linear combination of the Bessel functions with indices $\lambda_i + 1/2$ where $\lambda_i$ are related to the eigenvalues $\Lambda_i$ of the matrix $L$ by

$$\Lambda_i = \lambda_i(\lambda_i + 1), \quad i = 0, 1, \ldots \tag{11}$$

The form of the threshold law critically depends on the lowest eigenvalue $\Lambda_0$ (Gailitis and Damburg, 1963). If $\Lambda_0 > -1/4$, all $\lambda_i$ are real, the $T$-matrix element for inelastic processes is proportional to $k^{\lambda_0 + 1/2}$, and the cross-section to $k^{2\lambda_0 + 1}$. This happens if the dipole moment of the molecule is lower than the critical dipole moment $\mu_{cr} = 0.6395\,\text{a.u.} = 1.625\,\text{D}$. If $\mu > \mu_{cr}$, or $\Lambda_0 < -1/4$, $\lambda_0 + 1/2$ is purely imaginary, and the cross-section is finite at the threshold. The cross-section for an inelastic process can be written as (Fabrikant, 1977, 1978) ($k \equiv k_f$).

$$\sigma_{fi} = \text{const} \, |e^{i\beta} + e^{\pi\tau} k^{2i\tau}|^{-2}, \tag{12}$$

where $\tau = \text{Im}\lambda$ and the parameter $\beta$ depends on elements of the $M$ matrix as well as on the dipole moment. Although $\beta$ is generally complex, its imaginary part is small if the interaction with other channels (other than dipole-coupled near-threshold channels) is weak. In particular $\beta$ is real for

pure elastic scattering. In this case analytical continuation of the $T$ matrix below the threshold into the region of negative $k_f^2$ allows us to find the poles whose positions are given by the equation

$$k^2 = -\exp\{-[\pi(2n+1)+\beta]\tau^{-1}\} \tag{13}$$

These are the well-known dipole-supported states, discussed originally by Fermi and Teller (1947, see also Turner, 1977) and observed in a series of experiments on charge transfer from Rydberg atoms to polar molecules and clusters (Desfrançois *et al.*, 1994a, b, c; Desfrançois *et al.*, 1996; Compton and Hammer, 2001). Note that these states are very rapidly (exponentially) converging to the threshold, and this is what makes them very different from the Coulomb Rydberg states. The rotational splitting reduces the number of these states from infinity to very few, sometimes even to zero. For example, the HF molecule and water molecule have supercritical dipole moments, however they do not have stable anion states. Crawford and Garrett (1977), by performing model calculations for various molecules, concluded that a dipole-supported state remains bound after inclusion of rotation, if its fixed-nuclei binding energy exceeds approximately ten percent of the rotational constant.

If there are open channels below the threshold, the discussed bound states become dipole-supported Feshbach resonances. If the vibrational motion of the molecule is included, each dipole-supported state can generate a series of vibrational Feshbach resonances, originally called 'nuclear-excited' Feshbach resonances (Bardsley and Mandl, 1968; Domcke and Cederbaum, 1981; Gauyacq and Herzenberg, 1982).

Above the threshold the analytical structure of Eq. (12) leads to oscillations of the cross-section as a function of energy. However, these oscillations cannot be observed in practice (Fabrikant, 1977, 1978). If the dipole moment is just above the critical, the period of oscillations exceeds the rotational spacing whereas for higher dipole moments the amplitude of oscillations becomes exponentially small.

### A.3.  Rotating Dipole

Turning to the more complicated case of a rotating dipole, we have to distinguish between two cases. In the first, rotation removes all degeneracies of the dipole-coupled channels. In the second, some degenerate channels coupled by the dipolar interaction still remain. The second case is typical for symmetric-top molecules and molecules with nonzero projection of the electronic angular momentum on the internuclear axis (e.g., molecules in a $\Pi$ state).

If the electron energy in the final state is small compared to the rotational spacing, the dipole coupling becomes equivalent to the action of a diagonal potential which behaves at large distances as a polarization potential $\alpha_{eff}/(2r^4)$ (note that the effective polarizability $\alpha_{eff}$ can be both positive and negative). In the case of scattering by polar molecules the long-range behavior of the effective diagonal potential depends on the total angular momentum $J$. If $J=0$ the effective polarizability is given by (Clark, 1979; Fabrikant, 1983) $\alpha_{eff}=\mu^2/(3B)$ where $\mu$ is the permanent dipole moment and $B$ the rotational constant. For $J > 0$ and s-wave electrons the effective (static) polarizability turns to zero, and the long-range behavior is determined by the dynamical polarization interaction decaying as $r^{-6}$. In all cases the Wigner threshold law is restored, and it is also possible to find an analytical correction to the Wigner law of the order of $\alpha_{eff} k_f^2 \ln k_f$ (O'Malley, 1965; Damburg, 1968; Gailitis, 1970). The region of the transition between the Wigner law and the dipole threshold law is much more complicated. Even in the simplest two-channel case the solution has a very complicated analytical structure (Gailitis, 1970). Therefore most of the studies in this region were performed by numerical integration of the coupled equations (Fabrikant, 1978, 1983).

If the dipole moment of the molecule is supercritical, there is an infinite number of dipole-supported states in the fixed-nuclei approximation. When the rotational splitting is included, all or most of them disappear because of the effective cut-off of the dipole potential. At large distances the effective electron–dipole interaction decays as $r^{-4}$ or even faster. At shorter distances, where the rotational spacing is smaller than the electron–dipole interaction, the adiabatic body-frame representation (Clark, 1979; Fabrikant, 1983) is more appropriate for description of the physics. In this region the dipole potential leads to binding and anisotropy of the electron wavefunction. The size of the inner (adiabatic) region may be as large as a few hundred a.u. It means that the dipolar interaction may be strong enough to create a diffuse bound or a virtual state (Frey et al., 1994). In particular very diffuse virtual states were found in scattering of Rydberg electrons by HF molecules (Hill et al., 1996) and $CH_3Cl$ molecules (Frey et al., 1995; Fabrikant and Wilde, 1999).

In the presence of a bound or a virtual state near the threshold the analysis based on the multichannel formula of Ross and Shaw (1961), Eq. (6), leads to the following result for the transition cross-section ($k \equiv k_f$)

$$\sigma_{fi} = \frac{ak}{k^2 + 2k \mathrm{Im}\kappa + |\kappa|^2}. \tag{14}$$

The parameters $\kappa$ and $a$, as well as the positions of the $S$-matrix poles depend on $J$. This dependence was calculated for HF (Fabrikant, 1996) molecules. For higher $J$ the pole is moving farther away from the origin, and its influence on the threshold behavior becomes weaker.

In symmetric-top molecules and diatomic molecules with nonzero $\Lambda$, rotation reduces the dipole moment, but does not average it to zero, as for diatomic molecules in a $\Sigma$ state and nonsymmetric polyatomic molecules. In diatomic molecules with $\Lambda \neq 0$ the channels with the projection of the electronic angular momentum $M = \pm \Lambda$ remain degenerate if $\Lambda$-doubling is neglected. For symmetric tops there is a degeneracy with respect to the sign of projection of the rotation angular momentum on the symmetry axis. The reduced dipole moment $\mu_{av}$ can be defined as $\mu_{av} = K/[J(J+1)]^{1/2}$, where $J$ is the total rotational angular momentum and $K$ its component about the symmetry axis. $K$-doubling and inversion splitting are neglected in this approximation. Detailed analyses of the threshold exponents for these cases was done by Engelking (1982) and Engelking and Herrick (1984). Application to the near-threshold photodetachment of $OH^-$ was presented by Smith *et al.* (1997). The position of the virtual-state poles as a function of $J$ and $K$ was calculated for the $CH_3Cl$ molecule by Fabrikant and Wilde (1999).

### A.4. Vibrational Dynamics

At ultralow electron energies when the collision time is much longer than the vibrational period, the projectile electron "sees" the potential averaged over vibrations, therefore the theoretical description of vibrational motion is rather simple in this case. At electron energies which are substantially higher than the vibrational spacing, one can use the adiabatic approximation (Chase, 1956) whereby the transition amplitude is calculated by taking the matrix element of the fixed-nuclei amplitude between the initial and final vibrational states. The intermediate region, where the electron energy becomes comparable to the vibrational spacing, is the most challenging for theoretical calculations. On the other hand, due to the very large difference in masses of the projectile and the target, vibrational excitation of molecules by electrons and DA processes occur with substantial rates only when a resonance mechanism is involved whereby at first stage the electron is captured by the molecule forming a temporary negative-ion state. Inclusion of the resonance mechanism into the theory makes it simpler and more physically transparent, although alternative descriptions without the explicit use of the resonance states are possible (e.g. the zero-range-potential (ZRP) description applied by Gauyacq, 1982).

There are two methods for inclusion of the resonance mechanism into the theory of electron–molecule collisions: the Feshbach projection operator technique and the $R$-matrix approach. The first is more convenient for *ab initio* calculations of VE and DA. However, because of substantial computational challenges, this approach has been applied so far only to diatomic molecules. Even a relatively simple triatomic molecule, $CO_2$, has been treated (Kazansky, 1995; Rescigno *et al.*, 2002) only in the so-called local approximation. The idea of the local approximation (O'Malley, 1966; Bardsley, 1968; Herzenberg, 1968), also called the boomerang model (Birtwistle and Herzenberg, 1971; Dubé and Herzenberg, 1979), is to describe the motion of the negative-ion state by the Schrödinger equation with a local complex potential whereas the actual potential describing this motion is a nonlocal energy-dependent operator (Domcke, 1991). The nonlocal effects become particularly important near vibrational excitation thresholds where the local theory fails to describe vibrational Feshbach resonances and threshold cusps.

The nonlocal effects can be successfully described within the framework of the projection-operator approach (Domcke, 1991; Meyer *et al.*, 1991; Čížek *et al.*, 1999) or the resonance $R$-matrix theory. The *ab initio* $R$-matrix method (Schneider *et al.*, 1979) requires several terms in the $R$-matrix expansion to describe a single resonance. This is not physically transparent and causes difficulties in the calculation of DA processes. In contrast, the effective $R$-matrix model (Wong and Light, 1984, 1986) and the resonance $R$-matrix model (Fabrikant, 1986) use only one $R$-matrix state corresponding to the physical resonance. This allows us to find the direct connection between the parameters of the $R$-matrix theory and parameters of the Feshbach projection operator approach, particularly the position and the width of the negative-ion resonance.

For model calculations we present the fixed-nuclei $R$ matrix in the form

$$R = \frac{\gamma^2(\rho)}{W(\rho) - E_e} + R_b, \tag{15}$$

where the surface amplitude $\gamma(\rho)$ and the $R$-matrix pole $W(\rho)$ are standard parameters of the $R$-matrix theory, and $R_b$ is a background term which is assumed to be weakly dependent on electron energy $E_e$ and internuclear distance $\rho$ (here, $\rho$ is understood to represent its deviation from the equilibrium distance in the neutral potential energy curve). For simplicity we assume that only one angular mode dominates the resonance scattering, therefore the fixed-nuclei $R$ matrix includes only one channel. For example, the resonance scattering by the $N_2$ molecule is dominated by the d-wave,

whereas the resonant scattering by polar molecules is typically dominated by the lowest angular mode resulting from the diagonalization of the operator (10).

The nuclear motion is included by replacing function (15) by the operator (Schneider *et al.*, 1979).

$$R = \gamma(\rho)(T + U(\rho) - E)^{-1}\gamma(\rho) + R_{\mathrm{b}} \tag{16}$$

where $T$ is the kinetic energy operator for the nuclear motion, $E$ is the total energy of the system (including the vibrational energy), and $U(\rho) = W(\rho) + V(\rho)$ is the potential energy of the negative-ion state (whereas $V(\rho)$ is the potential energy of the neutral molecule). Function $U(\rho)$ is equivalent to the diabatic negative-ion state of the projection-operator theory, although these two are not identical. In particular $U(\rho)$ depends on the $R$-matrix radius $r_0$. In model calculations we try to choose $r_0$ and other $R$-matrix parameters in such a way that *one* curve $U(\rho)$ represents the resonance which we want to describe.

The basic equation of the $R$-matrix theory (5) can then be formally solved. We introduce a diagonal matrix $\boldsymbol{u}^+$ of radial electron wavefunctions in different vibrational channels and the surface amplitude matrix $\gamma$ for transitions between vibrational states of the neutral molecule and negative-ion states. Then the $S$ matrix for DA can be written in the following form

$$\boldsymbol{S}_{\mathrm{DA}} = 2\pi(\tilde{\boldsymbol{u}}^+)^{-1}(1 + \gamma\mathbf{G}^{(+)}\gamma\mathbf{L}^+)^{-1}\boldsymbol{y}, \tag{17}$$

where $\tilde{\boldsymbol{u}}^+ = \boldsymbol{u}^+ - R_{\mathrm{b}}(\boldsymbol{u}^+)'$, $\mathbf{L}^+ = (\boldsymbol{u}^+)'(\tilde{\boldsymbol{u}}^+)^{-1}$, $\mathbf{G}^{(+)}$ is the Green operator for the nuclear motion in the negative-ion state, and $\mathbf{y}$ is the column of the first-order DA amplitudes

$$y_v = \langle v|\gamma|\psi^{(+)}\rangle \tag{18}$$

where $|v\rangle$ is the eigenstate of the vibrational Hamiltonian for the neutral molecule, and $\psi^{(+)}$ is the nuclear wavefunction describing the motion in the negative-ion state corresponding to the outgoing-wave boundary condition. Because of the importance of the vibrational continuum for the calculation of the DA processes, Eq. (17) is actually an integral equation for $S_{DA}$. It is solved by the quasiclassical technique (Kalin and Kazansky, 1990) based on the quasiseparable representation of the Green operator.

The matrix $\mathbf{L}^+$ in Eq. (17) is responsible for near-threshold resonances and cusps in partial cross-sections (including dissociative attachment) at

each VE threshold. For example, in the absence of long-range electron–molecule interactions we obtain for the s-wave case

$$L_v^+ = \frac{ik_v}{1 - iR_b k_v}. \tag{19}$$

This behavior gives a cusp in $S_{DA}$ at the threshold for vibrational excitation of the level $v$. However, the cusps are not very pronounced in the absence of long-range interactions. Much more pronounced cusps appear when we include polarization and/or dipolar interactions outside the $R$-matrix sphere. If this interaction is attractive enough, it leads to a vibrational Feshbach resonance below the threshold. Mathematically it corresponds to a pole of $S_{DA}$, Eq. (17), in the complex plane of the energy $E_v = k_v^2/2$ whose imaginary part is negative and gives the resonance halfwidth. If the imaginary part of the pole is positive, the pole corresponds to a virtual state shifted into the complex plane of $E_v$ because of the interchannel interaction. If the virtual state pole is close to $E_v = 0$, we obtain a very sharp cusp at threshold. If we decrease the interaction in the channel $v$, the pole moves away from $E_v = 0$, and the cusp becomes weaker. This situation is schematically represented in Fig. 5.

An alternative, and perhaps physically more transparent description of vibrational Feshbach resonances and threshold effects starts with the neutral curve $V(\rho)$ and the "diabatic" negative-ion curve $U(\rho)$. The adiabatic negative-ion curve can be obtained from the basic equation of the $R$-matrix theory, Eq. (5), but using now the fixed-nuclei approximation.
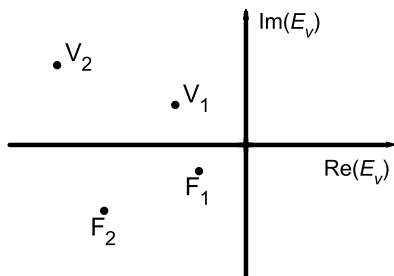


FIG. 5. Poles of the dynamical $S$ matrix describing vibrational excitation and dissociative attachment near the threshold $E_v = 0$. The pole $F_1$ represents a sharp vibrational Feshbach resonance just below the threshold; the pole $F_2$ a broader VFR farther away from the threshold. The pole $V_1$ represents a sharp virtual-state cusp; the pole $V_2$ a weaker virtual state cusp. Note that the poles $F_1$ and $F_2$ lie on the physical sheet, whereas $V_1$ and $V_2$ on the nonphysical sheet of the Riemann surface.
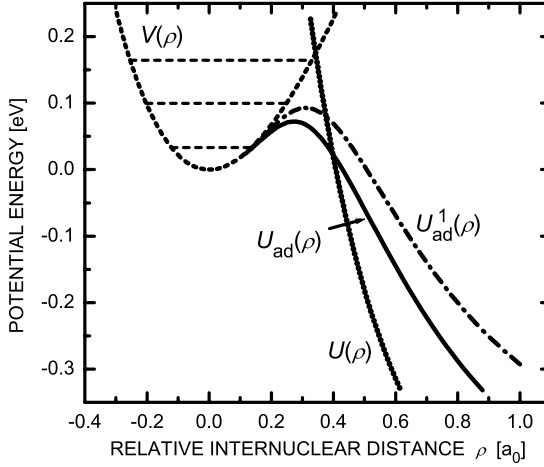
Fig. 6. Potential energy curves for a model electron scattering problem. $V(\rho)$, a curve for the neutral molecule; $U(\rho)$, the $R$-matrix pole; $U_{ad}(\rho)$, the adiabatic anion curve obtained with the polarizability $\alpha = 54\,a.u.$ and the dipole moment $\mu = 0.638\,a.u.$ The chain curve $U_{ad}^1(\rho)$ illustrates the change of the adiabatic curve when $U(\rho)$ is shifted upwards by $\Delta E_S = 0.1\,eV$. The vibrational levels of the neutral molecule are indicated by horizontal solid lines.

In the presence of a strong long-range interaction between the electron and the molecule, the adiabatic curve turns down near the crossing point and follows the neutral curve down to the internuclear distances close to equilibrium. This behavior is illustrated in Fig. 6 by choosing model potential energy curves $V(\rho)$ and $U(\rho)$ and calculating the adiabatic energy curve $U_{ad}(\rho)$ for a given polarizability of the molecule $\alpha$ and its dipole moment $\mu$. The exact position of the crossing between the neutral and the adiabatic negative-ion curves depends on the details of the long-range interaction. In particular, if the dipole moment is supercritical and remains supercritical down to small internuclear distances $\rho$, the curves do not cross, although in practice the dipole-supported state eventually disappears because of rotational effects, as discussed above. But generally, such a behavior of the adiabatic anion curve leads to vibrational states which lie below, but very close to the vibrational states of the neutral molecule. Typically, lower vibrational states correspond to sharper resonances whereas for higher vibrational states we observe cusps which become weaker with increasing $v$.

We illustrate these results in Figs. 7 and 8 by presenting DA cross-sections calculated with the potential curves presented in Fig. 6. In Fig. 7 we increase polarizability that allows us to go from virtual-state cusps to sharp VFRs,
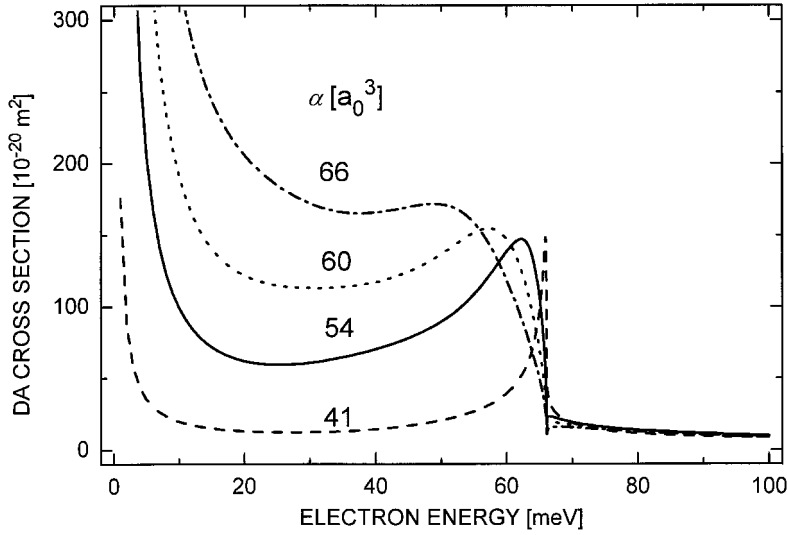
FIG. 7. Dissociative attachment cross-section obtained with potential energy curves $V(\rho)$ and $U(\rho)$ from Fig. 6 and different values of the polarizability $\alpha$ (in a.u.).
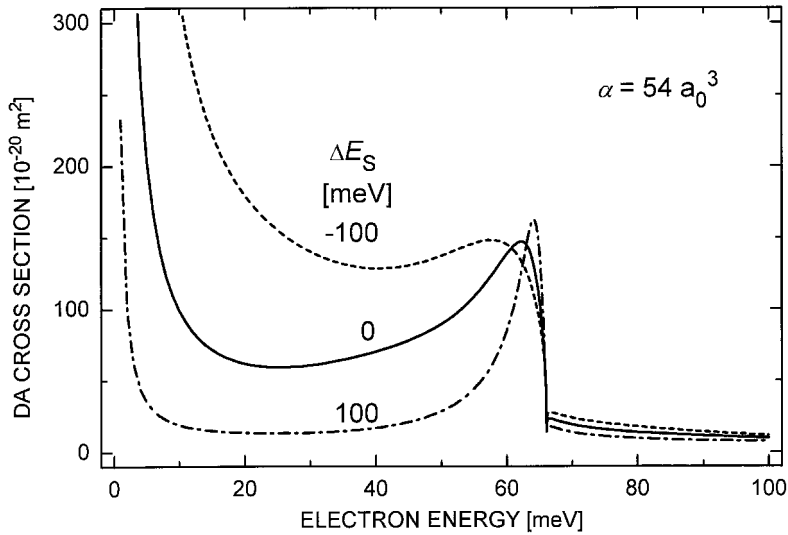


FIG. 8. Dissociative attachment cross-sections obtained from the model of Fig. 6 modified by shifting the curve $U(\rho)$ by different amounts $\Delta E_S$.

and then to broader VFRs well below the threshold. Changing the dipole moment $\mu$ from 0.4 to 0.9 a.u. (while keeping the polarizability fixed at $\alpha = 54$ a.u.) produces similar effects (Leber *et al.*, 2000a). A variation of the crossing point (e.g. through shifting $U(\rho)$ by simply adding or subtracting a $\rho$-independent energy $\Delta E_S$) also produces strong changes in the DA line shape. Introduction of a negative shift (lowering $U(\rho)$) corresponds to the solvation energy effect when the molecule is placed in a cluster or a condensed-matter environment. In Fig. 8 we show how the shape of the cusp and VFR is changing when $U(\rho)$ is shifted.

In conclusion we should stress that VFRs and cusps appear only in the dynamical *R*-matrix theory, or in the nonlocal complex potential theory which are basically equivalent. The local theory is not capable to describe the threshold effects. The effective-range-potential approximation can be considered as a limiting case of the *R*-matrix method and therefore is able to describe threshold effects, too (Gauyacq, 1982; Gauyacq and Herzenberg, 1984).

## B. Vogt-Wannier and Extended Vogt-Wannier Models

A completely different approach to the description of inelastic collisions with zero-energy threshold is used in the Vogt-Wannier (VW) model for the capture into polarization well (Vogt and Wannier, 1954). It is assumed there that the reactive process occurs with 100% probability if the electron falls into the singularity created by the polarization potential $V_{pol} = -\alpha/(2r^4)$. The cross-section depends only on energy and the molecular polarizability $\alpha$, and in the s-wave regime at very low energies, it is given by the simple formula

$$\sigma_{VW}(E \to 0) = 4\pi[\alpha/(2E)]^{1/2}. \tag{20}$$

The original VW result, Eq. (37) of Vogt and Wannier (1954), was derived from the theory of Mathieu functions. For the s-wave contribution Klots (1976) proposed a simple expression

$$\sigma_K(E) = [\pi/(2E)]\{1 - \exp[-4(2\alpha E)^{1/2}]\} \tag{21}$$

which fits the exact Vogt-Wannier result for $l = 0$ to within 8% (see Fig. 9) and describes the transition from the low-energy behavior (20) to the unitarity limit $\pi/(2E) = \pi \lambdabar^2$ at higher energies ($\lambdabar$ = reduced de Broglie wavelength).

$\alpha = 558\, a_0^3$
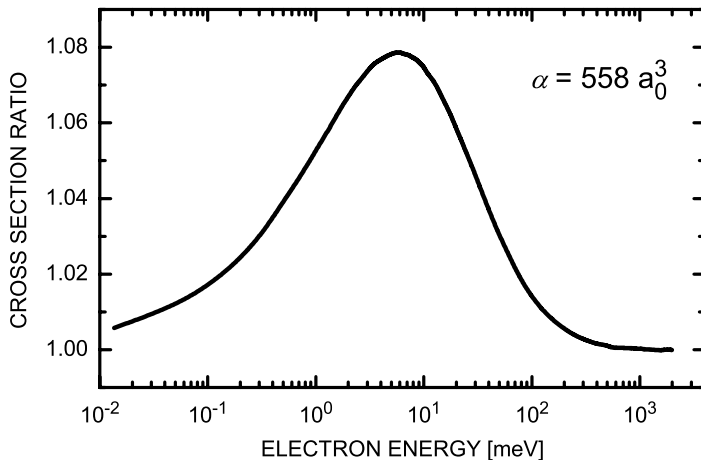
FIG. 9. Ratio $\sigma_K(E)/\sigma_{VW}(E;\ l=0)$ of the approximate s-wave capture cross-section due to Klots to the s-wave capture cross-section of Vogt and Wannier for a spherically symmetric target with a polarizability of $\alpha = 558$ a.u.

For molecules with high polarizabilities (such as $C_{60}$, $\alpha(C_{60}) \approx 558$ a.u., Bonin and Kresin, 1997) higher partial waves may become important even at rather low electron energies. Near zero energy the cross-section for capture of an $l \geq 1$ partial wave ($\sigma_{VW}(E;\ l \geq 1) \propto E^{l-1/2}$) is suppressed by the centrifugal barrier which the electron has to penetrate by tunneling. Inspection of the numerically computed partial capture cross-sections $\sigma_{VW}(E;\ l \geq 1)$ shows that they exhibit a maximum at an electron energy $E_{\mathrm{max},l}$ which is close to the maximum value $V_{\mathrm{eff}}(r_{\mathrm{max}};l) = [l(l+1)]^2/(8\alpha)$ (a.u.) of the effective potential $V_{\mathrm{eff}}(r;l) = -\alpha/(2r^4) + l(l+1)/(2r^2)$ where $r_{\mathrm{max},l} = [2\alpha/(l(l+1))]^{1/2}$. For $\alpha = 558$ a.u., the maximum values of $V_{\mathrm{eff}}$ for $l = 1, 2$ and $3$ are given by 24.4, 219, and 878 meV; the maxima are located at 23.6, 13.6, and 9.6 $a_0$, respectively. In Fig. 10 we show the $l = 0 - 4$ Vogt-Wannier capture cross-sections for electron capture by the $C_{60}$ molecule. At very low energies the Wigner threshold behaviour ($\propto E^{l-1/2}$) is observed while towards high energies the respective unitary limit $\sigma_l = \pi(2l+1)/k^2$ is reached. It is interesting to note (see also Vogt and Wannier, 1954; Klots and Compton, 1996) that the total VW cross-section $\sigma_{VW,\mathrm{tot}}(E)$ is found to agree with the classical Langevin cross-section $\sigma_{\mathrm{Lang}}(E) = 2\pi[\alpha/(2E)]^{1/2}$ (Langevin, 1905) to within 5% for energies above about 4 meV (more generally for $\alpha E > 0.08$ a.u.). Towards lower energies the ratio $\sigma_{VW,\mathrm{tot}}(E)/\sigma_{\mathrm{Lang}}(E)$ continuously rises towards the value 2 which is reached in the limit of zero energy, as illustrated in Fig. 11.
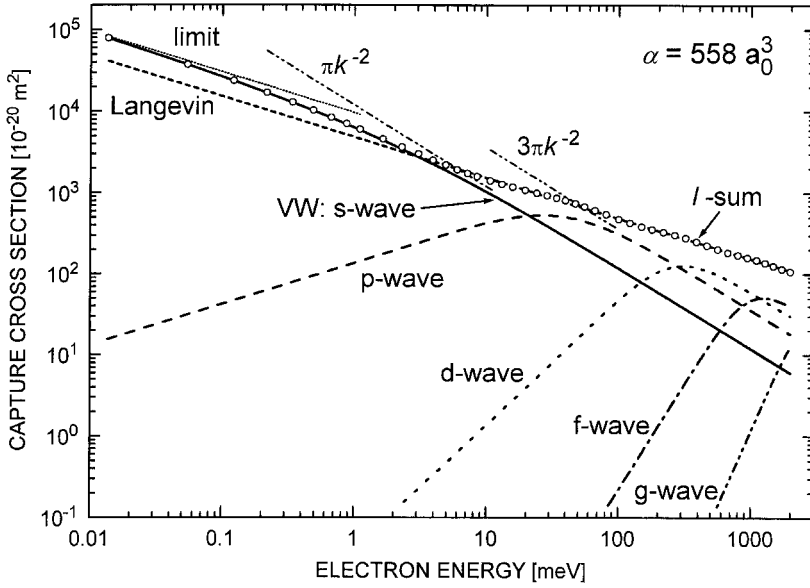
FIG. 10. Partial $l = 0$–4 VW cross-sections and the resulting total VW cross-section (open circles) for electron capture by a spherically symmetric target with a polarizability of $\alpha = 558$ a.u. In addition the figure presents the limiting s-wave Vogt-Wannier capture cross-section Eq. (20) (dotted line), the classical Langevin cross-section (short dashes) as well as the unitary limits $\pi k^{-2}$ and $3\pi k^{-2}$ for reactive s-wave and p-wave scattering, respectively.
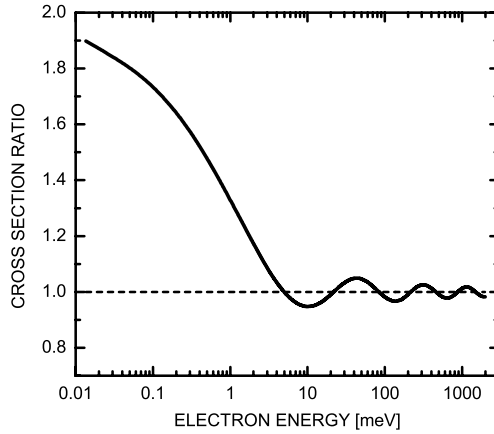


FIG. 11. Energy dependence of the ratio of the total Vogt-Wannier capture cross-section to the classical Langevin capture cross-section for a spherically symmetric target with a polarizability of $\alpha = 558$ a.u.

The Vogt-Wannier (VW) model seems to be unphysical in the sense that the actual long-range potential does not have a $r^{-4}$ singularity. Although both Eq. (20) and the resonance theory give the same energy dependence for s-wave electrons, there is no relation between them otherwise. The VW model does not incorporate the resonance mechanism, therefore there is no resonance characteristics like a width in its equation.

The situation turns out to be even more complicated for dipolar molecules. If the electron energy is large compared to the rotational spacing (an assumption which holds down to sub-meV energies for relatively heavy molecules), the Bethe-Wigner threshold law should be modified (Fabrikant, 1977). For subcritical dipole moments, $\mu < \mu_{cr} = 0.6395$ a.u., the cross-section becomes proportional to $E^{\lambda - 1/2}$ where $\lambda$ is a threshold exponent whose value varies between 0 for $\mu = 0$ and $-1/2$ (for $\mu = \mu_{cr}$). The resonance theory is consistent with this modification.

An extension of the VW theory for polar targets was given by Fabrikant and Hotop (2001). We will outline briefly the approach which they used. It follows closely the original derivation of Vogt and Wannier. The VW theory assumes the absorption boundary condition at the origin due to capture into the polarization well. The reaction cross-section $\sigma_r$ in this case is given by (Landau and Lifshitz, 1977)

$$\sigma_r = \frac{\pi}{k^2} \sum_{ll'} (\delta_{ll'} - |S_{ll'}|^2), \tag{22}$$

where $S_{ll'}$ are the matrix elements of the scattering operator in the angular momentum representation.

The Schrödinger equation for a superposition of the dipolar and polarization potentials allows separation of the variables. The wavefunction can be expanded in the dipolar angular harmonics (Mittleman and von Holdt, 1965) and the radial equation has the form

$$\left( \frac{d^2}{dr^2} + k^2 - \frac{\lambda(\lambda + 1)}{r^2} + \frac{\alpha}{r^4} \right) u(r) = 0, \tag{23}$$

where $k^2 = 2E$. For subcritical dipole moments considered here $\lambda(\lambda + 1) > -1/4$ and $\lambda$ is real.

The scattering matrix can also be transformed into the dipolar angular harmonics representation where it becomes diagonal. In the low-energy region only the lowest eigenvalue $\lambda$ makes a contribution to the inelastic

cross-section which can now be written in the form

$$\sigma_r = \frac{\pi}{k^2}(1 - |S_0|^2), \tag{24}$$

where $S_0$ is the matrix element of the scattering operator corresponding to the lowest $\lambda$.

The required solution of the radial equation with the ingoing-wave boundary conditions at the origin has a simple analytical form in the low-energy region (Fabrikant, 1979). For $S_0$ we obtain

$$S_0 = \frac{1/b - b}{1/b + b \ \exp(-2\pi i\lambda)}, \tag{25}$$

and

$$1 - |S_0|^2 = \frac{4 \ \cos^2 \pi\lambda}{b^2 + 1/b^2 + 2 \ \cos 2\pi\lambda} \tag{26}$$

where $b^2 = [(\Gamma(1 - \lambda - ½)/(2^{2\lambda+1} \ (\Gamma(1 + \lambda + 1/2))]^2(\alpha^{1/2}k)^{2\lambda+1}$, and $\lambda(\lambda + 1)$ is an eigenvalue of the operator $L^2 - 2\mu \cos\theta$ (see above). Note that although $b$ is asymptotically small, the threshold exponent $\tau$ might be close to 0, as, for example, in the case of $CH_3I$, therefore Eqs. (25), (26) should not be simplified further. In particular, using $1 - |S_0|^2 = 4b^2 \cos^2 \pi\lambda$ for the $CH_3I$ molecule violates the unitarity limit even at the electron energy $E = 0.01$ meV.

For a target with a given polarizability $\alpha$, a sub-critical dipole moment ($\mu < \mu_c$, $\mu_c = 0.6395$ a.u. $= 1.625$ D) and at electron energies sufficiently high to view the molecular rotation as frozen, we thus obtain the s-wave capture cross-section (labelled 'Extended Vogt–Wannier', EVW) in the form

$$\sigma_{EVW}(E) = (\pi k^{-2})[4\cos^2 \pi\lambda(b^2 + 1/b^2 + 2\cos 2\pi\lambda)^{-1}] \tag{27}$$

For dipole moments in the range $0 \leq \mu < \mu_c$ and $l = 0$, $\lambda$ takes values in the range $0 \geq \lambda > -1/2$; the relation between $\lambda$ and $\mu$ is to a good approximation described by the equation ($\mu$ in atomic units) (Klar *et al.*, 2001b)

$$\lambda(\mu) = -(1/2) + (1/2)[1 - 4\mu^2(0.66655 - 0.15646\mu^2 + 0.050418\mu^4)]^{1/2}. \tag{28}$$

Correspondingly, the cross-section (27) exhibits an energy dependence $\sigma_{EVW}(E) \propto E^{-X}$ with $0.5 < X < 1$. At fixed polarizability $\alpha$, the absolute values of the EVW cross-section (27) for nonzero dipole moment exceeds the Vogt-Wannier cross-section. The EVW formula (27) is a reasonable approximation to the exact cross-section for electron capture by combined polarization and dipolar forces for electron energies lower than $0.25/\alpha$ (a.u.). For zero dipole moment, formula (27) represents a good approximation to the exact s-wave VW cross-section for energies such that $\alpha E < 2$ a.u. (deviations $< 11\%$); towards higher energies formula (27) attains too low values and does not join the unitary limit while the Klots formula (21) remains a good approximation from low to high energies.

It should be noted, however, that the EVW expression (27) as well as the original VW and the Klots formula can be considered only as an estimate of the capture cross-section in the s-wave regime since the resonance mechanism and the actual nuclear motion (survival probability in the anion state) are not included. Typically, the VW and EVW formulae work well if the negative-ion curve crosses the neutral curve in the vicinity of the minimum of the latter, i.e. in the case of a favourable Franck-Condon factor (which, however, does not enter the EVW formula), as for the $CCl_4$ (Klar et al., 2001a) and the $CFCl_3$ molecule (Klar et al., 2001b). Another limitation of EVW/VW theory is related to the coupling of the attachment process to vibrationally inelastic channels. As a result, the EVW/VW cross-section is expected to be valid only up to the first threshold for excitation of vibrational levels whose symmetry allows strong coupling to the s-wave attachment process.

In Fig. 12 we present the DA cross-section for methyl iodide molecules in the vibrational ground state $CH_3I(\nu_3 = 0)$, calculated using different theories: the Klots fit of the VW result, the EVW (including the dipole moment) result, the complete $R$-matrix calculation and the results of the local complex potential (LCP) approximation. The equation for the DA cross-section in the LCP approximation was derived from the nonlocal theory by O'Malley (1966) and Bardsley (1968), and can be summarized (for a nondegenerate doublet resonance) as:

$$\sigma_{DA}(E) = (2\pi^2/k^2)\Gamma|FC|^2 S \qquad (29)$$

where $\Gamma$ is the resonance width, $S$ is the survival factor, and FC denotes the Franck-Condon overlap between the initial vibrational level of the neutral molecule and the continuum nuclear wave function in the dissociative resonance anion state, normalized to the delta function of energy. Note that with this normalization $|FC|^2$ has the dimension energy$^{-1}$, and we do not
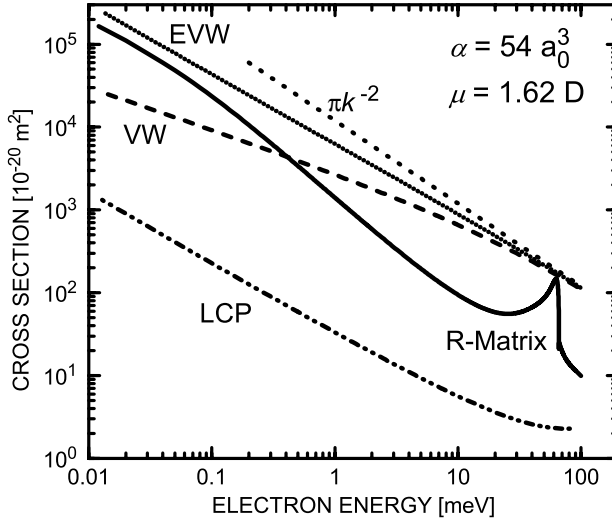
F<small>IG</small>. 12. Illustration of the EVW result compared with the VW result for s-wave attachment to $CH_3I$ ($\alpha = 54\,a_0^3$, $\mu = 1.62\,D$) and comparison with the $R$-matrix result and LCP theory (see Fig. 1 in Fabrikant and Hotop, 2001).

use O'Malley's delta function approximation for the dissociating state. The calculation of FC was done, however, assuming that the energy of the dissociating state is real.

Large deviations between the different theories are observed in Fig. 12, reaching two orders of magnitude at a fixed energy and with the lowest cross sections obtained with the local theory and the highest with the EVW. The energy dependence of the cross-section at ultralow energies is determined by the threshold exponent ($\lambda - 1/2$) which is $-0.965$ for $CH_3I$. Therefore both the extended Vogt-Wannier model and the local theory predict a fast growth of the cross-section towards zero energy, approaching $E^{-0.965}$. However, the nonlocal $R$-matrix results above $0.1\,meV$ exhibit an even faster variation. In addition, the nonlocal cross-sections are much greater (typically almost two orders of magnitude) than those of the local calculations, in agreement with the experiment. The $R$-matrix cross-section near the threshold for vibrational excitation of the symmetric C−I stretch is dominated by the vibrational Feshbach resonance which was discussed above in Section II.A.4. All other calculations do not exhibit this resonance. The strong enhancement (as compared to the local approximation) of the DA cross-section close to zero energy is caused by the same weakly bound state which supports the VFR near the $v_3 = 1$ threshold (Fabrikant and

Hotop, 2001). The analytical expression, describing this enhancement for a molecule with a subcritical dipole moment, can be written as (Fabrikant, 1977, 1978)

$$\sigma = ck^{2\lambda-1}/|\eta - ik^{2\lambda+1}\exp(-i\pi\lambda)|^2, \tag{30}$$

where $\eta$ is a complex parameter. This is similar to Eq. (12) written for a supercritical dipole moment. This expression has a pole in the complex $k$ plane corresponding to a bound or a virtual state, if $\eta$ is real. Because of the coupling with the DA channel this state, even if it is bound, can decay. However, the decay width is small because of the potential barrier towards dissociation. The width of the VFR below the $v_3 = 1$ threshold is substantially larger because of the lower potential barrier for the nuclear motion in the $v_3 = 1$ state. The resonance disappears at $v_3 = 2$. In summary, the big value of the DA cross-section for methyl iodide in the ultra-low energy region can be explained by the influence of the dipole-supported state which is not incorporated into the local version of the resonance theory.

# III. Experimental Aspects

In this section we discuss three different experimental setups for studies of electron–molecule collisions at *low* energies with *high* resolution (< 10 meV). We note that most low-energy electron collision studies in the gas phase have been and are being carried out at broader energy widths (typically in the range 30–150 meV), e.g. using trochoidal electron monochromators (TEM) which – by virtue of the magnetic guiding field – rather easily allow studies down to zero energy and – in conjunction with a TEM for energy analysis – also provide access to investigations of inelastic scattering with high sensitivity (Allan, 1989).

## A. Setup Involving Angle- and Energy-Resolved Detection of Scattered Electrons

A typical apparatus for studies of angle-dependent elastic and inelastic scattering consists of a hot filament electron source followed by an electrostatic monochromator, a target beam (of either effusive or supersonic character) and an angle-variable electrostatic energy analyzer (Allan, 1989; Brunger and Buckman, 2002). Using such an optimized instrument, as shown in Fig. 13, Allan has recently achieved energy widths down to 7 meV at high signal to background ratio in energy loss spectra and excitation
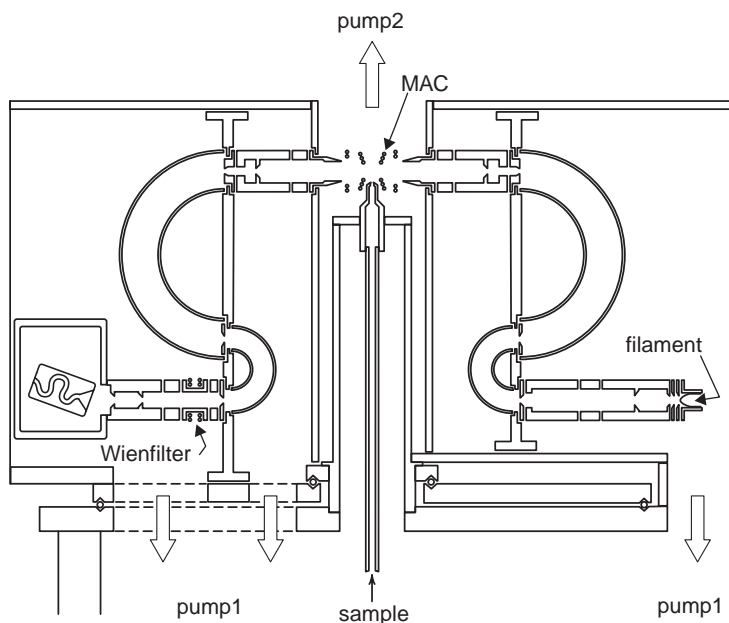
F<small>IG</small>. 13. The Fribourg apparatus for angle-differential low-energy electron scattering from a gaseous target beam. A small Wien-type mass filter is used to separate scattered electrons and fragment anions from dissociative attachment. The analyzers and the electron optics are differentially pumped as indicated by the arrows. The dots around the collision region (labelled MAC) represent the 'magnetic angle-changing device' (seen in cross-section).

functions involving elastic and vibrational inelastic scattering (Allan, 2001a; Allan and Moreira, 2002; Skalický *et al.*, 2002). Through careful calibration procedures absolute differential cross-sections are obtained.

Using optimized conventional electron sources, Ibach's group (1991, 1993) have achieved energy widths down to 1 meV in electron scattering from molecules adsorbed at surfaces under ultrahigh vacuum and low current conditions.

Photoelectron sources have been used for angle differential gas phase scattering experiments by Gallagher and coworkers (van Brunt and Gallagher 1978; Kennerly *et al.*, 1981), Field *et al.* (1988, 1991a, b) and, more recently, by Gopalan *et al.* (2003). In order to avoid the Doppler effect, differentially-pumped supersonic beam targets were used (see, e.g., Götte *et al.*, 2000). In principle an energy width down to 1 meV should be achievable at electron currents around 50 pA (Bömmels *et al.*, 2001; Gopalan *et al.*, 2003), but the full potential of this approach has yet to be demonstrated and exploited for angle-differential scattering experiments.

A long-standing problem, namely the detection of electrons scattered into angles around 180°, was recently solved by the introduction of 'magnetic angle-changing devices' by Read and coworkers (Read and Channing 1996; Zubek *et al.*, 1996). They typically consist of two Helmholtz-type pairs of current coils (coaxial solenoids around a common axis) and are designed such that the resultant magnetic field is zero in the outer region (allowing to keep electrostatic energy selectors) and nonzero in the region around the beam target. So far, the method has been applied mainly to electron scattering from rare gas atoms (e.g. Cubric *et al.*, 1999; Zubek *et al.*, 1999, 2000; Allan, 2000). An elegant version which is well suited for electron scattering studies involving collimated supersonic beams has been implemented by Allan (2000).

## B. Measurement of Total Scattering Cross-Sections

Experimental setups for the determination of total electron scattering cross-sections (comprising elastic as well as all inelastic collisions including attachment processes) involve a well-collimated electron beam of variable energy which is transmitted through a collision cell containing the static target gas. Non-scattered electrons are detected within a narrow angular range in the forward direction. Some energy analysing device is included to prevent inelastically forward scattered electrons from being detected; normally, however, the resolution is not sufficiently high to exclude electrons which have undergone rotational energy losses in the forward scattering. This aspect is critical for molecules with dipole moments. The energy resolution in these experiments is limited by the energy width of the electron source ($\Delta E_S$), by the potential variations in the target region ($\Delta E_T$), and ultimately by the Doppler effect ($\Delta E_D$) due to the random motion of the target molecules (mass $m_T$, average velocity $\mathbf{v}_T$, kinetic energy $E_T$) with respect to the directed electron beam (mass $m_e$, velocity $\mathbf{v}_e$, kinetic energy $E_e$). The collision energy $E$ of the electron–molecule system in the center-of-mass frame is given by

$$E \approx E_e - (m_e/m_T)E_e - 2(m_e E_e E_T/m_T)^{1/2} \cos\theta \qquad (31)$$

where $\theta$ is the angle between $v_e$ and $v_T$. In (31) the second term is the recoil energy which can be neglected at low collision energies. The third term is the energy shift $E_D$ due to the first order Doppler effect. Here we simply estimate the Doppler energy width $\Delta E_D$ by

$$\Delta E_D = (1/2)[E_D(180°) - E_D(0°)] = 2(m_e E_e E_T/m_T)^{1/2} \qquad (32)$$
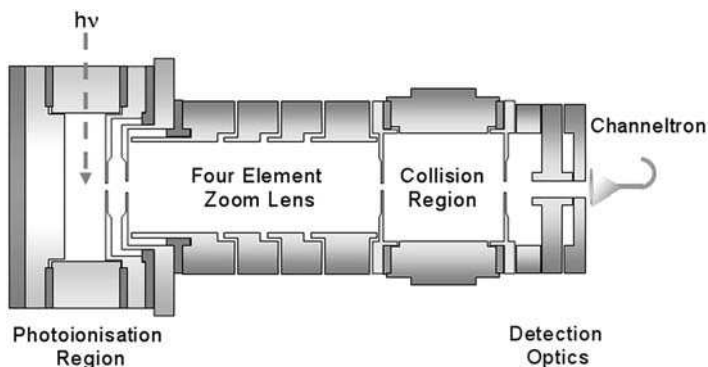
F<small>IG</small>. 14. Schematic diagram of the apparatus for studies of total electron scattering cross sections involving a VUV photoelectron source (from Hoffmann *et al.*, 2002).

For electron energies below 1 eV and thermal targets ($T_T = 300$ K) with a mass above 28 u the Doppler width stays below 2 meV, but is has to be taken into account when (sub) meV resolution is to be achieved.

In Fig. 14 we show an apparatus (Hoffmann *et al.*, 2002) which has been used in this or similar form by Field and Ziesel with coworkers (Field *et al.*, 1991a; Ziesel *et al.*, 1993; Gulley *et al.*, 1998a, b; Field *et al.*, 2000; Lunt *et al.*, 2001; Field *et al.*, 2001a, b, c; Jones *et al.*, 2002; Ziesel *et al.*, 2003) to investigate total electron scattering cross-sections for a large number of molecules from low (about 20 meV) to medium electron energies (around 10 eV). Electrons are created in the source region by photoionization of ground state argon atoms (at a pressure of a few tens of mPa) through the narrow Ar(11s′, $J = 1$) resonance at 78.65 nm (about 4 meV above the photoionization threshold), using focussed (10–20 μm) monochromatized synchrotron radiation. The photoelectrons (current up to 1 pA) are extracted by a weak electric field (20–40 V m$^{-1}$) and formed into a focussed beam with a four-element electrostatic lens. The energy width of this beam is determined mainly by the ionizing photon bandwidth; in the earlier experiments at SuperACO (LURE, Orsay, FR) and SRS (Daresbury, UK) the photon energy width amounted typically to 5–6 meV while in the recent experiments at ASTRID (Aarhus, DK) widths around 1 meV were achieved (Field *et al.*, 2000, 2001a, b; Hoffmann *et al.*, 2002).

The electron beam passes through the collision chamber which contains the target gas at a known number density $\rho_T$. The beam attenuation as a function of electron energy is measured by recording the electron current on a channel electron multiplier situated beyond further optical elements. The electron energy is scanned by varying the potential in the photoionization

source. The whole apparatus can be immersed in an axial magnetic field (typically 2 mT), thus allowing the determination of cross-sections for backward scattering to be compared with the total cross-sections, measured in the absence of magnetic fields. Absolute cross-sections $\sigma$ are evaluated using Beer's law

$$I_t = I_0 \exp(-\sigma(E)\rho_T z) \qquad (33)$$

where $I_t$ and $I_0$ are the attenuated and the unattenuated electron currents, respectively, $\sigma(E)$ is the enery dependent scattering cross-section, and $z$ is effective electron path length in the target gas. Uncertainties for the absolute values of the cross-sections are around 10%. The absolute energy scale is calibrated to within $\pm 5$ meV. Under optimum conditions cross-sections are determined at energies down to 10 meV. Measurements of backward cross-sections are limited to incident energies below 650 meV; this limit is imposed by the size of the exit hole (3 mm) of the scattering chamber in conjunction with the value of the guiding axial magnetic field (2 mT): above 650 meV, forward scattering will contribute to the measured cross-section.

## C. Measurement of Cross-Sections for Electron Attachment

The use of VUV photoelectron sources for high resolution studies of electron attachment to molecules has been initiated by Chutjian and coworkers (Ajello and Chutjian, 1979; Chutjian and Alajajian, 1985) under the acronym TPSA (Threshold Photoelectron Spectroscopy for Attachment). In these experiments, rare gas atoms Rg (Rg = Kr or Xe) were photoionized above the second ionization threshold (formation of $Rg^+(^2P_{1/2})$ + $e^-(E_e)$) to create electrons with variable energy by tuning the wavelength of monochromatized VUV radiation from a Hopfield continuum light source. By choosing this ionization path, higher energy electrons are simultaneously created due to formation of $Rg^+(^2P_{3/2})$ ions. The contribution of these electrons to the attachment signal is only negligible as long as the attachment cross-section drops sufficiently rapidly with increasing electron energy. The source volume contained both the rare gas atoms and the target molecules as static gases at rather high densities (about 0.01 Pa and 0.45 Pa, resp.). Negative ions, resulting from electron attachment to the molecules, were extracted with a weak electric field and detected with a quadrupole mass spectrometer. Attachment spectra for a large number of molecules were thus obtained over the energy range 0–160 meV (Chutjian, 1992; Chutjian et al., 1996). The energy resolution in the TPSA experiments was limited by the photon bandwidth (typically 6–8 meV) and by the

extraction field. When the wavelength is set close to the $Rg^+(^2P_{1/2})$ threshold the interpretation of the attachment signals may get complicated by the fact that autoionizing Rydberg resonances $Rg^{**}(^2P_{1/2}ns', nd')$ are created apart from free electrons. At principal quantum numbers $n$ above about 150, the lifetime of these resonances may become sufficiently long by field- and collision-induced mixing with high angular momentum states that contributions to the anion signal due to Rydberg electron transfer cannot be ruled out (Klar *et al.*, 1994a). Recently, Chutjian and coworkers have used an improved TPSA setup in which coherent VUV radiation, produced by frequency mixing techniques involving pulsed narrow-band (sub-meV) lasers, is used to photoionize Xe atoms above the $Xe^+(^2P_{1/2})$ threshold (Howe *et al.*, 2001). The Xe atoms are provided in conjunction with the target molecules as a collimated pulsed seeded supersonic beam. The experiment has the drawback of rather low pulse repetition rate (about $10\,s^{-1}$) which makes it difficult to achieve good statistical quality of the data and to follow attachment cross-sections over several orders of magnitude.

A powerful variant of the TPSA method has been developed by Klar *et al.* (1992a, b, 1994a) which produces monoenergetic electrons by photoionization of laser-excited $^{40}Ar^*(4p\,^3D_3)$ atoms (Klar *et al.*, 1994a; Schohl *et al.*, 1997) or laser excited $^{39}K^*(4p_{3/2})$ atoms (Weber *et al.*, 1999a, b; Petrov *et al.*, 2000) with a tunable blue dye laser of narrow bandwidth (typically 0.15 meV or 0.05 meV). These laser photoelectron sources have been used in a series of laser photoelectron attachment (LPA) studies involving molecules and molecular clusters. A recent version of the experimental setup is shown schematically in Fig. 15 (Weber *et al.*, 1999b; Barsotti *et al.*, 2002a).

For the first time electron collision experiments in the gas phase have been thus carried out at sub-meV resolution (Klar *et al.*, 1992a, b) and at incident energies down to 20 μeV (Schramm *et al.*, 1998). While the excited atoms are provided at low density (about $2 \times 10^6\,cm^{-3}$ for $Ar^*(4p\,^3D_3)$, $10^8\,cm^{-3}$ for $K^*(4p_{3/2})$) in a collimated atomic beam, the continuous ionizing intracavity laser is sufficiently intense (power 1–5 W) to achieve typical currents around 1 pA ($Ar^*$) or 50 pA ($K^*$). The two-step ionization path, involving efficient primary laser excitation of metastable $^{40}Ar(4s\,^3P_2)$ and ground state.

$^{39}K(4s_{1/2}$, F = 1, 2) atoms to the intermediate levels $^{40}Ar^*(4p\,^3D_3)$ or $^{39}K^*(4p_{3/2}$, F' = 2, 3) (quasi-stationary excited state population nearly 50%), is optimized in the sense that the cross-section for ionization of $Ar^*(4p\,^3D_3)$ (Schohl *et al.*, 1997) as well as for $K^*(4p_{3/2})$ atoms (Petrov *et al.*, 2000) is substantial (around $10^{-21}\,m^2$) and three to four orders of magnitude higher than that for ionization of metastable $Ar^*(4s\,^3P_2)$ atoms (Kau *et al.*, 1998; Petrov *et al.*, 1999) or ground state K(4s) atoms (Sandner *et al.*, 1981), respectively. We note that an analogous two-step photoionization scheme
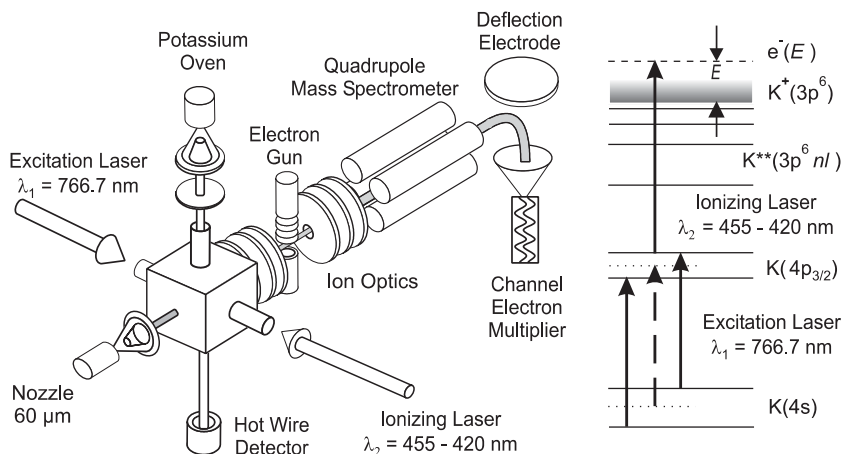
FIG. 15. Laser photoelectron attachment experiment involving two-step photoionization of potassium atoms, a supersonic target beam (differentially pumped nozzle) and mass spectrometric detection of the anions. The auxiliary electron gun is used for diagnostics of the target beam and of the residual gas by means of electron impact ionization. The laser photoelectron production scheme is shown on the right side (after Weber *et al.*, 2000).

involving ground state $Na(3s_{1/2})$ atoms has been recently applied by Keil *et al.* (1999) to study laser photoelectron attachment to vibrationally excited $Na_2$ molecules (see Section IV.B). The use of an ionizing laser at rather long visible wavelengths in all these two-step ionization schemes is advantageous for several reasons: (i) the high continuous laser intensity, available with an intracavity Stilbene 3 dye laser, allows substantial photoelectron currents to be produced from a *thin* atomic target; (ii) the bandwidth of the laser can be made sufficiently narrow (e.g. by using a single mode laser) to allow *in situ* diagnostics of residual dc electric fields in the photoionization/attachment volume by studies of the Stark effect (Frey *et al.*, 1993; Osterwalder and Merkt, 1999) or of the shift of the ionization threshold (Klar *et al.*, 1994a; Schramm *et al.*, 1998); (iii) the production of electrons emitted from surfaces by scattered laser light is negligible in the LPA experiment (wavelengths around 450 nm) while it is difficult to avoid in the TPSA experiment at VUV wavelengths (Howe *et al.*, 2001).

Using laser photoionization of $Ar^*(4p\,^3D_3)$ atoms over the range 462–433 nm, Klar *et al.* (1992a, b, 1994a, b, 2001a, b) and Schramm *et al.* (1998, 1999, 2002) have carried out the first series of LPA experiments at (sub) meV resolution over the typical energy range 0.2–173 meV for selected molecules ($SF_6$, $CCl_4$, $CFCl_3$, HI, $CH_3I$, $CH_2Br_2$, $CCl_3Br$, $1,1,1$-$C_2Cl_3F_3$),

present in the photoionization region as a static gas. In order to achieve a sufficient anion detection efficiency without the loss of energy resolution, the experiment was pulsed at high repetition rates (up to 140 kHz), alternating between the electron production/attachment period and the anion extraction interval, as described in detail in Klar *et al.* (1992b, 1994a, 2001a, b) and Schramm *et al.* (1999, 2002). Mass analysis was performed with a quadrupole filter (Klar *et al.*, 1992a, b, 1994a, 2001a, b) or with a time-of-flight spectrometer (Schramm *et al.*, 1999, 2002).

A more recent version of the LPA experiment (Fig. 15) is based on two-step photoionization of potassium atoms in a collimated differentially pumped beam; by tuning the ionizing wavelength from 455.2 to 424 nm, the electron energy is continuously varied from zero to 200 meV. Typically, electron currents in the range 20–50 pA are used to limit the energy broadening effects associated with the photoion space charge (FWHM about 30 μeV/pA) (Bömmels *et al.*, 2001). A differentially pumped supersonic beam serves as a well collimated target, allowing – in conjunction with the increased current – for the first time electron attachment studies of molecular clusters at meV energy width (Weber *et al.*, 1999a). Negative ions which are created by electron attachment and drift out of the essentially field free reaction chamber, are imaged into a quadrupole mass spectrometer ($m/q \leq 2000$ u/e) with a combination of two electrostatic lenses. The transmitted ions are accelerated to an energy of 1 keV and detected by a differentially pumped off-axis channel electron multiplier (Sjuts) with low background ($< 0.02 \, \mathrm{s}^{-1}$). For diagnostics of the target beam (especially with respect to possible cluster formation), positive ion mass spectra can be generated by electron impact ionization with an auxiliary electron gun (current around 0.1–1 μA, energy 75–85 eV).

The reaction volume is surrounded by a cubic chamber, made of six insulated copper plates. To improve the homogeneity of the surface potentials, the inner walls are coated with colloidal graphite. By applying bias potentials to each plate, residual dc electric fields are reduced to values $F_S < 0.2 \, \mathrm{V \, m}^{-1}$; the reduction procedure involves an iterative optimization of the shape of the attachment spectrum due to $SF_6^-$ formation around zero electron energy (Klar *et al.*, 1994a; Schramm *et al.*, 1998). Magnetic fields are reduced to values below 2 μT by compensation coils located outside the vacuum apparatus (Klar *et al.*, 1994a; Weber *et al.*, 1999b) or by the use of reaction chambers fabricated of mu metal (Schramm *et al.*, 1998, 1999, 2002). The electron energy resolution is limited by the bandwidth of the ionizing laser (normally $\Delta E_L \approx 0.15$ meV), residual electric fields ($\Delta E_F \leq 0.3$ meV), the Doppler effect (present in both the photoionization and in the attachment process, $\Delta E_D \approx 0.06 \, E^{1/2}$ for target velocities similar to the potassium atom velocity (600 ms$^{-1}$) with $\Delta E_D$ and $E$ in meV), and

space charge broadening $\Delta E_{SC}$ due to $K^+$ photoions generated in the reaction volume ($\Delta E_{SC} \approx 0.9$ meV at 30 pA photocurrent, see Fig. 7 in Bömmels et al., 2001). For the sake of normalization, in situ resolution testing, and compensation of electric stray fields, measurements of $SF_6^-$ formation are carried out, using a seeded supersonic beam of about 0.05% $SF_6$ in He ($p_0 = 1$ bar, $T_0 = 300$ K). By comparison of the measured anion yield with the known cross-section for $SF_6^-$ formation (Klar et al., 1992a, b, 1994a; Schramm et al., 1998) near 0 eV (convoluted with adjustable resolution functions), the effective electron energy spread at low energies can be inferred.

The use of a supersonic beam target has the substantial advantage of a spatially confined reaction volume. When the molecules of interest are seeded in light carrier gas (such as helium) the kinetic energy of the molecules is raised substantially above its thermal value which – under conditions of weak extraction fields – results in a higher detection efficiency of the product ions due to dissociative attachment (Barsotti et al., 2002b). In a mixed supersonic beam, containing the seeded minority component with molecular mass $m_S$ at a fraction $x$ and the atomic carrier gas with mass $m_C$ (fraction $1 - x$), the flow velocity $u_S$ of the seeded component can be estimated (in the absence of velocity slip) by (Miller, 1988)

$$u_S \approx \{5k_B T_0 / [x m_S + (1 - x) m_C]\}^{1/2} \qquad (34)$$

with $k_B$ = Boltzmann constant.

A nontrivial aspect of DA experiments is a possible influence associated with the angular distribution of dissociating anions with respect to the momentum vector of the electron (Massey, 1976), as shown, e.g., for DA to $Cl_2$ by Azria et al. (1982). This problem is relevant in DA experiments with a well-defined direction of the electron beam when resonances with different symmetries are involved, leading to different anion detection efficiencies, as long as the anions are detected in an angle-sensitive manner. In the TPSA and LPA experiments angular distribution effects are expected to be negligible (or small) because the photoelectrons, created in the center of the reaction region, are emitted in all directions (albeit not fully isotropically).

The LPA experiment provides highly resolved attachment yield spectra $Y_e(E)$ for anion formation over the typical energy range 0.1–200 meV. The yield is proportional to the absolute cross-section $\sigma_e(E) = N Y_e(E)$ for anion formation due to free electron attachment. The normalization constant $N$ is conveniently determined with reference to known thermal energy attachment rate coefficients $k_e(T)$ (Smith and Španel, 1994;

Christophorou, 1996) using the expression (Chutjian and Alajajian, 1985; Klar *et al.*, 1992b, 2001a, b; Chutjian *et al.*, 1996; Schramm *et al.*, 1999, 2002)

$$k_e(T) = N(2/m_e)^{1/2} \int_0^\infty Y_e(E) E^{1/2} f(E; T) dE \tag{35}$$

with the Maxwellian distribution function $f(E; T) = (4/\pi)^{1/2} (k_B T)^{-3/2} E^{1/2}$ $\exp[-E/(k_B T)]$ where $k_B T = 25.85$ meV for $T = 300$ K and $\int_0^\infty f(E; T) dE = 1$. In the rate coefficient $k_e(T)$ the temperature $T$ addresses both the electron temperature $T_e$ and the gas temperature $T_G$ which are assumed to be identical. In the TPSA and the LPA experiments the gas temperature was typically $T_G = 300$ K; thus, rate coefficients $k_e(T)$ obtained at $T = T_e = T_G = 300$ K were used for normalization. As shown by Klar *et al.* (1992b, 2001a) for the cases of $SF_6$ and $CCl_4$ (s-wave attachment, peaking at zero energy) an integration interval (0, 170) meV in (35) is sufficient to guarantee errors below 1% in the normalization. In the evaluation the near-zero energy range requires some care. Klar *et al.* (1992b, 2001a, b) and Schramm *et al.* (1999, 2002) used an analytical cross-section similar to the Klots cross-section (21) to extrapolate to zero energy (see Section IV.B). It has to be stressed that the normalization procedure (35) can only be carried out in a reliable way if the anion yield function is obtained at sufficiently narrow electron energy width and down to sufficiently low energies. We also emphasize that the gas temperature is an important parameter since attachment cross-sections may depend very strongly on the rovibrational distribution of the molecules (O'Malley, 1967; Chantry, 1969; Massey, 1976; Christophorou, 1987; Smith and Španel, 1994; Hahndorf and Illenberger, 1997).

We conclude this section by briefly mentioning another approach to study electron–molecule collisions at very low energies. Going back to ideas of Fermi (1934), electrons in Rydberg orbits can be used as a source of very slow electrons (Stebbings and Dunning, 1983; Klar *et al.*, 1994b; Dunning, 1995). The concept of the quasi-free electron model (Fermi, 1934; Matsuzawa, 1972) allows us to express the rate coefficient $k_{nl}$ for a particular process to occur with Rydberg electrons in specified orbits $nl$ through the cross-section $\sigma_e(v)$ for the same process involving free electrons (Matsuzawa, 1972):

$$k_{nl} = \int_0^\infty \sigma_e(v) v f_{nl}(v) dv \tag{36}$$

where $f_{nl}(v)$ represents the velocity distribution function of the highly excited $nl$ electron in the Rydberg atom $A^{**}(nl)$. This equation assumes that the interaction of the electron with the ion core $A^+$ and that of the ion core $A^+$

with the target system is negligible throughout the collision process. At sufficiently low $n$ this assumption is no longer valid (Dunning, 1995; Desfrançois *et al.*, 1996; Compton and Hammer, 2001). Free electron cross-sections $\sigma_e(v)$ at very low velocities may be tested by comparing measured rate coefficients $k_{nl}$ with those calculated through Eq. (36) on the basis of the quasi-free electron model. The inverse procedure of deriving free electron cross-sections from a measured $n$ dependence for a RET process is not unique and so far has not been demonstrated in a convincing way.

# IV.  Case Studies

In the following section we shall discuss in some detail recent results which highlight resonance and threshold effects in low-energy electron collisions with selected molecules and molecular clusters, as obtained at very high resolution (i.e. energy widths in the few meV range). The emphasis will be on angle-differential elastic and vibrationally inelastic electron scattering as well as on electron attachment studies, but examples for total scattering cross-sections will also be included. Moreover, we shall briefly discuss important recent observations made for annihilation of positrons traversing molecular gases at energies below 1 eV at sufficiently low energy widths to resolve vibrational structure. Since the long-range electron–molecule interaction plays a decisive role at the considered low collision energies the molecules are grouped accordingly.

## A. Electron Collisions with Polar Molecules

Most molecules in nature are polar species. The presence of a permanent dipole moment has strong effects on electron–molecule scattering at low energies since the electron–dipole interaction and the centrifugal potential have to be treated on an equal footing as pointed out in the theory section. In Section IV.A we first discuss two groups of such molecular species (the hydrogen and methyl halides) which exhibit a rich spectrum of resonance and threshold effects and which have played an important role in the development of the theory for electron–molecule collisions. In addition we discuss as a special case of interest the molecule 1,2-$C_2H_2F_2$: a comparative investigation of elastic and inelastic electron scattering has been carried for both the *cis*-form (dipole moment $\mu = 2.42$ D) and the *trans*-form ($\mu = 0$).

### A.1.  Hydrogen Halides

Studies of threshold behavior in electron collisions with hydrogen halides H$X$ (where $X$ stands for F, Cl, Br and I atoms) started with the pioneering

work of Rohr and Linder (1975, 1976) and Rohr (1977, 1978) who discovered
threshold peaks in VE of HF, HCl, and HBr molecules. Threshold
structures were also found in the elastic cross-section (Burrow 1974) and
in transmission spectra (Ziesel *et al.*, 1975a).

It was realized later that these peaks are related to the stepwise structure
in the DA cross-section at VE thresholds, observed first by Ziesel *et al.*
(1975a) for HCl and later by Abouaf and Teillet-Billy (1977,1980) for HCl,
DCl, HBr and HF molecules and explained by nonlocal effects as early as
in 1974 (Fiquet-Fayard, 1974). Another distinctive property of DA cross-
sections to hydrogen halides is a vertical threshold onset which is a general
feature of an endothermic DA process without a reaction barrier (O'Malley,
1966). More detailed experimental data on VE were obtained in the late
1980s in Ehrhardt's group (Knoth *et al.*, 1989a,b; Rädle *et al.*, 1989). In the
$0 \rightarrow 3$ VE cross-section for HF, they found a dip-like resonance structure
*below* the $v = 4$ threshold (Knoth *et al.*, 1989a), thus providing the first
experimental evidence for a vibrational Feshbach resonance (VFR, then
addressed as nuclear-excited resonance). Recently, the Fribourg group
reported improved results for VE of all the hydrogen halide molecules
(Allan *et al.*, 2000, Sergenton *et al.*, 2000, Sergenton and Allan, 2000; Čížek
*et al.*, 2001a; Allan, 2001b), as will be in part discussed below.

Initial attempts to explain threshold peaks in VE were based on model
calculations involving enhancement by a virtual state (Dubé and Herzen-
berg, 1977; Kazansky, 1978, 1982), s-wave bound states (Gauyacq, 1983;
Teillet-Billy and Gauyacq, 1984), or the long-range dipolar interaction
between the electron and the target (Fabrikant, 1977, 1983). (see Morrison,
1988 for a more complete review of the work done before 1988). An
important paper of Domcke and Mündel (1985), based on the nonlocal
complex potential approach (Domcke, 1991), showed that the situation is
much more complex. In the nonlocal treatment the effects of resonances,
virtual states and bound states are all included and distinction between
them is not easily possible. The long range dipolar interaction between the
electron and the molecule leads to a very strong energy dependence of
the resonance capture amplitudes and an unusual behavior of an s-wave
resonance in an adiabatic fixed-nuclei approximation.

In the early 1990s a series of model and semiempirical calculations of DA
and VE for hydrogen halides were performed which led to an understanding
of the basic mechanisms. Some of these calculations were based on the
quasiclassical version of the nonlocal complex potential theory (Kalin and
Kazansky, 1990), and some on the quasiclassical version of the resonance
*R*-matrix theory (Fabrikant, 1991a) which was shown (Fabrikant, 1990)
to be equivalent to the nonlocal approach. For model or semiempirical
calculations the *R*-matrix version is more convenient since it allows for

a simpler parameterization of the input parameters. Quasiclassical *R*-matrix calculations for HCl and HF (Fabrikant, 1991a; Fabrikant *et al.*, 1991, 1992) reproduced the major features in VE and DA cross-sections, showing essential agreement with earlier calculations (Domcke and Mündel, 1985) for HCl. Variational *R*-matrix calculations (Thümmel *et al.*, 1992, 1993) obtained individual rotational contributions to vibrational excitation of HF, but did not produce results for DA. The effective range approximation was applied by Gauyacq (1987).

Further development of theoretical methods allowed obtaining accurate *ab initio* cross-sections for HF (Gallup *et al.*, 1998), HCl (Horáček *et al.*, 1998; Čížek *et al.*, 1999; Allan *et al.*, 2000), HBr and DBr (Horáček and Domcke, 1996, Čížek *et al.*, 2001), and HI (Horáček *et al.*, 1997; Kolorenc *et al.*, 2002). Near-threshold DA to vibrationally and rotationally excited molecules has been studied by Xu *et al.* (2000) for HF and Kolorenc *et al.* (2002) for HI.

Improved experimental techniques led to the discovery of unexpected oscillatory structures in VE of HCl below the DA threshold (Schafer and Allan, 1991; Cvejanović 1993). Figure 16 shows the more detailed
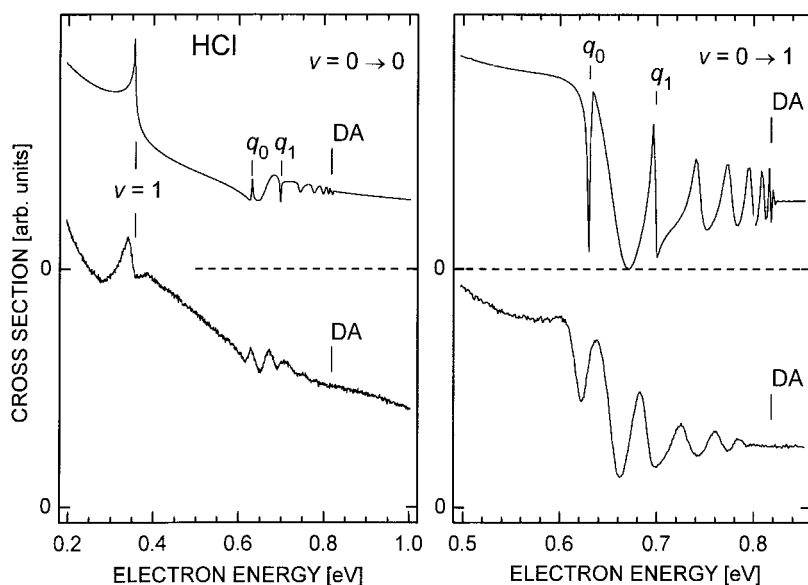


FIG. 16. Elastic (left) and $v = 0 \rightarrow 1$ VE cross-sections measured at 90° in HCl. Results of nonlocal resonance theory are shown on the top, experiment on the bottom. The sharp structures due to outer-well resonances ($q_0$ and $q_1$) are superimposed on broader boomerang type oscillations (Allan *et al.*, 2000).
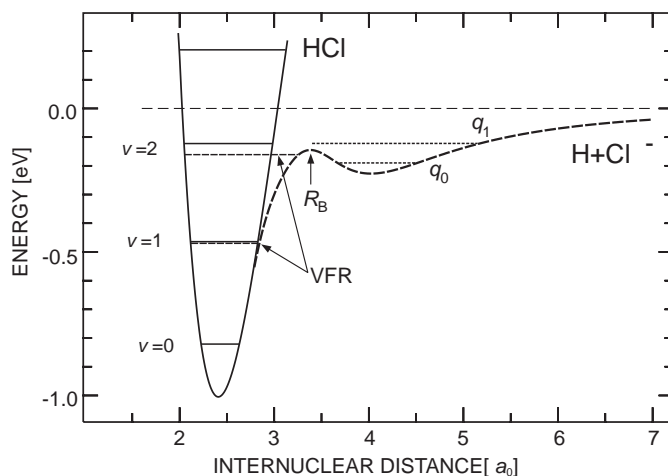
Fɪɢ. 17. Illustration of the outer- and inner-well resonances in HCl. The adiabatic potential curves of Čížek *et al.* (1999, 2001b) are shown as solid (HCl) and dashed (HCl⁻) curves (see also text).

measurements and results of advanced nonlocal resonance theory calculations of Allan *et al.* (2000). The theory (Čížek *et al.*, 1999; Allan *et al.*, 2000) permitted an interpretation of these structures as a combination of boomerang oscillations, reflecting short-lived wave-packet motion of the $HX^-$ anion, and so-called outer-well resonances, arising from quasibound energy levels in the outer well of the anion potential curve, as illustrated in Fig. 17. The $HCl^-$ curve follows the general model discussed in Sections I and II, Figs. 3 and 6. It has an inner and an outer well, separated by a potential barrier at $R_B$. The adiabatic potential curve of $HCl^-$ disappears below $R \approx 2.8\, a_0$, but vibrational motion of short duration is still possible on the inner well through nonadiabatic effects (partial re-capture of the electronic cloud as the nuclei swing back to large $R$), giving rise to the VFRs. Quasistationary vibrational levels whose wave function is localized predominantly in the outer well give rise to the outer-well resonances. They are coupled to the inner well by tunneling ($q_0$) or passage over the potential barrier ($q_1$). The outer well resonances appear as sharp dips at 0.632 and 0.699 eV, the VFR associated with the $v = 2$ level as a dip at 0.66 eV in the spectra of Fig. 16. Note the striking similarity with the situation encountered in $CO_2$ (Fig. 34). The outer-well resonances may be viewed as vibrational Feshbach resonances, albeit somewhat different in a quantitative sense from the 'inner well vibrational Feshbach resonances' discussed in the introduction. Similar structures as for HCl were observed in the elastic

and VE cross-sections of HBr and DBr by Čížek *et al.* (2001a), who also presented improved calculations and measurements of the dissociative attachment channel.

For HF, oscillatory structure below the DA threshold starts to be observed in the $v=0 \to 3$ VE channel and becomes very clear in $v=0 \to 4$ VE (Sergenton *et al.*, 2000). Recent high-resolution (15 meV) angle-differential VE results (Allan, 2001b; Čížek *et al.*, 2003) for $v=0 \to 1$, 2, 3, 4 exhibit a plethora of threshold and resonance features which are in full harmony with a nonlocal resonance model calculation of Čížek *et al.* (2003): in the $v=2$ channel, a sharp, dip-like VFR just below the $v=3$ onset is found (as predicted by Thümmel *et al.*, 1993); in the $v=3$ channel, a broader, deep dip below the $v=4$ threshold is observed (confirming and improving the results of Knoth *et al.*, 1989a), followed by oscillatory structure; in the $v=4$ channel a weak threshold peak is followed by impressive oscillations with decreasing energy spacings which cease at the DA threshold. These results are presented in Fig. 18a and compared with results of a nonlocal resonance model calculation (Čížek *et al.*, 2003).

Impressive agreement between theory and experiment is observed. The structures can be understood as VFR, which are sharp at lower energies
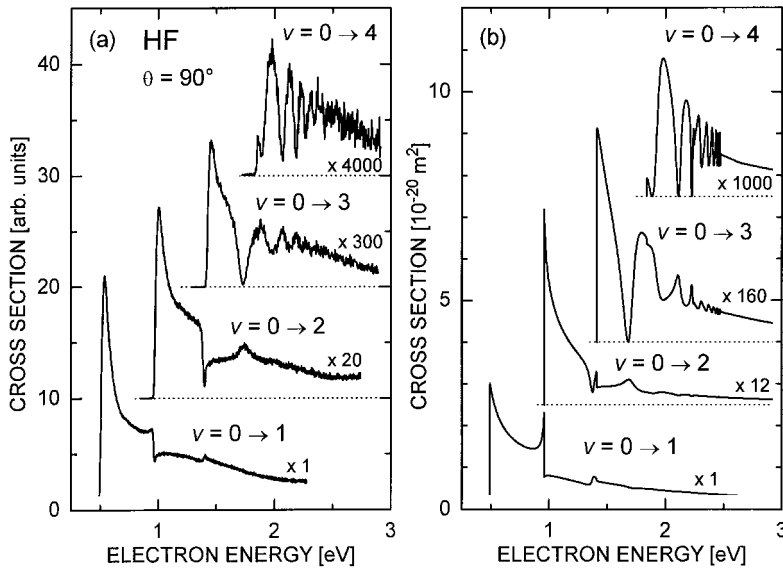


FIG. 18. VE cross-sections for HF($v=0$). (a): experiment ($\theta=90°$, Allan, 2001b; Čížek *et al.*, 2003) (b) theory (Čížek *et al.*, 2003).

and gradually become boomerang oscillations at higher energies, where the anion lifetime is just enough for nuclei to perform one classical oscillation. This interpretation might at first seem to cause a problem because H$X$ molecules do not support bound states at relatively small internuclear distances, close to the equilibrium separation and below (the same situation occurs for methyl halides discussed in Section IV.A.2). Appropriate theories predict VFRs even in this case, however (Section II). The qualitative picture (Gauyacq, private communication, see also Sergenton *et al.*, 2000) is that the electron escapes at small internuclear separations so slowly that it is recaptured with a large probability when the nuclei swing back to large $R$ where it is bound. Another interesting feature of boomerang oscillations is that they always occur below the DA threshold. Strictly speaking, boomerang structure could also occur above the DA threshold in the presence of potential barriers towards dissociation from which the nuclear wave packet would be reflected. No such case of boomerang structure above DA threshold has yet been reported, however. The same is true for threshold peaks in VE which are generally found only below the DA threshold (Domcke, 1991, Čížek *et al.*, 2001a), but may appear above it in the presence of a potential barrier towards dissociation. A specific example of the latter case was recently found, first theoretically (Schramm *et al.*, 1999) and then experimentally (Allan and Fabrikant, 2002), in methyl iodide. The fact that the DA channel is open in the VFR region simply means that there is an additional channel for the VFR decay: predissociation into the valence ionic state. Indeed, as will be discussed in Section IV.A.2, VFRs also appear in the DA channel in electron collisions with methyl halides. This mechanism is similar to what is called "indirect recombination" (O'Malley, 1981) in the theory of dissociative recombination and was discussed a lot in the relevant literature (Mitchell, 1990).

## A.2. Methyl Halides and Related Molecules

Dissociative attachment (DA) in low-energy electron collisions with methyl halide molecules $CH_3X$ ($X = $ F, Cl, Br, I), yielding $X^-$ anions, as well as vibrational excitation (VE) of the C-$X$ stretch mode $\nu_3$ may be described by a one-dimensional model involving just the $\nu_3$ mode. Although DA at zero electron energy is an exothermic process for the heavier methyl halides ($X = $ Cl, Br, I), the DA rate coefficients differ by orders of magnitudes at room temperature, rising from an extremely small value for $CH_3Cl$ (of order $10^{-15}\,cm^3\,s^{-1}$) via about $10^{-11}\,cm^3\,s^{-1}$ for $CH_3Br$ to about $10^{-7}\,cm^3\,s^{-1}$ for $CH_3I$ (Smith and Španel, 1994; Christophorou, 1996). A comparative study of DA to these molecules can help understand the basic physics governing the magnitudes of the DA cross-sections for different

molecules and the dependence of the DA cross-sections on vibrational temperature and electron energy.

DA to $CH_3Cl$ was investigated by swarm and beam techniques (for more recent studies and references to earlier work see Petrović *et al.*, 1989; Chu and Burrow, 1990; Datskos *et al.*, 1990; Pearl and Burrow, 1993). Widely different results for the DA cross-sections were reported that disagree by many orders of magnitude. Careful experimental investigations (Pearl and Burrow; 1993, Pearl *et al.*, 1995), supported by semiempirical calculations (Fabrikant, 1991b, 1994; Pearl *et al.*, 1995), showed that most of the earlier measurements were affected by contaminants, and the actual value of the low-energy DA cross section for $CH_3Cl$ gas at room temperature is so small that the process can hardly be detected. However, an increase in molecular temperature leads to a very rapid exponential rise of the cross-section. Theory and experiment agree well for temperatures above about $500\,K$ (Pearl *et al.*, 1995). DA cross-sections for $CH_3Br$ are substantially larger than for $CH_3Cl$, but still rather small at room temperature. At $T = 300\,K$ the swarm unfolded DA cross section of Datskos *et al.* (1992) shows a peak at $E \approx 0.38\,eV$ with a size of about $1.8 \times 10^{-22}\,cm^2$. Both the energy integrated cross section and the rate coefficient for electron attachment to $CH_3Br$ exhibit a strong increase with rising molecular temperature (Spence and Schulz, 1973; Alge *et al.*, 1984; Petrović and Crompton, 1987; Datskos *et al.*, 1992). So far high-resolution electron attachment spectra for $CH_3Cl$ and $CH_3Br$ have not been reported. DA to $CH_3I$ was studied experimentally by electron beam (Spence and Schulz, 1973) and swarm (Christophorou, 1976; Alge *et al.*, 1984; Shimamori and Nakatani, 1988; Shimamori *et al.*, 1992a; Speck *et al.*, 2000) methods and by the threshold photoelectron attachment technique (Alajajian *et al.*, 1988). In recent LPA studies of DA to the $CH_3I$ molecule (Hotop *et al.*, 1995; Schramm *et al.*, 1999), performed with meV resolution, a sharp variation of the cross section within a narrow energy interval below the first threshold for vibrational excitation of the symmetric stretch $v_3 = 1$ was observed. This was interpreted in terms of a vibrational Feshbach resonance (Schramm *et al.*, 1999). Higher vibrational thresholds do not exhibit resonance behaviour, but show pronounced cusps of the Baz'-Wigner type (Baz' 1958).

Using the model outlined in II.A.4, $R$-matrix calculations were performed (Schramm *et al.*, 1999; Wilde *et al.*, 2000) with the aim to theoretically characterize vibrational structure in the DA cross-sections for the methyl halides and to understand the strong size variation and temperature dependences of the DA rates for $CH_3Cl$ and $CH_3Br$. The parameters of the neutral potential curve $V(\rho)$, described in Morse form, were chosen to reproduce the experimental values for the dissociation energy $D_0$ as well as the vibrational spacing $\Delta G_{0-1}(v_3)$. For the negative ion curve $U(\rho)$,

described by an exponentially decaying function plus a constant, the vertical attachment energy (i.e. the value at $\rho = 0$, the equilibrium distance of the neutral potential) was chosen to agree with estimates of Modelli *et al.* (1992) (obtained from electron transmission spectra). The asymptotic value of $U(\rho)$ is fixed by the combined value of $D_0(CH_3-X)$ and the well-known electron affinity of $X$ ($X = Cl$, Br, I) (Andersen *et al.*, 1999). This leaves as unknown quantities in the semiempirical *R*-matrix model the parameter $\beta$ of the exponential repulsion in $U(\rho)$ and the surface amplitude (related to the width function), described by $\gamma(\rho) = \gamma_0 + \gamma_1/[\exp(\zeta\rho) + \eta]$. Moreover, the important long-range interactions between the electron and the molecule were taken into account in an appropriate way.

For methyl chloride, the *R*-matrix parameters were fixed by using information from *ab initio* calculations for the anion curve at distances $\rho > \rho_c$ ($\rho_c$ denotes the crossing point between $V(\rho)$ and $U(\rho)$) and from features observed in measurements of the differential VE cross section for $CH_3Cl$. For methyl iodide, the parameters were obtained by fitting to the highly resolved absolute DA cross-section, obtained by Schramm *et al.* (1999) with reference to swarm data at 300 K. For methyl bromide, two approaches were used which gave quite different results; we here report the results from model 2 which incorporated information from *ab initio* calculations for the anion curve as well as use of the experimental DA rate coefficient of Petrović and Crompton (1987) at $T = 440$ K.

In Fig. 19 we show the relevant potential curves for the three methyl halides of interest. The most important characteristic and difference between the three molecules is the location of the crossing point between the potential curve of the neutral molecule and that of the diabatic anion state which is close to the outer classical turning point of the $\nu_3 = 8$, 5, and 2 vibrational level for $CH_3Cl$, $CH_3Br$, and $CH_3I$, respectively.

In Fig. 20 we present DA cross-sections for two different initial vibrational states of $CH_3Cl$, namely for $\nu_3 = 0$ and for $\nu_3 = 7$; note that the cross-section scales differ by more than eight orders of magnitude. Just below the onset for vibrational excitation of the $\nu_3 = 8$ level, a very sharp resonance is observed which is interpreted as a VFR (Wilde *et al.*, 2000). When excited from the $\nu_3 = 0$ initial level, this VFR occurs at an energy of 0.68 eV (peak cross section about $3 \times 10^{-27}\,\mathrm{m}^2$) whereas in the attachment spectrum for $CH_3Cl(\nu_3 = 7)$ the same VFR shows up at 0.085 eV with a peak cross section of about $1.1 \times 10^{-18}\,\mathrm{m}^2$. The prominent VFR is present in all $CH_3Cl(\nu_3)$ attachment spectra for initial levels $\nu_3 = 0 - 7$. Sharp downward steps (cusps) are observed at the onsets for $\nu_3 > 8$ while a small peak (indicative of a virtual state) is present at the $\nu_3 = 7$ onset in the spectra for $CH_3Cl(\nu_3 = 0–6)$. The adiabatic potential curve for the $CH_3Cl^-$ anion follows the neutral curve in the region close to equilibrium internuclear
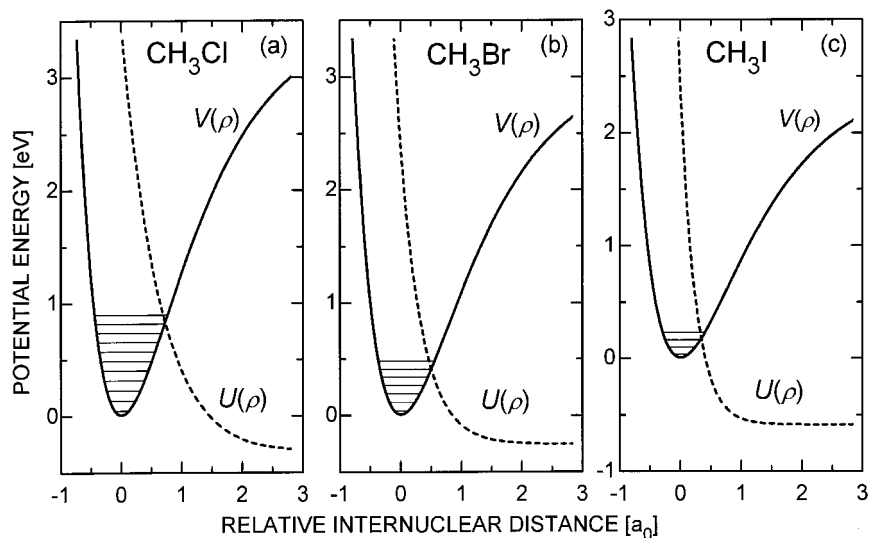
FIG. 19. Potential energy curves for $CH_3Cl$ (a) $CH_3Br$ (b) and $CH_3I$ (c) and their anions. The neutral curves (full) are denoted by $V(\rho)$, the diabatic anion curves (broken) by $U(\rho)$ where $\rho$ denotes the C–X distance relative to its equilibrium value ($\rho = 0$) (from Wilde et al., 2000).
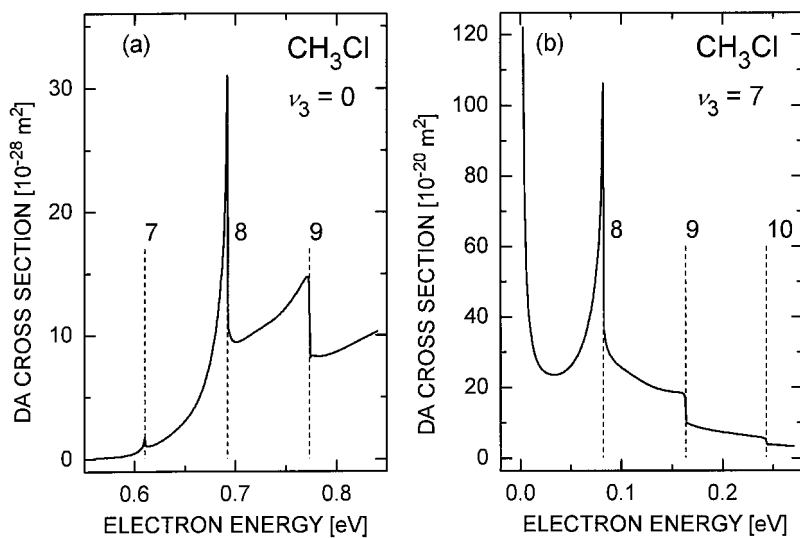


FIG. 20. Calculated DA cross-sections for $CH_3Cl$ ((a) $v_3 = 0$, (b) $v_3 = 7$). The quantum number $v_3$ labels the initially populated C–Cl stretch vibrational mode. Vertical broken lines denote the indicated vibrational thresholds (from Wilde et al., 2000).

separation (Wilde *et al.*, 2000; see also the general case illustrated in Fig. 3b), producing about eight vibrationally excited states of $CH_3Cl^-$ with a loosely bound electron, reflected as sharp peaks in the DA cross-sections (Fig. 20). In the case of $CH_3I$ we have only one vibrationally excited state of this type, therefore the resonance occurs only at the $\nu_3 = 1$ threshold. Although there are eight such states in $CH_3Cl^-$, the resonances at the thresholds with $\nu_3 < 7$ are masked by a rapid decrease of the DA cross-section towards lower energies due to the very fast drop of the Franck-Condon overlap between the initial vibrational state and the dissociating state.

A similar picture is observed for $CH_3Br$. Here the adiabatic negative-ion curve supports four excited vibrational states. Due to the lower a diabatic anion curve in the region of the crossing point, we observe two vibrational Feshbach resonances at the $\nu_3 = 3$ and $\nu_3 = 4$ thresholds (see Fig. 21; note that VFR at the $\nu_3 = 3$ threshold is barely seen on the scale of drawing). In the DA spectrum for $CH_3Br(\nu_3 = 0)$ the $\nu_3 = 4$ VFR has a peak cross-section of about $2 \times 10^{-22}\,m^2$ while in the spectrum for $CH_3Br(\nu_3 = 3)$ it reaches $1.2 \times 10^{-18}\,m^2$. The attachment spectrum for $CH_3Br$ molecules at room temperature is predicted to exhibit the $\nu_3 = 4$ VFR at four different energies in about equal strength (effective peak cross-sections around $3 \times 10^{-22}\,m^2$), corresponding to excitation from the thermally populated $\nu_3 = 0$, 1, 2, and 3
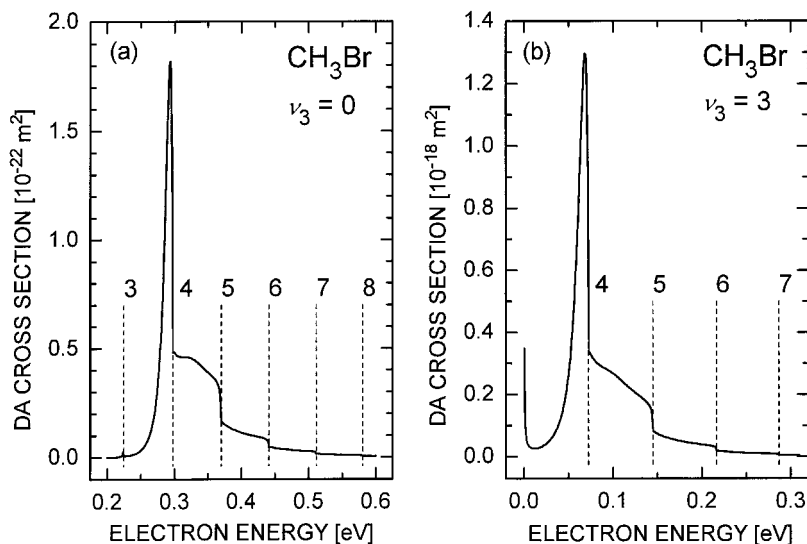


FIG. 21. Calculated DA cross-sections for $CH_3Br$ ((a) $\nu_3 = 0$, (b) $\nu_3 = 3$). Vertical broken lines denote the indicated vibrational thresholds (from Wilde *et al.*, 2000).

vibrational levels (Wilde *et al.*, 2000). As mentioned above, two different models with more or less equal diabatic curves, but rather different surface amplitudes were used which yielded rather different cross-sections. The results shown here were obtained with the higher surface amplitude (model 2). High-resolution DA experiments for methyl bromide are needed to prove the presence of the prominent VFR associated with the $\nu_3 = 4$ level.

The first clear experimental observation of a VFR in the DA channel was made for $CH_3I$ by the Kaiserslautern group (Hotop *et al.*, 1995; Schramm *et al.*, 1999). Results were obtained with a thermal target (300 K, population of $\nu_3 = 1$ relative to $\nu_3 = 0$ about 7.8%) as well as with vibrationally cooled molecules in a seeded supersonic beam. In Fig. 22 the supersonic beam data (open circles, adjusted in absolute size to theory) are compared with the *R*-matrix fit over the range 0–115 meV. Note that at the $\nu_3 = 2$ threshold VFR peak structure is absent in agreement with the experimental data, taken over a broader electron energy range at $T_G = 300$ K (insert in Fig. 22; note that the experimental cross-section has been multiplied by 0.5 for this comparison). Weak structure is observed in the measured spectrum close
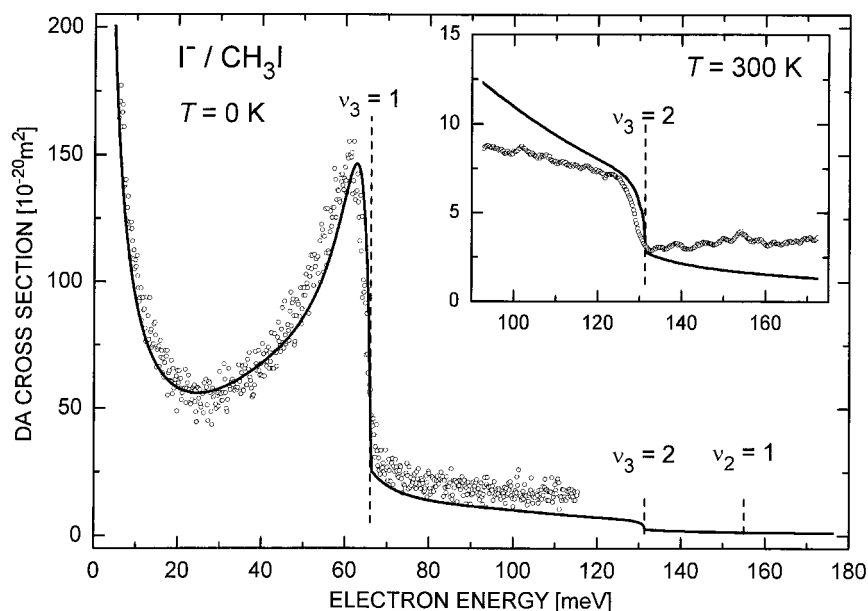


FIG. 22. Comparison of measured (open circles) and calculated (full curves) DA cross-sections for $CH_3I$. The LPA data in the main frame were measured with a supersonic beam target, whereas for the LPA data in the inset (measured cross-section multiplied by 0.5) a diffuse gas target at room temperature was used (from Schramm *et al.*, 1999).

to the $\nu_2 = 1$ onset ($E = 155$ meV) which is not reflected by theory because only the $\nu_3$ mode is included in the model. The *R*-matrix results for the shape of the VFR were found to be very sensitive to the *R*-matrix parameters including the long-range electron–molecule interaction, associated with the permanent electric dipole moment and the polarizability of methyl iodide (Schramm *et al.*, 1999; Leber *et al.*, 2000a, see also Section II).

   In view of the good quality in the description of both the shape and the absolute value of the DA cross-section one may hope that the *R*-matrix model be able to correctly predict electron scattering cross-sections, especially for VE involving the $\nu_3$ mode. In Fig. 23 we compare the calculated cross-sections for elastic and vibrationally inelastic ($\nu_3 = 0 \rightarrow 1$) scattering with recent experimental results, with an energy width of 10 meV in the incident beam (Allan and Fabrikant, 2002). In the elastic channel the VFR just below the $\nu_3 = 1$ onset shows up as a sharp dip whose depth is reduced in the experimental spectrum due to the energy spread. The $\nu_3 = 0 \rightarrow 1$ VE spectrum exhibits a prominent threshold peak, an upward step at the $\nu_3 = 2$ threshold, and an upward cusp at the $\nu_3 = 3$ onset in very good agreement between theory and experiment. Similarly good agreement is observed for $\nu_3 = 0 \rightarrow 2$ and higher channels VE. We conclude that semiempirical *R*-matrix calculations have substantial predictive power once the model parameters have been appropriately fixed by using information from either VE or DA experiments in combination with *ab initio* molecular structure theory.
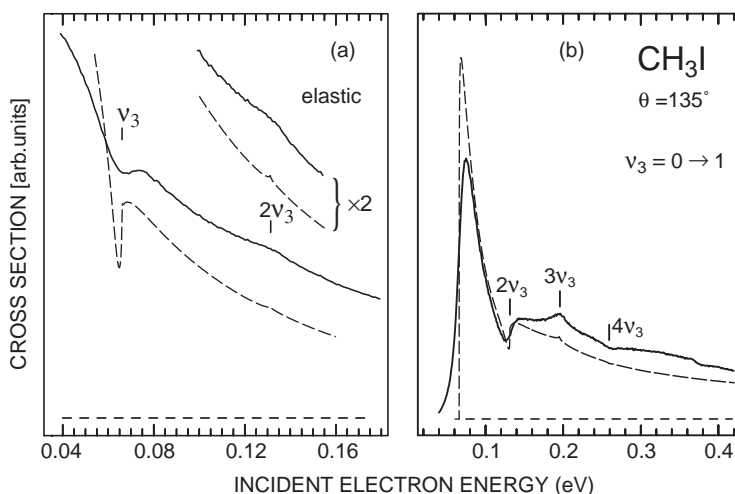


Fig. 23. Theoretical (dashed) and experimental elastic scattering (a) and $\nu_3 = 0 \rightarrow 1$ VE (b) in electron-$CH_3I$ collisions. Vibrational thresholds are marked (from Allan and Fabrikant, 2002).
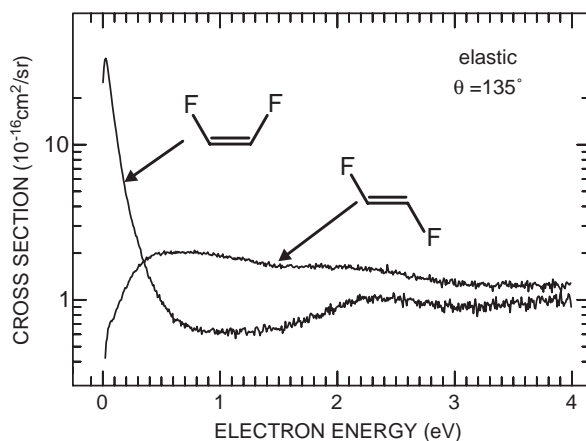
F<small>IG</small>. 24. Differential elastic cross-sections in *cis*- and *trans*-difluoroethenes (Allan *et al.*, 2002).

A similar treatment can be applied to the perfluoromethyl chloride ($CF_3Cl$) molecule. However, since its dipole moment is relatively small ($\mu = 0.196$ a.u.), no VFRs were found there. A strong temperature effect in DA to $CF_3Cl$ was detected by Hahndorf *et al.* (1994) in the low-energy region (energy width around 0.1 eV). Theoretical calculations have been performed in the classical approximation (Lehr and Miller 1996; Lehr *et al.*, 1997) and by the use of the resonance *R*-matrix method (Wilde *et al.*, 1999). Recent *ab initio* calculations of Beyer *et al.* (2001) combine the *R*-matrix method with the projection operator technique to treat the vibrational dynamics. The semiempirical classical and the *R*-matrix calculations reproduce (albeit only qualitatively) the experimental zero-energy peak at $T = 800$ K. For a more detailed comparison between theory and experiment, high resolution DA measurements as a function of gas temperature would be interesting.

The LPA method has been applied to investigate DA to the dipolar halogenated methanes $CH_3I$ (see above), $CFCl_3$, $CBrCl_3$, and $CH_2Br_2$ at meV energy width. In all cases s-wave attachment was confirmed at very low energies where the DA cross-sections showed an energy dependence between $E^{-1/2}$ and $E^{-1}$ (Klar *et al.*, 2001b; Schramm *et al.*, 2002). For $CH_2Br_2$ (which has similar dipole moment and polarizability as $CH_3I$) a clear VFR just below the onset for the $\nu_3 = 1$ symmetric $CBr_2$ stretch vibration was observed (Schramm *et al.*, 2002). While clear cusp structure was detected at several vibrational thresholds for $CFCl_3$ (Klar *et al.*, 2001b), such structure was nearly absent for $CBrCl_3$ (Schramm *et al.*, 2002). *R*-matrix calculations demonstrated that $Br^-$ formation from DA to $CBrCl_3$

proceeds by s-wave attachment to the ground anion state at low energies while a broad peak, observed around 0.6 eV and evolving predominantly into the statistically favoured Cl⁻ channel, is due to an excited anion state.

### A.3. Electron Scattering from cis- and trans-Difluoroethenes

Use of polyatomic organic compounds allows introducing a "chemical dimension" into the study of electron scattering by *designing* molecules with the desired physical and electronic properties. *Cis*- and *trans*-difluoroethenes (1,2-$C_2H_2F_2$) represent an example where use is made of this possibility. Both molecules are virtually identical in terms of size, the nature of chemical bonding and of electronic structure, but differ dramatically in the magnitudes of the permanent dipole moments (2.42 Debye in *cis* and zero by symmetry in *trans*). This pair of compounds thus allowed Allan *et al.* (2002) to study the effect of dipole moment on the threshold peaks, while keeping the effect of other factors like polarizability, presence or absence of double bonds, number of halogens, etc., unchanged.

Figure 24 illustrates the trivial effect on the elastic cross-section. The size of the elastic cross-section is strongly enhanced at low energies by the long-range force of the permanent dipole moment of *cis*-difluoroethene, as expected.

Figures 25 and 26 compare the cross-sections of the C=C stretch and the C–F stretch vibrations for the two isomers. A band due to the $\pi^*$ shape resonance is seen for both types of vibrations, yielding vertical electron attachment energies of 2.37 eV for *cis*-difluoroethene and 2.05 eV for *trans*-difluoroethene. The resonances thus lie slightly higher than in the parent compound ethene, which has a resonance at 1.78 eV (Jordan and Burrow, 1978). The effect of the fluorine substituents may be viewed as a stabilizing inductive effect due to the large electronegativity of fluorine and a destabilizing conjugative effect due to admixture of the occupied lone pair orbitals of $\pi$ symmetry on the fluorines. The higher energy of the resonance in the *cis*- compound can be visualized within this picture as due to destabilizing through-space interaction of the fluorine lone pairs of $\pi$ symmetry.

Both the C=C stretch vibrations (Fig. 25) and the C–F stretch vibrations (Fig. 26) are excited to about the same degree in the $\pi^*$ shape resonance region. This reflects the fact that the $\pi^*$ antibonding orbital, which is temporarily occupied in the shape resonance, is antibonding with respect to both the C=C and the C–F distances, and is little influenced by whether the fluorines are arranged *cis* or *trans*.
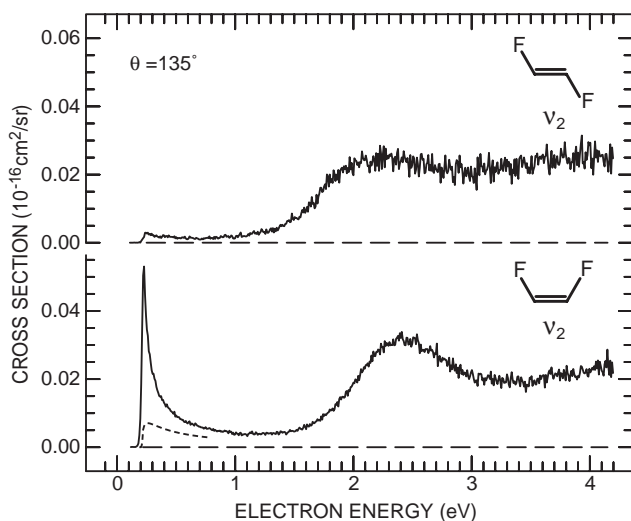
FIG. 25. Cross-sections for the excitation of the C=C stretch vibrations $\nu_2$ in *cis*- and *trans*-difluoroethenes. The dashed curve is a cross-section calculated from the infrared intensities using the Born approximation. $\nu_2$ is IR inactive in the *trans* compound and the Born cross-section is consequently zero. (from Allan *et al.*, 2002).
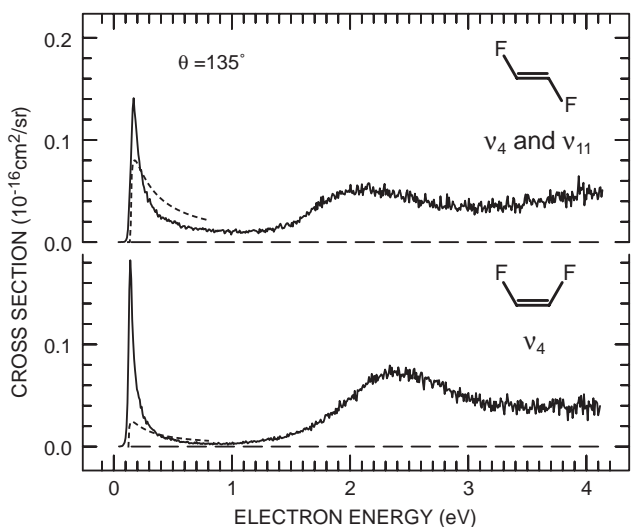


FIG. 26. Cross-sections for the excitation of the C–F stretch vibrations in *cis*- and *trans*-difluoroethenes ($\nu_4$ in *cis*-difluoroethene and overlapping $\nu_4$ and $\nu_{11}$ in *trans*-difluoroethene). Born cross sections are shown dashed (from Allan *et al.*, 2002).

Substantial differences appear in the threshold region, however. These differences were discussed in terms of two effects. The first is the trivial excitation of infrared active vibrations near threshold by the dipole mechanism. This excitation is forward-peaked and its extent in Figs. 25 and 26 has been reduced by the large scattering angle of 135°. The remaining contribution of the excitation by this mechanism was estimated by calculating the cross-sections within the Born approximation from the experimental infrared band intensities. This approximation is primarily intended for forward scattering, but can be assumed to be qualitatively useful even at the large scattering angle. Threshold cross-sections exceeding substantially the Born prediction were interpreted as 'true' threshold peaks, in the same sense as in the examples of HF and other halogen halides described above.

Two observations are made in the excitation of the C=C stretch vibrations in Fig. 25. This vibration is excited at threshold only in the *cis* isomer where it is infrared active, and nearly absent in the *trans* isomer where it is infrared inactive. The cross-section in the former case is, in addition, substantially higher than the Born prediction.

Threshold peaks are found in the cross-sections for the C–F stretch excitation for both the *cis* and the *trans* isomers in Fig. 26, but only in the *cis* isomer, with permanent dipole moment, does the observed cross-section substantially exceed the Born prediction. (Two C–F stretch vibrations overlap in the *trans* compound and both the experimental cross-section and the Born prediction are the sums for both vibrations.). It was consequently concluded that two conditions strongly contribute to the presence of 'true' threshold peaks. One is a permanent dipole moment and the other a dipole moment being a function of nuclear coordinate for the normal mode in question (i.e., the mode must be IR active). This conclusion holds also for a number of other normal modes of *cis* and *trans* difluoroethenes measured by Allan *et al.* (2002) but not shown here.

These conclusions are compatible with the notion that the threshold peaks are closely related with a negative ion state where an electron is bound (in an electronic sense) by a dipole force in a spatially diffuse wave function, but only for a certain range of configurations of the nuclei. HF is a prototype of this mechanism and the present molecules extend it to a case with many normal modes and a variable permanent dipole moment. The permanent dipole moment is important by providing a sufficient 'dipole binding' in the first place. The binding energy is further enhanced and becomes a function of vibrational coordinate (for the normal mode in question) for IR active vibrations. The permanent dipole moment is not absolutely indispensable, however, as exemplified by $CO_2$ and $CS_2$. A sufficiently strong polarization force can replace its effect.

## B. Electron Collisions with Nonpolar Molecules

In this subsection we shall discuss molecules which do not possess a permanent electric dipole moment (i.e. $\mu = 0$). Most of these molecules exhibit, however, a permanent electric quadrupole moment $Q \neq 0$, leading to an interaction $V_Q(r) \propto -1/r^3$ which has to be considered in addition to the polarization interaction $V_{pol}(r) \propto -1/r^4$. Here we consider the three cases $Na_2$, $F_2$ and $Cl_2$ for which we focus on the threshold behaviour of the electron attachment cross-section. Very few molecules, characterized by a high symmetry, neither possess a permanent electric dipole moment nor a permanent electric quadrupole moment, among them $SF_6$, $CCl_4$ and $C_{60}$. These molecules are known as very efficient electron scavengers, and $SF_6$ is being used as a gaseous dielectric in many applications (Christophorou and Olthoff, 2000). We further discuss the low-energy scattering behaviour of two linear, symmetric triatomic molecules which exhibit strong enhancements of elastic and inelastic scattering through a virtual state ($CO_2$) or a bound anion state ($CS_2$) and also include the weakly polar molecule $N_2O$ ($\mu = 0.16\,D$) which is isoelectronic with $CO_2$ and has exhibited intriguing vibrational structure in a recent high resolution DA study. These findings are also relevant to the observations of vibrational resonance structure made for clusters composed of these and related molecules.

### B.1. Electron Attachment to Vibrationally Excited Sodium Molecules

Among the *nonpolar* diatomic molecules $Y_2$ only a few cases (including the halogen molecules) exhibit anion formation by dissociative electron attachment at near-zero electron energies. The threshold behaviour of DA to the halogen molecules is still under debate (see next subsection). DA to the alkali dimers is endothermic by a few tenths of an eV. Zero energy attachment, may, however, be investigated if a sufficient amount of vibrational energy is present in the molecule. Here we describe the results of a recent experiment in which high resolution near-zero energy electron attachment to sodium dimers in a *controlled* vibrational level $v$ has been carried out (Keil *et al.*, 1999):

$$e^-(E) + Na_2(X^1\Sigma_g^+, v) \rightarrow Na_2^-(A^2\Sigma_g^+) \rightarrow Na^-(^1S) + Na(3^2S). \quad (37)$$
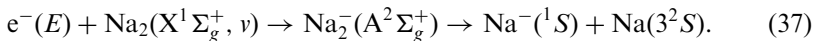
Figure 27 illustrates the relevant potential energy curves (Külz *et al.*, 1996, Keil *et al.*, 1999), as obtained in a high level electronic structure calculation. The electronic configuration of the $Na_2^-(^2\Sigma_u^+)$ ground state (chain curve) is $1\sigma_g^2 1\sigma_u$; it is stable for lower vibrational levels (adiabatic electron
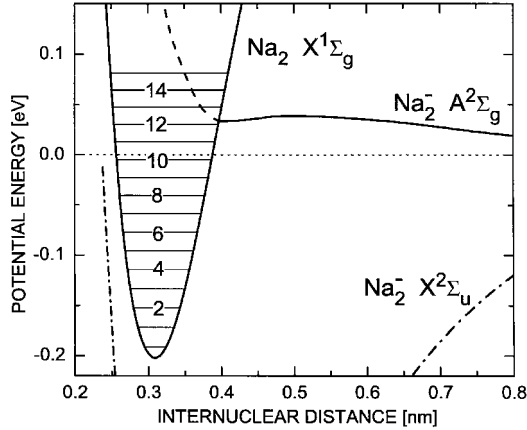
FIG. 27. Potential energy curves for $Na_2$ and $Na_2^-$, relevant for threshold electron attachment to $Na_2(v > 0)$ molecules (from Keil *et al.*, 1999).

affinity $+0.44\,eV$) and is not involved in the processes discussed here. The $Na_2^-(A^2\Sigma_g^+)$ state is stable for internuclear distances $R > R_C = 0.38\,nm$ and turns into a resonance state for smaller $R$. At long range it is dominated by the $1\sigma_g 1\sigma_u^2$ configuration. It acquires significant admixture of a $1\sigma_g^2 2\sigma_g$ configuration at distances below $0.5\,nm$. For $R < R_C$ the $2\sigma_g$ orbital turns into a continuum wave function; anion formation involves a two-electron process in which the incoming s-wave electron and one of the molecular $1\sigma_g$ electrons form the $1\sigma_u^2$ part of the Feshbach-type $Na_2^-(A^2\Sigma_g^+)$ resonance state. Reaction (37) becomes exothermic for $v = 11$, but due to the barrier in the $Na_2^-(A^2\Sigma_g^+)$ potential energy curve near $0.47\,nm$ the DA cross-sections for both $v = 11$ and 12 are predicted to be suppressed at very low energies.

Using a collimated supersonic beam, containing both Na(3s) atoms and $Na_2(v = 0)$ molecules, the experiment (Keil *et al.*, 1999) combined the laser photoelectron attachment method (here two-step photoionization of Na(3s) through the excited Na(3p$_{3/2}$) level) with selective vibrational excitation by means of a two-photon Raman technique with acronym STIRAP (Stimulated Raman with Adiabatic Passage) (Vitanov *et al.*, 2001). Na$^-$ ions due to the DA process (37) are detected with a time-of-flight mass spectrometer. In Fig. 28 the attachment spectra for the four selected vibrational levels $v = 12$, 13, 14, and 22 are shown; they were obtained at an electron current of about $0.2\,nA$. There is a clear change in the threshold behaviour when going from $v = 12$ to higher vibrational levels; for $v \geq 13$, the calculations and the experimental results both exhibit a strong rise of the
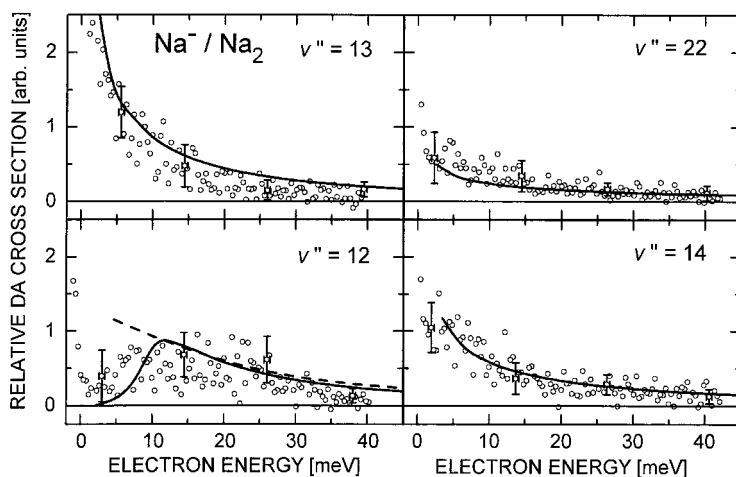
F<small>IG</small>. 28. Electron attachment cross-sections for selectively vibrationally excited $Na_2(v)$ molecules (from Keil *et al.*, 1999).

cross-section towards zero electron energy which is characteristic for s-wave capture. Note that the theoretical data for $v = 12$ (which show a sharp rise above 8 meV) have been convoluted by a Gaussian with 6 meV width to simulate the effects of experimental resolution. The overall agreement between the experimental and theoretical results is quite satisfactory although the experimental anion yields seem to decrease somewhat more rapidly towards higher energies than the theoretical cross-sections.

### B.2. Electron Attachment to Fluorine and Chlorine Molecules

Dissociative electron attachment to the halogen molecules $Y_2$ ($Y = F$, Cl, Br, I) at energies below 1 eV is expected to occur through formation of the lowest negative-ion state with $^2\Sigma_u^+$ symmetry according to the scheme (see, e.g., Domcke, 1991; Christophorou and Olthoff, 1999)

$$e^-(E) + Y_2(X^1\Sigma_g^+) \to Y_2^-(^2\Sigma_u^+) \to Y^-(^1S) + Y(^2P). \qquad (38)$$
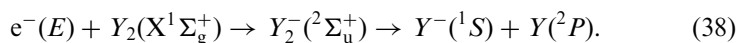
This process has been observed in several experimental studies (e.g. Kurepa and Belić, 1978, Tam and Wong, 1978, Chantry, 1982) as a peak at or close to zero energy with a width which was to a large extent limited by the experimental resolution (between 0.08 and 0.2 eV). For $F_2$ Chutjian and Alajajian (1987) reported s-wave behaviour of the DA cross-section at an energy width of 6–12 meV, using the TPSA method. From a theoretical

point of view the process is expected to be dominated by the p-wave because of the ungerade parity of the resonance state which rules out s-wave attachment. According to the Wigner threshold law the cross-section should thus grow with the square root of the electron energy at sufficiently low energies, as predicted in several theoretical calculations for $F_2$ (Hazi *et al.*, 1981; Bardsley and Wadehra, 1983; Brems *et al.*, 2002) and for $Cl_2$ (Fabrikant *et al.*, 2000).

Brems *et al.* (2002) carried out high level *ab initio* calculations of the lowest $F_2^-$ resonance state by the *R*-matrix method with the Feshbach-Fano partitioning technique to treat the nuclear dynamics. Their DA cross-section exhibits p-wave threshold behavior and reaches a peak around 0.2 eV with a size of about $1.5 \times 10^{-20}\,m^2$. The experimental DA cross-section of Chantry (1982) is in satisfactory agreement with the theoretical results over the range 0.6–2 eV, but the increase towards lower energies (compatible with the TPSA data) remains unexplained. There is clearly a need for a new high-resolution experiment with the aim to clarify the situation.

For the chlorine molecule, a similar discrepancy as for $F_2$ appeared to exist. A critical analysis of the early and more recent low resolution data (Kurepa and Belic, 1978; Tam and Wong, 1978; Feketeova *et al.*, 2003), based on their comparison with convoluted theoretical cross-section shapes (using appropriate energy distribution functions), reveals that they are in fact not contradictory to p-wave attachment (Ruf *et al.*, 2003). In a recent LPA experiment (energy width near threshold 1 meV) Barsotti *et al.* (2002b) provided conclusive experimental evidence for p-wave behaviour of the attachment cross-section for $Cl_2$ by demonstrating the steep rise from threshold to a maximum located around 50 meV.

Recent accurate calculations (Leininger and Gadea, 2000) of potential curves for $Cl_2$ and $Cl_2^-$ provide useful information regarding the dynamics of the process. The curve crossing between the $Cl_2(X^1\Sigma_g^+)$ and $Cl_2^-(^2\Sigma_u^+)$ states occurs below the left classical turning point for the nuclear motion in $Cl_2$. Typically the Franck-Condon factor changes relatively slowly in the near-threshold region, and the energy dependence of the cross-section is mainly determined by the capture width $\Gamma$ which gives the $E^{-1/2}$ law in the case of s-wave attachment and the $E^{1/2}$ law in the case of the p-wave attachment. However, in the case of attachment to $Cl_2$ the Franck-Condon factor drops very rapidly with rising energy, therefore the DA cross-section should exhibit a rather narrow peak near threshold with the $E^{1/2}$ behavior limited to energies below 10 meV.

To confirm this conjecture, the DA cross-section was calculated by Fabrikant *et al.* (2000), using the resonance *R*-matrix theory. The surface amplitude $\gamma$ was adjusted to reproduce the recommended value of the DA cross-section (Christophorou and Olthoff, 1999) at 0.1 eV and the
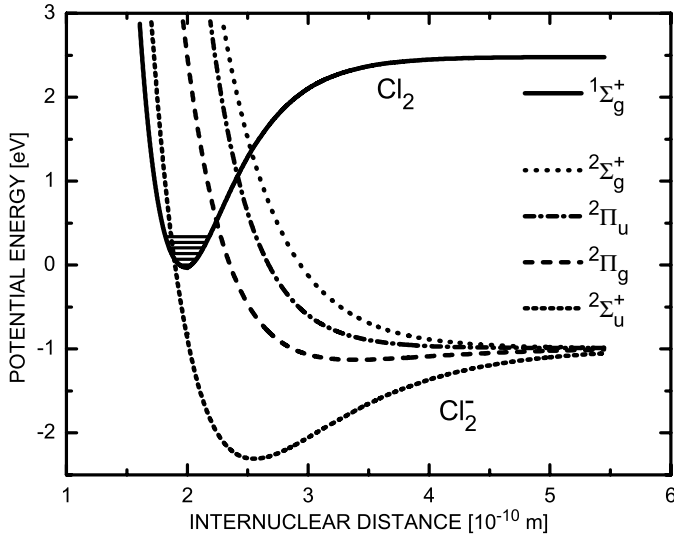
Fig. 29. Potential energy curves for $Cl_2$ and $Cl_2^-$, relevant for electron attachment to $Cl_2(X\,^1\Sigma_g^+)$ molecules (from Barsotti *et al.*, 2002b).

magnitude of the swarm-derived DA rate coefficients (McCorkle *et al.*, 1984). In Fig. 29 we present the fitted potential curves of the problem. The neutral curve $V(\rho)$ and the "diabatic" curve $U(\rho)$ were parameterized by Morse functions.

In Fig. 30 we show the calculated DA cross-section (full curve) in the low-energy region (0–200 meV) and compare it with the measured LPA cross-section (open circles, normalized in absolute size to the calculated value at the maximum, assuming a vibrational temperature of $Cl_2$ of $T_i = 500\,K$). The shapes of the experimental and theoretical cross-sections are in good agreement. We emphasize that the *shape* of the DA cross-section for different initial vibrational levels $v_i$ is almost independent of $v_i$ (see broken line in Fig. 30, calculated with $T_i = 300\,K$) while the *absolute size* rises strongly with increasing $v_i$, reflecting mainly the changes of the Franck-Condon factors. The rather sharp decrease of the DA cross-section above $E = 0.05\,eV$ is caused by two reasons: the fast drop of the Franck-Condon factor with rising energy mentioned above and the decrease of the survival probability of the intermediate negative ion against autodetachment. It is essential that this behavior is independent of our normalization procedure. If we vary $\gamma$, but keep the adiabatic anion curve fixed, the shape of the cross-section does not change.

The *R*-matrix calculations were extended to provide semiempirical predictions for vibrational excitation (VE) cross-sections for this molecule of
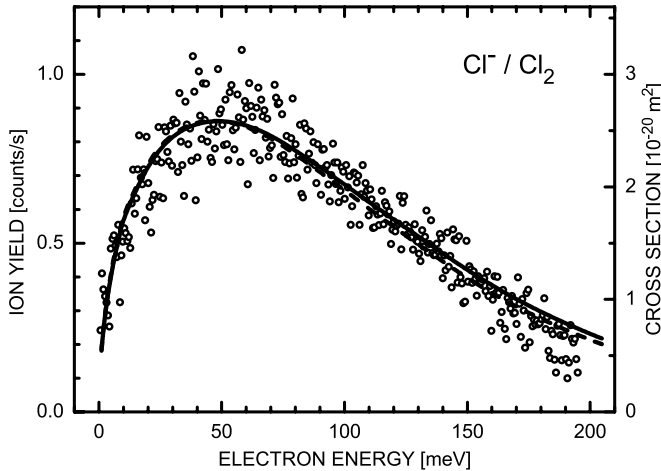
F<small>IG</small>. 30. Cross-section for dissociative electron attachment to $Cl_2$. The absolute scale refers to the calculation which assumes a vibrational temperature of $T_i = 500$ K (full curve). The LPA data (open circles) and the calculation with $T_i = 300$ K (broken curve) have been normalized to the maximum of the full curve (from Barsotti *et al.*, 2002b).

substantial practical interest, not only though the $Cl_2^-(^2\Sigma_u^+)$ resonance, but also through the higher lying $^2\Pi_g$ and $^2\Pi_u$ resonances (Ruf *et al.*, 2003). So far no direct measurements for these VE cross-sections have been carried out.

## B.3. Electron Attachment to $SF_6$ and $CCl_4$

Both $SF_6$ and $CCl_4$ belong to the few molecules for which the Vogt-Wannier capture model should be applicable in view of missing electric dipole and quadrupole moments, and it is thus of interest to compare the prediction of the VW theory with experimental results for the energy dependent attachment cross-section, obtained at very low energies and high resolution. To illustrate the importance of the reactive attachment channel, we also present the total electron scattering cross-sections.

Using energy-variable photoelectrons from VUV photoionization of rare gas atoms (energy range 0–160 meV, energy width 6–8 meV), Chutjian and Alajajian (1985) obtained clear evidence for s-wave behavior of the attachment cross-section for $SF_6$ and $CCl_4$ at low energies. They used the following analytical form for the attachment cross-section to describe the TPSA data over the range from 0 to 140 meV (see also Chutjian, 1992; Chutjian *et al.*, 1996):

$$\sigma_{\text{TPSA}}(E) = N_{\text{TPSA}}[aE^{-1/2}\exp(-E^2/\lambda^2) + \exp(-E/\gamma)]. \qquad (39)$$

It contains three fit parameters $a$, $\lambda$, and $\gamma$ and a normalization constant $N_{\text{TPSA}}$; the latter is determined by use of Eq. (35). The analytical form of the cross-section (39) has the deficiency that the second exponential term (which serves to describe the fast decrease of the cross-section at higher energies) is not cut off towards very low energies where the first term (which describes the limiting s-wave behavior) should take over. As long as the first term is not very much larger than the second one, this leads to a more or less substantial perturbation of the s-wave term (Klar *et al.*, 2001a).

Subsequently, Klar *et al.* (1992a, b, 2001a), Hotop *et al.* (1995) and Schramm *et al.* (1998) used the laser photoelectron attachment (LPA) method to investigate anion formation from these two molecules over a similar energy range, but with substantially reduced energy width (below 1 meV). As an important ingredient and improvement over previous work, they analyzed the effects of residual electric fields (reduced to values below 1 V/m) on the near-threshold attachment yield through model calculations of the attachment yield (Klar *et al.*, 1992b; 1994a, b; 2001a, b; Schramm *et al.*, 1998). In the spirit of the s-wave capture formula (21) due to Klots they used the analytical cross-section

$$\sigma_e(E) = (\sigma_0/E)[1 - \exp(-\beta E^{1/2})] \tag{40}$$

which was found to provide a very good description of the experimental attachment yield from threshold up to the first vibrationally inelastic onset for both $SF_6$ (Klar *et al.*, 1992b; 1994a, b) and $CCl_4$ (Hotop *et al.*, 1995; Klar *et al* 2001a). In this way they were able to determine the parameter $\beta$ in Eq. (40) to within 10% and thereby quantify the deviations of the cross section from the limiting behavior $\sigma_e(E \to 0)$ which – in terms of Eq. (40) – is given by $\sigma_e(E \to 0) = \sigma_0 \beta / E^{1/2}$. With $\beta$ expressed in units of $(\text{meV})^{-1/2}$, Klar *et al.* obtained $\beta = 0.405(40)$ for $SF_6$ (Klar *et al.*, 1992b) and $\beta = 0.59(6)$ for $CCl_4$ (Hotop *et al.*, 1995; Klar *et al.*, 2001a), in both cases distinctly larger than the prediction obtained from the Klots formula (21), namely $\beta_K = 0.228$ for $SF_6$ and $\beta_K = 0.299$ for $CCl_4$. For $SF_6$, Schramm *et al.* (1998) measured the attachment yield at residual electric fields as low as 0.01 V/m and negligible laser bandwidth for electron energies from 10 meV down to 20 $\mu$eV; they confirmed the results of Klar *et al.* (1992b) for the parameter $\beta$. The limiting LPA rate coefficient $k_e(E \to 0) = \sigma_e(E \to 0)(2E/m_e)^{1/2} = \sigma_0 \beta (2/m_e)^{1/2}$ ($5.4(8) \times 10^{-7}$ cm$^3$ s$^{-1}$) is in good agreement with the Vogt-Wannier prediction $k_c = 5.15 \times 10^{-7}$ cm$^3$ s$^{-1}$ (Klar *et al.*, 1992b) and with RET data for $SF_6^-$ formation from $SF_6$ at high principal quantum numbers $n$ ($k_{nl} = 4.0(10) \times 10^{-7}$ cm$^3$ s$^{-1}$, Ling *et al.*, 1992; Klar *et al.*, 1994b; Dunning, 1995).
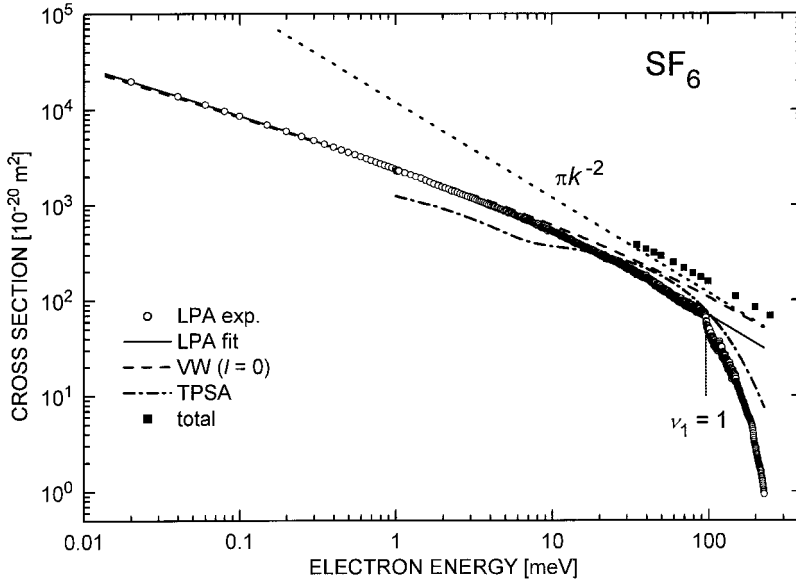
FIG. 31. Absolute cross-sections for electron collisions with $SF_6$. LPA: Laser photoelectron attachment ($SF_6^-$ formation, Klar *et al.*, 1992b; Hotop *et al.*, 1995), TPSA: Threshold photoelectron attachment (($SF_6^-$ formation, Chutjian and Alajajian, 1985), see text. For comparison, we have included the total cross-sections due to Ferch *et al.* (1982) (full squares), the Vogt-Wannier s-wave capture cross-section VW($l=0$), the limiting s-wave reaction cross section $\pi k^{-2}$ and the LPA fit according to Eq. (40).

In Fig. 31 we present a comparison of the LPA cross-section (normalized in absolute size to the thermal rate coefficient due to Petrović and Crompton, 1985) with the VW result for s-wave attachment (p-wave capture would reach its peak at an electron energy of about 330 meV and is neglected), with the fit (39) to the TPSA data (Chutjian and Alajajian, 1985) and with the empirical fit (40) of Klar *et al.* (1992b). The fit (40) gives a good description of the LPA data up to the threshold for $\nu_1 = 1$ vibrational excitation where the cross-section exhibits a sharp downward cusp, predicted theoretically by Gauyacq and Herzenberg (1984) and confirmed by Klar *et al.* (1992a, b). Systematic deviations between the LPA and TPSA results are observed (in spite of using the same thermal rate coefficient for normalization) here and also for other molecules, as discussed and explained by Klar *et al.* (1992b; 1994a; 2001a, b) and Schramm *et al.* (1999, 2002). In a more recent study Howe *et al.* (2001) confirmed the smooth Klots-type behavior of the $SF_6^-$ cross-section (see also below).

For comparison with the (nondissociative) attachment channel, we have included in Fig. 31 the total scattering cross-section, as presented in the

survey of Christophorou and Olthoff (2000, Table 9) and due to Ferch *et al.* (1982) at low energies. Below the onset for vibrational excitation of the symmetric stretch mode $\nu_1 = 1$, the total cross-section is 2.23 (90 meV) to 2.05 (35 meV) times higher than the fitted LPA attachment cross-section. A decrease of the ratio between the total cross-section and the attachment cross-section towards very low energies is expected on theoretical grounds; the ratio should be a linear function of wave vector $k$ at very low energies and take the value unity for $E \rightarrow 0$. Assuming that VE cross-sections of the lower energy modes (e.g. $\nu_6 = 1$, onset at 44 meV) can be neglected, the elastic scattering cross-section $\sigma_{ES}$ can be calculated from the difference between the total cross-section and the LPA attachment cross-section. The resulting values for $\sigma_{ES}$ rise from $95 \times 10^{-20}\,\mathrm{m}^2$ at 90 meV to $195 \times 10^{-20}\,\mathrm{m}^2$ at 35 meV while the LPA cross-section rises from $78 \times 10^{-20}\,\mathrm{m}^2$ to $185 \times 10^{-20}\,\mathrm{m}^2$, respectively. A preliminary analysis of these data (Fabrikant, unpublished) within the framework of the modified effective range theory (O'Malley *et al.*, 1962) yields two possible solutions for the electron scattering length of $SF_6$, namely $A \approx 7.3\,a_0$ and $A \approx -10.0\,a_0$. In the first case a weakly bound state would exist for which no evidence exists so far (Christophorou and Olthoff, 2000). The second case would indicate a virtual state and would make the case of low-energy e–$SF_6$ scattering similar to that of $CO_2$ (see below). In order to clarify the situation, new measurements of the total cross-sections down to very low energies are needed. In recent theoretical calculations of electron scattering from $SF_6$ over the broad energy range from a few meV to 100 eV, Gianturco and Lucchese (2001) obtained total cross-sections which are substantially lower than the experimental results at energies below 1 eV. They attributed the differences to inelastic channels (vibrational excitation), but did not consider electron attachment which is the major reaction channel at the lowest energies. Their elastic cross-section at 35 meV is about 40 times lower than the estimate given above.

Since in the case of s-wave scattering there is no centrifugal barrier to support the resonance state, the process of low-energy attachment can be viewed as a direct nonadiabatic capture (Crawford and Koch, 1974; Gauyacq, 1982). Attachment to $SF_6$ was discussed in terms of nonadiabatic coupling by Gauyacq and Herzenberg (1984): the low-energy electron can give up its energy to become bound if the crossing of the negative-ion curve with the neutral curve occurs close to the equilibrium internuclear separation. However, there should be a mechanism that is preventing the electron from escaping into the continuum. In the case of $SF_6$ this occurs due to a fast intramolecular vibrational redistribution (IVR) of the available energy over many vibrational modes, before the nuclear framework can oscillate back to its initial configuration (Gauyacq and Herzenberg, 1984).

The $SF_6^-$ anion becomes metastable, and this explains the nondissociative feature of low-energy attachment to $SF_6$ (see also Thoss and Domcke, 1998). Since the capture in this case is nonresonant, the VW model becomes appropriate. Of course a $-\alpha/(2r^4)$ singularity, which plays an essential role in the VW model, is unphysical. However, for sufficiently high $\alpha$ it describes quite well the probability to find the electron within the molecule where the direct energy exchange is likely to occur.

The metastability of the $SF_6^-$ anion has been the subject of many studies aiming to determine its lifetime (see Christophorou and Olthoff, 2000, Suess et al., 2002, and references therein). This lifetime is expected to depend on the internal energy (i.e. vibrational energy) of the anion and on the energy $E$ of the electron attached in the primary capture process. Using a permanent magnet Penning trap, Suess et al. (2002) measured the lifetime of $SF_6^-$ ions, produced by electron transfer from $K^{**}(30p)$ and $K^{**}(60p)$ Rydberg atoms to a beam of thermal (300 K) $SF_6$ molecules. In both cases, they obtained a lifetime of about 10 ms. Previously reported lifetimes for $SF_6^-$ ions formed by free thermal electron capture depend strongly on the experimental technique used. Experiments using time-of-flight methods typically yield values of a few tens of microseconds, whereas ion-cyclotron-resonance methods suggest lifetimes of a millisecond or longer (Christophorou and Olthoff, 2000). In part, these differences might be explained by differences in the $SF_6$ gas temperature and the energy of the attached electrons, leading to $SF_6^-$ ions in a variety of states that auto-detach at different rates. A recent time-of-flight measurement, using a jet-cooled $SF_6$ target and a laser photoelectron source (LeGarrec et al., 2001), yielded a lifetime of about 19 μs that was independent of electron energy in the range 0.4–120 meV. This value is difficult to reconcile with the much longer lifetimes of Dunning's group (Suess et al., 2002) and with the results of our laser photoelectron attachment experiments in which the $SF_6^-$ ions, formed by electron capture in the energy range 0–200 meV, are detected 100–200 μs after their generation at intensities which indicate that losses due to autodetachment during this time interval must be small at $T = 300$ K.

At elevated temperatures, autodetachment and especially dissociation of the primary $SF_6^-$ anion into the products $SF_5^- + F$ are known to occur (Chen and Chantry, 1979). High-resolution data on the temperature dependence of the cross-sections for $SF_6^-$ and $SF_5^-$ formation have recently become available (Barsotti et al., 2003a). With the anion detected about 100 μs after their production, it was found that the general shape for the $SF_6^-$ cross-section varied little with a tendency that the decrease towards higher energies became somewhat steeper with rising temperature. This effect can be attributed to both autodetachment and dissociation towards $SF_5^- + F$. For sub-thermal temperatures (due to cooling in a supersonic expansion at

higher stagnation pressures) cusp structure at vibrational onsets was found to become clearer. The latter finding is in agreement with recent photo-electron attachment experiments of Chutjian's group (Howe *et al.*, 2001) in which a pulsed, seeded supersonic beam of 10% $SF_6$ in Xenon was used; it is expected that a considerable amount of vibrational cooling occurs in such an expansion. Howe *et al.* (2001) found clear cusp structure around the vibrational onsets $\nu_6$, $\nu_1$, and $\nu_3$ and a decrease of the cross-section which was characterized by a parameter $\beta$ (see Eq. (40)) smaller than the one obtained by Klar *et al.* (1992b) at $T_G = 300$ K.

For the $CCl_4$ molecule, attachment of electrons with very low energies leads to a $CCl_4^{-*}$ complex with a lifetime of 7.5(25) ps (Popple *et al.*, 1996) which dissociates to the observed anion products $Cl^-$ and $CCl_3$; only a small fraction of the available excess energy (about 0.6 eV) appears as translational energy (Popple *et al.*, 1996). In the LPA study of DA to $CCl_4$ (Hotop *et al.*, 1995; Klar *et al.*, 2001a; normalization of LPA cross-section to thermal rate coefficient of Orient *et al.*, 1989) the experimental energy resolution was about 0.8 meV, as limited by residual electric fields of about 0.5 V/m (Klar *et al.*, 2001a). Correspondingly, the extrapolation to the VW limit is somewhat less certain than for $SF_6$, but model calculations including the residual field and the cross-section (40) yielded very good agreement between the modelled and the measured attachment yield for $CCl_4$ in the threshold region (Klar *et al.*, 2001a).

In Fig. 32 we compare the recommended experimental DA cross-section for $CCl_4$ (consisting of the LPA cross-section at energies below 173 meV and electron beam data due to Chu and Burrow (1990) at higher energies, see also Klar *et al.*, 2001a) with the VW s-wave prediction and the LPA fit of Klar *et al.* (2001a). The slope of the experimental curve is steeper than that given by the VW model. This might be indicative – according to the theoretical discussion of the DA cross-section for methyl iodide (Fig. 12) – of a weakly bound negative-ion state. Indeed, as was suggested by Burrow *et al.* (1982) and Gallup *et al.* (2003), the ground state $^2A_1$ of the $CCl_4^-$ anion is bound with a very small binding energy, whereas the first repulsive excited state $^2T_2$ (to which the DA peak at 0.8 eV is attributed) has a vertical attachment energy of 0.94 eV. It is likely that the $^2T_2$ state drives the resonant DA process whereas the $^2A_1$ state enhances this process at low energies.

For comparison with the reactive attachment channel, we have included in Fig. 32 the total scattering cross-section, measured at high resolution by Ziesel *et al.* (2003) over the range 15–200 meV. Below the onset for vibrational excitation of the symmetric stretch mode $\nu_1 = 1$ (where the DA cross-section exhibits a clear downward cusp) the total cross-section is nearly parallel to the DA cross-section (which is close to the unitary limit $\pi/k^2$) at
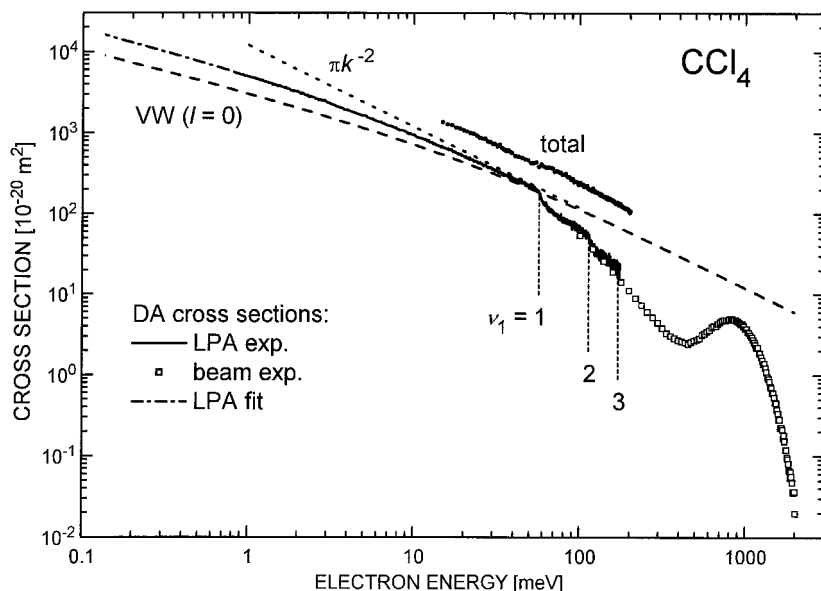
Fig. 32. Absolute cross-section for dissociative electron attachment to $CCl_4$ molecules ($Cl^-$ formation, from Klar *et al.*, 2001a), as compared to the Vogt-Wannier s-wave capture cross-section $VW(l=0)$, the limiting s-wave reaction cross section $\pi/k^2$ and the LPA fit according to Eq. (40). For comparison the total scattering cross section (full circles, Ziesel *et al.*, 2003) is included.

essentially twice the size. Apparently the very low energy region where the ratio between the total cross-section and the attachment cross-section becomes a linear function of wave vector $k$ has not been reached yet. Using the DA cross-section of Klar *et al.* (2001a) in conjunction with their total and backward scattering cross-sections (the latter measured down to 8 meV), Ziesel *et al.* (2003) derived phase shifts for s-wave and p-wave scattering over the energy range 8–55 meV. Below 25 meV, the s-wave phase shift varies rather little and takes values around 0.65 rad. In order to reach the expected limit of 0 or $\pi$ rad (in the absence or presence of a bound state compatible with s-wave symmetry) the s-wave phase shift has to change dramatically from 8 meV down to 0 meV; this is in sharp contrast to the weak variation in the range 8–25 meV.

In Fig. 33a we present the energy-dependent rate coefficient $k_e(E)$ for free electron attachment to $CCl_4$ over the range (0.8–173) meV (Hotop *et al.*, 1995; Klar *et al.*, 2001a). The limiting LPA value $12.3(19) \times 10^{-7} \text{ cm}^3 \text{ s}^{-1}$ (full circle, Klar *et al.*, 2001a) is in good agreement with the most recent
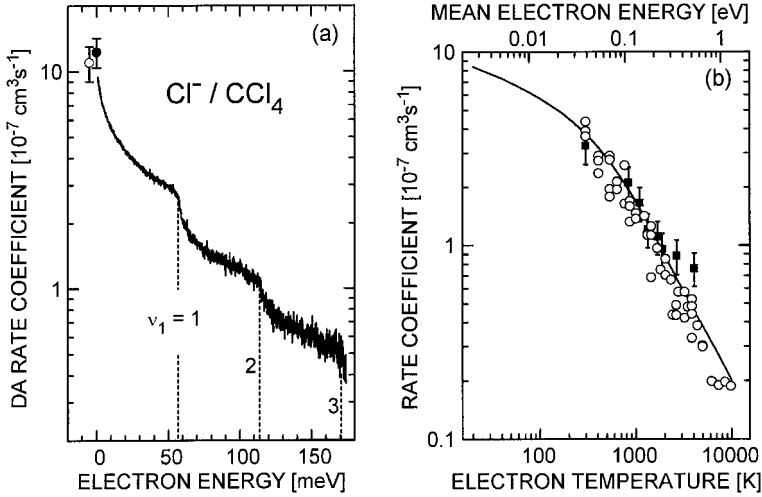
FIG. 33. Dissociative electron attachment to $CCl_4$ molecules: (a) energy dependence of DA rate coefficient $k_e(E)$; (b) thermal rate coefficient $k_e(T_e)$ for a Maxwellian electron energy distribution and fixed gas temperature $T_G = 300\,K$ (from Klar *et al.*, 2001a). For details see text.

rate coefficient $k_{nl} \approx 11(2) \times 10^{-7}\,cm^3\,s^{-1}$ (open circle, Dunning, 1995; Frey *et al.*, 1995) for RET in $K^{**}(np) + CCl_4$ collisions at high principal quantum numbers ($n \geq 70$); they are both distinctly higher than the VW capture rate coefficient $k_c(E \to 0) = 6.74 \times 10^{-7}\,cm^3\,s^{-1}$, possibly due to the influence of the bound $^2A_1$ anion state (see above). As compared to their appearance in the DA cross-section (Fig. 32), the downward steps at the onsets for excitation of one ($\nu_1 = 1$), two ($\nu_1 = 2$), and three quanta ($\nu_1 = 3$) of the symmetric stretch vibration show up more clearly in the plot of the DA rate coefficient $k_e(E)$. The vertical dashed lines at the three vibrational onsets label the respective vibrational energy positions determined by Raman spectroscopy. So far, no theoretical calculations for DA involving $CCl_4$ are available to our knowledge.

Using the combined DA cross-section shown in Fig. 32, Klar *et al.* (2001a) calculated thermal DA rate coefficients $k_e(T_e)$ for fixed gas temperature $T_G = 300\,K$ as a function of electron temperature $T_e$. In Fig. 33b the obtained results (full line) are compared with two sets of swarm data, obtained by Shimamori *et al.* (1992b) with a microwave cavity pulse radiolysis − microwave heating (MWPR−MH) method (open circles) and by Španel *et al.* (1995) with a flowing afterglow/Langmuir probe (FALP) apparatus involving an electron swarm with a variable temperature (full squares). We note that the respective rate coefficients at

$T = T_e = T_G = 300$ K agree within their mutual experimental uncertainties (see Klar *et al.*, 2001a). Good overall agreement with regard to the dependence on electron temperature is observed between the calculated results and the swarm data although it appears – as discussed by Klar *et al.* (2001a) – that the drop in the rate coefficients towards higher temperatures is somewhat slower in the FALP data than in both the LPA derived and in the MWPR−MH results. We emphasize that it is important that the beam data include results obtained with very high resolution in order to avoid uncertainties associated with the true behavior of the attachment cross-section at the lowest energies. For $CCl_4$, about 60% of the total thermal rate coefficient $k_e(T_e = T_G = T = 300$ K) stem from electrons with energies $E \leq k_B T$ (Klar *et al.*, 2001a).

### B.4. Electron Attachment to $C_{60}$

The fullerene molecule $C_{60}$ has astounding electron attachment properties; long-lived $C_{60}^-$ anions are formed from near zero to above 10 eV electron energy (Lezius *et al.*, 1993). Here we dwell on the threshold behavior of the cross-section which has been a subject of some controversy. Flowing afterglow/Langmuir probe (FALP) measurements (Smith *et al.*, 1993; Smith and Španel, 1996) indicated that electron capture by $C_{60}$ is characterized by an activation barrier of 0.26 eV. This was interpreted as a p-wave process by Tosatti and Manini (1994) who showed that an s state of the $C_{60}^-$ anion is prohibited by symmetry. Their calculations of the capture rates, based on a finite potential well model, are in good agreement with the FALP measurements (Smith *et al.*, 1993; Smith and Španel, 1996), both in terms of the absolute magnitude and the slope of the rate dependence on the inverse electron temperature which gives the magnitude of the activation barrier.

However, as noted previously by Huang *et al.* (1995), the model used by Tosatti and Manini (1994) and later by Matejcik *et al.* (1995), does not seem to represent the physics of the process correctly. First, it ignores the polarizability of $C_{60}$ which is very large (558 a.u.). Furthermore, it regards the capture cross-section as being identical to the elastic cross-section which is physically incorrect. The simplest way to see this is by looking at the threshold behavior: whereas the p-wave capture cross-section behaves as $E^{1/2}$ at low energies, the elastic p-wave scattering cross-section is proportional to $E^2$. The extra factor $E^{3/2}$ in the elastic cross-section appears because the electron has to tunnel through the centrifugal barrier a second time when leaving the interaction zone. Therefore the good agreement between the FALP experiments and the calculations of Tosatti and Manini (1994) seems to be fortuitous.

Several beam measurements (Jaffke *et al.*, 1994; Huang *et al.*, 1995; Matejcik *et al.*, 1995) also claim the existence of an activation barrier with a height of 0.24 (Jaffke *et al.*, 1994) or 0.15 eV (Huang *et al.*, 1995). The measurements of Jaffke *et al.* (1994) were reinterpreted by Weber *et al.* (1996) who concluded that they can only be understood if an s-wave contribution or a resonance close to zero energy are present. Note that the deconvoluted results of Jaffke *et al.* (1994) were incorrectly shifted on the energy scale by 0.4 eV (see appendix in Weber *et al.*, 1996), thereby suggesting a barrier; this, however, was an artifact of the deconvolution procedure of Jaffke *et al.* (1994). The presence of the 0.15(5) eV threshold in the experiment of Huang *et al.* (1995) is not yet understood; in Fig. 7 of Huang *et al.* (1995) the low-energy peak for $C_{60}^-$ formation is found to be shifted by about +80 meV relative to the peak for $SF_6^-$ formation.

The absence of an activation barrier is indicated by experiments on Rydberg electron attachment to $C_{60}$ (Finch *et al.*, 1995; Huang *et al.*, 1995; Weber *et al.*, 1996). They exhibit a flat dependence of the attachment rate on the principal quantum number $n$ of the Rydberg electron at high $n$, indicating an s-wave attachment process. In addition, more recent beam experiments (Elhamidi *et al.*, 1997; Vasil'ev *et al.*, 1997; Kasperovich *et al.*, 2001) with free electrons have found evidence for a zero-energy attachment process (within about 0.03 eV). Several mechanisms for s-wave attachment involving formation of weakly bound (Weber *et al.*, 1996) or virtual (Lucchese *et al.*, 1999) states of $C_{60}^-$, supported by the long-range polarization interaction, have been discussed.

Here we compare the obtained experimental information with the results of the application of the VW model. In Fig. 10 we presented the $l=0$ through $l=4$ contributions to the cross-sections for a capture by a target with the polarizability 558 a.u., as appropriate for $C_{60}$ (Bonin and Kresin, 1997). We see that the $E^{1/2}$ behavior for the p wave occurs within a very narrow energy range: the p-wave cross-section peaks at $E = 26$ meV. This means that the near-zero energy peaks in the $C_{60}^-$ yield, observed in electron beam experiments by several groups, could – at least in part – reflect such a p-wave contribution.

Recent *ab initio* theoretical calculations (Gianturco *et al.*, 1999; Lucchese *et al.*, 1999) of elastic e-$C_{60}$ scattering suggest that in the low-energy region this process is dominated by a virtual state in the $a_g$ symmetry, whose lowest partial wave component is $l=0$, and a resonance state in the $t_{1u}$ symmetry whose lowest partial-wave component is $l=1$. Therefore one may assume that the attachment process at low energies is controlled by a combination of direct capture mediated by a virtual state (similar to low-energy attachment to $SF_6$) and resonance capture into the $t_{1u}$ state. In model calculations of the threshold behaviour for $C_{60}^-$ formation in RET and free

electron attachment to $C_{60}$, Fabrikant and Hotop (2001) correspondingly described the capture cross-section by combining the s-wave and the p-wave VW cross-sections, $\sigma_0$ and $\sigma_1$:

$$\sigma(E) = c(\varepsilon\sigma_0 + \sigma_1) \tag{41}$$

where $c$ and $\varepsilon$ are adjustable parameters: $\varepsilon$ characterizes the relative contribution of the s-wave and $c$ the absolute value of the cross-section which was estimated from experimental RET attachment rate coefficients (Finch *et al.*, 1995; Huang *et al.*, 1995; Weber *et al.*, 1996). A combined fit to these *n*-dependent RET data and to the free electron data of Elhamidi *et al.* (1997) yielded $c = 0.1$ and $\varepsilon = 0.1$–0.2 (Fabrikant and Hotop, 2001). The s-wave zero energy peak dominates the cross-section only at very low energies (below 3 meV). High-resolution free electron attachment experiments are necessary to confirm this prediction.

Note that only 1–2% ($c\varepsilon = 0.01$ or 0.02) of the s-wave VW cross-section appears to contribute to the capture process, in contrast with attachment to $SF_6$. Apparently the stabilization mechanism discussed for $SF_6$ is not as efficient for $C_{60}$. The 1–2% fraction can be considered as an efficiency for conversion of the $C_{60}^-$ virtual state into a bound state, something similar to the survival probability in the resonance attachment. It has to be mentioned that the temperature dependence of the attachment rate coefficient observed in the FALP experiments (Smith *et al.*, 1993; Smith and Španel, 1996) was found to be not in accord with the combined s- and p-wave model. Possibly, the electron energy distribution in the temperature-variable FALP apparatus are not completely thermalized and short of low-energy electrons. Another possibility is a significant dependence of the negative ion yield on the rovibrational temperature of $C_{60}$ (Fabrikant and Hotop, 2001). At higher temperatures many nontotally symmetric vibrations are excited, and s-wave attachment might play a more substantial role (Vasil'ev *et al.*, 2001).

## B.5. Electron Scattering from $CO_2$, $CS_2$, and $N_2O$

### 5.a. Carbon Dioxide

Carbon dioxide is linear in its electronic ground state. The lowest vibrationally excited states, labelled as $(v_1v_2v_3)$, include the bending mode (010) (82.7 meV), the Fermi-coupled pair of the bending overtone and the symmetric stretch mode (020)/(100) (159.4/172.1 meV, average energy 165.7 meV), the Fermi-coupled pair (030)/(110) (239.6/257.5 meV; average energy 248.3 meV), the asymmetric stretch mode (001) (291.3 meV), and the Fermi-coupled triplet (040)/(120)/(200) (317/342/348 meV, average energy

336 meV) (Herzberg, 1945). $CO_2^-$ has long been known to have a bent equilibrium configuration, generally made responsible for the mass spectrometric observation of metastable $CO_2^-$ anions. In recent *ab initio* work, Gutsev *et al.* (1998) obtained a bond angle of 137.8°, an electric dipole moment of $-0.90$ D and a negative adiabatic electron affinity of $EA_{ad}(CO_2) = -0.66$ eV for this state of the anion.

Vibrational excitation in $CO_2$ has two distinct energy ranges. The first is around the $^2\Pi_u$ shape resonance at 3.6 eV, where boomerang structures have long been known (Boness and Schulz, 1974). The second is dominated by a virtual state below 2 eV (Morrison, 1982; Herzenberg, 1984; Estrada and Domcke, 1985; Kochem *et al.*, 1985; Morgan, 1998; Rescigno *et al.*, 1999; Mazevet *et al.*, 2001; Field *et al.*, 2001b). The virtual state causes dramatic enhancement of the cross-section near threshold for the excitation of the symmetric stretch vibration (100), Fermi-coupled with two quanta of the bending vibration $(02^00)$ (Kochem *et al.*, 1985; Field *et al.*, 1991b; Allan, 2001a). The cross-sections for the excitation of the infrared active fundamental vibrations, (010) and (001), also exhibit threshold peaks, but these can be ascribed, at least to a large degree, to direct dipole scattering (Kochem *et al.*, 1985). Pronounced selectivity was observed in the excitation of the Fermi-coupled vibrations $\{(10^00), (02^00)\}$ in the virtual state range (Antoni *et al.*, 1986; Allan, 2001a). Selectivity in the excitation of the Fermi-coupled vibrations was also observed in the shape resonance region (Johnstone *et al.*, 1995; Kitajima *et al.*, 2000; Allan, 2001a), but this energy range does not fall into the scope of the present review.

In contrast to the halogen hydrides the elastic cross-section and the cross-sections for the excitation of the *fundamental* vibrations do not exhibit structures of vibrational origin (Kochem *et al.*, 1985; Field *et al.*, 1991b). This corresponds to the expectation, reflecting the fact that the cross-section enhancement at threshold is due to a virtual state, which is not associated with a time delay (Herzenberg, 1984), and consequently cannot support vibrational structure. Tennysson and Morgan (1999) predicted, however, on theoretical grounds, that the virtual state becomes bound in the electronic sense upon sufficiently strong bending of the $CO_2$.

This idea has received strong support from the experimental observation of vibrational Feshbach resonances and boomerang oscillations in the excitation of certain higher-lying Fermi-coupled vibrations involving symmetric stretch and bending by Allan (2002a), as shown in Fig. 34. Allan (2002a) discussed two possible explanations of these structures. The first, considered less probable, is that these structures are due to metastable vibrational levels around the minimum of the valence ground state of $CO_2^-$ at a bend geometry, that is that they correspond to the outer well resonances discussed in this review already in connection with HCl. The second
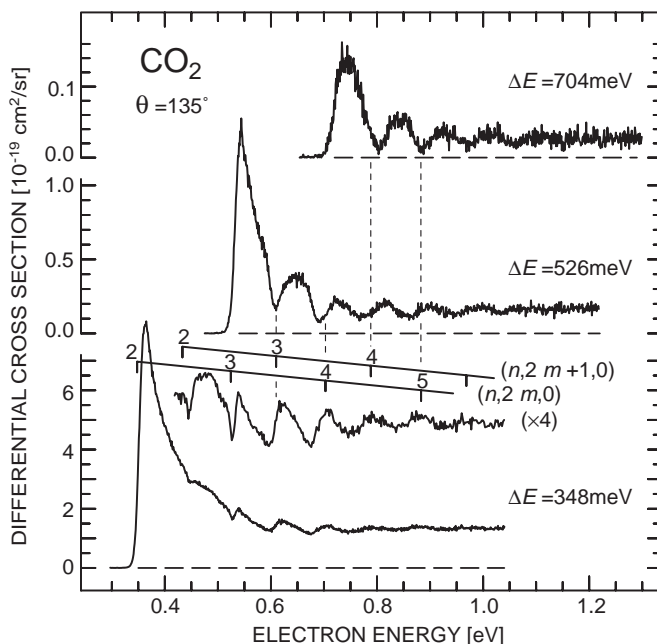
FIG. 34. Cross-sections for exciting vibrational overtones in $CO_2$, specifically the highest-energy components of the Fermi polyads $\{(n, 2m^0, 0)\}$ where $n$ and $m$ are zero or positive integers such that (from bottom to top) $n + m = 2$, 3, and 4. (i.e., $\{(n, 2m^0, 0)\}$, $n + m = 3$, stands for four Fermi-coupled states resulting from Fermi-mixing of the first order states $(3, 0^0, 0)$, $(2, 2^0, 0)$, $(1, 4^0, 0)$, $(0, 6^0, 0)$.) The grids above the bottom spectrum show the thresholds for exciting the highest-energy components of the polayds $\{(n, 2m^0, 0)\}$ and $\{(n, 2m+1^1, 0)\}$, with the sums $n + m$ given (from Allan, 2002a).

explanation, considered more probable, is that the structures are due to 'inner well' vibrational Feshbach resonances and boomerang oscillations supported by a potential surface of the $CO_2^-$ where an electron is weakly electronically bound by dipole and polarization force in the bent and stretched geometry. The wave function of the electron is spatially very diffuse. This 'diffuse' state of $CO_2^-$ becomes the (unbound) virtual state at the linear geometry.

   The latter explanation has received strong support from the $CO_2^-$ potential surface calculated by Sommerfeld (2003). His elaborate calculation succeeded in reproducing both the valence and the diffuse states of $CO_2^-$ within the same model. The cut through the adiabatic surface along the bending coordinate, shown in Fig. 35, shows that the valence ground state of $CO_2^-$, which has a shallow minimum at bent geometries, rapidly acquires
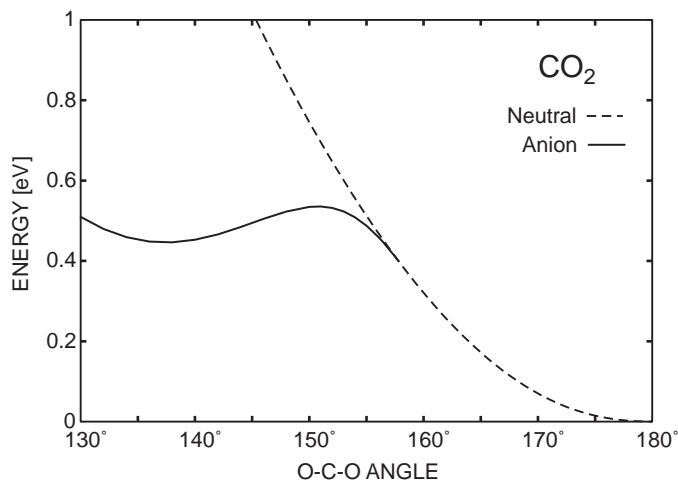
FIG. 35. Adiabatic potential curves for $CO_2$ (dashed) and $CO_2^-$ (solid line). The electronic wave function of $CO_2^-$ is valence-like for O–C–O angles below about $150°$, where it forms the outer well. It sharply bends down and becomes diffuse between about 150 and $160°$. It disappears (becomes a resonance and finally a virtual state) at angles above about $160°$ (Sommerfeld, 2003).

diffuse character and turns sharply down as the $CO_2$ framework is straightened towards the linear geometry. Below a certain bending angle the anion and neutral surfaces cross and the anionic surface disappears in the adiabatic sense. The situation is closely related to that discussed in Section II in connection with Fig. 6. Qualitatively, the oscillations of the nuclear wave packet on the 'inner well' of the $CO_2^-$ potential surface can be pictured in the same way as already discussed for $HF^-$. Around the linear geometry the $CO_2^-$ starts to loose the extra electron since it is no longer bound in the adiabatic sense. The electron departs only slowly, however, since we are near threshold. Part of the electron wave function is recaptured when the nuclei swing over to bent geometry again, giving rise to VFRs of varying width. The similarity between the HF and $CO_2$ cases is born out by the striking phenomenological similarity of the HF and $CO_2$ spectra (Figs. 18 and 34).

It is interesting to compare the present structures to those reported by Leber *et al.* (2000b) in dissociative electron attachment to $CO_2$ clusters (see also Section IV.C). They observed structures below the (010) and the $\{(1,0^00), (02^00)\}$ thresholds, with the difference that a structure was observed for each member of the latter Fermi dyad in their spectra, whereas in the present study a structure is observed only for the topmost members of the Fermi polyads.

## 5.b. Carbon Disulfide

$CS_2$ is isovalent with $CO_2$. Like $CO_2$ it does not have a permanent dipole moment, and it possesses – like $CO_2$ ($Q = -3.1$ a.u.) – a sizeable permanent quadrupole moment ($Q(CS_2) = +3.3$ a.u.) (Compton and Hammer, 2001). It differs from $CO_2$ in several important aspects, however. It is much more polarizable than $CO_2$ (average polarizability $59.4\,a_0^3$ for $CS_2$ and $19.4\,a_0^3$ for $CO_2$, Lide, 1995) and has a positive adiabatic electron affinity associated with the bent valence ground electronic state of $CS_2^-$ (Gutsev *et al.*, 1998), see also Section IV.C.5.

Sohn *et al.* (1987) measured absolute differential cross-sections in $CS_2$ at a number of discrete energies between 0.3 and 5 eV. Allan (2001c) reported deep narrow structures in the elastic and vibrationally inelastic cross-sections in a crossed-beam study. Jones *et al.* (2002) found deep structures in their very low-energy and very high-resolution measurements of the total integral and backward cross-sections using a synchrotron radiation photoelectron source. Jones *et al.* interpreted them in terms of giant resonances and symmetry selection rules. The total and the differential cross-sections (the latter multiplied by $4\pi$ to obtain an estimate of the integral cross-section) are compared in Fig. 36. There is a striking agreement of the shapes of the resonant structures. The 30% difference of the magnitudes could be in part of instrumental origin, in part due to an anisotropy of the differential cross-section. Figure 37 shows the crossed-beam
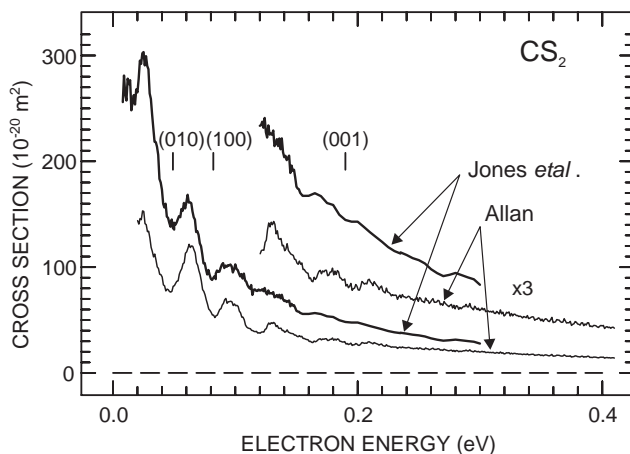


FIG. 36. Comparison of the total cross-section of Jones *et al.* (2002) with the $\theta = 135°$ differential elastic cross-section of Allan (2003). The latter was multiplied by $4\pi$ to obtain an estimate of the integral cross-section.
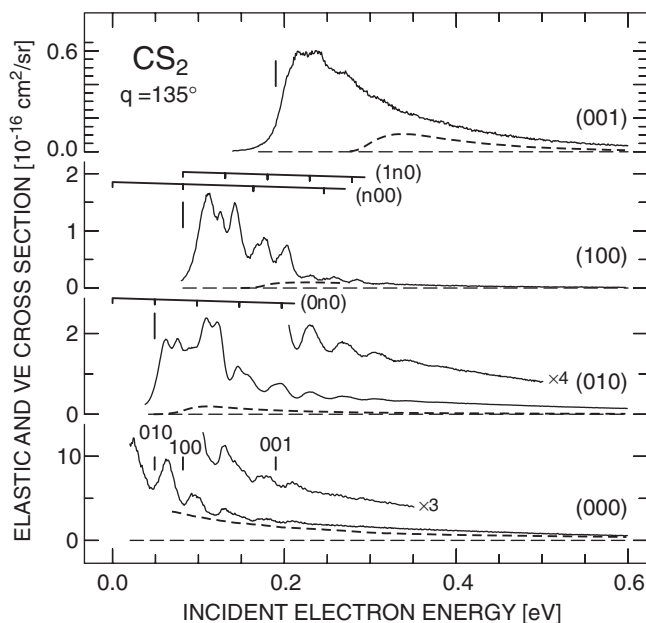
FIG. 37. Differential elastic and vibrationally inelastic cross-sections in $CS_2$ (Allan, 2003). $CO_2$ cross-sections (Allan, 2001a and 2002a, b) are shown for comparison as dashed curves. Vibrational thresholds are indicated by vertical bars above the elastic and to the left of the inelastic cross sections. Grids indicate selected progressions of vibrational energies of neutral $CS_2$.

results of Allan (2001c, 2003) for the elastic cross-section and the excitation of the fundamental vibrations. It shows that near-threshold the elastic, and to an even more dramatic degree the inelastic cross-sections, are larger in $CS_2$ than in $CO_2$. In addition, the elastic and the (010) and (100) cross-sections have deep narrow structures, also in contrast to $CO_2$, where the threshold peaks in the cross-sections for the *fundamental* vibrations are structureless and only certain overtone cross-sections exhibit structure (Fig. 34). The structure in the (001) cross-section is much less pronounced – like in $CO_2$.

The structures in the cross-sections are undoubtedly caused by vibrational activity in the negative ion. In contrast to $CO_2^-$, it is much harder to assign this activity to a certain electronic state of the anion. The vertical electronic affinity, corresponding to the lowest valence state $^2\Pi_u$ of $CS_2^-$ in its linear geometry, is around 0 eV (Gutsev *et al.*, 1998). This state splits into the $^2A_1$ and $^2B_2$ branches upon bending. The minimum of the lower branch corresponds to the adiabatic electron affinity, the experimental and

theoretical results for which range between about $+0.3$ and $+0.9\,\mathrm{eV}$ (Gutsev *et al.*, 1998). This means that the vibrational levels on both branches of the $^2\Pi_u$ state of $CS_2^-$ lie in the same energy range as the structures in the cross-sections and could be responsible for them, apart from the 'diffuse' state which has been invoked to explain the structure in $CO_2$.

The vibrational grids in Fig. 37 indicate that the structures do not, in contrast to $CO_2$, correspond to vibrational thresholds in a consistent manner. It is also impossible to assign the observed structures to vibrational levels of the valence electronic states of $CS_2^-$ in a convincing manner. These vibrations have been calculated at a very high degree of sophistication by Rosmus and Hochlaf (2002). An assignment is impossible, however, because the calculated density of $CS_2^-$ vibrational states is very high in this energy range, two branches of the $^2\Pi_u$ state are present, the vibrational origins of which are not exactly known, and because of further complications due to spin-orbit splitting and the pronounced anharmonicity of the potentials (Rosmus and Hochlaf, 2002).

In addition, $CS_2$ is likely, with its larger polarizability, to exert a higher polarization attraction to an extra electron than $CO_2$. A diffuse electronic state was postulated experimentally and theoretically already in the less polarizable $CO_2$, and it is thus very likely that $CS_2$ also supports a diffuse state, presumably over an even larger range of geometries of the nuclei than $CO_2$. Avoided crossings, similar to those found in $CO_2$ (Fig. 35), are likely to cause a complicated adiabatic potential surfaces of the ground and low-lying excited states of $CS_2^-$. This is probably the reason why the structures in the $CS_2$ cross-sections, unlike $CO_2$ (Fig. 34), cannot be convincingly associated with vibrational thresholds. An exception is the total cross-section, very similar to the elastic cross-section, where the dips (not peaks) could be associated with the thresholds for the fundamental vibrations by Jones *et al.* (2002). The remaining sharp structures, at least in the vibrationally inelastic cross-sections, lack detailed explanation at present.

### 5.c. *Nitrous Oxide*

$N_2O$ is isoelectronic with $CO_2$. Their (average) polarizabilities ($\alpha(N_2O) = 20.4\,a_0{}^3$, Lide, 1995) agree to within 5%. $N_2O$ differs from $CO_2$ in that it has a small permanent dipole moment (0.16 Debye, Lide, 1995) and, more importantly, in the much lower lying threshold for dissociative electron attachment. Cross sections above about $1\,\mathrm{eV}$ have been studied both experimentally and theoretically (see for example Winstead and McKoy, 1998, and the experimental work cited therein). Allan and Skalický (2003) recently measured the cross-sections below $1\,\mathrm{eV}$, in an energy range with which this review is concerned.
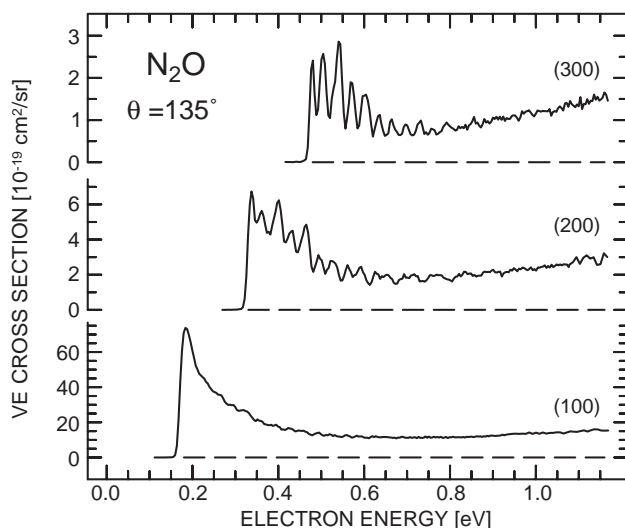
Fɪɢ. 38. Differential cross-sections for exciting the symmetric stretch vibration in $N_2O$ and its overtones (from Allan and Skalický, 2003).

The vibrationally inelastic cross-sections shown in Fig. 38 reveal a close phenomenological similarity with $CO_2$. The cross-section for the excitation of the fundamental vibrations are structureless (or nearly so) in both $N_2O$ and $CO_2$, but structures appear in the excitation of overtones. The structure in $N_2O$ is richer and deeper than in $CO_2$. In analogy with $CO_2$ we assign it to vibrational Feshbach resonances supported by an electronic state of $N_2O^-$ with a spatially diffuse electron wave function.

The low threshold to dissociative electron attachment permits the study of the vibrational Feshbach resonances in the dissociative channel, as shown in Fig. 39. The spectra were recorded with a resolution of about 10 meV in the incident beam, using an electron spectrometer with hemispherical analysers and a Wien filter to separate electrons and ions (Fig. 13). For energetic reasons, the ions can only be $O^-$. The spectrum on the left resembles closely the spectra of Chantry (1969), Brüning *et al.* (1998) and Krishnakumar and Srivastava (1990). The detail of the spectrum on the right reveals that what initially appeared as a continuous band consists in reality of narrow peaks (vibrational Feshbach resonances VFR), whose spacings and positions are related to the bending vibration of $N_2O$. It thus appears that the mechanism of dissociative electron attachment in $N_2O$ is more complex than the simple picture presented in Fig. 2 in the introduction. The VFRs act as ''doorway states'' and then predissociate into
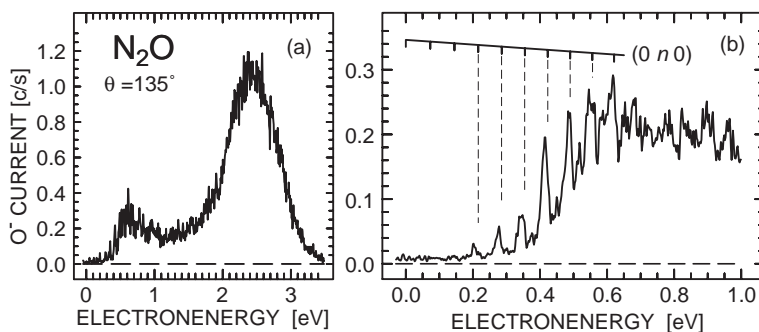
FIG. 39. Dissociative electron attachment spectrum in $N_2O$. A wider energy range is shown at left (a), detail at low energies at right (b) (from Allan and Skalický, 2003).

the dissociative continuum. This mechanism is analogous to that invoked theoretically for $CH_3Cl$ in connection with Fig. 20. Experimentally, it has been invoked previously in the strongly polar molecule ethylene carbonate (Stepanović *et al.*, 1999), although the individual VFRs were not resolved there. Sommerfeld (2002) discussed the role of VFRs as doorway states from the theoretical point of view in nitromethane. $N_2O$ represents a particularly convincing case because the individual VFRs could be resolved.

These results shed new light on the astounding observation of extremely narrow peaks (with widths down to 2.3 meV) in the laser photoelectron attachment spectra of $N_2O$ clusters yielding both heterogeneous $(N_2O)_qO^-$ and homogeneous $(N_2O)_q^-$ cluster anions (Weber *et al.*, 1999a; Leber *et al.*, 2000c). These peaks were found to be located just below the onsets for vibrational modes of the free $N_2O$ molecule (redshifts in the meV range) and interpreted as VFRs. Similar VFRs with substantially larger redshifts were subsequently found in attachment spectra for $CO_2$ cluster anions (Leber *et al.*, 2000b; Barsotti *et al.*, 2002a) as well as for OCS cluster anions. Evidence for VFRs in $O_2$ cluster anion production has been obtained by Matejcik *et al.* (1996, 1999). See Section IV.C for further discussion.

## C. Electron Attachment to Molecular Clusters

In this section we discuss resonance phenomena in low-energy electron attachment to molecular clusters, yielding stable or long-lived anions detected by mass spectrometers. The reaction scheme can be characterized

as follows ($\{\alpha\}$ denotes a set of quantum numbers for the electronic and ro-vibrational states in question):

$$(XY)_N(\alpha) + e^-(E) \rightarrow (XY)_N^{-*} \rightarrow (XY)_N\{\alpha'\} + e^-(E') \tag{42a}$$

$$\rightarrow (XY)_{q-1}Y^- + X + (N-q)XY$$

$$(q \leq N) \tag{42b}$$

$$\rightarrow (XY)_q^- + (N-q)XY \quad (q \leq N1) \tag{42c}$$

$$\rightarrow (XY)_N^{-\ddagger} \quad (\tau > 100\,\mu s) \tag{42d}$$
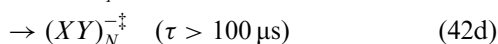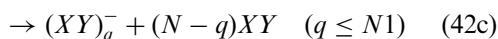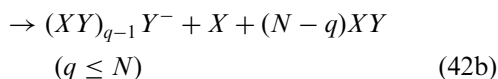
Here path (42a) describes elastic ($\alpha = \alpha'$) or inelastic scattering. Process (42b) represents dissociative electron attachment (DA) while in the reaction (42c) (only relevant for clusters, i.e. $N \geq 2$) anion formation proceeds through evaporation of $XY$ constituents. Even if no other stabilizing process occurs, the temporary negative ion $(XY)_N^{-*}$ ($N \geq 1$) can become metastable with respect to spontaneous re-emission (autodetachment) of the electron, if the electronic energy is rapidly redistributed into internal degrees of freedom (intra- and intermolecular vibration, rotation), thereby yielding long-lived negative ions $(XY)_N^{-\ddagger}$ in path (42d), e.g. $SF_6^{\ddagger}$ from $SF_6$ (see section IV.B) or small $(H_2O)_N^{-\ddagger}$ anions ($N = 2, 6, 7$) (Weber $et\ al.$, 1999b).

Beams of molecular clusters are typically created in supersonic beams (often using molecules as a minority seed gas in a rare gas atom carrier gas). Thus a broad size distribution of molecular clusters is produced. The correlation of the observed anion cluster size $q$ with the size $N$ of the neutral cluster precursor relevant for the reactions (42) is thus not a priori known. Positive cluster ion mass spectra, induced by electron impact at typically 70–100 eV electron energy, help to diagnose the presence of neutral clusters, but normally do not directly reflect the neutral cluster size distribution due to fragmentation effects which may be very strong for weakly bound molecular clusters (Buck, 1988). Comparisons of the mass spectra for positive and negative cluster ions due to electron impact ionization and electron attachment, respectively, are nevertheless useful in that peculiarities of anion formation become visible in a rather direct, albeit qualitative way. Schemes for size selection of neutral cluster beams, based on scattering from atomic beams, have been developed (Buck and Meyer, 1986), but they yield rather low size-selected target densities. To our knowledge, size-selected targets of molecular clusters have not been used in electron attachment work so far.

One of the interesting features of clusters is their role as nanoscale prototypes for studying the effects of solvation on the characteristics of both solvent and solvated particle, due to the interaction between a solvated molecule or ion and its surrounding solvent environment. Solvation effects

also play a key role in the formation of negative ions by attachment of slow electrons to clusters. The investigation of cluster anion formation in collisions of energy-controlled electrons with molecular clusters was pioneered by the Oak Ridge group (Klots and Compton, 1977, 1978) and subsequently studied by groups in Konstanz (Knapp *et al.*, 1985, 1986a, b, 1987), Innsbruck (Märk *et al.*, 1985, 1986; Stamatovic *et al.*, 1985a, b; Märk, 1991; Rauth *et al.*, 1992; Matejcik *et al.*, 1996, 1999), and Berlin (Hashemi *et al.*, 1990, 1991, 1992; Illenberger, 1992, 2000; Jaffke *et al.*, 1992; Ingolfsson *et al.*, 1996); typical electron energy widths ranged from 0.1 to 1 eV. It was shown that the repulsive negative ion resonances which dominate anion formation for the monomer molecules via dissociative attachment at energies in the range 1–10 eV are also important for cluster anion formation. In clusters, the resonances appear shifted towards lower energies due to the effects of solvation. For molecular clusters $(XY)_N$ additional features may be observed which reflect the effects of the cluster environment on the resonance energy and symmetry (Compton, 1980; Märk, 1991; Ingolfsson *et al.*, 1996). One aspect is the appearance of anion resonances in clusters whose formation is symmetry-forbidden for the isolated molecule (Märk, 1991; Illenberger, 1992). Another intriguing result in cluster anion formation is the observation of a prominent resonance at zero energy (indicative of an s-wave attachment process) in cases where such a feature is absent in the monomer (Märk *et al.*, 1985; Stamatović, 1988; Märk, 1991). The first observations of these 'zero energy resonances' for clusters of oxygen (Märk *et al.*, 1985), carbon dioxide (Stamatovic *et al.*, 1985a, b; Knapp *et al.*, 1985, 1986a) and water (Knapp *et al.*, 1986b, 1987) were made by groups at Innsbruck and Konstanz at too broad energy widths (0.5–1.0 eV), as to elucidate possible structure (e.g. due to vibrational effects) and to thoroughly understand the origin of these zero energy peaks.

Anion formation in collisions of molecular clusters with near-zero energy electrons can also be studied by Rydberg electron transfer (RET), as initiated by Kondow *et al.* (Kondow 1987), who used electron impact to produce $Kr^{**}(n)$ Rydberg atoms with a band of principal quantum numbers $n$ around 25. RET to molecular clusters with state-selected Rydberg atoms was pioneered by groups at Kaiserslautern (Kraft *et al.*, 1989) and Villetaneuse (Desfrançois *et al.*, 1989). Interesting structure was observed in the size dependence of several RET-induced anion cluster mass spectra such as those for $(CO_2)_q^-$ (Kondow, 1987; Kraft *et al.*, 1989) and $(N_2O)_qO^-$ formation (Kraft *et al.*, 1990), but the origin remained unclear. Rather sharp peaks in the *n*-dependence of the RET yield for anion formation involving strongly dipolar molecules and clusters were observed by the Villetaneuse group (Desfrançois *et al.*, 1994a, b, c) and interpreted as being due to a rather *n*-selective curve-crossing mechanism. In combination with studies of

field detachment, valuable information on binding energies of electrons, weakly bound to molecules and clusters by long-range forces, was derived (Desfrançois *et al.*, 1996, Compton and Hammer, 2001).

In the following subsections we shall discuss free electron attachment to homogeneous molecular clusters in the range of the 'zero energy resonance', carried out with sufficiently high resolution to resolve vibrational structure. To put the results for clusters into a proper perspective we include brief discussions of the characteristics for electron scattering from the respective monomer molecule. Although not covered in detail here, we mention that in mixed clusters (i.e. either molecule–atom or molecule–molecule clusters) interesting features in the energy dependence for anion formation have been observed which occur close to thresholds for sufficiently strong inelastic processes in one of the constituents (Illenberger, 1992; Rauth *et al.*, 1992). The underlying process is addressed as 'autoscavenging' (Rauth *et al.*, 1992): as a result of the inelastic event the scattered electron propagates as a near-zero energy electron which may be efficiently captured within the cluster if the other constituent has a prominent zero energy resonance. Autoscavenging can also occur in homogeneous clusters if the constituents exhibit both a prominent zero energy resonance and a strong inelastic channel at higher energies. It was discovered by Klots and Compton (1980) for the case of methyl iodide clusters and addressed as 'self-scavenging'. Both autoscavenging and self-scavenging should not be confused with true resonances (such as vibrational Feshbach resonances) of the electron-cluster system.

### C.1. Oxygen Clusters

Electron scattering from oxygen molecules at energies below 1 eV is strongly influenced by the well-known $O_2^-(^2\Pi_g)$ resonance (Schulz, 1973b; Allan, 1995). Addition of a $\pi_g$ electron to the oxygen molecule yields a stable negative ion with an adiabatic binding energy of 0.451(7) eV (Travers *et al.*, 1989) and an equilibrium distance about 12% longer than that of neutral $O_2$. The four lowest vibrational levels $v' = 0$–3 of the $O_2^-(^2\Pi_g, v')$ anion are truly bound with a vibrational quantum of $\Delta G_{01} = 134.4(8)$ meV (Bailey *et al.*, 1996). The center-of-gravity of the fine-structure split $v' = 4$ anion state is located 0.09 eV above the neutral ground state of $O_2(X, v'' = 0)$ (Land and Raith, 1974), and the states with $v' \geq 4$ are thus subject to autodetachment with decay widths $\Gamma_{v'}(E)$, rising strongly ($\propto E^{5/2}$) with electron energy $E$, as characteristic for a $d\pi_g$-wave shape resonance for the electron-$O_2$ system; for $v' = 6$, the width is about 1 meV (Field *et al.*, 1988; Allan, 1995; Higgins *et al.*, 1995). Correspondingly, the formation of

long-lived oxygen anions in electron collisions at sub-eV energies requires rapid collisional stabilization of the temporary $O_2^-$ anion, as possible in high-pressure media (Bloch and Bradbury, 1935; Christophorou, 1978; Hatano and Shimamori, 1981) or for oxygen bound in aggregates (homogeneous or heterogeneous clusters) (Märk, 1991; Illenberger, 1992; Hatano, 1997). The built-in stabilization capability of clusters was, e.g., demonstrated in a recent RET study involving oxygen monomers and dimers (Kreil *et al.*, 1998): while $O_2^-$ formation from $O_2$ molecules is very inefficient (and only possible through efficient postattachment interactions with the Rydberg ion core) (Walter *et al.*, 1986; Harth *et al.*, 1989) the rate coefficient for $O_2^-$ formation from oxygen dimers was found to exceed that involving monomers by four orders of magnitude (Kreil *et al.*, 1998).

In free electron attachment to oxygen clusters at low energies, only homogeneous $(O_2)_q^-$ anions ($q \geq 1$) can be formed. In the yield for anions with $q = 1, 2, 10$, measured with about 0.5 eV electron energy width, Märk *et al.* (1985) found a prominent peak near zero eV; for large $q$, the width of this peak was narrower than for $q = 1$ and 2. Later, Illenberger and coworkers studied $(O_2)_q^-$ ($q = 1$–4) anion formation from oxygen clusters with an energy-selected electron beam of about 0.2 eV width (Hashemi *et al.*, 1991, 1992; Jaffke *et al.*, 1992); they detected the maximum respective anion yield at energies clearly above zero energy. More recently, the Innsbruck group (Matejcik *et al.*, 1996, 1999) had a closer look at anion formation from oxygen clusters, using an energy-selected, magnetically–collimated electron beam with a stated energy width around 0.03 eV. They reported the yield for small cluster anions $(O_2)_q^-$ ($q = 1, 2, 3$) over the energy range 0–1 eV. Apart from a resolution-limited peak near-zero energy they detected peak structure starting at about 80 meV with spacings around 110 meV and superimposed on the general drop of the attachment yield towards higher energies. This structure was ascribed to vibrational levels of the oxygen anion solvated in oxygen molecules (Matejcik *et al.*, 1999).

In contrast to the findings of the Innsbruck group for $(O_2)_q^-$ formation ($q = 1$–3), no clear peak structure is observed in the attachment spectra for $(O_2)_q^-$ formation with $q = 5$–14 (Fig. 40), measured by the Kaiserslautern group with the LPA method at energy widths around 2 meV (Barsotti *et al.*, 2002a). In view of the much improved resolution of the LPA experiment, at least the peak structure, located near 80 meV in the Innsbruck data, should be present in the LPA data. Reasons for the different observations may possibly be found in the scenario, by which $(O_2)_q^-$ anions ($q = 1$–3) are formed. According to Matejcik *et al.* (1999) the attachment process proceeds in such a way that the incoming electron is primarily trapped at one oxygen molecule in neutral clusters with sizes dominated by the range $N = 10$–20. Subsequent substantial evaporation then yields the observed
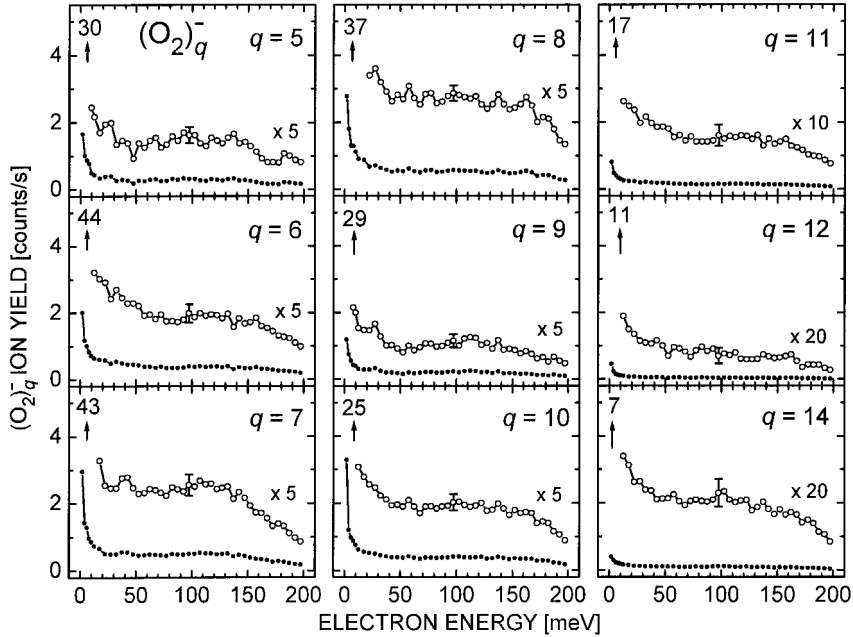
FIG. 40. Low-energy electron attachment spectra for formation of oxygen cluster anions $(O_2)_q^-$, measured with about 2 meV resolution. The numbers above the arrows near-zero energy give the cluster anion yields for RET at $n \approx 260$ (from Barsotti *et al.*, 2002a).

anions according to the following reaction scheme:

$$e^-(E) + (O_2)_N \to (O_2)_N^{-*} \to (O_2)_q^- + (N - q)O_2 \tag{43}$$
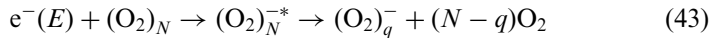
For this reaction to be exothermic at zero electron energy, the total binding energy of the $(O_2)_q^-$ ion (composed of the adiabatic electron affinity of $O_2$ plus the bond energies of the additional $(q - 1)$ $O_2$ molecules) has to exceed the total binding energy $E_N$ of the neutral precursor cluster of size $N$. In particular, $O_2^-$ formation requires that $E_N$ be smaller than $EA_{ad}(O_2) = 0.451(7)$ eV. According to calculations by Matejcik *et al.* (1999), scaled to reproduce the cohesive energy of bulk oxygen, the total binding energy of neutral $(O_2)_N$ clusters becomes larger than $EA_{ad}(O_2)$ for $N \geq 14$. Correspondingly, process (43) for $q = 1$ is energetically not possible when zero energy electrons attach to very cold clusters with $N \geq 14$, but may proceed when the electrons possess a sufficient amount of kinetic energy $E$ (for $N = 20$, the threshold energy for $O_2^-$ formation amounts to about

$E = 0.3$ eV). In contrast, formation of $(O_2)_q^-$ anions with $q \geq 2$ is exothermic for all neutral sizes up to about $N = 25$ even at zero electron energy. If a size *range* of neutral clusters is active as precursor in the cluster anion formation of a particular anion size $q$ according to (43), the observation of vibrational structure implies a sufficiently small inhomogeneous broadening of the vibrational resonance. Model calculations of the distribution function of the adiabatic electron affinity of clusters with sizes $N = 10$, 15 and 20 (Fig. 8 in Matejcik *et al.*, 1999) for the various cluster structures and positions of the solvated $O_2^-$ in the cluster showed the following behavior at low cluster temperatures $T_C$: for sufficiently cold (i.e. solid) clusters ($T_C \leq 20$ K), the width (FWHM) of the distribution function for a particular $N$ amounted to about 0.07 eV. Moreover, the peak position of the distribution remained nearly the same (close to 0.8 eV) for $N = 15$ and 20 while it shifted to 0.7 eV for $N = 10$. For (partially) molten clusters, as shown for $T_C = 40$ K (Matejcik *et al.*, 1999), the distribution was found to become wider by about a factor of 2 and thus too broad as to resolve vibrational structure even for a single precursor size. These calculations thus suggest that the absence of vibrational structure in our attachment spectra may be due to the fact that the oxygen clusters in our experiment were not sufficiently cold. From simulations of the peak structure, assuming solid oxygen clusters with a certain size range, Matejcik *et al.* concluded that neutral clusters around $N = 15$ (ranging from 13 to 20) are responsible for their attachment spectra with $q = 1$, 2, 3. This size selectivity was not explained. The authors also did not comment why the same range should be responsible for the formation of $O_2^-$, $O_4^-$, and $O_6^-$ ions (note that the peak structures for cluster anions with $q = 1$, 2, and 3 was found to be located – within their uncertainties – at the same energies). For $O_2^-$ formation, one would actually expect (in view of the energetic restriction that $N$ may not be larger than 13) that the average size of the neutral clusters involved in anion formation is significantly smaller than for dimer and trimer anion formation with the result that the peaks in the $O_2^-$ attachment spectrum appear at higher energies than those in the dimer and trimer anion spectra.

In this connection it is appropriate to recall that the Berlin group found a clear difference in the peak location of the yield for $(O_2)_q^-$ formation between $q = 1$ (0.7 eV) and $q \geq 2$ (0.4 eV) (Hashemi *et al.*, 1992). This difference is, on the one hand, compatible with a scenario that, on average, $O_2^-$ formation involves neutral clusters of smaller size than those responsible for $(O_2)_q^-$ ($q \geq 2$) formation. In the light of the Innsbruck observations (yielding the maximum yield of small oxygen cluster anions at 0 eV) the Berlin results may be possibly understood if – as proposed by Matejcik *et al.* (1999) – the neutral precursor clusters had a substantially smaller size in the

Berlin experiment. It is desirable for a better understanding of these different observations to carry out additional high resolution experiments which allow to vary the neutral cluster size distribution and the cluster temperature.

## C.2. Nitrous Oxide Clusters

Threshold electron attachment to $N_2O$ clusters via Rydberg electron transfer (RET) close to zero energy (Rydberg binding energy 0.2 meV) produces heterogeneous $(N_2O)_qO^-$ and homogeneous $(N_2O)_p^-$ cluster anions in a highly size selective way (Kraft et al., 1990). The dominant anion species were observed to be $(N_2O)_qO^-$ with $q = 5, 6$ and $(N_2O)_p^-$ with $p = 7, 8$, the latter being generally less intense than the former. These cluster anion intensities suggest resonant capture of zero energy electrons for neutral cluster size $N \approx 8$ with subsequent stabilization by intermolecular vibrational redistribution, by evaporation ($N_2O$ emission) or by dissociation (release of $N_2$ fragments).

In Fig. 41 we present the energy dependent yield for formation of heterogeneous $(N_2O)_qO^-$ ions ($q = 4–9, 11, 13$) and in Fig. 42 that of homogeneous $(N_2O)_p^-$ ions ($p = 8, 9, 11, 13$), as observed over the energy range 1.5–178 meV by Leber et al. (2000c). For all sizes $q$ and $p$ a sharp increase towards 0 eV is observed below $E \approx 15$ meV, indicative of an s-wave attachment process. In all these spectra, astoundingly narrow peaks are observed at energies $E_R$ close to, but not identical with the excitation energies $E(v_i)$ for the bending ($v_2 = 1, 2$) and the N–O stretching ($v_1 = 1$) vibrational mode of free $N_2O$ molecules. The widths (FWHM) of these peaks (around 2.5 meV for the bending fundamental, around 4–5 meV for the bending overtone and the N–O stretching mode (i.e. substantially broader than the experimental resolution of 1.2 meV) are essentially independent of cluster ion size. They are the narrowest resonances detected so far in electron scattering for any cluster or polyatomic molecule. They have been interpreted as vibrational Feshbach resonances (VFRs) (Weber et al., 1999a, Leber et al., 2000c), i.e. temporary anion states of the type $[(N_2O)_{N-1}(N_2O(v_i > 0)]^-$. The energy location and the long lifetime of these resonances (on the order of $2 \times 10^{-13}$ s for the $v_2 = 1$ VFRs, if inhomogeneous broadening due to contributions from different neutral precursors is neglected) are compatible with the idea of a weakly bound diffuse excess electron attached to an essentially unperturbed neutral $(N_2O)_{N-1}N_2O(v_i > 0)$ cluster by long range forces. The widths of the resonances increase with electron energy, probably due to rising phase space for the most probable decay mechanism of the resonances, namely autodetachment of the captured electron. The peak positions exhibit small
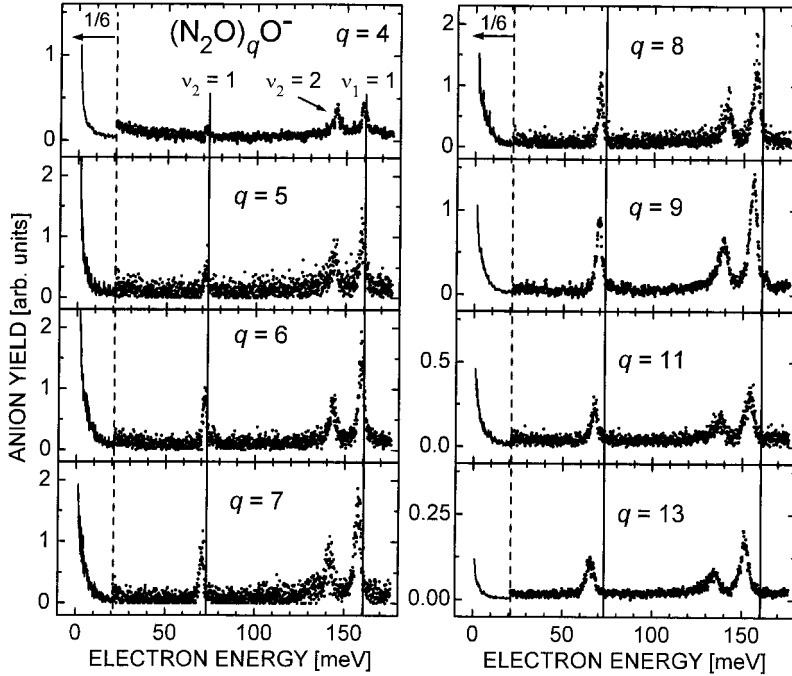
F<span style="font-variant:small-caps">IG</span>. 41. Low-energy electron attachment spectra for formation of heterogeneous $(N_2O)_qO^-$ cluster anions from $(N_2O)_N$ clusters ($q < N$). The full vertical lines denote the energy positions of the $\nu_2 = 1$ and the $\nu_1 = 1$ intramolecular vibrational excitation in $N_2O$ (from Leber et al., 2000c).

redshifts, defined as the quantity $\Delta \equiv E(\nu_i; N)_C - E_R$, which increase with cluster ion size; here $E(\nu_i; N)_C$ denotes the intramolecular excitation energy of the $\nu_i$ mode in the neutral cluster with size $N$ which acts as the precursor for the observed anion of size $q$ or $p$. It has to be emphasized that attachment processes involving slow secondary electrons from inelastic collisions with $N_2O$ monomers are ruled out for reasons of low target density and the inability to produce the observed cluster size dependent redshift.

The VFRs evolve to the observed homogeneous and heterogeneous cluster anions in different ways. Energy redistribution into soft inter-molecular modes may lead to long-lived homogeneous ions with size $p = N$. Homogeneous cluster anions with $p < N$ are produced upon evaporation of at least one $N_2O$ molecule. Formation of heterogeneous cluster anions involves removal of one $N_2$ fragment, possibly accompanied by release of
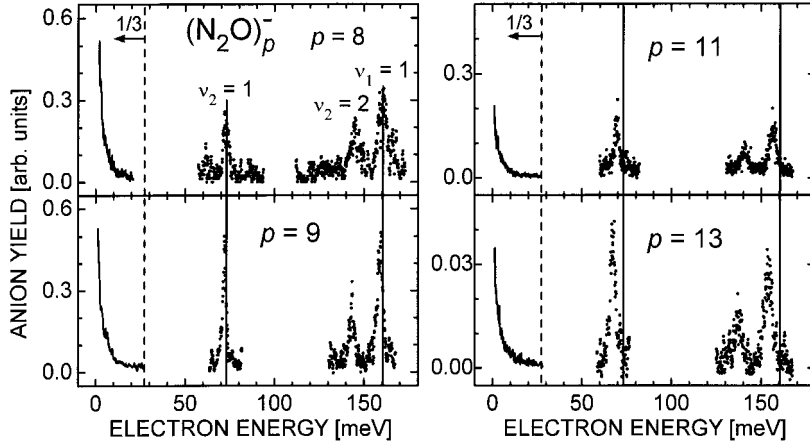
FIG. 42. Low-energy electron attachment spectra for formation of homogeneous $(N_2O)_p^-$ cluster anions from $(N_2O)_N$ clusters ($p \leq N$). The full vertical lines denote the energy positions of the $\nu_2 = 1$ and the $\nu_1 = 1$ intramolecular vibrational excitation in $N_2O$ (from Leber *et al.*, 2000c).

$N_2O$ units. The anion intensities in the threshold mass spectrum and correlations in the redshifts of the heterogeneous anions $\Delta_{het}(q)$ and of the homogeneous anions $\Delta_{hom}(p)$ suggest that neutral precursor clusters with size $N$ on average are correlated with homogeneous anions of size $p$ ($\leq N$) and heterogeneous cluster anions $(N_2O)_qO^-$ with size $q = p$-(2 or 3) (Leber *et al.*, 2000c).

In view of the existence of the vibrational Feshbach resonances $[(N_2O)_{N-1}(N_2O(\nu_i > 0)]^-$, it is natural to infer the presence of truly bound, nonautodetaching anion states $[(N_2O)_{N-1}(N_2O(\nu_i = 0)]^-$ without intramolecular vibrational excitation (see the model calculations below). Such bound states are not accessible in free electron collisions, but can be formed by Rydberg electron transfer (RET) as shown, e.g., by Desfrançois *et al.* (1996) for dipole bound anions. The strong rise in the free electron attachment yield towards zero energy is attributed to the influence of these weakly bound $(N_2O)_N^-$ capture states without intramolecular excitation (but possibly with some intermolecular excitation). The rather sharp drop in the RET-induced anion intensities, as observed at threshold ($n \cong 250$) for $q > 6$ and $p > 9$, appears to be mainly due to the increasing binding energies of the $[(N_2O)_{N-1}(N_2O(\nu_i = 0)]^-$ states with rising $N$ which correlate with a shift of the maximum RET rate coefficient towards lower principal quantum numbers $n$ (Desfrançois *et al.*, 1996), as in fact observed experimentally (Kraft *et al.*, 1990).

In the discussion above, it has been assumed for simplicity that a particular observed VFR is associated with a single size $N$ only. This assumption, however, is uncertain in view of the fact that the resonance widths, especially for the two higher lying VFRs, are larger than or at least similar to the redshift. Even if the observed VFRs correspond to a mixture of neighbouring sizes $N$ with a mean value $\langle N \rangle$ and if $N$ is not identical to $p$, it is still true, however, that the relation $q = p\text{-}(2 \text{ or } 3)$ holds.

In order to provide a qualitative understanding of the small VFR redshifts, Leber *et al.* (2000c) performed simple model calculations for the binding energy $E_B = -\Delta$ of the captured electron in the VFR state $[(N_2O)_{N-1}N_2O(\nu_i > 0)]^-$ relative to the energy $E_N$ of the neutral $[(N_2O)_{N-1}N_2O(\nu_i > 0)]$ cluster which carries the same amount of intra-molecular vibrational energy ($E_R = E_N + E_B$). The authors ignored geometrical arrangement effects of the cluster constituents as well as the intramolecular vibration and assumed that the binding energy $E_B$ is simply due to the combined effects of the long-range attraction between the electron and the cluster and the short range interaction $U_0$ at distances smaller than the cluster radius $R_N$. Leber *et al.* (2000c) took into account the polarization attraction $V_{pol} = -Ne^2\alpha(N_2O)/(2r^4)$ (neglecting, in the average over the cluster, the effects associated with the weak dipole moment and the quadrupole moment of the $N_2O$ molecules) and cut it off at the cluster radius; at electron-cluster distances smaller than $R_N = R_0(1.5N)^{1/3}$ ($R_0 =$ effective radius of a monomer) a constant potential energy $U_0$ was used and treated as a parameter. In Fig. 43 we sketch the potential model for $U_0 = +0.2\,\text{eV}$ and $N = 11$ and the probability density for the wave function of the corresponding weakly bound electron (Leber *et al.*, 2000c). As expected in view of the weak binding energies, the radial extension of the electron in these resonance states is quite large as illustrated in Fig. 43 for the VFR state with size $N = 11$.

Figure 44 shows the results of these calculations for the electron binding energies to clusters with $N = 4$–$15$, using several constant, *repulsive* values for the short range potential $U_0$, the isotropic monomer polarizability $\alpha(N_2O) = 20.4\,a_0^3$ [25] and $R_0 = 3\,a_0$ ($a_0 =$ Bohr radius). For comparison with the calculated binding energies (curves), the experimentally derived binding energies $E_{B,het}(N, q) = -\Delta_{het}(q + 2)$ (full symbols) and $E_{B,hom}(N, p) = -\Delta_{hom}(p)$ (open symbols) (i.e. we assume $N = p = q + 2$) are included in Fig. 44. For the intramolecular excitation energies $E(\nu_i; N)_C$ in $N_2O$ clusters the values, reported by Gauthier (1988) for $\nu_2 = 2$ and $\nu_1 = 1$, and for $\nu_2 = 1$ the monomer value were adopted. One observes reasonable agreement between the thus calculated and the observed resonance positions for $U_0 = +0.2\,\text{eV}$. The use of more elaborate potentials $U_0$ (Stampfli, 1995) does not provide deeper insight at the present level of accuracy.
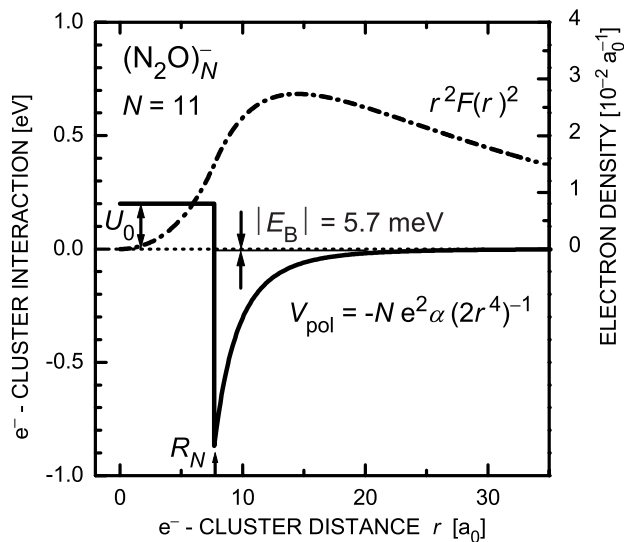
FIG. 43. Probability density (chain curve) for the radial wave function of the electron, weakly bound to the $(N_2O)_{11}$ cluster and the model potential (full curve) used to calculate this wave function (Leber *et al.*, 2000c).
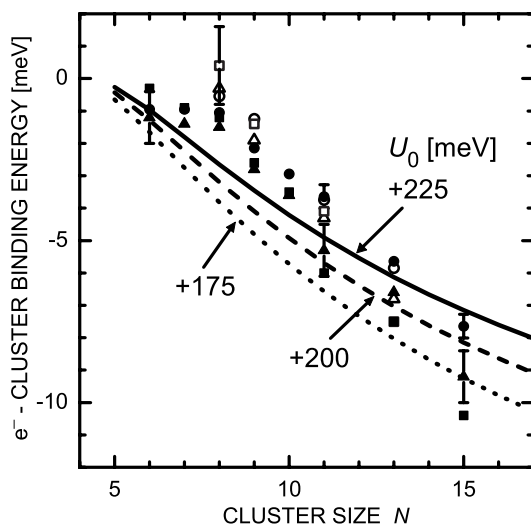


FIG. 44. Comparison of calculated and experimentally determined binding energies for weakly bound $(N_2O)_N^-$ anions, for details see text (Leber *et al.*, 2000c).
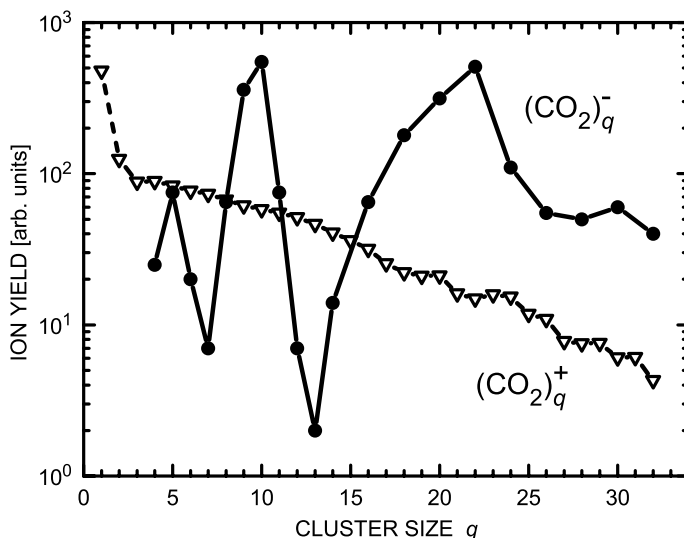
FIG. 45. Cluster ion mass spectra for $CO_2$ clusters (after Barsotti *et al.*, 2002a). Open triangles: mass spectrum of positive ions resulting from 85 eV electron impact ionization; full circles: mass spectrum of anions due to threshold electron attachment involving $K^{**}(nd, n \approx 260)$ Rydberg atoms.

### C.3. Carbon Dioxide Clusters

Some properties of the $CO_2$ molecule have been discused in Section IV.B5. According to molecular dynamics simulations (Etters *et al.*, 1981; Tsukada *et al.*, 1987; Torchet *et al.*, 1996; Maillet *et al.*, 1998), neutral carbon dioxide clusters possess icosahedral structure (at least for sizes up to about $N = 20$) with predicted binding energies around 0.14 eV per molecule for $N = 13$ (Maillet *et al.*, 1998); at sizes above about $N = 30$, a transition to bulk cubic structure has been predicted, and this bulk structure has been experimentally verified for $N$ above about 100 (Torchet *et al.*, 1996). Some information on cluster anion structures is also available. In agreement with photoelectron spectroscopic observations (Tsukda *et al.*, 1997a), *ab initio* calculations of the equilibrium structures and stabilities for different isomers of small $(CO_2)_q^-$ cluster anions ($q \leq 6$) find (Saeki *et al.*, 2001) that the dimer $C_2O_4^-$ acts as the core in clusters with $q = 2 - 5$. They predict evaporation energies for dissociation of one $CO_2$ unit from various isomers of $(CO_2)_q^-$ anions in the range 0.1–0.4 eV, rising substantially (by about 0.15 eV) when going from $q = 5$ to $q = 4$. Tsukada *et al.* (1987) developed a theory for the attachment of slow electrons to van der Waals clusters and applied it to $CO_2$ clusters. They predicted the existence of

a threshold size for attachment and a sharp decrease of the attachment cross-section with rising electron energy.

Previous experimental work of cluster anion formation in energy-controlled electron collisions with carbon dioxide clusters includes low-resolution beam studies over extended energy ranges (Compton, 1980, Stamatovic *et al.*, 1985a, b; Knapp *et al.*, 1985, 1986a), investigations by Rydberg electron transfer (RET) (Kondow, 1987; Kraft *et al.*, 1989, 1991; Misaizu *et al.*, 1991) and the recent LPA studies (energy width about 1 meV) (Leber *et al.*, 2000b; Barsotti *et al.*, 2002a). Anion mass spectra obtained by RET revealed an intriguing anion cluster size dependence. In Fig. 45, the relative intensities for $(CO_2)_q^+$ cluster ions due to 85 eV electron impact (open triangles) are compared with the relative intensities of the $(CO_2)_q^-$ cluster anions (full circles), obtained in RET with a narrow $n$ band of $K^{**}(nd)$ Rydberg atoms, centered around $n = 260$ (electron binding energy 0.2 meV). Note that, in contrast to the anion mass spectra shown in Fig. 2 of Barsotti *et al.* (2002a), the anion yield in Fig. 45 was obtained with the ion optics optimized for each cluster size. $(CO_2)_q^+$ ions ($q \geq 1$) dominate the positive ion mass spectrum and exhibit a nearly exponential intensity decrease with rising cluster size $q$. As expected on energetic grounds, only homogeneous ions $(CO_2)_q^-$ ($q > 3$) are observed in the anion mass spectra due to electron attachment to carbon dioxide clusters, both in Rydberg electron transfer (RET) involving $K^{**}(nd)$ atoms ($n = 14$–260) and in free electron attachment ($E = 1$–200 meV). Compared with the positive ion spectrum, the RET-induced anion cluster mass spectrum is completely different: the threshold anion spectrum exhibits local maxima at $q = 5$ and 10 as well as a broad maximum around $q = 22$, and deep, local minima at $q = 7$ and 13. Anion cluster mass spectra at lower principal quantum numbers ($n \leq 30$) (Kondow, 1987; Kraft *et al.*, 1989; Leber, 2000b) differ significantly from the threshold spectrum in Fig. 45 and indicate a substantial dependence on electron energy over a narrow range, as will be understood through the observations in the free electron attachment spectra.

In Fig. 46 we present the energy dependent yield for $(CO_2)_q^-$ cluster anions for selected sizes $q$ from the covered range $q = 4$–32 over the energy range from 1 meV up to 200 meV (Barsotti *et al.*, 2000a). For small cluster sizes, two clearly separated series of resonances are observed which exhibit redshifts increasing by about 12 meV per monomer unit. The key spectrum observed for $q = 5$ (in which the peaks exhibit the narrowest widths) shows a distinct zero energy peak (indicative of s-wave attachment), a rather sharp resonance peaking at about 52 meV and a double-peak structure with a center-of-gravity around 134 meV. These three peaks are attributed to vibrationally excited temporary cluster anion states (vibrational Feshbach
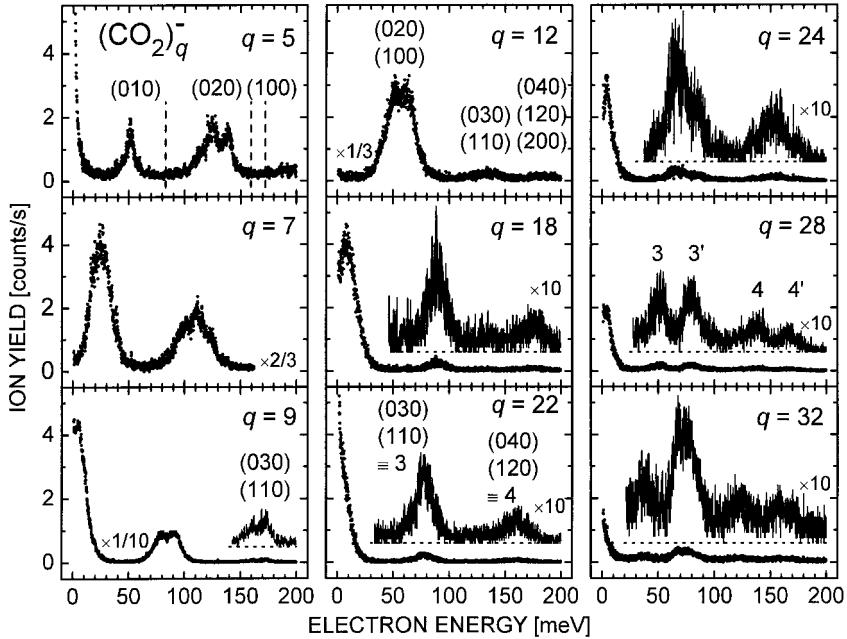
FIG. 46. Low-energy electron attachment spectra for formation of $(CO_2)_q^-$ cluster anions ($q = 4$–$32$) from $(CO_2)_N$ clusters ($q \leq N$). For $q = 5$, the energy positions of the $(v_1v_2v_3) = (010)$ and the Fermi-coupled $(020)/(100)$ vibrational modes of the $CO_2$ monomer are indicated by vertical dashed lines. The incremental redshift of the vibrational Feshbach resonances amounts to about 12 meV per monomer unit. For $q > 7$, the $3 \equiv (030)/(110)$ and, for $q > 10$, the $4 \equiv (040)/(120)/(200)$ vibrational modes are shifted into the electron energy range covered by the LPA experiment. For $q > 24$, a doubling of the Feshbach resonance peak structure is observed ($3/3'$ and $4/4'$) (after Barsotti et al., 2002a).

resonances VFRs) of the type $[(CO_2)_{N-1} CO_2(v_1v_2v_3)]^-$ with $(v_1v_2v_3) = (010)$ and $(020)/(100)$, respectively, which evolve into the observed long-lived $(CO_2)_{q=5}^-$ anions either by redistribution of the vibrational energy among soft modes of the cluster with formation of a metastable cluster ion with $q = N$ or by evaporation of a small number of $CO_2$ units (most likely $N - q = 1$, see below). As expected for VFRs, their energies are redshifted from those of the neutral $[(CO_2)_{N-1}CO_2(v_1v_2v_3)]$ precursor. In contrast to the sharp VFRs observed for $N_2O$ clusters which exhibit small redshifts in the meV range (see above), the redshift is substantially larger for $CO_2$ clusters, indicating a stronger interaction of the resonantly–captured electron with $CO_2$ clusters than with $N_2O$ clusters. In line with this observation the resonance widths are larger for $CO_2$ clusters than for $N_2O$ clusters. For any particular $(CO_2)_q^-$ cluster ion, the width of the observed resonances
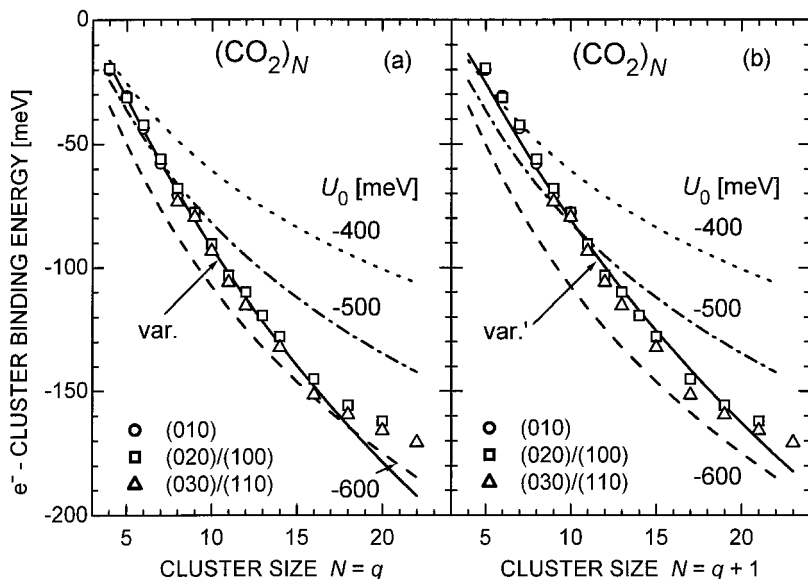
F$_{IG}$. 47. Comparison of calculated and measured binding energies for VFRs in $CO_2$ clusters, assuming $N = q$ (a) and $N = q + 1$ (b), for details see text (after Barsotti *et al.*, 2002a).

contains contributions due to the intrinsic resonance widths and resonance positions of all involved neutral precursors which participate in VFR formation, i.e. the observed resonances are in general inhomogeneously broadened. In view of the substantial redshift of about 12 meV per added $CO_2$ unit and the comparatively narrow intrinsic width of the VFRs, the width in conjunction with the redshift of the VFR allows rather direct conclusions to be drawn on the size *range* of the involved neutral precursors. For $q = 5$ the resonances exhibit the smallest widths, and it is plausible that the attachment spectrum is predominantly associated with a single neutral precursor size (with the possibility of inhomogeneous broadening due to contributions from different conformations for that cluster size). At this narrow peak width, the Fermi-coupled pair (020)/(100) is quite well resolved. Interestingly, we find the two peaks at similar intensities in contrast to the situation for vibrationally inelastic scattering of low energy electrons from $CO_2$ molecules where, close to the threshold for the pair (020)/(100), the higher energy component is excited almost exclusively (Allan, 2001a). This finding has been associated with the influence of a virtual state which has been theoretically predicted for low-energy electron scattering from carbon dioxide (Morrison, 1982;

Estrada and Domcke, 1985; Morgan, 1998) and recently also been confirmed by total scattering studies at very low energies (Field *et al.*, 2001b).

For $q = 4$ and $q \geq 6$, the (010) resonances appear to be significantly broader than for $q = 5$; this may indicate contributions from two neighbouring neutral precursor sizes, but could also be caused (at least in part) by the influence of different conformations for a particular $N$. For larger sizes ($q > 7$), additional series of peaks, attributed to resonances associated with the Fermi-coupled pair (030)/(110) and the triplet (040)/(120)/(200), are successively shifted into the studied energy range. The evolution of these series is clearly seen in the attachment spectra for the clusters anions with sizes $q = 14$–32. The trends are similar to those observed at smaller anion size, but the redshifts per added molecular unit decrease somewhat at higher $q$. For cluster sizes $q$ above 24 an interesting doubling of the VFR peak structure is observed in both the (030)/(110) $\equiv 3$ and (040)/(120)/(200) $\equiv 4$ series; the 3 and 4 series evolve 'normally' towards lower energies with intensities decreasing towards higher $q$ while the 'new' series 3′ and 4′ are observed at 30–40 meV higher energies relative to the 3 and 4 series, respectively, with intensities rising towards larger $N$. We tentatively attribute these two series to arise from the coexisting icosahedral (series 3, 4) and bulk cubic (series 3′, 4′) cluster structures, with the former losing and the latter gaining importance towards higher $N$. According to molecular dynamics simulations for carbon dioxide clusters, the icosahedral (low $N$) to bulk cubic (high $N$) transition is predicted to occur for sizes around $N = 30$ (Torchet *et al.*, 1996).

The attachment spectra shown in Fig. 46 offer the following explanation for the strongly $q$-dependent ion intensities in the mass spectrum resulting from threshold electron attachment (Fig. 45) with minima at $q = 7$ and 13, a clear maximum at $q = 10$ and another broad maximum for $q$ around 21. Enhanced cluster ion intensities are found for $q$-values for which a substantial overlap of a VFR with zero electron energy exists. For $q = 9$, 10, the (010) resonance has moved close to zero energy, for $q = 16$–22, the (020)/(100) resonance pair has a more or less substantial overlap with zero energy. The intensity rise in the threshold attachment mass spectrum from $q = 6$ to $q = 5$ may be attributed to an influence of $(CO_2)_N^-$ capture states without intramolecular excitation (but possibly some intermolecular excitation). One would expect such an influence to be even stronger for $(CO_2)_4^-$ formation, but the autodetachment rates of the temporary $(CO_2)_N^{-*}$ negative ions are expected to rise towards low $N$ and thus their survival probability towards stabilization and detection as long-lived anions should decrease. For further discussions including variations of the cluster anion mass spectrum with increasing electron energy see Barsotti *et al.* (2002a).

Application of the simple spherical model for the electron binding energies $E_B$, sketched in Section C.2, reproduces the redshifts when – in contrast to the situation for $N_2O$ clusters – *attractive* short range potentials are used (Leber *et al.*, 2000b; Barsotti *et al.*, 2002a). Figure 47 shows calculated electron binding energies to clusters with $N = 4 - 22$ (dashed curves), as obtained with realistic choices of the short range potential $U_0$ (for further results see Leber *et al.* (2000b)). For comparison, the experimentally derived binding energies $E_{B,exp}$ for the (010), (020)/(100), (030)/(110) and (040)/(120)/(200) resonance series, as calculated from the center-of-gravity resonance positions $E_R$ through $E_{B,exp} = E_R - E_q$, are included, using two different assumptions: (a) $N = q$ and (b) $N = q + 1$. In view of the fact that the intramolecular excitation energies $E_N$ in $CO_2$ clusters deviate from those in the $CO_2$ monomer $E_1$ (see IV.B.5.a) by no more than about $\pm 1$ meV (see references in Leber *et al.* (2000b)) we approximate $E_N$ by $E_1$ for all sizes $N$ of interest.

Reasonable agreement between the calculated and the observed average resonance positions is observed for the choice $U_0 = -0.5$ eV at low $N$ and $U_0 = -0.6$ eV at higher $N$. With the weakly $N$-dependent choice (Stampfli, 1995)

$$U_0(N) = aN^{-1/3} + b, \tag{44}$$

using $a = +0.7$ (0.8) eV for $N = q$ ($N = q + 1$) and $b = -0.866$ eV in both cases, the full curves (labeled var. in (a) and (b)) are obtained, showing good agreement with the experimentally found binding energies over a broad range of $N$. The combined information contained in the $q$-dependent redshifts, in the respective resonance widths, in the calculated absolute values of the electron binding energies and in the slopes of the calculated $E_B(N)$ and of the experimental $E_R(q)$ curves allows the conclusion that the main contributions to cluster anion formation stem from neutral clusters with sizes $N = q$ and/or $N = q + 1$. Note that in view of the rather narrow width of the observed VFRs a particular cluster anion size $q$ cannot be associated with a broad range of precursor sizes $N$ in view of the differential redshift of about 12 meV per added $CO_2$ unit.

The substantially larger binding energies observed for the VFRs in $CO_2$ clusters as compared to those for the VFRs in $N_2O$ clusters (see Section C.2) are due to the fact that the short-range interaction $U_0$ for $CO_2$ is attractive (note that the polarizabilities of $N_2O$ and $CO_2$ agree to within 5%). This conclusion is confirmed by analysis of experimental results and theoretical calculations of low-energy electron scattering by $CO_2$ and $N_2O$ molecules. Cross-sections for low-energy electron scattering by $CO_2$ are rapidly

increasing towards lower energies (Morrison *et al.*, 1982; Field *et al.*, 2001b) approaching $200 \times 10^{-20}\,m^2$ which corresponds to a large negative scattering length whose value lies between $-7.2\,a_0$ and $-6.3\,a_0$ (Fabrikant, 1984; Mazevet *et al.*, 2001; Field *et al.*, 2001b). On the other hand, experimental (Szmytkowski *et al.*, 1984) and theoretical (Sarpal *et al.*, 1996; Winstead and McKoy, 1998) data on electron scattering by the $N_2O$ molecule show that the low-energy cross-section in this case is much smaller and does not exceed $8 \times 10^{-20}\,m^2$ below $E = 1\,eV$. At ultralow energies, the cross-section should increase due to the (albeit very small, $\mu = 0.16\,D$) dipole moment; but this effect should not be important for clusters. Note that the quadrupole moment of the molecule, although relevant, does not affect the energy *dependence* of the cross-section at low energies (Fabrikant, 1984; Leber *et al.*, 2000b). For the clusters of interest here, the effects of the molecular dipole and quadrupole moments should be small as a result of cancellation due to mixed orientations. Therefore the observed redshifts of the VFRs can be reproduced by modelling the $e^-$–$CO_2$ and $e^-$–$N_2O$ interaction potentials as a well or a repulsive barrier with a polarization tail. In the more general expression (44) for the short-range contribution to the electron interaction with clusters the parameter $b$ is the excess energy of the electron in the infinite medium and the factor $a$ is a constant which depends on the dielectric properties of the cluster. Our estimate of $b$ which employs the effective potentials of monomers and the concept of the Wigner-Seitz cell (Stampfli, 1995) shows that $b$ for bulk $N_2O$ exceeds the value of $b$ for bulk $CO_2$ by $1\,eV$ which agrees well with our empirical values for $b$ of $-0.87\,eV$ for $CO_2$ and about $+0.2\,eV$ for $N_2O$ (Leber *et al.*, 2000c). The described model is of course very simple. For a detailed understanding of these fascinating vibrational resonances large-scale *ab initio* calculations are needed.

### C.4. Carbonyl Sulfide Clusters

Carbonyl sulfide OCS in its ground electronic state is a linear molecule with an electric dipole moment of $\mu = 0.715\,D$ (Gutsev *et al.*, 1998). The lowest vibrationally excited states, labelled $(v_1 v_2 v_3)$, include the bending mode (010) (64.5 meV), the asymmetric stretch mode (001) (106.5 meV) and the bending overtone (020) (129.0 meV). The ground state of the anion $OCS^-$ is bent with an angle of $136°$. The adiabatic electron affinity (*AEA*) of OCS is not yet well known. Gutsev *et al.* (1998) report a calculated value of $AEA(OCS) = -0.22\,eV$ (CCSD(T) method), while Surber *et al.* (2002) conclude that $AEA(OCS)$ is close to zero. Values of this magnitude are supported by the fact that the properties of OCS are intermediate between those of $CO_2$ and $CS_2$ which have adiabatic electron affinities

of $AEA(CO_2) \approx -0.66\,\text{eV}$ (Gutsev $et\,al.$, 1998) and $AEA(CS_2) = 0.9 - 1.0\,\text{eV}$ (Oakes and Ellison, 1986). The theoretical results for $AEA(OCS)$, however, differ from the experimental value of $AEA(OCS) \approx 0.4\,\text{eV}$ (Compton $et\,al.$, 1975; Chen and Wentworth, 1983).

The dissociation energy of OCS towards $S + CO$ amounts to $D_0(OC-S) = 3.13(4)\,\text{eV}$ (Ziesel $et\,al.$, 1975b) and the electron affinity of S to $EA(S) = 2.0772\,\text{eV}$ (Andersen $et\,al.$, 1999). $S^-$ formation in dissociative attachment to OCS is thus accessible at energies above about $1.05\,\text{eV}$ in agreement with experimental findings (Ziesel $et\,al.$, 1975b; Iga $et\,al.$, 1996). which show a prominent peak for $S^-$ formation, centered at about $1.35\,\text{eV}$ (cross-section of about $2.7 \times 10^{-21}\,\text{m}^2$). This peak is connected with a resonance peak found at about $1.15\,\text{eV}$ in elastic scattering from OCS (Karwacz $et\,al.$, 2001a).

Rather little is known up to now on the formation of carbonyl sulfide cluster anions and on their geometrical structure. Kondow and Mitsuke (1985) investigated formation of negative cluster ions of OCS produced by electron transfer from a range of Rydberg rare gas atoms around $n = 25$. Their mass spectrum is dominated by $(OCS)_q^-$ ions with a maximum at $q = 10$. To our knowledge no free electron attachment spectra for OCS clusters have been reported prior to the LPA work discussed below. Regarding cluster anion spectroscopy and structure, Sanov $et\,al.$ (1998) studied the photochemistry of $(OCS)_n^-$ cluster ions following excitation by $395\,\text{nm}$ and $790\,\text{nm}$ photons. They also presented possible equilibrium geometries of $(OCS)_2^-$ and the relative potential energy curves for the neutral dimer $(OCS)_2$ and the anion $(OCS)_2^-$.

Using the laser photoelectron attachment method, Barsotti $et\,al.$ (2003b) have recently studied the formation of cluster anions in RET and in low-energy free electron attachment ($E = 1$–$200\,\text{meV}$) to molecular clusters of carbonyl sulfide OCS at energy widths of $1$–$2\,\text{meV}$. In Fig. 48 the intensities, for positive $(OCS)_q^+$ ions (due to $85\,\text{eV}$ electron impact) and normalized to the anion signal at $q = 2$ and for negative $(OCS)_q$ ions (resulting from RET at high $n \approx 260$) are compared. The anion mass spectrum shows a clear peak at the dimer, but little structure otherwise.

The energy dependences for $(OCS)_q^-$ anion formation by free electron attachment, shown in Fig. 49 for $q = 1 - 9$, are characterized by a strong rise towards zero energy (attributed to s-wave attachment) as well as by vibrational Feshbach resonances (VFR) whose importance decreases towards larger cluster sizes $q$. The electron attachment behavior of OCS clusters is thus intermediate between that of $CO_2$ clusters (which is dominated by VFRs) and that of $CS_2$ (which exhibits a strong zero-energy peak, but no VFRs, see Section C5). Formation of the $(OCS)_2^-$ dimer anion is especially enhanced; its attachment spectrum exhibits a sharp vibrational
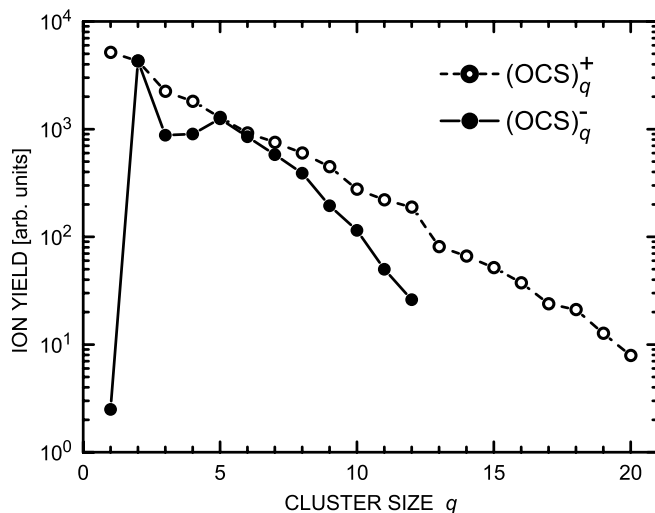
FIG. 48. Intensities of homogenous positive/negative ions (normalized at $q = 2$) due to $85\,eV$ electron impact/threshold electron attachment involving OCS clusters (Barsotti *et al.*, 2003b).
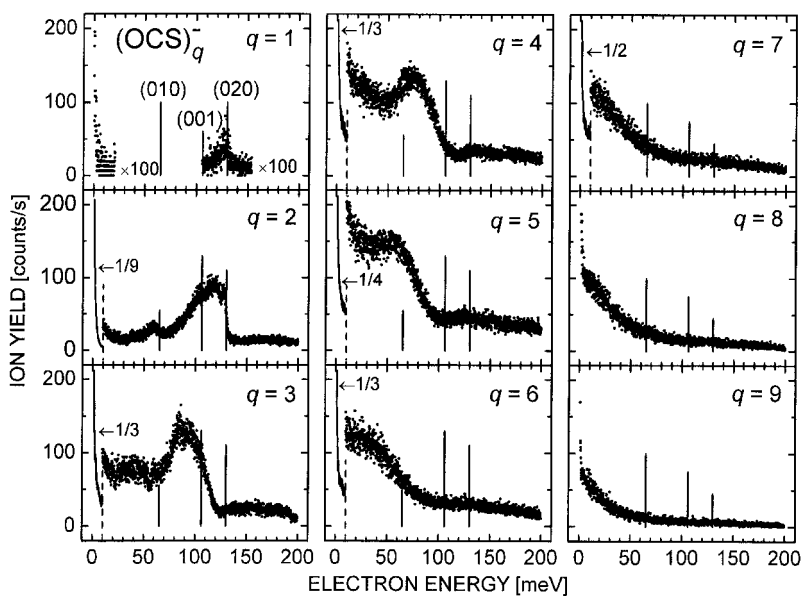


FIG. 49. Low-energy electron attachment spectra for formation of $(OCS)_q^-$ anions from $(OCS)_N$ clusters ($q \leq N$). The full vertical lines denote the energy positions of the listed vibrational modes in the OCS monomer (from Barsotti *et al.*, 2003b).

Feshbach resonance at 128 meV, just below the (020) onset for excitation of the $(\nu_1\nu_2\nu_3)$ normal modes in the OCS molecule, a broad structure centered at about 117 meV, a weak structure at about 103 meV (just below the $\nu_3 = 1$ onset) and a peak at about 59 meV below the $\nu_2 = 1$ onset. The attachment spectrum observed for $q = 1$ shows a low counting rate; it also exhibits a rather sharp resonance peaking at about 128 meV. The low intensity may indicate that OCS$^-$ only exists in a few stable or even metastable rovibrational states, in line with the theoretical results of Surber *et al.* (2002). Since the spectra for $q = 1$ and $q = 2$ both exhibit the (020)-peak essentially at the same energy position, it is plausible that the yield for the monomer anion OCS$^-$ is due to formation of the dimer $(OCS)_2^-$ with subsequent evaporation of a single OCS unit (and not due to attachment of clusters with sizes $q \geq 3$; it is also not expected that (long-lived) OCS$^-$ anions are formed through free electron attachment to OCS monomers).

For $q = 3$ the very sharp peak present in the spectrum at $q = 2$ and assigned to the vibrational Feshbach resonance of the type $\nu_2 = 2$ is no longer observed, the broad structure appears red-shifted by about 20 meV, and a peak at lower energies is weakly observed, also red-shifted by about 20 meV. With the increase of the cluster size ($4 \leq q \leq 7$) only a broad structure is left in the spectra, red-shifted by about 20 meV per added OCS unit. For $q > 8$ no clear structure is left in the spectra which are dominated by the rise towards zero energy. The missing of the sharp resonance for $q > 2$ is similar to the findings for electron attachment to methyl iodide clusters (Weber *et al.*, 2000, see also subsection C.6). The sharp vibrational Feshbach resonance, observed at about 61 meV (just below the onset for the C–I stretch vibration $\nu_3 = 1$) for dissociative attachment to CH$_3$I monomers (yielding I$^-$ ions), is almost missing in attachment spectra for $(CH_3I)I^-$ and $(CH_3I)_2I^-$, which weakly exhibit broad red-shifted structure.

### C.5. *Carbon Disulfide Clusters*

Carbon disulfide CS$_2$ is linear in its electronic ground state. According to *ab initio* calculations (Gutsev *et al.*, 1998) the adiabatic electron affinity is positive with a value of $EA_{ad} = 0.30$ eV; the stable anion is bent with a bond angle of about 144.5° and an electric dipole moment of $+0.46$ D. The difference between the theoretical value for $EA_{ad}$ and the experimental result (0.89 eV, Oakes and Ellison, 1986) might in part be due to very unfavourable Franck-Condon-factors for the transition connecting the respective vibrational ground levels from the anion to the neutral, precluding observation of this transition in the experiment (Gutsev *et al.*, 1998). For optimized linear configurations of CS$_2$ and CS$_2^-$, their energies are almost identical with the possibility that the linear anion is stable against
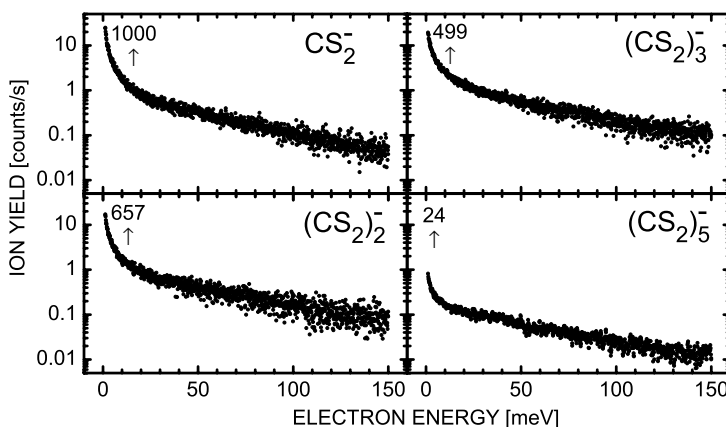
FIG. 50. Low-energy electron attachment spectra for formation of $(CS_2)_q^-$ anions from $(CS_2)_N$ clusters ($N \geq q = 1, 2, 3, 5$). The numbers above the arrows near zero energy give the cluster anion yields for RET at $n \approx 260$ (from Barsotti *et al.*, 2002a).

autodetachment by a few millielectron volts. This finding is compatible with substantial rate coefficients for the formation of $CS_2^-$ ions in RET experiments (Kalamarides *et al.*, 1988; Harth *et al.*, 1989; Carman *et al.*, 1990) and can explain observations of long-lived weakly bound $CS_2^-$ ions which undergo electric-field-induced detachment when subjected to fields of only a few kilovolts per centimeter (Kalamarides *et al.*, 1988). Anion formation involving carbon disulfide clusters has been studied by RET (Kondow, 1987; Desfrançois *et al.*, 1993) and, more recently, in free electron attachment experiments with the LPA method (Barsotti *et al.*, 2002a). Photodetachment and photodestruction studies of $(CS_2)_q^-$ cluster anions (e.g. Maeyama *et al.*, 1998) in conjunction with *ab initio* calculations of the anion structures and binding energies (e.g. Sanov *et al.*, 1998) indicate that a $C_2S_4^-$ core is involved in the $(CS_2)_q^-$ cluster anions with $q \geq 2$.

Figure 51 presents the attachment spectra for formation of small carbon disulfide cluster anions with sizes $q = 1, 2, 3, 5$, as measured with the LPA method over the energy range 1–150 meV (Barsotti *et al.*, 2002a); $CS_2$ molecules (0.34 bar) were coexpanded with helium carrier gas at a total stagnation pressure of 4.5 bar). For all cluster anion sizes, the attachment yield shows a monotonous decline towards higher electron energies. Within the statistical uncertainties no structure is observed. The anion cluster size distribution in the free electron attachment spectra, viewed at any particular electron energy, was found to be close to that observed in the threshold attachment RET mass spectrum which decreased monotonically with
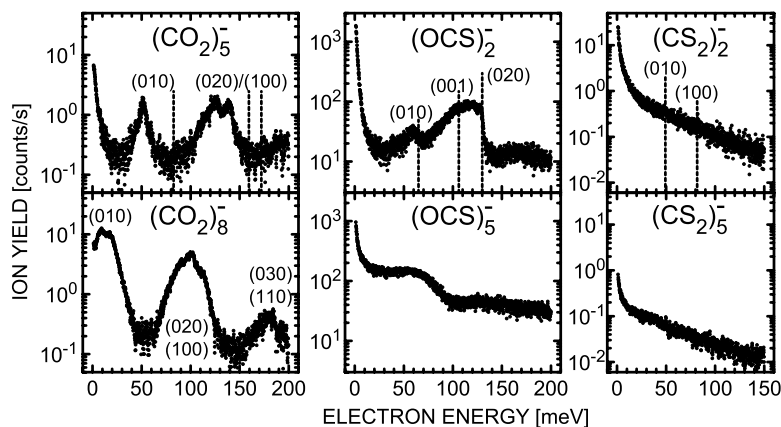
FIG. 51. Comparison of attachment spectra for formation of homogenous cluster anions $(CO_2)_q$ $(q = 5, 8)$, $(OCS)_q$ $(q = 2, 5)$, and $(CS_2)_q$ $(q = 2, 5)$. Vibrational Feshbach resonance dominate the spectra for $(CO_2)_q$ formation and are still prominent (though broader) in the $(OCS)_q$ spectra (from Barsotti *et al.*, 2002a, 2003b).

rising $q \geq 1$. Electron attachment at near-zero energies is efficient for any size (including the monomer); the formed temporary cluster anion may evaporate monomers at an energy expense of about $0.17\,\mathrm{eV}$ per molecule (Desfrançois *et al.*, 1993). In this way reaction (42c) can proceed with an evaporation of one or more monomers (depending on the values of the respective electron affinities and evaporation energies). In collisions with free electrons or Rydberg electrons with sufficiently high principal quantum number long-lived monomer $CS_2^-$ anions are not formed from the neutral monomer; in these cases, the yield for $CS_2^-$ formation originates from neutral clusters with sizes $N \geq 2$.

In comparison with the observations made for cluster anion formation from $CO_2$ and OCS clusters, in particular with regard to the presence of vibrational resonances, (see Fig. 1) the question arises why no vibrational structure is observed at all for carbon disulfide clusters. Note that 'giant' scattering resonances have been observed in the energy dependence of the total cross-section (Jones *et al.*, 2002) as well as in the angle differential elastic cross-section (Allan, 2001c) for electron scattering from $CS_2$ molecules at very low energies, as discussed in Section B.6 of this chapter. One essential difference between $CO_2$, OCS and $CS_2$ is the substantial rise in the adiabatic (as well as in the vertical) electron affinity from $CO_2$ to $CS_2$. Carbon dioxide does not form a stable negative ion, OCS anions are just about stable while $CS_2$ possesses states bound by several tenths of an eV

(see above). For $CS_2$ clusters the stronger valence-type electron binding and the expected stronger effects due to solvation in the cluster anions may thus preclude the formation of VFRs which reflect long-range electron binding.

### C.6. Methyl Iodide Clusters

As described in Section IV.A, a prominent VFR has been observed (Schramm *et al.*, 1999) in dissociative attachment to $CH_3I$ molecules (yielding $I^-$ ions) directly below the onset for the $v_3 = 1$ C−I stretch vibration. It was shown that the VFR occurs due to the combined effects of the dipole and the polarization attraction, and it may thus be expected that this VFR will look quite different in clusters of methyl iodide, if present at all. We note that the $v_3 = 1$ VFR has been suggested to play a role in photofragmentation of the $I^- \cdot CH_3I$ anion yielding $I^-$ ions (Dessent *et al.*, 1996).

The cross-sections for $(CH_3I)_q\,I^-$ ($q = 1, 2$) cluster anion formation reveal in fact a dramatic influence of the cluster environment on the VFR observed for methyl iodide monomers: for $q = 1$ a weak, broad shoulder, shifted to lower energy, remains while for $q = 2$, no significant structure is observed. This behavior was attributed to solvation effects which move the resonance position to lower energies and substantially increase the resonance width. In Fig. 52 we show calculated cross-sections for different solvation energies (but for a fixed polarizability) using a modified $R$-matrix model (Weber *et al.*, 2000).

However, the cusp structure associated with the threshold for vibrational excitation of the symmetric C–I stretch at $E = 66.1$ meV is still clearly seen in Fig. 52, whereas experimental data do not exhibit the cusp. This can be explained by interaction of the C–I stretch mode with other modes in the complex. In particular, the vibrational dynamics of the dimer is influenced by interaction between the I atoms. To account for this effect, a model (Thoss and Domcke, 1998) describing interaction between a specific (system) vibrational mode with a background (bath) mode was adopted in Weber *et al.* (2000). The background mode was described by the displaced harmonic oscillator model (Domcke and Cederbaum, 1977). This approach allows to construct the Green's function describing both C−I and soft-mode vibrations. After calculation of its matrix elements, the problem is reduced to solving a system of $N_v \times N_p$ linear algebraic equations for $N_v \times N_p$ attachment amplitudes, where $N_v$ is the number of states describing C–I stretch vibrations, and $N_p$ the number of states describing the soft-mode vibrations. The bath mode is characterized by the frequency parameter $\omega$ and the coupling parameter $\Theta = (1/2)\mu\omega R_0^{\,2}$ where $\mu$ is the reduced mass corresponding to soft-mode vibrations and $R_0$ is the distance between the
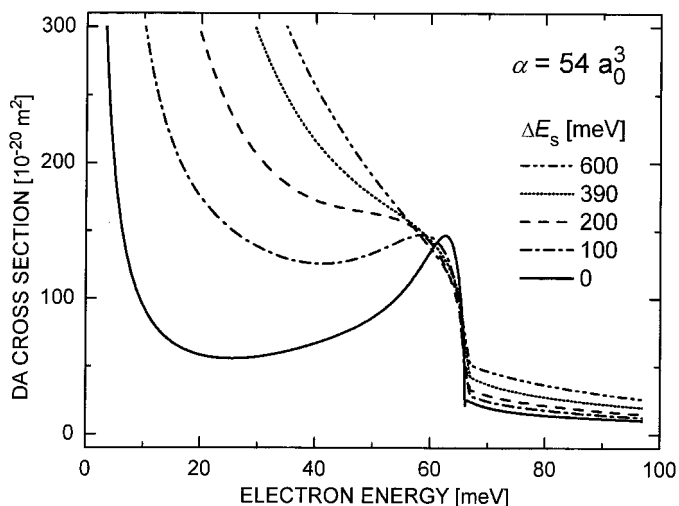
FIG. 52. Calculated cross-sections for dissociative attachment to $CH_3I$ monomers with potential curves, "solvation"-shifted by the indicated amounts (from Weber *et al.*, 2000).

minima of the two porential curves describing the neutral molecule and the negative ion. Another effect which was included in the calculations is an additional polarization interaction for the incident electron due to the presence of the second molecule in the dimer. Some sample results for the DA rate coefficients and their comparison with experiment are presented in Fig. 53.

Agreement between theory and experiment should be considered more qualitative than quantitative at the present stage: the theory confirms that the solvation and polarization effects destroy the vibrational Feshbach resonance and lead to almost complete disappearance of the threshold cusp due to coupling with the bath mode. On the other hand, the theoretical rate coefficient drops with energy too fast as compared to the experimental observations. One of the possible reasons for this is an overestimation of the polarization energy in the theoretical model. Indeed, calculations with a polarization potential whose strength is reduced at shorter distances lead to a better agreement with experiment, as we can see from Fig. 53.

## D. Related Topic: Positron Annihilation

Although this review is focused on electron–molecule collisions, a related topic of positron–molecule collisions is important and will be briefly
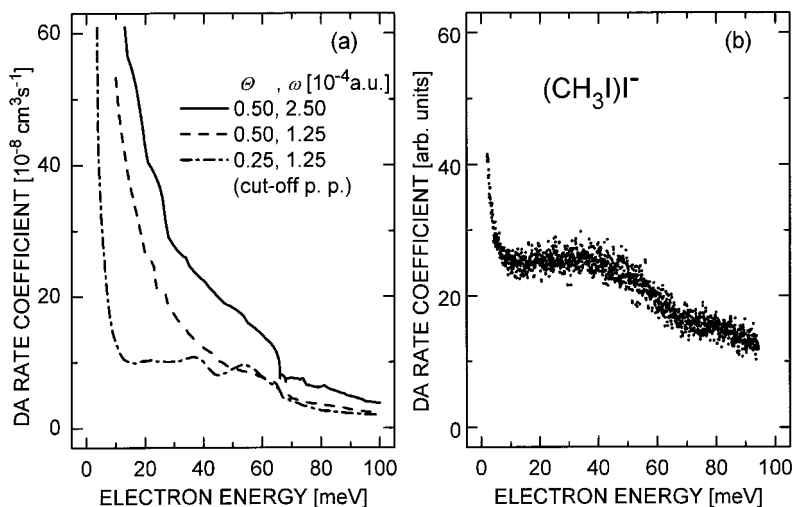
Fig. 53. Comparison between (a) calculated and (b) experimental rate coefficients for dissociative attachment to methyl iodide dimers yielding $(CH_3I)I^-$ ions. The theoretical curves correspond to different choices of the bath-mode parameters. The chain curve represents a model with a reduced polarization interaction (from Weber *et al.*, 2000).

discussed here. Resonances in positron collisions with atomic and molecular systems were predicted in several theoretical works (for a more complete review of the subject the reader is referred to the paper of Kimura *et al.* (2000)), however until recently there was no direct experimental evidence for them. Indirect evidence for these resonances was obtained in 1963 when Paul and Saint-Pierre (1963) observed very high annihilation rates in thermal positron collisions with certain large molecules. Surko *et al.* (1988) extended these studies to larger organic molecules. More recently these findings were confirmed by a series of experiments performed at the University of San Diego (Murphy and Surko, 1991; Iwata *et al.*, 1995; Iwata *et al.*, 2000).

The annihilation rate is usually characterized by the parameter

$$Z_{\text{eff}} = \lambda(\pi r_0^2 cn)^{-1}, \tag{45}$$

where $\lambda$ is the observed annihilation rate, $r_0$ is the classical electron radius, $c$ is the speed of light, and $n$ is the molecule number density. Equation (45) reflects a naive view of the annihilation process according to which the annihilation rate can be obtained by multiplication of the Dirac annihilation

rate of positronium (Ps) by an effective number $Z_{eff}$ of electrons in the target molecule. However measurements for many hydrocarbons and partially fluorinated hydrocarbons yield values of $Z_{eff}$ which exceed the actual number of electrons by several (sometimes 4 or even 5) orders of magnitude. This is particularly surprising because the measurements are pertinent to positron energies *below* the positronium formation threshold. However, Murphy and Surko (1991) found a simple (albeit pure empirical) scaling relation for all studied atoms and single-bonded nonpolar molecules.

$$\ln(Z_{eff}) = A(E_i - E_{Ps})^{-1}, \tag{46}$$

where $E_i$ is the ionization energy of the target and $E_{Ps}$ is the binding energy of positronium. Other interesting observations are: (i) the annihilation rates for the deuterated and protonated alkanes are very similar if not identical at room temperatures; (ii) singly fluorinated hydrocarbons have even higher annihilation rates whereas further fluorination leads to a decrease of annihilation rate with the perfluorinated molecule having the lowest rate; (iii) there is no strong correlation between $Z_{eff}$ and molecular dipole moment.

A theoretical model (Gribakin, 2000, 2001; Iwata *et al.*, 2000) with two regimes was proposed to explain the observed rates. According to the first mechanism, annihilation enhancement can occur due to a weakly bound or a virtual state in the positron–molecule complex. This mechanism (direct annihilation) can explain a moderate ($Z_{eff}$ below about 1000) enhancement of the rate. For higher rates a resonant mechanism associated with a temporary capture of the positron into the field of vibrationally excited molecules (VFR) is introduced.

The influence of VFRs on the annihilation rates was recently confirmed by experiments (Gilbert *et al.*, 2002; Barnes *et al.*, 2003) with positron beams whereby Ps annihilation rates were investigated as a function of the positron energies from 50 meV to several eV at an energy width of about 25 meV. Pronounced peaks below several vibrational excitation thresholds have been observed providing the first direct evidence for long-lived vibrational resonances of the positron–molecule complex. Two examples are shown in Fig. 54. The redshifts of the vibrational resonances (relative to the position of the C–H stretch mode, dashed line) amount to 0.03 eV in propane and 0.13 eV in heptane; they are interpreted as a measure of the positron–molecule binding energy (see Barnes *et al.*, 2003 for details).

The existence of VFRs in positron–molecule systems suggests that there should be bound states of positron–molecule systems. However, very little
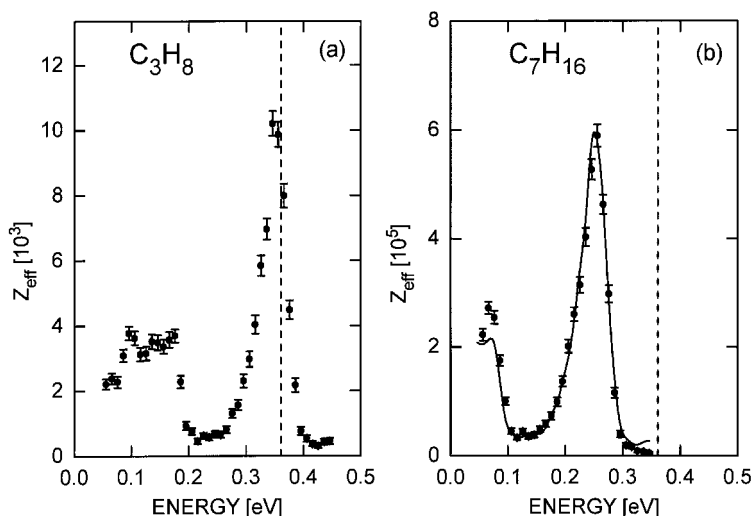
FIG. 54. Energy-resolved annihilation rates, $Z_{eff}$, for (a) propane and (b) heptane. For comparison, the solid line in (b) shows $Z_{eff}$ for propane, scaled by 60 and shifted downward in energy by 0.1 eV (Barnes *et al.*, 2003).

is known about such systems. Even for positron–atom bound states, calculations became possible only recently (Dzuba *et al.*, 1995; Ryzhikh and Mitroy, 1997), and virtually nothing is known about molecules, although some results were obtained for the relation between positron affinities and molecular dipole moments (Tachikawa *et al.*, 2001). However, experimental data do not indicate any significance of the dipole moment for enhanced annihilation. Theoretical calculations of positron affinities of molecules are particularly difficult because of the relative weakness of positron–molecule interactions as compared to the electron–molecule interaction. The reason is simple: the static potential for the positron–molecule interaction is repulsive and therefore it strongly reduces the attraction due to the polarization interaction (Kimura *et al.*, 2000). This makes inclusion of positron–electron correlations especially important, therefore calculations of positron affinities are more difficult than those of electron affinities.

Another theoretical challenge has to do with the density of VFRs. According to recent work on positron annihilation rates (Gribakin, 2000, 2001), a high density of VFRs, growing exponentially with the number of atoms in the molecule, is required in order to explain the measured annihilation rates. This was confirmed by recent experiments of Barnes *et al.* (2003) which indicate a strong correlation between the spectrum of

vibrational modes and the annihilation spectrum for propane and heptane (see Fig. 54). Although we can expect that VFRs are a quite common phenomenon in electron and positron scattering by polyatomic systems, there are no theoretical calculations to confirm this judgement. Finally, studies of VFRs in electron–molecule scattering show that VFRs are typically supported by the long-range field of the molecule, whereas annihilation data do not exhibit any correlation between the observed rates and molecular dipole moments. Certainly, more experimental and theoretical studies are required to explain this interesting phenomenon. The theory is still in a very preliminary stage at this point. No calculations of VFRs and corresponding annihilation rates are available even for simple diatomic molecules.

However, one aspect of the theory, namely the behavior of the annihilation cross-section near the threshold for positronium formation, has been studied in some detail. Equation (46) might suggest that the annihilation cross-section exhibits a singularity near the threshold. Indeed, according to the model of Laricchia and Wilkin (1997), $Z_{eff}$ grows as $|E_i - E_{Ps}|^{-1}$. Variational calculations (Van Reeth and Humberston, 1998) demonstrate a weaker divergence $|E_i - E_{Ps}|^{-1/2}$. However, any divergence would violate unitarity of the $S$ matrix. To resolve this controversy one has to introduce the coupling between the Ps formation channel and the annihilation channel (Gribakin and Ludlow 2002; Igarashi $et$ $al.$, 2002). Due to this coupling the Ps formation channel is blurred by the annihilation energy width, and the $|E_i - E_{Ps}|^{-1/2}$ singularity is removed. Recent calculations (Gribakin and Ludlow, 2002; Igarashi $et$ $al.$, 2002) for annihilation in e$^+$–H collisions demonstrate that the cross-section behaves as a continuous function of positron energy near the Ps formation threshold. This result actually follows from a general theory of threshold behavior for creation of an unstable particle (Baz', 1961).

# V. Conclusions and Perspectives

As shown in this review, significant progress has been made over the past decade in our understanding of resonance and threshold phenomena in low-energy electron interactions with molecules and clusters. At very low energies (below about 0.2 eV) novel photoelectron techniques have allowed to study attachment cross-sections for both molecules and molecular clusters at unprecedented (sub-) meV resolution and down to sub- meV energies. Sharp vibrational Feshbach resonances have been discovered in molecules as well as molecular clusters, and the fundamental threshold behaviour was convincingly demonstrated for several polar and nonpolar

molecules. With free electron cross-sections measured to sub- meV energies, a realistic extrapolation to zero energy became possible, and accurate absolute attachment cross-sections were established with reference to reliable thermal rate coefficients due to electron swarm experiments. For the first time a critical comparison between free electron attachment and Rydberg electron transfer data became possible by calculating – within the quasi-free electron model for Rydberg electron collisions – the RET rate coefficient from measured free electron attachment cross-sections, and good agreement was observed for several molecules (Klar *et al.*, 1994b, 2001a, b; Dunning, 1995).

Using synchrotron-based VUV photoelectron sources, measurements of total cross-sections have been extended down to about 10 meV. Strong resonances have been detected in $CS_2$ which are similarly present in the differential elastic cross-section. It can be expected that these observations are just the beginning of an exciting future of 'cold electron collisions' (Field *et al.*, 2001a) with many resonances yet to discover in electron scattering and attachment cross-sections. Intriguing examples of such features are the observation of a deep dip in the total scattering cross-section at 0.1 eV for nitrobenzene (Lunt *et al.*, 2001) and at 0.07 eV for the $CF_3Cl$ molecule (Field *et al.*, 2001c), tentatively ascribed to interference between a direct channel of rotational excitation and indirect excitation via a short-lived negative ion state. Their observation and explanation poses a challenge to theory.

Substantial progress has also been made in angle-differential electron scattering studies, using optimized and well-calibrated electrostatic spectrometers at energy widths below 10 meV. Theoretical *ab initio* DA and VE cross-sections for hydrogen halides, obtained with the nonlocal resonance model, agree very well with accurate measurements, and, what is even more important, many features observed there, like threshold peaks, boomerang oscillations and VFRs, are now well understood. However, for several other diatomic molecules the situation is not as clear. In important cases such as chlorine, no reliable experimental cross-sections for vibrational excitation are available, and *R*-matrix calculations of VE and DA cross-sections in part had to use semiempirical input. A fully *ab initio* calculation of VE and DA involving fluorine molecules has been carried out, but the controversy related to the low-energy behavior of DA (p-wave versus s-wave) is still unresolved. Certainly more experimental results are needed here.

The situation with polyatomic molecules is even more complicated. We have achieved a qualitative understanding of some important features. The known cases suggest that threshold peaks and possibly also sharp structures due to VFR may be found in many, presumably most polyatomic

molecules. They are linked to anion states with an electron in a spatially diffuse wave function, bound by a combination of dipolar and polarization forces; the dipolar forces may be active even in molecules without a permanent dipole moment (such as $CO_2$) when the parent vibrational state of the VFR is not totally symmetric and acquires a nonzero dipole moment upon variation of its normal coordinate. The VFRs may substantially affect the cross-sections by acting as doorways into valence, possibly dissociative states. The outer wells in anion potentials and the associated outer well resonances described here are likely to represent prototype cases for outer wells in many polyatomic molecules. Here the electron is in a valence orbital whose antibonding properties are responsible for the substantially different geometry. More studies of polyatomic molecules at energies below about 1 eV will be needed to confirm these expectations.

Completely *ab initio* calculations of near-threshold and resonance processes for polyatomic molecules are still very difficult. In this field model and semiempirical calculations continue to play an important role. Approaches such as the resonance $R$-matrix method allow us to produce cross-sections for many transitions using just a few adjustable parameters. This method was particularly successful for our understanding of VFRs and threshold features in electron collisions with methyl halides. The major challenge in this field is extension of the existing methods towards incorporation of several vibrational modes. For this purpose the wave-packet propagation method (McCurdy and Turner, 1983; Kazansky, 1995) seems to be very promising. Some results have been recently obtained for dissociative attachment (Kazansky, 1995) and vibrational excitation (Rescigno *et al.*, 2002) of the $CO_2$ molecule. However, the split time propagation method has been implemented so far only within the framework of the local resonance model which is not able to describe correctly threshold phenomena and VFRs. A relevant example is dissociative attachment to the $CH_2Br_2$ molecule with the formation of $Br^-$. This process cannot be described in a one vibrational mode approximation. On the other hand, a multidimensional description of the vibrational dynamics should also include nonlocal effects in order to reproduce the VFR observed below the threshold for excitation of the symmetric C–Br stretch. Another challenging example is a recent discovery of a zero energy peak in $O^-$ formation due to dissociative electron attachment to ozone (Senn *et al.*, 1999), which may play an important role in the destruction of ozone in the earth's atmosphere; it is still waiting for an explanation, also in view of the fact that thermal rate coefficients for electron attachment to ozone are not compatible with a zero energy resonance (van Doren *et al.*, 2003).

With the increasing complexity of the target, the situation is becoming even more challenging. In particular, we do not have a general theory of electron attachment to clusters, although some observed features in electron-cluster interactions, like VFRs and their dependence on cluster environment, have received an explanation recently. The resonance $R$-matrix theory has been generalized to describe DA to methyl iodide clusters. However, almost no calculations, except some preliminary results for $CO_2$ clusters (Tsukada *et al.*, 1987), were done for nondissociative attachment. The major remaining task here is the correct account for the coupling between the phonon modes in the cluster and the vibrational modes of individual molecules leading to VFRs in nondissociative attachment. Several controversies in low-energy electron attachment to $C_{60}$ remain unresolved and demand further work.

Although not dealt with in this review, we mention metal clusters as another object for future studies. One-electron shape resonances in elastic scattering (Bernath *et al.*, 1995; Ipatov *et al.*, 1998a) and collective plasmon resonances in elastic and inelastic electron collisions with metal clusters (Gerchikov *et al.*, 1998; Ipatov *et al.*, 1998b; Connerade *et al.*, 2000) have been predicted in theoretical calculations and wait for experimental confirmation. Measurements of electron capture by sodium clusters (Kasperovich *et al.*, 2000a, b) indicate the validity of the Langevin formula for capture, as modified by employing the full image-charge interaction potential which accounts for the finite size of the cluster (Kasperovich *et al.*, 2000b). Evidence for resonance-enhanced electron capture by potassium clusters has been reported by Sentürk *et al.* (2000). Another class of objects, attracting strongly rising interest recently, are biomolecules. One of the driving motivations is the question how radiation damage is induced by the interaction of slow (secondary) electrons with the constituents of biological systems. Here we just mention pioneering work by Boudaïffa *et al.* (2000) who reported resonant formation of DNA strand breaks by low-energy electrons.

Studies of vibrational resonances in positron–molecule collisions are only at the beginning stage. Their important observation in recent experiments has received only qualitative explanation so far, and many unanswered questions exist in this field. In particular we do not know yet why the annihilation rates are high in the thermal-energy region, well below the threshold for vibrational excitation. No calculations of electron affinities of molecular targets, supporting the assumption about VFRs in positron-molecule scattering, exist. The observed widths of VFRs in these processes are also awaiting for theoretical explanations.

Progress in future work on high-resolution low-energy electron (as well as positron) collisions will inevitably be bound to improved experimental

techniques. Higher electron currents at energy widths in the meV range are mandatory for cases in which the product of cross-section and target density is intrinsically low. While laser photoelectron sources involving *gas phase* atoms are increasingly affected by energy broadening due to photoion space charge at currents above about $100\,pA$, photoemission from suitably prepared solid state surfaces (e.g. doped GaAs) holds promise for major progress (e.g. Pastuszka *et al.*, 2000) when much higher electron currents at energy widths around $10\,meV$ are needed. This technique is, however, technologically demanding in that ultrahigh vacuum requirements for the electron source have to be combined with a gaseous target of sufficient density.

Most of the work discussed in this review dealt with molecules and clusters in their electronic and vibrational ground state. Regarding electron collisions with electronically excited atoms and molecules, the status of the field has been recently surveyed by Christophorou and Olthoff (2001b). The obvious experimental challenge lies in the preparation of a sufficient density of selectively excited states to allow electron collision studies at a decent energy resolution. Advances in laser technology (i.e. high intensity laser diodes as pumps of solid state lasers in combination with efficient nonlinear frequency conversion techniques) hold hope for the availability of broadly tunable, narrowband lasers with *high* repetition rate *and* intensity. Such laser systems could access electronically excited molecules with intermediate lifetimes comparable to the molecular transit time through the collision region with the electron beam.

For molecules in the electronic ground state, it is known that electron collision processes can depend very strongly on the initial vibrational state, yet rather few studies went beyond the conventional approach of thermally heating the target molecules in investigating the effects of vibrational excitation. However, the hope for efficient preparation of selectively excited vibrational modes has recently substantially increased. Although the STIRAP method (Vitanov *et al.*, 2001) involving cw lasers is suitable only in few cases (as discussed for $Na_2$ in this review), it may be applied to a broader range of molecules when pulsed lasers with sufficient coherence, pulse energy and repetition rate become available. With the advent of efficient optical parametric oscillators (OPO) and generators (OPG) in the infrared region (so far up to about $4\,\mu m$), which involve quasi-phase matching in periodically poled solid state crystals such as $LiNbO_3$ (see, e.g., Kovalchuk *et al.*, 1997, for a cw single mode OPO and Bäder et al., 2003, for a transform-limited, seeded nanosecond OPG with $10\,kHz$ repetition rate), the future looks promising for efficient excitation of many dipole-allowed vibrational transitions, including the C–H stretch mode. This should allow a broad range of high resolution

studies of electron scattering and attachment involving vibrationally excited molecules.

## VI. Acknowledgements

## VII. References

Abouaf, R., and Teillet-Billy, D. (1977). Fine structure in dissociative attachment cross sections for HCl and DCl. *J. Phys. B* **10**, 2261–2268.

Abouaf, R., and Teillet-Billy, D. (1980). Fine structure in the dissociative attachment cross sections for HBr and HF. *Chem. Phys. Lett.* **73**, 106–109.

Ajello, J. M., and Chutjian, A. (1979). Line shapes for attachment of threshold electrons to $SF_6$ and $CFCl_3$: Threshold photoelectron (TPSA) studies of Xe, CO, and $C_2H_2$. *J. Chem. Phys.* **71**, 1079–1087.

Alajajian, S. H., Bernius, M. T., and Chutjian, A. (1988). Electron attachment lineshapes, cross sections and rate constants at ultra-low energies in several halomethyl and haloethyl molecules. *J. Phys. B* **21**, 4021–4033.

Alge, E., Adams, N. G., and Smith, D. (1984). Rate coefficients for the attachment reactions of electrons with c-$C_7F_{14}$, $CH_3Br$, $CF_3Br$, $CH_2Br_2$ and $CH_3I$ determined between 200 and 600 K using the FALP technique. *J. Phys. B*. **17**, 3827–3833.

Allan, M. (1989). Study of triplet states and short-lived negative ions by means of electron impact spectroscopy. *J. Electron Spectrosc.* **48**, 219–351.

Allan, M. (1995). Measurement of absolute differential cross sections for vibrational excitation of $O_2$ by electron impact. *J. Phys. B* **28**, 5163–5175.

Allan, M. (2000). Excitation of the $2^3S$ state of helium by electron impact from threshold to 24 eV: measurements with the 'magnetic angle changer'. *J. Phys. B* **33**, L215–L220.

Allan, M. (2001a). Selectivity in the excitation of fermi-coupled vibrations in $CO_2$ by impact of slow electrons. *Phys. Rev. Lett.* **87**, 033201 (1–4).

Allan, M. (2001b). Threshold peaks in vibrational excitation by electron impact, In: I. I. Fabrikant, G. A. Gallup, and P. D. Burrow, Eds. "Int. Symp. on Electron-Molecule Collisions and Swarms," Abstracts. pp. 67–70, Lincoln, NE, USA.

Allan, M. (2001c). Threshold peaks in vibrational excitation of polyatomic molecules. In: S. Datz, M. E. Bannister, H. F. Krause, L. H. Saddiq, D. R. Schultz, And C. R. Vane, Eds. "Abstracts of contributed papers of the 22. Int. Conf. on Photonic Electronic and Atomic Collisions (XXII ICPEAC)," pp. 275, Santa Fe, N.M., USA.

Allan, M. (2002a). Vibrational structures in electron-$CO_2$ scattering below the $^2\Pi_u$ shape resonance. *J. Phys. B* **35**, L387–L395.

Allan, M. (2002b). Selective excitation of fermi-coupled vibrations in $CO_2$ by impact of slow electrons. In J. Burgdörfer, J. S. Cohen, S. Datz, C. R. Vane, Eds. "Photonic, Electronic, and Atomic Collisions," pp. 284–287, Rinton Press, Princeton, NY, USA.

Allan, M., and Fabrikant, I. I. (2002). Threshold peaks and structures in vibrational excitation of $CH_3I$ by electron impact. *J. Phys. B* **35**, 1025–1034.

Allan, M., and Moreira, O. (2002). Excitation of the symmetric and antisymmetric stretch vibrations of $H_2O$ by electron impact. *J. Phys. B*. **35**, L37–L42.

Allan, M., Čížek, M., Horáček, J., and Domcke, W. (2000). Electron scattering in cooled HCl: boomerang structures and outer-well resonances in elastic and vibrational excitation cross sections. *J. Phys. B* **33**, L209-L213.

Allan, M., Craig, N. C., and McCarty, L. V. (2002). Vibrational excitation of *cis*- and *trans*-1,2-difluoroethenes by electron impact: effect of dipole moment on the threshold peaks. *J. Phys. B* **35**, 523–532.

Allan, M. (2003). Threshold peaks and structures in elastic and vibrationally inelastic electron impact cross sections for $CS_2$. *J. Phys. B* **36**, 2489–2500.

Allan, M. and Skalický, T. (2003). Structures in elastic vibrational, and dissociative electron attachment cross sections in $N_2O$ near threshold. *J. Phys. B*. 3397–3409.

Andersen, N., and Bartschat, K. (1996). Complete experiments in electron-atom collisions. *Adv. At. Mol. Opt. Phys.* **36**, 1–87.

Andersen, T., Haugen, H. K., and Hotop, H. (1999). Binding energies in atomic negative ions: III. *J. Phys. Chem. Ref. Data* **28**, 1511–1533.

Antoni, T., Jung, K., Ehrhardt, H., and Chang, E. S. (1986). Rotational branch analysis of the excitation of the fundamental vibrational modes of $CO_2$ by slow electron collisions. *J. Phys. B* **19**, 1377–1396.

Azria, R., Abouaf, R., and Teillet-Billy, D. (1982). Symmetry of $Cl_2^{-*}$ resonant states formed in dissociative electron attachment reaction on $Cl_2$. *J. Phys. B* **15**, L569–L574.

Bäder, U., Mattern, T., Bauer, T., Bartschke, J., Rahm, M., Borsutzky, A., and Wallenstein, R. (2003). Pulsed nanosecond optical parametric generator based on periodically poled lithium niobate. *Opt. Commun.* **217**, 375–380.

Bailey, C. G., Lavrich, D. J., Serxner, D., and Johnson, M. A. (1996). Autodetachment from vibrational levels of the $O_2^- \ A \ ^2\Pi_u$ resonance across its dissociation limit by photoexcitation from $O_2^- \ X \ ^2\Pi_g$. *J. Chem. Phys.* **105**, 1807–1814.

Bardsley, J. N. (1968). Configuration interaction in the continuum states of molecules. *J. Phys. B* **1**, 349–364.

Bardsley, J. N., and Mandl, F. (1968). Resonant scattering of electrons by molecules. *Rep. Prog. Phys.* **31**, 471–511.

Bardsley, J. N., and Wadehra, J. M. (1983). Dissociative attachment in HCl, $D_2$, and $F_2$. *J. Chem. Phys.* **78**, 7227–7234.

Barnes, L. D., Gilbert, S. J., and Surko, C. M. (2003). Energy-resolved positron annihilation for molecules. *Phys. Rev. A* 67, 032706 (1–11).

Barsotti, S., Leber, E., Ruf, M.-W., and Hotop, H. (2002a). High resolution study of cluster anion formation in low-energy electron collisions with molecular clusters of $CO_2$, $CS_2$, and $O_2$. *Int. J. Mass Spectrom.* **220**, 313–330.

Barsotti, S., Ruf, M.-W., and Hotop, H. (2002b). Clear experimental evidence for p-wave attachment-threshold behavior in electron attachment to chlorine molecules. *Phys. Rev. Lett.* **89**, 083201 (1–4).

Barsotti, S., Ruf, M.-W., and Hotop, H. (2003a). Laser photoelectron attachment to $SF_6$ molecules in a seeded supersonic beam at temperatures from 300 K to 600 K. (in preparation).

Barsotti, S., Sommerfeld, T., Ruf, M.-W., and Hotop, H. (2003b). High resolution study of cluster anion formation in low-energy electron collisions with OCS clusters. *Int. J. Mass. Spectrom.* (submitted).

Baz', A. I. (1958). The energy dependence of a scattering cross section near the threshold of a reaction. *Sov. Phys. JETP* **6**, 709–713.

Baz', A. I. (1961). Energy dependence of cross sections near the "threshold" for unstable particle production. *Sov. Phys. JETP* **13**, 1058–1061.

Becker, K. H., McCurdy, C. W., Orlando, T. W., and Rescigno, T. M. (Eds.) (2000). "Current Status and Future Perspectives of Electron Interactions with Molecules, Clusters, Surfaces, and Interfaces," Stevens Inst. Technol., Hoboken, NJ, USA.

Bernath, M., Dragún, O., Spinella, M. R., Massmann, H., and Pacheco, J. M. (1995). Response of metal clusters to elastic electron impact. *Phys. Rev. A* **52**, 2173–2178.

Bethe, H. A. (1935). Theory of disintegration of nuclei by neutrons. *Phys. Rev.* **47**, 747–759.

Beyer, T., Nestmann, B. M., Peyerimhoff, S. D. (2001). Resonant features of inelastic electron scattering off $CF_3Cl$ in the low-energy region. *J. Phys. B* **34**, 3703–3716.

Birtwistle, D. T., and Herzenberg, A. (1971). Vibrational excitation of $N_2$ by resonance scattering of electrons. *J. Phys. B* **4**, 53–70.

Blatt, J. M., and Weisskopf, V. F. (1952). "Theoretical Nuclear Physics," Wiley, NY, USA.

Bloch, F., and Bradbury, N. E. (1935). On the Mechanism of Unimolecular Electron Capture. *Phys. Rev.* **48**, 689–695.

Bömmels, J., Leber, E., Gopalan, A., Weber, J. M., Barsotti, S., Ruf, M.-W., and Hotop, H. (2001). Energy broadening due to photoion space charge in a high resolution laser photoelectron source. *Rev. Scient. Instrum.* **72**, 4098–4105.

Boness, M. J. W., and Schulz, G. J. (1974). Vibrational excitation in $CO_2$ via the 3.8 eV resonance. *Phys. Rev. A* **9**, 1969–1979.

Bonin, K., and Kresin, V. (1997). "Electric-Dipole Polarizabilities of Atoms, Molecules, and Clusters," World Scientific, Singapore.

Boudaïffa, B., Cloutier, P., Hunting, D., Huels, M. A., and Sanche, L. (2000). Resonant formation of DNA strand breaks by low-energy (3–20 eV) electrons. *Science* 287, 1658–1660.

Brems, V., Beyer, T., Nestmann, B. M., Meyer, H.-D., and Cederbaum, L. S. (2002). *Ab initio* study of the resonant electron attachment top the $F_2$ molecule. *J. Chem. Phys.* **117**, 10635–10647.

Brunger, M. J., and Buckman, S. J. (2002). Electron-molecule scattering cross-sections. I. Experimental techniques and data for diatomic molecules. *Phys. Rep.* **357**, 215–458.

Brüning, F., Matejcik, S., Illenberger, E., Chu, Y., Senn, G., Muigg, D., Denifl, G., and Märk, T. D. (1998). Effects of temperature on the dissociative electron attachment to $N_2O$. *Chem. Phys. Lett.* **292**, 177–182.

Buck, U., and Meyer, D. (1986). Electron bombardment fragmentation of Ar van der Waals clusters by scattering analysis. *J. Chem. Phys.* **84**, 4854–4861.

Buck, U. (1988). Properties of neutral clusters from scattering experiments. *J. Phys. Chem.* **92**, 1023–1031.

Buckman, S. J., and Clark, C. W. (1994). Atomic negative-ion resonances. *Rev. Mod. Phys.* **66**, 539–655.

Burke, P. G. (1979). Theory of low energy electron-molecule collisions. *Adv. At. Mol. Phys.* **15**, 471–506.

Burrow, P. D. (1974). Threshold structure in the elastic cross section for scattering of slow electrons from HCl and HBr. *J. Phys. B* **7**, L385–L388.

Burrow, P. D., Modelli, A., Chiu, N. S., and Jordan, K. D. (1982). Temporary negative ions in the chloromethanes $CHCl_2F$ and $CCl_2F_2$: Characterization of the $\sigma^*$ orbitals. *J. Chem. Phys.* **77**, 2699–2701.

Burrow, P. D., Gallup, G. A., Fabrikant, I. I., and Jordan, K. D. (1997). Dissociative attachment studies of halogen-containing molecules: Problems, applications and challenges. *Aust. J. Phys.* **49**, 403–423.

Carman, H. S. Jr., Klots, C. E., and Compton, R. N. (1990). Isotope-dependent rate constants for $CS_2^-$ formation in $Cs(ns, nd) + CS_2$ collisions. *J. Chem. Phys.* **92**, 5751–5752.

Chantry, P. J. (1969). Temperature dependence of dissociative attachment in $N_2O$. *J. Chem. Phys.* **51**, 3369–3379.

Chantry, P. J. (1982). Negative ion formation in gas lasers. In E. W. McDaniel and W. L. Nighan, Eds. "Gas Lasers. Applied Atomic Collision Physics 3," pp. 35–70, Academic Press, New York.

Chase, D. M. (1956). Adiabatic approximation for scattering processes. *Phys. Rev.* **104**, 838–842.

Chen, C. L., and Chantry, P. J. (1979). Photon-enhanced dissociative electron attachment in $SF_6$ and its isotopic selectivity. *J. Chem. Phys.* **71**, 3897–3907.

Chen, E. C. M., and Wentworth, W. R. (1983). Determination of molecular electron affinities using the electron capture detector in the pulse sampling mode at steady state. *J. Phys. Chem.* **87**, 45–49.

Christophorou, L. G. (1976). Electron attachment to molecules in dense gases ("quasi-liquids"). *Chem. Rev.* **76**, 409–423.

Christophorou, L. G. (1978). The lifetimes of metastable negative ions. *Adv. in Electronics and Electron Physics* **46**, 55–129.

Christophorou, L. G. (Ed.) (1984). "Electron-Molecule Interactions and their Applications," Vols. 1 and 2, Academic Press, New York.

Christophorou, L. G. (1987). Electron attachment and detachment processes in electronegative gases. *Contrib. Plasma Phys.* **27** (4), 237–281.

Christophorou, L. G. (1996). The dependence of the thermal electron attachment rate constant in gases and liquids on the energy position of the electron attaching state. *Z. Phys. Chem.* **195**, 195–215.

Christophorou, L. G., and Olthoff, J. K. (1999). Electron interactions with $Cl_2$. *J. Phys. Chem. Ref. Data* **28**, 131–169.

Christophorou, L. G., and Olthoff, J. K. (2000). Electron interactions with $SF_6$. *J. Phys. Chem. Ref. Data* **29**, 267–330.

Christophorou, L. G., and Olthoff, J. K. (2001a). Electron collision data for plasma-processing gases. *Adv. At. Mol. Opt. Phys.* **44**, 59–98.

Christophorou, L. G., and Olthoff, J. K. (2001b). Electron Interactions with Excited Atoms and Molecules. *Adv. At. Mol. Opt. Phys.* **44**, 155–293.

Chu, S. C., and Burrow, P. D. (1990). Dissociative attachment of electrons in the chloromethanes. *Chem. Phys. Lett.* **172**, 17–22.

Chutjian, A., and Alajajian, S. H. (1985). *s*-wave threshold in electron attachment: Observations and cross sections in $CCl_4$ and $SF_6$ at ultralow electron energies. *Phys. Rev. A* **31**, 2885–2892.

Chutjian, A., and Alajajian, S. H. (1987). Electron attachment in $F_2$: Conclusive demonstration of nonresonant, s-wave coupling in the limit of zero electron energy. *Phys. Rev. A* **35**, 4512–4514.

Chutjian, A. (1992). Electron attachment to molecules at ultralow electron energies. In: W. R. MacGillivray, I. E. McCarthy, M. C. Standage, Eds. "Electronic and Atomic Collisions," pp. 127–138, Adam Hilger, Bristol.

Chutjian, A., Garscadden, A., and Wadehra, J. M. (1996). Electron attachment to molecules at low electron energies. *Phys. Rep.* **264**, 393–470.

Čížek, M., Horáček, J., and Domcke, W. (1999). Associative detachment, dissociative attachment, and vibrational excitation of HCl by low-energy electrons. *Phys. Rev. A* **60**, 2873–2881.

Čížek, M., Horáček, J., Sergenton, A.-Ch., Popovic, D. B., Allan, M., Domcke, W., Leininger, T., and Gadea, F. X. (2001a). Inelastic low-energy electron collisions with the HBr and DBr molecules: Experiment and theory. *Phys. Rev. A* **63**, 062710(1–14).

Čížek, M., Horáček, J., Thiel, F. A. U., and Hotop, H. (2001b). Associative detachment in low-energy collisions between hydrogen atoms and atomic halogen anions. *J. Phys. B* **34**, 983–1004.

Čížek, M., Horáček, J., Allan, M., Fabrikant, I. I., Domeke, W. (2003). Vibrational excitation of hydrogen fluoride by low-energy electrons: theory and experiment. *J. Phys. B* **36**, 2837–2849.

Clark, C. W. (1979). Electron scattering from diatomic polar molecules. II. Treatment by frame transformations. *Phys. Rev. A* **20**, 1875–1889.

Compton, R. N. (1980). Electron attachment to molecules. In: N. Oda and, K. Takayanagi, Eds. "Electronic and Atomic Collisions," pp. 251–262, North-Holland, Amsterdam.

Compton, R. N., and Hammer, N. I. (2001). Multipole-bound molecular anions. *Adv. in Gas-Phase Ion Chemistry*, Vol. **4**, 257–305. Elsevier Science B.V.

Compton, R. N., Reinhardt, P. W., and Cooper, C. D. (1975). Collisional ionisation of Na, K, and Cs by $CO_2$, COS, and $CS_2$: molecular electron affinities. *J. Chem. Phys.* **63**, 3821–3827.

Compton, R. N., Carman, H. S. Jr., Desfrançois, C., Abdoul-Carmine, H., Schermann, J.-P., Hendricks, J. H., Lyapustina, S. A., and Bowen, K. H. (1996). On the binding of electrons to nitromethane: dipole and valence bound anions. *J. Chem. Phys.* **105**, 3472–3478.

Connerade, J.-P., Gerchikov, L. G., Ipatov, A. N., and Senturk, Ş. (2000). Resonance effects in inelastic scattering of low-energy electrons from metallic clusters. *J. Phys. B* **33**, 5109–5120.

Crawford, O. H., and Garrett, W. R. (1977). Electron affinities of polar molecules. *J. Chem. Phys.* **66**, 4968–4970.

Crawford, O. H., and Koch, B. J. D. (1974). Diabatic capture in dissociative attachment. *J. Chem. Phys.* **60**, 4512–4519.

Crompton, R. W. (1994). Benchmark measurements of cross sections for electron collisions: Electron swarm methods. *Adv. At. Mol. Opt. Phys.* **33**, 97–148.

Cubric, Mercer, D. J. L., Channing, J. M., King, G. C., and Read, F. H. (1999) A study of inelastic electron scattering in He covering the complete angular range from 0° to 180°. *J. Phys. B* **32**, L45–L50.

Cvejanovic, S. (1993). Threshold and resonant features in the vibrational excitation functions of hydrogen halides. In: T. Andersen, B. Fastrup, F. Folkmann, H. Knudsen, Eds. "The Physics of Electronic and Atomic Collisions," AIP Conf. Proc. Vol. 295, pp. 390–401, A.I.P., New York.

Damburg, R. J. (1968). Threshold law for model with long-range interaction. *J. Phys. B* **1**, 1001–1003.

Datskos, P. G., Christophorou, L. G., and Carter, J. G. (1990). Temperature-enhanced electron attachment to $CH_3Cl$. *Chem. Phys. Lett.* **168**, 324–329.

Datskos, P. G., Christophorou, L. G., and Carter, J. G. (1992). Effect of temperature on the attachment of slow ($\leq 1\,eV$) electrons to $CH_3Br$. *J. Chem. Phys.* **97**, 9031–9035.

Desfrançois, C., Khelifa, N., Schermann, J. P. (1989). Very low energy electron attachment to $SF_6$ clusters. *J. Chem. Phys.* **91**, 5853–5854.

Desfrançois, C., Khelifa, N., Schermann, J.-P., Kraft, T., Ruf, M.-W., and Hotop, H. (1993). Energy exchanges following very low energy electron attachment to neat $CS_2$ and $CS_2$-containing clusters. *Z. Phys. D* **27**, 365–369.

Desfrançois, C., Abdoul-Carime, H., Adjouri, C., Khelifa, N., Schermann, J. P. (1994a). Dipole binding to a strongly polar molecule and its homogeneous clusters: Magic distribution of Acetonitrile cluster anions. *Europhys. Lett.* **26**, 25–30.

Desfrançois, C., Baillon, B., Schermann, J.-P., Arnold, S. T., Hendricks, J. H., and Bowen, K. H. (1994b). Prediction and observation of a new, ground state, dipole-bound dimer anion: the mixed water/ammonia system. *Phys. Rev. Lett.* **72**, 48–51.

Desfrançois, C., Abdoul-Carime, H., Khelifa, N., and Schermann, J.-P. (1994c). From $1/r$ to $1/r^2$ potentials: electron exchange between Rydberg atoms and polar molecules. *Phys. Rev. Lett.* **73**, 2436–2439.

Desfrançois, C., Abdoul-Carime, H., and Schermann, J.-P. (1996). Ground-state dipole-bound anions. *Int. J. Mod. Phys. B* **10**, 1339–1395.

Dessent, C. E. H., Bailey, C. G., and Johnson, M. A. (1996). *J. Chem. Phys.* **105**, 10416–10423.

Domcke, W. (1991). Theory of resonance and threshold effects in electron-molecule collisions: the projection-operator approach. *Phys. Rep.* **208**, 97–188.

Domcke, W., and Cederbaum, L. S. (1977). Theory of the vibrational structure of resonances in electron-molecule scattering. *Phys. Rev. A* **16**, 1465–1482.

Domcke, W., and Cederbaum, L. S. (1981). On the interpretation of low-energy electron-HCl scattering phenomena. *J. Phys. B* **14**, 149–173.

Domcke, W., and Mündel, C. (1985). Calculation of cross sections for vibrational excitation and dissociative attachment in HCl and DCl beyond the local-complex-potential approximation. *J. Phys. B* **18**, 4491–4509.

Dubé, L., and Herzenberg, A. (1977). Vibrational excitation of polar molecules by slow electrons: HCl. *Phys. Rev. Lett.* **38**, 820–823.

Dubé, L., and Herzenberg, A. (1979). Absolute cross sections from the "boomerang model" for resonant electron-molecule scattering. *Phys. Rev. A* **20**, 194–213.

Dunning, F. B. (1995). Electron-molecule collisions at very low electron energies. *J. Phys. B* **28**, 1645–1672.

Dzuba, V. A., Flambaum, V. V., Gribakin, G. F., and King, W. A. (1995). Bound states of positrons and neutral atoms. *Phys. Rev. A* **52**, 4541–4546.

Elhamidi, O., Pommier, J., and Abouaf, R. (1997). Low-energy attachment to fullerenes $C_{60}$ and $C_{70}$ in the gas phase. *J. Phys. B* **30**, 4633–4642.

Engelking, P. C. (1982). Strong electron-dipole coupling in photodetachment of molecular negative ions: Anomalous rotational thresholds. *Phys. Rev. A* **26**, 740–745.

Engelking, P. C., and Herrick, D. R. (1984). Effects of rotational doubling on the anomalous photodetachment thresholds resulting from electron-dipole interaction. *Phys. Rev. A* **29**, 2425–2428.

Estrada, H., and Domcke, W. (1985). On the virtual-state effect in low-energy electron-$CO_2$ scattering. *J. Phys. B* **18**, 4469–4479.

Etters, R. D., Flurchick, K., Pan, R. P., Chandrasekharan, V. (1981). Thermodynamic properties and phase transitions in $CO_2$ molecular clusters. *J. Chem. Phys.* **75**, 929–936.

Fabrikant, I. I. (1977). Threshold behavior of the cross sections for scattering of electrons by polar molecules. *Sov. Phys. JETP* **46**, 693–697.

Fabrikant, I. I. (1978). The influence of long-range interaction on the vibrational excitation of polar molecules by electrons. *J. Phys. B* **11**, 3621–3633.

Fabrikant, I. I. (1979). The influence of a $r^{-s}$ potential on electron scattering by polar molecules. *J. Phys. B* **12**, 3599–3610.

Fabrikant, I. I. (1983). Frame transformation effective-range theory: application to interaction of polar molecules with electrons. *J. Phys. B* **16**, 1269–1282.

Fabrikant, I. I. (1984). Effective-range analysis of low-energy electron scattering by non-polar molecules. *J. Phys. B* **17**, 4223–4233.

Fabrikant, I. I. (1985). *R*-matrix theory of vibrational excitation of the HCl molecule by slow electrons in the adiabatic approximation. *J. Phys. B* **18**, 1873–1879.

Fabrikant, I. I. (1986). *R*-matrix theory of inelastic processes in low-energy electron collisions with HCl molecule. *Z. Physik* **3**, 401–410.

Fabrikant, I. I. (1990). Resonance processes in e-HCl collisions: comparison of the *R*-Matrix and the nonlocal-complex-potential methods. *Comments At. Mol. Phys.* **24**, 37–52.

Fabrikant, I. I. (1991a). Quasiclassical *R*-matrix theory of inelastic processes in collisions of electrons with HCl molecules. *Phys. Rev. A* **43**, 3478–3486.

Fabrikant, I. I. (1991b). A model describing inelastic processes in low-energy electron collisions with methyl chloride. *J. Phys. B* **24**, 2213–2225.

Fabrikant, I. I., Kalin, S. A., and Kazansky, A. K. (1991). Inelastic processes in e-HCl collisions in the energy range including the dissociation threshold. *J. Chem. Phys.* **95**, 4966–4971.

Fabrikant, I. I., Kalin, S. A., and Kazansky, A. K. (1992). Resonant *R*-matrix theory of inelastic processes in collisions of electrons with HF molecules. *J. Phys. B* **25**, 2885–2898.

Fabrikant, I. I. (1994). Semiempirical calculations of inelastic electron-methylchloride scattering. *J. Phys. B* **27**, 4325–4336.

Fabrikant, I. I. (1996). Electron scattering by neutral targets at milli- and submilli-electron-volt energies. *Comments At. Mol. Phys.* **32**, 267–279.

Fabrikant, I. I., and Hotop, H. (2001). Low-energy behavior of exothermic dissociative electron attachment. *Phys. Rev. A* **63**, 022706(1–10).

Fabrikant, I. I., and Wilde, R. S. (1999). Evidence of virtual dipole-supported states in electron scattering by methyl chloride. *J. Phys. B* **32**, 235–240.

Fabrikant, I. I., Leininger, T., and Gadéa, F. X. (2000). Low-energy dissociative electron attachment to $Cl_2$ molecules. *J. Phys. B* **33**, 4575–4580.

Feketeova, L., Skalny, D. J., Hanel, G., Gstir, B., Francis, M., and Märk, T. D. (2003). Production of $Cl^-$ via dissociative electron attachment to $Cl_2$. *Int. J. Mass Spectrom.* **223–224**, 661–667.

Ferch, J., Raith, W., Schröder, K. (1982). Total cross section measurement for $e-SF_6$ scattering down to 0.036 eV. *J. Phys. B* **15**, L175–L178.

Fermi, E. (1934). Sopra lo spostamento per pressione delle righe elevate delle serie spettrali. *Nuovo Cimento* **11**, 157–166.

Fermi, E., and Teller, E. (1947). The capture of negative mesotrons in matter. *Phys. Rev.* **72**, 399–408.

Field, D., Mrotzek, G., Knight, D. W., Lunt, S. L., and Ziesel, J.-P. (1988). High-resolution studies of electron scattering by molecular oxygen. *J. Phys. B* **21**, 171–188.

Field, D., Knight, D. W., Mrotzek, G., Randell, J., Lunt, S. L., Ozenne, J. B., and Ziesel, J. P. (1991a). A high-resolution synchrotron photoionization spectrometer for the study of low-energy electron-molecule scattering. *Meas. Sci. Technol.* **2**, 757–769.

Field, D., Lunt, S. L., Mrotzek, G., Randell, J., and Ziesel, J. P. (1991b). High resolution electron scattering from carbon dioxide. *J. Phys. B* **24**, 3497–3506.

Field, D., Jones, N. C., Gingell, J. M., Mason, N. J., Lunt, S. L., and Ziesel, J.-P. (2000). Electron scattering in chlorine dioxide. *J. Phys. B.* **33**, 1039–1046.

Field, D., Lunt, S. L., and Ziesel, J.-P. (2001a). The quantum world of cold electron collisions. *Acc. Chem. Res.* **34**, 291–296.

Field, D., Jones, N. C., Lunt, S. L., and Ziesel, J.-P. (2001b). Experimental evidence for a virtual state in a cold collision: electrons and carbon dioxide. *Phys. Rev. A* **64**, 022708 (1–6).

Field, D., Jones, N. C., Lunt, S. L., Ziesel, J.-L., and Gulley, R. G. (2001c). Low energy electron scattering in $CF_2Cl_2$ and $CF_3Cl$. *J. Chem. Phys.* **115**, 3045–3052.

Filippelli, A. R., Lin, C. C., Anderson, L. W., and McConkey, J. W. (1994). Principles and methods for measurement of electron impact excitation cross sections for atoms and molecules by optical techniques. *Adv. At. Mol. Opt. Phys.* **33**, 1–62.

Finch, C. D., Popple, R. A., Nordlander, P., and Dunning, F. B. (1995). Formation of long-lived $C_{60}^-$ ions in Rydberg atom-$C_{60}$ collisions. *Chem. Phys. Lett.* **244**, 345–349.

Fiquet-Fayard, F. (1974). Theoretical investigation of dissociative attachment in HCl and DCl. *J. Phys. B* **7**, 810–816.

Frey, M. T., Hill, S. B., Ling, X., Smith, K. A., Dunning, F. B., and Fabrikant, I. I. (1994). Inelastic electron-dipole-molecule scattering at sub-milli-electron-volt energies: Possible role of dipole-supported states. *Phys. Rev. A* **50**, 3124–3128.

Frey, M. T., Hill, S. B., Smith, K. A., Dunning, F. B., and Fabrikant, I. I. (1995). Studies of electron-molecule scattering at microelectronvolt energies using very-high-$n$ Rydberg atoms. *Phys. Rev. Lett.* **75**, 810–813.

Frey, M. T., Ling, X., Lindsay, B. G., Smith, K. A., and Dunning, F. B. (1993). Use of the Stark effect to minimize residual electric fields in an experimental volume. *Rev. Sci. Instrum.* **64** (12), 3649–3650.

Gailitis, M. (1970). Influence of close coupling on the threshold behavior of the cross sections for the excitation of atoms by electrons. *Theor. Math. Phys.* **3**, 572–581.

Gailitis, M., and Damburg, R. (1963). The influence of close coupling on the threshold behaviour of cross sections of electron-hydrogen scattering. *Proc. Phys. Soc.* **82**, 192–200.

Gallup, G. A., Xu, Y., and Fabrikant, I. I. (1998). Nonlocal theory of dissociative electron attachment to $H_2$ and HF molecules. *Phys. Rev. A* **57**, 2596–2607.

Gallup, G. A., Aflatooni, K., and Burrow, P. D. (2003). Dissociative electron attachment near threshold, thermal attachment rates, and vertical attachment energies of chloroalkanes. *J. Chem. Phys.* **118**, 2562–2574.

Gauthier, M. (1988). Spectra and structure of nitrous oxide dimers and clusters. *J. Chem. Phys.* **88**, 5439–5449.

Gauyacq, J. P. (1982). Associative detachment in collisions between negative halogen ions and hydrogen atoms. *J. Phys. B* **15**, 2721–2739.

Gauyacq, J. P. (1983). Associative detachment and vibrational excitation in the $e^-$-HF system. *J. Phys. B* **16**, 4049–4058.

Gauyacq, J.-P. (1987). "Dynamics of Negative Ions," World Scientific, Singapore.

Gauyacq, J. P., and Herzenberg, A. (1982). Nuclear-excited Feshbach resonances in e+HCl scattering. *Phys. Rev. A* **25**, 2959–2967.

Gauyacq, J. P., and Herzenberg, A. (1984). The attachment of very slow electrons to polyatomic molecules. *J. Phys. B* **17**, 1155–1171.

Gerchikov, L. G., Ipatov, A. N., and Solov'yov, A. V., and Greiner, W. (1998). Excitation of multipole plasmon resonances in clusters by electron impact. *J. Phys. B* **31**, 3065–3078.

Gianturco, F. A., and Lucchese, R. R. (2001). Electron scattering from gaseous $SF_6$: comparing calculations with experiments. *J. Chem. Phys.* **114**, 3429–3439.

Gianturco, F. A., Lucchese, R. R., and Sanna, N. (1999). Computed elastic cross sections and angular distributions of low-energy electron scattering from gas phase $C_{60}$ fullerene. *J. Phys. B* **32**, 2181–2193.

Gilbert, S. J., Barnes, L. D., Sullivan, J. P., and Surko, C. M. (2002). Vibrational-resonance enhancement of positron annihilation in molecules. *Phys. Rev. Lett.* **88**, 043201(1–4).

Gopalan, A., Bömmels, J., Götte, S., Landwehr, A., Franz, K., Ruf, M.-W., Hotop, H., and Bartschat, K. (2003). A novel electron scattering apparatus combining a laser photoelectron source and a triply differentially pumped supersonic beam target: characterization and results for the $He^-(1s2s^2)$ resonance. *Eur. Phys. J. D* **22**, 17–29.

Götte, S., Gopalan, A., Bömmels, J., Ruf, M.-W., and Hotop, H. (2000). A triply differentially pumped supersonic beam target for high-resolution collision studies. *Rev. Scient. Instrum.* **71**, 4070–4077.

Gribakin, G. F. (2000). Mechanisms of positron annihilation on molecules. *Phys. Rev. A* **61**, 022720(1–13).

Gribakin, G. F. (2001). Theory of positron annihilation on molecules. In: F. A. Gianturco and C. M. Surko, Eds. "New Directions in Antimatter Chemistry and Physics," pp. 413–435, Kluwer Academic.

Gribakin, G. F., and Ludlow, J. (2002). Enhancement of Positron-Atom Annihilation near the positronium formation threshold. *Phys. Rev. Lett.* **88**, 163202(1–4).

Gulley, R. J., Lunt, S. L., Ziesel, J.-P., and Field D. (1998a). Very low energy electron scattering from benzene and deuterated benzenes. *J. Phys. B.* **31**, 2735–2751.

Gulley, R. J., Field, T. A., Steer, W. A., Mason, N. J., Lunt, S. L., Ziesel, J.-P., and Field, D. (1998b). Very low energy electron collisions with molecular chlorine. *J. Phys. B.* **31**, 2971–2980.

Gutsev, G. L., Bartlett, R. J., and Compton, R. N. (1998). Electron affinities of $CO_2$, OCS, and $CS_2$. *J. Chem. Phys.* **108**, 6756–6762.

Hahndorf, I., and Illlenberger, E. (1997). Temperature dependence of electron attachment processes. *Int. J. Mass Spectrom. Ion Proc.* **167/168**, 87–101.

Hahndorf, I., Illenberger, E., Lehr, L., and Manz, J. (1994). Temperature effects of dissociative electron attachment to $CF_3Cl$. *Chem. Phys. Lett.* **231**, 460–466.

Harth, K., Ruf, M.-W., and Hotop, H. (1989). Electron transfer from laser excited Rydberg

atoms to molecules. Absolute rate constants at low and intermediate principal quantum numbers. *Z. Phys. D* **14**, 149–165.

Hashemi, R., and Illenberger, E. (1991). Violation of the $\sigma^-$ selection rule in electron attachment to $O_2$ clusters. *Chem. Phys. Lett.* **187**, 623–627.

Hashemi, R., Kühn, A., and Illenberger, E. (1990). Electron capture induced processes in molecules and molecular aggregates. *Int. J. Mass Spectrom. Ion Proc.* **100**, 753–784.

Hashemi, R., Jaffke, T., Christophorou, L. G., and Illenberger, E. (1992). Role of inelastic electron scattering by $N_2$ in the formation of $(O_2)_n^-$ anions in mixed $O_2/N_2$ clusters. *J. Phys. Chem.* **96**, 10605–10607.

Hatano, Y. (1997). Electron attachment and recombination in dense molecular media. *Aust. J. Phys.* **50**, 615–625.

Hatano, Y., and Shimamori, H. (1981). Electron attachment in dense gases. In: L. G. Christophorou, Ed. "Electron and Ion Swarms," p. 103–116, Pergamon, New York.

Hazi, A. U., Orel, A. E., and Rescigno, T. N. (1981). Ab initio study of dissociative attachment of low-energy electrons to $F_2$. *Phys. Rev. Lett.* **46**, 918–922.

Herrick, D. R. (1975). Resonance-channel quantum numbers in electron-hydrogen and proton-hydrogen scattering from group theory of the long-range dipole interaction. *Phys. Rev. A* **12**, 413–424.

Herrick, D. R., and Engelking, P. C. (1984). Dipole coupling channels for molecular anions. *Phys. Rev. A* **29**, 2421–2424.

Herzberg, G. (1945). Infrared and Raman spectra of polyatomic molecules. *Molecular Spectra and Molecular Structure II*. Van Nostrand Reinhold, N. Y.

Herzenberg, A. (1968). Oscillatory energy dependence of resonant electron-molecule scattering. *J. Phys. B* **1**, 548–558.

Herzenberg, A. (1984). Vibrational excitation of molecules by slow electrons. In: I. Shimamura and K. Takayanagi, Eds. "Electron-Molecule Collisions," pp. 191–274, Plenum Press, New York.

Higgins, K., Gillan, C. J., Burke, P. G., and Noble, C. J. (1995). Low-energy electron scattering by oxygen molecules: II. Vibrational excitation. *J. Phys. B* **28**, 3391–3402.

Hill, S. B., Frey, M. T., Dunning, F. B., and Fabrikant, I. I. (1996). Electron-hydrogen fluoride scattering at ultralow electron energies: possible role of dipole-supported states. *Phys. Rev. A* **53**, 3348–3357.

Hoffmann, S. V., Lunt, S. L., Jones, N. C., Field, D., and Ziesel, J.-P. (2002). An undulator-based spherical grating monochromator beamline for low energy electron-molecule scattering experiments. *Rev. Sci. Instrum.* **73**, 4157–4163.

Horáček, J., and Domcke, W. (1996). Calculation of cross sections for vibrational excitation and dissociative attachment in electron collisions with HBr and DBr. *Phys. Rev. A* **53**, 2262–2271.

Horáček, J., Domcke, W., and Nakamura, H. (1997). Electron attachment and vibrational excitation in hydrogen iodide: calculations based on the nonlocal resonance model. *Z. Phys. D* **42**, 181–185.

Horáček, J., Čížek, M., and Domcke, W. (1998). Generalization of the nonlocal resonance model for low-energy electron collisions with hydrogen halides: the variable threshold exponent. *Theor. Chem. Acc.* **100**, 31–35.

Hotop, H. (2001). Dynamics of low energy electron collisions with molecules and clusters. In: L. G. Christophorou and J. K. Olthoff, Eds. "Gaseous Dielectrics IX," pp. 3–14, Kluwer Academic/Plenum Publ., New York.

Hotop, H., Klar, D., Kreil, J., Ruf, M.-W., Schramm, A., and Weber, J. M. (1995). Studies of low energy electron collisions at sub-meV resolution. In: L. J. Dube, J. B. A. Mitchell, J. W. McConkey, and C. E. Brion, Eds. "The Physics of Electronic and Atomic Collisions," AIP Conf. Proc. Vol. 360, pp. 267–278. AIP Press, Woodbury, New York.

Howe, P.-T., Kortyna, A., Darrach, M., and Chutjian, A. (2001). Low-energy electron attachment to $SF_6$ at sub-meV resolution using a tunable laser photoelectron method. *Phys. Rev. A* **64**, 042706 (1–8).

Huang, J., Carman, H. S. Jr., and Compton, R. N. (1995). Low-energy electron attachment to $C_{60}$. *J. Phys. Chem.* **99**, 1719–1726.

Huo, W. H., and Gianturco, F. A. (Eds.) (1995). "Computational Methods for Electron-Molecule Collisions," Plenum, New York.

Ibach, H. (1991). "Electron Energy Loss Spectrometers," Springer Ser. Opt. Sciences, Vol. 63, Springer, Berlin, Heidelberg.

Ibach, H. (1993). Electron energy loss spectroscopy with resolution below 1 meV. *J. Electron Spectrosc.* **64/65**, 819–823.

Iga, I., Rao, M. V. V. S., Srivastava, S. K., and Nogueira, J. C. (1996). Cross sections for the formation of $S^-$ ions by electron impact on OCS. *Int. J. Mass Spectrom. Ion Proc.* **155**, 99–105.

Igarashi, A., Kimura, M., and Shimamura, I. (2002). Unified treatment of positron annihilation and positronium formation. *Phys. Rev. Lett.* **89**, 123201(1–4).

Illenberger, E. (1992). Electron-attachment reactions in molecular clusters. *Chem. Rev.* **92**, 1589–1609.

Illenberger, E. (2000). Electron capture processes by free and bound molecules. In: C.-Y. Ng (Ed.) "Photoionization and Photodetachment (Part II)," *Adv. Series in Physical Chemistry*, Vol. 10 B, pp. 1063–1160, World Scientific, Singapore.

Ingólfsson, O., Weik, F., Illenberger, E. (1996). The reactivity of slow electrons with molecules at different degrees of aggregation: gas phase, clusters and condensed phase. *Int. J. Mass Spectrom. Ion Processes* **155**, 1–68.

Ipatov, A. N., Ivanov, V. K., Agap'ev, B. D., and Ekardt, W. (1998a). Exchange and polarization effects in elastic electron scattering by metallic clusters. *J. Phys. B* **31**, 925–934.

Ipatov, A., Connerade, J.-P., Gerchikov, L. G., and Solov'yov, A. V. (1998b). Electron attachment to metallic clusters. *J. Phys. B* **31**, L27–L34.

Iwata, K., Greaves, R. G., Murphy, T. J., Tinkle, M. D., and Surko, C. M. (1995). Measurements of positron-annihilation rates on molecules. *Phys. Rev. A* **51**, 473–487.

Iwata, K., Gribakin, G. F., Greaves, R. G., Kurz, C., and Surko, C. M. (2000). Positron annihilation on large molecules. *Phys. Rev. A* **61**, 022719(1–17).

Jaffke, T., Hashemi, R., Christophorou, L. G., Illenberger, E. (1992). Mechanisms of anion formation in $O_2$, $O_2/Ar$ and $O_2/Ne$ clusters; the role of inelastic electron scattering. *Z. Phys. D* **25**, 77–85.

Jaffke, T., Illenberger, E., Lezius, M., Matejcik, S., Smith, D., and Märk, T. D. (1994). Formation of $C_{60}^-$ and $C_{70}^-$ by free electron capture. Activation energy and effect of the internal energy on lifetime. *Chem. Phys. Lett.* **226**, 213–218.

Johnstone, W. M., Akther, P., and Newell, W. R. (1995). Resonant vibrational excitation of carbon dioxide. *J. Phys. B* **28**, 743–753.

Jones, N. C., Field, D., Ziesel, J.-P., and Field, T. A. (2002). Giant resonances in cold electron scattering by $CS_2$. *Phys. Rev. Lett.* **89**, 093201(1–4).

Jordan, K. D., and Burrow, P.D. (1978). Studies of temporary anion states of unsaturated hydrocarbons by electron transmission spectroscopy. *Acc. Chem. Res.* **11**(9), 341–348.

Kalamarides, A., Walter, C. W., Smith, K. A., and Dunning, F. B. (1988). Negative ion formation in K($nd$)-$CS_2$ collisions: detection of electric-field-induced detachment from $CS_2^-$. *J. Chem. Phys*. **89**, 7226–7228.

Kalin, S. A., and Kazansky, A. K. (1990). The semiclassical version of the non-local resonance theory of electron-molecule collisions. *J. Phys. B* **23**, 4377–4400.

Karwasz, G. P., Brusa, R. S., and Zecca, A. (2001a). One century of experiments on electron-atom and molecule scattering: a critical review of integral cross sections. II. Polyatomic molecules. *Riv. Nuovo Cim*. **24(1)**, 1–118.

Karwasz, G. P., Brusa, R. S., and Zecca, A. (2001b). One century of experiments on electron-atom and molecule scattering: a critical review of integral cross-sections. III. Hydrocarbons and halides. *Riv. Nuovo Cim*. **24(4)**, 1–101.

Kasperovich, V., Tikhonov, G., Wong, K., and Kresin, V. V. (2000a). Negative-ion formation in collisions of low-energy electrons with neutral sodium clusters. *Phys. Rev. A* **62**, 063201(1–6).

Kasperovich, V., Wong, K., Tikhonov, G., and Kresin, V. V. (2000b). Electron capture by the image charge of a metal nanoparticle. *Phys. Rev. Lett*. **85**, 2729–2732.

Kasperovich, V., Tikhonov, G., and Kresin, V. V. (2001). Low-energy electron capture by free $C_{60}$ and the importance of polarization interaction. *Chem. Phys. Lett*. **337**, 55–60.

Kau, R., Petrov, I. D., Sukhorukov, V. L., and Hotop, H. (1998). Experimental and theoretical cross sections for photoionization of metastable Ar* and Kr* atoms near threshold. *J. Phys. B*. **31**, 1011–1027.

Kazansky, A. K. (1978). Model of the passing of the s term through the parabolic boundary of the continuum. *Theor. Math. Phys*. **36**, 825–832.

Kazansky, A. K. (1982). Antibonding intermediate state in the theory of vibrational excitation of diatomic molecules by slow electrons. *Sov. Phys. JETP* **55**, 824–827.

Kazansky, A. K. (1995). A model study of dissociative attachment of slow electrons to the carbon dioxide molecule. *J. Phys. B* **28**, 3987–4004.

Kazansky, A. K., and Fabrikant, I. I. (1984). Scattering of slow electrons by molecules. *Sov. Phys. Usp*. **27**, 607–630.

Keil, M., Kolling, T., Bergmann, K. and Meyer, W. (1999). Dissociative attachment of low-energy electrons to vibrationally excited $Na_2$ molecules using a photoelectron source. *Eur. Phys. J. D* **7**, 55–64.

Kennerly, R. E., Van Brunt, R. J., and Gallagher, A. C. (1981). High-resolution measurement of the helium $1s2s^2$ $^2S$ resonance profile. *Phys. Rev. A* **23**, 2430–2442.

Kimura, M., Sueoka, O., Hamada, A., and Itikawa, Y. (2000). A comparative study of electron- and positron-polyatomic molecule scattering. *Adv. Chem. Phys*. **111**, 537–622.

Kitajima, M., Watanabe, S., Tanaka, H., Takekawa, M., Kimura, M., and Itikawa, Y. (2000). Strong mode dependence of the 3.8-eV resonance in $CO_2$ vibrational excitation by electron impact. *Phys. Rev. A* **61**, 060701 (R1–R4).

Klar, D., Ruf, M.-W., and Hotop, H. (1992a). Attachment of electrons to molecules at submillielectronvolt resolution. *Chem. Phys. Lett*. **189**, 448–454.

Klar, D., Ruf, M.-W., and Hotop, H. (1992b). Attachment of electrons to molecules at meV resolution. *Aust. J. Phys*. **45**, 263–291.

Klar, D., Ruf, M.-W., and Hotop, H. (1994a). A tunable laser-atomic beam photoelectron source with sub-milli-electron-volt resolution: design, operation and application to threshold electron attachment studies. *Meas. Sci. Technol*. **5**, 1248–1261.

Klar, D., Mirbach, B., Korsch, H. J., Ruf, M.-W., and Hotop, H. (1994b). Comparison of rate coefficients for Rydberg electron and free electron attachment. *Z. Phys. D* **31**, 235–244.

Klar, D., Ruf, M.-W., and Hotop, H. (2001a). Dissociative electron attachment to $CCl_4$ molecules at low electron energies with meV resolution. *Int. J. Mass Spectrom*. **205**, 93–110.

Klar, D., Ruf, M.-W., Fabrikant, I. I., and Hotop, H. (2001b). Dissociative electron attachment to dipolar molecules at low energies with meV resolution: $CFCl_3$, $1,1,1-C_2Cl_3F_3$, and HI. *J. Phys. B* **34**, 3855–3878.

Klots, C. E. (1976). Rate constants for unimolecular decomposition at threshold. *Chem. Phys. Lett.* **38**, 61–64.

Klots, C. E., and Compton, R. N. (1977). Electron attachment to carbon dioxide clusters in a supersonic beam. *J. Chem. Phys.* **67**, 1779–1780.

Klots, C. E., and Compton, R. N. (1978). Electron attachment to van der Waals polymers of carbon dioxide and nitrous oxide. *J. Chem. Phys.* **69**, 1636–1643.

Klots, C. E., and Compton, R. N. (1980). Self-scavenging of electrons in van der Waals molecules of methyl iodide. *Chem. Phys. Lett.* **73**, 589–591.

Klots, C. E., and Compton, R. N. (1996). Evidence for thermionic emission from small aggregates. *Surf. Rev. Lett.* **3**, 535–540.

Knapp, M., Kreisle, D., Echt, O., Sattler, K., and Recknagel, E. (1985). Size distributions of negatively and positively charged clusters: $CO_2$ and $N_2O$. *Surf. Science* **156**, 313–320.

Knapp, M., Echt, O., Kreisle, D., Märk, T. D., and Recknagel, E. (1986a). Formation of long-lived $CO_2^-$, $N_2O^-$, and their dimer anions, by electron attachment to van der Waals clusters. *Chem. Phys. Lett.* **126**, 225- 231.

Knapp, M., Echt, O., Kreisle, D., and Recknagel, E. (1986b). Trapping of low energy electrons at preexisting, cold water clusters. *J. Chem. Phys.* **85**, 636–637.

Knapp, M., Echt, O., Kreisle, D., and Recknagel, E. (1987). Electron attachment to water clusters under collision-free conditions. *J. Phys. Chem.* **91**, 2601–2607.

Knoth, G., Gote, M., Rädle, M., Jung, K., and Ehrhardt, H. (1989a). Nuclear-excited feshbach resonances in the electron scattering from hydrogen halides. *Phys. Rev. Lett.* **62**, 1735–1737.

Knoth, G., Rädle, M., Gote, M., Ehrhardt, H., and Jung, K. (1989b). Near-threshold electron impact rovibrational excitation of HCl and HF. *J. Phys. B* **22**, 299–326.

Kochem, K. H., Sohn, W., Hebel, N., Jung, K., and Ehrhardt, H. (1985). Elastic electron scattering and vibrational excitation of $CO_2$ in the threshold energy region. *J. Phys. B* **18**, 4455–4467.

Kolorenc, P., Čizek, M., Horáček, J., Mil'nikov, G., and Nakamura, H. (2002). Study of dissociative electron attachment to HI molecule by using *R*-matrix representation for Green's function. *Physica Scripta* **65**, 328–335.

Kondow, T., and Mitsuke, K. (1985). Formation of negative cluster ions of $CO_2$, OCS, and $CS_2$ produced by electron transfer from high-Rydberg rare gas atoms. *J. Chem. Phys.* **83**, 212–213.

Kondow, T. (1987). Ionization of clusters in collision with high-Rydberg rare gas atoms. *J. Phys. Chem.* **91**, 1307–1316.

Kovalchuk, E. V., Dekorsy, D., Lvovsky, A. I., Braxmaier, C., Mlynek, J., Peters, A., and Schiller, S. (2001). High-resolution Doppler-free molecular spectroscopy with a continuous-wave optical parametric oscillator. *Opt. Lett.* **26**, 1430–1432.

Kraft, T., Ruf, M.-W., and Hotop, H. (1989). Formation of negatively-charged cluster ions in thermal energy collisions with state-selected Rydberg atoms. *Z. Phys. D* **14**, 179–185.

Kraft, T., Ruf, M.-W., and Hotop, H. (1990). Strong dependence of negative cluster ion spectra on principal quantum number *n* in collisions of state-selected $Ar^{**}(nd)$ Rydberg atoms with $N_2O$ clusters. *Z. Phys. D* **17**, 37–434.

Kraft, T., Ruf, M.-W., and Hotop, H. (1991). Effective absolute rate constant for the formation of negatively-charged $CO_2$ cluster ions by electron transfer from state-selected Rydberg atoms. *Z. Phys. D* **18**, 403–407.

Kreil, J., Ruf, M.-W., Hotop, H., Ettischer, I., and Buck, U. (1998). Threshold electron attachment and electron impact ionization involving oxygen dimers. *Chem. Phys.* **239**, 459–473.

Krishnakumar, E., and Srivastava, S. K. (1990). Dissociative attachment of electrons to $N_2O$. *Phys. Rev. A* **41**, 2445–2452.

Külz, M., Keil, M., Kortyna, M., Schellhaaß, B., Hauck, J., Bergmann, K., and Meyer, W. and Weyh, D. (1996). Dissociative attachment of low-energy electrons to state-selected diatomic molecules. *Phys. Rev. A* **53**, 3324–3334.

Kurepa, M. V., and Belić, D. S. (1978). Electron-chlorine molecule total ionisation and electron attachment cross sections. *J. Phys. B* **11**, 3719–3729.

Land, J. E., and Raith, W. (1974). High-resolution measurement of resonances in $e$-$O_2$ scattering by electron time-of-flight spectroscopy. *Phys. Rev. A* **9**, 1592–1602.

Landau, L. D., and Lifshitz, E. M. (1977). "Quantum Mechanics, Non-relativistic Theory," 3rd Edn., Pergamon, Oxford.

Lane, A. M., and Thomas, R. G. (1958). *R*-matrix theory of nuclear reactions. *Rev. Mod. Phys.* **30**, 257–353.

Lane, N. F. (1980). The theory of electron-molecule collisions, *Rev. Mod. Phys.* **52**, 29–119.

Langevin, P. (1905). Une formule fondamentale de théorie cinétique. *Ann. chim. et phys.* **5**, 245–288.

Larrichia, G., and Wilkin, C. (1997). Semiempirical approach to positron annihilation in molecules. *Phys. Rev. Lett.* **79**, 2241–2244.

Leber, E., Fabrikant, I. I., Weber, J. M., Ruf, M.-W., and Hotop, H. (2000a). Resonance and threshold phenomena in electron attachment to molecules and clusters. In: M. Larsson, J. B. A. Mitchell, and I. F. Schneider, Eds. "Dissociative Recombination: Theory, experiment and applications IV," pp. 69–76, World Scientific, Singapore.

Leber, E., Barsotti, S., Fabrikant, I. I., Weber, J. M., Ruf, M.-W., and Hotop, H. (2000b). Vibrational feshbach resonances in electron attachment to carbon dioxide clusters. *Eur. Phys. J. D* **12**, 125–131.

Leber, E., Barsotti, S., Bömmels, J., Weber, J. M., Fabrikant, I. I., Ruf, M.-W., and Hotop, H. (2000c). Vibrational Feshbach resonances in electron attachment to nitrous oxide clusters: decay into heterogeneous and homogeneous cluster anions. *Chem. Phys. Lett.* **325**, 345–353.

LeGarrec, J.-L., Steinhurst, D. A., and Smith, M. A. (2001). Measurement of the autodetachment lifetime of $SF_6^-$ as a function of electron energy in a free jet expansion. *J. Chem. Phys.* **114**, 8831–8835.

Lehr, L., and Miller, W. H. (1996). A classical approach to dissociative electron attachment DA: application to temperature effects in the DA cross section of $CF_3Cl$. *Chem. Phys. Lett.* **250**, 515–522.

Lehr, L., Manz, J., and Miller, W. H. (1997). A classical approach to resonant low-energy electron scattering of molecules: application to the $a_1$-shape resonance of $CF_3Cl$. *Chem. Phys.* **214**, 301–312.

Leininger, T., and Gadea, F. X. (2000). *Ab initio* calculations for electron attachment to $Cl_2$. *J. Phys. B* **33**, 735–744.

Lezius, M., Scheier, P., and Märk, T. D. (1993). Free electron attachment to $C_{60}$ and $C_{70}$. *Chem. Phys. Lett.* **203**, 232–236.

Lide, D. R. (Ed.) (1995). "CRC Handbook of Chemistry and Physics," 76th Edn. Boca Raton, FL: Chemical Rubber Company.

Ling, X., Lindsay, B. G., Smith, K. A., and Dunning, F. B. (1992). Rydberg-atom collisions with $SF_6$ and $CCl_4$ at very high *n*. *Phys. Rev. A* **45**, 242–246.

Lucchese, R. R., Gianturco, F. A., and Sanna, N. (1999). Low-energy electron scattering from $C_{60}$ molecules. *Chem. Phys. Lett.* **305**, 413–418.

Lunt, S. L., Field, D., Ziesel, J.-P., Jones, N. C., and Gulley, R. J. (2001). Very low energy electron scattering in nitromethane, nitroethane, and nitrobenzene. *Int. J. Mass Spectrom.* **205**, 197–208.

Maeyama, T., Oikawa, T., Tsumura, T., and Mikami, N. (1998). Photodestruction spectroscopy of carbon disulfide cluster anions $(CS_2)_n^-$, $n = 1$–4: evidence for the dimer core structure and competitive reactions of the dimer anion. *J. Chem. Phys.* **108**, 1368–1376.

Maillet, J.-B., Boutin, A., Buttefey, S., Calvo, F., Fuchs, A. H. (1998). From molecular clusters to bulk matter. I. Structure and thermodynamics of small $CO_2$, $N_2$, and $SF_6$ clusters. *J. Chem. Phys.* **109**, 329–337.

Märk, T. D. (1991). Free electron attachment to van der Waals clusters. *Int. J. Mass Spectrom. Ion Processes* **107**, 143–163.

Märk, T. D., Leiter, K., Ritter, W., and Stamatovic, A. (1985). Low-energy-electron attachment to oxygen clusters produced by nozzle expansion. *Phys. Rev. Lett.* **55**, 2559–2562.

Märk, T. D., Leiter, K., Ritter, and W., Stamatovic, A. (1986). Electron attachment to oxygen clusters at low electron energies. Formation and stability of $(O_2)_n^-$ and $(O_2)_nO^-$. *Int. J. Mass Spectrom. Ion Proc.* **74**, 265–279.

Massey, H. S. W. (1976). "Negative Ions," 3rd Edn. Cambridge Univ. Press, Cambridge.

Matejčik, Š., Märk, T. D., Španel, P., Smith, D., Jaffke, T., and Illenberger, E. (1995). Formation and decay of $C_{60}^-$ following free electron capture by $C_{60}$. *J. Chem. Phys.* **102**, 2516–2521.

Matejcik, S., Kiendler, A., Stampfli, P., Stamatovic, A., and Märk, T. D. (1996). Vibrationally resolved electron attachment to oxygen clusters. *Phys. Rev. Lett.* **77**, 3771–3774.

Matejcik, S., Stampfli, P., Stamatovic, A., Scheier, P., and Märk, T. D. (1999). Electron attachment to oxygen clusters studied with high energy resolution. *J. Chem. Phys.* **111**, 3548–3558.

Matsuzawa, M. (1972). Reactions of highly excited atoms with molecules $A^{**} + BC \rightarrow A^+ + B + C^-$. *J. Phys. Soc. Japan* **32**, 1108–1119.

Mazevet, S., Morrison, M. A., Morgan, L. A., and Nesbet, R. K. (2001). Virtual-state effects on elastic scattering and vibrational excitation of $CO_2$ by electron impact. *Phys. Rev. A* **64**, 040701(1–4).

McCorkle, D. L., Christodoulides, A. A., and Christophorou, L. G. (1984). Electron attachment to $Cl_2$. *Chem. Phys. Lett.* **109**, 276–279.

McCurdy, C. W., and Turner, J. L. (1983). Wave packet formulation of the boomerang model for resonant electron-molecule scattering. *J. Chem. Phys.* **78**, 6773–6779.

Meyer, H.-D., Horáček, J., and Cederbaum, L. S. (1991). Schwinger and anomaly-free Kohn variational principles and a generalized Lanczos algorithm for nonsymmetric operators. *Phys. Rev. A* **43**, 3587–3596.

Miller, D. R. (1988). Free jet sources. In: G. Scoles, Ed. "Atomic and molecular beam methods," Vol. 1, pp. 14–53, Oxford Univ. Press, New York.

Misaizu, F., Mitsuke, K., Kondow, T., and Kuchitsu, K. (1991). Formation of negative cluster ions from $(CO_2)_m$ in collision with high-Rydberg atoms. *J. Chem. Phys.* **94**, 243–249.

Mitchell, J. B. A. (1990). The dissociative recombination of molecular ions. *Phys. Rep.* **186**, 215–248.

Mittleman, M. H., and von Holdt, R. E. (1965). Theory of low-energy-electron scattering by polar molecules. *Phys. Rev.* **140**, A726–A729.

Modelli, A., Scagnolari, F., Distefano, G., Jones D., and Guerra, M. (1992). Electron attachment to the fluoro-, bromo-, and iodomethanes studied by means of electron transmission spectroscopy and Xα calculations. *J. Chem. Phys.* **96**, 2061–2070.

Morgan, L. A. (1998). Virtual states and resonances in electron scattering by $CO_2$. *Phys. Rev. Lett.* **80**, 1873–1875.

Morrison, M. A. (1982). Interpretation of the near-threshold behavior of cross sections for $e-CO_2$ scattering. *Phys. Rev. A* **25**, 1445–1449.

Morrison, M. A. (1988). Near-threshold electron-molecule scattering. *Adv. At. Mol. Phys.* **24**, 51–156.

Murphy, T. J., and Surko, C. M. (1991). Annihilation of positrons on organic molecules. *Phys. Rev. Lett.* **67**, 2954–2957.

Oakes, J. M., and Ellison, G. B. (1986). Photoelectron spectroscopy of radical anions. *Tetrahedron* **42**, 6263–6267.

O'Malley, T. F. (1965). Effect of long-range final-state forces on the negative-ion photodetachment cross section near threshold. *Phys. Rev.* **137**, A1668–A1672.

O'Malley, T. F. (1966). Theory of dissociative attachment. *Phys. Rev.* **150**, 14–29.

O'Malley, T. F. (1967). Calculation of dissociative attachment in hot $O_2$. *Phys. Rev.* **155**, 59–63.

O'Malley, T. F. (1981). Rydberg levels and structure in dissociative recombination cross sections. *J. Phys. B* **14**, 1229–1238.

O'Malley, T. F., Rosenberg, L., and Spruch, L. (1962). Low-energy scattering of a charged particle by a neutral polarizable system. *Phys. Rev.* **125**, 1300–1310.

Orient, O. J., Chutjian, A., Crompton, R. W., and Cheung, B. (1989). Comparison of experimental and calculated attachment rate constants for $CFCl_3$ and $CCl_4$ in the temperature range 294–500 K. *Phys. Rev. A* **39**, 4494–4501.

Osterwalder, A., and Merkt, F. (1999). Using high rydberg states as electric field sensors. *Phys. Rev. Lett.* **82**, 1831–1834.

Pastuszka, S., Hoppe, M., Kratzmann, D., Schwalm, D., Wolf, A., Jaroshevich, A. S., Kosolobov, S. N., Orlov, D. A., and Terekhov, A. S. (2000). Preparation and performance of transmission-mode GaAs photocathodes as sources for cold dc electron beams. *J. Appl. Phys.* **88**, 6788–6800.

Paul, D. A. L., and Saint-Pierre, L. (1963). Rapid annihilations of positrons in polyatomic gases. *Phys. Rev. Lett.* **11**, 493–496.

Pearl, D. M., and Burrow, P. D. (1993). Thermal decomposition and the apparent dissociative attachment cross section of heated methyl-, ethyl- and *t*-butyl-chloride. *Chem. Phys. Lett.* **206**, 483–487.

Pearl, D. M., Burrow, P. D., Fabrikant, I. I., and Gallup, G. A. (1995). Dissociative attachment in hot $CH_3Cl$: experiment and theory. *J. Chem. Phys.* **102**, 2737–2743.

Petrov, I. D., Sukhorukov, V. L., and Hotop, H. (1999). The influence of core polarization on photoionization of alkali and metastable rare gas atoms near threshold. *J. Phys. B* **32**, 973–986.

Petrov, I. D., Sukhorukov, V. L., Leber, E., and Hotop, H. (2000). Near threshold photoionization of excited alkali atoms Ak(np) (Ak = Na, K, Rb, Cs; n = 3–6). *Eur. Phys. J. D* **10**, 53–65.

Petrović, Z. Lj., and Crompton, R. W. (1985). Thermal-electron attachment to $SF_6$ at room temperature and 500 K. *J. Phys. B* **18**, 2777–2791.

Petrović, Z. Lj., and Crompton, R. W. (1987). Attachment and diffusion of thermal electrons in methyl bromide. *J. Phys. B* **20**, 5557–5565.

Petrović, Z. Lj., Wang, W. C., and Lee, L. C. (1989). Dissociative electron attachment to some chlorine-containing molecules. *J. Chem. Phys.* **90**, 3145–3152.

Popple, R. A., Finch, C. D., Smith, K. A., and Dunning, F. B. (1996). Dissociative electron attachment to $CCl_4$: lifetime of the $CCl_4^{-*}$ intermediate. *J. Chem. Phys.* **104**, 8485–8489.

Rädle, M., Knoth, G., Jung, K., and Ehrhardt, H. (1989). Rotational and rovibrational excitation of HCl and HF by low-energy electron impact. *J. Phys. B* **22**, 1455–1476.

Randell, J., Field, D., Lunt, S. L., Mrotzek, G., and Ziesel, J. P. (1992). Low-energy electron scattering by $SF_6$. *J. Phys. B* **25**, 2899–2909.

Rauth, T., Foltin, M., and Märk, T. D. (1992). Autoscavenging of electrons in mixed van der Waals clusters: a new approach to the spectroscopy of cluster anions. *J. Phys. Chem.* **96**, 1528–1530.

Read, F. H., and Channing, J. M. (1996). Production and optical properties of an unscreened but localized magnetic field. *Rev. Sci. Instrum.* **67**, 2372–2377.

Rescigno, T. N., Byrum, D. A., Isaacs, W. A., and McCurdy, C. W. (1999). Theoretical studies of low-energy electron-$CO_2$ scattering: total, elastic, and differential cross sections. *Phys. Rev. A* **60**, 2186–2193.

Rescigno, T. N., Isaacs, W. A., Orel, A. E., Meyer, H.-D., and McCurdy, C. W. (2002). Theoretical study of resonant vibrational excitation of $CO_2$ by electron impact. *Phys. Rev. A* **65**, 032716 (1–13).

Rohr, K. (1977). Threshold resonances in vibrational excitation of HBr molecules by electron impact. *J. Phys. B* **10**, L399–L402.

Rohr, K. (1978). Interaction mechanismus and cross sections for the scattering of low-energy electrons from HBr. *J. Phys. B* **11**, 1849–1860.

Rohr, K., and Linder, F. (1975). Vibrational excitation in e-HCl collisions at low energies. *J. Phys. B* **8**, L200–L204.

Rohr, K., and Linder, F. (1976). Vibrational excitation of polar molecules by electron impact. I. Threshold resonance in HF and HCl. *J. Phys. B* **9**, 2521–2537.

Rosmus, P., and Hochlaf, M. (2002). Private communication.

Ross, M. H., and Shaw, G. L. (1961). Multichannel effective range theory. *Ann. Phys.* **13**, 147–186.

Ruf, M.-W., Barsotti, S., Braun, M., Hotop, H., and Fabrikant, I. I. (2003). Attachment and vibrational excitation in low-energy electron collisions with chlorine molecules. *J. Phys. B* (submitted).

Ryzhikh, G. G., and Mitroy, J. (1997). Positronic Lithium, an electronically stable $Li-e^+$ ground state. *Phys. Rev. Lett.* **79**, 4124–4126.

Sadeghpour, H. R., Bohn, J. L., Cavagnero, M. J., Esry, B. D., Fabrikant, I. I., Macek, J. H., and Rau, A. R. P. (2000). Collisions near threshold in atomic and molecules physics. *J. Phys. B* **33**, R93–R140.

Sandner, W., Gallagher, T. F., Safinya, K. A., and Gounand, F. (1981). Photoionization of potassium in the vicinity of the minimum in the cross section. *Phys. Rev. A* **23**, 2732–2735.

Saeki, M., Tsukuda, T., and Nagata, T. (2001). Ab initio study of $(CO_2)_n^-$: Structures and stabilities of isomers. *Chem. Phys. Lett.* **340**, 376–384.

Sanov, A., Lineberger, W. C., and Jordan, K. D. (1998). Electronic structure of $(CS_2)_2^-$. *J. Phys. Chem. A* **102**, 2509–2511.

Sarpal, B. K., Pfingst, K., Nestmann, B. M., and Peyerimhoff, S. D. (1996). Study of electron scattering by $N_2O$ using the polyatomic *R*-matrix method. *J. Phys. B* **29**, 857–873; *J. Phys. Chem. A* **102**, 1877(E).

Schafer, O., and Allan, M. (1991). Measurement of near-threshold vibrational excitation of HCl by electron impact. *J. Phys. B* **24**, 3069–3076.

Schneider, B. I., LeDourneuf, M., and Burke, P. G. (1979). Theory of vibrational excitation and dissociative attachment: an *R*-matrix approach. *J. Phys. B* **12**, L365–L369.

Schohl, S., Klar, D., Cherepkov, N. A., Petrov, I. D., Ueda, K., Baier, S., Kau, R., and Hotop, H. (1997). Photoionization of polarized Ar* (4p, $J = 3$) atoms near threshold. *J. Phys. B* **30**, 609–631.

Schramm, A., Fabrikant, I. I., Weber, J. M., Leber, E., Ruf, M.-W., and Hotop, H. (1999). Vibrational resonance and threshold effects in inelastic electron collisions with methyl iodide molecules. *J. Phys. B* **32**, 2153–2171.

Schramm, A., Ruf, M.-W., Stano, M., Matejcik, S., Fabrikant, I. I., and Hotop, H. (2002). High-resolution study of dissociative electron attachment to dipolar molecules at low energies: $CH_2Br_2$ and $CCl_3Br$. *J. Phys. B* **35**, 4179–4202.

Schramm, A., Weber, J. M., Kreil, J., Klar, D., Ruf, M.-W., and Hotop, H. (1998). Laser photoelectron attachment to molecules in a skimmed supersonic beam: diagnostics of weak electric fields and attachment cross sections down to $20\,\mu eV$. *Phys. Rev. Lett.* **81**, 778–781.

Schulz, G. J. (1973a). Resonances in electron impact on atoms. *Rev. Mod. Phys.* **45**, 378–422.

Schulz, G. J. (1973b). Resonances in electron impact on diatomic molecules. *Rev. Mod. Phys.* **45**, 423–486.

Senn, G., Skalny, J. D., Stamatovic, A., Mason, N. J., Scheier, P., and Märk, T. D. (1999). Low energy dissociative electron attachment to ozone. *Phys. Rev. Lett.* **82**, 5028–5031.

Sentürk, Ş., Connerade, J. P., Burgess, D. D., and Mason, N. J. (2000). Enhanced electron capture by metallic clusters. *J. Phys. B* **33**, 2763–2774.

Sergenton, A.-Ch., and Allan, M. (2000). Excitation of vibrational levels of HI up to $v = 8$ by electron impact. *Chem. Phys. Lett.* **319**, 179–183.

Sergenton, A.-Ch., Jungo, L., and Allan, M. (2000). Excitation of vibrational levels of HF up to $v = 4$ by electron impact. *Phys. Rev. A* **61**, 062702(1–6).

Shi, X., Chan, V. K., Gallup, G. A., and Burrow, P. D. (1996). Low energy electron scattering from $CH_3Cl$. *J. Chem. Phys.* **104**, 1855–1863.

Shi, X. (1992). *Ph.D. Thesis*, Univ. of Nebraska, Lincoln, NE, USA.

Shimamori, H., and Nakatani, Y. (1988). Rate constants for thermal electron attachment to $CF_3I$, $CH_3I$, $C_2H_5I$, $1\text{-}C_3H_7I$ and $2\text{-}C_3H_7I$ determined between 250 and $350\,K$. *Chem. Phys. Lett.* **150**, 109–112.

Shimamori, H., Tatsumi, Y., Ogawa, Y., and Sunagawa, T. (1992a). Electron-energy dependence of electron attachment to $c\text{-}C_7F_{14}$, $CH_3I$ and $CH_2Br_2$ studied by the pulse-radiolysis microwave-cavity technique combined with microwave heating. *Chem. Phys. Lett.* **194**, 223–229.

Shimamori, H., Tatsumi, Y., Ogawa, Y., and Sunagawa, T. (1992b). Low-energy electron attachment to molecules studied by pulse-radiolysis microwave-cavity technique combined with microwave heating. *J. Chem. Phys.* **97**, 6335–6347.

Shimamura, I., and Takayanagi, K. (Eds.) (1984). "Electron-Molecule Collisions," Plenum Press, New York.

Skalický, T., Chollet, C., Pasquier, N., and Allan, M. (2002). Properties of the $\pi^*$ and $\sigma^*$ states of chlorobenzene anion determined by electron impact spectroscopy. *Phys. Chem. Chem. Phys.* **4**, 3583–3590.

Smith, D., and Španel, P. (1994). Studies of electron attachment at thermal energies using the flowing Afterglow-Langmuir probe technique. *Adv. At. Mol. Opt. Phys.* **32**, 307–343.

Smith, D., and Španel, P. (1996). Electron attachment to $C_{60}$ and $C_{70}$ in the gas phase. *J. Phys. B* **29**, 5199–5212.

Smith, D., Španel, P., and Märk, T. D. (1993). Electron attachment to $C_{60}$ at low energies. *Chem. Phys. Lett.* **213**, 202–206.

Smith, J. R., Kim, J. B., and Lineberger, W. C. (1997). High-resolution threshold photodetachment spectroscopy of $OH^-$. *Phys. Rev. A* **55**, 2036–2043.

Sohn, W., Kochem, K.-H., Scheuerlein, K. M., Jung, K., and Ehrhardt, H. (1987). Low-energy electron impact spectroscopy of OCS and $CS_2$. *J. Phys. B* **20**, 3217–3236.

Sommerfeld, T. (2002). Coupling between dipole-bound and valence states: the nitromethane anion. *Phys. Chem. Chem. Phys.* **4**, 2511–2516.

Sommerfeld, T. (2003). A fresh look at the $^2A_1$ $CO_2^-$ potential energy surface. *J. Phys. B* **36**, L127–L133.

Španel, P., Matejcik, S., and Smith, D. (1995). The varying influences of gas and electron temperatures on the rates of electron attachment to some selected molecules. *J. Phys. B* **28**, 2941–2957.

Speck, T., Mostefaoui, T., Rebrion-Rowe, C., Mitchell, J. B. A., and Rowe, B. R. (2000). Low temperature electron attachment to $CH_3I$. *J. Phys. B* **33**, 3575–3582.

Spence, D., and Schulz, G. J. (1973). Temperature dependence of electron attachment at low energies for polyatomic molecules. *J. Chem. Phys.* **58**, 1800–1803.

Stamatovic, A. (1988). Electron attachment to van der Waals clusters: the zero energy resonance. In: H. B. Gilbody, W. R. Newell, F. H. Read, A. C. H. Smith, Eds. "Electronic and Atomic Collisions," pp. 729–735, North Holland, Amsterdam.

Stamatovic, A., Stephan, K., and Märk, T. D. (1985a). Electron attachment and electron ionisation of van der Waals clusters of carbon dioxide. *Int. J. Mass Spectrom. Ion Proc.* **63**, 37–47.

Stamatovic, A., Leiter, K., Ritter, W., Stephan, K., and Märk, T. D. (1985b). Electron attachment to carbon dioxide clusters at very low electron energies. *J. Chem. Phys.* **83**, 2942–2946.

Stampfli, P. (1995). Theory for the electron affinity of clusters of rare gas atoms and polar molecules. *Phys. Rep.* **255**, 1–77.

Stebbings, R. F., and Dunning, F. B. (Eds.) (1983). "Rydberg States of Atoms and Molecules," Cambridge Univ. Press, Cambridge.

Stepanović, M., Pariat, Y., and Allan, M. (1999). Dissociative electron attachment in cyclopentanone, $\gamma$-butyrolactone, ethylene carbonate, and ethylene carbonate-$d_4$: role of dipole-bound resonances. *J. Chem. Phys.* **110**, 11376–11382.

Suess, L., Parthasarathy, R., and Dunning, F. B. (2002). Nondissociative low-energy electron attachment to $SF_6$, $C_6F_6$, $C_{10}F_8$, and c-$C_7F_{14}$: negative ion lifetimes. *J. Chem. Phys.* **117**, 11222–11227.

Surber, E., Ananthavel, S. P., and Sanov, A. (2002). Nonexistent electron affinity of OCS and the stabilization of carbonyl sulfide anions by gas phase hydration. *J. Chem. Phys.* **116**, 1920–1929.

Surko, C. M., Passner, A., Leventhal, M., and Wysocki, F. J. (1988). Bound states of positrons and large molecules. *Phys. Rev. Lett.* **61**, 1831–1834.

Szmytkowski, C., Karwacz, G., and Maciag, K. (1984). Absolute total electron-scattering cross sections of $N_2O$ and OCS in the low-energy region. *Chem. Phys. Lett.* **107**, 481–484.

Tachikawa, M., Shimamura, I., Buenker, R. J., and Kimura, M. (2001). In: F. Gianturco and C. Surko, Eds. "New Directions in Antimatter Chemistry and Physics," p. 437, Kluwer Academic.

Tam, W.-C., and Wong, S. F. (1978). Dissociative attachment of halogen molecules by 0–8 eV electrons. *J. Chem. Phys.* **68**, 5626–5630.

Tanaka, H., and Sueoka, O. (2001). Mechanisms of electron transport in electrical discharges and electron collision cross sections. *Adv. At. Mol. Opt. Phys.* **44**, 1–32.

Teillet-Billy, D., and Gauyacq, J. P. (1984). Dissociative attachment in e⁻-HCl, DCl collisions. *J. Phys. B* **17**, 4041–4058.

Tennysson, J., and Morgan, L. (1999). Electron collisions with polyatomic molecules using the R-matrix method. *Phil. Trans. R. Soc. Lond. A* **357**, 1161–1173.

Thoss, M., and Domcke, W. (1998). Theory of vibrational relaxation processes in resonant collisions of low-energy electrons with large molecules. *J. Chem. Phys.* **109**, 6577–6595.

Thümmel, H. T., Nesbet, R. K., and Peyerimhoff, S. D. (1992). Near-threshold rotational excitation in electron-polar-molecule scattering. *J. Phys. B* **25**, 4553–4579.

Thümmel, H. T., Nesbet, R. K., and Peyerimhoff, S. D. (1993). Near-threshold rovibrational excitation of HF by electron impact. *J. Phys. B* **26**, 1233–1251.

Torchet, G., Feraudy, M.-F., Boutin, A., and Fuchs, A. H. (1996). Structural transformation in $(CO_2)_N$ clusters, $N < 100$. *J. Chem. Phys.* **105**, 3671–3678.

Tosatti, E., and Manini, N. (1994). Anomalous attachment of low-energy electrons to $C_{60}$. *Chem. Phys Lett.* **223**, 61–64.

Trajmar, S., and McConkey, J. W. (1994). Benchmark measurements of cross sections for electron collisions: analysis of scattered electrons. *Adv. At. Mol. Opt. Phys.* **33**, 63–96.

Trajmar, S., Register, D. F., and Chutjian, A. (1983). Electron scattering by molecules. II. Experimental methods and data. *Phys. Rep.* **97**, 219–356.

Travers, M. J., Cowles, D. C., and Ellison, G. B. (1989). Reinvestigation of the electron affinities of $O_2$ and NO. *Chem. Phys. Lett.* **164**, 449–455.

Tsukada, M., Shima, N., Tsuneyuki, S., Kageshima, H., and Kondow, T. (1987). Mechanism of electron attachment to van der Waals clusters: application to carbon dioxide clusters. *J. Chem. Phys.* **87**, 3927–3933.

Tsukuda, T., Johnson, M. A., and Nagata, T. (1997a). Photoelectron spectroscopy of $(CO_2)_n^-$ revisited: core switching in the $2 \le n \le 16$ range. *Chem. Phys. Lett.* **268**, 429–433.

Tsukuda, T., Hirose, T., and Nagata, T. (1997b). Negative-ion photoelectron spectroscopy of $(CS_2)_n^-$: coexistence of electronic isomers. *Chem. Phys. Lett.* **279**, 179–184.

Turner, J. E. (1977). Minimum dipole moment required to bind an electron – molecular theorists rediscover phenomenon mentioned in Fermi-Teller paper 20 years earlier. *Am. J. Phys.* **45**, 758–766.

Van Brunt, R. J., and Gallagher, A. (1978). Electron scattering with 1 meV resolution. In: G. Watel (Ed.) "Electronic and Atomic Collisions," Proc. X. ICPEAC, Paris, 1977, pp. 129–142, North Holland Publ., Amsterdam.

Van Doren, J. M., Miller, T. M., Williams, S., and Viggiano, A. A. (2003). Thermal electron attachment to ozone, 296–550 K. *Phys. Rev. Lett* (submitted).

Van Reeth, P., and Humberston, J. W. (1998). The energy dependence of the annihilation rate in positron–atom scattering. *J. Phys. B* **31**, L231–L238.

Vasil'ev, Y. V., Tuktarov, R. F., and Mazunov, V. A. (1997). Resonant electron capture mass spectra of fullerenes $C_{60}$ and $C_{70}$. *Rapid Comm. Mass Spectrom.* **11**, 757–761.

Vasil'ev, Y. V., Abzalimov, R. R., Nasibullaev, S. K., Tuktarov, R. F., Pogulay, A. V., and Drewello, T. (2001). Low energy electron-molecule interactions of fullerene $C_{60}$ and its hydro- and fluoro-derivatives. In: I. I. Fabrikant, G. A. Gallup, and P. D. Burrow, Eds. "Int. Symp. On Electron-Molecule Collisions and Swarms," Abstracts, pp. 57–58, Lincoln, NE, USA.

Vitanov, N. V., Fleischhauer, M., Shore, B. W., and Bergmann, K. (2001). Coherent manipulation of atoms and molecules by sequential laser pulses. *Adv. At. Mol. Opt. Phys.* **46**, 55–190.

Vogt, E., and Wannier, G. H. (1954). Scattering of ions by polarization forces. *Phys. Rev.* **95**, 1190–1198.

Walter, C. W., Zollars, B. G., Johnson, C. B., Smith, K. A., and Dunning, F. B. (1986). Formation of $O_2^-$ ions in K($nd$)-$O_2$ collisions at intermediate $n$. *Phys. Rev. A* **34**, 4431–4432.

Weber, J. M., Fabrikant, I. I., Leber, E., Ruf, M.-W., and Hotop, H. (2000). Effects of solvation on dissociative electron attachment to methyl iodide clusters. *Eur. Phys. J. D* **11**, 247–256.

Weber, J. M., Leber, E., Ruf, M.-W., and Hotop, H. (1999a). Nuclear-excited Feshbach resonances in electron attachment to molecular clusters. *Phys. Rev. Lett.* **82**, 516–519.

Weber, J. M., Leber, E., Ruf, M.-W., and Hotop, H. (1999b). Formation of small water cluster anions by attachment of very slow electrons at high resolution. *Eur. Phys. J. D* **7**, 587–594.

Weber, J. M., Ruf, M.-W., and Hotop, H. (1996). Rydberg electron transfer to $C_{60}$ and $C_{70}$. *Z. Phys. D* **37**, 351–357.

Wigner, E. P. (1948). On the behavior of cross sections near thresholds. *Phys. Rev.* **73**, 1002–1009.

Wigner, E. P., and Eisenbud, L. (1947). Higher angular momenta and long range interaction in resonance reactions. *Phys. Rev.* **72**, 29–41.

Wilde, R. S., Gallup, G. A., and Fabrikant, I. I. (1999). Semiempirical *R*-matrix theory of low energy electron-$CF_3Cl$ inelastic scattering. *J. Phys. B* **32**, 663–673.

Wilde, R. S., Gallup, G. A., and Fabrikant, I. I. (2000). Comparative studies of dissociative electron attachment to methyl halides. *J. Phys. B* **33**, 5479–5492.

Winstead, C., and McKoy, V. (1998). Electron collisions with nitrous oxide. *Phys. Rev. A* **57**, 3589–3597.

Winstead, C., and McKoy, V. (2000). Electron-molecule collisions in low-temperature plasmas. *Adv. At. Mol. Opt. Phys.* **43**, 111–145.

Wong, C. F., and Light, J. C. (1984). Application of *R*-matrix theory to resonant reactive electron-molecule scattering: vibrational excitation and dissociative attachment of $N_2$ and $F_2$. *Phys. Rev. A* **30**, 2264–2273.

Wong, C. F., and Light, J. C. (1986). Vibrational excitation and dissociative attachment of a triatomic molecule: $CO_2$ in the collinear approximation. *Phys. Rev. A* **33**, 954–967.

Xu, Y., Gallup, G. A., and Fabrikant, I. I. (2000). Dissociative electron attachment to vibrationally and rotationally excited $H_2$ and HF molecules. *Phys. Rev. A* **61**, 052705(1–7).

Zecca, A., Karwasz, G. P., and Brusa, R. S. (1996). One century of experiments on electron-atom and molecule scattering: a critical review of integral cross-section. I. Atoms and diatomic molecules. *Riv. Nuovo Cim.* **19(3)**, 1–146.

Ziesel, J. P., Nenner, I., and Schulz, G. J. (1975a). Negative ion formation, vibrational excitation, and transmission spectroscopy in hydrogen halides. *J. Chem. Phys.* **63**, 1943–1949.

Ziesel, J. P., Schulz, G. J., and Milhaud, J. (1975b). $S^-$ formation by dissociative attachment in OCS and $CS_2$. *J. Chem. Phys.* **62**, 1936–1940.

Ziesel, J. P., Randell, J., Field, D., Lunt, S. L., Mrotzek, G. and Martin, P. (1993). Very low energy electron scattering by $O_2$. *J. Phys. B* **26**, 527–533.

Ziesel, J. P., Jones, N. C., Field, D., and Madsen, L. B. (2003). Reaction and scattering in cold electron collisions. *Phys. Rev. Lett.* **90**, 083201 (1–4).

Zubek, M., Gulley, N., King, G. C., and Read, F. H. (1996). Measurements of elastic electron scattering in the backward hemisphere. *J. Phys. B* **29**, L239–L244.

Zubek, M., Mielewska, B., Channing, J. M., King, G. C., and Read, F. H. (1999). A study of resonance structures in elastic electron scattering from helium, neon, argon, krypton, and xenon over the angular range from 100 to 180°. *J. Phys. B* **32**, 1351–1363.

Zubek, M., Mielewska, B., Channing, J., King, G. C., and Read, F. H. (2000). Absolute differential cross sections for electron elastic scattering and vibrational excitation in nitrogen in the angular range from 120 to 180°. *J. Phys. B* **33**, L527–L532.

# COHERENCE ANALYSIS AND TENSOR POLARIZATION PARAMETERS OF $(\gamma, e\gamma)$ PHOTOIONIZATION PROCESSES IN ATOMIC COINCIDENCE MEASUREMENTS

*B. LOHMANN[1,2], B. ZIMMERMANN[1], H. KLEINPOPPEN[1,3] and U. BECKER[1]*

[1]*Fritz-Haber-Institut der Max-Planck-Gesellschaft, Faradayweg 4 – 6, D-14195 Berlin, Dahlem, Germany;* [2]*Westfälische Wilhelms-Universität Münster, Institut für Theoretische Physik, Wilhelm-Klemm-Str. 9, D-48149 Münster, Germany;* [3]*University of Stirling, Atomic and Molecular Physics, Stirling FK9 4LA, Scotland, UK*

*E-mail: lohmanb@uni-muenster.de

# I. Introduction

Photoionization of atoms can be linked to the original discovery of the photoelectric effect by Hertz (1887) and almost simultaneously by Hallwachs (1888) in the 19th century. Sophisticated investigations on photoionization of free atoms were first primarily related to total and differential cross-section measurements. Photoelectron spectroscopy refers to measurements of energies and intensities often including their angular distributions (Berkowitz, 1979). So-called *complete* or *perfect* atomic collision and photoionization experiments were based on analysis of particle-photon-, particle-particle-coincident correlations and electron- and atomic spin and orientation effects. References to recent developments of such investigations can be linked to the monograph by Schmidt (1997) and the conference report by Becker and Crowe (2001).

Photoionization and atomic collision processes can quantum mechanically be completely described by a limited number of amplitudes and their phase differences and thus the experiment from which the relevant amplitudes and phase differences can be extracted has been referred to as a *complete* or *perfect* experiment. The first complete atomic collision experiment was realized in the early electron–atom collision experiments of Eminyan *et al.* (1973) and of Standage and Kleinpoppen (1975). The first

complete experiment in photoionization of atoms was reported by Heinzmann and co-workers (see, for example, Heinzman (1980) and Heckenkamp *et al.* (1984)). These authors measured the angular distribution and the spin polarization of photoelectrons for Xe 5p photoionization from which all the relevant dipole amplitudes and phase differences were determined. A series of further studies of this kind were mainly restricted to rare gas atoms (Kessler, 1985).

While the suggestion of quantum mechanically complete collision experiments as most sensitive and crucial tests on the validities of theoretical approaches for the understanding of the relevant dynamic process has been around already since about the middle of the last century (e.g. Fano (1957) and Jacobs (1972)) further and new kinds of methods for complete atomic photoionization experiments have only been suggested and carried out recently. We mention the suggestion by Klar and Klienpoppen (1982) for which photoionization of polarized atoms with polarized light may lead to a complete analysis of relevant amplitudes and phases. Various successful experiments based upon this method have already been reported (Siegel *et al.*, 1983; Kerling *et al.*, 1990; Plotzke *et al.*, 1986, Godehusen *et al.*, 1998, Prümper *et al.*, 2000). Magnetic circular dichroism (MCD) describes the different response of a magnetized piece of material to left- and right handed circular polarized light. Prümper *et al.* (2001) performed the first MCD experiment for polarized iron in the gas phase and observed a remarkable large MCD effect[1] of the ion yield of Fe-vapor far away from any absorption edge. This large MCD effect in the Fe gas phase is contrary to MCD of less than $10^{-4}$ in thin iron films.

A further approach to a complete photoionization analysis has been reported by Hausmann *et al.* (1988); in their experiment on the photoionization of atomic magnesium, the angular distributions of the photoelectrons and Auger electrons provide full *complete* description in terms of complex matrix elements for continuum s- and d-electrons and their relative phase (or cosine of the phase).

Lörch *et al.* (1999) have also reported on a group of studies in which photoionization data and non-coincident subsequent Auger decay for the $3p_{3/2}$ photoionization in atomic calcium leads to a complete extraction of dipole matrix elements and their phase difference, i.e. $|R_{\varepsilon d}|$, $|R_{\varepsilon s}|$ and $\Delta$, from the partial cross-sections, the photoelectron angular distribution parameter $\beta$ and the angular distribution parameter of two fine structure components of the subsequent Auger transition for photon energies near the Cooper minimum.

---

[1] Between 2 and 6%.

Related experiments and theoretical studies of the 3p photoionization of Ca in the vicinity of its ionization threshold were reported by de Fanis *et al.* (1999); angular correlation measurements between the 3p photoelectron and the $M_3N_1N_1$ Auger electron and conventional angular distribution measurements for both the 3p photoelectron and $M_3N_1N_1$ Auger electron were carried out. Random phase approximation calculations for the Ca 3p photoionization are in good agreement with the amplitudes and phases extracted from the experimental data.

An interesting experimental determination of the ratios of the s and d Auger decay amplitudes and their phase difference for the resonant Auger transition $2p_{3/2}^{-1}4s \longrightarrow 3s^{-1}3p^{-1}4s(^2P_J)$ in argon has been reported by Ueda *et al.* (1999); they measured the angular correlation between the resonant Auger emission and the subsequent second-step Auger emission as well as the angular distributions of these two electron emissions.

A comprehensive problematic of the impossibility to perform complete valence shell photoionization experiments with closed shell atoms (Schmidtke *et al.*, 2000a), of the feasibility of a complete Auger decay experiment by spin and angle resolved electron spectroscopy (Schmidtke *et al.*, 2000b) on Xe $N_4O_{2,3}O_{2,3}\,^3P_1$ and of measurements of the transferred spin polarization and analysis of Auger amplitudes in Kr $M_{4,5}N_1N_{2,3}\,^1P_1$ Auger decay (Schmidtke *et al.*, 2001) highlights present-day research.

These experiments have been accompanied and are partly related to theoretical studies and numerical calculations of the angular distribution and spin polarization parameters of Auger emission of the rare gases (Lohmann *et al.*, 1993; Lohmann and Larkins, 1994). More recently, Lohmann (1999a) has been able to derive so-called *propensity rules* in order to predict large dynamic spin polarization parameters for resonant Auger transitions avoiding numerical calculations.

There has been considerable success in describing relative intensities, angular distribution and spin polarization of the emitted Augers electrons numerically for the $N_5O_{2,3}O_{2,3}$ Auger decay of the Xe I $(4d_{5/2}^{-1}6p_{3/2}\,J=1)$ photoexcited state (Lohmann, 1999b) while Lohmann and Kleiman (2000) particularly focussed on the spin-flip transitions.

Other partial stages of developments of complete photoionization experiments have been reported in connection with alignment measurements of the produced ions in which separately angular distributions of Auger and photoelectrons or the polarization of fluorescence radiation is determined (e.g. the papers on Sr and Ca by Hamdy *et al.* (1991a,b), and review on present and future experiments by Mehlhorn (1991)).

We also refer to measurements of alignment parameters of Ar 2p hole states produced by photoionization in the soft X-ray region (Becker *et al.*, 1988; Becker, 1989). For the first time these authors measured partial

photoionization cross-sections and angular distributions of the Ar 2p photo-lines and their subsequent LMM Auger lines. The latter have been supplemented by numerical calculations of the Auger angular distribution parameter by Kabachnik *et al.* (1991).

A series of alignment studies on atomic ions have been reported of which we selectively mention those for cadmium ions $Cd^+(4d^{-1}5s^2\ ^2D_{5/2}, ^2D_{3/2})$ by using the He I 584 Å radiation (Caldwell and Zare, 1977) or synchrotron radiation for photoionization (Kronast *et al.*, 1994; Goodman *et al.*, 1985). In addition to these studies alignment tensor values of $Zn^+$ $(3d^{-1}4s^2\ ^2D_{3/2})$ have been determined (Kronast *et al.*, 1986). For $Cd^+$ ions relativistic random phase approximation in conjunction with quantum defect theory describe the experimental alignment reasonable well.

Detailed papers on alignment through synchrotron radiation have particularly been reported with heavy rare gas ions; we list here those with Kr and Xe. The alignment of Kr II $4p^45p$ states after the Auger decay of the Kr I $(3d_{5/2}^{-1}5p\ J = 1)$ resonance was measured by using the photon induced fluorescence spectroscopy (Zimmermann *et al.*, 2000).

The angular dependence of the ultraviolet fluorescence radiation was (measured by Ehresmann *et al.* (1988)) in order to determine the alignment of Xe II and Xe III ionic states populated via the decay of the Xe I $(4d_{5/2}^{-1}6p\ ^1P_1)$ autoionization resonance through spectator-Auger or Auger-shake transitions. The alignment of the $5p^46p$ levels after the decay of the Xe I $(4d_{5/2}^{-1}6p\ J = 1)$ resonance was studied experimentally and theoretically (Lagutin *et al.*, 2000; Meyer *et al.*, 2001).

Photon induced fluorescence spectroscopy was applied for the first time by Schmoranzer *et al.* (1997) to study the anisotropy of the vacuum UV radiation emitted from Kr II satellite states with total angular momentum $J \geq 3/2$ after the photoionization of Kr atoms by linearly polarized synchrotron radiation near the 4s threshold. The measurements gave evidence of the fact that the sign of the alignment parameter is practically independent of the exciting photon energy for the ionic state with $J = 5/2$ whereas with $J = 3/2$ states the alignment changes sign with varying energy.

While it is well established that the $L_3$ subshell X-ray emission from charged particle impact ionization has anisotropic angular radiation (Wille and Hippler, 1986) equivalent non-statistical population of magnetic substates of atoms in Photoionization has been studied for the erbium atom by Papp and Campbell (1992). The observed angular distributions of the $L_3$ photons were well described by the usual function $I(\theta) = I_0(1 + \beta P_2(\cos\theta))$, e.g. Berezhko *et al.* (1978), with regard to the anisotropy parameter $\beta$ of the $L\ell$, $L\alpha_{1,2}$ and $L\beta_{2,15}$ photon transitions and unpolarized ionizing photons.

The angular asymmetry parameter $\beta_{fl}$ for the resonance enhanced photon induced production of $Ar^+(3s^23p^44p\ ^{2,4}L_J)$ fine structure resolved satellites

were measured by Mentzel *et al.* (1998) from threshold to 38.4 eV. The $\beta_{fl}$ data can be interpreted by a partial wave analysis of photofragmentation products.

New types of complete photoionization experiments have only recently been reported by Beyer *et al.* (1995) and by West *et al.* (1996). These are based upon a coincidence analysis of photoelectrons and fluorescence photons from the decay of excited atoms $^2P_{3/2}$-state ions. A combination of applying linearly and circularly polarized synchrotron radiation for the ionization provided relative *s*- and *d*-wave amplitudes and their phase differences (*including the sign*). A first approach of the theoretical analysis was included in the above papers and has been extended by Kabachnik and Ueda (1995). Their theory, however, is restricted to applications for which the initial state of the atom is in an S-configuration, i.e. closed shell atoms.

In this paper we would like to give up this restriction and generalize the initial state for the photoionization such that any arbitrary state can be chosen. This should enable experimentalists to systematically study through the periodic table photoionization into excited ions and completely analyze the relevant amplitudes to a larger degree of completeness. In order to illustrate the general applicability of our formalism, we partly review specific experimental setups which occur to be special cases of our general approach. Using a different notation these cases may be found in the literature (e.g. Kabachnik and Sazhina, 1976; Bussert and Klar, 1983; Cherepkov, 1983; Kabachnik and Ueda, 1995; Balashov *et al.*, 2000).

The paper is organized as follows. In the next section a general theory for the description of $(\gamma, e\gamma)$ coincidence experiments is derived. This is done by means of the density matrix and statistical tensor methods (e.g. Devons and Goldfarb, 1957; Blum, 1996; Andersen and Bartschat, 2000; Balashov *et al.*, 2000). In particular, the appropriate parameters containing the ionization and decay dynamics and the angular dependency are derived. In Section III the possible different experimental setups are discussed where special attention is given to additional selection rules which may occur for the specific experiments. In Section IV we derive the general equations of angular distribution and of spin and fluorescence polarization, respectively. In order to express these relation in terms of relative parameters we introduce the so-called generalized irreducible anisotropy tensors of alignment and orientation. Besides the common Stokes parameters and the spin polarization vector of the emitted photoelectron we introduce so-called tensor polarization parameters. The analysis of special cases of simultaneous photoelectron fluorescence photon emission will be discussed in Section V. Section VI summarizes previous and recent developments related to experimental approaches to complete scattering experiments in connection with $(\gamma, e\gamma)$ processes and reports of some recent experimental

investigations of $(\gamma, e\gamma)$ processes for calcium and strontium atoms. Synchrotron radiation of fixed energy and polarization state simultaneously photoionizes the atom and excites the ion into a higher state from which fluorescence photons are emitted. The experimental coincidence analysis of the photoelectron and the emitted fluorescence photon can lead to results for relevant amplitudes and phase differences which describe such processes. Eventually, a short conclusion is given in the last section. Throughout the paper atomic units, i.e. $\hbar = e = m_e = 1$, are used.

## II. Theory

### A. GENERAL CONSIDERATIONS

For observing the photoelectron and the subsequently emitted photon radiation in a coincidence experiment a two-step model is assumed. In a first step, e.g. by absorption of synchrotron radiation, a simultaneous photoionization/excitation takes place, i.e. one electron is excited into a Rydberg state, while the other is emitted into the continuum which leaves the atom in a singly ionized excited state. In a second step, the ionic state de-excites via emission of fluorescence radiation.

$$\gamma_{\mathrm{Syn}} + A \longrightarrow A^{+*} + e^-_{\mathrm{Phot}}$$
$$\phantom{xxxxxxxxxx} \llcorner\!\!\longrightarrow A^+ + h\nu \tag{1}$$

The combined photoionization/excitation; and fluorescence emission process is illustrated in Fig. 1. The process of a simple inner shell photoionization with a subsequent fluorescence emission is included in this approach, too. Fluorescence radiation and the photoelectron shall be observed in coincidence. This requires explicit knowledge of the total density matrix $\hat{\boldsymbol{\rho}}_{\mathrm{out}}$ of the combined ensemble of the excited intermediate ionic state $A^{+*}$ and the photoelectron $e^-_{\mathrm{Phot}}$, i.e.

$$\hat{\boldsymbol{\rho}}_{\mathrm{out}} = \hat{\boldsymbol{\rho}}_{\mathrm{out}}(A^{+*} + e^-_{\mathrm{Phot}}). \tag{2}$$

The total density matrix $\hat{\boldsymbol{\rho}}_{\mathrm{in}}$ describing the uncorrelated ensemble of the initial photon $\gamma_{\mathrm{Syn}}$ and the atomic state $A$ can be written as a direct product

$$\hat{\boldsymbol{\rho}}_{\mathrm{in}} = \hat{\boldsymbol{\rho}}(A) \times \hat{\boldsymbol{\rho}}(\gamma_{\mathrm{Syn}}). \tag{3}$$

In particular, assuming an arbitrarily polarized synchrotron radiation beam and choosing the quantization axis along the incoming beam direction, the

FIG. 1. The combined photoionization/excitation and fluorescence emission process. After ionization of an inner shell the residual ion remains in an excited state which eventually decays via emission of fluorescence radiation.

density matrix of the synchrotron radiation photon can be expressed in terms of *Stokes parameters*,

$$\hat{\boldsymbol{\rho}}(\gamma_{\text{Syn}}) = \frac{I}{2}\begin{pmatrix} 1 + \eta_2 & -\eta_3 + i\eta_1 \\ -\eta_3 - i\eta_1 & 1 - \eta_2 \end{pmatrix}, \tag{4}$$

where the notation of Blum, (1996) has been adopted. Here, $\eta_1$ and $\eta_3$ denote the Stokes parameters describing the linear polarization state of the photon beam, whereas $\eta_2$ gives the circular polarization.

Both ensembles are connected by the transition operator $T_i$

$$\hat{\boldsymbol{\rho}}_{\text{out}} = T_i \hat{\boldsymbol{\rho}}_{\text{in}} T_i^+. \tag{5}$$

On the other hand, the final state ensemble consists of the ion $A^+$ and the fluorescence photon

$$\hat{\boldsymbol{\rho}}_{\text{fin}} = \hat{\boldsymbol{\rho}}_{\text{fin}}(A^+ + h\nu). \tag{6}$$

They are connected with the intermediate state ensemble by

$$\hat{\boldsymbol{\rho}}_{\text{fin}} = T_f \hat{\boldsymbol{\rho}}_{\text{out}} T_f^+, \tag{7}$$

where $T_f$ is the transition operator to the final state.

## B. PRIMARY PHOTOIONIZATION/EXCITATION

In the following, the initial atomic state is denoted as $|J_0 M_0\rangle$ where $J_0$ and $M_0$ denote the total angular momentum and magnetic quantum number, respectively. The initial synchrotron radiation photon is characterized as $|\omega \mathbf{n} \lambda\rangle$ where $\omega$ is the photon energy, $\mathbf{n}$ the incoming beam direction, and $\lambda$ the helicity of the photon state. Analogously, the intermediate ionic state is described as $|JM\rangle$ and the photoelectron as $|\mathbf{p} m_s\rangle$ where $\mathbf{p}$ is the electron momentum and $m_s$ the electronic magnetic spin quantum number.

Following textbooks on density matrix formalism, e.g. Devons and Goldfarb, 1957, Blum, 1996, Andersen and Bartschat, 2000, Balashov *et al.*, 2000, and expressing the ionic and electronic states in terms of statistical tensorial sets Eq. (2) may be expressed as

$$\langle T(J)^+_{KQ} \times t(\hat{\mathbf{p}})^+_{kq} \rangle = \mathrm{tr}\,(\hat{\boldsymbol{\rho}}_{\mathrm{out}} T(J)^+_{KQ} \times t(\hat{\mathbf{p}})^+_{kq}), \tag{8}$$

where tr denotes the trace. The statistical tensorial sets $T(J)^+_{KQ}$ and $t(\hat{\mathbf{p}})^+_{kq}$ refer to the intermediate excited ionic state and the photoelectron, respectively. The angular dependency of the photoelectron is given by the solid angle $\hat{\mathbf{p}}$ which denotes the direction of emission. In particular, we may write $t(\hat{\mathbf{p}})^+_{kq} = t^+_{kq} \times 1_{\hat{\mathbf{p}}}$ where $1_{\hat{\mathbf{p}}} = |\hat{\mathbf{p}}\rangle\langle\hat{\mathbf{p}}|$. Analogously, using tensorial sets for the initial photonic, $\mathcal{T}^+_{\Gamma\gamma}$, and atomic states, $T(J_0)^+_{K_0 Q_0}$, and by using Eq. (5) we obtain

$$\langle T(J)^+_{KQ} \times t(\hat{\mathbf{p}})^+_{kq} \rangle = \sum_{K_0 Q_0 \Gamma\gamma} \langle T(J_0)^+_{K_0 Q_0} \rangle \langle \mathcal{T}^+_{\Gamma\gamma} \rangle B(K_0 Q_0, \Gamma\gamma; KQ, kq), \tag{9}$$

where the anisotropy parameter $B$ is defined as

$$B(K_0 Q_0, \Gamma\gamma; KQ, kq) = \mathrm{tr}\Big( T[T(J_0)_{K_0 Q_0} \times \mathcal{T}_{\Gamma\gamma}] T^+ [T(J)^+_{KQ} \times t(\hat{\mathbf{p}})^+_{kq}] \Big). \tag{10}$$

The state multipoles $\langle \mathcal{T}^+_{\Gamma\gamma} \rangle$ describing the synchrotron radiation photon can be connected to the Stokes parameters which is shown in table I. In particular, we note that for an arbitrarily polarized photon beam the tensors $\langle \mathcal{T}^+_{K0} \rangle$, $K \leq 2$ and $\langle \mathcal{T}^+_{2\pm 2} \rangle$ can be non-zero, only.[2]

---

[2] Note, that this depends on the choice of quantization axis. In the so-called *natural coordinate frame* one would obtain different tensors to be non-zero.

Table I

The state multipoles of an arbitrarily polarized photon beam and their connection
to the Stokes parameters. The photon beam axis has been chosen as quantization
axis. Multipoles of rank $K > 2$ must be zero due to dipole-selection rules.

| State multipoles | | Stokes parameters | Stokes parameters | | State multipoles |
|---|---|---|---|---|---|
| | $\langle T_{00}^+ \rangle$ | $= \dfrac{I}{\sqrt{3}}$ | $I$ | $=$ | $\sqrt{3}\langle T_{00}^+ \rangle$ |
| | $\langle T_{10}^+ \rangle$ | $= \dfrac{I}{\sqrt{2}}\eta_2$ | $I\eta_2$ | $=$ | $\sqrt{2}\langle T_{10}^+ \rangle$ |
| | $\langle T_{1\pm1}^+ \rangle$ | $= 0$ | | | |
| $\langle T_{20}^+ \rangle = \dfrac{1}{\sqrt{2}}\langle T_{00}^+ \rangle$ | | $= \dfrac{I}{\sqrt{6}}$ | $I = \sqrt{6}\langle T_{20}^+ \rangle$ | $=$ | $\dfrac{\sqrt{3}}{2}(\langle T_{00}^+ \rangle + \sqrt{2}\langle T_{20}^+ \rangle)$ |
| | $\langle T_{2\pm1}^+ \rangle$ | $= 0$ | | | |
| | $\langle T_{22}^+ \rangle$ | $= \dfrac{I}{2}(-\eta_3 + i\eta_1)$ | $I\eta_3$ | $=$ | $-2\mathrm{Re}\langle T_{22}^+ \rangle$ |
| $\langle T_{2-2}^+ \rangle = \langle T_{22}^+ \rangle^*$ | | $= \dfrac{I}{2}(-\eta_3 - i\eta_1)$ | $I\eta_1$ | $=$ | $2\mathrm{Im}\langle T_{22}^+ \rangle$ |

Inserting complete basis sets the anisotropy parameter $B$ can be expressed as

$$B(K_0 Q_0, \Gamma\gamma; KQ, kq) = \sum_{\substack{MM'm_s m_s' \\ M_0 M_0' \lambda\lambda'}} \langle JM'|T(J)_{KQ}^+|JM\rangle \langle m_s'|t_{kq}^+|m_s\rangle \langle\lambda|\mathcal{T}_{\Gamma\gamma}|\lambda'\rangle$$

$$\times \langle J_0 M_0|T(J_0)_{K_0 Q_0}|J_0 M_0'\rangle \langle JM\mathbf{p}^{(-)}m_s|T_i|J_0 M_0\omega\mathbf{n}\lambda\rangle$$

$$\times \langle JM'\mathbf{p}^{(-)}m_s'|T_i^+|J_0 M_0'\omega\mathbf{n}\lambda'\rangle^* \tag{11}$$

where the asterisk denotes the conjugate complex matrix. The angular dependency is now contained in the transition matrix elements.

The matrix elements of the irreducible tensors may be expressed in terms of 3$j$-symbols

$$B(K_0 Q_0, \Gamma\gamma; KQ, kq)$$

$$= \sum_{\substack{MM'm_s m_s' \\ M_0 M_0' \lambda\lambda'}} \langle JM\mathbf{p}^{(-)}m_s|T_i|J_0 M_0\omega\mathbf{n}\lambda\rangle \langle JM'\mathbf{p}^{(-)}m_s'|T_i^+|J_0 M_0'\omega\mathbf{n}\lambda'\rangle^*$$

$$\times (-1)^{J-M+J_0-M_0+3/2-m_s-\lambda}\sqrt{(2K+1)(2K_0+1)(2k+1)(2\Gamma+1)}$$

$$\times \begin{pmatrix} 1/2 & 1/2 & k \\ m_s & -m_s' & -q \end{pmatrix} \begin{pmatrix} 1 & 1 & \Gamma \\ \lambda & -\lambda' & -\gamma \end{pmatrix} \begin{pmatrix} J_0 & J_0 & K_0 \\ M_0 & -M_0' & -Q_0 \end{pmatrix} \begin{pmatrix} J & J & K \\ M & -M' & -Q \end{pmatrix}.$$

$$\tag{12}$$

Following some textbooks on scattering theory, e.g. Amusia (1990), we expand the transition matrix elements in terms of dipole matrix elements (see Appendix A).

$$\langle JM\mathbf{p}^{(-)}m_s|T_i|J_0M_0\omega\mathbf{n}\lambda\rangle$$

$$= \langle JM\mathbf{p}^{(-)}m_s|d_\lambda|J_0M_0\rangle$$

$$= \frac{1}{\sqrt{|p|^2}}\sum_{\substack{\ell m j m_j \\ J_1 M_1}}(-i)^\ell e^{i\sigma_\ell^j} Y_{\ell m}(\hat{\mathbf{p}})\langle(Jj)J_1\|d\|J_0\rangle(-1)^{-\ell+1/2+m_j-J+j+J_1}$$

$$\times \sqrt{(2j+1)(2J_1+1)}\begin{pmatrix}\ell & 1/2 & j\\ m & m_s & -m_j\end{pmatrix}\begin{pmatrix}J & j & J_1\\ M & m_j & -M_1\end{pmatrix}\begin{pmatrix}J_1 & 1 & J_0\\ -M_1 & \lambda & M_0\end{pmatrix}.$$

$$(13)$$

Inserting Eq. (13) twice into Eq. (12) and rearranging the phase factors the $B$ coefficient can be contracted and we remain with (see Appendix B)

$$B(K_0 Q_0, \Gamma\gamma; KQ, kq)$$

$$= \frac{1}{4\pi|p|^2}\sqrt{(2K+1)(2K_0+1)(2k+1)(2\Gamma+1)}$$

$$\times \sum_{\substack{\mathcal{L}\mathcal{M}\\ a\alpha b\beta}}\sum_{\substack{\ell jJ_1\\ \ell'j'J_1'}}i^{\ell+\ell'}e^{i(\sigma_\ell^j-\sigma_{\ell'}^{j'})}(2a+1)(2b+1)(2\mathcal{L}+1)\sqrt{(2\ell+1)(2\ell'+1)}\mathcal{D}_{\mathcal{M}0}^{(\mathcal{L})}(\hat{\mathbf{p}})^*$$

$$\times \sqrt{(2j+1)(2j'+1)(2J_1+1)(2J_1'+1)}\langle(Jj)J_1\|d\|J_0\rangle\langle(Jj')J_1'\|d\|J_0\rangle^*$$

$$\times (-1)^{J_1'-J_1+\mathcal{L}+\mathcal{M}+k-q}$$

$$\times \begin{pmatrix}\ell & \ell' & \mathcal{L}\\ 0 & 0 & 0\end{pmatrix}\begin{pmatrix}\mathcal{L} & k & a\\ \mathcal{M} & q & \alpha\end{pmatrix}\begin{pmatrix}K_0 & b & \Gamma\\ -Q_0 & \beta & -\gamma\end{pmatrix}\begin{pmatrix}K & a & b\\ -Q & \alpha & \beta\end{pmatrix}$$

$$\times \begin{Bmatrix}K_0 & b & \Gamma\\ J_0 & J_1 & 1\\ J_0 & J_1' & 1\end{Bmatrix}\begin{Bmatrix}K & a & b\\ J & j & J_1\\ J & j' & J_1'\end{Bmatrix}\begin{Bmatrix}\mathcal{L} & k & a\\ \ell & 1/2 & j\\ \ell' & 1/2 & j'\end{Bmatrix}.$$

$$(14)$$

Equation (14) gives an important result. It represents the most general contracted form of the anisotropy parameter $B$. Within the applied two-step

model, the $B$ parameters provide the full information about the primary photoionization/excitation process. They contain the ionization dynamics via the transition matrixs and the scattering phases, as well as the angular dependency which is given via the rotation matrices. So far, an arbitrarily polarized synchrotron radiation beam has been assumed. Besides the fact that we are considering transitions with a resolved initial and final state fine structure, no further assumptions have been made on the polarization state of the atom and excited ion, respectively. Thus, the possibility of coincidence experiments with polarized atoms is included, too. Equation (14) allows also for an electron–photon coincidence experiment where the spin polarization of the photelectron is observed together with the polarization of the emitted fluorescence radiation.

Inspecting Eq. (14) more closely, due to coupling rules, we find the following general restrictions for the quantum numbers

$$0 \leq \Gamma \leq 2, \quad 0 \leq K_0 \leq 2J_0, \quad 0 \leq K \leq 2J \quad \text{and} \quad 0 \leq k \leq 1. \tag{15}$$

The restriction on $\Gamma$ is a result of the dipole approximation, whereas $K_0$ and $K$ are limited by the total angular momenta $J_0$ and $J$ of the initial and intermediate state of the target. The restriction on $k$ is due to the fact that the observed photoelectrons are spin 1/2 particles.

Note, that due to parity conservation in photoionization the emitted partial waves must have the same parity. Therefore, the angular momentum coupling rule of the first 3$j$-symbol restricts $\mathcal{L}$ to even values, i.e.

$$(-1)^{\mathcal{L}} = 1. \tag{16}$$

Further, we note that due to the dipole approximation either $J_1 = J_0$ or $J_1 = J_0 \pm 1$ must be fulfilled.

It is often more convenient to introduce a so-called irreducible statistical product tensor $\langle \mathcal{T}(T_K, t_k; \hat{\mathbf{p}})^+_{\mathcal{K}\kappa} \rangle$, see e.g. Brink and Satchler (1962), eq. (4.6), combining the tensorial sets $T(J)^+_{KQ}$ and $t(\hat{\mathbf{p}})^+_{kq}$, referring to the excited intermediate ionic and photoelectronic states, respectively.

$$\langle \mathcal{T}(T_K, t_k; \hat{\mathbf{p}})^+_{\mathcal{K}\kappa} \rangle = \sum_{Qq} (-1)^{k-K+\kappa} \sqrt{(2\mathcal{K}+1)} \begin{pmatrix} K & k & \mathcal{K} \\ Q & q & -\kappa \end{pmatrix} \langle T(J)^+_{KQ} \times t(\hat{\mathbf{p}})^+_{kq} \rangle.$$
$$\tag{17}$$

Note, that the product tensor is defined with respect to a fixed direction $\hat{\mathbf{p}}$ of photoelectron emission.

Expressing the product tensors $\langle \mathcal{T}(T_K, t_k; \hat{\mathbf{p}})^+_{\mathcal{K}\kappa} \rangle$ with the help of Eq. (9) and including the remaining phase factor, we may write

$$\langle \mathcal{T}(T_K, t_k; \hat{\mathbf{p}})^+_{\mathcal{K}\kappa} \rangle = \sum_{K_0 Q_0 \Gamma\gamma} \langle T(J_0)^+_{K_0 Q_0} \rangle \langle \mathcal{T}^+_{\Gamma\gamma} \rangle C(K_0 Q_0, \Gamma\gamma; K, k, \mathcal{K}\kappa), \quad (18)$$

where the introduced $C$ coefficient is defined as

$$C(K_0 Q_0, \Gamma\gamma; K, k, \mathcal{K}\kappa) = \sum_{Qq} (-1)^{k-K+\kappa} \sqrt{(2\mathcal{K}+1)} \begin{pmatrix} K & k & \mathcal{K} \\ Q & q & -\kappa \end{pmatrix}$$

$$\times B(K_0 Q_0, \Gamma\gamma; KQ, kq). \quad (19)$$

For the remainder of this work we will use the irreducible product tensors introduced by Eq. (17). Therefore, it is appropriate to use the introduced $C$ coefficients instead of the $B$ coefficients. That is, we will deal with the $C$ coefficients as the general anisotropy parameters describing the primary ionization/excitation process. Inserting Eq. (14) into the above expression the summation over the magnetic quantum numbers $Q$, $q$, and $\alpha$ can be carried out, where the 1st, 3rd, and 5th 3$j$-symbols can be combined to form a 6$j$-symbol. This yields

$$C(K_0 Q_0, \Gamma\gamma; K, k, \mathcal{K}\kappa)$$

$$= \frac{1}{4\pi|p|^2} \sqrt{(2\mathcal{K}+1)(2K+1)(2K_0+1)(2k+1)(2\Gamma+1)}$$

$$\times \sum_{\substack{\mathcal{L}\mathcal{M} \\ ab\beta}} \sum_{\substack{\ell j J_1 \\ \ell' j' J_1'}} i^{\ell+\ell'} e^{i(\sigma^j_\ell - \sigma^{j'}_{\ell'})} (2a+1)(2b+1) \langle (Jj)J_1 \| d \| J_0 \rangle \langle (Jj')J_1' \| d \| J_0 \rangle^* \mathcal{D}^{(\mathcal{L})}_{\mathcal{M}0}(\hat{\mathbf{p}})^*$$

$$\times (2\mathcal{L}+1) \sqrt{(2\ell+1)(2\ell'+1)} \sqrt{(2j+1)(2j'+1)(2J_1+1)(2J_1'+1)}$$

$$\times (-1)^{K+J_1'-J_1-a-b}$$

$$\times \begin{pmatrix} \ell & \ell' & \mathcal{L} \\ 0 & 0 & 0 \end{pmatrix} \begin{pmatrix} \mathcal{L} & b & \mathcal{K} \\ -\mathcal{M} & \beta & -\kappa \end{pmatrix} \begin{pmatrix} K_0 & b & \Gamma \\ -Q_0 & \beta & -\gamma \end{pmatrix}$$

$$\times \begin{Bmatrix} \mathcal{L} & b & \mathcal{K} \\ K & k & a \end{Bmatrix} \begin{Bmatrix} K_0 & b & \Gamma \\ J_0 & J_1 & 1 \\ J_0 & J_1' & 1 \end{Bmatrix} \begin{Bmatrix} K & a & b \\ J & j & J_1 \\ J & j' & J_1' \end{Bmatrix} \begin{Bmatrix} \mathcal{L} & k & a \\ \ell & 1/2 & j \\ \ell' & 1/2 & j' \end{Bmatrix}, \quad (20)$$

where $(-1)^{2(\mathcal{M}+q)} = 1$ has been used. Eventually, we note that the restrictions of Eqs. (15) and (16) for the quantum numbers do apply for the $C$ coefficients, too. An extensive discussion of the $C$ coefficients for different experimental set-ups will be given in Section III.

Especially, the selection rule for $\mathcal{L}$ to be an even number needs some further considerations since it implies that the angular dependency of the photoelectrons is given by rotation matrices of even rank, only.

$$\mathcal{D}_{\mathcal{M}0}^{(\mathcal{L})}(\hat{\mathbf{p}})^* \neq 0 \quad \text{for } \mathcal{L} \text{ even.} \tag{21}$$

Where it is a well-known fact that for an unpolarized synchrotron radiation beam and an unpolarized target the angular dependency of a photoionization process is given by the second Legendre polynomial, the usual so-called $\beta$-dependency of the photoelectron, it might be somewhat surprising to find the spherical harmonics restricted to those of even rank. Mainly, if one considers that this is a general result which is also valid, e.g. for a polarized atom *and/or* an arbitrarily polarized synchrotron radiation beam. This result can be however explained by keeping in mind that we applied the dipole approximation.

Generally, the radiation field can be expressed as a linear combination of its electric and magnetic components of the transverse field, having parity $(-1)^{L+1}$ and $(-1)^L$, respectively.

In the dipole approximation the magnetic component of the radiation field is neglected and only the zero-order part, i.e. $L = 0$, of its electric component is taken into account. Due to this, the parity of all emitted partial waves must be the same for electric dipole transitions, which eventually restricts the spherical harmonics to even rank. That is, spherical harmonics of an odd rank can contribute to the angular distribution of emitted photoelectrons only if magnetic multipole transitions or higher order terms of the electric component of the radiation field are taken into account.

## C. Emission of Fluorescence Radiation

Considering the final state and using Eqs. (6) and (7) the fluorescence radiation to be detected can be expressed in terms of state multipoles as

$$\langle \mathcal{T}(\hat{\boldsymbol{\omega}})_{h\nu}^+ \times t(\hat{\mathbf{p}})_{kq}^+ \rangle = \text{tr}\left( \hat{\boldsymbol{\rho}}_{\text{fin}} \mathcal{T}(\hat{\boldsymbol{\omega}})_{h\nu}^+ \times t(\hat{\mathbf{p}})_{kq}^+ \right)$$

$$= \text{tr}\left( T_f \hat{\boldsymbol{\rho}}_{\text{out}} T_f^+ [\mathcal{T}(\hat{\boldsymbol{\omega}})_{h\nu}^+ \times t(\hat{\mathbf{p}})_{kq}^+] \right), \tag{22}$$

where the tensors $\mathcal{T}(\hat{\boldsymbol{\omega}})_{hv}^+$ refer to the fluorescence photon. Its direction of emission is given by the solid angle $\hat{\boldsymbol{\omega}}$. By using

$$\hat{\boldsymbol{\rho}}_{\text{out}} = \sum_{KQ'\overline{k}\overline{q}} \langle T(J)_{KQ'}^+ \times t(\hat{\mathbf{p}})_{\overline{k}\overline{q}}^+ \rangle T(J)_{KQ'} \times t(\hat{\mathbf{p}})_{\overline{k}\overline{q}} \tag{23}$$

we get

$$\langle \mathcal{T}(\hat{\boldsymbol{\omega}})_{hv}^+ \times t(\hat{\mathbf{p}})_{kq}^+ \rangle = \sum_{KQ'\overline{k}\overline{q}} \langle T(J)_{KQ'}^+ \times t(\hat{\mathbf{p}})_{\overline{k}\overline{q}}^+ \rangle A(KQ', \overline{k}\overline{q}, hv, kq), \tag{24}$$

where the anisotropy parameter $A$ is defined as

$$A(KQ', \overline{k}\overline{q}, hv, kq) = \text{tr}\left( T_f [T(J)_{KQ'} \times t(\hat{\mathbf{p}})_{\overline{k}\overline{q}}] T_f^+ [\mathcal{T}(\hat{\boldsymbol{\omega}})_{hv}^+ \times t(\hat{\mathbf{p}})_{kq}^+] \right). \tag{25}$$

The introduction of the anisotropy parameter $A$ is analogously to the discussion in the previous section. While the $B$ or $C$ coefficients contain the information on the primary ionization/excitation; dynamics, the $A$ coefficients yield information on the dynamics of the fluorescence radiation emission, i.e. the second step according to Eq. (1), respectively.

Inserting complete basis sets the anisotropy parameter $A$ can be expressed as

$$A(KQ', \overline{k}\overline{q}, hv, kq) = \sum_{\substack{M_f m_s m_s' \Lambda\Lambda' \\ MM'M_sM_s'}} \langle J_f M_f \Omega \mathbf{N} \Lambda \mathbf{p}^{(-)} m_s | T_f | JM\mathbf{p}^{(-)}M_s \rangle$$

$$\times \langle JM\mathbf{p}^{(-)}M_s | T(J)_{KQ'} \times t_{\overline{k}\overline{q}} | JM'\mathbf{p}^{(-)}M_s' \rangle$$

$$\times \langle JM'\mathbf{p}^{(-)}M_s' | T_f^+ | J_f M_f \Omega \mathbf{N}\Lambda' \mathbf{p}^{(-)}m_s' \rangle$$

$$\times \langle \Lambda' | \mathcal{T}_{hv}^+ | \Lambda \rangle \langle m_s' | t_{kq}^+ | m_s \rangle. \tag{26}$$

Here, $|J_f M_f\rangle$ denotes total angular momentum and its magnetic component of the final ionic state. The fluorescence photon is described by $|\Omega \mathbf{N}\Lambda\rangle$ where $\Omega$ is the photon energy, $\mathbf{N}$ denotes the direction of emission of the emitted fluorescence photon, and $\Lambda$ is the helicity of the photon state.

The transition operator $T_f$ describes the de-excitation via fluorescence photon emission. Thus, the transition matrix elements are orthogonal with respect to the magnetic spin quantum numbers of the photoelectron. This immediately yields the selection rules

$$m_s = M_s \quad \text{and} \quad m_s' = M_s', \tag{27}$$

and the anisotropy parameter $A$ can be reduced to

$$A(KQ', \overline{kq}, hv, kq) = \sum_{\substack{M_f m_s m'_s \\ \Lambda\Lambda' MM'}} \langle J_f M_f \Omega \mathbf{N} \Lambda | T_f | JM \rangle \langle JM | T(J)_{KQ'} | JM' \rangle$$

$$\times \langle m_s | t_{\overline{kq}} | m'_s \rangle \langle JM' | T_f^+ | J_f M_f \Omega \mathbf{N} \Lambda' \rangle \langle \Lambda' | \mathcal{T}_{hv}^+ | \Lambda \rangle \langle m'_s | t_{kq}^+ | m_s \rangle$$

Applying the orthonormality condition of the 3$j$-symbols the sum over $m_s$ and $m'_s$ can be carried out which yields

$$tr(t_{\overline{kq}} t_{kq}^+) = \sum_{m_s m'_s} \langle m_s | t_{\overline{kq}} | m'_s \rangle \langle m'_s | t_{kq}^+ | m_s \rangle = \delta_{\overline{k}k} \delta_{\overline{q}q}, \qquad (29)$$

where $\delta_{xy}$ denotes the Kronecker symbol.

Thus, $A$ can be further reduced and results in

$$A(KQ', \overline{kq}, hv, kq) = \sum_{\substack{M_f \Lambda\Lambda' \\ MM'}} \langle J_f M_f \Omega \mathbf{N} \Lambda | T_f | JM \rangle$$

$$\times \langle JM | T(J)_{KQ'} | JM' \rangle \langle JM' | T_f^+ | J_f M_f \Omega \mathbf{N} \Lambda' \rangle \langle \Lambda' | \mathcal{T}_{hv} | \Lambda \rangle$$

$$= A(KQ', hv). \qquad (30)$$

Expressing the irreducible tensors in terms of 3$j$-symbols we get

$$A(KQ', hv) = \sum_{\substack{M_f \Lambda\Lambda' \\ MM'}} \langle J_f M_f \Omega \mathbf{N} \Lambda | T_f | JM \rangle \langle J_f M_f \Omega \mathbf{N} \Lambda' | T_f^+ | JM' \rangle^*$$

$$\times (-1)^{J-M+1-\Lambda'} \sqrt{(2K+1)(2h+1)} \begin{pmatrix} J & J & K \\ M & -M' & -Q' \end{pmatrix} \begin{pmatrix} 1 & 1 & h \\ \Lambda & -\Lambda' & -v \end{pmatrix}.$$

$$\qquad (31)$$

Thus, the anisotropy parameter $A$ depends on the tensorial rank of the fluorescence photon and the intermediate excited ionic state, only. With this, Eq. (24) simplifies, too.

$$\langle \mathcal{T}(\hat{\boldsymbol{\omega}})_{hv}^+ \times t(\hat{\mathbf{p}})_{kq}^+ \rangle = \sum_{KQ'} \langle T(J)_{KQ'}^+ \times t(\hat{\mathbf{p}})_{kq}^+ \rangle A(KQ', hv). \qquad (32)$$

Following a similar procedure as for the anisotropy parameter $B$ (see Appendix C), the dipole approximation can be applied to the fluorescence transition matrix elements. By using the Wigner–Eckart theorem the matrix elements can be replaced by the reduced transition matrices and by summing over all magnetic quantum numbers the anisotropy parameter $A$ can be written as

$$A(K) = A(KQ', h\nu)$$
$$= \delta_{hK}\delta_{\nu Q'}(-1)^{J+J_f+1-K}|\langle J_f\|D\|J\rangle|^2 \begin{Bmatrix} J & J & K \\ 1 & 1 & J_f \end{Bmatrix}. \qquad (33)$$

This is the angular distribution parameter of photon emission derived by Berezhko and Kabachnik (1977) using a slightly different notation. It is discussed in the book by Balashov *et al.*, (2000), too. In particular, we obtain the normalization parameter $A(0)$ as

$$A(0) = \frac{1}{\sqrt{3(2J+1)}}|\langle J_f\|D\|J\rangle|^2. \qquad (34)$$

This yields some important properties. As can be seen from Eq. (33) all anisotropy parameters are real numbers. The rank of tensors describing the fluorescence photon must be the same as for the intermediate ionic state. The same holds for their magnetic quantum numbers, i.e.

$$K = h \quad \text{and} \quad Q' = \nu. \qquad (35)$$

The anisotropy parameter $A$ eventually depends only on the tensorial rank of the intermediate excited ionic state, and it is independent of the magnetic quantum number.

With this, Eq. (32) simplifies further. The sum over $K$ and $Q'$ vanishes and we finally get

$$\langle \mathcal{T}(\hat{\boldsymbol{\omega}})_{h\nu}^+ \times t(\hat{\mathbf{p}})_{kq}^+\rangle = A(K)\langle T(J)_{KQ'}^+ \times t(\hat{\mathbf{p}})_{kq}^+\rangle \delta_{hK}\delta_{\nu Q'}. \qquad (36)$$

Whereas in Eq. (36) the state multipoles $\langle t_{kq}^+\rangle$ are already defined with respect to the incoming synchrotron radiation beam axis as quantization axis, the tensors $\langle \mathcal{T}_{KQ'}^+\rangle$ and thus the anisotropy parameter $A$ are defined with respect to the axis of radiation emission as quantization axis. Therefore we need to rotate the quantization axis of the photon system back to the axis

parallel to the synchrotron radiation beam axis. Using Blum, (1996), Eq. (4.3.13), and the basic properties of the state multipoles we get

$$
\begin{aligned}
\langle T(J)_{KQ'}^{+} \times t(\hat{\mathbf{p}})_{kq}^{+} \rangle &= \left\langle T(J)_{KQ'} \times t(\hat{\mathbf{p}})_{kq} \right\rangle^{*} = \left[ \mathrm{tr}(\hat{\boldsymbol{\rho}}_{\mathrm{out}} T(J)_{KQ'} \times t(\hat{\mathbf{p}})_{kq}) \right]^{*} \\
&= \left[ \sum_{Q} \mathcal{D}_{QQ'}^{(K)}(\hat{\boldsymbol{\omega}}) \mathrm{tr}(\hat{\boldsymbol{\rho}}_{\mathrm{out}} T(J)_{KQ} \times t(\hat{\mathbf{p}})_{kq}) \right]^{*} \\
&= \sum_{Q} \mathcal{D}_{QQ'}^{(K)}(\hat{\boldsymbol{\omega}})^{*} \langle T(J)_{KQ}^{+} \times t(\hat{\mathbf{p}})_{kq}^{+} \rangle.
\end{aligned} \tag{37}
$$

Inserting the above result into Eq. (36) and using Eq. (9) we get

$$
\langle \mathcal{T}(\hat{\boldsymbol{\omega}})_{KQ'}^{+} \times t(\hat{\mathbf{p}})_{kq}^{+} \rangle = A(K) \sum_{Q} \langle T(J)_{KQ}^{+} \times t(\hat{\mathbf{p}})_{kq}^{+} \rangle \mathcal{D}_{QQ'}^{(K)}(\hat{\boldsymbol{\omega}})^{*}, \tag{38}
$$

where

$$
\langle T(J)_{KQ}^{+} \times t(\hat{\mathbf{p}})_{kq}^{+} \rangle = \sum_{K_0 Q_0 \Gamma \gamma} \langle T(J_0)_{K_0 Q_0}^{+} \rangle \langle \mathcal{T}_{\Gamma\gamma}^{+} \rangle B(K_0 Q_0, \Gamma\gamma; KQ, kq). \tag{39}
$$

Equations (38) and (39) are the most general expressions for any type of electron–photon coincidence experiment as described in Eq. (1), i.e. so far, no assumptions have been made on the degree of polarization of the incoming synchrotron radiation nor on the polarization state of the initial atomic ensemble. As a matter of fact, by using Eqs. (38) and (39) electron–photon coincidence experiments of the most general type can be described, i.e. a simultaneous detection of both, the degree of polarization of the emitted fluorescence photon, as well as the degree of spin polarization of the emitted photoelectron.

The dynamics of the primary simultaneous photoionization/excitation is fully described by the anisotropy parameter $B$. The information on the intermediate state ensemble, i.e. the combined system of the singly ionized excited atom, and of the photoelectron, emitted into a fixed spatial direction, is given by the state multipoles $\langle T(J)_{KQ}^{+} \times t(\hat{\mathbf{p}})_{kq}^{+} \rangle$. The dynamics of de-excitation of the intermediate Rydberg state via fluorescence photon emission is contained in the anisotropy parameter $A$, the angular dependency of the photon system to be observed is provided by the rotation matrix $\mathcal{D}_{Q'Q}^{(K)}(\hat{\boldsymbol{\omega}})$, whereas the angular dependency of the photo-electron is, according to Eq. (14), contained in the $B$ coefficients.

Equations (38) and (39) may be also expressed by means of the introduced irreducible statistical product tensors $\langle \mathcal{T}(T_K, t_k; \hat{\mathbf{p}})_{\mathcal{K}\kappa}^+ \rangle$ and the $C$ coefficients,

$$\langle \mathcal{T}(\hat{\boldsymbol{\omega}})_{KQ'}^+ \times t(\hat{\mathbf{p}})_{kq}^+ \rangle = A(K) \sum_{\mathcal{K}\kappa Q} (-1)^{K-k+\kappa} \sqrt{(2\mathcal{K}+1)} \begin{pmatrix} K & k & \mathcal{K} \\ Q & q & -\kappa \end{pmatrix}$$

$$\times \langle \mathcal{T}(T_K, t_k; \hat{\mathbf{p}})_{\mathcal{K}\kappa}^+ \rangle \mathcal{D}_{QQ'}^{(K)}(\hat{\boldsymbol{\omega}})^*, \tag{40}$$

and

$$\langle \mathcal{T}(T_K, t_k; \hat{\mathbf{p}})_{\mathcal{K}\kappa}^+ \rangle = \sum_{K_0 Q_0 \Gamma\gamma} \langle T(J_0)_{K_0 Q_0}^+ \rangle \langle \mathcal{T}_{\Gamma\gamma}^+ \rangle C(K_0 Q_0, \Gamma\gamma; K, k, \mathcal{K}\kappa). \tag{41}$$

Inserting the appropriate quantum numbers into Eqs. (40) and (41), the general expressions for the angular distribution and spin polarization of the photoelectron and for the angular distribution and degree of polarization of the fluorescence radiation can be obtained. We leave this to the discussion in Section IV.


### D. SELECTION OF THE COORDINATE FRAME

Besides the fact that we have initially chosen our quantization axis as parallel to the synchrotron radiation beam axis, no further assumptions for the explicit choice of our coordinate system have been made so far. That is, in our above derivation of the general formalism, the photoelectron is emitted under the solid angle $\hat{\mathbf{p}} = (\vartheta_e, \varphi_e)$ whereas the fluorescence photon is emitted under the angle $\hat{\boldsymbol{\omega}} = (\theta_\gamma, \phi_\gamma)$. The third Euler angles $\psi_\gamma$ and $\psi_e$ can be generally chosen as zero. The angular dependency of the photoelectron enters Eq. (20) via the rotation matrices $\mathcal{D}_{\mathcal{M}0}^{(\mathcal{L})}(0, \vartheta_e, \varphi_e)$ whereas the angular distribution of the fluorescence photon is contained in the rotation matrices $\mathcal{D}_{Q'Q}^{(K)}(0, \theta_\gamma, \phi_\gamma)$ of Eq. (40).

For our type of electron–photon coincidence experiment the angular correlation between photoelectron and fluorescence photon can be sufficiently described by three angles. That is we may choose an appropriate coordinate system which suits the experimental setup. We will discuss two possibilities.

First, suppose a reaction plane defined by the incoming beam axis and the direction of emission of the fluorescence photon (see Fig. 2). It is then sufficient to describe the direction of emission by a single angle
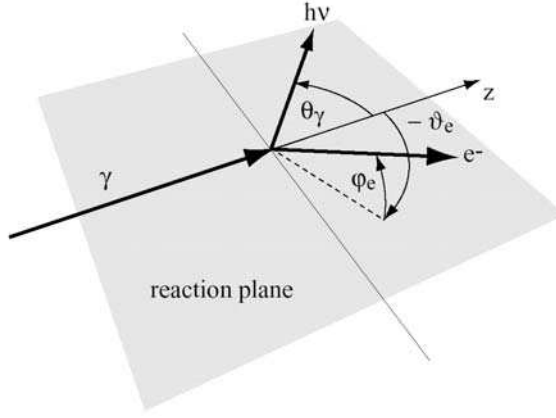
FIG. 2. The choice of the coordinate system for $(\gamma, e\gamma)$ coincidence experiments. The reaction plane is spanned by the incoming synchrotron beam axis $\gamma$ and the direction of emission of the fluorescence photon $h\nu$. $\theta_\gamma$ is the angle of photon emission. The photoelectron $e^-$ is generally observed outside the reaction plane. The direction of photoelectron emission is denoted by the azimuthal angle $\vartheta_e$ and polar angle $\varphi_e$, respectively.

$\hat{\boldsymbol{\omega}} = (0, \theta_\gamma, 0)$. The rotation matrix can then be reduced to a real matrix and Eq. (40) may be written as

$$\langle \mathcal{T}(\hat{\boldsymbol{\omega}})^+_{KQ'} \times t(\hat{\mathbf{p}})^+_{kq} \rangle = A(K) \sum_{\mathcal{K}\kappa Q} (-1)^{K-k+\kappa} \sqrt{(2\mathcal{K}+1)} \begin{pmatrix} K & k & \mathcal{K} \\ Q & q & -\kappa \end{pmatrix}$$
$$\times \langle \mathcal{T}(T_K, t_k; \hat{\mathbf{p}})^+_{\mathcal{K}\kappa} \rangle d^{(K)}_{QQ'}(\theta_\gamma). \qquad (42)$$

The angular dependency of the photoelectron must then be expressed by the complex rotation matrices $\mathcal{D}^{(\mathcal{L})}_{\mathcal{M}0}(0, \vartheta_e, \varphi_e)$.

On the other hand, we may define our reaction plane by the incoming beam axis and the direction of photoelectron emission (see Fig. 3). Thus, the angular dependency of the photoelectron becomes independent on the polar angle $\varphi_e$, and the complex rotation matrices can be reduced to real matrices

$$\mathcal{D}^{(\mathcal{L})}_{\mathcal{M}0}(0, \vartheta_e, 0)^* = d^{(\mathcal{L})}_{\mathcal{M}0}(\vartheta)_e. \qquad (43)$$

However, the angular distribution of the fluorescence photon is then expressed by the complex rotation matrices $\mathcal{D}^{(K)}_{QQ'}(0, \theta_\gamma, \phi_\gamma)$ and Eq. (40) must be used.
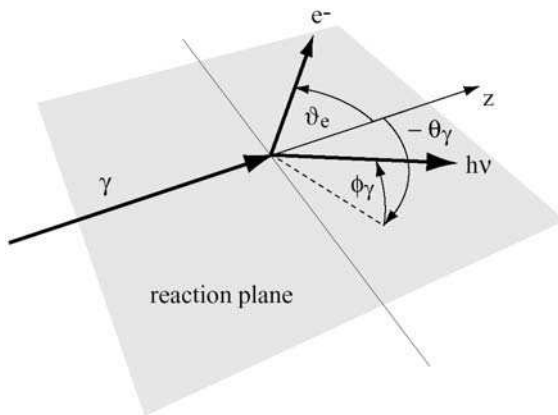
FIG. 3. The alternative choice of the coordinate system for $(\gamma, e\gamma)$ coincidence experiments. The reaction plane is spanned by the incoming synchrotron beam axis $\gamma$ and the direction of emission of the outgoing photoelectron $e^-$. $\vartheta_e$ denotes the photoelectron emission angle. The fluorescence photon $h\nu$ is generally observed outside the reaction plane. The direction of fluorescence photon emission is denoted by the azimuthal angle $\theta_\gamma$ and polar angle $\phi_\gamma$, respectively.

This definition has been widely used in the description of electron–photon coincidence experiments, e.g. Beyer *et al.* (1995), West *et al.* (1996). Throughout the remainder of the discussion we will use this choice of coordinate frame. That is, we have $\hat{\mathbf{p}} = (0, \vartheta_e, 0)$.

Unfortunately, a contraction of the two rotation matrices is not possible for the general case. Only in the special case that either $Q$ or $Q'$ of the rotation matrix $\mathcal{D}_{QQ'}^{(K)}(0, \theta_\gamma, \phi_\gamma)$ is equal to zero, both rotation matrices can be expressed in terms of spherical harmonics which then can be contracted to form bipolar spherical harmonics. Therefore, we leave the angular dependency in the uncoupled form.

## E. SYMMETRIES OF THE $C$ COEFFICIENTS

In order to minimize the calculational effort we can derive symmetry relations for the introduced $C$ coefficients. Forming the complex conjugate of Eq. (20) and using the fact that $(-1)^{\ell+\ell'} = 1$, since $\ell$ and $\ell'$ must have the same parity, we interchange the indices of summation according to

$$j \longleftrightarrow j', \quad \ell \longleftrightarrow \ell', \quad J_1 \longleftrightarrow J_1', \quad \mathcal{M} \longleftrightarrow -\mathcal{M}, \quad \text{and} \quad \beta \longleftrightarrow -\beta. \quad (44)$$

Using the symmetry relations of the 9$j$-symbols and those of the rotation matrices and the 3$j$-symbols, i.e. $\mathcal{M} = \kappa - \gamma - Q_0$, and, eventually the fact that, according to Eq. (21), $\mathcal{L}$ is even, we obtain as symmetry relation for the $C$ coefficients

$$C(K_0 Q_0, \Gamma\gamma; K, k, \mathcal{K}\kappa)^* = (-1)^{K+k+\mathcal{K}+1+\kappa-\gamma-Q_0}$$
$$\times C(K_0 - Q_0, \Gamma - \gamma; K, k, \mathcal{K} - \kappa). \quad (45)$$

The symmetry relation (45) is generally valid for any of the $C$ coefficients. However, for a particular choice of the coordinate frame we might be able to find additional symmetries. As has been discussed in Section II.D, we choose our coordinate frame as is shown in Fig. 3. Then, our reaction plane is spanned by the incoming synchrotron beam and the direction of photoelectron emission and according to Eq. (43) the angular dependency of the $C$ coefficients can be written in form of the real, reduced rotation matrices.

$$C(K_0 Q_0, \Gamma\gamma; K, k, \mathcal{K}\kappa)$$

$$= \frac{1}{4\pi|p|^2} \sqrt{(2\mathcal{K}+1)(2K+1)(2K_0+1)(2k+1)(2\Gamma+1)}$$

$$\times \sum_{\substack{\mathcal{L}\mathcal{M} \\ ab\beta}} \sum_{\substack{\ell j J_1 \\ \ell' j' J_1'}} i^{\ell+\ell'} e^{i(\sigma_\ell^j - \sigma_{\ell'}^{j'})} (2a+1)(2b+1) \langle (Jj)J_1 \| d \| J_0 \rangle \langle (Jj')J_1' \| d \| J_0 \rangle^* d_{\mathcal{M}0}^{(\mathcal{L})}(\vartheta_e)$$

$$\times (2\mathcal{L}+1)\sqrt{(2\ell+1)(2\ell'+1)}\sqrt{(2j+1)(2j'+1)(2J_1+1)(2J_1'+1)}$$

$$\times (-1)^{K+J_1'-J_1-a-b}$$

$$\times \begin{pmatrix} \ell & \ell' & \mathcal{L} \\ 0 & 0 & 0 \end{pmatrix} \begin{pmatrix} \mathcal{L} & b & \mathcal{K} \\ -\mathcal{M} & \beta & -\kappa \end{pmatrix} \begin{pmatrix} K_0 & b & \Gamma \\ -Q_0 & \beta & -\gamma \end{pmatrix}$$

$$\times \begin{Bmatrix} \mathcal{L} & b & \mathcal{K} \\ K & k & a \end{Bmatrix} \begin{Bmatrix} K_0 & b & \Gamma \\ J_0 & J_1 & 1 \\ J_0 & J_1' & 1 \end{Bmatrix} \begin{Bmatrix} K & a & b \\ J & j & J_1 \\ J & j' & J_1' \end{Bmatrix} \begin{Bmatrix} \mathcal{L} & k & a \\ \ell & 1/2 & j \\ \ell' & 1/2 & j' \end{Bmatrix}. \quad (46)$$

Following the same method as above, we form the complex conjugate of Eq. (46) and interchange the indices of

$$j \longleftrightarrow j', \quad \ell \longleftrightarrow \ell', \quad \text{and} \quad J_1 \longleftrightarrow J_1', \quad (47)$$

only. Applying the symmetry relations of the *nj*-symbols and re-arranging the phase factor, we obtain

$$
\begin{aligned}
&C(K_0 Q_0, \Gamma\gamma; K, k, \mathcal{K}\kappa)^* \\
&\quad = (-1)^{\mathcal{K}+K_0+\Gamma-\kappa-Q_0-\gamma} C(K_0 - Q_0, \Gamma - \gamma; K, k, \mathcal{K} - \kappa). \quad (48)
\end{aligned}
$$

In a similar way but interchanging

$$
\mathcal{M} \longleftrightarrow -\mathcal{M}, \quad \text{and} \quad \beta \longleftrightarrow -\beta, \quad (49)
$$

only, we obtain

$$
\begin{aligned}
&C(K_0 Q_0, \Gamma\gamma; K, k, \mathcal{K}\kappa)^* \\
&\quad = (-1)^{K_0+K+k+\Gamma+1} C(K_0 - Q_0, \Gamma - \gamma; K, k, \mathcal{K} - \kappa). \quad (50)
\end{aligned}
$$

The symmetry relations (48) and (50) are valid for our specific choice of the coordinate frame. Both can be identified as special cases of the general symmetry relation (45). This becomes obvious by noting the fact that combining relations (48) and (50) yields Eq. (45) again.

The relations (45)–(50) can be further simplified for a specific experimental setup. For example, let us assume an unpolarized target which is simultaneously ionized and excited by an unpolarized synchrotron beam. Then, the target state is sufficiently described by the monopole tensor $\langle T(J_0)_{00}^+ \rangle$, and the synchrotron beam by tensors $\langle \mathcal{T}_{\Gamma 0}^+ \rangle$, with $\Gamma =$ even, respectively. Thus, we have $K_0 = Q_0 = \gamma = 0$, and $(-1)^\Gamma = 1$, and the symmetry relations can be reduced which yields

$$
C(00, \Gamma 0; K, k, \mathcal{K}\kappa)^* = (-1)^{K+k+\mathcal{K}+1+\kappa} C(00, \Gamma 0; K, k, \mathcal{K} - \kappa), \quad (51)
$$

for the general case. The symmetry relations depending on the coordinate frame can be reduced to

$$
C(00, \Gamma 0; K, k, \mathcal{K}\kappa)^* = (-1)^{\mathcal{K}-\kappa} C(00, \Gamma 0; K, k, \mathcal{K} - \kappa), \quad (52)
$$

and

$$
C(00, \Gamma 0; K, k, \mathcal{K}\kappa)^* = (-1)^{K+k+1} C(00, \Gamma 0; K, k, \mathcal{K} - \kappa), \quad (53)
$$

respectively.

## III. Different Experimental Setups

In this section, we will consider different possible experimental setups in more detail, to point out the general applicability of the derived formalism. Particularly, the different occurring $C$ coefficients are considered and reduced where applicable in order to simplify the complex general expressions.

### A. UNPOLARIZED TARGET

The most simple type of coincidence experiments can be done by using an ensemble of unpolarized atoms. The atomic charge cloud is then isotropic and therefore, the atomic ensemble is sufficiently described by the zero-rank state multipole

$$\langle T(J_0)^+_{K_0 Q_0} \rangle = \delta_{K_0,0} \delta_{Q_0,0} \frac{1}{\sqrt{2J_0 + 1}}. \tag{54}$$

Thus, Eq. (41) can be reduced to

$$\langle \mathcal{T}(T_K, t_k; \hat{\mathbf{p}})^+_{\mathcal{K}\kappa} \rangle = \frac{1}{\sqrt{2J_0 + 1}} \sum_{\Gamma\gamma} \langle \mathcal{T}^+_{\Gamma\gamma} \rangle C_{\text{un}}(\Gamma\gamma; K, k, \mathcal{K}\kappa), \tag{55}$$

where the coefficient $C_{\text{un}}$ has been defined as

$$C_{\text{un}}(\Gamma\gamma; K, k, \mathcal{K}\kappa) = C(00, \Gamma\gamma; K, k, \mathcal{K}\kappa). \tag{56}$$

That is, the coefficient $C_{\text{un}}$ is a special case of the general anisotropy parameter $C$. Inserting Eq. (55) into Eq. (40) yields

$$\langle \mathcal{T}(\hat{\boldsymbol{\omega}})^+_{KQ'} \times t(\hat{\mathbf{p}})^+_{kq} \rangle$$
$$= \frac{1}{\sqrt{2J_0 + 1}} A(K) \sum_{\mathcal{K}\kappa Q} \mathcal{D}^{(K)}_{QQ'}(\hat{\boldsymbol{\omega}})^*$$
$$\times (-1)^{K-k+\kappa} \sqrt{(2\mathcal{K}+1)} \begin{pmatrix} K & k & \mathcal{K} \\ Q & q & -\kappa \end{pmatrix} \sum_{\Gamma\gamma} \langle \mathcal{T}^+_{\Gamma\gamma} \rangle C_{\text{un}}(\Gamma\gamma; K, k, \mathcal{K}\kappa). \tag{57}$$

Inserting $K_0 = Q_0 = 0$ into Eq. (20) yields the selection rules

$$\Gamma = b \quad \text{and} \quad \gamma = \beta. \tag{58}$$

Thus, the sum over $b$ and $\beta$ can be omitted and the $C$ coefficient can be further contracted,

$$C_{\mathrm{un}}(\Gamma\gamma; K, k, \mathcal{K}\kappa)$$

$$= \frac{1}{4\pi|p|^2} \sqrt{\frac{(2\mathcal{K}+1)(2K+1)(2k+1)(2\Gamma+1)}{(2J_0+1)}}$$

$$\times \sum_{a\mathcal{L}} \sum_{\substack{\ell j J_1 \\ \ell' j' J_1'}} i^{\ell+\ell'} e^{i(\sigma_\ell^j - \sigma_{\ell'}^{j'})} (2a+1) \langle (Jj)J_1\|d\|J_0\rangle \langle (Jj')J_1'\|d\|J_0\rangle^* \mathcal{D}_{\mathcal{M}0}^{(\mathcal{L})}(\hat{\mathbf{p}})^*$$

$$\times (2\mathcal{L}+1)\sqrt{(2\ell+1)(2\ell'+1)}\sqrt{(2j+1)(2j'+1)(2J_1+1)(2J_1'+1)}$$

$$\times (-1)^{1+J_0+J_1+a-\mathcal{K}+\Gamma+\gamma} \begin{pmatrix} \ell & \ell' & \mathcal{L} \\ 0 & 0 & 0 \end{pmatrix} \begin{pmatrix} \mathcal{L} & \Gamma & \mathcal{K} \\ -\mathcal{M} & \gamma & -\kappa \end{pmatrix}$$

$$\times \begin{Bmatrix} \mathcal{L} & \Gamma & \mathcal{K} \\ K & k & a \end{Bmatrix} \begin{Bmatrix} J_1 & 1 & J_0 \\ 1 & J_1' & \Gamma \end{Bmatrix} \begin{Bmatrix} K & a & \Gamma \\ J & j & J_1 \\ J & j' & J_1' \end{Bmatrix} \begin{Bmatrix} \mathcal{L} & k & a \\ \ell & 1/2 & j \\ \ell' & 1/2 & j' \end{Bmatrix}. \quad (59)$$

Note, that the sum over $\mathcal{M}$ can be omitted since $\gamma$ and $\kappa$ are arbitrary but fixed numbers. Hence, $\mathcal{M}$ is restricted to one value via the selection rule of the 3$j$-symbol,

$$\mathcal{M} = \gamma - \kappa. \quad (60)$$

If we further assume that the initial atomic state has a total angular momentum $J_0 = 0$, e.g. a ${}^1S_0$ ground state, the second 6$j$-symbol yields an additional selection rule

$$J_1 = J_1' = 1. \quad (61)$$

Thus, the summation over $J_1$ and $J_1'$ can be omitted and we remain with

$$C_{\mathrm{un}}^{J_0=0}(\Gamma\gamma; K, k, \mathcal{K}\kappa)$$

$$= \frac{1}{4\pi|p|^2} \sqrt{(2\mathcal{K}+1)(2K+1)(2k+1)(2\Gamma+1)}$$

$$\times \sum_{a\mathcal{L}} \sum_{\ell j \ell' j'} i^{\ell+\ell'} e^{i(\sigma_\ell^j - \sigma_{\ell'}^{j'})} (2a+1) \langle (Jj)1\|d\|0\rangle \langle (Jj')1\|d\|0\rangle^* \mathcal{D}_{\mathcal{M}0}^{(\mathcal{L})}(\hat{\mathbf{p}})^*$$

$$\times (2\mathcal{L} + 1)\sqrt{(2\ell + 1)(2\ell' + 1)}\sqrt{(2j + 1)(2j' + 1)}$$

$$\times (-1)^{a-K+\gamma} \begin{pmatrix} \ell & \ell' & \mathcal{L} \\ 0 & 0 & 0 \end{pmatrix} \begin{pmatrix} \mathcal{L} & \Gamma & \mathcal{K} \\ -\mathcal{M} & \gamma & -\kappa \end{pmatrix}$$

$$\times \begin{Bmatrix} \mathcal{L} & \Gamma & \mathcal{K} \\ K & k & a \end{Bmatrix} \begin{Bmatrix} K & a & \Gamma \\ J & j & 1 \\ J & j' & 1 \end{Bmatrix} \begin{Bmatrix} \mathcal{L} & k & a \\ \ell & 1/2 & j \\ \ell' & 1/2 & j' \end{Bmatrix}. \tag{62}$$

## B. Unobserved Photoelectron Spin

In a recent experiment by Beyer *et al.* (1995) the degree of polarization of the fluorescence radiation has been detected angle resolved in coincidence with the emitted photoelectron. However, the spin polarization of the photoelectron has not been detected. Theoretically, this case has been discussed by Kabachnik and Ueda (1995).

For such type of experiment only the monopole terms of the tensors $t(\hat{\mathbf{p}})_{kq}^+$ are necessary to describe the photoelectron. Inserting $k = q = 0$ into Eq. (40) we get

$$\langle \mathcal{T}(\hat{\boldsymbol{\omega}})_{KQ'}^+ \times t(\hat{\mathbf{p}})_{00}^+ \rangle = A(K) \sum_{\mathcal{K}\kappa Q} (-1)^{K+\kappa} \sqrt{(2\mathcal{K}+1)} \begin{pmatrix} K & 0 & \mathcal{K} \\ Q & 0 & -\kappa \end{pmatrix}$$

$$\times \langle \mathcal{T}(T_K, t_0; \hat{\mathbf{p}})_{\mathcal{K}\kappa}^+ \rangle \mathcal{D}_{QQ'}^{(K)}(\hat{\boldsymbol{\omega}})^*. \tag{63}$$

From the $3j$-symbol we get the selection rules

$$K = \mathcal{K} \quad \text{and} \quad Q = \kappa. \tag{64}$$

Thus, the summation over $\mathcal{K}$ and $\kappa$ vanishes and we obtain

$$\langle \mathcal{T}(\hat{\boldsymbol{\omega}})_{KQ'}^+ \times t(\hat{\mathbf{p}})_{00}^+ \rangle = A(K) \sum_Q \langle \mathcal{T}(T_K, t_0; \hat{\mathbf{p}})_{KQ}^+ \rangle \mathcal{D}_{QQ'}^{(K)}(\hat{\boldsymbol{\omega}})^*. \tag{65}$$

Using Eq. (41), we express the irreducible product tensor in terms of $C$ coefficients and Eq. (65) may be written as

$$\langle \mathcal{T}(\hat{\boldsymbol{\omega}})_{KQ'}^+ \times t(\hat{\mathbf{p}})_{00}^+ \rangle = A(K) \sum_Q \mathcal{D}_{QQ'}^{(K)}(\hat{\boldsymbol{\omega}})^*$$

$$\times \sum_{K_0 Q_0 \Gamma\gamma} \langle T(J_0)_{K_0 Q_0}^+ \rangle \langle \mathcal{T}_{\Gamma\gamma}^+ \rangle C(K_0 Q_0, \Gamma\gamma; K, 0, KQ), \tag{66}$$

where the angular dependency on the solid angle $\hat{\mathbf{p}}$ of the emitted photoelectron is contained in the $C$ coefficient.

Inserting $k = 0$ into Eq. (20) and using the above selection rules the 6$j$- and 9$j$-symbols can be further reduced and give the additional selection rule

$$\mathcal{L} = a. \tag{67}$$

Thus, the sum over $a$ can be omitted which yields

$$
\begin{aligned}
&C(K_0 Q_0, \Gamma\gamma; K, 0, KQ) \\
&= \frac{1}{4\pi|p|^2} \frac{1}{\sqrt{2}} \sqrt{(2K_0 + 1)(2\Gamma + 1)(2K + 1)} \\
&\quad \times \sum_{\substack{\mathcal{L}M \\ b\beta}} \sum_{\substack{\ell j J_1 \\ \ell' j' J_1'}} i^{\ell+\ell'} e^{i(\sigma_\ell^j - \sigma_{\ell'}^{j'})} (2b+1) \langle (Jj)J_1 \| d \| J_0 \rangle \, \langle (Jj')J_1' \| d \| J_0 \rangle^* \mathcal{D}_{\mathcal{M}0}^{(\mathcal{L})}(\hat{\mathbf{p}})^* \\
&\quad \times (2\mathcal{L}+1)\sqrt{(2\ell+1)(2\ell'+1)} \sqrt{(2j+1)(2j'+1)(2J_1+1)(2J_1'+1)} \\
&\quad \times (-1)^{J_1' - J_1 + \mathcal{L} + j' + \ell + 1/2} \begin{pmatrix} \ell & \ell' & \mathcal{L} \\ 0 & 0 & 0 \end{pmatrix} \begin{pmatrix} \mathcal{L} & b & K \\ -\mathcal{M} & \beta & -Q \end{pmatrix} \begin{pmatrix} K_0 & b & \Gamma \\ -Q_0 & \beta & -\gamma \end{pmatrix} \\
&\quad \times \begin{Bmatrix} j & j' & \mathcal{L} \\ \ell' & \ell & 1/2 \end{Bmatrix} \begin{Bmatrix} K & \mathcal{L} & b \\ J & j & J_1 \\ J & j' & J_1' \end{Bmatrix} \begin{Bmatrix} K_0 & b & \Gamma \\ J_0 & J_1 & 1 \\ J_0 & J_1' & 1 \end{Bmatrix}.
\end{aligned} \tag{68}
$$

An interesting relation can be obtained considering an initial $^1S_0$ ground state , i.e. $J_0 = 0$. Then, the selection rule $J_1 = J_1' = 1$ applies and therefore the sum over $J_1$ and $J_1'$ disappears. The last 9$j$-symbol yields $K_0 = 0$ which implies $Q_0 = 0$. This yields additional selection rules

$$b = \Gamma \quad \text{and} \quad \beta = \gamma. \tag{69}$$

Thus, the sum over $b$ and $\beta$ vanishes and we remain with

$$
\begin{aligned}
C^{J_0=0}(K_0 Q_0, \Gamma\gamma; K, 0, KQ) &= C^{J_0=0}(00, \Gamma\gamma; K, 0, KQ) \\
&= \sqrt{\frac{(2K+1)(2\Gamma+1)}{2}} \\
&\quad \times \sum_{\mathcal{L}} \sum_{\ell j \ell' j'} i^{\ell+\ell'} e^{i(\sigma_\ell^j - \sigma_{\ell'}^{j'})} \langle (Jj)1 \| d \| 0 \rangle \langle (Jj')1 \| d \| 0 \rangle^* \mathcal{D}_{\mathcal{M}0}^{(\mathcal{L})}(\hat{\mathbf{p}})^*
\end{aligned}
$$

$$\times (2\mathcal{L} + 1)\sqrt{(2\ell + 1)(2\ell' + 1)}\sqrt{(2j + 1)(2j' + 1)}$$

$$\times (-1)^{\Gamma - \gamma + \mathcal{L} + j' + \ell + 1/2} \begin{pmatrix} \ell & \ell' & \mathcal{L} \\ 0 & 0 & 0 \end{pmatrix} \begin{pmatrix} \mathcal{L} & \Gamma & K \\ -\mathcal{M} & \gamma & -Q \end{pmatrix}$$

$$\times \begin{Bmatrix} j & j' & \mathcal{L} \\ \ell' & \ell & 1/2 \end{Bmatrix} \begin{Bmatrix} K & \mathcal{L} & \Gamma \\ J & j & 1 \\ J & j' & 1 \end{Bmatrix}. \tag{70}$$

Note, that $\gamma$ and $Q$ are arbitrary but fixed numbers for each $C$ coefficient. Thus, $\mathcal{M}$ is also fixed and the sum over $\mathcal{M}$ can be omitted.

   Comparing this result with the discussion of Section IV.A we find Eq. (70) as a special case of Eq. (62)

$$C^{J_0 = 0}(00, \Gamma\gamma; K, 0, KQ) = C_{\mathrm{un}}^{J_0 = 0}(\Gamma\gamma; K, 0, KQ). \tag{71}$$

This result is not that surprising since the considered $^1S_0$ ground state cannot be polarized. Therefore, for the case $J_0 = 0$ Eq. (71) must exist. On the other hand, this confirms the fact that additional information in a coincidence experiment can be obtained only if the target is initially not in a $^1S_0$ ground state.

## C. Undetected Photoelectron

Often, information on the excited ionic system is only required. In such a situation the photoelectron is not detected, a case which has been considered by Bussert and Klar (1983). An appropriate example is the description of the Auger emission within a two-step model. Here, the anisotropy parameters of angular distribution and spin polarization of the emitted Auger can be factorized into a parameter describing the Auger emission and a coefficient containing the dynamics of the primary ionization/excitation process. As can be seen from Eq. (41), the latter is proportional to our $C$ coefficient averaged over the electronic spin, i.e. $k = 0$, and integrated over the solid angle $\hat{\mathbf{p}}$ of the direction of photoelectron emission. For our general case of $(\gamma, e\gamma)$ experiments an undetected photoelectron simply refers to a photo-excitation followed by a photoemission

$$\gamma_{\mathrm{Syn}} + A \longrightarrow A^* \longrightarrow A + h\nu, \tag{72}$$

i.e. a two-step, non-coincidence experiment. Integrating Eq. (65) over the solid angle $\hat{\mathbf{p}}$ yields

$$\int \langle \mathcal{T}(\hat{\boldsymbol{\omega}})_{KQ'}^+ \times t(\hat{\mathbf{p}})_{00}^+ \rangle d\hat{\mathbf{p}} = A(K) \sum_Q \int \langle \mathcal{T}(T_K, t_0; \hat{\mathbf{p}})_{KQ}^+ \rangle d\hat{\mathbf{p}} \mathcal{D}_{QQ'}^{(K)}(\hat{\boldsymbol{\omega}})^*. \tag{73}$$

Expressing the integrated irreducible product tensors in terms of $C$ coefficients we may write Eq. (73) as

$$\int \langle \mathcal{T}(\hat{\boldsymbol{\omega}})_{KQ'}^+ \times t(\hat{\mathbf{p}})_{00}^+ \rangle d\hat{\mathbf{p}} = A(K) \sum_Q \mathcal{D}_{QQ'}^{(K)}(\hat{\boldsymbol{\omega}})^*$$

$$\times \sum_{K_0 Q_0 \Gamma \gamma} \langle T(J_0)_{K_0 Q_0}^+ \rangle \langle \mathcal{T}_{\Gamma\gamma}^+ \rangle C_{\text{ion}}(K_0 Q_0, \Gamma\gamma; K, 0, \mathcal{K}\kappa),$$

(74)

where we introduced the coefficient $C_{\text{ion}}$ by using Eq. (68) of Section III.B as

$$C_{\text{ion}}(K_0 Q_0, \Gamma\gamma; K, 0, KQ) = \int C(K_0 Q_0, \Gamma\gamma; K, 0, KQ) \, d\hat{\mathbf{p}}.$$

(75)

Using the orthogonality relations of the rotation matrices

$$\int \mathcal{D}_{\mathcal{M}0}^{(\mathcal{L})}(\hat{\mathbf{p}})^* d\hat{\mathbf{p}} = \delta_{\mathcal{L},0}\delta_{\mathcal{M},0}8\pi^2,$$

(76)

and applying the symmetry relations of the $nj$-symbols we obtain the following selection rules

$$\ell = \ell', \quad j = j' \quad \text{and} \quad b = K, \quad \beta = Q.$$

(77)

Thus, the summation over $b$, $\beta$, $j'$, and $\ell'$ can be omitted and by further reducing the 9$j$-symbol we eventually get

$$C_{\text{ion}}(K_0 Q_0, \Gamma\gamma; K, 0, KQ)$$

$$= \frac{\sqrt{2}\pi}{|p|^2}\sqrt{(2K_0 + 1)(2\Gamma + 1)(2K + 1)}$$

$$\times \sum_{\ell j J_1 J_1'} \sqrt{(2J_1 + 1)(2J_1' + 1)}\langle (Jj)J_1 \|d\| J_0 \rangle \langle (Jj)J_1' \|d\| J_0 \rangle^*$$

$$\times (-1)^{J+j+J_1+Q} \begin{pmatrix} K_0 & K & \Gamma \\ -Q_0 & Q & -\gamma \end{pmatrix} \begin{Bmatrix} J & J & K \\ J_1 & J_1' & j \end{Bmatrix} \begin{Bmatrix} K_0 & K & \Gamma \\ J_0 & J_1 & 1 \\ J_0 & J_1' & 1 \end{Bmatrix},$$

(78)

as the general parameter describing the dynamics of the primary ionization/ excitation process for a non-coincidence experiment.

Considering the case of an unpolarized atom (see Section III.A and Bussert and Klar, 1983) Eq. (78) can be further reduced. Inserting $K_0 = Q_0 = 0$ and reducing the $nj$-symbols we obtain

$$C_{\text{ion}}(K) = C_{\text{ion}}(00, \Gamma\gamma; K, 0, KQ)\delta_{K, \Gamma}\delta_{Q, \gamma}$$

$$= \frac{\pi}{|p|^2}\sqrt{\frac{2}{2J_0 + 1}}\sum_{\ell j J_1 J_1'}\sqrt{(2J_1 + 1)(2J_1' + 1)}\langle(Jj)J_1\|d\|J_0\rangle\langle(Jj)J_1'\|d\|J_0\rangle^*$$

$$\times (-1)^{J_0+1+J_1'+J_1+J+j}\begin{Bmatrix} J & J & K \\ J_1 & J_1' & j \end{Bmatrix}\begin{Bmatrix} 1 & 1 & K \\ J_1 & J_1' & J_0 \end{Bmatrix}. \tag{79}$$

Thus, the $C$ coefficient depends on the tensorial rank $\Gamma$ of the photonic states, only. Therefore, combining Eqs. (55) and (79), Eq. (74) can be reduced to

$$\int\langle\mathcal{T}(\hat{\boldsymbol{\omega}})_{KQ'}^+ \times t(\hat{\mathbf{p}})_{00}^+\rangle d\hat{\mathbf{p}} = \delta_{K, \Gamma}\delta_{Q, \gamma}\frac{1}{\sqrt{2J_0 + 1}}A(K)\sum_Q \mathcal{D}_{QQ'}^{(K)}(\hat{\boldsymbol{\omega}})^*\langle\mathcal{T}_{\Gamma\gamma}^+\rangle C_{\text{ion}}(K). \tag{80}$$

Eventually, assuming the initially unpolarized atoms to be in a $J_0 = 0$ ground state, e.g. the rare gases, we obtain an additional selection rule

$$J_1 = J_1' = 1, \tag{81}$$

and the above expression can be further reduced which eventually yields

$$C_{\text{ion}}^{J_0=0}(K) = \frac{\sqrt{2}\pi}{|p|^2}\sum_{\ell j}(-1)^{J_0+J_1'+J+j-K}|\langle(Jj)1\|d\|0\rangle|^2\begin{Bmatrix} J & J & K \\ 1 & 1 & j \end{Bmatrix}. \tag{82}$$

## D. Unpolarized Atoms and Undetected Electron Spin

If the photoelectron spin is not detected the selection rules of Eq. (64) apply. Thus, Eq. (66) reduces to

$$\langle\mathcal{T}(\hat{\boldsymbol{\omega}})_{KQ'}^+ \times t(\hat{\mathbf{p}})_{00}^+\rangle = \frac{1}{\sqrt{2J_0 + 1}}A(K)\sum_Q \mathcal{D}_{QQ'}^{(K)}(\hat{\boldsymbol{\omega}})^*$$

$$\times \sum_{\Gamma\gamma}\langle\mathcal{T}_{\Gamma\gamma}^+\rangle C_{\text{un}}(\Gamma\gamma; K, 0, KQ), \tag{83}$$

where the coefficient $C_{un}$ has been given in Eq. (59). Inserting $k = 0$ into Eq. (59) and reducing the $nj$-symbols yield $\mathcal{L} = a$ and we remain with

$$C_{un}(\Gamma\gamma; K, 0, KQ)$$

$$= \frac{1}{4\pi|p|^2} \sqrt{\frac{(2K+1)(2\Gamma+1)}{2(2J_0+1)}}$$

$$\times \sum_{\mathcal{L}} \sum_{\substack{\ell j J_1 \\ \ell' j' J_1'}} i^{\ell+\ell'} e^{i(\sigma_\ell^j - \sigma_{\ell'}^{j'})} \langle (Jj)J_1 \| d \| J_0 \rangle \langle (Jj')J_1' \| d \| J_0 \rangle^* \mathcal{D}_{\mathcal{M}0}^{(\mathcal{L})}(\hat{\mathbf{p}})^*$$

$$\times (2\mathcal{L}+1)\sqrt{(2\ell+1)(2\ell'+1)}\sqrt{(2j+1)(2j'+1)(2J_1+1)(2J_1'+1)}$$

$$\times (-1)^{J_0+J_1+\gamma+\mathcal{L}+\ell+j'+3/2} \begin{pmatrix} \ell & \ell' & \mathcal{L} \\ 0 & 0 & 0 \end{pmatrix} \begin{pmatrix} \mathcal{L} & \Gamma & K \\ -\mathcal{M} & \gamma & -Q \end{pmatrix}$$

$$\times \begin{Bmatrix} J_1 & 1 & J_0 \\ 1 & J_1' & \Gamma \end{Bmatrix} \begin{Bmatrix} \ell' & \ell & \mathcal{L} \\ j & j' & 1/2 \end{Bmatrix} \begin{Bmatrix} K & \mathcal{L} & \Gamma \\ J & j & J_1 \\ J & j' & J_1' \end{Bmatrix}, \tag{84}$$

where $(-1)^{2K} = 1$ has been used. Note, that $\mathcal{M} = \gamma - \kappa$ and thus $\mathcal{M} = \gamma - Q$ still holds.

For an initial $^1S_0$ ground state we have $J_0 = 0$ which implies $J_1 = J_1' = 1$ which eventually yields

$$C_{un}^{J_0=0}(\Gamma\gamma; K, 0, KQ)$$

$$= \frac{1}{4\pi|p|^2} \sqrt{\frac{(2K+1)(2\Gamma+1)}{2}}$$

$$\times \sum_{\mathcal{L}} \sum_{\ell j \ell' j'} i^{\ell+\ell'} e^{i(\sigma_\ell^j - \sigma_{\ell'}^{j'})} \langle (Jj)1 \| d \| 0 \rangle \langle (Jj')1 \| d \| 0 \rangle^* \mathcal{D}_{\mathcal{M}0}^{(\mathcal{L})}(\hat{\mathbf{p}})^*$$

$$\times (-1)^{\Gamma-\gamma+\mathcal{L}+\ell+j'+1/2}(2\mathcal{L}+1)\sqrt{(2\ell+1)(2\ell'+1)}\sqrt{(2j+1)(2j'+1)}$$

$$\times \begin{pmatrix} \ell & \ell' & \mathcal{L} \\ 0 & 0 & 0 \end{pmatrix} \begin{pmatrix} \mathcal{L} & \Gamma & K \\ -\mathcal{M} & \gamma & -Q \end{pmatrix} \begin{Bmatrix} \ell' & \ell & \mathcal{L} \\ j & j' & 1/2 \end{Bmatrix} \begin{Bmatrix} K & \mathcal{L} & \Gamma \\ J & j & 1 \\ J & j' & 1 \end{Bmatrix}. \tag{85}$$

This result is not surprising since it is identical to the special case of Eq. (70) which has been discussed in Section III.B.

Integrating Eq. (84) over the solid angle $\hat{\mathbf{p}}$ we should end up with the result of Section III.C for an unpolarized target, i.e. Eq. (79). Using the orthogonality of the rotation matrices, Eq. (76), and reducing the *nj*-symbols gives the additional selection rules

$$\ell = \ell', \quad j = j' \quad \text{and} \quad \Gamma = K, \quad \gamma = Q, \tag{86}$$

and we obtain

$$\int C_{\text{un}}(\Gamma\gamma; K, 0, KQ)\, d\hat{\mathbf{p}}$$

$$= \delta_{\mathcal{L},0}\delta_{\mathcal{M},0}\delta_{\ell,\ell'}\delta_{j,j'}\delta_{\Gamma,K}\delta_{\gamma,Q}$$

$$\times \frac{\pi}{|p|^2}\sqrt{\frac{2}{(2J_0+1)}}\sum_{\ell j J_1 J_1'}\langle(Jj)J_1\|d\|J_0\rangle\langle(Jj)J_1'\|d\|J_0\rangle^*\sqrt{(2J_1+1)(2J_1'+1)}$$

$$\times (-1)^{J_0+J_1+J_1'+J+j+1}\begin{Bmatrix} 1 & 1 & K \\ J_1 & J_1' & J_0 \end{Bmatrix}\begin{Bmatrix} J & J & K \\ J_1 & J_1' & j \end{Bmatrix}. \tag{87}$$

Thus, we end up with the expected result

$$\int C_{\text{un}}(\Gamma\gamma; K, 0, KQ)\, d\hat{\mathbf{p}} = C_{\text{ion}}(K). \tag{88}$$

### E. Unobserved Ion State

For this case we observe the photoelectron while the ion remains undetected. This case has been widely discussed throughout the literature. It has been first investigated by Jacobs (1972), Kabachnik and Sazhina (1976) and reviewed by Cherepkov (1983). A further discussion has been given more recently by Balashov *et al.* (2000). However, we include it since it occurs as a special case of our general approach. Here, the ionic state is fully described by the isotropic monopole terms of the tensors $T(J)_{KQ}$. Thus, we have $K = 0$ which requires $Q = Q' = 0$, too. Inserting into Eq. (40) gives

$$\langle \mathcal{T}(\hat{\boldsymbol{\omega}})_{00}^+ \times t(\hat{\mathbf{p}})_{kq}^+ \rangle = \sum_{\mathcal{K}\kappa}(-1)^{k-\kappa}\sqrt{(2\mathcal{K}+1)}\begin{pmatrix} 0 & k & \mathcal{K} \\ 0 & q & -\kappa \end{pmatrix} \times \langle \mathcal{T}(T_0, t_k; \hat{\mathbf{p}})_{\mathcal{K}\kappa}^+ \rangle, \tag{89}$$

The 3$j$-symbol yields the selection rules

$$k = \mathcal{K} \quad \text{and} \quad q = \kappa. \tag{90}$$

Thus, the summation over $\mathcal{K}$ and $\kappa$ vanishes and we obtain the simple relation

$$\langle \mathcal{T}(\hat{\boldsymbol{\omega}})_{00}^+ \times t(\hat{\mathbf{p}})_{kq}^+ \rangle = \langle \mathcal{T}(T_0, t_k; \hat{\mathbf{p}})_{kq}^+ \rangle, \tag{91}$$

Due to the selection rules for the photoelectron tensors $t(\hat{\mathbf{p}})_{kq}^+$, generalized product tensors of rank $k \leq 1$ can occur, only. Therefore, the number of independent parameters to be determined in such type of experiment is significantly reduced compared to the general case. We will consider this point in more detail in Section IV.

Using Eq. (41), we express the irreducible product tensor in terms of $C$ coefficients and Eq. (91) may be written as

$$\langle \mathcal{T}(\hat{\boldsymbol{\omega}})_{00}^+ \times t(\hat{\mathbf{p}})_{kq}^+ \rangle = \sum_{K_0 Q_0 \Gamma \gamma} \langle T(J_0)_{K_0 Q_0}^+ \rangle \langle \mathcal{T}_{\Gamma \gamma}^+ \rangle C(K_0 Q_0, \Gamma \gamma; 0, k, kq), \tag{92}$$

where the angular dependence on the solid angle $\hat{\mathbf{p}}$ is contained in the $C$ coefficient.

Inserting $K = 0$ and using the selection rules of Eq. (90) in Eq. (20) we get the selection rule $a = b$ from the 6$j$-symbol, and reduction of the $nj$-symbols yields

$C(K_0 Q_0, \Gamma \gamma; 0, k, kq)$

$$= \frac{1}{4\pi |p|^2} \sqrt{\frac{(2K_0 + 1)(2k + 1)(2\Gamma + 1)}{(2J + 1)}}$$

$$\times \sum_{\substack{\mathcal{L}\mathcal{M} \\ b\beta}} \sum_{\substack{\ell j J_1 \\ \ell' j' J_1'}} i^{\ell + \ell'} e^{i(\sigma_\ell^j - \sigma_{\ell'}^{j'})} (2b + 1) \langle (Jj)J_1 \| d \| J_0 \rangle \langle (Jj')J_1' \| d \| J_0 \rangle^* \mathcal{D}_{\mathcal{M}0}^{(\mathcal{L})}(\hat{\mathbf{p}})^*$$

$$\times (2\mathcal{L} + 1)\sqrt{(2\ell + 1)(2\ell' + 1)}\sqrt{(2j + 1)(2j' + 1)(2J_1 + 1)(2J_1' + 1)}$$

$$\times (-1)^{k + \mathcal{L} + J + J_1' + j'}$$

$$
\times \begin{pmatrix} \ell & \ell' & \mathcal{L} \\ 0 & 0 & 0 \end{pmatrix} \begin{pmatrix} \mathcal{L} & b & k \\ -\mathcal{M} & \beta & -q \end{pmatrix} \begin{pmatrix} K_0 & b & \Gamma \\ -Q_0 & \beta & -\gamma \end{pmatrix}
$$

$$
\times \begin{Bmatrix} j & j' & b \\ J_1' & J_1 & J \end{Bmatrix} \begin{Bmatrix} K_0 & b & \Gamma \\ J_0 & J_1 & 1 \\ J_0 & J_1' & 1 \end{Bmatrix} \begin{Bmatrix} \mathcal{L} & k & b \\ \ell & 1/2 & j \\ \ell' & 1/2 & j' \end{Bmatrix}. \tag{93}
$$

Equation (93) is the general result for the $C$ coefficient for the considered type of experiment.

If we further assume an unpolarized target we have $K_0 = Q_0 = 0$. Inserting into Eq. (92) gives

$$
\langle \mathcal{T}(\hat{\boldsymbol{\omega}})_{00}^+ \times t(\hat{\mathbf{p}})_{kq}^+ \rangle = \frac{1}{\sqrt{2J_0 + 1}} \sum_{\Gamma\gamma} \langle \mathcal{T}_{\Gamma\gamma}^+ \rangle C(00, \Gamma\gamma; 0, k, kq). \tag{94}
$$

After reducing Eq. (93) we get further selection rules

$$
b = \Gamma \quad \text{and} \quad \beta = \gamma, \tag{95}
$$

and we end up with

$$
C(00, \Gamma\gamma; 0, k, kq)
$$

$$
= \frac{1}{4\pi|p|^2} \sqrt{\frac{(2k+1)(2\Gamma+1)}{(2J_0+1)(2J+1)}}
$$

$$
\times \sum_{\mathcal{L}} \sum_{\substack{\ell j J_1 \\ \ell' j' J_1'}} i^{\ell+\ell'} e^{i(\sigma_\ell^j - \sigma_{\ell'}^{j'})} \langle (Jj)J_1 \| d \| J_0 \rangle \langle (Jj')J_1' \| d \| J_0 \rangle^* \mathcal{D}_{\mathcal{M}0}^{(\mathcal{L})}(\hat{\mathbf{p}})^*
$$

$$
\times (2\mathcal{L}+1)\sqrt{(2\ell+1)(2\ell'+1)} \sqrt{(2j+1)(2j'+1)(2J_1+1)(2J_1'+1)}
$$

$$
\times (-1)^{k+\mathcal{L}+J+J_0+2J_1'+j'+1-\gamma} \begin{pmatrix} \ell & \ell' & \mathcal{L} \\ 0 & 0 & 0 \end{pmatrix} \begin{pmatrix} \mathcal{L} & \Gamma & k \\ -\mathcal{M} & \gamma & -q \end{pmatrix}
$$

$$
\times \begin{Bmatrix} J_1' & J_1 & \Gamma \\ j & j' & J \end{Bmatrix} \begin{Bmatrix} J_1' & J_1 & \Gamma \\ 1 & 1 & J_0 \end{Bmatrix} \begin{Bmatrix} \mathcal{L} & k & \Gamma \\ \ell & 1/2 & j \\ \ell' & 1/2 & j' \end{Bmatrix}. \tag{96}
$$

In Eq. (96) the sum over $\mathcal{M}$ can be omitted since the selection rule of Eq. (60) applies. Equation (96) is a special case of Eq. (59)

$$
C(00, \Gamma\gamma; 0, k, kq) = C_{\text{un}}(\Gamma\gamma; 0, k, kq). \tag{97}
$$

Supposing a $^1S_0$ atomic ground state we have $J_0 = 0$ which yields $J_1 = J_1' = 1$, and the sum over $J_1$ and $J_1'$ can be omitted. After some reduction we arrive at

$$
\begin{aligned}
C(00, \Gamma\gamma; 0, k, kq) = {} & \frac{1}{4\pi|p|^2} \sqrt{\frac{(2k+1)(2\Gamma+1)}{(2J+1)}} \\
& \times \sum_{\mathcal{L}} \sum_{\ell j \ell' j'} i^{\ell+\ell'} e^{i(\sigma_\ell^j - \sigma_{\ell'}^{j'})} \langle (Jj)1 \| d \| 0 \rangle \langle (Jj')1 \| d \| 0 \rangle^* \mathcal{D}_{\mathcal{M}0}^{(\mathcal{L})}(\hat{\mathbf{p}})^* \\
& \times (2\mathcal{L}+1)\sqrt{(2\ell+1)(2\ell'+1)}\sqrt{(2j+1)(2j'+1)} \\
& \times (-1)^{k+\mathcal{L}+J+j'+1+\Gamma-\gamma} \begin{pmatrix} \ell & \ell' & \mathcal{L} \\ 0 & 0 & 0 \end{pmatrix} \begin{pmatrix} \mathcal{L} & \Gamma & k \\ -\mathcal{M} & \gamma & -q \end{pmatrix} \\
& \times \begin{Bmatrix} 1 & 1 & \Gamma \\ j & j' & J \end{Bmatrix} \begin{Bmatrix} \mathcal{L} & k & \Gamma \\ \ell & 1/2 & j \\ \ell' & 1/2 & j' \end{Bmatrix}.
\end{aligned} \tag{98}
$$

Eventually, if not observing the photoelectron spin we have $k = q = 0$, and the $nj$-symbols yield further selection rules

$$
\Gamma = \mathcal{L} \quad \text{and} \quad \mathcal{M} = \gamma, \tag{99}
$$

and after some reduction we obtain

$$
\begin{aligned}
C(00, \Gamma\gamma; 0, 0, 00) = {} & \frac{1}{4\pi|p|^2} \sqrt{\frac{(2\Gamma+1)}{2(2J_0+1)(2J+1)}} \\
& \times \sum_{\substack{\ell j J_1 \\ \ell' j' J_1'}} i^{\ell+\ell'} e^{i(\sigma_\ell^j - \sigma_{\ell'}^{j'})} \langle (Jj)J_1 \| d \| J_0 \rangle \langle (Jj')J_1' \| d \| J_0 \rangle^* \mathcal{D}_{\gamma 0}^{(\Gamma)}(\hat{\mathbf{p}})^* \\
& \times \sqrt{(2\ell+1)(2\ell'+1)}\,\sqrt{(2j+1)(2j'+1)(2J_1+1)(2J_1'+1)} \\
& \times (-1)^{\Gamma+J+J_0+2J_1'+\ell+1/2} \begin{pmatrix} \ell & \ell' & \Gamma \\ 0 & 0 & 0 \end{pmatrix} \\
& \times \begin{Bmatrix} \ell & \ell' & \Gamma \\ j' & j & 1/2 \end{Bmatrix} \begin{Bmatrix} J_1' & J_1 & \Gamma \\ j & j' & J \end{Bmatrix} \begin{Bmatrix} J_1' & J_1 & \Gamma \\ 1 & 1 & J_0 \end{Bmatrix}.
\end{aligned} \tag{100}
$$

Equation (100) is related to the well-known angular distribution parameter of photoelectron emission, the $\beta$ parameter of photoionization, e.g Kabachnik and Sazhina (1976), Berezhko and Kabachnik (1977), Balashov *et al.*, 2000.

For completeness we consider the $^1S_0$ ground state, i.e. we have $J_1 = J_1' = 1$, and we remain with

$$
C^{J_0=0}(00, \Gamma\gamma; 0, 0, 00)
$$

$$
= \frac{1}{4\pi|p|^2} \sqrt{\frac{(2\Gamma+1)}{2(2J+1)}}
$$

$$
\times \sum_{\ell j \ell' j'} i^{\ell+\ell'} e^{i(\sigma_\ell^j - \sigma_{\ell'}^{j'})} \langle (Jj)1\|d\|0 \rangle \langle (Jj')1\|d\|0 \rangle^* \mathcal{D}_{\gamma 0}^{(\Gamma)}(\hat{\mathbf{p}})^*
$$

$$
\times \sqrt{(2\ell+1)(2\ell'+1)} \sqrt{(2j+1)(2j'+1)}
$$

$$
\times (-1)^{J+\ell+1/2} \begin{pmatrix} \ell & \ell' & \Gamma \\ 0 & 0 & 0 \end{pmatrix} \begin{Bmatrix} \ell & \ell' & \Gamma \\ j' & j & 1/2 \end{Bmatrix} \begin{Bmatrix} 1 & 1 & \Gamma \\ j & j' & J \end{Bmatrix}. \quad (101)
$$

## F. The Normalization Parameter

In order to express the $C$ coefficient in terms of relative parameters we eventually consider the normalization coefficient $C(00, 00; 0, 0, 00)$. Using the results of Section III.E and inserting $\Gamma = \gamma = 0$ into Eq. (100) the $nj$-symbols give additional selection rules

$$
\ell = \ell', \quad j = j' \quad \text{and} \quad J_1 = J_1', \quad (102)
$$

and reducing the relevant $nj$-symbols eventually yields

$$
C(00, 00; 0, 0, 00) = \frac{1}{4\pi|p|^2} \frac{1}{\sqrt{6(2J_0+1)(2J+1)}} \sum_{\ell j J_1} |\langle (Jj)J_1\|d\|J_0 \rangle|^2 \quad (103).
$$

Thus, we find the normalization parameter $C(00, 00; 0, 0, 00)$ proportional to the transition rate of photoionization.

## G. Normalization of Generalized Anisotropy Parameters

In Section IV we will derive the general equations of angular distribution and of spin and fluorescence polarization, respectively. Therefore, we need to consider the normalization of the occurring parameters. As we will see later on, the photoelectron intensity $I(\hat{\mathbf{p}})$ as well as the total intensity $I_0$ are both related to the zero-order generalized tensor $\langle \mathcal{T}(T_0, t_0; \hat{\mathbf{p}})_{00}^+ \rangle$.

Its determination is also necessary for defining the generalized irreducible anisotropy parameters of alignment and orientation in terms of relative parameters. From Eq. (41) we find

$$\langle \mathcal{T}(T_0, t_0; \hat{\mathbf{p}})_{00}^+ \rangle = \sum_{K_0 Q_0 \Gamma\gamma} \langle T(J_0)_{K_0 Q_0}^+ \rangle \langle \mathcal{T}_{\Gamma\gamma}^+ \rangle C(K_0 Q_0, \Gamma\gamma; 0, 0, 00). \quad (104)$$

Thus, we need to determine the relevant $C$ coefficients of Eq. (104) Using the result of Eq. (93), inserting $k = \mathcal{K} = \kappa = 0$, reducing the $nj$-symbols, and applying the additional selection rules

$$\mathcal{L} = b \quad \text{and} \quad \mathcal{M} = \beta, \quad (105)$$

results in

$$C(K_0 Q_0, \Gamma\gamma; 0, 0, 00)$$

$$= \frac{1}{4\pi |p|^2} \sqrt{\frac{(2K_0 + 1)(2\Gamma + 1)}{2(2J + 1)}}$$

$$\times \sum_{\mathcal{L}} \sum_{\substack{\ell j J_1 \\ \ell' j' J_1'}} i^{\ell + \ell'} e^{i(\sigma_\ell^j - \sigma_{\ell'}^{j'})} \langle (Jj)J_1 \| d \| J_0 \rangle \langle (Jj')J_1' \| d \| J_0 \rangle^* \mathcal{D}_{\mathcal{M}0}^{(\mathcal{L})}(\hat{\mathbf{p}})^*$$

$$\times (2\mathcal{L} + 1)\sqrt{(2\ell + 1)(2\ell' + 1)} \sqrt{(2j + 1)(2j' + 1)(2J_1 + 1)(2J_1' + 1)}$$

$$\times (-1)^{3\mathcal{L} + J + J_1' + 2j' + \ell + 1/2 + \mathcal{M}} \begin{pmatrix} \ell & \ell' & \mathcal{L} \\ 0 & 0 & 0 \end{pmatrix} \begin{pmatrix} K_0 & \mathcal{L} & \Gamma \\ -Q_0 & \mathcal{M} & -\gamma \end{pmatrix}$$

$$\times \begin{Bmatrix} j & j' & \mathcal{L} \\ J_1' & J_1 & J \end{Bmatrix} \begin{Bmatrix} j & j' & \mathcal{L} \\ \ell & \ell' & 1/2 \end{Bmatrix} \begin{Bmatrix} K_0 & \mathcal{L} & \Gamma \\ J_0 & J_1 & 1 \\ J_0 & J_1' & 1 \end{Bmatrix}. \quad (106)$$

The sum over $\mathcal{M}$ can be omitted since $\gamma$ and $Q_0$ are arbitrary but fixed numbers.

The total intensity $I_0$ is proportional to the angle integrated generalized zero-order tensor. According to Eq. (104) we find

$$\int \langle \mathcal{T}(T_0, t_0; \hat{\mathbf{p}})_{00}^+ \rangle d\hat{\mathbf{p}} = \sum_{K_0 Q_0 \Gamma\gamma} \langle T(J_0)_{K_0 Q_0}^+ \rangle \langle \mathcal{T}_{\Gamma\gamma}^+ \rangle \int C(K_0 Q_0, \Gamma\gamma; 0, 0, 00) \, d\hat{\mathbf{p}}.$$

$$(107)$$

Integrating Eq. (106) over the solid angle $\hat{\mathbf{p}}$ and applying the orthogonality of the rotation matrices, Eq. (76), yields the selection rules

$$\ell = \ell', \quad j = j', \quad J_1 = J_1' \quad \text{and} \quad \Gamma = K_0, \quad \gamma = Q_0, \quad (108)$$

and after some reduction we eventually get

$$\int C(K_0 Q_0, \Gamma\gamma; 0, 0, 00)\, d\hat{\mathbf{p}};$$

$$= \frac{\pi}{|p|^2} \sqrt{\frac{2}{2J+1}} \sum_{\ell j J_1} |\langle (Jj)J_1 \|d\| J_0 \rangle|^2 (-1)^{J_1+J_0} \begin{Bmatrix} J_0 & J_0 & K_0 \\ 1 & 1 & J_1 \end{Bmatrix}. \qquad (109)$$

Reducing the phase factor we used the fact that $Q_0$ is always even since $Q_0 = \gamma$ must be fulfilled.

## IV. Angular Distribution and Electron–Photon Polarization

We will now derive the general equations of angular distribution and of spin and fluorescence polarization, respectively. The fluorescence polarization may be expressed in terms of Stokes parameters. Their connection with the state multipoles have been already given in table I. For the photoelectron, the cartesian components of the spin polarization vector can be connected to the electronic state multipoles by

$$Ip_x = -(\langle t_{11}^+ \rangle - \langle t_{1-1}^+ \rangle) = -2\mathrm{Re}\langle t_{11}^+ \rangle,$$
$$Ip_y = -i(\langle t_{11}^+ \rangle + \langle t_{1-1}^+ \rangle) = 2\mathrm{Im}\langle t_{11}^+ \rangle, \qquad (110)$$
$$Ip_z = \sqrt{2}\langle t_{10}^+ \rangle,$$

and $\langle t_{00}^+ \rangle$ as a normalization factor is given as

$$\langle t_{00} \rangle = I/\sqrt{2}\,. \qquad (111)$$

### A. Angular Distribution

To obtain the general expression for the electron–photon angular distribution only the monopole terms $\langle t_{00}^+ \rangle$ of the electronic tensors have to be taken into account. For the description of the photonic state, this is however not sufficient. According to table I, the tensors $\langle \mathcal{T}_{00}^+ \rangle$ as well as $\langle \mathcal{T}_{20}^+ \rangle$ both contribute to the angular distribution. This can be explained by the transversely character of light. Due to the fact that a photon state with helicity $\lambda = 0$ cannot be populated a photon beam is *always* aligned, and thus the second rank tensor must be included even in the description of an unpolarized photon beam.

Using Eq. (40), the total intensity $I = I(\hat{\boldsymbol{\omega}}, \hat{\mathbf{p}})$ to detect a photon emitted into direction $\hat{\boldsymbol{\omega}}$ while a photoelectron has been emitted under the angle $\hat{\mathbf{p}}$ can then be written as

$$
\begin{aligned}
I(\hat{\boldsymbol{\omega}}, \hat{\mathbf{p}}) &= \frac{\sqrt{6}}{2} \Big( \langle \mathcal{T}(\hat{\boldsymbol{\omega}})_{00}^+ \times t(\hat{\mathbf{p}})_{00}^+ \rangle + \sqrt{2} \langle \mathcal{T}(\hat{\boldsymbol{\omega}})_{20}^+ \times t(\hat{\mathbf{p}})_{00}^+ \rangle \Big) \\
&= \frac{\sqrt{6}}{2} \Bigg( A(0) \langle \mathcal{T}(T_0, t_0; \hat{\mathbf{p}})_{00}^+ \rangle + \sqrt{2} A(2) \sum_Q \langle \mathcal{T}(T_2, t_0; \hat{\mathbf{p}})_{2Q}^+ \rangle \mathcal{D}_{Q0}^{(2)}(\hat{\boldsymbol{\omega}})^* \Bigg).
\end{aligned}
$$

(112)

Integrating over the solid angle $\hat{\boldsymbol{\omega}}$ of photon emission the photoelectron intensity $I(\hat{\mathbf{p}})$ is given as

$$
I(\hat{\mathbf{p}}) = \int I(\hat{\boldsymbol{\omega}}, \hat{\mathbf{p}}) \, d\hat{\boldsymbol{\omega}} = 2\pi \sqrt{6} A(0) \langle \mathcal{T}(T_0, t_0; \hat{\mathbf{p}})_{00}^+ \rangle.
$$

(113)

Eventually, integrating over the solid angle of photelectron emission the total intensity $I_0$ is

$$
I_0 = \int I(\hat{\mathbf{p}}) \, d\hat{\mathbf{p}} = \iint I(\hat{\boldsymbol{\omega}}, \hat{\mathbf{p}}) \, d\hat{\boldsymbol{\omega}}; \, d\hat{\mathbf{p}}; = 2\pi \sqrt{6} A(0) \int \langle \mathcal{T}(T_0, t_0; \hat{\mathbf{p}})_{00}^+ \rangle \, d\hat{\mathbf{p}}.
$$

(114)

Using the relative coefficients of photoemission introduced by Berezhko and Kabachnik (1977) (see also Balashov *et al.*, 2000)

$$
\alpha_K = \delta_{K0} + \sqrt{K} \frac{A(K)}{A(0)},
$$

(115)

and introducing the so-called generalized irreducible anisotropy tensors of alignment and orientation

$$
\mathcal{A}_{\mathcal{K}\kappa}(T_K, t_k; \hat{\mathbf{p}}) = \frac{\langle \mathcal{T}(T_K, t_k; \hat{\mathbf{p}})_{\mathcal{K}\kappa}^+ \rangle}{\int \langle \mathcal{T}(T_0, t_0; \hat{\mathbf{p}})_{00}^+ \rangle \, d\hat{\mathbf{p}}},
$$

(116)

we are able to express the photoelectron intensity $I(\hat{\mathbf{p}})$ in terms of relative parameters

$$
I(\hat{\mathbf{p}}) = I_0 \mathcal{A}_{00}(T_0, t_0; \hat{\mathbf{p}}).
$$

(117)

Note, that the zero rank tensor $\mathcal{A}_{00}(T_0, t_0; \hat{\mathbf{p}})$ is still a function of the photoelectron emission angle. Integrating over the solid angle $\hat{\mathbf{p}}$ yields

however the simple relation

$$\int \mathcal{A}_{00}(T_0, t_0; \hat{\mathbf{p}}) \, d\hat{\mathbf{p}} = 1 \tag{118}$$

This result is consistent with Eq. (114) since integrating Eq. (117) over the solid angle $\hat{\mathbf{p}}$ yields the total intensity which is the expected result.

Then, by using the total intensity $I_0$, Eq. (112) may be eventually expressed as

$$I(\hat{\boldsymbol{\omega}}, \hat{\mathbf{p}}) = \frac{I_0}{4\pi} \left( \mathcal{A}_{00}(T_0, t_0; \hat{\mathbf{p}}) + \alpha_2 \sum_Q \mathcal{A}_{2Q}(T_2, t_0; \hat{\mathbf{p}}) \mathcal{D}_{Q0}^{(2)}(\hat{\boldsymbol{\omega}})^* \right). \tag{119}$$

Using the photoelectron intensity $I(\hat{\mathbf{p}})$ Eq. (119) may be expressed in a different way

$$I(\hat{\boldsymbol{\omega}}, \hat{\mathbf{p}}) = \frac{I(\hat{\mathbf{p}})}{4\pi} \left( 1 + \frac{\alpha_2}{\mathcal{A}_{00}(T_0, t_0; \hat{\mathbf{p}})} \sum_Q \mathcal{A}_{2Q}(T_2, t_0; \hat{\mathbf{p}}) \mathcal{D}_{Q0}^{(2)}(\hat{\boldsymbol{\omega}})^* \right). \tag{120}$$

An alternative form can be obtained by applying Eq. (117)

$$I(\hat{\boldsymbol{\omega}}, \hat{\mathbf{p}}) = \frac{I_0}{4\pi} \left( \frac{I(\hat{\mathbf{p}})}{I_0} + \alpha_2 \sum_Q \mathcal{A}_{2Q}(T_2, t_0; \hat{\mathbf{p}}) \mathcal{D}_{Q0}^{(2)}(\hat{\boldsymbol{\omega}})^* \right). \tag{121}$$

On the other hand, the fluorescence photon intensity $I(\hat{\boldsymbol{\omega}})$ can be obtained from Eq. (119) by integrating over the solid angle $\hat{\mathbf{p}}$ of photoelectron emission and using Eq. (118) as

$$I(\hat{\boldsymbol{\omega}}) = \int I(\hat{\boldsymbol{\omega}}, \hat{\mathbf{p}}) \, d\hat{\mathbf{p}} = \frac{I_0}{4\pi} \left( 1 + \alpha_2 \sum_Q \mathcal{D}_{Q0}^{(2)}(\hat{\boldsymbol{\omega}})^* \int \mathcal{A}_{2Q}(T_2, t_0; \hat{\mathbf{p}}) \, d\hat{\mathbf{p}} \right). \tag{122}$$

Using Eq. (117) in Eq. (122) yields an interesting relation between the angle dependent fluorescence photon intensity $I(\hat{\boldsymbol{\omega}})$ and the angular dependency of the photoelectron intensity $I(\hat{\mathbf{p}})$

$$I(\hat{\boldsymbol{\omega}}) = \int I(\hat{\boldsymbol{\omega}}, \hat{\mathbf{p}}) \, d\hat{\mathbf{p}}$$

$$= \frac{1}{4\pi} \frac{I(\hat{\mathbf{p}})}{\mathcal{A}_{00}(T_0, t_0; \hat{\mathbf{p}})} \left( 1 + \alpha_2 \sum_Q \mathcal{D}_{Q0}^{(2)}(\hat{\boldsymbol{\omega}})^* \int \mathcal{A}_{2Q}(T_2, t_0; \hat{\mathbf{p}}) \, d\hat{\mathbf{p}} \right). \tag{123}$$

## B. POLARIZATION OF FLUORESCENCE RADIATION

The degree of polarization of the emitted fluorescence radiation is usually best described by the use of Stokes parameters. Their connection with the photon tensors $\langle T_{KQ}^{+} \rangle$ is given in table I. Inserting the appropriate quantum numbers into Eq. (40) we obtain the following expressions for the Stokes parameters.

$$I\eta_2(\hat{\boldsymbol{\omega}}, \hat{\mathbf{p}}) = 2\langle \mathcal{T}(\hat{\boldsymbol{\omega}})_{10}^{+} \times t(\hat{\mathbf{p}})_{00}^{+} \rangle = 2A(1) \sum_Q \langle \mathcal{T}(T_1, t_0; \hat{\mathbf{p}})_{1Q}^{+} \rangle \mathcal{D}_{Q0}^{(1)}(\hat{\boldsymbol{\omega}})^*, \quad (124)$$

$$I\eta_1(\hat{\boldsymbol{\omega}}, \hat{\mathbf{p}}) = \sqrt{8}\langle \mathrm{Im}\, \mathcal{T}(\hat{\boldsymbol{\omega}})_{22}^{+} \times t(\hat{\mathbf{p}})_{00}^{+} \rangle$$

$$= \sqrt{8}A(2) \sum_Q \langle \mathcal{T}(\mathrm{Im}\, T_2, t_0; \hat{\mathbf{p}})_{2Q}^{+} \rangle \mathcal{D}_{Q2}^{(2)}(\hat{\boldsymbol{\omega}})^*, \quad (125)$$

and

$$I\eta_3(\hat{\boldsymbol{\omega}}, \hat{\mathbf{p}}) = -\sqrt{8}\langle \mathrm{Re}\, \mathcal{T}(\hat{\boldsymbol{\omega}})_{22}^{+} \times t(\hat{\mathbf{p}})_{00}^{+} \rangle$$

$$= -\sqrt{8}A(2) \sum_Q \langle \mathcal{T}(\mathrm{Re}\, T_2, t_0; \hat{\mathbf{p}})_{2Q}^{+} \rangle \mathcal{D}_{Q2}^{(2)}(\hat{\boldsymbol{\omega}})^*. \quad (126)$$

Expressing our results by means of relative parameters, i.e. using Eqs. (115) and (116), and introducing the abbreviation

$$N(\hat{\boldsymbol{\omega}}, \hat{\mathbf{p}}) = \mathcal{A}_{00}(T_0, t_0; \hat{\mathbf{p}}) + \alpha_2 \sum_Q \mathcal{A}_{2Q}(T_2, t_0; \hat{\mathbf{p}}) \mathcal{D}_{Q0}^{(2)}(\hat{\boldsymbol{\omega}})^*, \quad (127)$$

we eventually get

$$\eta_2(\hat{\boldsymbol{\omega}}, \hat{\mathbf{p}}) = \frac{1}{N(\hat{\boldsymbol{\omega}}, \hat{\mathbf{p}})} \sqrt{\frac{8}{3}} \,\alpha_1 \sum_Q \mathcal{A}_{1Q}(T_1, t_0; \hat{\mathbf{p}}) \mathcal{D}_{Q0}^{(1)}(\hat{\boldsymbol{\omega}})^*, \quad (128)$$

$$\eta_1(\hat{\boldsymbol{\omega}}, \hat{\mathbf{p}}) = \frac{1}{N(\hat{\boldsymbol{\omega}}, \hat{\mathbf{p}})} \sqrt{\frac{8}{3}} \,\alpha_2 \sum_Q \mathcal{A}_{2Q}(\mathrm{Im}\, T_2, t_0; \hat{\mathbf{p}}) \mathcal{D}_{Q2}^{(2)}(\hat{\boldsymbol{\omega}})^*, \quad (129)$$

and

$$\eta_3(\hat{\boldsymbol{\omega}}, \hat{\mathbf{p}}) = \frac{-1}{N(\hat{\boldsymbol{\omega}}, \hat{\mathbf{p}})} \sqrt{\frac{8}{3}} \,\alpha_2 \sum_Q \mathcal{A}_{2Q}(\mathrm{Re}\, T_2, t_0; \hat{\mathbf{p}}) \mathcal{D}_{Q2}^{(2)}(\hat{\boldsymbol{\omega}})^*. \quad (130)$$

## C. Non-coincident Polarization of Fluorescence Radiation

In order to demonstrate the general applicability of the theory we consider the observation of polarization of the emitted fluorescence radiation in a non-coincidence experiment. The related expressions for the Stokes parameters can be easily obtained by integrating the results of Section III.B over the solid angle $\hat{\mathbf{p}}$. In particular, we obtain for the Stokes parameter $\eta_2$

$$I\eta_2(\hat{\boldsymbol{\omega}}) = I \int \eta_2(\hat{\boldsymbol{\omega}}, \hat{\mathbf{p}}) \, d\hat{\mathbf{p}} = 2 \int \langle \mathcal{T}(\hat{\boldsymbol{\omega}})_{10}^+ \times t(\hat{\mathbf{p}})_{00}^+ \rangle \, d\hat{\mathbf{p}}$$

$$= 2A(1) \sum_Q \int \langle \mathcal{T}(T_1, t_0; \hat{\mathbf{p}})_{1Q}^+ \rangle \, d\hat{\mathbf{p}} \mathcal{D}_{Q0}^{(1)}(\hat{\boldsymbol{\omega}})^*, \tag{131}$$

Using Eq. (127) we introduce the angle integrated parameter $N_1$

$$N_1(\hat{\boldsymbol{\omega}}) = \int N d\hat{\mathbf{p}} = 1 + \alpha_2 \sum_Q \int \mathcal{A}_{2Q}(T_2, t_0; \hat{\mathbf{p}}) \, d\hat{\mathbf{p}} \mathcal{D}_{Q0}^{(2)}(\hat{\boldsymbol{\omega}})^*. \tag{132}$$

With Eq. (132) we obtain the angle integrated Stokes parameters in terms of relative parameters as

$$\eta_2(\hat{\boldsymbol{\omega}}) = \int \eta_2(\hat{\boldsymbol{\omega}}, \hat{\mathbf{p}}) \, d\hat{\mathbf{p}} = \frac{1}{N_1(\hat{\boldsymbol{\omega}})} \sqrt{\frac{8}{3}} \, \alpha_1 \sum_Q \int \mathcal{A}_{1Q}(T_1, t_0; \hat{\mathbf{p}}) \, d\hat{\mathbf{p}} \mathcal{D}_{Q0}^{(1)}(\hat{\boldsymbol{\omega}})^*, \tag{133}$$

$$\eta_1(\hat{\boldsymbol{\omega}}) = \int \eta_1(\hat{\boldsymbol{\omega}}, \hat{\mathbf{p}}) \, d\hat{\mathbf{p}} = \frac{1}{N_1(\hat{\boldsymbol{\omega}})} \sqrt{\frac{8}{3}} \, \alpha_2 \sum_Q \int \mathcal{A}_{2Q}(\text{Im } T_2, t_0; \hat{\mathbf{p}}) \, d\hat{\mathbf{p}} \mathcal{D}_{Q2}^{(2)}(\hat{\boldsymbol{\omega}})^*, \tag{134}$$

and

$$\eta_3(\hat{\boldsymbol{\omega}}) = \int \eta_3(\hat{\boldsymbol{\omega}}, \hat{\mathbf{p}}) \, d\hat{\mathbf{p}} = \frac{-1}{N_1(\hat{\boldsymbol{\omega}})} \sqrt{\frac{8}{3}} \, \alpha_2 \sum_Q \int \mathcal{A}_{2Q}(\text{Re } T_2, t_0; \hat{\mathbf{p}}) \, d\hat{\mathbf{p}} \mathcal{D}_{Q2}^{(2)}(\hat{\boldsymbol{\omega}})^*. \tag{135}$$

## D. Spin Polarization of Photoelectrons

We will now express the spin polarization vector of the photoelectron by its cartesian components. Therefore we assume the *y*-axis as perpendicular

to the reaction plane defined by the incoming synchrotron radiation beam and the axis of photoelectron emission. Using Eqs. (110) and (111) we obtain

$$
Ip_x(\hat{\boldsymbol{\omega}}, \hat{\mathbf{p}}) = -\sqrt{3}(\langle \mathcal{T}(\hat{\boldsymbol{\omega}})_{00}^+ \times \operatorname{Re} t(\hat{\mathbf{p}})_{11}^+\rangle \sqrt{2}\langle \mathcal{T}(\hat{\boldsymbol{\omega}})_{20}^+ \times \operatorname{Re} t(\hat{\mathbf{p}})_{11}^+\rangle)
$$

$$
= -\sqrt{3}\Bigg( A(0)\langle \mathcal{T}(T_0, \operatorname{Re} t_1; \hat{\mathbf{p}})_{11}^+\rangle
$$

$$
+ \sqrt{2}A(2)\sum_{\mathcal{K}\kappa Q}(-1)^{\kappa-1}\sqrt{2\mathcal{K}+1}\begin{pmatrix} 2 & 1 & \mathcal{K} \\ Q & 1 & -\kappa \end{pmatrix}
$$

$$
\times \langle \mathcal{T}(T_2, \operatorname{Re} t_1; \hat{\mathbf{p}})_{\mathcal{K}\kappa}^+\rangle \mathcal{D}_{Q0}^{(2)}(\hat{\boldsymbol{\omega}})^* \Bigg). \tag{136}
$$

Note, that the summation over $Q$ and $\kappa$ in the above equation is not independent. Due to the fact that the fluorescence photon is always aligned the number of product tensors $\langle \mathcal{T}(T_K, t_k; \hat{\mathbf{p}})_{\mathcal{K}\kappa}^+\rangle$ increases rapidly. It is therefore no longer possible to adopt the common picture of alignment and orientation tensors which has been successfully used in a large variety of experiments.

Expressing Eq. (136) with relative parameters and using Eq. (127) we obtain

$$
p_x(\hat{\boldsymbol{\omega}}, \hat{\mathbf{p}}) = \frac{-\sqrt{2}}{N(\hat{\boldsymbol{\omega}}, \hat{\mathbf{p}})}\Bigg( \mathcal{A}_{11}(T_0, \operatorname{Re} t_1; \hat{\mathbf{p}})
$$

$$
+ \alpha_2 \sum_{\mathcal{K}Q}(-1)^Q\sqrt{2\mathcal{K}+1}\begin{pmatrix} 2 & 1 & \mathcal{K} \\ Q & 1 & -Q-1 \end{pmatrix}
$$

$$
\times \mathcal{A}_{\mathcal{K}Q+1}(T_2, \operatorname{Re} t_1; \hat{\mathbf{p}})\mathcal{D}_{Q0}^{(2)}(\hat{\boldsymbol{\omega}})^* \Bigg). \tag{137}
$$

Applying the same method we obtain the $y$-component as

$$
p_y(\hat{\boldsymbol{\omega}}, \hat{\mathbf{p}}) = \frac{\sqrt{2}}{N(\hat{\boldsymbol{\omega}}, \hat{\mathbf{p}})}\Bigg( \mathcal{A}_{11}(T_0, \operatorname{Im} t_1; \hat{\mathbf{p}})
$$

$$
+ \alpha_2 \sum_{\mathcal{K}Q}(-1)^Q\sqrt{2\mathcal{K}+1}\begin{pmatrix} 2 & 1 & \mathcal{K} \\ Q & 1 & -Q-1 \end{pmatrix}
$$

$$
\times \mathcal{A}_{\mathcal{K}Q+1}(T_2, \operatorname{Im} t_1; \hat{\mathbf{p}})\mathcal{D}_{Q0}^{(2)}(\hat{\boldsymbol{\omega}})^* \Bigg), \tag{138}
$$

and for the $z$-component we get

$$
p_z(\hat{\boldsymbol{\omega}}, \hat{\mathbf{p}}) = \frac{1}{N(\hat{\boldsymbol{\omega}}, \hat{\mathbf{p}})} \Bigg( \mathcal{A}_{10}(T_0, t_1; \hat{\mathbf{p}})
$$

$$
+ \alpha_2 \sum_{\mathcal{K}Q} (-1)^{Q-1} \sqrt{2\mathcal{K}+1} \begin{pmatrix} 2 & 1 & \mathcal{K} \\ Q & 0 & -Q \end{pmatrix} \mathcal{A}_{\mathcal{K}_Q}(T_2, t_1; \hat{\mathbf{p}}) \mathcal{D}_{Q0}^{(2)}(\hat{\boldsymbol{\omega}})^* \Bigg).
$$

$$(139)$$

### E. Non-coincident Spin Polarization of Photoelectrons

In analogy to the discussion of Section III.C we consider the detection of the spin polarization of the emitted photoelectrons in a non-coincidence experiment. The related expressions for the cartesian components of the spin polarization vector can be obtained by integrating the results of Section II.D over the solid angle $\hat{\boldsymbol{\omega}}$. Using the orthogonality conditions of the rotation matrices, only the first term of Eq. (137) survives and we get for the $x$-component of the spin polarization vector

$$
p_x(\hat{\mathbf{p}}) = \int p_x(\hat{\boldsymbol{\omega}}, \hat{\mathbf{p}}) \, d\hat{\boldsymbol{\omega}} = \frac{-\sqrt{2}}{4\pi} \frac{\mathcal{A}_{11}(T_0, \operatorname{Re} t_1; \hat{\mathbf{p}})}{\mathcal{A}_{00}(T_0, t_0; \hat{\mathbf{p}})}. \tag{140}
$$

Here, we used that the integral over the parameter $N$ yields

$$
\int N(\hat{\boldsymbol{\omega}}, \hat{\mathbf{p}}) \, d\hat{\boldsymbol{\omega}} = 4\pi \mathcal{A}_{00}(T_0, t_0; \hat{\mathbf{p}}). \tag{141}
$$

Analogously we obtain the angle integrated $y$-component as

$$
p_y(\hat{\mathbf{p}}) = \int p_y(\hat{\boldsymbol{\omega}}, \hat{\mathbf{p}}) \, d\hat{\boldsymbol{\omega}} = \frac{\sqrt{2}}{4\pi} \frac{\mathcal{A}_{11}(T_0, \operatorname{Im} t_1; \hat{\mathbf{p}})}{\mathcal{A}_{00}(T_0, t_0; \hat{\mathbf{p}})}, \tag{142}
$$

and for the $z$-component we get

$$
p_z(\hat{\mathbf{p}}) = \int p_z(\hat{\boldsymbol{\omega}}, \hat{\mathbf{p}}) \, d\hat{\boldsymbol{\omega}} = \frac{1}{4\pi} \frac{\mathcal{A}_{10}(T_0, t_1; \hat{\mathbf{p}})}{\mathcal{A}_{00}(T_0, t_0; \hat{\mathbf{p}})}. \tag{143}
$$

### F. Tensor Polarization

Present experimental techniques do not allow to detect both, the electron and the photon spin, in coincidence. Their theoretical analysis can, however,

result in new experimental approaches, e.g. a new method of indirectly determining the electronic spin polarization. For the complete analysis of such experiments, we introduce the so-called components of tensor polarization. That is, we have to determine all combinations of the type $\langle \eta_i \times p_j \rangle$, where $i = 1, 2, 3$ and $j = x, y, z$, respectively. This yields the expressions

$$I\langle \eta_2(\hat{\boldsymbol{\omega}}) \times p_x(\hat{\mathbf{p}}) \rangle = -\sqrt{8}\langle \mathcal{T}(\hat{\boldsymbol{\omega}})^+_{10} \times \text{Re } t(\hat{\mathbf{p}})^+_{11} \rangle, \tag{144}$$

$$I\langle \eta_2(\hat{\boldsymbol{\omega}}) \times p_y(\hat{\mathbf{p}}) \rangle = \sqrt{8}\langle \mathcal{T}(\hat{\boldsymbol{\omega}})^+_{10} \times \text{Im } t(\hat{\mathbf{p}})^+_{11} \rangle, \tag{145}$$

and

$$I\langle \eta_2(\hat{\boldsymbol{\omega}}) \times p_z(\hat{\mathbf{p}}) \rangle = 2\langle \mathcal{T}(\hat{\boldsymbol{\omega}})^+_{10} \times t(\hat{\mathbf{p}})^+_{10} \rangle. \tag{146}$$

Here we have used the fact that all state multipoles with a magnetic component $q = 0$ are real numbers.

The remaining six expressions may be written as

$$I\langle \eta_1(\hat{\boldsymbol{\omega}}) \times p_x(\hat{\mathbf{p}}) \rangle = -4\langle \text{Im } \mathcal{T}(\hat{\boldsymbol{\omega}})^+_{22} \times \text{Re } t(\hat{\mathbf{p}})^+_{11} \rangle, \tag{147}$$

$$I\langle \eta_1(\hat{\boldsymbol{\omega}}) \times p_y(\hat{\mathbf{p}}) \rangle = 4\langle \text{Im } \mathcal{T}(\hat{\boldsymbol{\omega}})^+_{22} \times \text{Im } t(\hat{\mathbf{p}})^+_{11} \rangle, \tag{148}$$

$$I\langle \eta_1(\hat{\boldsymbol{\omega}}) \times p_z(\hat{\mathbf{p}}) \rangle = \sqrt{8}\langle \text{Im } \mathcal{T}(\hat{\boldsymbol{\omega}})^+_{22} \times t(\hat{\mathbf{p}})^+_{10} \rangle, \tag{149}$$

and

$$I\langle \eta_3(\hat{\boldsymbol{\omega}}) \times p_x(\hat{\mathbf{p}}) \rangle = 4\langle \text{Re } \mathcal{T}(\hat{\boldsymbol{\omega}})^+_{22} \times \text{Re } t(\hat{\mathbf{p}})^+_{11} \rangle, \tag{150}$$

$$I\langle \eta_3(\hat{\boldsymbol{\omega}}) \times p_y(\hat{\mathbf{p}}) \rangle = -4\langle \text{Re } \mathcal{T}(\hat{\boldsymbol{\omega}})^+_{22} \times \text{Im } t(\hat{\mathbf{p}})^+_{11} \rangle, \tag{151}$$

$$I\langle \eta_3(\hat{\boldsymbol{\omega}}) \times p_z(\hat{\mathbf{p}}) \rangle = -\sqrt{8}\langle \text{Re } \mathcal{T}(\hat{\boldsymbol{\omega}})^+_{22} \times t(\hat{\mathbf{p}})^+_{10} \rangle, \tag{152}$$

respectively. Thus, using Eq. (40), Eq. (144) yields

$$I\langle \eta_2(\hat{\boldsymbol{\omega}}) \times p_x(\hat{\mathbf{p}}) \rangle = -\sqrt{8}A(1) \times \sum_{\mathcal{K}\kappa Q} (-1)^\kappa \sqrt{2\mathcal{K}+1} \begin{pmatrix} 1 & 1 & \mathcal{K} \\ Q & 1 & -\kappa \end{pmatrix}$$
$$\times \langle \mathcal{T}(T_1, \text{Re } t_1; \hat{\mathbf{p}})^+_{\mathcal{K}\kappa} \rangle \mathcal{D}^{(1)}_{Q0}(\hat{\boldsymbol{\omega}})^*, \tag{153}$$

Using the normalization of Eq. (127), the above result can be expressed with relative parameters,

$$\langle \eta_2(\hat{\boldsymbol{\omega}}) \times p_x(\hat{\mathbf{p}}) \rangle = \frac{-4}{N(\hat{\boldsymbol{\omega}}, \hat{\mathbf{p}})\sqrt{3}} \alpha_1 \sum_{\mathcal{K}Q} (-1)^{Q+1} \sqrt{2\mathcal{K}+1} \begin{pmatrix} 1 & 1 & \mathcal{K} \\ Q & 1 & -Q-1 \end{pmatrix}$$
$$\times \mathcal{A}_{\mathcal{K}Q+1}(T_1, \operatorname{Re} t_1; \hat{\mathbf{p}}) \mathcal{D}_{Q0}^{(1)}(\hat{\boldsymbol{\omega}})^*. \tag{154}$$

For the components $\langle \eta_2 \times p_y \rangle$ and $\langle \eta_2 \times p_z \rangle$ we obtain

$$\langle \eta_2(\hat{\boldsymbol{\omega}}) \times p_y(\hat{\mathbf{p}}) \rangle = \frac{4}{N(\hat{\boldsymbol{\omega}}, \hat{\mathbf{p}})\sqrt{3}} \alpha_1 \sum_{\mathcal{K}Q} (-1)^{Q+1} \sqrt{2\mathcal{K}+1} \begin{pmatrix} 1 & 1 & \mathcal{K} \\ Q & 1 & -Q-1 \end{pmatrix}$$
$$\times \mathcal{A}_{\mathcal{K}Q+1}(T_1, \operatorname{Im} t_1; \hat{\mathbf{p}}) \mathcal{D}_{Q0}^{(1)}(\hat{\boldsymbol{\omega}})^*, \tag{155}$$

and

$$\langle \eta_2(\hat{\boldsymbol{\omega}}) \times p_z(\hat{\mathbf{p}}) \rangle = \frac{\sqrt{8}}{N(\hat{\boldsymbol{\omega}}, \hat{\mathbf{p}})\sqrt{3}} \alpha_1 \sum_{\mathcal{K}Q} (-1)^{Q} \sqrt{2\mathcal{K}+1} \begin{pmatrix} 1 & 1 & \mathcal{K} \\ Q & 0 & -Q \end{pmatrix}$$
$$\times \mathcal{A}_{\mathcal{K}Q}(T_1, t_1; \hat{\mathbf{p}}) \mathcal{D}_{Q0}^{(1)}(\hat{\boldsymbol{\omega}})^* \tag{156}$$

Analogously, the components $\langle \eta_1 \times p_j \rangle$ can be expressed as

$$\langle \eta_1(\hat{\boldsymbol{\omega}}) \times p_x(\hat{\mathbf{p}}) \rangle = \frac{-\sqrt{32}}{N(\hat{\boldsymbol{\omega}}, \hat{\mathbf{p}})\sqrt{3}} \alpha_2 \sum_{\mathcal{K}Q} (-1)^{Q} \sqrt{2\mathcal{K}+1} \begin{pmatrix} 2 & 1 & \mathcal{K} \\ Q & 1 & -Q-1 \end{pmatrix}$$
$$\times \mathcal{A}_{\mathcal{K}Q+1}(\operatorname{Im} T_2, \operatorname{Re} t_1; \hat{\mathbf{p}}) \mathcal{D}_{Q2}^{(2)}(\hat{\boldsymbol{\omega}})^*, \tag{157}$$

$$\langle \eta_1(\hat{\boldsymbol{\omega}}) \times p_y(\hat{\mathbf{p}}) \rangle = \frac{\sqrt{32}}{N(\hat{\boldsymbol{\omega}}, \hat{\mathbf{p}})\sqrt{3}} \alpha_2 \sum_{\mathcal{K}Q} (-1)^{Q} \sqrt{2\mathcal{K}+1} \begin{pmatrix} 2 & 1 & \mathcal{K} \\ Q & 1 & -Q-1 \end{pmatrix}$$
$$\times \mathcal{A}_{\mathcal{K}Q+1}(\operatorname{Im} T_2, \operatorname{Im} t_1; \hat{\mathbf{p}}) \mathcal{D}_{Q2}^{(2)}(\hat{\boldsymbol{\omega}})^*, \tag{158}$$

and

$$\langle \eta_1(\hat{\boldsymbol{\omega}}) \times p_z(\hat{\mathbf{p}}) \rangle = \frac{4}{N(\hat{\boldsymbol{\omega}}, \hat{\mathbf{p}})\sqrt{3}} \alpha_2 \sum_{\mathcal{K}Q} (-1)^{Q+1} \sqrt{2\mathcal{K}+1} \begin{pmatrix} 2 & 1 & \mathcal{K} \\ Q & 0 & -Q \end{pmatrix}$$
$$\times \mathcal{A}_{\mathcal{K}Q}(\operatorname{Im} T_2, t_1; \hat{\mathbf{p}}) \mathcal{D}_{Q2}^{(2)}(\hat{\boldsymbol{\omega}})^*, \tag{159}$$

and for the components $\langle \eta_3 \times p_j \rangle$ we write

$$\langle \eta_3(\hat{\boldsymbol{\omega}}) \times p_x(\hat{\mathbf{p}}) \rangle = \frac{\sqrt{32}}{N(\hat{\boldsymbol{\omega}}, \hat{\mathbf{p}})\sqrt{3}} \, \alpha_2 \sum_{\mathcal{K}Q} (-1)^Q \sqrt{2\mathcal{K}+1} \begin{pmatrix} 2 & 1 & \mathcal{K} \\ Q & 1 & -Q-1 \end{pmatrix}$$

$$\times \mathcal{A}_{\mathcal{K}Q+1}(\operatorname{Re} T_2, \operatorname{Re} t_1; \hat{\mathbf{p}}) \mathcal{D}_{Q2}^{(2)}(\hat{\boldsymbol{\omega}})^*, \tag{160}$$

$$\langle \eta_3(\hat{\boldsymbol{\omega}}) \times p_y(\hat{\mathbf{p}}) \rangle = \frac{-\sqrt{32}}{N(\hat{\boldsymbol{\omega}}, \hat{\mathbf{p}})\sqrt{3}} \, \alpha_2 \sum_{\mathcal{K}Q} (-1)^Q \sqrt{2\mathcal{K}+1} \begin{pmatrix} 2 & 1 & \mathcal{K} \\ Q & 1 & -Q-1 \end{pmatrix}$$

$$\times \mathcal{A}_{\mathcal{K}Q+1}(\operatorname{Re} T_2, \operatorname{Im} t_1; \hat{\mathbf{p}}) \mathcal{D}_{Q2}^{(2)}(\hat{\boldsymbol{\omega}})^*, \tag{161}$$

and

$$\langle \eta_3(\hat{\boldsymbol{\omega}}) \times p_z(\hat{\mathbf{p}}) \rangle = \frac{-4}{N(\hat{\boldsymbol{\omega}}, \hat{\mathbf{p}})\sqrt{3}} \, \alpha_2 \sum_{\mathcal{K}Q} (-1)^{Q+1} \sqrt{2\mathcal{K}+1} \begin{pmatrix} 2 & 1 & \mathcal{K} \\ Q & 0 & -Q \end{pmatrix}$$

$$\times \mathcal{A}_{\mathcal{K}Q}(\operatorname{Re} T_2, t_1; \hat{\mathbf{p}}) \mathcal{D}_{Q2}^{(2)}(\hat{\boldsymbol{\omega}})^*. \tag{162}$$

As we have seen from the general expression for the tensor polarization parameters as well as for the other cases discussed in Section IV, there is, for the most general case, a large number of irreducible anisotropy parameters $\mathcal{A}_{\mathcal{K}\kappa}(T_K, t_k; \hat{\mathbf{p}})$ to determine. The maximum number of anisotropy parameter to occur for a certain type of the experiments discussed is given in table II. For example if the angular distribution intensity is measured in a coincidence experiment, the quantity $I(\hat{\boldsymbol{\omega}}, \hat{\mathbf{p}})$, in general, depends on the zero rank tensor parameter $\mathcal{A}_{00}(T_0, t_0; \hat{\mathbf{p}})$ and on the five components of the second rank tensor $\mathcal{A}_{2\kappa}(T_2, t_0; \hat{\mathbf{p}})$, with $\kappa = -2, -1, 0, 1, 2$. Thus, $I(\hat{\boldsymbol{\omega}}, \hat{\mathbf{p}})$ can be a function of six independent parameters in the general case. The number of independent parameters may reduce depending on the specific type of experiment, see the discussion in Section III, as well as on the quantum numbers of a specific transition. This will be discussed in the next section.

## V.  Analysis of a Special Case $J_0 = 0 \longrightarrow J = 1/2$ Transitions

In order to clarify the derived formalism we will now consider a case of an *ideal* transitions in more detail. It is illustrated that for a certain transition

Table II

The generalized irreducible anisotropy parameters $\mathcal{A}_{\mathcal{K}\kappa}(T_K, t_k; \hat{\mathbf{p}})$ occurring for the different experimentally observable parameters of angular distribution, spin polarization, Stokes and tensor polarization, respectively. The angle integrated parameters are abbreviated as $\mathcal{A}_{\mathcal{K}\kappa}(T_K, t_k)$.

| Exp. | Observ. | Irr. aniso. par. | Mag. comp. $\kappa$ | No. of coef. |
|---|---|---|---|---|
| Ang. distrib. | $I(\hat{\boldsymbol{\omega}}, \hat{\mathbf{p}})$ | $\mathcal{A}_{00}(T_0, t_0; \hat{\mathbf{p}})$ | $0$ | 1 |
| | | $\mathcal{A}_{2\kappa}(T_2, t_0; \hat{\mathbf{p}})$ | $-2, -1, 0, 1, 2$ | 5 |
| | $I(\hat{\mathbf{p}})$ | $\mathcal{A}_{00}(T_0, t_0; \hat{\mathbf{p}})$ | $0$ | 1 |
| | $I(\hat{\boldsymbol{\omega}})$ | $\mathcal{A}_{2\kappa}(T_2, t_0)$ | $-2, -1, 0, 1, 2$ | 5 |
| Fluo. pol. | $\eta_2(\hat{\boldsymbol{\omega}}, \hat{\mathbf{p}})$ | $\mathcal{A}_{1\kappa}(T_1, t_0; \hat{\mathbf{p}})$ | $-1, 0, 1$ | 3 |
| | $\eta_1(\hat{\boldsymbol{\omega}}, \hat{\mathbf{p}})$ | $\mathcal{A}_{2\kappa}(\mathrm{Im}\,T_2, t_0; \hat{\mathbf{p}})$ | $-2, -1, 0, 1, 2$ | 5 |
| | $\eta_3(\hat{\boldsymbol{\omega}}, \hat{\mathbf{p}})$ | $\mathcal{A}_{2\kappa}(\mathrm{Re}\,T_2, t_0; \hat{\mathbf{p}})$ | $-2, -1, 0, 1, 2$ | 5 |
| | $\eta_2(\hat{\boldsymbol{\omega}})$ | $\mathcal{A}_{1\kappa}(T_1, t_0)$ | $-1, 0, 1$ | 3 |
| | $\eta_1(\hat{\boldsymbol{\omega}})$ | $\mathcal{A}_{2\kappa}(\mathrm{Im}\,T_2, t_0)$ | $-2, -1, 0, 1, 2$ | 5 |
| | $\eta_3(\hat{\boldsymbol{\omega}})$ | $\mathcal{A}_{2\kappa}(\mathrm{Re}\,T_2, t_0)$ | $-2, -1, 0, 1, 2$ | 5 |
| Spin pol. | $p_x(\hat{\boldsymbol{\omega}}, \hat{\mathbf{p}})$ | $\mathcal{A}_{11}(T_0, \mathrm{Re}\,t_1; \hat{\mathbf{p}})$ | $1$ | 1 |
| | | $\mathcal{A}_{1\kappa}(T_2, \mathrm{Re}\,t_1; \hat{\mathbf{p}})$ | $-1, 0, 1$ | 3 |
| | | $\mathcal{A}_{2\kappa}(T_2, \mathrm{Re}\,t_1; \hat{\mathbf{p}})$ | $-1, 0, 1, 2$ | 4 |
| | | $\mathcal{A}_{3\kappa}(T_2, \mathrm{Re}\,t_1; \hat{\mathbf{p}})$ | $-1, 0, 1, 2, 3$ | 5 |
| | $p_y(\hat{\boldsymbol{\omega}}, \hat{\mathbf{p}})$ | $\mathcal{A}_{11}(T_0, \mathrm{Im}\,t_1; \hat{\mathbf{p}})$ | $1$ | 1 |
| | | $\mathcal{A}_{1\kappa}(T_2, \mathrm{Im}\,t_1; \hat{\mathbf{p}})$ | $-1, 0, 1$ | 3 |
| | | $\mathcal{A}_{2\kappa}(T_2, \mathrm{Im}\,t_1; \hat{\mathbf{p}})$ | $-1, 0, 1, 2$ | 4 |
| | | $\mathcal{A}_{3\kappa}(T_2, \mathrm{Im}\,t_1; \hat{\mathbf{p}})$ | $-1, 0, 1, 2, 3$ | 5 |
| | $p_z(\hat{\boldsymbol{\omega}}, \hat{\mathbf{p}})$ | $\mathcal{A}_{10}(T_0, t_1; \hat{\mathbf{p}})$ | $0$ | 1 |
| | | $\mathcal{A}_{1\kappa}(T_2, t_1; \hat{\mathbf{p}})$ | $-1, 0, 1$ | 3 |
| | | $\mathcal{A}_{2\kappa}(T_2, t_1; \hat{\mathbf{p}})$ | $-2, -1, 1, 2$ | 4 |
| | | $\mathcal{A}_{3\kappa}(T_2, t_1; \hat{\mathbf{p}})$ | $-2, -1, 0, 1, 2$ | 5 |
| | $p_x(\hat{\mathbf{p}})$ | $\mathcal{A}_{11}(T_0, \mathrm{Re}\,t_1; \hat{\mathbf{p}})$ | $1$ | 1 |
| | $p_y(\hat{\mathbf{p}})$ | $\mathcal{A}_{11}(T_0, \mathrm{Im}\,t_1; \hat{\mathbf{p}})$ | $1$ | 1 |
| | $p_z(\hat{\mathbf{p}})$ | $\mathcal{A}_{10}(T_0, t_1; \hat{\mathbf{p}})$ | $0$ | 1 |
| Tensor pol. | $\langle \eta_2(\hat{\boldsymbol{\omega}}) \times p_x(\hat{\mathbf{p}}) \rangle$ | $\mathcal{A}_{00}(T_1, \mathrm{Re}\,t_1; \hat{\mathbf{p}})$ | $0$ | 1 |
| | | $\mathcal{A}_{1\kappa}(T_1, \mathrm{Re}\,t_1; \hat{\mathbf{p}})$ | $0, 1$ | 2 |
| | | $\mathcal{A}_{2\kappa}(T_1, \mathrm{Re}\,t_1; \hat{\mathbf{p}})$ | $0, 1, 2$ | 3 |

*(continued)*

Table II
Continued.

| Exp. | Observ. | Irr. aniso. par. | Mag. comp. $\kappa$ | No. of coef. |
|------|---------|------------------|---------------------|--------------|
| | $\langle \eta_2(\hat{\boldsymbol{\omega}}) \times p_y(\hat{\mathbf{p}})\rangle$ | $\mathcal{A}_{00}(T_1, \operatorname{Im} t_1; \hat{\mathbf{p}})$ | $0$ | 1 |
| | | $\mathcal{A}_{1\kappa}(T_1, \operatorname{Im} t_1; \hat{\mathbf{p}})$ | $0, 1$ | 2 |
| | | $\mathcal{A}_{2\kappa}(T_1, \operatorname{Im} t_1; \hat{\mathbf{p}})$ | $0, 1, 2$ | 3 |
| | $\langle \eta_2(\hat{\boldsymbol{\omega}}) \times p_z(\hat{\mathbf{p}})\rangle$ | $\mathcal{A}_{00}(T_1, t_1; \hat{\mathbf{p}})$ | $0$ | 1 |
| | | $\mathcal{A}_{1\kappa}(T_1, t_1; \hat{\mathbf{p}})$ | $-1, 1$ | 2 |
| | | $\mathcal{A}_{2\kappa}(T_1, t_1; \hat{\mathbf{p}})$ | $-1, 0, 1$ | 3 |
| | $\langle \eta_1(\hat{\boldsymbol{\omega}}) \times p_x(\hat{\mathbf{p}})\rangle$ | $\mathcal{A}_{1\kappa}(\operatorname{Im} T_2, \operatorname{Re} t_1; \hat{\mathbf{p}})$ | $-1, 0, 1$ | 3 |
| | | $\mathcal{A}_{2\kappa}(\operatorname{Im} T_2, \operatorname{Re} t_1; \hat{\mathbf{p}})$ | $-1, 0, 1, 2$ | 4 |
| | | $\mathcal{A}_{3\kappa}(\operatorname{Im} T_2, \operatorname{Re} t_1; \hat{\mathbf{p}})$ | $-1, 0, 1, 2, 3$ | 5 |
| | $\langle \eta_1(\hat{\boldsymbol{\omega}}) \times p_y(\hat{\mathbf{p}})\rangle$ | $\mathcal{A}_{1\kappa}(\operatorname{Im} T_2, \operatorname{Im} t_1; \hat{\mathbf{p}})$ | $-1, 0, 1$ | 3 |
| | | $\mathcal{A}_{2\kappa}(\operatorname{Im} T_2, \operatorname{Im} t_1; \hat{\mathbf{p}})$ | $-1, 0, 1, 2$ | 4 |
| | | $\mathcal{A}_{3\kappa}(\operatorname{Im} T_2, \operatorname{Im} t_1; \hat{\mathbf{p}})$ | $-1, 0, 1, 2, 3$ | 5 |
| | $\langle \eta_1(\hat{\boldsymbol{\omega}}) \times p_z(\hat{\mathbf{p}})\rangle$ | $\mathcal{A}_{1\kappa}(\operatorname{Im} T_2, t_1; \hat{\mathbf{p}})$ | $-1, 0, 1$ | 3 |
| | | $\mathcal{A}_{2\kappa}(\operatorname{Im} T_2, t_1; \hat{\mathbf{p}})$ | $-2, -1, 1, 2$ | 4 |
| | | $\mathcal{A}_{3\kappa}(\operatorname{Im} T_2, t_1; \hat{\mathbf{p}})$ | $-2, -1, 0, 1, 2$ | 5 |
| | $\langle \eta_3(\hat{\boldsymbol{\omega}}) \times p_x(\hat{\mathbf{p}})\rangle$ | $\mathcal{A}_{1\kappa}(\operatorname{Re} T_2, \operatorname{Re} t_1; \hat{\mathbf{p}})$ | $-1, 0, 1$ | 3 |
| | | $\mathcal{A}_{2\kappa}(\operatorname{Re} T_2, \operatorname{Re} t_1; \hat{\mathbf{p}})$ | $-1, 0, 1, 2$ | 4 |
| | | $\mathcal{A}_{3\kappa}(\operatorname{Re} T_2, \operatorname{Re} t_1; \hat{\mathbf{p}})$ | $-1, 0, 1, 2, 3$ | 5 |
| | $\langle \eta_3(\hat{\boldsymbol{\omega}}) \times p_y(\hat{\mathbf{p}})\rangle$ | $\mathcal{A}_{1\kappa}(\operatorname{Re} T_2, \operatorname{Im} t_1; \hat{\mathbf{p}})$ | $-1, 0, 1$ | 3 |
| | | $\mathcal{A}_{2\kappa}(\operatorname{Re} T_2, \operatorname{Im} t_1; \hat{\mathbf{p}})$ | $-1, 0, 1, 2$ | 4 |
| | | $\mathcal{A}_{3\kappa}(\operatorname{Re} T_2, \operatorname{Im} t_1; \hat{\mathbf{p}})$ | $-1, 0, 1, 2, 3$ | 5 |
| | $\langle \eta_3(\hat{\boldsymbol{\omega}}) \times p_z(\hat{\mathbf{p}})\rangle$ | $\mathcal{A}_{1\kappa}(\operatorname{Re} T_2, t_1; \hat{\mathbf{p}})$ | $-1, 0, 1$ | 3 |
| | | $\mathcal{A}_{2\kappa}(\operatorname{Re} T_2, t_1; \hat{\mathbf{p}})$ | $-2, -1, 1, 2$ | 4 |
| | | $\mathcal{A}_{3\kappa}(\operatorname{Re} T_2, t_1; \hat{\mathbf{p}})$ | $-2, -1, 0, 1, 2$ | 5 |

additional selection rules may occur which allow for a reduction of the general equations.

The simple most case is that of an atomic closed shell target being in its ground state. For example, for the rare gases this refers to a $^1S_0$ state. For this case, additional selection rules apply since the atomic charge cloud is isotropic. This yields a reduced $C$ coefficient which has been derived in Section III.A.

Now, let us consider a primary photoionization

$$\gamma + A(J_0 = 0) \longrightarrow A^{+^*}(J = 1/2) + e^-, \tag{163}$$

and the subsequent de-excitation of the residual ionic state via fluorescence photon emission

$$A^{+^*}(J = 1/2) \longrightarrow A^{+^*}(J_f = 3/2) + h\nu. \tag{164}$$

Inserting $J = 1/2$ into Eq. (62) yields

$$C_{\mathrm{un}}^{J_0=0}(\Gamma\gamma; K, k, \mathcal{K}\kappa)$$

$$= \frac{1}{4\pi|p|^2} \sqrt{(2\mathcal{K}+1)(2K+1)(2k+1)(2\Gamma+1)}$$

$$\times \sum_{a\mathcal{L}} \sum_{\ell j \ell' j'} i^{\ell+\ell'} e^{i(\sigma_\ell^j - \sigma_{\ell'}^{j'})} (2a+1) \langle (1/2j)1\|d\|0\rangle \langle (1/2j')1\|d\|0\rangle^* \mathcal{D}_{\mathcal{M}0}^{(\mathcal{L})}(\hat{\mathbf{p}})^*$$

$$\times (2\mathcal{L}+1)\sqrt{(2\ell+1)(2\ell'+1)} \sqrt{(2j+1)(2j'+1)}$$

$$\times (-1)^{a-K+\gamma} \begin{pmatrix} \ell & \ell' & \mathcal{L} \\ 0 & 0 & 0 \end{pmatrix} \begin{pmatrix} \mathcal{L} & \Gamma & \mathcal{K} \\ -\mathcal{M} & \gamma & -\kappa \end{pmatrix}$$

$$\times \begin{Bmatrix} \mathcal{L} & \Gamma & \mathcal{K} \\ K & k & a \end{Bmatrix} \begin{Bmatrix} K & a & \Gamma \\ 1/2 & j & 1 \\ 1/2 & j' & 1 \end{Bmatrix} \begin{Bmatrix} \mathcal{L} & k & a \\ \ell & 1/2 & j \\ \ell' & 1/2 & j' \end{Bmatrix}. \tag{165}$$

The 9$j$-symbol yields an important restriction to the rank $K$ of the tensors describing the ionic state

$$K \leq 1. \tag{166}$$

Thus, the residual ionic state cannot be aligned though oriented. Therefore, only few of the generalized anisotropy parameters

survive. The possible non-zero parameters $\mathcal{A}_{\mathcal{K}\kappa}(T_K, t_k; \hat{\mathbf{p}})$ are listed in table III.

Due to this, the general equations of angular distribution and fluorescence and spin polarization can be significantly reduced.

Table III

The possible non-zero generalized irreducible anisotropy parameters $\mathcal{A}_{\mathcal{K}\kappa}(T_K, t_k; \hat{\mathbf{p}})$ for $J_0 = 0 \longrightarrow J = 1/2$ transitions, occurring for the different experimentally observable parameters of angular distribution, spin polarization, Stokes and tensor polarization, respectively. The angle integrated parameters are abbreviated as $\mathcal{A}_{\mathcal{K}\kappa}(T_K, t_k)$. Parameters not shown are zero.

| Exp. | Observ. | Irr. aniso. par. | Mag. comp. $\kappa$ | No. of coef. |
|---|---|---|---|---|
| Ang. distrib. | $I(\hat{\boldsymbol{\omega}}, \hat{\mathbf{p}})$ | $\mathcal{A}_{00}(T_0, t_0; \hat{\mathbf{p}})$ | 0 | 1 |
| | $I(\hat{\mathbf{p}})$ | $\mathcal{A}_{00}(T_0, t_0; \hat{\mathbf{p}})$ | 0 | 1 |
| | $I(\hat{\boldsymbol{\omega}})$ | $= I_0/4\pi$ | | |
| Fluo. pol. | $\eta_2(\hat{\boldsymbol{\omega}}, \hat{\mathbf{p}})$ | $\mathcal{A}_{1\kappa}(T_1, t_0; \hat{\mathbf{p}})$ | $-1, 0, 1$ | 3 |
| | $\eta_1(\hat{\boldsymbol{\omega}}, \hat{\mathbf{p}})$ | $= \eta_3(\hat{\boldsymbol{\omega}}, \hat{\mathbf{p}}) = 0$ | | |
| | $\eta_2(\hat{\boldsymbol{\omega}})$ | $\mathcal{A}_{1\kappa}(T_1, t_0)$ | $-1, 0, 1$ | 3 |
| | $\eta_1(\hat{\boldsymbol{\omega}})$ | $= \eta_3(\hat{\boldsymbol{\omega}}) = 0$ | | |
| Spin pol. | $p_x(\hat{\boldsymbol{\omega}}, \hat{\mathbf{p}})$ | $\mathcal{A}_{11}(T_0, \mathrm{Re}\, t_1; \hat{\mathbf{p}})$ | 1 | 1 |
| | $p_y(\hat{\boldsymbol{\omega}}, \hat{\mathbf{p}})$ | $\mathcal{A}_{11}(T_0, \mathrm{Im}\, t_1; \hat{\mathbf{p}})$ | 1 | 1 |
| | $p_z(\hat{\boldsymbol{\omega}}, \hat{\mathbf{p}})$ | $\mathcal{A}_{10}(T_0, t_1; \hat{\mathbf{p}})$ | 0 | 1 |
| | $p_x(\hat{\mathbf{p}})$ | $\mathcal{A}_{11}(T_0, \mathrm{Re}\, t_1; \hat{\mathbf{p}})$ | 1 | 1 |
| | $p_y(\hat{\mathbf{p}})$ | $\mathcal{A}_{11}(T_0, \mathrm{Im}\, t_1; \hat{\mathbf{p}})$ | 1 | 1 |
| | $p_z(\hat{\mathbf{p}})$ | $\mathcal{A}_{10}(T_0, t_1; \hat{\mathbf{p}})$ | 0 | 1 |
| Tensor pol. | $\langle \eta_2(\hat{\boldsymbol{\omega}}) \times p_x(\hat{\mathbf{p}}) \rangle$ | $\mathcal{A}_{00}(T_1, \mathrm{Re}\, t_1; \hat{\mathbf{p}})$ | 0 | 1 |
| | | $\mathcal{A}_{1\kappa}(T_1, \mathrm{Re}\, t_1; \hat{\mathbf{p}})$ | 0, 1 | 2 |
| | | $\mathcal{A}_{2\kappa}(T_1, \mathrm{Re}\, t_1; \hat{\mathbf{p}})$ | 0, 1, 2 | 3 |
| | $\langle \eta_2(\hat{\boldsymbol{\omega}}) \times p_y(\hat{\mathbf{p}}) \rangle$ | $\mathcal{A}_{11}(T_1, \mathrm{Im}\, t_1; \hat{\mathbf{p}})$ | 0 | 1 |
| | | $\mathcal{A}_{1\kappa}(T_1, \mathrm{Im}\, t_1; \hat{\mathbf{p}})$ | 0, 1 | 2 |
| | | $\mathcal{A}_{2\kappa}(T_1, \mathrm{Im}\, t_1; \hat{\mathbf{p}})$ | 0, 1, 2 | 3 |
| | $\langle \eta_2(\hat{\boldsymbol{\omega}}) \times p_z(\hat{\mathbf{p}}) \rangle$ | $\mathcal{A}_{00}(T_1, t_1; \hat{\mathbf{p}})$ | 0 | 1 |
| | | $\mathcal{A}_{1\kappa}(T_1, t_1; \hat{\mathbf{p}})$ | $-1, 1$ | 2 |
| | | $\mathcal{A}_{2\kappa}(T_1, t_1; \hat{\mathbf{p}})$ | $-1, 0, 1$ | 3 |
| | $\langle \eta_1(\hat{\boldsymbol{\omega}}) \times p_x(\hat{\mathbf{p}}) \rangle$ | $= \langle \eta_1(\hat{\boldsymbol{\omega}}) \times p_y(\hat{\mathbf{p}}) \rangle$ | $= \langle \eta_1(\hat{\boldsymbol{\omega}}) \times p_z(\hat{\mathbf{p}}) \rangle$ | $= 0$ |
| | $\langle \eta_3(\hat{\boldsymbol{\omega}}) \times p_x(\hat{\mathbf{p}}) \rangle$ | $= \langle \eta_3(\hat{\boldsymbol{\omega}}) \times p_y(\hat{\mathbf{p}}) \rangle$ | $= \langle \eta_3(\hat{\boldsymbol{\omega}}) \times p_z(\hat{\mathbf{p}}) \rangle$ | $= 0$ |

## A. Angular Distribution

The total intensity $I = I(\hat{\boldsymbol{\omega}}, \hat{\mathbf{p}})$ to detect a photon emitted into direction $\hat{\boldsymbol{\omega}}$ while a photoelectron has been emitted under the angle $\hat{\mathbf{p}}$ reduces to

$$I(\hat{\boldsymbol{\omega}}, \hat{\mathbf{p}}) = \frac{I_0}{4\pi} \mathcal{A}_{00}(T_0, t_0; \hat{\mathbf{p}}), \qquad (167)$$

whereas the expression for the photoelectron intensity $I(\hat{\mathbf{p}})$ remains as has been given in Eq. (117). Connecting Eq. (117) and Eq. (167) yields

$$I(\hat{\mathbf{p}}) = 4\pi I(\hat{\boldsymbol{\omega}}, \hat{\mathbf{p}}). \qquad (168)$$

Thus, for the considered type of transition, observation of the angle resolved intensity $I(\hat{\boldsymbol{\omega}}, \hat{\mathbf{p}})$ yields no additional information that cannot be obtained from observing the angular distribution of the photoelectron, only. This is not surprising since an angular dependence of the emitted fluorescence radiation depends on the existence of an alignment in the residual ion. Since its total angular momentum is, however, $J = 1/2$, an alignment cannot be generated in the final ionic state. As a matter of fact we find from Eq. (122)

$$I(\hat{\boldsymbol{\omega}}) = \frac{I_0}{4\pi}. \qquad (169)$$

## B. Polarization of Fluorescence Radiation

Reducing the expressions for the Stokes parameters according to table III, we find from Eqs. (128)–(130) that only the Stokes parameter $\eta_2$ survives,

$$\eta_2(\hat{\boldsymbol{\omega}}, \hat{\mathbf{p}}) = \frac{1}{N(\hat{\mathbf{p}})} \sqrt{\frac{8}{3}} \alpha_1 \sum_Q \mathcal{A}_{1Q}(T_1, t_0; \hat{\mathbf{p}}) \mathcal{D}_{Q0}^{(1)}(\hat{\boldsymbol{\omega}})^*, \qquad (170)$$

where the normalization parameter simply reduces to

$$N(\hat{\boldsymbol{\omega}}, \hat{\mathbf{p}}) = N(\hat{\mathbf{p}}) = \mathcal{A}_{00}(T_0, t_0; \hat{\mathbf{p}}). \qquad (171)$$

The two other Stokes parameters $\eta_1$ and $\eta_3$ cannot be observed in such type of coincidence experiment due to the $J = 1/2$ residual ionic state.

$$\eta_1(\hat{\boldsymbol{\omega}}, \hat{\mathbf{p}}) = \eta_3(\hat{\boldsymbol{\omega}}, \hat{\mathbf{p}}) = 0. \qquad (172)$$

### C. Non-coincident Polarization of Fluorescence Radiation

For the case of a non-coincident experiment, we obtain a similar reduction. Again, only the $\eta_2$ parameter can be observed. From Eq. (132) we obtain the normalization parameter as $N_1(\hat{\boldsymbol{\omega}}) = 1$ which yields for the Stokes parameters

$$\eta_2(\hat{\boldsymbol{\omega}}) = \sqrt{\frac{8}{3}}\, \alpha_1 \sum_Q \int \mathcal{A}_{1\,Q}(T_1, t_0; \hat{\mathbf{p}})\, d\hat{\mathbf{p}}\, \mathcal{D}_{Q0}^{(1)}(\hat{\boldsymbol{\omega}})^*, \tag{173}$$

and

$$\eta_1(\hat{\boldsymbol{\omega}}) = \eta_3(\hat{\boldsymbol{\omega}}) = 0. \tag{174}$$

### D. Spin Polarization of Photoelectrons

Though the fluorescence photon is always aligned the restriction of Eq. (166) again reduces the dependence on the generalized anisotropy parameters to one coefficient. Using Eq. (171), Eqs. (137)–(139) can be reduced to the simple expressions

$$p_x(\hat{\boldsymbol{\omega}}, \hat{\mathbf{p}}) = \frac{-\sqrt{2}\mathcal{A}_{1\,1}(T_0, \mathrm{Re}\, t_1; \hat{\mathbf{p}})}{\mathcal{A}_{0\,0}(T_0, t_0; \hat{\mathbf{p}})}, \tag{175}$$

$$p_y(\hat{\boldsymbol{\omega}}, \hat{\mathbf{p}}) = \frac{\sqrt{2}\mathcal{A}_{1\,1}(T_0, \mathrm{Im}\, t_1; \hat{\mathbf{p}})}{\mathcal{A}_{0\,0}(T_0, t_0; \hat{\mathbf{p}})}, \tag{176}$$

and

$$p_z(\hat{\boldsymbol{\omega}}, \hat{\mathbf{p}}) = \frac{\mathcal{A}_{1\,0}(T_0, t_1; \hat{\mathbf{p}})}{\mathcal{A}_{0\,0}(T_0, t_0; \hat{\mathbf{p}})}. \tag{177}$$

### E. Non-coincident Spin Polarization of Photoelectrons

As for the case of angular distribution, the relations for the non-coincident measurement of the photoelectron spin polarization can be related to the

coincident case discussed in the previous section. For the considered case of transitions Eqs. (140–143) remain the same. Thus, we obtain the relations

$$p_x(\hat{\mathbf{p}}) = \frac{1}{4\pi} p_x(\hat{\boldsymbol{\omega}}, \hat{\mathbf{p}}), \tag{178}$$

$$p_y(\hat{\mathbf{p}}) = \frac{1}{4\pi} p_y(\hat{\boldsymbol{\omega}}, \hat{\mathbf{p}}), \tag{179}$$

and

$$p_z(\hat{\mathbf{p}}) = \frac{1}{4\pi} p_z(\hat{\boldsymbol{\omega}}, \hat{\mathbf{p}}). \tag{180}$$

That is, for the considered type of transitions the information which can be obtained from a measurement of the spin polarization of the emitted photoelectron in a coincidence experiment is redundant.

## F. TENSOR POLARIZATION

Interesting information can be, however, obtained by inspecting the introduced tensor polarization parameters. Using the normalization of Eq. (171), we may write Eqs. (154)–(156) as

$$\langle \eta_2(\hat{\boldsymbol{\omega}}) \times p_x(\hat{\mathbf{p}}) \rangle = \frac{-4\alpha_1}{\sqrt{3} \mathcal{A}_{0\,0}(T_0, t_0; \hat{\mathbf{p}})} \sum_{\mathcal{K}Q} (-1)^{Q+1} \sqrt{2\mathcal{K}+1} \begin{pmatrix} 1 & 1 & \mathcal{K} \\ Q & 1 & -Q-1 \end{pmatrix}$$
$$\times \mathcal{A}_{\mathcal{K}Q+1}(T_1, \mathrm{Re}\, t_1; \hat{\mathbf{p}}) \, \mathcal{D}_{Q\,0}^{(1)}(\hat{\boldsymbol{\omega}})^*, \tag{181}$$

$$\langle \eta_2(\hat{\boldsymbol{\omega}}) \times p_y(\hat{\mathbf{p}}) \rangle = \frac{4\alpha_1}{\sqrt{3} \mathcal{A}_{0\,0}(T_0, t_0; \hat{\mathbf{p}})} \sum_{\mathcal{K}Q} (-1)^{Q+1} \sqrt{2\mathcal{K}+1} \begin{pmatrix} 1 & 1 & \mathcal{K} \\ Q & 1 & -Q-1 \end{pmatrix}$$
$$\times \mathcal{A}_{\mathcal{K}Q+1}(T_1, \mathrm{Im}\, t_1; \hat{\mathbf{p}}) \, \mathcal{D}_{Q\,0}^{(1)}(\hat{\boldsymbol{\omega}})^*, \tag{182}$$

and

$$\langle \eta_2(\hat{\boldsymbol{\omega}}) \times p_z(\hat{\mathbf{p}}) \rangle = \frac{\sqrt{8}\alpha_1}{\sqrt{3} \mathcal{A}_{0\,0}(T_0, t_0; \hat{\mathbf{p}})} \sum_{\mathcal{K}Q} (-1)^{Q} \sqrt{2\mathcal{K}+1} \begin{pmatrix} 1 & 1 & \mathcal{K} \\ Q & 0 & -Q \end{pmatrix}$$
$$\times \mathcal{A}_{\mathcal{K}Q}(T_1, t_1; \hat{\mathbf{p}}) \mathcal{D}_{Q\,0}^{(1)}(\hat{\boldsymbol{\omega}})^*. \tag{183}$$

Thus, even for the considered type of a simple $J_0 = 0 \longrightarrow J = 1/2$ ionic transition we obtain information from the tensor polarization parameters.

However, inspecting Eq. (165) more closely, one has to realize the fact that for the case of $0 \longrightarrow 1/2$ transitions, we have only three independent parameters in the $C$ coefficients to determine. In detail, the $C$ coefficient is a function of the modulus of the $\langle (1/2, j)1 \| d \| 0 \rangle$, $j = 1/2, 3/2$ transition matrix elements and the phase difference of the emitted $\varepsilon s_{1/2}$ and $\varepsilon d_{3/2}$ partial waves. Thus, the information which is contained in the tensor polarization parameters can be achieved, too, within a more simple experiment. For example, measuring the photoelectron spin polarization in a non-coincidental setup.

The other tensor polarization parameters which connect the linear components of the Stokes parameters with the spin polarization of the photoelectron cannot be observed since their detection requires the existence of an alignment in the residual ionic core which cannot be generated for a $J = 1/2$ state. Therefore, Eqs. (157)–(162) simply yield

$$\langle \eta_1(\hat{\boldsymbol{\omega}}) \times p_j(\hat{\mathbf{p}}) \rangle = \langle \eta_3(\hat{\boldsymbol{\omega}}) \times p_j(\hat{\mathbf{p}}) \rangle = 0 \quad \text{for } j = x, y, z. \tag{184}$$

Inserting the possible quantum numbers for $\mathcal{K}$ and $Q$ – see table III – expressing the $3j$ symbols by their actual values and writing the rotation matrices $\mathcal{D}_{Q0}^{(1)}(\hat{\boldsymbol{\omega}})^*$ in terms of the explicit angular functions, the non-zero tensor polarization parameters may be expressed as

$$\langle \eta_2(\hat{\boldsymbol{\omega}}) \times p_x(\hat{\mathbf{p}}) \rangle = \frac{\sqrt{8}\alpha_1}{\sqrt{3}\mathcal{A}_{00}(T_0, t_0; \hat{\mathbf{p}})} \Bigg( [\mathcal{A}_{11}(T_1, \mathrm{Re}\, t_1; \hat{\mathbf{p}}) - \mathcal{A}_{21}(T_1, \mathrm{Re}\, t_1; \hat{\mathbf{p}})] \cos\theta_\gamma$$

$$+ \Bigg[ \frac{-1}{\sqrt{3}} \mathcal{A}_{00}(T_1, \mathrm{Re}\, t_1; \hat{\mathbf{p}}) + \frac{1}{\sqrt{2}} \mathcal{A}_{10}(T_1, \mathrm{Re}\, t_1; \hat{\mathbf{p}})$$

$$- \frac{1}{\sqrt{6}} \mathcal{A}_{20}(T_1, \mathrm{Re}\, t_1; \hat{\mathbf{p}}) \Bigg] \sin\theta_\gamma \exp{-i\phi_\gamma}$$

$$+ \mathcal{A}_{22}(T_1, \mathrm{Re}\, t_1; \hat{\mathbf{p}}) \sin\theta_\gamma \exp{i\phi_\gamma} \Bigg), \tag{185}$$

$$\langle \eta_2(\hat{\boldsymbol{\omega}}) \times p_y(\hat{\mathbf{p}}) \rangle = \frac{-\sqrt{8}\alpha_1}{\sqrt{3}\mathcal{A}_{00}(T_0, t_0; \hat{\mathbf{p}})} \Bigg( [\mathcal{A}_{11}(T_1, \mathrm{Im}\, t_1; \hat{\mathbf{p}}) - \mathcal{A}_{21}(T_1, \mathrm{Im}\, t_1; \hat{\mathbf{p}})] \cos\theta_\gamma$$

$$+ \Bigg[ \frac{-1}{\sqrt{3}} \mathcal{A}_{00}(T_1, \mathrm{Im}\, t_1; \hat{\mathbf{p}}) + \frac{1}{\sqrt{2}} \mathcal{A}_{10}(T_1, \mathrm{Im}\, t_1; \hat{\mathbf{p}})$$

$$- \frac{1}{\sqrt{6}} \mathcal{A}_{20}(T_1, \mathrm{Im}\, t_1; \hat{\mathbf{p}}) \Bigg] \sin\theta_\gamma \exp{-i\phi_\gamma}$$

$$+ \mathcal{A}_{22}(T_1, \mathrm{Im}\, t_1; \hat{\mathbf{p}}) \sin\theta_\gamma \exp{i\phi_\gamma} \Bigg), \tag{186}$$

and

$$\langle\eta_2(\hat{\boldsymbol{\omega}})\times p_z(\hat{\mathbf{p}})\rangle = \frac{-\sqrt{8}\alpha_1}{\sqrt{3}\mathcal{A}_{00}(T_0,t_0;\hat{\mathbf{p}})}\left(\frac{1}{\sqrt{3}}[\mathcal{A}_{00}(T_1,t_1;\hat{\mathbf{p}})-\sqrt{2}\mathcal{A}_{20}(T_1,t_1;\hat{\mathbf{p}})]\cos\theta_\gamma\right.$$

$$+\frac{1}{2}[\mathcal{A}_{1-1}(T_1,t_1;\hat{\mathbf{p}})-\mathcal{A}_{2-1}(T_1,t_1;\hat{\mathbf{p}})]\sin\theta_\gamma\exp-i\phi_\gamma$$

$$\left.-\frac{1}{2}[-\mathcal{A}_{11}(T_1,t_1;\hat{\mathbf{p}})+\mathcal{A}_{21}(T_1,t_1;\hat{\mathbf{p}})]\sin\theta_\gamma\exp i\phi_\gamma\right). \qquad (187)$$

Thus, for the three non-zero tensor polarization parameters the angular dependency on the angles $\theta_\gamma$ and $\phi_\gamma$ is given by the same angular functions weighted, however, by different combinations $\mathcal{A}_{\mathcal{K}\kappa}(T_K,t_k;\hat{\mathbf{p}})$ of the generalized irreducible anisotropy tensors of alignment and orientation.

# VI. Experimental Approaches and Results

A. Complete Photoionization and $(\gamma,e\gamma)$ Coincidence Experiments

While photoionization experiments with free atoms have been carried out with regard to measurements of total cross sections and photoelectron angular distributions selectively during the first half of the last century, approaches to so-called *complete photoionization experiments* started about the eighties (see, e.g., Schmidt, 1997; Becker and Crowe, 2001). *Complete* means perfect results of the analysis of the relevant photoionization in terms of a quantum mechanical description with amplitudes (Bederson, 1963; Fano, 1957), i.e. their real parts and relative phases. In atomic collision physics complete experiments were reported with electron–photon angular coincidence measurements from helium electron impact excitation; since about the seventies (Eminyan *et al.*, 1973). Macek and Jaecks (1971) first described a concise theory. Further developments towards complete scattering experiments can be listed as follows: the early pioneering electron-polarized atom recoil experiment by Rubin *et al.* (1969) and the spin filter experiment of atoms by Bederson *et al.* (1960); the unpolarized electron scattered by partially polarized atoms (Hils *et al.*, 1972); superelastic electron scattering from laser-excited atoms (Hertel and Stoll, 1974); analysis of production of photoelectrons from heavy atoms (Heinzmann *et al.*, 1970; Heinzman, 1980); electron–photon coincidences by laser excitation of atoms (MacGillivray and Standage, 1988); towards complete photoionization Auger electron experiments (Grum-Grzhmailo *et al.*, 2001; Scherer *et al.*, 2001); alignment measurements in $H^+ + H$

collisions (Hippler *et al.*, 1988); complete photoionization experiments with polarized atoms as targets (Cherepkov, 1983; Siegel *et al.*, 1983; Kerling *et al.*, 1990; Becker and Kleinpoppen, 1999; Sonntag and Zimmermann, 1995; Plotzke *et al.*, 1986; Klar and Kleinpoppen, 1982); double photoionization of atoms whereby two electrons are ejected (Schwarzpkopf *et al.*, 1993; Cvejanovic and Reddish, 2000; Cvejanovic *et al.*, 2002); spin-asymmetries in polarized electron/polarized atom scattering (Alguard *et al.*, 1977; Hils and Kleinpoppen, 1978; Berger and Kessler, 1986; Baum *et al.*, 1999).

The *ultimate complete* atomic collision experiment requires application of polarized incoming (atomic) beams and polarized atomic targets with a combined coincidence and spin analysis of the collision partners. Mainly because of lack of intensities for such an ultimate complete collision experiment we are, however, in a position of restricting ourselves to feasible types of experiments and processes. With regard to more comprehensive arguments on this issue we like to refer to the paper by Datz *et al.* (1999). The $(\gamma, e\gamma)$ process is expected to be such process with regard to theoretical analysis and experimental feasibility. We will report now selectively on some results of recent $(\gamma, e\gamma)$ experiments.

### B. Coincidence Measurements on Calcium Atoms

The main example for the $(\gamma, e\gamma)$ process was the photoionization of an atom into an excited ion state and the subsequent decay into the ionic ground state with the simultaneous emission and observation of the fluorescence radiation in coincidence which eliminates cascading problems. In principle, the description of photoelectron–fluorescent photon coincidence measurements is similar to that of photoelectron–Auger coincidence experiments of the type reported by Kämmerling and Schmidt (1991). In order to avoid spin complications the initial ground state of the atom has been elected to be a singlet state, i.e. $^1S_0$. The obvious choice of first experimental studies was connected with Ca and Sr atoms. In its ground state calcium has the electron configuration of $Ca(1s^2 2s^2 2p^6 3s^2 3p^6 4s^2)\,^1S_0$. Photoionization into an excited $Ca^+$ ion of the $(1s^2 \ldots 3p^6 4p)\,^2P_{3/2}$ configuration works particularly efficient with high peak cross sections, $\sim 10^{-15}\,cm^2$, through resonance regions, i.e. initially, the direct ionization and excitation process to be studied was

$$\gamma + Ca(4s^2, {}^1S_0) \longrightarrow Ca^{+*}(4p, {}^2P_{1/2,3/2}) + e^- \tag{188a}$$

$$\begin{array}{l}\quad\ \ \vdash\!\!\longrightarrow Ca^+(4s, {}^2S_{1/2}) + \gamma',\end{array} \tag{188b}$$

while $\gamma$ is the synchrotron photon, $\gamma'$ denotes the fluorescence photon with wave lengths of $\lambda = 393.3$ and $396.8\,\text{nm}$, respectively. While this $(\gamma, e\gamma)$ direct process has a very low cross section ($\lesssim 10^{-19}\,\text{cm}^2$), calculations by Altun and Kelly (1985) indicated a much larger cross section ($\simeq 10^{-15}\,\text{cm}^2$) into the 4p, $^2$P state by correlation with excitation of the 3p electrons via the 3p–3d giant resonance according to

$$\gamma + \text{Ca}(4\text{s}^2, {}^1\text{S}_0) \longrightarrow \text{Ca}^*(3\text{p}^5, \text{n}\{^\text{s}_\text{d}\}, n'\ell', n''\ell'') \tag{189a}$$

$$\hookrightarrow \text{Ca}^{+*}(3\text{p}^6 4\text{p}, {}^2\text{P}_{1/2,3/2}) + e^- \tag{189b}$$

$$\hookrightarrow \text{Ca}^+(4\text{s}, {}^2\text{S}_{1/2}) + \gamma''. \tag{189c}$$

In fact there are several transitions of the 3p–3d resonance depending on the values of $n\ell, n'\ell', n''\ell''$ and their couplings. $\text{Ca}(4\text{s}^2, {}^1\text{S}_0) \longrightarrow \text{Ca}(3\text{p}^5 4\text{s}^2 3\text{d}, {}^1\text{P}_1)$ at the synchrotron energy of $31.4\,\text{eV}$ and the overlapping resonances $\text{Ca}(4\text{s}^2, {}^1\text{S}_0) \longrightarrow \text{Ca}(3\text{p}^5 3\text{d}^3, {}^1\text{P}_1)$, $\text{Ca}(3\text{p}^5 4\text{s}^2 3\text{d}, {}^3\text{D}_1)$, $\text{Ca}(3\text{p}^5 4\text{s} 3\text{d}^2, {}^1\text{P}_1)$, or $\text{Ca}(3\text{p}^5 4\text{s}^2 4\text{d}, {}^3\text{P}_1)$ at about $31.5\,\text{eV}$. Accordingly these resonances are called Ca 3p–3d resonances and have been extensively studied. Correspondingly strontium with the ground state configuration of $\text{Sr}(1\text{s}^2 2\text{s}^2\, 2\text{p}^6 3\text{s}^2 3\text{p}^6 3\text{d}^{10} 4\text{s}^2 4\text{p}^6 5\text{s}^2)\, {}^1\text{S}_0$ has Sr 4p–4d resonances. The object of previous photoelectron studies was not only to provide quantitative information about the decay channels of the complex Ca 3p–3d and Sr 4p–4d resonances, but also to obtain a complete description for the photoionization channel leaving the ion in the $\text{Ca}^+ 4\text{p}\,^2\text{P}_{3/2}$ and $\text{Sr}^+ 5\text{p}\,^2\text{P}_{3/2}$ levels. Hamdy *et al.* (1991a, b) had previously made polarization measurements of the fluorescence radiation into the ion ground state and determined the alignment tensors for $\text{Ca}^+$ in the $4\text{p}\,^2\text{P}_{3/2}$ state and the $\text{Sr}^+$ in the $5\text{p}\,^2\text{P}_{3/2}$ state.

The geometry of the coincidence experiments for the photoelectrons and fluorescence-polarized photons of Ca and Sr by Beyer *et al.* (1995) and Ueda *et al.* (1998) was such that the polarization of the coincident fluorescence radiation was referred to the linear polarization of the incoming synchrotron radiation. Figure 4 shows the experimental results with regard to the Ca 3p–3d resonance region: the upper part (a) has a peak at $31.4\,\text{eV}$ which corresponds to the above resonance $3\text{p}^5 4\text{s}^2 3\text{d}, {}^1\text{P}_1$ whereas the peak at $31.5\,\text{eV}$ shows the overlapping four resonances characterized above according to the identification of Mansfield and Newsom (1977, 1981). Curve (b) is the asymmetry parameter $\beta$ for the corresponding photoelectron. Curves (c) and (d) show the polarization as characterized above of the fluorescence photons taken in coincidence with

Fig. 4. Experimental results of the $(\gamma, e\gamma)$ coincidence studies in the Ca $3p \longrightarrow 3d$ resonance region: (a) relative partial cross-section for photoelectron ejection leaving the $Ca^+$ ion in the $4p$ excited state; (b) asymmetry parameter $\beta$ for the photoelectrons; (c) and polarization of the fluorescent photons taken in coincidence with the photoelectrons at the detection angles $\theta = -135°$; and (d) $\theta = -90°$, note the principle direction of the polarization is parallel to the $z$-axis; (e) fluorescence polarization calculated from non-coincidence experiments.

the photoelectrons. The data in curve (c) were taken at an angle $\theta_e = -135°$ and in curve (d) at $\theta_e = -90°$. Curve (e) shows non-coincidence data of fluorescence polarization which agree well with earlier data of Hamdy *et al.* (1991a). Obviously, there is a large difference between the non-coincidence data and the coincidence data. If we assume that the 31.4 eV resonance, i.e. $3p^54s^23d$, $^1P_1$ agrees well with LS coupling and apply the analysis and formalism of Berezhko *et al.* (1978) the photoelectron emission into s- and d-waves give ratios of their photoionization amplitudes and their phase differences and can be extracted as follows: $|D_s|/|D_d| = 1.4\,^{+0.6}_{-0.3}$ and $|\Delta| = 44.2°\,^{+2°}_{-5°}$. The errors include uncertainties in the polarization of the fluorescence, the $\beta$ parameter and the polarization of the linear polarization of the synchrotron radiation (their circular polarization has been taken as zero).

## C. Coincidence Measurements on Strontium Atoms

A second $(\gamma, e\gamma)$ study case we like to discuss is related to the $Sr(1s^2 \ldots 4p^65s^2)\,^1S_0$ atom. For the whole of this photoionization process of this atom *LS* coupling cannot be assumed as compared to the case of calcium. Therefore, the resonantly enhanced photoionization channel of Sr at a synchrotron energy of about 25 eV has been applied to populate the excited state of the $Sr^+$ ion. The radiative decay $5p\,^2P_{3/2} \longrightarrow 5s\,^2S_{1/2}$ of this ion state is connected to a coincidence measurement with the relevant photoelectron whereby an optical filter will be used to remove the unpolarized $5p\,^2P_{1/2}$ component. We focus our interest on a well separated resonance at 25.105 eV (see number 2 of Fig. 5) whose excited state is dominated by the $4p^5(4d^3,\,^4F)\,^5F_1$ component. The resulting photoionization of interest for the experiment can be summarized by the following sub-processes

$$h\nu(25.105\,\text{eV}) + Sr(5s^2,\,^1S_0) \longrightarrow Sr^*(4p^5[4d^3,\,^4F],\,^5F_1) \qquad (190a)$$

$$\qquad\qquad \longrightarrow Sr^{+*}(4p^65p,\,^2P_{1/2,\,3/2}) + e^- \qquad (190b)$$

$$\qquad\qquad\qquad \longrightarrow Sr^+(5s,\,^2S_{1/2}) + h\nu(3.040\,\text{eV}), \qquad (190c)$$

The fluorescence lines from the $P_{1/2,\,3/2}$ states can be separated by about 100 meV. An optical filter can be used to entirely distinguish the $Sr^+\ 4p^65p\,^2P_{3/2,\,1/2}$ and $4p^65s\,^2S_{1/2}$ components. The experimental photoelectron fluorescent photon coincidence rates of the above Sr atom

FIG. 5. Yield of photoelectrons as a function of the photon energy of the synchrotron radiation, where the strontium ion is left in the Sr$^+$ 5p $^2$P$_{1/2, 3/2}$ excited state. The data were taken at $\theta \cong 10°$ whereby the $^2$P$_{1/2, 3/2}$ levels could be resolved by the wave lengths of the fluorescence photons (Ueda *et al.*, 1998).

has been analyzed in detail by Kabachnik and Ueda (1995) as follows. Assuming that the incident synchrotron radiation is partially linearly polarized ($P_{\text{lin}} \leq 1$) and its circular polarization zero ($P_{\text{circ}} = 0$) the reference frame is chosen in such a way that the z-axis is along the principal axis of the linear polarization of the incoming photon and the y-axis along the photon beam. The photoelectron is detected in the x–z-plane at an angle $\theta$ with respect to the z-axis while the fluorescent photon is detected along the x-axis. The chosen experimental geometry varies slightly from the reaction plane geometry (see Fig. 3) which has been discussed in Section II.E used for the present theoretical analysis where the incoming synchrotron beam axis has been chosen as z-axis. By resolving the spin-orbit components of the 5p $^2$P$_{1/2}$ and 5p $^2$P$_{3/2}$ states of Sr$^+$ the photoelectron angular distributions were measured with an electron spectrometer of only 40 meV for the coincidence measurements. From these data at the photon energy of autoionization of Sr at 25.105 eV the following branching ratios of the relevant differential cross-sections and anisotropy parameters can be derived

$$\sigma_{5p^2P}1/2/\sigma_{5p^2P_{3/2}} = 0.85 \pm 0.08, \tag{191}$$

$$\beta_{5p^2P_{1/2}} = 1.28 \pm 0.09, \tag{192}$$

$$\beta_{5p^2P_{3/2}} = 0.67. \tag{193}$$

Note that the branching ratio is far away from the statistical value of 0.5 and the two $\beta$ values are significantly different.

Ueda *et al.* (1998) demonstrated by their above coincidence measurements in the resonance illustrated in Fig. 5 that they depend on ratios of five amplitudes $D_j^{(J)}$ of photoejected electron waves leaving the Sr$^+$ ion in the 5p $^2P_J$ states; $D_j^{(J)}$ are characterized by the $J = 1/2$ and $J = 3/2$ values of $^2P_{1/2,3/2}$ states and the $j$ corresponding to the $s$ wave with $j = 1/2$ and $j = 3/2$ and $j = 5/2$ to the $d$ waves, and one phase difference between the $s$ and $d$ waves. By using a combination of coincidence data from the angular correlation between the photoejected electron and the subsequent fluorescent photons and electron angular distribution measurements, the relevant $\beta$ values and the dipole amplitudes can be determined in the region of an autoionization resonance (Kabachnik and Sazhina, 1976).

In Fig. 5 the yield of photoelectrons, where the Sr$^+$ ion is left in the 5p excited state, is shown as a function of the synchrotron photon energy of the 4p excitation. The resonances have been identified in connection with the photoabsorption measurements of Mansfield and Newsom (1981). Coincidence measurements were carried out at energies indicated by arrows. They were analyzed by Kabachnik and Ueda (1995), and based upon the autoionization of strong resonances in the framework of Fano's theory for $q \gg 0$ Fano (1961) and Kabachnik and Sazhina's (1976) representation of the above dipole amplitudes. We are picking out results as examples of the peaks 2 and 4 of Fig. 5.

The branching ratios $D_{1/2}^{(1/2)} : D_{1/2}^{(3/2)}$ and $D_{3/2}^{(1/2)} : D_{3/2}^{(3/2)} : D_{5/2}^{(3/2)}$ extracted from the angular correlation experiment characterize the relative contribution of the fine structure subchannels of the s or d continua. For the resonance peaks 2 and 4 of Fig. 5 we summarize the data in tables IV–VI extracted from experiments using the following normalization convention

$$\overline{D}_s^2 : \overline{D}_d^2 \equiv \frac{[D_{1/2}^{(1/2)}]^2 + [D_{1/2}^{(3/2)}]^2}{[D_{3/2}^{(1/2)}]^2 + [D_{3/2}^{(3/2)}]^2 + [D_{5/2}^{(3/2)}]^2}, \tag{194}$$

$$\overline{D}_s^2 + \overline{D}_d^2 = 1, \tag{195}$$

$$\overline{D}_{1/2}^{(1/2)} : \overline{D}_{1/2}^{(3/2)} \equiv D_{1/2}^{(1/2)} : D_{1/2}^{(3/2)}, \tag{196}$$

Table IV

Photoelectron anisotropy parameters and branching ratio of the cross-sections in the 4p excited autoionization resonances in Sr (with peak numbers of Fig. 5).

| Peak no. | Phot. energy | Assignment | $\beta^{(1/2)}$ | $\beta^{(3/2)}$ | $\sigma^{(1/2)}/\sigma^{(3/2)}$ |
|---|---|---|---|---|---|
| 2 | 25.105 eV | $4p^5(4d^3, {}^4F)\,{}^5F_1$ | $1.28 \pm 0.09$ | $0.67 \pm 0.09$ | $0.85 \pm 0.08$ |
| 4 | 25.256 eV | $4p^5(5s^24d^1, {}^2D)\,{}^1P_1$ | $1.87 \pm 0.02$ | $1.53 \pm 0.03$ | $0.57 \pm 0.01$ |

Table V

Phase difference $\Delta = \delta_{1/2}^{(3/2)} - \delta_{3/2}^{(3/2)}$ and ratios of dipole amplitudes of the 4p excited autoionization resonances in Sr.

| Peak no. | $\Delta\,[\pi\,\mathrm{rad}]$ | $D_{1/2}^{(3/2)} : D_{3/2}^{(3/2)}$ | $D_{3/2}^{(3/2)} : D_{5/2}^{(3/2)}$ | $R = D_{1/2}^{(1/2)} : D_{3/2}^{(1/2)}$ |
|---|---|---|---|---|
| 2 | $0.77 \pm 0.13$ | $1.3 \pm 0.3$ | $2.3 \pm 1.3$ | $0.14 \pm 0.13,\ 1.51 \pm 0.48$ |
| 4 | $1.01 \pm 0.79$ | $0.9 \pm 0.4$ | $1.1 \pm 0.6$ | $0.43 \pm 0.79,\ 1.08 \pm 1.90$ |

Table VI

Branching ratio $\overline{D}_s^2 : \overline{D}_d^2$ and ratios of dipole amplitudes $\overline{D}_{1/2}^{(1/2)} : \overline{D}_{1/2}^{(3/2)}$ and $\overline{D}_{3/2}^{(1/2)} : \overline{D}_{3/2}^{(3/2)} : \overline{D}_{5/2}^{(3/2)}$. Where two sets of values are shown they correspond to the two solutions for $R$; see text.

| Peak no. | $\overline{D}_s^2 : \overline{D}_d^2$ | $\overline{D}_{1/2}^{(1/2)} : \overline{D}_{1/2}^{(3/2)}$ | $\overline{D}_{3/2}^{(1/2)} : \overline{D}_{3/2}^{(3/2)} : \overline{D}_{5/2}^{(3/2)}$ |
|---|---|---|---|
| 2 | $0.33 \pm 0.39{:}0.67 \pm 0.39$ | $0.16 \pm 0.15{:}0.99 \pm 0.03$ | $0.82 \pm 1.28{:}0.53 \pm 0.48{:}0.23 \pm 0.25$ |
| 2 | $0.64 \pm 0.13{:}0.36 \pm 0.13$ | $0.71 \pm 0.11{:}0.71 \pm 0.47$ | $0.62 \pm 0.24{:}0.72 \pm 0.22{:}0.31 \pm 0.20$ |
| 4 | $0.26 \pm 0.15{:}0.74 \pm 0.15$ | $0.46 \pm 0.22{:}0.89 \pm 0.09$ | $0.64 \pm 0.48{:}0.57 \pm 0.31{:}0.51 \pm 0.38$ |
| 4 | $0.40 \pm 0.21{:}0.60 \pm 0.21$ | $0.70 \pm 0.26{:}0.72 \pm 0.12$ | $0.53 \pm 0.34{:}0.63 \pm 0.33{:}0.57 \pm 0.42$ |
| ${}^1P_1$ | | $0.577{:}0.816$ | $0.577{:}0.258{:}0.775$ |
| ${}^3P_1$ | | $0.816{:}0.577$ | $0.408{:}0.730{:}0.548$ |
| ${}^3D_1$ | | | $0.707{:}0.632{:}0.316$ |

$$[\overline{D}_{1/2}^{(1/2)}]^2 + [\overline{D}_{1/2}^{(3/2)}]^2 = 1, \tag{197}$$

$$\overline{D}_{3/2}^{(1/2)} : \overline{D}_{3/2}^{(3/2)} : \overline{D}_{5/2}^{(3/2)} \equiv D_{3/2}^{(1/2)} : D_{3/2}^{(3/2)} : D_{5/2}^{(3/2)}, \tag{198}$$

and

$$[\overline{D}_{3/2}^{(1/2)}]^2 + [\overline{D}_{3/2}^{(3/2)}]^2 + [\overline{D}_{5/2}^{(3/2)}]^2 = 1. \tag{199}$$

The physical significance of the two values of $R$ in table V, leading to two sets of resonances 2, 4 (and also 6) is not yet clarified in the paper of Ueda *et al.* (1998). From the ratios of $D_j^{(J)}$ in table V and the experimental values of $\sigma^{(1/2)}/\sigma^{(3/2)}$ in table IV relative values of the five amplitudes (normalized on the unit scale introduced above) are summarized in table VI in the form of three ratios. The physical meaning of $\overline{D}_s^2 : \overline{D}_d^2$ is the branching ratio between the $s$ and $d$ electron waves. It was found that the $s$ wave is as strong as the $d$ wave in most resonances.

The ratios $\overline{D}_{1/2}^{(1/2)} : \overline{D}_{1/2}^{(3/2)}$ and $\overline{D}_{3/2}^{(3/2)} : \overline{D}_{3/2}^{(3/2)} : \overline{D}_{5/2}^{(3/2)}$ which are determined from experiment characterize the relative contribution of the fine structure subchannels in the $s$ or $d$ continua. Within the $LS$ coupling approximation, direct photoionization of the $^1S_0$ ground state of Sr, leaving the ion in the 5p excited level of Sr$^+$, leads to $5p\varepsilon s$ and $5p\varepsilon d$ $^1P_1$ continuum states. These $^1P_1$ continua, consisting of the ion and photoelectron, can be described in the $jj$ coupling scheme using an $LS - jj$ recoupling matrix, leading to the states $5p\,^2P_{1/2} + \varepsilon s_{1/2}$ and $\varepsilon d_{3/2}$ or $5p\,^2P_{3/2} + \varepsilon s_{1/2}, \varepsilon d_{3/2}$ and $\varepsilon d_{5/2}$. The ratios $\overline{D}_{1/2}^{(1/2)} : \overline{D}_{1/2}^{(3/2)}$ and $\overline{D}_{3/2}^{(1/2)} : \overline{D}_{3/2}^{(3/2)} : \overline{D}_{5/2}^{(3/2)}$ will then correspond to the amplitudes of the $LS - jj$ recoupling matrix elements themselves. This holds also for the strong $^1P_1$ autoionization resonance, as in the case of the Ca $3p^54s^23d\,^1P_1$ resonance which has been discussed before (Beyer *et al.*, 1995, 1996; West *et al.*, 1996), because the selection rules dictate that the continuum into which the resonance decays is also $^1P_1$.

Amplitudes estimated from the $LS - jj$ recoupling matrix for $^1P_1$ are also given in table VI. We can clearly see that the experimental ratios are in general far from the predictions based on the assumption that the final continuum states are $^1P_1$. According to Mansfield and Newsom (1981), resonance number 4 is 97% $4p^55s^24d\,^1P_1$. The result of Ueda *et al.* (1998), however, clearly indicates that this resonance is certainly not a pure $^1P_1$ resonance. Further evidence that this line is not a pure $^1P_1$ resonance comes from measurements of the fluorescence polarization when the electron ejection angle is 270°. According to Kabachnik and Ueda (1995) in this case the polarization should be 0.6 if the resonance is pure $^1P_1$. This result is based only on momentum conservation and therefore, in a sense, is model-independent.

Previously, Ueda *et al.* (1993) tried to extract the ratio $\overline{D}_s^2 : \overline{D}_d^2$ and the phase difference $\Delta$ from the measured values of alignment and photo-electron asymmetry parameter $\beta^{3/2}$ at the peak of resonance number 4, assuming that it is purely $LS$ coupled. These results indicate that the pure $LS$ coupling approximation is inappropriate, and the earlier values therefore should not be compared directly with those discussed here.

The breakdown of the assumption of $^1P_1$ for the final continuum states of the resonances studied is already evident in table IV. If the assumption held,

then the branching ratio $\sigma^{(1/2)}/\sigma^{(3/2)}$ would have the statistical value of 0.5, and $\beta^{(1/2)}$ should be equal to $\beta^{(3/2)}$. Such predictions do not agree with any experimental results.

The reason for the breakdown of the assumption of $^1P_1$ symmetry for the final continuum states is that all the resonances investigated here have large $^3P_1$ and $^3D_1$ components, and possibly others as well. As a result the resonances can autoionize into the $^3P_1$ and $^3D_1$ continua. If the resonance is predominantly $^3P_1$ ($^3D_1$), the continuum into which the resonance decays is also predominantly $^3P_1$ ($^3D_1$). The amplitudes expected from $LS - jj$ recoupling for pure $^3P_1$ and $^3D_1$ states are also given in table VI. It should be noted that none of the resonance states is pure $^3P_1$ or $^3D_1$; photoexcitation to these resonances takes place via the $^1P_1$ component.

In conclusion, one can show that the ratios of five amplitudes and one phase difference for the photoejected electron waves can be determined, in the case where the $Sr^+$ ion is left in the $5p\,^2P_{1/2}$ and $5p\,^2P_{3/2}$ states. The analysis of the amplitudes and phase difference shows that the major contribution of this technique is that it can identify the presence of components of different symmetries within a resonance line, giving quantitative information difficult to obtain from other experimental methods. Furthermore, since one is able to determine branching ratios for the amplitudes of the outgoing waves, it is now possible to make a direct comparison of these fundamental parameters with theoretical calculations, though it must be pointed out that such calculations are complex for an atom such as Sr because of the large number of channels involved. In a subsequent paper by West *et al.* (1998) it was demonstrated for the case of measuring the angular correlation of the photoejected electron and polarized fluorescence photon according to the reactions (190a)–(190c) that all photoionization parameters of dipole amplitude ratios and phases can be determined even for the relativistic case.

# VII. Conclusion and Outlook

In parts of this paper we referred on the developments of so-called *complete* atomic collision and photoionization experiments with free atoms. However, we concentrated extensively on the analysis of angle and spin resolved $(\gamma, e\gamma)$ coincidence experiments. By means of the density matrix and statistical tensor methods we derived a general theory which allows for a description of a large variety of $(\gamma, e\gamma)$ coincidence experiments. Applying a two step model the primary photoionization process has been dealt with independent of the subsequent fluorescence photon emission. For the

description of the photoionization we introduced $C$ coefficients which fully contain the dynamics of the photoelectron emission, whereas the $A$ coefficients contain the dynamics of the fluorescence photon emission. The latter have been already used for the interpretation of non-coincidence fluorescence photon emission experiments by many research groups. For the $C$ coefficients, the general symmetry relations have been derived. For such type of $(\gamma, e\gamma)$ coincidence experiments different experimental geometries are possible. Therefore, we discussed two different choices of the coordinate frame in more detail.

A large variety of different experimental setups have been discussed. Here, our focus has been on the additional selection rules due to the considered experiments and on the possible reduction of the general equations. In particular, we have been able to demonstrate, that the introduced $C$ coefficients do considerably reduce for certain types of experiments. We discussed the cases of experiments with an unpolarized target, the case of not observing the photoelectron spin, as well as not observing the photoelectron at all. Combining these results we considered the case of an unpolarized target and carrying out the coincidence experiment though not detecting the photoelectron spin. On the other hand, we investigated experiments without observing the residual ionic state, i.e. not observing the emitted fluorescence. This case has been demonstrated to be the one of non-coincidence photoelectron emission. In particular, we considered the additional selection rules for each type of experiment which occur when using a target with an initial $^1S_0$ ground state.

In order to introduce relative parameters we discussed the occurring normalization parameters. Using the introduced generalized irreducible anisotropy tensor of alignment and orientation we have been able to express the coupled statistical tensorial sets in terms of relative quantities. With this, the general equations of angular distribution and spin polarization for electron–photon coincidence experiments are derived. We discussed the angular distribution coincidence intensities in detail, and considered the case of detecting the fluorescence photon polarization in coincidence with the emitted photoelectron. Detailed examples related to Ca and Sr atoms have been discussed; they show examples of *complete scattering experiments* (Becker and Crowe, 2001) by which all relevant amplitudes and phase differences can be determined. Another special case of experiments is related to the non-coincident measurement of the fluorescence radiation polarized. For both experiments, information can be obtained from measuring the angle dependent Stokes parameters. For experiments observing the spin polarization of the emitted photoelectrons in coincidence with the emitted fluorescence radiation, information can be obtained by measuring the angle dependent cartesian components of the spin polarization vector of the

photoelectron. Again, a special case is the non-coincident measurement of the spin polarization of the photoelectron. A more complicated, and up today not possible, experiment is the simultaneous detection of the polarization of the emitted fluorescence photon and the spin polarization of the outgoing photoelectron. Here, we introduced the new tensor polarization parameters determined as the outer product of the components of the Stokes parameters and the spin polarization vector, respectively. Observing these new set of parameters may allow for obtaining an even more refined information on $(\gamma, e\gamma)$ coincidence experiments in the near future. However, these new parameters are related to a large number of anisotropy tensor parameters which makes their theoretical interpretation feasible.

In order to give a more simple example we have therefore discussed the simple most case of a $J_0 = 0 \longrightarrow J = 1/2$ transition in more detail. We have shown, that the general expressions for the observable quantities of angular distribution, spin and fluorescence polarization, as well as for the tensor polarization parameters considerably reduce for this case. The remaining expression are, however, still voluminous. Therefore, we have postponed a more detailed analysis, i.e. expressing the observable quantities simply in terms of modulo of the transition matrix elements and the occurring phase differences, to a more extended work in the near future.

# VIII. Acknowledgments

# IX. Appendix A: Expansion of Dipole Matrix Elements

Following Amusia (1990), pp. 16 the $T$-matrix of photoionization may be written as

$$\langle JM\mathbf{p}^{(-)}m_s|T_i|J_0 M_0 \omega \mathbf{n}\lambda\rangle = \sum_{q=1}^{N}\langle JM\mathbf{p}^{(-)}m_s|\exp^{i\mathbf{k}\cdot\mathbf{r}}(\mathbf{e}_\lambda \cdot \mathbf{p}_q^*)|J_0 M_0\rangle, \quad (200)$$

where $N$ denotes the number of electrons in the atomic shell, $\mathbf{e}_\lambda$ ($\lambda = \pm 1$) is the photon polarization vector which is chosen that $\mathbf{e}_\lambda \cdot \mathbf{n} = 0$, and $\mathbf{p}_q$ is the momentum of the $q$th electron of the atom. Note, that for the case of fluorescence photon emission (see Section II.C and Appendix C) the complex conjugate operator must be used.

Applying the long-wavelength limit of the dipole approximation, i.e. $kr_q \ll 1$, the exponential function can be replaced by unity $\exp^{i\mathbf{k}\cdot\mathbf{r}} \approx 1$.

Thus, for an arbitrarily polarized photon beam, the $T$-matrix elements may be written as

$$\langle JM\mathbf{p}^{(-)}m_s|T_i|J_0M_0\omega\mathbf{n}\lambda\rangle = \sum_{q=1}^{N}\langle JM\mathbf{p}^{(-)}m_s|(\mathbf{e}_\lambda \cdot \mathbf{p}_q^*)|J_0M_0\rangle$$

$$= \sum_{q=1}^{N} i\omega\langle JM\mathbf{p}^{(-)}m_s|(\mathbf{e}_\lambda \cdot \mathbf{r}_q^*)|J_0M_0\rangle, \quad (201)$$

where the first term denotes the "velocity form" and the latter the "length form" of the dipole transition matrix elements. The dipole approximation is valid in a rather broad region of energy (Amusia, 1990)

$$Z^2 < \omega \ll Z\alpha^{-1} \quad (202)$$

where $\alpha^{-1} = 137$ denotes the fine structure constant. Throughout the paper we will use the length form of the dipole matrix elements.

In our chosen coordinate frame the polarization vector $\mathbf{e}_\lambda$ can be eliminated by noting that in the helicity system the coordinate system is "spanned" by the three unit vectors $\mathbf{e}_{+1}$, $\mathbf{e}_{-1}$, $\mathbf{n}$, and that the dipole operator $\mathbf{r}$ can be therefore expanded in terms of this basis[3]

$$\mathbf{r} = r_{+1}^*\mathbf{e}_{+1} + r_{-1}^*\mathbf{e}_{-1} + r_0^*\mathbf{n}, \quad (203)$$

where $r_{\pm 1}$ and $r_0$ are the components of $\mathbf{r}$ along the directions of $\mathbf{e}_{\pm 1}$ and $\mathbf{n}$, respectively. That is, $r_{\pm 1}$ and $r_0$ are the spherical components of the vector $\mathbf{r}$. In this system the scalar product of $\mathbf{r}$ and $\mathbf{e}_\lambda$ is given by

$$\mathbf{e}_\lambda \cdot \mathbf{r}^* = r_\lambda. \quad (204)$$

---

[3] Here, and throughout the following the index $q$ and the summation over $q$, referring to the $q$th electron, are suppressed if not causing ambiguities.

The final state electron wavefunction can be expanded into partial waves. Applying the results of Lohmann (1990) we get

$$|\mathbf{p}^{(-)}m_s\rangle = \psi_{\mathbf{p}m_s}^{(-)}(\mathbf{r}) = \frac{1}{\sqrt{|p|^2}} \sum_{\substack{\ell m j m_j \\ m'\mu}} i^\ell\, e^{-i\sigma_\ell^j}\, Y_{\ell m}^*(\hat{\mathbf{p}})\, R_{\varepsilon\ell}^j(r)\, Y_{\ell m'}(\hat{\mathbf{r}})\, \chi_\mu$$

$$\times\, (\ell m 1/2 m_s | j m_j)(\ell m' 1/2\mu | j m_j)\,, \tag{205}$$

which yields for the expansion coefficients

$$a_{\ell m}^j = \langle j\ell m|\mathbf{p}^{(-)}\rangle = \frac{1}{\sqrt{|p|^2}}\, i^\ell\, e^{-i\sigma_\ell^j}\, Y_{\ell m}^*(\hat{\mathbf{p}})\,. \tag{206}$$

Inserting the partial wave expansions into the transition matrix elements we get

$$\langle JM\mathbf{p}^{(-)}m_s|r_\lambda|J_0 M_0\rangle$$
$$= \sum_{\ell m} a_{\ell m}^{j*}\langle JM\ell m 1/2 m_s|r_\lambda|J_0 M_0\rangle$$
$$= \sum_{\substack{\ell m j m_j \\ J_1 M_1}} a_{\ell m}^{j*}\langle (Jj)J_1 M_1|r_\lambda|J_0 M_0\rangle(\ell m 1/2 m_s|j m_j)(JM j m_j|J_1 M_1). \tag{207}$$

Using the fact that $\hat{\mathbf{r}}_\lambda$ is a tensor operator of rank one and applying the Wigner–Eckart theorem we get

$$\langle J_1 M_1|r_\lambda|J_0 M_0\rangle = (-1)^{J_1 - M_1} \begin{pmatrix} J_1 & 1 & J_0 \\ -M_1 & \lambda & M_0 \end{pmatrix}\langle J_1\|r\|J_0\rangle. \tag{208}$$

With this, we obtain for the dipole matrix element

$$\langle JM\mathbf{p}^{(-)}m_s|T_i|J_0 M_0\omega\mathbf{n}\lambda\rangle$$
$$= \langle JM\mathbf{p}^{(-)}m_s|d_\lambda|J_0 M_0\rangle$$
$$= \sum_{\substack{\ell m j m_j \\ J_1 M_1}} a_{\ell m}^{j*}\langle (Jj)J_1\|d\|J_0\rangle(-1)^{-\ell+1/2+m_j-J+j+J_1}\sqrt{(2j+1)(2J_1+1)}$$

$$\times \begin{pmatrix} \ell & 1/2 & j \\ m & m_s & -m_j \end{pmatrix}\begin{pmatrix} J & j & J_1 \\ M & m_j & -M_1 \end{pmatrix}\begin{pmatrix} J_1 & 1 & J_0 \\ -M_1 & \lambda & M_0 \end{pmatrix}, \tag{209}$$

where we introduced the abbreviation $d_\lambda = i\omega r_\lambda$. Inserting the expansion coefficients we finally end up with Eq. (13).

## X. Appendix B: Contraction of B Coefficients

Inserting Eq. (13) twice into Eq. (12) and re-arranging all factors yields

$$B(K_0Q_0, \Gamma\gamma; KQ, kq)$$

$$= \frac{1}{|p|^2} \sum_{\substack{MM'm_sm'_s \\ M_0M'_0\lambda\lambda' \\ }} \sum_{\substack{\ell m j m_j \\ J_1M_1}} \sum_{\substack{\ell'm'j'm'_j \\ J'_1M'_1}} (-1)^\ell i^{\ell+\ell'} e^{i(\sigma^j_\ell - \sigma^{j'}_{\ell'})}$$

$$\times Y_{\ell m}(\hat{\mathbf{p}}) Y^*_{\ell'm'}(\hat{\mathbf{p}}) \langle (Jj)J_1\|d\|J_0\rangle \langle (Jj')J'_1\|d\|J_0\rangle^*$$

$$\times \sqrt{(2K+1)(2K_0+1)(2k+1)(2\Gamma+1)}\sqrt{(2j+1)(2j'+1)(2J_1+1)(2J'_1+1)}$$

$$\times (-1)^{-\ell+1/2+m_j-J+j+J_1}(-1)^{-\ell'+1/2+m'_j-J+j'+J'_1}(-1)^{J-M+J_0-M_0+3/2-m_s-\lambda}$$

$$\times \begin{pmatrix} \ell & 1/2 & j \\ m & m_s & -m_j \end{pmatrix} \begin{pmatrix} J & j & J_1 \\ M & m_j & -M_1 \end{pmatrix} \begin{pmatrix} J_1 & 1 & J_0 \\ -M_1 & \lambda & M_0 \end{pmatrix}$$

$$\times \begin{pmatrix} \ell' & 1/2 & j' \\ m' & m'_s & -m'_j \end{pmatrix} \begin{pmatrix} J & j' & J'_1 \\ M' & m'_j & -M'_1 \end{pmatrix} \begin{pmatrix} J'_1 & 1 & J_0 \\ -M'_1 & \lambda' & M'_0 \end{pmatrix}$$

$$\times \begin{pmatrix} 1/2 & 1/2 & k \\ m_s & -m'_s & -q \end{pmatrix} \begin{pmatrix} 1 & 1 & \Gamma \\ \lambda & -\lambda' & -\gamma \end{pmatrix} \begin{pmatrix} J_0 & J_0 & K_0 \\ M_0 & -M'_0 & -Q_0 \end{pmatrix} \begin{pmatrix} J & J & K \\ M & -M' & -Q \end{pmatrix}.$$

$$(210)$$

Applying Brink and Satchler (1962), appendix III, p. 119, the summation over quantum numbers $M_0$, $M'_0$, $\lambda$, and $\lambda'$ can be carried out and by contracting the 3rd, 6th, 8th, and 9th 3$j$-symbols to a 9$j$-symbol we get

$$B(K_0Q_0, \Gamma\gamma; KQ, kq)$$

$$= \frac{1}{|p|^2} \sum_{\substack{MM'm_sm'_s \\ b\beta}} \sum_{\substack{\ell m j m_j \\ J_1M_1}} \sum_{\substack{\ell'm'j'm'_j \\ J'_1M'_1}} i^{\ell+\ell'} e^{i(\sigma^j_\ell - \sigma^{j'}_{\ell'})}$$

$$\times (2b+1) Y_{\ell m(\hat{\mathbf{p}})} Y^*_{\ell'm'}(\hat{\mathbf{p}}) \langle (Jj)J_1\|d\|J_0\rangle \langle (Jj')J'_1\|d\|J_0\rangle^*$$

$$\times \sqrt{(2K+1)(2K_0+1)(2k+1)(2\Gamma+1)}\sqrt{(2j+1)(2j'+1)(2J_1+1)(2J'_1+1)}$$

$$\times (-1)^{m_j-J+j+J_1}(-1)^{-\ell'+m'_j-J+j'}(-1)^{J-M+3/2-m_s+J_1-M_1}$$

$$\times \begin{pmatrix} 1/2 & 1/2 & k \\ m_s & -m'_s & -q \end{pmatrix} \begin{pmatrix} \ell & 1/2 & j \\ m & m_s & -m_j \end{pmatrix} \begin{pmatrix} \ell' & 1/2 & j' \\ m' & m'_s & -m'_j \end{pmatrix}$$

$$\times \begin{pmatrix} J & J & K \\ M & -M' & -Q \end{pmatrix} \begin{pmatrix} J & j & J_1 \\ M & m_j & -M_1 \end{pmatrix} \begin{pmatrix} J & j' & J'_1 \\ M' & m'_j & -M'_1 \end{pmatrix}$$

$$\times \begin{pmatrix} K_0 & b & \Gamma \\ -Q_0 & \beta & -\gamma \end{pmatrix} \begin{pmatrix} b & J_1 & J'_1 \\ \beta & -M_1 & M'_1 \end{pmatrix} \begin{Bmatrix} K_0 & b & \Gamma \\ J_0 & J_1 & 1 \\ J_0 & J'_1 & 1 \end{Bmatrix}. \tag{211}$$

Here, $M_0 + \lambda = M_1$ has been used and the artificial angular momentum $b$ and $z$-component $\beta$ has been introduced. By using the same formula we sum over $M$, $M'$, $M_1$, and $M'_1$ by contracting the 3$j$-symbols 4, 5, 6, and 8 which yields another 9$j$-symbol,

$$B(K_0 Q_0, \Gamma\gamma; KQ, kq)$$

$$= \frac{1}{|p|^2} \sum_{\substack{m_s m'_s \\ \alpha\alpha b\beta}} \sum_{\substack{\ell m j m_j J_1 \\ \ell' m' j' m'_j J'_1}} i^{\ell+\ell'} e^{i(\sigma^j_\ell - \sigma^{j'}_{\ell'})}$$

$$\times (2a+1)(2b+1) Y_{\ell m}(\hat{\mathbf{p}}) Y^*_{\ell' m'}(\hat{\mathbf{p}}) \langle (Jj)J_1 \| d \| J_0 \rangle \langle (Jj')J'_1 \| d \| J_0 \rangle^*$$

$$\times \sqrt{(2K+1)(2K_0+1)(2k+1)(2\Gamma+1)} \sqrt{(2j+1)(2j'+1)(2J_1+1)(2J'_1+1)}$$

$$\times (-1)^{3/2 - m_s - \ell' + m'_j + j + J_1 - J'_1}$$

$$\times \begin{pmatrix} 1/2 & 1/2 & k \\ m_s & -m'_s & -q \end{pmatrix} \begin{pmatrix} \ell & 1/2 & j \\ m & m_s & -m_j \end{pmatrix} \begin{pmatrix} \ell' & 1/2 & j' \\ m' & m'_s & -m'_j \end{pmatrix} \begin{pmatrix} a & j & j' \\ \alpha & m_j & -m'_j \end{pmatrix}$$

$$\times \begin{pmatrix} K_0 & b & \Gamma \\ -Q_0 & \beta & -\gamma \end{pmatrix} \begin{pmatrix} K & a & b \\ -Q & \alpha & \beta \end{pmatrix} \begin{Bmatrix} K_0 & b & \Gamma \\ J_0 & J_1 & 1 \\ J_0 & J'_1 & 1 \end{Bmatrix} \begin{Bmatrix} K & a & b \\ J & j & J_1 \\ J & j' & J'_1 \end{Bmatrix}, \tag{212}$$

where $(-1)^{2(J-M)} = 1$ and $M + m_j = M_1$ have been used. Applying Brink and Satchler (1962), app. IV, p 121, the two spherical harmonics can be contracted. This yields

$$B(K_0 Q_0, \Gamma\gamma; KQ, kq)$$

$$= \frac{1}{4\pi|p|^2} \sum_{\substack{m_s m'_s \mathcal{L} \mathcal{M} \\ \alpha\alpha b\beta}} \sum_{\substack{\ell m j m_j J_1 \\ \ell' m' j' m'_j J'_1}} i^{\ell+\ell'} e^{i(\sigma^j_\ell - \sigma^j_\ell)}(2a+1)(2b+1)$$

$$\times \sqrt{(2\ell+1)(2\ell'+1)}\,(2\mathcal{L}+1)\mathcal{D}^{(\mathcal{L})}_{\mathcal{M} 0}(\hat{\mathbf{p}})^* \langle (Jj)J_1 \| d \| J_0 \rangle \langle (Jj')J'_1 \| d \| J_0 \rangle^*$$

$$\times \sqrt{(2K+1)(2K_0+1)(2k+1)(2\Gamma+1)}\sqrt{(2j+1)(2j'+1)(2J_1+1)(2J_1'+1)}$$

$$\times (-1)^{3/2-m_s-\ell'+m_j'+j+J_1-J_1'+m'+\mathcal{M}}$$

$$\times \begin{pmatrix} \ell & \ell' & \mathcal{L} \\ 0 & 0 & 0 \end{pmatrix} \begin{pmatrix} \ell & \ell' & \mathcal{L} \\ m & -m' & -\mathcal{M} \end{pmatrix} \begin{pmatrix} a & j & j' \\ \alpha & m_j & -m_j' \end{pmatrix}$$

$$\times \begin{pmatrix} 1/2 & 1/2 & k \\ m_s & -m_s' & -q \end{pmatrix} \begin{pmatrix} \ell & 1/2 & j \\ m & m_s & -m_j \end{pmatrix} \begin{pmatrix} \ell' & 1/2 & j' \\ m' & m_s' & -m_j' \end{pmatrix}$$

$$\times \begin{pmatrix} K_0 & b & \Gamma \\ -Q_0 & \beta & -\gamma \end{pmatrix} \begin{pmatrix} K & a & b \\ -Q & \alpha & \beta \end{pmatrix} \begin{Bmatrix} K_0 & b & \Gamma \\ J_0 & J_1 & 1 \\ J_0 & J_1' & 1 \end{Bmatrix} \begin{Bmatrix} K & a & b \\ J & j & J_1 \\ J & j' & J_1' \end{Bmatrix}, \qquad (213)$$

where we expressed the spherical harmonics in terms of rotation matrices.

$$Y_{\mathcal{L}\mathcal{M}}(\hat{\mathbf{p}}) = \sqrt{\frac{2\mathcal{L}+1}{4\pi}} \mathcal{D}_{\mathcal{M}0}^{(\mathcal{L})}(\hat{\mathbf{p}})^*. \qquad (214)$$

Using Brink and Satchler (1962), appendix III, p 119, rearranging the phase factor, where $(-1)^{2m'} = 1$, $(-1)^{2(j'+j+a)} = 1$, $m_j' = m' + m_s'$ and $m_s' - m_s = -q'$ have been used, the 3$j$-symbols 2–6 can be contracted to another 9$j$-symbol and by summing over $m$, $m'$, $m_s$, $m_s'$, $m_j$, and $m_j'$, we eventually obtain Eq. (14).

## XI. Appendix C: Reduction of A Coefficients

Applying a similar procedure as for the anisotropy parameter $B$, the dipole approximation can be applied to the fluorescence transition matrix elements,

$$\langle J_f M_f \Omega \mathbf{N} \Lambda | T_f | J M \rangle = \sum_{q=1}^{N} \langle J_f M_f (\mathbf{e}_\Lambda^* \cdot \mathbf{P}_q) | J | M \rangle$$

$$= \sum_{q=1}^{N} -i\Omega \langle J_f M_f | (\mathbf{e}_\Lambda^* \cdot \mathbf{R}_q) | J M \rangle. \qquad (215)$$

Again, expanding the dipole operator $\mathbf{R}$ in a helicity basis, suppressing the electronic index $q$, and by applying the Wigner–Eckart theorem we get

$$\langle J_f M_f \Omega \mathbf{N} \Lambda | T_f | J M \rangle = i\Omega \langle J_f M_f | R_{-\Lambda} | J M \rangle$$

$$= (-1)^{J_f - M_f + 1} \begin{pmatrix} J_f & 1 & J \\ -M_f & -\Lambda & M \end{pmatrix} \langle J_f \| D \| J \rangle, \qquad (216)$$

where we used $D = -i\Omega R$ and the fact that $\mathbf{e}_\Lambda^* \cdot \mathbf{R} = R_\Lambda^* = -R_{-\Lambda}$.

Inserting Eq. (216) twice into Eq. (31) we obtain

$$A(KQ', h\nu) = \sum_{\substack{M_f \Lambda \Lambda' \\ MM'}} (-1)^{J-M+1-\Lambda'} \sqrt{(2K+1)(2h+1)} \, \langle J_f \| D \| J \rangle \langle J_f \| D \| J \rangle^*$$

$$\times \begin{pmatrix} J_f & 1 & J \\ -M_f & -\Lambda & M \end{pmatrix} \begin{pmatrix} J_f & 1 & J \\ -M_f & -\Lambda' & M' \end{pmatrix}$$

$$\times \begin{pmatrix} J & J & K \\ M & -M' & -Q' \end{pmatrix} \begin{pmatrix} 1 & 1 & h \\ \Lambda & -\Lambda' & -\nu \end{pmatrix}. \qquad (217)$$

Applying Blum, (1996), appendix (C9), the summation over $\Lambda$, $\Lambda'$, and $M_f$ can be carried out. Re-arranging the phase factor yields

$$A(KQ', h\nu) = \sum_{MM'} (-1)^{J-J_f-1} \sqrt{(2K+1)(2h+1)} \, \langle J_f \| D \| J \rangle \langle J_f \| D \| J \rangle^*$$

$$\times \begin{pmatrix} J & J & K \\ M & -M' & -Q' \end{pmatrix} \begin{pmatrix} J & J & h \\ -M' & M & -\nu \end{pmatrix} \begin{Bmatrix} J & J & h \\ 1 & 1 & J_f \end{Bmatrix}, \quad (218)$$

and by using the orthogonality relation of the 3$j$-symbols we get with Blum, (1996), eq. C4b

$$A(KQ', h\nu) = (-1)^{J+J_f+1-h} \sqrt{(2K+1)(2h+1)} \langle J_f \| D \| J \rangle \langle J_f \| D \| J \rangle^*$$

$$\times \frac{1}{2h+1} \delta_{hK} \delta_{\nu Q'} \begin{Bmatrix} J & J & h \\ 1 & 1 & J_f \end{Bmatrix}, \qquad (219)$$

which finally gives Eq. (33).

# XII.  References

Amusia, M. Ya. (1990). In: K.T. Taylor (Ed.) "Atomic Photoeffect trans." Plenum, New York, London.

Andersen, N., and Bartschat, K. (2000). "Polarization, Alignment, and Orientation in Atomic Collisions." Springer.

Alguard, M.J., Hughes, V.W, Lubell, M.S, and Weinwright. (1977). *Phys. Rev. Lett.* **39,** 334.

Altun, Z., and Kelly, H.P. (1985). *Phys. Rev. A* **31,** 3711.

Balashov, V.V., Grum-Grzhimailo, A.N., and Kabachnik, N.M. (2000). "Polarization and Correlation Phenomena in Atomic Collisions. A Practical Theory Course." Kluwer Academic/Plenum Publishers, New York.

Baum, G., Raith, W., Roth, B., Tondera, M., Bartschat, K., Bray, I., Ait-Tahar, S., Grant, I.P., and Norrinmgton, P.H. (1999). *Phys. Rev. Lett.* **82,** 1128.

Becker, U., Langer, B., Kohler, E., Heiser, F., Kerkhoff, H.G., and Wehlitz, R. (1988). In: C. Fabre and D. Delande (Ed.), "Book of Abstracts," p. V7. 11th ICAP, Paris.

Becker, U. (1989). In: A. Dalgarno, R.S. Freund, M.S. Lubell, and T.B. Lucatorto (Eds.), *XVII ICPEAC, AIP Conference Proceedings*. p. 162.

Becker, U., and Kleinpoppen, H. (1999). *Phil. Trans. Roy. Soc.* **357**, London, p. 1229.

Becker, U., and Crowe, A. (2001). "Complete Scattering Experiments." Kluwer Academic/ Plenum Publishers, New York.

Bederson, B. (1963). *Comm. At. Mol. Phys.* **1**, 41 and 65.

Bederson, B., Eisinger, J., Rubin, K., and Salop, A. (1960). *Rev. Sci. Instr.* **31**, 852.

Berger, O., and Kessler, J. (1986). *J. Phys. B: At. Mol. Opt. Phys.* **19**, 3539.

Berkowitz, J. (1979). "Photoabsorption, Photoionization and Photoelectron Spectroscopy." Academic Press, New York, San Francisco, London.

Berezhko, E.G., and Kabachnik, N.M. (1977). *J. Phys. B: At. Mol. Opt. Phys.* **10**, 2467.

Berezhko, E.G., Kabachnik, N.M., and Sizov, V.V., (1978). *J. Phys. B: At. Mol. Opt. Phys.* **11**, 1819.

Beyer, H.J., West, J.B., Ross, K.J., Ueda, K., Kabachnik, N.M., Hamdy, H., and Kleinpoppen, H. (1995). *J. Phys. B: At. Mol. Opt. Phys.* **28**, L47.

Beyer, H.J., West, J.B., Ross, K.J., Kabachnik, N.M., Hamdy, H., and Kleinpoppen, H. (1996). *J. Electr. Spectr. & Rel. Phen.* **79**, 339.

Blum, K. (1996). "Density Matrix Theory and Applications." 2nd Edn., Plenum Press, New York, London.

Brink, D.M., and Satchler, G.R., (1962). "Angular Momentum." Oxford University Press.

Bussert, W., and Klar, H. (1983). *Z. f. Physik A* **312**, 315.

Caldwell, C.D., and Zare, R.N. (1977). *Phys. Rev.* **16**, 255.

Cherepkov, N.A. (1983). *Adv. At. Mol. Phys.* **19**, 395.

Cvejanovic, S., and Reddish, J. (2000). *J. Phys. B: At. Mol. Opt. Phys.* **33**, 4691.

Cvejanovic, S., Viefhaus, J., Becker, U., Wiedenhöft, M., and Berrah, N. (2002). BESSY Annual Report 2001, to be published.

Datz, S., Drake, G.WF., Gallagher, T.F., Kleinpoppen, H., and zu Putlitz, G. (1999). *Rev. Mod. Phys.* **71**, 223.

Devons, S., and Goldfarb, L.JB. (1957). In: "Handbuch Der Physik," Vol. 42, p. 362. Springer-Verlag.

Ehresmann, A., Schäfer, H., Vollweiler, F., Mentzel, G., Magel, B., Schartner, K.H., and Schmoranzer, H. (1998). *J. Phys. B: At. Mol. Opt. Phys.* **31**, 1487.

Eminyan, M., Mac Adam, K., Slevin, J., and Kleinpoppen, H. (1973). *Phys. Rev. Lett.* **13**, 576.

Fano, U. (1957). *Rev. Mod. Phys.* **29**, 74.

Fano, U. (1961). *Phys. Rev.* **124**, 1866.

De fanis, A., West, J.B., Ross, K.J., Ueda, K., Beyer, H.J., Amusia M.Ya., and Chernysheva, L.V. (1999). *J. Phys. B: At. Mol. Opt. Phys.* **32**, 5739.

Godehusen, K., Zimmermann, P., Verweyen, A., von dem Borne, A., Wernet Ph, and Sonntag, B. (1998). *Phys. Rev. A* **58**, R3371.

Goodman, Z.M., Caldwell, C.D., and White, M.G. (1985). *Phys. Rev. Lett.* **54**, 1156.

Grum-Grzhmailo, A.N., Dorn, A., and Mehlhorn, W. (2001). In: U. Becker, and A. Crowe (Eds.), "Complete Scattering Experiments," p. 111. Kluwer Academic/Plenum Publishers, New York.

Hallwachs, W. (1888). *Ann. Phys. & Chem.* **33**, 301.

Hamdy, H., Beyer, H.J., West, J.B., and Kleinpoppen, H. (1991a). *J. Phys. B: At. Mol. Opt. Phys.* **24**, 4957.

Hamdy, H., Beyer, H.J., Mahmoud, K.R., Zohny, E.I.M., Hassan, G., and Kleinpoppen, H. (1991b). In: I.E. McCarthy, W.R. MacGillivray, and M.C. Standage (Eds.), "XVIIIth ICPEAC Book of Abstracts," p. 132. Griffith Univ., Brisbane.

Hausmann, A., Kämmerling, B., Kossman, H., and Schmidt, V. (1988). *Phys. Rev. Lett.* **61**, 2669.

Heckenkamp, Ch, Schafers, F., Schönhense, G., and Heinzmann, U. (1984). *Phys. Rev. Lett.* **52**, 421.

Heinzmann, U., Kessler, J., and Lorenz, J. (1970). *Z. Phys.* **240**, 42.

Heinzmann, U. (1980). *J. Phys. B: At. Mol. Opt. Phys.* **13**, 4353 and 4367.

Hertel, I.V., and Stoll, W. (1974). *J. Phys. B: At. Mol. Opt. Phys.* **7**, 570 and 583.

Hertz, H. (1887). *Ann. Phys. & Chem.* **31**, 983.

Hils, D., Mc Cusker, V., Kleinpoppen, H., and Smith, S.J. (1972). *J. Phys. B: At. Mol. Opt. Phys.* **29**, 398.

Hils, D., and Kleinpoppen, H. (1978). *J. Phys. B: At. Mol. Opt. Phys.* **11**, L 283.

Hippler, R., Madeheim, H., Harbich, W.Q., Kleinpoppen, H., and Lutz, H.O. (1988). *Phys. Rev. A* **38**, 1662.

Jacobs, V.L., (1972). *J. Phys. B: At. Mol. Opt. Phys.* **5**, 2257.

Kabachnik, N.M., and Sazhina, I.P. (1976). *J. Phys. B: At. Mol. Opt. Phys.* **9**, 1681.

Kabachnik, N.M., Lohmann, B., and Mehlhorn, W. (1991). *J. Phys. B: At. Mol. Opt. Phys.* **24**, 2249.

Kabachnik, N.M., and Ueda, K. (1995). *J. Phys. B: At. Mol. Opt. Phys.* **28**, 5013.

Kämmerling, B., and Schmidt, V. (1991). *J. Phys. B: At. Mol. Opt. Phys.* **67**, 1848.

Kerling, C., Böwering, N., and Heinzmann, U. (1990). *J. Phys. B: At. Mol. Opt. Phys.* **23**, L629.

Kessler, J. (1985). "Polarized Electrons." 2nd Edn. Springer, Berlin.

Klar, H., and Kleinpoppen, H. (1982). *J. Phys. B: At. Mol. Opt. Phys.* **15**, 933.

Kronast, W., Huster, R., and Mehlhorn, W. (1984). *J. Phys. B: At. Mol. Opt. Phys.* **17**, L51.

Kronast, W., Huster, R., and Mehlhorn, W. (1986). *Z. Phys. D* **2**, 285.

Lagutin, R.M., Petrov, I.D., Demekhin Ph, V., Sukhorukov, V.L., Vollweiler, F., Liebel, H., Ehresmann, A., Lauer, S., Schmoranzer, H., Wilhelmi, O., Zimmermann, B., and Schartner, K.H., (2000). *J. Phys. B: At. Mol. Opt. Phys.* **33**, 1337.

Lohmann, B. (1990). *J. Phys. B: At. Mol. Opt. Phys.* **23**, 3147.

Lohmann, B., Hergenhahn, U., and Kabachnik, N.M. (1993). *J. Phys. B: At. Mol. Opt. Phys.* **26**, 3327.

Lohmann, B., and Larkins, F.P. (1994). *J. Phys. B: At. Mol. Opt. Phys.* **27**, L143.

Lohmann, B. (1999a). *J. Phys. B: At. Mol. Opt. Phys.* **32**, L643.

Lohmann, B. (1999b). *Aust. J. Phys.* **52**, 397.

Lohmann, B., and Kleiman, U. (2001). In: J. Berakdar, and J. Kirschner (Eds.), "Many-Particle Spectroscopy of Atoms, Molecules, Clusters and Surfaces," p. 173. Kluwer Academic/ Plenum Publishers, New York.

Lörch, H., Bizau, J.M., Scherer, N., Diehl, S., Cubayanes, D., Zerouni, O., Wuilleumier, F.J., Schmidt, V., and Johnson, W.R. (1999). *J. Phys. B: At. Mol. Opt. Phys.* **32**, 2215.

Macek, J., and Jaecks (1971). *Phys. Rev. A* **4**, 1288.

MacGillivray, W.R., and Standage, M.C., *Physics Reports* **168**, 1.

Mansfield, M.W.D., and Newsom, G.H. (1977). *Proc. Roy. Soc. A* **357**, 77.

Mansfield, M.W.D., and Newsom, G.H. (1981). *Proc. Roy. Soc. A* **377**, 431.

Mehlhorn, W. (1991). In: M.Y. Amusia and J.B. West (Eds.), "Today and Tomorrow in Photoionization," p. 15. Proceedings of U.K./U.S.S.R. Seminar, St Petersburg SERC publication DL/Sci/R19.

Mentzel, G., Schartner, K.H., Wilhelmi, O., Magel, B., Staude, U., Vollweiler, F., Lauer, S., Liebel, H., Schmoranzer, H., Sukhorukov, V.L., and Lagutin, B.M. (1998). *J. Phys. B: At. Mol. Opt. Phys.* **31**, 227.

Meyer, M., Marquette, A., Grum-Grzhmailo, A.N., Kleiman, U., and Lohmann, B. (2001). *Phys. Rev. A* **64**, 022703-1.

Papp, T., and Campbell, J.L. (1992). *J. Phys. B: At. Mol. Opt. Phys.* **25**, 3765.

Plotzke, O., Prümper, G., Zimmermann, B., Becker, U., and Kleinpoppen, H. (1996). *Phys. Rev. Lett.* **77**, 2646.

Prümper, G., Zimmermann, B., Langer, B., Viefhaus, J., Hentges, R., Cherepkov, N.A., Schmidtke, B., Drescher, M., Heinzmann, U., Becker, U., and Kleinpoppen, H. (2000). *Phys. Rev. Lett.* **85**, 5074.

Prümper, G., Geßner, O., Zimmermann, B., Viefhaus, J., Hentges, R., Becker, U., and Kleinpoppen, H. (2001). *J. Phys. B: At. Mol. Opt. Phys.* **34**, 2707.

Rubin, K., Bederson, B., Goldstein, M., and Collins, R.E. (1969). *Phys. Rev.* **182**, 201.

Scherer, N., Schaphorst, and Schmidt, V. (2001). In U. Becker, and A. Crowe (Eds.), "Complete Scattering Experiments." Kluwer Academic/Plenum Publishers, New York, p. 155.

Schmidt, V. (1997). "Electron Spectrometry of Atoms using Synchrotron Radiation." Cambridge University Press.

Schmidtke, B., Drescher, M., Cherepkov, N.A., and Heinzmann, U. (2000a). *J. Phys. B: At. Mol. Opt. Phys.* **33**, 2451.

Schmidtke, B., Khalil, T., Drescher, M., Müller, N., Kabachnik, N.M., and Heinzmann, U. (2000b). *J. Phys. B: At. Mol. Opt. Phys.* **33**, 5225.

Schmidtke, B., Khalil, T., Drescher, M., Müller, N., Kabachnik, N.M., and Heinzmann, U. (2001). *J. Phys. B: At. Mol. Opt. Phys.* **34**, 4293.

Schmoranzer, H., Lauer, S., Vollweiler, F., Ehresmann, A., Sukhorukov, V.L., Lagutin, B.M., Petrov, I.D., Demekhin Ph D, Schartner, K.H., Magel, B., and Mentzel, G. (1997). *J. Phys. B: At. Mol. Opt. Phys.* **30**, 4463.

Schwarzkopf, O., Krässig, B., Elminger, J., and Schmidt, V. (1993). *Phys. Rev. Lett.* **70**, 3008.

Siegel, A., Ganz, J., Bussert, W., and Hotop, H. (1983). *J. Phys. B: At. Mol. Opt. Phys.* **16**, 2945.

Sonntag, B., and Zimmermann, P. (1995). *Physik. Blätter* **51**, 279.

Standage, M.C., and Kleinpoppen, H. (1975). *Phys. Rev. Lett.* **36**, 577.

Ueda, K., West, J.B., Ross, K.J., Hamdy, H., Beyer, H.J., and Kleinpoppen, H. (1993). *Phys. Rev. A* **48**, R863 and *J. Phys. B: At. Mol. Opt. Phys.* **26**, L347.

Ueda, K., West, J.B., Ross, K.J., Beyer, H.J., and Kabachnik, N.M. (1998). *J. Phys. B: At. Mol. Opt. Phys.* **31**, 4801.

Ueda, K., Shimizu, Y., Chiba, H., Sato, Y., Kitajima, M., Tanaka, H., and Kabachnik, N.M. (1999). *Phys. Rev. Lett.* **83**, 5463.

West, J.B., Ueda, K., Kabachnik, N.M., Ross, K.J., Beyer, H.J., and Kleinpoppen, H. (1996). *Phys. Rev. A* **53**, R9.

West, J.B., Ross, K.J., Ueda, K., and Beyer, H.J. (1998). *J. Phys. B: At. Mol. Opt. Phys.* **31**, L647.

Wille, U., and Hippler, R. (1986). *Phys. Rep.* **132**, 129.

Zimmermann, B., Wilhelmi, O., Schartner, K.H., Vollweiler, F., Liebel, H., Ehresmann, A., Lauer, S., Schmoranzer, H., Lagutin, B.M., Petrov, I.D., and Sukhorukov, V.L. (2000). *J. Phys. B: At. Mol. Opt. Phys.* **33**, 2467.

# QUANTUM MEASUREMENTS AND NEW CONCEPTS FOR EXPERIMENTS WITH TRAPPED IONS

*CH. WUNDERLICH and CH. BALZER*

*Institut für Laser-Physik, Universität Hamburg, Jungiusstr. 9, 20355 Hamburg, Germany*

## I. Overview

Quantum mechanics is a tremendously successful theory playing a central role in natural sciences even beyond physics, and has been verified in countless experiments, some of which were carried out with very high

*E-mail: wunderlich@phys.uni-hamburg.de

precision. Despite its great success and its history reaching back more than hundred years, still today the interpretation of quantum mechanics challenges our intuition that has been formed by an environment governed by classical physical laws.

Quantum optical experiments may come very close to idealized situations of gedanken experiments originally conceived to test and better understand the predictions and implications of quantum theory. An experimental system ideally suited to carry out such experiments will be dealt with in this work: electrodynamically trapped ions provide us with individual localized quantum systems well isolated from the environment. The interaction with electromagnetic radiation allows for preparation and detection of quantum states, even of single ions (Neuhauser *et al.*, 1980). Since the first storage and detection of a collection of ions in Paul and Penning traps has been reported (Fischer, 1959; Church and Dehmelt, 1969; Ifflander and Werth, 1977), a large variety of intriguing experiments were carried out, for instance, the demonstration of optical cooling (Neuhauser *et al.*, 1978; Wineland *et al.*, 1978) and experiments related to fundamental physical questions (for instance, Bergquist *et al.*, 1986; Sauter *et al.*, 1986; Diedrich and Walther, 1987; Schubert *et al.*, 1992; Guthöhrlein *et al.*, 2001; Howe *et al.*, 2001). Also, for precision measurements and frequency standards the use of trapped ions is well established (for instance, (Becker *et al.*, 2001; Diddams *et al.*, 2001; Stenger *et al.*, 2001).

The fact that quantum mechanics makes only statistical predictions let Albert Einstein and others doubt whether this theory is correct, or more specific, whether it gives a complete description of physical reality as they perceived it. Einstein cast part of his doubts about this theory in the words "Gott würfelt nicht" ("God doesn't roll dice") that is, according to his opinion laws of nature do *not* contain this intrinsic randomness and a proper theory should account for that.

Another puzzling feature of quantum mechanics was pointed out by Einstein, Podolsky, and Rosen (EPR) in Einstein *et al.* (1935). Quantum theory predicts correlations between two or more quantum systems once an entangled state of these systems has been generated. These correlations persist even after the quantum systems have been brought to spacelike separated points. The statistical nature of quantum mechanical predictions, and the superposition principle, together with quantum mechanical commutation relations give rise to such nonlocal correlations (Einstein *et al.*, 1935). Einstein found this, what he later called "spukhafte Fernwirkung" ("spooky action at a distance") deeply disturbing and concluded that quantum mechanics is an incomplete theory. The term "Verschränkung" (entanglement) has been coined by E. Schrödinger to describe such correlated quantum systems (Schrödinger, 1935). Recently,

entangled states of various physical systems have been created and analyzed in experiments (a review can be found in Whitaker, 2000). All experimental findings have been in agreement with quantum mechanical predictions.

There is no *a priori* reason not to apply quantum mechanics to objects like a measurement apparatus made up from a large number of elementary constituents each of which is perfectly described by quantum theory. This, however, may be a cause for yet more discomfort, since it leads to seemingly paradoxical or absurd consequences as Erwin Schrödinger pointed out (Schrödinger, 1935). With a gedanken experiment he illustrated the consequences of including an object usually described by classical physics (he chose a cat) into a quantum mechanical description.[1] The cat is 'coupled' to a quantum system prepared in a superposition state, and in the course of the gedanken experiment the cat, too, assumes a superposition state of 'being dead' and 'being alive' (Schrödinger, 1935): an entangled state of quantum system and cat results.

The cat can be viewed as a macroscopic apparatus that is used to measure the state of a quantum system. Thus, if the quantum system initially is in a superposition of two states, then linearity of quantum mechanics demands the measurement apparatus, too, to be in a superposition of two of its meter states. This is clearly not what we usually observe in experiments. Reference (Brune *et al.*, 1996) describes a cavity QED experiment where an electromagnetic field acts as meter for the quantum state of individual atoms. It is shown how the decay of the initially prepared superposition of meter states is the faster the larger the initial separation of these states is. For macroscopically distinct meter states this decay of a superposition state into a statistical mixture of states (that is, either one *or* the other is realized) is usually too fast to be observable experimentally. Thus, superpositions of macroscopically distinct states are never observed. Schrödinger-cat like states have also been investigated with trapped ions (Myatt *et al.*, 2000) and superconducting quantum interference devices (Friedman *et al.*, 2000).

The first step in a measurement process requires some interaction between the quantum system and a second system (the probe), and consequently a correlation is established between the two systems. (In general, this will result in an entangled state between quantum system and probe.) This correlation reduces or even destroys the quantum system's capability to display characteristics of a superposition state in subsequent local operations, and the appropriate description of the quantum system alone is a statistical mixture of states. The coupling of the probe to a macroscopic apparatus leads to a reduction of the probe itself from a coherent superposition into a

---

[1] Arguably classical physics is not sufficient to describe a cat. For the purpose of the gedanken experiment, therefore, it might be useful to choose an inanimate macroscopic object.

statistical mixture (for instance, Zurek, 1991; Giulini *et al.*, 1996 and references therein). When the apparatus is finally found in one of its meter states, quantum mechanics tells us that the quantum system is reset to the state correlated with this particular meter state. This will be evident in any subsequent manipulation the quantum system is subjected to. If the quantum system would undergo some kind of evolution as long as it is not being measured, then the measurement process might impede or even freeze this evolution. This slowing down (or coming to a complete halt) of the dynamics of a quantum system when subjected to frequent measurements has been termed quantum Zeno effect or quantum Zeno paradox (Misra and Sudarshan, 1977).

An unambiguous demonstration of this effect requires measurements on individual quantum systems as opposed to ensemble measurements. Such an experiment has been carried out with individual electrodynamically trapped $Yb^+$ ions prepared in a well-defined quantum state, and it is shown that even negative-result measurements (which do not involve local interaction between quantum system and apparatus in a "classical" sense) impede the quantum system's evolution (Section IV).

Now we turn to the concept of a quantum state that is a central ingredient of quantum theory. How can an arbitrary *unknown* state of a quantum system be determined accurately? The determination of the set of expectation values of the observables associated with a specific quantum state is complicated by the fact that after a measurement of one observable, information on the complementary observable is no longer available. Only if infinitely many identical copies of a given state were available could this task be achieved. Since this requirement cannot be fulfilled in experiments, it is of interest to investigate ways to gain optimal knowledge of a given quantum state making use of *finite* resources. In addition, quantum state estimation is, for instance, relevant for quantum communication where quantum information at the receiver end of a quantum channel has to be deciphered.

If $N$ identically prepared quantum systems in an unknown arbitrary state are available, how can this state be determined? In other words, what is the optimal strategy to gain the maximal amount of information about the state of a quantum system using finite physical resources? Quantum states of various physical systems such as light fields, molecular wave packets, motional states of trapped ions, and atomic beams have been determined experimentally (for a review of recent work see, for instance, (Freyberger *et al.*, 1997; Schleich and Raymer, 1997; Bužek *et al.*, 1998; Walmsley and Waxer, 1998; White *et al.*, 1999; Lvovsky *et al.*, 2001).

Optimal strategies to read out information encoded in the quantum state of a given number $N$ of identical *two-state* systems (qubits) have been

proposed in recent years. However, they require intricate measurements using a basis of entangled states. It is desirable to have a measurement strategy at hand that gives an estimate of a quantum state with high fidelity, even if $N$ measurements are performed separately (even sequentially) on each individual qubit, that is, if a factorizing basis is employed for state estimation. Sequential measurements on arbitrary but identically prepared states of a qubit, the ground state hyperfine levels of electrodynamically trapped $^{171}Yb^+$, are described in Section V. The measurement basis is varied during a sequence of $N$ measurements conditioned on the results of previous measurements in this sequence. The experimental efficiency and fidelity of such a self-learning measurement (Fischer *et al.*, 2000) is compared with strategies where the measurement basis is randomly chosen during a sequence of $N$ measurements.

In addition to puzzling us with fundamental questions regarding, for example, the measurement process, quantum mechanics holds the opportunity to put its laws to practical use. In the field of quantum information processing (QIP) and communication basic elements of computers are explored that would be able to solve problems that, for all practical purposes, cannot be handled by classical computers and communication devices (Feynman, 1982; Deutsch, 1985; Gruska, 1999; Nielsen and Chuang, 2000, and references therein). The computation of properties of quantum systems themselves is particularly suited to be performed on a quantum computer, even on a device where logic operations can only be carried out with limited precision. Exchange of information can be made secure by using encrypting methods that rely on quantum properties, for instance, of optical radiation. While exploring these routes to new types of computing and communication, again much will be learned about still unsolved issues in quantum mechanics, for instance, regarding the characterization of entanglement (Lewenstein *et al.*, 2000). The experimental system described in this work is well suited to conduct investigations in this new field.

The great potential that trapped ions have as a physical system for quantum information processing (QIP) was first recognized in Cirac and Zoller (1995), and important experimental steps have been undertaken toward the realization of an elementary quantum computer with this system (for instance, Appasamy *et al.*, 1998; Wineland *et al.*, 1998; Roos *et al.*, 1999; Hannemann *et al.*, 2002). At the same time, the advanced state of experiments with trapped ions reveals the difficulties that still have to be overcome.

Using $^{171}Yb^+$ ions we have realized a quantum channel, that is, propagation of quantum information in time or space, under the influence of well-controlled disturbances. The parameters characterizing the quantum

channel can be adjusted at will and various types of quantum channels (that may occur in other experimental systems, too) can be implemented with individual ions. Thus a model system is realized to investigate, for example, the reconstruction of quantum information after transmission through a noisy quantum channel (Section VI.A). Transfer of quantum states becomes important when quantum information is distributed between different quantum processors, as is envisaged, for instance, for ion trap quantum information processing (Pellizzari, 1997; van Enk *et al.*, 1999). Furthermore, codes for quantum information processing, and in particular error correction codes may be tested for their applicability under well-defined, non-ideal conditions.

These experiments demonstrate the ability to prepare arbitrary states of this SU2 system with very high precision – a prerequisite for quantum information processing. The coherence time of the hyperfine qubit in $^{171}$Yb$^+$ is long on the timescale of qubit operations and is essentially limited by the coherence time of microwave radiation used to drive the qubit transition.

In addition to the ability to perform arbitrary single-qubit operations, a second fundamental type of operation is required for QIP: conditional quantum dynamics with, at least, two qubits. Any quantum algorithm can then be synthesized using these elementary building blocks (Barenco *et al.*, 1995; DiVincenzo, 1995). While two internal states of each trapped ion serve as a qubit, communication between these qubits, necessary for conditional dynamics, is achieved via the vibrational motion of the ion string in a linear trap (the "bus-qubit") (Cirac and Zoller (1995)). Thus, it is necessary to couple external (motional) and internal degrees of freedom. Common to all experiments performed to date – related either to QIP or other research fields – that require some kind of coupling between internal and external degrees of freedom of atoms is the use of *optical* radiation for this purpose. The recoil energy $E_r = (\hbar k)^2/2m$ taken up by an atom upon absorption or emission of a photon may change the atom's motional state ($k = 2\pi/\lambda$, $\lambda$ is the wavelength of the applied electromagnetic radiation, and $m$ is the mass of the ion). In order for this to happen with appreciable probability with a harmonically trapped atom, the ratio between $E_r$ and the quantized motional energy of the trapped atom, $\hbar\nu$ should not be too small ($\nu$ is the angular frequency of the vibrational mode to be excited). Therefore, in usual traps, driving radiation in the optical regime is necessary to couple internal and external dynamics of trapped atoms.

The distance between neighboring ions $\delta z$ in a linear electrodynamic ion trap is determined by the mutual Coulomb repulsion of the ions and the time-averaged force exerted on the ions by the electrodynamic trapping field. Manipulation of individual ions is usually achieved by

focusing electromagnetic radiation to a spot size much smaller than $\delta z$. Again, only optical radiation is useful for this purpose.

In Section VI.B a new concept for ion traps is described that allows for experiments requiring individual addressing of ions and conditional dynamics with several ions even with radiation in the *radio frequency* (rf) or *microwave* (mw) regime. It is shown how an additional magnetic field gradient applied to an electrodynamic trap individually shifts ionic qubit resonances making them distinguishable in frequency space. Thus, individual addressing for the purpose of single qubit operations becomes possible using long-wavelength radiation. At the same time, a coupling term between internal and motional states arises even when rf or mw radiation is applied to drive qubit transitions. Thus, conditional quantum dynamics can be carried out in this modified electrodynamic trap, and in such a new type of trap all schemes originally devised for *optical* QIP in ion traps can be applied in the rf or mw regime, too.

Many phenomena that were only recently studied in the optical domain form the basis for techniques belonging to the standard repertoire of coherent manipulation of nuclear and electronic magnetic moments associated with their spins. Nuclear magnetic resonance (NMR) experiments have been tremendously successful in the field of QIP taking advantage of highly sophisticated experimental techniques. However NMR experiments usually work with macroscopic ensembles of spins and considerable effort has to be devoted to the preparation of pseudo-pure states of spins with initial thermal population distribution. This preparation leads to an exponentially growing cost (with the number $N$ of qubits) either in signal strength or the number of experiments involved (Vandersypen *et al.*, 2000), since the fraction of spins in their ground state is proportional to $N/2^N$.

Trapped ions, on the other hand, provide individual qubits – for example, hyperfine states as described in this work – well isolated from their environment with read-out efficiency near unity. It would be desirable to combine the advantages of trapped ions and NMR techniques in future experiments using either "conventional" ion trap methods, but now with mw radiation as outlined above, or, as described in the second part of Section VI.B.2, treating the ion string as a $N$-qubit molecule with adjustable spin-spin coupling constants: In a suitably modified ion trap, ionic qubit states are pairwise coupled. This spin–spin coupling can be formally described in the same way as J-coupling in molecules used for NMR, even though the physical origin of the interaction is very different. Thus, successful techniques and technology developed in spin resonance experiments, like NMR or ESR, can immediately be applied to trapped ions. An advantage of an artificial "molecule" in a trap is that the coupling constants $J_{ij}$ between qubits $i$ and $j$ can be chosen by the experimenter by setting the

magnetic field gradient, the secular trap frequency, and the type of ions used. In addition, *individual* spins can be detected state selectively with an efficiency close to 100% by collecting scattered resonance fluorescence.

Another avenue toward quantum computation with trapped ions is the use of an electric quadrupole transition (E2 transition) as a qubit (Appasamy *et al.*, 1998; Hughes *et al.*, 1998; Barton *et al.*, 2000; Schmidt-Kaler *et al.*, 2000). Section VI.G gives an account of experiments carried out with $Ba^+$ and $^{172}Yb^+$ ions where the E2 transition between the ground state $S_{1/2}$ and the metastable excited $D_{5/2}$ state is investigated.

Cooling of the collective motion of several particles is prerequisite for implementing conditional quantum dynamics on trapped ions. A study of the collective vibrational motion of two trapped $^{138}Ba^+$ ions cooled by two light fields is described in Section VI.C.3. Parameter regimes of the laser light irradiating the ions can be identified that imply most efficient laser cooling and are least susceptible to drifts, fluctuations, and uncertainties in laser parameters (Reiß *et al.*, 2002).

# II. Spin Resonance with Single $Yb^+$ Ions

In this section we introduce experiments with $^{171}Yb^+$ ions demonstrating the precise manipulation of hyperfine states of single ions essentially free of longitudinal and transverse relaxation. The experimental techniques outlined here, form the basis for further experiments with individual $Yb^+$ ions described in Sections IV, V, and VI.

## A. Experimental Setup for Yb+

$^{171}Yb^+$ and $^{172}Yb^+$ ions are confined in a miniature Paul trap (diameter of 2 mm). Excitation of the $S_{1/2} - P_{1/2}$ transition of $Yb^+$ serves for initial cooling and detection of resonantly scattered light near 369 nm (Fig. 1). For this purpose, infrared light near 738 nm is generated by a laser system based on a commercial Ti:Sapphire laser and frequency doubled using a $LiIO_3$ crystal mounted at the center of a homemade ring resonator. The emission frequency is stabilized against drift using an additional reference resonator.

Optical pumping into the $D_{3/2}$ state is prevented by illuminating the ions with laser light near 935 nm. This couples state $|D_{3/2}, F = 1\rangle$ via a dipole allowed transition to state $|[3/2]_{1/2}, F = 0\rangle$ that in turn decays to the ground state $|S_{1/2}, F = 1\rangle$. Light near 935 nm is produced by a homemade tunable, stabilized diode laser. Excitation spectra recorded with this laser have been recorded that exhibit sidebands due to micromotion of an ion in the trap. Making these sidebands disappear by adjusting the voltages applied to

$4f^{13}5d6s\ ^3D[3/2]_{1/2}$

$4f^{13}5d6s\ ^1D[5/2]_{5/2}$

935 nm

638 nm

$4f^{14}6p\ ^2P_{1/2}$

$4f^{14}5d\ ^2D_{5/2}$

369 nm

$4f^{14}5d\ ^2D_{3/2}$

411 nm

$4f^{13}6s^2\ ^2F_{7/2}$

F = 1

12.6 GHz

$4f^{14}6s\ ^2S_{1/2}$

F = 0

Ti:Sa Laser
738 nm

Diode Laser
935 nm

Diode Laser
822 nm

Diode Laser
638 nm

Frequency
Doubling

Frequency
Doubling

AOM

AOM

AOM

MW Source

DSP System

Personal
Computer

PMT
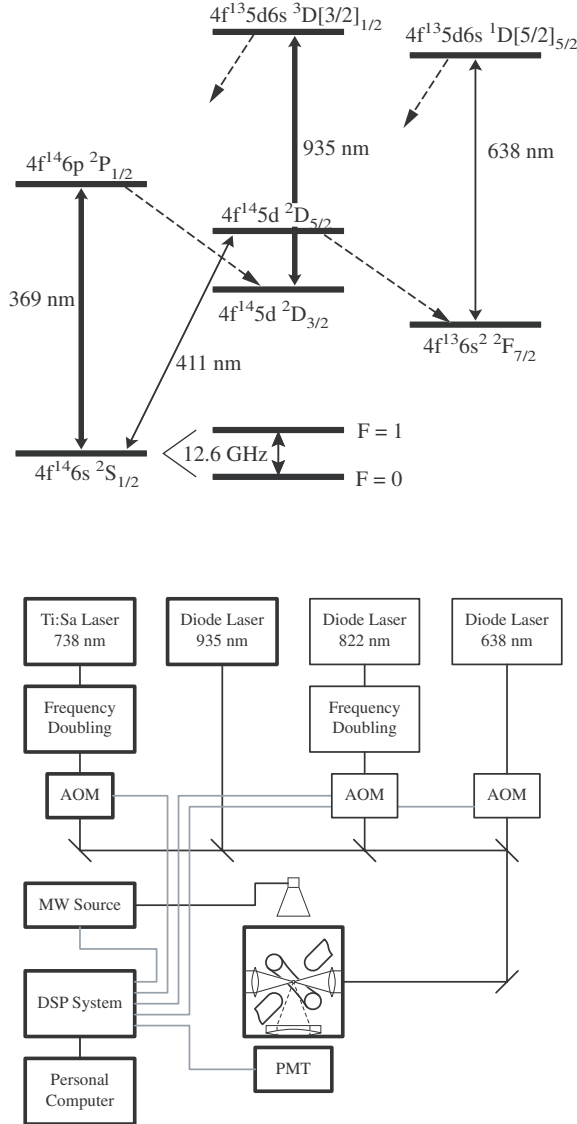
FIG. 1. (Top) Relevant energy levels of $^{171}$Yb$^+$. The hyperfine splitting is shown only for the ground state (not to scale). (Bottom) Schematic drawing of major experimental elements. All lasers are frequency stabilized employing reference resonators (not shown.) MW: microwave; PMT: photo multiplier tube; DSP: digital signal processing; AOM: acousto optic modulator. For most experiments described in this work (using $^{171}$Yb$^+$) the elements drawn with bold lines are used.

additional electrodes close to the trap serves for positioning the ion the field free potential minimum at the center of the trap.

The quantum mechanical two-state system used for the experiments described in Sections IV, V, and VI is the $S_{1/2}$ ground-state hyperfine doublet with total angular momentum $F = 0, 1$ of $^{171}$Yb$^+$. The

$$|0\rangle \equiv |S_{1/2}, F = 0\rangle \leftrightarrow |S_{1/2}, F = 1, \ m_F = 0\rangle \equiv |1\rangle \qquad (1)$$

transition with Bohr frequency $\omega_0$ is driven by a quasiresonant microwave (mw) field with angular frequency near $\omega = 2\pi\, 12.6\,\text{GHz}$. The time evolution of the system is virtually free of decoherence, that is, transversal and longitudinal relaxation rates are negligible. However, imperfect preparation and detection may limit the purity of the states. Photon-counting resonance fluorescence on the $S_{1/2}(F=1) \leftrightarrow P_{1/2}(F=0)$ transition at 369 nm serves for state-selective detection with efficiency $>98\%$. Optical pumping into the $|F = 1, m_F = \pm1\rangle$ levels during a detection period is avoided when the $E$ vector of the linearly polarized light subtends $45°$ with the direction of the applied dc magnetic field. The light is usually detuned to the red side of the resonance line by a few MHz in order to laser-cool the ion. Cooling is achieved by simultaneously irradiating the ion with light from both laser sources and with microwave radiation (Fig. 1).

When exciting the electric quadrupole transition $S_{1/2} - D_{5/2}$ (Section VI.C), the Yb$^+$ ion may decay into the extremely long-lived $F_{7/2}$ state. Light generated by a tunable diode laser near 638 nm resonantly couples this state to the excited state $D[5/2]_{5/2}$ such that optical pumping is avoided. The time needed to repump the ion from the $F_{7/2}$ state to the $S_{1/2}$ state has been determined as a function of the intensity of the laser light near 638 nm (Riebe, 2000). It saturates at $\approx$ ms.

## B. Ground State Hyperfine Transition in $^{171}$Yb$^+$

The two hyperfine states of Yb$^+$, $|0\rangle$ and $|1\rangle$ are coupled by a resonant, linearly polarized microwave field coherently driving transitions on this resonance. In a semiclassical description of the magnetic dipole interaction between a microwave field travelling in the $y$-direction and the hyperfine states of $^{171}$Yb$^+$ the Hamiltonian reads

$$\begin{aligned} H &= \frac{\hbar}{2}\omega_0\sigma_z - \vec{\mu} \cdot \vec{B} \\ &= \frac{\hbar}{2}\omega_0\sigma_z + \frac{\hbar}{2}\gamma B_x \cos(ky - \omega t + \phi')\sigma_x \end{aligned} \qquad (2)$$

where $\vec{\mu}$ is the magnetic dipole operator of the ion, $\vec{B} = (B_x \times \cos(ky - \omega t + \phi'), 0, 0)^T$ is the magnetic field associated with the microwave radiation, and $\gamma$ is the gyromagnetic ratio. The initial phase of the mw field, $\phi = ky + \phi'$ at the location of the ion is set to zero in what follows. Transforming this Hamiltonian according to $\tilde{H} = \exp(i(\omega/2)t\sigma_z)H \times \exp(-i(\omega/2)t\sigma_z)$, and invoking the rotating wave approximation yields the time evolution operator

$$U(t) = \exp\left[-\frac{i}{2}t(\delta\sigma_z + \Omega\sigma_x)\right] \tag{3}$$

governing the dynamics of the two-state system. The detuning $\delta \equiv \omega_0 - \omega$, the Rabi frequency is denoted by $\Omega = \gamma B_x/2$, and $\sigma_{z,x}$ represent the usual Pauli matrices. If the ion is initially prepared in state $|0\rangle$, then the probability to find it in state $|1\rangle$ after time $t$ is

$$P_1(t) = \left(\frac{\Omega}{\Omega_R}\right)^2 \sin^2\left(\frac{\Omega_R}{2}t\right) \tag{4}$$

where $\Omega_R \equiv \sqrt{\Omega^2 + \delta^2}$. A pure state $|\theta, \phi\rangle = \cos(\theta/2)|0\rangle + \sin(\theta/2)e^{i\phi}|1\rangle$ represented by a unit vector in 3D configuration space (Bloch vector) is prepared by driving the hyperfine doublet with mw pulses with appropriately chosen detuning $\delta \equiv \omega_0 - \omega$, and duration $t_{mw} = \theta/\Omega$, and by allowing for free precession for a prescribed time $t_p = \phi/\delta$.

The vertical bars in Fig. 2 indicate the experimentally determined excitation probability of state $|1\rangle$ (single $^{171}$Yb$^+$ ion) as a function of the mw pulse length $t_{mw}$; the solid line is a fit using Eq. 4 (Rabi oscillations). The observed Rabi oscillations are free of decoherence over experimentally relevant timescales. However, the contrast of the oscillations is below unity, since the initial state $|0\rangle$ was prepared with probability 0.89. This limitation will be addressed in future experiments. Figure 3 displays data from a Ramsey-type experiment (Ramsey, 1956) where the ion undergoes free precession for time $t_p$ between two subsequent mw pulses. This experimental signal, too, is essentially free of decoherence, and the contrast of the Ramsey fringes is only limited by the finite preparation efficiency. The data in Figs. 2 and 3 show that single-qubit operations are carried out with high precision, an important prerequisite for scalable quantum computing.
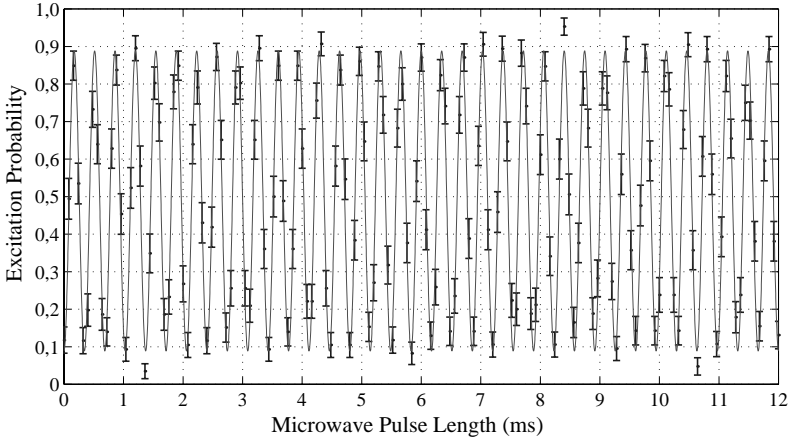
FIG. 2. Rabi oscillations: Excitation probability of state $|1\rangle \equiv |S_{1/2} F = 0, m_F = 0\rangle$ of a single $Yb^+$ ion averaged over 85 preparation–detection cycles as a function of mw pulse length $t_{mw}$. The solid line results from a fit using Eq. 4 giving $\Omega_R = 2.9165 \times 2\pi$ kHz. The error bars indicate one standard deviation of the statistical error resulting from the finite number of preparation–detection cycles. The sub-unity contrast of the signal is due to imperfect initial state preparation by optical pumping (which will be improved in future experiments).
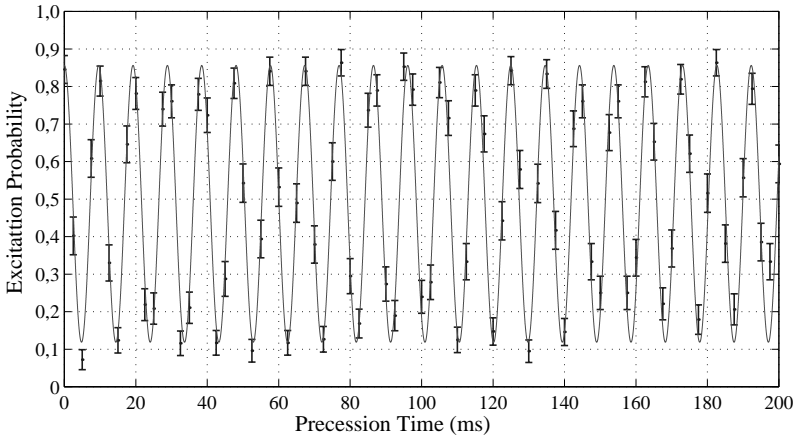


FIG. 3. Data from a Ramsey-type experiment where the ion undergoes free precession between two subsequent mw pulses (detuning $\delta = 103.9 \times 2\pi$ Hz, averaged over 100 realizations). The error bars are of statistical origin. This experimental signal, too, is essentially free of decoherence and the contrast of the so-called Ramsey fringes is only limited by the finite preparation efficiency. The data displayed in Fig. 2 and in this figure show that single-qubit operations are carried out with high precision, an important prerequisite for scalable quantum computing.

# III. Elements of Quantum Measurements

A. MEASUREMENTS AND DECOHERENCE

In what follows, we consider the process of performing a measurement on a quantum system. We start by considering the interaction between the quantum system to be measured and a second system, the quantum probe, assuming that pure states of both are prepared before an interaction between the two takes place. Initially, the state of the (unknown) quantum system $|\psi_i\rangle = \sum_n c_n|n\rangle$ ($|n\rangle$ are the eigenstates of the system Hamiltonian with complex coefficients $c_n$) and of the (known) state of the quantum probe $|\phi_i\rangle$ factorizes, that is we have $|\psi_i\rangle \otimes |\phi_i\rangle$. The interaction between system and probe is assumed to be governed by a Hamiltonian of the form (Giulini *et al.*, 1996, Chapter 3)

$$H_{\text{int}} = \sum_n |n\rangle\langle n| \otimes \hat{A}_n \tag{5}$$

where $\hat{A}_n$ are operators acting only in the Hilbert space of the probe. They transform the probe conditioned on the state of the quantum system. If $|\psi_i\rangle = |n\rangle$, then, after the interaction has taken place the combined state of system and probe reads

$$|n\rangle|\phi_i\rangle \xrightarrow{H_{\text{int}}} |n\rangle|\phi_n\rangle. \tag{6}$$

For the sake of a clearer discussion in the following paragraphs we assume that $\langle\phi_k|\phi_l\rangle = \delta_{kl}$. In general, if the quantum system is initially prepared in a superposition state, the first step of the measurement will result in an entangled state between system and probe

$$|\psi_i\rangle|\phi_i\rangle = \sum_n c_n|n\rangle|\phi_i\rangle \xrightarrow{H_{\text{int}}} \sum_n c_n|n\rangle|\phi_n\rangle. \tag{7}$$

Thus, if the quantum system initially is in a superposition of states, then linearity of quantum mechanics demands the probe, too, to be in a superposition of its states.

There is no *a priori* reason not to apply quantum mechanics, and, in particular the above treatment, to objects used as a probe that are made up of a large number of elementary constituents each of which is perfectly described by quantum mechanics. E. Schrödinger (Schrödinger, 1935) illustrated how quantum theory, if applied to macroscopic objects, may lead to predictions that are not in agreement with our observations. He imagined

a cat coupled to an individual quantum system that may exist in a superposition of states, say $|e\rangle$ and $|g\rangle$. The apparatus is constructed such that if the quantum system is in $|e\rangle$, the cat remains untouched, whereas state $|g\rangle$ means the cat will be killed by an intricate mechanism. The formal quantum mechanical description of this situation leads to the conclusion that the cat is in a superposition state of being dead and being alive, once the quantum system assumes a superposition state.

If the cat is replaced by an apparatus that is used to measure the state of the quantum system, one immediately sees that Schrödinger's gedanken experiment illustrates part of the measurement problem in quantum mechanics: Why does a macroscopic probe correlated to the quantum system's state not exist in a superposition of its possible states, but instead always assumes one *or* the other?

The Kopenhagen interpretation solves this contradiction between quantum mechanical predictions and actual observations by postulating that quantum mechanics does not apply to a classical apparatus. Following this interpretation there exists a border beyond which quantum mechanics is no longer valid. This, of course, provokes the questions where exactly this borderline should be drawn and what parameter(s) have to be changed in order to turn a given quantum system into a classical device.

The mathematical counterpart of this view was formulated by von Neumann: he postulated two possible time evolutions in quantum mechanics (von Neumann, 1932): One is the unitary time evolution that a quantum system undergoes according to Schrödinger's equation in absence of any attempt to perform a measurement (von Neumann's "zweiter Eingriff" or "second intervention"). This evolution is reversible. The other process is the irreversible quasi instantaneous time evolution when a measurement on the system is performed. It leads to a projection of the wave function on one of the eigenfunctions of the measured observable (called the "first intervention" by von Neumann).

The theory of decoherence (Zurch, 1991; Giulini *et al.*, 1996) answers the question how a *superposition* of a quantum system in the course of a measurement is reduced to a state described by a local diagonal density matrix (after tracing out the probe degrees of freedom), a mathematical entity describing possible alternative outcomes, but not a superposition of states. We will consider this approach in more detail in the following paragraphs.

A cavity-QED experiment similar to the gedanken experiment envisioned by Schrödinger is realized by first preparing a Rydberg atom in a super-position of two internal energy eigenstates $|e\rangle$ and $|g\rangle$ (Brune *et al.* (1996)). Then, this quantum system is sent through a cavity containing an electromagnetic field in a Glauber state (coherent state corresponding to the cat in the gedankan experiment), $|\alpha\rangle$ whose phase is changed by

dispersive interaction (no energy exchange takes place between atom and field) depending on the state of the atom. The combined atom–field state after the interaction reads

$$|\Psi\rangle_{\text{atom, cav}} = 1/\sqrt{2}(|e\rangle|\alpha e^{i\varphi}\rangle_C + |g\rangle|\alpha e^{-i\varphi}\rangle_C). \qquad (8)$$

The decay of this coherent superposition of probe states correlated with a quantum system (Rydberg atom) toward a statistical mixture was indeed experimentally observed and quantitatively compared with theoretical predictions (Brune *et al.*, 1996). It could be shown that the decay of the superposition becomes faster with increasing distinguishability of the two probe states involved in the measurement of the quantum system.

This decay from a superposition toward a statistical mixture is monitored by sending a second atom through the cavity (a time $\tau$ after the first atom) and detecting this second atom's state after it has interacted dispersively with the cavity field. The analysis of the correlations between the first and second atom's measurement results then reveals to what degree the off-diagonal elements of the density matrix (the coherences, created through the interaction with the first atom) describing the cavity field have decayed at time $\tau$ when the second atom was passing through the cavity (Maitre *et al.*, 1997).

(Gedanken) experiments on quantum complementary, too, have dealt with the influence of correlations and measurements on an observed system. As an example we consider first the diffraction of electrons when passing through a double slit resulting in an interference pattern on a screen mounted behind the double slit (Feynman *et al.*, 1965; Messiah, 1976). Any attempt to determine the path the electrons have taken, that is through which slit they passed, destroys the interference pattern. This can be explained by showing that the act of position measurement imposes an uncontrollable momentum kick on the electrons in accordance with Heisenberg's uncertainty principle (Bohr, 1949; reprinted in Bohr, 1983). This is to be regarded as a local physical interaction (Knight, 1998).

In Scully *et al.* (1991) it is shown by means of a gedanken experiment, without making use of the uncertainty principle, that the loss of interference may be caused by a nonlocal correlation of a welcher weg detector with the observed system: An atomic beam is detected on a screen after it has passed through a double slit. After having passed the double slit, the wave function describing the center-of-mass (COM) motion of the atoms is

$$\Psi(\vec{r}) = \frac{1}{\sqrt{2}}\left(\psi_1(\vec{r}) + \psi_2(\vec{r})\right) \qquad (9)$$

where the subscripts 1 and 2 refer to the two slits. The probability to detect an atom at location $\vec{R}$ on the screen is then given by

$$\left|\Psi(\vec{R})\right|^2 = \frac{1}{2}|\psi_1(\vec{R})|^2 + |\psi_2(\vec{R})|^2 + \psi_1^*\psi_2 + \psi_2^*\psi_1 \qquad (10)$$

where the last two terms are responsible for the appearance of interference fringes on the screen.

Now an empty (vacuum state) micromaser cavity is placed in front of each slit and the atoms are brought into an excited internal state, $|e\rangle$, before they reach one of the cavities. The interaction between atom and cavity is adjusted such that upon passing through a cavity an atom will emit a photon in the cavity and return to its lower state, $|g\rangle$. Consequently, the combined state of atomic COM wave function and cavity field is now an entangled one and reads

$$\Psi(\vec{r}) = \frac{1}{\sqrt{2}} \left( \psi_1(\vec{r})|1\rangle_1|0\rangle_2 + \psi_2(\vec{r})|0\rangle_1|1\rangle_2 \right). \qquad (11)$$

Here, the state ket representing a cavity field is labeled with the number of photons present in the cavity, and the subscripts indicate in front of which slit the respective cavity is placed. Calculating again the probability distribution on the screen now gives

$$\left|\Psi(\vec{R})\right|^2 = \frac{1}{2}|\psi_1(\vec{R})|^2 + |\psi_2(\vec{R})|^2 + \psi_1^*\psi_2\langle1|0\rangle_1\langle0|1\rangle_2 + \psi_2^*\psi_1\langle0|1\rangle_1\langle1|0\rangle_2.$$
$$(12)$$

The two last terms responsible for the appearance of interference fringes disappear, since the cavity states are orthogonal, and with them the interference pattern on the screen. It is emphasized in Scully *et al.* (1991) that the welcher weg detector functions without recoil on the atoms and negligible change of the spatial wave function of the atoms. The atoms, after having interacted with the welcher weg detector behave like a statistical ensemble, and the loss of the atomic spatial coherences is due to the nonlocal correlation of the atom with the detector. Such a correlation is generally produced in every welcher weg scheme, but its effect of suppressing interference is often covered by local physical back action on the observed quantum object (Dürr *et al.*, 1998).

The ability of the atomic COM wave function to display interference can be restored in this gedanken experiment by erasing the welcher weg

information (Scully *et al.*, 1991, and references therein; Scully and Walther, 1998). However, the interference is regained only, if the detection events due to atoms arriving at the screen are sorted according to the final state of the device used to erase the Welcher Weg information (a detector for the photons in this gedanken experiment). Experiments along these lines have demonstrated such quantum erasers (Kwiat *et al.*, 1992; Chapman *et al.*, 1995; Herzog *et al.*, 1995).

Here, we have considered the extreme case that complete information on the atoms path is available and the interference disappears completely. A general quantitative relation between the amount of welcher weg information stored in a detector and the visibility of interference fringes has been given in Englert (1996). In order to verify this relation, a welcher weg experiment using an atom interferometer was carried out and is described in Dürr *et al.* (1998a,b). In that experiment the amount of information stored in the detector and the contrast of interference fringes were determined independently.

The first part of the cavity-QED experiment described by Brune *et al.* (1996) (that is, before the second atom is sent through the cavity) can be interpreted as an atom interferometer with a welcher weg detector in one of the arms of the interferometer (compare also Gerry, 1996): Before the atom enters the cavity a coherent superposition of its energy eigenstates $1/\sqrt{2}(|e\rangle + |g\rangle)$ is prepared by applying a $\pi/2$-pulse to the atom. The analogy with an optical Mach–Zehnder interferometer where a photon is sent along one of two possible paths after the first beam splitter (in a classical view) is manifest in the fact that the atom may cross the cavity either in state $|e\rangle$ or state $|g\rangle$ (again classically speaking). After the atom has passed through the cavity, a second $\pi/2$-pulse is applied corresponding to the second beam splitter (or combiner) in an optical interferometer.

Placing a photodetector in one of the arms of the Mach–Zehnder interferometer would reveal information on which path the photon took. Here, the coherent field in the cavity that undergoes a phase shift correlated to the atom's state acts as a welcher weg detector. The cavity field does not act as a "digital" detector indicating the state of the atom with certainty. Instead, the two coherent field components correlated with the two atomic states may have some overlap (i.e., $\langle \alpha e^{i\varphi} | \alpha e^{-i\varphi} \rangle \neq 0$) such that they cannot be distinguished with certainty. Consequently, the correct state of the atom could only be inferred with probability below unity, if a measurement of the cavity field were performed. Therefore, the interference fringes do not completely disappear, but instead a reduced contrast of the fringes is observed (Fig. 3 in Brune *et al.*, 1996).

After the welcher weg detector (the field in the cavity-QED experiment) and the atom have become entangled, the atom's capability to display

interference vanishes. If only the atom is considered, that is, only one part of the entangled entities quantum system and quantum probe, then it appears as if the atom had been reduced to a statistical mixture of states as opposed to a coherent superposition. This is evident when considering the reduced density matrix of the atom obtained by "tracing out" the probe degrees of freedom. By applying a suitable global operation on probe and the atom together, the capability of the atomic states to show interference can be restored. This has been demonstrated in a different experiment where the Welcher Weg information is encoded in the photon number instead of the phase of the field (Bertet *et al.*, 2001). Thus, the reversibility of the interaction of system and probe is demonstrated.

The quantum probe itself – in the experiment described in Brune *et al.* (1996) represented by the mesoscopic cavity field initially prepared in a superposition of two states by the interaction with the atom – eventually undergoes decoherence: photons escaping from the resonator into the environment lead to entanglement between the atom, cavity field, and the previously empty, but now occupied "free space" modes of the electromagnetic field. Finally, this process results in a local diagonal density matrix (after tracing out the "free" field modes) describing a statistical mixture of the state of the atom (system) *and* the cavity field (probe). That is, the outcome of any subsequent manipulation of only the atom and/or cavity field will be characterized by the initial absence (before this further manipulation takes place) of coherent superpositions.

This argument can, of course, be extended further, including into the description also the environment with which the photons escaping from the cavity may eventually interact. Taking this argument consecutively further, always leaves behind some entities (the atom, cavity field, "free" field, ...) that will behave as statistical mixtures, if the next entity is not included in the theoretical description and further experiments. In practical experiments it seems impossible to include the whole chain of entities in further manipulations. Therefore, for all practical purposes, the correlation established between system, probe, and environment irreversibly destroys the system's and probe's superposition state. For a macroscopic environment (e.g., a measurement apparatus) this reduction to a statistical mixture occurs quasi-instantaneously (Giulini *et al.*, 1996).

In the considerations to follow, we divide the measurement apparatus, used to extract information about the state of a quantum system, into a quantum probe that interacts with the observed quantum system and a macroscopic device (called "apparatus" henceforth) coupled to the probe and yielding macroscopically distinct read-outs. The measurement process is then formally composed of two stages (von Neumann, 1932; Braginsky and Khalili, 1992; Alter and Yamamoto, 2001). First a unitary interaction

between quantum probe and the quantum system takes place. Then the quantum probe is coupled to the apparatus that indicates the state of the probe by assuming macroscopically distinct states (e.g., pointer positions.) The "environment" in the cavity-QED experiment described above takes on only part of the role of the apparatus: in principle, information about the probe's state is available in the environment after a time determined by the decay constant of the cavity field. However, it will be difficult for an experimenter to extract this information by translating it into distinct read-outs of a macroscopic meter.

## B. Measurements on Individual Quantum Systems

The theory of decoherence explains the appearance of local alternatives with certain statistical weights instead of coherent superpositions in quantum mechanical measurements. But it does not give an indication of which eigenstate the probe (and consequently the system) will be reduced to as the final result of the measurement. The density matrix describing system and probe, according to decoherence theory, becomes diagonal as a result of the interaction with the apparatus, but, in general, still has more than one diagonal element larger than zero. This will be a valid description, if after a measurement has been performed on an *ensemble* of quantum systems, further manipulations of this ensemble are carried out. However, such a density matrix is not in agreement with the experimental observation that after a measurement has taken place on an *individual* quantum system, and a particular eigenvalue of the measured observable has been obtained, subsequent measurements again yield the same result. After such a measurement, the state of this single quantum system has to be described by the density operator $\rho = |n\rangle\langle n|$ of a pure state, that is all diagonal elements vanish except one. Decoherence cannot explain or predict what particular outcome a given measurement on an individual quantum system has (i.e., which diagonal element becomes unity). The measurement of a single quantum system corresponds to a projection of the system's (and probe's) wave function on a particular eigenstate $|n\rangle$ ($|\phi_n\rangle$) in accord with von Neumann's first intervention (the projection postulate).

According to the projection postulate, the wave function of the object collapses into an eigenfunction of the measured observable due to the interaction between the measurement apparatus and the measured quantum object. The result of the measurement will be the corresponding eigenvalue. One could suspect that the statistical character of the measurement process described by the projection postulate is due to incomplete knowledge of the quantum state of the measurement apparatus. However, von Neumann

showed that the measurement process remains stochastic even if the state of the measurement apparatus were known (Chapter VI.C in von Neumann, 1932). We have seen that decoherence can account for the quasi-instantaneous disappearance of superpositions and the appearance of distinct measurement outcomes with certain probabilities, but not for the "choice" of a particular outcome of a measurement on an individual system (the projection postulate, too, does not explain this last point).

A quantum mechanical wave function can be determined experimentally from an ensemble experiment. Either a series of measurements is performed on identically prepared single systems, or a single measurement on an ensemble of identical systems is carried out (von Neumann, 1932; Raymer, 1997; Alter and Yamamoto, 2001). The wave function is interpreted as a probability amplitude that defines a probability density $P(a) = |\langle\psi|\psi\rangle|^2$, the distribution of possible results $a \in \mathbb{R}$ of measurements of an observable $\hat{A}$. The corresponding expectation value $\langle a\rangle = \langle\psi|\hat{A}|\psi\rangle$ defines the center position and the width $\langle(\Delta a)^2\rangle = \langle a^2\rangle - \langle a\rangle^2$ of the probability density. It is possible to determine *both* quantities in an *ensemble* measurement, and therefore to infer the quantum wave function up to a phase.

The expectation value might be estimated from

$$\langle a\rangle \approx \frac{1}{N}\sum_{n=1}^{N} a_n \tag{13}$$

where the $a_n$ are the results of local measurements on identically prepared independent quantum systems. In a similar way $\langle a^2\rangle$ and $\langle a\rangle^2$ can be determined, and thus $\langle(\Delta a)^2\rangle$. Though it is possible to determine an unknown quantum wave function from an ensemble measurement, it is impossible with a *single* quantum system, neither from a single measurement nor from a series of subsequent measurements. If $a_1$ is the result of a *single* measurement, the estimated expectation value $\langle a_s\rangle = a_1$, and in general $\langle a\rangle \neq \langle a_s\rangle$. The quantum uncertainty, $\langle(\Delta a)^2\rangle$ of the measured observable remains undetermined, since $\langle a_s^2\rangle = \langle a_s\rangle^2 = a_1^2$. Even if a *series* of measurements on the *same* single system is performed, it is not possible to infer the probability distribution $P(a)$. The results of $N$ subsequent measurements of $\hat{A}$ on a single system are not independent, and one will obtain the same eigenvalue $a_1 = a_2 = \cdots = a_N$ for every observation. The estimated expectation value will then again be $\langle a_s\rangle = \langle a_1\rangle = a_1$, and the variance $\langle\Delta a\rangle = 0$ (compare also Chapter 2 in Alter and Yamamoto, 2001).

In this sense, quantum mechanics is *not* an ergodic theory, in contrast to classical statistics where a series of measurements on a single system is equivalent to a single measurement on an ensemble of identical systems. Only if an observed single quantum system is identically prepared in

advance of every subsequent measurement, a series of measurements on a single quantum system is equivalent to a single measurement of an ensemble of quantum systems.

In general, it is not possible to predict the outcome of a measurement on an individual quantum system with certainty, even if complete knowledge of the initial quantum wave function is available. The obtained results are statistical, if the system is not initially prepared in an eigenstate of the observable being measured. On the other hand, if the initial state is an eigenstate, then the measurement is compatible to the preparation. Therefore, even a single measurement may yield *partial* information about the systems initial state. If an eigenvalue is obtained corresponding to a particular eigenstate $|n\rangle$, the observed system was initially not in an eigenstate $|n'\rangle$ orthogonal to the measured one.

So far, in the discussion of measurements on quantum systems we have not explicitly considered the case of negative result measurements (for a recent review see Whitaker, 2000). We will restrict the following discussion to quantum mechanical two-state systems for clarity. In some experimental situations (real or gedanken) the apparatus coupled to the quantum probe and quantum system, may respond (for example by a "click" or the deflection of a pointer) indicating one state of the measured system, or not respond at all indicating the other. Such measurements where the experimental result is the absence of a physical event rather than the occurrence of an event have been described, for instance, in Renninger (1960) and Dicke (1981). A negative-result measurement or observation leads to a collapse of the wave function *without* local physical interaction involved between measurement apparatus and observed quantum system. This will be discussed in more detail in the following paragraphs. In particular, the meaning of the concept "local physical interaction" is looked at in this context.

The situation described above is analogue to a gedanken experiment depicted in Chapter 3.3.2.3 in Giulini *et al.*, 1996. There, a Stern–Gerlach (SG) apparatus is considered that is oriented to yield at its exit spin-1/2 particles with their spin pointing either in the positive or negative $z$ direction. Particles with different spin directions propagate along spatially separate trajectories upon exiting the SG device (Fig. 4). A non-absorbing detector, $D_A$ is placed in only one of the exit "channels" A of the device SG such that it will register a particle passing through. If the particle takes the other channel B (corresponding to the orthogonal spin direction) then the detector $D_A$ does not respond. If for times greater than $t_A$ (the time needed for the particle to travel from the entrance of SG to $D_A$), $D_A$ has not indicated the passing through of a particle, and if an additional auxiliary detector $D_B$ were used in channel B, placed far away from SG and $D_A$
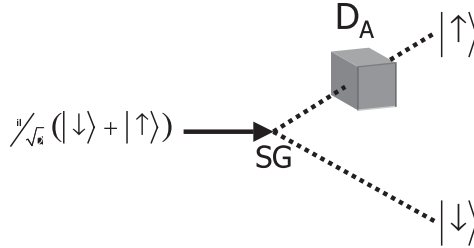
Fig. 4. Illustration of a negative result measurement using a Stern–Gerlach apparatus (SG) with a nonabsorbing detector ($D_A$) at one of its exits (see text).

(we take $t_B \gg t_A$), then this detector $D_B$ would register the particle with certainty at time $t_B$ after it was launched at the entrance of SG. Even though in this example, in a classical sense, the particle and the detector $D_A$ never interacted, since they are located in regions of space separated by a distance much larger than the deBroglie wavelength of the particle, the mere possibility for detection may change the behavior of the particle: a spin-1/2 at the entrance of SG initially prepared in a *superposition* of eigenstates of $\sigma_z$ is effectively reduced to an eigenstate of $\sigma_z$. In Giulini *et al.*, 1996 it is argued: "The claim that the particle did not interact at all with the detector [$D_A$] in the case of a spin-down result (detector $D_A$ does not "click") must be wrong, since a (superposition state) is different from an ensemble of *z*-up and *z*-down states." In this argument, the change of a quantum state is taken as a sufficient condition for "interaction" between the quantum system and some device (quantum or macroscopic). What is termed "interaction" in Giulini *et al.*, 1996, we consider as the consequence of a negative result measurement, a measurement not involving a local physical interaction between detector and system.

If detector $D_A$ did not respond (a negative-result measurement occurred) then the quantum state has nevertheless changed as described above: a coherent superposition is reduced not only to a statistical mixture, but to a definite state. In a classical sense, no interaction between the particle and the detector took place, since the particle is travelling along path B for $t > t_A$. This we consider the absence of *local* physical interaction. The Hamiltonian describing the quantum system (spin-1/2 after having passed through SG) and the detector ($D_A$) contains a term coupling the spin system to the detector $D_A$, *only* if the spin is in the *z*-up state, thus describing a conditional local physical interaction (which is absent if the spin is in *z*-down state). In general, a Hamiltonian determines eigenstates and -values, and fixes a range of *possible* measurement outcomes, some of which may be obtained without local physical interaction.

## IV. Impeded Quantum Evolution: the Quantum Zeno Effect

The nonlocal character of negative result measurements manifests itself in an effect that Misra and Sudarshan named "Zeno's paradox in quantum theory" (or "quantum Zeno effect") alluding to the paradoxes of the greek philosopher Zeno of Elea (born around 490 BC), who claimed that motion of classical objects is an illusion. Zeno illustrated his point of view with various examples one of which is the following: before an object can reach a point at a distance $d$ from its present location, it must have passed through the point at distance $d/2$. Carrying this argument further, it means that infinitely many points have to be passed in finite time before $d$ can be reached. Therefore motion is not possible according to this argument. Modern Mathematics resolves this apparent "paradox" making use of real numbers and convergent infinite series. In the quantum domain the notion "quantum Zeno effect" refers to the impediment or even suppression of the dynamical evolution of a quantum system by frequent measurements of the system's state (see, for instance, Khalfin, 1968; Fonda *et al.*, 1973; Misra and Sudarshan, 1977; Beige and Hegerfeldt, 1996; Home and Whitaker (1997)) and references therein, and also Chapter V.2 in von Neumann, 1932).

How does a quantum system behave, whose evolution in time is unitary, under repeated measurements separated by the time $\triangle t$? This will be considered for the case of ideal measurements, that is, the measurement is instantaneous and leaves the quantum system in an eigenstate of the observable being measured (Beige and Hegerfeldt, 1997). Let $|a\rangle$ be an eigenstate of observable $\hat{A}$, and $\hat{P}_a = |a\rangle\langle a|$ the corresponding projector. If a quantum system, initially prepared in state $|\psi(0)\rangle$, undergoes ideal measurements at times $t_1, t_2, \ldots$ with $\triangle t = t_i - t_{i-1}$ $(i = 1, 2, \ldots, N)$, then after $N$ successive measurements the system is found in state

$$|\psi(t_N, 0)\rangle = \hat{P}_a \hat{U}(t_N, t_{N-1}) \, \hat{P}_a \ldots \hat{P}_a \, \hat{U}(t_1, 0)|\psi(0)\rangle \tag{14}$$

where $\hat{U}(t_i, t_{i-1})$ denotes the unitary time evolution operator for the quantum system between two measurements. The probability to find the quantum system in the state $|a\rangle$ after $N$ ideal measurements is

$$P_a = |\langle a|\psi(t_n, 0)\rangle|^2 \tag{15}$$

$$= |\langle a|\hat{U}(t_1, 0)|\psi(0)\rangle|^2 \prod_{i=2}^{n} |\langle a|\hat{U}(t_i, t_{i-1})|a\rangle|^2, \tag{16}$$

and an expansion gives:

$$|\langle a|\hat{U}(t_i, t_{i-1})|a\rangle|^2 \simeq 1 - \triangle t^2 (\triangle \hat{H})^2 \tag{17}$$

If the time interval between subsequent measurements goes to zero, $\triangle t \to 0$, then $P_a$ tends to 1 and the survival probability becomes $P_a = |\langle a|\psi(0)\rangle|^2$. This simple argument shows that a quantum system initially in a state $|\psi_i\rangle$ turns into an eigenstate $|a\rangle$ under repeated ideal measurements for $\triangle t \to 0$ with probability $|\langle a|\psi(0)\rangle|^2$ (von Neumann, 1932). If $|\psi(0)\rangle = |a\rangle$, the system remains in $|a\rangle$ for $\triangle t \to 0$.

For short times the survival probability of the state will be proportional to $t^2$, and the decay rate of this state is proportional to $t$. In contrast, an exponential decay occurs with a constant rate, and a decay for time $t_1$, followed by an interruption (or measurement), followed by further decay for a time $t_2$ is equivalent to uninterrupted decay for a time $t_1 + t_2$ (Home and Whitaker (1997)).

A simple quantum system to demonstrate the quantum Zeno effect is a stable two-level system (states $|0\rangle$ and $|1\rangle$ with energy separation $\hbar\omega_0$) driven by a resonant harmonic perturbation. After unitary time evolution of duration $\triangle t$, the probability of finding the system in the initially prepared eigenstate, e.g. (the survival probability), $P_0 = \cos^2(\theta/2)$, where $\theta = \Omega \cdot \triangle t$, and $\Omega$ is the Rabi frequency. The corresponding transition probability $P_1 = \sin^2(\theta/2)$. For small time intervals $\triangle t$ the survival probability becomes

$$P_0 = \cos^2\left(\frac{\Omega \cdot \triangle t}{2}\right) \simeq 1 - \frac{\Omega^2 \triangle t^2}{4} \tag{18}$$

displaying the initial quadratic time dependence required for the quantum Zeno effect.

When an ideal measurement is carried out at the end of a period of evolution $\triangle t$, the quantum system is reset to one of its eigenstates. If during time evolution one performs $q$ successive ideal measurements a time $\triangle t$ apart, the survival probability to find the system in the initial eigenstate in measurement $q$ under the condition that it was found $q - 1$ times in this state before,

$$P_{00} = \cos^{2 \cdot q}(\theta/2) \ . \tag{19}$$
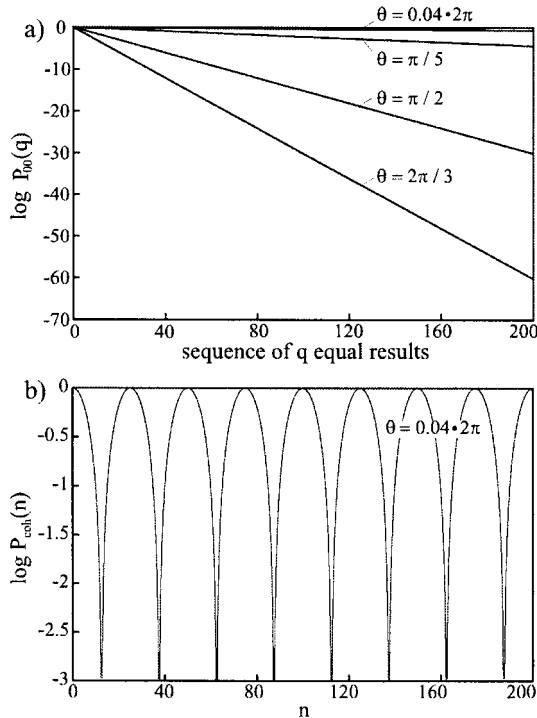
FIG. 5. (a) Probability, $P_{00}(q)$ to find a harmonically driven two-state system in the initially prepared state $|0\rangle$ in each one of $q$ successive measurements, resulting in uninterrupted sequences of $q$ equal results (for several nutation angles $\theta = \Omega\Delta t$). (b) *A priori* probability for the system to be in state $|0\rangle$ after time $n \cdot \Delta t$, if no measurements are performed.

In Fig. 5a $P_{00}$ is shown for several values of $\theta$. On the other hand, if no measurements were performed and the system evolve coherently, the (*a priori*) probability that the system is in the initial state after time $t = n \cdot \Delta t$ is $P_{coh}(n) = \cos^2(n \cdot \theta/2)$ (Fig. 5b).

In their original proposal of the quantum Zeno effect Misra and Sudarshan used the term "quantum Zeno paradox" for the case of "freezing" the system to a particular state by means of continuous observation of the systems unitary evolution (Misra and Sudarshan, 1977), while the term "quantum Zeno effect" was used to characterize its impediment (Peres, 1980; Pascazio and Namiki, 1994; Cook, 1998). Other authors distinguish between unitary evolution of the quantum system and exponential decay of an unstable system, and the suppression of the latter is regarded paradoxical (Block and Berman, 1991). In Home and Whitaker (1997) it is pointed out that the quantum Zeno effect is a quantum effect due

to the initial quadratic time dependence of quantum mechanical evolution. In contrast, a strictly exponential decay is a classical concept. In order for the quantum Zeno effect to take place when the system is characterized by an exponential decay, deviations from the exponential law at short times would be required (an initial quadratic time dependence). For unstable *quantum* systems these short time deviations were indeed predicted (Winter, 1961, Fonda *et al.*, 1978), and observed experimentally in the tunneling of atoms from a trapped state into the continuum (Wilkinson *et al.*, 1997). The use of the term quantum Zeno paradox to describe the inhibition of an exponential decay, therefore, seems inappropriate, since it requires the same initial time dependence to take place as in the unitary case.

What can be regarded as paradoxical about the quantum Zeno effect? In the comprehensive review by Home and Whitaker (1997), it is stressed that the paradoxical aspect is the retardation of evolution without any back action on the observed quantum system during the measurement process, as a consequence of negative result measurements. In the terminology used in this article this would correspond to the absence of local physical interaction in the course of a negative result measurement. The mere presence of the macroscopic measurement apparatus (like the detector $D_A$ in the Stern–Gerlach scheme discussed above) may affect the quantum system due to the nonlocal correlation between the two. Home and Whitaker (1997) suggest that a nonlocal negative result measurement on a microscopic system characterizes the quantum Zeno *paradox*.

It seems sensible to extend this definition of the quantum Zeno paradox to two more classes of measurements that are *not* of the negative-result type (Toschek and Wunderlich, 2001): (i) measurements free of back action (quantum nondemolition measurement (Braginsky and Khalili, 1992; Alter and Yamamoto, 2001), that in fact give rise to positive results, and (ii) measurements whose back action cannot account for the retarding effect. In both cases the local interaction (in connection with positive results) alone, cannot explain the change in the dynamics of the quantum system, and experiments that obey those criteria would show the quantum Zeno paradox.

In the theoretical considerations at the beginning of this section state vectors have been used, that is, the behavior of individual quantum systems was investigated. Why is it necessary to carry out experiments on the quantum Zeno paradox with individual quantum systems? Important work related to this question is found, for instance, in Spiller (1994), Nakazato *et al.* (1996), Alter and Yamamoto (1997), Wawer *et al.* (1998). The next paragraphs will be concerned with some aspects connected to this question. A more detailed discussion, concerning in particular experiments

with trapped ions, is given in Toschek and Wunderlich (2001) and Wunderlich *et al.* (2001).

The original formulation of the quantum Zeno effect considered the probability for the observed system to stay in its initial state throughout the time interval during which measurements are made. It has been pointed out (Nakazato *et al.*, 1996) that in ensemble measurements it is not possible to record this probability, unless different subensembles are chosen for each measurement, conditioned on previous measurement results. In usual ensemble experiments only the *net* probability of making or not making a transition from 0 to 1 *after* a series of *N* measurements is recorded and calculated to interpret the experiment. Experiments with single quantum system permit to record each individual measurement result and thus to select sequences of results where the system remained in its initial state.

Furthermore, by making a series of measurements on an ensemble of identically prepared quantum systems the effect of the measurement on the quantum systems' evolution cannot be distinguished from mere dephasing of the members of the ensemble (Spiller, 1994). (For example, collisions between atoms lead to dephasing of the atoms' wave functions.) Both processes lead to the destruction of coherences (off-diagonal elements of the density matrix) and give rise to identical dynamical behavior when the quantum system, after the measurement has been performed or dephasing has set in, will be subjected to subsequent manipulations. When investigating the quantum Zeno paradox we are interested in the change in the system's dynamics conditioned on the outcome of the measurement, in particular of negative-result measurements. Since dephasing of an ensemble as described above might occur *independently* of the measurement results, the question whether and how a series of particular measurement results is correlated with, and influences the quantum system's dynamics cannot be answered by an ensemble experiment. One might argue that dephasing *is* a measurement no matter how it comes about. During the process where the wave functions of the members of an otherwise isolated ensemble loose their initial phase relation via some mutual interaction (they have been identically prepared initially) correlations are established between members of this ensemble. This, however, does not establish a measurement of the initial state of the quantum systems.

In accordance with the discussion in Section III, the following condition is taken as a necessary one to constitute a measurement: some correlation is established between the quantum system (or an ensemble of quantum systems) and the "outside world" (not described by the elements of the Hilbert space(s) of the quantum system(s) under investigation). This could be an apparatus that assumes classically distinct states correlated to the quantum system's state.

A. Experiments

An experiment with several thousand $Be^+$ ions stored in an electromagnetic trap (Itano *et al.*, 1990, 1991) (based on a proposal by Cook for a single ion (Cook, 1988)) indeed shows the reduction of the transition probability between coherently driven hyperfine states (here, we label them $|0\rangle$ and $|1\rangle$) when the ions' state was frequently probed. Probing the ions' state is achieved by irradiating them with light resonantly coupling one of the hyperfine states to a third level $|2\rangle$ such that scattering of light occurs, if and only if an ion occupies, say state $|0\rangle$.

After initial preparation of the ions in $|0\rangle$, they are driven by a microwave $\pi$-pulse inverting the population of the hyperfine states. To investigate the effect of repeated measurements on the transition probability between states $|0\rangle$ and $|1\rangle$, the sample of ions is irradiated, during the driving pulse, by $N$ resonant probe light pulses. At the end of the microwave pulse the population of state $|0\rangle$ is measured by again applying a probe pulse and detecting scattered light. The outcome of the experiment shows a reduction of the observed transition probability in agreement with the predicted *net* transition probability

$$P_{e1}(T) = \frac{1}{2}[1 - \cos^N(\theta/N)] \qquad (20)$$

where $\theta = \pi$, and $T$ is the duration of the microwave pulse. The index $e1$ indicates that the ions in this ensemble experiment are found in state $|1\rangle$ irrespective of the results of intermediate probing (taking place between initial preparation and final probing $N$). The corresponding survival probability $P_{e0} = 1 - P_{e1}$. The theoretical transition probability is derived from a quantum mechanical model taking into account the probe light pulses that leave the population of states $|0\rangle$ and $|1\rangle$ unchanged and just set the coherences to zero (Itano *et al.*, 1990).

The inhibition of the quantum system's evolution was considered to be a consequence of measurements (light scattering) frequently projecting the ions back to their initial state. In Frerichs and Schenzle (1991), calculations of the dynamics of such a three level system are reported. It is deemed not necessary to invoke the notion of measurement together with state reduction to explain that the quantum system's evolution was impeded in the experiment. Instead, the retardation of the 2-state system's evolution is interpreted as a dynamical effect that can be explained when the third level is included in the quantum mechanical description (Block and Berman, 1991; Frerichs and Schenzle, 1991; Gagen and Milburn, 1993). Indeed, good agreement is found with experimental data gathered from the ensemble of

Be$^+$ ions. This is not so surprising, since the results of the experiment are expectation values of an ensemble of ions, and one would not expect quantum mechanics to fail in predicting the correct ensemble average. Each measurement leads to a diagonal density matrix describing the ions ($\rho_{00} \neq 0 \neq \rho_{11}$), however, with *both* diagonal elements different from zero. However the paradoxical aspect of quantum mechanics, and in particular of quantum Zeno, comes into focus when the eigenvalue of every single system as a result of a measurement is revealed.

Both state reduction and Bloch equations may lead to identical results when measurements on an ensemble are performed. This has been shown in Power and Knight (1996) and Beige and Hegerfeldt (1996) where the ensemble quantum Zeno experiment with Be$^+$ ions is simulated using quantum jump techniques in order to test whether the projection postulate is applicable to describe the observed results. It is pointed out that for an ensemble, the quantum trajectories produced by the quantum jump approach reproduce the density matrix probabilities resulting from the Bloch equations. In the latter model the decay of the coherences is due to coupling of the driven transition to the strong monitor transition (Frerichs and Schenzle, 1991; Power and Knight, 1996). Therefore, to understand the ensemble-averaged relaxation, it is not necessary to refer to state reduction. In Beige and Hegerfeldt (1996) it is suggested that under particular conditions (that were fulfilled in the experiment) the projection postulate is a useful tool that gives the right results. On the other hand, in Power and Knight (1996) it is pointed out that the Bloch equations do not hold for the description of the quantum Zeno effect with a *single* ion, since one of the diagonal elements of the density matrix disappears whereas in an ensemble, in general, both diagonal elements assume nonzero values.

Another aspect (connected to the above argument) to mention is that in the Be$^+$ experiment only the net transition probability at the end of the microwave pulse is recorded. Intermediate back-and-forth transitions between states $|0\rangle$ and $|1\rangle$ of individual members of the ensemble, as well as correlated transitions of ions, could not be detected. In Nakazato *et al.* (1996) it is worked out that, if one takes into account the result of every intermediate measurement, the probability in Eq. 20 describes *not* the quantum Zeno effect of a two-level system, but includes these intermediate back-and-forth transitions, which means the system does not necessarily stay in the initial state. The correct description is the one in Eq. 19. Both Eqs. 20 and 19 imply that an ensemble (for $N \rightarrow \infty$ nonselective measurements) and a single quantum system ($q \rightarrow \infty$ selective measurements) are found in the initial state. However, for small $N$ ($q$), expression 20 and 19 yield markedly different results (Section IV.C.)

The experiment described in Kwiat *et al.* (1995) aimed at the demonstration of an optical version of the quantum Zeno effect. Based on a suggestion put forth in Elitzur and Vaidman (1993), the propagation of a photon in a sequence of Mach–Zehnder interferometers is restricted to only one arm of the interferometers due to interaction-free measurements. Even though the outcome of the experiment obeys the mathematics of the quantum Zeno effect, the physics seems different as pointed out in Home and Whitaker (1997) where it is argued that the result of this experiment is explicable, as far as the quantum Zeno effect is concerned, in terms of classical physics. A modification of this experiment shows the polarization rotation of photons to be impeded because of an interaction-free measurement within the Mach–Zehnder interferometer (Kwiat *et al.*, 1999). As in the previous experiment the mathematics of the quantum Zeno effect describes well the dynamical behavior of the system. According to the arguments in Home and Whitaker (1997) and Whitaker (2000), it appears that again the physics necessary for the quantum Zeno effect is not involved. An experiment that can be classically described gives equivalent results: the rotation of the polarization of light passing through an optically active substance is retarded by means of a sequence of polarization analyzers (Peres, 1980).

Recently an experiment was performed to demonstrate the quantum Zeno effect and the anti-Zeno effect in an unstable system (Fischer *et al.*, 2001). The anti-Zeno effect describes an acceleration of the decay of an unstable system under repeated observation (Kofman and Kurizki, 2000; Facchi *et al.*, 2001). As stated previously, the quantum Zeno effect may occur, if the short time evolution of the decay deviates from a purely exponential one (Winter, 1961; Fonda *et al.*, 1978; Wilkinson *et al.*, 1997). Reference (Fischer *et al.*, 2001) describes the decay via tunneling of an ensemble of atoms trapped in an optical potential created by a standing light wave. Acceleration of the standing wave leads to a deformed potential, thus admitting tunneling of some atoms out of the optical potential wells. The tunneling probability shows a marked deviation from exponential decay for short times that has its origin in the initial reversibility of the decay process. Tunneling is initiated by applying high acceleration to the atoms trapped in the standing wave for a time $t_{\text{tunnel}}$, and interrupted for time $t_{\text{interr}}$ during which the acceleration was low. The interruption of tunneling is considered a measurement of the number of atoms that remain trapped, since $t_{\text{interr}}$ is chosen such that the fraction of trapped atoms separate in momentum space from the atoms that have tunneled during $t_{\text{tunnel}}$. The insertion of periods of low acceleration indeed leads to a slower decay of the survival probability of trapped atoms. It seems that this experiment does not satisfy the criteria for the quantum Zeno paradox for

similar reasons as the experiment with an ensemble of Be$^+$ ions outlined above. The final measurement of the spatial distribution of all atoms yields an ensemble average in agreement with the unitary time evolution predicted by the Schrödinger equation. The intermediate measurement results (obtained after periods of low acceleration) were not recorded; even if this had been the case, back-and-forth transitions between trapped and free states of individual members of the ensemble during the initial period (reversible dynamics) would have gone unnoticed.

The discussed experiments appear not suitable to demonstrate the Quantum-Zeno-Effect, or rather the quantum Zeno paradox, for they do not address a key point that makes up the nature of the effect: the retardation of the evolution of a quantum system due to a (possibly nonlocal) correlation between the observed individual quantum system and the macroscopic measurement apparatus during the repeated measurement process. This correlation leads to an irreversible change in the system's wave function and is evident even in negative result measurements where its effect is not concealed by local physical interaction. The latter, too, may indeed affect the system's transition probability under the condition of an initial quadratic time dependence. However, such a change in the time evolution is necessary but not sufficient for the quantum Zeno effect.

## B. Quantum Zeno Experiment on an Optical Transition

An experiment with a single $^{172}$Yb$^+$ ion demonstrating the quantum Zeno effect will be outlined in what follows (Balzer *et al.*, 2000). The electronic states S$_{1/2} \equiv |0\rangle$ and D$_{5/2} \equiv |1\rangle$, connected via an optical electric quadrupole transition close to 411 nm, serve as a two-level quantum system. State $|0\rangle$ is probed by coupling it to state P$_{1/2}$ via a strong dipole transition and detecting resonance fluorescence close to 369 nm. The quadrupole transition $|0\rangle - |1\rangle$ was coherently driven using light emitted by a diode laser with emission bandwidth 30 Hz (in 2 ms). To demonstrate the retardation of quantum evolution, driving light pulses close to 411 nm alternated with probe pulses at 396 nm. The duration, $\Delta t$ and the Rabi-frequency, $\Omega$ of the driving pulse were set to fixed values, and the frequency of the light field was slightly detuned from exact resonance in order to vary the effective nutation angle $\theta_{\text{eff}} = \sqrt{\Omega^2 + \delta^2} \cdot \Delta t$. The intensity and the duration of the probe field were adjusted such that the observation of resonance fluorescence results in state reduction to state $|0\rangle$, while the absence of fluorescence results in state $|1\rangle$ with near-unity probability. *Each* outcome of probing was registered, and a complete record of the evolution of the single quantum system was acquired. Thus, a trajectory of "on" results (resonance

fluorescence was observed) and ''off'' (no fluorescence, i.e. negative) results is obtained. The statistical distribution of uninterrupted sequences of $q$ equal results was found in good agreement with $P_{00}(q-1) = U(q)/U(1)$ where $U(q)$ is the normalized number of sequences with $q$ equal results, and $U(1)$ denotes the probability for this result at the beginning of the sequence. This shows the impediment of the system's evolution under repeated measurements, and thus the quantum Zeno effect. A theoretical model taking into account spontaneous decay of the $D_{5/2}$ state fits well the recorded series of ''off'' events (negative-result measurements) as well as to the ''on'' events (positive-result measurements). It has been shown that the effect of the measurement on the ion's evolution is not intertwined with additional dephasing effects (Balzer *et al.*, 2000; Toschek and Wunderlich, 2001). The observed impediment of the driven evolution of the system's population is a consequence of the correlation between the observed quantum system and the macroscopic meter.

In this experiment the angle of nutation $\theta$ was not exactly predetermined. During the driving pulse, the system's population undergoes multiple Rabi oscillations giving an effective nutation angle $\theta_{\text{eff}} = \theta \mod 2\pi$ at the end of the interaction that varies in a small range due to not perfect experimental conditions. Therefore, the exact nutation angle was obtained from a fit of experimental data. The analysis of the experiment is further complicated by spontaneous decay from the relatively short-lived $D_{5/2}$ state (lifetime of 6 ms (Fawcett and Wilson, 1991)) into the $S_{1/2}$ ground state and the extremely long-lived $F_{7/2}$ state of $^{172}\text{Yb}^{+}$ (lifetime of about 10 years (Roberts *et al.*, 1997)). In addition, the relatively short time series recorded in this experiment may cause interpretational difficulties.

## C. Quantum Zeno Experiment on a Hyperfine Transition

In this section we describe an experiment with a single $^{171}\text{Yb}^{+}$ ion whose ground-state hyperfine states are used as the quantum system to be measured. Here, the quantum Zeno paradox is demonstrated avoiding the complications associated with relaxation processes and optical pumping as in the experiment described in the previous section (Balzer *et al.*, 2002). The hyperfine transition is free of spontaneous decay and the use of microwave radiation allows for the precise preparation of states with a desired mutation angle $\theta$. Sufficiently extensive data records ensure an unambiguous interpretation of these experiments.

A semiclassical treatment of the magnetic dipole interaction between microwave field and hyperfine states of $\text{Yb}^{+}$ in an interaction picture (and making the rotating wave approximation) yields the time evolution

operator $U(t) = \exp[-i/2t(\delta\sigma_z + \Omega\sigma_x)]$. (compare Section II). For $t > 0$ the ion evolves into a superposition state

$$|\psi\rangle_I = \cos\frac{\theta}{2}|0\rangle + \sin\frac{\theta}{2}e^{i\phi}|1\rangle, \tag{21}$$

and the probability, $P_1(t)$ to find the system in $|1\rangle$ is proportional to $t^2$ for small $t$. In the experiment the resonance condition $\omega_0 = \omega$ is fulfilled to good approximation, and after time $T = \pi/\Omega$ of unperturbed evolution, a measurement of the ion's state will reveal it to be in state $|1\rangle$ with close to unit probability.

### C.1. State-selective detection

The relevant energy levels of the $^{171}$Yb$^+$ ion are schematically shown in Fig. 1. Sufficiently long irradiating the ion with UV laser light will prepare the ion in the ground state $F=0$ by optical pumping. The occupation of the $F=1$ level (after interaction with the microwave field) is probed by irradiating the ion with light at 369 nm (UV laser light,) thus exciting resonance fluorescence on the electric dipole transition $S_{1/2}, F = 1 \leftrightarrow P_{1/2}$, and detecting scattered photons using a photomultiplier tube. An "on" result (scattered photons are registered) leaves the ion in state $|1\rangle$, otherwise the ion is in the $|0\rangle$ ("off" result; no photons are registered.)

While the UV light is turned on for detection of the ion's state, the ion may be viewed as a beam splitter for the incident light beam: Either the light is completely "transmitted", that is, the initially populated light mode (characterized by annihilation operator $b$) remains unchanged. This will occur with probability, $w_0$ close to unity, if the ion is in state $|0\rangle$ during the UV laser pulse (we take $w_0 = 1$ in what follows). Or, photons are scattered into some other mode $b' \neq b$ (that may be different for every scattered photon) if the ion resides in $|1\rangle$. The latter occurs with probability $w_1$ determined by the detuning relative to the $S_{1/2}, F = 1 \leftrightarrow P_{1/2}, F = 0$ resonance, intensity, and duration of the incident UV light. For a sufficiently long UV light pulse eventually a photon will be scattered into mode $b'$, and we may take $w_1 = 1$. After one photon has been scattered into mode $b'$, the ionic state correlated with this electromagnetic field mode $b'$ is $|1\rangle$. Thus, the correlation established between the state of the light field and the ion's state is

$$\begin{aligned} |0\rangle|b\rangle &\rightarrow |0\rangle|b\rangle \\ |1\rangle|b\rangle &\rightarrow |1\rangle|b'\rangle, \end{aligned} \tag{22}$$

and consequently

$$\alpha|0\rangle + \beta|1\rangle \rightarrow \alpha|0\rangle|b\rangle + \beta|1\rangle|b'\rangle \qquad (23)$$

In this (simplified) description $|b\rangle$ represents the em field in its initial mode, and $|b'\rangle$ stands for a different mode occupied by a single photon. Since the field states $|b\rangle$ and $|b'\rangle$ are orthogonal, the density matrix describing the ion's state (obtained by tracing over the field states) becomes diagonal, and coherences of the ion's states $|0\rangle$ and $|1\rangle$ that may have existed are no longer observable (Giulini *et al.*, 1996). The field carries information about the ion's state, thus destroying the ion's ability to display characteristics of a superposition state in subsequent manipulations it may be subjected to.

The scattered photon in mode $|b\rangle$ may be absorbed by the photo cathode of a photomultiplier tube leading, after several amplification stages, to the ejection of a large number of photo electrons from the surface of the last dynode of the photo multiplier. This current pulse strikes the anode of the multiplier and is further amplified and finally registered as a voltage pulse by a suitable counter. Thus, the ion's state is eventually correlated irreversibly with the macroscopic environment. The irreversible correlation will actually take place much earlier in the detection chain. Irreversibility here means it is not possible, or rather very improbable, to restore the photo cathode (which would include, for instance, the power supply connected to it) to its state before an electron was ejected in response to an impinging photon.

Does the finite detection efficiency for photons (only the small fraction of about $4 \times 10^{-3}$ of scattered photons are detected during an ''on'' event) influence the interpretation of and conclusions drawn from the experiment described here? In order to answer this question we look in some more detail at the process of correlation between the ion's state and the rest of the world.

After the first photon has been scattered from mode $b$ into an orthogonal mode $b'$, a correlation between the ion and its macroscopic environment has been established, even if this photon is not registered by the photomultiplier tube, but instead is absorbed, for instance, by the wall of the vacuum recipient housing the ion trap. Welcher weg information about the state of the ion is available, and the ion is left in a statistical mixture of states, corresponding to a density matrix with two diagonal elements different from zero (if one uses the density matrix formalism to describe an ensemble of such individual quantum systems). The quantum Zeno experiment described below shows that the correct description of the single ion's state after a measurement pulse is either $|0\rangle$ *or* $|1\rangle$ (corresponding to a density

matrix with only *one* diagonal element). One may wonder whether (after a single photon has been scattered and absorbed by a wall) the ion is already reduced to the $F = 1$ state, or, alternatively if it is necessary for the scattered photon to hit the photo detector and thus yield a macroscopically distinct read-out for this to happen.

The second alternative does not seem plausible, since it would mean that the macroscopic photo detector plays a distinctive role compared with other macroscopic entities, like the wall of the vacuum recipient. No matter where the photon is absorbed, the absorption will result in an irreversible correlation of the ion with its environment, thus destroying the ion's coherences. However, the absorption in the wall does not yield macroscopically distinct states in the sense that an observer could access the information on the ion's state stored in the post-absorption state of the wall (as opposed to the case when the photon hits the detector). Should the ion's state reduction (here to state $|1\rangle$) only happen if an apparatus yields distinct read-outs, then this would mean that the ion's dynamics depends on whether the photo detector is switched on or off during a sequence of $N$ measurements (which seems implausible). Such a sequence of measurements (only the last one of $N$ measurement results is actually registered) has not been performed experimentally with a single ion. One would assume that the ion's dynamics is not changed during such a sequence compared to one where all intermediate results are "amplified" to distinct read-outs (as was actually done, and is necessary to demonstrate the quantum Zeno effect). If this assumption is correct, then this together with the experimental results described below, implies that state reduction of the ion occurs independently of the information gain of any observer. In addition, it means that after one photon has been scattered by the ion, the ion is in state $|1\rangle$. Once it is in state $|1\rangle$, it will scatter many more photons during the detection interval (about $10^7\,\mathrm{s}^{-1}$), some of which will be registered by the photo detector. Therefore, if and only if the ion is in state $|1\rangle$, will a distinctive macroscopic read-out be obtained (resulting from photo detection) corresponding to this state. Similar reasoning shows that the absence of photo counts correlates with the ion being in state $|0\rangle$.

### C.2. Fractionated $\pi$-pulse

To demonstrate the quantum Zeno paradox we investigate the impediment of an induced transition by means of measurements, similar to the proposal in Cook (1988). First, an $^{171}\mathrm{Yb}^+$ ion is illuminated for 50 ms with UV light and thus prepared in state $|0\rangle$. The intensity, detuning, and duration of microwave radiation applied to the ion is adjusted such that a $\pi$-pulse results, inducing a transition to state $|1\rangle$. This is achieved, if subsequent
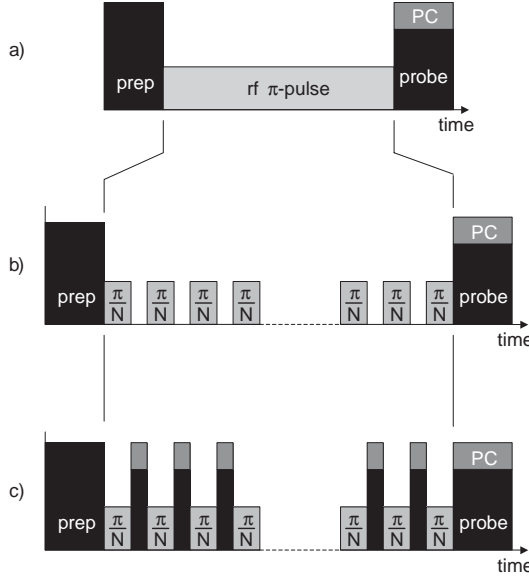
F<sub>IG</sub>. 6. (a) Excitation of the hyperfine transition in $^{171}$Yb$^+$ by applying a microwave $\pi$-pulse. (b) Fractionated $\pi$-pulse without intermediate probing, and (c) with intermediate probing using light at 369 nm and simultaneous detection of the scattered photons (PC: photon counter, prep: initial preparation by a light pulse at 369 nm).

probing using UV light invariably leads to registration of fluorescence yielding an "on" result (Fig. 6a). The duration of the $\pi$-pulse was 2.9 ms.

In order to separate the influence of the measurement pulses clearly from the driving field, the applied $\pi$-pulse is fractionated in $N$ pulses of equal area $\pi/N$ a time $\tau_{probe} = 3$ ms apart (Fig. 6b). The frequency of microwave radiation is carefully set to resonance with the ionic transition by means of Ramsey-type experiments (compare Section II). Thus, there is no dephasing between driving field and ion due to free precession during the intermissions, and the fractionated excitation will again result in a transition with nutation angle $N \times \pi/N$. Pulses of probe light are applied during the $N - 1$ "gaps" of duration $\tau_{probe}$, and the photon counter is gated open synchronously in order to register or not register scattered photons indicating the ions excitation to state $|1\rangle$ or survival in the initially prepared state $|0\rangle$, respectively (Fig. 6c.) The experimental succession of initial preparation in $|0\rangle$, applying $N$ microwave pulses and $N$ probe pulse is repeated $2000/N$ times.

The experiment is carried out for $N = 1, 2, 3, 4$, and 10. We are interested in those sequences where all $N$ measurements give a negative ("off") result, indicating the survival of the ion in its initially prepared state. The number
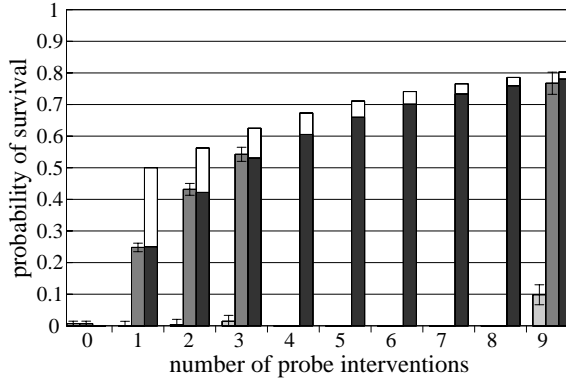
Fɪɢ. 7. Probability of survival in the initially prepared state versus the number, $N$–1 of probe interventions. The gray bars indicate the corrected (see text) measurement results which agree well with the calculated values of the survival probability $P_{00}$ (black bars). This demonstrates the quantum Zeno effect. The light gray bars give the survival probability when no measurement pulses are applied. The measured values differ significantly from the values of the probability $P_{e0}$ (white bars), that does not properly describe the quantum Zeno effect (see text).

of these sequences normalized by the total number of sequences is plotted in Fig. 7 versus the number of probe interventions (grey bars). The data shown in Fig. 7 have been corrected to account for the imperfect initial state preparation with an efficiency of 82%, as well as possible false detection of one of the $N$ results. The number of photo counts during a detection interval are Poisson distributed characterized by mean photon numbers of about 5 ("on" results) and 0.2 ("off" result), respectively. Since the two distributions overlap to some degree, wrong assignments may occur. To distinguish between "on" and "off" a fixed threshold is used. This threshold is chosen such that in less than 0.5% of the cases an "on" result is mistaken as "off". The error bars represent the variance of the binomial distribution of the number of recorded sequences of "on" and "off" results. In contrast to the proposal by Cook (1988) the result of each of $N$ measurements is registered. Therefore, it is possible to identify sequences of results that represent survival of the ion in the initially prepared state, $|0\rangle$ during the $N$ observations. The survival probability vanishes for $N=1$ and increases to 77% for $N=10$ showing that the evolution is impeded by frequent measurements.

The occurrence of sequences of $N$ equal results ("off") follows $P_{00}(N) = \cos^{2N}(\pi/2N)$, according to Eq. (19). This is different from the "net" probability $P_{e0}(N) = 1/2(1 + \cos^N(\pi/N))$ where intermediate

transitions between $|0\rangle$ and $|1\rangle$ are taken into account as discussed above. These two probabilities are significantly different for small values of $N$. The quantum Zeno paradox is evident in the correspondence of the experimental data in Fig. 7 with $P_{00}$.

In principle it is possible to analyze the recorded data by ignoring the results of the first $N-1$ probe interventions in each sequence. More specifically, one could extract from the data the probability for the ion to end up in state $|0\rangle$ after the $N$th measurement *irrespective* of its history. This probability would then be expected to agree with results from an ensemble experiment, provided no dephasing in the ensemble occurred. However, owing to the population accumulating in the Zeeman sublevels $|F = 1, m_F = \pm 1\rangle$ during an "on" detection interval, the upper state $|1\rangle$ may be decoupled by the probe light from the two-level system (Balzer *et al.*, 2002a): once an "on" result has been obtained, the ion may have made a transition to one of the Zeeman levels $|F = 1, m_F = \pm 1\rangle$ and is no longer affected by the subsequent microwave driving pulse. (This does not affect the determination of the survival probability in state $|0\rangle$.)

## C.3. Statistics of sequences of equal results

In the experiment described in the previous section, the quantum Zeno effect is manifest in the survival probability of the initially prepared state $|0\rangle$ growing with the number of intermediate measurements during the driving $\pi$-pulse. In other words, frequent measurements hinder the transition to state $|1\rangle$, in accordance with Cook's suggestion to demonstrate the quantum Zeno effect. However, to demonstrate the quantum Zeno effect, it is not necessary to employ a fractionated $\pi$-pulse. The retardation of the evolution of an initially prepared state will show up in a sequence of alternated driving and probing, too. We have recorded series of 10 000 pairs each consisting of a drive pulse and a probe pulse as shown in Fig. 8 (top) resulting in trajectories of alternating sequences of "on" and "off" results (Fig. 8, bottom). The normalized number of sequences of $q$ equal results, $U(q)$ corresponds, to good approximation, to the probability of survival in one of the eigenstates, $P_{00}$:

$$U(q)/U(1) = P_{00}(q-1) \,, \tag{24}$$

where $U(1)$ denotes the probability to find the ion in this state at the very beginning of sequence. $P_{00}$ is the conditional probability according to Eq. 19.

The statistical distributions of the "off" sequences, $P_{00}(q-1) = U(q)/U(1)$ is shown in Fig. 9 for the nutation angles $\theta = \pi, \pi/2, \pi/5$ and $\theta = 2\pi - 0.1$ (dashed lines). The duration of a microwave pulse that
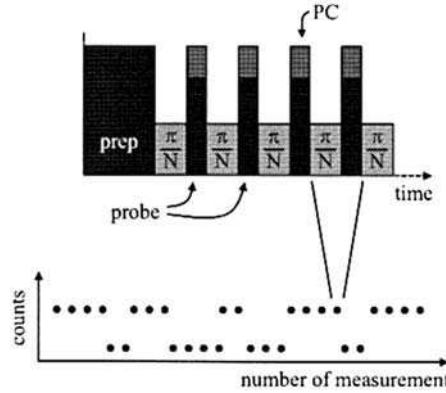
FIG. 8. Top: Measurement scheme of alternating excitation and detection. Bottom: Schematic of a trajectory of results.
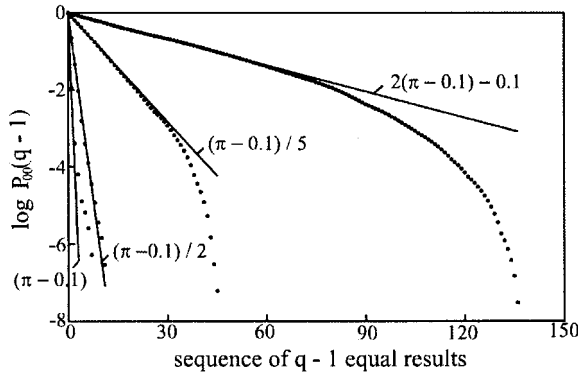


FIG. 9. Statistical distribution of "off" sequences, $P_{00}(q-1) = U(q)/U(1)$ versus $q-1$ (for different values of the nutation angle $\theta$ indicated in the figure). The correspondence of the measurement results (dots) with the survival probabilities $P_{00}(q-1)$ (solid lines) verifies the quantum Zeno effect. Deviations between measured and calculated values for large $q$ are due to the finite length of the experimental trajectories of measurement results.

corresponds to $\theta = 2\pi$ was set here to 4.9 ms. The interval of probing was 2 ms. The solid lines indicate the survival probabilities $P_{00}(q-1)$. A systematic deviation of 3% from the preset values of $\theta$ emerges from slightly varying the preset areas of the driving pulse while fitting $P_{00}$ to the data. For long sequences (large $q$), the data show strong deviations from the calculated survival probability. This is due to the finite length of the experimental trajectory.

Both experiments on the hyperfine transition of the $^{171}Yb+$-ion show clearly the quantum Zeno effect, the retardation of the evolution of an individual quantum system as a consequence of measurements. In particular, they demonstrate the quantum Zeno *paradox*, since the measurement results are of the negative-result type, indicating a correlation between the observed individual quantum system and the measurement apparatus without local physical interaction.

# V. Quantum State Estimation Using Adaptive Measurements

## A. INTRODUCTION

Determining an arbitrary state of a quantum system is a task of central importance in quantum physics, and in particular, in quantum information processing and communication where quantum mechanical 2-state systems (qubits) are elementary constituents. In order to gain complete knowledge about the state of a quantum system infinitely many measurements have to be performed on infinitely many identical copies of this quantum state. Naturally, the question arises how much information about a quantum state can be extracted using finite resources and what strategies are best suited for this purpose. A first indication of the appropriate operations to be carried out with two identically prepared qubits in order to gain maximal information about their state was given by Peres and Wootters (1991). It was strongly suggested that optimal information gain is achieved when a suitable measurement on both particles together is performed. The measure that served to quantify the gain of information in these theoretical considerations was the Shannon information.

The Shannon information (or entropy) $-\sum_n p_n \log_2 p_n$ (Shannon, 1948) is a measure for the uncertainty about the true value of some variable before a measurement of this variable takes place. The variable may take on $m$ different values with probability $p_n$, $n = 1 \ldots m$. Alternatively, the Shannon information can be viewed as giving a measure for the information that is gained by ascertaining the value of this variable. In Brukner and Zeilinger (2001) it is argued that this measure is not adequate in the quantum domain, since the state of a quantum system is not well defined prior to observation. Only if the quantum system is in an eigenstate before and after a measurement is performed, does the measurement indeed reveal a preexisting property. In general, however, this is deemed not the case in the quantum domain, and therefore, the Shannon information is not suitable as a measure for the uncertainty associated with an observable

before a measurement takes place. This statement may also be expressed in different words: In the quantum world not even the possible alternatives of measurement outcomes are fixed before a measurement is carried out. This fact is also at the core of the EPR program where quantum mechanics predicts nonclassical correlations between two particles (Einstein *et al.*, 1935). An alternative measure for the information content of a quantum system invariant under unitary transformations has been suggested in Brukner and Zeilinger (1999).

The suggestion in Peres and Wootters (1991) that the optimal measurement for determining a quantum state of two identically prepared particles needs to be carried out on both particles together, was proven in Massar and Popescu (1995). In more technical terms this means that the operator characterizing the measurement does not factorize into components that act in the Hilbert spaces of individual particles only. In Massar and Popescu (1995) it was also shown that the same is true when $N = 1, 2, 3, \ldots$ identically prepared qubits are available. The states to be estimated were drawn randomly from a uniform distribution over the Bloch sphere and the cost function that has been optimized was the fidelity $\cos^2(\theta/2)$ where $\theta$ is the angle between the actual and estimated directions. The optimal fidelity that can be reached is $(N + 1)/(N + 2)$. As a special case of optimal quantum state estimation of systems of arbitrary finite dimension the upper bound $(N + 1)/(N + 2)$ for the mean fidelity of an estimate of $N$ qubits was rederived in Derka *et al.* (1998). In addition, it was shown that *finite* positive operator valued measurements (POVMs) are sufficient for optimal state estimation. This result implied that an experimental realization of such measurements is feasible, at least *in principle*. Subsequently, optimal POVMs were derived to determine the pure state of a qubit with the *minimal* number of projectors when up to $N = 5$ copies of the unknown state are available (Latorre *et al.*, 1998). Still, the proposed optimal and minimal strategy requires the experimental implementation of rather intricate non-factorizing measurement operators. In addition, all $N$ qubits have to be available simultaneously for a measurement.

In Bužek *et al.* (1999, 2000) investigations are reported on how an arbitrary qubit state $|\psi\rangle$ can be turned into the state $|\psi^\perp\rangle$ orthogonal to the initial one. Such a quantum mechanical universal NOT (U-NOT) operation would correspond to the classical NOT gate that changes the value of a classical bit. It is shown that a U-NOT gate corresponds to an anti-unitary operation, and an ideal gate transforming an unknown quantum state into its orthogonal state does not exist. If a single qubit in a pure state is given and no *a priori* information on this state is available, then measuring the quantum state and using this information to prepare a state $|\psi^\perp\rangle$ gives

the optimal result. If $N$ qubits in state $|\psi\rangle$ are available, then too, the optimal U-NOT operation can be attained by estimating the initial quantum state using these $N$ qubits and subsequently preparing the desired state. Thus, the optimal fidelity $(N + 1)/(N + 2)$ for a U-NOT is reached which coincides with the optimal fidelity for state estimation.

Gill and Massar (2000) consider the problem of quantum state reconstruction when taking advantage of a large ensemble of identically prepared quantum states in a finite dimensional Hilbert space. For $N \to \infty$ any sensible measurement strategy yields a perfect estimate of a given quantum state, and since for large $N$ the estimate drawn from any strategy comes very close to the true value, the distinguishing feature between different strategies applied to large ensembles is the *rate* at which neighboring states can be distinguished. A quantitative measure for this rate is introduced and an upper bound for any type of estimation strategy is derived in Gill and Massar (2000). For the case of a 2-dimensional Hilbert space (qubits) an explicit measurement strategy for pure states is given attaining this upper bound when using separate measurements on each particle. It turned out that for mixed states this upper bound is also valid as long as measurements are carried out in a factorizing basis. However, if collective measurements are allowed for, then this bound is not necessarily valid. Therefore, mixed states exhibit nonlocality without entanglement when large ensembles are available whereas pure states do not show this feature.

Nonlocality without entanglement has been described in Bennett *et al.* (1999). There *unentangled* quantum states of a composite quantum system are described that can only be distinguished by a joint measurement on the whole system, but not by separate measurements on the individual constituents, not even when exchange of classical information between the observers measuring the individual objects is allowed for. A joint measurement on the quantum system reveals more information than any "classically" coordinated measurements of the individual parts.

In Massar and Popescu (2000) it is shown that different definitions for the target function that is to be maximized in quantum state estimation may lead to different recipes for optimal measurements. This in turn will determine the properties of the quantum state that is revealed in a quantum measurement. It is shown that no matter what type of target function is chosen, the maximum amount of information that can be obtained from one qubit is one bit.

Estimating a quantum state can also be viewed as the decoding procedure at the receiver end of a quantum channel necessary to recover elements of an alphabet that have been encoded in quantum states by a sender (see, for instance, Jones (1994). A sketch of the steps necessary for the
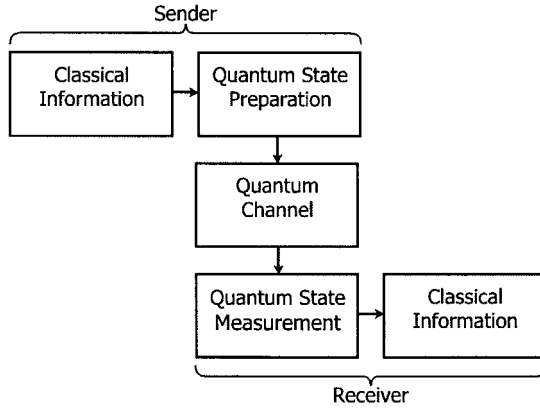
FIG. 10. The steps necessary for transmission of information using quantum systems are schematically shown.

transmission of quantum information is displayed in Fig. 10. The sender prepares a quantum state by setting the classical parameters of an appropriate device that prepares the desired quantum state. Then, the quantum system propagates in space or time until it reaches the receiver equipped with an apparatus capable of performing measurements in any basis, and it is her/his task to give the best possible estimate of this quantum state after $N$ identically prepared copies of the quantum system have been sent. In order to specify what "best possible" means, the Shannon information and von Neumann entropy for this situation have been computed, and an upper bound for the information obtainable from $N$ identically prepared quantum states as well as a lower bound on the entropy have been derived (Jones, 1994).

The quantum information associated with a state of a qubit to be transmitted can be viewed as a unit vector indicating a direction in space. If no common coordinate system has been established, then the transmission of a direction in space between two distant parties requires a physical object. In the quantum domain, $N$ identically prepared spin-1/2 systems may serve for this purpose. It has been shown that the optimal state, that is, the one that yields the highest average fidelity $F = \langle \cos^2(\theta/2) \rangle$ of transmission is an entangled one for $N > 2$ (Bagan *et al.*, 2000, 2001; Peres and Scudo, 2001) ($\theta$ is the angle between the estimated and the actual direction to be transmitted). The use of product states for communication of a spin direction has been investigated in Bagan *et al.* (2001).

Debugging of a quantum algorithm is another possible application for quantum state estimation (Fischer *et al.*, 2000). Once a quantum algorithm has been implemented, it has to be tested, for instance by checking the state of a certain qubit in the course of the computation. In such a case the qubits are only available sequentially and efficient estimation is desirable, that is, a large overlap of the estimated state with the true one while keeping the number of repetitions of the algorithm as small as possible.

First experimental steps toward entanglement-enhanced determination ($N=2$) of a quantum state have been undertaken (Meyer *et al.*, 2001). The rotation angle around a specific axis of the total angular momentum of 2 spin systems has been estimated with an uncertainty below the standard quantum limit. The related problem of measuring in an optimal way the phase difference $\phi$ between the two arms of a Mach–Zehnder interferometer has been addressed in Berry and Wiseman (2000). The optimal input state has been derived and an adaptive measurement scheme is proposed that relies on the detection of photon counts and yields a variance in $\phi$ close to the optimal result.

We have seen that optimal strategies to read out information encoded in the quantum state of a limited number of identical qubits require intricate measurements using a basis of entangled states. The first experimental demonstration of a self-learning measurement (employing a factorizing basis) of an arbitrary quantum state (Hannemann *et al.*, 2002) and an experimental comparison with other strategies is reviewed in what follows.

## B. Elements of the Theory of Self-Learning Measurements

It was recently shown that quantum state estimation of qubits with fidelity close to the optimum is possible when a self-learning algorithm is used (Fischer *et al.*, 2000). When using this algorithm, $N$ members of an ensemble of identically prepared quantum systems in a pure state,

$$|\psi\rangle = |\psi\rangle_1 \otimes |\psi\rangle_2 \otimes \cdots \otimes |\psi\rangle_N, \tag{25}$$

can be measured individually, that is, they do not have to be available simultaneously. In other words, the measurement operator $\hat{M}$ employed to estimate the state can be written as a tensor product and we have

$$\hat{M}|\psi\rangle = \hat{m}_1|\psi\rangle_1 \otimes \hat{m}_2|\psi\rangle_2 \otimes \cdots \otimes \hat{m}_N|\psi\rangle_N \tag{26}$$

The operators $\hat{m}_n$ project onto the orthonormal basis states

$$|\theta_m^{(n)}, \phi_m^{(n)}\rangle = \cos\frac{\theta_m^{(n)}}{2}|0\rangle + \sin\frac{\theta_m^{(n)}}{2}e^{i\phi_m^{(n)}}|1\rangle \quad \text{and} \quad |\pi - \theta_m^{(n)}, \pi + \phi_m^{(n)}\rangle \qquad (27)$$

An experimental realization of a self-learning measurement on an individual quantum system in order to estimate its state is reported in Hannemann *et al.* (2002). The projector $\hat{m}_n$ of measurement $n$ is varied in real time during a sequence of $N$ measurements conditioned on the results of previous measurements $\hat{m}_l, l < n$ in this sequence (for the first measurement, $n=1$, obviously no prior knowledge of the state is available and the first measurement basis can be chosen arbitrarily). The cost function that is optimized when proceeding from measurement $n$ to $n+1$ is the fidelity of the estimated state after measurement $n+1$. This will be detailed in the following paragraphs.

Prior to the first measurement no information on the qubit state is available and the corresponding density matrix $\varrho_0$ reflecting this ignorance is

$$\varrho_0 = \int_0^\pi d\theta \sin\theta \int_0^{2\pi} d\phi w_0(\theta, \phi) |\theta, \phi\rangle\langle\theta, \phi|, \qquad (28)$$

where $w_0(\theta, \phi) = 1/4\pi$ is the probability density on the Bloch sphere. After the qubit has been measured in the direction $(\theta_m, \phi_m)$ the new distribution $w_n(\theta, \phi)$ is obtained from Bayes rule (Bayes, 1763), reprinted in Bayes (1958):

$$w_n(\theta, \phi|\theta_m, \phi_m) = \frac{w_{n-1}(\theta, \phi) \,|\langle\theta_m, \phi_m|\theta, \phi\rangle|^2}{p_n(\theta_m, \phi_m)}, \qquad (29)$$

where $w_{n-1}(\theta, \phi)$ gives the *a priori* probability density to find the qubit along the direction indicated by $\theta$ and $\phi$. The conditional probability to measure the qubit along the direction $|\theta_m, \phi_m\rangle$ if it is in state $|\theta, \phi\rangle$ is given by $|\langle\theta_m, \phi_m|\theta, \phi\rangle|^2$. Correct normalization is ensured by the denominator

$$p_n(\theta_m, \phi_m) = \int_0^\pi d\theta \sin\theta \int_0^{2\pi} d\phi \, w_{n-1}(\theta, \phi) \,|\langle\theta_m, \phi_m|\theta, \phi\rangle|^2 \qquad (30)$$

that gives the probability to measure the qubit along the direction $|\theta_m, \phi_m\rangle$ irrespective of its actual state, that is, integrated over all possible *a priori* directions.

The adaptive algorithm needs to find optimal measurement axes $(\theta_m, \phi_m)_n$ after each step. The optimization is based on the knowledge gained from the preceding measurements as represented by $w_{n-1}(\theta, \phi)$.

The cost function used to find the optimal measurement is the fidelity

$$F_{n-1}(\theta, \phi) = \langle \theta, \phi | \varrho_{n-1} | \theta, \phi \rangle. \tag{31}$$

After $n-1$ measurements the knowledge of the state is represented by $w_{n-1}(\theta, \phi)$ and the fidelity of any state $|\theta, \phi\rangle$ is

$$F_{n-1}(\theta, \phi) = \int_0^\pi d\theta' \sin \theta' \int_0^{2\pi} d\phi' w_{n-1}(\theta', \phi') |\langle \theta, \phi | \theta', \phi' \rangle|^2 \tag{32}$$

The estimated state after $n-1$ measurements $|\theta_{\text{est}}, \phi_{\text{est}}\rangle_{n-1}$ has to maximize this fidelity:

$$F_{n-1}(\theta_{\text{est}}, \phi_{\text{est}}) = F_{n1}^{\text{opt}} \equiv \max F_{n-1}(\theta, \phi) \tag{33}$$

In order to find the optimal direction for the next measurement $n$, the *expected* mean fidelity after the next measurement is maximized as a function of the measurement axis. Suppose the system will be found in the direction $(\theta_m, \phi_m)$. Then the fidelity would be given by:

$$F_n(\theta, \phi | \theta_m, \phi_m) = \int_0^\pi d\theta' \sin \theta' \int_0^{2\pi} d\phi' \, w_n(\theta', \phi' | \theta_m, \phi_m) \, |\langle \theta, \phi | \theta', \phi' \rangle|^2 \tag{34}$$

where the *expected* distribution *after* this measurement, $w_n(\theta', \phi' | \theta_m, \phi_m)$ is obtained from Bayes rule (Eq. 29). The optimal fidelity $F_n^{\text{opt}}(\theta_m, \phi_m)$ is then found by maximizing this function with respect to $(\theta, \phi)$.

A measurement along a certain axis will reveal the system to be in one of two possible states: Either it is found along this axis $(\theta_m, \phi_m)$, or in the opposite direction $(\bar{\theta}_m, \bar{\phi}_m) \equiv (\pi - \theta_m, \pi + \phi_m)$. So far we have only taken into account the first of these two possible outcomes of the measurement. The optimized fidelity for the second result is calculated analogously and occurs with probability $p_n(\bar{\theta}_m, \bar{\phi}_m)$ (Eq. 30). Thus the expected mean fidelity after the next measurement is given by the optimized fidelities for each outcome, weighted by the estimated probability for that outcome:

$$\bar{F}_n(\theta_m, \phi_m) = p_n(\theta_m, \phi_m) F_n^{\text{opt}}(\theta_m, \phi_m) + p_n(\bar{\theta}_m, \bar{\phi}_m) F_n^{\text{opt}}(\bar{\theta}_m, \bar{\phi}_m) \tag{35}$$

The optimal measurement direction $(\theta_m^{\mathrm{opt}}, \phi_m^{\mathrm{opt}})$ has to maximize this function.

The direction of the first ($n=1$) measurement is of course arbitrary, since there is no *a priori* information on the state. The expected mean fidelity in this case is $\bar{F}_1 = 2/3$, independently of $(\theta_m, \phi_m)_1$. For measurements two and three the following analytical expressions have been derived: $\bar{F}_2 = (1/2 + \cos(\alpha/2 - \pi/4)/\sqrt{18})$, where the expected mean fidelity depends on the relative angle $\alpha$ between the second and the first measurement direction. Thus the optimal second measurement direction has to be orthogonal to the first one, yielding $\bar{F}_2^{\mathrm{opt}} = (1/2 + 1/\sqrt{18})$. The optimal third measurement axis is orthogonal to both previous directions and yields $\bar{F}_3^{\mathrm{opt}} = (1/2 + 1/\sqrt{12})$.

Interestingly, if the Shannon information is used as a cost function to find the optimal measurement directions, then the theoretically obtained fidelity of the estimated state after $N$ measurements is not as high as is the case, if the fidelity is employed as outlined above (Fischer *et al.*, 2000). This may hint at the inadequacy of the use of the Shannon measure in the quantum domain as pointed out by Brukner and Zeilinger (2001). However, the $\log_2$ function occurring in the Shannon measure for information poses some difficulties when numerically optimizing the cost function, and the less precise final estimate of the quantum state in our numerical studies could be caused by accumulating round-off errors.

## C. Experiment

A typical sequence of measurements where the adaptive algorithm outlined above has been realized is depicted in Fig. 11. The probability density $w_n(\theta, \phi)$ is shown on the surface of the Bloch sphere and the measurement directions $n$ (dashed line with open arrow head) and $n+1$ (solid line with solid arrow head) are indicated. Here, the state to be estimated is $|\theta_{\mathrm{prep}}, \phi_{\mathrm{prep}}\rangle = |3\pi/4, \pi/4\rangle$. The white solid circle on the Bloch sphere represents the parameters $\theta_p$ and $\phi_p$ of the state to be estimated, and does not indicate a quantum mechanical uncertainty. These parameters are part of a recipe to prepare the desired quantum state using a classical apparatus. When such a quantum state is subjected to a measurement, for instance, along the $z$-direction, then after this measurement, of course, there will be no more information available about the components of the initial state in the $x$- and $y$-directions in accordance with the uncertainty relation derived from the commutators of the spin-1/2 operators. Only in the limit $N \to \infty$ for $N$ suitably chosen measurements of $N$ states prepared according to the same recipe, the parameters $\theta$ and $\phi$ could be recovered. The
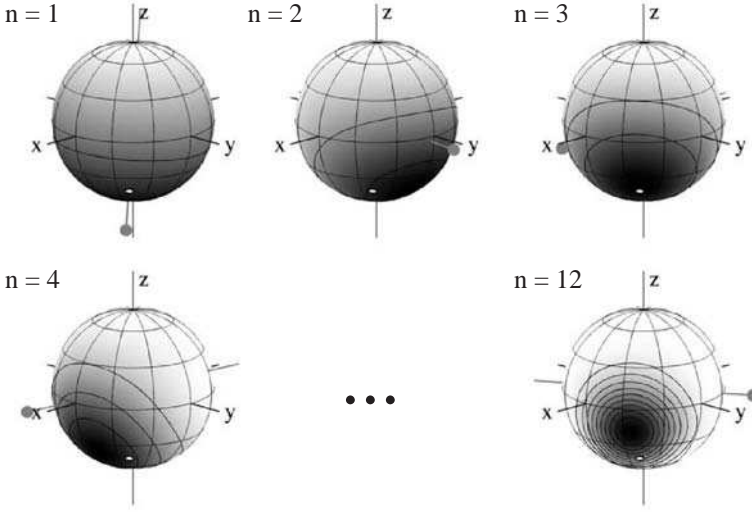
F̲ɪɢ. 11. A sequence of $N = 12$ adaptive measurements carried out on identically prepared qubits in order to estimate their state ($|3\pi/4, \pi/4\rangle$, marked by a white solid circle). The probability density $w_n(\theta, \phi)$ is gray scale coded on the surface of the Bloch sphere (the gray scale code is different for each measurement). In addition, contour lines indicate where $w_n$ takes on the values $0.1, 0.2, \ldots$ A gray straight line through each Bloch sphere shows the measurement direction and the filled gray circle indicates the measurement outcome. The fidelity of state estimation of this particular run is 94.9%.

uncertainty associated with the preparation of a specific quantum state, $|\theta, \phi\rangle$ is not a quantum mechanical one, it is determined by technical issues. If the electromagnetic field used for preparation of an ionic quantum state contains a large number of photons, for example, a coherent intense field emitted by a mw source with mean photon number $\langle M \rangle$ satisfying $\langle \triangle M \rangle / \langle M \rangle \ll 1$ (Haroche, 1971), then the "graininess" of the field can be safely neglected, and the amplitude stability of the applied mw field determined by technical specifications of the mw source would limit the precision of state preparation. The time resolution (25 ns) of the digital signal processing system controlling the mw source is another technical limitation for the accuracy and precision of state preparation. (In the actual experiment, the initial preparation of state is the main source of imprecision when an arbitrary quantum state is generated.)

Imprecision in the initial preparation of $|0\rangle$ and in the subsequent preparation of a desired quantum state, relaxation and dephasing of the quantum state before it is being measured, and the effect of an imperfect

measurement can be concisely summarized as the action of a depolarizing quantum channel together with a systematic bias.

$$\varrho \to (1 - 2\lambda)\varrho + \lambda I + \Delta\eta\sigma_z \ , \tag{36}$$

where $\Delta\eta \equiv (\eta_1 - \eta_0)/2$ is the difference in detection efficiencies for state $|1\rangle$ and $|0\rangle$, respectively; $0 \le \lambda \le 1/2$, and here we have $\lambda \le 1 - \bar\eta \equiv 1 - (\eta_1 + \eta_0)/2$ with $1/2 \le \eta_{0,1} \le 1$. This description is also applicable to other types of experiments where imperfections may be due to other physical reasons. The third term on the rhs in 36 arises whenever the efficiencies of detection for states $|0\rangle$ and $|1\rangle$ differ from each other, and has a specific influence on different estimation strategies. For any strategy, $\Delta\eta \ne 0$ means that the fidelity of state estimation depends on the state to be measured as can be seen in Fig. 12. Figure 12 also displays data obtained from experimental runs where the $N$ measurement directions are chosen randomly.

Experiments are necessarily imperfect, that is, they never perfectly reflect results obtained from theoretical considerations. In the case of quantum state estimation this means that an estimate with fidelity equal to the theoretical value cannot be obtained. Here, the performance of the experimental apparatus has been characterized quantitatively and completely (that is, the features that are relevant for the experiment). Taking into account the known experimental imperfections, the theoretical value for the fidelity of state estimation is numerically calculated for an ensemble of 10 000 states drawn randomly from a uniform distribution on the Bloch sphere. This theoretical mean fidelity is then compared to the experimental result of the self-learning algorithm and the random strategy (Fig. 13).

Decoherence inevitably occurs in any experiment and it has been shown that under this commonplace condition the self-learning strategy still yields the best results. Even more, the self-learning and the random strategy show a larger difference in mean fidelity (85.0% compared to 81.9%, the difference exceeding 5 standard errors) in the 'real' experimental world than the difference between the ideal theoretical values (92.5% and 91%, respectively, for $N = 12$).

The estimation procedure discussed here allows for separate (local) measurements on each qubit. Following each measurement on a particular qubit, classical information is used to determine the best measurement to be performed on the next qubit. In reference (Bagan *et al.*, 2002) the optimal LOCC scheme (performing local operations with exchange of classical information) is introduced for arbitrary states on the Bloch sphere (3D case).

a)



b)
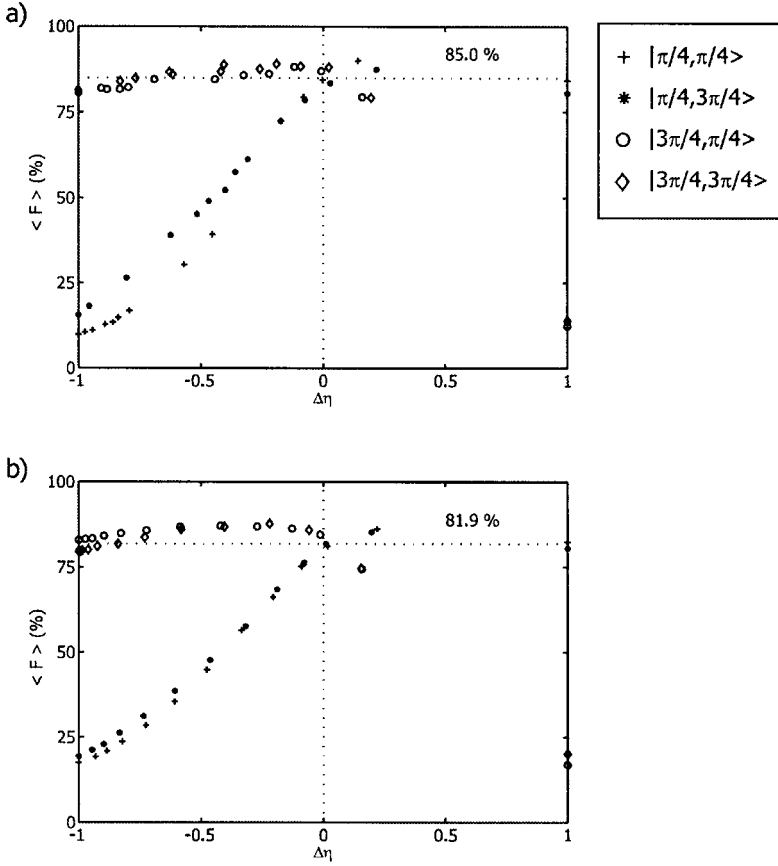


FIG. 12. The experimentally determined average fidelity of state estimation as a function of the difference in detection efficiency, $\Delta\eta$ for states $|0\rangle$ and $|1\rangle$, respectively. The fidelity is plotted for different states to be estimated. For $\Delta\eta = 0$ the fidelity should be independent of the initial state which is indeed observed in the experiment. (a) Self-learning estimation; (b) Random choice of basis.

Interestingly, if the state to be estimated lies in the *xy*-plane (2D case), then local operations alone suffice to obtain the optimal state estimate and classical communication is not necessary. This optimal LO(CC) scheme exhibits the same asymptotic behavior with the number $N$ of qubits as the optimal scheme taking advantage of collective measurements, and yields (according to theory) a slightly better average fidelity than the adaptive scheme presented here.
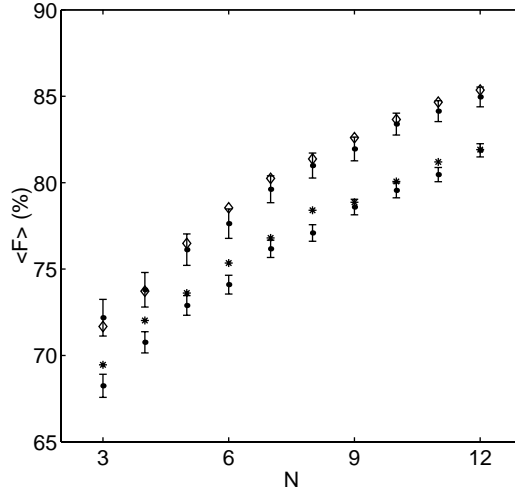
F<sub>IG</sub>. 13. The average fidelity of state estimation as a function of the number $N$ of available qubits. Diamonds and stars indicate theoretical values for the self-learning algorithm and the random choice of measurement basis, respectively (taking into account the experimental preparation and detection efficiencies). Solid squares show the experimentally determined values for these two measurement strategies.

# VI. Quantum Information

The investigations of fundamental questions of quantum mechanics, in addition to their intrinsic interest, may also prove useful to construct an information processor functioning according to the principles of quantum mechanics. If such a quantum computer were available, it could be used for a variety of tasks a classical computer, for all practical purposes, could not handle. A famous example for such a task is the factoring of large numbers. The difficulty of this task ensures the security of communication encrypted according to the RSA procedure (developed by R. Rivest; A. Shamir; and L. Adleman (Rivest *et al.*, 1978)), if the large number the encryption is based on, is changed after a time interval short compared to the computational time needed to carry out the factorization of this number. In Shor (1994, 1997) an algorithm is described, based on the laws of quantum mechanics, that could be used to find the prime factors of a given number of the order $10^N$ in time $T$ proportional to $(\ln N)^3$, as compared to the best known classical algorithm where $T \propto \exp(s(\ln N)^{1/3}(\ln \ln N)^{2/3})$ with $O(s) = 2$.

For $N = 130$ (a typical order of magnitude of today's RSA-type encrypting schemes) a classical computer using the best known algorithm

would need about $10^{17}$ instructions, whereas a quantum computer running Shor's algorithm (Shor, 1994) could solve the same task using $10^{10}$ instructions, thus reducing the time needed for this computation by a factor $10^7$, if the same speed for an elementary operation is assumed for both types of computers. The efficiency of the Shor algorithm relies on the efficient implementation of Fourier transformations with quantum logic. Its advantage over the classical algorithm increases with increasing complexity of the problem to be solved (here with $N$). It was shown, that a single qubit in a pure state together with $\log_2 N$ qubits in arbitrary mixed states suffice to implement Shor's factoring algorithm (Parker and Plenio, 2000).

The calculation of properties or dynamics of quantum systems is a promising line of action for a quantum computer, even one with only few qubits and operating with limited precision (Feynman, 1982; Molmer and Sorensen, 2000). In Abrams and Lloyd (1999) it is shown how a quantum computer consisting of about 100 qubits can be used to calculate eigenvalues and eigenvectors of Hamilton operators. Computing, for instance, energy levels and correlation energies of a Boron atom with 5 electrons is a rather intricate problem: if 20 angular wave functions and 40 radial wave functions are used, then this amounts to a total of about $10^{15}$ many body basis states to be considered in such a calculation. Sophisticated classical techniques have been developed to circumvent problems arising from the exponentially growing space of basis states. Still, a quantum computer of very limited size may be able to perform more accurate calculations (Abrams and Lloyd, 1999). Somaroo *et al.* (1999) describes how proton nuclear spins have been used to simulate the dynamics of a truncated quantum harmonic oscillator employing nuclear magnetic resonance techniques. Nonlinear dynamical problems that are hard or impossible (for all practical purposes) to solve on a classical computer due to accumulating round-off errors may also be simulated efficiently on a quantum computer (Georgeot and Shepelyansky, 2001a,b, 2002).

What is the origin of the computational power of a quantum computer? The elementary switching unit (bit) of usual classical computers is a transistor that may assume two distinct macroscopic states that can be identified with the computational binary states 0 and 1. In a quantum computer transistors are replaced by two-state quantum systems (qubits) that may exist in arbitrary superposition states $\alpha|0\rangle + \beta|1\rangle$ with the complex numbers $\alpha, \beta$ satisfying $|\alpha|^2 + |\beta|^2 = 1$. The possibility to exploit the quantum mechanical superposition principle and the linearity of operations in Hilbert space for massive parallel computing is one ingredient for a quantum computer. The art of designing quantum algorithms makes use of another feature of quantum mechanics: the ability to display interference.

Roughly speaking, a quantum algorithm has to be designed such that different computational paths interfere in such a way that at the end of the algorithm the correct result survives with probability near unity (Cleve *et al.*, 1998). Recent introductions to quantum computing can be found, for instance, in Nielsen and Chuang (2000) and Gruska (1999).

To date, nuclear magnetic resonance applied to macroscopic ensembles of molecules (Gershenfeld and Chuang, 1997) and electrodynamically trapped ions (Cirac and Zoller, 1995) are the two physical systems that have been most successfully used to demonstrate quantum logic operations, and even complete quantum algorithms (Jones and Mosca, 1998; Chuang *et al.*, 1998; Vandersypen *et al.*, 2001). Also, their specific advantages and shortcomings have been thoroughly investigated, experimentally and theoretically. Introductions to quantum computing with an emphasis on ion traps or nuclear magnetic resonance are given, for instance, in Steane (1997); Wineland *et al.* (1998); Sasura and Buzek (2002), and Jones (2001), respectively.

Sections V and VI.A describe experiments with trapped $^{171}\text{Yb}^+$ ions addressing basic questions of quantum mechanics that, at the same time, are relevant for QIP: the self-learning measurement of arbitrary qubit states and the realization and characterization of various quantum channels. These experiments also demonstrate the ability to perform arbitrary single-qubit gates with individual $^{171}\text{Yb}^+$ ions with high precision – a prerequisite for QIP. The coherence time of the hyperfine qubit in $^{171}\text{Yb}^+$ is, for all practical purposes, limited by the coherence time of microwave (mw) radiation used to drive the qubit transition.

In addition to single-qubit operations, a second basic ingredient is required for QIP with trapped ions: conditional quantum dynamics with, at least, two qubits. Any quantum algorithm can then be synthesized using these elementary building blocks (Barenco *et al.* 1995; DiVincenzo, 1995). Communication between qubits, necessary for conditional quantum dynamics, is achieved via the vibrational motion of the whole ion string (Cirac and Zoller, 1995; Jonathan *et al.*, 2000; Sorensen and Molmer, 2000). Thus, external (motional) and internal degrees of freedom need to be coupled. Driving a hyperfine transition with mw radiation (as in the experiments described in this article) does not allow for such a coupling, since the Lamb–Dicke parameter is essentially zero for long-wavelength radiation. Also, the inter-ion spacing in usual traps is much smaller than the wavelength of mw radiation and, therefore, individual addressing of ions is not possible. Section VI.B.2 describes how an additional magnetic field gradient applied to an electrodynamic trap individually shifts ionic qubit resonances thus making them distinguishable in frequency space. At the same time, coupling of internal and motional states is possible even

for mw radiation. With the introduction of this additional static field, all optical schemes devised for QIP in ion traps can be applied in the mw regime, too.

Instead of applying usual methods for coherent manipulation of trapped ions, a string of ions in such a modified trap can be treated like a molecule in NMR experiments taking advantage of spin–spin coupling. A collection of trapped ions forms a *N*-qubit "molecule" with adjustable spin–spin coupling constants (second part of Section VI.B.2.)

## A. Realization of Quantum Channels

Quantum logic operations, and other experiments where coherent super-positions of quantum states have to remain intact for a certain time, are carried out ideally under perfect, noiseless conditions. However, the inevitable coupling of qubits to their environment and the imperfection inherent to any physical operation with qubits invariably degrade the performance of quantum logic operations.

A quantum channel describes the general dynamics of a qubit under propagation in space and/or time. This evolution of qubits can be associated with a physical device used to transmit quantum information (like an optical fiber). When employing quantum states to transmit information, the sequence of necessary steps can be visualized as follows (compare Fig. 10): some physical apparatus is used to prepare a quantum state using a set of classical variables. The quantum state propagates, signified by the quantum channel until it is measured by a receiver again using a suitable apparatus to extract the values of classical variables. The optimal reconstruction of quantum states has been the topic of experiments described in the previous section. Now we consider explicitly the influence of the environment on a quantum state once it has been prepared, that is, we investigate the influence of the quantum channel on the transmission of quantum information (Hannemann *et al.*, n.d).

The state of a qubit is completely determined by the expectation values $\langle \sigma_x \rangle$, $\langle \sigma_y \rangle$, and $\langle \sigma_z \rangle$, and the density matrix describing its state can be written as

$$\rho = \frac{1}{2}(I + \vec{s} \cdot \vec{\sigma}) \tag{37}$$

where $\vec{s} \cdot \vec{\sigma} = \langle \sigma_x \rangle \sigma_x + \langle \sigma_y \rangle \sigma_y + \langle \sigma_z \rangle \sigma_z$, and $\sigma_{x,y,z}$ are the Pauli matrices. Ideally, while being transmitted through the quantum channel, the qubit's state described by the Bloch vector $\vec{s}$ is not changed. However, in general, the propagation of the qubit through a quantum channel will alter the

qubit's state and $\vec{s}'$ will be obtained at the quantum channel's exit. This change of the qubits state can be of reversible or irreversible nature. The quantum channel may also stand for a quantum memory storing a qubit state which may undergo some change until it is 'activated' again, that is, transferred to another quantum system or being subjected to a measurement. It can also represent the dynamics of a qubit during a quantum computation. The most economical error correcting and avoiding codes used to correct or stabilize quantum information depend on the type of quantum channel the qubits are exposed to.

Two examples for detrimental effects acting on qubit states (the consequence of "noise") are given in what follows. A phase damping channel leads to decoherence of a qubit state, affecting the off-diagonal elements $\rho_{10} = \rho_{01}^* = \langle\sigma_x\rangle - i\langle\sigma_y\rangle$ of the density matrix that are diminished or disappear completely while the diagonal elements remain unchanged. It transforms a Bloch vector according to

$$\vec{s}' = \begin{pmatrix} 1-2\lambda & 0 & 0 \\ 0 & 1-2\lambda & 0 \\ 0 & 0 & 1 \end{pmatrix}\vec{s}, \tag{38}$$

with $0 \leq \lambda \leq 1/2$. The $\sigma_x$ and $\sigma_y$ components of the Bloch vector shrink by a factor $1 - 2\lambda$.

A quantum channel that fully depolarizes the quantum state of a qubit transforms any state $\rho$ into a completely mixed state $\rho' = 1/2\,I$. A partially depolarizing channel can be characterized by a parameter $0 \leq \lambda \leq 1/2$ that is interpreted as the probability for changing the qubit's state into its orthogonal state: if the input state is pure, then we choose the basis such that the qubit's initial density matrix reads

$$\rho = \frac{1}{2}(I + \sigma_z). \tag{39}$$

After the quantum channel

$$\rho' = (1-\lambda)\frac{1}{2}(I + \sigma_z) + \lambda\frac{1}{2}(I - \sigma_z). \tag{40}$$

The action of the depolarizing channel is independent of the initial polarization of the qubit, hence can be described by

$$\vec{s} \rightarrow \vec{s}' = (1-2\lambda)\vec{s}. \tag{41}$$

In (Fujiwara and Algoet, 1999) it is shown that any quantum channel for qubits can be cast in the form

$$\vec{s}\,' = \hat{M}\vec{s} + \vec{v} \; . \tag{42}$$

where $\hat{M} \in \mathbb{R}^{3\times3}$ and $\vec{v} \in \mathbb{R}^3$. Equation 42 yields $\vec{s}\,'$, the Bloch vector of the qubit after it has traversed the quantum channel characterized by $\hat{M}$ and $\vec{v}$.

Various quantum channels have been realized experimentally with $^{171}$Yb$^+$ ions (Hannemann *et al.*, n.d) and the matrix and vector elements

$$M_{ij} = 2P_{ij} - P_{iz} - P_{i(-z)}$$
$$v_i = P_{iz} + P_{i(-z)} - 1 \tag{43}$$

are determined by measuring the probabilities (or rather relative frequencies) $P_{ij} = \langle i|\rho'|j\rangle$, where $\rho'$ is the density matrix describing the qubit state after the quantum channel, and $i,j \in \{x,y,z\}$ (Hannemann *et al.*, n.d).

Exploiting coherent and incoherent operations on the hyperfine qubits of Yb$^+$ we realized and completely characterized a polarization rotating quantum channel, a phase damping quantum channel acting in the $xy$-plane, and a phase damping quantum channel acting in an arbitrary plane. A Pauli channel and combinations of the aforementioned channels can also be realized. Incoherent disturbances to a quantum channel are realized by applying to the qubit a noisy magnetic field with well-defined spectral properties in conjunction with coherent microwave operations. Another possibility to produce a desired quantum channel is realized by applying to the qubit small amounts of light close to 369 nm, thus inducing well-defined quantities of longitudinal and/or transversal relaxation during coherent microwave operations (Balzer *et al.*, 2002b). This light-induced decoherence is readily applicable to individually addressed quantum systems, it may be switched on and off immediately, and it is reproducible. Although, in the present experiment, the coherent drive was microwave radiation resonant with a ground-state hyperfine transition in Yb$^+$, the same principle seems to apply to a system where a dipole-forbidden optical transition is driven by laser light (for example in Ca$^+$ or Ba$^+$).

An example of an experimentally realized quantum channel is displayed in Fig. 14. Here, a channel affected by controlled amounts of phase damping in the plane normal to the unit vector $\vec{n} = (1, \pi/6, 0)^T$ (in polar coordinates) has been implemented. The applied noisy magnetic field causes in addition a small amount of amplitude damping (detailed in Hannemann *et al.*, n.d). Each matrix element is plotted as a function of the amplitude of the additional noisy magnetic field.
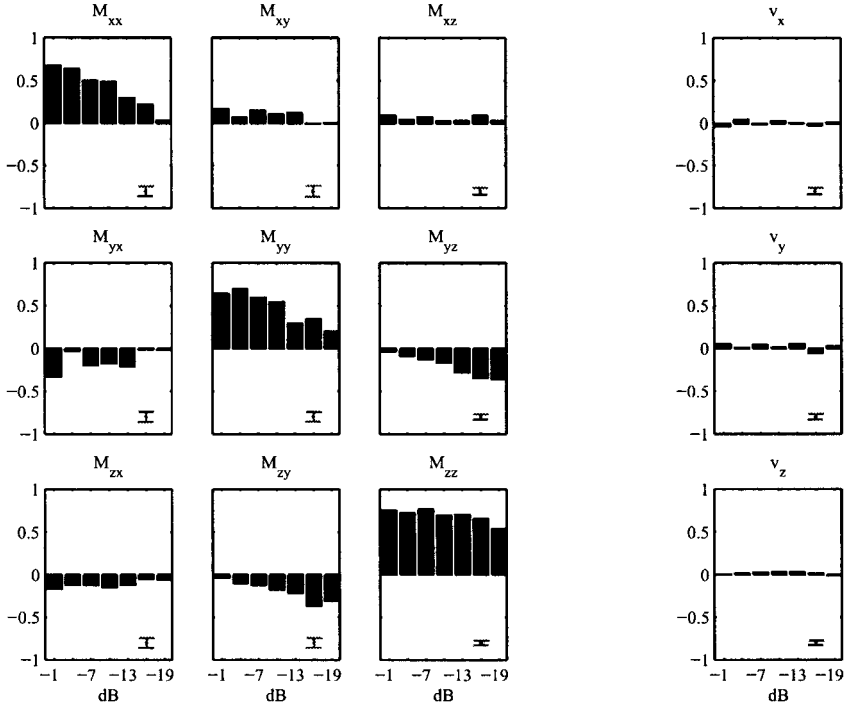
FIG. 14. Experimentally realized quantum channel with designed phase damping in the plane normal to the unit vector $\vec{n} = (1, \pi/6, 0)^T$ (in polar coordinates). In addition, a small amount of amplitude damping is present. The relative amplitude of the noise magnetic field was varied between $-19\,\mathrm{dB}$ and $-1\,\mathrm{dB}$.

Since the elements of the matrix describing the quantum channel can be varied over a wide range, this experimental system can be used to simulate specific quantum channels characteristic for other physical implementations of QIP, too. Error correction is essential for QIP, since decoherence is ubiquitous. We have implemented different quantum channels characterized by reversible and irreversible dynamics that can be used, for instance, to experimentally test the capabilities of different types of quantum error correcting codes under varying conditions.

If spatially separated quantum information processors, for example, ion traps each containing a limited number of qubits are connected to allow for the exchange of quantum information, then it will also be useful to be able to first characterize the quantum channel and then apply the appropriate strategy to avoid or correct these specific errors.

B. New Concepts for Spin Resonance with Trapped Ions

The discussion of a new approach to ion trap quantum computing in this
section is restricted to the use of electrodynamic Paul traps, even though this
concept should also be applicable when other trapping techniques are
employed, for example, Penning traps (Powell *et al.*, 2002).

### B.1. Linear ion trap

In a linear Paul trap (Paul *et al.*, 1958), a time-dependent two-dimensional
quadrupole field strongly confines the ions in the radial direction yielding an
average effective harmonic potential (Ghosh, 1995). An additional static
electric field is applied to harmonically confine the ions also in the
axial direction (Prestage *et al.*, 1989; Raizen *et al.*, 1992). If the confinement
of $N$ ions is much stronger in the radial than in the axial direction, the
ions will form a linear chain (Dubin, 1993; Schiffer, 1993) with inter-ion
spacing

$$\delta z \approx \zeta \, 2 N^{-0.56} \tag{44}$$

where

$$\zeta \equiv (e^2/4\pi\epsilon_0 m v_1^2)^{1/3}, \tag{45}$$

$m$ is the mass of one singly charged ion, $e$ the elementary charge, and $v_1$ is
the angular vibrational frequency of the center-of-mass (COM) mode of the
ion string (Steane, 1997; James, 1998). The distance between neighboring
ions, $\delta z$ is determined by the mutual Coulomb repulsion of the ions and the
trapping potential. Typically, $\delta z$ is of the order of a few μm; for example,
$\delta z \approx 7\,\mu m$ for $N = 10$ $^{171}\text{Yb}^+$ ions with $v_1 = 100 \times 2\pi\,\text{kHz}$.

Two appropriately chosen internal states of each ion confined in a linear
electrodynamic trap represent a quantum mechanical 2-state system that
may serve as one qubit. In order to prepare these quantum mechanical
2-state systems individually (single qubit operations), electromagnetic
radiation is aimed at one ion at a time, that is, it must be focused to a
spot size much smaller than $\delta z$. Therefore, optical radiation is usually
required for individual addressing of qubits in ion traps (Nägerl *et al.*, 1999).

In order to implement conditional quantum dynamics with ionic qubits,
it is necessary (in addition to single qubit operations) to couple external
and internal degrees of freedom. The interaction Hamiltonian governing the

dynamics of a particular ion $j$ at position $z_j$ subjected to an electromagnetic field with angular frequency $\omega$ and initial phase $\phi'$ reads

$$
\begin{aligned}
H_I &= \frac{\hbar}{2}\Omega(\sigma_j^+ + \sigma_j^-)\big[\exp[i(kz_j - \omega t + \phi')] + \exp[-i(kz_j - \omega t + \phi')]\big] \\
&= \frac{\hbar}{2}\Omega(\sigma_j^+ + \sigma_j^-)\left[\exp\left[\sum_n^N iS_{nj}\eta_n(a_n^\dagger + a_n) - i\omega t + i\phi\right] + h.c.\right]
\end{aligned}
\tag{46}
$$

where $\Omega = \vec{d}\cdot\vec{F}/\hbar$ is the Rabi frequency with $\vec{d}\cdot\vec{F}$ signifying either magnetic or electric coupling between the atomic dipole and the respective field component. $\sigma_{+,-} = 1/2(\sigma_x \pm \sigma_y)$ represent the atomic raising and lowering operators, respectively, ($a_n^\dagger$ and $a_n$ are the creation and annihilation operators of vibrational mode $n$, and $S_{nj}$ are the coefficients of the unitary transformation matrix that diagonalizes the dynamical matrix describing the axial degrees of freedom of a linear string of $N$ ions (Wunderlich, 2001). The Lamb–Dicke parameters $\eta_n$ determining the coupling strength between internal and motional dynamics are given by

$$
\eta_n \equiv \sqrt{\frac{(\hbar k)^2}{2m}/\hbar\nu_n} = \frac{\hbar k}{2\Delta p_n} = \frac{\Delta z_n\, 2\pi}{\lambda}.
\tag{47}
$$

The square of $\eta_n$ gives the ratio between the change in kinetic energy of the atom due to the absorption or emission of a photon and the quantized energy spacing of the harmonic oscillator mode characterized by angular frequency $\nu_n$. The mean square deviation of the vibrational mode's ground state wave function in momentum space, $(\Delta p_n)^2 = \hbar m\nu_n/2$, and the corresponding quantity in position space, $(\Delta z_n)^2 = \hbar/2m\nu_n$. Only if $\eta_n$ is nonvanishing, will the absorption or emission of photons be possibly accompanied by a change of the motional state of the atom. Trapping a $^{171}$Yb$^+$ ion, for example, with $\nu_1 = 100 \times 2\pi$ kHz gives $\Delta z_1 \approx 17$ nm and it is clear from Eq. (47) that driving radiation in the optical regime is necessary to couple internal and external dynamics of these trapped ions (Fig. 15).

## B.2. Spin resonance with trapped ions

As was briefly outlined in the introductory Section I, it would be beneficial for ion trap experiments to take advantage of the highly developed technological resources used in spin resonance (e.g., NMR) experiments. In particular, employing microwave radiation with extremely long coherence
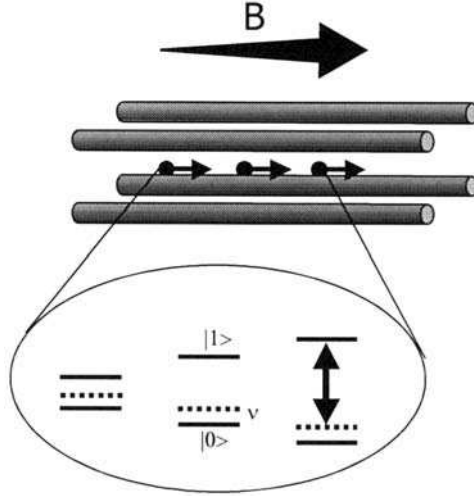
F_IG_. 15. Illustration of a linear ion trap including an axial magnetic field gradient. The static field makes individual ions distinguishable in frequency space by Zeeman-shifting their internal energy levels (solid horizontal lines represent qubit states). In addition, it mediates the coupling between internal and external degrees of freedom when a driving field is applied (dashed horizontal lines stand for vibrational energy levels of the ion string, see text).

time compared to optical radiation allows for precise and, on the timescale of typical experiments, virtually decoherence free manipulation of qubits.[2] In what follows it is outlined how in a linear ion trap with an additional axial magnetic field gradient, $\partial_z B$ (i) ions can be individually addressed in frequency space, and (ii) the Hamiltonian governing the interaction between microwave radiation and ions is formally identical with Eq. (46), with the usual Lamb–Dicke parameter $\eta$ replaced by a new effective LDP $\eta'$ scaling with $\partial_z B / v_1^{3/2}$ (Mintert and Wunderlich, 2001; Wunderlich, 2001).

**Individual addressing of qubits in a modified ion trap** Applying a magnetic field gradient $\vec{B} = bz \cdot \hat{z} + B_0$ along the axial direction of a linear ion trap causes a $z$-dependent Zeeman shift of the internal ionic states $|0\rangle$ and $|1\rangle$. Thus the transition frequency $\omega_{01}^{(j)}, j = 1 \dots N$, of each ion is individually shifted and the qubits can be addressed in frequency space. The Breit–Rabi

---

[2] Optical radiation with a long coherence time has been realized experimentally (for instance, Rafac *et al.*, 2000). However, building and maintaining such intricate light sources is exceedingly challenging compared to the case of rf or mw radiation.

formula (Corney, 1977)

$$E_{m_I m_J} = \frac{E_{\text{HFS}}}{2(2I+1)} - g_I \mu_N B m_q \pm \frac{E_{\text{HFS}}}{2}\left[1 + \frac{4m_q \chi_j}{2I+1} + \chi_j^2\right]^{\frac{1}{2}} \qquad (48)$$

gives the energy levels of the hyperfine levels for electron total angular momentum $J = 1/2$ and arbitrary values of the nuclear spin $I$. The hyperfine splitting between levels with total angular momentum $F = I + 1/2$ and $F = I - 1/2$ in zero magnetic field is denoted by $E_{\text{HFS}}$, $m_q = m_I \pm 1/2$, and the plus (minus) sign in front of the last term in Eq. (48) is to be used for levels originating from zero-field levels $F = I + 1/2$ ($F = I - 1/2$). The dimensionless quantity $\chi_j$ is defined as

$$\chi_j \equiv \frac{(g_J + g_I m_e/m_p)\mu_B B(z_j)}{E_{\text{HFS}}} \qquad (49)$$

where $m_e$ and $m_p$ indicate the electron and proton mass, respectively, $g_J$ and $g_I$ are the electronic and nuclear g-factor, and $\mu_B$ is the Bohr magneton.

Figure 16 shows a plot of the hyperfine levels of the ground state of $\text{Yb}^+$ as a function of the scaled magnetic field, $\chi$, and the allowed magnetic
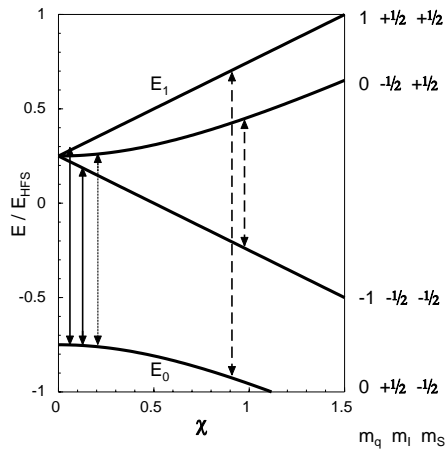


FIG. 16. Hyperfine levels of an atom with nuclear spin $I = 1/2$ and electron angular momentum $J = 1/2$ (for $\text{Yb}^+$ $J = 1/2 = s$) as a function of scaled magnetic field. Magnetic dipole transitions are indicated for $\pi$-polarized radiation (solid lines, weak field; dashed lines, strong field), and for $\sigma$-polarization (dotted line). The levels marked $E_0$ and $E_1$ are well suited to serve as qubit states.

dipole transitions are also displayed. In a weak static magnetic field $\vec{B}$ the selection rules $\Delta m_F = \pm 1$ and $\Delta F = 0, \pm 1$ hold for $\pi$-polarized radiation (that is, the electric field vector is parallel to $\vec{B}$; solid lines in Fig. 16), and $\Delta m_F = 0$ and $\Delta F = \pm 1$ are valid for $\sigma$-polarization (dotted line in Fig. 16). In a strong static field the selection rules are $\Delta m_S = \pm 1$ and $\Delta m_I = 0$ for $\pi$-polarized radiation (dashed lines) and $\Delta m_S = 0$ and $\Delta m_I = 0$ for $\sigma$-polarization (no allowed transitions). Therefore, in order to avoid unwanted overlap of resonance frequencies, $E_0$ and $E_1$ are the appropriate choice as qubit states. For the case of the ground state of $^{171}\text{Yb}^+$ where $E_{\text{HFS}}/\hbar = 12.6 \times 2\pi\,\text{GHz}$, a strong magnetic field (i.e., $\chi \approx 1$) amounts to $0.45\,\text{T}$.

Choosing the levels $E_0$ and $E_1$ indicated in Fig. 16 as qubit states and neglecting the contribution of the nuclear spin to the total energy (since the nuclear magneton $\mu_N \ll \mu_B$), the dependence of the qubit resonance frequency on the axial coordinate is given by

$$\frac{\partial \omega_{01}^{(j)}}{\partial z} = \frac{1}{2\hbar} g_J \mu_B \frac{\partial B(z)}{\partial z} \left( 1 + \frac{\chi_j}{\sqrt{1 + \chi_j^2}} \right). \tag{50}$$

The electronic angular momentum is due to the spin of a valence electron and we have $g_J = g_S = 2$.

When separating the qubit resonance frequencies through the application of a magnetic field gradient, overlap between the motional sidebands of the qubit transitions has to be avoided. Therefore, the gradient has to be chosen such that

$$\delta\omega \geq 2\nu_N + \nu_1 \tag{51}$$

where $\delta\omega = (\partial\omega_{01}/\partial z)\delta z$ is the frequency shift between two neighboring ions (compare Fig. 17), and $\nu_N$ is the angular frequency of the highest axial vibrational mode. Together with expression (44) giving the distance between two ions, $\delta z$, the requirement (51) leads to an estimate of the necessary field gradient in the weak field limit:

$$\frac{\partial B}{\partial z} \geq \frac{\hbar}{2\mu_B} \left( \frac{4\pi\varepsilon_0 m}{e^2} \right)^{1/3} \nu_1^{5/3} \left( 4.7 N^{0.56} + 0.5 N^{1.56} \right). \tag{52}$$

Thus, for example, $N = 10$ $^{171}\text{Yb}^+$ ions with $\nu_1 = 100 \times 2\pi\,\text{kHz}$ require $\partial B/\partial z \approx 10\,\text{T/m}$ (Mintert and Wunderlich, 2001).
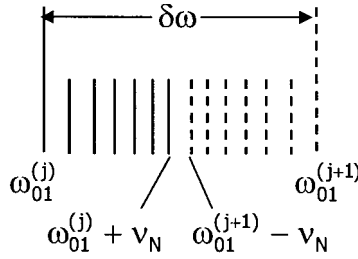
FIG. 17. Schematic drawing of the resonances of qubits $j$ and $j+1$ with some accompanying sideband resonances. The angular frequency $\nu_N$ corresponds to the $N$th axial vibrational mode, and the frequency separation between carrier resonances is denoted by $\delta\omega$.

The expression (52) for the required field gradient gives an order of magnitude estimate that is necessary to assess whether the necessary gradients are feasible. The exact magnitude of the field gradient has to be determined individually for a given experimental situation in order to also avoid possible interference from second order (in $\eta'$) motional sideband resonances. If, for example, 10 $Yb^+$ ions are used, a constant gradient can be chosen such that it leads to a frequency shift between neighboring ions of $8.8\nu_1$ (while equation (52) yields a gradient equivalent to a frequency shift $\geq 8.6\nu_1$). Then all second-order resonances are separated from the carrier and the respective upper and lower sidebands by at least $0.2\ \nu_1$. Since the distance between neighboring ions depends on the position of two ions in the linear string, not all ions' resonances will be centered in the desired frequency gap for a constant field gradient. This can be corrected by a slight variation of the gradient along the trap axis (which can be achieved when current carrying coils are used). Note that the local variation of the field gradient over the extent of the spatial wave function of an individual laser-cooled ion would still essentially be zero. Simply increasing the field gradient given in (52) by a factor 2 removes all possible coincidences of first-order and second-order resonances. Resonances of order three or higher in the effective Lamb–Dicke parameter $\eta'$ possibly still coincide with the useful ones. However their excitation will be suppressed by at least a factor $(\eta')^2$ compared to the first-order resonances.

An example may illustrate how the required gradients can be generated: Using a coil of 1 mm diameter (approximately the size of the ion traps employed for the experimental work described in this article) with 3 windings and running a current of 3.3 A through them produces a field gradient up to 20 T/m over the required distance. With additional coils the gradient can be modeled to have a desired spatial dependence. With small permanent magnets gradients of a few hundred T/m are easily generated.

**Coupling internal and external dynamics**    In the previous paragraphs it was shown that a magnetic field gradient applied to a linear ion trap allows for individual addressing of ions in frequency space. In order to create entangled states between internal and motional degrees of freedom of one particular ion it is obviously necessary to couple internal and external dynamics. If this coupling is possible, then the qubit state of a particular ion may be "written" into the vibrational motion of the ion string, and in subsequent operations transferred to another qubit, or quantum dynamics of one qubit conditioned on the state of another can be performed. At the beginning of this section, the physical reason for coupling of internal and external states was outlined, if laser light is used to drive an internal resonance. If mw or rf radiation is used, the recoil on the ion upon absorption or emission of a photon is not sufficient to excite motional states of the ion (the LDP is vanishingly small). However, in the presence of a magnetic field gradient motional quanta can nevertheless be created or annihilated in conjunction with changing the internal state of an ion (Mintert and Wunderlich, 2001). The physical origin of this effect will be discussed in what follows.

Figure 18 displays two internal states of an ion and a phase space diagram of a harmonic oscillator (an eigenmode of the ion string). The internal states of the ion are, in the presence of an axial magnetic field gradient, Zeeman shifted as a function of position along the axial direction. In Fig. 18 the derivative of the Zeeman shift with respect to the magnetic field has a different sign for the lower energy state $|0\rangle$ and the upper state $|1\rangle$. The position-dependent Zeeman shift gives rise to a force acting on the ion in addition to the electrodynamic and Coulomb potentials such that its equilibrium position is slightly different, depending on whether it is in state
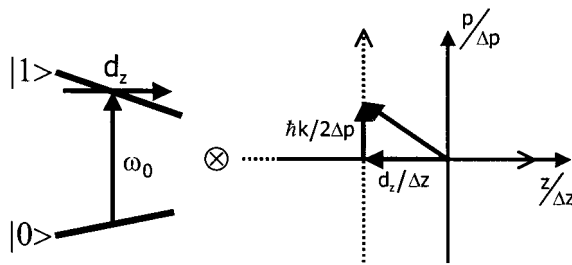


FIG. 18. Illustration of the coupled system 'qubit $\otimes$ harmonic oscillator' in a trap with magnetic field gradient. Internal qubit transitions lead to a displacement $d_z$ of the ion from its initial equilibrium position and consequently to the excitation of vibrational motion. In the formal description the usual Lamb–Dicke parameter is replaced by a new effective one (see text).

$|0\rangle$ or $|1\rangle$. Consequently, if an electromagnetic field is applied to drive this qubit resonance, a transition between the two states $|0\rangle$ and $|1\rangle$ will be accompanied by a change of the equilibrium position of the ion,

$$d_z^{(nj)} = -\hbar \frac{\partial_z \omega_{01}^{(j)}}{m v_n^2}. \tag{53}$$

In the phase space diagram of the harmonic oscillator this gives rise to a corresponding shift along the position coordinate together with a shift along the momentum coordinate. (The latter, however, is negligibly small in the microwave regime and is exaggerated in the sketch in Fig. 18). Thus, the oscillator will be excited and oscillate about its new equilibrium position. In Mintert and Wunderlich (2001) it is shown that the formal description of this coupling between internal and external dynamics is identical to the one used for the coupling induced by optical radiation (Eq. 46). The usual LDP is replaced by an effective new parameter

$$\eta'_{nj} e^{i\phi_j} \equiv \eta_n S_{nj} + i\epsilon_{nj}. \tag{54}$$

When using mw radiation and appropriately choosing the trap parameters secular axial frequency $v_1$ and magnetic field gradient, then $\eta_n S_{nj} \ll \epsilon_{nj}$ and we have $\eta_{nj} \approx \epsilon_{nj}$ with

$$\epsilon_{nj} \equiv S_{nj} \frac{-d_z^{(nj)}}{\Delta z_n} = S_{nj} \frac{\Delta z_n \partial_z \omega_{01}^{(j)}}{v_n}. \tag{55}$$

The numerator on the rhs of Eq. (55) contains the spatial derivative of the resonance frequency of qubit $j$ times the extension $\Delta z_n$ of the ground state wave function of mode $n$, that is, the variation of the internal transition frequency of qubit $j$ when it is moved by a distance $\Delta z$. Thus, the coupling constant $\epsilon_{nj}$ is proportional to the ratio between this frequency variation and the frequency of vibrational mode $n$. The strength of the coupling between an ion's internal dynamics and the motion of the ion string is different for each ion $j$ and depends on the vibrational mode $n$: $S_{nj}$ is a measure for how much ion $j$ participates in the motion of vibrational mode $n$.

All optical schemes devised for conditional quantum dynamics with trapped ions can also be applied in the microwave regime, despite the negligible recoil associated with this type of radiation. This includes, for instance, the proposal presented in Cirac and Zoller (1995) that requires cooling to the motional ground state, and the proposals reported in

Sørensen and Mølmer (2000) and Jonathan and Plenio (2000) (the latter two work also with ions in thermal motion).

**Trapped ions as a *N*-qubit molecule**   The Hamiltonian describing a string of trapped two-level ions in a trap with axial magnetic field gradient (without additional radiation used to drive internal transitions) has been shown to read (Wunderlich, 2001)

$$H = \frac{\hbar}{2}\sum_{j=1}^{N}\omega_j(z_{0,j})\sigma_{z,j} + \sum_{n=1}^{N}\hbar\nu_n(a_n^\dagger a_n) - \frac{\hbar}{2}\sum_{i<j}^{N}J_{ij}\sigma_{z,i}\sigma_{z,j}. \tag{56}$$

The first sum on the rhs of Eq. (56) represents the internal energy of the collection of $N$ ions. The qubit angular resonance of ion $j$ at its equilibrium position $z_{0,j}$ is $\omega_j$. The second term sums the energy of $N$ axial vibrational modes. These first two terms represent the usual Hamiltonian for a string of two-level ions confined in a harmonic potential (James, 1998). The new spin–spin coupling term (last sum in Eq. 56) arises due to the presence of the magnetic field gradient. Here,

$$J_{ij} \equiv \sum_{n=1}^{N}\nu_n\epsilon_{ni}\epsilon_{nj}. \tag{57}$$

The pairwise coupling (57) between qubits $i$ and $j$ is mediated by the vibrational motion. Therefore, it contains terms quadratic in $\epsilon$, and the coupling of qubit $i$ and $j$ to the vibrational motion has to be summed over all modes.

As an example, Table 1 shows the spin–spin coupling constants between 10 $^{171}\mathrm{Yb}^+$ ions confined in a linear trap ($\nu_1 = 100 \times 2\pi\,\mathrm{kHz}$) with a magnetic field gradient of 25 T/m. The application of NMR-type quantum logic operations to such an artificial molecule is facilitated by the fact that individual qubit resonances are widely separated in frequency (in this example the frequency "gap" between neighboring ions is about 1 MHz) as compared to typical NMR experiments (Vandersypen *et al.*, 2001). In addition, the coupling constants $J_{ij}$ have similar and nonzero values for all pairs of spins.

In a "real" molecule different nuclear spins share binding electrons that generate a magnetic field at the location of the nuclei, and the energy of a nuclear spin exposed to the electrons' magnetic field depends on the charge distribution of the binding electrons. If a particular nuclear spin is flipped, the interaction with the surrounding electrons will slightly change the electrons' charge distribution which in turn may affect the energy of other

Table I

Spin–spin coupling constants $J_{ij}/2\pi$ in units of Hz for 10 $^{171}$Yb$^+$ ions in a linear trap characterized by the angular frequency of the COM vibrational mode $\nu_1 = 100 \times 2\pi$ kHz using a static field gradient of 25 T/m.

| $i$ | $J_{i1}$ | $J_{i2}$ | $J_{i3}$ | $J_{i4}$ | $J_{i5}$ | $J_{i6}$ | $J_{i7}$ | $J_{i8}$ | $J_{i9}$ |
|---|---|---|---|---|---|---|---|---|---|
| 1 | | | | | | | | | |
| 2 | 54.61 | | | | | | | | |
| 3 | 41.36 | 48.12 | | | | | | | |
| 4 | 34.15 | 38.89 | 44.74 | | | | | | |
| 5 | 29.40 | 33.17 | 37.44 | 43.04 | | | | | |
| 6 | 25.92 | 29.09 | 32.55 | 36.77 | 42.52 | | | | |
| 7 | 23.19 | 25.93 | 28.88 | 32.35 | 36.77 | 43.04 | | | |
| 8 | 20.92 | 23.33 | 25.90 | 28.88 | 32.55 | 37.44 | 44.74 | | |
| 9 | 18.93 | 21.07 | 23.33 | 25.93 | 29.09 | 33.17 | 38.89 | 48.12 | |
| 10 | 17.04 | 18.93 | 20.92 | 23.19 | 25.92 | 29.40 | 34.15 | 41.36 | 54.61 |

nuclear spins. This indirect spin–spin coupling is realized here in a different way: the role of the electrons' magnetic field is replaced by the vibrational motion of the ions.

Usual ion trap schemes take advantage of motional sidebands that accompany qubit transitions. Instead, the spin–spin coupling that arises in a suitably modified trap may be directly used to implement conditional dynamics using NMR methods. The collection of trapped ions can thus be viewed as a $N$-qubit molecule with adjustable coupling constants (Wunderlich, 2001). Making use of this spin–spin coupling does not involve real excitation of vibrational motion. In this sense it is similar to a scheme for conditional quantum dynamics that uses optical 2-photon transitions detuned from vibrational resonances (Sorensen and Molmer, 2000), and, thus should be tolerant against thermal motion of the ions.

## C. COHERENT OPTICAL EXCITATION WITH BA$^+$ AND YB$^+$ IONS

This section is devoted to another possible, more "traditional" avenue toward quantum computation with trapped ions: employing an optical transition as a qubit. Since the relaxation rates of the states acting as a qubit eventually limit the time available for coherent manipulation, the use of two states connected via an electric dipole allowed transition is not a good

choice. Therefore, the electronic ground state of an ion (usually one specific Zeeman sublevel) and a metastable excited state have been chosen as qubit states in various experiments (Appasamy *et al.*, 1998; Roos *et al.*, 1999; Barton *et al.*, 2000). Here, we report on experiments with $Ba^+$ and $^{172}Yb^+$ ions where the electric quadrupole (E2) resonance $^2S_{1/2} - ^2D_{5/2}$ serves as the qubit.

### C.1. Rabi oscillations on optical E2 resonance in $Ba^+$

The lifetime of the metastable state $^2D_{5/2}$ ($\approx 34\,s$) is long on the timescale of typical coherent operations on this transition. Thus, the useful coherence time for quantum logic operations with this qubit transition is essentially limited (*i*) by the inverse emission bandwidth of laser light close to $1.76\,\mu m$ driving the E2 resonance, and (*ii*) by the stability of static magnetic fields that lift the degeneracy of Zeeman states. Exciting sideband resonances of this E2 transition allows for coupling of internal and external degrees of freedom (compare Section VI.B).

   $Ba^+$-ions are confined in a 1-mm-diameter Paul trap and irradiated by laser light at 493 nm (green light) for excitation of resonance fluorescence on the $^2S_{1/2} - ^2P_{1/2}$ transition (compare Fig. 19). This laser is usually detuned a few ten MHz below resonance for cooling the ions. Tunable light close to 493 nm is obtained by first generating light near 986 nm by a diode laser (stabilized to a reference resonator), and then frequency doubling the infrared light in a ring resonator containing a $KNbO_3$ crystal as a nonlinear element. A dye laser at 650 nm (red light) prevents optical pumping into the $^2D_{3/2}$ level. The fluorescence signal is recorded by photon counting. A static magnetic field defines the quantization axis and lifts the degeneracy of the magnetic sublevels. The direction of propagation and the polarization of both light beams (green and red) are set perpendicular to the magnetic field. The power levels of the light fields are stabilized by electro-optic modulators.

   The attainable Rabi frequency on the optical E2 resonance $S_{1/2}–D_{5/2}$ near 1762 nm (having a spectral width of 5 mHz) is limited by the available intensity of the light exciting this transition, and by the emission bandwidth, $\Delta\omega$ of the laser light. In addition, $\Delta\omega$ determines the coherence time of the qubit. A color-center laser that delivered up to 150 mW of light near 1762 nm with an effective emission bandwidth $\Delta\omega \approx 30 \times 2\pi\,kHz$ ($1/e^2$ full width of a Gaussian profile) was previously in use to excite this resonance (Appasamy *et al.*, 1998). The considerable effort that has to be devoted to the preparation of suitable NaCl crystals, the necessity to always maintain the laser medium at liquid nitrogen temperature, and the need for an Argon ion laser that ensures the correct polarization of the color-centers, in
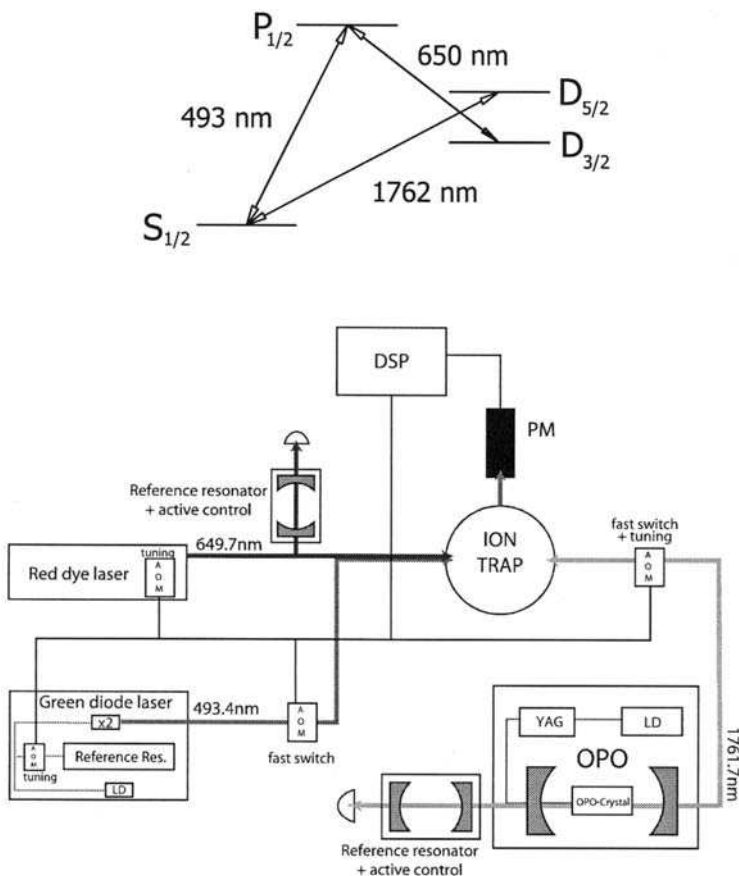
FIG. 19. (a) Relevant energy levels and transitions in $^{138}$Ba$^+$. (b) Schematic drawing of major experimental elements. OPO: Optical parametric oscillator; YAG: Nd:YAG laser; LD: laser diode; DSP: Digital signal processing system allows for real time control of experimental parameters; AOM: Acousto-optic modulators used as optical switches and for tuning of laser light; PM: Photo multiplier tube, serves for detection of resonance fluorescence. All lasers are frequency and intensity stabilized (not shown).

addition to the pump laser at 1064 nm are but a few of the obstacles that make such a laser a time consuming and not very economical instrument. This laser was replaced by a continuous wave optical parametric oscillator (Linos AG) emitting light in the required wavelength range. In order to attain the desired long-term stability of the emission frequency, a highly stable reference resonator suspended in ultra-high vacuum was used.

Insensitivity against vibrations and variations in temperature and air pressure is thus ensured (Leick, 2000).

Figure 20 shows Rabi oscillations on the carrier transition of the E2-resonance in $Ba^+$. Each data point is obtained by executing the following sequence 600 times: (i) the infrared light driving the E2 transition is switched on for a time $\tau$ indicated on the abscissa in Fig. 20 while the green light exciting the dipole resonance $S_{1/2}$–$P_{1/2}$ is turned off. (ii) Laser light near 493 nm is turned on for 1 ms, and scattered light is collected during this time for state-selective detection. Either scattered photons will be detected during the last step, indicating that the state of the ion is $S_{1/2}$ at the end of step ii (the registered number of photons is Poisson distributed around a mean value of typically 10 counts). Or, if no photon counts are registered, the ion was in state $D_{5/2}$. Thus, a trajectory of "on" (resonance fluorescence is observed) and "off" (absence of resonance fluorescence) events is recorded. A pair of "on"–"off" events indicates a transition from state $S_{1/2}$ to state $D_{5/2}$. The probability for absorption of an IR photon is calculated by dividing the number of these excitation events by the number of "on" events (total number of tries of excitation) in a trajectory. The probability for emission is obtained analogously. In Fig. 20 absorption and emission probability from one trajectory for a given time $\tau$ have been averaged to yield the transition probability between states $S_{1/2}$ and

$D_{5/2}$. A fit of the data displayed in Fig. 20 yields a Rabi frequency of $71.4 \times 2\pi$ kHz and a transversal relaxation time of $100\,\mu$s. Dephasing is determined by the emission bandwidth of the IR laser which will be further narrowed by improved frequency locking of the IR laser in future experiments.

## C.2. Lifetime measurement of the $D_{5/2}$ state in $Ba^+$

When using the metastable $D_{5/2}$ state in $Ba^+$ as one quantum state of a qubit, or for the potential application of electrodynamically trapped $Ba^+$ as a frequency standard, it is useful to know the lifetime of this state. $Ba^+$ is also a promising candidate to measure parity nonconserving interactions in atoms complementing high-energy experiments in search of new physics beyond the standard model (Fortson, 1993; Geetha *et al.*, 1998). Comparison between results obtained from atomic structure theory and experimentally determined values are thus important. Previous attempts of determining the lifetime of the $D_{5/2}$ state have yielded different values in experiments with single and many ions, respectively (Plumelle *et al.*, 1980, Nagourney *et al.*, 1986; Madej and Sankey, 1990). In recent experiments on $Ca^+$ it was found that the lifetime of the $D_{5/2}$ state in this ion species depended on the power of an additional laser used to repump the ion from the metastable $D_{3/2}$ state (Block *et al.*, 1999).

We have determined the lifetime of the $D_{5/2}$ state in $Ba^+$ using the quantum jump method. The resulting experimental lifetime is limited by collisions with background gas to 21 s which agrees well with the results reported in Madej and Sankey (1990). We did not find a dependence on the power or detuning of the laser used to scatter resonant light on the $S_{1/2}$–$P_{1/2}$ transition or of the "repumper" from the $D_{3/2}$ state.

## C.3. Cooling of a pair of $Ba^+$ ions

Cooling of the collective motion of several particles, not necessarily to the motional ground state (Sørensen and Mølmer, 2000; Jonathan and Plenio, 2001) is prerequisite for implementing conditional quantum dynamics with trapped ions. We have studied the collective vibrational motion of two trapped $^{138}Ba^+$ ions cooled by laser light close to the resonances corresponding to the $S_{1/2}$–$P_{1/2}$ (493 nm, green light) and $P_{1/2}$–$D_{3/2}$ (650 nm, red light) transition, respectively.

When two ions are confined in a nearly spherically symmetric Paul trap, and if they are sufficiently laser cooled, then we always observe them crystallizing at the same locations. The crystallization at preferred locations is explained by the slight asymmetry of the effective trapping potential, that is, $\nu_x \neq \nu_y \neq \nu_z$, where $\nu_{x,y,z}$ are the angular frequencies of the center-

of-mass-mode of the secular motion in different spatial directions. The Coulomb potential makes the ions repel each other, and the ion crystal tends to align along the axis of weakest confinement by the electrodynamic potential.

The potential along the $z$-direction is steeper than in the $xy$-plane. Consequently, if cooled well enough, the ions stay in this plane. Since $\nu_y > \nu_x$ they are not free to rotate in the $xy$-plane, and instead would have to surmount an azimuthal potential barrier at $\phi = \pi/2$ ($\phi = \arctan(y/x)$) in order to exchange places. However, if the vibrational energy of the relative motion of the two ions in the $\tilde{y}$-mode (Reiß *et al.*, 2002) exceeds the azimuthal barrier height, then the ions are free to rotate in the $xy$-plane. Depending on the parameter settings (detuning and intensity) of the cooling lasers, these different motional states corresponding to different temperatures are indeed observed experimentally.

If, for instance, the intensity and frequency of the green laser is held fixed and the red laser's frequency is scanned, then a characteristic spectrum displaying dark resonances is obtained (Fig. 21). Whenever the detuning of the red laser, with respect to a resonance between a Zeeman level of the $D_{3/2}$ state and one of the $P_{1/2}$ state equals the detuning of the green laser with respect to a resonance between Zeeman levels of the $P_{1/2}$ and $S_{1/2}$ states, a coherent superposition of the Zeeman levels of $S_{1/2}$ and $D_{3/2}$ is created that does not couple to the light field anymore. The appearance of four dark resonances is due to the selection rules for dipole allowed transitions between Zeeman sublevels of the $S_{1/2}$, $P_{1/2}$, and $D_{3/2}$ electronic states when both light fields are linearly polarized perpendicular to the magnetic field that defines the quantization axis. Fitting such an excitation spectrum using the optical Bloch equations allows for the determination of intensity and detuning of the laser light, as well as of the strength of the applied magnetic field. Upon scanning the red laser it is observed that ions take on different states of motion: either they crystallize at fixed locations or they form a ring-shaped structure when their thermal energy is sufficient to surmount the azimuthal potential barrier.

Using the laser parameters determined from a fit of the excitation spectrum, the expected temperature of the ions can be derived from detailed numerical calculations of laser cooling taking into account the Zeeman structure of the energy levels (Reiß *et al.*, 2002). It turns out that the transition from an ion crystal to the ring structure occurs at that detunings of the red laser where theory predicts laser cooling to turn into heating. The ions gain enough energy from scattering photons to surmount the azimuthal potential barrier and appear as a ring on the spatially resolving photo detector. The transition from cooling to heating occurs when the red laser is
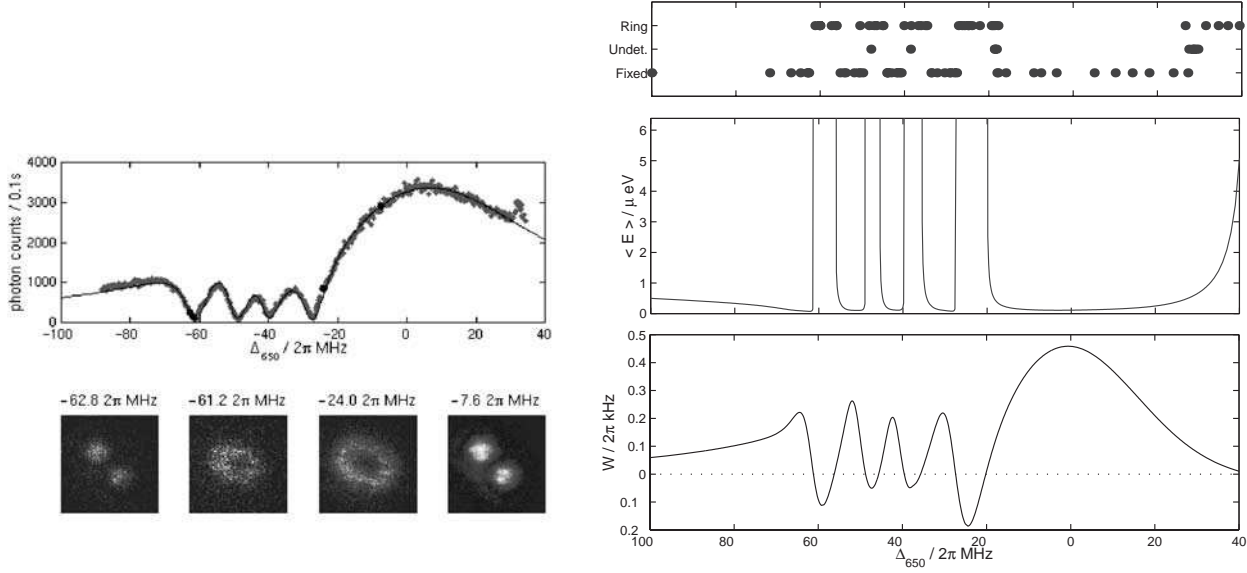
FIG. 21. Left top: Fluorescence of two trapped ions as a function of laser detuning. Left bottom: Two trapped Ba$^+$ ions show different motional states depending on laser parameters. Spatial distribution of the two ions at the detunings indicated above. Right top: Observed motional states for different detunings of the 650 nm light. The dots correspond to individual observations. Right middle: Mean motional energy in the $\tilde{y}$-mode calculated from theory. Right bottom: Cooling rate for the $\tilde{y}$-mode calculated from theory. Figure taken from (Reiß *et al.*, 2002)

scanned across a dark resonance with increasing frequency: as soon as it is blue detuned with respect to the closest dark resonance, the cooling rate is reduced to zero and with further increasing laser frequency becomes negative (that is, heating occurs). Increasing the laser's frequency even more means that the red laser is further blue detuned with respect to the dark resonance that was just passed. At the same time, however, the next resonance is approached relative to which the laser is red detuned and the cooling rate increases again. It should be noted that Raman scattering responsible for these processes occurs when both lasers are *red* detuned relative to the main resonance.

Very good agreement is found between the theoretical prediction of the transition of the ions' motional state and experimental observations. In addition, parameter regimes of the laser light irradiating the ions are identified that imply most efficient laser cooling and are least susceptible to drifts, fluctuations, and uncertainties in laser parameters. When applied to cooling of a string of ions in a linear trap, the multidimensional parameter space allows to identify regions where cooling is most efficient for all vibrational modes. In particular, the magnetic field can be increased for a larger separation of the dark resonances.

Cooling of different vibrational modes is also achieved with electromagnetically induced transparency (EIT) cooling (Morigi *et al.*, 2000; Roos *et al.*, 2000). In that scheme, too, atomic resonances are shaped by two laser fields such that most efficient cooling for as many vibrational modes as possible is achieved.

### C.4. Coherent excitation of an E2 resonance in $^{172}Yb^+$

The electric quadrupole resonance $S_{1/2} \leftrightarrow D_{5/2}$ in $^{172}Yb^+$ with a natural linewidth of $6 \times 2\pi$ Hz (Fawcett and Wilson, 1991) may be used as a qubit, too. The relevant energy levels involved in the investigation of coherent excitation of this transition are shown in Fig. 1. The E2-transition is driven by light of a frequency-doubled diode laser at 411 nm. The population of the $S_{1/2}$ ground state is probed by exciting resonance fluorescence on the strong monitor transition $S_{1/2} \leftrightarrow P_{1/2}$. In addition to spontaneous decay into the $S_{1/2}$ ground state, the state $D_{5/2}$ might decay into the extremely long-lived level $F_{7/2}$ (lifetime $> 10$ years (Roberts *et al.*, 1997)) with probability 0.81. The population trapped in the $F_{7/2}$ state is brought back into the $S_{1/2}$ ground state via the jk-coupled (Cowan, 2001) level $D[5/2]_{5/2}$ by illuminating the ion continuously with laser light at 638 nm. The depopulation time depends on the laser intensity and is found to be $\tau_{638} =$ ms in the limit of high intensity.
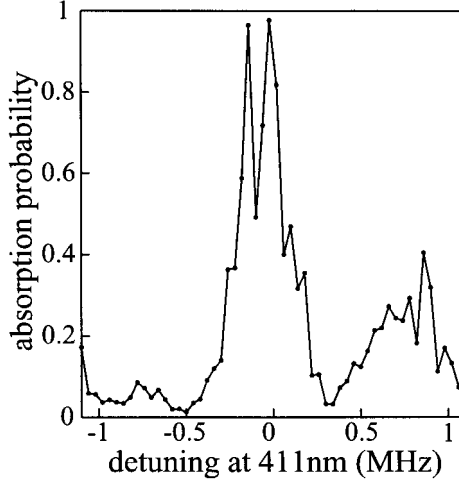
FIG. 22. Absorption spectrum between the Zeeman states $|S_{1/2}, m_j = 1/2\rangle \leftrightarrow |D_{5/2},$ $m_j = 1/2\rangle$ (E2-transition). The absorption probability on resonance exceeds 0.9 which proves coherent excitation. The sidebands at $\pm 750$ kHz next to the carrier are caused by the secular motion of the ion.

An absorption spectrum of the E2 transition is obtained by scanning the frequency of the light at 411 nm in steps of 40 kHz across the resonance of a selected Zeeman component. At every frequency step a series of 500 pairs of driving pulses ($\tau_{411} = 5$ ms) and probing pulses ($\tau_{369} = 10$ ms) is recorded resulting in a trajectory of "on" and "off" observations. The absorption probability on the $|S_{1/2}, m_j = 1/2\rangle \leftrightarrow |D_{5/2}, m_j = 1/2\rangle$ transition, determined in the same way as described in the previous section, is plotted in Fig. 22 versus the detuning of the frequency of the light field at 411 nm.

The measured absorption probability on the carrier transition exceeds 0.9 verifying coherent excitation of the E2 resonance. The structure seen in the carrier is due to Rabi oscillations (Balzer *et al.*, 2000; Wunderlich *et al.*, 2001). From the width of the carrier resonance the Rabi frequency is estimated to be $\approx 110$ kHz. A comparison of the experimental spectrum with numerical simulations using optical Bloch equations shows that the emission bandwidth of the laser field at 411 nm is less than 5 Hz in 5 ms.

Next to the carrier two sidebands are visible at $\pm 750$ kHz arising from the ion's axial secular motion in the pseudo harmonic potential of the electrodynamic trap. The asymmetry in the absorption probability between upper and lower sideband is due to sideband cooling on the E2 transition (to be detailed elsewhere.)

Employing optical E2 transitions, too, important steps toward quantum information processing have been experimentally realized. Because of the simple level structure of $^{138}$Ba$^+$, and of the long lifetime of its metastable D$_{5/2}$ state, this ion is well suited for experiments where coherent optical excitation is desired (for instance, in QIP).

# VII.  References

Abrams, D.S., and Lloyd, S. (1999). *Phys. Rev. Lett.* **83**, 5162.

Alter, O., and Yamamoto, Y. (1997). *Phys. Rev. A* **55**, R2499.

Alter, O., and Yamamoto, Y. (2001). "Quantum Measurement of a Single System." John Wiley and Sons Inc., New York.

Appasamy, B., Stalgies, Y., and Toschek, P.E. (1998). *Phys. Rev. Lett.* **80**, 2805.

Bagan, E., Baig, M., Brey, A., and Munoz-Tapia, R. (2000). *Phys. Rev. Lett.* **85**, 5230.

Bagan, E., Baig, M., Brey, A., and Munoz-Tapia, R. (2001). *Phys. Rev. A* **63**, 052309.

Bagan, E., Baig, M., and Munoz-Tapia. R. (2001). *Phys. Rev. A* **64**, 022305-1.

Bagan, E., Baig, M., and Munoz-Tapia, R. (2002). *arXiv guant-ph/0205026*.

Balzer, C., Hannemann, T., Reiß D, Neuhauser, W., Toschek, P.E., and Wunderlich, C. (2002a). *Laser Phys.* **12**, 729.

Balzer, C., Hannemann, T., Reiß D, Wunderlich, C., Neuhauser, W., and Toschek, P.E. (2002). *Opt. Commun.* **211**, 235.

Balzer, C., Huesmann, R., Neuhauser, W., and Toschek, P.E. (2000). *Opt. Commun.* **180**, 115.

Barenco, A., Bennett, C.H., Cleve, R., DiVincenzo, D.P., Margolus, N., Shor P., Sleator, T., Smolin, J.A., and Weinfurter, H. (1995). *Phys. Rev. A* **52**, 3457.

Barton, P.A., Donald, C.J.S., Lucas, D.M., Stevens, D.A., Steane, A.M., and Stacey, D.N. (2000). *Phys. Rev. A* **62**, 032503.

Bayes, T. (1763). *Phil. Trams. Roy. Soc. (London)* **53**, 370.

Bayes, T. (1958). *Biometrika* **45**, 293.

Becker, T., Zanthier, J., Nevsky, A., Schwedes, C., Skvortsov, M., Walther, H., and Peik, E. (2001). *Phys. Rev. A* **63**, 051802.

Beige, A., and Hegerfeldt, G. (1996). *Phys. Rev. A* **53**, 53.

Beige, A., and Hegerfeldt, G. (1997). *J. Phys. A: Math. Gen.* **30**, 1323.

Bennett, C.H., DiVincenzo, D.P., Fuchs, C.A., Mor, T., Rains, E., Shor, P.W., Smolin, J.A., and Wootters, W.K. (1999). *Phys. Rev. A* **59**, 1070.

Bergquist, J., Hulet, R., Itano, W., and Wineland, D. (1986). *Phys. Rev. Lett.* **57**, 1699.

Berry, D., and Wiseman, H. (2000). *Phys. Rev. Lett.* **85**, 5098.

Bertet, P., Osnaghi, S., Rauschenheutel, A., Nogues, G., Auffeves, A., Brune, M., Raimond, J.M., and Haroche, S. (2001). *Nature* **411**, 166.

Block, E., and Berman, P. (1991). *Phys. Rev. A.* **44**, 1466.

Block, M., Rehm, O., Seibert, P., and Werth, G. (1999). *Eur. Phys. J. D* **7**, 461.

Bohr, N. (1949). Ed. P.A. Schilipp, Library of Living Philosophers, Evaston, pp. 200–241.

Bohr, N. (1983). Ed. J.A. Wheeler, W.H. Zurek, Princeton University Press, Princeton, pp. 200–241.

Braginsky, V.B., and Khalili, F.Y. (1992). "Quantum Measurement." Cambridge University Press, Cambridge, UK.

Brukner, C., and Zeilinger, A. (1999). *Phys. Rev. Lett.* **83**, 3354.

Brukner, C., and Zeilinger, A. (2001). *Phys. Rev. A* **63**, 022113.

Brune, M., Hagley, E., Dreyer, J., Maitre, X., Maali, A., Wunderlich, C., Raimond, J.M., and Haroche, S. (1996). *Phys. Rev. Lett.* **77**, 4887.

Bužek, V., Derka, R., Adam, G., and Knight, P.L. (1998). *Ann. Phys.* **266**, 454.

Bužek, V., Hillery, M., and Werner, R.F. (1999). *Phys. Rev. A* **60**, R2626.

Bužek, V., Hillery, M., and Werner, R.F. (2000). *J. Mod. Opt* **47**, 211.

Chapman, M.S., Hammond, T.D., Lenef, A., Schmiedmayer, J., Rubenstein, R.A., Smith, E., and Pritchard, D.E. (1995). *Phys. Rev. Lett.* **75**, 3783.

Chuang, I.L., Vandersypen, L.M.K., Zhou, X., Leung, D.W., and Lloyd, S. (1998). *Nature* **393**, 143.

Church, D., and Dehmelt, H. (1969). *J. Appl. Phys.* **40**, 3421.

Cirac, J.I., and Zoller, P. (1995). *Phys. Rev. Lett.* **74**, 4091.

Cleve, R., Ekert, A., Macchiavello, C., and Mosca, M. (1998). *Proc. R. Soc. Lond. A* **454**, 339.

Cook, R. (1988). *Phys. Scrip.* **T21**, 49.

Corney, A. (1977). "Atomic and Laser Spectroscopy." Clarendon Press, Oxford.

Cowan, R.D. (2001). "The theory of atomic structure and spectra." University of California Press, Berkeley.

Derka, R., Bužek, V., and Ekert, A.K. (1998). *Phys. Rev. Lett.* **80**, 1571.

Deutsch, D. (1985). *Proc. R. Soc. London A* **400**, 97.

Dicke, R.H. (1981). *Am. J. Phys.* **49**, 925.

Diddams, S., Udem, T., Bergquist, J., Curtis, E., Drullinger, R., Hollberg, L., Itano, W., Lee, W., Oates, C., Vogel, K., and Wineland, D. (2001). *Science* **293**, 825.

Diedrich, F., and Walther, H. (1987). *Phys. Rev. Lett.* **58**, 203.

DiVincenzo, D.P. (1995). *Phys. Rev. A* **51**, 1015.

Dubin, D.H.E. (1993). *Phys. Rev. Lett.* **71**, 2753.

Dürr, S., Nonn, T., and Rempe, G. (1998). *Nature* **395**, 33.

Dürr, S., Nonn, T., and Rempe, G. (1998a). *Phys. Rev. Lett.* **81**, 5705.

Dürr, S., Nonn, T., and Rempe, G. (1998b). *Nature* **395**, 33.

Einstein, A., Podolsky, B., and Rosen, N. (1935). *Phys. Rev.* **47**, 777.

Elitzur, A., and Vaidman, L. (1993). Found *Phys.* **23**, 987.

Englert, B.G. (1996). *Phys. Rev. Lett.* **77**, 2154.

Facchi, P., Nakazato, H., and Pascazio, S. (2001). *Phys. Rev. Lett.* **86**, 2699.

Fawcett, B.C., and Wilson, M. (1991). *At. Data Nucl. Data Tables* **47**, 241.

Feynman, R., Leighton, R., and Sands, M. (1965). "The Feynman Lectures on Physics." Vol. III, Addison Wesley Reading.

Feynman, R.P. (1982). *Int. J. Theoret. Phys.* **21**, 467.

Fischer, D.G., Kienle, S.H., and Freyberger, M. (2000). *Phys. Rev. A* **61**, 032306.

Fischer, E. (1959). *Z. Physik* **156**, 1.

Fischer, M., Gutierrez-Medina, B., and Raizen, M.G. (2001). *Phys. Rev. Lett* **87**, 040402.

Fonda, L., Ghiradi, G.C., and Rimini, A. (1978). *Rep. Prog. Phys.* **41**, 587.

Fonda, L., Ghirardi, G., Rimini, A., and Weber, T. (1973). *Nuovo Cimento A* **15**, 689.

Fortson, N. (1993). *Phys. Rev. Lett.* **70**, 2383.

Frerichs, V., and Schenzle, A. (1991). *Phys. Rev. A* **44**, 1962.

Freyberger, M., Bardroff, P., Leichtle, C., Schrade, G., and Schleich, W. (1997). *Phys. World* **10**(11), 41.

Friedman, J.R., Patel, V., Chen, W., Tolpygo, S., and Lukens, J. (2000). *Nature* **406**, 43.

Fujiwara, A., and Algoet, P. (1999). *Phys. Rev. A* **59**, 3290.

Gagen, M.J., and Milburn, G.J. (1993). *Phys. Rev. A* **47**, 1467.

Geetha, K., Dilip Singh, A., Das, B., and Unnikrishnan, C. (1998). *Phys. Rev. A* **58**, R16.

Georgeot, B., and Shepelyansky, D.L. (2001a). *Phys. Rev. Lett.* **86**, 2890.

Georgeot, B., and Shepelyansky, D.L. (2001b). *Phys. Rev. Lett.* **86**, 5393.

Georgeot, B., and Shepelyansky, D.L. (2002). *Eur. Phys. J. D* **19**, 263.

Gerry, C.C. (1996). *Phys. Rev. A* **53**(2), 1179.

Gershenfeld, N., and Chuang, I.L. (1997). *Science* **275**, 350.

Ghosh, P.K. (1995). "Ion Traps." Clarendon Press, Oxford.

Gill, R.D., and Massar, S. (2000). *Phys. Rev. A* **61**, 042312-1.

Giulini, D., Joos, E., Kiefer, C., Kupsch, J., Stamatescu, I.O., and Zeh, H.D. (1996). "Decoherence and the Appearance of a classical world in Quantum Theory." Springer, Berlin.

Gruska, J. (1999). "Quantum Computing." McGraw-Hill, London.

Guthöhrlein, G., Keller, M., Hayasaka, K., Lange, W., and Walther, H.

(2001). *Nature* **414**, 49.

Hannemann, T., Reiß D, Balzer, C., Neuhauser, W., Toschek, P.E., and Wunderlich, C. (2002). *Phys. Rev. A* **65**, 050303(R)/1.

Hannemann, T., Reiß D, Neuhauser, W., and Wunderlich, C. *n.d. in preparation*.

Haroche, S. (1971). *Ann. Phys.* (Paris) **6**, 189 and 327.

Herzog, T.J., Kwiat, P.G., Weinfurter, H., and Zeilinger, A. (1995). *Phys. Rev. Lett.* **75**, 3034.

Home, D., and Whitaker, M. (1997). *Ann. Phys. N.Y.* **258**, 237.

Howe, M.A., Kielpinski, D., Meyer, V., Sackett, C., Itano, W., Monroe, C., and Wineland, D. (2001). *Nature* **409**, 791.

Hughes, R., James, D., Gomez, J., Gulley, M., Holzscheiter, M., Kwiat, P., Lamoreaux, S., Peterson, C., Sandberg, V.D., Schauer, M., Summons, C.M., Thorburn, C., Tupa, D., Wang, P., and White, A. (1998). *Fortschritte der Physik* **46**, 329.

Ifflander, R., and Werth, G. (1977). *Opt. Comm.* **21**, 411.

Itano, W., Heinzen, D., Bollinger, J., and Wineland, D. (1990). *Phys. Rev. A* **41**, 2295.

Itano, W., Heinzen, D., Bollinger, J., and Wineland, D. (1991). *Phys. Rev. A* **43**, 5168.

James, D.F.V. (1998). *App. Phys. B* **66**, 181.

Jonathan, D., and Plenio, M.B. (2001). *Phys. Rev. Lett.* **87**, 127901.

Jonathan, D., Plenio, M.B., and Knight, P.L. (2000). *Phys. Rev. A* **62**, 042307.

Jones, J. (2001). *Progress in Nuclear Magnetic Resonance Spectroscopy* **38**, 325.

Jones, J.A., and Mosca, M. (1998). *J. Chem. Phys.* **109**, 1648.

Jones, K.R.W. (1994). *Phys. Rev. A* **50**, 3682.

Khalfin, L. (1968). *JETP Lett.* **8**, 65.

Knight, P. (1998). *Nature* **395**, 12.

Kofman, A.G., and Kurizki, G. (2000). *Nature* **405**, 546.

Kwiat, P.G., Steinberg, A.M., and Chiao, R.Y. (1992). *Phys. Rev. A* **45**, 7729.

Kwiat, P.G., Weinfurter, H., Herzog, T., Zeilinger, A., and Kasevich, M.A. (1995). *Phys. Rev. Lett.* **74**, 4763.

Kwiat, P.G., White, A.G., Mitchell, J.R., Nairz, O., Weihs, G., Weinfurter, H., and Zeilinger, A. (1999). *Phys. Rev. Lett.* **83**, 4725.

Latorre, J.I., Pascual, P., and Tarrach, R. (1998). *Phys. Rev. Lett.* **81**, 1351.

Leick, P. (2000). "Ein stabiler Referenzresonator für die Spektroskopie auf dem elektrischen Quadrupolübergang $6^2S_{1/2}$ $5^2D_{5/2}$ des Ba+-Ions." Diplomarbeit Institut für Laserphysik Universität, Hamburg.

Lewenstein, M., Bruss, D., Cirac, J., Kraus, B., Kus, M., Samsonowicz, J., Sanpera, A., and Tarrach, R. (2000). *J. Mod. Opt.* **47**, 2481.

Lvovsky, A.I., Hansen, H., Aichele, T., Benson, O., Mlynek, J., and Schiller, S. (2001). *Phys. Rev. Lett.* **87**, 050402.

Madej, A., and Sankey, J. (1990). *Phys. Rev. A* **41**, 2621.

Maitre, X., Hagley, E., Dreyer, J., Maali, A., Wunderlich, C., Brune, M., Raimond, J.M., and Haroche, S. (1997). *J. Mod. Opt.* **44**, 2023.

Massar, S., and Popescu, S. (1995). *Phys. Rev. Lett.* **74**, 1259.

Massar, S., and Popescu, S. (2000). *Phys. Rev. A* **61**, 062303-1.

Messiah, A. (1976). "Quantenmechanik, Bd. 1." Walter de Gruyter, Berlin.

Meyer, V., Rowe, M.A., Kielpinski, D., Sackett, C.A., Itano, W.M., Monroe, C., and Wineland, D.J. (2001). *Phys. Rev. Lett.* **86**, 5870.

Mintert, F., and Wunderlich, C. (2001). *Phys. Rev. Lett.* **87**, 257904.

Misra, B., and Sudarshan, E.C.G. (1977). *J. Math. Phys. (N.Y.)* **18**, 756.

Mølmer, K., and Sørensen, A. (2000). *J. Mod. Opt.* **47**, 2515.

Morigi, G., Eschner, J., and Keitel, C.H. (2000). *Phys. Rev. Lett.* **85**, 4458.

Myatt, C., King, B., Turchettte, Q., Sackett, C., Kielpinski, D., Itano, W., Monroe, C., and Wineland, D. (2000). *Nature* **403**, 269.

Nägerl, H.C., Leibfired, D., Rohde, H. Thalhammer, G., Eschner, J., Schmidt-Kaler, F., and Blatt, R. (1999). *Phys. Rev. A* **60**, 145.

Nagourney, W., Sandberg, J., and Dehmelt, H. (1986). *Phys. Rev. Lett.* **56**, 2797.

Nakazato, H., Namiki, M., Pascazio, S., and Rauch, H. (1996). *Phys. Lett. A* **217**, 203.

Neuhauser, W., Hohenstatt, M., Toschek, P.E., and Dehmelt, H.G. (1978). *Phys. Rev. Lett.* **41**, 233.

Neuhauser, W., Hohenstatt, M., Toschek, P.E., and Dehmelt, H.G. (1980). *Phys. Rev. A* **22**, 1137.

Nielsen, M.A., and Chuang, I.L. (2000). "Quantum Computation and Quantum Information." Cambridge University Press, Cambridge, UK.

Parker, S., and Plenio, M.B. (2000). *Phys. Rev. Lett.* **85**, 3049.

Pascazio, S., and Namiki, N. (1994). *Phys. Rev. A* **50**, 4582.

Paul, W., Osberghaus, O., and Fischer, E., Westdeutscher Verlag, Cologne, (1958). *Forschungsberichte des Wirtschafts- und Verkehrsministeriums Nordrhein Westfalen* **415**.

Pellizzari, T. (1997). *Phys. Rev. Lett.* **79**, 5242.

Peres, A. (1980). *Am. J. Phys.* **48**, 931.

Peres, A., and Scudo, P.F. (2001). *Phys. Rev. Lett.* **86**, 4160.

Peres, A., and Wootters, W. (1991). *Phys. Rev. Lett.* **66**, 1119.

Plumelle, F., Desaintfuscien, M., Duchene, J., and Audoin, C. (1980). *Opt. Comm.* **34**, 71.

Powell, H., Segal, D., and Thompson, R. (2002). *Phys. Rev. Lett.* **89**, 093003.

Power, W.L., and Knight, P.L. (1996). *Phys. Rev. A* **53**, 1052.

Prestage, J.D., Dick, G.J., and Maleki, L. (1989). *J. Appl. Phys.* **66**, 1013.

Rafac, R., Young, B., Beall, J., Itano, W., Wineland, D., and Bergquist, J. (2000). *Phys. Rev. Lett.* **85**, 2462.

Raizen, M.G., Gilligan, J.M., Bergquist, J.C., Itano, W.M., and Wineland, D.J. (1992). *Phys. Rev. A* **45**, 6493.

Ramsey, N.F. (1956). "Molecular Beams" Oxford University Press, Oxford.

Raymer, M.G. (1997) *Contemp. Phys.* **38**, 343.

Reiß D, Abich, K., Neuhauser, W., Wunderlich, C., and Toschek, P.E. (2002). *Phys. Rev. A* **65**, 053401/1.

Renninger, M. (1960). *Z. Phys* **158**, 417.

Riebe, M. (2000). "Aufbau and Caarakterisierung eines Diodenlasers bei 638 nm für die Spektroskopie an gespeicherten Ytterbium-Ionen." Diplomarbeit Institut fiir Laserphysik Universität, Hamburg.

Rivest, R.L., Shamir, A., and Adleman, L.M. (1978). *Communications of the ACM* **21**, 120.

Roberts, M., Taylor, P., Barwood, G.P., Gill, P., Klein, H.A., and Rowley, W.R.C. (1997). *Phys. Rev. Lett.* **78**, 1876.

Roos, C.F., Leibfried, D., Mundt, A., Schmidt-Kaler, F., Eschner, J., and Blatt, R. (2000). *Phys. Rev. Lett.* **85**, 5547.

Roos, C., Zeiger, T., Rohde, H., Nägerl, H., Eschner, J., Leibfried, D., Schmidt-Kaler, F., and Blatt, R. (1999). *Phys. Rev. Lett.* **83**, 4713.

Sasura, M., and Buzek, V. (2002). *J. Mod. Opt.* **49**, 1593.

Sauter, T., Neuhauser, W., Blatt, R., and Toschek, P. (1986). *Phys. Rev. Lett.* **57**, 1696.

Schiffer, J.P. (1993). *Phys. Rev. Lett.* **70**, 818.

Special issue on quantum state preparation and measurement (1997)., edited by W.P. Schleich and M. Raymer. *J. Mod. Opt.* **44**(11/12).

Schmidt-Kaler, F., Roos, C., Nagerl, H., Rohde, H., Guide, S., Mundt, A., Leder-bauer, M., Thalhammer, G., Zeiger, T., Barton, P., Hornekaer, L. Reymond, G., Leibfried, D., Eschner, J., and Blatt, R. (2000). *J. Mod. Opt.* **47**, 2573.

Schrödinger, E. (1935). *Die Naturwassenschaften* **23**, 807, 823, 844.

Schubert, M., Siemers, I., Blatt, R., Neuhauser, W., and Toschek, P. (1992). *Phys. Rev. Lett.* **68**, 3016.

Scully, M.O., Englert, B.E., and Walther, H. (1991). *Nature* **351**, 111.

Scully, M.O., and Walther, H. (1998). *Foundations of Physics* **28**, 399.

Shannon, C.E. (1948). *Bell Syst. Tech. J.* **27**, 379.

Shor, P. (1994) ''Proceedings, 35th, Annual Symposium on Foundations of Computer Science.'' Santa Fe, NM, USA, November 2022, IEEE Computer Society Press p. 124.

Shor, P. (1997). *SIAM Journal of Computing* **26**, 1484.

Somaroo, S., Tseng, C.H., Havel, T.F., Laflamme, R., and Cory, D.G. (1999). *Phys. Rev. Lett.* **82**, 5381.

Sorensen, A., and Molmer, K. (2000). *Phys. Rev. A* **62**, 022311/1.

Spiller, T. (1994). *Phys. Lett. A* **192**, 163.

Steane, A. (1997). *Appl. Phys. B* **64**, 623.

Stenger, J., Tamm, C., Haverkamp, N., Weyers, S., and Telle, H. (2001). *Opt. Lett.* **26**, 1589.

Toschek, P.E., and Wunderlich, C. (2001). *Eur. J. Phys. D* **14**, 387.

van Enk, S.J., Kimble, H.J., Cirac, J.I., and Zoller, P. (1999). *Phys. Rev. A* **59**, 2659.

Vandersypen, L.M.K., Steffen, M., Breyta, G., Yannoni, C.S., Sherwood, M.H., and Chuang, I.L. (2001) *Nature* **414**, 883.

Vandersypen, L.M.K., Yannoni, C.S., and Chuang, I.L. (2000). *arXiv quant-ph/0012108*

von Neumann, J. (1932). ''Mathematische Grundlagen der Quantenmechanik.'' Springer Verlag, Berlin.

Walmsley, I.A., and Waxer, L. (1998). *J. Phys. B* **31**, 1825.

Wawer, R., Keller, M., Liebman, A., and Mahler, G. (1998) *Eur. Phys. J. D* **1**, 15.

Whitaker, M.A.B. (2000). *Progress in Quantum Electronics* **24**, 51.

White, A., James, D.F.V., Eberhard, P.H., and Kwiat, P.G. (1999). *Phys. Rev. Lett.* **83**, 3103.

Wilkinson, S.R., Bhaucha, C.F., Fischer, M.C., Madison, K.W., Morrow, P.R., Niu, Q., Sundaram, B., and Raizen, M.G. (1997). *Nature* **387**, 575.

Wineland, D.J., Drullinger, R.E., and Walls, F.L. (1978). *Phys. Rev. Lett.* **40**, 1639.

Wineland, D.J., Monroe, C., Itano, W.M., Leibfried, D., King, B.E., and Meekhof, D.M. (1998). *J. Res. Natl. Inst. Stand. Technol* **103**, 259.

Winter, R.G. (1961). *Phys. Rev.* **123**, 1503.

Wunderlich, C. (2001). in ''Laser Physics at the Limit.'' Springer Verlag, Heidelberg, Berlin-New York pp. 261–271.

Wunderlich, C., Balzer, C., and Toschek, P.E. (2001). *Z. Naturforsch* **56a**, 160.

Zurek, W.H. (1991). *Phys. Today* **44**(10), 36.

# SCATTERING AND REACTION PROCESSES IN POWERFUL LASER FIELDS

*DEJAN B. MILOŠEVIĆ[1] and FRITZ EHLOTZKY[2]*

[1]*Faculty of Science, University of Sarajevo, Zmaja od Bosne 35, 71000 Sarajevo, Bosnia and Herzegovina;* [2]*Institute for Theoretical Physics, University of Innsbruck, Technikerstrasse 25, A-6020 Innsbruck, Austria*

# I. Scattering Processes

## A. INTRODUCTION

Since the invention of the laser, physicists have been supplied with strong sources of coherent radiation which are now available in the frequency

---

*E-mail: Theoretical-Physik@uibk.ac.at

range between the far infrared and, at present, up to the vacuum–ultraviolet (VUV) and soft x-ray region. The investigations in the new field of laser physics gradually shifted with the rapid development of better and more powerful laser sources of very short pulse duration to their applications in a growing variety of different branches of physical research. This was motivated by the large number of hitherto unknown laser-induced phenomena which emerged and by their importance for both basic insight into atomic, molecular, and solid-state structures and for their practical applications in a large number of different fields of research like holography, fiber optics, tele-communications, material sciences, biology, plasma physics, thermonuclear fusion, and so on.

Quite general the scattering and reaction processes which take place in a powerful laser field can be divided into two main groups

(a) laser-assisted processes,
(b) laser-induced processes.

In the case (a) a basic process exists in the absence of the laser field and it is modified by the simultaneous interaction with laser radiation. In particular, both types of processes differ fundamentally by their reaction rates at lower laser intensities where perturbation theory applies. In the first case we find $R_N \sim I^N (Q/\hbar k)^{2N}$ and in the second $R_N \sim I^N$. Here $N$ is the order of nonlinearity, $I$ the laser intensity, $k$ the wave number of the laser field, and $Q$ some basic momentum transfer such that usually $Q \gg \hbar k$. Moreover, very often, processes of class (b) require a threshold value for $N$ to take place at all. Hence, the processes (a) require a much lower intensity of the laser field than the processes (b) in order to obtain sufficiently large rates $R_N$ for the laser-induced nonlinearities of the order $N$ with the emission or absorption of $N$ laser quanta $\hbar\omega$. In the case (a) the required laser intensities turn out to be of the order of magnitude $10^8$–$10^{12}$ W cm$^{-2}$ and in the case (b) intensities between $10^{12}$–$10^{16}$ W cm$^{-2}$ are required, depending on the wavelength of the laser source employed. This was also the reason why in the early days of laser development it was thought that processes of class (a) would be more easily accessible to observation than those of class (b).

In our early review [1], published about 18 years ago, several processes of class (a) and (b) have been discussed. In particular, we investigated electron–atom collisions in a laser field belonging to case (a), and multiphoton above-threshold ionization (ATI), belonging to case (b). At that time ATI just started to become a fascinating new field of research. Today the research activities in ATI and the concomitant generation of higher harmonics (HHG) of the laser frequency by an atomic system, interacting with a powerful laser beam, have become the dominant field of multiphoton

physics and there was an excellent collection of reviews on this subject edited by Gavrila [2]. We also mention the two books by Delone and Krainov [3,4] and by Eberly *et al.* [5]. In addition, there have been published recently several other expert reviews by Eberly *et al.* [6], Mainfray and Manus [7], Freeman and Bucksbaum [8], L'Huillier *et al.* [9], Ammosov *et al.* [10], Shakeshaft [11], Balcou *et al.* [12], Reiss [13], Burnett *et al.* [14], Faisal *et al.* [15], DiMauro and Agostini [16], Protopapas *et al.* [17], Joachain *et al.* [18], Maquet *et al.* [19], Terao-Dunseath and Dunseath [20], and Becker *et al.* [21]. Finally we mention the recent proceedings volumes edited by Evans and Chin [22] and by Lambropoulos and Walther [23]. Consequently, our present report will be devoted, in particular, to some of the above processes at very high laser powers, as discussed for example by Mourou *et al.* [24], in which case a relativistic treatment will be necessary since for laser powers of the order of magnitude of $10^{18}\,\mathrm{W\,cm^{-2}}$ and above, the ponderomotive energy of an electron, of mass $m$, in the laser field, given by $U_P = mc^2\,\mu^2/4$, will become of the order of magnitude of the electron rest energy $mc^2$. In the above formula we introduced the dimensionless intensity parameter $\mu$, defined by $\mu = e\mathcal{E}_0/m\omega c$ where $\mathcal{E}_0$ is the laser field amplitude and $\omega$ its frequency. Such high laser powers can nowadays be achieved by generating very short radiation pulses that can yield either harmonic x-rays or laser pulses in the attosecond regime [25–28].

In the following, we shall first perform an elementary classical consideration of Thomson scattering and x-ray scattering in a laser field which are prototypes of a laser-induced and a laser-assisted processes, respectively. Then we shall go on to consider relativistically Compton scattering in a laser field of extreme radiation power, such that $U_P \approx mc^2$. Particular attention will be devoted to spin effects at such intensities. Next we shall reconsider electron–atom scattering in a laser field of moderate power and low frequency. This will be mainly done in order to discuss some very new experimental results and their comparison with presently available theoretical work and possible explanations of the experimental findings. For more details on earlier work on this topic we refer to our recent review [29]. A further section will then be devoted to a relativistic treatment of free–free transitions at extremely high laser powers and we shall discuss, in particular, angular asymmetries of the cross sections and their respective electron energies that can be observed. Here too, the relevance of the electron spin will be discussed. A rather long chapter will then be devoted to a detailed discussion of above-threshold ionization, electron–ion recombination, x-ray–atom scattering in a laser field, and harmonic generation. These processes are all strongly interrelated among each other on account of the unitarity of the $S$-matrix of scattering theory. Finally, we shall demonstrate for some particular processes the modifications of the

nonlinear cross sections or probabilities that can be induced by a powerful bichromatic radiation field, usually of frequencies $\omega$ and $r\omega$ (with $r = 2, 3$). These modifications can be achieved by changing the amplitudes of the two field components, $\mathcal{E}_0$ and $\mathcal{E}_0^{(r)}$, respectively, and their relative radiation phase $\phi$. The investigation of the nonlinear probabilities of these processes as a function of the amplitudes $\mathcal{E}_0$, $\mathcal{E}_0^{(r)}$ and the phase $\phi$ has been termed *coherent phase control*. More details on this topic can be found in our recent review [30].

## B. Classical Considerations

### B.1. Thomson scattering in a laser field

In the early days of laser research, many papers were devoted to the scattering of strong radiation fields by free electrons beginning with the pioneering work of Sen Gupta [31], Vachaspati [32], Gol'dman [33], Brown and Kibble [34], Fried and Eberly [35] and others [36–38]. Summaries of these works are reported in reviews by Eberly [36], Bunkin *et al.* [39], Mitter [40], and McDonald [41]. Although the investigation of this process is of fundamental interest for the understanding of quantum electrodynamics at high radiation field intensities, the experimental verification of the predicted nonlinear effects at intermediate laser field intensities is seriously hampered by two basic facts which have impeded for a long time all experiments in this direction, namely,

(a) the extreme smallness of the Thomson cross section, i.e., $\sigma_{\text{Th}} \approx 7 \times 10^{-25}\,\text{cm}^2$ and

(b) the high intensity, of the order of magnitude $10^{16} - 10^{18}\,\text{W}\,\text{cm}^{-2}$, required to make the nonlinearities appreciable.

Therefore, only recently it was possible to perform experiments to verify the predictions of the above relativistic calculations, since by now table-top lasers have become available with a power output of $10^{18}\,\text{W}\,\text{cm}^{-2}$ and above [42, 43]. The essential difficulties encountered can be most easily demonstrated by the following simple classical calculation which furnishes a valuable low-frequency formula that will be repeatedly encountered in our discussions later on. Consider for simplicity the motion of a nonrelativistic electron of mass $m$ and charge $e$ in a radiation field described by the electric-field strength in dipole approximation $\vec{\mathcal{E}}(t) = \mathcal{E}_0 \vec{\epsilon} \sin \omega t$ with $\vec{\epsilon}$ being the unit vector of linear polarization, $\mathcal{E}_0$ a real amplitude, and $\omega$ the frequency of the field. We assume adiabatic decoupling of the field and particle at $t \to -\infty$ by a factor $\exp(-\gamma|t|)$, with $\gamma \geqslant 0$, so that the Lorentz equation

of motion and its integration read

$$\frac{d\vec{v}}{dt} = \frac{e}{m}\vec{\mathcal{E}}(t), \qquad \vec{v} = -\mu c \vec{\epsilon} \cos \omega t, \qquad \vec{r} = -\alpha_0 \vec{\epsilon} \sin \omega t \qquad (1)$$

where $\alpha_0 = \mu c/\omega$ is the amplitude of the classical electron oscillations in the radiation field and $\mu$ is the corresponding velocity amplitude measured in units of the speed of light $c$. It was explicitly given above by $\mu = (e\mathcal{E}_0/m\omega c) = (I/I_c)^{1/2}$. This dimensionless parameter can also be used to measure the field intensity $I$ as the ratio $\mu^2 = I/I_c$ where $I_c = \alpha \hbar \omega^2/8\pi r_0^2$. Here $r_0 = e^2/mc^2 = 2.82 \times 10^{-15}$ m is the classical electron radius and $\alpha = e^2/\hbar c \approx 1/137$ is the fine structure constant. $I_c$ is the critical intensity at which $\mu^2$ becomes equal to unity, thus turning the problem into a relativistic one (compare Eq. (1)). Expressing the intensity of the laser field by $\mu^2$ is conveniently used in the treatment of laser-induced processes. The intensity $I = \langle |\vec{S}| \rangle = \mathcal{E}_0^2 c/8\pi$ is the average ingoing flux of the radiation field.

Next we shall assume that the radiation field is sufficiently strong and, therefore, the amplitude $\vec{r}(t)$ of the electron oscillations becomes so large that $|\vec{r}| \gtrsim c/\omega = \lambda/2\pi$ and, consequently, the space dependence of the radiation field has to be included in the expression for the electric field $\vec{\mathcal{E}}(t)$ of Eq. (1). This means we have to replace $t$ by $t - \vec{n} \cdot \vec{r}(t)/c$, $\vec{n}$ being the direction of propagation of the ingoing radiation field. As long as $\mu^2 \ll 1$, we may assume that the radiation emitted by the electron is determined by the retarded acceleration $\vec{v}' = d\vec{v}/d\tau$, where $\tau = t - |\vec{r}_0 - \vec{r}(\tau_0)|/c \approx \tau_0 + \vec{n}' \cdot \vec{r}(\tau_0)/c$ is the retarded time and we use the fact that usually for the point of observation $\vec{r}_0$ we have $|\vec{r}_0| \gg |\vec{r}|$. Moreover, we have introduced the average time of retardation $\tau_0 = t - |\vec{r}_0|/c$ and $\vec{n}'$ is the unit vector of the direction of emission of the scattered field. Therefore, with the above substitutions and approximations the acceleration $\vec{v}'(\tau_0)$, correct to first order in the retarded phase, takes the form

$$\vec{v}' = \alpha_0 \omega^2 \vec{\epsilon} \left[ 1 + \frac{1}{c}(\vec{n}' - \vec{n}) \cdot \vec{v}(\tau_0) \right] \sin \left[ \omega\tau_0 + \frac{1}{c}(\vec{n}' - \vec{n}) \cdot \vec{r}(\tau_0) \right] = \sum_{N=1}^{\infty} \vec{v}'_N \quad (2)$$

with

$$\vec{v}'_N = (-1)^N \alpha_0 N \omega^2 \vec{\epsilon} J_N \left( \frac{\vec{K} \cdot \vec{\epsilon}}{k} \right) \sin(N\omega\tau_0) \qquad (3)$$

where $\vec{K} = \vec{k}' - \vec{k}$. The last formula follows from Eq. (1) after the insertion of $\vec{r}(\tau_0)/c$ from (1), realizing that $\exp(-i\alpha_0\vec{K}\cdot\vec{\epsilon}\sin\omega\tau_0)$ is the generating function of the ordinary Bessel functions $J_N$ of integer order $N$. This finding may be interpreted as the result of a laser-induced Doppler shift of the scattered radiation which is periodically oscillating in time. From Eqs. (2) and (3) we infer that the retarded acceleration of the electron in the strong radiation field decomposes into incoherent accelerations $\vec{v}'_N$, which yield scattered radiation of frequencies $\omega' = N\omega$ and wave vectors $\vec{k}' = \omega'\vec{n}'$, with $N \geqslant 1$. Finally we calculate the differential scattering cross sections $d\sigma_N$ for the individual nonlinear processes of the order $N$ from the standard formula

$$d\sigma_N = \frac{e^2}{4\pi c^3 I}\langle\vec{v}'^2\rangle\sin^2\phi\,d\Omega = \left(\frac{\omega'}{\omega}\right)^2 J_{N-1}^2(\alpha_0\vec{K}\cdot\vec{\epsilon})d\sigma_{\text{Th}} \qquad (4)$$

where $\hbar\vec{K} = \hbar(\vec{k}' - \vec{k})$ is the momentum transfer and $d\sigma_{\text{Th}}/d\Omega = r_0^2\sin^2\phi$ is the differential Thomson cross section formula with $\phi = \angle(\vec{\epsilon},\vec{n}')$ being the angle of radiation emission. The exact formula for $d\sigma_N$ has to be deduced from a classical relativistic calculation [45–52]. This, however, yields little difference in our order of magnitude estimates we shall pursue in the following.

The Eq. (4), just derived, represents the low-frequency theorem of nonlinear Thomson scattering in the presence of a strong radiation field. It demonstrates the two basic features indicated at the beginning: (a) $\sigma_{\text{Th}} = (8\pi/3)r_0^2 \approx 7 \times 10^{-25}\text{ cm}^2$, i.e. extreme smallness of the cross sections, and (b) $J_{N-1}^2(z)$ can only have its maximum values for $|z| \geqslant N - 1$, as can be inferred from the diagrams shown in the book of Jahnke–Emde–Lösch [53]. This means that we must have $\alpha_0\vec{K}\cdot\vec{\epsilon}$ at least of the order $N - 1$ and for the maximum value of $\vec{K}\cdot\vec{\epsilon} \approx Nk$ we consequently have to require $\mu = \alpha_0 k \geqslant 1$. Therefore, from $\mu^2 = I/I_c$ it then follows that we must have $I \geqslant I_c$ which is roughly $10^{16} - 10^{18}\text{ W cm}^{-2}$ for frequencies in the range of $CO_2$ and Nd:YAG lasers. This means, however, according to Eq. (1) that $|\vec{v}/c| = \beta$ becomes equal to 1 and our nonrelativistic calculations break down. Hence, our cross section formula Eq. (4) is valid only for $\mu^2 \ll 1$ and in this case we can expand the Bessel function $J_{N-1}(z)$ into its power series and keep only the first term of this expansion. Thus we obtain from Eq. (4)

$$d\sigma_N = \left(\frac{\omega'_N}{\omega}\right)^2\left(\frac{\alpha_0\vec{K}\cdot\vec{\epsilon}}{2}\right)^{2(N-1)}d\sigma_{\text{Th}} \approx r_0^2 N^4\left(\frac{I}{I_c}\right)^{N-1} 2^{-2(N-1)} \qquad (5)$$

and the cross sections of these laser-induced processes are therefore proportional to $r_0^2(I/I_c)^{N-1}$. For moderate laser field intensities one will consequently have to look for other processes, in which the conditions for the observation of nonlinear phenomena may be considerably relaxed. Since a metal contains a large number of quasi-free electrons of the order of magnitude $10^{22}-10^{23}\,\mathrm{cm}^{-3}$, it is quite natural to consider the possibility of generating harmonics of the laser field by shining laser light at grazing incidence on a metal surface having the polarization vector $\vec{\epsilon}$ sufficiently close to the normal onto the surface, for under these conditions the harmonic production is most efficient. In this way, even for moderate intensities, the generation of harmonics by the quasi-free electrons of the metal is possible although the process cannot be simply described by Thomson scattering [54–57]. If the laser field is more powerful, then a surface plasma becomes formed and the harmonic production will be even more efficient [58–63]. Alternative methods of very high harmonic generation in crystals are discussed in refs. [64–68].

## B.2. Laser-assisted x-ray scattering

With the development of coherent VUV and x-ray sources it becomes of interest to consider the scattering of high-frequency radiation by free or bound electrons in the presence of a powerful laser field since such a background field can modify considerably the basic process which also exists in the absence of the laser radiation [69–71]. Hence, in contrast to the process discussed before, such processes are coined laser-assisted. In order to demonstrate the basic features of such a process, we perform the following elementary classical calculation using the results of the foregoing section.

If a classical high-frequency plane wave $\vec{\mathcal{E}}\cos[\omega_{\mathrm{X}}(t-\vec{n}\cdot\vec{r}/c)]$ of unit field amplitude expressed by the vector of linear polarization $\vec{\mathcal{E}}$, direction of propagation $\vec{n}$ and of frequency $\omega_{\mathrm{X}}$ is scattered by a free electron under the simultaneous action of a low-frequency strong background field, as described in the foregoing section, with $\omega_{\mathrm{X}} \gg \omega$, then the phase of the absorbed and scattered x-ray field will be periodically modulated on account of the electron oscillations of large amplitude in the intense laser field. This will induce an oscillating Doppler-shift of the x-ray emission of the electron and the spectrum of scattered radiation will have the form $\omega_{\mathrm{X}}' = \omega_{\mathrm{X}} + N\omega$ with $N$ being a positive or negative integer or zero. Mathematically this fact will be expressed by the retarded electron acceleration $\vec{V}'(\tau_0) = (e/m)\vec{\mathcal{E}}\cos\{\omega_{\mathrm{X}}[\tau_0-(\vec{n}'-\vec{n})\cdot\vec{r}(\tau_0)/c]\}$, where $\vec{r}(\tau_0)$ is the amplitude of electron oscillations in the background field as given by Eq. (1) taken at the average retarded time $\tau_0$. Calculations similar to those

indicated in Section I.B.1 thus yield the following differential cross sections of x-ray scattering by a free electron and concomitant laser-induced nonlinear scattering processes

$$d\sigma_N = d\sigma_{\text{Th}}^{\text{X}} J_N^2(\rho\vec{Q} \cdot \vec{\epsilon}). \tag{6}$$

Here, $d\sigma_{\text{Th}}^{\text{X}}$ is the Thomson cross section of x-ray scattering, and $\vec{Q} = \hbar(\vec{K'} - \vec{K})$ is now the momentum transfer in x-ray scattering with $\vec{K} = \omega_{\text{X}}\vec{n}$ and $\vec{K'} = \omega_{\text{X}}'\vec{n}'$, while $\varrho = \alpha_0/\hbar = \mu c/\hbar\omega$. If we consider the low-frequency limit of the laser field, then $\omega_{\text{X}}' \approx \omega_{\text{X}}$. We shall see that the Eq. (6) agrees very well with the corresponding low-frequency result for electron–atom scattering in a laser field. In order to recognize this similarity later on, we artificially introduced in Eq. (6) Planck's constant $\hbar$. In fact, however, the above x-ray scattering is of entirely classical origin like the Thomson scattering process discussed before.

In contrast to Thomson scattering, discussed in Section I.B.1 under the aspects of our two criteria (a) and (b), we find the present process of x-ray scattering to have the great advantage of strongly enhanced probabilities for the nonlinear scattering effects at intermediate laser beam intensities, since the momentum transfer $\vec{Q}$ in Eq. (6) is much larger in absolute magnitude than the corresponding quantity in Eq. (4). So, from our condition to have $J_N^2(z)$ appreciably large, namely $|z| \geqslant N$, according to Eq. (6) we must now require $\rho\vec{Q} \cdot \vec{\epsilon} \geqslant |N|$. Taking $\vec{Q} \| \vec{\epsilon}$ we thus obtain by analogy with our condition (b) in Section I.B.1 $\mu^2 = I/I_c \geqslant [(N\omega/\omega_{\text{X}})^2/4]\sin^2\theta/2$ (where $\theta$ is the scattering angle) and, consequently, for $\theta \approx \pi/2$ our condition reads $I/I_c \geqslant (N\omega/\omega_{\text{X}})^2$. For a $CO_2$ laser with $\hbar\omega = 0.117$ eV and x-ray quanta $\hbar\omega_{\text{X}}$ of the order of magnitude 1 keV we then obtain $I \geqslant N^2 \times 10^{-8}I_c$, which is equivalent to a laser beam intensity of about $10^8 - 10^{10}$ W cm$^{-2}$. Therefore, with the advent of sufficiently powerful coherent VUV and x-ray sources these nonlinear effects should become observable without great difficulties. Finally, we observe that for sufficiently low laser intensities we may again expand the Bessel function in Eq. (6) into its power series to find the approximation

$$d\sigma_N \approx d\sigma_{\text{Th}}^{\text{X}} \left(\frac{\rho\vec{Q} \cdot \vec{\epsilon}}{2}\right)^{2N} \approx r_0^2 \left(\frac{I}{I_c}\right)^N \left(\frac{\vec{Q} \cdot \vec{\epsilon}}{\hbar k}\right)^{2N}. \tag{7}$$

Comparing this formula with Eq. (5), we recognize the difference between a laser-induced and laser-assisted process at low intensities. The cross sections of the laser-assisted process have an enhancement factor $|Q/\hbar k|^{2N}$. The disadvantage of x-ray scattering in a laser field is still, however, the

smallness of the Thomson cross section. Therefore we shall consider in Sections I.D and I.E electron–atom scattering in a laser field and in Section II.E x-ray–atom scattering in a laser field.

## C. Compton Scattering

### C.1. Preliminaries

As indicated in Section I.B, laser-induced Compton scattering was one of the first nonlinear processes that was intensively investigated immediately after the first lasers were brought into operation. Nice surveys of this early work and discussions of the various questions raised at that time can be found in the reviews of Eberly [36], Bunkin *et al.* [39], Mitter [40], and Neville and Rohrlich [72]. However, a long time before the laser was invented, Thomson and Compton scattering, induced by a classical electromagnetic background field, was discussed in considerable detail by Sen Gupta [31]. This early work was also reviewed by one of us [73] where we reported that the first theoretical investigations of stimulated nonlinear Thomson scattering can be found in papers that were written in the forming years of the development of quantum mechanics in the 1920s. In the early days of laser research, the attainable powers of laser radiation were so low that the nonlinear effects predicted were not accessible to observation. The first experiment in which the second harmonic of nonlinear Compton scattering was observed is the one reported by Englert and Rinehart [74]. Therefore, one of the present authors reconsidered Compton scattering in an intense, linearly-polarized laser field in a semi-relativistic approximation and he envisaged also the process of laser-modified x-ray scattering in the relativistic regime [70,71], based on arguments like those presented in Section I.B. At about the same time, classical Thomson scattering in a powerful, linearly-polarized plane wave radiation field was analyzed numerically to a considerable extent by Puntajer and Leubner [46], while this process was considered analytically several years before in great detail for linear as well as circular laser polarization by Sarachik and Schappert [45]. With the advent of very powerful laser sources in recent years, the predicted energy and momentum shifts of an electron in a laser field became observable and were analyzed carefully by Meyerhofer and co-workers [42–44]. Their experimental results gave rise to renewed interest in the investigation of relativistic Thomson scattering in an extremely powerful radiation field by Hartemann and Kerman [75], and in a series of papers by Salamin and Faisal [49–52]. The corresponding quantum mechanical Compton process was reinvestigated by Narozhnyĭ and Fofanov [38],

describing the powerful laser pulse by a circularly polarized electro-magnetic plane wave field. Finally, the old question why the quantum-electrodynamic treatment of laser-induced processes, in which the laser-dressing of the electron was treated by summing up Feynman diagrams, as in the work of Fried and Eberly [35], does not yield laser-induced energy and momentum shifts, while the classical description of the laser field does, has been reconsidered by Eberly and Reiss [76] and more recently by Körmendi and Farkas [77] who apparently find a reasonable explanation for this discrepancy.

In the present section, we want to reanalyze laser-induced Compton scattering in a very powerful radiation field in which the ponderomotive energy $U_P$ of the electron in the field is of the order of magnitude of the electron's rest mass, $U_P \simeq mc^2$, or even larger. Since most calculations of this process, performed in the past, of which we became aware, were performed for a classical, circularly-polarized electromagnetic plane-wave field and mainly analytic formulae were presented, we shall consider here Compton scattering for a linearly-polarized radiation field in which case we expect a much richer and more complicated scattering spectrum. Moreover, we want to find out whether at the high laser powers envisaged above, of about $10^{18}$ W cm$^{-2}$ and beyond, spin effects are of importance or, whether the treatment of nonlinear Compton scattering for a Klein–Gordon particle or a Dirac particle lead essentially to the same results. We shall consider various different scattering configurations in which the electrons are moving at high speed initially, which historically was not the usual assumption, and we shall permit the collision of the laser beam and the electron beam at an arbitrary angle and investigate the angular dependence of the cross sections of the scattered radiation of harmonics $N\omega$. Our calculations will lead in the present case of linear laser polarization to generalized Bessel functions of the form

$$B_N(x, y) = \sum_{\lambda=-\infty}^{+\infty} J_{N-2\lambda}(x) J_\lambda(y). \tag{8}$$

The numerical evaluation of such functions has been analyzed some time ago in the complex plane by Leubner [78] whose investigations were based on earlier work by Bleistein and Ursell [79,80], by Nikishov and Ritus [81], and by Reiss [82,83]. We used these considerations and designed a computer program for the evaluation of the generalized Bessel functions $B_N(x, y)$ for large values of the parameters $x$, $y$, and $N$.

In order to show that spin effects in the present processes should be rather marginal, we shall perform the following quasi-classical consideration.

We start from the Dirac equation, in its quadratic form, for a particle in an electromagnetic field that can be found in Schiff's book on quantum mechanics [84] (using in this section units $\hbar = c = 1$)

$$[(E - e\phi)^2 - m^2]\psi = [(\vec{p} - e\vec{A})^2 - e\vec{\sigma}' \cdot \vec{B} + ie\vec{\alpha} \cdot \vec{\mathcal{E}}]\psi \tag{9}$$

in which $\vec{A}$ and $\phi$ are the electromagnetic potentials while $\vec{\mathcal{E}}$ and $\vec{B}$ are the electric and magnetic field strengths, respectively. $\vec{\sigma}'$ and $\vec{\alpha}$ are Dirac's spin matrices. Considering an electromagnetic, linearly-polarized plane-wave of frequency $\omega$, unit vector of polarization $\vec{\epsilon} = \vec{e}_y$ and direction of propagation $\vec{n} = \vec{e}_x$ in the Coulomb gauge, $\vec{A} = A_0 \vec{e}_y \cos \omega(t - x)$ and $\phi = 0$, we can infer from Eq. (9) a semi-classical expression for the final kinetic energy $E'_{\text{kin}} = E' - m$ of an electron placed into this field with initial momentum $\vec{p}$ along the $y$-axis. Since $\vec{\mathcal{E}}$ points along the $y$-axis, $\vec{B}$ will point into the $z$-direction. Therefore the magnetic term in Eq. (9) can be replaced by $-eA_0\omega\sigma'_z \sin \omega(t - x)$ and the electric term by $ieA_0\omega\alpha_y \sin \omega(t - x)$. For $\sigma'_z$ we can take in our quasi-classical calculation the two values $\pm 1$, while $\alpha_y$ couples in a matrix element the two large components of a Dirac spinor with the two small components and therefore we have to take $\pm ip/(E + m)$, where the initial energy is $E = E_{\text{kin}} + m$. Therefore we obtain from Eq. (9)

$$E'_{\text{kin}}\left(1 + \frac{E'_{\text{kin}}}{2m}\right) = E_{\text{kin}}\left(1 + \frac{E_{\text{kin}}}{2m}\right) - 2\sqrt{2E_{\text{kin}}\left(1 + \frac{E_{\text{kin}}}{2m}\right)U_p} \cos\omega(t - x)$$

$$+ U_p[1 + \cos 2\omega(t - x)] \mp \sqrt{\frac{U_p}{m}}\omega\left[1 + \sqrt{\frac{E_{\text{kin}}}{E_{\text{kin}} + 2m}}\right]\sin\omega(t - x). \tag{10}$$

From this expression we obtain the maximum electron kinetic energy $E_{\text{kin}}^{\max}$ in the laser field with maximum spin contribution, if we choose the radiation phase to be $\omega(t - x) = \pi/4$ or $3\pi/4$ in which case $\sin\omega(t - x) = \pm 1/\sqrt{2}$ and $\cos 2\omega(t - x) = 0$. With this choice we find

$$E_{\text{kin}}^{\max}\left(1 + \frac{E_{\text{kin}}^{\max}}{2m}\right) = E_{\text{kin}}\left(1 + \frac{E_{\text{kin}}}{2m}\right)$$

$$+ U_p \pm \frac{\omega}{\sqrt{2}}\sqrt{\frac{U_p}{m}}\left[1 + \sqrt{\frac{E_{\text{kin}}}{E_{\text{kin}} + 2m}}\right] \tag{11}$$

where $E_{kin}$ is the initial kinetic energy of the electron, entering the radiation field. $U_p = m\mu^2/4$ is the ponderomotive energy of the electron in the laser field with $\mu$ being the intensity parameter, defined in Section I.A. The formula Eq. (11) immediately tells us that for laser field intensities in the relativistic regime, i.e. for $\mu = 1$ and thus $U_P = m/4$, the ratio between laser-induced spin effects and laser-induced dynamical effects will be $2\omega/m \simeq 10^{-6}$ for a Nd:YAG laser with $\omega = 1.17\,\text{eV}$. Consequently, on the basis of these quasi-classical considerations spin effects in relativistic scattering process of electrons in a very powerful laser field should be marginal. It is also interesting to remark that according to Eq. (10) the contributions of the laser-induced spin effects and of the laser-induced dynamical effects are out of phase by $\pi/2$ in their influence on the total final energy of the electron in the field. Moreover, we recognize that for relativistic initial electron kinetic energies, $E_{kin} \simeq m$, the electric spin term in Eq. (9) will contribute in the square brackets of the last term of Eq. (11) a factor $\sqrt{1/3}$, showing that also in the relativistic case the magnetic spin term yields the dominant contribution. On the other hand, for lower laser intensities we usually have $U_P \ll E_{kin}$ and $\mu \ll 1$ so that in this case the relevant ratio is $\omega\mu/2E_{kin} \ll 1$ and therefore also in the nonrelativistic regime spin effects are negligible. Our numerical results, presented below and in Section I.E, will confirm the findings of these heuristic considerations. A detailed analysis of spin effects in free or bound electron-laser systems has recently been presented by Walser *et al.* [85,86] and the relativistic quantum dynamics of a localized Dirac electron driven by an intense laser-field pulse was considered by San Román *et al.* [87]. In a recent paper by Kirsebom *et al.* [88] it was shown experimentally that the electron spin has a dramatic influence on the energy loss of ultrarelativistic electrons in strong fields where the electric field strength approaches the critical "Schwinger" field strength $E_0^{(S)} = m^2c^3/e\hbar = 1.32 \times 10^{16}\,\text{V}\,\text{cm}^{-1}$.

In the next section we shall first derive the generalized Compton formula for scattering of a powerful laser beam by a Klein–Gordon particle of spin 0 and we shall then consider the same process for a Dirac particle of spin 1/2 [89]. In Section I.C.4 we shall present and discuss some numerical results for various scattering geometries and combinations of parameter values.

## C.2. *Scattering by a Klein–Gordon particle*

The derivation of the scattering formula for a Klein–Gordon particle is relatively simple and straightforward. We start by considering the exact solution of the Klein–Gordon equation for a particle of mass $m$ and charge

$e$ embedded in an electromagnetic plane wave of vector potential $\vec{A}(\tau)$ in the Coulomb gauge. Here, $\tau = t - \vec{n} \cdot \vec{r}$ and $\vec{n}$ is the direction of propagation of the plane wave field. If the particle has initial energy $E$ and momentum $\vec{p}$ and if adiabatic decoupling of the particle from the plane wave is assumed, the corresponding Gordon solution [90], normalized to the volume $V$, reads [91]

$$\psi_{\vec{p}} = \frac{1}{\sqrt{2EV}} \exp\left[-i(Et - \vec{p} \cdot \vec{r}]f(\tau) \tag{12}$$

with

$$f(\tau) = \exp\left\{ \frac{i}{E - \vec{p} \cdot \vec{n}} \int_{-\infty}^{\tau} \left[ e\vec{p} \cdot \vec{A}(\tau') - \frac{e^2}{2} \vec{A}^2(\tau') \right] d\tau' \right\}. \tag{13}$$

Describing the powerful laser field by a monochromatic plane-wave of amplitude $A_0$, linear polarization $\vec{\epsilon}$, frequency $\omega$ and wave vector $\vec{k} = k\vec{n}$, represented by the vector potential

$$\vec{A}(\tau) = A_0 \vec{\epsilon} \cos \omega\tau \tag{14}$$

we obtain from Eqs. (12) and (13) the corresponding solution for the initial particle state

$$\psi_{\vec{p}} = \frac{1}{\sqrt{2EV}} \exp\left[-i(\overline{E}t - \overline{\vec{p}} \cdot \vec{r})\right]$$
$$\times \exp[i(a \sin \omega\tau - b \sin 2\omega\tau)]. \tag{15}$$

Here we have introduced the abbreviations

$$\overline{E} = E + d, \qquad \overline{\vec{p}} = \vec{p} + d\vec{n}, \qquad d = \frac{m^2 \mu^2/4}{E - \vec{p} \cdot \vec{n}}$$

$$a = \frac{m(\mu/k)\vec{p} \cdot \vec{\epsilon}}{E - \vec{p} \cdot \vec{n}}, \qquad b = \frac{m^2 \mu^2/8\omega}{E - \vec{p} \cdot \vec{n}}, \qquad \mu^2 = \left(\frac{eA_0}{m}\right)^2. \tag{16}$$

The laser-dressed energy $\overline{E}$ and momentum $\overline{\vec{p}}$ fulfil the relation $\overline{E}^2 = \overline{m}^2 + \overline{\vec{p}}^2$ and correspond to an on-shell particle of effective mass $\overline{m} = m(1 + \mu^2/2)^{1/2}$ [34]. The characteristic parameter, determining all the

laser-induced nonlinear intensity effects, is given by $\mu^2 = I/I_c$ where $I$ is the average intensity of the laser field and $I_c = \alpha\omega^2/8\pi r_0^2$ ($\alpha = e^2$, $r_0 = e^2/m$), as discussed in Section I.B.1.

Writing down a corresponding wave function, $\psi_{\vec{p}'}^*$, for the scattered particle of energy $E'$ and momentum $\vec{p}'$ with appropriate coefficients $a'$, $b'$, and $d'$ in Eqs. (15) and (16), we can evaluate in lowest order of perturbation theory the $T$-matrix element of nonlinear Compton scattering by a Klein–Gordon particle, viz.

$$T_{fi} = -i \int d\vec{r}\, dt \psi_{\vec{p}'}^* H_{\text{int}} \psi_{\vec{p}} \tag{17}$$

in which the interaction Hamiltonian $H_{\text{int}}$ for a laser-dressed charged Boson of spin 0, interacting with a quantized electromagnetic field $\vec{A}'$ in the Coulomb gauge is given by [92]

$$H_{\text{int}} = ie[\vec{A}'(\tau')\cdot\overrightarrow{\nabla} - \overleftarrow{\nabla} \cdot \vec{A}'(\tau')] + 2e^2\vec{A}'(\tau') \cdot \vec{A}(\tau) \tag{18}$$

where $\vec{A}(\tau)$ represents the laser field, defined in Eq. (14), and the effective vector potential $\vec{A}'(\tau')$ of the spontaneously emitted photon of frequency $\omega'$, wave vector $\vec{k}'$ and polarization $\vec{\epsilon}'$ has to be evaluated from the quantized field operator $\vec{A}'$, by considering the matrix element

$$\left\langle 1_{\vec{k}'}|\vec{A}'|0_{\vec{k}'}\right\rangle = \sqrt{\frac{2\pi}{V\omega'}}\vec{\epsilon}'e^{i(\omega't-\vec{k}'\cdot\vec{r})}. \tag{19}$$

If we insert Eq. (19) into Eq. (18) and use the resulting expression in Eq. (17) together with the appropriate Gordon solutions Eq. (15), we obtain after Fourier decomposition of $T_{fi}$ and integration over space and time

$$T_{fi} = \sum_{N=-\infty}^{+\infty} T_N,$$

$$T_N = i(2\pi)^4 \frac{em}{2V\sqrt{E'E}} \sqrt{\frac{2\pi}{V\omega'}} M_N$$

$$\times \delta(\overline{E}' - \overline{E} + \omega' - N\omega)\delta^3\left(\overline{\vec{p}}' - \overline{\vec{p}} + \vec{k}' - N\vec{k}\right) \tag{20}$$

in which the matrix elements $M_N$ are given by

$$
\begin{aligned}
M_N = {} & \frac{\left(\vec{\bar{p}}' + \vec{\bar{p}}\right) \cdot \vec{\epsilon}'}{m} B_N(x, y) \\
& - \left[\frac{\omega}{2m}(a' + a)(\vec{n} \cdot \vec{\epsilon}') + \mu(\vec{\epsilon}' \cdot \vec{\epsilon})\right] \\
& \times [B_{N+1}(x, y) + B_{N-1}(x, y)] \\
& + \frac{\omega}{m}(b' + b)(\vec{n} \cdot \vec{\epsilon}')[B_{N+2}(x, y) + B_{N-2}(x, y)]
\end{aligned}
\tag{21}
$$

with the arguments $x$ and $y$ defined by

$$
x = a' - a, \qquad y = b - b'
\tag{22}
$$

where $a, b$ and, similarly, $a', b'$ are given in Eq. (16) and the generalized Bessel functions $B_N(x, y)$ are defined in Eq. (8).

The transition probability per unit space-time volume for nonlinear Compton scattering of a Klein–Gordon particle with the absorption of $N$ laser photons $\omega$, can be evaluated by standard methods. We find

$$
\begin{aligned}
w_N = {} & \int \frac{|T_N|^2}{V\mathcal{T}} \frac{V}{(2\pi)^3} d\vec{k}' \frac{V}{(2\pi)^3} d\vec{\bar{p}}' \\
= {} & \frac{e^2 m^2}{8\pi V E} \int \frac{|M_N|^2}{E'\omega'} d\Omega_{\vec{k}'} \omega'^2 d\omega' \delta(\overline{E}' - \overline{E} + \omega' - N\omega) \\
& \times d\vec{\bar{p}}' \delta^3(\vec{\bar{p}}' - \vec{\bar{p}} + \vec{k}' - N\vec{k}).
\end{aligned}
\tag{23}
$$

In order to obtain the nonlinear differential cross sections $d\sigma_N/d\Omega_{\vec{k}'}$, for the general case where the electron beam and laser beam cross each other under an arbitrary angle, we have to divide the expression, Eq. (23), by the relative average flux $j_{el}^\mu (j_{ph})_\mu$ of the ingoing electrons and photons. This expression is found by adapting the Lorentz invariant form of the relative particle flux of two-particle collisions, if one of the particles is massless [1, 92]. The fluxes of electrons and photons can be obtained from

$$
\vec{j}_{el} = \frac{\vec{p}}{EV} = \frac{m}{EV}\vec{\beta}, \qquad \vec{j}_{ph} = \frac{1}{\omega}\langle \vec{S} \rangle = \frac{A_0^2 \omega}{8\pi}\vec{n}
\tag{24}
$$

and therefore the relative flux is given by

$$j_{\text{rel}} = \frac{A_0^2 \omega m}{8\pi E V}(1 - \vec{n} \cdot \vec{\beta})$$

(25)

Consequently, the nonlinear cross sections of the order $N$ of laser-induced Compton scattering by a Klein–Gordon particle will read

$$\frac{d\sigma_N}{d\Omega_{\vec{k}'}} = r_0^2 \left(\frac{\omega'}{\omega}\right)\left(\frac{m}{E'}\right)\frac{|M_N|^2}{\mu^2\left(1 - \vec{n} \cdot \vec{\beta}\right)}$$

(26)

where $r_0 = e^2/m$ is the classical electron radius. Next we consider the energy and momentum conservation relations, expressed by the $\delta$-functions in Eq. (23). These can be squared and subtracted to yield

$$\omega'(\overline{E}' - \overline{\vec{p}}' \cdot \vec{n}') = N\omega\left(\overline{E} - \overline{\vec{p}} \cdot \vec{n}\right)$$

(27)

and by substituting on the left hand side of Eq. (27) $\overline{E}'$ and $\overline{\vec{p}}'$ again from the energy and momentum conservation relations in Eq. (23), we find for the frequencies of scattered radiation the generalized Compton formula

$$\omega' = \frac{N\omega\left(E - \vec{p} \cdot \vec{n}\right)}{E - \vec{p} \cdot \vec{n}' + (N\omega + d)\left(1 - \vec{n} \cdot \vec{n}'\right)}.$$

(28)

If the electron is initially at rest, $E$ has to be replaced by $m$ and $\vec{p} = 0$, while $d$ reduces to $U_P = m\mu^2/4$. In that case the Compton formula Eq. (28) reads

$$\omega' = \frac{N\omega}{1 + (N\omega/m + U_p/m)(1 - \vec{n} \cdot \vec{n}')}.$$

(29)

At very high laser powers with $\mu \simeq 1$ and for a large number $N$ of absorbed laser photons, the frequencies $\omega'$ of the scattered photons will strongly depend on the quantum-mechanical recoil effect, determined in the denominator of Eq. (29) by the factor $N\hbar\omega/mc^2$, as well as on the classical laser-induced drift motion of the electron, yielding in the denominator of that frequency formula the contribution $U_P/mc^2$.

### C.3. Scattering by a Dirac particle

The treatment of laser-induced Compton scattering by a Dirac particle of spin 1/2 can follow similar lines, as in our discussion in the previous subsection for a particle of spin 0. We start from the Dirac equation for an electron moving in an arbitrary electromagnetic plane wave field

$$(i\gamma^\mu \partial_\mu - e\gamma^\mu A_\mu - m)\psi(x) = 0 \tag{30}$$

where the vector potential $A_\mu$ has the general form

$$A_\mu = A_\mu(k \cdot x), \qquad A \cdot k = k \cdot k = 0. \tag{31}$$

We use the Einstein summation convention and notation, namely $v^\mu w_\mu = v \cdot w$, where $\mu = 0, 1, 2, 3$. The solution of the above equation (Eq. (30)) was derived by Volkov [93] and its explicit form can be found in the paper by Denisov and Fedorov [94]. Assuming adiabatic decoupling along the light-cone in the past between the particle and the field we obtain

$$\psi(x) = [1 + \kappa \gamma^\mu k_\mu \gamma^\nu A_\nu (k \cdot x)]$$
$$\times \exp[-ip \cdot x - i \int_{-\infty}^{k \cdot x} S(\phi) d\phi] u_p \tag{32}$$

where $u_p$ is a free-particle solution of the equation $(\gamma^\mu p_\mu - m)u_p = 0$ with $p_\mu$ being a four-vector of energy and momentum. The constant $\kappa$ and the function $S(\phi)$ can be evaluated and we find

$$S(\phi) = \frac{eA(\phi) \cdot p}{p \cdot k} - \frac{e^2 A^2(\phi)}{2p \cdot k}, \qquad \kappa = \frac{e}{2p \cdot k}. \tag{33}$$

After normalization to the volume $V$, the required Volkov solution for an electron of initial four-momentum $p_\mu$ reads

$$\psi_p(x) = \sqrt{\frac{m}{VE_p}} \left[ 1 - \frac{e\gamma^\mu A_\mu(k \cdot x)\gamma^\nu k_\nu}{2k \cdot p} \right]$$
$$\times \exp\left[-ip \cdot x - i \int_{-\infty}^{k \cdot x} \left( \frac{eA(\phi) \cdot p}{p \cdot k} - \frac{e^2 A^2(\phi)}{2p \cdot k} \right) d\phi \right] u_p. \tag{34}$$

A similar solution, $\psi_{p'}(x)$, can be written down for the scattered electron of four-momentum $p'_\mu$.

The *T*-matrix element of laser-induced Compton scattering by a Dirac particle can be easily evaluated, since the interaction Hamiltonian of this process is determined by [92]

$$H_{\text{int}} = e\overline{\psi}_{p'}(x)\gamma^\lambda\psi_p(x)A'_\lambda(x). \tag{35}$$

Therefore, by choosing the appropriate Volkov solutions Eq. (34) for the ingoing and the corresponding outgoing electron in Eq. (35) and by using the effective vector potential $A'_\lambda(x)$ for the scattered photon, given by Eq. (19) and taken in its covariant form, we obtain

$$T_{fi} = -ie\frac{m}{V\sqrt{E_pE_{p'}}}\sqrt{\frac{2\pi}{V\omega'}}\int d^4x$$

$$\times \overline{u}_{p'}\left[1 + \frac{e\gamma^\sigma A_\sigma(k\cdot x)\gamma^\tau k_\tau}{2k\cdot p'}\right]\gamma^\lambda\epsilon'_\lambda\left[1 - \frac{e\gamma^\mu A_\mu(k\cdot x)\gamma^\nu k_\nu}{2k\cdot p}\right]u_p$$

$$\times \exp[i(p' - p + k')\cdot x]$$

$$\times \exp\left[ie\left(\frac{p'}{p'\cdot k} - \frac{p}{p\cdot k}\right)\cdot\int^{k\cdot x}A(\phi)d\phi\right]$$

$$\times \exp\left[-ie^2\left(\frac{1}{2p'\cdot k} - \frac{1}{2p\cdot k}\right)\int^{k\cdot x}A^2(\phi)d\phi\right]. \tag{36}$$

By inserting the vector potential Eq. (31) of the laser field, used in its covariant version, we can easily perform the Fourier decomposition of the matrix element Eq. (36) and we obtain, as in the previous case, $T_{fi} = \sum_{N=-\infty}^{+\infty} T_N$ where the transition matrix elements $T_N$ of the different nonlinear processes of the order $N$ have exactly the same structure as for Compton scattering by a Klein–Gordon particle, shown in Eq. (20), except that the matrix elements $M_N$ are different for the present process. The same conclusion also holds for the differential cross section formula $d\sigma_N/d\Omega_{\vec{k}'}$ in Eq. (26) and for the frequencies $\omega'$ of the scattered radiation in Eq. (28). The above matrix elements $M_N$ are found in the present case to be

$$M_N = 2(\mathcal{A} - \mathcal{C})B_N(x, y) + 2\mathcal{B}[B_{N+1}(x, y) + B_{N-1}(x, y)]$$

$$- \mathcal{C}[B_{N+2}(x, y) + B_{N-2}(x, y)] \tag{37}$$

where the coefficients $\mathcal{A}$, $\mathcal{B}$, and $\mathcal{C}$ have the explicit form

$$\mathcal{A} = \bar{u}_{p'} \gamma^\lambda \epsilon'_\lambda u_p$$

$$\mathcal{B} = \frac{eA_0}{4} \bar{u}_{p'} \left[ \frac{\gamma^\sigma \epsilon_\sigma \gamma^\tau n_\tau \gamma^\lambda \epsilon'_\lambda}{p' \cdot n} - \frac{\gamma^\lambda \epsilon'_\lambda \gamma^\mu \epsilon_\mu \gamma^\nu n_\nu}{p \cdot n} \right] u_p$$

$$\mathcal{C} = \frac{e^2 A_0^2}{8(p' \cdot n)(p \cdot n)} \bar{u}_{p'} \left( \gamma^\sigma \epsilon_\sigma \gamma^\tau n_\tau \gamma^\lambda \epsilon'_\lambda \gamma^\mu \epsilon_\mu \gamma^\nu n_\nu \right) u_p \qquad (38)$$

and the $B_N(x, y)$ are the generalized Bessel functions, defined in Eq. (8), with the arguments $x$ and $y$ given in Eq. (22). In writing down these expressions, we introduced the notation $k_\mu = \omega n_\mu$ where $n_\mu$ is a unit four vector. The evaluation of the matrix elements $\mathcal{A}$, $\mathcal{B}$, and $\mathcal{C}$ in Eq. (38) do not need to be done analytically, since these coefficients can be calculated, using appropriate software. In evaluating the differential cross sections of nonlinear Compton scattering for a Dirac particle, we have to be aware of the two possible spin polarizations, $s = \pm 1/2$, with respect to the $z$-axis of the electron in its rest frame, taken before and after the scattering, leading to cross sections with and without spin-flip during the nonlinear process. We shall therefore denote the cross sections of these processes by $d\sigma_N^{(s,\,s')}/d\Omega_{\vec{k}'}$ where in an abbreviated notation $(s = +, s' = +)$ and $(s = -, s' = -)$ will refer to the cross sections with no spin-flip and, correspondingly, $(s = +, s' = -)$ and $(s = -, s' = +)$ will denote the cross sections with spin-flip.

### C.4. Numerical examples

For the presentation of our numerical examples [89], we shall consider the scattering geometry depicted in Fig. 1. The laser beam and the electron beam are counter-propagating, as indicated by the arrows denoted by $\omega$ for the laser beam and by $e^-$ for the electron beam. The scattered radiation of frequency $\omega'$, wave vector $\vec{k}'$, and linear polarization $\vec{\epsilon}'$ is emitted with an angle $\theta'$ and the linear polarizations $\vec{\epsilon}$ and $\vec{\epsilon}'$ are oriented in the scattering plane. The scattering angle $\theta'$, defined as the angle between the wave vectors $\vec{k}$ and $\vec{k}'$, can vary between $0°$ and $360°$.

In Fig. 2 we show the nonlinear differential cross sections $d\sigma_N/d\Omega_{\vec{k}'}$ as a function of the scattering angle $\theta'$, evaluated from Eqs. (21) and (26) for a Klein–Gordon particle. The data turn out to be identical with those calculated for a Dirac particle, using for $M_N$ the expression Eqs. (37) and (38), if spin-flip is not taken into account. The data are expressed in
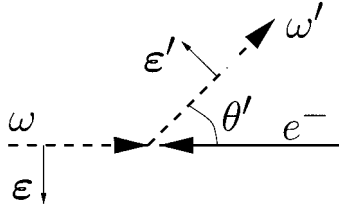
Fig. 1. Presents the scattering geometry considered. The wave vector $\vec{k}$ of the laser beam, the momentum $\vec{p}$ of the counter-propagating electrons and the wave vector $\vec{k}'$ of the emitted photons define the scattering plane. The polarization vectors $\vec{\epsilon}$ of the laser radiation and $\vec{\epsilon}'$ of the emitted field are located in this plane.

units of $r_0^2$ where $r_0$ is the classical electron radius. We used for the laser frequency $\omega = 1.54\,\text{eV}$ of a Ti-sapphire laser and the intensity of the laser beam is $I = 10^{22}\,\text{W}\,\text{cm}^{-2}$. The data presented in the panels (a)–(f) correspond respectively to the initial kinetic electron energies $E - mc^2$ equal to 10, $10^3$, $10^5$, $10^6$, $10^7$, and finally $10^8\,\text{eV}$. The number of absorbed laser photons is for all panels $N = 10^3$. The numbers along the circumferences of the circles in the panels (a)–(f) indicate the scattering angles $\theta'$ in degrees. By inspecting these data, we observe that for such intense laser fields the nonlinear Compton radiation is predominantly emitted into the forward direction with respect to the direction of propagation $\vec{n} = \vec{k}/k$ of the laser beam, as is also known to be the case for the generation of harmonics. This is even true for electron kinetic energies of the order of magnitude $mc^2$, as shown in panel (*d*). However, if the electron kinetic energy is increased still further, the scattering pattern becomes reversed so that for highly relativistic electron energies of the order of magnitude 100 MeV the Compton radiation will be emitted into the backward direction with respect to the direction of propagation $\vec{n}$ of the laser beam. Moreover, we find that with increasing electron energy the maximum values of the differential cross sections drop down significantly as indicated by the numbers inside the circles.

In Fig. 3 we present the cross sections of Compton scattering for a Dirac particle as a function of the nonlinear order $N$ for the large scattering angle $\theta' = 178°$, the kinetic electron energy $E - mc^2 = 10^7\,\text{eV}$, the laser frequency $\omega = 1.54\,\text{eV}$ and the laser power $I = 10^{22}\,\text{W}\,\text{cm}^{-2}$. All data have the property that for no spin-flip we find $d\sigma_N^{(+,+)} = d\sigma_N^{(-,-)}$, as shown in panel (a) and that for spin-flip $d\sigma_N^{(+,-)} = d\sigma_N^{(-,+)}$, depicted in panel (*b*). Moreover, the data for no spin-flip are evidently many orders of magnitude larger than those for spin-flip. For much smaller intensities than $I = 10^{22}\,\text{Wcm}^{-2}$ the cross section data drop down to zero very rapidly. However, for intensities $I \gtrsim 10^{22}\,\text{W}\,\text{cm}^{-2}$ the scattering spectrum extends to very large values of
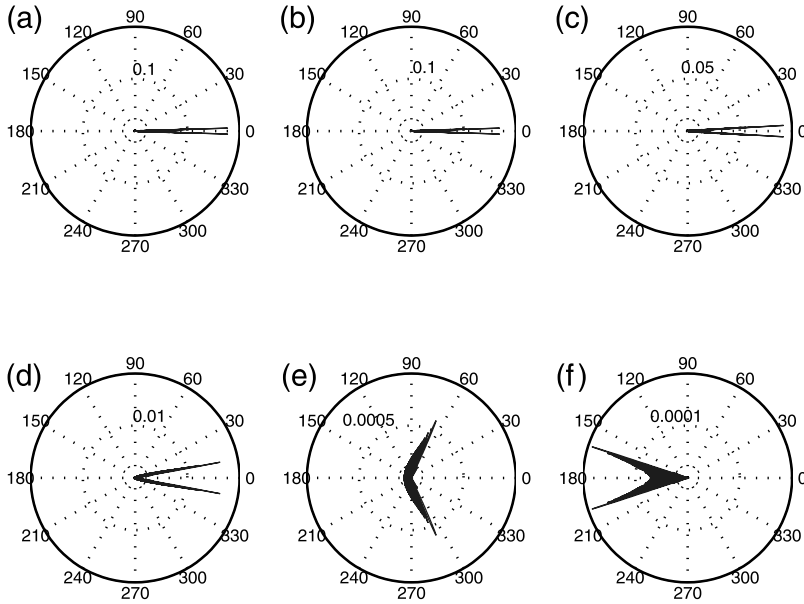
Fig. 2. Shows the differential cross sections $d\sigma_N/d\Omega_{\vec{k}'}$ evaluated for a Klein–Gordon particle and the identical cross sections $d\sigma_N^{(s,s')}/d\Omega_{\vec{k}'}$ for a Dirac particle with no spin-flip, i.e. either ($s=+$, $s'=+$) or ($s=-$, $s'=-$). The data are measured in units of $r_0^2$, where $r_0 = 2.82 \times 10^{-15}$ m is the classical electron radius. The scattering angle $\theta'$, defined in Fig. 1, is measured in degrees, as indicated by the numbers along the circumferences of the circles in the panels (a)–(f). The laser frequency is $\omega = 1.54$ eV, the radiation intensity $I = 10^{22}$ Wcm$^{-2}$ and the number of absorbed photons $N = 10^3$. In the panels (a)–(f) we consider increasing electron kinetic energies, namely $E - mc^2 = 10$, $10^3$, $10^5$, $10^6$, $10^7$, and $10^8$ eV, respectively. Evidently, for most of the electron energies considered the nonlinear Compton radiation is predominantly emitted into the forward direction with respect to $\vec{k}$ (or $\theta' \simeq 0$) and only for the highest electron energy of 100 MeV in the panel (f) the radiation is emitted mainly into the backward direction in the vicinity of $\theta' = 180°$ (see ref. [89]).

nonlinearity $N$ and shows rapid oscillations. Nevertheless, the spin non-flip process dominates over the spin-flip effects. The above oscillations of the cross section data are general features that we have found for all parameter values considered, stemming from the properties of the generalized Bessel functions, Eq. (8). Moreover, it appears that the cross sections for a Klein–Gordon particle are almost identical with those for a Dirac particle in the no spin-flip case. This demonstrates that even for such huge laser field intensities the spin effects are only marginally present and, therefore, from the practical point of view, the dynamics of the scattering process is very well described by the solutions of the Klein–Gordon equation.
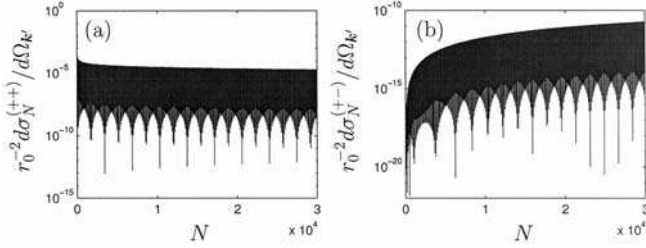
FIG. 3. Depicts the Compton cross sections in units of $r_0^2$ for a Dirac particle as a function of the nonlinear order $N$. The scattering angle is taken as $\theta' = 178°$, the electron kinetic energy is $E - mc^2 = 10^7$ eV, the laser frequency $\omega = 1.54$ eV, and the laser intensity $I = 10^{22}$ Wcm$^{-2}$. For all data presented, we find that $d\sigma_N^{(+,+)}/d\Omega_{\vec{k}'} = d\sigma_N^{(-,-)}/d\Omega_{\vec{k}'}$ and, similarly, $d\sigma_N^{(+,-)}/d\Omega_{\vec{k}'} = d\sigma_N^{(-,+)}/d\Omega_{\vec{k}'}$. For much smaller laser intensities the cross sections drop down to zero very rapidly, whereas for higher intensities the spectrum of cross sections extends to very large $N$. Moreover, the cross section values for no spin-flip dominate by far over those for spin-flip by about a factor of $10^7$ and the data for no spin-flip are identical with those for a Klein–Gordon particle (see ref. [89]).

## C.5. *Applications*

Short-pulse x-ray sources are under development as important tools for material, medical, and life sciences. Laser-Compton scattering was first used for the generation of short-pulse x-rays in 1996 [95–97]. The advantages of laser-Compton x-rays are that they have a tunable and semi-monochromatic photon energy, good directivity and controllability with a femtosecond pulse width. Various studies and projects have been proposed and demonstrated to date [98–102].

## D. Free–Free Transitions

### D.1. *Elementary considerations*

To simplify the present discussion, we consider the nonrelativistic potential scattering of electrons in a laser field. We assume that in the absence of the field the electron has the initial momentum $\vec{p}$ and the final momentum $\vec{p}'$ with corresponding energies $E = \vec{p}^2/2m$ and $E' = \vec{p}'^2/2m$, respectively. The laser field will be described, as in Section I.B.1, by the electric field in dipole approximation $\vec{\mathcal{E}}(t) = \mathcal{E}_0 \vec{\epsilon} \sin \omega t$ yielding the classical electron oscillation $\vec{r}(t) = -\alpha_0 \vec{\epsilon} \sin \omega t$. As will be shown in greater detail, in such a field a free electron plane wave $\exp[-i(Et - \vec{p} \cdot \vec{r})/\hbar]$ suffers a similar phase oscillation as we have observed in Section I.B.1 and thus the above plane wave will change into $\exp[-i(Et - \vec{p} \cdot \vec{r} - \alpha_0 \vec{p} \cdot \vec{\epsilon} \sin \omega t)/\hbar]$. Hence, during scattering of

the electron by the potential, we will obtain a phase-modulation factor similar to what we found in x-ray scattering, namely $\exp(-i\rho\vec{Q} \cdot \vec{\epsilon} \sin \omega t)$, and consequently by analogy the differential scattering cross sections of laser-assisted electron scattering will read

$$d\sigma_N = \frac{p'}{p} J_N^2(\rho\vec{Q} \cdot \vec{\epsilon}) d\sigma_{\text{el}}. \tag{39}$$

Here $d\sigma_{\text{el}}$ is the differential cross section of elastic electron scattering in the absence of the field and $\vec{Q} = \vec{p} - \vec{p}'$ is the momentum transfer during scattering. The energy of the scattered electrons is given by $E' = E + N\hbar\omega$ and thus $p' = \sqrt{2mE'}$. If $N > 0$ then $N$ laser quanta are absorbed during the scattering process and if $N < 0$ then $|N|$ quanta are emitted. Hence these processes are occasionally called induced and inverse bremsstrahlung, respectively or, generally speaking, they are named free–free transitions. The reason for the above similarity between Thomson scattering and electron scattering in a laser field simply stems from the fact that we may understand electron scattering to emerge from laser-induced Thomson scattering (or, more correctly, Compton scattering) by replacing the spontaneously emitted radiation field by the exchange of virtual quanta between the electron and the potential, observing that in Compton scattering we have the momentum conserving relation $\hbar(\vec{k} - \vec{k}') = \vec{p}' - \vec{p} = -\vec{Q}$.

Contrary to Thomson and x-ray scattering, electron–atom scattering in a laser field cannot be described classically in such a simple manner as to yield the scattering formula Eq. (39). There are, moreover, other fundamental differences which make the concomitant induced nonlinear processes in electron scattering much more easily accessible to observation in the laboratory, than in the case of Thomson or x-ray scattering. By comparing the corresponding formulas Eqs. (4) and (6) with Eq. (39) we find that:

(a) The average total cross section of elastic electron–atom scattering is of the order of magnitude $\sigma_{\text{el}} \approx Z^2 a_{\text{B}}^2$ where $Z$ is the nuclear charge and $a_{\text{B}} = \hbar^2/me^2 = 0.53 \times 10^{-8}$ cm is the Bohr radius. Thus $\sigma_{\text{el}} \approx 0.25 Z^2 \times 10^{-16}$ cm$^2$ and consequently it is by a factor $10^9$ larger than the Thomson cross section for which we found $10^{-25}$ cm$^2$.

(b) From the condition $|z| \geqslant |N|$, discussed in Sections I.B.1 and I.B.2, for having $J_N^2(z)$ sufficiently large (i.e., appreciable nonlinear contributions), now follows the requirement to have $\rho\vec{Q} \cdot \vec{\epsilon}$ at least of the order $|N|$. Taking at best $\vec{Q} \cdot \vec{\epsilon} \approx p'$, this means $\mu^2 = I/I_c \geqslant (N\hbar\omega)^2/2mc^2E'$. For a $CO_2$ laser with $\hbar\omega = 0.117$ eV and electron kinetic energies of the

order of $10\,\mathrm{eV}$ we thus find $I \geqslant 10^{-9}\,N^2 I_c$ which is according to our earlier estimates a moderate intensity of some $10^8\,\mathrm{W\,cm^{-2}}$.

These facts indicate that induced and inverse bremsstrahlung are sufficiently effective processes which show the way for directly observing these nonlinear effects as has been successfully demonstrated and will be discussed in some detail below. Of course, potential scattering is only a very crude approximation and in a more precise investigation of electron–atom scattering in a laser field also the structure of the atom will have to be taken into account.

### D.2. Nonrelativistic scattering

We consider a particle of charge $e$ and mass $m$ moving in a powerful laser field. In this case the field can be described to a very good approximation by a classical electromagnetic plane wave. For simplicity, we assume the field to be monochromatic with frequency $\omega$ and to have linear polarization $\vec{\epsilon}$. Moreover, for nonrelativistic particles it is sufficient to consider the dipole approximation. Hence, the vector potential can be taken in the form

$$\vec{A}(t) = A_0 \vec{\epsilon} \cos(\omega t), \quad A_0 = \frac{c\mathcal{E}_0}{\omega}, \tag{40}$$

where it is often more convenient to choose the electric field amplitude $\mathcal{E}_0$ instead of $A_0$. In the field Eq. (40) the Schrödinger equation of the charged particle reads

$$i\hbar\partial_t\psi = \frac{1}{2m}\left[-i\hbar\nabla - \frac{e}{c}\vec{A}(t)\right]^2\psi. \tag{41}$$

By means of the ansatz

$$\psi_{\vec{p}}(\vec{r}, t) = \frac{1}{\sqrt{V}}\exp\left[-\frac{i}{\hbar}(Et - \vec{p}\cdot\vec{r})\right]f_{\vec{p}}(t), \tag{42}$$

where $V$ denotes the normalization volume, the exact solution for $f_{\vec{p}}(t)$ is found to be

$$f_{\vec{p}}(t) = \exp\left\{\frac{i}{\hbar}\left[\vec{p}\cdot\vec{\alpha}_0\sin(\omega t) - \widetilde{\mathcal{E}}(t)\right]\right\}, \tag{43}$$

where it is implicitly assumed that for $t \to \pm\infty$ the field adiabatically decouples from the particle of momentum $\vec{p}$ and energy $E = \vec{p}^2/2m$. In Eq. (43) we find $\vec{r}(t) = \vec{\alpha}(t) = -\vec{\alpha}_0 \sin(\omega t)$ to describe the classical oscillations of the electron in the laser field and the amplitude $\vec{\alpha}_0$ is given by

$$\frac{1}{\hbar}\vec{\alpha}_0 = \frac{\mu}{\hbar k}\vec{\epsilon} = \rho\vec{\epsilon}, \quad \mu = \frac{e\mathcal{E}_0}{m\omega c}, \quad k = \frac{\omega}{c}. \tag{44}$$

$\mu$ is again the dimensionless intensity parameter, that determines the strength of the laser–particle interaction and we may write

$$\mu^2 = \left(\frac{eA_0}{mc^2}\right)^2 = \frac{I}{I_c}, \quad I_c = \frac{\alpha\hbar\omega^2}{8\pi r_0^2}, \tag{45}$$

with $\alpha = e^2/\hbar c \approx 1/137$ being the fine structure constant and $r_0 = e^2/mc^2 \approx 2.82 \times 10^{-15}$ m the classical electron radius. According to Eq. (45), $I_c$ denotes the critical laser intensity at which $\mu$ becomes equal to one and $I_c$ decreases with decreasing laser frequency $\omega$. For a Nd:YAG laser ($\hbar\omega = 1.17\,\text{eV}$) $I_c \approx 10^{18}\,\text{W cm}^{-2}$ and for a $CO_2$ laser ($\hbar\omega = 0.117\,\text{eV}$) $I_c \approx 10^{16}\,\text{W cm}^{-2}$. It is important to point out that our nonrelativistic theory in dipole approximation of the radiation field is valid only for $\mu^2 \ll 1$, which is fulfilled for most of the presently performed laser experiments.

As we infer from Eq. (43), the coupling strength between particle and laser field is determined by $\vec{p} \cdot \vec{\alpha}_0 / \hbar$ and we therefore expect large nonlinear effects in the laser field if

$$\mu \geqslant \frac{\hbar k}{p}, \tag{46}$$

where for processes of class (a) usually $\hbar k/p \ll 1$ and for processes of class (b) $\hbar k/p \leqslant 1$. Hence, as pointed out in Section I.B.2, processes (a) require less laser intensity then processes (b).

Moreover, we find in Eq. (43) an expression $\widetilde{\mathcal{E}}(t)$ which is determined by

$$\widetilde{\mathcal{E}}(t) = \frac{1}{4}mc^2\mu^2\left(t + \frac{\sin(2\omega t)}{2\omega}\right). \tag{47}$$

Here the component oscillating in time with twice the laser frequency $\omega$ contributes in dipole approximation, if at all, comparatively little to the

cross sections. The other term, however, turns out to be very important, since it yields an overall Stark shift of the electron energies in the laser field and it is given by $\sigma = mc^2\mu^2/4$. This energy shift, for example, is of great interest in the discussion of multiphoton above-threshold ionization. There it turns out that $\sigma$ is identical with the maximum of the classical ponderomotive potential $U_P$ of a charged particle in a laser pulse, namely

$$\sigma = U_P = \frac{1}{4}mc^2\mu^2. \tag{48}$$

In our present discussion of electron–atom scattering in a laser field, the energy term $\widetilde{\mathcal{E}}(t)$ of Eq. (47) drops out in the dipole approximation as a time-dependent phase factor. Hence, we may use in dipole approximation instead of Eqs. (42) and (43)

$$\psi_{\vec{p}}(\vec{r}, t) = \frac{1}{\sqrt{V}}\exp\left\{-\frac{i}{\hbar}[(Et - \vec{p}\cdot(\vec{r} + \vec{\alpha}_0\sin\omega t)]\right\}. \tag{49}$$

This wave function can be used to immediately write down the corresponding retarded Green's function

$$
\begin{aligned}
G^{(+)}(\vec{r}', t'; \vec{r}, t) &= \theta(t' - t)V\int\frac{d^3p}{(2\pi\hbar)^3}\,\psi_{\vec{p}}(\vec{r}', t')\psi_{\vec{p}}^*(\vec{r}, t) \\
&= \theta(t' - t)\int\frac{d^3p}{(2\pi\hbar)^3} \\
&\quad \times \exp\left\{-\frac{i}{\hbar}[E(t' - t) \quad -\vec{p}\cdot(\vec{r}' - \vec{r}) - \vec{p}\cdot\vec{\alpha}_0(\sin\omega t' - \sin\omega t)]\right\}
\end{aligned}
\tag{50}
$$

describing a charged particle that is propagating in the laser field. In Eq. (50), $\theta(t)$ is the step function with $\theta(t) = 1$ for $t > 0$ and $\theta(t) = 0$ for $t < 0$. The above nonrelativistic Gordon–Volkov solution has been introduced by Keldysh [103].

In the pioneering work by Bunkin and Fedorov [104] the potential scattering of electrons in a powerful laser field was considered in the first Born approximation in $V(\vec{r})$, describing the radiation field by a monochromatic plane wave in the dipole approximation, Eq. (40). Representing the laser-dressed ingoing and outgoing electron by nonrelativistic

Gordon–Volkov states Eq. (49), Bunkin and Fedorov found in the low frequency limit [1]

$$d\sigma_N = J_N^2(\rho\vec{\epsilon} \cdot \vec{Q})d\sigma_{\text{el}}^{(B)}, \quad \rho = \frac{1}{\hbar}|\vec{\alpha}_0|, \tag{51}$$

where $d\sigma_{\text{el}}^{(B)}$ is the differential cross section of elastic scattering in the first Born approximation and $J_N(z)$ is an ordinary Bessel function of the first kind of the integer order $N$, where $N > 0$ corresponds to stimulated absorption of $N$ laser quanta $\hbar\omega$, and $N < 0$ describes the corresponding emission. A simple rederivation has been presented by Bergou [105] and further discussions are outlined in recent work by Pert [106]. Moreover, the appearance of universal minima in differential cross sections for potential scattering of comparatively high energy electrons in the presence of a laser beam was discussed by Faisal [107] quite some time ago. More details can be found in several books and reviews [108–115] and, in particular, in the recent surveys [18, 29].

In the fundamental paper of Kroll and Watson [116], the formula (51) of Bunkin and Fedorov [104] was generalized such as to include the contributions of all higher order terms of the Born expansion in $V(\vec{r})$ as well as to lowest order in $\hbar\omega$ the contributions of the laser field in the intermediate states, as has been shown by Mittleman [117]. Using our approximate Green's function, $G_{\text{ST}}$, in the space-translated form [29]

$$G_{\text{ST}}^{(+)}(\vec{r}', t'; \vec{r}, t) = \theta(t' - t) \int \frac{dE}{2\pi\hbar} \exp\left\{-\frac{i}{\hbar}[E(t' - t)\right.$$
$$\left. -\vec{p}_E \cdot \vec{\alpha}_0(\sin\omega t' - \sin\omega t)]\right\} G_E^{(+)}(\vec{r}'; \vec{r}), \tag{52}$$

describing a charged particle propagating simultaneously in the potential field $V(\vec{r})$ and in the radiation field Eq. (40), we can easily derive the Kroll–Watson cross section formula for moderate field intensities by straightforward application of scattering theory in the Furry-picture with respect to the radiation field. The exact transition matrix element for our process is thus given by

$$T_{fi} = -\frac{i}{\hbar} \int dt\, d^3r\, \psi_{\vec{p}'}^*(\vec{r}, t) V(\vec{r}) \psi_{\vec{p}}^{(+)}(\vec{r}, t), \tag{53}$$

where $\psi_{\vec{p}}^{(+)}$ obeys the equation

$$\psi_{\vec{p}}^{(+)} = \psi_{\vec{p}} + G^{(+)} V \psi_{\vec{p}}, \tag{54}$$

while $\psi_{\vec{p}'}^*$ is an outgoing and $\psi_{\vec{p}}$ an ingoing Gordon–Volkov state Eq. (49) and $G^{(+)}$ is the exact retarded Green's function. If we replace this Green's function by our space-translated approximation $G_{\mathrm{ST}}^{(+)}$ (52), we find from Eqs. (53) and (54)

$$
\begin{aligned}
T_{fi} = &-\frac{i}{\hbar}\int dt\, d^3r\, \psi_{\vec{p}'}^*(\vec{r},t)V(\vec{r})\psi_{\vec{p}}(\vec{r},t) \\
&+\left(-\frac{i}{\hbar}\right)^2\int dt'\, d^3r'\int dt\, d^3r\, \psi_{\vec{p}'}^*(\vec{r}',t')V(\vec{r}') \\
&\times G_{\mathrm{ST}}^{(+)}(\vec{r}',t';\vec{r},t)V(\vec{r})\psi_{\vec{p}}(\vec{r},t),
\end{aligned}
\tag{55}
$$

where the evaluation of the first integral above just yields the matrix elements of the Bunkin–Fedorov formula, whereas the second integral can be evaluated in the limiting cases considered below:

If the scattering amplitude in the absence of the radiation field is a smooth function of the energy $E$, then one can expand the second integral, after having performed the time-integration, in powers of $\hbar\omega$ retaining only the linear terms and we arrive at the Kroll–Watson matrix elements

$$
\begin{aligned}
T_{fi} &= \sum_N T_N^{\mathrm{KW}}, \\
T_N^{\mathrm{KW}} &= -2\pi i\delta(E'-E-N\hbar\omega)f(\tilde{E},\vec{Q})J_N(\rho\vec{Q}\cdot\vec{\epsilon}),
\end{aligned}
\tag{56}
$$

where $f(\tilde{E},\vec{Q})$ is the on-shell matrix element without the laser field at renormalized energy $\tilde{E}$ given by

$$
\tilde{E} = \frac{(\tilde{\vec{p}})^2}{2m}, \quad \tilde{\vec{p}} = \vec{p} - \vec{\Delta}, \quad \vec{\Delta} = \frac{mcN\,\hbar k}{\vec{Q}\cdot\vec{\epsilon}}\vec{\epsilon},
\tag{57}
$$

and $\vec{\Delta}$ defines the laser-dependent renormalizing momentum. From Eq. (56) we thus find the Kroll–Watson cross section formula

$$
d\sigma_N^{\mathrm{KW}} = d\sigma_{\mathrm{el}}(\tilde{E},\vec{Q})J_N^2(\rho\vec{Q}\cdot\vec{\epsilon}).
\tag{58}
$$

For the relative order of magnitude of the momentum renormalization we find

$$
\frac{|\vec{\Delta}|}{p} \approx \frac{|N|\hbar\omega}{4E\sin^2\theta/2},
$$

where $\theta$ is the scattering angle, so that for a laser-assisted electron-scattering experiment in which $E \approx 10\,\text{eV}$ and $\hbar\omega \approx 0.1\,\text{eV}$ we find $|\vec{\Delta}|/p \approx 0.25(|N|/\sin^2\theta/2) \times 10^{-2}$. Hence $\vec{\Delta}$ is only a small momentum correction for sufficiently large scattering angles.

With two statistical models, combined with convenient space–time profiles of the laser pulse, Bivona *et al.* [118] were able to interpret in a satisfactory manner the scattering data of the experiment by Weingartshofer *et al.* [119–121]. As it turned out, the similarities of the electron scattering spectra in relation to the two laser models indicate that they are largely due to the effect of the spatial and temporal inhomogeneities of the laser pulse. Similar conclusions were reached in the analysis by Weingartshofer and Jung [122]. Although the above interpretation of the experiments suggested that in fact free–free transitions have been observed, more exact experiments and analysis of the field parameters were performed by Wallbank *et al.* [123,124].

However, it is of interest to discuss the more recent experiments on free–free transitions at small scattering angles performed by Wallbank and Holmes [125–127]. These authors considered the scattering of electrons by helium and argon atoms in a $CO_2$-laser field of about $10^8\,\text{Wcm}^{-2}$ intensity at a small scattering angle of $9°$–$10°$. The electrons have initial energies between 6.2 and 32 eV. Contrary to what has been found in previous experiments at large scattering angles, discussed before, the nonlinear cross section data measured cannot be interpreted by means of the Kroll–Watson scattering formula Eq. (58), since these data are by many orders of magnitude larger than the values predicted by Eq. (58). Wallbank and Holmes suggested that laser-induced polarization of the target atoms may be responsible for these discrepancies. In a series of papers by Rabadán *et al.* [128], Geltman [129] and ourselves [130] it has been shown, however, that these polarization effects are negligibly small for the experimental conditions considered.

We tried to interpret the above experimental results by suggesting a collective model of electron–atom scattering in a laser beam, taking into account the high density of atoms in the target beam [131]. Though this model quite nicely reproduced the experimental data, it was shown by Dickinson [132] and Robicheaux [133] that by taking into account the laser-dressing of the atomic target our collective effect becomes marginal. A detailed investigation of the Kroll–Watson formula was presented by Madsen and Taulbjerg [134] but their results did not agree with the above experiments. The same authors [135] also considered laser-assisted electron–atom resonance scattering and laser-induced resonance interference as possible explanations of the above experiments by Wallbank and Holmes. In a paper by Geltman [136] it was shown within the framework of

perturbation theory that by a different choice of the scattering boundary conditions, agreement between theory and experiment can be achieved. This approach, however, is not very satisfactory. Then Rabadàn *et al.* [137] have suggested that double scattering might be a possible mechanism to interpret the experimental data and they appear to obtain a reasonable fit. Finally Cionga *et al.* [138] have considered scattering at small angles for hydrogen, taking into account the detailed interaction of the ingoing electron with the atomic electron in the presence of the laser field using the Floquet method. Although their results indicate effects close to the observations of Wallbank and Holmes [125–127], their data are evaluated for hydrogen and at much lower laser field intensities. On the other hand, we were able to show that off-shell effects play no role at the electron energies and laser intensities considered in the experiments by Wallbank and Holmes, but we confirmed the conclusions of Rabadàn *et al.* [137] that double scattering is a possible explanation [139]. Hence, all interpretations, presented so far, are inconclusive and further work is necessary. This is also true for the very recent experiments by Wallbank and Holmes [140] in which free–free transitions are investigated for very slow electrons such that $E \approx \hbar\omega$, in which case no agreement with the Kroll–Watson formula Eq. (58) can be expected. To interpret these experiments, Geltman studied laser-assisted electron–helium scattering in the perturbative regime for electron energies less or equal to 2.6 eV and $CO_2$ laser intensities less or equal to $10^6$ W cm$^{-2}$ and presented results for one and two photon processes in which case the absorption cross sections are larger than those for emission. Large discrepancies between these perturbative results and the predictions of the Kroll–Watson theory are found [141] as in his foregoing paper.

In the most recent experiments by Wallbank and Holmes [142], the scattering of low-energy electrons between 1 and 20 eV by helium in the presence of a $CO_2$-laser field of peak power $10^8$ W cm$^{-2}$ is considered in the scattering configuration of Fig. 4. In this configuration the momentum transfer $\vec{Q} = \vec{p}_i - \vec{p}_f$ is perpendicular to the laser field polarization $\vec{\epsilon}$ in which case the Kroll–Watson scattering formula Eq. (58) yields vanishing results. On the other hand, the experimental data shown in Fig. 5 for electron energies of 8, 14, and 20 eV, respectively, and the absorption or emission of 0, 1, and 2 laser photons are of considerable magnitude. These data cannot be explained by double scattering [137,139] since in that case the angular dependence of the scattering data calculated is rather flat, as shown in Fig. 6 [139], while the experimental data of Fig. 5 show considerable variations as a function of the scattering angle $\theta$. If one considers free–free transitions in a laser field by including the contributions of the second order Born-term [143], it is possible to obtain for the
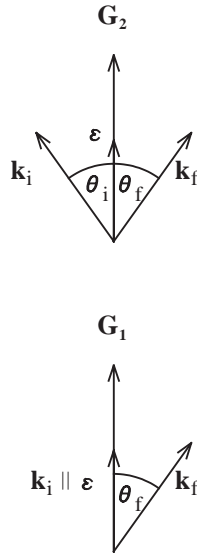
F$_{IG}$. 4. The scattering geometry, denoted by G$_2$, is considered in the recent experiments by Wallbank and Holmes [142] for observing free–free transitions. The laser polarization $\vec{\epsilon}$ is chosen perpendicular to the momentum transfer $\vec{Q} = \vec{p}_i - \vec{p}_f$ in which case the Bunkin–Fedorov and Kroll–Watson formulas yield vanishing cross sections. For the scattering geometry, called G$_1$, appreciable off-shell effects were found for free–free transitions in the most recent investigation [150], not, however, for the geometry G$_2$, in accordance with our previous work [139].

configuration of Fig. 4 nonvanishing scattering data. In that case the integration over the intermediate states of the scattering matrix element leads to a similar smearing out of $\vec{Q}$ as in the case of double scattering but the results are equally not well compatible with the experimental data. The only calculation that has lead to increased scattering data for the configuration in Fig. 4 is the one of Jarón and Kamiński [144] and their results are shown in Fig. 7, although they have not considered larger scattering angles as in Fig. 5. These authors demonstrate that off-shell effects are important in order to obtain these results. They consider a static scattering potential consisting of two parts, namely a short range contribution for the atomic core and, in addition, they introduce the Buckingham polarization potential [145] that leads to large off-shell effects. The relevance of off-shell effects was confirmed by Madsen and Taulbjerg [146,147]. On the other hand, in the investigations of Kylstra and Joachain
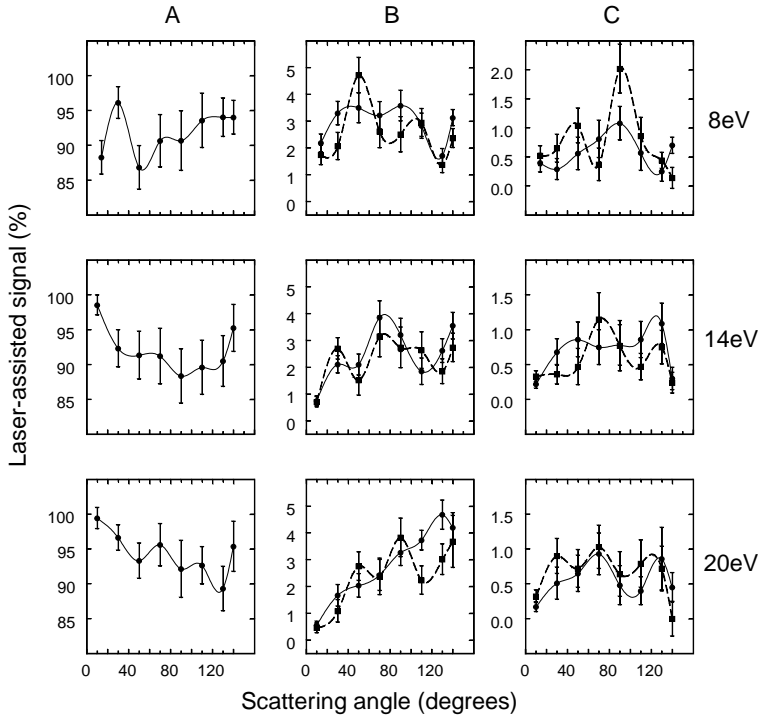
FIG. 5. The relative laser-assisted free–free signals expressed as percentages of the field–free scattering signals over the first two microseconds of the laser pulse for scattering from helium at incident electron energies of 8, 14, and 20 eV. Column A: zero photon; column B one-photon absorption (●) and emission (□); column C: two photon absorption (●) and emission (□). The lines drawn through the data points are simply cubic splines [142].

[148,149] no large off-shell effects were found. These authors solve the Floquet–Lippmann–Schwinger equation, using a static potential derived from the Hartree–Fock helium ground-state wave function, and they find no large effects if they add a contribution from the Buckingham potential. The above controversial results about the importance of off-shell effects has finally led to another investigation by Garland *et al.* [150]. These authors analyze free–free transitions for the two scattering configurations of Fig. 4 by comparing the results of exact Floquet calculations with those data they obtain by using the impulse approximation and the Kroll–Watson approximation. They find that in the case of the scattering configuration $G_1$ the off-shell effects can be considerable and can lead to an enhancement of the cross section data in comparison with the predictions of the
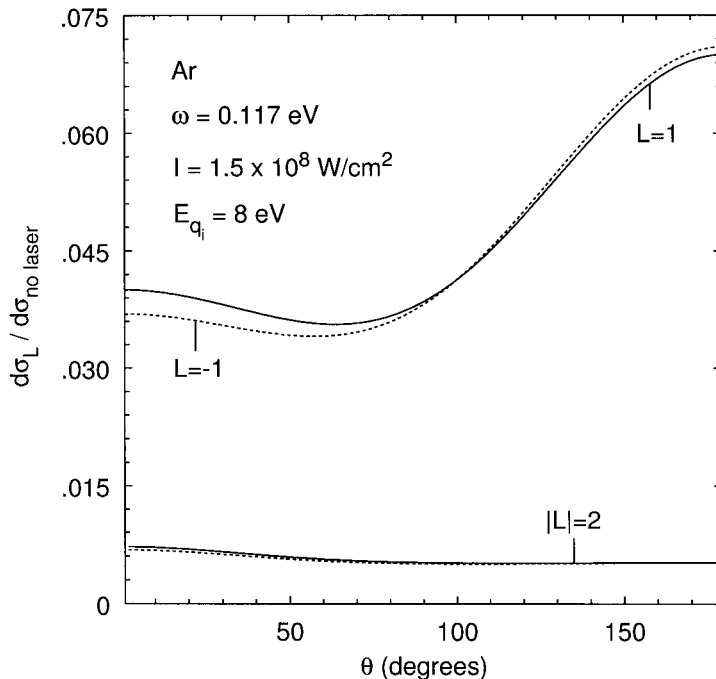
FIG. 6. The Kroll–Watson relative DCS, with double scattering effects included, for scattering from argon in the perpendicular configuration $\vec{\epsilon} \perp \vec{Q}$ as a function of the scattering angle $\theta$ for different number of absorbed (full curves: $L = 1$, 2) or emitted (dotted curves: $L = -1$, $-2$) photons and for incident electron energy 8 eV. The laser field parameters are $\omega = 0.117$ eV and $I = 1.5 \times 10^8$ Wcm$^{-2}$ [139].

Kroll–Watson formula Eq. (58). On the other hand, for the scattering configuration $G_2$ no appreciable off-shell enhancements of the cross sections were obtained. Summarizing, the most recent experimental results of Wallbank and Holmes [142], in particular for the scattering configuration $G_2$, shown in Fig. 4, are still awaiting a satisfactory interpretation. Further details on the topic of electron–atom scattering at moderate laser field intensities can be found in the reviews [29,18].

## E. Relativistic Scattering

### E.1. Introductory remarks

With the advent of very powerful laser sources, yielding intensities of $10^{18}$ W cm$^{-2}$ and above, it has become important to consider laser-assisted
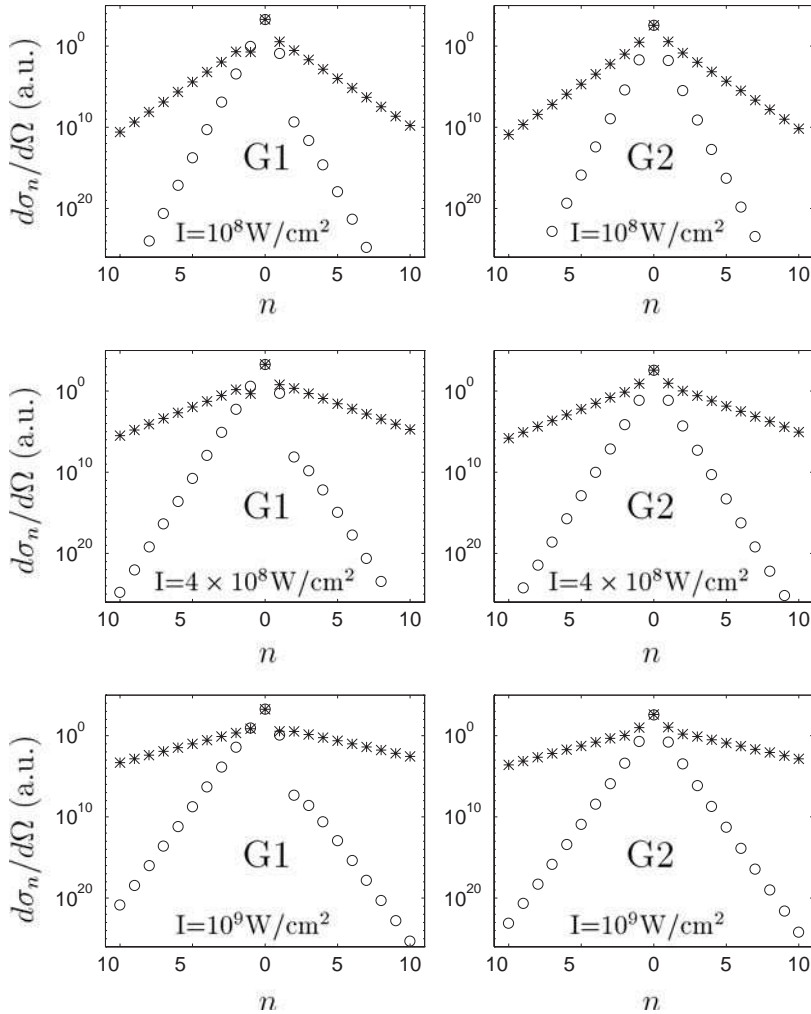
FIG. 7. Inelastic differential cross sections (in a.u.) for scattering of electrons as a function of the absorbed ($N > 0$) or emitted ($N < 0$) laser photons for an initial energy of electrons $E_{\vec{p}_i} = 10\,\text{eV}$ and for three laser intensities $I = 10^8\,\text{Wcm}^{-2}$, $I = 4 \times 10^8\,\text{Wcm}^{-2}$ and $I = 10^9\,\text{Wcm}^{-2}$. The electron–atom interaction is modeled by a square well potential of depth $V_0 = 0.5$ a.u. and width $a = 10.0$ a.u. The scattering geometry $G_1$ refers to $\vec{p}_i \parallel \vec{\epsilon}$ and is not considered in the most recent experiment by Wallbank and Holmes [142], whereas $G_2$ corresponds to $\theta_i = 4.5°$, $\varphi_i = 180°$ and $\theta_f = 4.5°$, $\varphi_f = 0°$, where $\varphi_{i(f)}$ are the corresponding azimuthal angles. In all cases the polarization vector $\vec{\epsilon}$ is parallel to the $z$-axis. Stars correspond to the low-frequency off-shell theory [144] and open circles to the Kroll–Watson formula. The large discrepancies between these two approaches are remarkable, but the results for $G_2$ are not confirmed by the most recent calculations [150].

and laser-induced processes relativistically [17,44]. Recently, Mott scattering in a powerful, circularly polarized radiation field was reconsidered by Szymanowski *et al.* [151] with reference to previous works [94,152–157]. We should also mention the detailed analysis of the laser-assisted relativistic scattering problem by Milošević and Krstić [158,159]. By evaluating the nonlinear cross sections numerically, large relativistic corrections were found by these authors if compared with the results of the Bunkin–Fedorov [104] or Kroll–Watson [116] formulae. On the other hand, this work showed that electron spin effects become essential only if the laser intensity is such that the critical parameter $\mu = e\mathcal{E}_0/m\omega c$ comes close to unity. For a Nd:YAG laser this value of $\mu$ corresponds to a laser field intensity of the order of magnitude mentioned above. For somewhat lower field intensities, it was found in the above work that spin effects are negligible and instead of using the Volkov solution of the Dirac equation [93] for describing the laser-dressed electron one may safely use the Gordon solution [90] of the Klein–Gordon equation. To simplify the calculations, Szymanowski *et al.* [151] considered electron scattering in a powerful circularly polarized laser field. The scattering process in this configuration is, however, not so effective and rich in details as in the case of linear polarization. In the case of linear polarization the electron will encounter more often the target during the scattering process and one can expect on classical grounds that here the collision process of electron–atom scattering in a laser field will, in the relativistic case, be much more effective and richer in its angular and polarization dependences. It is the purpose of the present section to analyze these effects in more detail and to show that phenomena can be encountered which are strong enough to be accessible to observation in the near relativistic regime of laser-field intensities. We also compare the results of the fully relativistic calculations with those of the nonrelativistic ones and we shall analyze the relevance of electron spin effects for a linearly-polarized radiation field at very high electron energies and laser powers such that the kinetic energy of the scattered electron, $E - mc^2$, and the ponderomotive energy of the electron in the laser field, $U_P = mc^2\mu^2/4$, are of the order of magnitude of the electron rest energy $mc^2$.

In the early days of laser physics, laser-induced Compton scattering was intensively investigated by many authors [36] (and reinvestigated very recently [89]) and a laser-induced electron drift motion and consequently a frequency shift of the Compton light was predicted (see Eq. (28)). This shift is proportional to $\mu^2$ and was very small for the available laser intensities at that time. Controversy had arisen about the existence or nonexistence of this frequency shift. One of the present authors was looking for a process that would more easily permit to observe the effect of the laser-induced drift motion of the electron. Considering in a semi-relativistic approximation

potential scattering of electrons in a laser field, he found in the low-frequency limit the following asymmetry in the total laser-assisted differential scattering cross sections [160,161]

$$\frac{d\sigma^{(-)} - d\sigma^{(+)}}{d\sigma^{(-)} + d\sigma^{(+)}} \simeq \frac{\mu^2}{2\beta} \sin\theta, \tag{59}$$

where $\mu$ is related to the electron drift velocity in the laser field by the relation $v_d = \mu^2 c$. Correspondingly $\beta = v/c$ where $v$ is the velocity of the scattered electron. Finally, $\theta$ is the scattering angle. The scattering configuration considered leading to the above asymmetry relation is depicted in Fig. 8. The scattering plane is determined by the vector $\vec{\epsilon}$ of linear polarization of the laser beam and by the direction $\vec{n}$ of its propagation. The momentum $\vec{p}$ of the ingoing electrons is oriented parallel to $\vec{\epsilon}$ and the momentum $\vec{p}\,'$ of the outgoing electrons can be either in the direction denoted by $(-)$, having an angle $\pi/2 + \theta$ with the direction $\vec{n}$, or in the direction $(+)$ with an angle $\pi/2 - \theta$ with respect to $\vec{n}$. Even though the laser-induced effect is here proportional to $\mu^2/\beta$ and not like the Compton drift effect proportional to $\mu^2$, at the time of writing the above paper laser powers and thus $\mu^2$ were still much too low and therefore the paper remained of little interest. Since, however, nowadays the experimental situation has drastically changed and the electron's drift motion in a powerful laser field has been verified experimentally [44], the above effect may become accessible to experimental verification.

   It is the purpose of the present analysis, to consider the above effects more carefully without the limitations of the low-frequency approximation. Considering laser powers of $10^{16}$ W cm$^{-2}$ and above, so that $\mu^2 \simeq 10^{-2} - 1$, and taking scattered electrons between $E_{\text{kin}} \simeq 100$ eV and $\simeq mc^2$ and hence
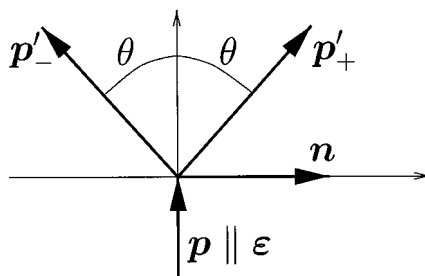


FIG. 8. Shows the scattering configuration considered for the numerical evaluation of $d\sigma_N^{(+)}$ and $d\sigma_N^{(-)}$ as well as of $\Delta E'/E_{\text{kin}}$ as a function of the scattering angle $\theta$ (see ref. [166]).

$\beta \simeq 10^{-2}$ up to $\lessgtr 1$, we find $\mu^2/2\beta \simeq 1$. We shall therefore rederive in the following the differential cross sections $d\sigma_N/d\Omega$ of induced and inverse bremsstrahlung for a Klein–Gordon and Dirac particle and we shall analyze numerically the asymmetry and spin effects that will turn out to be much more complicated than the one described by the simple formula Eq. (59).

### E.2. Relativistic scattering of a Bose particle

Several years ago, one of the present authors studied relativistic potential scattering in a laser field concentrating at that time on the low-frequency problem [91]. In this paper the laser-dressed electron was described by the Gordon solution [90] of the Klein–Gordon equation and the scattering process was described in first-order Born approximation using as target a screened Coulomb potential. Since in the present investigation we shall consider electron scattering in the near relativistic and relativistic region of the laser-field intensity and use electrons of $\geq 100$ eV kinetic energy, the first-order Born approximation should be sufficiently accurate and we can take over the main results from our above paper. We start with the exact solution of the Klein–Gordon equation for a particle of mass $m$ and charge $e$ moving in an electromagnetic plane wave field. This field is described by the vector potential $\vec{A}(\tau) = A_0 \vec{\epsilon} \cos \omega\tau$ in the Coulomb gauge where $\tau = t - \vec{n} \cdot \vec{x}$ and $\vec{n}$ is the direction of propagation of the field. We continue to use the units $\hbar = c = 1$. For a particle of initial energy $E$ and momentum $\vec{p}$, the normalized Gordon solution can be written in the form, introduced by Eqs. (15) and (16) in Section I.C.2

$$\psi_{\vec{p}} = (2EV)^{-1/2} \exp[-i(\overline{E}t - \overline{\vec{p}} \cdot \vec{r})] \exp[ia \sin \omega\tau - b \sin 2\omega\tau] \qquad (60)$$

with the abbreviations

$$\overline{E} = E + d, \qquad \overline{\vec{p}} = \vec{p} + d\vec{n}, \quad d = \frac{m^2\mu^2/4}{E - \vec{p} \cdot \vec{n}},$$

$$a = \frac{m(\mu/k)\vec{p} \cdot \vec{\epsilon}}{E - \vec{p} \cdot \vec{n}}, \qquad b = \frac{m^2\mu^2/8\omega}{E - \vec{p} \cdot \vec{n}}, \quad \mu^2 = (eA_0/m)^2. \tag{61}$$

Similarly, we can find the wave function $\psi_{\vec{p}'}^*$ which describes the scattered electron of energy $E'$ and momentum $\vec{p}'$ with the corresponding coefficients $a', b'$, and $d'$ like in Eq. (61). Then we find in first-order Born approximation

the following matrix element for our scattering process

$$T = -i \int d^4x [-i(\psi_{\vec{p}} \partial_t \psi_{\vec{p}'}^* - \psi_{\vec{p}'}^* \partial_t \psi_{\vec{p}})] U(\vec{r}). \tag{62}$$

For the scattering potential $U(\vec{r})$ we take a screened Coulomb potential of charge $eZ$ and screening length $\ell$ and in our calculations later on we use $Z = 1$ and $\ell = 1$ a.u. If we introduce into Eq. (62) all the quantities defined above, we find in a straightforward manner the differential cross sections of the laser-induced nonlinear bremstrahlung processes to be [91]

$$d\sigma_N = \frac{(e^2 Z)^2 (\overline{E}_N' + \overline{E})^2 d\Omega'}{[(\vec{\overline{p}}' - \vec{\overline{p}} - N\vec{k})^2 + \ell^{-2}]^2} \frac{p_N'}{p F_N} M_N^2, \tag{63}$$

where scattering takes place into the solid angle $d\Omega'$ and the energy conservation relation reads

$$\overline{E}_N' = \overline{E} + N\omega, \qquad \overline{p}_N' = (\overline{E}_N'^2 - \overline{m}^2)^{1/2}. \tag{64}$$

The factor $F_N$ that appears in the denominator of the cross section formula Eq. (63) has the form

$$F_N = 1 - \frac{d_N'}{E_N' - \vec{p}_N' \cdot \vec{n}} \left( 1 - \frac{E_N'}{p_N'^2} \vec{p}_N' \cdot \vec{n} \right). \tag{65}$$

Moreover, the matrix elements $M_N$ are found to be

$$M_N = B_N(x, y) - \frac{\omega(a' + a)}{2(\overline{E}' + \overline{E})} [B_{N+1}(x, y) + B_{N-1}(x, y)]$$

$$+ \frac{\omega(b' + b)}{\overline{E}' + \overline{E}} [B_{N+2}(x, y) + B_{N-2}(x, y)]. \tag{66}$$

In this expression we again have introduced the following generalized Bessel functions Eq. (8)

$$B_N(x, y) = \sum_{\lambda=-\infty}^{+\infty} J_{N-2\lambda}(x) J_\lambda(y), \tag{67}$$

in which the $J_{N-2\lambda}(x)$ and $J_\lambda(y)$ are ordinary Bessel functions of the first kind. The coefficients $x$ and $y$ in these functions are defined by

$$x = a' - a, \qquad y = b - b', \tag{68}$$

where $a$ and $b$ and similarly $a'$ and $b'$ are defined in Eq. (61). From the energy conservation relation equation (Eq. (64)) it becomes clear that all primed quantities are depending on the order of nonlinearity $N$. In the case of low intensities, $\mu^2 \ll 1$, and small kinetic energies, i.e. $(E - m)/m \ll 1$, the Eq. (63) reduces to the nonrelativistic formula of Bunkin and Fedorov [104] (see Eq. (51))

$$d\sigma_N^{NR} = \frac{(2r_0 Z)^2 m^4 d\Omega'}{\left(\vec{Q}_N^2 + \ell^{-2}\right)^2} \frac{p'_N}{p} J_N^2(\mu \vec{Q}_N \cdot \vec{\epsilon}/\omega), \tag{69}$$

where $\vec{Q}_N = \vec{p} - \vec{p}'_N$. The corresponding nonrelativistic energy conservation relation reads $E'_{\rm kin} = E_{\rm kin} + N\omega$. To these formulae we shall refer later on in our discussion of the numerical data obtained from the relativistic and nonrelativistic theories, respectively.

Let us consider the energy conservation relation, expressed by the Eq. (64), $\overline{E}_N = \overline{E} + N\omega$ and express $\overline{E}_N$ and $\overline{E}$ according to the definitions in Eq. (61) by $E'_N + d'$ and $E + d$, respectively. Then, by introducing the explicit expressions for $d'$ and $d$, we find on account of $p'/E' \ll 1$ and $p/E \ll 1$

$$E'_N = E - \frac{m^2 \mu^2}{4}\left[\frac{1}{E'}\left(1 + \frac{\vec{p}' \cdot \vec{n}}{E'}\right) - \frac{1}{E}\left(1 + \frac{\vec{p} \cdot \vec{n}}{E}\right)\right] + N\omega. \tag{70}$$

In the semi-relativistic limit [1] we may write in the denominators of this expression $E' \simeq E \simeq m$ and introduce the nonrelativistic kinetic energies by the relations $E' = m + \vec{p}'^2/2m$ and $E = m + \vec{p}^2/2m$. Then we obtain the semi-relativistic energy relation

$$E'_{\rm kin} = E_{\rm kin} - \frac{\mu^2}{4}(\vec{p}' - \vec{p}) \cdot \vec{n} + N\omega. \tag{71}$$

In the scattering configuration considered in Fig. 8, $\vec{p} \cdot \vec{n} = 0$. Denoting by $E_{\rm kin}^{'(+)}$ the kinetic energy of scattered electrons observed in the direction $(+)$ of Fig. 8 and by $E_{\rm kin}^{'(-)}$ the corresponding energy of electrons scattered in the direction $(-)$, we find the following asymmetry relation for the relative

energy difference in the low-frequency limit

$$\frac{\Delta E'_{\text{kin}}}{2E_{\text{kin}}} = \frac{\mu^2}{2\beta}\sin\theta \qquad (72)$$

in analogy to the relation of Eq. (59) for the asymmetry in the nonlinear cross sections. In the following section, we shall analyze numerically the asymmetry relations Eqs. (59) and (72) more precisely, using the exact cross section formula Eq. (63) and energy relation Eq. (64).

### E.3. *Asymmetries and angular windows*

For the following considerations, we fix the screening length $\ell$ of the scattering potential to $\ell = 1$ a.u. and the nuclear charge to $Z = 1$. Then we numerically evaluate the differential cross sections $d\sigma_N/d\Omega'$ from Eq. (63), taking selected values of the laser field intensity $I$, the kinetic energy $E_{\text{kin}}$ of the ingoing electrons, the order $N$ of nonlinearity of the scattering process and for the fixed laser frequency $\omega = 1.17$ eV. As the results of these calculations show, the elementary asymmetry relation Eq. (59) is in the general case by no means fulfilled in this particular form, but instead this asymmetry performs as a function of the scattering angle $\theta$ in certain angular regions more or less rapid oscillations and in other angular domains there may even appear "dark windows" in which the scattering data are very close to zero. Many years ago, such zeros of the differential cross sections were analyzed for the first time and their possible experimental implications discussed by Faisal [107] in the nonrelativistic regime. In this case they have their origin in the zeros of the Bessel functions in Eq. (69) for particular values of the arguments. In the present relativistic problem, such dark windows show up when the momentum transfer is perpendicular to the field polarization vector $\vec{\epsilon}$, just like in the recent experiments by Wallbank and Holmes [125–127, 142]. In the nonrelativistic scattering, however, the "dark windows" appear for small scattering angles only, if the Born approximation is considered. This is due to the applicability of the low-frequency approximation in which the absolute values of the ingoing and outgoing electron momenta are almost the same. In our case, however, this is not valid any longer and therefore "dark windows" can also show up for large scattering angles. We should also mention that such a situation can only appear for those inverse bremsstrahlung processes in which a certain number of laser photons becomes absorbed, while for the induced bremsstrahlung with the emission of laser photons "dark windows" cannot be encountered at large scattering angles, for in this case the momentum transfer can never be perpendicular to the laser polarization

vector $\vec{\epsilon}$, at least for the laser intensities considered here. The strength of the asymmetries, their oscillations and the angular location and width of the "dark windows" turn out to depend strongly on the parameter values of $I$, $E_{\mathrm{kin}}$, and $N$. For particular configurations of $I$, $E_{\mathrm{kin}}$, and $N$ the asymmetries can be considerable and we showed recently that they will be even more pronounced at higher laser-field intensities [163]. Concerning the second asymmetry relation Eq. (72) of the electron kinetic energies observed in the directions $(+)$ and $(-)$ of Fig. 4 the situation is insofar better as the deviation of the results, calculated from this semi-relativistic formula, from the corresponding data evaluated from the exact energy conservation relation Eq. (64) is less pronounced but still, depending on the values of $I$, $E_{\mathrm{kin}}$, and $N$, the deviations can be noticeable.

In Fig. 9 we show $\Delta E'/E_{\mathrm{kin}}$ evaluated from Eq. (64) as a function of the scattering angle $\theta$ as a full line and compare it with those data obtained from $\Delta E'_{\mathrm{kin}}/E_{\mathrm{kin}}$ of Eq. (72) represented by a dashed line. The parameter values used for this calculation are $I = 10^{15}\,\mathrm{W\,cm^{-2}}$, $E_{\mathrm{kin}} = 200\,\mathrm{eV}$, and $N = 20$. As one can see, the agreement of the data, evaluated from the two formulae, is quite good. Correspondingly, we present in Fig. 10 the differential cross sections $d\sigma_N^{(+)}/d\Omega$ as a full line and $d\sigma_N^{(-)}/d\Omega$ as a dashed line for the same parameter values of $I$, $E_{\mathrm{kin}}$, and $N$ as in Fig. 9 and we recognize an appreciable asymmetry at small scattering angles up to about $\theta = 30°$. On the other hand, a dark window shows up in the angular range $\theta = 10°-25°$ where the cross sections are almost zero.

In Fig. 11 we present the cross-sectional asymmetry, obtained from the cross section data for the directions $(+)$ and $(-)$ of Fig. 8, for the same
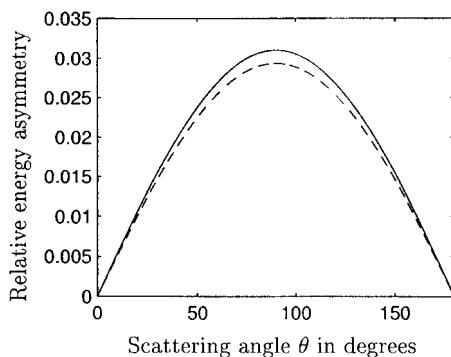


FIG. 9. Presents for comparison $\Delta E'/E_{\mathrm{kin}}$ as a full line and the low-frequency approximation, Eq. (72), as a dashed line as a function of the scattering angle $\theta$. The scattering parameter values are in this case $I = 10^{15}\,\mathrm{Wcm^{-2}}$, $E_{\mathrm{kin}} = 200\,\mathrm{eV}$ and $N = 20$. The agreement between both sets of data is reasonable (see ref. [166]).
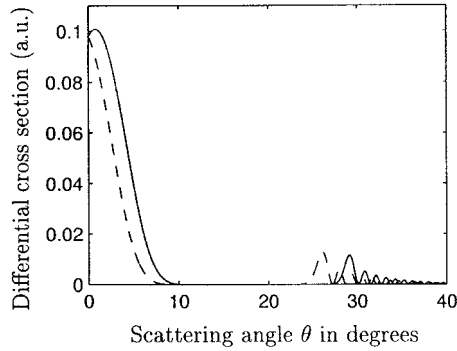
FIG. 10. Shows $d\sigma_N^{(+)}$ (full line) and $d\sigma_N^{(-)}$ (dashed line) as a function of $\theta$ for the same parameter values as in Fig. 9. We observe the appreciable scattering asymmetry at small angles $\theta$ up to about $30°$ and a dark window from $10°$ to $25°$. The data are presented in atomic units a.u. (see ref. [166]).
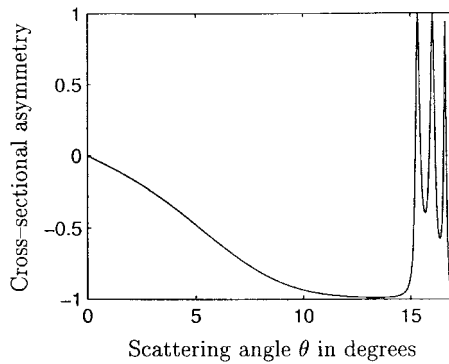


FIG. 11. Presents the cross-sectional asymmetry $(d\sigma^{(-)} - d\sigma^{(+)})/(d\sigma^{(-)} + d\sigma^{(+)})$, evaluated from Eq. (63) for the same parameter values as in Fig. 9. The discrepancies in relation to Eq. (59), are considerable, although the low-frequency approximation should be applicable (see ref. [166]).

parameter values as in Fig. 9 and for small scattering angles $\theta$. We see that the differences in relation to the predictions of Eq. (59) are significant. The asymmetry parameter defined in this equation approaches the values $+1$ or $-1$ in those cases where one of the cross sections ($d\sigma^{(+)}$ or $d\sigma^{(-)}$) is almost equal to zero. Since this happens very frequently for large scattering angles $\theta$, the asymmetry parameter will therefore oscillate very rapidly between $-1$ and $+1$. This is the reason why we have limited the presentation of our data to small scattering angles only.

### E.4. Cross section formula for a Dirac particle

In order to be able to determine the relevance of electron spin effects at high electron energies and laser powers for the present process, we have also to evaluate the nonlinear cross section formula for the potential scattering of a Dirac electron of spin 1/2, embedded in a powerful electromagnetic plane-wave field of linear polarization. This calculation can proceed in a very similar manner as was done for a Klein–Gordon particle in Section I.E.2. We start as in Section I.C.3 from the Dirac equation in an arbitrary plane wave field

$$(i\gamma^\mu \partial_\mu - e\gamma^\mu A_\mu - m)\psi(x) = 0, \tag{73}$$

where the vector potential $A_\mu$ has the general form

$$A_\mu = A_\mu(k \cdot x), \quad A \cdot k = k \cdot k = 0 \tag{74}$$

and we obtain according to Section I.C.3 the required Volkov solution [93] for an electron of initial four-momentum $p$ to read

$$
\begin{aligned}
\psi_p(x) = \sqrt{\frac{m}{VE_p}} &\left[1 - \frac{e\gamma^\mu A_\mu(k \cdot x)\gamma^\nu k_\nu}{2k \cdot p}\right] \\
&\times \exp\left[-ip \cdot x - i\int_0^{k \cdot x}\left(\frac{eA(\phi) \cdot p}{p \cdot k} - \frac{e^2 A^2(\phi)}{2p \cdot k}\right)d\phi\right]u_p.
\end{aligned}
\tag{75}
$$

For considering Mott scattering in a powerful laser field in the first-order Born approximation we have to evaluate the $T$-matrix element

$$T_{fi} = -i\int dx \, \overline{\psi}_{p'}(x)\gamma^\mu U_\mu(x)\psi_p \tag{76}$$

where scattering takes place for an electron of initial four-momentum $p$ to a final momentum $p'$. In Eq. (76) we describe the ingoing and outgoing electron by Volkov waves of the form Eq. (75) and we decompose this matrix element into its Fourier components in space and time, using the definition of the generalized Bessel functions Eq. (8). Then we find by straightforward calculation

$$
\begin{aligned}
T_{fi} = -i\frac{m}{V\sqrt{E'E}}\sum_N &\int dt \exp[i(\overline{E}' - \overline{E} - N\omega)t] \\
&\times \int d\vec{r}\, U(\vec{r})\exp\left[-i(\overline{\vec{p}}' - \overline{\vec{p}} - N\omega\vec{n}) \cdot \vec{r}\right]M_N,
\end{aligned}
\tag{77}
$$

where $U(\vec{r})$ is again a screened Coulomb potential of charge $eZ$ and screening length $\ell$ and the nonlinear matrix elements $M_N$ are given by

$$
\begin{aligned}
M_N = B_N \bar{u}_{p'} \gamma^0 u_p &+ \frac{eA_0}{4k \cdot p'}(B_{N+1} + B_{N-1})\bar{u}_{p'}\gamma^\mu \epsilon_\mu k^\nu \gamma_\nu \gamma^0 u_p \\
&- \frac{eA_0}{4k \cdot p}(B_{N+1} + B_{N-1})\bar{u}_{p'}\gamma^0 \gamma^\mu \epsilon_\mu k^\nu \gamma_\nu u_p \\
&- \frac{e^2 A_0^2}{8(k \cdot p')(k \cdot p)}\left[B_N + \frac{1}{2}(B_{N+2} + B_{N-2})\right]\bar{u}_{p'}\gamma^\mu \epsilon_\mu k^\nu \gamma_\nu \gamma^0 \gamma^\sigma \epsilon_\sigma k^\tau \gamma_\tau u_p,
\end{aligned}
$$

(78)

in which we now assumed the plane-wave field to be monochromatic and linearly polarized so that in the Coulomb gauge $A_\mu$ has the explicit form

$$
A^\mu(k \cdot x) = A_0 \epsilon^\mu \cos(k \cdot x), \quad \epsilon^\mu \equiv (0, \vec{\epsilon}), \quad \epsilon^2 = -1, \quad \vec{\epsilon}^2 = 1.
$$

(79)

Under these conditions, in the matrix element of Eq. (78) the arguments $x$ and $y$, defined in Eq. (68) of the generalized Bessel functions are determined by the same parameters as those in Eq. (61) for a Klein–Gordon particle. Since the Fourier transform $U(\vec{q})$ of the screened Coulomb potential in Eq. (77) can be easily calculated, we are able to evaluate from the Eqs. (77) and (78) the transition probability per unit time to read

$$
w_{fi} = \lim_{T \to \infty} \frac{|T_{fi}|^2}{T} = \sum_N \frac{2\pi m^2}{V^2 E'E}|U(\vec{p}' - \vec{p} - N\omega\vec{n})\ M_N|^2\ \delta(\overline{E}' - \overline{E} - N\omega),
$$

(80)

where for the laser-dressed electron momenta and energies the same notation is used as in Eq. (61) of Section I.E.2. From the transition probabilities, Eq. (80), we can finally evaluate the differential cross sections of the nonlinear scattering processes of the order $N$. We find

$$
\frac{d\sigma_N^{(s,s')}}{d\Omega'} = \frac{p'_N}{p}\frac{4(mZ\alpha)^2}{F_N}\frac{|M_N|^2}{[(\vec{\overline{p}}' - \vec{\overline{p}} - N\vec{k})^2 + \ell^{-2}]^2}.
$$

(81)

In Eq. (81), the indices $s$ and $s'$ are labelling the spin polarizations of the incoming and outgoing electrons and have the possible values $+$ or $-$. These indices, $\pm$, have the meaning that the spin polarization of an electron in its rest frame has the values $\pm 1/2$ with respect to the $z$-axis. For an

unpolarized beam of electrons, we should average over the initial and sum over the final spin polarizations, *viz.*

$$\frac{d\sigma_N}{d\Omega'} = \frac{1}{2} \sum_{s,\,s'=\pm} \frac{d\sigma_N^{(s,\,s')}}{d\Omega'}.$$    (82)

The energy conservation relation, that follows from Eq. (80), is the same as in Eq. (64) for scattering of a Klein–Gordon particle and the same is true for the generalized Bessel functions $B_N$ and their arguments, defined in the Eqs. (8) and (68). Similarly, we obtain in calculating the phase space the same function $F_N$, defined in Eq. (65). The evaluation of the matrix elements, appearing in the Eq. (78) and containing Dirac spinors and $\gamma$-matrices, is performed numerically, using appropriate software, and therefore their explicit result will not be written down here. In the following section, we shall present a comparison of the cross sections calculated for scattering of a spin 0 or a spin 1/2 particle in a very powerful laser field and we shall see that spin effects are marginal even at very high laser powers and/or electron energies, which is similar to what we found for Compton scattering in Section I.C.4. On the other hand, there are some interesting phenomena observable at very powerful laser fields, as we shall discuss in more detail below.

### E.5. *Analysis of spin effects at high laser powers*

For the following numerical analysis of the differential cross sections Eqs. (63), (81), and (82) for a linearly-polarized electromagnetic plane-wave field we shall fix the screening length $\ell$ of the scattering potential as before to $\ell = 1$ a.u. and take for the nuclear charge $Z = 1$. As frequency of the radiation field we shall consider $\omega = 1.17\,\text{eV}$ of a Nd:YAG laser. We investigate the angular and intensity dependence of the differential cross sections $d\sigma_N/d\Omega'$, given by the Eqs. (63), (81), and (82), for selected values of the laser field intensity $I$, initial kinetic electron energy $E_{\text{kin}}$ and order of nonlinearity $N$. As it turns out, it is of particular interest to consider high-energy electrons in the MeV range and, similarly, to choose radiation powers for which the ponderomotive energy $U_p = m\mu^2/4$ is of the order of magnitude of the electron rest energy $m$.

In Fig. 12 we analyze the dependence of the differential cross sections, either evaluated from Eq. (63) for a Klein–Gordon particle or from Eqs. (81) and (82) for a Dirac particle. For presenting our data, we chose in this figure the laser beam to propagate along the $x$-axis, i.e. $\vec{n}\|\vec{e}_x$, and its unit vector of linear polarization, $\vec{\epsilon}$, to define the $z$-direction, or $\vec{\epsilon}\|\vec{e}_z$, which
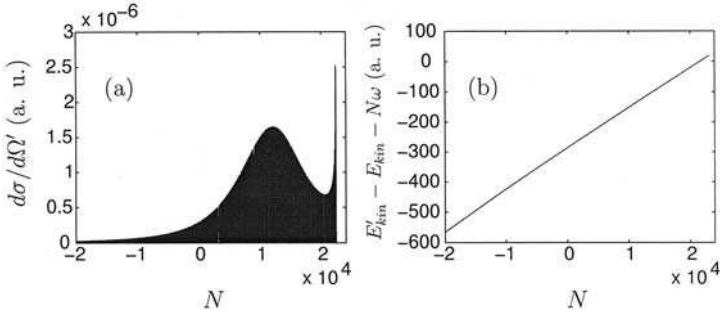
FIG. 12. Presents for the parameters $I = 10^{19}\,\text{Wcm}^{-2}$ and $E_{\text{kin}} = 2m$ in panel (a) the differential cross sections as a function of $N \lessgtr 0$ for $\theta' = 1°$, $\varphi' = 0°$ and electron incidence along the polarization $\vec{\epsilon}$. The cross sections are large for $N \gg 0$ and the cutoff is near $N_0 = 22352$. Panel (b) demonstrates the deviation of the relativistic energy conservation law from the nonrelativistic one (see ref. [163]).

also determines our polar axis whereas the azimuthal angle $\varphi$ is measured with respect to the $x$-axis in the $(x, y)$-plane. Our results are shown for fixed polar angles of electron incidence $(\theta, \varphi)$ and of scattering $(\theta', \varphi')$ as a function of the number $N$ of absorbed or emitted laser photons $\omega$. Both relativistic cross section formulae yield, in general, the same results. We shall discuss deviations between the data for a particle of spin 0 and spin 1/2 further below. As it turns out, the cross sections are particularly large for small scattering angles. Therefore the angles of electron incidence with respect to the $z$-axis are chosen $\theta = 0°$ and $\varphi = 0°$ and we consider scattering at a very small angle with $\theta' = 1°$ and $\varphi' = 0°$. The laser frequency $\omega$ will be the same as above and for the intensity we took $I = 10^{19}\,\text{W}\,\text{cm}^{-2}$ while the initial kinetic electron energy we assumed to be $E_{\text{kin}} = E - m = 2m$. In our present figure we show the evaluated differential cross sections as a function of $N$ in panel (a), which is demonstrating that these cross sections (presented in atomic units, denoted by a.u.) are considerably larger for photon absorption than for photon emission. A reasonable estimate for the cutoff value $N_0$ of the electron spectrum can be found from the approximate formula $N_0 = \pm|x| \pm 2|y|$, where $x$ and $y$ are the two arguments of the generalized Bessel functions, Eqs. (61) and (68). In our present case, the numerical calculations for the data shown in panel (a) yield the cutoff at $N_0 \simeq 22352$. For this case, the arguments $x$ and $y$ are found to be $x \simeq -23238$ and $y \simeq 126$ so that $|x| - 2|y| \simeq 22986$, which is in reasonable agreement with the value of $N_0$, given before. In panel (b) we show the deviation of the relativistic energy conservation law, Eq. (64), from the nonrelativistic energy relation $E'_{\text{kin}} = E_{\text{kin}} + N\omega$. This deviation represents an intensity-dependent energy excess. One can also show that the cross

section data perform rapid oscillations as a function of the nonlinear order
$N$. Such rapid changes with an almost periodic sequence of maxima and
minima can be qualitatively well explained by analyzing the properties of the
generalized Bessel functions $B_N$, defined in Eqs. (8) and (68). This analysis,
however, cannot be done analytically, due to the complicated dependence of
both arguments in Eq. (68), via the Eqs. (61) and (64), on the number $N$
of emitted or absorbed photons, but requires a numerical evaluation. This
result is very much different from the findings in non-relativistic potential
scattering in a laser field, since in the low-frequency limit the argument of
the Bessel functions $J_N$ in Eq. (69) becomes independent of $N$.

As we have indicated before, in the relativistic regime of electron kinetic
energies $E_{\text{kin}}$, being of the same order of magnitude as the electron
rest energy $m$, the scattering formulas for a Klein–Gordon particle and a
Dirac particle yield almost the same cross section values, in particular,
for close to forward scattering where the cross section data are largest.
On the other hand, the two expressions Eq. (63) and Eqs. (81) and (82) yield
significantly different values for the cross sections in the backward direction
where, however, the cross section values are particularly small. In order
to show this, we present in panel (a) of Fig. 13 a comparison of the
Klein–Gordon and Mott scattering data for the same scattering geometry
as before, i.e. with electrons impinging on the target along the $z$-axis
($\theta = \varphi = 0°$) and scattered by an angle $\theta' > 0°$ for $\varphi' = 0°$ or scattered by an
angle $\theta' < 0°$ for $\varphi' = 180°$. The ingoing kinetic energy of the electron is
$E_{\text{kin}} = 1$ MeV$\simeq 2m$ and we consider the elastic case with $N = 0$. As we
recognize, the cross section data (dashed line for Klein–Gordon particles
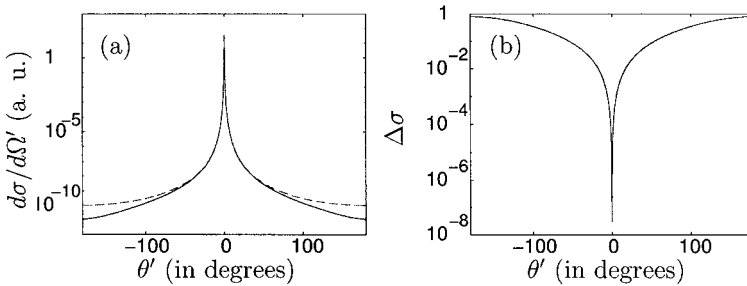


FIG. 13. Presents for the same scattering configuration and parameter values as in Fig. 12
and for elastic scattering, with $N = 0$, in the left panel the differential cross sections of
Mott-scattering (solid line) and Klein–Gordon scattering (dashed line) as a function of $\theta'$. In the
right panel is shown the normalized difference $\Delta\sigma$ of these cross sections. Apparently, spin
effects are visible only at large scattering angles (see ref. [163]).

and solid line for Dirac particles) are almost identical except for backward scattering. This can be seen even more clearly in panel (b) of Fig. 13, where we present the normalized difference $\Delta\sigma$ of these cross section data, defined by

$$\Delta\sigma \equiv \frac{|d\sigma_{\mathrm{D}}/d\Omega - d\sigma_{\mathrm{KG}}/d\Omega|}{d\sigma_{\mathrm{D}}/d\Omega + d\sigma_{\mathrm{KG}}/d\Omega} \tag{83}$$

which can have the values $0 \leq \Delta\sigma \leq 1$. As this panel shows, for $|\theta'| \simeq 0°$ the deviations between the cross section data for Dirac and Klein–Gordon particles are very small and only gradually increase for $|\theta'|$ approaching backscattering at $180°$.

The properties of the differential cross sections, presented in Fig. 13, can be found in general for values of $N \neq 0$ and for relativistic electron energies and laser intensities where $E_{\mathrm{kin}}$ and $U_P$ are in the MeV energy range. The differences between the cross sections for a Dirac and a Klein–Gordon particle will be significant only at large scattering angles where we shall simultaneously find a dip in the final electron energy $E'_{\mathrm{kin}}$.

Finally, we can also investigate in some detail the dependence of the nonlinear cross sections for a Dirac particle on the spin orientation and spin-flip. The differential cross sections, evaluated from Eq. (81) for the spin orientations $(s = +, s' = +)$ and for $(s = -, s' = -)$, turn out to be identical and the same holds for the cross sections with spin-flip $(s = +, s' = -)$ and $(s = -, s' = +)$. Moreover, we find that spin-flip leads to cross sections which are by about one order of magnitude smaller than the data for no flip and we also recognize differences in the angular behavior. We may therefore conclude that the probabilities of changing the spin orientation during scattering are in general very much smaller than for no change of the spin orientation, at least for the highly relativistic electron energies and laser intensities considered. More details on this topic can be found in ref. [163].

### E.6. Concluding remarks

In conclusion, we have considered in the present section potential scattering of electrons in a powerful laser field in the semi-relativistic and relativistic regions. We compared, on the basis of the scattering configuration of Fig. 8, the differential cross section data in the directions (+) and (−) and found considerable asymmetries that, however, do not follow the elementary asymmetry relation Eq. (59) of the low frequency limit. Characteristic "dark

windows" in the scattering cross sections were observed for certain regions of the scattering angle $\theta$ and rapid oscillations of the scattering data were found in other angular domains. Moreover, a similar asymmetry relation as Eq. (59) was derived for the relative energy change $\Delta E'_{\text{kin}}/E_{\text{kin}}$ in the semi-relativistic limit, Eq. (72), and the numerical data obtained from it were compared with the exact results for $\Delta E'/E_{\text{kin}}$ evaluated from the relativistic energy conservation relation, Eq. (64). Here the results of the semi-relativistic calculations agreed reasonably well with the exact calculations. Moreover, we have shown that even for moderate laser field intensities of some $10^{15}\,\text{W}\,\text{cm}^{-2}$, still far below the critical intensity $I_c \simeq 10^{18}\,\text{W}\,\text{cm}^{-2}$, for certain scattering geometries considerable differences are found between the predictions of the relativistic and nonrelativistic scattering formulas and energy conservation relations. These discrepancies originate in the space-dependence of the radiation field. This indicates that the use of nonrelativistic calculations for the description of laser-induced and laser-assisted processes may break down at much lower laser intensities than commonly expected. In particular, the use of the dipole approximation for the laser intensities considered above may become questionable. Further details of the above investigations can be found in our very recent work on this topic [164–166].

As our numerical analysis of the spin effects has shown, these effects on the differential cross sections $d\sigma_N/d\Omega'$ with the emission or absorption of $N$ laser photons, are in general marginal in the present process, in particular, for scattering in close to forward direction. Small spin effects by spin-flip can be observed at large scattering angles where, however, the cross sections are very small. Even in this case, the data with spin-flip are by orders of magnitude smaller than those with no flip. In this latter case, the cross sections for a Dirac particle are almost identical with those for a Klein–Gordon particle over the whole range of scattering angles. Of particular interest, as in our previous investigations of this scattering problem at lower laser field intensities, is a scattering configuration in which the electrons impinge on the target in the direction of the laser polarization $\vec{\epsilon}$ and the scattering plane is determined by the direction of propagation $\vec{n}$ of the laser field and its polarization $\vec{\epsilon}$, as shown in Fig. 8. We expect, on the basis of the results of our investigation, for laser powers (measured by the ponderomotive energy) and for electron energies in the MeV range, being equivalent to energies of the electron's rest mass, that similar conclusions can also be drawn for other fundamental scattering processes, namely that spin effects are in general marginal for laser-induced or laser-assisted processes even at very high laser powers. These conclusions were confirmed by our recent investigations of Compton scattering at very high laser powers [89], about which we reported in Section I.C.

# II. Reactions

If we consider a laser source, like a Nd:YAG laser with quanta of energy $\hbar\omega = 1.17\,\text{eV}$, then in general the simultaneous absorption of several photons will be required to ionize an atom whose ionization energy $I_{io} \gg \hbar\omega$. Thus, the atom poses a certain threshold beyond which multiphoton ionization is possible. With increasing power of the laser sources available, it turned out, however, that the ionized electron can also absorb photons beyond a certain threshold value $N_0\hbar\omega$ and a whole spectrum of above-threshold ionization (ATI) peaks can be observed [167,168]. This ATI, in particular of noble gases, has been predicted many years ago by Keldysh [103] who performed a simple model calculation which we shall present in a slightly modified form below. The same model has been reinvestigated later on by Faisal [169] and by Reiss [83]. Hence, this model has been termed the KFR-model. In the following we shall analyze ATI on the basis of the KFR-model in the one-electron approximation, although this model only describes the basic features of this process correctly but not the finer details.

In this model it is assumed that initially the electron to be ionized is in the ground state $\Psi_0(\vec{r}, t) = u_0(\vec{r})\exp(-iE_0t/\hbar)$ of the atomic system where the Coulomb field strength $\mathcal{E}_c$ is much larger than the laser field strength $\mathcal{E}_0$ so that the laser field can be considered as a perturbation. Then, in lowest order of perturbation theory, the electron becomes virtually scattered by the atomic potential $V(r) = -Ze^2/r$ and turns into a free particle embedded in the laser field which yields to ionization. During ionization the laser field strength is now much larger than the Coulomb field so that it can be considered as a perturbation. In this way one may envisage ATI as a "single-armed" potential scattering of electrons in a laser field. It is therefore not surprising that most of the theoretical methods developed for investigating free–free transitions are equally useful in the detailed treatment of ATI and vice versa. The ionized electron will be described by a similar laser-modulated plane-wave as we used for the free–free transitions in Section I.D. Thus the $T$-matrix element of ATI will read in the KFR-model

$$T = -\frac{i}{\hbar}\int d\vec{r}\,dt\,\exp[(i/\hbar)(Et + \sigma t - \vec{p}\cdot\vec{r} - \alpha_0\vec{p}\cdot\vec{\epsilon}\sin\omega t)]$$
$$\times\,V(r)u_0(\vec{r})\exp(-iE_0t/\hbar) \tag{84}$$

where the electron suffers in the powerful laser field a Stark shift $\sigma$ which is equal to the ponderomotive energy $U_P$ of the electron. This is defined as the

average kinetic energy of the electron in the field which is equivalent to the energy of its quiver motion. Hence we obtain from Eq. (1) $\sigma = U_P = m\langle \vec{v}^2 \rangle / 2 = mc^2 \mu^2 / 4$. For the ground state of the atom we use for simplicity the wave function of a hydrogen-like atom, i.e., $u_0(\vec{r}) = (4\pi)^{-1/2} \times (Z/a_B)^{3/2} \exp(-Zr/a_B)$, where $Z$ is the nuclear charge and $a_B$ the Bohr radius. The evaluation of the $T$-matrix element (84) is then straightforward and yields

$$T = \sum_N T_N, \; T_N = -\frac{8\pi i Z e^2}{(Z/a_B)^2 + (p/\hbar)^2} \left(\frac{Z}{a_B}\right)^{3/2}$$
$$\times J_N(\rho \vec{p} \cdot \vec{\epsilon}) \delta(E + U_P + I_{io} - N\hbar\omega) \tag{85}$$

from which we evaluate the differential cross sections of above threshold ionization to be given by

$$\frac{d\sigma_N}{d\Omega} = r_0^2 \frac{32 Z p c}{\mu^2 \hbar\omega [1 + (pa_B/Z\hbar)^2]^2} J_N^2(\rho \vec{p} \cdot \vec{\epsilon}) \tag{86}$$

where, as before, $r_0$ is the classical electron radius while $\varrho = \mu c/\hbar\omega$. The kinetic energy of the ionized electron is determined by the energy conservation relation found from Eq. (85) to be given by $E = N\hbar\omega - I_{io} - U_P$ where $I_{io} = -E_0$ is equal to the ionization energy. As we can see, the threshold condition for ionization is given by $N_0 \hbar\omega \geqslant I_{io} + U_P$. Thus we may write $N = N_0 + S$ where $S \geqslant 0$ counts the order of the above-threshold ionization peaks. For the corresponding electron momenta we find $p = \sqrt{2m(N\hbar\omega - I_{io} - U_P)}$. With increasing intensity of the laser field, the number $N_0$ of photons required to yield ionization will increase, since the ponderomotive energy $U_P$ is a linear function of the intensity $I$ and thus raises the ionization limit. Near the ionization threshold the energy of the ionized electron will be $E \leqslant \hbar\omega$ and thus $pc/\hbar\omega \leqslant \sqrt{2mc^2/\hbar\omega} \approx 10^3$ for a Nd:YAG laser. If we want to have the cross sections near threshold sufficiently large, i.e., $J_N^2(\mu pc/\hbar\omega)$ of appreciable magnitude, we will have to require $N_0 \approx \mu pc/\hbar\omega$. Therefore, with our above estimate, we must have $\mu \approx 10^{-3} N_0$. For xenon as target atom, with $I_{io} = 12.13$ eV, we need $N_0 = 12$ and consequently we must take $\mu \approx 10^{-2}$ which corresponds to a laser-field intensity of about $10^{14}$ W cm$^{-2}$.

In this case the prefactor of Eq. (86) becomes $32 r_0^2 Z \times 10^7$ so that this factor has roughly the value $a_B^2$. Thus, in this idealized case, the cross section turns out to be approximately of the same order of magnitude as the cross section of elastic electron–atom scattering in Section I.D. However, in order

to achieve this, a considerable higher laser field intensity is required than was necessary to observe free–free transitions. At lower laser-field intensities we can again expand the Bessel function into its power series keeping only the first term of the expansion. In this case we find from Eq. (86)

$$\frac{d\sigma_N}{d\Omega} = \frac{32 r_0^2 Z}{2^{2N}} \left(\frac{I}{I_c}\right)^{N-1} \left(\frac{pc}{\hbar\omega}\right)^{2N+1} (\vec{n} \cdot \vec{\epsilon})^{2N} \tag{87}$$

where $\vec{n}$ is the direction of emission of the ionized electron and $I/I_c = \mu^2$. However, these cross section values are considerably enhanced near threshold due to the action of the Coulomb field of the residual ion on the ionized electron [170].

Turning next to higher harmonic generation (HHG), we perform the following simple calculation. In the presence of a strong laser field the wave function of an atom becomes a periodic function of time $\Psi(\vec{r}, t) = \Psi(\vec{r}, t + T)$ where $T = 2\pi/\omega$ is the period of the laser field. Thus we may expand this wave function into its Fourier components and evaluate the dipole matrix elements to obtain

$$\begin{aligned}
\langle \Psi(t)|\vec{d}|\Psi(t)\rangle &= \int d\vec{r} dt \Psi^*(\vec{r}, t) \vec{d} \Psi(\vec{r}, t) \\
&= \sum_{m,n} \vec{d}_{m,n} \exp[-i(m-n)\omega t] \\
&= \sum_{M} \vec{d}_N \exp[-i(2M+1)\omega t].
\end{aligned} \tag{88}$$

Consequently, we obtain dipole elements $\vec{d}_N = \vec{d}_{2M+1}$ corresponding to the emission of harmonics of frequencies $\omega' = N\omega$ with $N = 2M + 1$ where $M = 1, 2, 3, \ldots$ The reason why only odd harmonics are generated is related to the spherical symmetry of the atomic ground state which has parity $P = 1$. Since during the harmonic generation the atom becomes excited by absorbing $N$ photons from the laser beam and then returns to the ground state by emitting a harmonic quantum, the parity of the total system must remain unchanged during the process. But the parity of the absorbed photons is $P = (-1)^N$ and the parity of the emitted photon $P = -1$ and consequently parity conservation requires that $(-1)^N = -1$ (since the parity of the ground state remains unchanged) from which the above restriction to odd harmonics follows. This is contrary to what happens in the case of harmonic generation at a solid surface, discussed previously, where there is no spherical symmetry of the system. Using the fact that $\vec{d}_N = -e\vec{r}_N$ and that the corresponding classical acceleration $\vec{v}_N' = -\omega_N^2 \vec{r}$ we may

employ Thomson's cross section formula Eq. (4), adapted to our problem, to evaluate the cross sections of the generated harmonics. We thus find

$$\frac{d\sigma_N}{d\Omega} = \left(\frac{\omega'^4}{4\pi c^3 I}\right)|\vec{d}_N|^2 \sin^2\phi = \left(\frac{8N^4}{\mu^2}\right)\left(\frac{\hbar\omega}{2mc^2}\right)^2 \alpha^2 |\vec{r}_N|^2 (\vec{\epsilon}' \cdot \vec{\epsilon})^2 \qquad (89)$$

where $\vec{\epsilon}'$ is the vector of linear polarization of the harmonic field and we have used the identity $\sin\phi = \vec{n}' \cdot \vec{\epsilon} = \cos\theta = \vec{\epsilon} \cdot \vec{\epsilon}'$. $\alpha = e^2/\hbar c$ is the fine structure constant. From our elementary results on laser-induced Thomson scattering in Section I.B.1 and on account of some considerations on harmonic generation, using time-dependent perturbation theory, we conclude that in the perturbative regime $|\vec{r}_N|$ is of the order of magnitude $[\mu\alpha(mc^2/\hbar\omega)]^N a_B$ so that we obtain from Eq. (89) the approximation

$$\sigma_N \approx \frac{16\pi}{3} N^4 \left(\frac{I}{I_c}\right)^{N-1} \alpha^{2(N+1)} \left(\frac{mc^2}{\hbar\omega}\right)^{2(N-1)} a_B^2. \qquad (90)$$

Considering the production of the third harmonic by irradiating an atom with a Nd:YAG laser pulse of an intensity of $10^{14}$ W cm$^{-2}$ for which $I/I_c \approx 10^{-4}$, we then find from Eq. (90) $\sigma_3 \approx a_B^2$. Hence, under these conditions, the cross sections of harmonic generation are of about the same order of magnitude as those for free–free transitions, considered in Section I.D, but the laser power required is considerably higher. Hence free–free transitions have the favorable property of requiring comparatively low laser power for observing the laser-induced nonlinearities. This is also the reason why rather early a considerable number of investigations has been devoted to this process quite a long time before ATI and HHG were considered.

A considerable amount of insight into the above processes can be gained by the following simple semi-classical considerations, suggested in various forms by several authors [171–173]. In this so-called "*three-step model*" the first step describes the ionization of an atomic electron, while the second step regards the propagation of the free electron in the laser field. The third step considers the collision between the electron, driven back by the laser field, and the atomic core, whereupon the electron either recombines, emitting a harmonic photon, or rescatters at the atomic core to gain in the laser field further energy by absorbing additional photons in the ATI process (see, for example, the reviews [174,175]). This model is schematically presented in Fig. 14 for the HHG process. In this figure, the above-mentioned steps are denoted by the numbers 1, 2, and 3, respectively. The atom, having the ionization energy $I_{io}$, is in its ground state when the laser field is switched on. The atomic potential becomes lowered by the

$$\hbar\Omega = I_{io} + E_k = I_{io} + 3.17 U_P$$
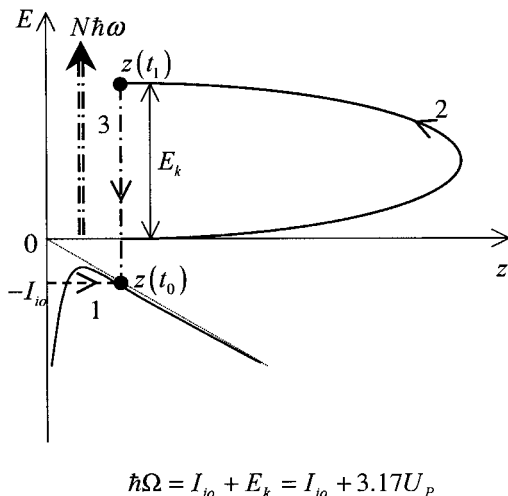
F<span style="font-variant:small-caps">IG</span>. 14. Schematic presentation of high-harmonic generation according to the three-step model. The laser field is linearly polarized along the $z$-axis. The numbers 1, 2, and 3 denote the steps of the three-step model. The $E$-axis denotes the electron energy coordinate. See the text for more detailed explanation.

superposition of the Coulomb field and the laser field so that the atom can be ionized either by tunneling or by multiphoton ionization. The atomic electron is born at the point $\vec{r}(t_0)$ with the velocity $\vec{v}_0$ where both are usually assumed to be zero (i.e. the electron has absorbed the minimum number $N_0$ of photons required for ionization). The free electron now propagates in the laser field and aquires an energy $E_k$. When the electron has come back to the origin ($\vec{r}(t_1) = \vec{r}(t_0)$), it can recombine, emitting a harmonic photon of energy $\hbar\omega' = I_{io} + E_k$. The observed HHG spectrum forms an extended plateau which consists of many harmonics with comparable intensities. The maximum kinetic energy which the ionized electron can acquire in a linearly-polarized laser field, will be shown below to be $E_k = 3U_P$ (or more precisely $3.17U_P$) where $U_P$ is the ponderomotive energy, defined before.

Before presenting a classical analysis of the above cutoff law of harmonics, $\hbar\omega'_{\max} = I_{io} + 3.17U_P$, we shall discuss a simple derivation of the parameter $\gamma$, introduced by Keldysh [103]. This parameter permits to characterize the difference between tunneling and multiphoton ionization. The Keldysh parameter can be defined by the ratio $\gamma = \tau/T$. Here $\tau$ is the time required by the atomic electron to tunnel through the potential barrier, formed at a certain instant of time $t$ by the overlap of the atomic

Coulomb potential $V_c(r)$ and the electric dipole potential $V_L(z, t) = -ez\mathcal{E}_0 \sin \omega t$ of the laser field (see Fig. 14), whereas $T = 2\pi/\omega$ is the period of the radiation field oscillations. If $\gamma \ll 1$, then the ionization took place quasi-instantaneously by tunneling of the electron through the potenial at a particular instant of time $t$, whereas for $\gamma \gg 1$ the laser field performs during ionization many oscillations and therefore multiphoton ionization will prevail. A more convenient definition of the Keldysh parameter is to consider the expression $\gamma = \tau\omega$. In order to obtain the maximum average value of the tunnel time $\tau$, we consider the corresponding maximum value of the tunnel length $l = v_\tau\tau$ which, by inspecting the Fig. 14, is determined by the relation $I_{io} = el\mathcal{E}_0/2$, since we have to consider the average over one period, $\langle \sin^2 \omega t \rangle = 1/2$, of the oscillatory electric dipole potential. If, on the other hand, we assume that, on account of Bohr's correspondence principle and the virial theorem, the tunnel velocity $v_\tau$ is equal to the electron velocity on the first Bohr orbit $v_\tau = v_0 = \alpha c$, where $\alpha = e^2/\hbar c$ is the fine structure constant, then we find from the foregoing two relations $\tau = l/v_\tau = 2I_{io}/e\mathcal{E}_0\alpha c$ and consequently the Keldysh parameter can be expressed in the form [103]

$$\gamma = \tau\omega = \sqrt{\frac{I_{io}}{2U_P}}. \tag{91}$$

In order to present a classical analysis of the energies which an ionized electron can gain, moving after ionization freely in the laser field, we perform the following simple calculation, based on considerations on the energy spectrum of electrons obtained from Rydberg atoms placed into a microwave field [176,177]. With reference to our Fig. 14, we shall assume that at the instant of ionization $t = t_0$ the ionized electron has the initial velocity $\vec{v}_0 = 0$. Neglecting the interaction with the residual ion, the electron follows for $t \geq t_0$ the classical Lorentz equation of motion, neglecting in dipole approximation the magnetic term $(e/c)(\vec{v} \times \vec{\mathcal{B}})$

$$\frac{d\vec{v}}{dt} = \frac{e\mathcal{E}_0}{m}\vec{\epsilon} \sin \omega t \tag{92}$$

and after integration with the above initial condition we find

$$\vec{v} = -\mu c\vec{\epsilon}(\cos \omega t - \cos \omega t_0) \tag{93}$$

from which we evaluate the kinetic energy $E_{kin}$ of the ionized electron averaged over one period of the laser field

$$\langle E_{kin} \rangle = \frac{m}{2}\langle \vec{v}^2 \rangle = U_P(1 + 2\cos^2 \omega t_0). \tag{94}$$

Hence the kinetic energy of the ionized electron will lie within the limits

$$U_P \leq E_{\text{kin}} \leq 3U_P, \tag{95}$$

as in fact was experimentally observed for the energy spectrum of electrons obtained by the ionization of Rydberg atoms in a microwave field [178,179]. Applying the result Eq. (95) to the ionization of an atom in a laser field, we immediately conclude, if the ionized electron recombines with the residual ion (following the three-step model discussed above) that the maximum photon energy of HHG will be given by

$$\hbar\omega_{\text{max}} = I_{io} + 3U_P, \tag{96}$$

where the more precise cutoff law for HHG, $I_{io} + 3.17U_P$, can also be obtained classically by calculating, instead of the average kinetic energy, the maximum kinetic energy of the electron with the additional condition (constraint) that the electron returns to the atomic core. The factor 3.17 is obtained as the solution of a nonlinear equation that is obtained in this way (see ref. [21] and references therein). More precise quantum mechanical calculations yield in addition a prefactor in front of the ionization potential $I_{io}$ so that the cutoff law reads $\hbar\omega_{\text{max}} = 1.32I_{io} + 3.17U_P$ [180,181].

Instead of recombining and emitting harmonic photons, the ionized electron can also rescatter at its ionic core thereby picking up further photons from the laser field thanks to free–free transitions. In this way an extended plateau of ATI peaks becomes generated as we shall discuss in more detail in the next section. The maximum energy that can be gained by the ionized electron in this way can also be evaluated, using our above simple classical calculation [170]. Since according to Eq. (95) the average energy acquired by the electron during the second step of the ionization process is $E_{\text{kin}} = 2U_P$, we can reconsider the Eq. (95) and solve it with the initial condition $\vec{v}(t_0) = \vec{v}_0$. In this way we find for the average kinetic energy $\langle E_{\text{kin}} \rangle$ gained by the electron in the laser field during the rescattering process

$$\langle E_{\text{kin}} \rangle = U_P[1 + 2\cos^2 \omega t_0] + \frac{1}{2}m\vec{v}_0^2 - 2\sqrt{mU_P}\vec{v}_0 \cdot \vec{\epsilon}\cos \omega t_0. \tag{97}$$

If we then choose for the initial electron velocity at the rescattering process, $\vec{v}_0 = -2(\sqrt{U_P/m})\vec{\epsilon}$, assuming that $\frac{1}{2}m\vec{v}_0^2 = 2U_P$, then we find from Eq. (97) for the maximum kinetic energy of the electron after rescattering

$$\langle E_{\text{kin}} \rangle = 3U_P + 2U_P + 4U_P = 9U_P \tag{98}$$

and this is the energy at which the sidelobes in the angular distributions of the ionized electrons are observed [174]. If, however, the electrons are rescattered with the initial energy $3U_P$, then the maximum energy the electrons can acquire in the laser field during rescattering will follow from Eq. (97) to be

$$\langle E_{\text{kin}} \rangle = 3U_P + 3U_P + 2\sqrt{6}U_P \approx 11U_P \tag{99}$$

which quite well agrees with the cutoff energy of the plateau found experimentally [174]. Also here, as in the case of the cutoff law for HHG, a more precise cutoff energy can be evaluated by maximizing the average electron energy with the condition that the electron rescatters at the atomic core. To this end, one solves the system of equations $\vec{r}(t_1) = 0$ and $\partial\langle E_{\text{kin}}\rangle/\partial t_o = 0$ where $t_o$ and $t_1$ are the instant of ionization and the instant of rescattering, respectively. In this way we obtain for the maximum energy of the rescattered electrons $\langle E_{\text{kin}}\rangle_{\text{max}} = 10.007\, U_P$ (see ref. [21] and references therein).

Finally, the reader might think that by going to increasingly higher laser powers, such that a relativistic treatment of ATI and HHG will become important, we should be able to achieve very much higher harmonic frequencies and, similarly, a more extended plateau of ATI peaks. Unfortunately, this is not true as the following simple classical calculation will show. For higher laser powers we have to add in the Lorentz equation of motion Eq. (92) the magnetic term $(e/c)(\vec{v} \times \vec{\mathcal{B}})$. But for a plane-wave field $\vec{\mathcal{B}} = \vec{n} \times \vec{\mathcal{E}}$, where $\vec{n}$ is the direction of propagation of the plane wave, and in an iterative solution of the Lorentz equation we may introduce into the above magnetic term for $\vec{v}$ the approximation $\vec{v} = -\mu c\vec{\epsilon} \cos \omega t$. Then the Lorentz equation can be written in the form

$$\frac{d\vec{v}}{dt} = \frac{e\mathcal{E}_0}{m}\{\vec{\epsilon}\sin \omega t - \mu[\vec{\epsilon} \times (\vec{n} \times \vec{\epsilon})]\cos \omega t \sin \omega t\} \tag{100}$$

and its integration yields with the initial condition $\vec{v}(t_0 = 0) = 0$

$$\vec{v} = -\mu c\{\vec{\epsilon}\cos \omega t + (\mu/4)\vec{n}(1 - \cos 2\omega t)\} \tag{101}$$

from which follows that the ionized electron experiences in addition to its oscillatory motion in the direction of laser polarization $\vec{\epsilon}$, driving the electron back to the residual ion, also a drift motion in the direction $\vec{n}$ of laser-field propagation, perpendicular to the direction $\vec{\epsilon}$. Therefore, with increasing laser-field intensity, the electron will not come back so easily to the ion to either recombine, emitting a harmonic photon, or to rescatter at

the ion to lead to an extended plateau of ATI peaks. This conclusion is confirmed quantum mechanically and we shall therefore restrict our considerations below to laser field intensities for which $\mu^2 \ll 1$ such that nonrelativistic calculations are adequate and the laser field can be treated in the dipole approximation. There are, however, exceptions where relativistic calculations for very high laser powers become of interest, namely, if ATI, HHG and related processes are considered for highly charged ions. This topic has been investigated in some detail by Keitel and coworkers [182–189] in whose papers further references can be found but we shall not go into details here. Very short and ultra-intense laser pulses of some $10^{21}$ W cm$^{-2}$, interacting with highly charged ions, can also be used to generate electrons with kinetic energy in the GeV range. Discussions and references on this topic can be found in refs. [190–192].

Additional information can be obtained from the books and reviews [2, 3, 6–18, 21–24]. Since ATI and HHG are presently the main subjects of investigation in the regime of high laser powers, we shall discuss the various interesting features of these processes in more detail in the following. Our considerations and calculations will be based on the *S*-matrix approach for evaluating the required transition probabilities. In the domain of high laser powers various approximations can be made to achieve this goal, at least in an approximate way, thanks to the fact that in many cases the atomic binding effects can be neglected or approximated by some effective potential. Moreover, we shall concentrate in the present work on the *single active electron approximation* of an atomic species. Only recently double ionization of atoms at high laser powers has been observed. We shall not discuss this research topic further in detail in the present review but we refer to recent work [189, 193] for further references.

## B. ABOVE-THRESHOLD IONIZATION

### B.1. Introductory remarks

As we have seen before, above-threshold ionization (ATI) is a process in which more photons are absorbed than is necessary for ionization. In this case, the photoelectron energy spectrum consists of a series of peaks separated by the photon energy. Since the detection of ATI [167] there has been considerable progress in understanding this process. Reviews concerning ATI can be found in the books by Mittleman [109] and Delone and Krainov [3,4] or in the articles [16, 194, 195]. Recently, it became evident that the ATI process is considerably more complex than has been assumed. The experimental findings [196–203] and theoretical analysis [204] have shown new features of the ATI process, such as the appearance of a plateau

in the ATI spectrum with a cutoff around $10U_P$, and the sidelobes (or rings as some authors call them). Therefore, it was necessary to improve the existing theories in order to explain these features.

The main theoretical approaches can be divided into two groups (for an overview see ref. [205]). The first [206–213] is rather complicated, requiring a large amount of computation time either for Floquet calculations or direct integration of the time-dependent Schrödinger equation. The origin of the second group is found in the theory of ionization in strong electromagnetic fields which was formulated by Keldysh [103] in 1964. Many authors have presented modifications of this theory which is now known as the Keldysh–Faisal–Reiss (KFR) model [83,103,169,214] or strong-field approximation (SFA) [194, 205]. Essentially, the KFR model is determined by the zeroth-order term of an expansion of the $S$-matrix in terms of the atomic potential $V$, while the interaction with the laser field is implicitly taken care of to all orders by the Gordon–Volkov wave that describes the outgoing electron in the laser field (see Eq. (84)). An improvement of the KFR theory can be obtained by taking into account the Coulomb effects of the residual ion. This was first done by replacing the Gordon–Volkov wave by the Coulomb–Volkov wave, and later on by using an improved version of the Coulomb–Volkov wave [170, 215–218]. Unfortunately, even by using this improved KFR model, it was not possible to explain the appearance of the experimentally observed second plateau of ATI peaks due to the rescattering process. Therefore, it becomes clear that the higher-order terms of the $S$-matrix expansion should be taken into account in order to explain the experimental findings. Such corrections have to take care of the rescattering of the ionized electron at the atomic core. As it turns out, the rescattering effects can be modeled by a short-range potential. In ref. [219] a separable short-range potential was used, while in refs. [174, 220–223] a zero-range potential model was considered. Finally, in our work [224] a more realistic screened Coulomb potential was considered. In all these investigations the second plateau was predicted and in ref. [223] the height of the plateau was controlled by changing the screening parameter. In the present section on ATI we shall present our model which includes both the Coulomb and the rescattering effects [225].

## B.2. The S-matrix theory

Our starting point is the $S$-matrix (using throughout the atomic system of units)

$$S_{fi} = i \lim_{t' \to \infty} \lim_{t \to -\infty} \langle \Phi_{\text{out}}(t') | G(t', t) | \Phi_{\text{in}}(t) \rangle, \tag{102}$$

where the in- and out-states depend on the boundary conditions, and $G$ is the total Green's operator which satisfies the Lippmann–Schwinger equation

$$G(t, t') = G_x(t, t') + \int dt'' G(t, t'') V_x G_x(t'', t'). \tag{103}$$

$G$ and $G_x$ satisfy the time-dependent Schrödinger equation with the total Hamiltonian $H = H_x + V_x$ and the Hamiltonian $H_x$, respectively. In the case of ionization, our in-state is a solution of the Schrödinger equation with the atomic binding potential $V$. This solution is outside the laser field and propagates under the influence of the Green's operator $G_v$. The final state at time $t$ satisfies

$$\langle \Phi_f^{(-)}(t)| = i\langle \Phi_{\text{out}}(\infty)|G^{(+)}(\infty, t). \tag{104}$$

Using this and the orthogonality of the in- and out-states, we obtain by substituting Eq. (103) into Eq. (102) and by choosing $V_x = H_L$ (where $H_L$ is the interaction Hamiltonian with the laser field)

$$S_{fi} = -i \int_{-\infty}^{\infty} dt \langle \Phi_f^{(-)}(t)|H_L(t)|\Phi_{\text{in}}(t)\rangle. \tag{105}$$

This is one of the possible forms of the photoionization $S$-matrix element [109, 205]. We now assume that the potential $V$ contains, besides the long-range Coulomb part $V_c$, a short-range part $V_s$, i.e., $V = V_c + V_s$. This short-range part becomes effective when the ionized electron rescatters at the atomic core (therefore it is not always present and may be considered as time-dependent). If we now insert Eq. (104) into Eq. (105) and use Eq. (103), by putting $V_x = V_s$, we find

$$S_{fi} = \int_{-\infty}^{\infty} dt \langle \Phi_{\text{out}}(\infty)|[G_x(\infty, t)$$
$$+ \int dt' G(\infty, t') V_s G_x(t', t)]H_L(t)|\Phi_{\text{in}}(t)\rangle. \tag{106}$$

Introducing the states $\Phi_{f,x}^{(-)}$ which propagate under the influence of the Hamiltonian $H_x = \vec{p}^2/2 + H_L + V_c$, and obey Eq. (104) with $G$ replaced by $G_x$, we obtain

$$S_{fi} = S_{fi}^{(0)} + S_{fi}^{(1)} + \cdots, \tag{107}$$

$$S_{fi}^{(0)} = -i \int_{-\infty}^{\infty} dt \langle \Phi_{f,x}^{(-)}(t) | H_L(t) | \Phi_{\text{in}}(t) \rangle, \tag{108}$$

$$S_{fi}^{(1)} = -i \int_{-\infty}^{\infty} dt \int_{t}^{\infty} dt' \langle \Phi_{f,x}^{(-)}(t') | V_s G_x(t', t) H_L(t) | \Phi_{\text{in}}(t) \rangle. \tag{109}$$

The physical interpretation of the results, Eqs. (106)–(109), is the following. Due to the interaction with the laser field $H_L$, the electron is ionized from the in-state. After ionization, the electron propagates in the laser field and it also feels the long-range Coulomb field. It can then leave these fields and become observed experimentally (this corresponds to the term $S_{fi}^{(0)}$ considered in [170, 215–218, 291]). However, it can happen that during the propagation of the ionized electron in the field it comes back to the atomic core and scatters at the short-range part of the ionic potential (while the long-range part was already included in $\Phi_{f,x}^{(-)}$ and $G_x$). After rescattering, the electron propagates out of the fields and can be observed. Of course, both contributions of Eqs. (108) and (109) interfere quantum-mechanically, as is evident from Eq. (107). We rewrite the integrals in Eq. (109) in a more convenient form. Using the identity $\int_{-\infty}^{\infty} dt \int_{t}^{\infty} dt'[\cdots] = \int_{-\infty}^{\infty} dt' \int_{-\infty}^{t'} dt[\cdots]$, after the substitutions $t'' = t'$, $\tau = t'' - t$, and writing $t$ instead of $t''$ in the final expression, we obtain

$$\begin{aligned} S_{fi}^{(0)} + S_{fi}^{(1)} = -i \int_{-\infty}^{\infty} dt \langle \Phi_{f,x}^{(-)}(t) | \{ H_L(t) | \Phi_{\text{in}}(t) \rangle \\ + \int_{0}^{\infty} d\tau V_s G_x(t, t - \tau) H_L(t - \tau) | \Phi_{\text{in}}(t - \tau) \rangle \}. \end{aligned} \tag{110}$$

The time $\tau$ is usually called the return or travel time because the electron is ionized at the moment $t - \tau$ and it rescatters after the time interval $\tau$ at the atomic core at the moment $t$. For the initial state we can write $|\Phi_{\text{in}}(t)\rangle = |\psi_0\rangle \exp(iI_{io}t)$, where $|\psi_0\rangle$ and $I_{io}$ are the atomic ground state and its ionization energy, respectively. Because $\Phi_{f,x}^{(-)}$ is the scattered wave which propagates under the influence of both, the laser field and the Coulomb field, we shall approximate it by the improved Coulomb–Volkov state ansatz [170, 215–218, 224–230, 291]

$$|\Phi_{\vec{k}_f, x}^{(-)}(t)\rangle = \left| \psi_{\vec{k}_f + \vec{A}(t)}^{(-)} \right\rangle \exp\{-i[\vec{k}_f \cdot \vec{\alpha}(t) + \mathcal{U}(t) + E_{\vec{k}_f} t]\}, \tag{111}$$

where $\vec{A}(t)$ and $\vec{\mathcal{E}}(t) = -\partial \vec{A}(t)/\partial t$ are the vector potential of the laser field and its electric field vector, respectively, and $\vec{\alpha}(t) = \int^{t} dt' \vec{A}(t')$,

$\mathcal{U}(t) = (1/2) \int^t dt' \vec{A}^2(t')$. $|\psi_{\vec{k}}^{(-)}\rangle$ is the Coulomb wave vector

$$
\begin{aligned}
\psi_{\vec{k}}^{(-)}(\vec{r}) &= (2\pi)^{-3/2} \exp[\pi/(2k)]\, \Gamma(1 + i/k) \\
&\times \exp(i\vec{k} \cdot \vec{r})_1 F_1[-i/k, 1, -i(kr + \vec{k} \cdot \vec{r})].
\end{aligned} \tag{112}
$$

Our next approximation is to replace the intermediate Green's propagator $G_x$ by the Gordon–Volkov Green's operator, which is the usual approximation within the *Strong-Field-Approximation* (SFA). The Gordon–Volkov Green's operator reads

$$
G_L(t, t') = -i\theta(t - t') \int d\vec{k} |\chi_{\vec{k}}(t)\rangle \langle \chi_{\vec{k}}(t')|, \tag{113}
$$

where in the length gauge, in which $H_L(t) = \vec{r} \cdot \vec{E}(t)$, the Gordon–Volkov state vectors are

$$
|\chi_{\vec{k}}(t)\rangle = |\vec{k} + \vec{A}(t)\rangle \exp\{-i[\vec{k} \cdot \vec{\alpha}(t) + \mathcal{U}(t) + E_{\vec{k}} t]\}. \tag{114}
$$

Introducing Eqs. (111)–(114) into Eq. (110) we obtain

$$
\begin{aligned}
S_{fi}^{(0)} + S_{fi}^{(1)} &= -i \int_{-\infty}^{\infty} dt \exp\left\{ i\left[ \vec{k}_f \cdot \vec{\alpha}(t) + \mathcal{U}(t) + (E_{\vec{k}_f} + I_{io})t \right] \right\} \\
&\times \left\{ \left\langle \psi_{\vec{k}_f + \vec{A}(t)}^{(-)} | \vec{r} \cdot \vec{\mathcal{E}}(t) | \psi_0 \right\rangle - i \int d\vec{k} \left\langle \psi_{\vec{k}_f + \vec{A}(t)}^{(-)} | V_s | \vec{k} + \vec{A}(t) \right\rangle \right. \\
&\times \int_0^{\infty} d\tau \left\langle \vec{k} + \vec{A}(t - \tau) | \vec{r} \cdot \vec{\mathcal{E}}(t - \tau) | \psi_0 \right\rangle \\
&\times \left. \exp\left[ -iS(\vec{k}; t, \tau) \right] \right\},
\end{aligned} \tag{115}
$$

where

$$
\begin{aligned}
S(\vec{k}; t, \tau) &= \int_{t-\tau}^{t} dt' \{(1/2)[\vec{k} + \vec{A}(t')]^2 + I_{io}\} \\
&= (E_{\vec{k}} + I_{io})\tau + \vec{k} \cdot [\vec{\alpha}(t) - \vec{\alpha}(t - \tau)] + \mathcal{U}(t) - \mathcal{U}(t - \tau) \tag{116}
\end{aligned}
$$

is the semiclassical action which we introduced in analogy to previous work [174, 181, 219, 233], in which the process of harmonic generation was

considered. The integral over the momenta in Eq. (115) can be performed using the saddle-point method, with the result [233]

$$
\int d\vec{k}\, h(\vec{k};\, t, \tau) \exp[-iS(\vec{k};\, t, \tau)] = \left(\frac{2\pi}{i\tau}\right)^{3/2}
$$
$$
\exp[-iS(\vec{k};\, t, \tau)]\left(1 - \frac{i}{2\tau}\frac{\partial^2}{\partial\vec{k}^2} + \cdots\right)h(\vec{k};\, t, \tau)\,|_{\vec{k}=\vec{k}_s}, \tag{117}
$$

where we denoted with $h$ the product of the matrix elements which appear under the integral over $\vec{k}$ in Eq. (115), and

$$
\vec{k}_s = -\frac{1}{\tau}\int_{t-\tau}^{t} dt'\,\vec{A}(t') = \frac{1}{\tau}[\vec{\alpha}(t-\tau) - \vec{\alpha}(t)] \tag{118}
$$

is the solution of the equation $\vec{\nabla}_{\vec{k}}S(\vec{k};\, t, \tau) = 0$. If we do not use the atomic units, then the corrections in Eq. (117) are of the order $(\hbar/\tau)^m$, where $\hbar$ is Planck's constant divided by $2\pi$ and $m = 1, 2, \ldots$. In this sense our expansion is a time-dependent Wentzel–Kramers–Brillouin approximation (see, for example, ref. [234]). The factor $\tau^{-m}$ corresponds to the spreading of the wave packet. Obviously, for large return times, which are needed in the case of higher energies of rescattering, these terms can be neglected. Retaining only the zeroth-order term in Eq. (117), we obtain

$$
S_{fi} = -i\int_{-\infty}^{\infty} dt\,\exp[i(E_{\vec{k}_f} + I_{io} + U_P)t]\,\mathcal{T}_{fi}(\varphi)
$$
$$
= -2\pi i\sum_N \delta(E_{\vec{k}_f} + I_{io} + U_P - N\omega)T_{fi}(N), \tag{119}
$$

where

$$
\mathcal{T}_{fi}(\varphi) = \exp\{i[\vec{k}_f \cdot \vec{\alpha}(\varphi) + \mathcal{U}_1(\varphi)]\}\left\{\left\langle\psi_{\vec{k}_f+\vec{A}(\varphi)}^{(-)}\,|\vec{r}\cdot\vec{\mathcal{E}}(\varphi)|\psi_0\right\rangle\right.
$$
$$
-i\int_0^{\infty} d\tau\left(\frac{2\pi}{i\tau}\right)^{3/2}\left\langle\psi_{\vec{k}_f+\vec{A}(\varphi)}^{(-)}\,|V_s|\vec{k}_s + \vec{A}(\varphi)\right\rangle \tag{120}
$$
$$
\left.\times\langle\vec{k}_s + \vec{A}(\varphi')|\vec{r}\cdot\vec{\mathcal{E}}(\varphi')|\psi_0\rangle\exp[-iS(\vec{k}_s;\, \varphi, \omega\tau)]\right\},
$$

and $\mathcal{U}(t) = \mathcal{U}_1(\varphi) + U_P t$, $\varphi = \omega t$, $\varphi' = \varphi - \omega\tau$. $\mathcal{T}_{fi}(\varphi)$ is a $2\pi/\omega$-periodic function of $t$, which can be expanded into a Fourier series

$$
\mathcal{T}_{fi}(\varphi) = \sum_{N=-\infty}^{\infty} T_{fi}(N)\exp(-iN\varphi), \quad T_{fi}(N) = \int_0^{2\pi}\frac{d\varphi}{2\pi}\mathcal{T}_{fi}(\varphi)\exp(iN\varphi). \tag{121}
$$

$T_{fi}(N)$ is the $T$-matrix element for ionization with the absorption of $N$ photons. The corresponding differential ionization rate of the order $N$ is

$$w_{fi}(N, \theta) = 2\pi k_f \, |T_{fi}(N)|^2, \tag{122}$$

where $k_f = (2E_{\vec{k}_f})^{1/2}$ satisfies the energy conserving condition $E_{\vec{k}_f} = N\omega - I_{io} - U_P$, and $\theta$ is the angle between $\vec{k}_f$ and the laser-field polarization vector $\vec{\epsilon}$. The matrix elements in Eq. (120) have simple analytic form [235], so that the differential ionization rates can be easily computed by performing the integration over the return time $\tau$ and by using the fast Fourier transform method.

Below, we shall present some results for a monochromatic, linearly-polarized laser field. Our target will be a hydrogen atom in its ground state ($\psi_0(\vec{r}) = \pi^{-1/2} \exp(-r)$ and $I_{io} = 0.5$ a.u.) and for the short-range potential we take $V_s = -\exp(-r)/r$, i.e. a potential of the Yukawa type. It should be stressed that the theory presented is quite general and can also be applied to ATI in a bichromatic laser field [236] and to the inert gases. Ground-state wave functions of inert gases can be found in ref. [237], while the short-range potential can be modeled by the Slater potential [238, 239] or by a potential of the form $-(a + b/r)\exp(-\lambda r)$ [240]. The short-range potential could also be computed directly by using the formula [241] $V(\vec{r}) = \int d\vec{r}' |\psi^+(\vec{r}')|^2/ |\vec{r} - \vec{r}'| - Z/r$, where the first term is the interaction of the ionized electron with the electron core cloud and $Z$ is the nuclear charge. For example, for helium we have $Z = 2$ and the ground-state wave function of a He$^+$ ion is $\psi_{1s}^+ = (8/\pi)^{1/2} \exp(-2r)$ so that $V(\vec{r}) = -1/r - (2 + 1/r)\exp(-4r)$. Therefore, the desired short-range potential in the case of helium is $V_s(\vec{r}) = -(2 + 1/r)\times \exp(-4r)$ and all our matrix elements can be easily obtained using this result and the ground-state wave function of helium [235]. Without going into these more complex considerations, we shall show here that all the main features of the earlier experiment [201] can be reproduced by only considering the hydrogen atom and the Yukawa-type short-range potential.

### B.3. Numerical examples

In Fig. 15 we present the differential ionization rates as a function of the kinetic energy of the outgoing electron in units of $U_P$ for the laser field parameters used in the experiment by Walker *et al.* [201], i.e., the laser-field frequency $\omega = 1.58$ eV and the intensity $I = 10^{15}$ W cm$^{-2}$. The short-range part of the core potential is $V_s(r) = -\exp(-r)/r$. The upper curve represents the results of the present model which includes both, rescattering and Coulomb effects, while the lower curve corresponds to a model which includes rescattering effects only. Both curves are for $\theta = 0°$. In the model
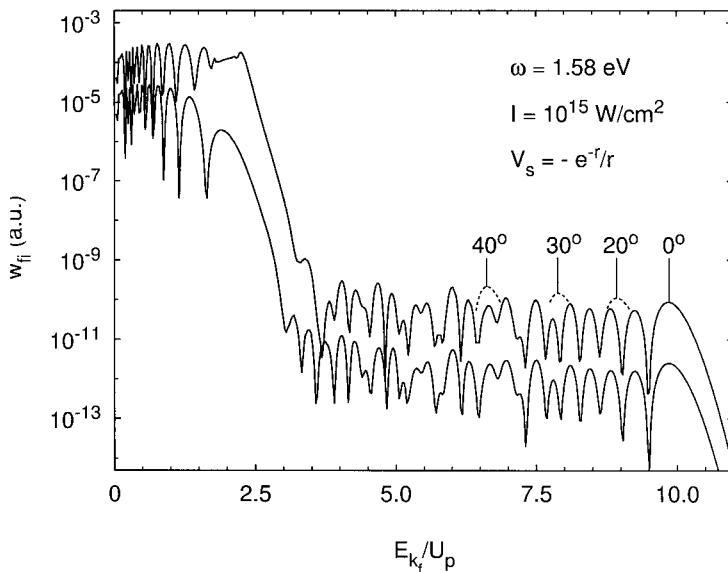
FIG. 15. Differential ionization rates for the hydrogen atom as functions of the kinetic energy $E_{\vec{k}_f}$ of the ionized electron scaled to the ponderomotive potential $U_P$, for the laser field frequency $\omega = 1.58\,\text{eV}$ and intensity $I = 10^{15}\,\text{Wcm}^{-2}$. The short-range part of the core potential is $V_s(\vec{r}) = -\exp(-r)/r$. The lower curve is obtained by using the model in which the Coulomb effects are not included, while in the upper curve both are taken into account, i.e., the Coulomb and rescattering effects. The data in both curves are for the angle $\theta = 0°$ between the polarization vector $\vec{\epsilon}$ of the laser and the momentum of the ionized electron. The rounded tops (dotted line) refer to the angles $\theta = 20°$, $30°$, and $40°$, as indicated in the figure. For each angle, only the last rounded top (at the cutoff) is presented so that the spectrum for $\theta = 0°$ is more easily seen, for otherwise too many interfering curves for the different angles would be superimposed (see ref. [225]).

which only includes the rescattering effects [225], it is assumed that the atomic potential is of short range, i.e., $V(r) = -\exp(-r)/r$. In this case, the first two terms of the $S$-matrix can be combined to give a term of the form $VG_LV$, while the final state is a Gordon–Volkov wave, instead of a modified Coulomb–Volkov wave [224]. In Fig. 15 one can see that the Coulomb effects increase the rates by two orders of magnitude and make the first plateau more pronounced. This plateau corresponds to the direct ionization process (with no rescattering) and the present results agree with the previous findings, in which the Coulomb effects were considered without rescattering [215–218]. In both cases, the second plateau has a sharp cutoff at $10U_P$ which agrees with the classical considerations of rescattering [218, 242, 243]. This value can also be obtained from a semiclassical analysis of Eq. (120)

in the limit $I_{io} \to 0$. The energy of $10U_P$ corresponds to $N = 409$ absorbed photons, so that the process is highly nonlinear. The cutoff position depends on the angle $\theta$ of electron emission. In Fig. 15 the cutoff regions of the ionization rates for angles $\theta = 20°$, $30°$, and $40°$ are also presented. One can see that the cutoff energy decreases with the increase of $\theta$, which is in agreement with the experimental [201] and theoretical [174, 220–225, 236, 242, 243] findings. The shapes of the second plateau of the ionization rates with and without the Coulomb effects are qualitatively similar, except that the rates which include the Coulomb effects are considerably higher. The plateau consists of a sequence of rounded tops and sharp suppressions similar to what is found for the spectra of high-order harmonic generation [181, 233]. This can be ascribed to the interference of tunneling trajectories [222, 223] (see also the last reference in ref. [221]). These sharp suppressions were recently observed experimentally [201] and cannot be explained within the semiclassical rescattering model presented in that same paper. It is important that the last rounded top that corresponds to the cutoff is the largest of all. Using this fact, we can explain the appearance of the sidelobes in the high-energy parts of the spectra. Namely, the sidelobes for the angle $\theta$ correspond to the last rounded top of the photoelectron spectrum for the same angle. Therefore, according to Fig. 15, the last rounded top for $\theta = 20°$ is at $9U_P$, while for $\theta = 30°$ it is at $8U_P$. This is in agreement with the data in Fig. 16, where the angular distributions of the rates for fixed $E_{\vec{k}_f} = 9U_P$, $8U_P$, $7.3U_P$, and $6.6U_P$ are presented. The sidelobes for $E_{\vec{k}_f} = 9U_P$ and $8U_P$ are just at $\theta = 20°$ and $30°$, respectively. With the decrease of $E_{\vec{k}_f}$ the angular distributions become more complicated but the sidelobe structures are still evident. For $E_{\vec{k}_f} = 7.3U_P$ and $E_{\vec{k}_f} = 6.6U_P$ we have sidelobes at $35°$ and $40°$, respectively. The presented results also agree with the following symmetry of the $T$-matrix: $T_{fi}(N, \pi - \theta) = (-1)^N T_{fi}(N, \theta)$. From our analysis, we can conclude that by using a generalization of the KFR model, which includes both the Coulomb and the rescattering effects, we were able to explain the more recent experimental results, i.e., the second plateau and the sidelobes in the photoelectron spectra. We were also able to predict the right position of the sidelobes. The advantage of our model is that it can be easily applied to more complicated systems than the hydrogen atom. For example, the inert gases can be modeled by choosing the initial wave functions from ref. [237] and the core potentials from refs. [236, 237].

### B.4. *More recent developments*

The strong species dependence of the high-order photoelectron production in alkali metal atoms was discussed by Gaarde *et al.* [244], presenting a
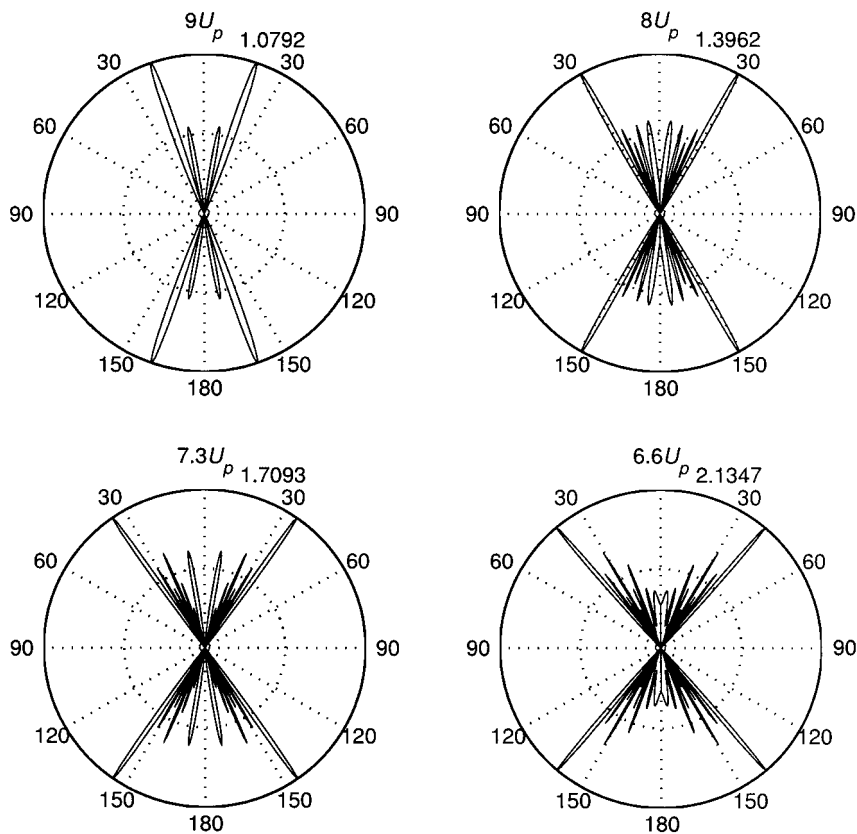
FIG. 16. For the same laser field and short-range potential parameters, as in Fig. 15, the sidelobe structures of the ATI spectra of high-energy electrons are shown. The differential rates $w_{fi}(N, \theta)$ are presented as functions of the polar angle $\theta$ (in degrees) for fixed values of $N$ that correspond to $E_{\vec{k}_f} = 9U_P$ (upper left subplot), $8U_P$ (upper right subplot), $7.3U_P$ (lower left subplot), and $6.6U_P$ (lower right subplot). The rates are in units $10^{-10}$ a.u., and the data are normalized to their maximum value in each subplot separately. For example, the maximum rate for $E_{\vec{k}_f} = 9U_P$ is $1.0792 \times 10^{-10}$ a.u. (see ref. [225]).

theoretical and experimental study of these atoms interacting with intense, mid-infrared radiation. The strength of this process shows an unexpected strong species dependence that can be explained via the difference in the cross section for electron–ion scattering from the different atoms. This permits to directly relate the high-energy portion of the photoelectron spectrum to specific features of the electron–ion potential. This dependence we have anticipated in our discussions at the end of Subsection II.B.2.

The interplay between different electronic quantum trajectories in ATI by an elliptically-polarized laser field has been analyzed experimentally and theoretically by Paulus *et al.* [245] as a generalization of the results of earlier investigations for a linearly-polarized field [222, 223]. The data show a second plateau at a specific angle with respect to the large component of the laser field and can be explained by the strong-field rescattering approximation. Another investigation by these authors [246] was concerned with the channel-closing-induced resonances in the ATI plateau. Apparently, multiphoton resonances with ponderomotively upshifted Rydberg states have dramatic effects on the plateau of high-order ATI. Certain groups of the ATI peaks are significantly enhanced. For short pulses and intense laser fields, individual Rydberg states lose their physical significance. Under these conditions, thanks to the experimental and theoretical investigations of the dependence of the photoelectron spectra on the laser field, these authors propose that the observed effects can be largely understood in terms of channel closings that are characteristic of a short-range model potential of rescattering (see the recent review article [21] and references therein). Borca *et al.* [247] considered the same threshold-related enhancement of the high-energy plateau in ATI. In particular, they demonstrated the enhancement of the above-threshold detachment spectra at channel closing and explained this by the effect of the well-known threshold anomalies of general scattering theory.

The relevance of Coulomb effects, that we have discussed at various places in this review, was considered recently by Duchateau *et al.* [248, 249] by investigating the ionization of atoms by intense and ultrashort laser pulses. They present a nonperturbative approach, based on the Coulomb–Volkov-type of states, suggested many years ago by Jain and Tzoar [250], which is able to predict both angular and energy distributions of ejected electrons when atoms interact with a very short and intense laser pulse. It is shown that, for atomic hydrogen targets, this theory makes accurate predictions as long as the interaction time does not allow more than two optical cycles. This was found by comparison with an "exact" treatment of the problem. Taking into account the long-range ionic Coulomb field, the ATI of rare-gas atoms was analyzed experimentally and theoretically for 200 fs, 800 nm Ti:sapphire laser pulses by Larochelle *et al.* [251] who found that by comparing the experimental curves for the ion yield as a function of the laser intensity with a theory by Perelomov *et al.* and Krainov [252–255], a rather good overlap between experimental and theoretical results can be achieved. We should mention, however, that considerable doubts have been raised concerning the validity of the above Coulomb–Volkov wave at high laser-field strength $\mathcal{E}_0$ [256, 257]. The necessity of a careful analysis of gauge invariance in the interaction between atoms and few-cycle laser pulses

was recently stressed by Madsen [258]. For few-cycle laser pulses the effects of the leading and of the trailing edge of the pulse on the ATI spectrum are crucial. In practice, the shape of the envelope can be parametrized by the pulse length and the "absolute phase", that is, the phase difference between the maximum of the envelope and a maximum of the carrier-wave electric field. The effect of the absolute phase is a pronounced backward–forward asymmetry of the ATI yields in two opposite directions. This was recently observed in a "stereo" ATI experiment [259] and explained theoretically by using a generalization of the KFR model [260].

In our present work, the main approach of solving the laser-assisted and laser-induced processes is the $S$-matrix theory. There are, however, several other methods that have been successfully used, like the Floquet approximation, described in some detail in the recent review by Joachain et al. [18]. This theory is applicable for a laser pulse that can be described by a harmonic wave train of infinite extent. A more flexible method that has become applicable thanks to the development of fast computers is the direct numerical solution of the time-dependent Schrödinger equation. This method can be applied to laser pulses consisting of a few radiation cycles as they have become available recently in the course of the development of femto- and atto-second physics. But, even nowadays, this numerical methods usually require a considerable computer time. In the domain of ATI, this method has been applied recently by Muller et al. [261, 262] to investigate the bunching and focusing of tunneling wave packets in high-order ATI and to the tunneling excitation to resonant states in helium as the main source of "superponderomotive" photoelectrons in the tunneling regime. On the whole, the tunneling theory of Ammosov, Delone, and Krainov (ADK) [263] has turned out to be very successful in interpreting ATI data at high laser-field intensities at which the Keldysh parameter $\gamma \ll 1$. A review of this approach has recently been presented by Delone and Krainov [264]. The method has been applied by McNaught et al. [265] to investigate the photoelectron initial conditions for tunneling ionization in a powerful linearly-polarized laser field in the long-pulse tunneling limit. The method has also been applied successfully by several authors to the ATI process in the tunneling limit [266–271]. The above-barrier ionization regime, i.e., the regime of ionization in which the barrier of the Coulomb potential becomes suppressed by the electric field and the electron escapes directly from the potential well without tunneling, was recently considered by Scrinzi et al. [272].

Although we indicated in the introductory Section II.B.1 of this chapter that at relativistically high laser powers, where the dipole approximation for describing the laser pulse breaks down, the ATI yields after rescattering will decrease thanks to the sideways motion of the ionized electrons, it has

become of interest to investigate certain features of this relativistic process in more detail. In the work of Ortner [273], the relativistic photoelectron spectra in the ionization of atoms by elliptically-polarized laser light have been evaluated in the tunneling limit using the relativistic version of the Landau–Dykhne formula and have been compared with recent calculations by Krainov [274]. A relativistic theory of ATI of hydrogen-like atoms in ultrastrong laser fields was presented recently by Avetissian *et al.* [275] but unfortunately there are no numerical data presented which would lead to some insight into the relativistic effects. Finally, we mention a similar analysis by Taïeb *et al.* [276] in which a comparison is made between the results obtained by the ADK theory, mentioned before, and the numerical solution of the time-dependent Schrödinger equation.

Another interesting approach to the investigation of ATI and HHG has recently been formulated by Roy and Chu [277]. These authors suggest a quantum-fluid-dynamic treatment of strong-field processes applied to the study of ATI and HHG of helium and neon. They explore the feasibility of extending the quantum-fluid dynamics method for the quantitative investigation of nonlinear optical processes of many-electron quantum systems in intense laser fields. Through the amalgamation of the quantum-fluid dynamics and density-functional theory, a single time-dependent hydrodynamical equation of motion can be derived. This equation has the form of a generalized nonlinear Schrödinger equation but includes the many-body effects through a local time-dependent exchange-correlation potential. The time-dependent generalized pseudospectral method is extended to the solution of the generalized nonlinear Schrödinger equation in spherical coordinates, allowing nonuniform spacial discretization and efficient, accurate solution of the hydrodynamical density and wave function in space and time. The procedure is applied to the study of multiphoton ionization and HHG of He and Ne atoms in intense laser fields. Excellent agreement with other recent self-interaction-free time-dependent density-functional theory calculations is obtained for He, while for Ne, good agreement is achieved. The method offers a conceptually appealing and computationally practical approach for nonperturbative treatment of strong-field processes of many-electron systems beyond the time-dependent Hartree–Fock level.

## C. Electron–Ion Recombination

### C.1. Introductory remarks

Presently much work is devoted to the generation of x-ray fields whose frequencies are in the "water window" [278, 279]. One of the processes,

which is very promising to reach this goal, is the laser heating of plasmas. Here high-frequency radiation becomes emitted which has its origin in the following three main processes: (i) higher harmonic generation (HHG to be discussed in Section II.F), (ii) laser-induced bremsstrahlung (discussed in Sections I.D and I.E), and (iii) laser-assisted electron–ion recombination. As we saw, the first of these processes yields maximum frequencies given by $\hbar\omega_{max} = 1.32\, I_{io} + 3.17 U_P$ where $I_{io}$ is the ionization energy of the atom and $U_P = mc^2\mu^2/4$, the ponderomotive- (or quiver-) energy of an electron in the laser field, which is proportional to the field intensity $I$. Presently, these frequencies are usually not enough to reach directly into the water window [17, 280]. The second process leads to the heating of the plasma, thanks to inverse bremsstrahlung at high laser power, discussed in Section I.E, by which energetic electrons are created and high frequency spontaneous bremsstrahlung is produced in electron–ion collisions [29]. Finally, during the laser-stimulated electron–ion recombination high-frequency radiation of maximum energy $\hbar\omega_{max} = E_{\vec{p}} + I_{io} + U_P + 2\sqrt{2E_{\vec{p}}U_P}$ can be generated where $E_{\vec{p}}$ is the initial kinetic energy of the recombining electron. In the absence of a laser field, the process of electron–ion recombination has been investigated in great detail in the past [281]. The laser-stimulated recombination process (LSR) will be analyzed in greater detail in the present section with reference to our previous work [282] and similar considerations on this topic by Kuchiev and Ostrovsky [283]. Since we are interested to obtain in this process sufficiently high radiation frequencies, our above formula for $\omega_{max}$ indicates that for a given laser field intensity $I$ the high-energy electrons generated by the laser heating of the plasma will correspondingly yield the desired high radiation frequencies. Therefore the inverse form of the Keldysh–Faisal–Reiss (KFR) model [83, 103, 169] should be very suitable to evaluate the laser-stimulated recombination probabilities. Moreover, we shall show that even at initial electron kinetic energies in the 100 eV range the Coulomb effect of an ion on the recombining electron is considerable and we shall therefore consider a Coulomb-modified version of the KFR model [170].

We shall first present the inverse form of the KFR theory applied to the LSR process and we shall formulate its modification for including the Coulomb effects of the ion in the recombination process. Then we shall discuss a number of specific applications of our theory and we shall analyze our recombination spectra. Finally, we shall summarize our results and present some concluding remarks, in particular, on the possibility of rescattering in electron–ion recombination in a powerful laser field.

## C.2. Theory of laser-stimulated recombination (LSR)

**The differential power spectrum**    We consider the process of recombination of electrons with ions in the presence of a strong laser beam, described by a vector potential $\vec{A}_L(t)$ in the dipole approximation. During the action of the laser field the emission of x-ray photons of frequency $\omega_X$, wave vector $k_X\vec{n}$ and linear polarization $\vec{\epsilon}_X$ takes place. We continue to work in units $\hbar = c = 1$. The Hamiltonian in the length gauge which describes such a process is of the form

$$\hat{H}(t) = \hat{H}_{\mathrm{at}} - e\vec{\mathcal{E}}_L(t) \cdot \hat{\vec{r}} - e\widehat{\vec{\mathcal{E}}}_X(\hat{\vec{r}}, t) \cdot \hat{\vec{r}}, \tag{123}$$

in which $\hat{H}_{\mathrm{at}}$ is the radiation-free atomic Hamiltonian,

$$\hat{H}_{\mathrm{at}} = \frac{1}{2m}\hat{\vec{p}}^2 + \hat{V}. \tag{124}$$

Moreover, $\vec{\mathcal{E}}_L(t)$ is the electric-field of the laser beam in the dipole approximation, and $\widehat{\vec{\mathcal{E}}}_X(\hat{\vec{r}}, t)$ is the electric field operator of the x-ray radiation. In our analysis the laser field is treated classically, whereas the spontaneously emitted x-ray radiation is described quantum-mechanically. For a one-mode x-ray radiation the electric field operator is equal to

$$\widehat{\vec{\mathcal{E}}}_X(\hat{\vec{r}}, t) = i\sqrt{\frac{\omega_X}{2V}}\vec{\epsilon}_X(\hat{a}_X\mathrm{e}^{-i\omega_X t + ik_X\vec{n}\cdot\hat{\vec{r}}} - \hat{a}_X^\dagger\mathrm{e}^{i\omega_X t - ik_X\vec{n}\cdot\hat{\vec{r}}}), \tag{125}$$

where $\vec{\epsilon}_X$ is the polarization vector, $\hat{a}_X$ and $\hat{a}_X^\dagger$ are the annihilation and creation operators, $\vec{n}$ is the direction of propagation of the x-ray radiation of frequency $\omega_X$, and finally $V$ is the quantization volume of the radiation field. For the recombination processes the initial state is equal to $|\psi_{\vec{p}}^{(+)}(t); 0\rangle$, i.e., it is the vacuum state for x-ray radiation and a scattering state of the electron in the laser field of energy $E_{\vec{p}}$. On the other hand, the final state equals to $|\psi_0(t); 1\rangle$, i.e., it is a one-photon state for the x-ray and for the electron a bound state in the laser field with binding energy $E_0 = -I_{io}$. Applying Fermi's golden rule, we find the probability of emitting an x-ray photon by an electron, recombining from a scattering state of momentum $\vec{p}$ into a quasi-bound state, to be equal to

$$P(\vec{n}, \vec{p}) = \left|\int dt\langle\psi_0(t); 1 - e\widehat{\vec{\mathcal{E}}}_X(\hat{\vec{r}}, t) \cdot \hat{\vec{r}} \mid \psi_{\vec{p}}^{(+)}(t); 0\rangle|^2\right|. \tag{126}$$

After simple algebraic manipulations we arrive at the probability rate ($\alpha = e^2$ is the fine structure constant)

$$w(\vec{n}, \vec{p}) = (2\pi)^2 \alpha \frac{\omega_X}{V} \delta(E_0 - E_{\vec{p}} - U_P - n\hbar\omega_L + \hbar\omega_X)$$

$$\times \left| \frac{\omega_L}{2\pi} \int_0^{2\pi/\omega_L} dt \langle \psi_0(t) | e^{-i\omega_X t + ik_X \vec{n}\cdot\hat{\vec{r}}} \hat{\vec{\epsilon}}_X \cdot \hat{\vec{r}} | \psi_{\vec{p}}^{(+)}(t) \rangle \right|^2. \quad (127)$$

In deriving this formula, we have assumed that the imaginary part of the quasi-energy for the final quasi-bound state is much smaller than the laser-photon energy $\omega_L$, and that the laser field is described by a monochromatic plane wave.

For scattering states, normalized to a plane-wave $\exp(i\vec{p} \cdot \vec{r})$, the density of electron states is equal to

$$\frac{d^3p}{(2\pi)^3} = \frac{mp}{(2\pi)^3} dE_{\vec{p}} d\Omega_{\vec{p}}, \quad (128)$$

whereas for the density of states of the x-ray radiation quantized in a volume $V$ we have

$$\frac{d^3k_X}{(2\pi)^3} V = \frac{V\omega_X^2}{(2\pi)^3} d\omega_X d\Omega_{\vec{n}}. \quad (129)$$

Hence, the total probability rate for emission of x-ray photons by electrons of arbitrary momenta equals

$$w = \int \frac{d^3p}{(2\pi)^3} \frac{d^3k_X}{(2\pi)^3} V w(\vec{n}, \vec{p}), \quad (130)$$

whereas for the total power of emitted x-rays we obtain

$$P = \int \frac{d^3p}{(2\pi)^3} \frac{d^3k_X}{(2\pi)^3} V \omega_X w(\vec{n}, \vec{p})$$

$$= \int dE_{\vec{p}} d\Omega_{\vec{p}} d\omega_X d\Omega_{\vec{n}} S(\omega_X, \vec{n}, \vec{p}) \delta(E_0 - E_{\vec{p}} - U_P - n\omega_L + \omega_X), \quad (131)$$

in which the so-called differential power spectrum is given by

$$S(\omega_X, \vec{n}, \vec{p}) = \frac{\alpha\omega_X^4 mp}{(2\pi)^4} \left| \frac{\omega_L}{2\pi} \int_0^{2\pi/\omega_L} dt \langle \psi_0(t) | e^{-i\omega_X t + ik_X \vec{n}\cdot\hat{\vec{r}}} \hat{\vec{\epsilon}}_X \cdot \hat{\vec{r}} | \psi_{\vec{p}}^{(+)}(t) \rangle \right|^2. \quad (132)$$

The above formulae have been derived in the length gauge. In the velocity gauge the Hamiltonian reads,

$$\hat{H}^{(v)}(t) = \frac{1}{2m}(\hat{\vec{p}} - e\vec{A}_L(t) - e\hat{\vec{A}}_X(\hat{\vec{r}}, t))^2 + \hat{V}, \tag{133}$$

where the superscript $(v)$ means that the corresponding quantity is expressed in the velocity gauge. We note that this form of the Hamiltonian is correct provided that the electron energy is nonrelativistic and the laser field intensity is not too large, i.e. $U_P \ll m$ (or $\mu^2 \ll 1$). The Hamiltonian in the length gauge can be derived from the above Hamiltonian provided that the wavelength of x-ray radiation is much larger than the size of an atom. However, the reason for using the length gauge is based on our consideration that the approximations for the exact initial and final states of electrons in a laser field, we shall use below, appears to be more justified in this gauge. In particular, in this gauge and for not too intense laser fields the exact quasi-bound ground state of an electron can be approximated reasonably well by the ground state in the absense of the laser field, as it was done in the original model, proposed by Keldysh [103].

Following the same steps as before, we arrive at the corresponding expression for the differential power spectrum

$$S^{(v)}(\omega_X, \vec{n}, \vec{p}) = \frac{\alpha\omega_X^2 p}{(2\pi)^4 m} \left|\frac{\omega_L}{2\pi} \int_0^{2\pi/\omega_L} dt \Big\langle \psi_0^{(v)}(t) \Big| e^{i\omega_X t - ik_X \vec{n}\cdot\hat{\vec{r}}} \right.$$
$$\left. \times \vec{\epsilon}_X \cdot \left(\hat{\vec{p}} - e\vec{A}_L(t)\right) \Big| \psi_{\vec{p}}^{(+)(v)}(t) \Big\rangle \right|^2. \tag{134}$$

Since

$$\psi_{\vec{p}}^{(+)}(\vec{r}, t) = \exp(ie\vec{A}_L(t) \cdot \vec{r})\psi_{\vec{p}}^{(+)(v)}(\vec{r}, t) \tag{135}$$

and a similar expression is valid for $\psi_0^{(v)}(\vec{r}, t)$, we conclude that both these differential power spectra, Eqs. (132) and (134) coincide, provided that the x-ray wavelength is larger than the size of the atom. If, however, the wavelength of the generated x-rays is comparable or smaller than the atomic size we should rather apply the formula in the velocity gauge. We also stress that this gauge-invariance becomes broken, if we make approximations for the initial and final states of the electron moving in both the laser field and the static potential of the ion.

In our further discussions, we shall deal with such incident electron energies and laser field intensities to permit the use of the formulas in the Eqs. (131) and (132) in the length gauge.

**The Coulomb–Volkov model**   According to our above discussion, in the electric-field gauge the differential power spectrum of high-energy photons radiated into the solid angle $d\Omega_{\vec{n}}$ is given by the following formula [282]

$$S(\omega_X, \vec{n}, \vec{p}) = \frac{\alpha \omega_X^4 p}{(2\pi)^4} \left|\frac{\omega_L}{2\pi} \int_0^{2\pi/\omega_L} dt\, I(t)\right|^2, \qquad (136)$$

where

$$I(t) = \int d\vec{r}\, \psi_0^*(\vec{r}, t)\, \vec{\epsilon}_X \cdot \vec{r}\, \mathrm{e}^{i(\omega_X t - k_X \vec{n}\cdot\vec{r})}\, \psi_{\vec{p}}^{(+)}(\vec{r}, t). \qquad (137)$$

Here $\psi_0(\vec{r}, t)$ is the wave function of the final quasi-bound state of the electron in the laser field and $\psi_{\vec{p}}^{(+)}(\vec{r}, t)$ is the scattering state of the electron in both, the laser field and the static binding potential of the ion. We shall further assume that $\psi_0(\vec{r}, t)$ can be approximated by the wave function of the ground state of the electron without the laser field, which for hydrogen takes the form

$$\psi_0(\vec{r}, t) = \sqrt{\frac{\beta^3}{\pi}} \mathrm{e}^{-iE_0 t} \mathrm{e}^{-\beta r}, \qquad (138)$$

with $\beta = 1$ and $E_0 = -0.5$ a.u., and that $\psi_{\vec{p}}^{(+)}(\vec{r}, t)$ can be represented by the Coulomb–Volkov solution [29,170]

$$\psi_{\vec{p}}^{(+)}(\vec{r}, t) \approx \exp\left[-iE_{\vec{p}} t - i\vec{\alpha}_L(t)\cdot\vec{p} - \frac{i}{2m}\int^t e^2 \vec{A}_L^2(t)\, dt\right] u_{\vec{p}-e\vec{A}_L(t)}^{(+)}(\vec{r}), \quad (139)$$

where $u_{\vec{p}}^{(+)}(\vec{r})$ is the Coulomb scattering state without the laser field. The laser field will be described by the vector potential $\vec{A}_L(t) = \vec{A}_0 \cos\omega_L t$. Hence, in Eq. (139), $\vec{\alpha}_L(t) = \vec{\alpha}_0 \sin\omega_L t$ with $\vec{\alpha}_0 = -e\vec{A}_0/\omega_L$. The first approximation, Eq. (138), is commonly applied in the KFR models [83,103,169], whereas the second one, Eq. (139), is justified for the high-energy electrons, considered here [116, 157].

### C.3. Numerical examples

For all the numerical data presented below, we chose the following geometry. The reference surface (which may be the surface of a solid target) will be taken parallel to the $(x, y)$-plane and both the laser field and the x-ray will propagate in the $x$-direction, whereas the polarization vectors of both radiations will be perpendicular to the reference plane, i.e. pointing in the $z$-direction. The incident electrons will come from above, i.e. their polar angles $\theta_{\vec{p}}$ will lie in the range $[\pi, \pi/2]$ and the corresponding azimuth $\varphi_{\vec{p}}$ can acquire any value in the interval $[0, 2\pi]$. For the presentation of the numerical data, we shall choose two types of laser sources, a Ti:Sapphire laser with wavelength $\lambda_L = 800$ nm and photon energy $\omega_L = 1.5498$ eV, or a Nd:YAG laser with wavelength $\lambda_L = 1064$ nm and $\omega_L = 1.17$ eV.

In Fig. 17 we compare the two power spectra of generated x-ray radiation obtained for a Ti:sapphire laser of power $10^{14}$ W cm$^{-2}$ by either using the Coulomb–Volkov or the KFR model. We see that for relatively small electron kinetic energies of 162.5 eV the differences between the results of the two models are quite significant, in particular, at the two maxima near the endpoints of the spectra, where the Coulomb–Volkov model yields a 2–3 times smaller power spectrum than the KFR model. This is in contradiction to what was found for the ionization process [284] where the
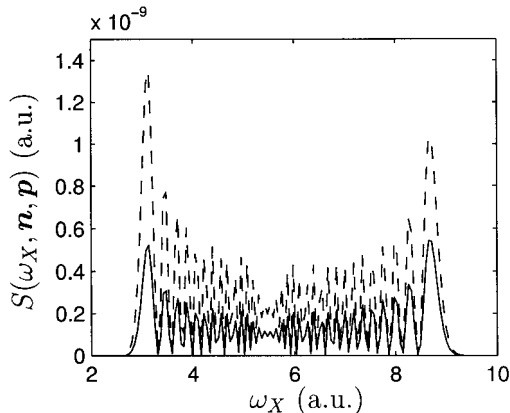


FIG. 17. For a Ti:Sapphire laser of power $10^{14}$ Wcm$^{-2}$ and perpendicular incidence of electrons of energy $E_{\vec{p}} = 5.974$ a.u. $= 162.5$ eV comparison is made between the power spectra predicted by the KFR (dashed line) and Coulomb–Volkov model (full line). Apparently, the KFR model overestimates the x-ray yields for the low electron energy considered, in particular, near the endpoints of the x-ray spectrum. However, the positions of the maxima of the spectrum coincide for both models. This latter finding shows that the KFR model can be used for a qualitative understanding of x-ray generation by laser-assisted recombination (see ref. [285]).

Coulomb–Volkov model was found to predict larger ionization rates. The discrepancies between the predictions of the above two models are decreasing with increasing energy of the ingoing electrons. Therefore one can use the KFR model for the analysis of the power spectrum of generated x-ray radiation at higher incident electron energies. In this way, we were able to estimate qualitatively the region of x-ray frequencies for which the power spectrum is significant (see the Eq. (142) below). At the end of this section we shall present a classical explanation for the range of x-ray frequencies $\omega_X$ that can be obtained in laser-assisted electron–ion recombination.

In Figs. 18 and 19 we present the power spectra, evaluated for a Ti:sapphire laser and for the intensities $10^{14}$ and $10^{15}\,\mathrm{W\,cm^{-2}}$, respectively, using both, logarithmic and linear scales for presenting the data. Here a much larger electron kinetic energy of $E_{\vec{p}} = 59.76\,\mathrm{a.u.} \simeq 1.62\,\mathrm{keV}$ was considered. Since in these two figures the electron energy is about 10 times larger than before, we only present the results for the power spectra evaluated from the Coulomb–Volkov model, since the results obtained from the KFR model are qualitatively the same. We recognize that the region of x-ray frequencies for which the power spectrum significantly differs from zero spreads out with increasing laser intensity and electron kinetic energy in agreement with the Eq. (142), presented below.

Our above findings concerning the spectrum of x-ray photons suggest a classical explanation for the position of its boundaries. An electron moving towards the solid surface and considered to be placed into a laser field, has the total classical energy given by

$$E_{\vec{p}}(t) = \frac{1}{2m}[\vec{p} - e\vec{A}_L(t)]^2 \qquad (140)$$

where it is assumed that initially the electron has the kinetic energy $E_{\vec{p}} = \vec{p}^2/2m$. Whenever the above energy reaches its maximum or minimum value, it will be directly converted into an x-ray photon during the recombination process with zero laser photons exchanged. This means that the upper and lower bounds of the plateau in the Figs. 17, 18, and 19 are in general given by the formula

$$\omega_{\mathrm{max/min}} = \mathrm{max/min}\left\{I_{io} + \frac{1}{2m}[\vec{p} - e\vec{A}_L(t)]^2\right\}. \qquad (141)$$

In the case of our choice for the geometry, in which $\vec{p}$ is parallel to $\vec{A}_L$, with $\vec{A}_L(t) = \vec{A}_0 \cos\omega_L t$, these bounds of the plateau turn out to be

$$\omega_{\mathrm{max/min}} = I_{io} + 2U_P + E_{\vec{p}} \pm 2\sqrt{2U_P E_{\vec{p}}} \qquad (142)$$
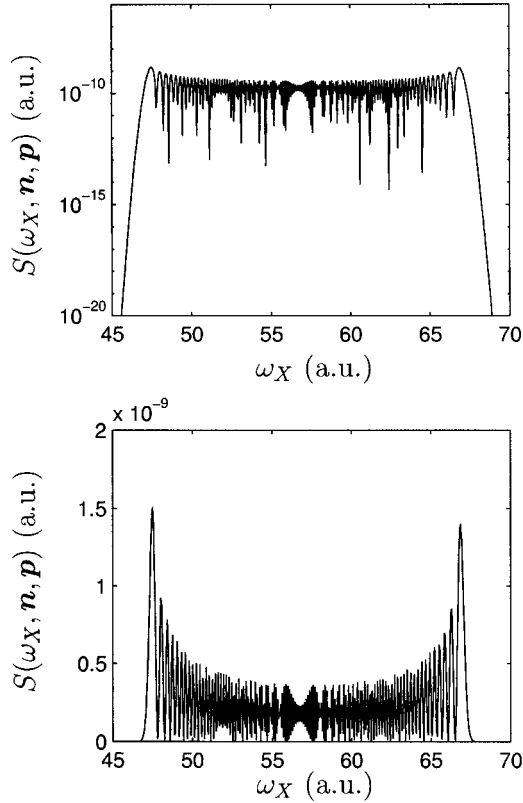
FIG. 18. Presents the power spectrum evaluated from the Coulomb–Volkov model on a logarithmic scale on the top, and on a linear scale on the bottom of the figure for the same laser frequency and intensity as in Fig. 17 but for a larger energy of impinging electrons of $E_{\bar{p}} = 59.76$ a.u. $= 1.62$ keV. At this energy, the KFR model yields similar results. We recognize the spreading of the x-ray spectrum with increasing electron energy by comparing the present results with the data in Fig. 17 (see ref. [285]).

in which $+$ refers to $\omega_{\max}$ and $-$ to $\omega_{\min}$. These classical limits represent a good estimate for the position and the width of the plateau even for small initial electron energy. This fact is clearly illustrated by the data shown in the Fig. 20.

Thus, on the basis of our work [282], and of similar investigations by Kuchiev and Ostrovsky [283], we have considered electron–ion recombination in the presence of a powerful laser field and we have evaluated the spectrum of x-rays that can be generated by this process. In particular, we
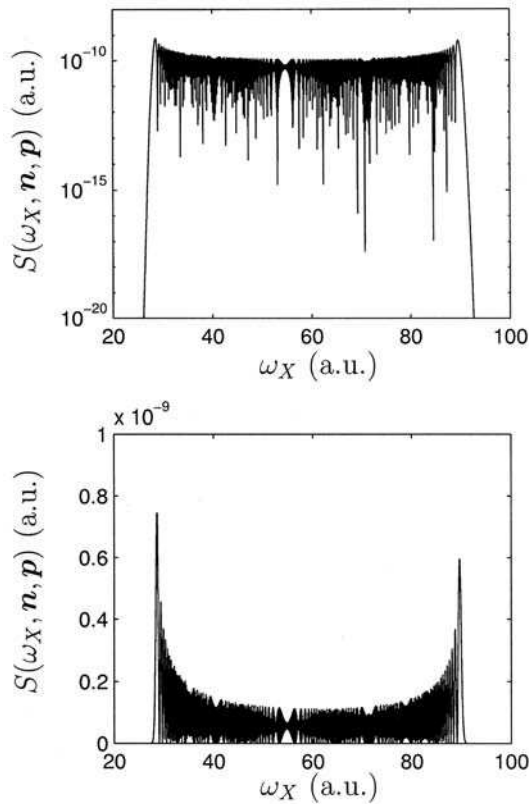
Fig. 19. Shows the same as in Fig. 17, except for a higher laser intensity of $10^{15}\,\mathrm{Wcm}^{-2}$, and indicates the spreading of the spectrum with increasing electron energy and laser intensity (compare Figs. 17 and 18) (see ref. [284]).

presented the derivation of an explicit expression for the differential power spectrum of the emitted radiation. In doing so, we compared the corresponding results obtained by using either the length- or the velocity-gauge and stressed the limits of validity of the formulas derived for the power spectrum. We also investigated for comparison the stimulated recombination process in the framework of the inverse KFR model, by either taking into account the Coulomb effects of the ionic target on the ingoing laser-dressed electron or by neglecting this effect using for the ingoing electron a Gordon–Volkov solution, Eq. (60), in the nonrelativistic limit and in the dipole-approximation. The Coulomb effects were found to be considerable even at higher electron kinetic energies. We evaluated on the
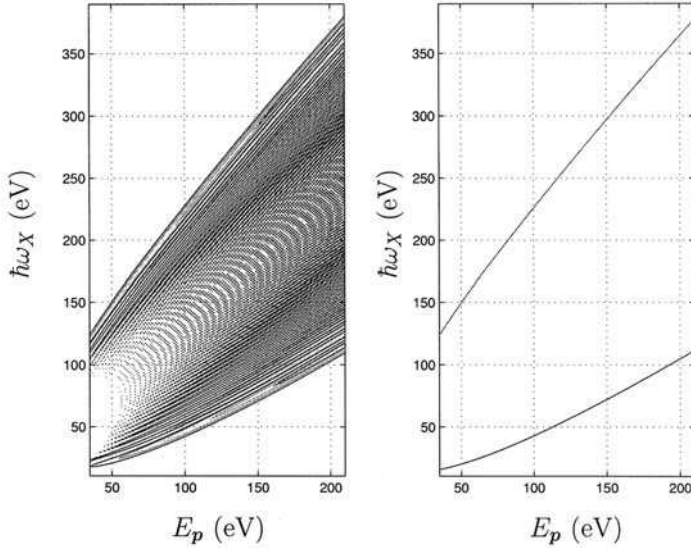
FIG. 20. Compares in the $(E_{\vec{p}}, \omega_X)$-plane the x-ray spectrum evaluated from the Coulomb–Volkov model and the classical predictions of the Eq. (142) as a function of the incident electron energy for a fixed laser-intensity of $10^{14}\,\mathrm{Wcm}^{-2}$ of a Nd:YAG laser. The limits of the quantum-mechanical x-ray spectrum are well reproduced by the classical considerations, using Eq. 142 (see ref. [285]).

basis of our model the power spectra for different laser frequencies and ingoing electron energies and estimated their orders of magnitude for the generated discrete x-ray spectrum. We also determined the dominant frequency range of this x-ray field and evaluated the laser intensity dependence of the rates of electron–ion recombination. Finally, we showed by means of a simple classical analysis of the electron energy in a time-dependent radiation field, how the domain of generated x-ray frequencies can be understood in an elementary classical way. In conclusion, we estimated that the energy conversion efficiency of x-ray radiation of about $20U_P$ will be of the order of magnitude $10^{-11}$. Further details can be found in our very recent work [285–287]. Plasma aspects of the LSR process were recently considered by Leone *et al.* [288].

## C.4. Rescattering

As it turns out, the study of the laser-assisted electron–ion recombination that includes the scattering of the electron at the ion prior to its recombination is important due to the two following main reasons.

(i) The laser-assisted electron–ion recombination could be another potential source for generating coherent soft x-rays and thus further informations about this process will be useful in achieving this goal. We have shown [289, 290] that the recombination process is more important for lower incident electron energies and that for a given high-intensity laser field the total power of the emitted x-rays as a function of the incident electron energy has its maximum if the incident electron energy is equal to a few times the ponderomotive energy. (ii) In our opinion, however, the more important reason for this investigation, was the existing complementarity between the recombination process (including rescattering, abbreviated as the SLSR process) and the well-known HHG and high-order ATI. In fact, all of them can be explained by using the three-step model. This implies the use of a similar theoretical formalism that is based on the $S$-matrix theory and on the semiclassical saddle-point solutions, discussed in Sections II.E and II.F. Equivalently, it can also be formulated by using the Feynman path integrals [291]. An important difference is, however, that HHG and high-order ATI are genuinely tunneling phenomena, whereas our SLSR process has in its initial state a free electron with a positive energy. Therefore, we have only complex solutions of the saddle-point equations for HHG and high-order ATI, while for SLSR also real solutions are possible. Using these real solutions, we were able to derive two cutoff laws for SLSR. One concerns the maximum incident electron energy for which the SLSR process is "classically" still possible. It is the same $10.007\,U_P$ cutoff law as that for the maximum outgoing electron energy in high-order ATI [196–201, 218–225, 242]. The second cutoff law determines the maximum energy of the emitted soft x-rays in SLSR, and it is the same $I_{io} + 3.17\,U_P$ cutoff law as for HHG. However, the SLSR saddle-point equations have also complex solutions. Their contribution becomes important for short electron travel times. Therefore, the $10.007\,U_P$ cutoff law is only classically valid but it is not a real limitation on the values of the incident electron energy, as is confirmed by our numerical calculations. Concerning the cutoff law for the high-energy photons, our results show [289] that it is given by the formula $\hbar\omega_{X,\,\max} = I_{io} + \max\{3.17U_P, E_{\vec{p}} + 2U_P + 2\sqrt{2E_{\vec{p}}U_P}\}$. The second term in this curly brackets is identical to what is found for the direct LSR cutoff law, as shown in by Eq. (142). For SLSR it corresponds to the complex solutions mentioned before. It is important that the probabilities of SLSR that belong to these solutions and for short travel times are much higher than expected. Namely, the ratio of the rates of the direct and the rescattering process (for high-order ATI, for example) is usually about $10^6$–$10^7$. We have shown, however, that in the present problem this ratio is only 10–100 or even less. We want to point out, that one possible explanation for this result is that the backscattered electron

recombines with a high probability immediately after the scattering event has taken place and when it is still in the vicinity of the nucleus. One can speculate whether in the case where the direct recombination process is not allowed (due to selection rules, for example) or is highly suppressed, SLSR presents a new channel for the energy transfer of the incoming electrons to the high-energy photons. The short-travel-time transfer mechanism is not characteristic of SLSR only. For the short travel times additional complex solutions (in comparison to those presented in ref. [292]) of the saddle-point equations for HHG exist, the contribution of which to the low-energy part of the spectrum is important. We expect a similar behavior in the case of high-order ATI. For HHG it can be connected to the so-called nontunneling harmonics [293, 294].

## D. X-ray–Atom Ionization

### D.1. Introductory remarks

Laser field induced transitions of an electron from one continuum state to another (free–free transitions) are of special interest because in such processes the absorption or emission of different number of photons can occur with comparable probability and the laser-field–matter interaction should be treated nonperturbatively. The first observation of the free–free transitions was reported by Weingartshofer *et al.* in experiments on laser field assisted electron–atom scattering [119]. Later on such transitions were observed in single and two-color above-threshold ionization [8, 295] and in laser-assisted Auger decay [296]. More recently, free–free transitions were studied through the observation of the laser-assisted photoelectric effect [297]. In this experiment soft x-ray pulses (generated as high-order harmonics of a Ti:sapphire laser) are used for ionization of helium atoms. The modifications of the photoelectron spectra are induced by the fundamental laser field pulse. In comparison with the photoelectron spectrum in the absence of the laser-field, one observes the following two modifications: (i) absorption and emission of laser photons during ionization gives rise to sidebands in the spectrum and (ii) the spectrum is shifted to a lower energy as a result of a laser-field-induced increase of the binding energy of the ionized atoms.

Before this first observation of the laser-assisted x-ray photoionization such processes were considered theoretically by several authors [69–71], [298–319]. In these papers the interaction between the atom and the weak high-frequency field (soft x-ray field which causes the ionization) is treated perturbatively to first order. For the soft x-rays the dipole approximation is also valid [320]. As concerns the interaction with the

strong low-frequency laser field, the approaches of these works are different. In the paper by Cionga *et al.* [319], the dressing of the atomic states by the laser field is taken into account. In [69–71, 298–301, 303–305, 307, 312] the outgoing electrons were described by the Gordon–Volkov waves, while in [306, 313–317, 319] more adequate Coulomb–Volkov waves were used. In [310, 311, 318] the low-frequency approximation was considered. It should also be noted that, according to the gauge-invariance requirements, some of the work mentioned is not reliable (see the reference in [314–316]). The process of laser-assisted x-ray photoionization has recently attracted much attention due to the possibility of investigating the relative phase of harmonics generated by a strong laser field [321] or to measure the XUV pulse duration [322–324] that can be important for attosecond physics [25, 28].

  In the next section we present a theory of photoionization of hydrogen by a high-frequency laser field in the presence of a low-frequency laser field [321]. Numerical results are then presented and compared with the results of other authors. In this section we use atomic units ($\hbar = e = m = 1$).

*D.2. S-matrix theory*

The *S*-matrix element for laser-assisted processes with the emission or absorption of one x-ray photon, in the $\vec{r} \cdot \vec{\mathcal{E}}$ gauge, is

$$S_{fi} = -i \int_{-\infty}^{\infty} dt \Big\langle \Phi_f(t) | \vec{r} \cdot \vec{\mathcal{E}}_X(t) | \Phi_i(t) \Big\rangle = S_{fi}^{(+)} + S_{fi}^{(-)}, \qquad (143)$$

where the electric-field vector of the x-ray is $\vec{\mathcal{E}}_X(t) = \mathcal{E}_{0X} \vec{\epsilon}_X \sin \omega_X t$, $\mathcal{E}_{0X} = I_X^{1/2}$, and $\omega_X$, $I_X$, and $\vec{\epsilon}_X$ are its frequency, intensity, and unit vector of polarization, respectively. The component $S_{fi}^{(-)} \propto -(1/2i) \exp(-i\omega_X t)$ belongs to the photoionization process we are considering. The initial and final state vectors $|\Phi_j(t)\rangle$, $j = i, f$, satisfy the Schrödinger equation

$$\left[ i\frac{\partial}{\partial t} - \frac{\vec{p}^2}{2} - V - \vec{r} \cdot \vec{\mathcal{E}}(t) \right] |\Phi_j(t)\rangle = 0, \quad j = i, f, \qquad (144)$$

where $V = -1/r$ is the Coulomb potential and the electric-field vector $\vec{\mathcal{E}}(t)$, in our case of a linearly-polarized laser field, is given by

$$\vec{\mathcal{E}}(t) = \mathcal{E}_0 \vec{\epsilon} \sin \omega t, \quad \mathcal{E}_0 = I^{1/2}. \qquad (145)$$

The initial state $|\Phi_i(t)\rangle$ describes the laser-modified atomic ground state of hydrogen which, in the first order of time-dependent perturbation theory, has the form ([326–328] and references therein)

$$|\Phi_i(t)\rangle = |\Phi_0(\omega t)\rangle \exp(iI_{io}t),$$
$$|\Phi_0(\varphi)\rangle = \{1 - (i/2)E_0[G_c(E_0 - \omega)e^{i\varphi} - G_c(E_0 + \omega)e^{-i\varphi}]\vec{r}\cdot\vec{\epsilon}\}|\psi_0\rangle. \quad (146)$$

$G_c(E)$ is the time-independent Coulomb Green function, $I_{io} = 0.5$ a.u. is the ionization energy, and $\psi_0(\vec{r}) = \pi^{-1/2}\exp(-r)$ is the wave function of the ground state of the hydrogen atom. The final state $|\Phi_f(t)\rangle$ represents the laser-modified continuum state of the hydrogen atom. This state can also be approximated by a perturbative solution, similar to Eq. (146) [327, 329], but instead we shall approximate $|\Phi_f(t)\rangle$ by the improved Coulomb–Volkov wave [170, 226, 230–232]

$$|\Phi_f(t)\rangle \approx |\Phi_{\vec{k}_f}(t)\rangle = |\psi_{\vec{k}_f + \vec{A}(\omega t)}\rangle \exp\{-i[\vec{k}_f \cdot \vec{\alpha}(\omega t) + \mathcal{U}(t) + E_{\vec{k}_f}t]\}. \quad (147)$$

Here $E_{\vec{k}_f} = \vec{k}_f^2/2$ is the kinetic energy of the outgoing electron and $\vec{A}(\varphi)$, with $\varphi = \omega t$, represents the vector potential of the laser field with $\vec{\mathcal{E}}(t) = -\partial\vec{A}(\omega t)/\partial t$, where

$$\vec{A}(\varphi) = A_0\vec{\epsilon}\cos\varphi \quad (148)$$

and for the parameters in Eq. (147) we find

$$\vec{\alpha}(\varphi) = \int^t dt' \vec{A}(\omega t') = \alpha_0\vec{\epsilon}\sin\varphi, \ \alpha_0 = \frac{A_0}{\omega} = \frac{\mathcal{E}_0}{\omega^2}, \quad (149)$$

$$\mathcal{U}(t) = (1/2)\int^t dt' \vec{A}^2(\omega t') = U_P t + \mathcal{U}_1(\omega t),$$
$$U_P = \frac{A_0^2}{4}, \ \mathcal{U}_1(\omega t) = \frac{U_P}{2\omega}\sin 2\omega t, \quad (150)$$

while $|\psi_{\vec{k}}\rangle$ is the Coulomb wave vector in the absence of the laser field

$$\psi_{\vec{k}}(\vec{r}) = (2\pi)^{-3/2}\exp\left(\frac{\pi}{2k}\right)\Gamma(1 + i/k)\exp(i\vec{k}\cdot\vec{r})$$
$$\times {}_1F_1[-i/k, 1, -i(kr + \vec{k}\cdot\vec{r})]. \quad (151)$$

Introducing the Eqs. (146) and (147) into Eq. (143) we obtain

$$S_{fi}^{(-)} = \frac{\mathcal{E}_{0X}}{2} \int_{-\infty}^{\infty} dt\, f(\omega t) \exp[i(E_{\vec{k}_f} - \omega_X + I_{io} + U_P)\, t], \qquad (152)$$

where

$$f(\varphi) = \left\langle \psi_{\vec{k}_f + \vec{A}(\varphi)} | \vec{r} \cdot \vec{\epsilon}_X | \Phi_0(\varphi) \right\rangle \exp\{i[\vec{k}_f \cdot \vec{\alpha}(\varphi) + \mathcal{U}_1(\varphi)]\} \qquad (153)$$

is a $2\pi/\omega$-periodic function of $t$ which can be expanded into a Fourier series

$$f(\varphi) = \sum_{N=-\infty}^{\infty} f_N \exp(-iN\varphi), \qquad f_N = \int_0^{2\pi} \frac{d\varphi}{2\pi} f(\varphi) \exp(iN\varphi), \qquad (154)$$

so that we obtain

$$S_{fi}^{(-)} = -2\pi i \sum_N \delta(E_{\vec{k}_f} + I_{io} + U_P - \omega_X - N\omega) T_{fi}(N), \qquad (155)$$

where $T_{fi}(N) = (i/2)E_X f_N$ is the $T$-matrix element for the exchange of $N$ laser photons (in addition to the absorption of one x-ray photon). The processes with $N < 0$ correspond to stimulated emission, while the processes with $N > 0$ correspond to the absorption of $N$ photons. The matrix elements which appear in $f(\varphi)$ can be computed analytically. For the evaluation of these matrix elements with the time-independent Coulomb Green functions its Sturmian representation can be used, but in the present case one can show [327] that the closure approximation with the mean energy $\bar{E}_0 = 4/9$ a.u. gives satisfactory results. Therefore we are left with one numerical integration over $\varphi$ which can be easily done. From the energy conserving condition $E_{\vec{k}_f} = \omega_X + N\omega - I_{io} - U_P$, we infer that the laser field induces an increase of the binding energy by $U_P$, as found experimentally [297].

The differential cross section (DCS) with the exchange of $N$ laser photons, normalized to the flux of incident x-ray photons, is defined by [320]

$$\frac{d\sigma(N)}{d\Omega} = 2\pi \frac{\omega_X}{I_X} k_f(N)\, |T_{fi}(N)|^2, \qquad (156)$$

where $k_f(N) = (2E_{\vec{k}_f})^{1/2}$ is determined by the energy-conserving condition. The total cross section (TCS) for the exchange of $N$ photons is

$$\sigma(N) = \int d\Omega \frac{d\sigma(N)}{d\Omega}. \qquad (157)$$

Denoting by $N_0$ the smallest negative integer for which $\vec{k}_f^2$ is still positive, we obtain for the TCS (summed over all $N$)

$$\sigma_{\text{tot}} = \sum_{N=N_0}^{\infty} \sigma(N).$$  (158)

### D.3. Numerical examples

In our paper [325] we compared our results for the x-ray photoionization cross sections in the presence of a monochromatic laser field with the results of other work [313, 319, 329]. In the paper by Leone *et al.* [313] the initial state was the ground state of the hydrogen atom and the final state was the Coulomb–Volkov wave with an extra gauge factor: $|\Phi_f(t)\rangle = \exp[\,i\vec{A}(\omega t)\cdot\vec{r}\,]|\psi_{\vec{k}_f}\rangle \exp\{-i[\vec{k}_f\cdot\vec{\alpha}(\omega t) + \mathcal{U}(t) + E_{\vec{k}_f}t]\}$. The agreement between their calculations and ours is good for low laser field intensities. For the higher intensities we have noticed some differences. As an example, we present in Fig. 21 the TCS as a function of the number $N$ of the exchanged photons for $\omega = 1.17\,\text{eV}$, $\omega_X = 50\,\text{eV}$, and $I = 5 \times 10^{12}\,\text{W cm}^{-2}$. These results correspond to the results shown in figure 5 of ref. [313]. In our figure, filled circles refer to the $\sigma(N)$ defined without the factor $k_f$ (as it was done in ref. [313] and where it was shown that this factor comes from the density of the final states). We notice that for $|N| < 8$, the sidebands corresponding to the stimulated emission processes are larger than those found for absorption. This fact is more pronounced in our case than in ref. [313]. For higher intensities and frequencies these differences become more important and they are significantly close to the threshold value $N = N_0$. For illustrating this, we have evaluated the TCS $\sigma(N)$ as a function of the photoelectron energy for $\omega = 1.55\,\text{eV}$, $\omega_X = 13\,\omega$, and: (a) $I = 5 \times 10^{11}\,\text{W cm}^{-2}$, (b) $I = 3 \times 10^{12}\,\text{W cm}^{-2}$, and (c) $I = 1.75 \times 10^{13}\,\text{W cm}^{-2}$. The results obtained are similar to those of figure 2 in the paper by Véniard *et al.* [329]. In ref. [329] the photoelectron spectra were obtained via the numerical solution of the time-dependent Schrödinger equation for a hydrogen atom in the presence of both fields. The authors claim that they verified that their results are quite different from the results of Leone *et al.* [313]. This indicates that the approach of Leone *et al.* is not applicable for the laser field parameters considered in ref. [329]. But, as our data [325] show, our method gives quite satisfactory results. The only difference between the work of Véniard *et al.* [329] and our results appear close to threshold, where our ionization peaks are slightly suppressed. This difference has to be expected, because for small values of $E_{\vec{k}_f}$ the influence of the bound states of atomic hydrogen
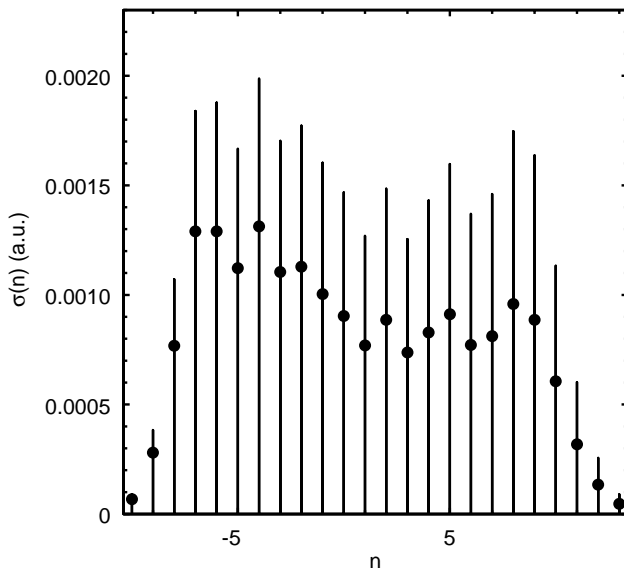
F‍IG. 21. The TCS (in a.u.) for the x-ray photoionization process in the presence of a linearly-polarized laser field as a function of the number $N$ of exchanged photons for $\omega = 1.17\,\text{eV}$, $\omega_X = 50\,\text{eV}$, and $I = 5 \times 10^{12}\,\text{Wcm}^{-2}$. Filled circles refer to the data for $\sigma(N)$ defined without the factor $k_f$ (see ref. [325]).

becomes important. This influence, however, is not taken into account if we use our improved Coulomb–Volkov waves. All other features of the photoelectron spectra, presented in the work of Véniard *et al.* [329], were recovered.

## E. X‍-‍R‍A‍Y‍–A‍T‍O‍M S‍C‍A‍T‍T‍E‍R‍I‍N‍G

### E.1. Preliminaries

As we have seen before, the investigation of atomic processes in the simultaneous presence of strong laser fields and soft x-ray pulses are presently attracting considerable interests, both experimentally and theoretically. This is connected with the possibility of an efficient generation of high-order harmonics of the driving laser field. The latest reports [330, 331] show that it is possible to generate harmonic photons of the energy 460 eV. The observation of the laser-assisted photoelectric effect [297] was just possible by using soft x-ray pulses generated as high-order

harmonics. There are also other schemes on which soft x-ray lasers can operate (see refs. [332, 333] and references therein). There are only a small number of theoretical contributions to this field (see, for example, our work [325] on x-ray photoionization of hydrogen in the presence of a bichromatic laser field, and references therein). In the present section, we shall consider x-ray–atom scattering in the presence of a laser field. The number of publications devoted to this process is even less than those investigations, considering the laser-assisted x-ray photoionization, we have considered before.

The elements of the x-ray scattering in the absence of a laser field can be found in the textbooks by Heitler [334] and by Loudon [335]. The differential cross-section (DCS) for light scattering is expressed in the quantum-mechanical scattering theory by the Kramers–Heisenberg formula, which includes both elastic Rayleigh scattering and inelastic Raman scattering. If the photon energy $\hbar\omega_{\vec{K}}$ of the x-ray is much larger than the atomic excitation energy (but still small enough so that the dipole approximation is valid [335]), then the DCS of elastic scattering process is described by the Thomson scattering formula $(d\sigma/d\Omega)_{\text{Th}} = Z^2 r_0^2 (\vec{\epsilon}_{\vec{K}} \cdot \vec{\epsilon}_{\vec{K}'})^2$, where $r_0 = 2.82 \times 10^{-15}$ m is the classical electron radius, $Z$ denotes the number of electrons in the atom, and $\vec{\epsilon}_{\vec{K}}$ and $\vec{\epsilon}_{\vec{K}'}$ are the unit polarization vectors of the incident and scattered x-ray photons, respectively. In the opposite case, where $\hbar\omega_{\vec{K}}$ is much smaller than the atomic excitation energy (which we shall not consider here), the elastic DCS is proportional to $\omega_{\vec{K}}^4$. The intermediate case was analyzed numerically for scattering by hydrogen in Gavrila's work [336]. There are a lot of investigations in which x-ray scattering by bound systems is considered in the absence of the laser field, of which we mention an early work by Levinger [337] and more recent work [338,339] on inelastic x-ray scattering (see also the references in ref. [339]). According to our knowledge, besides the references on x-ray photoionization mentioned in ref. [325], x-ray scattering in the presence of a laser field was considered only in earlier work by one of the present authors [69, 301, 302, 340] and in more recent work by Kálmán [314, 315, 341]. The latter work is devoted to the laser-assisted inelastic x-ray scattering as a tool for determining the length of ultrafast x-ray pulses and is of no interest for our present problem. For the laser-assisted x-ray scattering in the context of electron–atom collisions in a laser field, see the recent review article [29].

We shall first present the *S*-matrix theory of laser-assisted x-ray atom scattering. Then we introduce some approximations, explain their range of validity and define the *T*-matrices. This is followed by the derivation of an expression for the DCS for laser-assisted x-ray atom scattering and we apply the time-dependent WBK approximation to our problem and present

our final expression for the DCS of laser-assisted x-ray scattering by hydrogen atoms. The next subsection is devoted to the saddle-point method analysis of the x-ray spectra and the numerical results for a monochromatic linearly-polarized laser field are finally presented. This is followed by some concluding remarks. We use SI units and for a better visualization of the order of magnitude of the data obtained, we express the DCS in units of the Thomson DCS and this is for hydrogen atoms and for parallel scattering geometry equal to $r_0^2$.

### E.2. The S-matrix approach

In order to derive an expression for the DCS of laser-assisted x-ray atom scattering, we start from a general form of the $S$-matrix

$$S_{fi} = i\hbar \lim_{t' \to \infty} \lim_{t \to -\infty} \langle \Phi_{\text{out}}(t') | G(t', t) | \Phi_{\text{in}}(t) \rangle. \tag{159}$$

In the Eq. (159), $G$ is the total Green's operator which corresponds to the total Hamiltonian

$$H = H_0 + e\vec{r} \cdot \vec{\mathcal{E}}_{\text{X}}(t), \qquad H_0 = \frac{\vec{p}^2}{2m} + V + e\vec{r} \cdot \vec{\mathcal{E}}(t), \tag{160}$$

where $e\vec{r} \cdot \vec{\mathcal{E}}_{\text{X}}(t)$ describes the interaction of the atom with the x-ray field (using the length gauge and the dipole approximation), $e\vec{r} \cdot \vec{\mathcal{E}}(t)$ represents the laser-atom interaction, also in the length gauge, and $V$ is the atomic potential. We shall treat the laser field classically, so that in the case of a linearly-polarized and monochromatic field the laser electric-field vector $\vec{\mathcal{E}}(t)$, having the unit polarization vector $\vec{\epsilon}$, the frequency $\omega$ and the intensity $I$, is given by

$$\vec{\mathcal{E}}(t) = \mathcal{E}_0 \vec{\epsilon} \sin \omega t, \qquad I = \frac{1}{2} \varepsilon_0 c \mathcal{E}_0^2. \tag{161}$$

In order to distinguish the x-ray field from the laser field, we shall treat the x-ray radiation as quantized, i.e., according to ref. [335], we define

$$\vec{\mathcal{E}}_{\text{X}}(t) = \vec{\mathcal{E}}_{\text{X}}^{(+)}(t) + \vec{\mathcal{E}}_{\text{X}}^{(-)}(t),$$

$$\vec{\mathcal{E}}_{\text{X}}^{(+)}(t) = i \sum_{\vec{K}} \left( \frac{\hbar \omega_{\vec{K}}}{2\varepsilon_0 V} \right)^{1/2} \vec{\epsilon}_{\vec{K}} a_{\vec{K}} e^{-i\omega_{\vec{K}} t},$$

$$\vec{\mathcal{E}}_{\text{X}}^{(-)}(t) = -i \sum_{\vec{K}} \left( \frac{\hbar \omega_{\vec{K}}}{2\varepsilon_0 V} \right)^{1/2} \vec{\epsilon}_{\vec{K}} \hat{a}_{\vec{K}}^{\dagger} e^{i\omega_{\vec{K}} t}, \tag{162}$$

where $a_{\vec{K}}$ and $\hat{a}^{\dagger}_{\vec{K}}$ are the annihilation and creation operators of the x-ray field photons corresponding to the wave vectors $\vec{K}$, frequencies $\omega_{\vec{K}}$, and unit polarization vectors $\vec{\epsilon}_{\vec{K}}$. $V = L^3$ is the quantization volume. We consider the scattering of an x-ray photon with the initial wave vector $\vec{K}$ and energy $\hbar\omega_{\vec{K}}$ into a final state with the wave vector $\vec{K}'$ and energy $\hbar\omega_{\vec{K}'}$. If we denote the initial and the final atomic state vectors and ionization energies by $|\psi_0\rangle$ and $I_{io}$, respectively, then the *in*- and *out*-states, which appear in Eq. (159), can be written as

$$|\Phi_{\text{in}}(t)\rangle = |\psi_0\rangle e^{iI_{io}t/\hbar}|1_{\vec{K}}\rangle|0_{\vec{K}'}\rangle, \quad |\Phi_{\text{out}}(t)\rangle = |\psi_0\rangle e^{iI_{io}t/\hbar}|0_{\vec{K}}\rangle|1_{\vec{K}'}\rangle. \quad (163)$$

The total Green's operator satisfies the Lippmann–Schwinger equation

$$G(t, t') = G_0(t, t') + \int dt'' G(t, t'')\, e\vec{r}\cdot\vec{\mathcal{E}}_{\text{X}}(t'')G_0(t'', t'), \quad (164)$$

where the Green's operator $G_0$ of the Hamiltonian $H_0$ operates in the vector space of x-ray photons as a unit operator. Introducing Eq. (164) into Eq. (159) and taking into account that the total Green's operator, by acting on the out-state, yields a total final state at the time $t$ of the form, $\langle\Phi_f(t)| = i\hbar\langle\Phi_{\text{out}}(\infty)|G(\infty, t)$, while the operator $G_0$ only acts on the atomic part of the in-state as $i\hbar G_0(t, -\infty)|\psi_0\rangle\exp(iI_{io}t/\hbar) = |\psi_i(t)\rangle$, we obtain

$$(S - 1)_{fi} = -\frac{i}{\hbar}\int_{-\infty}^{\infty} dt\langle\Phi_f(t)|\ e\vec{r}\cdot\vec{\mathcal{E}}_{\text{X}}(t)|\psi_i(t)\rangle|1_{\vec{K}}\rangle|0_{\vec{K}'}\rangle. \quad (165)$$

By applying once more Eq. (164), we find for the final state

$$\langle\Phi_f(t)| = i\hbar\langle\Phi_{\text{out}}(\infty)|[G_0(\infty, t) + \int dt' G_0(\infty, t')\, e\vec{r}\cdot\vec{\mathcal{E}}_{\text{X}}(t')G(t', t)]. \quad (166)$$

Substituting Eq. (166) into Eq. (165) and taking into account that $\langle 0_{\vec{K}}|\langle 1_{\vec{K}'}|\vec{\mathcal{E}}_{\text{X}}(t)|1_{\vec{K}}\rangle|0_{\vec{K}'}\rangle = \vec{0}$ and that $\langle\Phi_{\text{out}}(\infty)|G_0(\infty, t) = (-i/\hbar)\langle\psi_f(t)|\ \langle 0_{\vec{K}}|\langle 1_{\vec{K}'}|$, we obtain

$$(S - 1)_{fi} = -\frac{i}{\hbar}\int_{-\infty}^{\infty} dt \int dt' \langle\psi_f(t')|\langle 0_{\vec{K}}|\langle 1_{\vec{K}'}|e\vec{r}\cdot\vec{\mathcal{E}}_{\text{X}}(t')$$
$$\times G(t', t)\, e\vec{r}\cdot\vec{\mathcal{E}}_{\text{X}}(t)\ |\psi_i(t)\rangle|1_{\vec{K}}\rangle|\ 0_{\vec{K}'}\rangle. \quad (167)$$

### E.3. Approximations and the T-matrices

By now the only simplifications we used were the nonrelativistic and the dipole approximation. They are satisfied for x-ray photon energies less than 100 eV, which we are considering [335]. Supposing that the x-ray field is not too strong, we obtain from Eq. (164) $G(t, t') \approx G_0(t, t')$. In this case, the remaining matrix elements in the vector space of the x-ray photons give the following result for the $S$-matrix

$$
\begin{aligned}
(S - 1)_{fi} = -\frac{i}{\hbar} \frac{\hbar e^2}{2\varepsilon_0 V} (\omega_{\vec{K}} \omega_{\vec{K}'})^{1/2} \int_{-\infty}^{\infty} dt \int dt' \Big\{ &\langle \psi_f(t') | \vec{r} \cdot \vec{\epsilon}_{\vec{K}} G_0(t', t) \\
\times \vec{r} \cdot \vec{\epsilon}_{\vec{K}'} | \psi_i(t) \rangle e^{-i\omega_{\vec{K}} t' + i\omega_{\vec{K}'} t} & \\
+ \langle \psi_f(t') | \vec{r} \cdot \vec{\epsilon}_{\vec{K}'} G_0(t', t) \vec{r} \cdot \vec{\epsilon}_{\vec{K}} | \psi_i(t) \rangle e^{i\omega_{\vec{K}'} t' - i\omega_{\vec{K}} t} & \Big\}.
\end{aligned} \tag{168}
$$

Our next approximation is to neglect the laser field dressing of the initial and final states, i.e., the substitution $|\psi_j(t)\rangle \approx |\psi_0\rangle \exp(iI_{io}t/\hbar)$, $j = i, f$. This approximation is valid for laser field intensities much less than the atomic unit of intensity $I_A = 3.51 \times 10^{16}$ W cm$^{-2}$, which is satisfied in our case. Furthermore, we have shown in ref. [325] that the first-order corrections, obtained for these wavefunctions from the time-dependent perturbation theory, give only small contributions to the DCS of photoionization processes. Using these approximations and transforming the integrals over the times in Eq. (168) by means of the identity $\int_{-\infty}^{\infty} dt \int_{t}^{\infty} dt' f(t', t) = \int_{-\infty}^{\infty} dt' \int_{-\infty}^{t'} dt f(t', t)$, upon introducing the new variables $t'' = t'$, $\tau = t' - t$, and after writing $t$ instead of $t''$ in the final expression, we obtain

$$
\begin{aligned}
(S - 1)_{fi} = -\frac{i}{\hbar} \frac{\hbar e^2}{2\varepsilon_0 V} (\omega_{\vec{K}} \omega_{\vec{K}'})^{1/2} \int_{-\infty}^{\infty} dt \int_{0}^{\infty} d\tau\, e^{-iI_{io}t/\hbar} \langle \psi_0| \\
\Big\{ \vec{r} \cdot \vec{\epsilon}_{\vec{K}} e^{-i\omega_{\vec{K}} t} G_0(t, t - \tau) \vec{r} \cdot \vec{\epsilon}_{\vec{K}'} e^{i\omega_{\vec{K}'}(t - \tau)} \\
+ \vec{r} \cdot \vec{\epsilon}_{\vec{K}'} e^{i\omega_{\vec{K}'} t} G_0(t, t - \tau) \vec{r} \cdot \vec{\epsilon}_{\vec{K}} e^{-i\omega_{\vec{K}}(t - \tau)} \Big\} |\psi_0\rangle e^{iI_{io}(t - \tau)/\hbar}.
\end{aligned} \tag{169}
$$

Our next approximation is to neglect in Eq. (169) the influence of the Coulomb field on the intermediate propagator, i.e., to replace the Green's operator $G_0$ by the Gordon–Volkov Green's operator

$$
G_0(t, t - \tau) \approx -\frac{i}{\hbar} \int d\vec{q}\, |\chi_{\vec{q}}(t)\rangle \langle \chi_{\vec{q}}(t - \tau)|, \tag{170}
$$

where the Gordon–Volkov state vectors in the length gauge are [with $\vec{\mathcal{E}}(t) = -\partial\vec{A}(t)/\partial t$, $e = |e|$]

$$|\chi_{\vec{q}}(t)\rangle = |\vec{q} + \frac{e}{\hbar}\vec{A}(t)\rangle \exp\{-i[\vec{q}\cdot\vec{\alpha}(t) + (\mathcal{U}(t) + E_{\vec{q}}t)/\hbar]\}, \qquad (171)$$

with

$$\vec{\alpha}(t) = \frac{e}{m}\int^t dt'\,\vec{A}(t'), \qquad \mathcal{U}(t) = \frac{e^2}{2m}\int^t dt'\,\vec{A}^2(t') = \mathcal{U}_1(t) + U_P t, \qquad (172)$$

where $U_P = e^2 A_0^2/4m$ is the ponderomotive potential, $E_{\vec{q}} = \hbar^2\vec{q}^2/2m$, and $A_0 = \mathcal{E}_0/\omega$. This approximation was successfully used in the analysis of high-order harmonics generation [181, 233] and above-threshold ionization [224, 342]. Corrections to this approximation can be obtained by replacing the Gordon–Volkov waves by the Coulomb–Volkov waves or by the laser-field modified Coulomb–Volkov waves, but we shall not consider this here (see ref. [325] and references therein). The quasi-classical action which corresponds to the propagation from the atomic ground state at time $t - \tau$ to the ground state at time $t$ is

$$\begin{aligned} S(\vec{q}; t, \tau) &= \int_{t-\tau}^t dt' \left\{\frac{\hbar^2}{2m}[\vec{q} + \frac{e}{\hbar}\vec{A}(t')]^2 + I_{io}\right\} \\ &= (E_{\vec{q}} + I_{io} + U_p)\tau + \hbar\vec{q}\cdot[\vec{\alpha}(t) - \vec{\alpha}(t-\tau)] + \mathcal{U}_1(t) - \mathcal{U}_1(t-\tau). \end{aligned} \tag{173}$$

Both matrix elements which appear in Eq. (169) contain the factor $\exp[-i(\omega_{\vec{K}} - \omega_{\vec{K}'})t]$. Taking into account that $\vec{\mathcal{E}}(t)$, $\vec{A}(t)$, $\vec{\alpha}(t)$, $\mathcal{U}_1(t)$, and $S(\vec{q}; t, \tau)$ are $2\pi/\omega$-periodic functions of $t$, the remaining part of the two matrix elements mentioned above can be written in the form $C_{\vec{K},\vec{K}'} \mathcal{T}_{\vec{K},\vec{K}'}^{(\pm)}(\varphi)$, with $C_{\vec{K},\vec{K}'} = (\hbar e^2/2\varepsilon_0 V)(\omega_{\vec{K}}\omega_{\vec{K}'})^{1/2}$, and $\varphi = \omega t$, while

$$\begin{aligned} \mathcal{T}_{\vec{K},\vec{K}'}^{(\pm)}(\varphi) &= \int_0^\infty d\tau \int d\vec{q}\langle\psi_0|\vec{r}\cdot\vec{\epsilon}_{\vec{K}}|\vec{q} + \frac{e}{\hbar}\vec{A}(t)\rangle \\ &\quad \times \left\langle\vec{q} + \frac{e}{\hbar}\vec{A}(t-\tau)|\vec{r}\cdot\vec{\epsilon}_{\vec{K}'}|\psi_0\right\rangle \exp\{-i[S(\vec{q}; t, \tau)/\hbar \pm \omega_{\vec{K}'}\tau]\}, \qquad (174) \end{aligned}$$

so that

$$(S - 1)_{fi} = (-i/\hbar)^2 C_{\vec{K},\vec{K}'} \int_{-\infty}^\infty dt\left[\mathcal{T}_{\vec{K},\vec{K}'}^{(+)}(\varphi) + \mathcal{T}_{\vec{K}',\vec{K}}^{(-)}(\varphi)\right]\exp[-i(\omega_{\vec{K}} - \omega_{\vec{K}'})t]. \tag{175}$$

By expanding the matrix elements $T^{(\pm)}_{\vec{K},\vec{K}'}(\varphi)$ into a Fourier series

$$T^{(\pm)}_{\vec{K},\vec{K}'}(\varphi) = \sum_{N=-\infty}^{\infty} T^{(\pm)}_{\vec{K},\vec{K}'}(N)\exp(-iN\varphi),$$

$$T^{(\pm)}_{\vec{K},\vec{K}'}(N) = \int_0^{2\pi} \frac{d\varphi}{2\pi} T^{(\pm)}_{\vec{K},\vec{K}'}(\varphi)\exp(iN\varphi), \tag{176}$$

we obtain

$$(S-1)_{fi} = (-i/\hbar)^2 C_{\vec{K},\vec{K}'} 2\pi \sum_n \delta(\omega_{\vec{K}'} - \omega_{\vec{K}} - N\omega)\, T_{fi}(N),$$

$$T_{fi}(N) = T^{(+)}_{\vec{K},\vec{K}'}(N) + T^{(-)}_{\vec{K}',\vec{K}}(N). \tag{177}$$

The physical meaning of the two $T$-matrix elements in Eq. (177) is the following. The matrix element $T^{(-)}_{\vec{K}',\vec{K}}(N)$ corresponds to the processes in which an x-ray photon of the wave vector $\vec{K}$ and energy $\hbar\omega_{\vec{K}}$ is absorbed first. The atom becomes ionized and the electron propagates under the influence of the laser field only during the time interval from $t-\tau$ to $t$ when it comes back to the atomic core (i.e., the return time $\tau$). At this instant the electron recombines, exchanging $N$ photons with the laser field and emitting an x-ray photon of the wave vector $\vec{K}'$ and of the energy $\hbar\omega_{\vec{K}'} = \hbar\omega_{\vec{K}} + n\hbar\omega$. For the matrix element $T^{(+)}_{\vec{K},\vec{K}'}(n)$ we have first the emission of the x-ray photon with the wave vector $\vec{K}'$ and the energy $\hbar\omega_{\vec{K}'}$, then the electron propagation and, finally, the absorption (or emission) of $N$ photons of the laser field and the absorption of one x-ray photon of the wave vector $\vec{K}$ and the energy $\hbar\omega_{\vec{K}}$.

### E.4. Differential cross-section

The rate (probability per unit time) of emission of x-ray photons of frequencies within the interval $(\omega_{\vec{K}'} - \varepsilon, \omega_{\vec{K}'} + \varepsilon)$ and with the polarization $\vec{\epsilon}_{\vec{K}'}$ into a solid angle $d\Omega_{\hat{K}'}$ is [335]

$$w_{fi}d\Omega_{\hat{K}'} = \frac{1}{T_p}\frac{V}{(2\pi c)^3}d\Omega_{\hat{K}'}\int_{\omega_{K'}-\varepsilon}^{\omega_{K'}+\varepsilon}d\omega_{\vec{K}}\omega_{\vec{K}}^2|(S-1)_{fi}|^2, \tag{178}$$

where $T_p$ is the laser pulse duration time and the connection $\sum_{\vec{K}} \to V/(2\pi)^3\int d\vec{K} = V/(2\pi c)^3\int d\omega_{\vec{K}}\omega_{\vec{K}}^2\int d\Omega_{\hat{K}}$ was used. $\varepsilon$ is considered small enough so that $\omega_{\vec{K}}^2|(S-1)_{fi}|^2$ is almost constant over the interval of integration. The duration time of x-ray pulses generated in high-order

harmonic generation processes is usually shorter than the duration of the laser field pulse. Hence one can assume that the x-ray scattering process happens at some instant $t_s \in [0, T_p]$. According to Eq. (177), we obtain for the absolute square of the $S$-matrix element

$$
\begin{aligned}
|(S-1)_{fi}|^2 &= \left(\frac{2\pi}{\hbar^2} C_{\vec{K},\vec{K}'}\right)^2 \sum_N T_{fi}(N)\delta(\omega_{\vec{K}'} - \omega_{\vec{K}} - N\omega) \\
&\quad \times \sum_{N'} T_{fi}^*(N')\delta(\omega_{\vec{K}'} - \omega_{\vec{K}} - N'\omega) \\
&= \frac{T_p}{2\pi}\left(\frac{2\pi}{\hbar^2} C_{\vec{K},\vec{K}'}\right)^2 \sum_N |T_{fi}(N)|^2 \delta(\omega_{\vec{K}'} - \omega_{\vec{K}} - N\omega), \quad (179)
\end{aligned}
$$

where we used the relation $2\pi\delta(0) = T_p$ (for $T_p \to \infty$). The differential cross section can be obtained by dividing the emission rate $w_{fi}(N)$ by the incident x-ray photon flux $j_{\vec{K}} = c/V$. Taking into account the quantity $C_{\vec{K},\vec{K}'}$, defined above Eq. (174), we obtain

$$
\frac{d\sigma(N)}{d\Omega_{\hat{\vec{K}}'}} = \left(\frac{e^2}{4\pi\varepsilon_0\hbar}\right)^{1/2} KK'^3 |T_{fi}(N)|^2, \quad \omega_{\vec{K}'} = \omega_{\vec{K}} + N\omega, \quad (180)
$$

where $K = \omega_{\vec{K}}/c$, $K' = \omega_{\vec{K}'}/c$, and the energy-conserving condition $\hbar\omega_{\vec{K}'} = \hbar\omega_{\vec{K}} + N\hbar\omega$ comes from the argument of the $\delta$-function. This is our final result for the DCS of x-ray atom scattering with the absorption ($N > 0$) or emission ($N < 0$) of $N$ laser photons.

### E.5. Time-dependent WBK approximation

In order to evaluate the DCS we have to compute the $T$-matrices which are the Fourier components of the matrix elements $\mathcal{T}^{(\pm)}_{\vec{K},\vec{K}'}(\varphi)$, defined by Eq. (174). The three-dimensional integral over the intermediate electron momenta $\hbar\vec{q}$ can be computed using the saddle-point method. This can be done in a similar way as shown in ref. [233]. Denoting the subintegral matrix elements by $h(\vec{q}; t, \tau)$, we obtain with $\vec{p} = \hbar\vec{q}$ the result

$$
\begin{aligned}
\hbar^3 \int d\vec{q}\, h(\vec{q}; t, \tau)&\exp[-iS(\vec{q}; t, \tau)/\hbar] \\
&= \left(\frac{2\pi m\hbar}{i\tau}\right)^{3/2} \exp[-iS(\vec{q}_s; t, \tau)/\hbar]\left(1 - i\frac{m\hbar}{2\tau}\frac{\partial^2}{\hbar^2\partial\vec{q}^2} + \cdots\right) \\
&\quad \times h(\vec{q}; t, \tau)\,|_{\vec{q}=\vec{q}_s(t,\tau)}, \quad (181)
\end{aligned}
$$

where the stationary momentum $\hbar\vec{q}_s$, given by

$$\hbar\vec{q}_s(t,\tau) = -\frac{e}{\tau}\int_{t-\tau}^{t} dt'\,\vec{A}(t') = \frac{m}{\tau}[\vec{\alpha}(t-\tau) - \vec{\alpha}(t)], \tag{182}$$

is the solution of the equation $\vec{\nabla}_{\vec{q}}S(\vec{q};t,\tau) = 0$. The result in Eq. (181) is a particular version of the time-dependent WBK approximation [234]. We have shown in the context of high-order harmonic generation and above-threshold ionization within the strong-field approximation [224, 233, 342] that satisfactory results can be obtained by keeping only the zeroth-order term of the expansion of the form Eq. (181). For the processes mentioned before, the number $N$ of the exchanged photons is large. It will be worthwhile to check whether this approximation is also applicable for relatively small $N$ which we shall consider here. In order to verify this, we computed the first-order correction (the term with $\partial^2/\partial\vec{q}^2$) and found that the above approximation is satisfactory for $|N| > 2$. This is an unexpected result which shows that the above approximation, Eq. (181), has a wider range of applicability than it was expected previously. The matrix elements which appear in $\mathcal{T}_{\vec{K},\vec{K}'}^{(\pm)}(\varphi)$ are of the form (for a hydrogen atom in its ground state $|\psi_0\rangle$)

$$\langle\vec{q}|\vec{\epsilon}_{\vec{K}}\cdot\vec{r}|\psi_0\rangle = -i\frac{2^{7/2}\vec{q}\cdot\vec{\epsilon}_{\vec{K}}}{\pi a_{\mathrm{B}}^{5/2}(\vec{q}^2 + a_{\mathrm{B}}^{-2})^3}, \tag{183}$$

where $a_{\mathrm{B}}$ is the Bohr radius. In the case of a linearly-polarized laser field we have $\vec{q} = \vec{q}_s \parallel \vec{\epsilon}$, so that the DCS contains the factor $(\vec{\epsilon}\cdot\vec{\epsilon}_{\vec{K}})^2(\vec{\epsilon}\cdot\vec{\epsilon}_{\vec{K}'})^2$. This factor has its maximum (equal to 1) for parallel geometry: $\vec{\epsilon} \parallel \vec{\epsilon}_{\vec{K}} \parallel \vec{\epsilon}_{\vec{K}'}$. In order to simplify the situation, we shall therefore present numerical results for this geometry only.

Our final result for the DCS, used for evaluating numerical result, is given by Eq. (180) in which

$$T_{fi}(N) = T_{\vec{K},\vec{K}'}^{(+)}(N) + T_{\vec{K}',\vec{K}}^{(-)}(N), \quad T_{\vec{K},\vec{K}'}^{(\pm)}(N) = \int_0^{2\pi}\frac{d\varphi}{2\pi}\mathcal{T}_{\vec{K},\vec{K}'}^{(\pm)}(\varphi)\exp(iN\varphi), \tag{184}$$

where the $\mathcal{T}_{\vec{K},\vec{K}'}^{(\pm)}(\varphi)$ are given by Eq. (174). According to Eq. (183), the zeroth-order term of the WBK expansion Eq. (181) yields for the parallel

geometry

$$
\mathcal{T}^{(\pm)(0)}_{\vec{K},\vec{K}'}(\varphi) = -\left(\frac{2\pi m}{i\hbar}\right)^{3/2} \frac{2^7}{\pi^2 a_{\mathrm{B}}^5} \int_0^\infty \frac{d\tau}{\tau^{3/2}} \exp\{-i[S(\vec{q}_s; t, \tau) \pm \hbar\omega_{\vec{K}'}\tau]/\hbar\}
$$

$$
\times \frac{[q_s + e/\hbar A(t)][q_s + e/\hbar A(t-\tau)]}{\{[q_s + e/\hbar A(t)]^2 + a_{\mathrm{B}}^{-2}\}^3 \{[q_s + e/\hbar A(t-\tau)]^2 + a_{\mathrm{B}}^{-2}\}^3}, \quad (185)
$$

where $S$ and $\vec{q}_s \equiv q_s\vec{\epsilon}$ are given by Eqs. (173) and (182), respectively, and $\vec{A}(t) \equiv A(t)\vec{\epsilon}$.

### E.6. Saddle-point method analysis of the x-ray spectra

According to Eqs. (177) and (180) the DCS for scattering in a laser field is determined by the $T$-matrix $T_{fi}(N) = T^{(+)}_{\vec{K},\vec{K}'}(N) + T^{(-)}_{\vec{K},\vec{K}'}(N)$. The matrix elements $T^{(\pm)}_{\vec{K},\vec{K}'}(N)$ can be evaluated by computing the five-dimensional integral over the time $t$, the return time $\tau$, and the intermediate electron momenta $\vec{q}$. We have shown in the previous section that the three-dimensional integral over the intermediate electron momenta can be replaced by an infinite sum of matrix elements. The resulting integrals can also be analyzed by applying the saddle-point method. The behavior of all these matrix elements is mainly determined by the factors which appear in the exponent. According to Eqs. (174)–(176) and (181) we have

$$
T^{(\pm)}_{\vec{K},\vec{K}'}(N) \propto \int dt \int d\tau\, \tau^{-3/2}\, h(\vec{q}_s; t, \tau) \exp\{-i[S(\vec{q}_s; t, \tau)/\hbar \pm \omega_{\vec{K}'}\tau - N\omega t]\}.
$$
$$(186)$$

By applying the saddle-point method to the integral over the time $t$ we obtain the condition $\partial S/\partial t = N\hbar\omega$, which can be written in the form

$$
\frac{\vec{\pi}^2(t)}{2m} - \frac{\vec{\pi}^2(t-\tau)}{2m} = N\hbar\omega, \quad (187)
$$

where $\vec{\pi}(t') = \hbar\vec{q}_s(t', \tau) + e\vec{A}(t')$ is the momentum of the electron in the laser field at time $t'$. The second condition can be obtained by applying the saddle-point method to the integral over $\tau$. This condition depends on the $T$-matrix element which we are considering and we obtain,

respectively

$$\text{for } T^{(+)}_{\vec{K},\vec{K}'}(N) : \frac{\vec{\pi}^2(t-\tau)}{2m} = -\hbar\omega_{\vec{K}'} - I_{io},$$

$$\text{for } T^{(-)}_{\vec{K}',\vec{K}}(N) : \frac{\vec{\pi}^2(t-\tau)}{2m} = +\hbar\omega_{\vec{K}} - I_{io}. \tag{188}$$

The right-hand side of the first of the above equations is always negative, so that the solutions for $t$ and $\tau$ are complex. A similar condition was obtained in the context of the analysis of the cutoff law in high-order harmonic generation [181, 233]. The more interesting is the second condition of Eq. (188), because for $\hbar\omega_{\vec{K}} \geq I_{io}$ it corresponds to real times $t$ and $\tau$. By considering numerical examples, we shall show in the next section that this term essentially determines the behavior of the final x-ray spectra. The matrix element $T^{(-)}_{\vec{K}',\vec{K}}(N)$ corresponds to a process in which an x-ray photon is absorbed first. For $\hbar\omega_{\vec{K}} \geq I_{io}$ the electron can really be ionized and it has the energy $\vec{\pi}^2(t-\tau)/2m$ in the laser field at the instant $t-\tau$. Then this electron moves under the influence of the laser field only. At some time $t$ it comes close to the atomic core and can be recaptured by the nucleus. The recombination process is the most probable one for low electron energies, i.e., for $\vec{\pi}^2(t)/2m \approx 0$. Introducing this condition into Eq. (187) we obtain $\vec{\pi}^2(t-\tau)/2m = -N\hbar\omega$, which, in combination with the second condition in Eq. (188), yields

$$N\hbar\omega = I_{io} - \hbar\omega_{\vec{K}}. \tag{189}$$

Therefore we obtain a simple linear dependence which connects the number $N$ of absorbed (or emitted) photons of the laser field, the atomic ionization potential $I_{io}$, and the energy of the incident x-ray photon $\hbar\omega_{\vec{K}}$. Besides this condition, we should take into account the energy conserving condition $\hbar\omega_{\vec{K}'} = \hbar\omega_{\vec{K}} + N\hbar\omega \geq 0$, which determines the cutoff of the spectrum at large negative values of $N$. Moreover we have to observe that, according to symmetry and parity considerations of the matrix elements the number $N$ of the exchanged photons must be even. As we shall show in the next section, the x-ray spectrum is mainly determined by these conditions. The condition Eq. (189), and consequently the values of $N$ which characterize the spectrum, do not depend on the intensity of the laser-field. We shall see that the DCS increase with the increase of the laser field intensity, but the general shape of the spectrum is determined by the simple condition Eq. (189).

### E.7.  Numerical results

First we shall check whether our time-dependent WBK approximation gives reasonable results. In Fig. 22 we present for two values of the laser-field intensity our data for the DCS (in units of $r_0^2$) of laser-assisted x-ray atom scattering as functions of the number $N$ of photons exchanged with the laser field. The triangles and squares refer to the results obtained with the zeroth- and the first-order term of the WBK expansion Eq. (181), while the dotted and the dashed line correspond to the use of the zeroth-order term only. As we can see, for $|N| > 2$ the zeroth-order approximation gives satisfactory results. Moreover, the results presented in Fig. 22 show the typical behavior of the x-ray spectra which we obtained in this calculation. First of all, only an even number of laser photons is absorbed or emitted. Second, for $N = 0, \pm 2$ the spectrum has a pronounced maximum and then there is a rapid drop at $N = \pm 4$. Beyond that there is a plateau which is quite different for the positive and the negative values of $N$. The height of the plateau is determined by the laser-field intensity. The plateau for positive $N$ is small
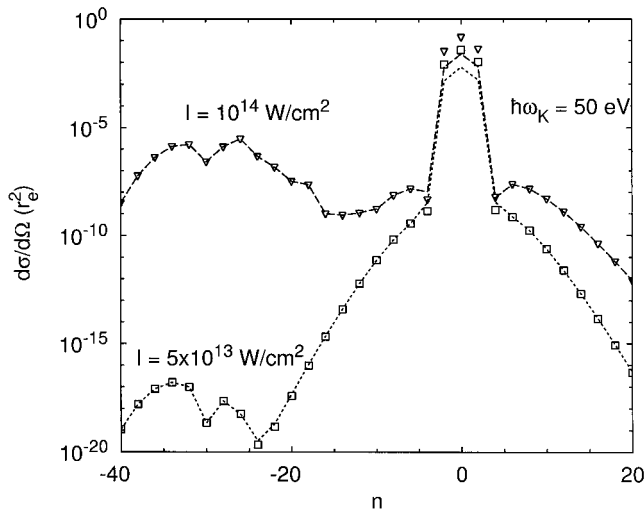


FIG. 22. The DCS of x-ray scattering in units of $r_0^2$ ($r_0 = 2.82 \times 10^{-15}$ m is the classical electron radius) as function of the number $N$ of absorbed (or emitted) laser field photons for two values of the laser field intensity: $I = 5 \times 10^{13}$ Wcm$^{-2}$ (squares and dotted curve) and $I = 10^{14}$ Wcm$^{-2}$ (triangles and dashed curve). The laser field is linearly polarized and monochromatic with the photon energy $\hbar\omega = 1.17$ eV. The energy of the incident x-ray photons is $\hbar\omega_{\vec{K}} = 50$ eV. The results presented by the dotted and dashed curves are obtained by using the zeroth-order term of the WBK approximation (see the text), while the triangles and squares refer to the results obtained by taking into account the first-order correction (see ref. [343]).
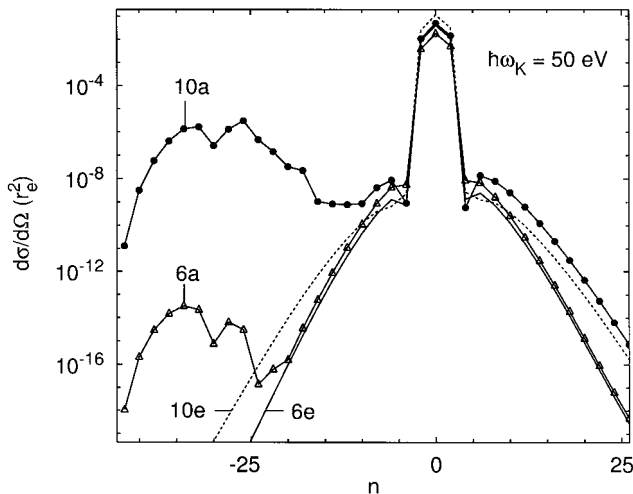
FIG. 23. The DCS of x-ray scattering in the presence of a laser field presented in the same way as in Fig. 22. The curves denoted by 6 and 10 refer to the laser field intensities $I = 6 \times 10^{13}\,\mathrm{Wcm^{-2}}$ and $I = 10^{14}\,\mathrm{Wcm^{-2}}$, respectively. The results obtained by using only the matrix element that belongs to the process in which an x-ray photon is absorbed first, are denoted by the letter "a", while the letter "e" refer to the process in which there is first the emission of an x-ray photon (see ref. [343]).

(almost negligible) in comparison with the plateau for the negative values of $N$. In Fig. 23 we analyze the contributions of the matrix elements $T_{\vec{K},\vec{K}'}^{(+)}(N)$ and $T_{\vec{K}',\vec{K}}^{(-)}(N)$ to the DCS. The results denoted by "a" correspond to the matrix elements $T_{\vec{K}',\vec{K}}^{(-)}(N)$ and refer to the processes in which an x-ray photon is absorbed first, while the results denoted by "e" belong to the elements $T_{\vec{K},\vec{K}'}^{(+)}(N)$ and refer to the processes in which we have first the emission of an x-ray photon. We see that the 'e'-spectrum is symmetric with respect to $N = 0$, while the 'a'-spectrum has a broad plateau for the negative values of $N$. Therefore, the x-ray spectra are mainly determined by those processes in which the x-ray photon is absorbed first and which is in accordance with our analysis presented in the previous section. For the results shown in Figs. 22 and 23 the incident x-ray photon energy was taken to be $\hbar\omega_{\vec{K}} = 50\,\mathrm{eV}$ and the laser field photon energy was chosen $\hbar\omega = 1.17\,\mathrm{eV}$, while the laser field intensities were $I = 5 \times 10^{13}\,\mathrm{W\,cm^{-2}}$, $I = 6 \times 10^{13}\,\mathrm{W\,cm^{-2}}$, and $I = 10^{14}\,\mathrm{W\,cm^{-2}}$.

### E.8. Concluding remarks

Only little work was so far devoted to x-ray–atom scattering in the presence of a laser field. We presented above our $S$-matrix theory of this process that

leads, after suitable approximations, to a relatively simple expression for the DCS, Eq. (180). The *T*-matrix element, contained in this expression, consists of two terms that can be explained in terms of two Feynman diagrams: one corresponds to the processes in which the x-ray photon is absorbed first, while in the other one the x-ray photon is emitted first. The intermediate propagator between the points of absorption and the emission of the x-ray photons is dressed by the laser field so that thanks to parity conservation in x-ray–atom scattering in a laser field only an even number of laser-field photons can be absorbed or emitted. We showed that the expression obtained for the DCS can be further simplified by applying a particular version of the time-dependent WBK approximation. This method was developed within the strong-field approximation for high-order harmonics generation [181, 233] and above-threshold ionization [224, 342] and is assumed to be applicable in those cases where the number $N$ of exchanged photons is large. Contrary to this assumption, we showed here that this method also works well for relatively low laser-field intensities and for small values of $N$. A further result of our application of the saddle-point method leads to the conclusion that the x-ray spectra are mainly determined by those processes in which the x-ray photon is absorbed first. In this case, the atom becomes ionized and the electron moves quasi-freely in the laser field. If its energy is small enough when it comes close to the atomic core, it can be recaptured and an x-ray photon is emitted. We demonstrated that this process is most probable when the number of the exchanged photons satisfies the condition Eq. (189), $N\hbar\omega = I_{io} - \hbar\omega_{\vec{K}}$. For $\hbar\omega_{\vec{K}} > I_{io}$ mostly an even number of photons is emitted into the laser field, and the energies of the scattered x-rays $\hbar\omega_{\vec{K}'} = \hbar\omega_{\vec{K}} + N\hbar\omega$, is thus smaller than the energy of the incident x-ray.

The above problem of x-ray–atom scattering in a monochromatic laser field was considered by the present authors in ref. [343], while the more general scattering process in a bichromatic field was investigated in ref. [344], emphasizing the coherent phase control of x-ray–atom scattering. The high-energy plateau of scattered x-ray photons, that is induced by the presence of a static electric field in the laser-assisted x-ray–atom scattering process, was analyzed in ref. [345]. In this investigation it was found that by adding a static electric field, the dynamics of the process becomes changed in the intermediate states, giving rise to an extended plateau of scattered x-rays of photon energies $\hbar\omega_{\vec{K}'} = \hbar\omega_{\vec{K}} + N\hbar\omega$ with $N > 0$. This leads to a substantial increase of the energies of the scattered x-rays which thus can reach into the frequency domain of the "water window" [346]. Finally, in ref. [347] Milošević and Starace investigated the intensity-dependence of the plateau structure in the laser-assisted x-ray–atom scattering process, considering the two cases: with and without a static electric field. Using

the "three-step model" of HHG and some semiclassical arguments, the connection between the laser-assisted x-ray–atom scattering process and HHG was established, and additional plateaus in the x-ray spectra were observed and analyzed.

## F. Generation of Harmonics

### F.1. Introduction

The generation of higher harmonics, besides the above-threshold ionization in laser–atom interactions, can also be understood on the basis of general scattering theory. From the unitarity of the scattering operator, $S^+S = 1$, and the definition of the transition operator, $S = 1 - 2\pi i T$, we obtain the relation $T - T^+ = -2\pi i T^+ T$. Now we apply this relation to atomic interactions with the radiation field, denoting by $\varepsilon$ the powers of interaction. Then we can make the formal expansion $T = T_0 + \varepsilon T_1 + \varepsilon^2 T_2 + \cdots$ and insert it into the above relation. Considering now second order processes in $\varepsilon$ and taking the same initial and final atomic state $|g\rangle$, we obtain

$$2\mathrm{Im}\langle g|T_2|g\rangle = -2\pi \sum_n |\langle n|T_1|g\rangle|^2. \tag{190}$$

Hence to every photon absorption process by an atomic system will correspond a dispersive photon scattering process and vice versa. Generalizing Eq. (190) to multiphoton processes, we expect that higher harmonic generation will be concomitant with multiphoton ionization.

High-harmonic generation (HHG) is one of the major topics of intense-field laser–atom physics [9, 17, 18, 21, 26, 174, 175, 280, 348–350]. When an atomic gas (or any nonlinear medium) is irradiated by a short intense laser pulse the atoms emit coherent radiation at frequencies that are multiples of the laser field frequency $\omega$. The generation efficiency of these harmonics is characterized by a rapid drop at low orders, followed by a broad plateau with approximately constant efficiency and a sharp cutoff. The plateau was experimentally observed at the end of the 1980s [351, 352]. The emitted high-harmonic photon energy in more recent experiments reaches several hundred eV, i.e., the harmonic order is above 300 [330, 331, 353, 354] (in ref. [350] the XUV spectrum is presented that extends beyond 500 eV, i.e., to the short-wavelength edge of the water window at 2.3 nm, the K-edge of oxygen). For a linearly-polarized laser field with the electric field vector $\vec{\mathcal{E}}_L$ and the frequency $\omega$, the cutoff corresponds to the emitted high-harmonic photon energy $N_{\max}\hbar\omega \approx |E_0| + 3.17\,U_P$, where $|E_0| = I_{io}$ is the atomic ionization energy and $U_P = \langle e\mathcal{E}_L\rangle^2/(2m\omega^2)$ is the ponderomotive energy of

the electron. The harmonics with the photon energies higher than $N_{\max}\,\hbar\omega$ are produced with an exponentially diminishing efficiency thus becoming rapidly indistinguishable from the background. The HHG process is entirely nonlinear and nonperturbative. It can be explained by using the three-step quasiclassical model [172, 173, 355], as discussed in the historical overview in Section II.A. According to this model, the atom is ionized by a tunneling process (step 1). The escaped electron is driven by the field and returns to the atomic core (step 2), emitting a harmonic photon during the transition back to the ground state (step 3). The maximum kinetic energy acquired by a free electron in a linearly-polarized laser field when it returns to the nucleus is 3.17 $U_P$, which explains the cutoff energy of the emitted harmonic photons. Both the classical [172, 173, 355] and quantum [180, 181, 356, 357] calculations have confirmed this model. A schematic diagram of the three-step model is presented in Fig. 14, while an example of the spectrum, calculated using the *S*-matrix method which will be presented below, is shown in Fig. 24.

In the present section we shall concentrate on the *microscopic single-atom theory of HHG* that describes the response of an atom to the fundamental
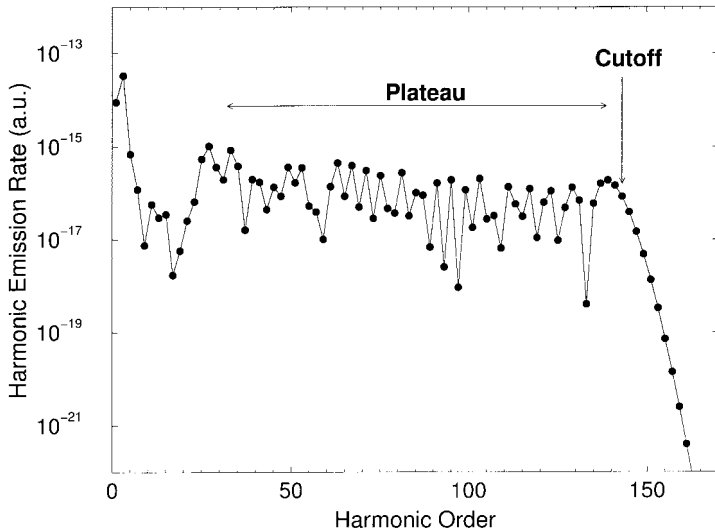


FIG. 24. Harmonic emission rate as a function of the harmonic order $N$ for HHG by He atoms (ionization energy $I_{io} = 24.588\,\text{eV}$) with a linearly polarized Ti:Sapphire laser (wavelength 800 nm) having the intensity $I = 10^{15}\,\text{Wcm}^{-2}$. The results are obtained by using the semi-analytical approach, described in the text. The plateau and the cutoff regions of the spectrum are marked in the figure. According to refs. [181, 358] the cutoff is at $N_{\max}\,\hbar\omega = 1.325\,|E_0| + 3.173 U_P$, which is in excellent agreement with the results presented ($N_{\max} = 143$).

laser field. A complete theory should also include the macroscopic response of the system and the coherent emission of all the atoms in the laser focus. HHG can only be observed by an ensemble of atoms that introduces phase matching. In this case, one has to solve Maxwell's equations for the fundamental field and the harmonic field, with the single-atom harmonic field as the source term. This is the so-called propagation theory [175], which we shall not consider here. The problem of the single-atom response can be solved by using different approaches. The classical phase space averaging method was considered in [359–361]. The characteristics of the high-harmonic spectra were also reproduced by using a simple two-level model, implying that these characteristics are common to strongly driven nonlinear systems (see ref. [362] for the first analysis and refs. [363, 364] for more recent contributions). Numerical methods based on the Floquet theory were presented in ref. [365] (see also the review article [18]). The method of direct integration of the three-dimensional time-dependent Schrödinger equation was initiated by Kulander [366]. This method was developed further by using different codes (see, for example, the references in the review articles [17, 175]). The above-mentioned numerical methods are within the single-active-electron approximation. According to a review article on two-electron atoms in strong fields by Lambropoulos *et al.* [367] and the recent Focus issue on laser-induced multiple ionization [368], HHG is basically a single electron phenomenon described quite well by the single-active-electron models. The correlation effects play little role in HHG for visible and near infrared light, while for higher laser frequencies they can be of importance (see references in ref. [369], where HHG with two active electrons was considered). Within the fully numerical approaches, but beyond the single-active-electron approximation, a variant of the time-dependent density functional theory was shown to be very useful [370,371]. The quantum-fluid-dynamics approach to HHG was explored in ref. [277]. A hydrodynamics model and a variant of the Thomas–Fermi model was used in ref. [372] to investigate the response of a multi-electron atom to an intense radiation field at high photon energies up to 40 eV. The limitations of the fully numerical approaches are that they are quite memory and time consuming. For more complicated cases, such as elliptically-polarized and bichromatic laser fields, the presence of static fields, relativistically-strong laser field, etc., semi-analytical methods are more useful.

The *semi-analytical approaches to HHG* based on the *strong-field approximation* (SFA) were developed in [180, 181, 356, 357]: the harmonic spectrum is obtained as the Fourier transform of the real time-dependent effective-dipole matrix element $\vec{d}_{\mathrm{ed}}(t) = \langle \Phi^{(+)}(t)|e\vec{r}|\Phi^{(+)}(t)\rangle$, where $|\Phi^{(+)}(t)\rangle$ is the wave vector which describes the electron in presence of both the laser field and the atomic potential. This real effective-dipole expectation value is

required as the source term for the integration of the Maxwell equations. However, if just the harmonic emission of a single atom is considered, then the $S$-matrix element, instead of the effective-dipole matrix element, is the useful quantity. The $S$-matrix formulation of the atomic processes in the laser field can be found in ref. [109]. We shall use the $S$-matrix theory that we have employed in previous sections. Instead of using $\vec{d}_{\mathrm{ed}}(t)$, we calculate in the *S-matrix approach* the complex quantity $\vec{d}_{\mathrm{sm}}(t) = \langle \Phi^{(-)}(t)|e\vec{r}|\Phi^{(+)}(t)\rangle$, where the wave vectors $|\Phi^{(+)}(t)\rangle$ and $|\Phi^{(-)}(t)\rangle$ evolve from the initial and final state, respectively, under the action of the corresponding total Green's operators $G^{(+)}$ and $G^{(-)}$. The first attempt to apply the $S$-matrix theory to HHG was made in ref. [373]. In ref. [374] the difference between the $S$-matrix approach and the effective-dipole method was discussed. Besides the effective-dipole vs. the $S$-matrix method, the semi-analytical approaches to HHG can also be distinguished, depending on how one treats the laser field and the harmonic field, either classically or quantum-electrodynamically (i.e., using the photon creation and annihilation operators). Usually, both fields are treated classically (see refs. [180,181] for the effective-dipole approach and [375, 376] for a method similar to the $S$-matrix approach that leads to the complex time-dependent dipole matrix element). In the refs. [377–380] both fields were treated quantum-electrodynamically, and the HHG problem was analyzed as a time-independent scattering process. However, by appropriate transformations one can introduce the time dependence into this approach that permits the interpretation in terms of the three-step model [381]. In our review, we shall use a mixed representation in which the laser field is considered as classical, while the harmonic field is treated by quantum electrodynamics. This approach is justified since the quantum-electrodynamical treatment of the electromagnetic field, taken in the laser-field approximation (i.e., for a large number of photons in the field mode), is equivalent to the classical treatment [109]. By means of this approach, we shall formulate a *general S-matrix theory for the HHG process*. This method was similar to our $S$-matrix theory for laser-assisted x-ray–atom scattering [343] developed in Section II.E. More recently, a similar approach was presented in refs. [382, 383].

In refs. [384–386] it was shown within the quasi-stationary quasi-energy approach that we have to use instead of the time-dependent effective-dipole matrix element the expression $\vec{d}_{\mathrm{dual}} = \langle \Phi^{(+)}_{\mathrm{dual}}(t)|e\vec{r}|\Phi^{(+)}(t)\rangle$, where $\Phi^{(+)}_{\mathrm{dual}}(t)$ is the dual state that corresponds to the state $\Phi^{(+)}(t)$. The dual quasi-stationary states were introduced in order to achieve the proper normalization condition. The results of the dual-space method coincide (within some approximations) with those of the $S$-matrix method. An advantage of the $S$-matrix calculation is that in this approach the initial and final states do not need to be the same.

Instead of computing the time-dependent dipole, one can calculate the time-dependent acceleration $\vec{a}(t) = \langle \Phi^{(+)}(t)|e\vec{r}|\Phi^{(+)}(t)\rangle$. This method allows to avoid some computational difficulties. The Fourier transforms of $\vec{a}(t)$ and $\vec{d}(t)$ are simply related by the formula $\mathcal{F}_N(\vec{a}) = (N\omega)^2 \mathcal{F}_N(\vec{d})$ [362, 387, 388].

*F.2. S-matrix theory of high-harmonic generation*

We shall start with a general form of the *S*-matrix [92] (in SI units)

$$S_{fi} = i\hbar \lim_{t' \to \infty} \lim_{t \to -\infty} \langle \Phi_{\text{out}}(t')|G^{(+)}(t', t)|\Phi_{\text{in}}(t)\rangle, \tag{191}$$

where the total Green's operator $G$ corresponds to the Hamiltonian

$$H(t) = H_0(t) + e\vec{r}\cdot\vec{\mathcal{E}}_{\text{H}}(t), \qquad H_0(t) = \frac{\vec{p}^2}{2m} + V_{\text{A}} + H_{\text{L}}(t). \tag{192}$$

Here $V_{\text{A}}$ is the atomic potential, while $e\vec{r}\cdot\vec{\mathcal{E}}_{\text{H}}(t)$ and $H_{\text{L}}(t) = e\vec{r}\cdot\vec{\mathcal{E}}_{\text{L}}(t)$ represent the interactions of the atom with the high-harmonic field and the laser field, respectively (in the length gauge; $e = |e|$). In order to distinguish the high-harmonic radiation field from the (classical) laser field, we treat it as a quantized field, i.e., according to ref. [335], we define

$$\vec{\mathcal{E}}_{\text{H}}(t) = \sum_{\vec{K}} c_{\vec{K}} \left[ a_{\vec{K}}^{\dagger} e^{i(\omega_{\vec{K}}t - \vec{K}\cdot\vec{R})}\vec{\epsilon}_{\vec{K}}^* - a_{\vec{K}} e^{-i(\omega_{\vec{K}}t - \vec{K}\cdot\vec{R})}\vec{\epsilon}_{\vec{K}} \right], \tag{193}$$

where $c_{\vec{K}} = -i[\hbar\omega_{\vec{K}}/(2\varepsilon_0\mathcal{V})]^{1/2}$, and $a_{\vec{K}}$ and $a_{\vec{K}}^{\dagger}$ are the annihilation and creation operators of the high-harmonic photon, having the wave vector $\vec{K}$, frequency $\omega_{\vec{K}}$, and complex unit polarization vector $\vec{\epsilon}_{\vec{K}}$. $\mathcal{V}$ is the quantization volume and $\vec{R}$ is the coordinate of the center of mass of the atom. The interaction with the laser field is turned off for the *in* and *out* states, so that

$$|\Phi_{\text{in}}(t)\rangle = |\psi_{0i}(t)\rangle|0_{\vec{K}}\rangle, \quad |\Phi_{\text{out}}(t)\rangle = |\psi_{0f}(t)\rangle|1_{\vec{K}}\rangle, \tag{194}$$

where $|\psi_{0j}(t)\rangle = |\psi_{0j}\rangle \exp(-iE_{0j}t/\hbar)$, $j = i, f$, and the ket vectors $|0_{\vec{K}}\rangle$ and $|1_{\vec{K}}\rangle$ refer to no high-harmonic photon in the initial state and to one high-harmonic photon in the final state, respectively. The atomic state vectors $|\psi_{0j}\rangle$ and energies $E_{0j}$ satisfy the stationary Schrödinger equation $[\vec{p}^2/2m + V_{\text{A}}]|\psi_{0j}\rangle = E_{0j}|\psi_{0j}\rangle$. The total Green's operator satisfies the

Lippmann–Schwinger equation

$$G^{(+)}(t,t') = G_0^{(+)}(t,t') + \int dt'' G^{(+)}(t,t'')\, e\vec{r}\cdot\vec{\mathcal{E}}_H(t'') G_0^{(+)}(t'',t'), \qquad (195)$$

where the Green's operator $G_0^{(+)}$ belongs to the Hamiltonian $H_0$ and operates in the vector space of high-harmonic photons as a unit operator. Introducing Eq. (195) into Eq. (191), we obtain

$$S_{fi} = i\hbar \lim_{t'\to\infty} \lim_{t\to-\infty} \langle \psi_{0f}(t')| \int dt'' \langle 1_{\vec{K}}|G^{(+)}(t',t'')|1_{\vec{K}}\rangle$$
$$\times\, c_{\vec{K}} e\vec{r}\cdot\vec{\epsilon}_{\vec{K}}^{\,*} e^{i(\omega_{\vec{K}}t''-\vec{K}\cdot\vec{R})} G_0^{(+)}(t'',t)|\psi_{0i}(t)\rangle. \qquad (196)$$

Using Eq. (195) we find $\langle 1_{\vec{K}}|G^{(+)}(t',t'')|1_{\vec{K}}\rangle = G_0^{(+)}(t',t'')[1+\mathcal{O}(H_H^2)]$, where $\mathcal{O}(H_H^2)$ denotes the second-order terms in the interaction with the high-harmonic field, that we shall neglect. We should mention that if we consider only the interaction for the emission of high-harmonics [i.e., the term with $a_{\vec{K}}^\dagger$ in Eq. (193)], then the relation $\langle 1_{\vec{K}}|G^{(+)}|1_{\vec{K}}\rangle = G_0^{(+)}$ is exact, since $\langle 1_{\vec{K}}|(a_{\vec{K}}^\dagger)^n|1_{\vec{K}}\rangle = \delta_{n,0}$. The S-matrix element Eq. (196) can be further transformed, using the relations

$$i\hbar \lim_{t'\to\infty} \langle\psi_{0f}(t')|G_0^{(+)}(t',t'') = \langle\Phi_f^{(-)}(t'')|,$$
$$i\hbar \lim_{t\to-\infty} G_0^{(+)}(t'',t)|\psi_{0i}(t)\rangle = |\Phi_i^{(+)}(t'')\rangle, \qquad (197)$$

where the states $|\Phi_j^{(\pm)}(t)\rangle$, $j=i,f$, satisfy the time-dependent Schrödinger equation for the Hamiltonian $H_0(t)$:

$$\left[i\hbar\frac{\partial}{\partial t} - H_0(t)\right]|\Phi_j^{(\pm)}(t)\rangle = 0. \qquad (198)$$

From Eqs. (196) and (197) we find

$$S_{fi} = -\frac{i}{\hbar} c_{\vec{K}} \int_{-\infty}^{\infty} dt\, e^{i(\omega_{\vec{K}}t-\vec{K}\cdot\vec{R})}\, \vec{\epsilon}_{\vec{K}}^{\,*}\cdot\vec{d}_{fi}(t), \qquad (199)$$

where $\vec{d}_{fi}(t)$ is the time-dependent dipole matrix element between the initial and final laser-field dressed atomic states:

$$\vec{d}_{fi}(t) = \left\langle \Phi_f^{(-)}(t)\left| e\vec{r}\right|\Phi_i^{(+)}(t)\right\rangle. \qquad (200)$$

Equations (199) and (200) represent a general form of the $S$-matrix element for the emission of one high-harmonic photon of frequency $\omega_{\vec{K}}$, wave vector $\vec{K}$, and polarization $\vec{\epsilon}_{\vec{K}}$. The fact that the $S$-matrix element depends on the atomic position $\vec{R}$ can be used to develop a kind of macroscopic theory, which is different from the propagation theory based on the Maxwell equations, mentioned in the introduction. One can sum over the atoms within the interaction volume and use the continuous-medium approximation [389, 390].

If the fundamental laser field with the frequency $\omega$ is $T = 2\pi/\omega$-periodic and the pulse envelope is constant, then $H_0(t + T) = H_0(t)$ and it is possible to introduce the $T$ matrix by the relation

$$S_{fi} = -2\pi i \sum_N \delta(\hbar\omega_{\vec{K}} + E_{0f} - E_{0i} - N\hbar\omega)c_{\vec{K}}T_{fi}(N), \qquad (201)$$

where

$$T_{fi}(N) = \int_0^T \frac{dt}{T} e^{i\omega_{\vec{K}}t}\vec{\epsilon}_{\vec{K}}^* \cdot \vec{d}_{fi}(t) \equiv \vec{\epsilon}_{\vec{K}}^* \cdot \mathcal{F}(\vec{d}_{fi}) \qquad (202)$$

is the corresponding $T$-matrix element and $\mathcal{F}$ denotes the Fourier transform. Using the standard procedure, we obtain for the rate of emission of a harmonic photon, having the frequency $\omega_{\vec{K}}$ and the polarization $\vec{\epsilon}_{\vec{K}}$, into a solid angle $d\vec{n}_{\vec{K}}$

$$w_{fi}(\omega_{\vec{K}}, \vec{\epsilon}_{\vec{K}}) = \frac{\omega_{\vec{K}}^3}{8\pi^2\varepsilon_0\hbar c^3}\left|T_{fi}(N)\right|^2, \quad \hbar\omega_{\vec{K}} + E_{0f} = N\hbar\omega + E_{0i}. \qquad (203)$$

Our final result is given by Eqs. (202) and (203), where the wave vectors $|\Phi_j^{(\pm)}(t)\rangle$ satisfy the Eqs. (197) and (198) together with Eq. (192). The power irradiated into the solid angle $d\vec{n}_{\vec{K}}$ is then $\hbar\omega_{\vec{K}}w_{fi}(\omega_{\vec{K}}, \vec{\epsilon}_{\vec{K}})$.

### F.3. Time-dependent dipole matrix element and the strong-field approximation

In this section we shall analyze the time-dependent dipole matrix element $\vec{d}_{fi}(t)$. Our starting point is Eq. (200) with Eq. (198). The wave vectors $|\Phi_j^{(\pm)}(t)\rangle$ $(j = i, f)$ satisfy

$$|\Phi_j^{(\pm)}(t)\rangle = |\psi_{0j}(t)\rangle + \int dt' G_0^{(\pm)}(t, t')H_L(t')|\psi_{0j}(t')\rangle, \qquad (204)$$

where the first term on the right-hand side is the solution of the homogeneous (field-free) equation. Introducing Eq. (204) into Eq. (200), we obtain

$$\vec{d}_{\mathrm{sm}}(t) \equiv \vec{d}_{fi}(t) = \langle\psi_{0f}(t)|\ e\vec{r}\ |\psi_{0i}(t)\rangle + \vec{d}_{\mathrm{a}}(t) + \vec{d}_{\mathrm{e}}(t) + \vec{d}_{\mathrm{cc}}(t), \qquad (205)$$

where

$$\vec{d}_{\mathrm{a}}(t) = \langle\psi_{0f}(t)|e\vec{r}\int dt' G_0^{(+)}(t,t')H_{\mathrm{L}}(t')|\psi_{0i}(t')\rangle, \qquad (206)$$

$$\vec{d}_{\mathrm{e}}(t) = \int dt' \langle\psi_{0f}(t')|H_{\mathrm{L}}(t')G_0^{(+)}(t',t)e\vec{r}|\psi_{0i}(t)\rangle, \qquad (207)$$

$$\vec{d}_{\mathrm{cc}}(t) = \int dt' \int dt'' \langle\psi_{0f}(t')|H_{\mathrm{L}}(t')G_0^{(+)}(t',t)e\vec{r}G_0^{(+)}(t,t'')H_{\mathrm{L}}(t'')|\psi_{0i}(t'')\rangle. \quad (208)$$

The above four terms, Eqs. (205)–(208), can be understood in terms of Feynman diagrams: the vertex ($e\vec{r}$) for the emission of a high-harmonic photon is inserted in all possible ways. For equal initial and final states, the term $\langle\psi_{0f}(t)|\ e\vec{r}\ |\psi_{0i}(t)\rangle$ is equal to zero for any spherically-symmetric potential. The term $\vec{d}_{\mathrm{a}}(t)$ describes a process in which we first have the laser–atom interaction at the time $t'$ when photons are absorbed from the laser field (the index "a" stands for "absorbed"). After that the system propagates until the instant $t$, where a high-harmonic photon is emitted during the transition to the final state $|\psi_{0f}(t)\rangle$. This term corresponds to the three-step model, described in the introduction. The term $\vec{d}_{\mathrm{e}}(t)$ belongs to the time-reversed version of the "a" process, described above (it is denoted with "e" because a harmonic photon is emitted first). Finally, the term $\vec{d}_{\mathrm{cc}}(t)$ describes a process which consists of five steps: laser–atom interaction at the time $t''$, propagation during the time interval from $t''$ to $t$, emission of the high-harmonic photon at the time $t$, propagation from the time $t$ to the time $t'$, and, finally, a laser–atom interaction at the time $t'$, accompanied by the transition to the final state. It is denoted by "cc" because the harmonic photon is emitted between the two propagations that mainly include continuum states (the "continuum–continuum" transition). We shall continue to analyze the result Eq. (205) by employing the SFA [83, 103, 169, 214]. We assume that in the intermediate states the atomic interaction $V_{\mathrm{A}}$ can be neglected in comparison with the interaction with the laser field $H_{\mathrm{L}}(t)$, so that the Green's operator $G_0$ can be approximated by the Gordon–Volkov Green's operator $G_{\mathrm{L}}$ [343, 374]. By expressing $G_{\mathrm{L}}$

through the Gordon–Volkov wave vectors in the length gauge, Eq. (171), we find

$$\vec{d}_a(t) \approx -\frac{i}{\hbar} \int d^3\vec{q} \, \langle \psi_{0f} | e\vec{r} | \vec{q} + \frac{e}{\hbar} \vec{A}(t) \rangle$$
$$\times \int_{-\infty}^{t} dt' \exp\left[\frac{i}{\hbar} S(\vec{q}; t, t')\right] \langle \vec{q} + \frac{e}{\hbar} \vec{A}(t') | H_L(t') | \psi_{0i} \rangle, \qquad (209)$$

where

$$S(\vec{q}; t, t') = E_{0f} t - \int_{t'}^{t} dt'' \frac{\hbar^2}{2m}\left[\vec{q} + \frac{e}{\hbar}\vec{A}(t'')\right]^2 - E_{0i} t', \qquad (210)$$

with $\vec{\mathcal{E}}(t) = -\partial\vec{A}(t)/\partial t$. The three-dimensional integral over the intermediate electron momenta $\hbar\vec{q}$ can be represented by a series [233]

$$\hbar^3 \int d^3\vec{q} \, M(\vec{q}; t, t') \exp\left[\frac{i}{\hbar} S(\vec{q}; t, t')\right] = \left[\frac{2\pi m\hbar}{i(t - t')}\right]^{3/2}$$
$$\times \exp\left[\frac{i}{\hbar} S(\vec{q}_s; t, t')\right]\left[1 - i\frac{m\hbar}{2(t - t')}\frac{\partial^2}{\hbar^2 \partial\vec{q}^2} + \cdots\right] M(\vec{q}; t, t')|_{\vec{q}=\vec{q}_s(t, t')}, \qquad (211)$$

where $M$ denotes the product of the matrix elements in Eq. (209). Using $m\vec{\alpha}(t) = e\int^t dt' \vec{A}(t')$, the stationary momentum $\hbar\vec{q}_s$ is defined by

$$\hbar\vec{q}_s(t, t') = -\frac{e}{t - t'}\int_{t'}^{t} dt'' \vec{A}(t'') = \frac{m}{t - t'}[\vec{\alpha}(t') - \vec{\alpha}(t)], \qquad (212)$$

and is the solution of the equation $\vec{\nabla}_{\vec{q}} S(\vec{q}; t, t') = \vec{0}$. The higher order terms in Eq. (211) can be neglected in the *semi-classical approximation* (which is an expansion in powers of $\hbar$). For some models this integral can be solved exactly. Similar expressions can be derived for Eqs. (207) and (208). The matrix elements $\vec{d}_a(t)$ and $\vec{d}_e(t)$ can be evaluated by numerical integration over a new variable of integration $\tau$. After the substitutions $t' = t - \tau$ in Eq. (206) and $t' = t + \tau$ in Eq. (207), we obtain

$$\vec{d}_a(t) \approx -\frac{i}{\hbar}\left(\frac{2\pi m}{i\hbar}\right)^{3/2} \int_0^{\infty} \frac{d\tau}{\tau^{3/2}} \exp\left[\frac{i}{\hbar} S(\vec{q}; t, t - \tau)\right]\left(1 - i\frac{m}{2\hbar\tau}\frac{\partial^2}{\partial\vec{q}^2} + \cdots\right)$$
$$\times \left\langle \psi_{0f} \left| e\vec{r} \right| \vec{q} + \frac{e}{\hbar}\vec{A}(t) \right\rangle \left\langle \vec{q} + \frac{e}{\hbar}\vec{A}(t - \tau) \left| H_L(t - \tau) \right| \psi_{0i} \right\rangle\Big|_{\vec{q}=\vec{q}_s(t, t-\tau)}, \quad (213)$$

and

$$\vec{d}_e(t) \approx -\frac{i}{\hbar}\left(\frac{2\pi m}{i\hbar}\right)^{3/2} \int_0^\infty \frac{d\tau}{\tau^{3/2}} \exp\left[\frac{i}{\hbar} S(\vec{q}; t+\tau, t)\right]\left(1 - i\frac{m}{2\hbar\tau}\frac{\partial^2}{\partial\vec{q}^2} + \cdots\right)$$

$$\times \left\langle \psi_{0f}\left|H_L(t+\tau)\right|\vec{q}+\frac{e}{\hbar}\vec{A}(t+\tau)\right\rangle\!\!\left\langle\vec{q}+\frac{e}{\hbar}\vec{A}(t)\right|e\vec{r}\left|\psi_{0i}\right\rangle\Big|_{\vec{q}=\vec{q}_s(t+\tau, t)}.$$

$$(214)$$

A similar, but longer derivation for the matrix element $\vec{d}_{cc}(t)$ leads to the following double integral over the variables $\tau = t' - t$ and $\tau' = t - t''$

$$\vec{d}_{cc}(t) \approx \left(\frac{-i}{\hbar}\right)^2\left(\frac{2\pi m}{i\hbar}\right)^{3/2} \int_0^\infty d\tau \int_0^\infty d\tau'(\tau+\tau')^{-3/2}\exp\left[\frac{i}{\hbar} S(\vec{q}; t+\tau, t-\tau')\right]$$

$$\times \left[1 - i\frac{m}{2\hbar(\tau+\tau')}\frac{\partial^2}{\partial\vec{q}^2} + \cdots\right]\langle\psi_{0f}|H_L(t+\tau)|\vec{q}+\frac{e}{\hbar}\vec{A}(t+\tau)\rangle$$

$$\times \left[\vec{\alpha}(t) - \vec{\alpha}(t-\tau') + \frac{\hbar}{m}\vec{q}\tau' + i\frac{\partial}{\partial\vec{q}}\right]$$

$$\times \langle\vec{q}+\frac{e}{\hbar}\vec{A}(t-\tau')|H_L(t-\tau')|\psi_{0i}\rangle\,|_{\vec{q}=\vec{q}_s(t+\tau, t-\tau')}.$$

$$(215)$$

There is another way of expressing the time-dependent dipole matrix element. Within the SFA, the sum of $\vec{d}_a(t)$ and $\vec{d}_e(t)$ can be rewritten as

$$\int dt' \langle\psi_{0f}(t')|V_A G_L^{(+)}(t', t)e\vec{r}\,|\psi_{0i}(t)\rangle + \int dt' \langle\psi_{0f}(t)|\,e\vec{r}G_L^{(+)}(t, t')V_A|\psi_{0i}(t')\rangle.$$

$$(216)$$

Similarly, the "continuum–continuum" coupling term $\vec{d}_{cc}(t)$ can be rewritten as the sum of three terms, the first two of which cancel the terms in Eq. (216), while the remaining one gives

$$\vec{d}_a(t) + \vec{d}_e(t) + \vec{d}_{cc}(t) \approx \int dt' \int dt'' \langle\psi_{0f}(t')|V_A G_L^{(+)}(t', t)$$

$$\times e\vec{r}\, G_L^{(+)}(t, t'')V_A|\psi_{0i}(t'')\rangle.$$

$$(217)$$

This result can be transformed with ($\tau = t' - t$, $\tau' = t - t''$) into

$$\vec{d}_a(t) + \vec{d}_e(t) + \vec{d}_{cc}(t) \approx \left(\frac{-i}{\hbar}\right)^2 \left(\frac{2\pi m}{i\hbar}\right)^{3/2} \int_0^\infty d\tau \int_0^\infty d\tau' (\tau + \tau')^{-3/2}$$

$$\times \exp\left[\frac{i}{\hbar} S(\vec{q}; t + \tau, t - \tau')\right]$$

$$\times \left[1 - i\frac{m}{2\hbar(\tau + \tau')}\frac{\partial^2}{\partial\vec{q}^2} + \cdots\right]\langle\psi_{0f}|V_A|\vec{q} + \frac{e}{\hbar}\vec{A}(t + \tau)\rangle$$

$$\times \left[\vec{\alpha}(t) - \vec{\alpha}(t - \tau') + \frac{\hbar}{m}\vec{q}\tau' + i\frac{\partial}{\partial\vec{q}}\right]$$

$$\times \langle\vec{q} + \frac{e}{\hbar}\vec{A}(t - \tau')|V_A|\psi_{0i}\rangle|_{\vec{q}=\vec{q}_s(t+\tau, t-\tau')}. \tag{218}$$

In the case of a zero-range potential, the matrix element in the momentum space is

$$\langle\vec{q}|V_A|\psi_{1s}\rangle = (2\pi)^{-3/2}\int d\vec{r}e^{-i\vec{q}\cdot\vec{r}}\frac{2\pi}{m\kappa}\delta(\vec{r})\frac{\partial}{\partial r}r\left(\frac{\kappa}{2\pi}\right)^{1/2}\frac{e^{-\kappa r}}{r} = -\frac{\kappa^{1/2}}{2\pi m}, \tag{219}$$

so that the matrix elements are constant and all the derivatives over $\vec{q}$ in Eq. (218) are equal to zero. By putting $\vec{q} = \vec{q}_s(t + \tau, t - \tau')$, the last square brackets in Eq. (218) reduce to

$$\vec{\alpha}(t) - \left[\tau\vec{\alpha}(t - \tau') + \tau'\vec{\alpha}(t + \tau)\right]/(\tau + \tau')$$

which, for $f = i$, is equivalent to the result of ref. [374]. In atomic units $e = \hbar = m = 1$, and for $|E_0| = \kappa^2/2$, the right-hand side of Eq. (218) simplifies to yield

$$-\left(\frac{|E_0|}{\pi}\right)^{1/2}\int_0^\infty d\tau \int_0^\infty \frac{d\tau'[\vec{\alpha}(t) - \vec{\alpha}(t + \tau) - \tau\vec{q}_s]}{[i(\tau + \tau')]^{3/2}}\exp\left[\frac{i}{\hbar}S(\vec{q}_s; t + \tau, t - \tau')\right], \tag{220}$$

where $\vec{q}_s \equiv \vec{q}_s(t + \tau, t - \tau')$ is given by Eq. (212). After the expansion of the exponential into a series of the Bessel functions, Eq. (220) reduces to a single integral (see, for example, ref. [357]). However, our calculations [382] show that the main contribution to our time-dependent dipole matrix element, Eq. (205), comes from the two parts: $\vec{d}_{sm}(t) \approx \vec{d}_a(t) + \vec{d}_e(t)$, which are much easier to evaluate. One example of the results obtained for the emission rates, using this method, is presented in Fig. 24. In the effective-dipole approach [180,181], the corresponding time-dependent dipole matrix

element can be written as: $\vec{d}_{\mathrm{ed}}(t) = \vec{d}_{\mathrm{a}}(t) + \vec{d}_{\mathrm{a}}^*(t) = 2\vec{d}_{\mathrm{a}}^{\mathrm{R}}(t)$, where $\vec{d}^{\mathrm{R}}$ ($\vec{d}^{\mathrm{I}}$) denote the real (imaginary) parts of $\vec{d}$. The corresponding $T$-matrix elements, Eq. (203), are: $T_{N,\mathrm{sm}} = \vec{\epsilon}_{\vec{K}}^* \cdot F(\vec{d}_{\mathrm{a}} + \vec{d}_{\mathrm{e}})$ and $T_{N,\mathrm{ed}} = \vec{\epsilon}_{\vec{K}}^* \cdot \mathcal{F}(2\vec{d}_{\mathrm{a}}^{\mathrm{R}})$. Our numerical calculations have shown that for high-harmonics we obtain: $\mathcal{F}(\vec{d}_{\mathrm{a}}^{\mathrm{R}}) \approx i\mathcal{F}(\vec{d}_{\mathrm{a}}^{\mathrm{I}})$ and $\mathcal{F}(\vec{d}_{\mathrm{e}}^{\mathrm{R}}) \approx -i\mathcal{F}(\vec{d}_{\mathrm{e}}^{\mathrm{I}})$, so that $\mathcal{F}(\vec{d}_{\mathrm{a}} + \vec{d}_{\mathrm{e}}) \approx 2\mathcal{F}(\vec{d}_{\mathrm{a}}^{\mathrm{R}})$ and $T_{N,\mathrm{sm}} \approx T_{N,\mathrm{ed}}$. Therefore, for $N \gg 1$, the harmonic emission rates, Eq. (203), obtained by means of the $S$-matrix approach, are approximately equal to those evaluated by means of the effective-dipole approach. This explains why the results of refs. [180, 181, 357] were such good approximations. For example, for the results presented in Fig. 24 the maximum relative difference between the $S$-matrix and the effective-dipole results was found to be 17% for $n = 5$, while for $n > 17$ it was less than 1%. Another consequence of the above results is that the contribution of the matrix element $\vec{d}_{\mathrm{e}}(t)$ to the high-harmonic emission can be neglected (for an explicit comparison see Fig. 2 in ref. [343] and ref. [382]).

### F.4. New developments and applications

The HHG process can be considered as a photon–atom scattering process with the absorption of $N$ laser photons having wavevectors $\vec{k}_\omega$ and the emission of a high-harmonic photon with the wavevector $\vec{K}$ and the frequency $\omega_{\vec{K}} = N\omega$. The change of the atomic momentum is then $\hbar\delta\vec{K}_{\mathrm{a}} = \hbar(N\vec{k}_\omega - \vec{K})$. For $N_{\mathrm{a}}$ atoms the emission of the high harmonic in the direction $\vec{K} = N\vec{k}_\omega$ (forward scattering) results from coherent contribution of different atoms and increases as $N_{\mathrm{a}}^2$, whereas the emission in other directions increases linearly with $N_{\mathrm{a}}$. Hence, the generated harmonics are coherent with a very narrow angular distribution. The energy of the emitted high-harmonic photons is up to several hundred times higher than the energy of the photons of the driving field. Also, the harmonic pulse duration is shorter than the duration of the driving laser pulse. Therefore, in the process of HHG one obtains high-frequency coherent radiation of unprecedented spatial and temporal characteristics with great potentials for various applications.

For applications it is necessary to control the harmonic emission and to increase the intensity of the emitted harmonics. A concept of quantum orbits, considered recently in a review article by Becker *et al.* [21], has shown to be extremely useful in this context. This concept is based on the saddle-point-method approximation to the five-dimensional integral that appears in the $S$-matrix element; namely the three-dimensional integration over the intermediate electron momenta $\vec{q}$, Eq. (209), one integration over the ionization time $t'$, Eq. (209), and one integration over the recombination time, i.e., the harmonic emission time $t$, Eq. (199). Without going into detail

here, we only mention that the corresponding $T$-matrix element can be expressed as

$$T_N \propto \sum_s M_s \left[ \det\left(\frac{\partial^2 S_s}{\partial q_k \partial q_l}\right) \right]^{-1/2} \exp\left(\frac{i}{\hbar} S_s\right), \qquad (221)$$

where the quasi-classical action $S_s \equiv S(\vec{q}_s, t_s, t'_s) + N\omega t_s$ is evaluated at the saddle points $q_i$ ($i = 1, \ldots, 5$) that comprises the five variables $\vec{q}_s \equiv (q_{1s}, q_{2s}, q_{3s})$, $t_s$, and $t'_s$. The summation in Eq. (221) runs over an appropriate subset of the saddle points $(\vec{q}_s, t_s, t'_s)$, which are the solutions of equations that express the energy conservation at times $t'$ and $t$ and, moreover, the condition that the electron returns to its starting point $\vec{r}(t) = \vec{r}(t')$. This leads to a generalization of the three-step model. Due to the tunneling nature of the first step of this process the solutions of these equations are complex. Projecting these solutions onto the real plane, one obtains the real-space electron trajectories (quantum orbits) which are very useful for a physical understanding of the process. This method is closely related to the Feynman path integral approach to quantum mechanics (see [291] and references therein).

The practical importance of the result of Eq. (221) is that only a few complex solutions (the shortest trajectories) give the main contribution, so that the numerical calculations are very fast. For a linearly-polarized laser field this method was first considered in [180, 181, 391]. The method is more useful for more complicated fields. For an elliptically-polarized field the quantum orbits yield a vivid generalization of the three-step model [291, 292, 358]. The results for a bichromatic, linearly-polarized laser field were presented in [392]. A particularly interesting case is, to consider a two-color bicircular field [393–396]. Using the concept of quantum-orbits, it was possible to explain the experimentally observed (see ref. [397]) high efficiency of HHG by such a field configuration. Further examples of the usefulness of the formalism of quantum-orbits are those problems in which there is a laser field and an additional static electric field [345, 347] or a laser field and an additional magnetic field [346, 398, 399]. The concept of quantum orbits was also successfully applied to calculate and explain the characteristics of HHG by a relativistically strong laser field [400, 401]. In that case, the most pronounced effects observed are the multiplateau structure of the high-harmonic spectrum, similar to the one observed for an elliptically polarized laser field, and the suppression of the ultrahigh-order harmonic generation due to the magnetic-field-induced drift motion of the electron on its orbit. Very similar effects were also observed in the investigations [402, 403]. The resonance-like enhancement of the harmonics in the first part of the plateau [407, 408] has also been explained by using

the formalism of quantum-orbits [407, 408]. This effect is connected with the closing of channels. The enhancements can be traced to multiphoton resonances due to the ponderomotively upshifted continuum threshold. In this case, the contributions of the quantum orbits add constructively and many more orbits have to be taken into account. On the contrary, only few orbits give satisfactory results for the harmonics in the central part and in the region at the end of the plateau. The resonant enhancement of low order harmonics, generated in argon with a KrF laser source was considered in ref. [386]. More recently, the threshold-related effects and enhancement in HHG were considered in some detail by Borca *et al.* [409]. For an early reference about the impact of channel closing on HHG we refer to the work of Becker *et al.* [410], in which the interplay between the above-threshold multiphoton detachment and HHG was considered. Namely, owing to conservation of probability, as expressed by the unitarity of the *S*-matrix, the opening or closing of a new inelastic channel affects the remaining channels. Therefore, pronounced cusps appear in the high-harmonic emission rates at intensities where a particular above-threshold multiphoton detachment channel closes. Most recently Milosevic and Becker [411] have explained the enhancement of HHG near channel closings by the constructive interference of a large number of quantum orbits. The enhancements exactly at the channel closings are extremely narrow and build up by the constructive interference of a very large number of quantum orbits. Additional broader enhancements occur slightly below channel closings and they are generated by the interplay of a medium number of orbits.

In ref. [412] the intra-atomic phase matching of HHG was proposed. The laser pulse shape is optimized so that a particular harmonic is enhanced. This "coherent control" is realized by the constructive interference of the contributions from different quantum orbits. A similar coherent control by means of a genetic algorithm optimization of the laser-pulse shape and intra-atomic phase matching was presented in ref. [413] (the different wave packets, calculated by numerical solutions of the time-dependent Schrödinger equation, instead of using the quantum orbits, are considered). The genetic algorithm was used to theoretically maximize the harmonic pulse energy, minimize the pulse duration or optimize the temporal coherence in [414, 415]. The feedback control of the phase of the laser pulse has recently enabled to experimentally realize the selective enhancement of a particular harmonic [416]. The self phase matching of very high harmonics (soft x-ray regime) was also explained in terms of the quasi-classical action [417]. For coherent control of HHG with chirped laser pulses see, for example, ref. [418].

The temporal behavior of HHG can be explained using both the three-step model and the intensity-dependent phase of the field-induced atomic

dipole [391, 394, 419]. The atomic dipole can be analyzed in terms of the quantum orbits. For a linearly polarized driving field the main contribution to any particular harmonic in the plateau comes from two different quantum orbits. In ref. [419] it was shown that, by judicious manipulation of the spatial and temporal profile of the driving laser pulse, it is possible to favor the contribution of one or the other orbit to the harmonics emitted by the atoms of an ensemble, and to obtain a train of attosecond pulses of linearly-polarized harmonics. Selection of high-order harmonics from quantum paths by controlling the phase-matching condition was also demonstrated [420–422]. On the other hand, in the investigations [393,394] it was shown that for a two-color bicircular field only one orbit contributes significantly to the harmonic spectrum in the plateau region, so that no collective effects are necessary to extract an attosecond pulse train. As a quantitative measure for the amount of phase locking of a group of subsequent harmonics, considered in ref. [394], the following ratio $R$ of the coherent over the incoherent sum of harmonic intensities was introduced

$$R(t) = \frac{\left|\sum_{N \in \mathcal{G}} E_N(t)\right|^2}{\sum_{N \in \mathcal{G}} \left|E_N(t)\right|^2}, \quad E_N(t) = N^2 T_N \exp(-iN\omega t), \qquad (222)$$

where $T_N$ is the $T$-matrix element of the effective-dipole approach. In Fig. 25 we present this ratio for the group $\mathcal{G}$ of the harmonics between $N = 91$ and $N = 121$ (16 odd harmonics), for the parameters of Fig. 24. One can see in this figure a train of attosecond pulses of the duration of 72 as.

Up to now we concentrated on the three-step or quantum-orbit physical model of HHG. As we have seen, the control of the plateau and of the cutoff of the harmonics can be achieved by manipulating the driving laser pulse in the intermediate (the second) step of the process. However, there are some situations in which this method fails and the influence of the atomic (ionic) potential becomes crucial. For example, the appearance of hyper-Raman lines can be explained by using the model of a two-level atom [363]. A possible enhancement of HHG by employing a gas that possesses permanent dipole moments, was presented in [423]. HHG that is obtained from the coherent superposition of the ground state and an excited atomic state was analyzed in [424, 425]. In ref. [426] HHG from a confined atom was proposed. By choosing the confinement parameters of a parabolic potential, the cutoff harmonic energy can be increased by 50%. This method leads to results that are similar to those obtained from the parallel-magnetic-field confinement scheme of refs. [346, 398, 399]. HHG for a configuration in which the static magnetic field is perpendicular to the laser polarization direction was considered in [427]. Increasing the efficiency of high-order harmonic generation using counterpropagating laser pulses was also
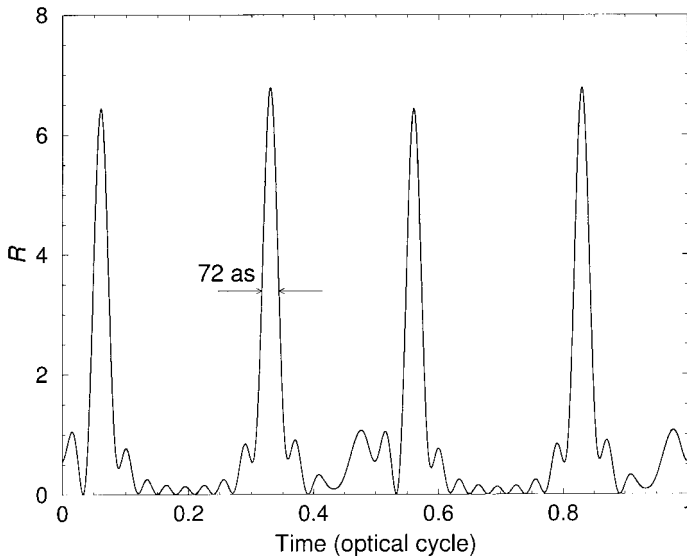
Fig. 25. The ratio $R$ of the coherent over the incoherent sum of the harmonic intensities as a function of the time during one optical cycle in the case of HHG by He atoms ($I_{io} = 24.588$ eV) with a linearly-polarized Ti:Sapphire laser (wavelength 800 nm) having the intensity $I = 10^{15}$ Wcm$^{-2}$ (see Fig. 24). The results are for a group of 16 plateau harmonics, between the 91st and the 121st. The FWHM is 72 attoseconds.

suggested [428]. More recently, HHG by multiply charged ions, such as $O^{7+}$, exposed to laser fields of the order of $10^{18}$ W cm$^{-2}$ at 248 nm was investigated theoretically. Nontunneling high-order harmonics were found that exhibit plateau and cutoff features [293,294]. A classical "surfing" mechanism for the generation of these harmonics was proposed. The electron gains its energy from the laser field by riding on an effective potential saddle, in a similar way as a surfer rides on a water wave. The gained energy is later on released as high-harmonic photon energy. In ref. [294] the influence of different shapes of the ionic potential on nontunneling HHG was investigated and the appearance of interesting hump-shaped plateau characteristics, hyper-Raman lines, etc., were explained.

Most of the considerations presented above are applicable to HHG from atoms or ions. However, also different media for HHG were proposed. Experimental studies of HHG in molecular gases (see [429, 430] and references therein) have shown harmonic spectra very similar to those obtained in atomic gases. Theoretical investigations of HHG by molecular ions such as $H_2^+$ were first presented in refs. [431, 432]. Due to the phenomenon of charge resonance enhanced ionization, HHG in molecular

ions should also be enhanced. Moreover, in such extended systems the (re)collision of electrons with neighboring ions can produce high harmonics well beyond the $I_{io} + 3.17\,U_P$ cutoff law (see refs. [433–435] and references therein). For more complex systems, the electron dynamics is enriched by the higher number of degrees of freedom so that new mechanisms can contribute to HHG. HHG from a linear chain of atoms was suggested in ref. [436]. In refs. [437, 438] experimental work was performed to study how the generation of HHG depends on the molecular orientation. The numerical solution of the time-dependent Schrödinger equation is used in ref. [439] in order to find the maxima and minima, due to intramolecular interferences, in the dependence of the harmonic emission rates on the internuclear distance and on the orientation of the molecules. For the HHG in cyclic organic molecules we refer to refs. [440–442] and to the references therein. HHG by molecules having discrete rotational symmetry (for example, benzene) interacting with circularly polarized laser light [443, 444] shows interesting dynamical symmetries and therefore satisfies certain selection rules [445, 446]. Such rules can also be applied to HHG by thin crystals [445]. As a medium for HHG carbon nanotubes were suggested in [447–449]. A comprehensive report on the laser–cluster interactions can be found in ref. [450]. HHG in atomic clusters was analyzed in refs. [451–456]. Although HHG at solid surfaces was observed earlier than HHG in gases, the method is still less developed. In ref. [457] harmonics up to the 11th order, and in refs. [458, 459], harmonics up to the 46th order were observed in the interaction of nanosecond $CO_2$ laser pulses with solid targets. More recently, harmonics up to the 75th order were observed during the interaction of 2.5 ps (1053 nm) laser pulses with solid targets [460]. The harmonics generated at high driving laser intensities are found to be emitted isotropically, which is not a very attractive characteristic for practical applications. For more details about HHG at solid surfaces see, for example, the review article [461]. From the experimental point of view, the solid targets are stable and easy to handle. However, from the theoretical point of view, the presence of the collective effects make the study of HHG at solid surfaces a formidable task. The two main approaches to the modeling of these complex systems are the solutions of the hydrodynamical equations and the solutions of the many particle equations. Among the latter schemes one of the most successful methods is the particle-in-cell (PIC) simulation [462]. For references to the quantum calculations see, for example, [463]. There is also a more recent experimental paper [464] and references therein about a simple physical model of an oscillating plasma mirror that explains the main mechanism of HHG by radiation reflection from solid targets. In ref. [465] HHG in stimulated bremsstrahlung by a very short and intense laser–crystal interaction is proposed.

During the last few years there was considerable progress in the development of high-intensity sources of radiation in vacuum and extreme ultraviolet (VUV-XUV) and soft x-ray regions, such as x-ray lasers, synchrotron radiation sources, free-electron lasers, and high-order harmonic sources. Among these sources, high-harmonic radiation has the advantage of being simple and easily produced by table-top devices. Only HHG provides the ultrashort pulses of high intensity in this spectral region. Therefore, the applications of high-harmonic sources of radiation are numerous. We mention here the nonlinear processes in the XUV range, such as the two- and three-photon ionization of rare gases [466, 467], the time-resolved x-ray spectroscopy of solid-state and molecular dynamics on a sub-100-fs timescale [468], and the extreme ultraviolet interferometry measurements [469, 470]. One of the most important applications of HHG is the attosecond physics. A. Zewail received the 1999 Nobel prize in chemistry for showing that it is possible with ultrafast laser techniques to see how the atoms in molecules move during a chemical reaction [471]. Attosecond pulses will be to atomic physics what femtosecond pulses are to chemistry. We have already seen in Fig. 25 how an attosecond pulse train can be generated by phase locking of several high harmonics. In a recent review article [26] more details and references about the generation of ultrashort pulses can be found. In refs. [472, 473] the first observation of attosecond light localization in HHG was claimed, but this is not generally accepted [474, 475]. These results can be considered as an experimental demonstration that high-order harmonics can be a source of trains of attosecond XUV pulses. This is similar to what was done in ref. [321], where a method was presented to measure the relative phase of the harmonics. The generation of isolated soft x-ray pulses was analyzed in ref. [25] and numerically characterized in ref. [476]. Finally, in refs. [28, 477] the first experimental observations of single harmonic pulses with the duration of $650 \pm 150$ attoseconds was demonstrated. According to remarks by Yaron Silberberg in an accompanying News and Views article in *Nature*, this "might be the dawn of attophysics".

# III.  Coherent Control

## A. The Fundamental Idea

### A.1.  Introduction

Controlling the yield of molecular reactions by means of lasers has been a longstanding goal in chemical dynamics. Early laser-based attempts at

control relied either on the frequency resolution of lasers to locate a frequency which maximizes the yield, or on the use of high-power lasers to alter the dynamics. Both methods suffer from severe drawbacks; the former depends on the chance existence of a favorable branching ratio and the latter requires extremely high powers which make it impracticable. In addition, both of these methods are passive in the sense that the yield is primarily determined by molecular properties and cannot be controlled by experimental design.

About 16 years ago, it was suggested in a series of pioneering papers by Shapiro, Brumer and coworkers [478–480] to actively manipulate chemical reactions by applying a bichromatic laser field of frequencies $\omega$ and $3\omega$ and by varying the relative phase $\varphi$ and amplitudes $\mathcal{E}$ of the two fields. The theoretical approach of these authors to actively control the yield of a chemical reaction is based on the following general idea. Suppose that we invoke two simultaneous coherent paths $a$ and $b$ to get to the reaction products. Under these circumstances the probability $P$ of producing products is given by

$$P = |A_a|^2 + (A_a A_b^* + A_a^* A_b) + |A_b|^2. \tag{223}$$

Here $A_i$ is the probability amplitude of obtaining products through path $i$, so that $|A_a|^2$ and $|A_b|^2$ are the probabilities for independently obtaining products from path $a$ and path $b$. The second term, the crossed term, can be positive or negative and arises from the quantum interference between the two paths. If both paths $a$ and $b$ lead to more than one product channel then the branching ratio $R_{qq'}$ for channel $q$ and $q'$ is of the form

$$R_{qq'} = P_q/P_{q'} \tag{224}$$

where now in Eq. (223) the amplitudes are $A_i^q$ and $A_i^{q'}$ $(i = a, b)$, respectively. To have active control over the product distribution means that one can experimentally manipulate the magnitude of the numerator or denominator of Eq. (224). Thus, if one can design an experimental scenario such that by varying laboratory parameters one varies the sign and magnitude of the cross term, then one gets control over the product distributions and product yields. The above authors termed this overall approach, which relies upon coherence and the use of interference between a minimum of two path, *coherent radiative control*. Alternative methods, based upon time-dependent wave packet approaches, have been developed by others to which we shall return later.

To be more specific, we consider a molecule, initially in a state $|E_i\rangle$ of energy $E_i$, that is subjected to two electric fields given by

$$\vec{\mathcal{E}}(t) = \vec{\mathcal{E}}_1 \cos(\omega_1 t + \vec{k}_1 \cdot \vec{R} + \theta_1) + \vec{\mathcal{E}}_3 \cos(\omega_3 t + \vec{k}_3 \cdot \vec{R} + \theta_3) \qquad (225)$$

Here $\omega_3 = 3\omega_1$ and both fields are taken to have the same directions of linear polarization and directions of propagation with $\vec{k}_3 = 3\vec{k}_1$. Then, as discussed above, the probability $P(E, q; E_i)$ of producing a molecular reaction product with energy $E$ along the channel $q$ from a state $|E_i\rangle$ is given by the probabilities $P_1(E, q; E_i)$ and $P_3(E, q; E_i)$ due to the $\omega_1$ and $\omega_3$ excitations, plus a cross term $P_{13}(E, q; E_i)$ due to the interference between the two excitations, thus

$$P(E, q; E_i) = P_3(E, q; E_i) + P_{13}(E, q; E_i) + P_1(E, q; E_i) \qquad (226)$$

Evaluating the corresponding probabilities in the weak radiation field limit by time-dependent perturbation theory [480], where in the case of excitation by the $\omega_1$ component of Eq. (225) application of third-order perturbation theory is required to get to the final state $|E\rangle$, we only need to consider first-order perturbation to arrive at the same final state $|E\rangle$ using the $\omega_3$ component of Eq. (225). Thus we get for the branching ratio $R_{qq'}$ for channels $q$ and $q'$

$$R_{qq'} = \frac{F_3^{(q)} - 2x \cos\left(\theta_3 - 3\theta_1 + \delta_{13}^{(q)}\right) |F_{13}^{(q)}| + x^2 \mathcal{E}_0^4 F_1^{(q)}}{F_3^{(q')} - 2x \cos\left(\theta_3 - 3\theta_1 + \delta_{13}^{(q')}\right) |F_{13}^{(q')}| + x^2 \mathcal{E}_0^4 F_1^{(q')}} \qquad (227)$$

where a normalized field amplitude $\mathcal{E}_0$ and field amplitude ratio $x$ have been introduced [495]. The experimental control over $R_{qq'}$ is therefore obtained by varying the difference $\phi = \theta_3 - 3\theta_1$ and the parameter $x$. The former is the phase difference between the $\omega_3$ and the $\omega_1$ laser fields and the latter incorporates the ratio of the two laser amplitudes. Since "*tripling*" is a common method to produce $\omega_3$ from $\omega_1$, of fixed relative phase, the subsequent variation of the phase of one of these beams provides a straightforward method of altering $\phi$. A summary of the method and its application to photodissociation reactions can be found in reviews by Shapiro and Brumer [481, 482]. Early experiments are reported by Lu *et al.* [483] and Zhu *et al.* [484] and a more recent summary can be found in the report by Gordon and Rice [485]. A large theoretical and experimental body of work, using the above method of influencing molecular properties and reactions, has accumulated by now. In particular, the method has been

extended to the use of powerful bichromatic laser fields thus going beyond the application of perturbation theory. A sufficient amount of references on these works can be found in the papers by Charron *et al.* [486] on photodissociation, by Thompson *et al.* [487] and Bandrauk and Chelkowski [488] on dissociative ionization, by Bandrauk *et al.* [489] on harmonic generation, by Dion *et al.* [490] on molecular orientation, by McCullough *et al.* [491] on the coherent control of refractive indices and by Shapiro *et al.* [492] on the control of asymmetric synthesis with achiral light.

Although we shall in our review mainly devote our attention to the application of *coherent phase control* (CPC), outlined above, to various atomic phenomena, we should also mention here other laser schemes that have been designed recently to tailor atomic and molecular processes. As suggested by Tannor and Rice [493] and improved by Kosloff *et al.* [494], the selectivity of molecular product formation can be induced by shaping and spacing pump and dump laser pulses. This pump–dump scheme for controlling the selectivity of product formation in a chemical reaction can be improved by developing a method for optimizing the field of a particular product with respect to the shapes of the pump and dump pulses. An even simpler scheme involves a series of identical laser pulses. By varying the delay time between two pump pulses with an accuracy better than the vibrational period, and probing the excited state population with a third pulse, Zewail and coworkers have shown that they could control selectively the wave packet motion in the $B$ state of $I_2$ [495]. More details of this method and its improvements can be found in the works of Blanchet *et al.* [496], Kohler *et al.* [497], and Lozovoy *et al.* [498] and references cited therein. A comprehensive review on wave packet dynamics and its application to physics and chemistry in femto-time is presented in the papers by Garraway and Suominen [499, 500] and Ficek and Freedhoff [501] discuss spectroscopy in polychromatic fields. Coherent control by single phase shaped femtosecond laser pulses is discussed, for example, by Assion *et al.* [502] and by Meshulach and Silberberg [503]. Finally, in the work of Bardeen *et al.* [504] feedback quantum control, where the sample "teaches" a computer-controlled arbitrary lightform generator to find the optimal light field, is experimentally demonstrated for a molecular system. Further details on the above control schemes can be obtained from an article by Manz [505] and an earlier review by Warren *et al.* [506].

### A.2. A simple classical example of CPC

In order to demonstrate how a laser-induced nonlinear process can be effectively controlled by changing the relative phase of the stimulating

bichromatic radiation field, we consider the following simple classical radiation problem that will be a generalization of the process discussed in Section I.B.2. If a classical high-frequency plane wave

$$\vec{\mathcal{E}}_x(t) = \vec{\epsilon}_x \cos \omega_x(t - \vec{n}\cdot\vec{r}/c) \tag{228}$$

of unit field amplitude, expressed by the vector of linear polarization $\vec{\epsilon}_x$, direction of propagation $\vec{n}$, and frequency $\omega_x$ is scattered by a free electron under the simultaneous action of a strong bichromatic, low-frequency background field

$$\vec{\mathcal{E}}(t) = \mathcal{E}_0\vec{\epsilon}\,[\sin \omega t + \sin(2\omega t + \phi)] \tag{229}$$

with $\omega_x \gg \omega$ and equal field amplitude $\mathcal{E}_0$ and linear polarization $\vec{\epsilon}$, then the phase of the absorbed and scattered x-ray field will be periodically modulated on account of the large amplitude electron oscillations in the intense background field. This will induce an oscillating Doppler shift of the x-ray emission of the electron and the spectrum of scattered radiation will have the form $\omega'_x = \omega_x + N\omega$ with $N$ being a positive or negative integer or zero. Mathematically this fact will be expressed by the retarded electron acceleration

$$\vec{V}'(\tau_0) = \frac{e}{m}\vec{\epsilon}_x \cos \omega_x[\tau_0 - (\vec{n}' - \vec{n}) \cdot \vec{r}(\tau_0)/c] \tag{230}$$

where $\vec{r}(\tau_0)$ is the amplitude of electron oscillations in the background field given by

$$\vec{r}(\tau_0) = -\alpha_0\vec{\epsilon}\,[\sin \omega\tau_0 + \frac{1}{4}\sin(2\omega\tau_0 + \phi)] \tag{231}$$

taken at the average retarded time $\tau_0$. $\alpha_0 = \mu c/\omega$ is the amplitude of the classical electron oscillations in the background field and $\mu$ is the corresponding velocity amplitude measured in units of the speed of light $c$. It is explicitly given by $\mu = e\mathcal{E}_0/m\omega c$ and we have discussed the relevance of this parameter at several places in this review before. By inserting Eq. (231) into Eq. (230) and then making a Fourier decomposition of the retarded acceleration into its infinite number of harmonic components, we can evaluate the differential cross sections of x-ray scattering by a free electron and the concomitant nonlinear scattering processes induced by the

bichromatic background field. We get

$$\frac{d\sigma_N}{d\Omega} = \frac{d\sigma_{\text{Th}}^x}{d\Omega} \left| B_N(a, b; \phi) \right|^2. \tag{232}$$

Here, $d\sigma_{\text{Th}}^x/d\Omega$ is the Thomson cross section of x-ray scattering and $B_N(a, b; \phi)$ is a generalized, phase-dependent Bessel function of the integer order $N$ defined by

$$B_N(a, b; \phi) = \sum_{\lambda=-\infty}^{+\infty} J_{N-2\lambda}(a) J_\lambda(b) e^{-i\lambda\phi} \tag{233}$$

where the $J_\lambda$ are ordinary Bessel functions of the integer order $\lambda$. The generalized Bessel functions Eq. (233) can be obtained by expanding its generating function into a Fourier series, viz.

$$\exp\{i[a\sin\omega t + b\sin(2\omega t + \phi)]\} = \sum_{N=-\infty}^{+\infty} B_N(a, b; \phi) \exp(iN\omega t). \tag{234}$$

Here the various different Fourier components of the expansions of the two exponentials on the left-hand side of Eq. (234) into ordinary Bessel functions $J_\lambda$, yielding the same final harmonic frequency $N\omega$, may be considered in this classical problem as the infinite number of different phase-dependent "reaction channels" contributing to the cross sections Eq. (232). The arguments $a$ and $b$ are given in the present case by

$$a = \alpha_0(\vec{K} - \vec{K}') \cdot \vec{\epsilon}, \quad b = a/4 \tag{235}$$

with $\vec{K}' - \vec{K}$ being the "*wave vector transfer*" in x-ray scattering where $\vec{K} = \omega_x \vec{n}$ and $\vec{K}' = \omega_x' \vec{n}'$, while $\vec{n}$ and $\vec{n}'$ are the directions of propagation of the ingoing and scattered x-ray fields. We shall see in the next chapter that formula Eq. (232) agrees very well with the corresponding low-frequency result of electron–atom scattering in a bichromatic low frequency laser field of frequencies $\omega$ and $2\omega$ and a relative phase $\phi$. From Eq. (234) it is quite clear that for a fixed value of $a$ the cross sections Eq. (232) will strongly depend on the relative phase $\phi$ of the two field component in Eq. (229).

## B. Examples of Application

Since the investigations of atomic phenomena in bichromatic laser fields have been discussed in considerable detail in our recent review [30], we shall

concentrate in the present chapter on the presentation of our theoretical results on the following three topics which are presently of particular interest. We shall consider above-threshold ionization, electron–ion recombination and higher harmonic generation in a bichromatic laser field of frequencies $\omega$ and $r\omega$ ($r = 2, 3$) and we shall discuss the coherent control of the transition probabilities as a function of the relative phase $\phi$ of the two fields.

### B.1. ATI in a bichromatic field

In the present section, we compute and discuss the electron energy spectra for a bichromatic laser field of linear polarization, frequencies $\omega$ and $2\omega$, and relative phase $\phi = 0$. We find that the plateau for the backward ($\theta = 180°$) emission of electrons extends up to $21U_{P_1}$, where $U_{P_1}$ is the ponderomotive energy of the first laser field component assuming equal intensities of both components. There are no such high energy electrons for $\theta = 0°$, in contrast to the symmetry $\theta \leftrightarrow 180° - \theta$, valid in the monochromatic case. In the bichromatic case the ionization rates possess the more general symmetry properties $(\phi, \theta) \leftrightarrow (\phi + \pi, 180° - \theta)$. Therefore, for $\phi = \pi$ we predict the emission of the high-energy electrons in the forward direction ($\theta = 0°$). In a bichromatic field the sidelobe stuctures are strongly influenced by quantum-mechanical interference effects. We also explore the $\theta$-dependence of the ionization rates for different relative phases $\phi$ and for these energies which correspond to the classical cutoff law.

***S-matrix formulation*** The general approach for treating the present problem can be found in [236] and will be the same as in our discussion of ATI for a monochromatic laser field in Section II.B.2. Therefore we can take over the basic results from this section and use as starting point of our calculations for the following formulas. The $S$-matrix element of our problem will be given by

$$
\begin{aligned}
S_{fi} &= -i \int_{-\infty}^{\infty} dt \, \exp[i(E_{\vec{k}_f} + I_{io} + U_P)t] \, \mathcal{T}_{fi}(\varphi) \\
&= -2\pi i \sum_N \delta(E_{\vec{k}_f} + I_{io} + U_P - N\omega) \, T_{fi}(N),
\end{aligned} \tag{236}
$$

where $I_{io} = -E_0$ is the ionization energy of the atom in its ground state while $E_{\vec{k}_f}$ and $\vec{k}_f$ are the final energy and momentum of the ionized electron, respectively. For the bichromatic field of frequencies $\omega$ and $2\omega$ and equal linear polarization $\vec{\epsilon}$ that we shall consider, we have $\vec{\alpha}(t) = \vec{\epsilon}\,[\alpha_0 \sin \omega t + \alpha_{02} \sin(2\omega t + \phi)]$ and, if both field components $\mathcal{E}_j$ ($j = 1, 2$)

have equal intensity, we find $\alpha_{02} = \alpha_0/4$. For the matrix element $\mathcal{T}_{fi}(\varphi)$ we obtain

$$
\mathcal{T}_{fi}(\varphi) = \exp\{i\,[\vec{k}_f \cdot \vec{\alpha}(\varphi) + \mathcal{U}_1(\varphi)]\} \left\{ \left\langle \psi^{(-)}_{\vec{k}_f + \vec{A}(\varphi)} \left| \vec{r} \cdot \vec{\mathcal{E}}(\varphi) \right| \psi_0 \right\rangle - i \int_0^\infty d\tau \left( \frac{2\pi}{i\tau} \right)^{3/2} \right.
$$

$$
\times \left\langle \psi^{(-)}_{\vec{k}_f + \vec{A}(\varphi)} \left| V_s \right| \vec{k}_s + \vec{A}(\varphi) \right\rangle \left\langle \vec{k}_s + \vec{A}(\varphi') \left| \vec{r} \cdot \vec{\mathcal{E}}(\varphi') \right| \psi_0 \right\rangle
$$

$$
\left. \times \exp[-iS(\vec{k}_s; \varphi, \omega\tau)] \right\}, \tag{237}
$$

where the evaluation of $S(\vec{k}_s; \varphi, \omega\tau)$ was discussed in Section II.B.2 and $\mathcal{U}(t) = \mathcal{U}_1(\varphi) + U_P t$, with $\varphi = \omega t$, $\varphi' = \varphi - \omega\tau$. The function $\mathcal{U}_1(\varphi)$ is explicitly given by

$$
\mathcal{U}_1(\varphi) = \frac{1}{4\omega} \left\{ 2U_{P_1} \sin 2\varphi + U_{P_2} \sin(4\varphi + 2\phi) \right.
$$
$$
\left. + 8\sqrt{U_{P_1} U_{P_2}} [\sin(\varphi + \phi) + \frac{1}{3}\sin(2\varphi + \phi)] \right\} \tag{238}
$$

where $U_{P_1}$ and $U_{P_2}$ are the ponderomotive energies of the two field components, separately and $U_P = U_{P_1} + U_{P_2}$ is the total ponderomotive energy of the two fields with $U_{P_j} = \mathcal{E}_j^2/4(j\omega)^2$ $(j = 1, 2)$. $\mathcal{T}_{fi}(\varphi)$ is a $2\pi/\omega$-periodic function of $t$, which can be expanded into a Fourier series

$$
\mathcal{T}_{fi}(\varphi) = \sum_{N=-\infty}^{\infty} T_{fi}(N) \exp(-iN\varphi), \quad T_{fi}(N) = \int_0^{2\pi} \frac{d\varphi}{2\pi} \mathcal{T}_{fi}(\varphi) \exp(iN\varphi). \tag{239}
$$

$T_{fi}(N)$ is the $T$-matrix element for ionization with the absorption of $N$ photons. The corresponding differential ionization rate of the order $N$ is

$$
w_{fi}(N, \theta) = 2\pi k_f |T_{fi}(N)|^2, \tag{240}
$$

where $k_f = (2E_{\vec{k}_f})^{1/2}$ satisfies the energy conserving condition $E_{\vec{k}_f} = N\omega - I_{io} - U_P$, and $\theta$ is the angle between $\vec{k}_f$ and the laser-field polarization vector $\vec{\epsilon}$. The matrix elements in Eq. (236) have a simple analytic form, so that the differential ionization rates can be easily computed by performing the integration over the return time $\tau$ and by using the fast Fourier transform method, as discussed in detail in Section II.B.2.

**Numerical results**   In this section we present our results for a bichromatic linearly-polarized laser field of frequencies $\omega$ and $2\omega$. The electric-field vector of our field is $\vec{\mathcal{E}}(t) = I^{1/2}\vec{\epsilon}\,[\sin\omega t + \sin(2\omega t + \phi)]$ where $I$ is the laser-field intensity (taken to be equal for both components) and $\phi$ is the phase difference between the two laser-field components. In this case, the total ponderomotive energy is $U_P = U_{P_1} + U_{P_2} = (5/4)U_{P_1}$, where $U_{p_1} = I/4\omega^2$. As target we consider a hydrogen atom in its ground state and for the short-range potential we chose the Yukawa-type potential $V_s = -\exp(-r)/r$. It should be stressed that our theory is quite general and can also be applied to inert gases by employing an appropriate effective ion potential $V = V_c + V_s$. For the strong laser fields we are considering ($I \sim 10^{15}\,\mathrm{W\,cm^{-2}}$) there are no experimental data available for ATI in a bichromatic laser field. There exist experimental results for a lower field intensity ($\sim 10^{13}\,\mathrm{W\,cm^{-2}}$) by Schumacher and Bucksbaum [507]. In an earlier paper [218], we compared their data with our results obtained from a modified KFR model, but without taking into account the rescattering effects. The second plateau in the photoelectron energy spectrum that originates in the rescattering process in the case of ionization by a bichromatic laser field, was not yet observed. In the same paper [218], mentioned before, (see also refs. [173, 242, 243]) we showed on the basis of classical considerations that the second plateau can extend to almost $21U_{P_1}$. Here we demonstrate in our quantum-mechanical calculation that the cutoff for certain values of $\theta$ and $\phi$ can really be at $21U_{P_1}$. Concerning the sidelobes, we should notice that in a bichromatic laser field of frequencies $\omega$ and $2\omega$ and relative phase $\phi$ the symmetry $180° - \theta \leftrightarrow \theta$ becomes broken. Therefore, in the present case the sidelobes found in Fig. 16 for a monochromatic field will not possess this symmetry any longer. In the bichromatic field instead, the differential ionization rates obey now the symmetry relation $(\phi + \pi, 180° - \theta) \leftrightarrow (\phi, \theta)$. This can be shown explicitly by considering the $T$-matrix elements in Eqs. (237) and (239) which satisfy the symmetry relations

$$T_{fi}(N, \phi + \pi, 180° - \theta) = (-1)^n\, T_{fi}(n, \phi, \theta). \tag{241}$$

According to this relation, the rates for the backward direction ($\theta = 180°$) and $\phi = 0$ are the same as the rates for forward direction ($\theta = 0°$) and $\phi = \pi$.

   In Fig. 26 we show the differential ionization rates as functions of $E_{\vec{k}_f}/U_{P_1}$ for different values of the angle $\theta$ of electron emission and for the relative phase $\phi = 0$. The direct ionization rates (computed from $S_{fi}^{(0)}$) and the ionization rates which include rescattering, described by $S_{fi}^{(0)} + S_{fi}^{(1)}$, are shown separately. For $\theta = 180°$ the direct rates are represented by a dotted line, while the rates which include rescattering are
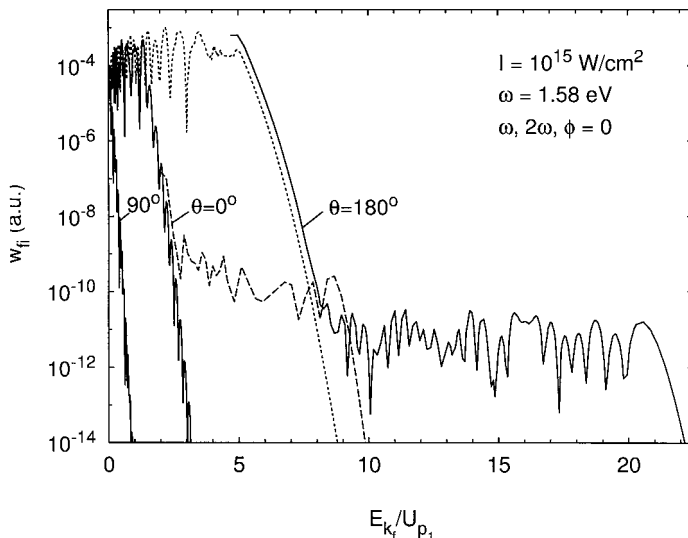
Fig. 26. Differential ionization rates presented in a similar way as in Fig. 15, but for a bichromatic field of frequencies $\omega = 1.58$ eV and $2\omega$, the relative phase $\phi = 0$, and equal intensity of both components. The direct ionization rates and the ionization rates which include rescattering are shown separately. For $\theta = 180°$ the direct rates are shown by a dotted line, while the rates which include rescattering are presented by a continuous curve. For $\theta = 90°$ only the rates of direct ionization are shown, while for $\theta = 0°$ the direct rates are depicted by a continuous line. The rates at $\theta = 0°$, which include rescattering, are presented as a dashed curve (see ref. [236]).

shown by a continuous curve. For $\theta = 90°$ only the direct rates are plotted, while for $\theta = 0°$ the direct rates are depicted as a continuous line. The rates which include rescattering for $\theta = 0°$ are represented by a dashed curve. As follows from this figure, the direct ionization rates contribute to the first plateau only, while the second plateau starts at the cutoff of the direct rates and represents the rescattering effects. The positions of the cutoff strongly depend on the angle $\theta$. The maximum outgoing electron energy, both for the first and the second plateau, is found at $\theta = 180°$. The cutoff of the first plateau is near $5 U_{P_1}$ which agrees with the results of [218]. The cutoff of the second plateau is at $20.6 \ U_{P_1}$ as predicted by the results of a classical consideration of rescattering. The maximum outgoing electron energies for smaller $\theta$ are much lower than for $\theta = 180°$. These energies also increase with the decrease of $\theta$ from $90°$ to $\theta = 0°$. The main conclusion drawn from Fig. 26 is that for $\phi = 0$ the backward emission of electrons is dominant and that in this direction we obtain many more high-energy electrons. According to the symmetry relation (241) this situation will be reversed for $\phi = \pi$.

In Fig. 27 we show polar plots similar to those presented in Fig. 16, but for a bichromatic linearly polarized laser field of frequencies $\omega$ and $2\omega$, for the relative phase $\phi = 0$, and for $E_{\vec{k}_f} = 8U_{P_1}$, $9U_{P_1}$, $12U_{P_1}$, $16U_{P_1}$, $20U_{P_1}$, and $21U_{P_1}$. The plots in Fig. 27 do not possess the symmetry $\theta \leftrightarrow 180° - \theta$ as in Fig. 16 for a monochromatic field. For $E_{\vec{k}_f} = 8U_{p_1}$, we can notice sidelobes at $\theta = 20°$ in addition to the emissions in forward and backward direction. These sidelobes are similar to those seen in the monochromatic case. Moreover, there are also smaller sidelobes for $\theta > 120°$. The behavior of the ionization rates for larger angles is different from those for smaller angles and different from the monochromatic case. They are characterized by rapid oscillations, very similar to previous findings [508, 509], and one can ascribe these oscillations to the behavior of the generalized Bessel functions, Eq. (233), with a large second argument. With increasing $E_{\vec{k}_f}$, this effect becomes dominant. For $E_{\vec{k}_f} = 9U_{P_1}$ there are no more sidelobes for small angles $\theta$. We only have emission of electrons in a small angular range near the forward direction and at $\theta > 123°$. The rates have maxima at $126.3°$, $132.3°$, and $141.1°$. For $E_{\vec{k}_f} = 12U_{P_1}$ we only have emission of electrons at $\theta > 132°$. On top of a background of oscillatory sidelobes, are those the most prominent ones at $152°$ and $136°$. For $E_{\vec{k}_f} = 16U_{p_1}$ the angular interval of electron emission becomes narrower ($145° - 180°$). The sidelobes are now at $150°$ and $170°$. For $E_{\vec{k}_f} = 20U_{p_1}$ we only obtain clear sidelobes at $170°$. There are no more rapid oscillations of the rates as a function of $\theta$. This shows that the origin of these oscillations can be found in the interferences of different electron trajectories. Namely, only a small number of trajectories can contribute to such large $E_{\vec{k}_f}$ and thus the interference effects are suppressed. Finally, for $E_{\vec{k}_f} = 21U_{p_1}$ we only find emission of electrons into a small range around the backward direction.

**Classical consideration** In previous investigations [218] (see also refs. [242, 243]), we performed classical considerations of the rescattering effects in a bichromatic laser field. According to the rescattering model, the electron is born at time $t_0$ with the initial momentum $\vec{p}_0$ and moves under the influence of the laser field. Solving the Lorentz equation of motion for the electron momentum and assuming that the electron scatters elastically at the atomic core at some instant $t_1$, we can obtain an expression for the cycle averaged kinetic energy $\langle E_k \rangle$ of this electron which depends on $\vec{p}_0$, $t_0$, and $t_1$. For a fixed $\vec{p}_0$ (chosen to be zero), the times $t_0$ and $t_1$ for which $\langle E_k \rangle$ has its maximum can be evaluated by solving the system of equations $\vec{r}(t_1) = \vec{0}$ (i.e. that the electron is at the nucleus at the time $t_1$) and $\partial \langle E_k \rangle / \partial t_0 = 0$. Solving numerically this system of equations, we obtained $\langle E_k \rangle_{\max}$ as a function of the relative phase $\phi$. This yields the maximum value $20.9\, U_{P_1}$
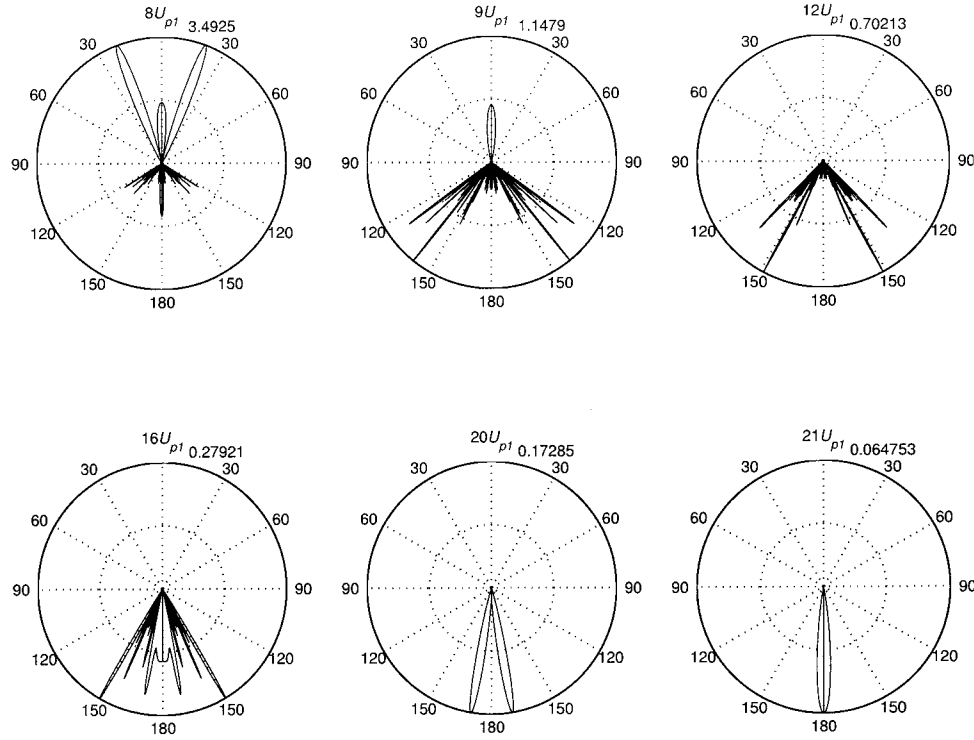
FIG. 27. The sidelobe structure of the ATI spectra are presented in similar fashion as in Fig. 16 for a single frequency $\omega$, but for the bichromatic laser field parameters of Fig. 26. The outgoing electron energies are $E_{\vec{k}_f} = 8U_{P_1}$ (upper left plot), $12U_{P_1}$ (upper right plot), $16U_{P_1}$ (lower left plot), and $20U_{P_1}$ (lower right plot) (see ref. [236]).

close to $\phi = 0$ and $\phi = \pi$ and the minimum value $17.3 U_{P_1}$ for $\phi = \pi/2$. Thus we find a classical cutoff law as a function of $\phi$. In order to check to which angles $\theta$ of electron emission these $\langle E_k \rangle_{\max}(\phi)$ would correspond, we computed by means of our quantum-mechanical approach, presented before, the $\theta$-dependence of the ionization rates for each "classical" pair of parameters chosen (i.e. $\langle E_k \rangle_{\max}, \phi$), for values of $\phi$ in the interval $[0, \pi]$, using steps of $\pi/10$. The results can be presented graphically and one notices that for $\phi < \pi/2$ the electrons are mostly emitted in the backward directions, while for $\phi > \pi/2$ the situation is opposite, i.e., the emission in forward direction is dominant. One also finds that the results for $\phi = 0$ and $\phi = \pi$ satisfy the symmetry relation of the ionization rates $w_{fi}(0, 180° - \theta) = w_{fi}(\pi, \theta)$ which is in accord with Eq. (241). There is no symmetry $\theta \leftrightarrow 180° - \theta$ for other pairs of curves.

**Conclusions**  Summarizing, we predict in the case of a bichromatic laser field interesting effects that should be accessible to observation. Namely, we obtained an extended second plateau for the emission of electrons in the backward direction ($\theta = 180°$) for the relative phase $\phi = 0$. According to the symmetry relation, Eq. (241), this plateau is expected for electrons emitted in the forward direction ($\theta = 180°$) if $\phi = \pi$. The sidelobe structures in the bichromatic case are more complicated, especially for large angles $\theta$ of electron emission. After the cutoff energy at $\theta = 0°$, which is $\sim 9 U_{P_1}$, there are no further electrons emitted at small angles close to forward direction, instead electrons are only emitted in a broad angular interval around the backward direction. With increasing energy of the outgoing electrons, these angular intervals become narrower and at the cutoff energy at $21 U_{P_1}$ the electrons are only emitted in the backward direction ($\theta = 180°$).

### B.2. CPC in electron–ion recombination

With refererence to our recent work [287], we consider electron–ion recombination in a powerful bichromatic laser field of frequencies $\omega_L$ and $3\omega_L$ and investigate the dependence of the recombination probabilities on the relative phase $\phi$ of the two field components. More recently, the case of recombination in a bichromatic field of the frequency components $\omega_L$ and $2\omega_L$ was considered in ref. [290]. During this process a certain number of laser photons can be absorbed or emitted yielding a spectrum of harmonics of the form $\hbar\omega_X = E_{\vec{p}} + N\hbar\omega_L + I_{io} + U_P^{\text{tot}}$ where $E_{\vec{p}}$ is the initial electron energy, $N$ the number of emitted or absorbed laser photons $\hbar\omega_L$, $I_{io}$ the ionization energy, and $U_P^{\text{tot}}$ the total ponderomotive energy of the bichromatic laser field. This process is of interest for the generation of high-frequency fields during the laser heating of plasmas, as we discussed in

Section II.C. We shall evaluate the nonlinear recombination probabilities as a function of the relative phase $\phi$ of the two field components using the inverse form of the Keldysh–Faisal–Reiss model, taking also into account in an approximate way the Coulomb effects of the ion on the recombining electron. We shall moreover compare our quantum-mechanical results with those obtained from a classical theory of recombination, developed recently, based on Bohr's correspondence principle of quantum mechanics.

**Quantum theoretical formulation**   We consider the recombination of electrons with ions in the presence of a strong bichromatic laser beam, described by the vector potential

$$\vec{A}_L(t) = \vec{A}_{01} \cos \omega_L t + \vec{A}_{03} \cos(3\omega_L t + \phi) \qquad (242)$$

in the dipole approximation and we assume that both field components have the same direction of linear polarization. In the presence of the laser field, x-ray photons of frequency $\omega_X$, wave vector $k_X \vec{n}$, and linear polarization $\vec{\epsilon}$ are emitted. In the length gauge, the Hamiltonian describing this process reads

$$\hat{H}(t) = \hat{H}_{\mathrm{at}} + \hat{H}_{\mathrm{rad}} - e\vec{E}_L(t) \cdot \vec{r} - e\vec{E}_X(\vec{r}, t) \cdot \vec{r}, \qquad (243)$$

in which $\hat{H}_{\mathrm{at}}$ is the atomic Hamiltonian in the absence of the fields and $\hat{H}_{\mathrm{rad}}$ is the Hamiltonian of the two free radiation fields. $\vec{E}_L(t)$ describes the electric field of the laser beam in the dipole approximation and $\vec{E}_X(\vec{r}, t)$ is the electric-field operator of the x-ray radiation. It will be permitted to use in Eq. (243) for the electron laser field coupling as well as for the electron x-ray field coupling the dipole interaction, as long as the wavelength of both fields will be larger than the Bohr radius. We treat the laser field classically while the spontaneously emitted x-ray is described quantum-mechanically. For our recombination process, the initial state is $\mid \psi_{\vec{p}}^{(+)}(t); 0\rangle$, namely the vacuum state for x-ray radiation and a scattering state for an electron in the laser field. On the other hand, the final state equals $\mid \psi_0(t); 1\rangle$, is describing a one-photon state for x-rays and a bound state of an electron in the laser field. Using Fermi's golden rule, we find for the probability of emitting a single x-ray photon by an electron recombining from a scattering state of momentum $\vec{p}$ into a quasi-bound state to be

$$P(\vec{n}, \vec{p}\,) = \left| \frac{1}{\hbar} \int dt \langle \psi_0(t); 1 \mid - e\vec{E}_X(\vec{r}, t) \cdot \vec{r} \mid \psi_{\vec{p}}^{(+)}(t); 0\rangle \right|^2 \qquad (244)$$

and straightforward calculations lead then to the total power of emitted x-rays to be

$$P = \int \frac{d^3p}{(2\pi\hbar)^3} \frac{d^3k_X}{(2\pi)^3} V \hbar\omega_X w(\vec{n}, \vec{p})$$

$$= \int dE_{\vec{p}} \, d\Omega_{\vec{p}} \, d\omega_X \, d\Omega_{\vec{n}} \, S(\omega_X, \vec{n}, \vec{p})$$

$$\times \delta(E_0 - E_{\vec{p}} - U_P^{\text{tot}} - N\hbar\omega_L + \hbar\omega_X), \qquad (245)$$

in which the differential power spectrum is defined by

$$S(\omega_X, \vec{n}, \vec{p}) = \frac{\alpha\omega_X^4 mp}{(2\pi)^4 \hbar c^2}$$

$$\times \left| \frac{\omega_L}{2\pi} \int_0^{2\pi/\omega_L} dt \langle \psi_0(t) \, | e^{-i\omega_X t + i(\omega_X/c)\vec{n}\cdot\vec{r}} \, \vec{\varepsilon} \cdot \vec{r} \, | \, \psi_{\vec{p}}^{(+)}(t) \rangle \right|^2. \qquad (246)$$

Our discussions below will be based on this quantity. We approximate $\psi_0(\vec{r}, t)$ by the ground-state wave function of hydrogen without the laser field and we replace $\psi_{\vec{p}}^{(+)}(\vec{r}, t)$ by our Coulomb–Volkov solution [29]. For the laser field, Eq. (242), we use in our approximation for $\psi_{\vec{p}}^{(+)}(\vec{r}, t)$, represented by a Coulomb–Volkov wave, $\vec{\alpha}_L(t) = \vec{\alpha}_{01} \sin\omega_L t + \vec{\alpha}_{03} \sin(3\omega_L t + \phi)$ with $\vec{\alpha}_{0j} = -e\vec{A}_{0j}/jm\omega_L$ ($j = 1, 3$). Our above calculations are entirely performed in the length gauge, as was originally done for ATI by Keldysh [103]. The Coulomb–Volkov solution used here, gives more reliable results than the one originally suggested by Jain and Tzoar [250] many years ago (using the velocity gauge). A comparison of the two Coulomb–Volkov approximations was made in ref. [170].

**Classical formulation**   Based on Bohr's correspondence principle, we shall outline in this section some classical considerations on the power spectrum of x-rays emitted during the recombination of electrons with ions in the presence of a strong laser field. We have shown [282] that the power spectrum of x-rays, evaluated for a single laser frequency, can be estimated from the quantum-mechanical calculations to have the shape of a plateau of the width $4\sqrt{2U_P E_{\vec{p}}}$ and the maximum/minimum energy of the emitted x-ray quanta can be found to be $\hbar\omega_{\max/\min} = E_{\vec{p}} + I_{io} + U_P \pm 2\sqrt{2U_P E_{\vec{p}}}$. We also demonstrated in another work [510], that a similar result can be obtained by analyzing a simple classical model for x-ray generation during the recombination process. However, for a single laser frequency this classical model apparently describes the shape of the power spectrum as well

as the position of its extrema more closely to the quantum-mechanical results than the above-made estimate. In the classical model the limits of the x-ray spectrum for a single laser frequency are found to be given by $\hbar\omega_{\max/\min} = E_{\vec{p}} + I_{io} + 2U_P \pm 2\sqrt{2U_P E_{\vec{p}}}$ and hence this calculation yields an x-ray spectrum which is shifted by a factor $U_P$ in comparison with the above estimate. We shall therefore also apply this classical model to recombination in a bichromatic field and compare the results of the quantum mechanical and classical models.

We consider the energy of a classical electron moving in a laser field in dipole approximation

$$E(t) = \frac{1}{2m}(\vec{p} - e\vec{A}_L(t))^2, \tag{247}$$

where $\vec{p}$ is the momentum of the electron's translational motion and $\vec{A}_L(t)$ is in the present case the vector potential, Eq. (242). If at time $t$ an electron is captured by an ion in the field, Eq. (242), then the energy of the emitted x-ray photon will be $\hbar\omega_X(t) = I_{io} + E(t)$. Hereby we assumed that the total kinetic electron energy was converted into an x-ray photon and that other processes, involving some laser photons, are much less probable. Moreover, we assume that the intensity of the emitted x-rays of energies in the interval $[\omega_X, \omega_X + d\omega_X]$ is proportional to the time during which a "*classical*" electron in the laser field Eq. (242) has energies in the interval $[E(t), E(t) + \hbar d\omega_X]$. Hence, the classical power spectrum of x-ray radiation $S_c(\omega_X, \vec{n}, \vec{p})$ will be proportional to the probability density of finding an electron with an instant energy $E(t) = \hbar\omega_X(t) - I_{io}$. This classical probability density can be evaluated to be [510]

$$\rho_c(\omega_X) = \frac{\omega_L}{2\pi} \sum_{t(\omega_X)} \frac{1}{|\omega'_X(t(\omega_X))|}, \tag{248}$$

where the prime denotes the derivative with respect to time and the values of $t(\omega_X)$ are the solutions of the equation

$$\hbar\omega_X = I_{io} + \frac{1}{2m}\left[\vec{p} - e\vec{A}_{01}\cos\omega_L t - e\vec{A}_{03}\cos(3\omega_L t + \phi)\right]^2. \tag{249}$$

The probability density Eq. (248) has been normalized to one, viz.

$$\int_{\omega_{\min}}^{\omega_{\max}} \rho_c(\omega_X)d\omega_X = 1, \tag{250}$$

with $\omega_{\min}$ and $\omega_{\max}$ being the classical minimum and maximum frequencies of generated x-rays.

We also took the electron momentum to point parallel to the polarization vectors of the bichromatic field, i.e. $\vec{p} \parallel \vec{A}_{01} \parallel \vec{A}_{03}$, corresponding to the most favorable geometry, as discussed in ref. [282]. For this geometry, the possible energies of x-ray photons $\hbar\omega_X$ lie within the range $[\omega_{\min}, \omega_{\max}]$, where in general the minimum and maximum frequencies have to be found numerically for our bichromatic field Eq. (242) using the extremum condition $\omega'_X(t) = 0$ to be derived from Eq. (249) which in general cannot be solved analytically, except for the two values $\varphi = 0$ and $\pi$. In this case we obtain

$$\hbar\omega_{\max/\min} = I_{io} + E_{\vec{p}} \pm 2\left(\sqrt{2U_{P_1}E_{\vec{p}}} + \sqrt{2U_{P_3}E_{\vec{p}}}\right) + 2\left(\sqrt{U_{P_1}} + \sqrt{U_{P_3}}\right)^2,$$

where $U_{P_i} = e^2 A_{0i}^2/4m$ $(i = 1, 3)$.

The above classical model predicts that for a given value of the electron momentum the power spectrum of x-ray radiation is limited to the range $[\omega_{\min}, \omega_{\max}]$. Since the classical probability density $\rho_c(\omega_X)$ is infinite at the endpoints of the interval $[\omega_{\min}, \omega_{\max}]$, we have to consider a realistic experiment in which the intensity of x-ray radiation is measured within a certain interval $[\omega_X, \omega_X + d\omega_X]$ due to the finite experimental resolution. Therefore, the density $\rho_c(\omega_X)$ has to be averaged over a frequency range in the vicinity of $\omega_X$. This leads to a finite and continuous classical probability density for the generation of x-rays. Assuming that the experimental apparatus counts all photons within the interval $[\omega_X - \delta, \omega_X + \delta]$, the averaged probability density becomes

$$\bar{\rho}_c(\omega_X) = \frac{1}{2\delta} \int_{\omega_X - \delta}^{\omega_X + \delta} d\omega \rho_c(\omega). \tag{251}$$

The averaged classical probability density $\bar{\rho}_c(\omega_X)$ is then a continuous function of $\omega_X$, while the quantum-mechanical formula Eq. (245) predicts that the x-ray frequencies can only differ by multiples of the laser frequency $\omega_L$. In order to compare the predictions of the classical and quantum models, we have to discretize the classical probability density. The most natural discretization prescription turns out to be

$$\bar{p}_c(\omega_X) = \int_{\omega_X - (1/2)\omega_L}^{\omega_X + (1/2)\omega_L} d\omega \bar{\rho}_c(\omega) \approx \omega_L \bar{\rho}_c(\omega_X), \tag{252}$$

yielding the probability that during the process of recombination a photon of energy within the interval $[\omega_X - (1/2)\omega_L, \omega_X + (1/2)\omega_L]$ is emitted. This classical result has to be compared with the corresponding averaged quantum probability $\bar{p}_q(\omega_X)$. This probability is proportional to the power spectrum $S(\omega_X, \vec{n}, \vec{p})$ of x-ray radiation, given by Eq. (246), where the total probability of emission of any x-ray photon is equal to one. Also in the quantum mechanical case we have to account for the finite resolution of the experimental apparatus and therefore $\bar{p}_q(\omega_X)$ will be proportional to the power spectrum $S(\omega_X, \vec{n}, \vec{p})$, averaged like the classical probability distribution, namely

$$\bar{p}_q(\omega_X) = N \sum_{\omega_X - \delta \,\leqslant\, \omega \,\leqslant\, \omega_X + \delta} S(\omega, \vec{n}, \vec{p}), \tag{253}$$

where $N$ is a normalization factor, determined from the condition

$$\sum_{\omega_X} \bar{p}_q(\omega_X) = 1. \tag{254}$$

Our numerical examples will be expressed in atomic units, if not stated otherwise.

**Numerical examples**   The numerical examples will demonstrate the validity of our classical model of recombination, based on Bohr's correspondence principle. It is applied in the present problem to the recombination in a bichromatic field, Eq. (242), of frequencies $\omega_L$ and $3\omega_L$ and we consider a Ti:sapphire laser of frequency $\omega_L = 1.5498\,\text{eV}$. We assume that the resolution of the experimental apparatus that measures the energy of the emitted x-ray photons is either $2\delta = 10\omega_L$ or $2\delta = 20\omega_L$. These are reasonable values for the energetic x-ray radiation generated by the recombination of ingoing electrons of kinetic energies of about $E_{\vec{p}} \simeq 56$ a.u. and laser intensities between $I = 10^{13}$ and $10^{14}\,\text{W\,cm}^{-2}$. In the following figures we compare the classical and quantum mechanical recombination probabilities $\bar{p}_c(\omega_X)$ and $\bar{p}_q(\omega_X)$, respectively. We show for comparison the corresponding differential power spectrum, $S(\omega, \vec{n}, \vec{p})$, for the above laser-field parameters and electron energies as a function of the relative phase $\varphi$ of the two field components. As anticipated from the results of our earlier work [510] for a single laser frequency $\omega_L$, the exact quantum mechanical results are smoothed out by the averaging procedure, but also in the bichromatic case the most important finding is that the shapes of the classical and quantum-mechanical probability distributions are almost identical. It may well be
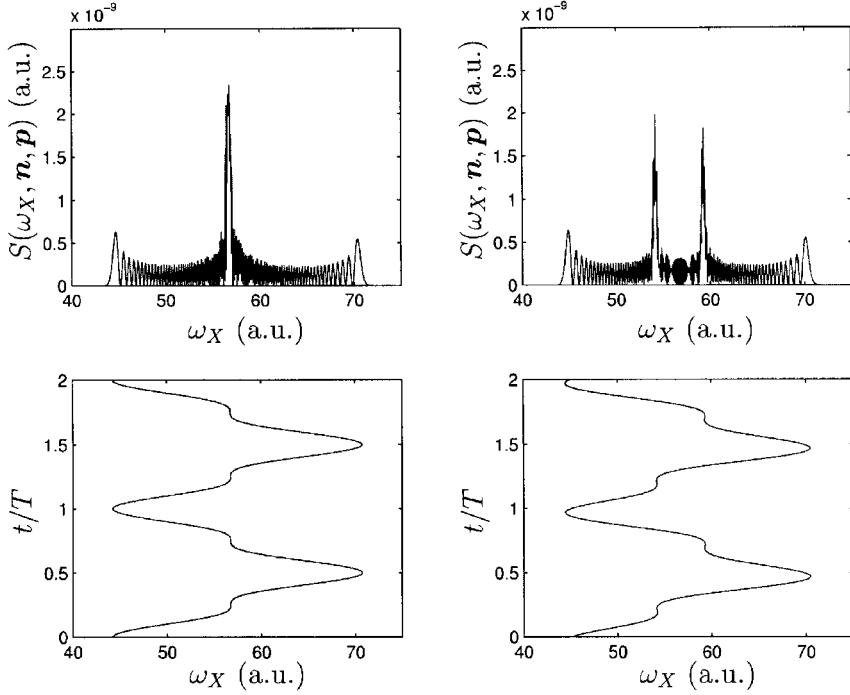
FIG. 28. Compares the power spectrum, Eq. (246), and the time-dependence of $\omega_X = I_{io} + (1/2m)(\vec{p} - (e/c)\vec{A}_L(t))^2$. The position of the dominant peaks of the quantum-mechanical spectrum is classically properly predicted by the condition $\omega'_X(t) \simeq 0$ demonstrating the usefulness of the classical model. The left frames refer to $\phi = 0°$ and the right ones to $\phi = 45°$. The other parameters are $\omega_L = 1.5498\,\text{eV}$, $I_1 = I_3 = 10^{14}\,\text{Wcm}^{-2}$, $E_{\vec{p}} = 56.213$ a.u. (see ref. [166]).

that for smaller laser-field frequencies, where the correspondence principle should be more reliable, the agreement will be even better.

In Fig. 28 we assume the same intensity $I_1 = I_3 = 10^{14}\,\text{W cm}^{-2}$ for both radiation-field components and we show for the rather high electron kinetic energy $E_p = 56.213$ a.u. in the upper two frames the power spectra Eq. (246) for $\varphi = 0°$ on the left hand side and for $\varphi = 45°$ on the right hand side. We immediately recognize that the dominant x-ray frequencies of the laser-assisted recombination spectrum can be manipulated by varying the relative phase $\varphi$ of the two laser field components. Moreover, we conclude that recombination in a bichromatic field can be used to promote particular x-ray frequencies to become dominant in the recombination spectrum. Furthermore, we plotted in the lower two frames the time-dependence of $\omega_X = I_{io} + (1/2m)(\vec{p} - e\vec{A}_L(t))^2$ (in units $\hbar = c = 1$) and we recognize that
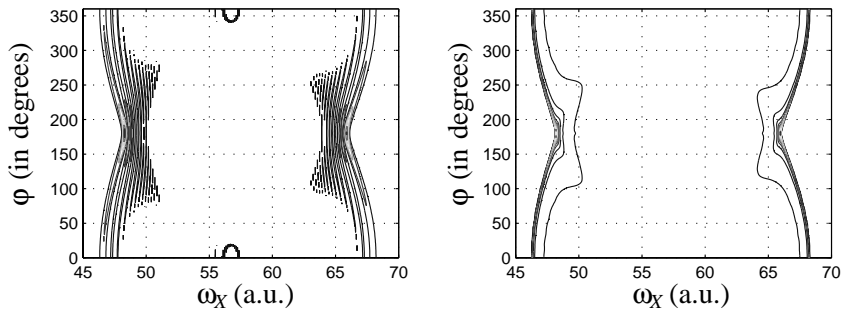
Fɪɢ. 29. Presents a comparison of the contour plots of the averaged quantum mechanical (left) and classical (right) recombination probabilities. Both probabilities have their maxima at the same positions but the quantum mechanical probabilities show oscillations due to interferences of quantum mechanical origin. In both cases the resolution $2\delta = \omega_L$ was chosen. The other parameters are the same as in Fig. 28, except that $0° \leq \phi \leq 360°$. Thanks to the equal intensity of both radiation components, the similarity of the $\phi$-dependence of the dominant peak structure of the quantum mechanical and classical probabilities becomes more evident (see ref. [166]).

the endpoints of the x-ray spectrum are, by comparison with the upper frames, correctly determined by the condition $\omega'_X(t) \simeq 0$. This demonstrates again the usefulness of the classical considerations to obtain in the present case insight into the extent of the recombination spectrum in a bichromatic laser field.

In Fig. 29 we compare the contour plots of the averaged recombination probabilities for the quantum case in the left frame and the classical case in the right frame. The laser and electron parameters are the same as in Fig. 28. In both cases the resolution was chosen to be $2\delta = \omega_L$. The maxima of the plotted quantum-mechanical and classical probabilities agree very well with each other although the oscillations of the quantum mechanical probability distribution are a clear indication of the interferences between different quantum path which are not present in the classical case. In both frames, however, the $\varphi$-dependence of the recombination probabilities is very similar in shape and extent. The more powerful second field component leads to a much more pronounced $\varphi$-dependence of the spectra and very sharp maxima of the recombination probabilities at characteristic x-ray frequencies $\omega_X(\varphi)$.

**Conclusions** Summarizing, we have discussed an example of the predictive power of our classical model of electron–ion recombination in a laser field. We saw that even the phase-dependences and peak structures of the recombination spectra in a bichromatic field are well described by this

model. We should emphasize, however, that our classical model cannot be used to estimate the absolute values of the recombination probabilities of the spectrum. This can only be done by a quantum mechanical calculation. As we pointed out earlier [510], the classical model can also not predict the rapid oscillations of the power distribution in the inner part of the frequency spectrum. While the classical distribution only shows some characteristic peaks, the quantum distribution contains additional rapid oscillations which originate in quantum interferences. These stem from the summation of the quantum mechanical probability amplitudes, referring to different quantum paths, but leading to the same final state. The very good agreement between the classical and quantum distributions for the main features of the spectrum in the case of a bichromatic field suggests that for the main peaks there will be only one dominant quantum path, namely the direct emission of an x-ray photon during the recombination process. The successful application of Bohr's correspondence principle to recombination in a bichromatic laser field is another example for the successful application of classical considerations to laser-induced phenomena as was done previously for HHG and ATI by Corkum [173] and Kulander *et al.* [172], and for potential scattering by Rabadán *et al.* [511, 512].

### B.3. *HHG by bichromatic fields*

Over the past decade HHG in laser-irradiated atomic gases has been extensively studied [17,175], as already discussed in Section II.F. Many efforts were made in order to control HHG, especially due to the potentially important applications of the coherent soft x-rays that might be produced via HHG [331]. It is known that the harmonic output can be manipulated by changing the driving field or altering the medium which generates harmonics. For example, a bichromatic driving laser field provides two additional parameters for the control of HHG, the relative intensity and the relative phase of the fields [233, 513–515]. Polarization of the laser field [213, 515–518], as well as the shape of the laser pulse [519, 520], are also parameters useful for such control. For ultra-short pulses, the initial phase of the laser field has a significant influence on the HHG process [354, 355]. The HHG process can also be controlled by adding a static electric field [521–523] or a static magnetic field [398, 524–526] to the driving laser field. The usual media used in HHG are atomic gases, but HHG has also been examined for ions [527], molecular gases [433] and atomic clusters [528]. In addition, control of HHG was explored theoretically for the case in which the initial state is prepared as a coherent superposition of states [424, 425].

**Theoretical approach** We consider the generation of harmonics by irradiating atoms with a powerful laser field described by an electromagnetic

plane wave in the dipole approximation with the electric field vector
defined by

$$\vec{\mathcal{E}}(t) = \vec{\epsilon}\mathcal{E}(t) = \vec{\epsilon}\sum_j \mathcal{E}_{0j}\cos(j\omega t + \phi_j), \tag{255}$$

where $\vec{\epsilon}$ is a unit vector of linear polarization oriented in the $z$-direction and
$\phi_j$ and $\mathcal{E}_{0j}$ ($j = 1, 2$ or $j = 1, 3$) are the phases and amplitudes of the driving
fields. The rate of emission of a harmonic photon of frequency $N\omega$
and polarization $\vec{\epsilon}$ into the solid angle $d\Omega$ is determined by the expression
(see Eq. (203) with Eqs. (202) and (205)–(208) in Section II.F, for $f = i$
and in atomic units)

$$w_N = \frac{1}{2\pi}\left(\frac{N\omega}{c}\right)^3 |D_N|^2, \tag{256}$$

with $D_N$ being the $N$th harmonic strength

$$D_N = \int_0^T \frac{dt}{T} d(t)\exp(iN\omega t), \tag{257}$$

where $d(t)$ is the time-dependent dipole matrix element. The corresponding
intensity of the harmonics is $|D_N|^2$ and their power is $N\omega w_N$. Using the
strong-field approximation, discussed in greater detail in Sections II.E and
II.F, and neglecting the continuum–continuum coupling, the time-depen-
dent dipole matrix element can be approximated by $d(t) \approx d_a(t) + d_e(t) \approx
d_a(t) + d_a^*(t)$, where according to Eq. (213) in Section II.F.3

$$d_a(t) \approx -i\int_0^\infty d\tau\left(\frac{2\pi}{i\tau}\right)^{3/2}\mathcal{E}(t-\tau)\langle\psi_0|z|q_s + A(t)\rangle\langle q_s + A(t-\tau)|z|\psi_0\rangle e^{iS_s} \tag{258}$$

with

$$q_s = \frac{1}{\tau}[\alpha(t-\tau) - \alpha(t)], \tag{259}$$

$$S_s \equiv S(q_s; t, t-\tau) = \int_t^{t-\tau} dt'\left\{\frac{1}{2}[q_s + A(t')]^2 + I_{io}\right\}$$

$$= [\alpha(t-\tau) - \alpha(t)]q_s + U(t-\tau) - U(t) - \left(I_{io} + \frac{q_s^2}{2}\right)\tau, \tag{260}$$

and

$$\alpha(t) = \int^t dt'\, A(t'), \;\; U(t) = \frac{1}{2}\int^t dt'\, A^2(t').  \tag{261}$$

The integral over the return time $\tau$ can be calculated by numerical integration and the harmonic strength Eq. (257) can then be evaluated by means of the fast Fourier transform method in a very similar fashion as explained in Sections II.E and II.F.

**Numerical examples**   First we present data that were evaluated in the work of Milošević and Piraux [233], who investigated HHG in a bichromatic elliptically polarized laser field. In their work, the strong-field approximation of HHG, developed by Lewenstein *et al.* [181], was generalized to the case of a bichromatic elliptically polarized radiation field. Numerical results for a linearly polarized laser field were presented and analyzed for different laser field frequencies, intensities and relative phases. The harmonic intensities turn out to be many orders of magnitude higher in the bichromatic case than in the monochromatic one. The plateau height can be controlled by changing the relative phase of the fields. A qualitative agreement of their results with the experiments [397, 529] was found by these authors. As a representative example for the CPC effects we depict in Fig. 30 their results for a linearly polarized bichromatic field of frequencies $\omega = 1\,\mathrm{eV}$ and $3\omega$ and field amplitudes $\mathcal{E}_{01}$ and $\mathcal{E}_{03} = 3\mathcal{E}_{01}$. The ionization energy and the laser intensity were $I_{io} = 13.6\,\mathrm{eV}$ and $I_{01} = \mathcal{E}_{01}^2 = 7 \times 10^{13}\,\mathrm{W\,cm^{-2}}$, respectively. In the figure presented, different values of the relative phase $\phi = \phi_2 - \phi_1$ are considered.

In Fig. 31 we present some more recent data on the harmonic spectra generated by a linearly polarized bichromatic laser field of frequencies $\omega$ and $2\omega$ with the electric field vector given by $\mathcal{E}(t) = \mathcal{E}_{01}\sin\omega t + \mathcal{E}_{02}\sin(2\omega t + \phi)$ where the field amplitudes are given by $\mathcal{E}_{01} = 0.1$ a.u. and $\mathcal{E}_{02} = 0.32\,\mathcal{E}_{01}$. The results shown are for the relative phases $\phi = 0$ and $\phi = 0.2\pi$. The laser frequency is chosen in this case $\omega = 0.057$ a.u. and the ionization energy of the target atom is $I_{io} = 0.58$ a.u. The results presented in this figure show two plateaus of generated harmonics and two cutoffs. For both relative phases the higher cutoff energy is at $63\omega$. At this cutoff, the harmonic intensity for $\phi = 0$ is by one order of magnitude higher than the corresponding intensity for $\phi = 0.2\pi$. In the shorter plateaus we find much higher harmonic intensities than in the longer plateaus and they have their cutoffs at $47\omega$ and $43\omega$ for $\phi = 0$ and $\phi = 0.2\pi$, respectively. All these features of the spectra presented can be explained by using two pairs of
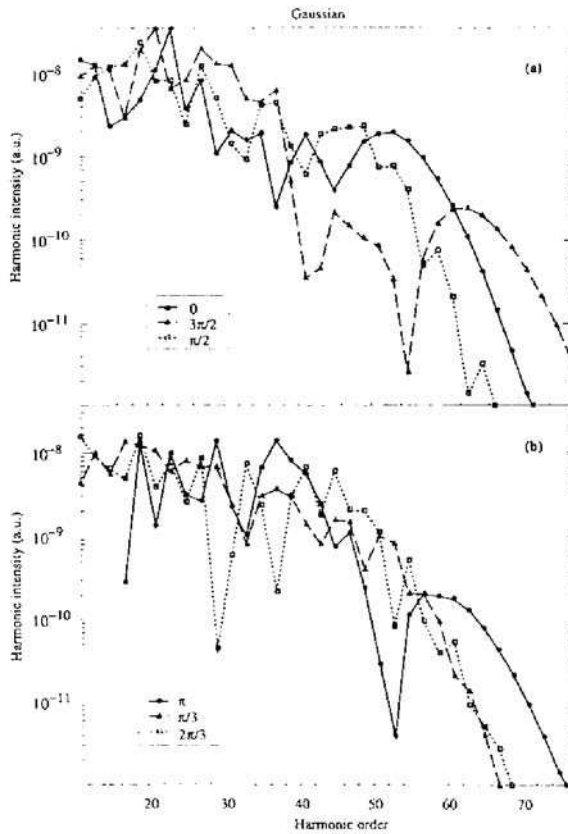
FIG. 30. Shows the harmonic intensity as a function of the harmonic order $N$ for the Gaussian model [181], for the $\omega$–$3\omega$ bichromatic laser field (255). The parameters are $I_{io} = 13.6\,\text{eV}$, $\omega = 1\,\text{eV}$, $I_{01} = 7 \times 10^{13}\,\text{W}\,\text{cm}^{-2}$, and the data presented are for different values of the relative phase $\phi = \phi_2 - \phi_1$: (a) $\phi = \{0, 3\pi/2, \pi/2\}$ and (b) $\phi = \{\pi, \pi/3, 2\pi/3\}$. From these figures we can infer that both, the height of the plateau and the position of the cutoff change with the change of $\phi$ (see ref. [233]).

quantum orbits which are the solutions of the corresponding saddle-point equations [392].

**Conclusions**   As it was shown, both theoretically and experimentally, it is possible to control HHG by employing a bichromatic radiation field of harmonic frequencies $\omega$ and $s\omega$ (usually, $s = 2, 3$). A considerable number of investigations of HHG in a bichromatic field have been performed to which we refer the reader for further details [233, 392, 515, 530–534].
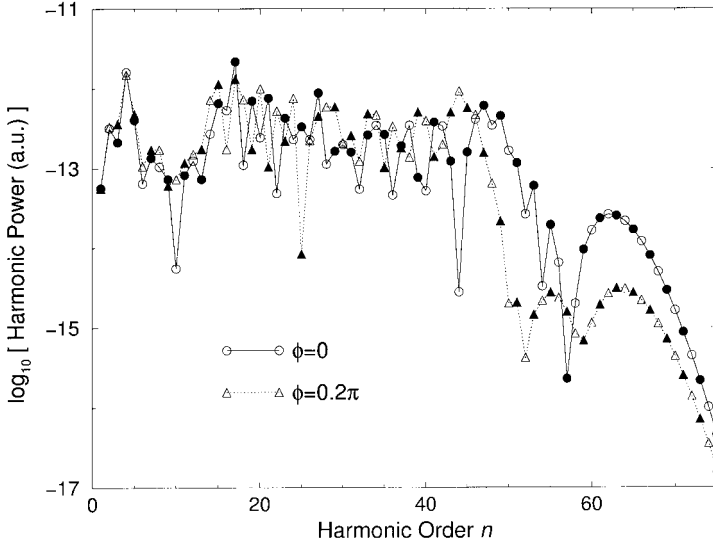
FIG. 31. Presents the harmonic power as a function of the harmonic order $N$, generated by a linearly polarized bichromatic laser field of frequencies $\omega_1$ and $2\omega_1$ with the field amplitudes $\mathcal{E}_{01} = 0.1$ a.u. and $\mathcal{E}_{02} = 0.32 \, \mathcal{E}_{01}$ for the laser frequency $\omega = 0.057$ a.u., while the ionization potential is $I_{io} = 0.58$ a.u. The relative phases are $\phi = 0$ (circles) and $\phi = \pi/2$ (triangles). Even harmonics are marked by open symbols, while odd harmonics are shown as filled symbols.

As the numerical analysis has shown [232, 392], we arrive at the following conclusions: (i) The harmonic intensities can be much larger in the bichromatic case. (ii) In the bichromatic case, the plateau of harmonics is not constant as in the monochromatic case, but has its own structure. Moreover, two plateaus in the harmonic spectrum are developed, a shorter and a longer one. The intensity of the harmonics in the shorter plateau is higher. (iii) The cutoff positions as well as the plateau heights can be controlled by changing the relative phase. (iv) In the $\omega$–$2\omega$ case there are both, even and odd harmonics generated and they have the same intensity. (v) The phase of the induced atomic dipole moment exhibits a quasilinear dependence on the ponderomotive energy, similar to the monochromatic case, but it has a lower slope. (vi) The behavior of the harmonic intensity as a function of the relative phase does not depend on the chosen atomic potential. Finally, the qualitative predictions of the theory are in agreement with experiments, but a quantitative analysis requires to take into account phase matching and propagation effects, as pointed out in Section II.F.

## IV.  Final Comments

In the present work, we have given an overview on various scattering and reaction processes taking place in a powerful laser field. These processes can be either laser-induced or laser-assisted. In the latter case a fundamental process exists in the absence of the laser field. We have concentrated in our discussions on laser interactions with atomic systems, though occasionally we also mentioned the corresponding molecular phenomena. In the case of molecules, the additional freedoms of motion lead in the presence of a laser field to a variety of more complicated effects, but the treatment of these processes also causes more computational difficulties. Our general approach to solving the problems considered, was adapted from the $S$-matrix theory, originally conceived for the solution of problems of quantum electrodynamics. This method turns out to be very efficient in the present case of treating atomic processes in powerful laser fields, since at high laser field intensities a number of approximations can be made, in particular, the "quasi-free" electron approximation in which it is assumed that an ionized or scattered electron is interacting with the laser field only, while the atomic binding effects can be neglected to a very large extent. Moreover, the unitarity of the $S$-matrix presents an intuitive link between various different laser-induced processes like, for example, the connection between ATI and HHG. Another approximation turns out to be very useful and, in many cases, leads to sufficiently good results. That is, to assume that there is only one single electron in the atomic system interacting with the laser field at a particular instant of time. Of course, this approximation is not always valid and more recently a number of experiments have shown where this approximation breaks down. We shall not go, however, into a detailed discussion of these phenomena, but we shall mention some experimental and theoretical work performed recently.

As we indicated, the dynamics of an atom in an intense laser field can be described in general quite accurately within the assumption of just one single active electron [535]. Experiments several years ago proved, however, that this is certainly not always the case for the laser-induced double ionization of atoms [536–539]. In fact, these experiments demonstrated that the yield of double ionization can be many orders of magnitude higher than predicted within a theory using one active electron at a time. Subsequently, several theories were put forward to understand the underlying physics of this nonsequential process. They were referred to as the shake-off [540], the recollision [173] and the collective-tunneling [541, 542] mechanisms. More insight into the dominating mechanism was most recently gained by the experiments of two groups [543–547] which involved very sensitive

measurements of the momentum distributions of doubly charged ions with the help of the COLTRIMS (cold target recoil-ion momentum spectroscopy) technique [548, 549]. The data have shown uniformly that one of the two electrons first tunnel alone through the Coulomb barrier, then return after the change of phase in the linearly-polarized laser field towards the ionic core and finally ionize the second electron via momentum transfer during the recollision process. We also mention some further recent experimental results [550–553]. The experimental development was accompanied by many supporting calculations of the correlated two-electron dynamics, including *S*-matrix theories [554–561], classical relativistic calculations [562], that were used in order to confirm the observed suppression of double ionization due to the magnetic field induced electron drift motion, semi-classical model calculations [563–567] and in most cases time-dependent numerical integration of the corresponding Schrödinger equation [568–587]. The corresponding problem at relativistic laser field intensities was also considered recently [189]. In the investigations mentioned and in the review by Lambropoulos *et al.* [367] and in the recent Focus issue [368] the interested reader will find more detailed information.

## V.  Acknowledgments

## VI.  References

1. Ehlotzky, F. (1985). *Can. J. Phys.* **63**, 907.
2. Gavrila, M., ed. (1992). "Atoms in Intense Laser Fields. Adv. At. Mol. Opt. Phys. Suppl. 1." Academic, New York.
3. Delone, N.B., and Krainov, V.P. (1994). "Multiphoton Processes in Atoms." Springer, Berlin.
4. Delone, N.B., and Krainov, V.P. (2000). "Multiphoton Processes in Atoms." 2nd. ed., Springer, Berlin.

5. Eberly, J.H., Grobe, R., Law, C.K., and Su, Q. (1992). In: M. Gavrila (ed.). *Atoms in Intense Laser Fields. Adv. At. Mol. Opt. Phys. Suppl. 1*, p. 301. Academic, New York.

6. Eberly, J.H., Javanainen, J., and Rzążewski, K. (1991). *Phys. Rep.* **204**, 331.

7. Mainfray, G., and Manus, C. (1991). *Rep. Prog. Phys.* **54**, 1333.

8. Freeman, R.R., and Bucksbaum, P.H. (1991). *J. Phys. B* **24**, 325.

9. L'Huillier, A., Schafer, K.J., and Kulander, K.C. (1991). *J. Phys. B* **24**, 3315.

10. Ammosov, M.V., Delone, N.B., Ivanov, M.Yu., Bondar, I.I., and Masalov, A.V. (1991). *Adv. At. Mol. Opt. Phys.* **29**, 33.

11. Shakeshaft, R. (1992). *Comments At. Mol. Phys.* **28**, 179.

12. Balcou, Ph., Cornaggia, C., Gomes, A.S.L., Lompre, L.A., and L'Huillier, A. (1992). *J. Phys. B* **25**, 4467.

13. Reiss, H.R. (1992). *Prog. Quantum. Electron.* **16**, 1.

14. Burnett, K., Reed, V.C., and Knight, P.L. (1993). *J. Phys. B* **26**, 561.

15. Faisal, F.H.M., Dimou, L., Stiemke, H.-J., and Nurhuda, M. (1995). *J. Nonlinear Opt. Phys. Materials* **4**, 707.

16. DiMauro, L.F., and Agostini, P. (1995). *Adv. At. Mol. Opt. Phys.* **35**, 79.

17. Protopapas, M., Keitel, C.H., and Knight, P.L. (1997). *Rep. Progr. Phys.* **60**, 389.

18. Joachain, C.J., Dörr, M., and Kylstra, N. (2000). *Adv. At. Mol. Opt. Phys.* **42**, 225.

19. Maquet, A., Véniard, V., and Marian, T.A. (1998). *J. Phys. B* **31**, 3743.

20. Terao-Dunseath, M., and Dunseath, K.M. (2002). *J. Phys. B* **35**, 125.

21. Becker, W., Grasbon, F., Kopold, R., Milošević, D.B., Paulus, G.G., and Walther, H. (2002). *Adv. At. Mol. Opt. Phys.* **48**, 35.

22. Evans, D.K., and Chin, S.L. (eds.) "Proceedings of the Sixth International Conference on Multiphoton Processes 1994." World Scientific (Singapore).

23. Lambropoulos, P., and Walther, H. (eds.) "Proceedings of the Seventh International Conference on Multiphoton Processes 1997." Institute of Physics (Bristol).

24. Mourou, G.A., Barty, C.P.J., and Perry, M.D. (1998). *Phys. Today* **51**, 22.

25. Drescher, M., Hentschel, M., Kienberger, R., Tempea, G., Spielmann, Ch., Reider, G.A., Corkum, P.B., and Krausz, F. (2001). *Science* **291**, 1923.

26. Brabec, T., and Krausz, F. (2000). *Rev. Mod. Phys.* **72**, 545.

27. Krausz, F. (2001). *Phys. World* **14**, 41.

28. Hentschel, M., Kienberger, R., Spielmann, Ch., Reider, G.A., Milosevic, N., Brabec, T., Corkum, P., Heinzmann, U., Drescher, M., and Krausz, F. (2001). *Nature* (London) **414**, 509.

29. Ehlotzky, F., Jaroń, A., and Kamiński, J.Z. (1998). *Phys. Rep.* **297**, 63.

30. Ehlotzky, F. (2001). *Phys. Rep.* **345**, 175.

31. Sen Gupta, N.D. (1949). *Bull. Math. Soc. Calcutta* **41**, 187; (1952). *ibid.* **44**, 157.

32. Vachaspati (1962). *Phys. Rev.* **128**, 664.

33. Gol'dman, I.I. (1964). *Zh. Éksp. Teor. Fiz.* **46**, 1412 [(1964). *Sov. Phys. JETP* **19**, 954].

34. Brown, L.S., and Kibble, T.W.B. (1964). *Phys. Rev.* **133**, A705.

35. Fried, Z., and Eberly, J.H. (1964). *Phys. Rev.* **136**, B871.

36. Eberly, J.H. (1969). *Progress in Optics* **VII**, 361; and references therein.

37. Bergou, J., and Varró, S. (1981). *J. Phys. A* **14**, 1469.

38. Narozhnyĭ, N.B., and Fofanov, M.S. (1996). *Zh. Éksp. Teor. Fiz.* **110**, 26 [(1996). *JETP* **38**, 14].

39. Bunkin, F.B., Kazakov, A.E., and Fedorov, M.V. (1972). *Usp. Fiz. Nauk* **107**, 559 [(1973). *Sov. Phys. Usp.* **15**, 416.]; and references quoted therein.

40. Mitter, H. (1975). *Acta Phys. Austriaca Suppl.* **14**, 397.

41. McDonald, K.T. (1986). *Princeton Univ. Preprint DOE/ER/3072-38.*

42. Moore, C.I., Knauer, J.P., and Meyerhofer, D.D. (1995). *Phys. Rev. Lett.* **74**, 2439.

43. Meyerhofer, D.D., Knauer, J.P., McNaught, S.J., and Moore, C.I. (1996). *J. Opt. Soc. Am. B* **13**, 113.
44. Meyerhofer, D.D. (1997). *IEEE J. Quantum. Elect.* **33**, 1935.
45. Sarachik, E.S., and Schappert, G.T. (1970). *Phys. Rev. D* **1**, 2738.
46. Puntajer, A.K., and Leubner, C. (1989). *Phys. Rev. A* **40**, 279.
47. Puntajer, A.K., and Leubner, C. (1989). *Opt. Commun.* **73**, 153.
48. Puntajer, A.K., and Leubner, C. (1990). *J. Appl. Phys.* **67**, 1606.
49. Salamin, Y.I., and Faisal, F.H.M. (1996). *Phys. Rev. A* **54**, 4383.
50. Salamin, Y.I., and Faisal, F.H.M. (1997). *Phys. Rev. A* **55**, 3678.
51. Salamin, Y.I., and Faisal, F.H.M. (1997). *Phys. Rev. A* **55**, 3964.
52. Salamin, Y.I., and Faisal, F.H.M. (1998). *J. Phys. A* **31**, 1319.
53. Lösch, F. (ed.) (1960). "Jahnke–Emde–Lösch, Tables of Higher Functions" (6th ed.). Teubner, Stuttgart.
54. Farkas, Gy., Tóth, Cs., Moustaizis, S.D., Papadogiannis, N.A., and Fotakis, C. (1992). *Phys. Rev. A* **46**, R3605.
55. Farkas, Gy., Tóth, Cs., Köházi-Kis, A., Agostini, P., Petite, G., Martin, P., Berset, J.M., and Ortega, J.M. (1998). *J. Phys. B* **31**, L461.
56. Varró, S., and Ehlotzky, F. (1994). *Phys. Rev. A* **49**, 3106.
57. Georges, A.T. (1996). *Phys. Rev. A* **54**, 2412.
58. Kohlweyer, S., Tsakiris, G.D., Wahlström, C.-G., Tillman, C., and Mercer, I. (1995). *Opt. Commun.* **117**, 431.
59. von der Linde, D., Engers, T., Jenke, G., Agostini, P., Grillon, G., Nibbering, E., Mysyrowicz, A., and Antonetti, A. (1995). *Phys. Rev. A* **52**, R25.
60. Lichters, R., Meyer-ter-Vehn, J., and Pukhov, A. (1996). *Phys. Plasmas* **3**, 3425.
61. Varró, S., and Ehlotzky, F. (1996). *Phys. Rev. A* **54**, 3245.
62. Varró, S., and Ehlotzky, F. (1997). *J. Phys. D* **30**, 3071.
63. Varró, S., and Ehlotzky, F. (1998). *Phys. Rev. A* **57**, 663.
64. Kálmán, P., and Brabec, T. (1995). *Phys. Rev. A* **52**, R21.
65. Faisal, F.H.M., and Kamiński, J.Z. (1996). *Phys. Rev. A* **54**, R1769.
66. Faisal, F.H.M., and Kamiński, J.Z. (1997). *Phys. Rev. A* **56**, 748.
67. Faisal, F.H.M., and Kamiński, J.Z. (1998). *Phys. Rev. A* **58**, R19.
68. Schwengelbeck, U., Plaja, L., Conejero Jarque, E., Roso, L., Varró, S., and Farkas, Gy. (2002). *J. Phys. B* **35**, L181.
69. Ehlotzky, F. (1978). *Opt. Commun.* **25**, 221.
70. Ehlotzky, F. (1987). *J. Phys. B* **20**, 2619.
71. Ehlotzky, F. (1989). *J. Phys. B* **22**, 601.
72. Neville, R.A., and Rohrlich, F. (1971). *Phys. Rev. D* **3**, 1692.
73. Ehlotzky, F. (1970). *Acta Phys. Austr.* **31**, 18; **31**, 31.
74. Englert, T.J., and Rinehart, E.A. (1983). *Phys. Rev. A* **28**, 1539.
75. Hartemann, F.V., and Kerman, A.K. (1996). *Phys. Rev. Lett.* **76**, 624.
76. Eberly, J.H., and Reiss, H.R. (1966). *Phys. Rev.* **145**, 1035, and references therein.
77. Körmendi, F.F., and Farkas, Gy. (1999). *Phys. Rev. A* **59**, 4172.
78. Leubner, C. (1981). *Phys. Rev. A* **23**, 2877.
79. Bleistein, N. (1967). *J. Math. Mech.* **17**, 533.
80. Ursell, F. (1972). *Proc. Cambridge Philos. Soc.* **72**, 49.
81. Nikishov, A.I., and Ritus, V.I. (1964). *Zh. Éksp. Teor. Fiz.* **46**, 776 [(1964). *Sov. Phys. JETP* **19**, 529]; (1964). *ibid.* **46**, 1768 [(1964). *ibid.* **19**, 1191].
82. Reiss, H.R. (1962). *J. Math. Phys.* **3**, 59; (1962). *ibid.* **3**, 387.
83. Reiss, H.R. (1980). *Phys. Rev. A* **22**, 1786, and references therein.
84. Schiff, L.I. (1968). "Quantum Mechanics." (3rd ed.) McGraw-Hill, New York.

85. Walser, M.W., Urbach, D.J., Hatsagortsyan, K.Z., Hu, S.X., and Keitel, C.H. (2002). *Phys. Rev. A* **65**, 043410.

86. Walser, M.W., and Keitel, C.H. (2001). *Opt. Commun.* **199**, 447.

87. San Román, J., Plaja, L., and Roso, L. (2001). *Phys. Rev. A* **64**, 063402.

88. Kirsebom, K., Mikkelsen, U., Uggerhøj, E., Elsener, K., Ballestrero, S., Sona, P., and Vilakazi, Z.Z. (2001). *Phys. Rev. Lett* **87**, 054801.

89. Panek, P., Kamiński, J.Z., and Ehlotzky, F. (2002). *Phys. Rev. A* **65**, 022712.

90. Gordon, W. (1926). *Z. Phys.* **40**, 117.

91. Ehlotzky, F. (1988). *Opt. Commun.* **66**, 265.

92. Bjorken, J.D., and Drell, S.D. (1964). "Relativistic Quantum Mechanics." McGraw-Hill, New York.

93. Volkov, D.M. (1935). *Z. Phys.* **94**, 250.

94. Denisov, M.M., and Fedorov, M.V. (1967). *Zh. Éksp. Teor. Fiz.* **53**, 1340 [(1968). *Sov. Phys. JETP* **26**, 779].

95. Schoenlein, R.W., Leemans, W.P., Chin, A.H., Volfbeyn, P., Glover, T.E., Balling, P., Zolotorev, M., Kim, K.J., Chattopadhyay, S., and Shank, C.V. (1996). *Science* **274**, 236.

96. Leemans, W.P., Schoenlein, R.W., Volfbeyn, P., Chin, A.H., Glover, T.E., Balling, P., Zolotorev, M., Kim, K.J., Chattopadhyay, S., and Shank, C.V. (1996). *Phys. Rev. Lett.* **77**, 4182.

97. Leemans, W.P., Schoenlein, R.W., Volfbeyn, P., Chin, A.H., Glover, T.E., Balling, P., Zolotorev, M., Kim, K.J., Chattopadhyay, S., and Shank, C.V. (1997). *IEEE J. Quantum Electron.* **QE-33**, 1925.

98. Ting, A., Fischer, R., Fisher, A., Moore, C.I., Hafizi, B., Elton, R., Krushelnik, K., Burris, R., Jackel, S., Evans, K., Weaver, J.N., Sprangle, P., Esarey, E., Baine, M., and Ride, S. (1996). *Nucl. Instrum. Meth. A* **375**, 68.

99. Kotaki, H., Kando, M., Dewa, H., Kondo, S., Watanabe, T., Ueda, T., Kinoshita, K., Yoshii, K., Uesaka, M., and Nakajima, K. (2000). *Proc. SPIE* **3935**, 149.

100. Endo, A., Kobayashi, K., Takasago, K., Ito, S., Yang, J., Okada, Y., Yorozu, M., Sakai, F., and Aoki, Y. (2000). *SPIE* **4144**, 16.

101. Yorozu, M., Yang, J.F., Okada, Y., Yanagida, T., Sakai, F., and Endo, A. (2001). *Jpn. J. Appl. Phys.* **40**, 4228.

102. Yorozu, M., Yang, J.F., Okada, Y., Yanagida, T., Sakai, F., Takasago, K., Ito, S., and Endo, A. (2002). *Appl. Phys. B* **74**, 327.

103. Keldysh, L.V. (1964). *Zh. Éksp. Teor. Fiz.* **47**, 1945 [(1965). *Sov. Phys. JETP* **20**, 1307].

104. Bunkin, F.V., and Fedorov, M.V. (1966). *Zh. Éksp. Teor. Fiz.* **49**, 1215 [(1966). *Sov. Phys. JETP* **22**, 844].

105. Bergou, J. (1980). *J. Phys. A* **13**, 2817.

106. Pert, G.J. (1996). *J. Phys. B* **29**, 1135.

107. Faisal, F.H.M. (1974). *Phys. Lett.* **50A**, 193.

108. Faisal, F.H.M. (1987). "Theory of Multiphoton Processes." Plenum, New York.

109. Mittleman, M.H. (1993). "Introduction to the Theory of Laser–Atom Interactions." Plenum, New York.

110. Rosenberg, L. (1982). *Adv. At. Mol. Phys.* **18**, 1.

111. Mittleman, M.H. (1982). *Comments At. Mol. Phys.* **11**, 91.

112. Fedorov, M.V. (1981). *Prog. Quant. Electr.* **7**, 73.

113. Gavrila, M., and van der Wiel, M. (1978). *Comments At. Mol. Phys.* **8**, 1.

114. Francken, P., and Joachain, C.J. (1990). *J. Opt. Soc. Am. B* **7**, 554.

115. Jung, C. (1979). *Phys. Rev. A* **20**, 1585.

116. Kroll, N.M., and Watson, K.M. (1973). *Phys. Rev. A* **8**, 804.

117. Mittleman, M.H. (1979). *Phys. Rev. A* **19**, 134.

118. Bivona, S., Burlon, R., Zangara, R., and Ferrante, G. (1985). *J. Phys. B* **18**, 3149.
119. Weingartshofer, A., Holmes, J.K., Caudle, G., Clarke, E.M., and Krüger, H. (1977). *Phys. Rev. Lett.* **39**, 269.
120. Weingartshofer, A., Clarke, E.M., Holmes, J.K., and Jung, C. (1979). *Phys. Rev. A* **19**, 2371.
121. Weingartshofer, A., Holmes, J.K., Sabbagh, J., and Chin, S.L. (1983). *J. Phys. B* **16**, 1805.
122. Weingartshofer, A., and Jung, C. (1984). In S.L. Chin and P. Lambropoulos (eds.) "Multiphoton Ionization of Atoms." Academic, New York, p. 155.
123. Wallbank, B., Holmes, J.K., and Weingartshofer, A. (1987). *J. Phys. B* **20**, 6121.
124. Wallbank, B., Connors, V.W., Holmes, J.K., and Weingartshofer, A. (1987). *J. Phys. B* **20**, L833.
125. Wallbank, B., and Holmes, J.K. (1993). *Phys. Rev. A* **48**, R2515.
126. Wallbank, B., and Holmes, J.K. (1994). *J. Phys. B* **27**, 1221.
127. Wallbank, B., and Holmes, J.K. (1994). *J. Phys. B* **27**, 5405.
128. Rabadán, I., Méndez, L., and Dickinson, A.S. (1994). *J. Phys. B* **27**, L535.
129. Geltman, S. (1995). *Phys. Rev. A* **51**, R34.
130. Varró, S., and Ehlotzky, F. (1995). *Phys. Lett. A* **203**, 203.
131. Varró, S., and Ehlotzky, F. (1995). *J. Phys. B* **28**, L673.
132. Dickinson, A.S. (1996). *J. Phys. B* **29**, 1569.
133. Robicheaux, F. (1996). *J. Phys. B* **29**, 2367.
134. Madsen, L.B., and Taulbjerg, K. (1995). *J. Phys. B* **28**, 5327.
135. Madsen, L.B., and Taulbjerg, K. (1997). *J. Phys. B* **30**, 1599.
136. Geltman, S. (1996). *Phys. Rev. A* **53**, 3473.
137. Rabadán, I., Méndez, L., and Dickinson, A.S. (1996). *J. Phys. B* **29**, L801.
138. Cionga, A., Dimou, L., and Faisal, F.H.M. (1997). *J. Phys. B* **30**, L361.
139. Milošević, D.B., and Ehlotzky, F. (1997). *J. Phys. B* **30**, 2999.
140. Wallbank, B., and Holmes, J.K. (1996). *J. Phys. B* **29**, 5881.
141. Geltman, S. (1997). *Phys. Rev. A* **55**, 3755.
142. Wallbank, B., and Holmes, J.K. (2001). *Can. J. Phys.* **79**, 1246.
143. Sun, J., Zhang, S., Jiang, Y., and Yu, G. (1998). *Phys. Rev. A* **58**, 2225.
144. Jaroń, A., and Kamiński, J.Z. (1997). *Phys. Rev. A* **56**, R4393.
145. Buckingham, R.A. (1937). *Proc. Roy. Soc. A* **160**, 94.
146. Madsen, L.B., and Taulbjerg, K. (1998). *J. Phys. B* **31**, 4701.
147. Madsen, L.B., and Taulbjerg, K. (2000). *J. Phys. B* **33**, 2869.
148. Kylstra, N.J., and Joachain, C.J. (1998). *Phys. Rev. A* **58**, R26.
149. Kylstra, N.J., and Joachain, C.J. (1999). *Phys. Rev. A* **60**, 2255.
150. Garland, L.W., Jaroń, A., Kamiński, J.Z., and Potvliege, R.M. (2002). *J. Phys. B* **35**, 2861.
151. Szymanowski, C., Véniard, V., Taïeb, R., Maquet, A., and Keitel, C.H. (1997). *Phys. Rev. A* **56**, 3846 and references therein.
152. Brehme, H. (1971). *Phys. Rev. C* **3**, 837.
153. Schlessinger, L., and Wright, J. (1979). *Phys. Rev. A* **20**, 1934.
154. Bergou, J., and Varró, S. (1980). *J. Phys. A* **13**, 2823.
155. Faisal, F.H.M., and Radożycki, T. (1993). *Phys. Rev. A* **47**, 4464.
156. Morales, F., Ferrante, G., and Daniele, R. (1997). *Nuovo Cimento* **19** D, 23.
157. Kamiński, J.Z. (1985). *J. Phys. A* **18**, 3365.
158. Milošević, D.B., and Krstić, P.S. (1988). *J. Phys. B* **21**, L303.
159. Milošević, D.B., and Krstić, P.S. (1989). *Phys. Rev. A* **39**, 1783.
160. Ehlotzky, F. (1970). *Nuovo Cimento* **69** B, 73.
161. Ehlotzky, F. (1978). *Opt. Commun.* **27**, 65.
162. Prakash, H., and Chandra, N. (1968). *Nuovo Cimento* **55** B, 404.

163. Panek, P., Kamiński, J.Z., and Ehlotzky, F. (2002). *Phys. Rev. A* **65**, 033408.
164. Kamiński, J.Z., and Ehlotzky, F. (1999). *Phys. Rev. A* **59**, 2105.
165. Panek, P., Kamiński, J.Z., and Ehlotzky, F. (2000). *Can. J. Phys.* **77**, 591.
166. Kamiński, J.Z., Panek, P., and Ehlotzky, F. (2000). *Laser Phys.* **10**, 163.
167. Agostini, P., Fabre, F., Mainfray, G., Petite, G., and Rahman, N.K. (1979). *Phys. Rev. Lett.* **42**, 1127.
168. Kruit, P., Kimman, J., Muller, H.G., and van der Wiel, M.J. (1983). *Phys. Rev. A* **28**, 248.
169. Faisal, F.H.M. (1973). *J. Phys. B* **6**, L89.
170. Kamiński, J.Z., Jaroń, A., and Ehlotzky, F. (1996). *Phys. Rev. A* **53**, 1756.
171. Kuchiev, M.Yu. (1987). *Pis'ma Zh. Éksp. Teor. Fiz.* **45**, 319 [(1987). *JEPT Lett.* **45**, 404].
172. Kulander, K.C., Schafer, K.J., and Krause, J.L. (1993). In B. Piraux, A. L'Huillier and K. Rzażewski (eds.). "*Super-Intense Laser-Atom Physics. Vol.* **316** *of NATO Advanced Studies Institute, Series B: Physics.*" Plenum, New York, p. 95.
173. Corkum, P.B. (1993). *Phys. Rev. Lett.* **71**, 1994.
174. Becker, W., Lohr, A., and Kleber, M. (1995). *Quantum Semiclass. Opt.* **7**, 423.
175. Salières, P., L'Huillier, A., Antoine, Ph., and Lewenstein, M. (1999). *Adv. At. Mol. Opt. Phys.* **41**, 83.
176. Gallagher, T.F. (1988). *Phys. Rev. Lett.* **61**, 2304.
177. van Linden van den Heuvell, H.B., and Muller, H.G. (1988). In S.J. Smith and P.L. Knight (eds.). "*Multiphoton Processes.*" Univ. Press, Cambridge.
178. Gallagher, T.F., and Scholz, T.J. (1989). *Phys. Rev. A* **40**, 2762.
179. Tate, D.A., Papaioannou, D.G., and Gallagher, T.F. (1990). *Phys. Rev. A* **42**, 5703.
180. L'Huillier, A., Lewenstein, M., Salières, P., Balcou, Ph., Ivanov, M.Yu., Larsson, J., and Wahlström, C.G. (1993). *Phys. Rev. A* **48**, R3433.
181. Lewenstein, M., Balcou, Ph., Ivanov, M.Yu., L'Huillier, A., and Corkum, P.B. (1994). *Phys. Rev. A* **49**, 2117.
182. Keitel, C.H. (2001). *Contemp. Physics* **42**, 353.
183. Hu, S.X., and Keitel, C.H. (1999). *Europhys. Lett.* **47**, 318.
184. Hu, S.X., and Keitel, C.H. (1999). *Phys. Rev. Lett.* **83**, 4709.
185. Urbach, D.J., and Keitel, C.H. (2000). *Phys. Rev. A* **61**, 043409.
186. Hu, S.X., and Keitel, C.H. (2001). *Phys. Rev. A* **63**, 053402.
187. Keitel, C.H., and Hu, S.X. (2002). *Appl. Phys. Lett.* **80**, 541.
188. Casu, M., and Keitel, C.H. (2002). *Europhys. Lett.* **58**, 496.
189. Prager, J., and Keitel, C.H. (2002). *J. Phys. B* **35**, L167.
190. Hu, S.X., and Starace, A.F. (2002). *Phys. Rev. Lett.* **88**, 245003.
191. Salamin, Y.I., and Keitel, C.H. (2002). *Phys. Rev. Lett.* **88**, 095005.
192. Salamin, Y.I., and Keitel, C.H. (2000). *Appl. Phys. Lett.* **77**, 1082.
193. Fu, L-B, Liu, J., and Chen, S-G. (2002). *Phys. Rev. A* **65**, 021406(R).
194. Reiss, H.R. (1990). In C.A. Nicolaides, C.W. Clark, and M.H. Nayfeh (eds.). "Atoms in Strong Fields." Plenum, New York, p. 425.
195. Muller, H.G., Agostini, P., and Petite, G. (1992). In M. Gavrila (ed.). Atoms in Intense Laser Fields. Adv. At. Mol. Opt. Phys. Suppl. 1, Academic, New York, p. 1.
196. Schafer, K.J., Yang, B., DiMauro, L.F., and Kulander, K.C. (1993). *Phys. Rev. Lett.* **70**, 1599.
197. Yang, B., Schafer, K.J., Walker, B., Kulander, K.C., Agostini, P., and DiMauro, L.F. (1993). *Phys. Rev. Lett.* **71**, 3770.
198. Paulus, G.G., Nicklich, W., Xu, H., Lambropoulos, P., and Walther, H. (1994). *Phys. Rev. Lett.* **72**, 2851.
199. Paulus, G.G., Nicklich, W., and Walther, H. (1994). *Europhys. Lett.* **27**, 267.
200. Paulus, G.G., Nicklich, W., Zacher, F., Lambropoulos, P., and Walther, H. (1996). *J. Phys. B* **29**, L249.

201. Walker, B., Sheehy, B., Kulander, K.C., and DiMauro, L.F. (1996). *Phys. Rev. Lett*. **77**, 5031.
202. Nandor, M.J., Walker, M.A., and Van Woerkom, L.D. (1998). *J. Phys. B* **31**, 4617.
203. Nandor, M.J., Walker, M.A., Van Woerkom, L.D., and Muller, H.G. (1999). *Phys. Rev. A* **60**, R1771.
204. Muller, H.G. (1999). *Phys. Rev. A* **60**, 1341.
205. Reiss, H.R. (1996). In H.G. Muller and M.V. Fedorov (eds.). "Super-Intense Laser-Atom Physics IV." Kluwer, Dordrecht, p. 143.
206. Kulander, K.C., Schafer, K.J., and Krause, J.L. (1992). In M. Gavrila (ed.). Atoms in Intense Laser Fields. Adv. At. Mol. Opt. Phys. Suppl. 1, Academic, New York, p. 247.
207. Rottke, H., Wolff-Rottke, B., Feldmann, D., Welge, K.H., Dörr, M., Potvliege, R.M., and Shakeshaft, R. (1994). *Phys. Rev. A* **49**, 4837.
208. Cormier, E., and Lambropoulos, P. (1997). *J. Phys. B* **30**, 77.
209. Huens, E., Piraux, B., Bugacov, A., and Gajda, M. (1997). *Phys. Rev. A* **55**, 2132.
210. Dionissopoulou, S., Mercouris, Th., Lyras, A., and Nicolaides, C.A. (1997). *Phys. Rev. A* **55**, 4397.
211. Ermolaev, A.M., Puzynin, I.V., Selin, A.V., and Vinitsky, S.I. (1999). *Phys. Rev. A* **60**, 4831.
212. Glass, D.H., and Burke, P.G. (2000). *J. Phys. B* **33**, 407.
213. Cormier, E., Garzella, D., Breger, P., Agostini, P., Chériaux, G., and Leblanc, C. (2001). *J. Phys. B* **34**, L9.
214. Reiss, H.R. (1990). *Phys. Rev. A* **42**, 1476.
215. Kamiński, J.Z., and Ehlotzky, F. (1997). *Phys. Rev. A*. **55**, 4625.
216. Kamiński, J.Z., and Ehlotzky, F. (1997). *J. Phys. B* **30**, 69.
217. Kamiński, J.Z., and Ehlotzky, F. (1997). *J. Phys. B* **30**, 5729.
218. Milošević, D.B., and Ehlotzky, F. (1998). *J. Phys. B* **31**, 4149.
219. Lewenstein, M., Kulander, K.C., Schafer, K.J., and Bucksbaum, P.H. (1995). *Phys. Rev. A* **51**, 1495.
220. Becker, W., Lohr, A., and Kleber, M. (1994). *J. Phys. B* **27**, L325. (1995). Corrigendum: *J. Phys. B* **28**, 1931.
221. Lohr, A., Kleber, M., Kopold, R., and Becker, W. (1997). *Phys. Rev. A* **55**, R4003.
222. Paulus, G.G., Zacher, F., Walther, H., Lohr, A., Becker, W., and Kleber, M. (1998). *Phys. Rev. Lett*. **80**, 484.
223. Kopold, R., and Becker, W. (1999). *J. Phys. B* **32**, L419.
224. Milošević, D.B., and Ehlotzky, F. (1998). *Phys. Rev. A* **57**, 5002.
225. Milošević, D.B., and Ehlotzky, F. (1998). *Phys. Rev. A* **58**, 3124.
226. Kamiński, J.Z. (1986). *Phys. Scripta* **34**, 770.
227. Kamiński, J.Z. (1990). *Phys. Scripta* **42**, 417.
228. Kamiński, J.Z. (1988). *Phys. Rev. A* **37**, 622.
229. Kamiński, J.Z. (1990). *J. Phys. C* **2**, 7719.
230. Krstić, P.S., and Milošević, D.B. (1987). *J. Phys. B* **20**, 3487.
231. Shakeshaft, R., and Potvliege, R.M. (1987). *Phys. Rev. A* **36**, 5478.
232. Mittleman, M.H. (1994). *Phys. Rev. A* **50**, 3249.
233. Milošević, D.B., and Piraux, B. (1996). *Phys. Rev. A* **54**, 1522.
234. Robert, D. (1998). *Helv. Phys. Acta* **71**, 44.
235. Akhiezer, A.I., and Berestetskii, V.B. (1965). "Quantum Electrodynamics." Interscience, New York.
236. Milošević, D.B., and Ehlotzky, F. (1999). *J. Phys. B* **32**, 1585.
237. Radzig, A.A., and Smirnov, B.M. (1985). "Reference Data on Atoms, Molecules and Ions." Springer, Berlin.

238. Cowan, R.D. (1981). "The Theory of Atomic Structure and Spectra." Univ. California Press, Berkeley.
239. Shevelko, V.P. (1997). "Atoms and Their Spectroscopic Properties." Springer, Berlin.
240. Hüpper, B., Main, J., and Wunner, G. (1995). *Phys. Rev. Lett.* **74**, 2650; (1996). *Phys. Rev. A* **53**, 744.
241. Drukarev, G.F. (1965). "The Theory of Electron-Atom Collisions." Academic, London.
242. Paulus, G.G., Becker, W., Nicklich, W., and Walther, H. (1994). *J. Phys. B* **27**, L703.
243. Paulus, G.G., Becker, W., and Walther, H. (1995). *Phys. Rev. A* **52**, 4043.
244. Gaarde, M.B., Schafer, K.J., Kulander, K.C., Sheehy, B., Kim, D., and DiMauro, L.F. (2000). *Phys. Rev. Lett.* **84**, 2822.
245. Paulus, G.G., Grasbon, F., Dreischuh, A., Walther, H., Kopold, R., and Becker, W. (2000). *Phys. Rev. Lett.* **84**, 3791.
246. Paulus, G.G., Grasbon, F., Walther, H., Kopold, R., and Becker, W. (2001). *Phys. Rev. A* **64**, 021401(R).
247. Borca, B., Frolov, M.V., Manakov, N.L., and Starace, A.F. (2002). *Phys. Rev. Lett.* **88**, 193001.
248. Duchateau, G., Cormier, E., Bachau, H., and Gayet, R. (2001). *Phys. Rev. A* **63**, 053411.
249. Duchateau, G., Cormier, E., and Gayet, R. (2000). *Eur. Phys. J. D* **11**, 191.
250. Jain, M., and Tzoar, N. (1978). *Phys. Rev. A* **18**, 538.
251. Larochelle, S.F.J., Talebpour, A., and Chin, S.L. (1998). *J. Phys. B* **31**, 1215.
252. Perelomov, A.M., Popov, V.S., and Terent'ev, M.V. (1966). *Zh. Éxp. Teor. Fiz.* **50**, 1393 [(1966). *Sov. Phys. JETP* **23**, 924].
253. Perelomov, A.M., and Popov, V.S. (1967). *Zh. Éxp. Teor. Fiz.* **52**, 514 [(1967). *Sov. Phys. JETP* **25**, 336].
254. Perelomov, A.M., Popov, V.S., and Kuznetsov, V.P. (1968). *Zh. Éxp. Teor. Fiz.* **54**, 451 [(1968). *Sov. Phys. JETP* **27**, 451].
255. Krainov, V.P. (1997). *J. Opt. Soc. Am B* **14**, 425.
256. Ehlotzky, F. (1990). *Opt. Commun.* **77**, 309.
257. Kornev, A.F., and Zon, B.A. (2002). *J. Phys. B* **35**, 2451.
258. Madsen, L.B. (2002). *Phys. Rev. A* **65**, 053417.
259. Paulus, G.G., Grasbon, F., Walther, H., Villoresi, P., Nisoli, M., Stagira, S., Priori, E., and De Silvestri, S. (2001). *Nature* (London) **414**, 182.
260. Milošević, D.B., Paulus, G.G., and Becker, W. (2002). *Phys. Rev. Lett.* **89**, xxx.
261. Muller, H.G., and Kooiman, F.C. (1998). *Phys. Rev. Lett.* **81**, 1207.
262. Muller, H.G. (1999). *Phys. Rev. Lett.* **83**, 3158.
263. Ammosov, M.V., Delone, N.B., and Krainov, V.P. (1986). *Zh. Éxp. Teor. Fiz.* **91**, 2008 [(1986). *Sov. Phys. JETP* **64**, 1191].
264. Delone, N.B., and Krainov, V.P. (1998). *Usp. Fiz. Nauk.* **168**, 531 [ *Physics Uspekhi* **41**, 469] and further references therein.
265. McNaught, S.J., Knauer, J.P., and Meyerhofer, D.D. (1998). *Phys. Rev. A* **58**, 1399.
266. Goreslavskii, S.P., and Popruzhenko, S.V. (1998). *Phys. Lett. A* **249**, 477.
267. Goreslavskii, S.P., and Popruzhenko, S.V. (1999). *J. Phys. B* **32**, L531.
268. Goreslavskii, S.P., and Popruzhenko, S.V. (2000). *Zh. Éxp. Teor. Fiz.* **117**, 895 [(2000). *JETP* **90**, 778].
269. Popov, V.S. (2000). *Zh. Éxp. Teor. Fiz.* **118**, 56 [(2000). *JETP* **91**, 48].
270. Smirnov, M.B., and Krainov, V.P. (1998). *J. Phys. B* **31**, L519.
271. Smirnov, M.B. (2000). *Phys. Scripta* **61**, 75.
272. Scrinzi, A., Geissler, M., and Brabec, T. (1999). *Phys. Rev. Lett.* **83**, 706 and references therein.
273. Ortner, J. (2000). *J. Phys. B* **33**, 383.

274. Krainov, V.P. (1999). *J. Phys. B* **32**, 1607.
275. Avetissian, H.K., Markossian, A.G., and Mkrtchian, G.F. (2001). *Phys. Rev. A* **64**, 053404.
276. Taïeb, R., Véniard, V., and Maquet, A. (2001). *Phys. Rev. Lett.* **87**, 053002.
277. Roy, A.K., and Chu, S.I. (2002). *Phys. Rev. A* **65**, 043402 and references quoted therein.
278. Teubner, U., Wülker, C., Theobald, W., and Förster, E. (1995). *Phys. Plasmas* **2**, 972.
279. Andreev, A.A., Teubner, U., Kurnin, I.V., and Förster, E. (2000). *Appl. Phys. B* **70**, 505.
280. Platonenko, V.T., and Strelkov, V.V. (1998). *Kvant. Elektron.* **25**, 582 [(1998). *Quantum Electron.* **28**, 564].
281. Hahn, Y. (1997). *Rep. Progr. Phys.* **60**, 691.
282. Jaroń, A., Kamiński, J.Z., and Ehlotzky, F. (2000). *Phys. Rev. A* **61**, 023404.
283. Kuchiev, M.Yu., and Ostrovsky, V.N. (2000). *Phys. Rev. A* **61**, 033414.
284. Jaroń, A., Kamiński, J.Z., and Ehlotzky, F. (1999). *Opt. Commun.* **163**, 115.
285. Jaroń, A., Kamiński, J.Z., and Ehlotzky, F. (2001). *Laser Phys.* **11**, 174.
286. Jaroń, A., Kamiński, J.Z., and Ehlotzky, F. (2001). *Phys. Rev. A* **63**, 055401.
287. Jaroń, A., Kamiński, J.Z., and Ehlotzky, F. (2001). *J. Phys. B* **34**, 1221.
288. Leone, C., Bivona, S., Burlon, R., and Ferrante, G. (2003). *Laser Phys.* (to be published).
289. Milošević, D.B., and Ehlotzky, F. (2002). *Phys. Rev. A* **65**, 042504.
290. Milošević, D.B., and Ehlotzky, F. (2002). *J. Mod. Opt.* (in press).
291. Salières, P., Carré, B., Le Déroff, L., Grasbon, F., Paulus, G.G., Walther, H., Kopold, R., Becker, W., Milošević, D.B., Sanpera, A., and Lewenstein, M. (2001). *Science* **292**, 902.
292. Kopold, R., Milošević, D.B., and Becker, W. (2000). *Phys. Rev. Lett.* **84**, 3831.
293. Hu, S.X., Milošević, D.B., Becker, W., and Sandner, W. (2001). *Phys. Rev. A* **64**, 013410.
294. Hu, S.X., Starace, A.F., Becker, W., Sandner, W., and Milošević, D.B. (2002). *J. Phys. B* **35**, 627.
295. Muller, H.G., van Linden van den Heuvell, H.B., and van der Wiel, M.J. (1986). *J. Phys. B* **19**, L733.
296. Schins, J.M., Breger, P., Agostini, P., Constantinescu, R.C., Muller, H.G., Grillon, G., Antonetti, A., and Mysyrowicz, A. (1994). *Phys. Rev. Lett.* **73**, 2180.
297. Glover, T.E., Schoenlein, R.W., Chin, A.H., and Shank, C.V. (1996). *Phys. Rev. Lett.* **76**, 2468.
298. Freund, I. (1973). *Opt. Commun.* **8**, 401.
299. Ehlotzky, F. (1975). *Opt. Commun.* **13**, 1.
300. Ehlotzky, F. (1981). *Opt. Commun.* **40**, 135.
301. Ehlotzky, F. (1978). *Phys. Lett.* **69A**, 24.
302. Ehlotzky, F. (1989). *J. Phys. B* **22**, 601.
303. Tzoar, N., and Jain, M. (1976). *Opt. Commun.* **19**, 417.
304. Tzoar, N., and Jain, M. (1978). *Opt. Commun.* **24**, 153.
305. Jain, M., and Tzoar, N. (1977). *Phys. Rev A* **15**, 147.
306. Ferrante, G., Fiordilino, E., and Lo Cascio, L. (1981). *Phys. Lett.* **81A**, 261.
307. Ferrante, G., Fiordilino, E., and Rapisarda, M. (1981). *J. Phys. B* **14**, L497.
308. Miranda, L.C.M. (1981). *Phys. Lett.* **86A**, 363.
309. Ferrante, G., Fiordilino, E., and Leone, C. (1982). *Phys. Lett.* **92A**, 276.
310. Fiordilino, E., and Mittleman, M.H. (1983). *Phys. Rev. A* **28**, 229.
311. Dörr, M., and Shakeshaft, R. (1987). *Phys. Rev. A* **36**, 421.
312. Fonseca, A.L.A., and Nunes, O.A.C. (1988). *Phys. Rev. A* **37**, 400.
313. Leone, C., Bivona, S., Burlon, R., and Ferrante, G. (1988). *Phys. Rev. A* **38**, 5642.
314. Kálmán, P. (1989). *Phys. Rev. A* **39**, 2428.
315. Kálmán, P. (1988). *Phys. Rev. A* **38**, 5458.
316. Kálmán, P. (1989). *Phys. Rev. A* **39**, 3200.

317. Bivona, S., Burlon, R., Leone, C., and Ferrante, G. (1989). *Nuovo Cimento D* **11**, 1751.

318. Ehlotzky, F. (1992). *Can. J. Phys.* **70**, 731.

319. Cionga, A., Florescu, V., Maquet, A., and Taïeb, R. (1993). *Phys. Rev. A* **47**, 1830.

320. Joachain, C.J. (1975). "Quantum Collision Theory." North-Holland, Amsterdam.

321. Paul, P.M., Toma, E.S., Breger, P., Mullot, G., Augé, F., Balcou, Ph., Muller, H.G., and Agostini, P. (2001). *Science* **292**, 1689.

322. Toma, E.S., Muller, H.G., Paul, P.M., Breger, P., Cheret, M., Agostini, P., Le Blanc, C., Mullot, G., and Cheriaux, G. (2000). *Phys. Rev. A* **62**, 061801(R).

323. Scrinzi, A., Geissler, M., and Brabec, T. (2001). *Phys. Rev. Lett.* **86**, 412.

324. Kitzler, M., Milosevic, N., Scrinzi, A., Krausz, F., and Brabec, T. (2002). *Phys. Rev. Lett.* **88**, 173904.

325. Milošević, D.B., and Ehlotzky, F. (1998). *Phys. Rev. A* **57**, 2859.

326. Milošević, D.B., and Ehlotzky, F. (1997). *Phys. Rev. A* **56**, 3879.

327. Milošević, D.B., Ehlotzky, F., and Piraux, B. (1997). *J. Phys. B* **30**, 4347.

328. Martin, P., Véniard, V., Maquet, A., Francken, P., and Joachain, C.J. (1989). *Phys. Rev. A* **39**, 6178.

329. Véniard, V., Taïeb, R., and Maquet, A. (1995). *Phys. Rev. Lett.* **74**, 4161.

330. Chang, Z., Rundquist, A., Wang, H., Murnane, M.M., and Kapteyn, H.C. (1997). *Phys. Rev. Lett.* **79**, 2967.

331. Spielmann, C., Burnett, N.H., Sartania, S., Koppitsch, R., Schnürer, M., Kan, C., Lenzner, M., Wobrauschek, P., and Krausz, F. (1997). *Science* **278**, 661.

332. Decker, C.D., and London, R.A. (1998). *Phys. Rev. A* **57**, 1395.

333. Dunn, J., Osterheld, A.L., Shepherd, R., White, W.E., Shlyaptsev, V.N., and Stewart, R.E. (1998). *Phys. Rev. Lett.* **80**, 2825.

334. Heitler, W. (1954). "The Quantum Theory of Radiation." Clarendon, Oxford.

335. Loudon, R. (1983). "The Quantum Theory of Light." Clarendon, Oxford.

336. Gavrila, M. (1967). *Phys. Rev.* **163**, 147.

337. Levinger, J.S. (1952). *Phys. Rev.* **87**, 656.

338. Parente, F. (1983). *J. Phys. B* **16**, 3487.

339. Åberg, T., and Heinäsmäki, S. (1997). *J. Phys. B* **30**, 4827.

340. Ehlotzky, F. (1975). *Z. Phys. A.* **272**, 155.

341. Kálmán, P., Krausz, F., and Wintner, E. (1993). *Phys. Rev. A* **47**, 729.

342. Milošević, D.B., and Ehlotzky, F. (1999). *Laser Phys.* **9**, 149.

343. Milošević, D.B., and Ehlotzky, F. (1998). *Phys. Rev. A* **58**, 2319.

344. Milošević, D.B., and Starace, A.F. (1999). *J. Phys. B* **32**, 1831.

345. Milošević, D.B., and Starace, A.F. (1998). *Phys. Rev. Lett.* **81**, 5097.

346. Milošević, D.B., and Starace, A.F. (2000). *Laser Phys.* **10**, 278.

347. Milošević, D.B., and Starace, A.F. (1999). *Phys. Rev. A* **60**, 3943.

348. Piraux, B., L'Huillier, A., and Rzażewski, K. (eds.). (1993). "*Super-Intense Laser-Atom Physics. Vol.* **316** *of NATO Advanced Studies Institute, Series B: Physics.*" Plenum, New York.

349. Fedorov, M.V. (1997). "Atomic and free electrons in a strong light field." World Scientific, Singapore.

350. Spielmann, Ch., Kan, C., Burnett, N.H., Brabec, T., Geissler, M., Scrinzi, A., Schnürer, M., and Krausz, F. (1998). *IEEE J. of Selected Topics in Quantum Electron.* **4**, 249.

351. McPherson, A., Gibson, G., Jara, H., Johann, U., Luk, T.S., McIntyre, I.A., Boyer, K., and Rhodes, C.K. (1987). *J. Opt. Soc. Am. B* **4**, 595.

352. Ferray, M., L'Huillier, A., Li, F.X., Lompré, L.A., Mainfray, G., and Manus, C. (1988). *J. Phys. B* **21**, L31.

353. Schnürer, M., Spielmann, Ch., Wobrauschek, P., Streli, C., Burnett, N.H., Kan, C., Ferensz, K., Koppitsch, R., Cheng, Z., Brabec, T., and Krausz, F. (1998). *Phys. Rev. Lett.* **80**, 3236.

354. Rundquist, A., Durfee, C.G., Chang, Z.H., Herne, C., Backus, S., Murnane, M.M., and Kapteyn, H.C. (1998). *Science* **280**, 1412.

355. Krause, J.L., Schafer, K.J., and Kulander, K.C. (1992). *Phys. Rev. Lett.* **68**, 3535.

356. Becker, W., Long, S., and McIver, J.K. (1990). *Phys. Rev. A* **41**, 4112.

357. Becker, W., Long, S., and McIver, J.K. (1994). *Phys. Rev. A* **50**, 1540.

358. Milošević, D.B. (2000). *J. Phys. B* **33**, 2479.

359. Bandarage, G., Maquet, A., Ménis, T., Taïeb, R., Véniard, V., and Cooper, J. (1992). *Phys. Rev. A* **46**, 380.

360. Balcou, Ph., and L'Huillier, A. (1993). *Phys. Rev. A* **47**, 1447.

361. Lee, C., Duan, Y., Liu, W.-K., Yuan, J.-M., Shi, L., Zhu, X., and Gao, K. (2001). *Phys. Rev. A* **64**, 043410.

362. Sundaram, B., and Milonni, P.W. (1990). *Phys. Rev. A* **41**, R6571.

363. Di Piazza, A., Fiordilino, E., and Mittleman, M.H. (2001). *Phys. Rev. A* **64**, 013414.

364. Figueira de Morisson Faria, C., and Rotter, I. (2002). *Phys. Rev. A* **66**, 013402.

365. Potvliege, R.M., and Shakeshaft, R. (1989). *Phys. Rev. A* **40**, 3061.

366. Kulander, K.C. (1987). *Phys. Rev. A* **35**, R445.

367. Lambropoulos, P., Maragakis, P., and Zhang, J. (1998). *Phys. Rep.* **305**, 203.

368. Focus issue: *Laser-induced multiple ionization.* (2001). *Optics Express* **8**, No. 7, pp. 351–446.

369. Prager, J., Hu, S.X., and Keitel, C.H. (2001). *Phys. Rev. A* **64**, 045402.

370. Tong, X.M., and Chu, S.I. (1998). *Phys. Rev. A* **57**, 452.

371. Chu, X., and Chu, S.I. (2001). *Phys. Rev. A* **63**, 023411; **64**, 013417; **64**, 063404.

372. Brewczyk, M., and Rzążewski, K. (2001). *J. Phys. B* **34**, L289.

373. Ehlotzky, F. (1992). *Nuovo Cimento* **14** D, 517.

374. Becker, W., Lohr, A., Kleber, M., and Lewenstein, M. (1997). *Phys. Rev. A* **56**, 645.

375. Kuchiev, M.Yu., and Ostrovsky, V.N. (1999). *J. Phys. B* **32**, L189.

376. Kuchiev, M.Yu., and Ostrovsky, V.N. (2001). *Phys. Rev. A* **60**, 3111; *J. Phys. B* **34**, 405.

377. Gao, J., Shen, F., and Eden, J.G. (1998). *Phys. Rev. Lett.* **81**, 1833.

378. Gao, J., Shen, F., and Eden, J.G. (1999). *J. Phys. B* **32**, 4153.

379. Gao, J., Shen, F., and Eden, J.G. (2000). *Phys. Rev. A* **61**, 043812.

380. Gao, L., Li, X., Fu, P., Freeman, R.R., and Guo, D.-S. (2000). *Phys. Rev. A* **61**, 063407.

381. Fu, P., Wang, B., Li, X., and Gao, L. (2001). *Phys. Rev. A* **64**, 063401; Milošević, D.B. (unpublished).

382. Milošević, D.B. (2001). In B. Piraux and K. Rzążewski (eds.). "Super-Intense Laser-Atom Physics." Kluwer, Amsterdam, p. 229.

383. Usachenko, V.I., and Pazdzersky, V.A. (2002). *J. Phys. B* **35**, 761.

384. Borca, B., Flegel, A.V., Frolov, M.V., Manakov, N.L., Milošević, D.B., and Starace, A.F. (2000). *Phys. Rev. Lett.* **85**, 732.

385. Manakov, N.L., Frolov, M.V., Starace, A.F., and Fabrikant, I.I. (2000). *J. Phys. B* **33**, R141.

386. Plummer, M., and Noble, C.J. (2002). *J. Phys. B* **35**, L51.

387. Burnett, K., Reed, V.C., Cooper, J., and Knight, P.L. (1992). *Phys. Rev. A* **45**, 3347.

388. Watson, J.B., Sanpera, A., and Burnett, K. (1995). *Phys. Rev. A* **51**, 1458.

389. Zaretskii, D.F., and Nersesov, E.A. (1996). *Zh. Éksp. Teor. Fiz.* **109**, 1994 [(1996). *JETP* **82**, 1073].

390. Nersesov, E.A., Popruzhenko, S.V., Zaretsky, D.F., and Becker, W. (2000). *Opt. Commun.* **183**, 289.

391. Lewenstein, M., Salières, P., and L'Huillier, A. (1995). *Phys. Rev. A* **52**, 4747.

392. Figueira de Morisson Faria, C., Milošević, D.B., and Paulus, G.G. (2000). *Phys. Rev. A* **61**, 063415.
393. Milošević, D.B., Becker, W., and Kopold, R. (2000). *Phys. Rev. A* **61**, 063403.
394. Milošević, D.B., and Becker, W. (2000). *Phys. Rev. A* **62**, 011403(R).
395. Milošević, D.B., and Sandner, W. (2000). *Opt. Lett.* **25**, 1532.
396. Milošević, D.B., Becker, W., Kopold, R., and Sandner, W. (2001). *Laser Phys.* **11**, 165.
397. Eichmann, H., Egbert, A., Nolte, S., Momma, C., Wellegehausen, B., Becker, W., Long, S., and McIver, J.K. (1995). *Phys. Rev. A* **51**, R3414.
398. Milošević, D.B., and Starace, A.F. (1999). *Phys. Rev. Lett.* **82**, 2653.
399. Milošević, D.B., and Starace, A.F. (1999). *Phys. Rev. A* **60**, 3160.
400. Milošević, D.B., Hu, S., and Becker, W. (2001). *Phys. Rev. A* **63**, 011403(R).
401. Milošević, D.B., Hu, S.X., and Becker, W. (2002). *Laser Phys.* **12**, 389.
402. Walser, M.W., Keitel, C.H., Scrinzi, A., and Brabec, T. (2000). *Phys. Rev. Lett.* **85**, 5082.
403. Kylstra, N.J., Potvliege, R.M., and Joachain, C.J. (2001). *J. Phys. B* **34**, L55.
404. Toma, E.S., Antoine, Ph., de Bohan, A., and Muller, H.G. (1999). *J. Phys. B* **32**, 5843.
405. Gaarde, M.B., and Schafer, K.J. (2001). *Phys Rev. A* **64**, 013820.
406. Chu, X., Chu, S.-I., and Laughlin, C. (2001). *Phys Rev. A* **64**, 013406.
407. Kopold, R., Becker, W., Kleber, M., and Paulus, G.G. (2002). *J. Phys. B* **35**, 217.
408. Figueira de Morisson Faria, C., Kopold, R., Becker, W., and Rost, J.M. (2002). *Phys. Rev. A* **65**, 023404.
409. Borca, B., Starace, A.F., Flegel, A.V., Frolov, M.V., and Manakov, N.L. (2002). *Phys. Rev. A* **65**, 051402(R).
410. Becker, W., Long, S., and McIver, J.K. (1992). *Phys. Rev. A* **46**, R5334.
411. Milošević, D.B., and Becker, W. (2002). *Phys. Rev. A* **66**, 063417.
412. Christov, I.P., Bartels, R., Kapteyn, H.C., and Murnane, M.M. (2001). *Phys. Rev. Lett.* **86**, 5458.
413. Chu, X., and Chu, S.-I. (2001). *Phys. Rev. A* **64**, 021403(R).
414. Roos, L., Gaarde, M.B., and L'Huillier, A. (2001). *J. Phys. B* **34**, 5041.
415. Roos, L., Gaarde, M.B., and L'Huillier, A. (2002). *J. Phys. B* **35**, 745.
416. Bartels, R., Backus, S., Zeek, E., Misoguti, L., Vdovin, G., Christov, I.P., Murnane, M.M., and Kapteyn, H.C. (2000). *Nature (London)* **406**, 164.
417. Tempea, G., Geissler, M., Schnürer, M., and Brabec, T. (2000). *Phys. Rev. Lett.* **84**, 4329.
418. Lee, D.G., Kim, J.-H., Hong K.-H., and Nam, C.H. (2001). *Phys. Rev. Lett.* **87**, 243902.
419. Antoine, Ph., L'Huillier, A., and Lewenstein, M. (1996). *Phys. Rev. Lett.* **77**, 1234.
420. Bellini, M., Lyngå, C., Tozzi, A., Gaarde, M.B., Hänsch, T.W., L'Huillier, A., Wahlström, C.-G. (1998). *Phys. Rev. Lett.* **81**, 297.
421. Balcou, Ph., Dederichs, A.S., Gaarde, M.B., and L'Huillier, A. (1999). *J. Phys. B* **32**, 2973.
422. Lee, D.G., Shin, H.J., Cha, Y.H., Hong, K.-H., Kim, J.-H., and Nam, C.H. (2001). *Phys. Rev. A* **63**, 021801(R).
423. Gavrilenko, V.P., and Oks, E. (2000). *J. Phys. B* **33**, 1629.
424. Watson, J.B., Sanpera, A., Chen, X., and Burnett, K. (1996). *Phys. Rev. A* **53**, R1962.
425. Sanpera, A., Watson, J.B., Lewenstein, M., and Burnett, K. (1996). *Phys. Rev. A* **54**, 4320.
426. Figueira de Morisson Faria, C., and Rost, J.-M. (2000). *Phys. Rev. A* **62**, 051402(R).
427. Tong, X.M., and Chu, S.I. (1999). *J. Phys. B* **32**, 5593.
428. Prokopovich, I.P., Khrutchinsky, A.A., Churmakov, D.Yu., Peatross, J., and Apolonsky, A.A. (2002). *Phys. Rev. A* **65**, 053823.
429. Lyngå, C., L'Huillier, A., and Wahlström, C.-G. (1996). *J. Phys. B* **29**, 3293.
430. Liang, Y., Talebpour, A., Chien, C.Y., Augst, S., and Chin, S.L. (1997). *J. Phys. B* **30**, 1369.
431. Ivanov, M.Yu., and Corkum, P.B. (1993). *Phys. Rev. A* **48**, 580.

432. Zuo, T., Chelkowski, S., and Bandrauk, A.D. (1993). *Phys. Rev. A* **48**, 3837.
433. Kopold, R., Becker, W., and Kleber, M. (1998). *Phys. Rev. A* **58**, 4022.
434. Moreno, P., Plaja, L., and Roso, L. (1997). *Phys. Rev. A* **55**, R1593.
435. Bandrauk, A.D., and Yu, H. (1999). *Phys. Rev. A* **59**, 539.
436. Numico, R., Giulietti, D., Giulietti, A., Gizzi, L.A., and Roso, L. (2000). *J. Phys. B* **33**, 2605.
437. Velotta, R., Hay, N., Mason, M.B., Castillejo, M., and Marangos, J.P. (2001). *Phys. Rev. Lett.* **87**, 183901.
438. Hay, N., Velotta, R., Lein, M., de Nalda, R., Heesel, E., Castillejo, M., and Marangos, J.P. (2002). *Phys. Rev. A* **65**, 053805.
439. Lein, M., Hay, N., Velotta, R., Marangos, J.P., Knight, P.L. (2002). *Phys. Rev. A* **66**, 023805.
440. Hay, N., Castillejo, M., de Nalda, R., Springate, E., Mendham, K.J., and Marangos, J.P. (2000). *Phys. Rev. A* **61**, 053810.
441. Hay, N., de Nalda, R., Halfmann, T., Mendham, K.J., Mason, M.B., Castillejo, M., and Marangos, J.P. (2000). *Phys. Rev. A* **62**, 041803(R).
442. Hay, N., de Nalda, R., Halfmann, T., Mendham, K.J., Mason, M.B., Castillejo, M., and Marangos, J.P. (2001). *Eur. Phys. J. D* **14**, 231.
443. Averbukh, V., Alon, O.E., and Moiseyev, N. (2001). *Phys. Rev. A* **64**, 033411.
444. Ceccherini, F., and Bauer, D. (2001). *Phys. Rev. A* **64**, 033423.
445. Alon, O.E., Averbukh, V., and Moiseyev, N. (1998). *Phys. Rev. Lett.* **80**, 3743.
446. Ceccherini, F., Bauer, D., and Cornolti, F. (2001). *J. Phys. B* **34**, 5017.
447. Slepyan, G.Ya., Maksimenko, S.A., Kalosha, V.P., Herrmann, J., Campbell, E.E.B., and Hertel, I.V. (1999). *Phys. Rev. A* **60**, R777.
448. Slepyan, G.Ya., Maksimenko, S.A., Kalosha, V.P., Gusakov, A.V., and Herrmann, J. (2001). *Phys. Rev. A* **63**, 053808.
449. Alon, O.E., Averbukh, V., and Moiseyev, N. (2000). *Phys. Rev. Lett.* **85**, 5218.
450. Ditmire, T. (1997). *Contemp. Phys.* **38**, 315.
451. Hu, S.X., and Xu, Z.Z. (1997). *Appl. Phys. Lett.* **71**, 2605.
452. Hu, S.X., and Xu, Z.Z. (1997). *Phys. Rev. A* **56**, 3916.
453. Véniard, V., Taïeb, R., and Maquet, A. (1999). *Phys. Rev. A* **60**, 3952.
454. Véniard, V., Taïeb, R., and Maquet, A. (2001). *Phys. Rev. A* **65**, 013202.
455. Tisch, J.W.G. (2000). *Phys. Rev. A* **62**, 041802(R).
456. de Aldana, J.R.V., and Roso, L. (2001). *J. Opt. Soc. Am. B* **18**, 325.
457. Burnett, N.H., Baldis, H.A., Richardson, M.C., and Enright, G.D. (1977). *Appl. Phys. Lett.* **31**, 172.
458. Carman, R.L., Forslund, D.W., and Kindel, J.M. (1981) *Phys. Rev. Lett.* **46**, 29.
459. Carman, R.L., Rhodes, C.K., and Benjamin, R.F. (1981). *Phys. Rev. A* **24**, 2649.
460. Norreys, P.A., Zepf, M., Moustaizis, S., Fews, A.P., Zhang, J., Lee, P., Bakarezos, M., Danson, C.N., Dyson, A., Gibbon, P., Loukakos, P., Neely, D., Walsh, F.N., Wark, J.S., and Dangor, A.E. (1996). *Phys. Rev. Lett.* **76**, 1832.
461. von der Linde, D. (1999). *Appl. Phys. B* **68**, 315.
462. Gibbon, P. (1996). *Phys. Rev. Lett.* **76**, 50.
463. Varró, S., Farkas, Gy., and Ehlotzky, F. (1999). *Opt. Commun.* **172**, 47.
464. Tarasevitch, A., Orisch, A., von der Linde, D., Balcou, Ph., Rey, G., Chambaret, J.-P., Teubner, U., Klöpfel, D., and Theobald, W. (2000). *Phys. Rev. A* **62**, 023816.
465. Hatsagortsyan, K.Z., and Keitel, C.H. (2001). *Phys. Rev. Lett.* **86**, 2277; (2002). *J. Phys. B* **35**, L175.
466. Kobayashi, Y., Ohno, T., Sekikawa, T., Nabekawa, Y., and Watanabe, S. (2000). *Appl. Phys. B: Lasers Opt.* **70**, 389.

467. Descamps, D., Roos, L., Delfin, C., L'Huillier, A., and Wahlström, C.-G. (2001). *Phys. Rev. A* **64**, 031404(R).

468. Schnürer, M., Streli, Ch., Wobrauschek, P., Hentschel, M., Kienberger, R., Spielmann, Ch., and Krausz, F. (2000). *Phys. Rev. Lett.* **85**, 3392.

469. Salières, P., Le Déroff, L., Auguste, T., Monot, P., d'Oliveira, P., Campo, D., Hergott, J.-F., Merdji, H., and Carré, B. (1999). *Phys. Rev. Lett.* **83**, 5483.

470. Descamps, D., Lyngå, C., Norin, J., L'Huillier, A., Wahlström, C.-G., Hergott, J.-F., Merdji, H., Salières, P., Bellini, M., and Hänsch, T.W. (2000). *Opt. Lett.* **25**, 135.

471. Zewail, A. (2000). Femtochemistry: Atomic scale dynamics of the chemical bond (adapted from the Nobel lecture) *J. Phys. Chem. A* **104**, 5660–5694.

472. Papadogiannis, N.A., Witzel, B., Kalpouzos, C., and Charalambidis, D. (1999). *Phys. Rev. Lett.* **83**, 4289.

473. Hertz, E., Papadogiannis, N.A., Nersisyan, G., Kalpouzos, C., Halfmann, T., Charalambidis, D., and Tsakiris, G.D. (2001). *Phys. Rev. A* **64**, 051801(R).

474. Tempea, G., Scrinzi, A., Krausz, F., and Brabec, T. (2001). *Phys. Rev. Lett.* **87**, 109401.

475. Papadogiannis, N.A., Witzel, B., Kalpouzos, C., and Charalambidis, D. (2001). *Phys. Rev. Lett.* **87**, 109402.

476. Milosevic, N., Scrinzi, A., and Brabec, T. (2002). *Phys. Rev. Lett.* **88**, 093905.

477. Silberberg, Y. (2001). *Nature (London)* **414**, 494.

478. Shapiro, M., Brumer, P. (1986). *J. Chem. Phys.* **84**, 4103.

479. Shapiro, M., Hepburn, J.W., and Brumer, P. (1988). *Chem. Phys. Lett.* **149**, 451.

480. Chan, C.K., Brumer, P., and Shapiro, M. (1991). *J. Chem. Phys.* **94**, 2688.

481. Shapiro, M., and Brumer, P. (1997). In: P. Lambropoulos and H. Walther (eds.). "Multiphoton Processes." Institute of Physics, Bristol, p. 231.

482. Shapiro, M., and Brumer, P. (2000). *Adv. At. Mol. Opt. Phys.* **42**, 287.

483. Lu, S-P., Park, S.M., Xie, Y.G., and Gordon, R.J. (1992). *J. Chem. Phys.* **96**, 6613.

484. Zhu, L.C., Kleiman, V., Li, X.N., Lu, S-P., Trentelman, K., and Gordon, R.J. (1995). *Science* **270**, 77.

485. Gordon, R.J., and Rice, S.A. (1997). *Annu. Rev. Phys. Chem.* **48**, 601.

486. Charron, E., Giusti-Suzor, A., and Mies, F.H. (1995). *J. Chem. Phys.* **103**, 7359.

487. Thompson, M.R., Thomas, M.K., Taday, P.F., Posthumus, J.H., Langley, A.J., Frasinski, L.J., and Codling, K. (1997). *J. Phys. B* **30**, 5755.

488. Bandrauk, A.D., and Chelkowski, S. (2000). *Phys. Rev. Lett.* **84**, 3562.

489. Bandrauk, A.D., Chelkowski, S., Yu, H., and Constant, E. (1997). *Phys. Rev. A* **56**, R2537.

490. Dion, C.M., Bandrauk, A.D., Atabek, O., Keller, A., Umeda, H., and Fujimura, Y. (1999). *Chem. Phys. Lett.* **302**, 215.

491. McCullough, E., Shapiro, M., and Brumer, P. (2000). *Phys. Rev. A* **61**, 041801(R).

492. Shapiro, M., Frishman, E., and Brumer, P. (2000). *Phys. Rev. Lett.* **84**, 1669.

493. Tannor, D.J., and Rice, S.A. (1985). *J. Chem. Phys.* **83**, 5013.

494. Kosloff, R., Rice, S.A., Gaspard, P., Tersigni, S., and Tannor, D.J. (1989). *Chem. Phys.* **139**, 201.

495. Gerdy, J.J., Dantus, M., Bowman, R.M., and Zewail, A.H. (1990). *Chem. Phys. Lett.* **171**, 1.

496. Blanchet, V., Bouchene, M.A., Cabrol, O., and Girard, B. (1995). *Chem. Phys. Lett.* **233**, 491.

497. Kohler, B., Yakovlev, V.V., Che, J., Krause, J.L., Messina, M., Wilson, K.R., Schwentner, N., Whitnell, R.M., Yan, Y-J. (1995). *Phys. Rev. Lett.* **74**, 3360.

498. Lozovoy, V.V., Antipin, S.A., Gostev, F.E., Titov, A.A., Tovbin, D.G., Sarkisov, O.M., Vetchinkin, A.S., Umanskii, S. Ya. (1998). *Chem. Phys. Lett.* **284**, 221.

499. Garraway, B.M., and Suominen, K-A. (1995). *Rep. Prog. Phys.* **58**, 365.

500. Garraway, B.M., and Suominen, K-A. (1998). *Phys. Rev. A* **58**, 440.

501. Ficek, Z., and Freedhoff, H.S. (2000). *Progress in Optics* **XL**, 389.

502. Assion, A., Baumert, T., Helbing, J., Seyfried, V., and Gerber, G. (1996). *Chem. Phys. Lett.* **259**, 488.

503. Meshulach, D., and Silberberg, Y. (1999). *Phys. Rev. A* **60**, 1287.

504. Bardeen, C.J., Yakovlev, V.V., Wilson, K.R., Carpenter, S.D., Weber, P.M., and Warren, W.S. (1997). *Chem. Phys. Lett.* **280**, 151.

505. Manz, J., (1997). In: V. Sundström (ed.). "Femtochemistry and Femtobiology: Ultrafast Reaction Dynamics at Atomic Scale Resolution." Imperial College Press, London, p. 80.

506. Warren, W.S., Rabitz, H., and Dahleh, M. (1993). *Science* **259**, 1581.

507. Schumacher, D.W., and Bucksbaum, P.H. (1996). *Phys. Rev. A* **54**, 4271.

508. Varró, S., and Ehlotzky, F. (1995). *J. Phys. B* **28**, 2729.

509. Milošević, D.B. (1996). *J. Phys. B* **29**, 875.

510. Jaroń, A., Kamiński, J.Z., and Ehlotzky, F. (2001). *Phys. Rev. A* **63**, 055401.

511. Rabadán, I., Méndez, L., and Dickinson, A.S. (1994). *J. Phys. B* **27**, 2089.

512. Rabadán, I., Méndez, L., and Dickinson, A.S. (1996). *J. Phys. B* **29**, 163.

513. Long, S., Becker, W., and McIver, J.K. (1995). *Phys. Rev. A* **52**, 2262.

514. Figueira de Morrison Faria, C., Becker, W., Dörr, M., and Sandner, W. (1999). *Laser Phys.* **9**, 388.

515. Gaarde, M.B., L'Huillier, A., and Lewenstein, M. (1996). *Phys. Rev. A* **54**, 4236.

516. Ivanov, M., Corkum, P.B., Zuo, T., and Bandrauk, A. (1995). *Phys. Rev. Lett.* **74**, 2933.

517. Antoine, Ph., Piraux, B., Milošević, D.B., and Gajda, M. (1996). *Phys. Rev. A* **54**, R1761.

518. Antoine, Ph., Milošević, D.B., L'Huillier, A., Gaarde, M.B., Salières, A., and Lewenstein, M. (1997). *Phys. Rev. A* **56**, 4960.

519. de Bohan, A., Antoine, Ph., Milošević, D.B., and Piraux, B. (1998). *Phys. Rev. Lett.* **81**, 1837.

520. de Bohan, A., Antoine, Ph., Milošević, D.B., Kamta, G.L., and Piraux, B. (1999). *Laser Phys.* **9**, 175.

521. Bao, M.Q., and Starace, A.F. (1996). *Phys. Rev. A* **53**, R3723.

522. Lohr, A., Becker, W., and Kleber, M. (1997). *Laser Phys.* **7**, 615.

523. Wang, B., Li, X., and Fu, P. (1998). *J. Phys. B* **31**, 1961.

524. Zuo, T., Bandrauk, A., Ivanov, M., and Corkum, P.B. (1995). *Phys. Rev. A* **51**, 3991.

525. Zuo, T., and Bandrauk, A. (1995). *J. Nonl. Opt. Phys. Mat.* **4**, 533.

526. Bandrauk, A., Ruel, J., Zuo, T., and Yu, H. (1997). *Int. J. Quant. Chem.* **64**, 613.

527. Preston, S.G., Sanpera, A., Zepf, M., Blyth, W.J., Smith, C.G., Wark, J.S., Key, M.H., Burnett, K., Nakai, M., Neely, D., and Offenberger, A.A. (1996). *Phys. Rev. A* **53**, R31.

528. Donnelly, T.D., Ditmire, T., Neuman, K., Perry, M.D., and Falcone, W. (1996). *Phys. Rev. Lett.* **76**, 2472.

529. Watanabe, S., Kondo, K., Nabekawa, Y., Sagisaka, A., and Kobayashi, Y. (1994). *Phys. Rev. Lett.* **73**, 2692.

530. Figueira de Morrison Faria, C., Dörr, M., Becker, W., and Sandner, W. (1999). *Phys. Rev. A* **60**, 1377.

531. Hasbani, R., Cormier, E., and Bachau, H. (1999). *J. Opt. Soc. Am. B* **16**, 1880.

532. Andiel, U., Tsakiris, G.D., Cormier, E., and Witte, K. (1999). *Europhys. Lett.* **47**, 42.

533. Cormier, E., and Lewenstein, M. (2000). *Eur. Phs. J. D* **12**, 227.

534. Figueira de Morrison Faria, C., and Du, M.L. (2001). *Phys. Rev. A* **64**, 023415.

535. Kulander, K.C. (1987). *Phys. Rev. A* **36**, 2726.

536. L'Huillier, A., Lompre, L.A., Mainfray, G., and Manus, C. (1983). *Phys. Rev. A* **27**, 2503.

537. Fittinghoff, D.N., Bolton, P.R., Chang, B., and Kulander, K.C. (1992). *Phys. Rev. Lett.* **69**, 2642.
538. Walker, B., Sheehy, B., DiMauro, L.F., Agostini, P., Schafer, K.J., and Kulander, K.C. (1994). *Phys. Rev. Lett.* **73**, 1227.
539. Larochelle, S., Talebpour, A., and Chin, S.L. (1998). *J. Phys. B* **31**, 1201.
540. Fittinghoff, D.N., Bolton, P.R., Chang, B., and Kulander, K.C. (1994). *Phys. Rev. A* **49**, 2174.
541. Eichmann, U., Dörr, M., Maeda, H., Becker, W., and Sandner, W. (2000). *Phys. Rev. Lett.* **84**, 3550.
542. Zon, B.A. (1999). *Źh. Eksp. Teor. Fiz.* **116**, 410 [ *JETP* **89**, 219].
543. Weber, Th., Weckenbrock, M., Staudte, A., Spielberger, L., Jagutzki, O., Mergel, V., Afaneh, F., Urbasch, G., Vollmer, M., Giessen, H., and Dörner, R. (2000). *Phys. Rev. Lett.* **84**, 443.
544. Weber, Th., Weckenbrock, M., Staudte, A., Spielberger, L., Jagutzki, O., Mergel, V., Afaneh, F., Urbasch, G., Vollmer, M., Giessen, H., and Dörner, R. (2000). *J. Phys. B* **33**, L127.
545. Weber, Th., Giessen, H., Weckenbrock, M., Urbasch, G., Staudte, A., Spielberger, L., Jagutzki, O., Mergel, V., Vollmer, M., and Dörner, R. (2000). *Nature (London)* **405**, 658.
546. Moshammer, R., Feuerstein, B., Schmitt, W., Dorn, A., Schröter, C.D., Ullrich, J., Rottke, H., Trump, C., Wittmann, M., Korn, G., Hoffmann, K., and Sandner, W. (2000). *Phys. Rev. Lett.* **84**, 447.
547. Feuerstein, B., Moshammer, R., and Ullrich, J., (2000). *J. Phys. B* **33**, L823.
548. Dörner, R., Mergel, V., Jagutzki, O., Spielberger, L., Ullrich, J., Moshammer, R., and Schmidt-Böcking, H. (2000). *Phys. Rep.* **330**, 95.
549. Ullrich, J., Moshammer, R., Dörner, R., Jagutzki, O., Mergel, V., Schmidt-Böcking, H., and Spielberger, L. (1997). *J. Phys. B* **30**, 2917.
550. Witzel, B., Papadogiannis, N.A., and Charalambidis, D. (2000). *Phys. Rev. Lett.* **85**, 2268.
551. Lafon, R., Chaloupka, J.L., Sheehy, B., Paul, P.M., Agostini, P., Kulander, K.C., and DiMauro, L.F. (2001). *Phys. Rev. Lett.* **86**, 2762.
552. Feuerstein, B., Moshammer, R., Fischer, D., Dorn, A., Schröter, C.D., Deipenwisch, J., Crespo Lopez-Urrutia, J.R., Höhr, C., Neumayer, P., Ullrich, J., Rottke, H., Trump, C., Wittmann, M., Korn, G., and Sandner, W. (2001). *Phys. Rev. Lett.* **87**, 043003.
553. Weckenbrock, M., Hattass, M., Czasch, A., Jagutzki, O., Schmidt, L., Weber, T., Roskos, H., Löffler, T., Thomson, M., and Dörner, R. (2001). *J. Phys. B* **34**, L449.
554. Becker, A., and Faisal, F.H.M. (1996). *J. Phys. B* **29**, L197.
555. Becker, A., and Faisal, F.H.M. (1999). *J. Phys. B* **32**, L335.
556. Becker, A., and Faisal, F.H.M. (1999). *Phys. Rev. A* **59**, R3182.
557. Becker, A., and Faisal, F.H.M. (2000). *Phys. Rev. Lett.* **84**, 3546 .
558. Kopold, R., Becker, W., Rottke, H., and Sandner, W. (2000). *Phys. Rev. Lett.* **85**, 3781.
559. Kuchiev, M.Yu. (1995). *J. Phys. B* **28**, 5093.
560. Popruzhenko, S.V., and Goreslavskii, S.P. (2001). *J. Phys. B* **34**, L239.
561. Goreslavskii, S.P., Popruzhenko, S.V., Kopold, R., and Becker, W. (2001). *Phys. Rev. A* **64**, 053402.
562. Dammasch, M., Dörr, M., Eichmann, U., Lenz, E., and Sandner, W. (2001). *Phys. Rev. A* **64**, 061402(R).
563. Sacha, K., and Eckhardt, B. (2001). *Phys. Rev. A* **63**, 043414.
564. Chen, J., Liu, J., Fu, L.B., and Zheng, W.M. (2001). *Phys. Rev. A* **63**, 011404(R).
565. Fu, L.B., Liu, J., Chen, J., and Chen, S.-G. (2001). *Phys. Rev. A* **63**, 043416.
566. Bhardwaj, V.R., Aseyev, S.A., Mehendale, M., Yudin, G.L., Villeneuve, D.M., Rayner, D.M., Ivanov, M.Yu., and Corkum, P.B. (2001). *Phys. Rev. Lett.* **86**, 3522.
567. Yudin, G.L., and Ivanov, M.Yu. (2001). *Phys. Rev. A* **63**, 033404.

568. Watson, J.B., Sanpera, A., Lappas, D.G., Knight, P.L., and Burnett, K. (1997). *Phys. Rev. Lett.* **78**, 1884.

569. Lappas, D.G., Sanpera, A., Watson, J.B., Burnett, K., Knight, P.L., Grobe, R., and Eberly, J.H. (1996). *J. Phys. B* **29**, L619.

570. Burnett, K., Watson, J.B., Sanpera, A., and Knight, P.L. (1998). *Phil. Trans. R. Soc. Lond. A* **356**, 317.

571. Sanpera, A., Watson, J.B., Shaw, S.E.J., Knight, P.L., Burnett, K., and Lewenstein, L. (1998). *J. Phys. B* **31**, L841.

572. Bauer, D. (1997). *Phys. Rev. A* **56**, 3028.

573. Bauer, D., and Ceccherini, F. (1999). *Phys. Rev. A* **60**, 2301.

574. Liu, W.-C., Eberly, J.H., Haan, S.L., and Grobe, R. (1999). *Phys. Rev. Lett.* **83**, 520.

575. Lein, M., Gross, E.K.U., and Engel, V. (2000). *Phys. Rev. Lett.* **85**, 4707.

576. Lein, M., Gross, E.K.U., and Engel, V. (2000). *Phys. Rev. A* **64**, 023406.

577. Lein, M., Gross, E.K.U., and Engel, V. (2000). *J. Phys. B* **33**, 433.

578. Zhang, J., and Lambropoulos, P. (1995). *J. Phys. B* **28**, L101.

579. Scrinzi, A., and Piraux, B. (1997). *Phys. Rev. A* **56**, R13.

580. van der Hart, H.W., and Burnett, K. (2000). *Phys. Rev. A* **62**, 013407.

581. Taylor, K.T., Parker, J.S., Dundas, D., Smyth, E., and Vivirito, S. (1999). *Laser Phys.* **9**, 98.

582. Dundas, D., Taylor, K.T., Parker, J.S., and Smyth, E.S. (1999). *J. Phys. B* **32**, L231.

583. Parker, J.S., Moore, L.R., Smyth, E.S., and Taylor, K.T. (2000). *J. Phys. B* **33**, 1057.

584. Parker, J.S., Moore, R.L., Meharg, K.J., Dundas, D., and Taylor, K.T. (2001). *J. Phys. B* **34**, L69.

585. Parker, J.S., Moore, R.L., and Taylor, K.T. (2001). *Opt. Express* **8**, 436.

586. Dörr, M. (2000). *Opt. Express* **6**, 111.

587. Muller, H.G. (2001). *Opt. Express* **8**, 417.

# HOT ATOMS IN THE TERRESTRIAL ATMOSPHERE

*VIJAY KUMAR\* and E. KRISHNAKUMAR*

*Tata Institute of Fundamental Research, Homi Bhabha Road,*
*Colaba, Mumbai-400 005, India*

## I. Introduction

The translationally energetic atoms, sometimes called hot/fast/energetic atoms, can be produced in the planetary atmospheres, interstellar medium and in the laboratory, both in ground and excited electronic states. In the terrestrial atmosphere, hot O, H, and N atoms are produced in the mesosphere and the lower thermosphere by different processes like dissociative recombination, collisional quenching, photodissociation, and

\*Present address: Institute for Plasma Research, Near Indira Bridge, Bhat, Gandhinagar – 382 428, India.
E-mail: ekkumar@tifr.res.in

photoelectron-impact dissociation. In the stratosphere, hot oxygen atoms are produced by photodissociation of ozone. In the interstellar medium, the interaction of stellar UV radiation with ice mixtures, especially nonpolar ice mixtures, leads to photolysis. As a result, hot atoms are liberated. The role of hot atoms in the terrestrial atmosphere could be understood only through the combined effort from different areas of activity. This includes quantum chemical calculations of potential energy surfaces and reaction dynamics, measurements of various branching ratios and cross sections, numerical as well as experimental simulation of the thermalization, *in situ* measurements of the velocity distribution of various species with specific internal energies, and modeling of the atmospheric processes.

The field of collision studies of fast atoms with other atoms/molecules is still in infancy. Though specific atom – molecule reactive scatterings have been investigated from the point of view of chemical dynamics at low energies, not much experimental and theoretical work on fast atom collisions relevant to atmospheric processes has been taken up, probably because of lack of thrill and proper motivation. Interest in the subject grew tremendously when it was realized that the optical "shuttle glow" phenomenon in the low-earth orbit was due to recombination of ground state hot O atoms ($\sim 5\,\text{eV}$ energy) in the thermosphere with surface-adsorbed (surface of the space vehicle) nitric oxide leading to formation of nitrogen dioxide in the excited state (Swenson *et al.*, 1985a,b; Orient *et al.*, 1992). Also, the infrared emissions from excited nitric oxide were detected during an experiment onboard space shuttle (Ahmadjian *et al.*, 1992; Zhou *et al.*, 1992) and it was suggested (Oakes *et al.*, 1994) by laboratory simulation experiments that these emissions were due to the reaction of energetic O atoms ($8\,\text{km}\,\text{s}^{-1}$) with molecular nitrogen. Also, cross section measurements in the laboratory for reactions of energetic oxygen atoms with CO, $CO_2$, and $CH_4$ (Upschulte *et al.*, 1992) and energetic nitrogen atoms with molecular oxygen (Caledonia *et al.*, 2000) have given a tremendous boost to this relatively new field. It has now been realized that the energetic atoms could play an important role in the chemical and heat balance of the terrestrial atmosphere through reactive collisions as well as thermalization with ambient/bath gases (Gorecki and Hanazaki, 1994 and references therein; Balakrishnan *et al.*, 1999, 2000 and references therein). The cross sections for energy relaxation and electronic quenching of hot $O(^1D)$ atoms in collision with $O_2$ and $N_2$ have recently been measured (Taniguchi *et al.*, 2000 and references therein) using time-resolved Doppler spectroscopy. In the laboratory, the energetic neutral atom beams of well-defined quantum states can now be produced by accelerating the species as negative or positive ions and neutralizing them using appropriate collision techniques. Also, the accelerated species can be produced directly in the laboratory through a

momentum-transfer step such as in a seeded supersonic beam, or in a plasma-ball explosion (Chutjian and Orient, 1996). The field of gas-phase collisions of fast atoms has suddenly opened up because beam–beam collision experiments are now possible and can be carried out with relatively greater ease.

The review article consists of seven sections. The subject is introduced in this section and the neutral terrestrial atmosphere and the day and nighttime ionosphere are discussed briefly in Section II. A detailed discussion on sources and sinks of hot oxygen and nitrogen atoms in the Earth's atmosphere is taken up in Sections III and IV. Thermalization of hot atoms in collision with ambient/bath gases is discussed in Section V taking into account, translational energy/velocity relaxation, electron quenching of hot atoms and inelastic excitation of product molecules. The computation of elastic cross sections and inelastic cross sections for the above processes and the corresponding Boltzmann kernels for thermalization are discussed in detail. The latest experiments to measure such cross sections are also included. Shuttle glow in the optical as well as infrared regions is discussed in Section VI along with the probable emission mechanisms. The section also contains description of the laboratory experiments to simulate the two types of glows and measurement of excitation cross sections for reactions of fast atoms in collision with ambient gases responsible for producing the glow. Finally, the problem of large NO density measured at an altitude of 105 km, which has so far not been accounted by the latest photochemical models even after including the hot nitrogen chemistry with an energy-dependent thermalization cross section, is discussed in Section VII.


## II. Terrestrial Neutral Atmosphere and Ionosphere

Before the discussion on hot atoms and their chemistry in the terrestrial atmosphere, it is desirable to review the neutral atmosphere and also, the daytime and nighttime ionosphere. In Fig. 1 are shown the variations in the number density of the neutral constituents like O, $O_2$, $N_2$, Ar, H, He, and total as a function of altitude up to 1000 km (Carrigan and Skrivanek, 1974). Widely used neutral atmosphere models by Jacchia (1972, 1977) and Hedin (1987) give similar results under different geophysical conditions. For most practical applications, the neutral atmosphere would be considered to consist mainly of atomic oxygen with traces of molecular oxygen, molecular nitrogen, and atomic hydrogen at altitudes above about 200/250 km. Atomic hydrogen, though, dominates occasionally above 500 km for low exospheric temperatures. Other minor constituents present above 200/250 km are nitric oxide, atomic nitrogen, and argon. Temperature in the terrestrial
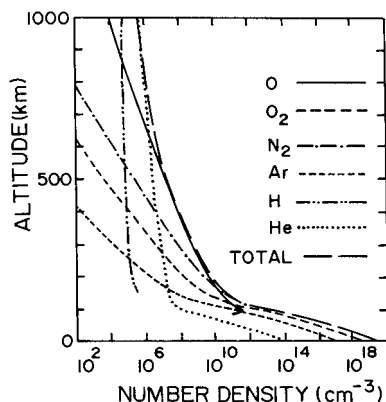
Fig. 1. Neutral atmosphere density profiles for average geophysical conditions on the dayside (Carrigan and Skrivanek, 1974).

atmosphere varies approximately exponentially from about 100 K at 100 km to 500–1000 K at 1000 km, depending up on latitude, local time, and solar cycle index. It may even go to as high as 2000 K at 1000 km during high levels of geomagnetic activity.

Another important parameter in the study of hot atoms is the terrestrial ionosphere. On the sun-lit side of the earth, X-rays and extreme ultraviolet radiation penetrate the neutral atmosphere leading to direct and dissociative ionization of the molecules. The whole process gives rise to photoelectrons, atomic and molecular ions. Figure 2a shows ion composition measured using a mass spectrometer (Johnson, 1966) above 100 km together with electron densities. The F-region above 150 km consists of atomic ions $O^+$ and $N^+$, which are dominant throughout most of the region, but at high altitudes, $H^+$ and $He^+$ are more abundant. Molecular ions ($NO^+$ and $O_2^+$) are the most important ions in the 100–150 km region. Although the mass spectrometric data (Fig. 2a) are quite old, models developed in the later part of 1990s using the best available chemical mechanisms and kinetic data reproduce the observations quite well. Figure 2b shows the predictions of a model developed in connection with European Incoherent **SCAT**ter (**EISCAT**) studies (Diloy *et al.*, 1996). Peaks in the electron concentrations are, in general, associated with different ion populations, $O_2^+$ in the E region and $O^+$ in the F region. Between these two peaks, $NO^+$ is the major ion having a maximum concentration at 180 km. $O^+$ begins to dominate above 190 km. Above the F region peak, $N^+$ becomes an important minor ion; the ratio of $[N^+]/[O^+]$ is about 5% at 1000 km. The concentration of $H^+$ according to the above model, is about 1% that of $O^+$ at 1000 km.
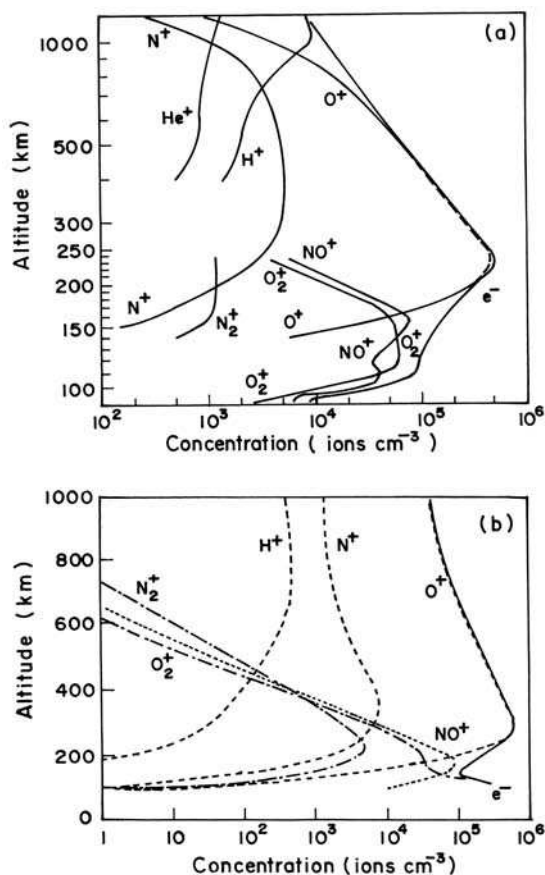
FIG. 2. Ion distributions during daytime: (a) mass spectrometer measurements at solar minimum (Johnson, 1966); (b) modeling for a quiet ionosphere (Diloy et al., 1996).

The ion and electron density profiles for quiescent nighttime conditions near solar maximum (Fig. 3) have been reported in the International Reference Ionosphere by Rawer et al. (1978). The nighttime ionosphere is, mainly, possible because solar radiation at 58.4 and 121.6 nm from dayside gets resonantly scattered into the night side from extended helium and hydrogen geocorona respectively. The 58.4 nm radiation is energetic enough to ionize most of the neutral species where as the radiation at 121.6 nm can ionize only NO molecules. The $N_2^+$ densities are too small to appear in Fig. 3.

The attenuation of solar radiation takes place at all heights of the terrestrial atmosphere. The extent of attenuation depends upon the
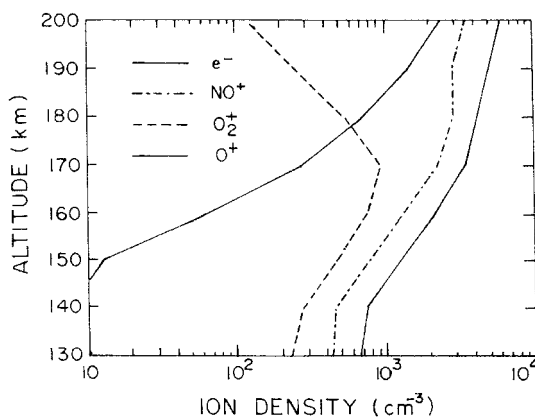
FIG. 3. The altitude profiles of ion and electron densities for quiescent nighttime conditions near solar maximum (Rawer *et al.*, 1978).

photoabsorption cross sections of atoms and molecules and their number densities at those altitudes. The different wavelength regions of the solar spectrum are therefore filtered out at different heights. Molecular oxygen filters out solar ultraviolet radiation at wavelengths between 100 and 200 nm at altitudes between 50 and 110 km, whereas ozone filters the radiation ($\sim$200 $-$300 nm) in the stratosphere.

## III. Sources of Hot Atoms

### A. Hot Oxygen Atoms

The hot oxygen atoms are formed in the Earth's atmosphere by various physical and chemical processes discussed below.

*Photodissociation of molecular oxygen and ozone.* Photodissociation of molecular oxygen by solar ultraviolet radiation is one of the foremost processes leading to the production of hot oxygen atoms at mesospheric and thermospheric heights. These hot atoms are produced not only in the ground state $^3P$, but also in $^1D$ and $^1S$ states by,

$$O_2 + h\nu \rightarrow O(^3P) + O(^3P, {}^1D, {}^1S) \tag{1}$$
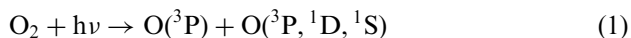
The potential energy curves of molecular oxygen (Fig. 4) show that one of the two atomic fragments produced in the B state because of photoabsorption of molecules in the ground X state is, in fact, itself excited. The
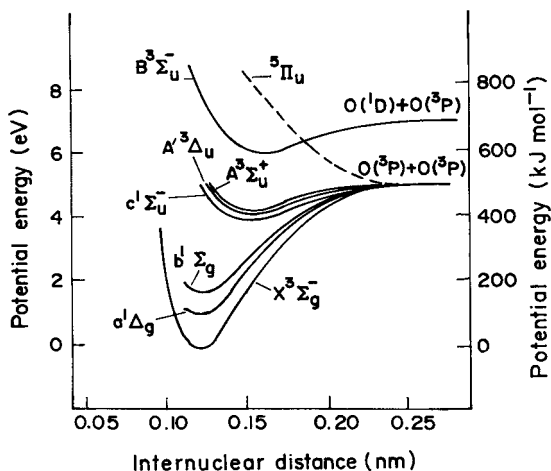
FIG. 4. Potential energy curves for some of the low-lying states of molecular oxygen. The dashed curve ($^5\Pi_u$) is representative of several repulsive states that correlate with the $O(^3P) + O(^3P)$ limit and cause the predissociation of the $B^3\Sigma_u^-$ state (Wayne, 2000).

convergence limit has been observed to be at 175 nm, which corresponds to the formation of one ground state ($^3P$) and one excited ($^1D$) atom. The A←X absorption is weak because it is forbidden for an electric dipole transition, and dissociation into two ground state atoms occurs for photon energies corresponding to its convergence limit. Above the convergence limit, the photoabsorption leads to the formation of energetic atoms with continuous distribution of kinetic energies. Thus, translationally "hot" $O(^3P)$ and $O(^1D)$ atoms are produced. Similar explanation could be given for the production of hot $O(^1S)$ atoms when the photoabsorption to another higher electronic state of $O_2$ takes place leading to dissociation into $O(^3P)$ and $O(^1S)$ or $O(^1D)$ and $O(^1S)$ atoms.

   In the stratosphere, the photodissociation of ozone leads to the formation of $O(^3P)$ along with $O_2(X^3\Sigma_g^-, A^3\Sigma_u^+, B^3\Sigma_u^-)$ states or $O(^1D)$ along with $O_2(^1\Delta_g, ^1\Sigma_g^+)$ states, depending on the photon energy. The O atoms produced may be translationally hot for the incident photon energies larger than the dissociation limit. For example, at 250 nm in the process leading to the formation of $O(^1D)$ and $O_2(^1\Delta_g)$, the excess energy is about 22 kcal mol$^{-1}$. The resultant translation energy of $O(^1D)$ atom is about 15 kcal mol$^{-1}$ in the space-fixed frame.

   *Dissociative recombination.* It was initially suggested (Rohrbaugh and Nisbet, 1973) that hot oxygen atoms in the F region of the terrestrial ionosphere could be produced by dissociative recombination of $O_2^+$ and

$NO^+$ with thermal electrons. This is, now, known to be one of the major processes for producing hot oxygen atoms in the daytime and probably the foremost process for nighttime production. In the case of $O_2^+$, the following processes release substantial energy to be shared equally between the atoms as kinetic energy:

$$O_2^+ + e \rightarrow O(^3P) + O(^3P) + 6.95\,eV \tag{2}$$

$$O_2^+ + e \rightarrow O(^3P) + O(^1D) + 4.98\,eV \tag{3}$$

$$\rightarrow O(^1D) + O(^1D) + 3.06\,eV \tag{4}$$

$$\rightarrow O(^1D) + O(^1S) + 0.79\,eV \tag{5}$$
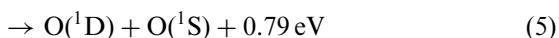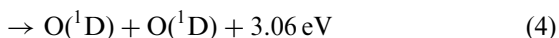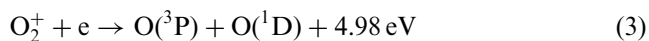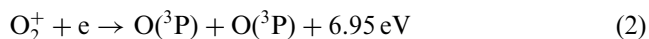
Assuming that the $O_2^+$ ions are in the ground vibrational level, the branching ratios for different reactions (2), (3), (4), and (5) have been reported to be 0.22:0.42:0.31:0.05 in an ion storage ring measurement (Kella *et al.*, 1997). In the case of $NO^+$, the reactions,

$$NO^+ + e \rightarrow N(^2D) + O(^3P) + 0.38eV \tag{6}$$

$$\rightarrow N(^4S) + O(^3P) + 2.75eV \tag{7}$$
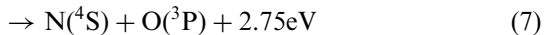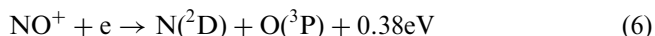
produce O atoms with energies of 0.18 and 1.28 eV respectively.

*Exothermic chemical reactions.* The third process to produce hot O atoms is exothermic chemical reactions. A set of 27 such reactions have been identified (Richards *et al.*, 1994; Hickey *et al.*, 1995) leading to the formation of hot $O(^3P)$ and $O(^1D)$ atoms. Most of these reactions were not considered earlier because they involve metastable species whose importance was established only through the Atmospheric Explorer (AE) programme (Torr and Torr, 1982). Metastable species contain electronic energy, which can be transferred to translational energy in quenching process. The metastable $N(^2D)$ produced very efficiently in the thermosphere through photodissociation has an electronic energy of 2.4 eV. When $N(^2D)$ is quenched by atomic oxygen, the electronic energy is made available as translational energy for the two product atoms, $N(^4S)$ and O which would then both be hot. The importance of the new chemical sources for hot oxygen geocorona, has been discussed in detail by Gérard *et al.* (1995).

Experimental evidence for the existence of hot oxygen in the thermosphere, was first presented by Yee *et al.* (1980) who made indirect

observations of hot O atoms from twilight measurements of $O^+$ emission at
732 nm. A number density of $10^5$ to $10^6$ cm$^{-3}$ at an altitude of 550 km, was
reported with a temperature of 4000 K or higher. Further experimental
evidence was supplied by Hedin (1989), who inferred densities of 1 to
$3 \times 10^5$ cm$^{-3}$ at 550 km based on differences between models on satellite
drag and mass spectrometer measurements and $5 \times 10^5$ to $2 \times 10^6$ cm$^{-3}$
at 1100 km from a limited number of Dynamics Explorer (DE) mass
spectrometer measurements. In another experiment during September 1988,
the Berkley EUV airglow rocket spectrometer (BEARS) made high-
resolution measurements of atomic oxygen day glow emissions at 135.6,
130.4, 102.7, and 98.9 nm between 150 and 960 km (Cotton *et al.*, 1993a).
It was found that the modeled 130.4 and 98.9 nm emissions underestimated
the measured intensities. Later on, Cotton *et al.* (1993b) reanalyzed the data
incorporating the effects of non-LTE on the $^3P_{2,1,0}$ sublevel populations and
a hot O component in the upper thermosphere and lower exosphere was
added to investigate the effects on the modeled emissions. A comparison of
the new results with those using a standard LTE model shows that hot O
geocorona has a peak intensity of $10^6$ cm$^{-3}$ at 550 km and a temperature of
4000 K as shown in Fig. 5. The figure also shows the mass spectrometer/
incoherent scatter (MSIS) model O densities. A more recent analysis
(Hubert *et al.*, 1999) has shown that the calculated intensity increase
associated with the perturbation of the Doppler profile by the presence of
hot O($^3P$) atoms is insufficient to account for the above sounding rocket
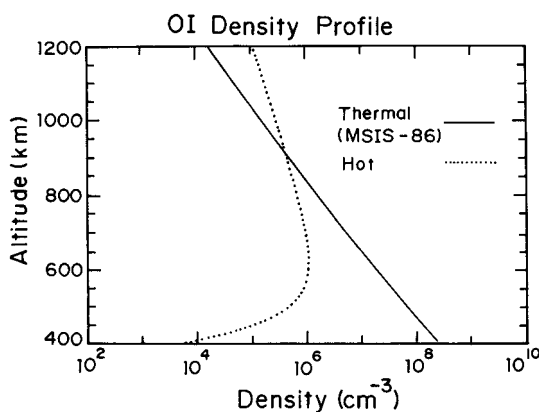


F IG . 5. Density profile for hot oxygen atom corresponding to a translational temperature of
4000 K (dotted line) along with MSIS-86 O-densities (solid curve) (Cotton *et al.*, 1993b.
Reproduced by permission of American Geophysical Union).

data. Reports on the observation of hot metastable $O(^1D)$ and $O(^1S)$ atoms and various models on the hot oxygen geocorona could be found in Hubert *et al.* (2001 and references therein).


## B. HOT NITROGEN ATOMS

Hot nitrogen atoms can be produced in the daytime thermosphere by photon and electron-impact dissociation and ion-chemical processes. The nitrogen atoms, thus, produced in various electronically excited states (principally $^2D$ and $^2P$) as well as in the ground state $(^4S)$ are characterized by thermal energy excess (Zipf and McLaughlin, 1978). The sources of hot nitrogen atoms are discussed below.

- Photodissociation of $N_2$ by solar photons (80–100 nm),

$$N_2 + h\nu \rightarrow N(^4S) + N(^4S, {}^2D, {}^2P) \tag{8}$$
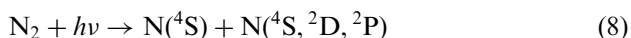
This yields translationally excited $N(^4S)$ atoms with kinetic energies varying from 0.1 to 1.26 eV (Hudson and Carter, 1969). The branching ratio between hot $N(^4S)$ and $N(^2D)$ atoms in the above reaction is usually assumed to be 0.5 : 0.5, with negligible contribution to $N(^2P)$.

- Electron-impact dissociation of $N_2$, is another source of $N(^4S)$ atoms in the daytime atmosphere:

$$N_2 + e \rightarrow N(^4S) + N(^4S, {}^2D, {}^2P) + e \tag{9}$$
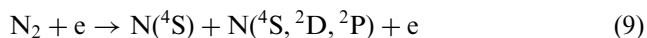
- Other important sources of hot $N(^4S)$ atoms include the recombination, charge transfer and quenching reactions of the type

$$NO^+ + e \rightarrow N(^4S) + O + 2.75 eV \tag{10}$$

$$O^+ + N_2 \rightarrow NO^+ + N(^4S) + 1.09 \, eV \tag{11}$$

$$N^+ + O \rightarrow O^+ + N(^4S) + 0.93 \, eV \tag{12}$$

$$N(^2D) + O \rightarrow O + N(^4S) + 2.38 \, eV \tag{13}$$
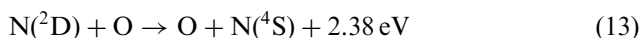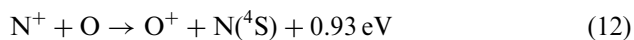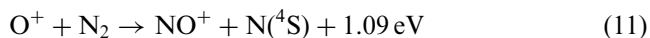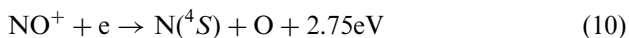
In the last reaction, $N(^2D)$ deactivation by atomic oxygen forms $N(^4S)$ hot atoms with a kinetic energy of about 1.27 eV (Shematovich *et al.*, 1991).

Some of the nocturnal sources of energetic nitrogen atoms in the thermosphere are given below:

(a) Solar radiation at 58.4 nm (He I line) from the dayside gets resonantly scattered into the night side by helium atoms in the extended helium geocorona. This radiation is energetic enough to ionize oxygen atoms. The $O^+$ ions so formed, then, react with $N_2$ (reaction 11) to produce hot $N(^4S)$ atoms with kinetic energies up to 0.74 eV with a temperature-dependent rate coefficient $k_1 = [1.553 - 0.592(T/300) + 0.086(T/300)^2] \times 10^{-12} \, cm^3 \, s^{-1}$ (Roble *et al.*, 1987). Some $O^+$ ions are also produced by charge exchange reaction between oxygen atoms present in the night side atmosphere with $H^+$ ions transported from the dayside.

(b) The resonantly scattered solar Lyman alpha (H I) radiation at 121.6 nm in the extended dayside hydrogen geocorona enters the night side and photoionizes NO molecules to produce $NO^+$ ions. These ions, in turn, undergo dissociative recombination (reaction 10) with a rate coefficient $k = 9.2 \times 10^{-8} \, (T_e/300)^{-0.85} \, cm^3 \, s^{-1}$ where $T_e$ is the electron temperature. Another dissociative recombination process

$$NO^+ + e \rightarrow N(^2D) + O + 0.38 \, eV \tag{14}$$
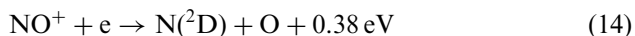
with a rate coefficient $k = 3.3 \times 10^{-7}(T_e/300)^{-0.85} \, cm^3 \, s^{-1}$ gives rise to non-thermal nitrogen atoms in the excited state. The rate coefficients for all the above three reactions were reported by Roble *et al.* (1987).

(c) Following reaction (14), $N(^2D)$ reacts with $O(^3P)$ to form hot $N(^4S)$ atoms at nighttime,

$$N(^2D) + O(^3P) \rightarrow N(^4S) + O(^3P) + 2.38 \, eV \tag{13}$$

$$N(^2D) + O(^3P) \rightarrow N(^4S) + O(^1D) + 0.41 \, eV \tag{15}$$
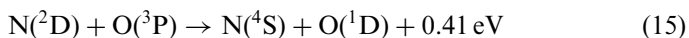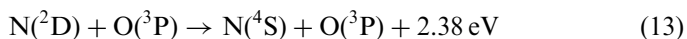
The second reaction is strongly favored (Bates, 1989).

## IV. Sinks of Hot Atoms

A. HOT OXYGEN ATOMS

The main sink for energetic $O(^3P)$ atoms in the upper atmosphere is the chemical reaction

$$O(^3P) + N_2 \rightarrow NO(v,j) + N \tag{16}$$
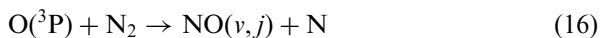
with reaction endothermicity of 3.26 eV. Hot $O(^3P)$ atoms also undergo elastic collisions with other ambient/bath gases like $N_2$, $O_2$, and O. The $O(^3P)$ atoms slowed down by this process involve the transfer of momenta among the colliding partners without introducing any change in their internal states. However, inelastic collisions with molecules in the ambient gas lead to rotational and vibrational excitation of the molecules.

The translationally hot $O(^1D)$ atoms are dominantly removed by three processes: thermalization (translational relaxation) with the bath gas,

$$\text{Fast } O(^1D) + [N_2, O_2, O] \rightarrow \text{Slow } O(^1D) + [N_2, O_2, O] \qquad (17)$$

collisional deactivation or quenching,

$$\text{Fast } O(^1D) + [N_2, O_2, O] \rightarrow \text{Fast } O(^3P) + [N_2, O_2, O] \qquad (18)$$
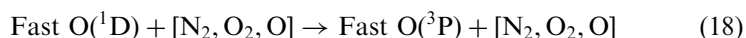
and the spontaneous radiation transition,

$$\text{Fast } O(^1D) \rightarrow \text{Fast } O(^3P) + h\nu \qquad (19)$$
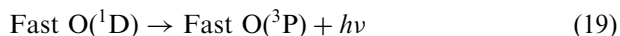
The rate for reaction (19) is described by an Einstein coefficient equal to $0.0056\,\text{s}^{-1}$ (Baluja and Zeippen, 1988).

The main sink for hot oxygen atoms in the stratosphere is through their reactions with $H_2O$, $CH_4$, $N_2O$, and $O_3$. These are all very important reactions from the point of view of stratospheric chemistry (Wayne, 2000).

## B. Hot Nitrogen Atoms

The main sink for hot $N(^4S)$ atoms is the chemical reaction

$$N(^4S) + O_2 \rightarrow NO + O \qquad (20)$$

This is an important source of thermospheric nitric oxide. In addition, the hot nitrogen atoms are thermalized by elastic and inelastic collisions with the ambient/bath gases $N_2$, $O_2$, and O. For hot $N(^2D)$ atoms, in addition to translational energy degradation, electronic quenching, like reactions (13) and (15) acts as a sink.

## V. Thermalization of Hot Atoms in Collision with Bath Gases

The hot atoms, produced in the upper atmosphere, are removed by thermalization. The process includes translational energy or velocity relaxation and electronic quenching of hot atoms in collision with ambient/bath gases. In the case of hot atoms, say $O(^1D)$ atoms, the velocity relaxation reaction

$$\text{Fast } O(^1D) + [N_2, O_2, \text{ or } O] \rightarrow \text{Slow } O(^1D) + [N_2, O_2, \text{ or } O] \qquad (17)$$
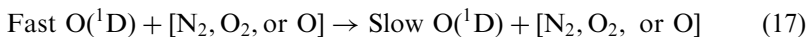
amounts to slowing down of the hot atoms by any of the bath gases. This is an elastic process in which there is a transfer of momenta among the colliding partners but there is no change in their internal state. There could also be inelastic collisions in which the kinetic energy of the atom is transferred to the rotational and vibrational motion of the bath gas molecules. The electronic quenching reaction of the type

$$O(^1D) + [N_2, O_2] \rightarrow O(^3P_j) + [N_2, O_2] \qquad (18)$$
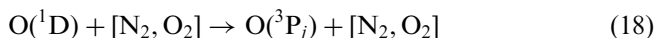
is an inelastic process in which the electronic energy of the atom is transferred to the translational energy of the products and/or the ro-vibrational energy of the molecules. These elastic and inelastic processes are important aspects of thermalization of the hot atoms. A detailed discussion of the experimental and theoretical work on this is given below.

### A. Theoretical Approach

#### A.1. Elastic Collisions

When an atom or molecule with relatively large but narrow velocity distribution is placed in a bath gas of molecules maintained at some equilibrium temperature, the velocity distribution relaxes to a Maxwell–Boltzmann distribution. Any anisotropy in the initial spatial distribution also becomes an isotropic one. This phenomenon is applicable, not only to hot atoms, but also to other collision phenomena involving electrons, ions, or neutrons (Shizgal and Blackmore, 1983, and references therein). Assuming only two-body collisions, the time-dependent velocity distribution is a solution to the Boltzmann integro-differential equation. This nonlinear equation could be linearized when the nonequilibrium component has no internal degrees of freedom and its number density is much smaller than that of the bath gas. In the case of hot $O(^1D)$ atoms in the upper atmosphere,

Shizgal and Blackmore (1983) solved numerically the Boltzmann equation for an initially non-Maxwellian anisotropic velocity distribution dispersed in a thermal bath. The eigen values of the collision operator depend upon the mass ratio ($R = M_b/M$) of the two components and the elastic scattering cross sections. Here, $M_b$ is the mass of the ambient/bath gas colliding component and $M$ is the mass of the hot target atom. For $R \ll 1$, that is, when the bath gas is lighter than the hot target atom, the degradation of the speed is faster than the degradation of the angular anisotropy. For $R \gg 1$, that is, when the bath gas is heavier than the hot target atom, the angular distribution becomes isotropic before appreciable velocity relaxation is achieved. Most of the work done in the past used the hard-sphere model. The hard-sphere approximation facilitates the evaluation of the differential cross section or collision kernel of the Boltzmann equation, but it ignores the energy and angular dependence of the cross sections (Anderson and Schuler, 1974; Shizgal and Blackmore, 1986) as well as the long-range interactions, which may lead to significant errors in the evaluation of the collision kernel. For energies below a few electron volts, where the Van der Waal's forces play an important role in the momentum and energy transfer, the collision cross sections show strong energy and angular dependence (Yee and Dlagarno, 1985, 1986). Kharchenko *et al.* (1998) and Balakrishnan *et al.* (1998a,b, 1999) constructed a procedure to calculate the parameters to describe translational relaxation of the energetic atoms in a bath gas. The procedure constructed by them is briefly described below.

The rate of energy/velocity relaxation of an energetic atom initially at an energy $E$ and a final energy $E'$ (both in the laboratory frame) in collision with an ambient/bath gas atom or molecule is given by the collision kernel, $B(E'|E)$, of the Boltzmann equation. In an isotropic bath gas whose density is much higher than the density of the hot atoms, the energy distribution $f(E, t)$ of the projectile is related to the kernel of the Boltzmann equation (Kharchenko *et al.*, 1998) by

$$\frac{\partial}{\partial t} f(E,t) = \int B(E'|E) f(E',t)\, dE' - f(E,t) \int B(E'|E)\, dE'$$

$$- \xi(E) f(E,t) + S(E,t) \tag{21}$$

where $S(E, t)$ is the rate of production of fast atoms at energy $E$ and $\xi(E)$ is the rate of the sink reactions that remove them. An analytical expression for $B(E'/E)$ has been derived taking into account the rate of binary collisions that change the momenta of the colliding partners from $p$, $p_b$ to $p'$, $p_b'$ in the laboratory frame (Kharchenko *et al.*, 1998); the subscript $b$ refers to the

bath gas. The rate of binary collisions is obtained from the doubly differential cross section, $d^2\sigma / d\Omega d\varepsilon$,

$$W(p',p_b|p,p_b) = \frac{|p - (M/M_b)p_b|}{|p' - (M/M_b)p_b'|} \frac{1}{\mu^2} \frac{d^2\sigma}{d\Omega d\varepsilon} \delta(p' + p_b' - p - p_b) \qquad (22)$$

where the laboratory frame momenta $p$, $p_b$ and $p'$, $p_b'$ are related to the initial and final relative energies $\varepsilon$ and $\varepsilon'$. $\Omega$ is the center of mass scattering angle and $\mu$ is the reduced mass of the atom and the bath gas molecule. The energy relaxation kernel is given by the integral of the rate of binary collisions with the bath gas, which transforms the magnitude of the projectile momentum $p = (2ME)^{1/2}$ to $p' = (2ME')^{1/2}$:

$$B(E'|E) = \frac{N_b M^{3/2}}{2\sqrt{2\pi}\mu^2} \sqrt{E'} \int \sqrt{\frac{\varepsilon}{\varepsilon'}} \frac{d^2\sigma(\varepsilon,\varepsilon',\cos\chi)}{d\Omega d\varepsilon} \rho(p_b)\, dp_b\, d\Omega_p\, d\Omega_{p'} \qquad (23)$$

where $\Omega_p$ and $\Omega_{p'}$ are the solid angles of the initial and final momenta in the laboratory frame for fixed values of $p$ and $p'$; $N_b$ is the density of the bath gas; $\rho(p_b)$ is the distribution function of the bath gas at the bath temperature; $\chi$ is the scattering angle between the initial and final momenta. From the kernel $B(E'|E)$, Kharchenko *et al.* have calculated a few important parameters which are given below. The average rate of energy loss is given by

$$\gamma(E) = \int_0^\infty B(E'|E)(E - E')\, dE' \qquad (24)$$

whereas the frequency of the thermalizing collision is

$$\omega(E) = \int_0^\infty B(E'|E)\, dE' \qquad (25)$$

The inverse of $\omega(E)$ is the mean time spent by the projectile between successive collisions. The ratio $\gamma(E)/\omega(E)$ is the mean energy loss of the projectile atom per collision and is given by

$$\Delta E(E) = \gamma(E)/\omega(E) = \frac{\int_0^\infty B(E'|E)(E - E')}{\int_0^\infty B(E'|E)\, dE'} \qquad (26)$$

Using $dE/dt = -\gamma(E)$, the characteristic time of energy loss of the projectile atom from an initial energy $E_0$ to a final energy $E$ is obtained as

$$t(E) = \int_E^{E_0} \frac{dE'}{\gamma(E')} \tag{27}$$

A small time increment $dt = dn/\omega(E)$ gives

$$dE/dt = dE/dn.\omega(E) = -\gamma(E)$$

$$\text{or} \quad dE/dn = -\gamma(E)/\omega(E) = -\Delta E(E) \tag{28}$$

where $n$ is the total number of collisions. From (28), one can compute the number of collisions required to slow down the fast atoms with initial energy $E_0$ to a final energy $E$:

$$n(E,E_0) = \int_E^{E_0} [1/\Delta E(E')] \, dE' \tag{29}$$

The integral elastic cross sections and the corresponding doubly differential cross sections have to be calculated precisely to evaluate the Boltzmann kernel. Calculations for such cross sections in the case of heavier systems like $N+N_2$, $N+O_2$, $O+N_2$, and $O+O_2$ are computationally prohibitive due to the large number of ro-vibrational levels to be included in the close-coupling calculation and due to the difficulty in obtaining accurate potential energy surfaces. An approximate quantum mechanical scheme based on sudden approximation of rotational motion, was used by Balakrishnan *et al.* (1998a). The infinite order sudden approximation (IOSA) calculations have been extensively applied to atom–diatom non-reactive and reactive scattering processes. The IOSA has been found to be appropriate for collisions between a heavy molecule and a light hot atom for which at higher energies, the basic assumptions behind the approximation are satisfied. In the present case, the calculations involve solving the vibrationally close-coupled radial Schrödinger equation for a number of orientation angles chosen as Gauss–Légendre quadrature points. By averaging over the angle dependence of the $S$-matrix elements, the orientation-averaged IOSA integral cross sections for state-to-state vibrational transitions are obtained:

$$\sigma_{v,v'} = \left(\frac{\pi}{k_v^2}\right) \sum_{l=0}^{\infty} (2l+1) \int_{-1}^{1} \left| S_{v,v'}^l(k_v,\gamma) \right|^2 d\cos\gamma \tag{30}$$

where $\varepsilon$ is the kinetic energy and $k_v$ is the momentum for the incoming channel wavefunction and $v$ and $v'$ are the initial and final vibrational levels. Morse oscillator wavefunctions with an appropriate quadrature rule were used to obtain the matrix elements $S^l_{vv'}$ of the interaction potential. The two lowest vibrational levels of the molecule were included in the coupled equations. A London–Eyring–Polanyi–Sato potential energy surface with an additional attractive term of the form $R^{-6}$ (Laganá and Garcia, 1994) was used to describe the potential energy surface of the hot atom + bath molecule system. Though the potential energy surface was, in general, not accurate to describe all aspects of hot atom + bath molecule collisions, it is believed that its features were realistic enough to provide useful description of hot atom thermalization.

The results obtained from the computations of elastic cross sections for specific hot atom–bath molecule collisions by the method discussed above are shown in Fig. 6. In general, the integral values for the elastic cross sections in all the four cases shown have relatively large values at low energies, with a rather steep drop as the energy is increased. The calculations also show interesting contrast with change in the collision partners. For example, as the bath gas is changed from $N_2$ to $O_2$ for the case of hot $N(^4S)$ atoms, there is a very perceptible difference in the rate at which the cross sections change between 0 and 0.5 eV, leading to more than a factor of two difference in the cross sections at higher energies. A similar contrasting behavior could be seen for the case of $O(^3P)$ and $N(^4S)$ atoms, both in their electronic ground states, colliding with the same bath gas $N_2$. The figure also provides a comparison between the situations where the hot
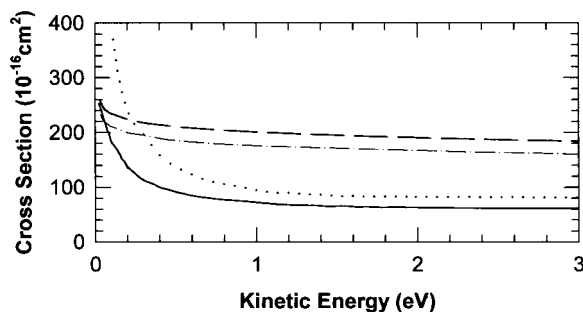


FIG. 6. Integral elastic cross sections for $N(^4S) + N_2$ (solid line: Balakrishnan *et al.*, 1998a), $O(^3P) + N_2$ (dashed line: Balakrishnan *et al.*, 1998b), $O(^1D) + N_2$ (dotted line: Balakrishnan *et al.*, 1999, extrapolated between 2 and 3 eV), and $N(^4S) + O_2$ (dash-dotted line: Balakrishnan *et al.*, 2000) as a function of center-of-mass kinetic energy.

atom is in the ground state (O $^3$P) in one case and in an excited state (O $^1$D) in the other with the same bath gas, $N_2$. The calculations also show relatively larger cross sections at very low energies, when the atom (O $^1$D) is in an excited state, as compared to that in which the atom is in the ground state. The results of these calculations (Balakrishnan *et al.*, 1998a,b, and 1999) could be contrasted with those of Shematovich *et al.* (1999) who used a hard-sphere collision model for the case of O($^1$D) in the terrestrial atmosphere to get an energy independent cross section of $3.0 \times 10^{-15}$ cm$^2$.

In Fig. 7 are shown the Boltzmann kernels in units of eV$^{-1}$ s$^{-1}$ for elastic collisions in two cases of interest. The Boltzmann kernel for the energy relaxation for O($^1$D) + $N_2$ collisions is shown in Fig. 7a for the bath gas density of $3.6 \times 10^{16}$ cm$^{-3}$ and bath temperature of 298 K which corresponds to an altitude of about 50 km in the terrestrial atmosphere where fast O($^1$D) is produced by the photodissociation of $O_3$ and is an important player in the stratospheric chemistry. Shown in Fig. 7b is the Boltzmann kernel for elastic N($^4$S) + $N_2$ collisions for the bath density of $2.743 \times 10^9$ cm$^{-3}$ and the bath temperature of 844 K characteristic of the upper atmosphere at 200 km altitude. Similar calculations for the O($^3$P) + $N_2$ collisions have been carried out for thermospheric conditions (Balakrishnan *et al.*, 1998b). All the Boltzmann kernels are highly anisotropic as the elastic cross sections are dominated by small angle scattering involving small energy losses. The results on translational energy degradation obtained from these calculations are compared with experimental data later.

### A.2. Inelastic collisions

Just like the computation of elastic cross sections for studying the energy/velocity relaxation of hot atoms, the inelastic cross sections for the rotational and vibrational excitation of product molecules have to be calculated precisely to evaluate the corresponding Boltzmann kernel. Thus, the evaluation of the doubly differential cross sections and the integral cross sections is a formidable computational problem. To overcome this difficulty, the semi-classical approach has been employed by Balakrishnan *et al.* (1998a and references therein). In this approach, the degrees of freedom for which the quantum effects are most important, are treated quantum mechanically and the remaining are treated classically. Balakrishnan *et al.* have employed a classical mechanical description for the rotational and relative translational motion of the system and a quantum mechanical treatment for the vibrational motion. The quantum and classical dynamics are solved self-consistently, and transition probabilities to open vibrational levels are obtained by projecting the final wavefunction onto different vibrational states of the bath molecule. Performing the
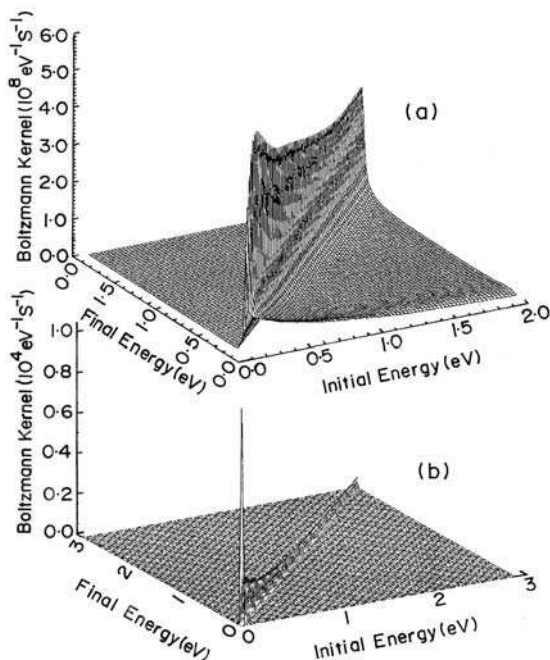
FIG. 7. Boltzmann kernels for thermalization by elastic collisions: (a) $O(^1D) + N_2$ collisions for a bath temperature of 298 K and an $N_2$ density of $3.6 \times 10^{16}$ cm$^{-3}$ (Reprinted with permission from Balakrishnan *et al.*, 1999. Copyright 1999 American Chemical Society); (b) $N(^4S) + N_2$ collisions for an $N_2$ density of $2.743 \times 10^9$ cm$^{-3}$ and temperature of 844 K (Balakrishnan *et al.*, 1998a).

computations for a range of impact parameters and averaging over an ensemble of trajectories with different initial conditions for the classical variables, the energy transfer cross sections for a $(v, v')$ transition have been computed as,

$$\sigma_{v,v'}(\varepsilon) = 2\pi \int P_{v,v'}(b) b \, db \qquad (31)$$

where $b_{max}$ is the maximum value of the impact parameter, $b$. The integral is evaluated by Monte Carlo method. The corresponding doubly differential cross section evaluated in a similar way by Balakrishnan *et al.* provides information regarding the dynamics including final angular and relative translational energy distributions of the scattered products.

In Fig. 8 is shown the inelastic Boltzmann kernel in units of eV$^{-1}$ s$^{-1}$ for $N(^4S) + N_2$ collisions for the bath gas $N_2$ density of $2.743 \times 10^9$ cm$^{-3}$ and bath temperature of 844 K. It is markedly anisotropic as compared to the

hard-sphere model and slightly less localized than its elastic counterpart because of additional energy loss in internal excitation of the molecule. Similar behavior has been seen in the case of $O(^3P) + N_2$ collisions (Balakrishnan *et al.*, 1998b).

The computed elastic and inelastic Boltzmann kernels can be used to derive the average rate of energy loss as well as the frequency of the thermalizing collisions. In Fig. 9a and b are shown the average rates of energy loss of fast $O(^3P)$ and $N(^4S)$ atoms respectively as a function of their initial energy in the laboratory frame for both elastic and inelastic $O(^3P) + N_2$ and $N(^4S) + N_2$ collisions. The average rate of energy loss for $O(^3P)$ atoms is larger than that for $N(^4S)$ atoms for both elastic and inelastic collisions. Also, in the case of both the fast atoms, the average rate of energy loss is much higher for elastic collisions than that for inelastic collisions.

The frequency of thermalizing collisions for both elastic and inelastic $N(^4S) + N_2$ encounters is shown in Fig. 10 as a function of the initial energy of the hot atoms in the laboratory frame. Its inverse is the time between thermalizing collisions. The main contribution of frequency to the elastic part arises from small angle scattering but such collisions are not very effective in energy transfer. For this reason, even though the frequency of elastic collisions is two times larger than that for inelastic collisions (Fig. 10), the latter contribute importantly to the slowing down of hot atoms and thus are only slightly less effective than elastic collisions as illustrated in Fig. 9b.
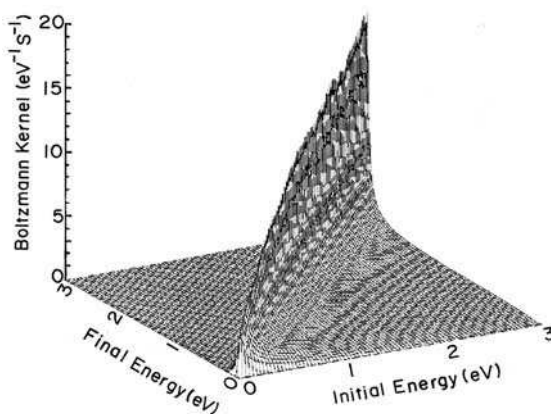


Fig. 8. Boltzmann kernel for inelastic $N(^4S) + N_2$ collisions for a $N_2$ density of $2.743 \times 10^9 \, \text{cm}^{-3}$ and temperature of 844 K (Balakrishnan *et al.*, 1998a).
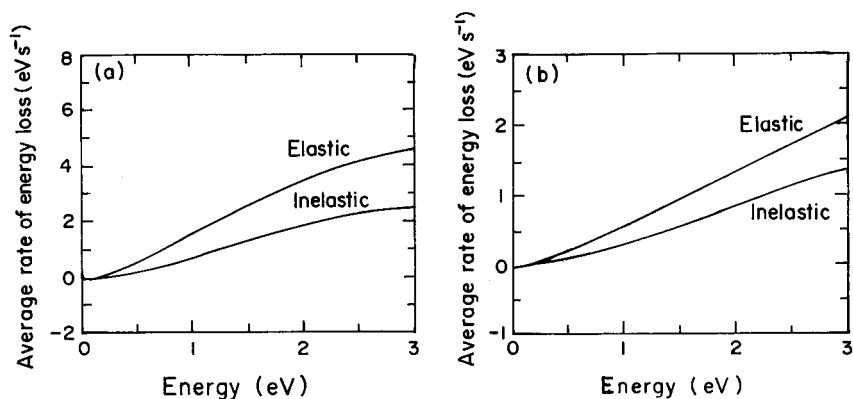
FIG. 9. Average rates of energy loss of fast $O(^3P)$ and $N(^4S)$ atoms as a function of their initial translational energy in the laboratory frame for (a) elastic and inelastic $O(^3P) + N_2$ (Balakrishnan *et al.*, 1998b. Reproduced by permission of American Geophysical Union) and (b) $N(^4S) + N_2$ collisions (Balakrishnan *et al.*, 1998a).
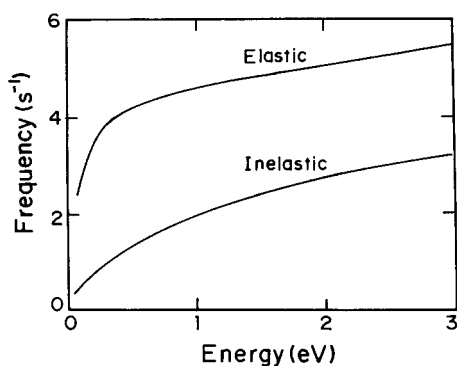


FIG. 10. Frequency of thermalizing collisions for both elastic and inelastic $N(^4S) + N_2$ encounters derived from the corresponding kernels as a function of N atom energy in the laboratory frame (Balakrishnan *et al.*, 1998a).

## B. EXPERIMENTAL APPROACH

Not enough experimental work has been carried out so far to study the translational relaxation of hot atoms. The major difficulty in carrying out the experiments is the preparation and energy measurement of the neutral particles as well as their detection. Unlike charged particles, which could be accelerated and detected using conventional detectors like Faraday cup or

channel electron multipliers, special spectroscopic techniques have to be used for the detection of neutral atoms. Also, preparing the atoms with specific energies and measuring their energies after collisions call for innovative experimental techniques like photodissociation followed by Doppler profile measurements. Park *et al.* (1989) investigated the relaxation of hot H atoms produced in the photodissociation of $H_2S$ by 193 nm laser photons in collision with helium, argon, krypton, xenon, molecular nitrogen, and molecular oxygen by measuring the Doppler profiles of Lyman alpha line in their time-resolved Doppler spectroscopy experiment. Mass of the H atoms being small compared to all collision partners, it was found that the spatial anisotropy was relaxed in a single collision whereas the velocity relaxation was achieved much more slowly. The relaxation processes of the hot $I(^2P_{1/2})$ atoms produced in the photodissociation of $n$-$C_3F_7I$ at 226 nm in collision with parent molecule/helium were reported by Cline *et al.* (1990). In the case of collisions of $I(^2P_{1/2})$ with $n$-$C_3F_7I$, the angular isotropy was found to degrade 2.5 times faster than the velocity degradation where as for iodine–helium collisions, the angular isotropy and the velocity relaxation occurred on the same timescale. Nan and Houston (1992) monitored the velocity relaxation of hot $S(^1D)$ atoms by helium, neon, and xenon. Relaxation processes of translationally hot $O(^1D)$ by collisions with rare gases, $N_2$, and $O_2$ have been studied experimentally by Matsumi *et al.* (1994), Matsumi and Chowdhury (1996) and Taniguchi *et al.* (2000). Similar experiments on hot $O(^3P)$ and $N(^4S)$ are yet to be done. The experimental work of Matsumi and his group would be discussed below in detail.

The experimental setup reported by Matsumi *et al.* (1994) is shown in Fig. 11. The hot $O(^1D)$ atoms were generated by photodissociation of $O_2$ and $N_2O$ with linearly polarized laser light of 157 nm and 193 nm from excimer laser operated in the $F_2$ and ArF modes respectively. The average translational energies of these hot atoms in the laboratory frame produced by the reactions

$$O_2 + h\nu(157\,\text{nm}) \rightarrow O(^1D) + O(^3P_j) \tag{32}$$

$$N_2O + h\nu(193\,\text{nm}) \rightarrow O(^1D) + N_2(v, J) \tag{33}$$
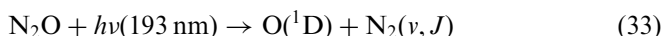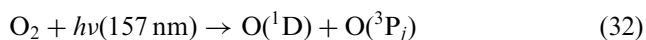
were 9.8 kcal mol$^{-1}$ and 18.2 kcal mol$^{-1}$, which correspond to 0.425 eV and 0.79 eV respectively. The velocity distribution of $O(^1D)$ was determined from the Doppler profiles measured by VUV laser-induced fluorescence (LIF) of $O(3s^1D^o \leftarrow 2p^1D)$ centered at 115.215 nm. The observation direction of the LIF was kept perpendicular to both the photolysis and the probe laser beams and also perpendicular to the polarization of the electric vector of the VUV probe laser. The probe efficiency using this
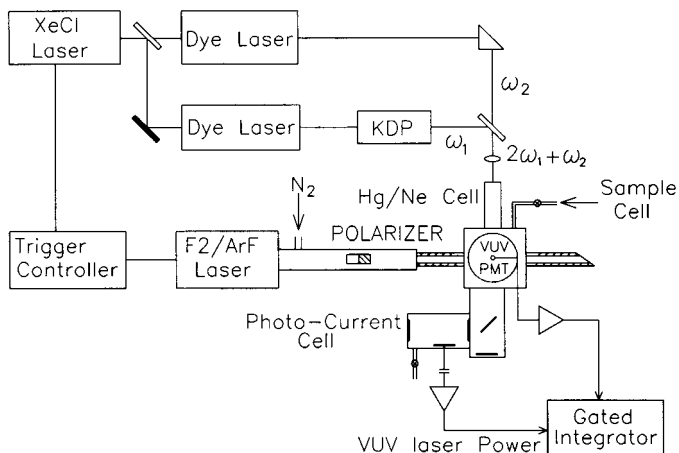
FIG. 11. The experimental setup to study the velocity relaxation of hot O($^1$D) atoms by collisions with bath gases (Matsumi *et al.*, 1994).

detection technique is independent of the polarization anisotropy for the electronic angular momentum of O($^1$D), even if it is produced by the photodissociation process (Springsteen *et al.*, 1993). The resonance frequency of O($^1$D) atom exhibits a Doppler shift of $\Delta v = v_o(\omega/c)$, where $\omega = \mathbf{v}.\mathbf{k_p}$ is the component of the atom's velocity $\mathbf{v}$ along the unit vector $\mathbf{k_p}$ in the direction of propagation of the probe laser and $v_o$ is the center frequency of the atomic transition. The probe laser beam propagated perpendicular to the direction of the dissociation laser beam, $\mathbf{k_d}$. The probe VUV laser light at 115.215 nm was generated by a four-wave sum mixing $(2\omega_1 + \omega_2)$ technique using the two-photon resonance at the $6s6d\,^1D_2$ state of mercury (Hilbig and Wallenstein, 1983). The $\omega_1$ wavelength at 280.3 nm was generated by frequency doubling the dye-laser output in a KDP crystal, and the $\omega_2$ wavelength was 647.0 nm. Both the dye lasers were pumped by a XeCl excimer laser at 308 nm. The intensity of the VUV light was monitored by the photoion current in a NO gas cell with LiF window.

In order to study the electronic quenching of O($^1$D) by the bath gases, the population of O($^3P_j$) atoms produced by the quenching process was monitored using the probe-laser system arranged to observe the VUV–LIF of the $3s\,^3S^0 - 2p\,^3P_j$ transition at 130.22 nm for $j=2$, 130.48 nm for $j=1$, and 130.60 nm for $j=0$. The VUV laser photon wavelength around 130 nm was generated by four-wave difference mixing $(2\omega_1 - \omega_2)$ in krypton gas using two dye lasers pumped by the XeCl excimer laser.

Doppler profiles of the laser excitation spectra at 115.215 nm for $O(^1D)$ at various delay times ($t = 50$–$1000$ ns) between the dissociation laser and the probe laser provided the time evolution of the energy distribution of the atoms. Typical profiles of hot $O(^1D)$ atoms having 0.79 eV initial energy at various delay times with bath gases $N_2$ and $O_2$ are shown in Fig. 12 for two geometrical configurations, $\mathbf{k_p} \parallel \mathbf{E_d}$ and $\mathbf{k_p} \perp \mathbf{E_d}$ where $\mathbf{E_d}$ is the polarization vector of the dissociation laser. Doppler spectra at $t = 0$ have wide widths and different shapes between the two configurations indicating large translational energy and strong anisotropy of the photodissociation process. At long delay times, the Doppler profiles become close to those of thermalized atoms.

Following the analysis procedure described by Matsumi *et al.* (1994), the velocity distributions of the atoms were computed from the Doppler profiles at different delay times to obtain the degradation of the average translational energy as a function of time. The degradation of the average energy of $O(^1D)$ with time as compared to initial energy for $N_2$ as the bath gas is shown in Fig. 13a along with the theoretical values of Balakrishnan *et al.* (1999). Figure 13b shows the translational energy degradation of $O(^1D)$ atoms for bath gas $O_2$ along with the theoretical results using the hard-sphere collision model. Comparison of the experimental results with the computationally obtained data shows a good agreement indicating that the energy losses arise prominently from elastic scattering, with small contribution from inelastic rotational and vibrational excitation.
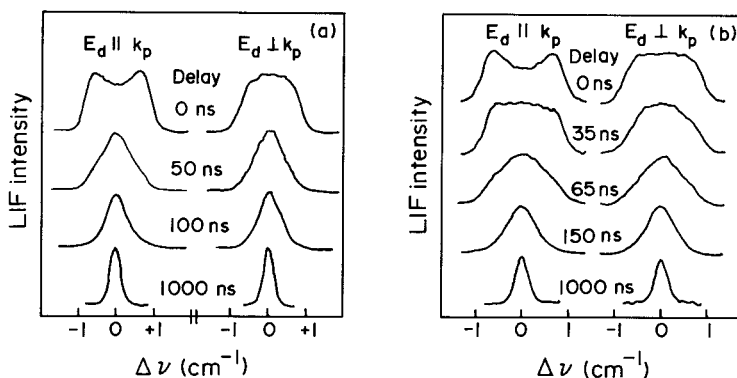


FIG. 12. Doppler profiles for $O(^1D)$ at various delay times between the photodissociation and probe laser pulses. The hot $O(^1D)$ atoms produced by photodissociation have energy of 0.79 eV. (a) Bath gas: $N_2$ (Matsumi and Chowdhury, 1996); (b) Bath gas: $O_2$ (Reprinted with permission from Taniguchi *et al.*, 2000. Copyright 2000 American Chemical Society).
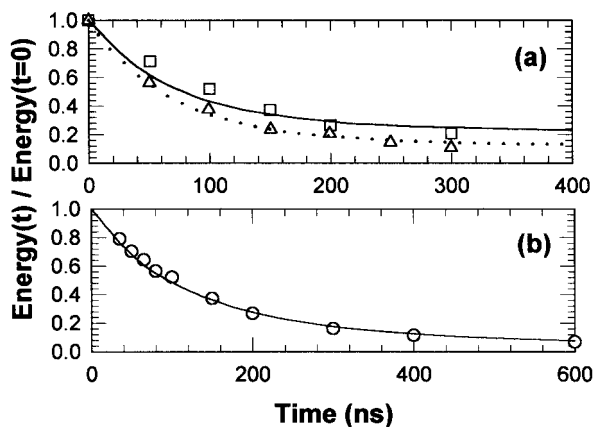
FIG. 13. The translational energy degradation of O($^1$D) atoms in collision with N$_2$ and O$_2$ as a function of delay time. (a) Bath gas N$_2$: Squares (Matsumi and Chowdhury, 1996) and solid line (Balakrishnan *et al.*, 1999) for 0.425 eV initial energy; triangles (Matsumi and Chowdhury, 1996) and dotted line (Balakrishnan *et al.*, 1999) for 0.79 eV initial energy. (b) Bath gas O$_2$: circles (experimental data) and solid line (hard sphere model) for 0.79 eV initial energy (Taniguchi *et al.*, 2000).

## C. QUENCHING AND THERMALIZATION OF O($^1$D)

Apart from the translational energy degradation through elastic and inelastic collisions, the quenching of electronically excited hot atoms play an important role in the terrestrial atmosphere. The cross sections for these three processes, i.e., elastic scattering, inelastic scattering with vibrational excitation of the bath gas molecules, and quenching of the electronically excited atoms are strongly dependent on the collision energy and they also do not vary in the same direction with energy. The energy dependence of the cross sections and the fact that all these processes occur in parallel, may have significant effects in the overall chemistry of the atmosphere. This may be particularly applicable to the upper stratosphere where 90% of the oxygen atoms are produced in the O($^1$D) state with considerable kinetic energy by the photodissociation of O$_3$. The reactions of O($^1$D) with H$_2$O to form OH, with N$_2$O to form NO, or N$_2$ and O$_2$ and with HCl to form OH+Cl or ClO+H are important in atmospheric chemistry (Wayne, 2000), though these reactions by themselves are not major sinks for O($^1$D). If the translational relaxation rate is not fast enough compared with the electronic quenching rate, there will be large number of translationally hot O($^1$D) atoms in the stratosphere in a steady-state condition and the above reactions of O($^1$D) will take place under nonequilibrated conditions.

As discussed earlier, the translational relaxation occurs through both elastic and inelastic collisions:

$$\text{Fast } O(^1D) + [N_2, O_2] \rightarrow \text{Slow } O(^1D) + [N_2, O_2] \qquad (17a)$$

$$\text{Fast } O(^1D) + [N_2, O_2] \rightarrow \text{Slow } O(^1D) + [N_2(v, J), O_2(v, J)] \qquad (17b)$$
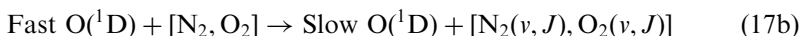
And the quenching through the reactions:

$$O(^1D) + N_2(X^1\Sigma_g^+) \rightarrow O(^3P_j) + N_2(X^1\Sigma_g^+, v, J) \qquad (18a)$$

$$O(^1D) + O_2(X^3\Sigma_g^-) \rightarrow O(^3P_j) + O_2(b^1\Sigma_g^+, {}^1\Delta g, X^3\Sigma_g^-, v, J) \qquad (18b)$$
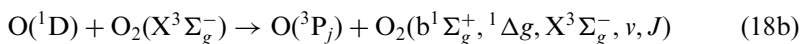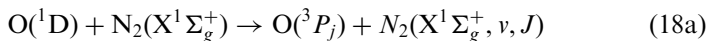
The reaction (18a) could lead to ro-vibrational excitation of $N_2$ and reaction (18b) could lead to the formation of $O_2(b^1\Sigma_g^+)$ and $O_2(^1\Delta_g)$ as they are energetically accessible. DeMore *et al.* (1997) suggest the branching ratio for the formation of $O_2(b^1\Sigma_g^+)$ to be $0.8 \pm 0.2$. This process is supposed to be a major source of $O_2(b^1\Sigma_g^+)$ in the atmosphere. The recommended (DeMore *et al.*, 1997) rate constants of the electronic quenching processes at 298 K are $2.6 \times 10^{-11}$ cm$^3$ molecule$^{-1}$ s$^{-1}$ for (18a) and $4.0 \times 10^{-11}$ cm$^3$ molecule$^{-1}$ s$^{-1}$ for (18b). The temperature dependence of these reactions have been measured by Streit *et al.* (1976) in the range of 104–354 K. The quenching process is exothermic by 1.97 eV and using Doppler spectroscopy, Matsumi *et al.* (1994) found that about 30% of this energy was released into the ro-vibrational excitation of $N_2$ for reaction (18a). They also measured the branching ratios among the fine structure levels of the product $O(^3P_j)$ atoms.

Along with the translational energy degradation measurements of $O(^1D)$, Matsumi and Chowdhury (1996) and Taniguchi *et al.* (2000) studied the electronic quenching processes (18a) and (18b) respectively using the experiment described earlier. To observe the quenching process, they monitored the increase in the population of $O(^3P_j)$ levels by LIF as a function of delay time after the formation of $O(^1D)$ through photodissociation. The $O(^3P_j)$ population was found to saturate within 12–15 μs at the bath gas pressures of 0.3 Torr and an initial $O(^1D)$ energy of 0.79 eV. The relative concentrations of $O(^3P_j)$ are shown in Fig. 14a as a function of delay time for the reaction (18a) with $N_2$ pressures at 1.00 and at 0.30 Torr. The horizontal scale has been made equivalent for the two $N_2$ pressures through proper normalization. Similar results are shown in Fig. 14b for the reaction (18b) at the $O_2$ pressure of 0.3 Torr. The smooth curves in Fig. 14a and b
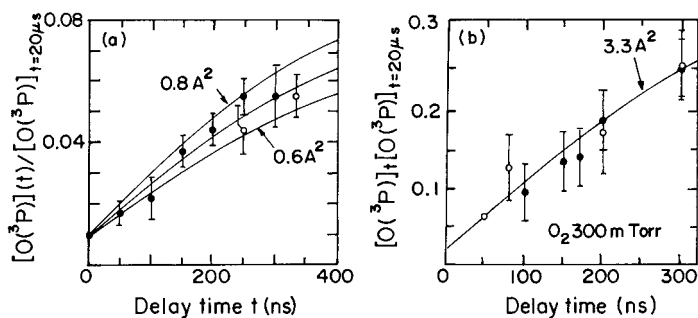
FIG. 14.  The concentrations of $O(^3P_j)$ formed by quenching of $O(^1D)$ as a function of delay time. (a) Quenching by $N_2$ at 1 Torr (filled circles) and 0.30 Torr (open circles) (Matsumi and Chowdhury, 1996). (b) Quenching by $O_2$ at 0.3 Torr with $N_2O$ pressure 1% (open circles) and 8% (filled circles) of $O_2$ (Reprinted with permission from Taniguchi *et al.*, 2000. Copyright 2000 American Chemical Society). Smooth curves are the result of simulation with reaction cross section (see text). The concentrations of $O(^3P_j)$ at a given time are normalized with that at large enough delay time (20 μs) by which there is complete quenching.

show the results of the simulation in which both velocity relaxation and reactive removal of $O(^1D)$ atoms in collision with $N_2$ and $O_2$ are taken into account. The reaction cross sections of the electronic quenching processes (18a) and (18b), $\sigma_r$, were taken as a fitting parameter. The best fit values of $\sigma_r$ for reactions (18a) and (18b) were found to be $(0.7 \pm 0.1)$ Å$^2$ and $(3.3 \pm 0.7)$ Å$^2$ respectively. Matsumi and Chowdhury (1996) also found that when the initial translational energy of $O(^1D)$ is 0.425 eV, about 40% of the $O(^1D)$ atoms are electronically quenched before the entire thermalization of the hot atoms takes place with $N_2$ as the bath gas, indicating that the translational relaxation rate of $O(^1D)$ by collisions with $N_2$ is not fast enough compared with the electronic quenching by $N_2$. A numerical simulation of the stratospheric conditions using the experimental data pointed to a steady-state distribution of the $O(^1D)$ translational energy in the upper stratosphere which is superthermal and that the populations at high translational energies are higher than that estimated from an equilibrated condition with the ambient air. They concluded that in the studies of reaction rates or product branching ratios in stratospheric reactions of $H_2O$, $N_2O$, and $HCl$ with $O(^1D)$, the contributions of superthermal distributions should be taken into account. This was supported by the measurements of Taniguchi *et al.* (2000) using $O_2$ as the bath gas.

For the quenching process (18a), the entrance channel potential has singlet spin-multiplicity, whereas the exit channel has triplet. Therefore the

quenching process by $N_2$ is spin-forbidden. The singlet and triplet potential surfaces could be connected only through a spin–orbit interaction, which is weak since the $N_2O$ complex is made of light atoms. Thus the transition probability between the two surfaces would be small. However, the strongly attractive entrance potential for the reaction results in long lifetimes of the singlet complex of $N_2O$. The trajectories of the collision complex on the singlet surface cross the seams to the triplet surface many times during their lifetimes. This mechanism has been proposed to explain the relatively fast rate of the quenching of $O(^1D)$ by $N_2$ (Tully, 1974). At higher collision energies, the lifetime of the $N_2O$ complex becomes shorter leading to less chance for crossing the seams between the singlet and triplet surfaces and the subsequent reduction in the quenching probability with increase in collision energy (Zahr *et al.*, 1975).

The *ab initio* molecular orbital (MO) and surface-hopping trajectory calculations by Tachikawa *et al.* (1995) showed that the quenching probability decreases with increasing collision energy and the electronic to ro-vibrational energy transfer occurs efficiently via an intermediate $N_2O$ complex on the singlet surface. This energy dependence of the quenching process is consistent with the experimental results of Matsumi and Chowdhury (1996) and earlier calculations of Zahr *et al.* (1975). The calculations by Tachikawa *et al.* (1997) using *ab initio* MO and classical trajectory calculations suggest that the cross section for the translational energy transfer process increases with increasing collision energy. According to their calculations, the translational relaxation dominates at high collision energies. At a collision energy of $10 \, \text{kcal} \, \text{mol}^{-1}$, the probability of translational energy transfer is 0.916 as compared to the remaining 0.084 for electronic quenching. As the collision energy is decreased to $5 \, \text{kcal} \, \text{mol}^{-1}$, the quenching probability increases to 0.432 and tends to dominate at lower collision energies. Based on these results Tachikawa *et al.* (1997) proposed that after the formation by photodissociation of $O_3$ in the upper stratosphere, the fast $O(^1D)$ atoms get thermalized through translational energy loss followed by electronic quenching. However, this model does not take into account the cross sections for momentum transfer by elastic collisions. These are more than two orders of magnitude higher than the inelastic and quenching cross sections even at high energies and increase very sharply below $10 \, \text{kcal} \, \text{mol}^{-1}$ as the energy decreases (Balakrishnan *et al.*, 1999). Considering the dominance of the elastic cross sections over the inelastic one, it may appear surprising that almost half of the $O(^1D)$ atoms are electronically quenched before entire thermalization as observed in the experiments of Matsumi and Chowdhury (1996). A qualitative explanation for this may lie in the fact

that as the collision energy decreases, the energy transfer per collision decreases in the case of elastic collisions. In the case of quenching, each collision releases relatively large energy (as much as $45\,\text{kcal}\,\text{mol}^{-1}$) into the translational motion, which needs to be thermalized further through elastic collisions. In this context it is important to note that although Matsumi and Chowdhury (1996) have presented a simulation on the energy distribution of $O(^1D)$ atoms in the stratosphere, detailed calculations using accurate energy-dependent cross sections are yet to be carried out.

As mentioned above, Taniguchi *et al.* (2000) obtained a quenching cross section of $(3.3\pm0.7)$ $\text{Å}^2$ for the quenching by $O_2$ as compared with $(0.7\pm0.1)$ $\text{Å}^2$ by $N_2$ at the same collision energy of $(8.7\pm6)$ $\text{kcal}\,\text{mol}^{-1}$. However, the cross section for the case of $O_2$ at this energy is slightly small as compared with that at room temperature. This is consistent with the temperature dependence of the quenching rate constant by $O_2$, $k(T)=3.2\times10^{-11}\exp[(70\pm100)/RT]$ (DeMore *et al.*, 1997) which shows a small negative or no activation energy. The small decrease in cross section with energy suggests that the entrance potential of the $O(^1D)+O_2(X\,^3\Sigma_g^-)$ is attractive and has no barrier for the reaction pathway. The potential energy surfaces for both the entrance channel and the dominant exit channel leading to the product $O(^3P_j)+O_2(b^1\Sigma_g^+)$ of the reaction, correlate to the triplet states of the $O_3$ molecule. Thus unlike the case of $N_2$, the quenching reaction by $O_2$ is spin-allowed and the transition probability at the seams between the two potential energy surfaces is expected to be large. As a result, the reaction probability may become independent of the lifetime of the collision complex. Taniguchi *et al.* (2000) explain the small variation of the quenching cross section with energy for reaction (18b) in terms of the addition of the centrifugal term to the attractive entrance potential. Unlike the case of $N_2$, no detailed molecular orbital calculations have been carried out for the quenching by $O_2$ as it involves potential energy surfaces of high-lying states of $O_3$. Banichevich *et al.* (1993) have calculated low-lying potential energy surfaces that correlate to $O(^3P)+O_2(X^3\Sigma_g^-)$ and $O(^3P)+O_2(^1\Delta_g)$. The triplet potential energy surface corresponding to the dominant exit channel, $O(^3P_j)+O_2(b^1\Sigma_g^+)$ has not been calculated. However, using a collinear $O-O_2$ geometry, Miura *et al.* (2002) calculated the collision energy dependence of the quenching probability for this reaction. They found that the ratio of probabilities for quenching reaction at higher energies to that at 298 K is close to unity. This is in fair agreement with the result of Taniguchi *et al.* (2000). Miura *et al.* (2002) also reported that the nonadiabatic transitions occurring at the large $O-O_2$ separation in the almost flat region of the potential energy surfaces is the major contributor to the quenching by $O_2$.

## VI. Hot Atoms and Space Vehicle Glow

The space shuttle and small satellites orbit around the earth between 100 and 1000 km with an orbital velocity of about 7.8 km s$^{-1}$. The resultant impact energy of the particles near the forward (or ram) surface of the spacecraft could reach values in excess of 5 eV, varying from 5.1 eV for O, 4.5 eV for N, and 10.2 eV for $O_2$. In addition, the atoms and molecules scattered from the ram direction would also gain energies in this range and could react with the ambient species. The collisions at such high energies have been found to give rise to the space vehicle glow.

The vehicle glow was suspected to be present on several rocket flights in the early seventies but went essentially undetected until the late seventies and early eighties. The glow was observed on satellites like AE-C, AE-E, and DE-B (Torr *et al.*, 1977) as well as on large space shuttles (Banks *et al.*, 1983). The satellite glow was dominated by discrete molecular band emissions from VUV to red, whereas the shuttle ram glow consisted of emissions both in the visible and infrared regions. In the visible region, the glow emitted a continuum extending from 420 to 800 nm having a broad peak intensity around 690 nm. The shuttle glow in the infrared region consisted of a few bands from 2.7 to 5.8 μm. The vehicle glow posed an across-the-board threat through contamination to the low-latitude optical sensor systems aboard satellites and space shuttles.

The satellite glow was observed to be maximum on surfaces facing into the velocity vector. Also, the intensity of glow decayed exponentially with altitude. The scale height was found to be about 35 km and the glow was found to extend well away from the satellite. Also, the glow was found to increase in brightness toward the red with a scale length of roughly 1–10 m. This implied that the emitters were long-lived species. Yee and Abreu (1983) found a strong correlation between ram emission intensity and altitude. It was found that at altitudes above 160 km, the brightness followed the atomic oxygen scale height. The most probable emission mechanism for the above glow came from Slanger (1983). He suggested that at these altitudes oxygen atoms could be impacting the surface of the satellite with as much as 5 eV energy and the interaction between these atoms and water adsorbed on the vehicle surface material led to the production of OH in the excited state. The de-excitation of OH$^{*}$ produced Meinel bands from 656.3 nm (6-1 band) to 732 nm (8-3 band).

We confine the discussion on the satellite glow to the above. However, the shuttle ram glow and its probable emission mechanisms in the optical and infrared regions are described below. The latest laboratory simulation experiments to test the proposed mechanisms are also discussed.

A. SHUTTLE RAM GLOW IN THE VISIBLE REGION

The first glow observations on shuttle in the optical region, were reported on STS-3 by Banks *et al.* (1983) followed by emissions observed from shuttle missions STS-4 and 5, STS-8 and 9, 41-D, 41-G, 51-D, and 61-C (Garrett *et al.*, 1988 and references therein) and STS-38 (Viereck *et al.*, 1992). These were observed using, either the orbiter television camera, a still camera or a grating in front of a photographic camera. On mission 41-D, the optical detection experiment was significantly upgraded with a special glow spectrometer. This spectrometer could be operated in three modes viz. image intensifier mode, grating-produced objective spectrum-slitless spectrum mode, and high-resolution spectrographic mode (3.4 nm resolution) with a slit to exclude contamination from the scattered airglow (Mende and Swenson, 1985). Results from the above instrument are shown in Fig. 15. The spectrum peaks at 680 nm and no distinct spectral features such as molecular band spectra were observed, indicating a continuum at 3.4 nm resolution of the 41-D instrument.

A few additional features of the measurements on the shuttle glow on different shuttle surfaces are given below:

- The scale length of the glowing layer in the ram direction is estimated at 20 cm above the large flat surfaces on the shuttle or perhaps 6 cm above rms. This is consistent with an effective radiative lifetime of emitting molecules, of about 0.6–0.7 ms for a mean emitter velocity of 0.3 km s$^{-1}$.
- The intensity of glow varies from material to material with black chemglaze (carbon-filled, urethane-base paint) and Z-302 (overcoated
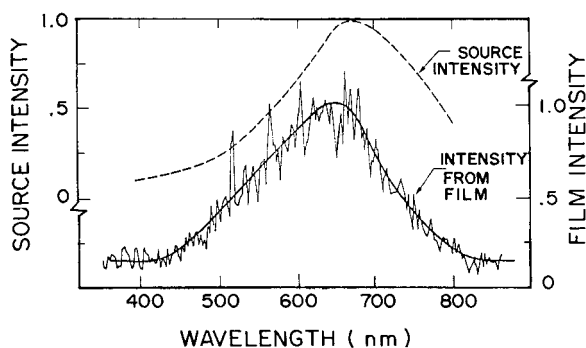


FIG. 15. Shuttle ram glow intensity (normalized at the peak) as observed on STS-41D as a function of emission wavelength. Bottom plot – film intensity after making correction for the film response; top plot – spectrum further corrected for the instrument response (Mende and Swenson, 1985. Reproduced by permission of American Geophysical Union).

with silicone) being the brightest followed by $MgF_2$. The glow intensity for polyurethane has been found to be the least intense. The scale length, however, was found to be similar in the case of each sample.

- The angular variation of intensity with ram angle is closer to $\cos(\varphi)$ with respect to the angle of attack, $\varphi$.
- There is a strong exponential correlation between the surface glow intensity and the surface temperature. The intensity has been observed to decrease with increasing temperature (Swenson *et al.*, 1986).

### A.1. Emission mechanism

Out of the many mechanisms proposed to explain the shuttle ram glow, the $NO_2$ recombination process is the leading contender. The source of $NO_2$ is the formation of NO by the Langmuir–Hinshelwood mechanism mediated by a surface (Gasser, 1985; von Zahn and Murad, 1986) followed by a few more chemical reactions. Basic steps in the surface recombination process are illustrated in Fig. 16. The surface recombination of atmospheric OI and
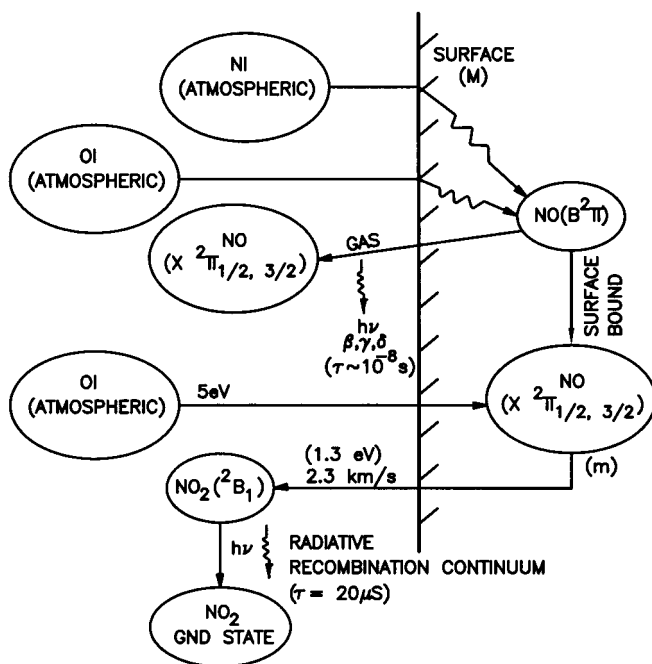


FIG. 16. Schematic of chemical processes that result in the $NO_2$ continuum emission believed to be responsible for shuttle ram glow (Swenson *et al.*, 1985b).

NI is assumed to yield $NO(B^2\pi)$ as suggested by Torr *et al.* (1977). The NO in the excited state gets deactivated to $NO(X^2\pi_{1/2, \; 3/2})$ ground state still remaining on the surface of the space shuttle. A portion of NO escapes the surface. Assuming that the escaping NO is $NO(B^2\pi)$, then one might observe the $\beta, \gamma, \ldots$ band emissions corresponding to $B^2\pi \rightarrow X^2\pi_{1/2, \; 3/2}$ transitions. These emissions are supposed to be near the spacecraft skin. Such emissions, under similar conditions, have been observed in the laboratory experiments (Kofsky and Barrett, 1986). The other portion of the deactivated $NO(X^2\pi_{1/2, 3/2})$ which is still remaining on the surface can react with ambient OI atoms (having about 5 eV energy) to form $NO_2(\tilde{A}^2B_1)$ which escapes the surface as a gas. The deactivation of $NO_2(^2B_1)$ to its ground electronic state, $NO_2(X^2A_1)$, gives rise to the continuum emission. If the recombined $NO_2$ retains 25% of the kinetic energy of the energetic ram O, the thickness of the shuttle glow layer can be explained by the above $NO_2$ continuum (Swenson *et al.*, 1985a).

It was pointed out by Green and Murad (1986) that the shuttle glow intensity as suggested in the above mechanism should scale as $[O]^2$ i.e. one O atom to form NO and a second one to form $NO_2$. But the actual observations of the shuttle glow show that the intensity scales as $[O]$ as reported by Dalgarno *et al.* (1985) and Slanger (1983). The latter observation might be explained by noting that the $NO_2$ emission will not vary as $[O]^2$ if the $N + O$ saturates on the surface at a given temperature as postulated by Swenson *et al.* (1986). If the $N + O$ creation goes faster than the removal but the saturation is maintained, the emission rate will be proportional to $[O]$.

### A.2. Laboratory simulation

A fast neutral beam technique has been developed to produce atomic oxygen at variable hyper-thermal energies (1–100 eV) by Orient *et al.* (1990, 1992) to study some of those surface-catalyzed reactions in the laboratory, which may be responsible for the chemiluminescent shuttle glow. A schematic diagram of the experimental setup is shown in Fig. 17. The magnetically confined electrons generated by a spiral-wound tungsten filament F are extracted at high energy and then decelerated to a final energy of 8 eV at the gas nozzle G. The electrons are allowed to react with the NO molecules effusing from G and dissociatively attach to form $O^-(^2P)$ ions. The confined ions and electrons are then accelerated to the desired final energy. The slower ions are separated from the faster electrons using a trochoidal deflector, $T_1$. The electrons are trapped in a Faraday cup and the negative ions, $O^-(^2P)$, are photodetached using emissions from a 20-W
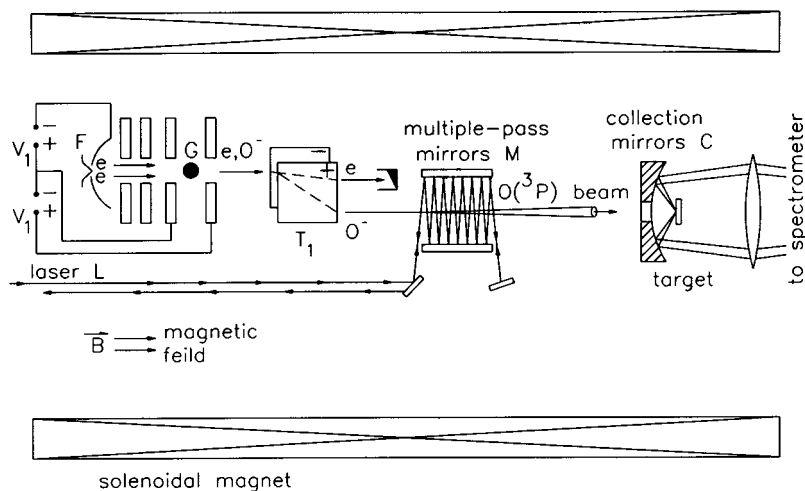
argon-ion laser in a multiple-pass mirror assembly (M) to form exclusively $O(^3P)$ atoms at desired energies. The detachment efficiency is about 15%. Finally, the O beam is directed and the undetached $O^-$ beam is reflected by negatively biasing the target. The magnetic confinement of the charged particles is carried out, by placing the complete system in a uniform, high-intensity (6T) solenoidal magnetic field. The O-atom flux as obtained from the decrease in $O^-$ flux with laser on is estimated to be $\sim 10^{13}$ atoms $cm^{-2}s^{-1}$. The targets were specially prepared with careful cleaning and cooled to temperatures in the range 240–340 K that could be varied accurately. A small gas jet of NO directed on to the target surfaces continuously. The chemiluminescence produced in the experiment was dispersed by a double-grating monochromator and detected using a photomultiplier tube.

Chemiluminescent spectra at a resolution of 10 nm and a temperature of 240 K obtained in this experiment with bombardment of 5 eV $O(^3P)$ atoms on NO adsorbed on $MgF_2$, Ni and Ti surfaces are shown in Fig. 18. The gap in the spectra above 400 nm was necessitated by the huge background light from the high-intensity laser used for detachment of $O^-$. The temperature of the target surface was varied and the recombination intensity was monitored at a particular wavelength. This way, the activation energy, $E_a$, for desorption of NO precursor from the surface could be obtained. $E_a$ was then
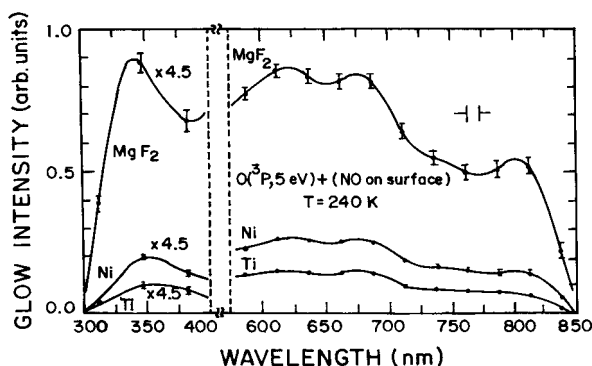
Fig. 18. Chemiluminescence spectra produced in collision of 5 eV oxygen atoms with NO-adsorbed MgF$_2$, Ni, and Ti surfaces at 240 K and the spectral resolution of 10 nm. The region between the dashed lines corresponds to the strong detaching laser wavelengths (Orient *et al.*, 1992. Copyright (1992) by the American Physical Society).

measured at 70 other wavelengths in the range 300–850 nm. The following conclusions were drawn from the above measurements (Orient *et al.*, 1992):

- The MgF$_2$ surface has the greatest tendency to chemiluminescence, followed by nickel and titanium.
- The chemiluminescence spectra are similar for the three surfaces with minor variations probably due to differences in the vibrational excitation of the excited electronic states.
- All three materials exhibit greater tendency to glow at lower temperatures. This is because of greater packing density of surface-adsorbed NO at lower temperature for each surface. As one warms the surface, more NO is lost by desorption, and hence the chemiluminescence diminishes.
- The activation energies of NO desorption are similar (about 0.12 eV) for the three surfaces. This indicates that the desorption is dominated by the release of a NO dimer or monomer physisorbed on the surface.
- The activation energy for each surface is independent of the emission wavelength. Hence, the same species is emitting throughout the wavelength range.

Comparison of chemiluminescence spectra reported by Orient *et al.* (1992) with the glow spectrum measured on space shuttle STS-38 (Viereck *et al.*, 1992) is given in Fig. 19. There seems to be a reasonable agreement between the spectra at wavelengths less than $\sim 640$ nm. At longer wavelengths, the shuttle-observed intensity is much larger. This could be because of different coating materials used on the shuttle surface. In general, most of the shuttle surfaces are coated with additional materials (CO, H$_2$O, hydrazine etc.), which may have their glow at wavelengths larger than 640 nm. But in the
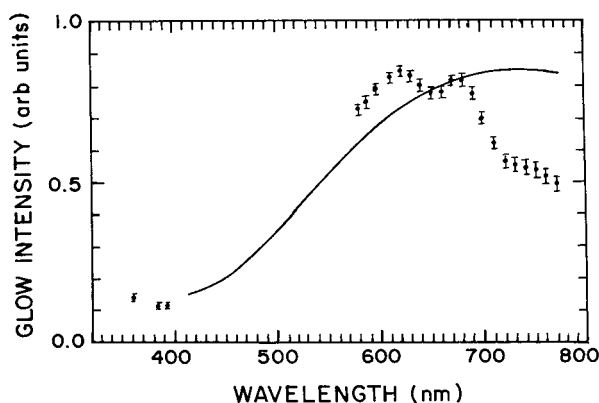
FIG. 19. Comparison of the glow spectrum (solid circles) produced in the laboratory by the collision of fast O atoms on NO adsorbed on a surface (Orient *et al.*, 1992) with the shuttle glow measurements (smooth curve) reported by Viereck *et al.* (1992). The two data are normalized at 650 nm (Copyright (1992) by the American Physical Society).

case of shuttle STS-38 (Viereck *et al.*, 1992), the surface viewed was shuttle tile, which is a porous, ceramic material and may have different emission characteristics of $NO_2^*$.

It is interesting to note that $MgF_2$ was also found to be the bright emitter when used in low-Earth-orbit (LEO) aboard shuttle 41-D (Mende *et al.*, 1986). Also, Swenson *et al.* (1986) estimated shuttle glow intensities and surface temperatures of various spacecrafts and derived an analogous "orbital" Arrhenius plot which gave an activation energy, $E_a = (0.14 \pm 0.2)$ eV. The laboratory measurements of Orient *et al.* (1992) are in good agreement with this, indicating that the same phenomenon was being observed both in LEO and the laboratory.

Taking the emitting species to be electronically excited $NO_2$, one can examine the energy balance in the process of chemiluminescence and calculate the threshold O-atom energy for the glow process (Orient *et al.*, 1992). The energy balance equation is given by

$$T_{\text{c.m.}} + D(\text{NO–O}) = E_{\text{phot}} + T_{\text{exit}} + E_a \qquad (34)$$

where $T_{\text{c.m.}}$ is the center-of-mass energy of the O-atom beam; $D(\text{NO–O})$ is the bond energy of $NO_2$ (3.11 eV); $E_{\text{phot}}$ is the maximum photon energy released (4.13 eV corresponding to 300 nm); $E_a$ is the activation energy for desorption of the precursor (0.12 eV); $T_{\text{exit}}$ is the kinetic energy of $NO_2^*$ as it leaves the surface and is about 1.5 eV as given by Swenson *et al.*

(1985a). From these values, one calculates the minimum required energy for the glow process for the O-atom beam, which comes out to be $T_{c.m.} \approx 2.6\,\text{eV}$. This is almost consistent with a value of about 3 eV observed by Orient *et al.* (1992). The difference in energy may be due to O-atom energy lost to surface heating, which has not been taken into account in the above equation. Based on the experiments by Orient *et al.*, it may be concluded that the shuttle glow in the visible region is due to the collision of fast O atoms with NO adsorbed on the surface forming $NO_2^*$ which emits the radiation.

### B. Shuttle Ram Glow in the Infrared Region

The infrared shuttle glow has been observed in the spectral region from 0.7 to 5.8 μm in a few different experiments on board the STS-39 space shuttle 'Discovery', which was launched on April 28, 1991 into a 260-km altitude circular orbit at an inclination of 57 deg for an eight-day mission. The experiments were different variations of **S**pacecraft **K**inetic **I**nfra**r**ed **T**est **(SKIRT)** and **C**ryogenic **I**nfra**r**ed **R**adiance **I**nstrumentation for **S**huttle **(CIRRIS-1A)**, which were operated both during 'non-glow' and 'glow' measurement times (Ahmadjian *et al.*, 1990, 1992; Zhou *et al.*, 1992). In the 'non-glow' measurement times, the experiments were operated to have an extensive infrared database on the *in situ* orbiter environment whereas 'glow' time measurements were carried out to provide near-field sources of infrared emissions.

   SKIRT consisted of two separate payloads, designated as SKIRT CVF (circular variable filter) and SKIRT GLOS (gaseous luminosity/optical surfaces). SKIRT GLOS contained six radiometer assemblies covering the large wavelength region in 42 band passes where as SKIRT CVF featured an infrared circular variable filter spectrometer and a long wavelength radiometer, both sharing common collection optics and were cooled with solid nitrogen. The spectrometer covered the wavelength region from 0.7 to 5.4 μm at about 3% spectral resolution using In:Sb detector whereas the radiometer had a Hg:Cd:Te detector, which sampled the wavelength interval from 9.9 to 10.4 μm. The CIRRIS-1A experiment consisted of a primary infrared sensor and a number of secondary sensors and subsystems. The main sensor was a cryogenic infrared interferometer/filter radiometer covering 2.5–25 μm spectral range. The Si:As detectors of various sizes were cooled with super-critical helium to temperatures of about 10 K.

   In Fig. 20a is shown the spectrum of space shuttle glow measured with SKIRT CVF sensor pointing into the ram direction while looking above the
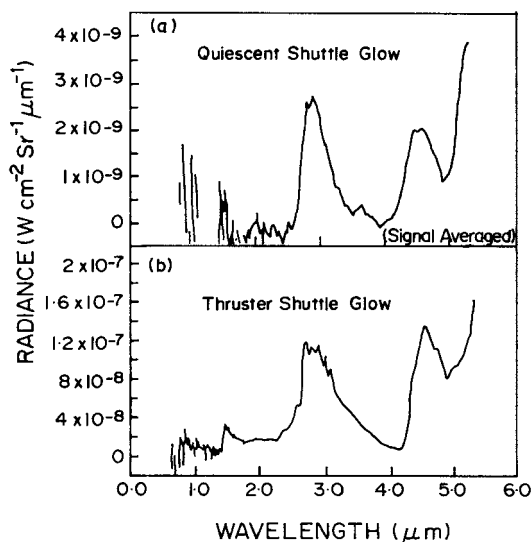
FIG. 20. (a) Signal-averaged spectrum of quiescent shuttle glow; (b) Spectrum of shuttle glow during a thruster firing (Ahmadjian *et al.*, 1992).

horizon, whereas Fig. 20b gives a glow spectrum taken during a thruster firing showing different spectral features and an increase in overall intensity. At the time of measurement, there were no thruster firings, water dumps, flash evaporators, and other contamination-generating activities. The glow spectra predicted to be in the fundamental, $NO(v) \rightarrow NO(v-1) + h\nu$ (5–6 μm) and overtone, $NO(v) \rightarrow NO(v-2) + h\nu$ (2.5–3 μm) bands, were observed along with $NO^+$ band. The emission features observed on shuttle STS-39 at 260 km (Ahmadjian *et al.*, 1992) were assigned as:

| | | |
|---|---|---|
| 2.7 μm | NO Overtone | Intense |
| 5.3 μm | NO Fundamental | Very Intense |
| 4.3 μm | $NO^+$ Fundamental | Intense |
| 1.4 μm | OH Overtone | Weak |
| 2.8 μm | OH Fundamental | Weak and unresolved |
| 4.6 μm | CO Fundamental | Unresolved |

The shuttle glow radiances are of the order of $10^{-9}\,\text{W}\,\text{cm}^{-2}\,\text{sr}^{-1}\,\mu\text{m}^{-1}$. Spectra during the day are twice as intense as those taken at night. This is consistent with the enhancement in concentrations of the assumed reaction precursors, O for NO and $O^+$ for $NO^+$ during the day.

The NO fundamental band has only been shown partly in Fig. 20a. But CIRRIS-1A interferometer on board STS-39 reported a high level of NO

emissions observed at a tangent height of 267 km (Zhou *et al.*, 1992). The radiation intensity at this altitude in the 5.3 μm NO band was reported to be $\sim 1.6 \times 10^{-9}\,\mathrm{W\,cm^{-2}\,sr^{-1}\,\mu m^{-1}}$ in line with the SKIRT observations. The CIRRIS data exhibits the additional fundamental band emission between 5.4 and 5.8 μm.

### B.1. Emission mechanism

The radiation intensity reported in SKIRT and CIRRIS experiments for NO and $NO^+$ bands is quite significant. Also, these emissions have been observed at altitudes between 260 and 270 km. At these high altitudes, such intense atmospheric $NO/NO^+$ emissions cannot be anticipated. It is, therefore, suggested (Green *et al.*, 1986) that there is a near-field source for these radiations.

The principal reaction of interest with energetic O atoms with $N_2$ produces vibrationally excited NO, i.e.,

$$O + N_2 \rightarrow NO(v,J) + N \qquad \Delta H_{300} = 3.26\,\mathrm{eV} \qquad (35)$$

where $\Delta H_{300}$ is the amount of enthalpy, at room temperature, released by the reaction. The above reaction is endothermic for center-of-mass energies less than 3.26 eV, which coincidentally corresponds to an O-atom velocity of $8\,\mathrm{km\,s^{-1}}$. Green *et al.* (1986) have modeled various chemiluminiscent processes that could occur above shuttle surfaces. They have pointed out that the above reaction could provide a significant source of infrared emissions. Also, the NO so created can react on the surface to produce vibrationally excited NO (Kofsky and Barrett, 1985).

The $NO^+$ fundamental emission at 4.3 μm as assigned by Ahmadjian *et al.* (1992) arises from the interaction of fast $O^+$ with $N_2$ i.e.

$$O^+ + N_2 \rightarrow NO^+(v,J) + N \qquad (36)$$

The above reaction is almost inefficient at thermal energies but the cross section of reaction increases rapidly at fast ion center-of-mass energies larger than 0.33 eV (Upschulte *et al.*, 1992).

### B.2. Laboratory simulation

Simulation experiments of infrared shuttle glow and measurement of cross sections for the reactions involving hot oxygen atoms and energetic oxygen ions with $N_2$, CO, $CO_2$, $CH_4$ has been carried out using a novel fast oxygen atom/ion source initially developed by Caledonia *et al.* (1987). The details of
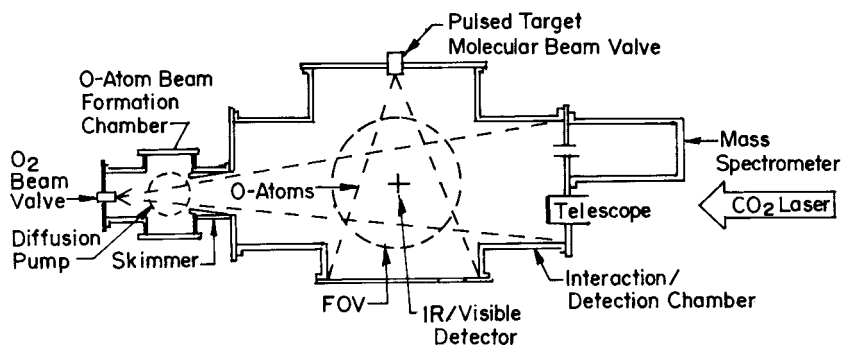
FIG. 21. Schematic diagram of the experimental system (Upschulte *et al.*, 1992; Upschulte and Caledonia, 1992; Oakes *et al.*, 1994) for carrying out reactions between hot atoms and molecules.

the experimental approach, which used a laser-surface "blow-off" scheme to produce the fast atoms have been discussed by Upschulte *et al.* (1992), Upschulte and Caledonia (1992), and Oakes *et al.* (1994). A 12-J per pulse $CO_2$ laser (Fig. 21) was used to heat and partially dissociate pure molecular oxygen. About one-third of the $CO_2$ laser energy was delivered in an initial 200 ns gain-switched spike, which induced a plasma break down in the high-pressure region of the throat via inverse Bremsstrahlung absorption mechanism. The resulting plasma, heated to about 24,000 K by a laser-supported detonation wave, absorbed the remaining energy in the remaining time of 2 μs laser pulse. The rapidly expanding plasma continued to dissociate the remaining molecular oxygen in the nozzle. During the expansion, the directed kinetic energy increased as the gas temperature and density dropped. The nozzle limited the expansion to favor electron–ion recombination while largely inhibiting the recombination of oxygen atoms into molecules. Consequently, a cold, high-energy, large area beam of atomic oxygen flowed out of the nozzle.

The atomic oxygen beam velocity was measured by determining the time delay of the radiation produced by $O^+ + e$ recombination on two, filtered photomultiplier tube radiometers separated by a fixed distance downstream of the nozzle exit. A mass flow meter was used to measure the oxygen input and a piezoelectric transducer was used to measure the temporal profile of the cold gas pulse. A mass spectrometer with a crossed beam ionizer was used to measure the beam composition. The reacting gas, molecular nitrogen, was introduced from another pulsed molecular beam valve located on the top of the beam interaction chamber.
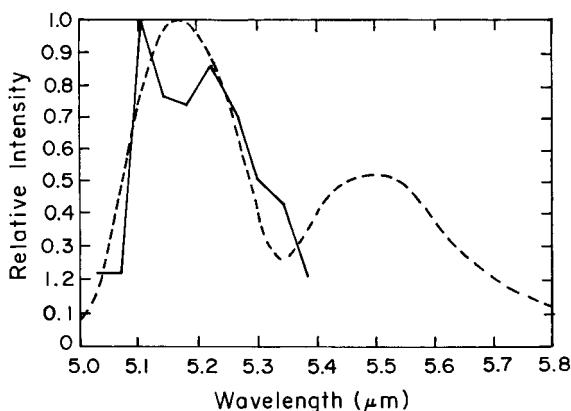
F<small>IG</small>. 22. Comparison of laboratory observations of infrared emission from the reaction of fast oxygen atoms with $N_2$ (solid line: Oakes *et al.*, 1994) and flight measurements performed with CIRRIS-1A instrument on STS-39 at a tangent height of 267 km (broken line: Zhou *et al.*, 1992). (Reproduced by permission of American Geophysical Union).

The temporally resolved measurements with 0.05 μm spectral resolution were made using a continuous variable filter (CVF) radiometer consisting of a three-segment 90° filter wheel, a pair of f/1.5 off-axis parabolic reflectors and an In-Sb detector. A second radiometer consisting of interference filters and an In-Sb detector views the whole of the interaction region of the crossed beams and was used to normalize the CVF spectra and to obtain lower-resolution, band-pass-filtered spectra.

The spectrum obtained by Oakes *et al.* (1994) for reaction (35) using the above experiment is shown in Fig. 22 along with the spectrum obtained using CIRRIS-1A interferometer on board STS-39 at a tangent height of 267 km by Zhou *et al.* (1992), both corresponding to the NO fundamental band. The laboratory spectrum was taken at a resolution of 0.08 μm and an oxygen atom velocity of 12 km s$^{-1}$. The data of Oakes *et al.* (1994) did not extend beyond 5.4 μm due to the negligibly small response function of the infrared detector used by them. That the NO was created rotationally hot in the laboratory experiment is evident from the finite intensity below 5.1 μm, which is the lower limit at room temperature. The comparison between the laboratory and flight data in the 5.0–5.4 μm spectral region appears to be quite good.

Using fast O$^+$ beam Upschulte *et al.* (1992) identified the observed emission in the 4–5 μm region in the shuttle glow (Fig. 20) as due to the reaction (36). They measured the cross section value to be $\sim 3.2 \times 10^{-16}$ cm$^2$ at the laboratory energy of 5 eV for this reaction, which is in agreement with

the value of $3 \times 10^{-16}\,\mathrm{cm}^2$ reported by Burley *et al.* (1987). The measurement of cross sections for some other important reactions with hot atoms is discussed below.

### B.3. *Measurement of excitation cross sections*

The excitation cross sections involving the collision of fast O and N atoms with molecules have been measured (Upschulte and Caledonia, 1992; Oakes *et al.*, 1994; Caledonia *et al.*, 2000). The cross section could be written as (Upschulte and Caledonia, 1992)

$$\sigma = \frac{J}{AC_0N_T} \tag{37}$$

where $J$ represents the peak radiance of the entire interaction volume and $A$ is the Einstein coefficient of the radiative transition. $C_0$ and $N_T$ would be defined later during the discussion leading to the calculation of $J$. All the emission intensity data is first converted into irradiance units using standard black body calibration procedures, taking into account filter and atmospheric transmission efficiencies. The gas targets are optically thin and the detector irradiances are, therefore, readily converted into the total photon emission rate within the field of view (FOV)

$$J = \int_{\mathrm{FOV}} N^* A\, dV \tag{38}$$

where $N^*$ is the local concentration of the excited state and the integral is over the radiating volume within the field of view. At the end of the pulse, the local excited state concentration at any point in the gaseous target is given by

$$N^* = \int_{\tau} \sigma V [HA][TM]\, dt \tag{39}$$

Here $V$ is the beam velocity of the interacting hot atoms, $[HA]$ and $[TM]$ are the local hot atom and target molecule density, respectively, and the integration is over the pulse time. The target beam intensity is steady over the time of the pulse and thus, the density of the local target molecule is independent of time. Therefore

$$N^* = \sigma [TM] \int V [HA]\, dt \tag{40}$$

The integral in the above equation is equivalent to $C_0$, the local line density of hot atoms in the pulse. Thus

$$N^* = \sigma[TM]C_0 \tag{41}$$

In terms of $J$, the number of photons per second,

$$J = A\sigma C_0 \int_{\text{FOV}} [TM]\,dV \tag{42}$$

where $C_0$ has been assumed to be constant over the interaction volume. If the experimental conditions are so chosen that the hot atom beam is larger than the target beam, the volume integral of the target beam density falls out of the gas dynamics and

$$\int [TM]\,dV \approx \frac{dm}{dt}\Delta H \frac{1}{U_{\text{max}}} \tag{43}$$

where $dm/dt$ is the measured mass flow rate through the target beam orifice, $U_{\text{max}}$ is the maximum attainable molecular beam velocity and $\Delta H$ is the height/length of the target beam, which is impacted by the hot atom beam within the field of view. For the sake of convenience, the whole integral in the above equation can be written as $N_T$ as given in Eq. (37).

The results of the measurement of excitation cross sections for some important reactions between hot atoms and molecular targets are discussed below.

*Fast O-atoms with molecular nitrogen.* The excitation cross sections for the reaction,

$$O(\text{Hot}) + N_2 \rightarrow NO(v, J) + N \tag{35}$$
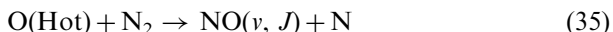
have been measured by Oakes *et al.* (1994) as a function of O-atom velocity ranging from 8 to $12\,\text{km s}^{-1}$ for both the fundamental (5.0–5.4 μm) and overtone (2.5–3.0 μm) NO bands. Since each vibrational transition has a distinct Einstein coefficient and since it is not known as to which vibrational states are radiating within the monitored band passes, only effective cross section values have been obtained under the assumption that all radiation arises from $v(1) \rightarrow v(0)$ and $v(2) \rightarrow v(0)$ for the fundamental and overtone bands respectively. The excitation cross sections are shown in Fig. 23 as a function of hot atom velocity. The effective Einstein coefficients for the fundamental and overtone band emissions have been taken as 13 and $1\,\text{s}^{-1}$
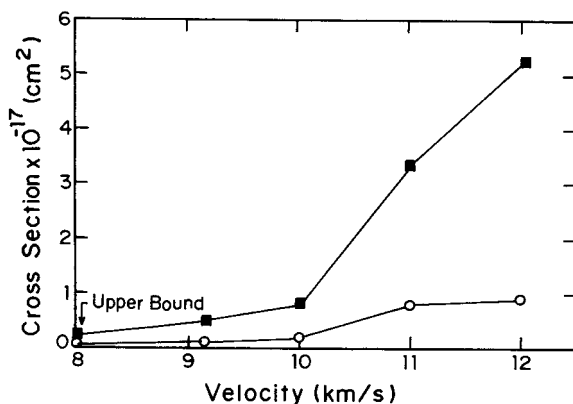
FIG. 23. Effective excitation cross sections for the reaction $O + N_2 \rightarrow NO(v, J) + N$ as a function of O-atom velocity (Oakes *et al.*, 1994. Reproduced by permission of American Geophysical Union). Squares: 2.5–3.0 μm emission band (Einstein coefficient $A = 1\,s^{-1}$). Circles: 5–5.4 μm emission band (Einstein coefficient $A = 13\,s^{-1}$) The upper bound value obtained at $8\,km\,s^{-1}$ has also been defined in the text.

Table I
Cross Sections for Collisional Excitation of O Atoms ($8\,km\,s^{-1}$) with CO, $CO_2$, and $CH_4$ (Upschulte and Caledonia, 1992).

| Reaction | Cross Section ($cm^2$) |
| --- | --- |
| $O + CO \rightarrow CO^*(v) + O$ | $7.3 \times 10^{-17}$ |
| $O + CO_2 \rightarrow CO_2^*(v_3) + O$ | $3.7 \times 10^{-18}$ |
| $O + CO_2 \rightarrow CO^*(v) + O_2$ | $6.4 \times 10^{-17}$ |
| $O + CH_4 \rightarrow CH_4^*(v_3) + O$ | $5.0 \times 10^{-19}$ |
| $O + CH_4 \rightarrow CH_3 + OH^((v)$ | $< 5 \times 10^{-19}$ |

respectively. The cross sections (Fig. 23) begin to rise significantly beyond $10\,km\,s^{-1}$ O-atom velocity. Also, the overtone cross sections are larger in value than those of the fundamental at all O-atom velocities, thereby suggesting that higher vibrational states are dominantly formed in the process. It may be noted here that the data for the overtone band pass at $8\,km\,s^{-1}$ are an upper bound corresponding to signal-to-noise ratio of 1.

*Fast O atoms with CO, $CO_2$, and $CH_4$.* The values of excitation cross sections measured by Upschulte and Caledonia (1992) for reactions involving hot O atoms at $8\,km\,s^{-1}$ with CO, $CO_2$, and $CH_4$ are given in table I. It appears that no other experimental or theoretical data exist on these reaction cross sections.

*Fast N atoms with $O_2$.* The reaction between the ground state nitrogen atoms at thermal energies and oxygen molecules

$$N(^4S) + O_2 \rightarrow NO(v, J) + O \qquad (44)$$
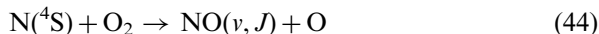
is exothermic by 1.38 eV (31.82 kcal mol$^{-1}$). This plus the activation energy of 7–8 kcal mol$^{-1}$ (Clyne and Thrush, 1961) released in this reaction is sufficient to populate $v = 0$ through 7 of NO at room temperature. There have been four measurements (Whitson *et al.*, 1976; Rahbee and Gibson, 1981; Herm *et al.*, 1983; Winkler *et al.*, 1986) and a few theoretical studies (Duff *et al.*, 1994; Gilbert *et al.*, 1995) under thermal conditions to obtain vibrational product distribution of this reaction. This reaction with hot atoms has been observed in the terrestrial upper atmosphere (Sharma *et al.*, 1993). The only measurement to study the above reaction at high collision energies has been carried out by Caledonia *et al.* (2000). They determined the distribution of vibrationally excited ground state of NO and the vibrational state-specific excitation cross sections using fast $N(^4S)$ atoms of velocity 8 km s$^{-1}$. The state-specific excitation cross section values are given in Fig. 24 as determined from NO fundamental band emission data. Also given in the figure are classical trajectory predictions (Duff *et al.*, 1994; Duff, 1997) and quasiclassical trajectory calculations by Ramachandran *et al.* (2000). There is good agreement between the experimental reaction cross sections for production of NO($v = 1$ to 7) and the results of Duff (1997). However, the results of Ramachandran *et al.* (2000) are systematically higher by a factor of $\pi$ (Ramachandran, 2002).
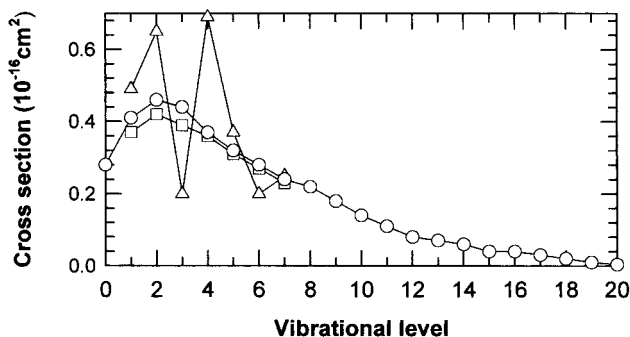


FIG. 24. Cross sections for the production of NO in different vibrational levels by the collision of $N(^4S)$ on $O_2$. $\Delta$ – Experimental data (Caledonia *et al.*, 2000); $\square$ – Calculations (Duff 1997); $\bigcirc$–Calculations (Ramachandran *et al.*, 2000). The data by Ramachandran *et al.* have been divided by a factor of $\pi$.

# VII. Large NO Densities at 105 km

Nitric oxide plays a critical role in the cooling of terrestrial atmosphere above 70 km. It is also one of the important catalytic destroyers of ozone in the stratosphere. Large NO densities of $\sim 10^8$ cm$^{-3}$ have been measured at an altitude of $\sim 105$ km. These values have been obtained from infrared and ultraviolet observations in different experiments aboard rockets, satellites, and space shuttles and from microwave measurements using ground-based millimeter wave telescopes. The reactions of N($^2$D) and N($^4$S) with O$_2$ are important sources of NO. The latest photochemical models have incorporated soft x-ray fluxes, new reaction sources, the new value of yield for N($^2$D) + O reaction as obtained in the latest laboratory measurements and over and above, the hot nitrogen chemistry with an energy-dependent thermalization cross sections. But all these efforts have failed to explain the high abundance of nitric oxide at 105 km. Though this still remains an open problem, we discuss in this section an aspect of the hot N atom chemistry, which has been subjected to detailed analysis as a source of NO.

The first measurement of the NO densities were carried out by Barth (1964) using an ultraviolet spectrometer on a sounding rocket by observing the resonant fluorescence of NO(1,0) $\gamma$-band near 215 nm. Subsequent rocket flights by Thomas (1978), McCoy (1983), and Cleary (1986) and experiments on satellites (OGO 4, AE C and D, and Solar Mission Explorer, SME) also observed the (1,0) $\gamma$-band to obtain NO densities (Barth *et al.*, 1973, 1998; Rusch, 1973; Barth, 1992). All this data underestimated the amount of NO due to the neglect of self-absorption in the calculation of NO $\gamma$-band emission rate. However, Epavier and Barth (1992) and Stevens (1995) have estimated the self-absorption correction and as a result, an increase in the peak NO densities by a factor of 2–3 was reported as compared to the results where self-absorption was not taken into account. The first microwave detection of the atmospheric NO (Clancy and Rusch, 1992) was carried out through ground-based observations of 1.2 mm (250.796 GHz) line emission using National Radio Astronomy Observatory millimeter wave telescope (Kitt Peak, Arizona). The values derived in this experiment for column density above 70 km and number density at an altitude of $110 \pm 10$ km are $\sim 5 \times 10^{14}$ cm$^{-2}$ and $\sim 3 \times 10^8$ cm$^{-3}$ respectively. The nitric oxide density measurements have also been carried out using the 5.3 µm solar occultation spectral data obtained by Atmospheric Trace Molecule Spectroscopy (ATMOS)/Atmospheric Laboratory for Applications and Science (ATLAS 1). The ATMOS observations were made in April and May, 1985 (Barth *et al.*, 1996) and the ATMOS/ATLAS1 observations during shuttle mission (March–April 1992) in the latitude

range $38°N$–$58°S$ (Krishna Kumar *et al.*, 1995). These measurements yielded peak NO densities of $\sim 10^8 \, cm^{-3}$ at $105 \pm 2.5 \, km$.

No reliable atmospheric model has succeeded in predicting the observed NO densities at these heights. This has stimulated a great deal of theoretical work (Gérard *et al.*, 1997; Balakrishnan *et al.*, 2000 and references therein). One of the additional sources proposed to account for the observations has been the reaction of hot $N(^4S)$ atoms with $O_2$. Though this reaction is exothermic by $1.38 \, eV$, the reaction is slow at room temperature due its activation energy of $0.3 \, eV$ and energetic $N(^4S)$ atoms are needed for this reaction to proceed efficiently. The presence of nonthermal distribution of $N(^4S)$ despite the thermalization by the ambient bath gases and the reaction of this nonthermal distribution with $O_2$ to contribute to the NO production has been suggested (Solomon, 1983; Gérard *et al.*, 1991; Lie-Svendsen *et al.*, 1991). Most of the calculations carried out for the energy distribution function of $N(^4S)$ do not incorporate the full energy and angular dependence of the elastic and inelastic cross sections with the bath gases. Often, the cross sections were assumed to be independent of energy, with an isotropic distribution in the scattering angle, the so-called hard-sphere approximation (Sharma *et al.*, 1996 and references therein). Later, Sharma *et al.* (1998) computed the energy distribution function of hot $N(^4S)$ atoms at an altitude of $110 \, km$ using energy and angle-dependent cross sections for collisions with O and $N_2$ obtained from quasiclassical trajectory calculations. It was assumed by them that both elastic and inelastic $N + O_2$ collisions have the same effect as for $N + N_2$ collisions. Recently, Swaminathan *et al.* (1998) presented an updated version of photochemical model of NO in the lower thermosphere which incorporated solar soft x-rays as an additional source of hot $N(^4S)$ atoms. The NO densities predicted by them are still significantly less than those observed in rocket, satellite, and space shuttle measurements. However, while accounting for the contribution of hot $N(^4S)$ atoms to the production of nitric oxide, Swaminathan *et al.* used cross sections derived from classical calculations (Gérard *et al.*, 1997) which did not take care of the angular distribution of the scattering event. In this context, Balakrishnan *et al.* (2000) have made a critical evaluation of the reaction hot $N(^4S) + O_2$ as a possible source of NO in the upper atmosphere.

Balakrishnan *et al.* (2000) used a quantum-mechanical approach to show that $N + O_2$ elastic collision cross sections have a different energy and angular dependence than those for $N + N_2$ collisions. A comparison of the integral elastic cross sections for these two collisions could be found in Section V and Fig. 6. The energy as well as angular anisotropy of the elastic and inelastic collision cross sections for collisions of hot $N(^4S)$ atoms with O, $N_2$, and $O_2$ were included the construction of the Boltzmann kernel
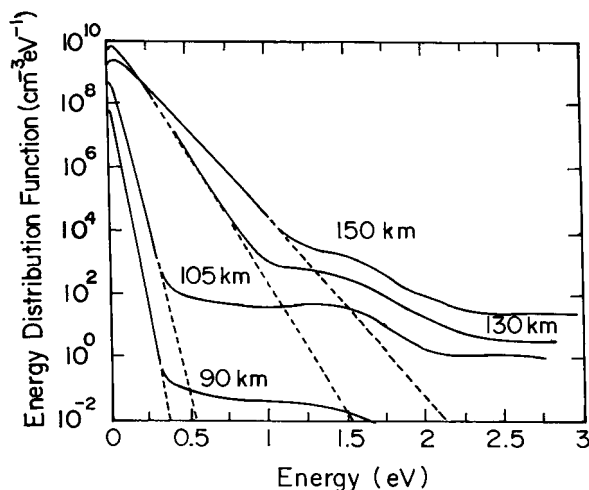
FIG. 25. Energy distribution function of N($^4$S) atoms in the thermosphere at 90, 105, 130, and 150 km (Balakrishnan *et al.*, 2000. Reproduced by permission of American Geophysical Union). The solid curves are computed non-thermal energy distribution functions and the dashed curves are the Maxwellians at the ambient temperatures.

which determine the rate of energy relaxation. Subsequently, the energy distribution function, f(E,T), under steady-state conditions with the weighted sum of the energy relaxation kernels for collisions with bath gases were obtained. The f(E,T) for 90, 105, 130, and 150 km altitudes, are shown in Fig. 25. These are similar to the Maxwellian distribution at low energies but are significantly different at higher energies having a pronounced non-thermal tail. Using the Maxwellian and the non-thermal energy distribution functions, the differential rate coefficients for N($^4$S) + O$_2$ reaction were calculated as a function of translational energy of N($^4$S) atoms. The rate coefficients at different hot atom energies are shown in Fig. 26 for the altitudes of 110 and 130 km, which correspond to thermospheric temperatures of 270 and 595 K respectively. At 110 km, the major contribution to the rate coefficient arises from the non-thermal part, whereas at 130 km, the contribution from the nonthermal part is relatively small. Using the average mid-latitude daytime number densities of N($^2$D) and N($^4$S) given by Swaminathan *et al.* (1998), the relative contribution to the formation of NO by these two states of N were calculated. Based on these, Balakrishnan *et al.* (2000) found that at altitudes below 130 km, where the nonthermal N($^4$S) atoms contribute more than their thermal counterparts, the overall contribution from the N($^4$S) is considerably smaller than that due to the
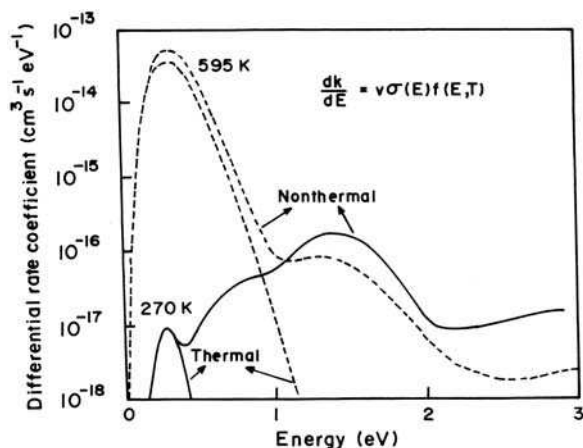
FIG. 26. Differential rate coefficients for $N(^4S) + O_2 \rightarrow NO + O$ reaction obtained from the non-thermal and the Maxwellian energy distribution functions at 270 K (110 km) and 595 K (130 km) as reported by Balakrishnan *et al*. (2000) (Reproduced by permission of American Geophysical Union).

$N(^2D)$, thus indicating that inclusion of the contribution due to hot $N(^4S)$ atoms will not explain the observed large abundance of NO at 105–110 km altitude.

# VIII.  References

Ahmadjian, M., Nadile, R.M., Wise, J.O., and Bertschi, B. (1990). *J. Spacecr. Rockets* **27**, 669.
Ahmadjian, M., Jennings, D.E., Mumma, M.J., Espenak, F., Rice, R.J., Russell, R.W., and Green, B.D. (1992). *Geophys. Res. Lett*. **19**, 989.
Anderson, K., and Schuler, K.E. (1974). *J. Chem. Phys*. **40**, 633.
Balakrishnan, N., Kharchenko, V., and Dalgarno, A. (1998a). *J. Chem. Phys*. **108**, 943.
Balakrishnan, N., Kharchenko, V., and Dalgarno, A. (1998b). *J. Geophys. Res*. **103**, 23393.
Balakrishnan, N., Kharchenko, V., and Dalgarno, A. (1999). *J. Phys. Chem. A* **103**, 3999.
Balakrishnan, N., Sergueeva, E., Kharchenko, V., and Dalgarno, A. (2000). *J. Geophys. Res*. **105**, 18549.
Baluja, K.L., and Zeippen, C.J. (1988). *J. Phys. B: At. Mol. Opt. Phys*. **21**, 1455.
Banichevich, A., Peyerimhoff, S.D., and Grein, F. (1993). *Chem. Phys*. **178**, 155.
Banks, P.M., Williamson, P.R., and Raitt, W.J. (1983). *Geophys. Res. Lett*. **10**, 118.
Barth, C.A. (1964). *J. Geophys. Res*. **69**, 3301.
Barth, C.A. (1992). *Planet. Space Sci*. **40**, 315.
Barth, C.A., Rusch, C.W., and Stewart, A.I. (1973). *Radio Sci*. **8**, 379.
Barth, C.A., Tobiska, W.K., Siskind, D.E., and Cleary, D.D. (1988). *Geophys. Res. Lett*. **15**, 92.
Barth, C.A., Farmer, C.B., Siskind, D.E., and Perich, J.P. (1996). *J. Geophys. Res*. **101**, 12489.
Bates, D.R. (1989). *Planet. Space Sci*. **37**, 363.

Burley, J.D., Ervin, K.M., and Armentrent, P.B. (1987). *J. Chem. Phys.* **86**, 1944.

Caledonia, G.E., Krech, R.H., and Green, B.D. (1987). *Aeronautics Astronautics J.* **25**, 59.

Caledonia, G.E., Krech, R.H., Oakes, D.B., Lipson, S.J., and Blumberg, W.A.M. (2000). *J. Geophys. Res.* **105**, 12833.

Carrigan, A.L., and Skrivanek, R.A. (1974). Air Force Cambridge Research Laboratories AFCRL Chart 1974.

Chutjian, A., and Orient, O.J. (1996). *Expt. Meth. Phys. Sci.* **29B**, 49.

Clancy, R.T., and Rusch, D.W. (1992). *Geophys. Res. Lett.* **19**, 261.

Cleary, D.D. (1986). *J. Geophys. Res.* **91**, 11337.

Cline, J.I., Taatjes, C.A., and Leone, S.R. (1990). *J. Chem. Phys.* **93**, 6543.

Clyne, M.A.A., and Thrush, B.A. (1961). *Proc. Roy. Soc.* (*London*) *Ser. A* **261**, 259.

Cotton, D.M., Chakrabarti, S., and Gladstone, G.R. (1993a). *J. Geophys. Res.* **98**, 21627.

Cotton, D.M., Gladstone, G.R., and Chakrabarti, S. (1993b). *J. Geophys. Res.* **98**, 21651.

Dalgarno, A., Yee, J.-H., and LeCompte, M. (1985). *Proc. Sec. Workshop on Spacecraft Glow*, NASA CP-2391, 55.

DeMore, W.B., Sander, S.P., Howard, C.J., Ravishankara, A.R., Golden, D.M., Kolb, C.E., Hampson, R.F., Kurylo, M.J., and Molina, M.J. (1997). "Chemical Kinetics and Photochemical Data for use in Stratospheric Modeling." No.12: JPL Publication 97–4, Pasadena, CA.

Diloy, P.-Y., Robineau, A., Lilensten, J., Blelly, P.-L., and Fontanari, J. (1996). *Ann. Geophys.* **14**, 191.

Duff, J.W., Bien, F., and Paulsen, D.E. (1994). *Geophys. Res. Lett.* **21**, 2043.

Duff, J.W. (1997). (As quoted by Caledonia *et al.* 2000).

Epavier, F.G., and Barth, C.A. (1992). *J. Geophys. Res.* **97**, 13723.

Garrett, H.B., Chutjian, A., and Gabriel, S. (1988). *J. Spacecr. Rockets* **25**, 321.

Gasser, R.P.H. (1985). "An Introduction to Chemisorption and Catalysis by Metals." Oxford, New York.

Gérard, J.C., Shematovich, V.I., and Bisikalo, D.V. (1991). *Geophys. Res. Lett.* **18**, 1695.

Gérard, J.C., Richards, P.G., Shematovich, V.I., and Bisikalo, D.V. (1995). *Geophys. Res. Lett.* **22**, 279.

Gérard, J.C., Bisikalo, D.V., Shematovich, V.I., and Duff, J.W. (1997). *J. Geophys. Res.* **102**, 285.

Gilbert, M., Gimenez, X., Gonzalez, M., Sayos, R., and Aguilar, A. (1995). *Chem. Phys.* **191**, 1.

Gorecki, J., and Hanazaki, I. (1994). *Chem. Phys.* **181**, 39.

Green, B.D., and Murad, E. (1986). *Planet. Space Sci.* **34**, 219.

Green, B.D., Rawlins, K.T., and Marinelli, W.J. (1986). *Planet. Space Sci.* **34**, 879.

Hedin, A.E. (1987). *J. Geophys. Res.* **92**, 4649.

Hedin, A.E. (1989). *J. Geophys. Res.* **94**, 5523.

Herm, R.R., Sullivan, B.J., and Whitson, M.E., Jr. (1983). *J. Chem. Phys.* **79**, 2221.

Hickey, M.P., Richards, P.G., and Torr, D.G. (1995). *J. Geophys. Res.* **100**, 17377.

Hilbig, R., and Wallenstein, R. (1983). *IEEE J. Quan. Electron.* QE-**19**, 1759.

Hubert, B., Gérard, J.C., Cotton, D.M., Bisikalo, D.V., and Shematovich, V.I. (1999). *J. Geophys. Res.* **104**, 17139.

Hubert, B., Gérard, J.C., Killeen, T.L., Wu. Q., D.M., Bisikalo, D.V., and Shematovich, V.I. (2001). *J. Geophys. Res.* **106**, 12753.

Hudson, R.D., and Carter, V.L. (1969). *J. Geophys. Res.* **74**, 393.

Jacchia, L.G. (1972). "COSPAR International Atmosphere." Akademie-Verlag, Berlin, p. 225.

Jacchia, L.G. (1977). Smithsonian Astrophysical Observatory, Harvard MA, Special Report, p. 375.

Johnson, C.Y. (1966). *J. Geophys. Res.* **71**, 330.

Kella, D., Johnson, P.J., Pedersen, H.B., Vejby-Christensen, L., and Andersen, L.H. (1997). *Science* **276**, 1530.

Kharchenko, V., Balakrishnan, N., and Dalgarno, A. (1998). *J. Atmos. Solar Terr. Phys.* **60**, 95.

Kofsky, I.L., and Barrett, J.L. (1985). Proc. Second Workshop on Spacecraft Glow, NASA CP-2391, p. 155.

Kofsky, I.L., and Barrett, J.L. (1986). *Planet. Space Sci.* **34**, 665.

Krishna Kumar, C., Swaminathan, P.K., Anderson, D.E., Yee, J.-H., Gunsen, M.R., and Abrams, M.C. (1995). *J. Geophys. Res.* **100**, 16839.

Laganá, A., and Garcia, E. (1994). *J. Phys. Chem.* **98**, 502.

Lie-Svendsen, O., Rees, M.H., Stamnes, K., and Whipple, E.C. (1991). *Plane. Space Sci.* **39**, 929.

Matsumi, Y., Shamsuddin, S.M., Sato, Y., and Kawasaki, M. (1994). *J. Chem. Phys.* **101**, 9610.

Matsumi, Y., and Chowdhury, A.M.S. (1996). *J. Chem. Phys.* **104**, 7036.

McCoy, R.P. (1983). *J. Geophys. Res.* **88**, 3197.

Mende, S.B., and Swenson, G.R. (1985). Proc. Second Workshop on Spacecraft Glow, NASA CP-2391, p. 1.

Mende, S.B., Swenson, G.R., Clifton, K.S., Gause, R., Leger, L., and Garriott, O.K. (1986). *J. Spacecr. Rockets* **23**, 189.

Miura, N., Hashimoto, K., Takahashi, K., Taniguchi, N., and Matsumi, Y. (2002). *J. Chem. Phys.* **116**, 5551.

Nan, G., and Houston, P.L. (1992). *J. Chem. Phys.* **97**, 7865.

Oakes, D.B., Sonnenfroh, D.M., and Caledonia, G.E. (1994). *J. Geophys. Res.* **99**, 23249.

Orient, O.J., Chutjian, A., and Murad, E. (1990). *Phys. Rev. A* **41**, 4106.

Orient, O.J., Martus, K.E., Chutjian, A., and Murad, E. (1992). *Phys. Rev. A* **45**, 2998.

Park, J., Shafer, N., and Bersohn, R. (1989). *J. Chem. Phys.* **91**, 7861.

Rahbee, A., and Gibson, J.J. (1981). *J. Chem. Phys.* **74**, 5143.

Ramachandran, B., Balakrishnan, N., and Dalgarno, A. (2000). *Chem. Phys. Lett.* **332**, 562.

Ramachandran, B. (2002). Private communication.

Rawer, K., Bilitza, D., and Ramakrishna, S. (1978). *Rev. Geophys.* **16**, 177.

Richards, P.G., Hickey, M.P., and Torr, D.G. (1994). *Geophys. Res. Lett.* **21**, 657.

Roble, R.G., Ridley, E.C., and Dickinson, R.E. (1987). *J. Geophys. Res.* **92**, 8745.

Rohrbaugh, R.P., and Nisbet, J.S. (1973). *J. Geophys. Res.* **78**, 6768.

Rusch, D.W. (1973). *J. Geophys. Res.* **78**, 5676.

Sharma, R.D., Sun, Y., and Dalgarno, A. (1993). *Geophys. Res. Lett.* **20**, 2043.

Sharma, R.D., Kharchenko, V.A., Sun, Y., and Dalgarno, A. (1996). *J. Geophys. Res.* **101**, 275.

Sharma, R.D., Dothe, H., and Duff, J. (1998). *J. Geophys. Res.* **103**, 14753.

Shematovich, V.I., Bisikalo, D.V., and Gérard, J.C. (1991). *Geophys. Res. Lett.* **18**, 1691.

Shematovich, V.I., Gérard, J.C., Bisikalo, D.V., and Hubert, B.J. (1999). *J. Geophys. Res.* **104**, 4287.

Shizgal, B., and Blackmore, R. (1983). *Chem. Phys.* **77**, 417.

Shizgal, B., and Blackmore, R. (1986). *Planet. Space Sci.* **34**, 279.

Slanger, T.G. (1983). *Geophys. Res. Lett.* **10**, 130.

Solomon, S. (1983). *Planet. Space Sci.* **31**, 135.

Springsteen, L.L., Satyapal, S., Matsumi, Y., Dobeck, L.M., and Houston, P.L. (1993). *J. Chem. Phys.* **97**, 7239.

Stevens, M.H. (1995). *J. Geophys. Res.* **100**, 14735.

Streit, G.E., Howard, C.J., Schmeltekopf, A.L., Davidson, J.A., and Schiff, H.I. (1976). *J. Chem. Phys.* **65**, 4761.

Swaminathan, P.K., Strobel, D.F., Kupperman, D.G., Krishna Kumar, C., Acton, L., DeMajistre, R., Yee, J.-H., Paxton, L., Anderson, D.E., Strickland, D.J., and Duff, J.W. (1998). *J. Geophys. Res.* **103**, 11579.

Swenson, G.R., Mende, S.B., and Clifton, K.S. (1985a). *Geophys. Res. Lett.* **12**, 97.

Swenson, G.R., Mende, S.B., and Clifton, K.S. (1985b). *Proc. Second Workshop on Spacecraft Glow*, NASA CP-2391, p. 35.

Swenson, G.R., Mende, S.B., and Llewellyn, E.J. (1986). *Nature* **323**, 519.

Tachikawa, H., Hamabayashi, T., and Yoshida, H. (1995). *J. Phys. Chem.* **99**, 16630.

Tachikawa, H., Ohnishi, K., Hamabayashi, T., and Yoshida, H. (1997). *J. Phys. Chem.* **101**, 2229.

Taniguchi, N., Hirai, K., Takahashi, K., and Matsumi, Y. (2000). *J. Phys. Chem. A* **104**, 3894.

Thomas, R.J. (1978). *J. Geophys. Res.* **83**, 513.

Torr, M.R., Hays, P.P., Kennedy, B.C., and Walker, J.C.G. (1977). *Planet. Space Sci.* **25**, 173.

Torr, M.R., and Torr, D.G. (1982). *Rev. Geophys.* **20**, 91.

Tully, C.J. (1974). *J. Chem. Phys.* **61**, 61.

Upschulte, B.L., and Caledonia, G.E. (1992). *J. Chem. Phys.* **96**, 2025.

Upschulte, B.L., Oakes, D.B., Caledonia, G.E., and Blumberg, W.A.M. (1992). *Geophys. Res. Lett.* **19**, 993.

Viereck, R.A., Mende, S.B., Murad, E., Swenson, G.R., Pike, C.P., Culbertson, F.L., and Springer, R.C. (1992). *Geophys. Res. Lett.* **19**, 1219.

von Zahn, U., and Murad, E. (1986). *Nature* **321**, 147.

Wayne, R.P., (2000). ''Chemistry of Atmospheres.'' Oxford University Press, New York.

Whitson, M.E., Jr., Darnton, L.A., and McNeal, R.J. (1976). *Chem. Phys. Lett.* **74**, 552.

Winkler, I.C., Stachnik, R.A., Steinfeld, J.I., and Miller, S.M. (1986). *J. Chem. Phys.* **85**, 890.

Yee, J.-H., and Abreu, V.J. (1983). *Geophys. Res. Lett.* **10**, 126.

Yee, J.-H., Meriwether, J.W., and Hays, P.B. (1980). *J. Geophys. Res.* **85**, 3396.

Yee, J.-H., and Dalgarno, A. (1985). *Planet. Space Sci.* **33**, 825.

Yee, J.-H., and Dalgarno, A. (1986). *Planet. Space Sci.* **35**, 399.

Zahr, G.E., Preston, R.K., and Miller, W.H. (1975). *J. Chem. Phys.* **62**, 1127.

Zhou, D.K., Pendleton, W.R., Bingham, G.E., Steed, A.J., Nadile, R.M., and Sharma, R.D. (1992). *EOS Trans. AGU* **73**, 421.

Zipf, E.C., and McLaughlin, R.W. (1978). *Planet. Space Sci.* **26**, 449.

# Index

This page
intentionally
left blank

# CONTENTS OF VOLUMES IN THIS SERIAL